THERMOLYSIS OF MULTIPLY-METHYLATED ACENES:

EXPERIMENTS AND MECHANISTIC MODELLING

by

Vikki J. Vlastnik

B.S., Chemistry,
Illinois Benedictine College, 1986

M.S.C.E.P., Massachusetts Institute of Technology, 1988

Submitted to the Department of Chemical Engineering
in Partial Fulfillment of the Requirements
for the Degree of

Doctor of Philosophy

at the

Massachusetts Institute of Technology
September 1993

© Massachusetts Institute of Technology, 1993

Signature of Author_____
Department of Chemical Engineering
September 2, 1993

Certified by_____
Preetinder S. Virk
Associate Professor of Chemical Engineering
Thesis Supervisor

Accepted by_____
Robert E. Cohen
Chairman, Committee for Graduate Students

MASSACHUSETTS INSTITUTE
OF TECHNOLOGY

SEP 22 1993   V. |

LIBRARIES

Science

Thermolysis of Multiply-Methylated Acenes: Experiments and Mechanistic Modelling

Vikki J. Vlastnik

ABSTRACT

The thermolysis of multiply-methylated acenes, namely 9,10-dimethylanthracene (910DMA), 9-methylanthracene (9MA) and 1,4-dimethylnaphthalene (14DMN), was experimentally studied in batch reactors, volume $V = 0.6$ cm^3, at temperatures from 315-550°C with initial concentrations from 0.081-2.47 mol/l and fractional conversions 0.05 - 0.99. All gaseous and up to 40 liquid thermolysis products were assayed by GC and certain heavy products were also detected and identified by GC/MS. The experiments provided, for the first time, quantitative experimental information concerning multiply-methylated acene thermolysis kinetics and reaction pathways.

910DMA thermolysis kinetics were found, overall, to be 3/2 order in substrate with activation energy $\sim$ 45 kcal/mol and Arrhenius parameters, $[\log_{10} A, E^*/\theta]$ = $[11.1 \pm 0.08, 44.6 \pm 2.1]$. 9MA thermolysis kinetics were found, overall, to be 3/2 order in substrate with activation energy $\sim$ 40 kcal/mol and Arrhenius parameters, $[\log_{10} A, E^*/\theta]$ = $[9.2 \pm 0.15, 39.7 \pm 3.9]$. 14DMN thermolysis kinetics were found, overall, to be 2nd order in substrate with activation energy $\sim$ 42 kcal/mol and Arrhenius parameters, $[\log_{10} A, E^*/\theta]$ = $[7.9 \pm 0.14, 40.1 \pm 2.3]$.

Three primary parallel pathways were identified for the general case of thermolysis of an X methyl acene, where X is the number of methyl groups on the acene, namely: (P1) hydrogenation to dihydro X methyl acene, (P2) demethylation to (X-1) methyl acene, and (P3) methylation to (X+1) methyl acene. For the specific case of 910DMA substrate, this leads to (P1) Hydrogenation, to 9,10-dihydro-9,10-dimethylanthracene (DHDMA), (P2) Demethylation to 9-methylanthracene (9MA), and (P3) Methylation, to 1,9,10-trimethylanthracene (and other isomers, TMAs). This pathway triad secondarily operates upon the primary products, forming 9,10-dihydro-9-methylanthracene (DHMA), a host of dimethylanthracenes (1,9-, 1,10- 2,9- and 3,9-isomers), and anthracene (ANT), as well as minor amounts of 9,10-dihydroanthracene and 1- and 2-methylanthracenes (1MA, 2MA).

A free-radical mechanism was formulated for the early stages of multiply-methylated acene thermolysis. In the general case, initiation occurs by substrate disproportionation, to form dehydrogenated and hydrogenated radical species. Of these, a hydrogenated radical species propagates the reaction. It can either abstract hydrogen from substrate or undergo β-scission, controlling the pathway ratio P1/P2. The methyl radical formed by β-scission of the hydrogenated radical species can subsequently either abstract H from substrate or add to it, setting the pathway ratio P2/P3. Termination occurs by pure- and cross-combination of the dehydrogenated and hydrogenated radical

species. For the specific case of 910DMA substrate, the mechanism comprised 10 elementary steps, with HDMA* the propagating radical species. For 9MA substrate, the mechanism comprised 19 elementary steps with two hydrogenated radical species, HMA9* and HMA10*, of which only HMA10* propagated the decomposition. For 14DMN, the mechanism was analogous to 910DMA.

The preceding mechanism served as a platform for the quantitative numerical simulation and modelling of the multiply-methylated acene thermolysis kinetics and product selectivities. Thermochemical and kinetic parameters required for the model were derived from first principles and the system of stiff differential conservation relations comprising the model was numerically solved with an appropriate computer code. A sensitivity analysis was performed to estimate the inherent uncertainties in model predictions. An optimized model was finally developed to best-fit the experimental observations. At $T = 355°C$ with $[910DMA]_o = 0.82$ mol/l, the optimized model was able to match within a factor of 2 the observed substrate decay half-life, the product selectivities of 9MA, DHDMA, TMA and dimers, and the product ratios R[DHDMA/9MA] and R[TMA/9MA]. At $T = 370°C$ with $[9MA]_o = 0.82$ mol/l, the optimized model was able to match within a factor of 2 the observed substrate decay half-life, the product selectivities of ANT, DHMA, 910DMA and dimers, and the product ratios R[DHMA/ANT] and R[910DMA/ANT]. At $T = 450°C$ with $[14DMN]_o = 0.87$ mol/l, the optimized model was within a factor of 10 of the observed substrate decay half-life; it also provided the product selectivities of 1MN, TMN and dimers, and the product ratios R[TMN/1MN] within a factor of 3 of the experimental; the 14DMN model also predicted selectivities of DHDMN that were so low as to have been below experimental detection limits.

The relative amounts of minor methylated products formed during 910DMA and 9MA thermolyses were modelled as arising from periselective methyl radical attack on an arene ring position, governed by the single-centered FMO stabilization energy. The approach predicted the relative abundances of both dimethylanthracene isomers (2,9- + 3,9-)DMA/(1,9- + 1,10-)DMA and the minor methylanthracene isomers 2MA/1MA from both 910DMA and 9MA thermolysis. Relative abundances of addition dimethylanthracene isomers (2,9- + 3,9-)DMA/9,10-DMA and (1,9- + 1,10-)DMA/9,10-DMA were also available from 9MA thermolysis.

Finally, a 48-step extended model of 910DMA thermolysis was developed by combining the basic 10-step 910DMA and 19-step 9MA models and accounting for additional reactions between the species therein. Numerical solution of the extended model at $T = 370°C$ for $[910DMA]_o = 0.82$ mol/l showed it to predict decay half-life, major product selectivities, namely S(9MA), S(TMA), S(DHDMA), S(DHMA), S(HVY), S(CH4) and S(ANT), and major product ratios R[TMA/9MA], R[DHDMA/9MA], R[ANT/9MA] and R[DHMA/ANT] that were significantly closer to experimental observations than the corresponding prediction of these quantities by the basic 910DMA thermolysis model.

Thesis Supervisor: Preetinder S. Virk
Title: Associate Professor

ACKNOWLEDGEMENTS

DEDICATION

This thesis is dedicated to the one man
who has made the greatest impact on my life
and helped make me who I am today,
my father Jerry C. Vlastnik, Jr
(1937 - 1992).

TABLE OF CONTENTS

11

LIST OF FIGURES

15

16

17

19

21

24

27

29

31

32

LIST OF TABLES

37

Chapter 1.

Summary

1.1 Objective and Approach

The objective of this thesis is to delineate, experimentally and theoretically,

the reaction pathways that control the thermolysis of multiply-methylated acenes.

These substrates, specifically 9,10-dimethylanthracene (910DMA), 9-

methylanthracene (9MA) and 1,4-methylanthracene (14DMN), were chosen to mimic

the essential aromatic character as well as the electron-donating substituents of the

chemical moieties found in petroleum, wood and fuels. Understanding how the

thermal reaction pathways that operate during the thermolysis of fuel materials

contribute to the structure and toxicity of the products that are ultimately emitted

into the environment could help control these processes and reduce toxic emissions. The present investigation comprised three related aspects: 1) Chemical modelling, to select simple substrates that mimicked both the chemical moieties found in the original complex materials to be thermolyzed as well as subsidiary moieties that might arise from secondary reactions during thermolysis. 2) Thermolyses of the model substrates in batch reactors to experimentally establish the pathways available to them. 3) Theoretical interpretation of the thermolysis data, to devise chemical mechanisms for the observed pathways, and thence to develop quantitative models for numerical simulations of the experimental results.

This summary chapter will focus almost exclusively on the 910DMA substrate, as representative of the methods used in and results obtained from the present work.

1.2 Background

There appear to be no previous studies of 910DMA thermolysis in the literature, save for a preliminary investigation in our laboratories (Pope, 1987) that is elaborated here. The literature contains two earlier references to 9MA thermolysis (Pomerantz, 1980; Smith and Savage, 1993). There appear to be no previous reports on 14DMN thermolysis.

The literature does contain much material on the pyrolysis of aromatic and alkylaromatic molecules, of which studies relevant to the present work include the following. Schaefgen (1955), pyrolysis of *p*-xylene; Badger (1965), a systematic study

of the vapor phase pyrolytic behavior of a host of hydrocarbons; Klein (1980),

thermolyses of lignin models; Stein (1980), anthracene pyrolysis; Wornat (1988),

pyrolysis products of coal; Savage and Klein (1987, 1989), pyrolysis of long chain

alkyl benzenes; and Smith and Savage (1991 - 1993), pyrolysis of alkyl-substituted

polycyclic aromatic hydrocarbons.
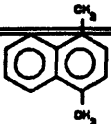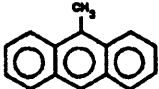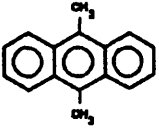
1.3 Experimental Procedures

Table 1.1 summarizes conditions for the experimental thermolyses, listing the

model substrates, their structures and ranges of temperatures, batch holding times

and initial concentrations studied, as well as the temperatures at which light gas

analyses were performed. Thermolyses were conducted in batch reactors, volume 0.6

ml, made from 1/4" stainless steel Swagelok parts. The reactors were charged with

weighed amounts of biphenyl (internal standard) and substrate (for example,

910DMA) totalling 0.30 g, sealed and placed in an isothermal, fluidized-sand bath

for the appropriate holding times, after which they were quenched in ice-water, and

their contents extracted into methylene chloride. Based on the melting and critical

properties of biphenyl and the substrates, reactor contents were in the liquid phase

during all experiments.

Liquid and gaseous thermolysis products were identified and analyzed by gas

chromatography and by gas chromatography/mass spectrometry. Figure 1.1 shows

the GCs from the 910DMA thermolysis gaseous and liquid products at 370°C for

Table 1.1

GRID FOR EXPERIMENTAL THERMOLYSES

Substrate[1]	Structure	Temperature Range (°C)	Holding Times (sec)	Concentration (moles/liter)	Light Gas Analysis
1,4-dimethyl-naphthalene		370-550	150-115200	0.081-2.07	450°C[2]
9-methyl-anthracene		315-409	450-57600	0.082-2.06	370°C
9,10-dimethyl-anthracene		315-409	450-57600	0.082-2.47	335&370°C

[1]   The chemicals used; 14DMN (Aldrich 95% purity), 9MA (Aldrich 98% purity), 910DMA (Aldrich 99% purity); biphenyl (Aldrich 99% purity) and methylene chloride (EM Science omnisolve), were all obtained commercially and used as received.

[2]   Detection only, not quantitative.

t = 1800 sec X = 0.1475

t = 7200 sec X = 0.4499

t = 28800 sec X = 0.8665
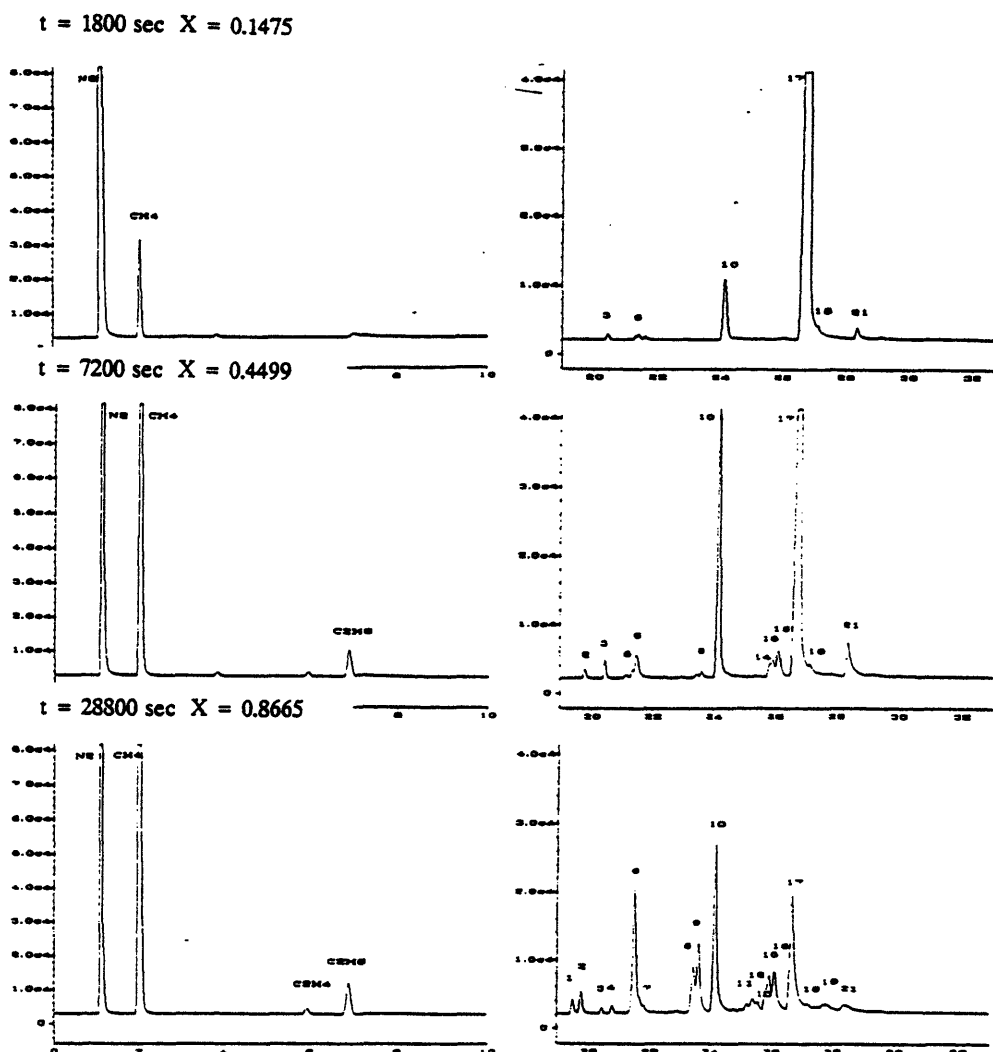
1 = 9,10-Dihydroanthracene (DHA)*	8 = 2-Methylanthracene (2MA)*
2 = Dihydro-methylanthracene (DHMA)	9 = 1-Methylanthracene (1MA)*
3 = cis-9,10-dihydro-9,10-dimethylanthracene (cDHDMA)*	10 = 9-Methylanthracene (9MA)*
4 = Unknown mass of 182 (UNK182)	11 = Dimethylanthracene (DMA)
5 = trans-9,10-dihydro-9,10-dimethylanthracene	12 = DMA
6 = Anthracene (ANT)*	13 = DMA
7 = DHDMA	14 = 2,9-&3,9-Dimethylanthracene

15 = 1,9-Dimethylanthracene (19DMA)
16 = 1,10-Dimethylanthracene (110DMA)
17 = 9,10-Dimethylanthracene (910DMA)*
18 = Trimethylanthracene (TMA)
19 = TMA
20 = TMA
21 = TMA

Figure 1.1: Gas chromatograms of 910DMA thermolysis gas (left) and liquid (right) products with identification of peaks from GC/MS.

each of three fractional substrate conversions of X = 0.15, 0.45 and 0.87. All gas peaks were identified by injections of standards. Liquid products that were identified by injections of standards are marked with an asterisk. All other peaks were identified by determining their mass on the GC/MS and correlating their retention time to times for known peaks.

Heavy thermolysis products, mostly dimers of the methylanthracenes and methylnaphthalenes, were analyzed and identified by GC/MS. For 910DMA, one large peak is detected at t ~ 29.5 min, with several smaller peaks in front of it, as shown in the upper panel of Figure 1.2. The fragmentation pattern and structure of the peak at 29.5 minutes are shown in the lower panel of Figure 1.2, the fragmentation pattern was deduced from the small molecular ion at 410 and large fragment peak at 205. The latter is indicative of the cleavage of an alkyl-substituted aromatic molecule at the bond beta to the ring, giving the resonance-stabilized benzylic ion. For this dimeric structure, the bond beta to both rings, as shown by the dotted lines on the structure, is the alkyl C-C bond, which yields a fragment of mass 205. The structures of the other dimers detected for the peaks at t = 28.1, 28.3 and 28.4 minutes are shown in Figure 1.2. Product array trains developed for each substrate using the preceding GC and GC/MS techniques typically accounted for ~ 15 reaction products. Identified products accounted for > 90% of the reacted mass at low substrate conversion, X < 0.4, and > 65% of the reacted mass at the highest conversions, X > 0.8.
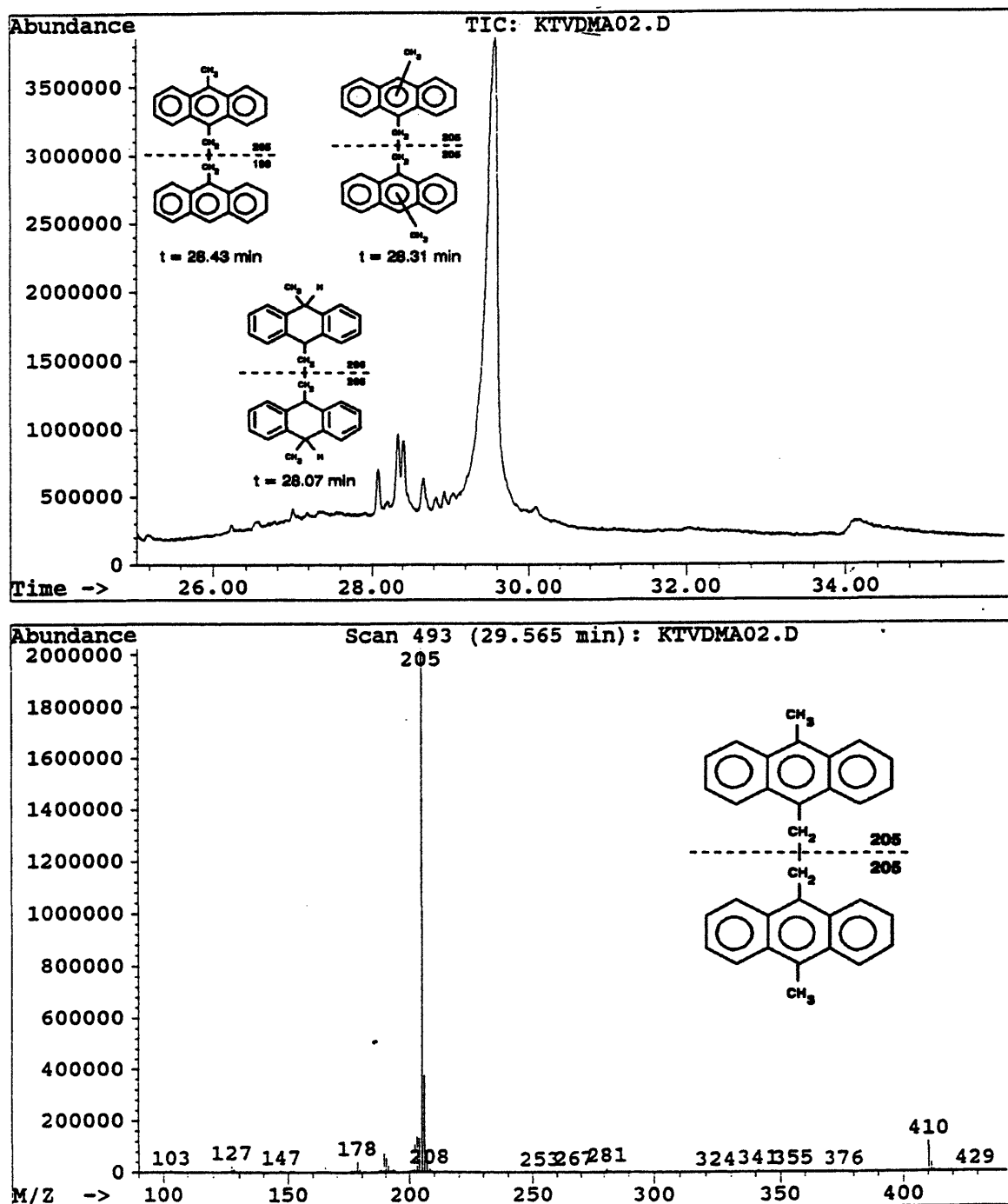
Figure 1.2: Gas chromatogram, fragmentation pattern and structure of heavy products in 910DMA thermolysis at t = 29.6 min and X = 0.24.

1.4 Thermolysis Experiments

1.4.1 A Representative Example

Figure 1.3 shows the histories of the major liquid and gaseous products (upper panel) and minor liquid products (lower panel) for 910DMA thermolysis at temperature $T = 370°C$ and initial concentration $[910DMA]_o = 0.82$ mol/l. The plot uses arithmetic coordinates of absolute substrate amounts J in the reactor in moles, versus reaction holding time t in seconds, with the appropriate, different, ordinal scales in the upper and lower panels; all data refer to fixed reactor volume $V = 0.60$ cm^3.

In the upper panel of Figure 1.3, the substrate 910DMA, symbol o, is seen to decay continuously from an initial $J = 4.9E-04$ moles to $J = 6.6E-05$ moles at $t = 28800$ s; the decay half-life is $t^* \sim 9900$ s. The principal product, 9-methylanthracene, abbreviated 9MA with symbol $\square$, increases from 0 initially to a maximum value $J = 1.3E-04$ moles at $t = 14400$ s and then decreases to $J = 7.8E-05$ moles at $t = 28800$ s. The sum of several trimethylanthracenes, abbreviated TMA with symbol $\triangle$, grow from 0 initially to $J = 2.3E-05$ moles at $t = 3000$ s, then maintains a plateau with shallow maximum $J = 2.9E-05$ moles at $t = 7200$ s, after which they decay slowly with increasing time to $J = 2.3E-05$ moles at $t = 28800$ s. Data labelled DHDMA, symbol •, represent the sum of four dihydrodimethylanthracene species actually detected, of which *cis*- and *trans*-9,10-dihydro-9,10-dimethylanthracenes are most abundant. The DHDMAs first appear

46
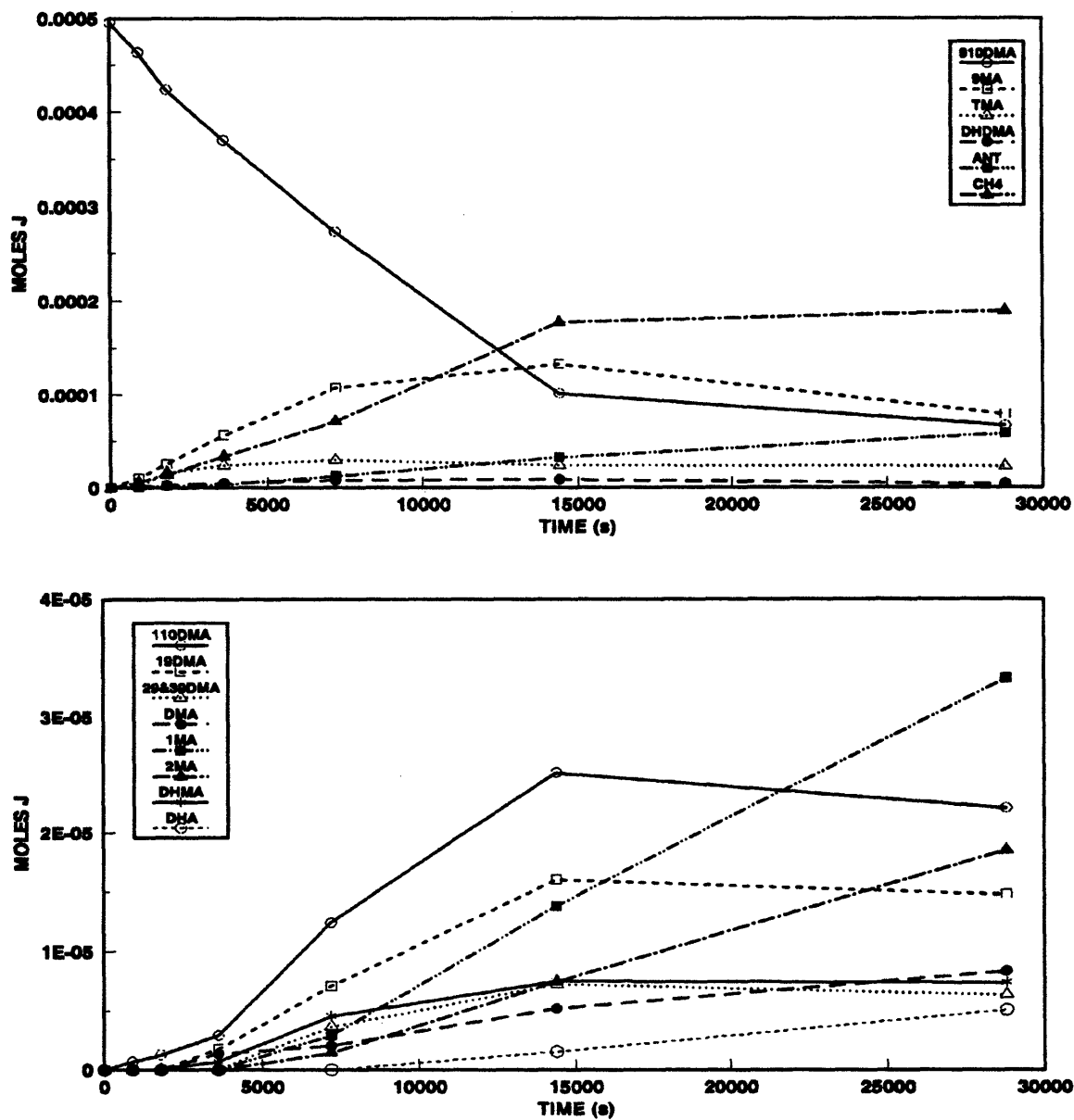
Figure 1.3: Product histories for 910DMA thermolysis at 370°C with [910DMA]$_0$ = 0.82 mol/l: major products (top) and minor products (bottom).

at t = 900 s with J = 1.9E-06 moles, reach a maximum value J = 8.4E-06 moles at

t = 14400 s and then slowly decay to J = 4.0E-06 moles at t = 28800 s. Anthracene,

abbreviated ANT with symbol ■, appears first at t = 900 s with J = 1.1E-05 moles,

and then rises monotonically with increasing reaction time to J = 5.8E-05 moles at

t = 28800 s. It should be noted here that *cis*-DHDMA and ANT eluted only 0.2 s

apart during GC analysis, leading to some uncertainties in their respective amounts

at the shortest times. The gaseous product methane, abbreviated CH4 with symbol

▲, increases monotonically from 0 initially to J = 1.8E-04 moles at t = 14400 s,

followed by a slight increase to J = 1.9E-04 moles at t = 28800 s; methane exceeds

the major liquid product 9MA for t > 10000 s. The substrate and major product

histories described above evidently depict a sequential reaction series A(910DMA)

→ B(9MA) → C(ANT).

The lower panel of Figure 1.3 shows the histories of several minor liquid

products that are formed during 910DMA thermolysis, including the 1,10-, 1,9-, and

2,9-&3,9-dimethylanthracene, and other dimethylanthracene isomers, the 1- and 2-

methylanthracene isomers, and the hydrogenated methylanthracene and anthracene

species. Of the dimethylanthracene isomers, in order of abundance, the 1,10-

dimethylanthracene, abbreviated 110DMA with symbol ○, first appears at t = 900 s

with J = 6.7E-07 moles, grows to a maximum J = 2.5E-05 moles at t = 14400 s, and

then decays slightly to J = 2.2E-05 moles at t = 28800 s. 1,9-dimethylanthracene,

abbreviated 19DMA with symbol ▢, first appears at t = 3600 s with J = 1.7E-06

moles, grows to a maximum J = 1.6E-05 moles at t = 14400 s, and then decays slightly to J = 1.5E-05 moles at t = 28800 s. 2,9&3,9-dimethylanthracenes, abbreviated 29&39DMA with symbol ▲, and other DMA isomers, abbreviated DMA with symbol •, also appear in small amounts. It is noteworthy that 110DMA appears at t ~ 900 s and 19DMA, 29&39DMA and other DMAs all appear at t ~ 3600 s, all subsequent to the appearance of 9MA at t < 900 s. 1-methylanthracene, abbreviated 1MA with symbol ■, and 2-methylanthracene, abbreviated 2MA with symbol ▲, respectively, appear at t = 7200 s and t = 14400 s with J = 2.9E-06 and 1.4E-06 moles, well after the first appearance of anthracene at t = 900 s. Both 1MA and 2MA grow monotonically with increasing time, to respectively, J = 3.3E-05 and J = 1.9E-05 moles at t = 28800 s, with 1MA the predominant of the two species. Finally, data labelled DHMA, symbol *, represent the sum of three dihydromethylanthracene species, of which one, likely 9,10-dihydromethylanthracene, is most abundant. The DHMAs first appear at t = 1800 s with J = 8.6E-08 moles, reach a maximum J ~ 7.5E-06 moles at t = 14000 to 28800 s. 9,10-dihydroanthracene, abbreviated DHA with symbol ○, first appears at t = 14400 s with J = 1.5E-06 moles, increasing to J = 5.1E-06 moles at t = 28800 s.

The data presented in Figure 1.3 are all displayed as selectivity diagrams in Figure 1.4, using ordinates of selectivity, S, defined as moles of product formed divided by moles of substrate 910DMA reacted, and an abscissae of substrate 910DMA fractional conversion, X. In the upper panel of Figure 1.4, the selectivity
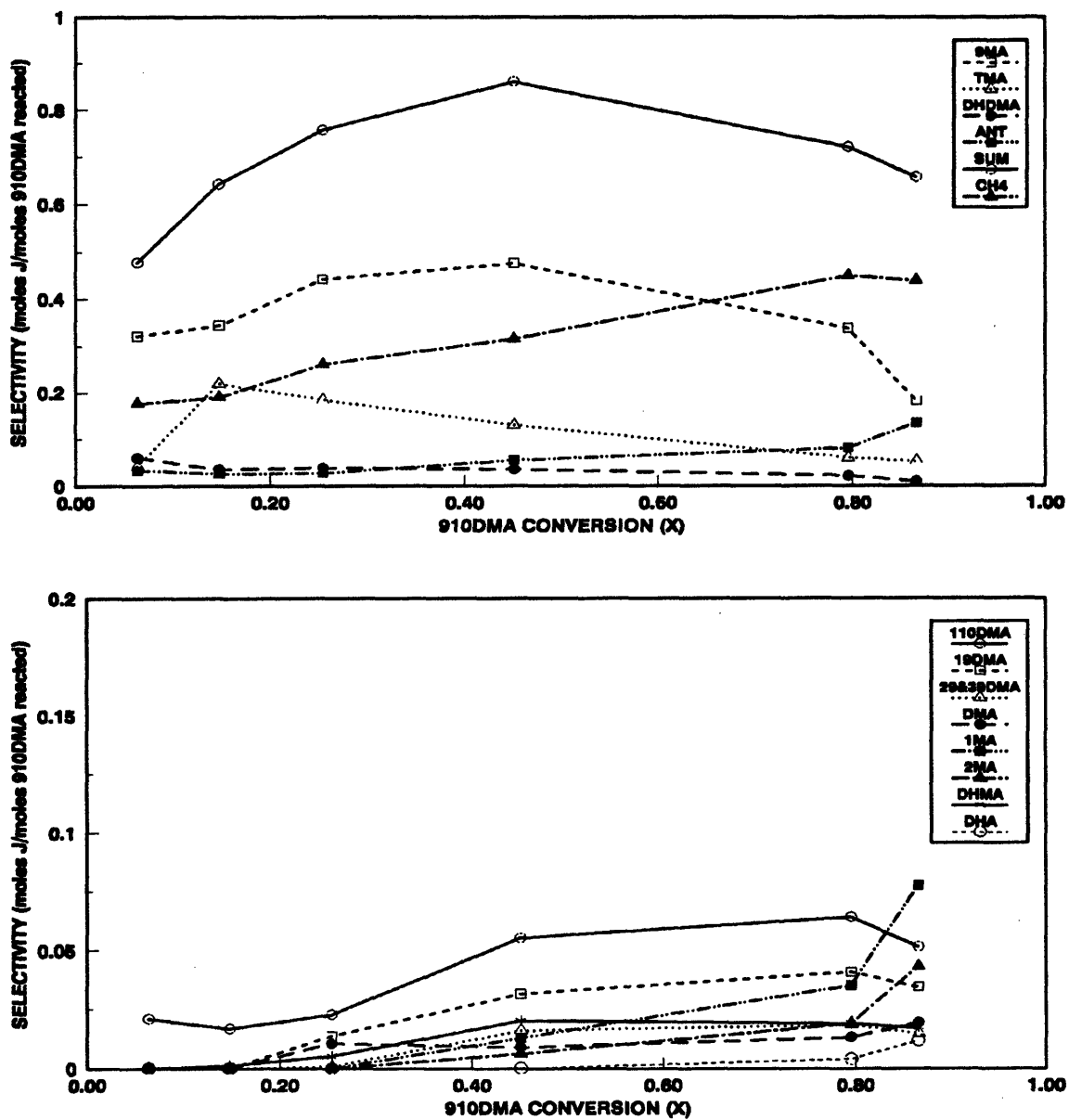
Figure 1.4: Selectivity diagram for 910DMA thermolysis at 370°C with [910DMA]$_o$ = 0.82 mol/l: major products (top) and minor products (bottom).

to 9MA, symbol □, is S ~ 0.33 at X = 0.06 and 0.15, then increases slowly to exhibit

a shallow maximum S = 0.48 at X = 0.45, before declining, at first slowly to S ~

0.34 at X = 0.80, then sharply to S = 0.19 at X = 0.87. Selectivity to TMA, symbol

△, is S = 0.042 at X = 0.06, increases sharply to S = 0.22 at X = 0.15, and then

declines steadily to S = 0.052 at X = 0.87. DHDMA, symbol •, exhibits its highest

S = 0.060 at the lowest X = 0.06, decreases to S = 0.030 ± 0.005 for 0.15 < X <

0.80 and then finally drops to S = 0.0093 at X = 0.87. ANT, symbol ■, appears with

S = 0.033 at X = 0.06, declines slightly to S = 0.027 at X = 0.25 and then increases

steadily to S = 0.082 at X = 0.8, after which it increases more steeply to S = 0.13

at X = 0.87. The selectivities of ANT at the low conversions, X < 0.20, are subject

to some analytical uncertainties, as noted in conjunction with Figure 1.3. The sum

of the selectivities of all identified products, Σ, abbreviated SUM with symbol ○,

increases from Σ = 0.48 at X = 0.06 to Σ = 0.86 at X = 0.45 and then declines

slightly to Σ = 0.66 at X = 0.87; over a wide range of 910DMA conversions, 0.2 <

X < 0.9, the selectivity sum is roughly constant, at Σ = 0.75 ± 0.08. The selectivity

to methane, symbol ▲, is S = 0.20 at X = 0.15 and 0.25, then increases slowly to S

= 0.45 at X = 0.80, and then remains roughly constant to X = 0.87.

In the bottom panel of Figure 1.4, selectivities of the dominant

dimethylanthracene isomers, 110DMA, symbol •, and 19DMA, symbol ■, both

increase monotonically, from S = 0.02 and 0, respectively, for X < 0.15 to S = 0.055

and 0.031 at X = 0.45, after which they exhibit a maximum S = 0.064 and 0.041 at

X = 0.80 before declining to S = 0.051 and 0.034 at X = 0.87. The small non-zero 110DMA selectivity seen at the lowest conversions likely arises from methylation of the 1% 9MA impurity present in the 910DMA substrate. The lesser dimethylanthracene isomers, 29&39DMA, symbol ▲, and other DMA selectivity, symbol •, obtain selectivities S ~ 0.015 for 0.3 < X < 0.8. The methylanthracene isomers 1MA, symbol ■, and 2MA, symbol ▲, start with S = 0.013 and 0.0062, respectively, at X = 0.45, rise slowly to S = 0.035 and 0.019 by X = 0.80, and then rise more quickly to S = 0.077 and 0.043 by X = 0.87. DHMA selectivity, symbol *, is S = 0.0012 at X = 0.15 and rises to S = 0.018 ± 0.002 for 0.45 < X < 0.87. DHA, symbol ○, appears first at X = 0.80 with S = 0.0038 and increases to S = 0.012 at X = 0.87.

The preceding selectivity diagrams show that 9MA, CH4, TMA and DHDMA, as well as ANT, are among the earliest products observed during 910DMA thermolysis. The pair of minor products 110DMA and 19DMA are observed after the appearance of 9MA, suggesting that they arose from methylation of 9MA, rather than from isomerization of the substrate 910DMA. Similarly, 1MA and 2MA are observed well after the appearance of ANT, suggesting that they likely arise from the methylation of ANT, rather than from isomerization of 9MA. The hydrogenated products DHMA and DHA both also arise subsequent to the appearance of their respective parents, 9MA and ANT.

1.4.2. Effect of Initial Concentration

In order to discuss its effects on reaction kinetics and product selectivities, the initial 910DMA concentration was varied in four steps from $[910DMA]_o$ = 0.082 to 2.47 mol/l at fixed reaction temperature T = 355°C.

Figure 1.5 shows substrate and product histories at T = 355°C and the lowest $[910DMA]_o$ = 0.082 mol/l. The data in Figure 1.5 are analogous to those shown for the representative example in Figure 1.3, but exhibit quantitative differences. The same major products, 9MA, TMA, DHDMA and ANT, appear in both cases (upper panels), but the substrate decay half-life t^* ~ 60000 s in Figure 1.5 appreciably exceeds t^* ~ 9900 s in Figure 1.3. The di- and mono-methylanthracene minor products (lower panels) seen in Figure 1.5 are the same as in Figure 1.3, but the latter also contains several minor products; namely 2MA, DHMA and DHA, not detected in the former.

Product selectivities derived from the data in Figure 1.5 are shown in Figure 1.6, using coordinates identical to the corresponding representative case, Figure 1.4. Among major products (upper panels), S(9MA) and S(DHDMA) are both higher, while S(TMA) is lower, in Figure 1.6 relative to Figure 1.4. Selectivity differences are also apparent among minor products (lower panels), with both S(110DMA) and S(19DMA) lower in Figure 1.6 than in Figure 1.4.

The observed influence of initial substrate concentration on reaction kinetics is summarized in Figure 1.7, a doubly logarithmic plot of t^* versus $[910DMA]_o$.
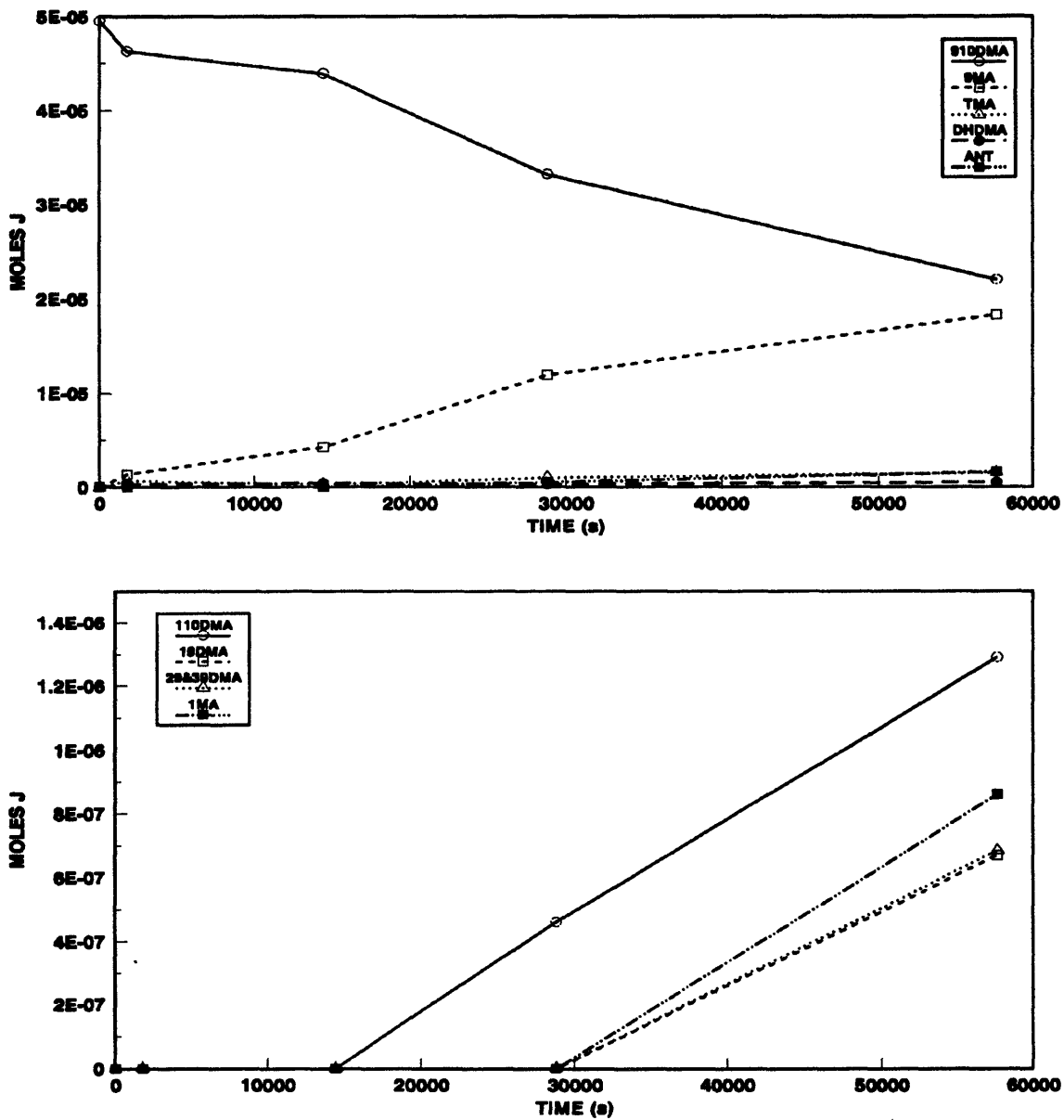
Figure 1.5: Products histories for 910DMA thermolysis at 355°C with [910DMA]$_o$ = 0.082 mol/l: major products (top) and minor products (bottom).
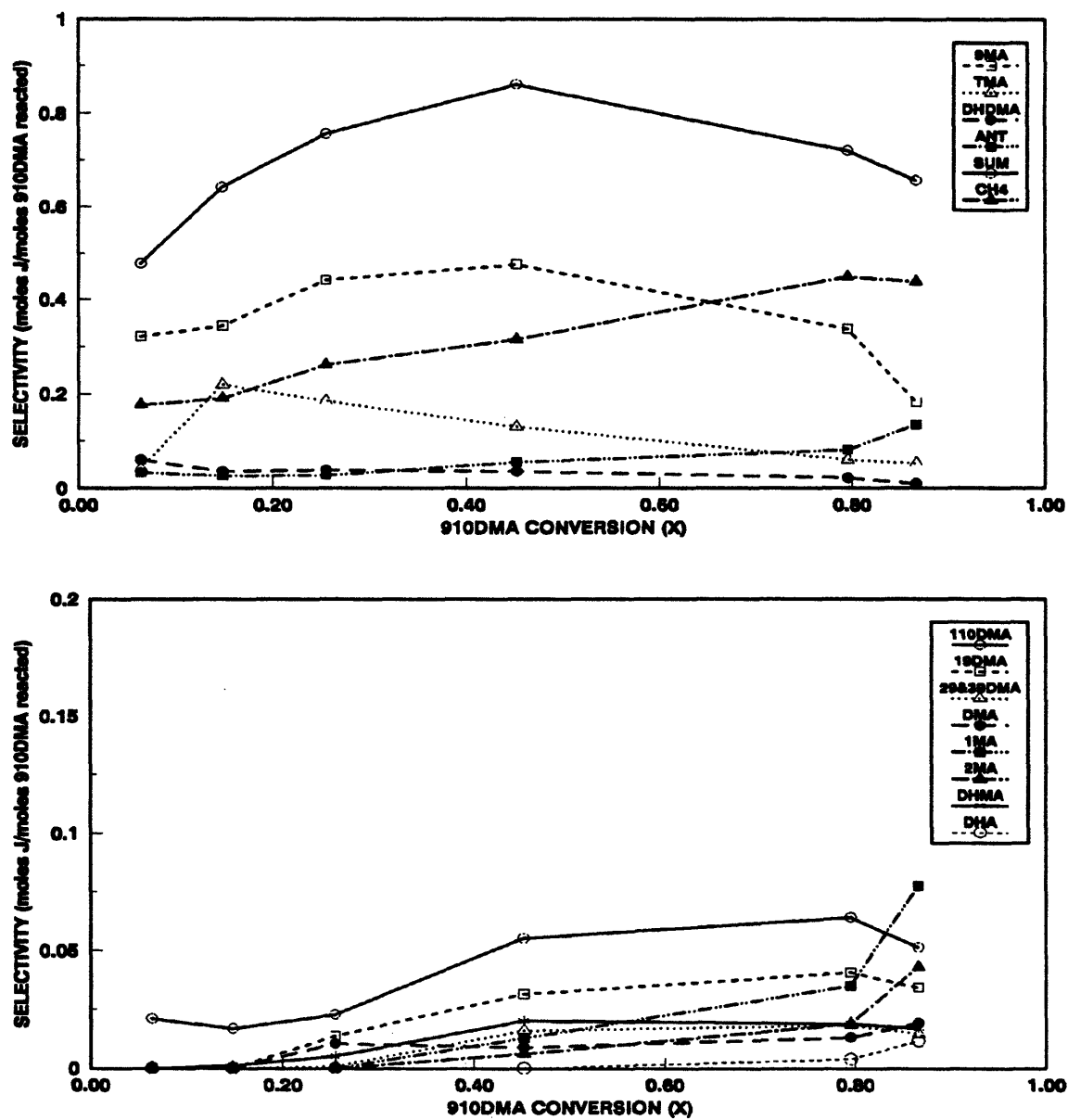
Figure 1.6: Selectivity diagrams for 910DMA thermolysis at 355°C with [910DMA]$_o$ = 0.082 mol/l: major products (top) and minor products (bottom).
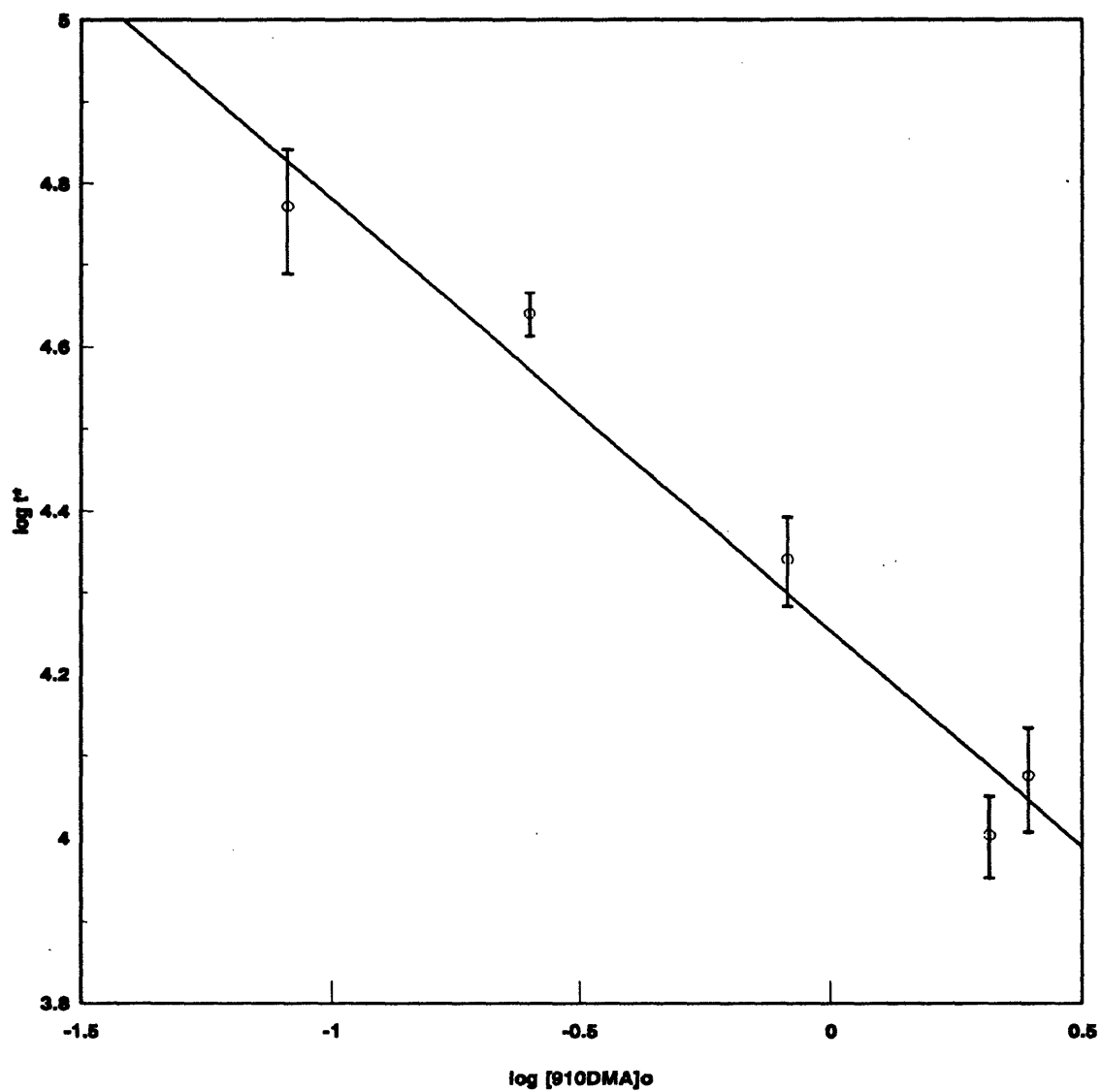
Figure 1.7: Decay half-life t^* for varying initial concentrations $[910DMA]_o$ at fixed $T = 355°C$.

Substrate decay half-life t^* decreased about 5-fold, from 59000 to 12000 s, as initial concentration $[910DMA]_o$ increased 30-fold, from 0.082 to 2.47 mol/l. The associated best-fit line shown in Figure 1.7 has a slope $\sim$ -1/2, which implies that 910DMA decomposition is 3/2 order in substrate; the intercept of this line also provides the 3/2 order rate constant at T = 355°C, namely k_1 = -4.34.

Table 1.2 summarizes the observed effect of initial 910DMA concentration on product selectivities. Part (a) shows that increasing $[910DMA]_o$ from 0.082 to 2.47 mol/l causes S(9MA) to decrease slightly from 0.65 to 0.45, and S(TMA) to increase appreciably from 0.04 to 0.16 at conversions 0.1 < X < 0.8. Part (b) shows that S(DHDMA) is essentially independent of $[910DMA]_o$ at a given conversion, despite decreasing greatly with increasing conversion, from S $\sim$ 0.08 at X = 0.06 to S $\sim$ 0.02 at X = 0.56. Part (c) shows that S(ANT) $\sim$ 0.055 is also essentially independent of $[910DMA]_o$ at fixed X = 0.56. Subtle variations of minor-product selectivities are also visible in parts (b) and (c) of Table 1.2.

1.4.3 Effect of Temperature

To study activation effects during 910DMA decomposition, reaction temperature was varied from T = 315 to 409°C at a fixed initial concentration of $[910DMA]_o$ = 0.82 mol/l in five steps.

Figure 1.8 shows substrate and product histories for $[910DMA]_o$ = 0.82 mol/l at the highest T = 409°C. The differences between Figure 1.8 and the representative

Table 1.2

EFFECT OF INITIAL 910DMA CONCENTRATION ON PRODUCT SELECTIVITIES AT T = 355°C

Part	Selectivity S of:	Conversion X Range:	[910DMA]$_o$ (mol/l)				
			0.082	0.25	0.82	2.06	2.47
a	9MA	0.1 - 0.8	0.65	0.51	0.48	0.46	0.45
	TMA	0.1 - 0.8	0.04	0.07	0.11	0.12	0.16
b	DHDMA	0.06 ± 0.02	0.089	0.078	0.076	0.081	0.076
		0.56 ± 0.02	0.017	0.003	0.012	0.019	0.024
	DHMA	0.56 ± 0.02	ND	ND	0.009	0.018	0.021
	DHA	0.8	ND	ND	ND	0.007	0.005
c	ANT	0.56 ± 0.02	0.057	0.051	0.054	0.055	0.051
	1MA	0.56 ± 0.02	0.030	0.013	0.015	0.023	0.020
	2MA	0.56 ± 0.02	ND	0.006	0.007	0.007	0.008
	110DMA	0.56 ± 0.02	0.045	0.054	0.061	0.076	0.064
	19DMA	0.56 ± 0.02	0.024	0.032	0.036	0.056[1]	0.059[1]
	29&39DMA	0.56 ± 0.02	0.024	0.027	0.030		
	DMA	0.56 ± 0.02	ND	ND	0.009	0.014	0.011

[1] Selectivity for 19DMA & 29&39DMA combined; these peaks are not resolvable on GC for [910DMA]$_o$ = 2.07 and 2.47 mol/l

Figure 1.8: Product histories for 910DMA thermolysis at 409°C with [910DMA]$_o$ = 0.82 mol/l: major products (top) and minor products (bottom).

Figure 1.3 reveal the effect of increasing temperature. In the respective upper panels of these figures, the substrate decay half-life decreases seven-fold to $t^* \sim 1300$ s from $t^* \sim 9900$ s. The same major products are seen in both figures but their proportions and behavior differ. In Figure 1.8, 9MA exhibits a sharp maximum at $t \sim 2000$ s and then decreases almost to zero by the longest time $t \sim 20000$ s; this contrasts with the shallow maximum exhibited at the longest time by 9MA in time Figure 1.3. Too, the amounts of DHDMA are much lower, and those of ANT far higher, in Figure 1.8; relative to Figure 1.3. Minor product amounts (lower panels) in both figures also differ. The dimethylanthracene isomers show more pronounced maxima and in some cases greater amounts at the higher temperature; methylanthracene isomer amounts are also significantly higher and among hydrogenated species, DHMA amounts are lower while DHA amounts are much higher.

Product selectivities derived from Figure 1.8 are shown in Figure 1.9, for comparison with the corresponding representative case, Figure 1.4. Both the upper and lower panels of Figure 1.9 differ from those in Figure 1.4 in the manner enunciated in the previous paragraph. A noteworthy aspect is the sharp decline in S(9MA) for X > 0.90 and the corresponding increase in S(ANT); these reflect the increasing extent of secondary reactions at the higher conversions.

The observed influence of temperature on reaction kinetics is summarized in Figure 1.10, a semi-log plot using Arrhenius-related coordinates of log t^* vs. $1/\theta$, where $\theta = 4.573 \times 10^{-3} T$ in Kelvins. Substrate decay half-life t^* decreased about 230-
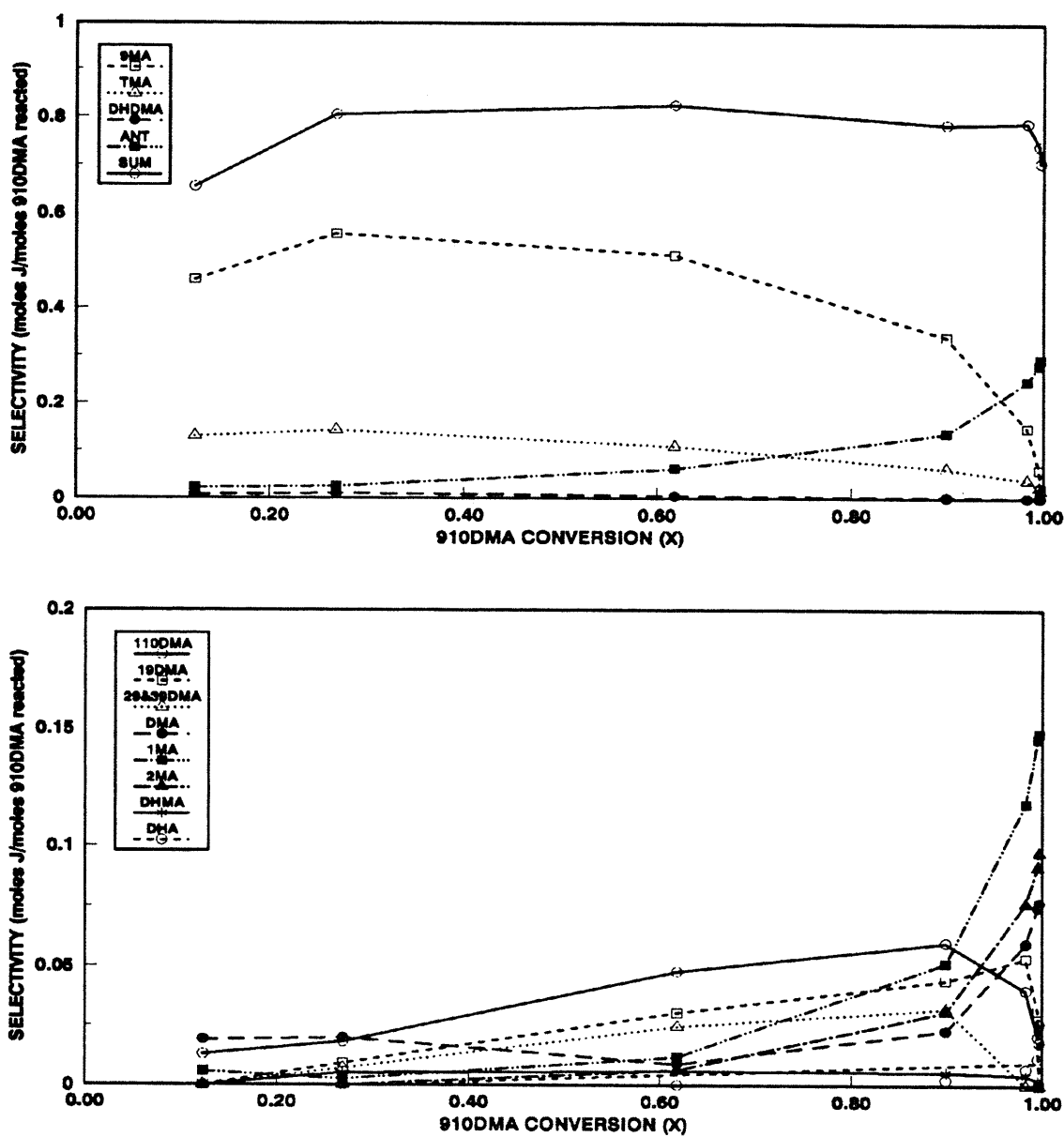
Figure 1.9: Selectivity diagrams for 910DMA thermolysis at 409°C with [910DMA]$_o$ = 0.82 mol/l: major products (top) and minor products (bottom).

61
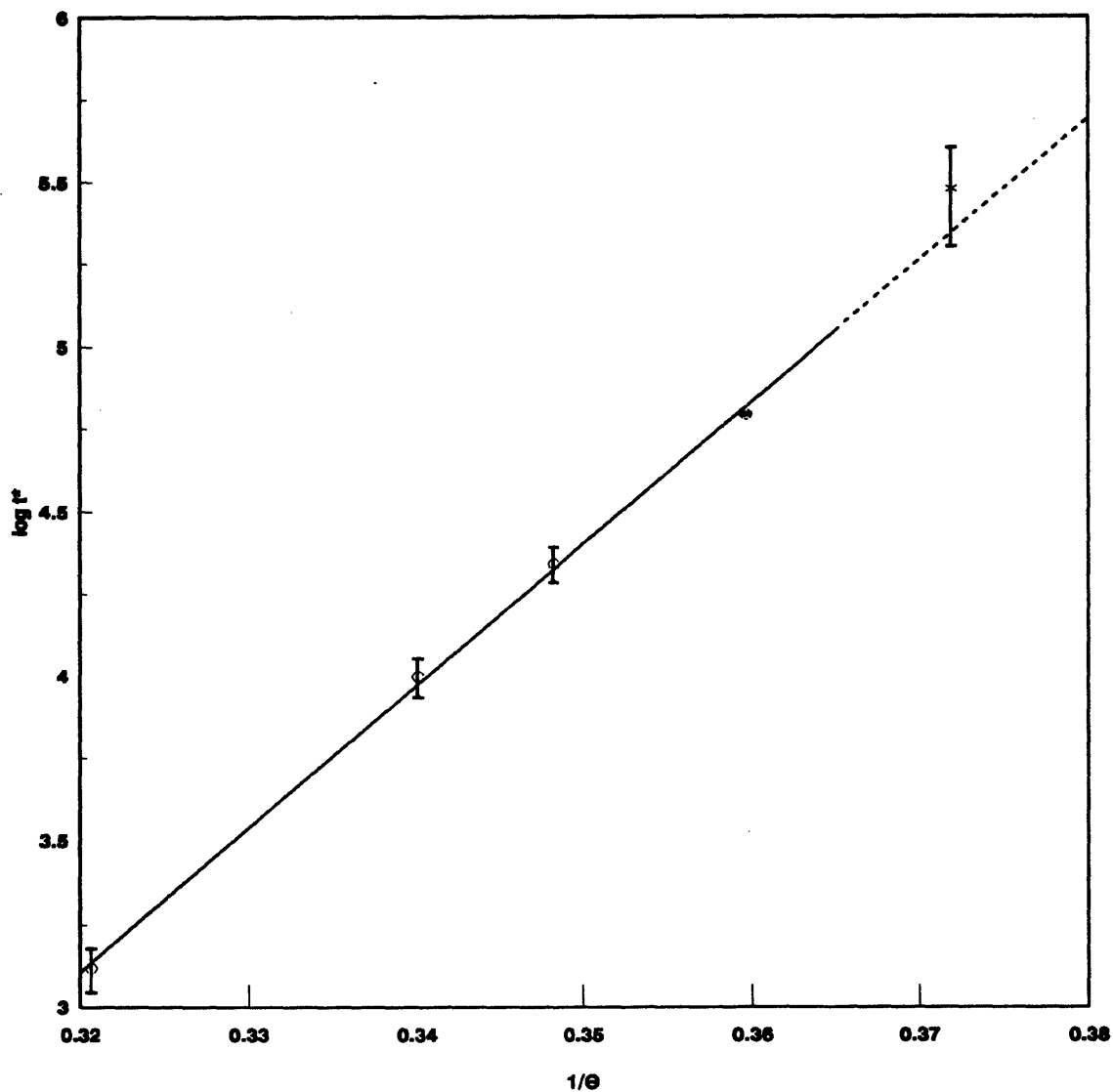
Figure 1.10: Decay half-life t^* for varying temperatures with fixed $[910DMA]_o$ = 0.82 mol/l.

fold, from 300000 to 1300 s, as reaction temperature T increased ~ 100°C, from 315 to 409°C. The best-fit line shown in Figure 1.10 has slope 43.1, which is the activation energy in kcal/mol of the overall reaction; also, for 3/2 order decomposition, the intercept of the line provides a pre-exponential factor of -10.7. Thus 910DMA thermolysis is 3/2 order in substrate with Arrhenius parameters $(\log_{10} A, E^*)$ ≈ (10.6 ± 0.03, 43.1 ± 1.0).

The observed effect of reaction temperature on product selectivities is summarized in Table 1.3. Part (a) shows that increasing T from 315 to 409°C had little effect on either S(9MA) ~ 0.48 of S(TMA) ~ 0.12, each of which remained relatively constant at conversions 0.1 < X < 0.8. Part (b) shows that S(DHDMA) ~ 0.05 was roughly independent of T at low conversion, X = 0.06, but decreased from S(DHDMA) ~ 0.02 at T = 335°C to S(DHDMA) ~ 0.004 at T = 409°C at higher conversion of X = 0.56. Part (c) shows that at fixed X = 0.56, S(ANT) increased with increasing T, from S(ANT) = 0.03 at T = 355°C to S(ANT) = 0.06 at T = 409°C. Minor product selectivity variations with temperature (and conversion) are also available in parts (b) and (c) of Table 1.3.

1.5 Kinetics

1.5.1 Overall Reaction Order

Decay half-life data for 910DMA substrate led to the approximate 3/2 order of decomposition and the approximate Arrhenius parameters $(\log_{10} A, E^*)$ ~ (10.7,

Table 1.3

EFFECT OF TEMPERATURE ON PRODUCT SELECTIVITIES FOR $[910DMA]_0$ = 0.82 mol/l

Part	Selectivity S of:	Conversion X Range:	Temperature (°C) 315[1]	335[2]	355	370	409
a	9MA	0.1 - 0.8	0.52	0.43	0.47	0.42	0.45
	TMA	0.1 - 0.8	0.20	0.12	0.11	0.11	0.11
b	DHDMA	0.06	0.053	0.041	0.048	0.060	0.007[3]
		0.56 ± 0.02	0.049	0.019	0.012	0.011	0.004
	DHMA	0.56 ± 0.02	0.017	0.011	0.009	0.008	0.006
	DHA	0.95	ND	ND	0.001[4]	0.010	0.010
c	ANT	0.56 ± 0.02	0.034	0.033	0.054	0.055	0.061
	1MA	0.56 ± 0.02	ND	0.007	0.015	0.013	0.012
	2MA	0.56 ± 0.02	ND	0.003	0.007	0.006	0.006
	110DMA	0.56 ± 0.02	0.035	0.054	0.061	0.055	0.048
		0.85 ± 0.05				0.064	0.060
		0.91 ± 0.05				0.051	0.040
	19DMA	0.56 ± 0.02	0.006	0.024	0.036	0.031	0.030
		0.85 ± 0.05				0.041	0.044
		0.91 ± 0.05				0.034	0.031
	29&39DMA	0.56 ± 0.02	ND	0.016	0.031	0.030	0.024
		0.85 ± 0.05				0.035	0.032
		0.91 ± 0.05				0.008	0
	DMA	0.56 ± 0.02	0.022	0.009	0.009	0.012	0.015
		0.91 ± 0.05				0.039	0.069

[1] For T = 315°C, all data at X = 0.10 except DHDMA at X = 0.06

[2] For T = 335°C, all data at X = 0.46 except DHDMA at X = 0.06

[3] This point at X = 0.12, the lowest conversion at T = 409°C

[4] This point at X = 0.68, the highest conversion at T = 355°C

43.1). True rate constants, $k_{3/2}$, were also derived from the 3/2 order rate expression:

$$r \left(\frac{mol}{l \ s}\right) = k_{3/2}[910DMA]^{3/2} \tag{1.1}$$

which, integrated with respect to time, reads:

$$\frac{1}{[910DMA]_t^{1/2}} - \frac{1}{[910DMA]_o^{1/2}} = \frac{k_{3/2}t}{2} \tag{1.2}$$

A plot of $1/[910DMA]_t^{1/2}$ versus time should therefore be linear, with slope $k_{3/2}/2$ and intercept $1/[910DMA]_o^{1/2}$. Figure 1.11 shows all the present data for 910DMA thermolysis at fixed T = 355°C on coordinates of $1/[910DMA]^{1/2}$ versus t along with the best-fit lines resulting from regression of the low conversion data, X < 0.4, for each $[910DMA]_o$. The light dashed-dotted diagonal line in the figure represents the locus of times and concentrations at which X = 0.4. The best-fit regressed lines are roughly parallel to one another, with slopes, that is $(k_{3/2}/2)$ = [1.70E-05, 1.53E-05, 1.66E-05, 2.49E-05, 1.86E-05] for $[910DMA]_o$ = [0.082, 0.25, 0.82, 2.06, 2.47 mol/l] respectively. The individual slopes vary by less than a factor of 2 over a 30-fold range of initial concentrations, affirming the validity of the chosen 3/2 order.

1.5.2 Activation Parameters

True 3/2 order rate constants were also derived from all 910DMA thermolyses for fixed $[910DMA]_o$ = 0.82 mol/l at varying temperatures 315 < T <
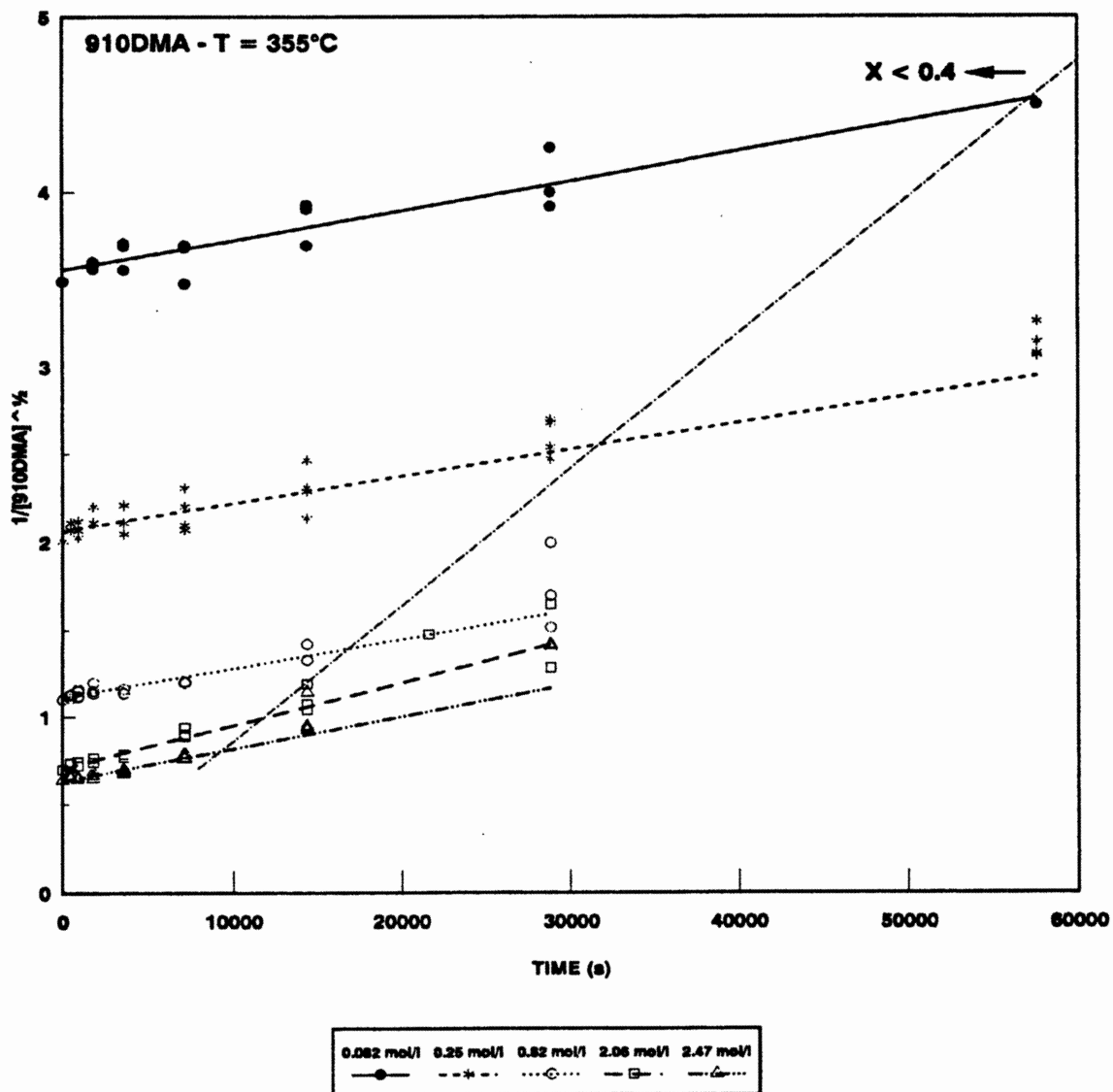
Figure 1.11: 3/2 order plot, $1/[910DMA]_t^{1/2}$ vs. t, for 910DMA thermolysis with varying $[910DMA]_o$ at fixed T = 355°C.

409°C; regressions were restricted to low conversions, X < 0.4.

The variation of rate constants $k_{3/2}$ with temperature shown in Figure 1.12, using Arrhenius coordinates of $\log_{10} k$ versus $1/\theta$, where $\theta = 4.573 \times 10^{-3}$ T in Kelvins; on these coordinates, an Arrhenius relation of form:

$$\log_{10} k = \log_{10} A - \frac{E^*}{\theta} \qquad (1.3)$$

is described by a straight line of slope equal to activation energy E^* in kcal/mol and intercept $\log_{10} A$, where the pre-exponential factor A has units of the rate constant. In the figure, the hollow circles represent twice the slope of the integrated 3/2 rate expression versus time while the error bars are the standard errors of these slopes. The best-fit Arrhenius parameters for $k_{3/2}$ are [$\log_{10} A$ ($l^{\frac{1}{2}}/mol^{\frac{1}{2}}$ s), E^* (kcal/mol)] = [11.1 ± 0.08, 44.6 ± 2.1]. These compare favorably with the approximate Arrhenius parameters derived from decay half-lifes.

1.6 Reaction Pathways

910DMA thermolysis pathways deduced from the present experiments are summarized in Figure 1.13 and Figure 1.14. As shown in Figure 1.13, three primary pathways operate in parallel upon the original 910DMA substrate, namely: (P1) hydrogenation to *cis*- and *trans*-9,10-dihydro-9,10-dimethylanthracene, (P2) demethylation to 9-methylanthracene, and (P3) methylation to 1,9,10-trimethylanthracene and other TMA isomers. The main demethylation sequence,

67
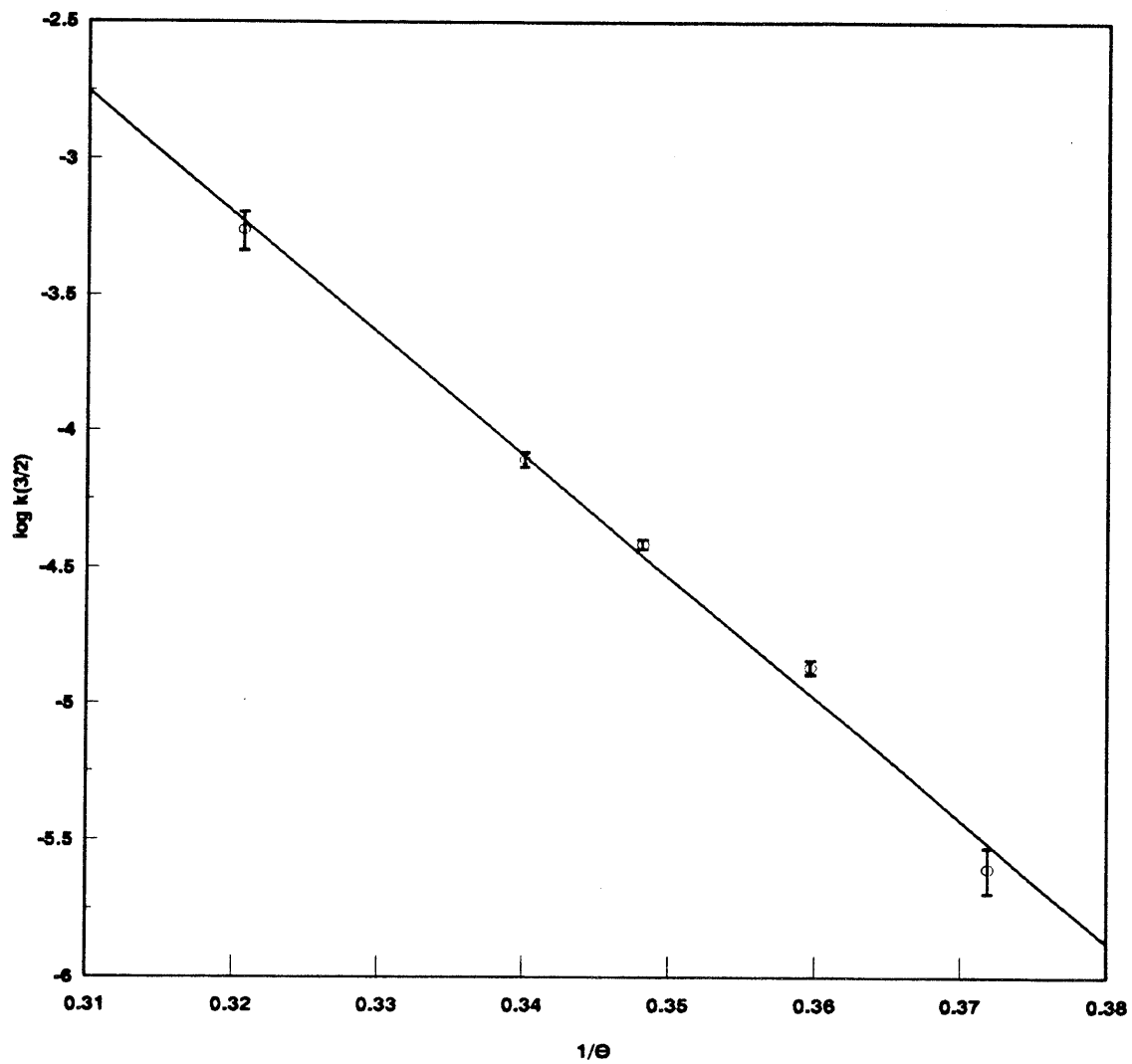
Figure 1.12: Arrhenius plot of $k_{3/2}$ derived for low conversions, $X < 0.4$, with $[910DMA]_o = 0.82$ mol/l at all temperatures $315 < T < 409°C$.
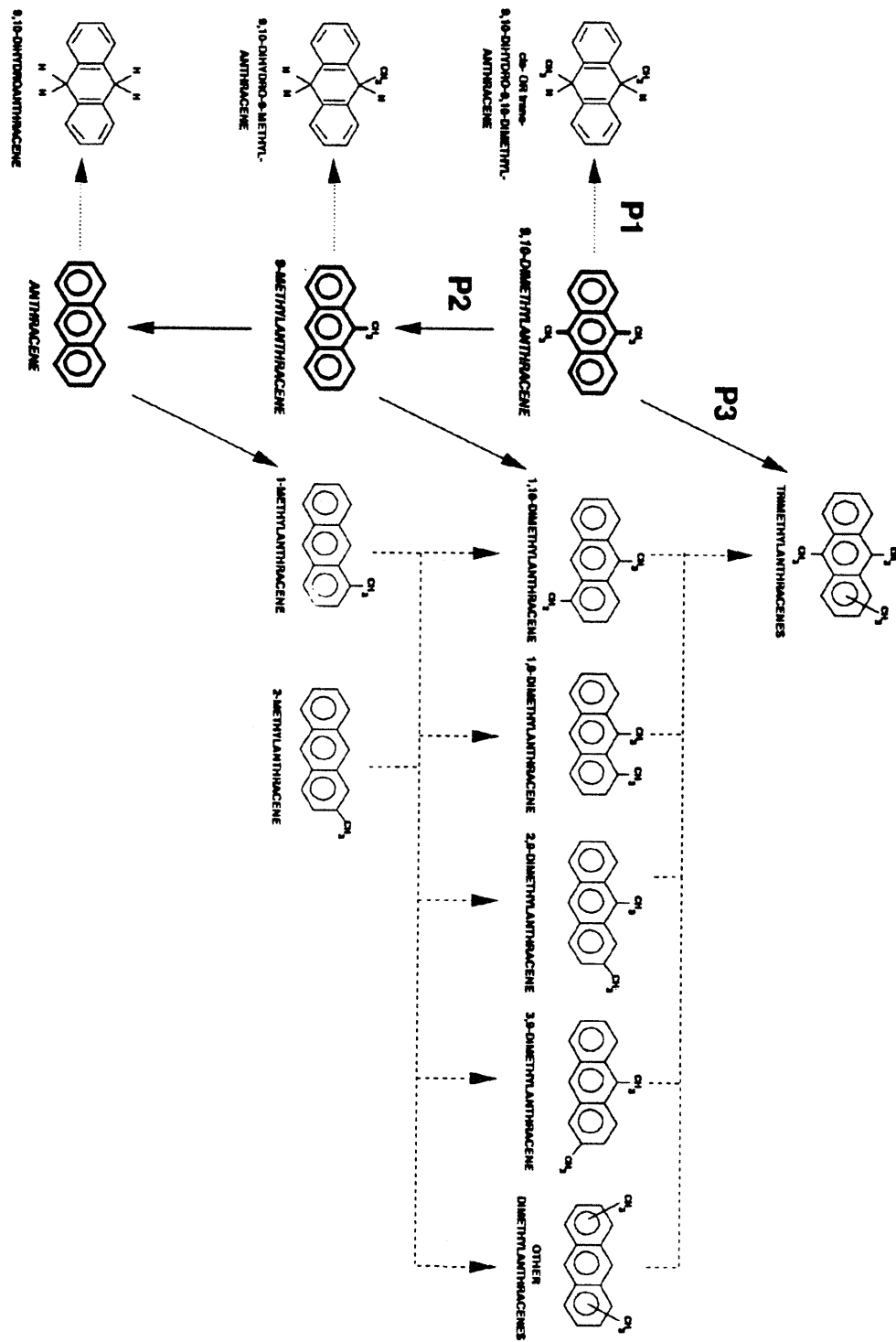
Figure 1.13: 910DMA primary decomposition pathways.
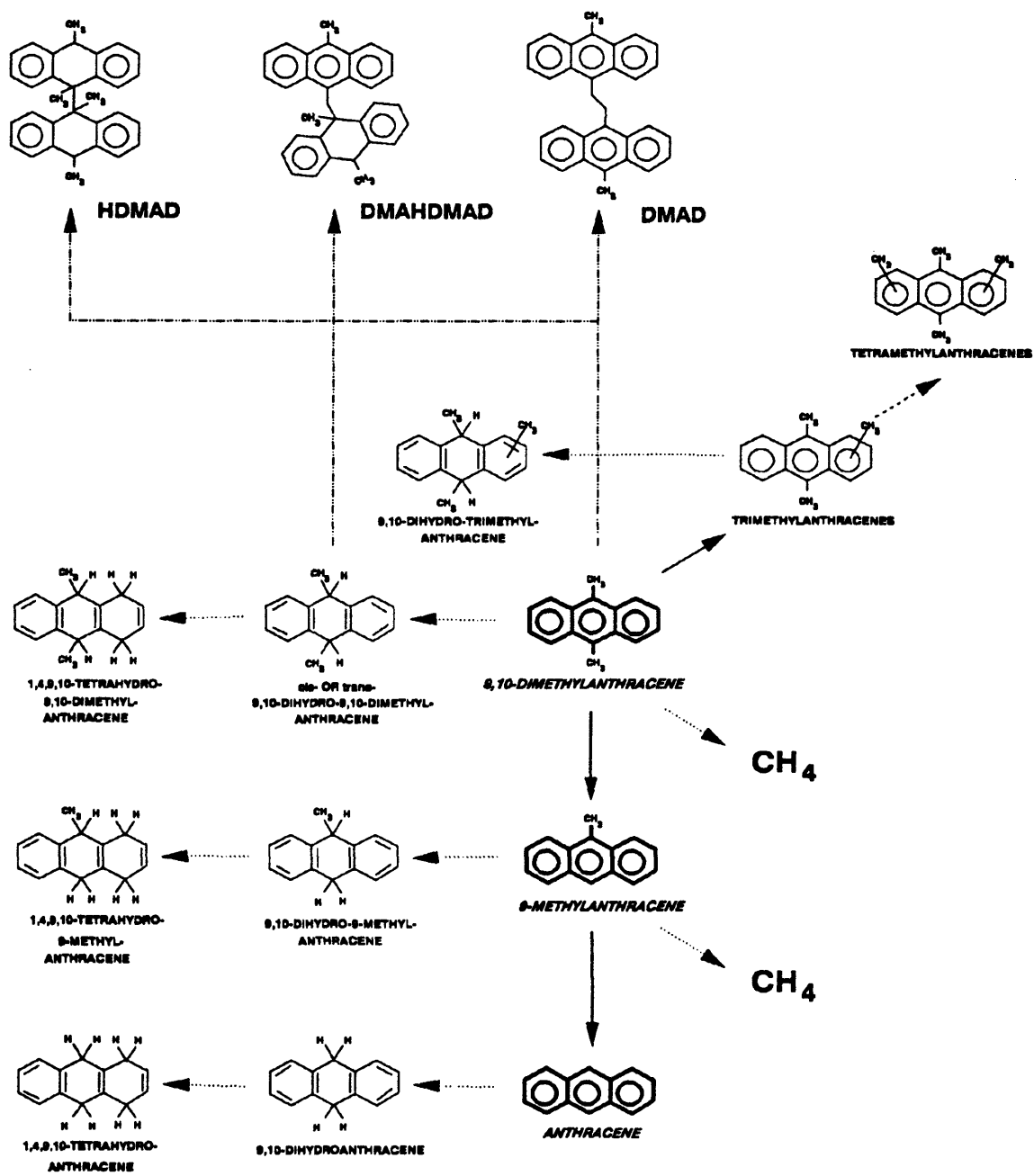
Figure 1.14: 910DMA secondary decomposition pathways.

shown bold, cascades from 910DMA to 9MA to ANT. The primary demethylation

product 9MA is secondarily operated upon by a pathway triad analogous to the

preceding primary triad, eventually forming 9,10-dihydro-9-methylanthracene, a host

of dimethylanthracenes (1,9-, 1,10-, 2,9-&3,9- and others) and anthracene. And at

the highest substrate conversions, even the terminal demethylation product ANT

suffers hydrogenation and methylation, as witnessed by the appearance of the minor

products DHA, 1MA and 2MA. Neither 910DMA nor 9MA isomerize to their

positional isomers, since the latter (methylated) species do not arise prior to the

appearance of their demethylated precursor, with 1,9-, 1,10- and other DMAs arising

only after 9MA, while 1MA and 2MA arise after ANT.

Figure 1.14 summarizes secondary and termination pathways. The main

demethylation sequence is shown again in bold. The primary demethylation product

of 910DMA, 9MA, is associated with methane gas. The primary methylation product

of 910DMA, TMA, is secondarily operated upon by a pathway triad analogous to the

primary triads, forming dihydrotrimethylanthracenes (not shown) and

tetramethylanthracenes. Hydrogenated products formed by the primary product

triads acting upon 910DMA, 9MA and ANT are further hydrogenated to yield

tetrahydrogenated products (far left). Termination products (top) include both pure-

and cross-termination species related to 910DMA and DHDMA.

The relative importance of primary pathways (P1 - P3) in Figure 1.13 is shown

in Figure 1.15, Figure 1.16 and Figure 1.17, which depict the variation of certain

71
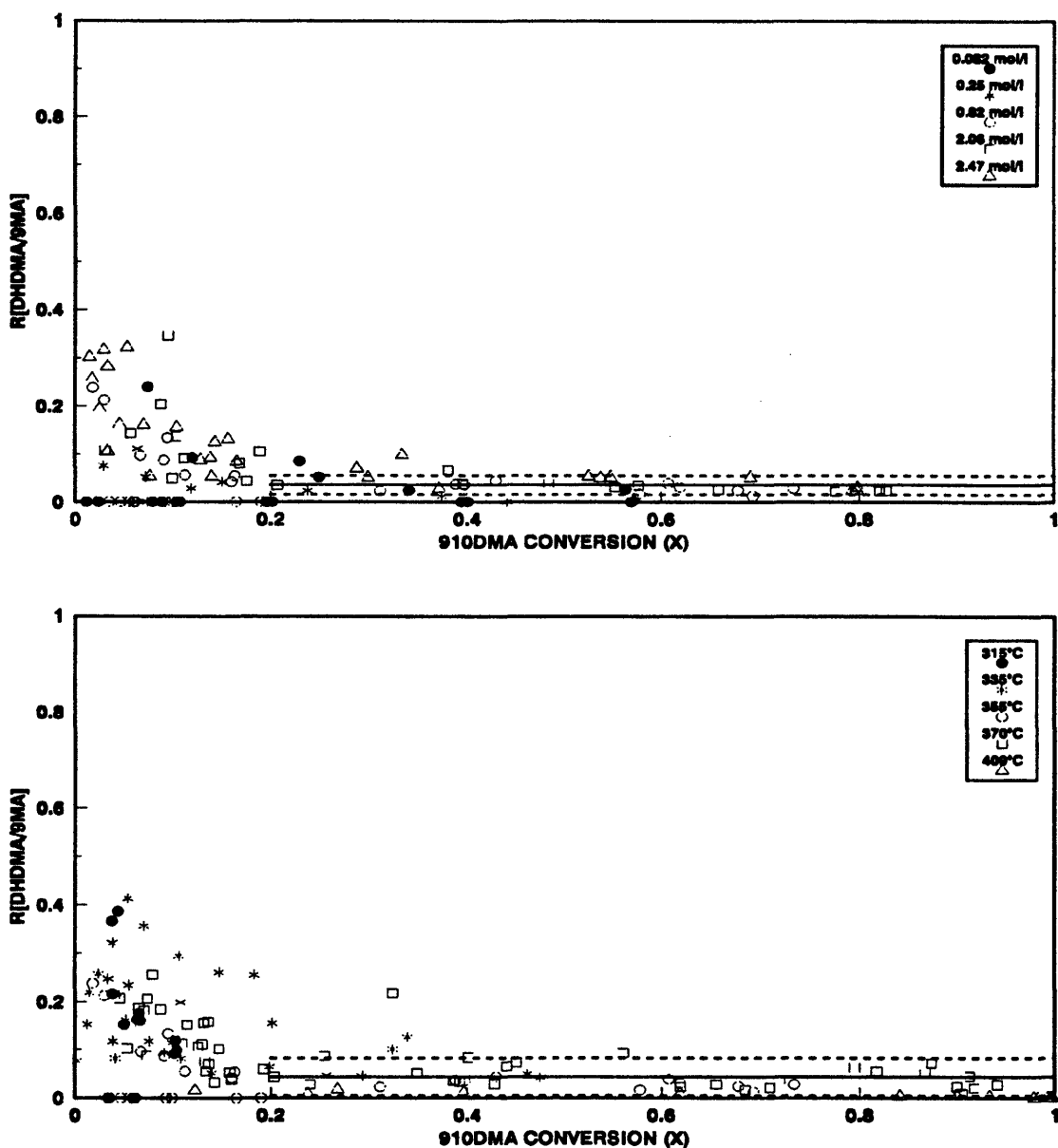
Figure 1.15: Ratio moles DHDMA to moles 9MA produced vs. 910DMA conversion (X) for varying $[910DMA]_o$ at T = 355°C (top) and for varying T with $[910DMA]_o$ = 0.82 mol/l (bottom).
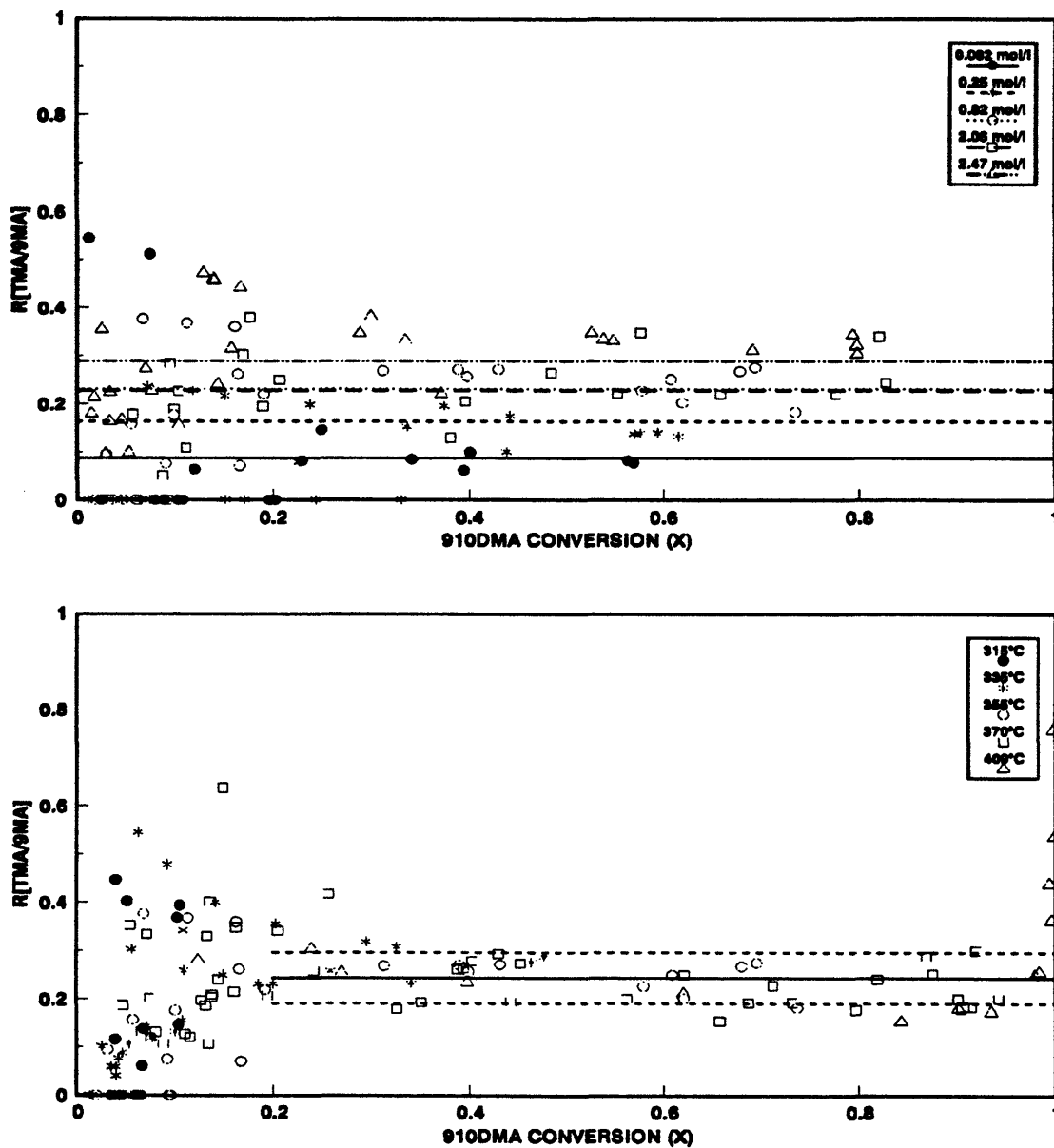
Figure 1.16: Ratio of moles TMA to moles 9MA produced vs. 910DMA conversion (X) for varying [910DMA]$_o$ at T = 355°C (top) and for varying T with [910DMA]$_o$ = 0.82 mol/l (bottom).
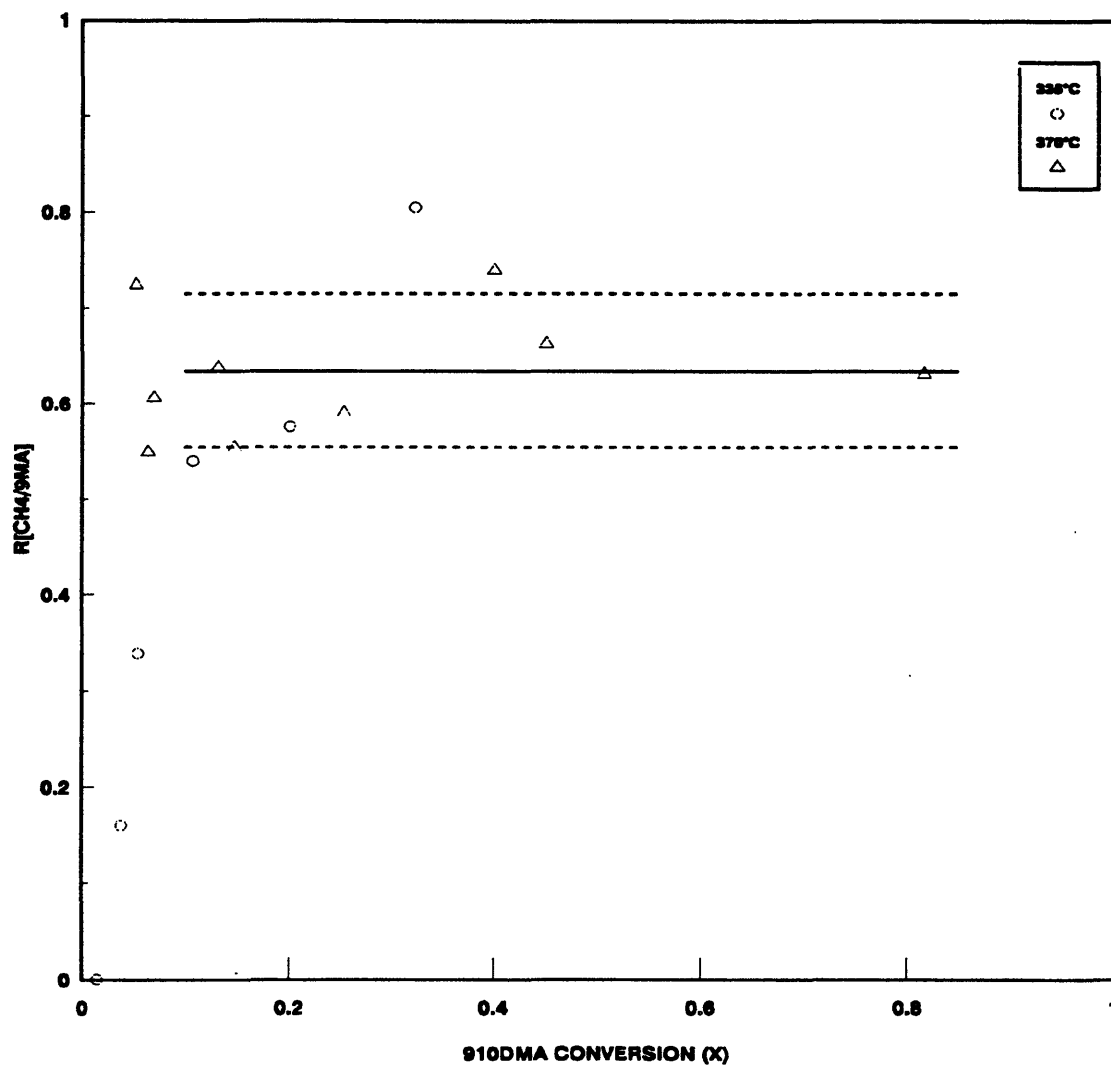
Figure 1.17: Ratio of moles CH4 to moles 9MA produced vs. 910DMA conversion (X) for varying T with $[910DMA]_o$ = 0.82 mol/l.

primary product ratios R, namely R[DHDMA/9MA], R[TMA/9MA] and R[CH4/9MA], versus conversion X.

R[DHDMA/9MA] measures the ratio of hydrogenation (P1) to demethylation (P2) pathways. The upper panel of Figure 1.15 shows that, for all initial 910DMA concentrations, R[DHDMA/9MA] ~ 0.4 at the lowest concentrations, X → 0, and then drops rapidly to 0.04 ± 0.02 for X > 0.20. The lower panel of Figure 1.15 shows that, at all temperatures, R[DHDMA/9MA] ~ 0.4 for X → 0 and then drops rapidly to a level of 0.04 ± 0.04 for X > 0.20. The ratio of hydrogenation to demethylation pathways being essentially independent of initial concentration and temperature implies that these pathways are of similar overall order with respect to substrate and possess similar activation energies.

R[TMA/9MA] measures the ratio of methylation (P3) to demethylation (P2) while R[CH4/9MA] measures the ratio of methane gas formed (roughly P2 - P3) relative to demethylation (P2). The upper panel of Figure 1.16 shows that R[TMA/9MA] is a weak function of initial concentration, with R[TMA/9MA] = [0.09 ± 0.02, 0.16 ± 0.05, 0.23 ± 0.09, 0.23 ± 0.08, 0.29 ± 0.10] for $[910DMA]_0$ = [0.082, 0.25, 0.82, 2.06, 2.47 mol/l] for X > 0.20; this implies that the methylation pathway P3 is of somewhat higher order in substrate than the demethylation pathway P2. The lower panel of Figure 1.16 shows that R[TMA/9MA] is essentially independent of temperature, with R[TMA/9MA] = 0.24 ± 0.10 for X > 0.20 at all temperatures; thus P3 and P2 possess similar activation energies.

Figure 1.17 shows that R[CH4/9MA] = 0.63 ± 0.08 for X > 0.20 at T = 355

and 370°C and [910DMA]$_o$ = 0.82 mol/l. Taken together, the data in the lower

panel of Figure 1.16 and in Figure 1.17 show that the sum of the ratios

R[TMA/9MA] + R[CH4/9MA] ~ 0.87 is close to unity, accounting for the methyl

radicals implicitly formed in the demethylation pathway P2. It is interesting that,

under the present experimental conditions, ~ 2/3 of the methyl radicals formed by

P2 are quenched by hydrogen abstraction, forming methane gas, while ~ 1/3 add to

the 910DMA substrate, eventually appearing as TMAs.

1.7 Mechanism

A possible mechanism for 910DMA thermolysis is summarized in Figure 1.18,

as an elementary step "graph". This is constructed such that the substrate and all

stable molecular products are arrayed in the bottom row while unstable radical

intermediates (the transition states) are arrayed in the top row. Reaction "nodes",

arrayed in the middle row, connect the individual species in the bottom and top rows

with arrows indicating the initial direction of reaction (all reactions are, of course,

reversible). Initiation reactions are denoted by solid interconnecting lines,

propagation reactions by various kinds of dashed lines and termination reactions by

dotted lines. Also, the substrate 910DMA is shown with heavy borders in the middle

of the bottom row, with light (propagation) products to its right and heavy

(termination) products, mostly dimers, to its left.
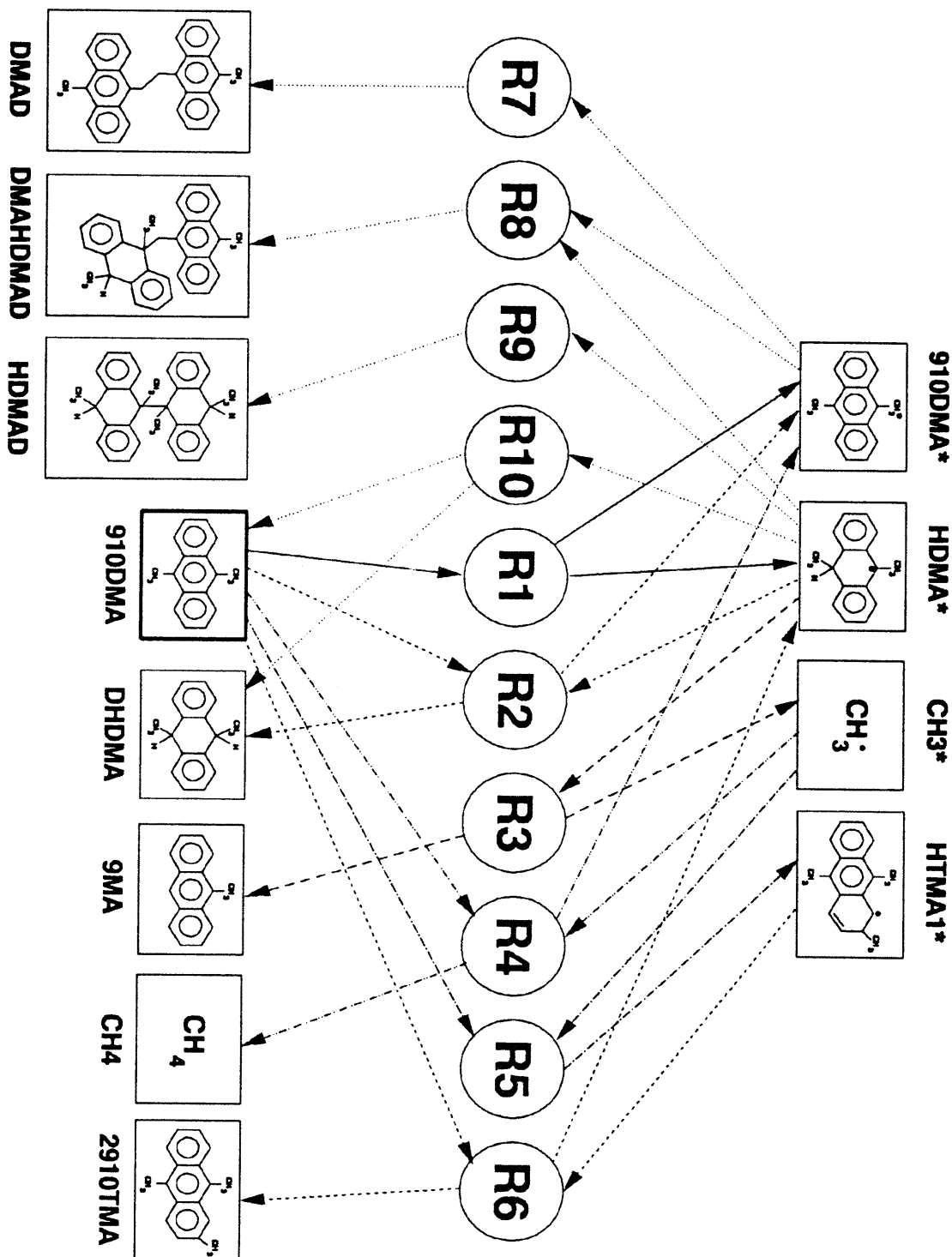
Figure 1.18: Elementary step graph of 910DMA thermolysis mechanism.

The free-radical cycle is initiated by the substrate 910DMA undergoing bimolecular disproportionation (R1), an intermolecular hydrogen transfer reaction, to form the respectively dehydrogenated and hydrogenated radical species 910DMA* and HDMA*. Of these, the latter can either abstract hydrogen from 910DMA substrate by (R2), to form DHDMA products (*cis-* and *trans-* not distinguished), or undergo a β-scission type of radical decomposition by (R3), forming 9MA product and a methyl radical CH_3*. The CH_3* can either abstract H from 910DMA substrate by (R4), to form methane product, or add to the 910DMA substrate by (R5), to form the trimethyl radical HTMA1*. The latter can then abstract H from substrate 910DMA via (R6) to form (the 2910 isomer of) the observed TMA product. Finally, the radical mechanism is terminated by the species 910DMA* and HDMA* engaging in both pure- and cross-combination, (R7-R9), to form various dimeric products. HDMA* radical can also terminate by disproportionation, (R10), to form 910DMA and DHDMA.

The proposed mechanism evidently accounts for all the major products, 9MA, TMA, DHDMA, CH4 and heavies, observed during the initial stages of 910DMA thermolysis. Each of the observed triad of primary pathways, namely, P1 hydrogenation, P2 demethylation and P3 methylation, also arise naturally as limiting cases of the elementary step graph, with P1 comprising the set [R1, R2, R7], P2 the set [R1, R3, R4, R7] and P3 the set [R1, R3, R5, R6, R8]. Note that the mechanism

stoichiometrically restricts the maximum selectivities of each of the major products to 1/3, which is well within a factor of 2 of the selectivities actually observed.

The mechanism shown in Figure 1.18 also offers some theoretical insights. It suggests that the relative kinetics of the observed hydrogenation and demethylation pathways, (P1)/(P2), are essentially controlled by the HDMA* radical, through the ratio of its H-abstraction to β-scission reactions (R2)/(R3). Further, the observed methylation to demethylation pathway ratio, (P3)/(P2), is essentially governed by competition between methyl radical reactions (R4) and (R5), in which CH3* either abstracts H from or adds to the 910DMA substrate. Finally, the mechanism presented in Figure 1.18 serves as a platform for the quantitative modelling of 910DMA thermolysis kinetics and product selectivities. This effort is described in the section that follows.

1.8 Modelling of 910DMA Thermolysis

Our modelling of 910DMA thermolysis, based on the mechanism derived above, involved the following steps. First, thermochemical parameters were obtained for all stable and radical species occurring in the mechanism, from first principles. Next, enthalpies of reaction were calculated for each elementary step and these were used to infer Arrhenius parameters for each step in both forward and reverse directions. Third, rate constants were calculated for each reaction at the selected temperature, say T = 355°C, and these were used in conjunction with the differential

conservation relations for each species to effect a full numerical solution of the model system, starting from an initial condition of pure substrate at concentration $[910DMA]_o$ = 0.82 mol/l, say. The preceding provided a numerical simulation of 910DMA thermolysis kinetics and product selectivities at the chosen T and $[910DMA]_o$; these "model" results could be directly compared to experimental observations at the same conditions. Fourth, a sensitivity analysis was performed to discern how errors in the estimated Arrhenius parameters affected the model results. Finally, the Arrhenius parameters of certain elementary steps were adjusted, within their estimated error limits; to provide model results that best-fit the experimental observations.

1.8.1 Thermochemical Properties

Enthalpies of formation, ΔH°_{f298}, for all chemical species participating in our 910DMA thermolysis model were derived by a "macro" group-additivity technique summarized in Table 1.4 and illustrated in Figure 1.19. In this, a basis set of bond strengths, D° kcal/mol, steric corrections, C° kcal/mol, and stable species enthalpies of formation, ΔH°_f, was assembled from a variety of literature sources, as shown in the bottom three rows of Table 1.4(a). The estimation of ΔH°_f for a model species, say 9MA as shown in the upper panel of Figure 1.19, began with the largest, most structurally similar basis species available, say ANT. Other basis species and steric corrections, in this case 1MN, NAP and an alkene gauche interaction, were then

Table 1.4(a)
MATRIX FOR THERMOCHEMICAL
PROPERTY ESTIMATION

ΔH°f (kcal/mol)	Model Species	ANT	DHA	14CHD	36DM-14CHD	CHX	MeCHX	NAP	12DHN	14DHN	1MN	2MN	17DMN	18DMN	14DHA	gauche alkene	DoC-H(ETBZ)	DoC-H(CUM)	DoC-H(12DHN)	DoC-H(14DHN)	DoC-H(DPM)	DoC-H(14DHA)	DoC-H(9MA)
38.8±1.0	910DMA	*						2*		2*					2*								
47.0±0.8	9MA	*						*		*					*								
28.3±1.3	2910TMA	*						2*		2*	*				2*								
35.7±1.4	1910TMA	*						2*		2*	*	*	*		2*								
23.0±1.6	cDHDMA		*	*	*																		
24.3±1.6	tDHDMA		*	*	*																		
23.6±1.6	DHDMA		*	*	*																		
30.7±1.2	DHMA		*			*	*																
68.7±2.3	910DMA*	*						2*		2*					2*								*
52.3±3.7	HDMA*		*	*	*												*	*	*		*		
55.0±4.2	HTMA1*					*	*	2*	*	2*				*	2*						*		
58.4±5.1	HTMA2*					*	*	2*	*	2*	*	*	*	2*		*	*			*			
76.9±2.2	9MA*	*						*		*													*
60.8±2.3	HMA10*	*				*	*								*	*	*				*		
59.6±3.1	HMA9*	*				*	*								*	*	*				*		

Bond Strengths or Basic Species	Do or ΔH°f (kcal/mol)	Reference
ANT	55.2±0.5	Pedley (1976)
DHA	38.2±1.1	Pedley (1976)
14CHD	25.9±0.5	SnGB (1977)
36DM-14CHD	11.3±1.0	SnGB (1977)
CHX	-29.5±0.2	SnGB (1977)
MeCHX	-37.0±0.4	Benson et al. (1969)
NAP	35.9±0.4	Pedley (1976)
12DHN	30.2±2.0	Benson et al. (1969)
14DHN	32.9±2.0	SnGB (1977)
1MN	27.2±0.5	SnGB (1977)
2MN	26.4±0.6	SnGB (1977)
17DMN	19.6±0.5	Stull (1969)
18DMN	26.0±0.5	Pedley (1976)
14DHA	49.7±2.0	SnGB (1977)
gauche alkene	0.5	Benson (1976)
DoC-H(ETBZ)	84.7±1.5	SPX (1991)
DoC-H(CUM)	82.5±1.5	SPX (1991)
DoC-H(12DHN)	84.0±2.0	NBMO estimate
DoC-H(14DHN)	81.0±2.0	NBMO estimate
DoC-H(DPM)	82.0±2.0	Bordwell et al. (1988)
DoC-H(14DHA)	84.0±2.0	NBMO estimate
DoC-H(9MA)	82.0±2.0	Stein & Brown (1991)

81

Table 1.4(b)

LIST OF ABBREVIATIONS IN THERMOCHEMICAL PROPERTY ESTIMATION MATRIX

Model Species

910DMA	9,10-dimethylanthracene
9MA	9-methylanthracene
2910TMA	2,9,10-trimethylanthracene
1910TMA	1,9,10-trimethylanthracene
cDHDMA	*cis*-9,10-dihydro-9,10-dimethylanthracene
tDHDMA	*trans*-9,10-dihydro-9,10-dimethylanthracene
DHDMA	9,10-dihydro-9,10-dimethylanthracene
DHMA	9,10-dihydro-9-methylanthracene
910DMA*	9,10-dimethylanthracene benzylic radical
HDMA*	9-hydro-9,10-dimethylanthracene (2°) radical
HTMA1*	1-hydro-2,9,10-trimethylanthracene radical
HTMA2*	2-hydro-1,9,10-trimethylanthracene radical
9MA*	9-methylanthracene benzylic radical
HMA10*	9-hydro-9-methylanthracene (2°) radical
HMA9*	10-hydro-9-methylanthracene (3°) radical

Bond Strengths

14DHA	1,4-dihydroanthracene
DPM	diphenylmethane
14DHN	1,4-dihydronaphthalene
12DHN	1,2-dihydronaphthalene
CUM	cummene
ETBZ	ethylbenzene

Table 1.4(c)

LIST OF ABBREVIATIONS IN THERMOCHEMICAL PROPERTY ESTIMATION MATRIX (con't)

Steric Corrections	
gauche alkene	1,5-gauche alkene repulsion interaction (Benson, 1976)

Basis Species	
18DMN	1,8-dimethylnaphthalene
17DMN	1,7-dimethylnaphthalene
2MN	2-methylnaphthalene
1MN	1-methylnaphthalene
NAP	naphthalene
MeCHX	methylcyclohexane
CHX	cyclohexane
14CHD	1,4-cyclohexadiene
36DM-14CHD	3,6-dimethyl-1,4-cyclohexadiene
DHA	9,10-dihydroanthracene
ANT	anthracene

References	
NBMO estimate	non-bonding molecular orbital estimate in present work
SPX (1991)	Structures & Properties Database and Estimation Program (Stein et al., (1991)
StGB (1977)	Stein, Golden and Benson (1977)
ShGB (1977)	Shaw, Golden and Benson (1977)

ANT
55.2 ± 0.5

1MN
27.2 ± 0.5

NAPH
35.9 ± 0.4

GAUCHE
ALKENE
0.5

9MA
55.2 + 27.2 - 35.9 + 0.5 = 47.0
$(0.5^2 + 0.5^2 + 0.4^2)^{\wedge} \frac{1}{2} = 0.8$

DPM
82.0 ± 2.0

H*
52.1 ± 0.1

DHA
38.2 ± 1.1

DHA*
68.1 ± 2.3

DHA*
68.1 ± 2.3

avgDHDMA
23.6 ± 1.6

DHA
38.2 ± 1.1

CUM
82.5 ± 1.5

ETBZ
84.7 ± 1.5

GAUCHE
ALKENE
0.5

HDMA*
68.1 + 23.6 - 38.2 + 82.5 - 84.7 + 2 * 0.5 = 52.3
$(2.3^2 + 1.6^2 + 1.1^2 + 1.5^2 + 1.5^2)^{\wedge} \frac{1}{2} = 3.7$
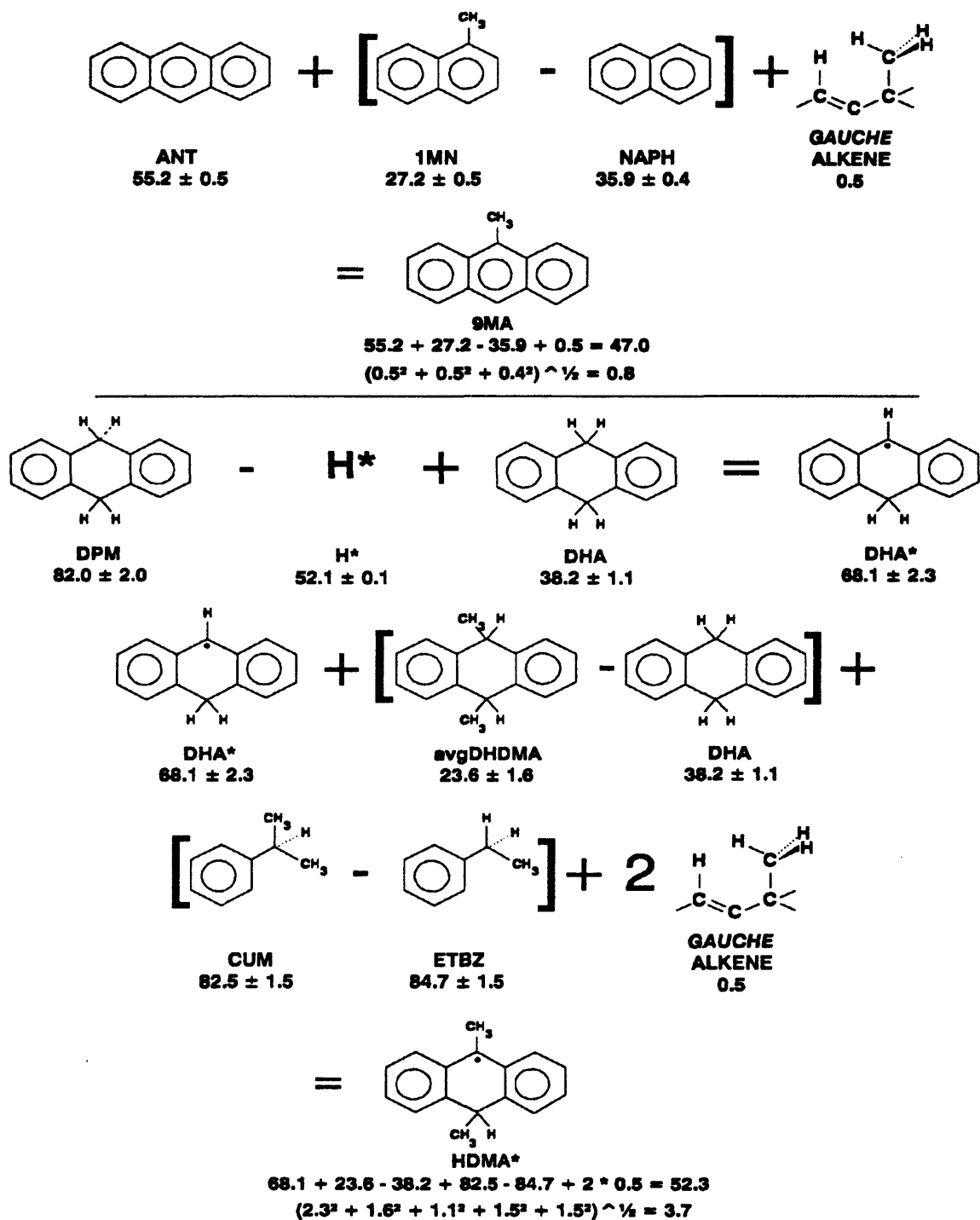
Figure 1.19: Example of the "macro" group additivity technique used to estimate enthalpies of formation for stable and radical species, and errors associated with the estimations.

added to and subtracted from the starting species to bridge the structural differences between it and the model species. The macro group-additivity procedure described for 9MA is summarized in row 2 of Table 1.4(a), with asterisks in columns 1, 7, 10, 14 indicating the basis set members involved; the estimated ΔH°_f and its estimated error ($\pm$) is noted to the left of the 9MA model species' name. A second example, for radical species HDMA*, is provided in the lower panel of Figure 1.19 and row 10 of Table 1.4(a).

1.8.2 Arrhenius Parameters

Arrhenius expressions, of the form $\log_{10} k = \log_{10} A - E^*/\theta$, with rate constant k (l, mol, s units), and pre-exponential factor A (same units as k), and activation energy E^* (kcal/mol), were generated for each elementary step of the 910DMA thermolysis mechanism, as summarized in Table 1.5. An elementary reaction was first classified (column 2), using standard free-radical reaction notation. Next, kinetic data reported in the literature for that type of reaction was analyzed to ascertain its activation parameters. Of these, $\log_{10} A$ was decomposed into an intrinsic portion, $\log_{10} A_{int}$ (column 3) and a reaction path degeneracy, rpd (column 4), with $\log_{10} A = \log_{10} A_{int} + \log_{10} (rpd)$. The activation energy E^* was determined by an Evans-Polanyi expression (column 5), of form $E^* = E_o + \alpha\Delta H^\circ_r$ with $\alpha = 0$ (combinations), 0.5 (H-abstraction and transfer) or 1 (homolysis, beta-scission). Values of the

Table 1.5

ARRHENIUS EXPRESSIONS FOR ELEMENTARY STEPS OF 910DMA THERMOLYSIS MECHANISM

	Type of Reaction	$\log_{10} A_{int}$ l mol^{-1} s^{-1}	rpd	Evans-Polanyi Relation: $E^* =$	$\Delta H_r°$ kcal/mol	E^* kcal/mol	Arrhenius Expression: $\log_{10} k =$
R1	molecular disproportionation	8.5	24	$\Delta H_r°$	43.4	43.4	9.9 - 43.4/θ
R-1	radical disproportionation	8.5	1	0	-43.4	0	8.5
R2	H-abstraction	8.1	6	$17.5 + \Delta H_r°/2$	1.2	18.1	8.9 - 18.1/θ
R-2	H-abstraction	8.1	2	$17.5 + \Delta H_r°/2$	-1.2	16.9	8.4 - 16.9/θ
R3	methyl scission	13.5	1	$2.1 + \Delta H_r°$	29.5	31.6	13.5 - 31.6/θ
R-3	CH3* addition	8.3	1	2.1	-29.5	2.1	8.3 - 2.1/θ
R4	H-abstraction	8.1	6	$17.5 + \Delta H_r°/2$	-22.7	6.2	8.9 - 6.2/θ
R-4	H-abstraction	8.1	4	$17.5 + \Delta H_r°/2$	22.7	28.9	8.7 - 28.9/θ
R5	CH3* addition	8.3	4	5.1	-18.6	5.1	8.9 - 5.1/θ
R-5	methyl scission	13.5	1	$5.1 + \Delta H_r°$	18.6	23.7	13.5 - 23.7/θ
R6	radical H transfer	8.1	2	$17.5 + \Delta H_r°/2$	-13.2	10.9	8.4 - 10.9/θ
R-6	radical H transfer	8.1	1	$17.5 + \Delta H_r°/2$	13.2	24.1	8.1 - 24.1/θ
R7	radical combination	9.3	1	0	-54.2	0	9.3
R-7	homolytic dissociation	15.5	1	$\Delta H_r°$	54.2	54.2	15.5 - 54.2/θ
R8	radical combination	9.3	1	0	-52.4	0	9.3
R-8	homolytic dissociation	15.5	1	$\Delta H_r°$	52.4	52.4	15.5 - 52.4/θ
R9	radical combination	9.3	1	0	-50.7	0	9.3
R-9	homolytic dissociation	15.5	1	$\Delta H_r°$	50.7	50.7	15.5 - 50.7/θ
R10	radical disproportionation	8.5	1	0	-42.2	0	8.5
R-10	molecular disproportionation	8.5	4	$\Delta H_r°$	42.2	42.2	9.1 - 42.2/θ

enthalpy of reaction ΔH°_r (column 6), derived from the data of Section 8.1, then led

to E^* (column 7) and the final Arrhenius expression (column 8).

1.8.3 Numerical Solution and Model Results

The model 910DMA thermolysis reaction system was solved by a computer

code called ACUCHEM (Braun et al., 1988). This program numerically solves a

system of differential equations that describe the temporal behavior of a spatially

homogeneous, isothermal, multicomponent chemical reaction system. ACUCHEM

performs integrations with a suite of subroutines (called DDRIV) designed to solve

general systems of stiff nonlinear ordinary differential equations by the method of

Gear (1971). Two types of tests were performed to ensure that ACUCHEM

produced reliable results. First, in regard to its stability, it was verified that the

program generated the same concentration profiles, regardless of the time step size.

Second, in regard to its fidelity, the concentrations of all species, both radical and

stable, calculated by the numerical solution at low conversions $X < 0.1$ were found

to agree quite closely, to within a factor of 2 or better, with corresponding

concentrations obtained from pseudo-steady-state algebraic solutions at similar

conditions.

Numerical solution of the 910DMA thermolysis model at $T = 355°C$ and

$[910DMA]_o = 0.82$ mol/l, the central point of the experimental grid provided

complete concentration histories of all radical and stable species, which were then used to obtain the model results presented in Figure 1.20, Figure 1.21 and Figure 1.22.

Figure 1.20 graphically depicts the elementary reaction traffic at a vary low conversion, X = 0.001, with the thicker arrows denoting reaction with the greater net (forward - reverse) rates. It is seen that 910DMA substrate decomposition occurs mainly, but not exclusively, by (R1). Also, the rates of hydrogenation (R2) and of demethylation (R3) are of comparable magnitudes, with (R3) > (R2). Methyl radical quenching by H-abstraction from substrate (R4) greatly exceeds its addition to the substrate (R5). Among termination reactions, (R7 - R10), 910DMA* combination (R7) is dominant.

Figure 1.21 depicts reaction traffic at a moderate conversion, X = 0.31, showing the substrate decomposition rate to be lower than it was at X = 0.001 and the rate of hydrogenation (R2) to be much smaller than the rate of demethylation (R3). However, H-abstraction by methyl radical (R4) continues to exceed its addition to substrate (R5) and (R7) remains the dominant termination.

Figure 1.22 compares the substrate and product histories (upper panel) and product selectivities (lower panel) obtained from the numerical solution to the experimental data for 910DMA, 9MA, TMA and CH4. In the upper panel of Figure 1.22, the model is seen to predict 910DMA decay, the solid line, that is too slow compared to the experimental observations, shown as asterisks. The model half-
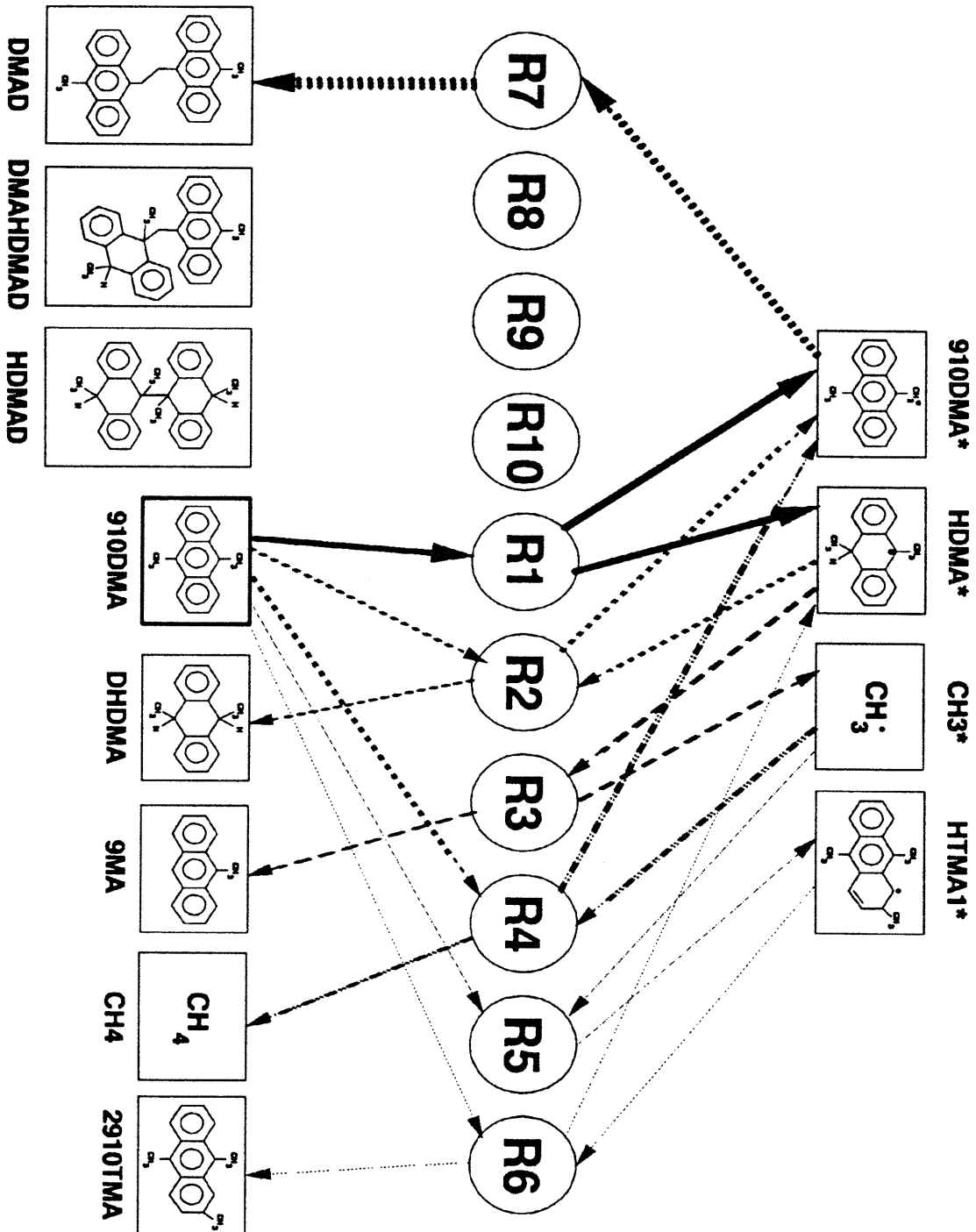
Figure 1.20: Relative elementary reaction rate traffic at T = 355°C with [910DMA]$_o$ = 0.82 mol/l for X → 0.
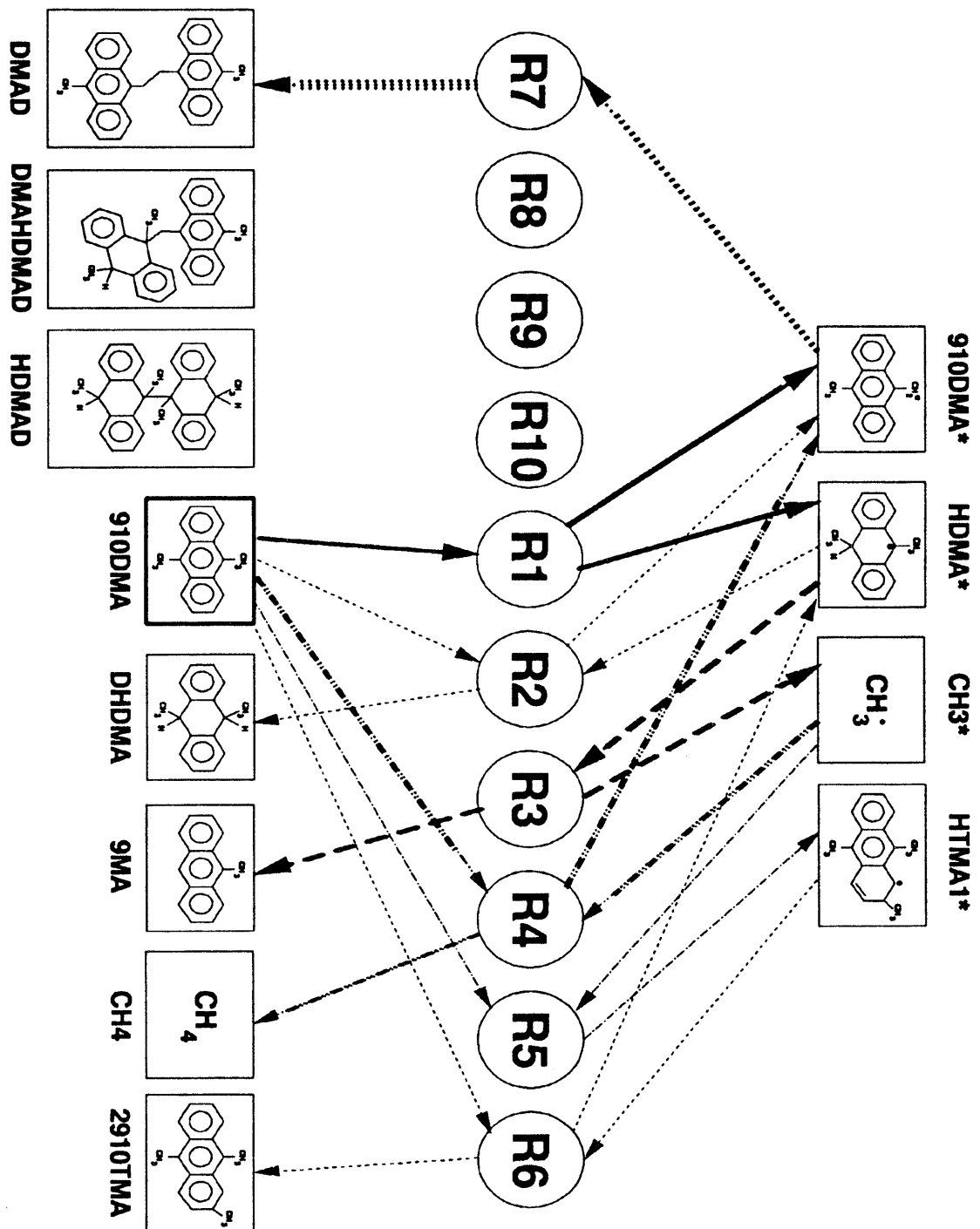
Figure 1.21: Relative elementary reaction rate traffic at T = 355°C with [910DMA]$_o$ = 0.82 mol/l for X = 0.31.
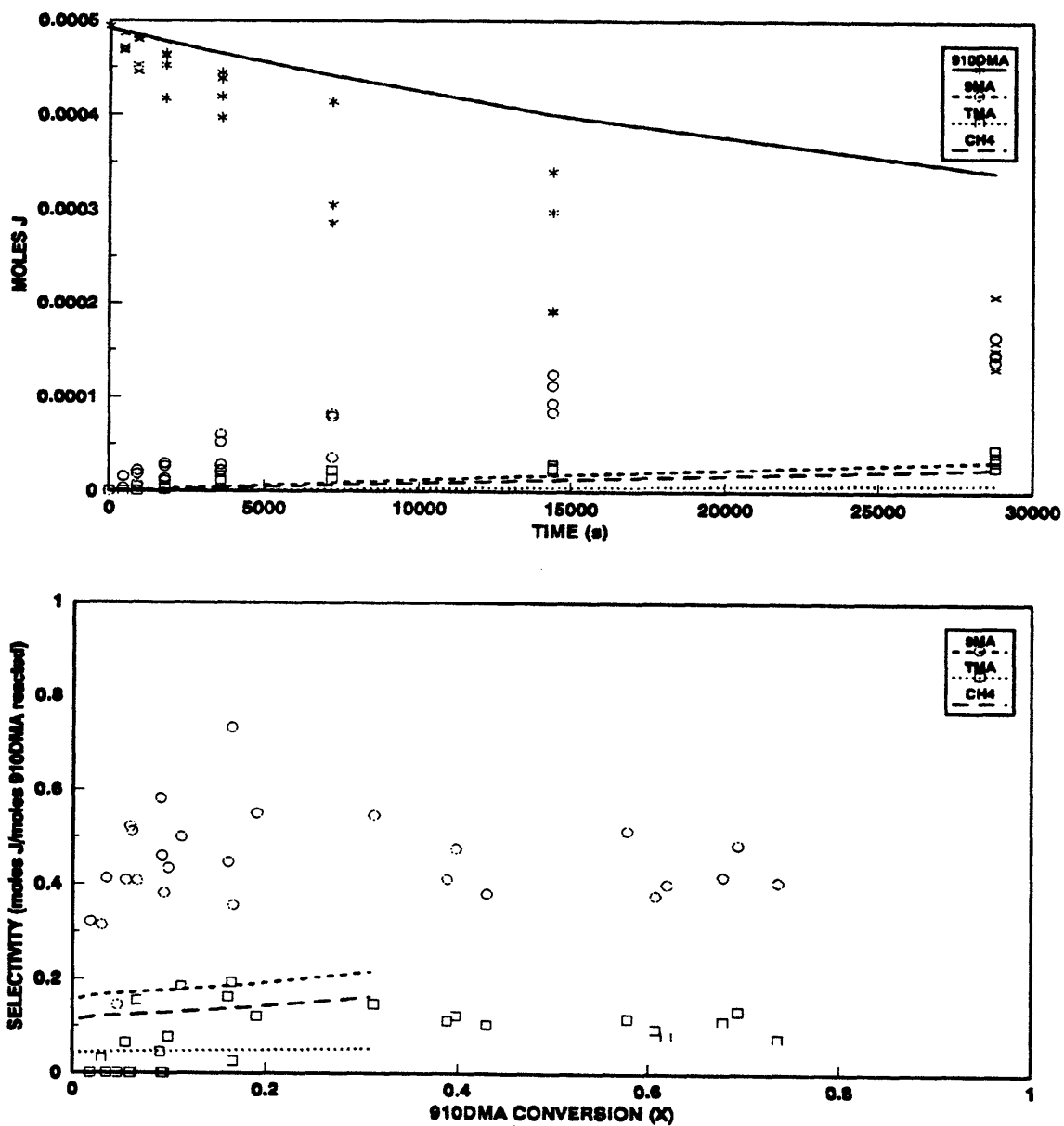
Figure 1.22: Product histories (top) and selectivity diagram (bottom) comparing model results (lines) to experimental data (symbols) for 910DMA, 9MA, TMA and CH4 at T = 355°C with $[910DMA]_o$ = 0.82 mol/l.

91

life, t^*, is 2.6-fold slower than the experimental. Also, the absolute amounts of 9MA, the short-dashed line versus the circles, and of TMA, the dotted line versus the squares, formed by the model are both lower than observed in the experiments. However, the model predicts the relative amounts of 9MA > CH4 > TMA and the sum of CH4 plus TMA equal to the 9MA produced, both of which accord with the experiment. The lower panel of Figure 1.22 shows that the selectivities S(9MA) and S(TMA) from the model are respectively 2.5 and 2.2-fold too low compared to the average values of S(9MA) and S(TMA) observed from the experiments between 0.1 < X < 0.8. However, the model ratio R[TMA/9MA] = 0.27, physically the methylation/demethylation pathway ratio P3/P2, is close to value of 0.24 observed experimentally.

1.8.4 Sensitivity Analysis

A sensitivity analysis of our 910DMA thermolysis model was conducted at the central point of the 910DMA experimental grid, T = 355°C and $[910DMA]_o$ = 0.82 mol/l, by separately perturbing the kinetics of selected elementary steps over their estimated uncertainty limits. The inherent errors in ΔH°_f are between 1 - 3 kcal/mol for stable species and 2 - 5 kcal/mol for radicals as shown in Table 1.4(a). These errors in ΔH°_f translate into errors of ± 2 - 5 kcal/mol for ΔH°_r which propagate through the Evans-Polanyi relations of Table 1.5 into errors of ± 2 - 5 kcal/mol for E^*; when coupled with a $\theta \sim 3$, which corresponds to the temperatures of the present

experiments, these lead to errors of $\pm$ 0.7 - 1.7 in $\log_{10}$ k. The errors in the $\log_{10}$ A

estimates are, at most, $\pm$ 0.5, which translate directly to errors of ± 0.5 in $\log_{10}$ k.

Thus, in general, the calculated rate constants of the elementary steps are beset more

by errors in their E^* than in their $\log_{10}$ A. For this reason, the sensitivity analysis was

performed by separately perturbing the E^* of selected elementary reactions over the

inherent errors in their ΔH°_r to show their effects on 910DMA decay half-life t^*,

9MA selectivity S(9MA), and the primary product ratios R[DHDMA/9MA] and

R[TMA/9MA]. Figure 1.23 and Figure 1.24 show results of a sensitivity analysis

applied to 910DMA decay half-lives. Since the elementary reaction R1 contributes

most heavily to the destruction of 910DMA substrate in our model, the sensitivity to

t^* was examined by perturbing the activation energy E^*, by its estimated uncertainty

of $\pm$ 4.4 kcal/mol, which is the inherent error in ΔH°_{R1}. Results are shown in

Figure 1.23, a doubly-logarithmic plot of t^* vs. $[910DMA]_o$ at T = 355°C, wherein

experimental observations, depicted by solid points with error bars and a solid line,

are compared with model predictions, shown by the hollow points and dashed line.

The upper and lower ends of the vertical dashed line at $[910DMA]_o$ = 0.82 mol/l

represent values of t^* obtained by negative and positive perturbations, respectively,

of E^*_1. This sensitivity analysis shows that the inherent uncertainties of $\pm$ 1.5 orders

of magnitude in values of t^* calculated by the model are considerably greater than

the 0.5 to 1.0 order of magnitude difference between the model results and

experimental observations. That is, within its (large) error limits, the model yields
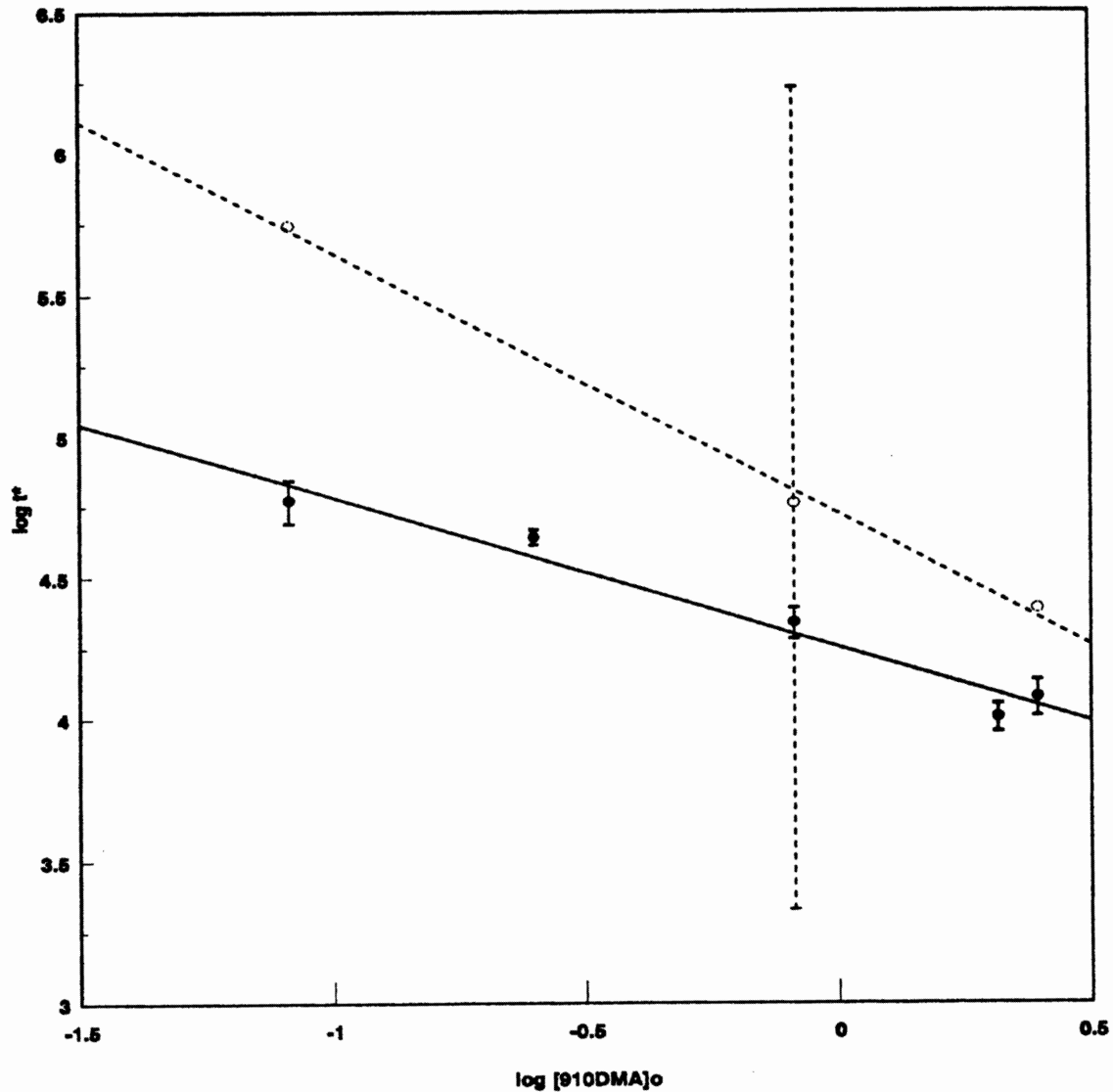
Figure 1.23: Decay half-life t^*_{exp} (solid line, circles) and t^*_{mod} (dashed line, hollow circles, vertical dashed lines indicates error band) for varying $[910DMA]_o$ at fixed T = 355°C.
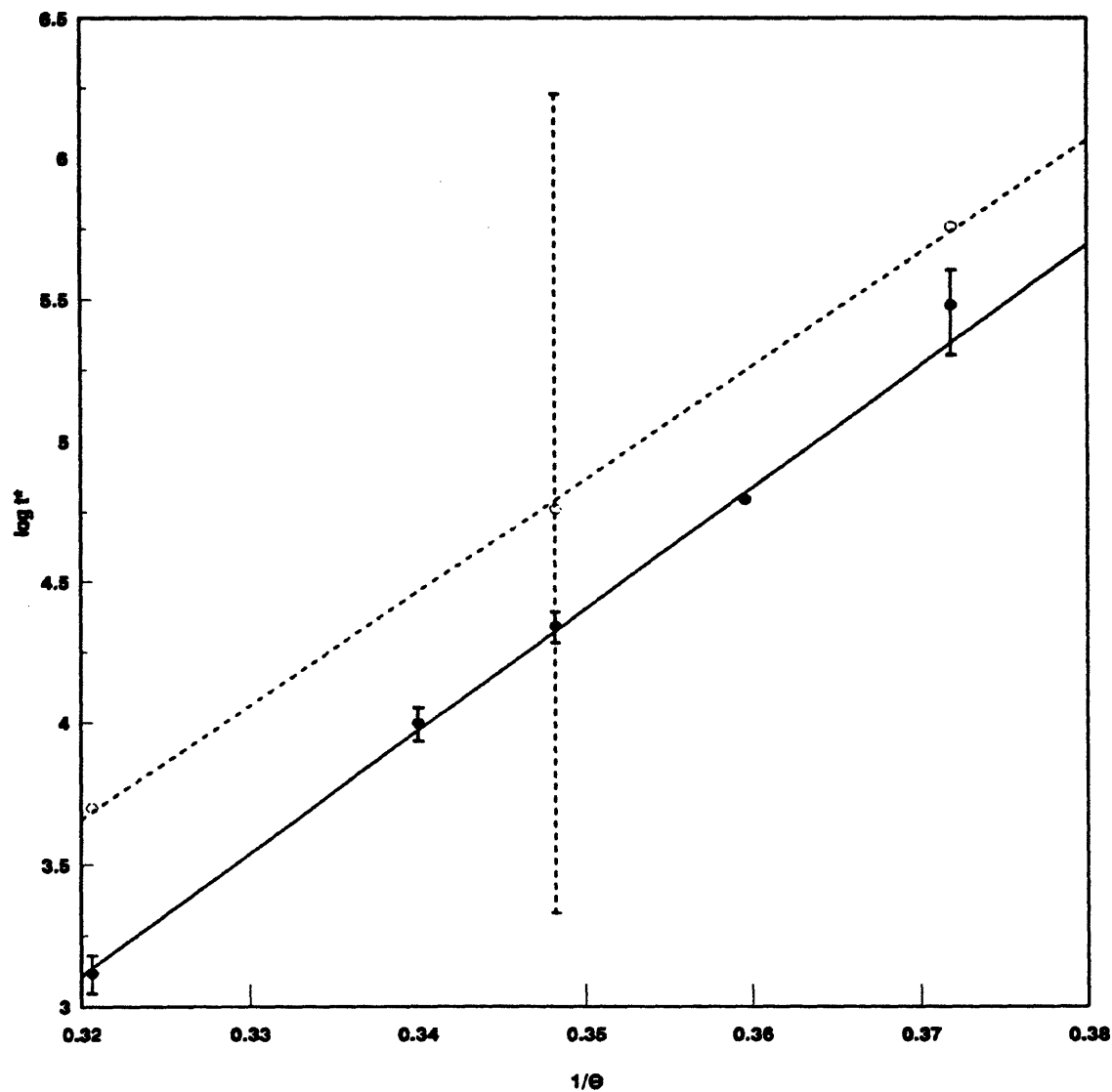
Figure 1.24: Decay half-life t^*_{exp} (solid line, circles) and t^*_{mod} (dashed line, hollow circles, vertical dashed line indicates error band) for varying T with fixed $[910DMA]_o$ = 0.82 mol/l.

half-lifes in agreement with experiments. This conclusion is reinforced by the results in Figure 1.24, a semi-logarithmic Arrhenius-related plot of t^* vs. $1/\theta$ wherein experimental observations are compared to model predictions and their uncertainties in a manner analogous to that used in Figure 1.23.

Figure 1.25 shows results of a sensitivity analysis applied to the selectivity of 9MA formation, S(9MA). According to the model, 9MA formation is governed by elementary reaction (R3), and therefore E^*_{R3} was perturbed by $\pm$ 3.7 kcal/mol, the inherent error in ΔH°_{R3}. In the upper panel of Figure 1.25, using log-log coordinates of S(9MA) vs. $[910DMA]_o$, the model is seen to predict S(9MA) from 0.2 to 0.5 orders of magnitude too low relative to experimental observations, while in the lower panel, using semi-log coordinates of S(9MA) vs. $1/\theta$, the model predicts S(9MA) from 0.1 to 0.7 orders of magnitude lower than observed. The sensitivity analysis, common to both panels, shows uncertainties of approximately + 0.4 and -1.1 orders of magnitude in the model predictions of S(9MA). Thus, within its error limits, the model predicts S(9MA) in accord with observations over the range of the present experiments; it should be noted, however, that of the lowest temperature and highest $[910DMA]_o$, the experimental values of S(9MA) lie at, even slightly above, the upper bound of model predictions.

Figure 1.26 shows results of a sensitivity analysis applied to the major product ratio R[TMA/9MA]. In our model, R[TMA/9MA] is directly governed by R4 and R5, that is, by the relative propensities of a methyl radical to either abstract H or
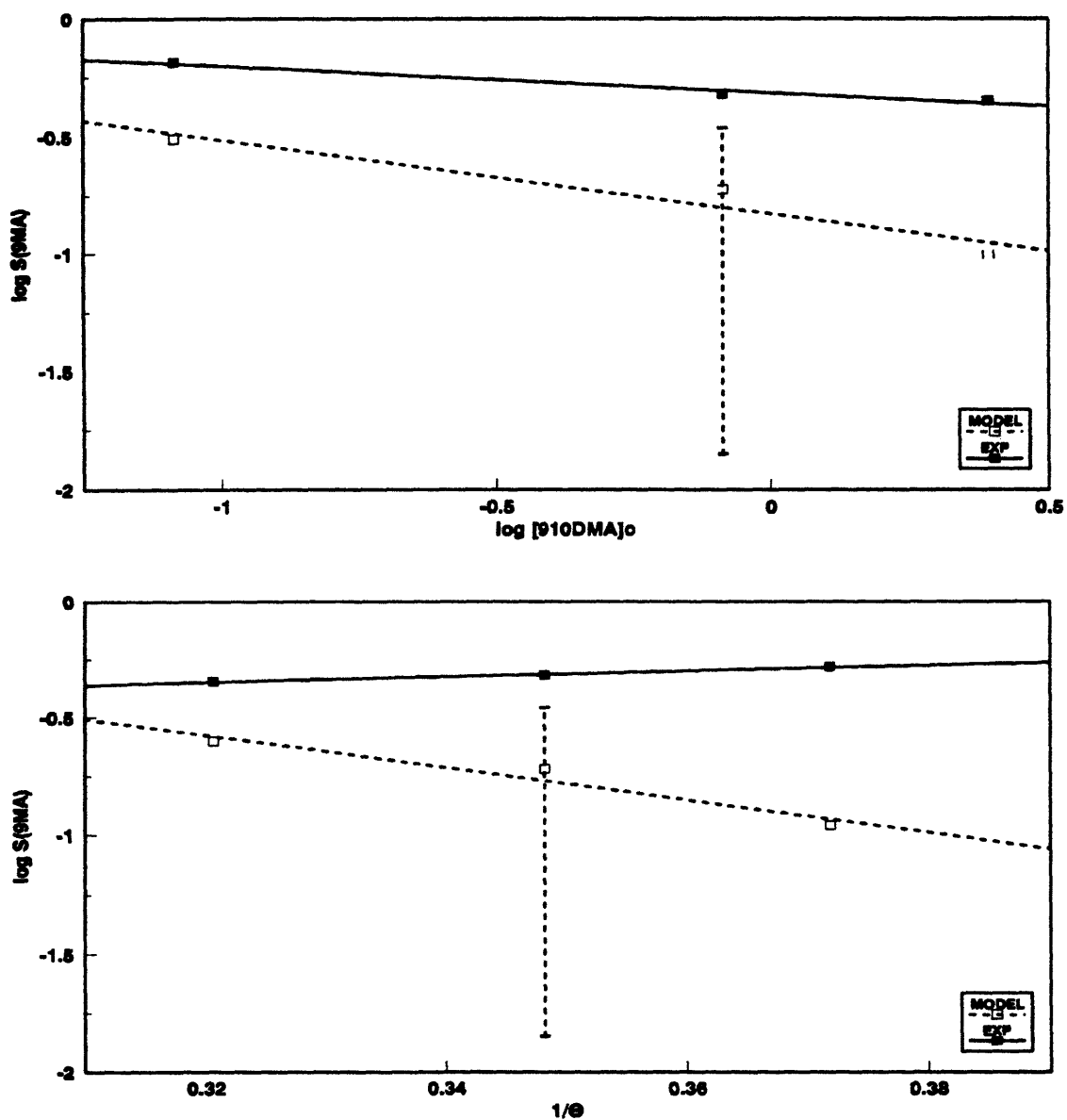
Figure 1.25: Comparison of experiment (solid squares) and model (hollow squares) S(9MA) for varying $[910DMA]_o$ at fixed $T=355°C$(top) and varying T with fixed $[910DMA]_o=0.82$ mol/l(bottom).
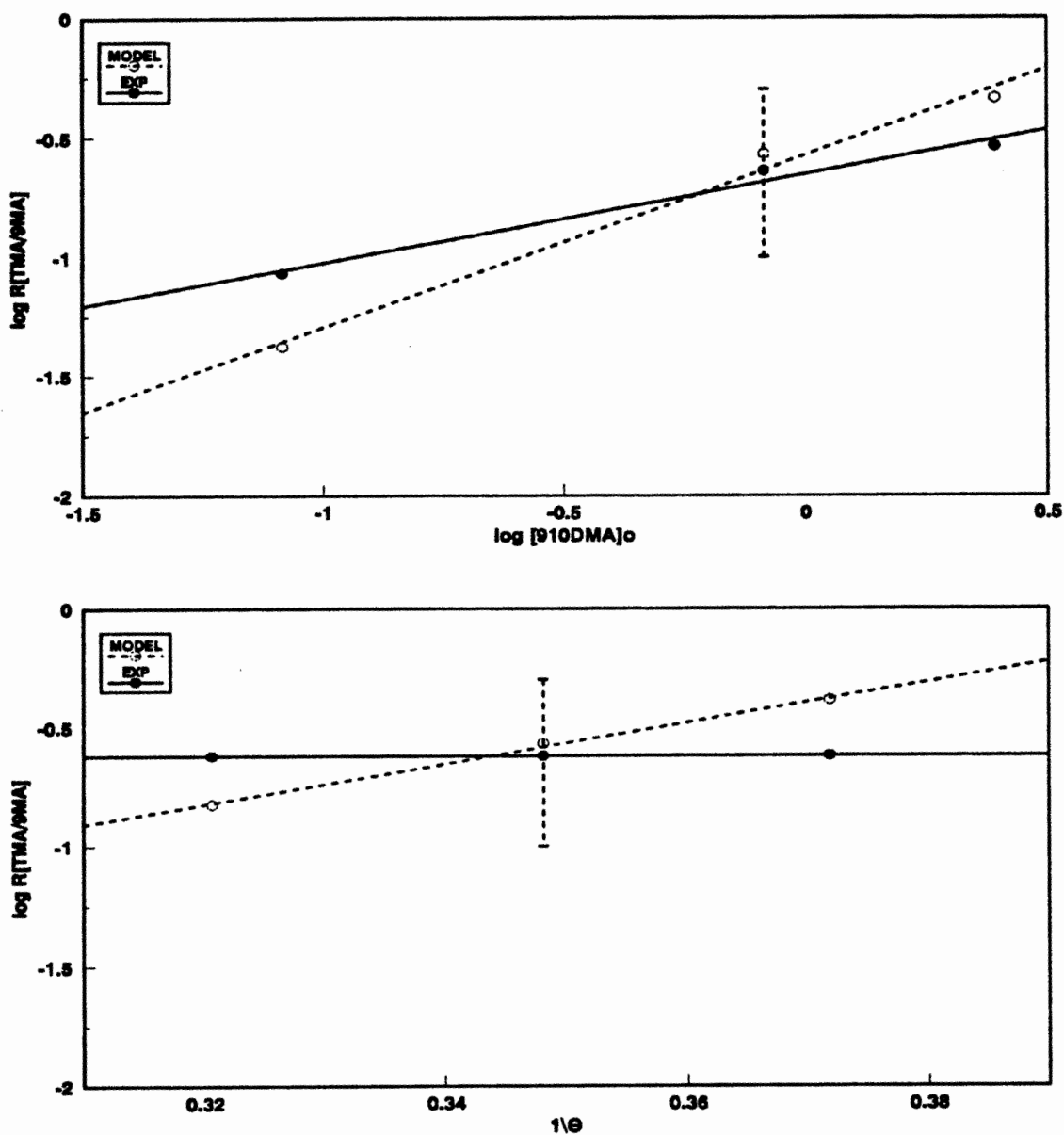
Figure 1.26: Comparison of experiment (solid circles) and model (circles) R[TMA/9MA] for varying [910DMA]$_o$ at fixed T=355°C(top) and varying T with fixed [910DMA]$_o$ = 0.82 mol/l(bottom).

add to the 910DMA substrate. The sensitivity of R[TMA/9MA] was thus examined by perturbing E^*_{R4} by ± 1.25 kcal/mol, which is the inherent error in ΔH°_{R4}, using the Evans-Polanyi relation $E^*_{R4} = 17.5 + \Delta H^\circ_{R4}/2$. The activation energy E^*_{R5} of the exothermic methyl addition in R5 was not affected by error in ΔH°_{R5}. In both the upper and lower panel of Figure 1.26, log-log coordinates of R[TMA/9MA] vs. [910DMA]$_o$, and the lower panel, semi-log coordinates of R[TMA/9MA] vs. $1/\theta$, the model predictions of R[TMA/9MA] lie within ± 0.5 orders of magnitude of the experimental observations. The sensitivity analysis shows uncertainties of ± 0.6 orders of magnitude in model predictions of R[TMA/9MA]. Within its error limits, the model thus predicts R[TMA/9MA] in accord with the experiments.

1.8.5 Optimized Model

The preceding comparisons between model and experimental results, along with the sensitivity analysis, established that at low X and within its inherent error limits, our model was able to predict 910DMA thermolysis kinetics, product selectivities and product ratios in accord with observations. This is noteworthy because all the kinetic parameters employed in the model were derived from first principles and used without adjustments. The aforementioned comparisons between model and experiments also revealed how empirical adjustments of the original model parameters might permit the model to best-fit all experimental results for engineering purposes. This led to an "optimized" model, described in this section.

The best-fit of all experimental data for 910DMA thermolysis at T = 355°C with $[910DMA]_o$ = 0.82 mol/l arose by altering the original activation energies E^*_1, E^*_2, E^*_{-2} and E^*_3 by respective amounts of -1.2, +1.2, -1.2 and -1.2 kcal/mol, all of these changes being well within the inherent uncertainties of these parameters, respectively, ±4.4, ±2.4, ±2.4 and ±3.7 kcal/mol.

Figure 1.27 compares the substrate and product histories (upper panel) and product selectivities (lower panel) obtained from the optimized model to the experimental data for 910DMA, 9MA, TMA and CH4. In the upper panel of Figure 1.27, the optimized model, solid line, is seen to well predict the observed 910DMA decay, shown by asterisks, with decay half-lives t^* = 25000 s from the model versus 22000 s experimental. Also, the absolute amounts of 9MA, the short-dashed line versus the circles, and of TMA, the dotted line versus the squares, formed by the model are both lower than observed in the experiments. In the lower panel of Figure 1.27, a selectivity diagram, S(9MA) and S(TMA) from the model are respectively 1.7 and 1.4-fold too low compared to the average values of S(9MA) and S(TMA) observed from the experiments between 0.1 < X < 0.8; however, the ratio R[TMA/9MA] = 0.27 from the model is close to the experimental values of 0.24.

Figure 1.28 continues the comparison between the optimized model (lines) and experimental (circle) product histories and selectivities for DHDMA product. In the upper panel the model is seen to predict DHDMA to within the scatter of the experimental data, while in the lower panel, we see that, relative to the experiments,
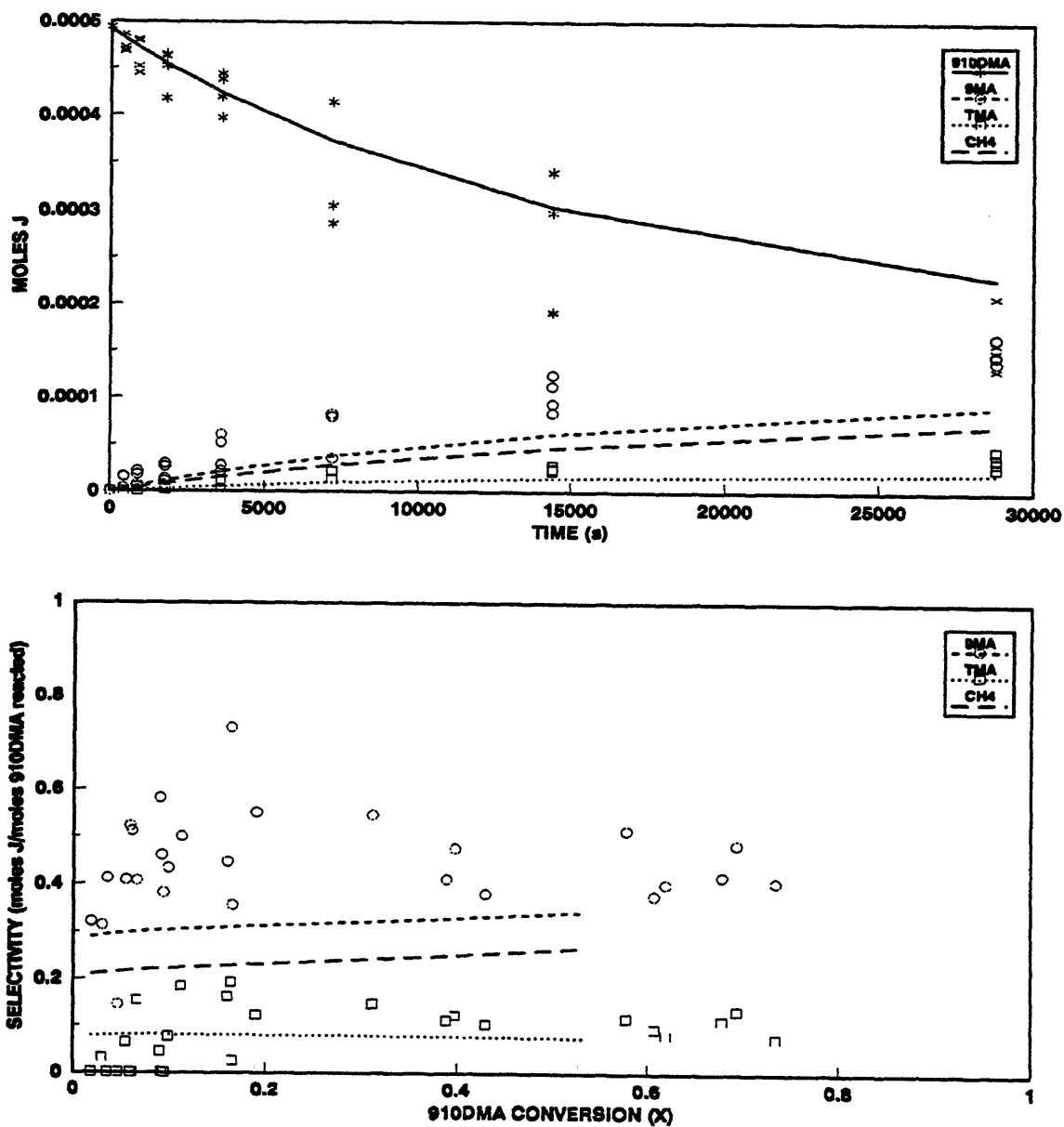
Figure 1.27: Product histories (top) and selectivity diagram (bottom) comparing optimized model (lines) to experimental data (symbols) for 910DMA, 9MA, TMA and CH4 at T = 355°C with $[910DMA]_o$ = 0.82 mol/l.

101
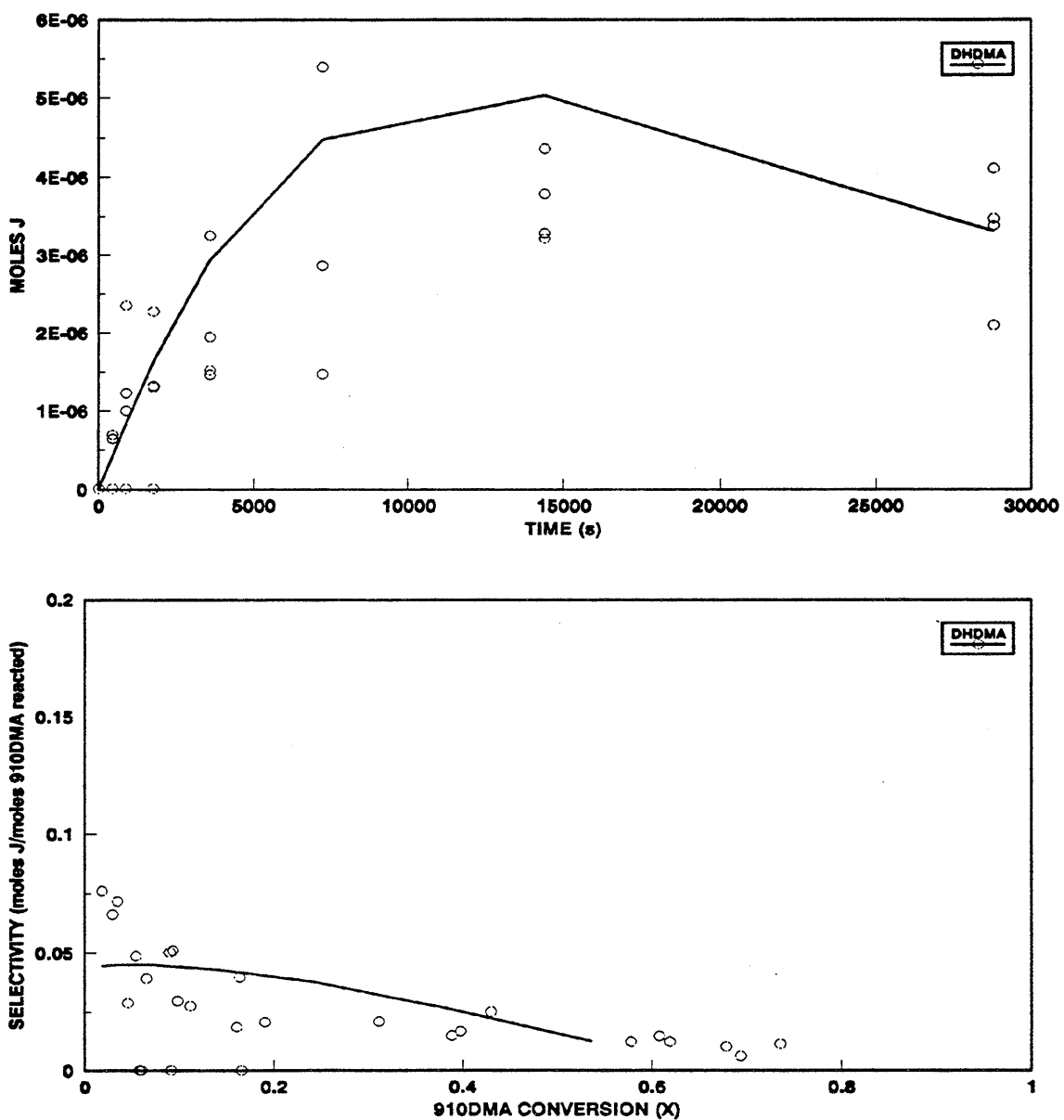
Figure 1.28: Product histories (top) and selectivity diagram (bottom) comparing optimized model results (lines) to experimental data (symbols) for DHDMA at T = 355°C with $[910DMA]_o$ = 0.82 mol/l.

S(DHDMA) from the model has the correct values at both low and high conversions, though the slope of the model line does not match that of the experimental data.

Figure 1.29 compares the model (lines) to the experimental data (solid circles) for heavies (DMAD, DMAHDMAD and HDMAD). In the upper panel, the model predicts heavies production approximately equal to that in the experiments at short times, but at long times produces more dimer than seen experimentally; the lower panel shows the dimer selectivity S(DMAD) ~ 0.27 calculated from the model is close to the experimental S(HVY) ~ 0.25 at low X < 0.1, but whereas the S(HVY) in the experiments decreases to ~0.10 with increasing conversion, X > 0.2, S(DMAD) from the model remains roughly constant at S(DMAD) ~ 0.27.

Figure 1.30 compares the product ratios R[DHDMA/9MA] and R[TMA/9MA] as functions of 910DMA conversion derived from the optimized model (lines) to those observed experimentally (symbols). In the upper panel the model predicts R[DHDMA/9MA] roughly equal to the experimental magnitudes at low and high conversions, but the slope of the line does not match that of the experimental data. In the lower panel model predicts R[TMA/9MA] approximately equal to that experimentally observed at all conversions 0 < X < 0.54.

It is finally instructive to compare the present Figure 1.27 containing optimized model results with the earlier Figure 1.22 that contained results from the original model at the same conditions of T = 355°C with $[910DMA]_o$ = 0.82 mol/l. In regard to both thermolysis kinetics and the selectivities of major products, the
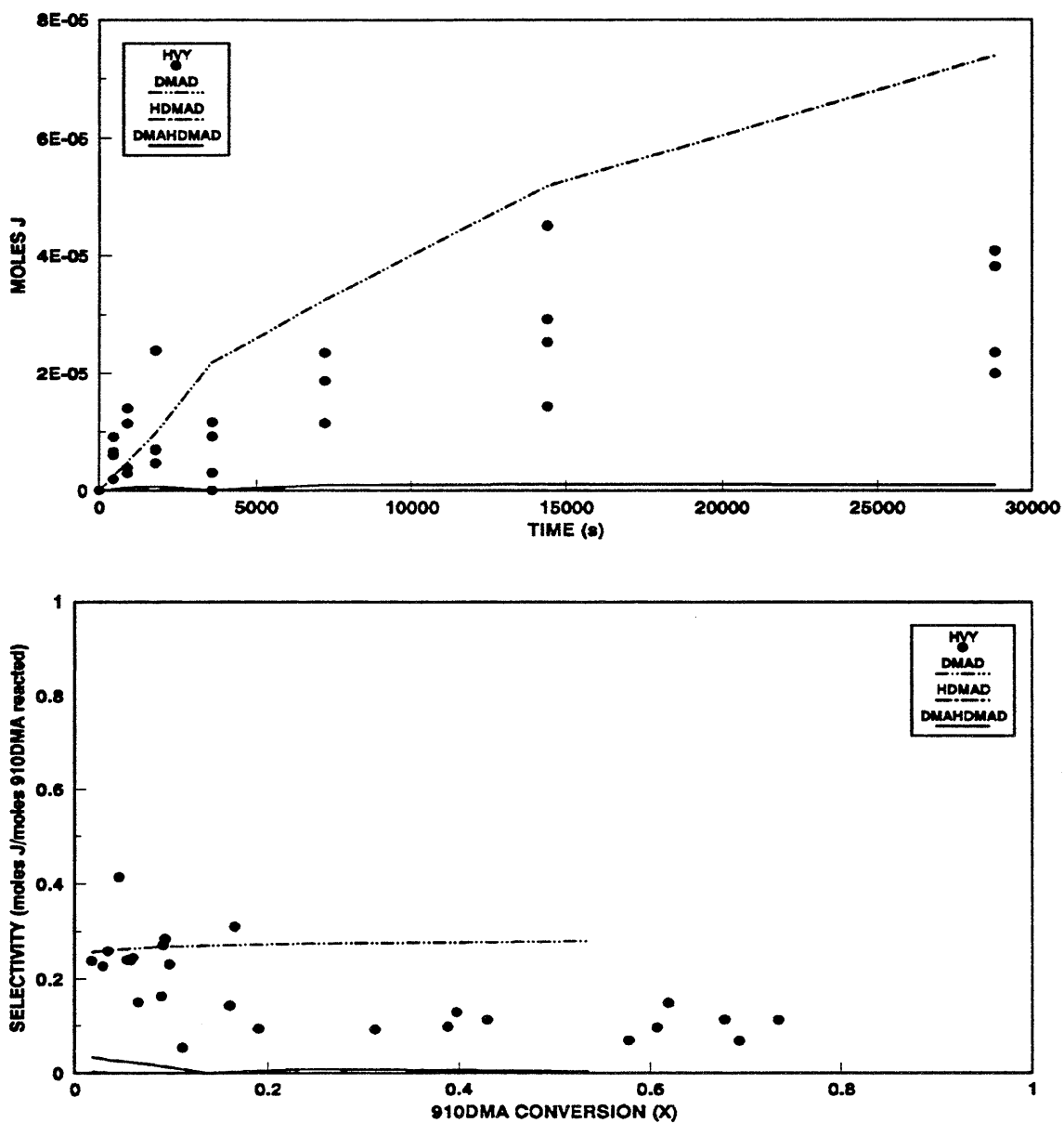
Figure 1.29: Product histories (top) and selectivity diagram (bottom) comparing optimized model results (lines) to experimental data (symbols) for heavies at T = 355°C with $[910DMA]_o$ = 0.82 mol/l.
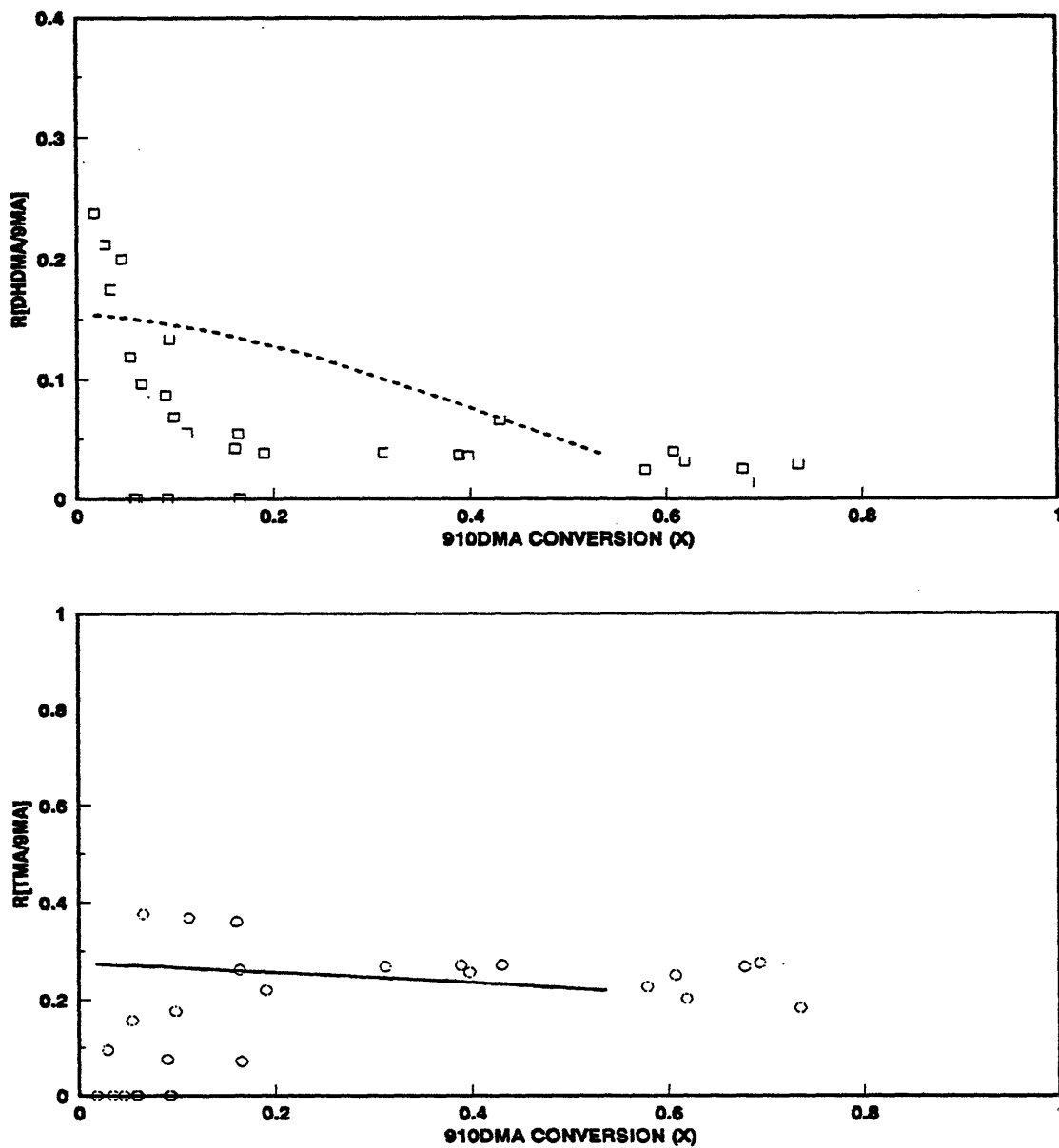
Figure 1.30: R[DHDMA/9MA] (top) and R[TMA/9MA] (bottom) comparing optimized model results (lines) to experimental data (symbols) at T = 355°C with [910DMA]$_o$ = 0.82 mol/l.

predictions of the optimized model are appreciably closer to the experimental

observations than those of the original model. It must be kept in mind, however, that

the differences between the activation parameters of the optimized and original

models, of order 1.2 kcal/mol, are small relative to the inherent uncertainties in

these parameters, of order 3.5 kcal/mol. Thus, although the optimized model effects

an appealing cosmetic improvement over the original model, of possible value in

engineering applications, the two models are statistically very similar. Substantive

scientific improvements in modelling thermolyses such as the present must await

better methods and more reliable data for deriving the kinetics of the underlying

elementary reactions.

1.9 Minor Methylated Products

The observed formations of dimethylanthracene isomers 1,9-, 1,10-, 2,9- and

3,9-DMA from 9MA and of methylanthracene isomers 1MA and 2MA from ANT

during 910DMA thermolysis at high severities invite interpretation by frontier orbital

theory, as examples of periselective methyl radical attack on the aromatic anthracene

nucleus.

1.9.1 Observed Product Ratios

Figure 1.31 and Figure 1.32, respectively, show the ratios of (2,9- + 3,9-

)DMA/(1,9- + 1,10-)DMA and of 2MA/1MA obtained as functions of 910DMA
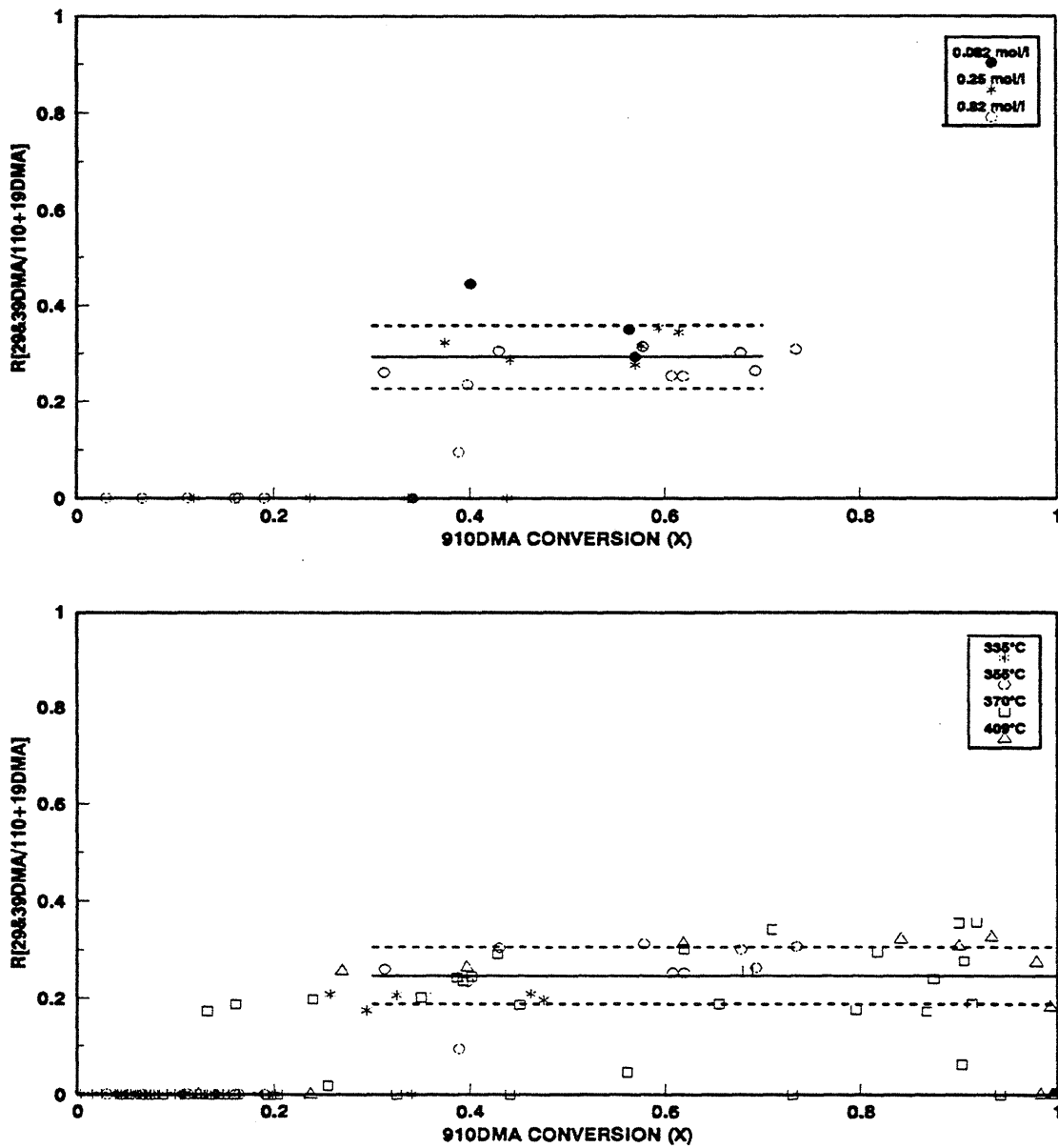
Figure 1.31: Ratio of moles (2,9-+3,9-)DMA to moles (1,9-+1,10-)DMA vs. 910DMA conversion(X) for varying $[910DMA]_o$ at T = 355°C(top) and for varying T with $[910DMA]_o$ = 0.82 mol/l(bottom).
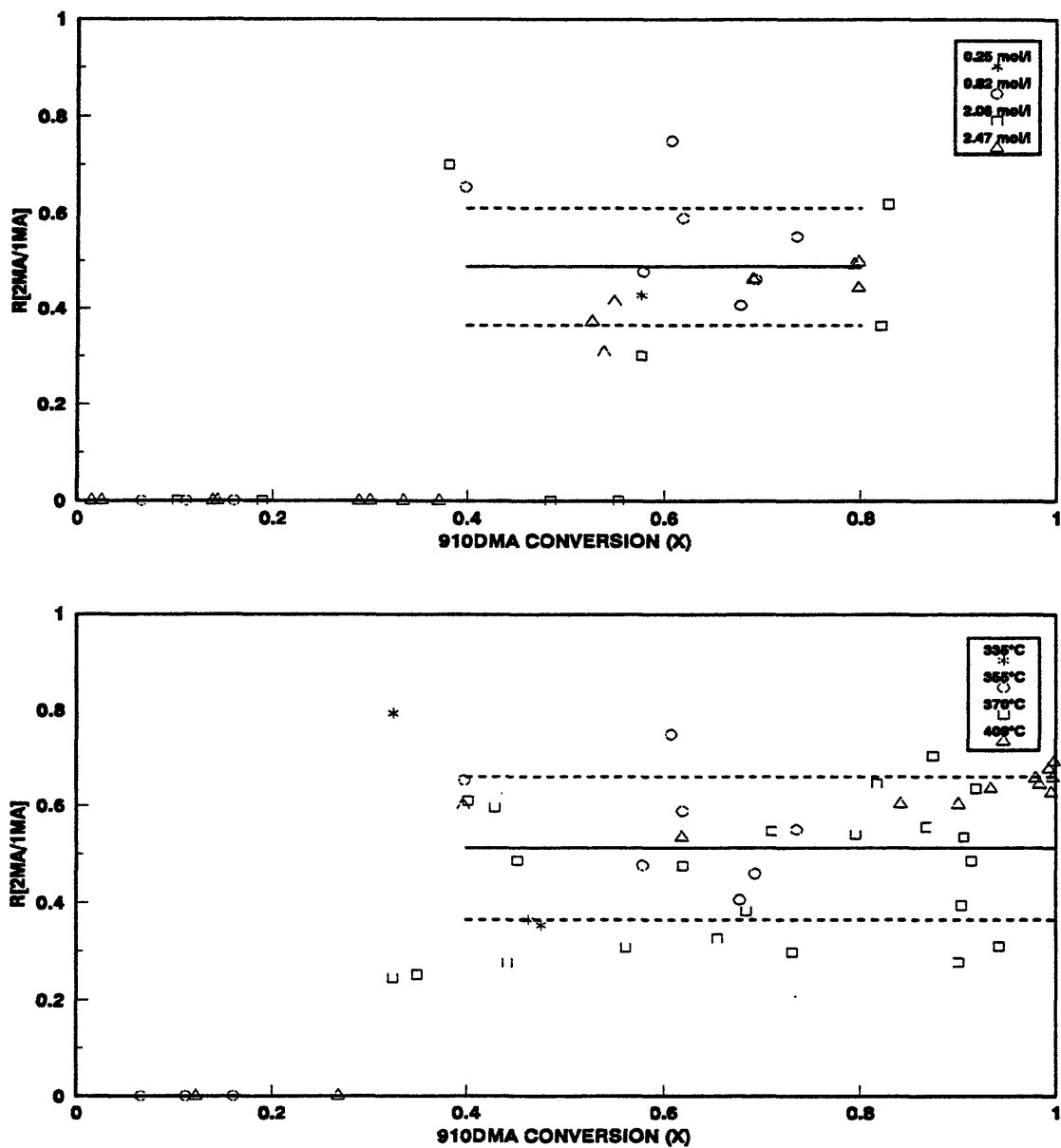
Figure 1.32: Ratio of moles 2MA/moles 1MA produced vs. 910DMA conversion for varying $[910DMA]_o$ at fixed T = 355°C(top) and varying T with fixed $[910DMA]_o$ = 0.82 mol/l(bottom).

conversion during the present experiments. The data in the upper and lower panels of these figures provide the ratios R[(2,9- + 3,9-)DMA/(1,9- + 1,10-)DMA] = 0.27 ± 0.07 for 0.3 < X < 0.98 and R[2MA/1MA] = 0.50 ± 0.15 for 0.4 < X < 0.99, with these ratios separately constant over the entire range of temperatures and initial substrate concentrations. The ratios R[(2,9- + 3,9-)DMA/(1,9- + 1,10-)DMA] and R[2MA/1MA] can both be viewed as the relative methyl affinities of positions 1 and 2 on the periphery of the anthracene ring, with methyl attack at position 2 less favored than at position 1 by a factor of 2 to 4.

1.9.2 Frontier Molecular Orbital Treatment using Hückel MOs

Theoretically, following Fukui (1975) for the interaction between the frontier orbitals of a radical and a molecule, the favorable, non-dimensional FMO stabilization energy E'(t) is given by the interaction between the singly-occupied MO (SOMO) of the CH3* radical and the highest-occupied and lowest-unoccupied MOs (HOMO and LUMO) of the ANT at position t:

$$E'(t) = \frac{c_{t,HO}^{2}}{-X_{HO}} + \frac{c_{t,LU}^{2}}{X_{LU}} = \frac{2c_{t,HO}^{2}}{-X_{HO}} \qquad (1.4)$$

where:

c_t =   MO coefficient at position t (Coulson and Streitwieser, 1960)

X_{HOorLU} =   nondimensionalized Hückel MO energy and the subscripts HO and LU refer to the frontier orbitals (Coulson and Streitwieser, 1960).
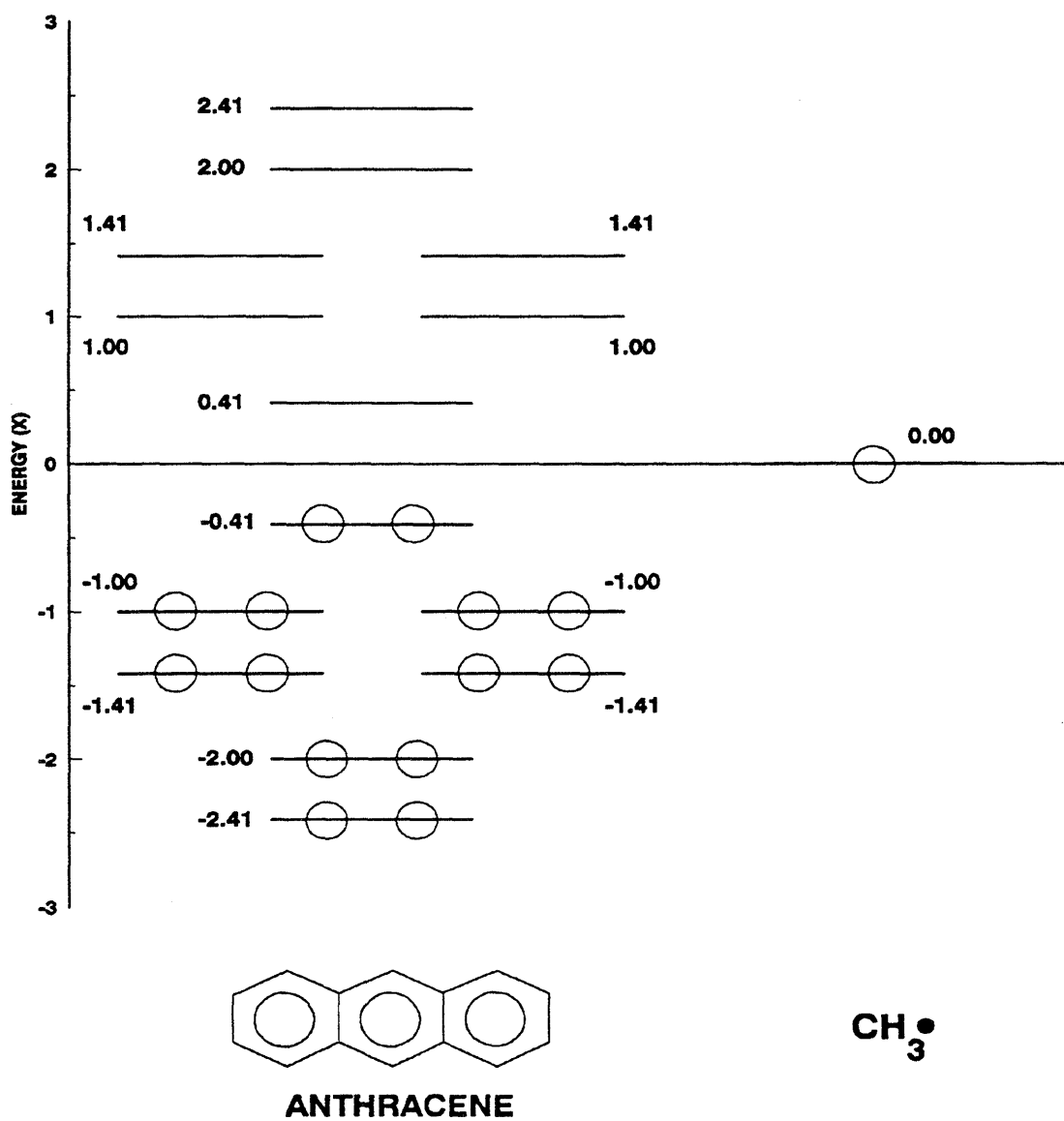
Figure 1.33: Frontier orbital interaction diagram for addition of methyl radical to anthracene using Hückel MOs.

Figure 1.33 is an orbital interaction diagram for the system comprising ANT and CH3*, with energy as ordinate and the molecules confined to separate columns. Equation (1.4) reduces to one term because, in the Hückel approximation, alterant hydrocarbons such as ANT have X_{LU} = $-X_{HO}$ and radicals such as CH3* have X_{SO} = 0. The dominant FMO interaction fixes the denominator of Equation (1.4), but since ANT possesses multiple reaction sites, the numerator can take several different values. The evaluation of these expressions is graphically depicted in Figure 1.34, a "periselectivity diagram" in which each position on the ANT ring framework is decorated with its HOMO coefficients, $C_{t(HO)}$, and then positions equivalent to the three distinct positions 9, 1, and 2, are shown interacting with the methyl radical SOMO, having $C_{u(SO)}$ = 1. For ANT positions t = (2,1,9), the respective E'(t) = (0.12, 0.23, 0.47); that is, FMO theory predicts CH3* attack favored in the order of positions 2 < 1 < 9. The predicted inequality between positions 2 and 1 of the ANT nucleus accords with the experimentally observed minor product ratios R[2MA/1MA] = 0.50 for methylation of ANT and R[(2,9- & 3,9-)DMA/(1,9- + 1,10-)DMA] ~ 0.27 for methylation of 9MA.

Finally, it is worth noting that in free-radical phenylation of ANT at T = 30°C, Dickerman (1973) reported relative phenyl affinities at position (2,1,9) in the ratio (0.28, 1.00, 14.32), that is, position 2 was less favored than position 1 by a factor of 3.5. The ratio of phenyl affinities at ANT positions 1 and 2 is of roughly the same
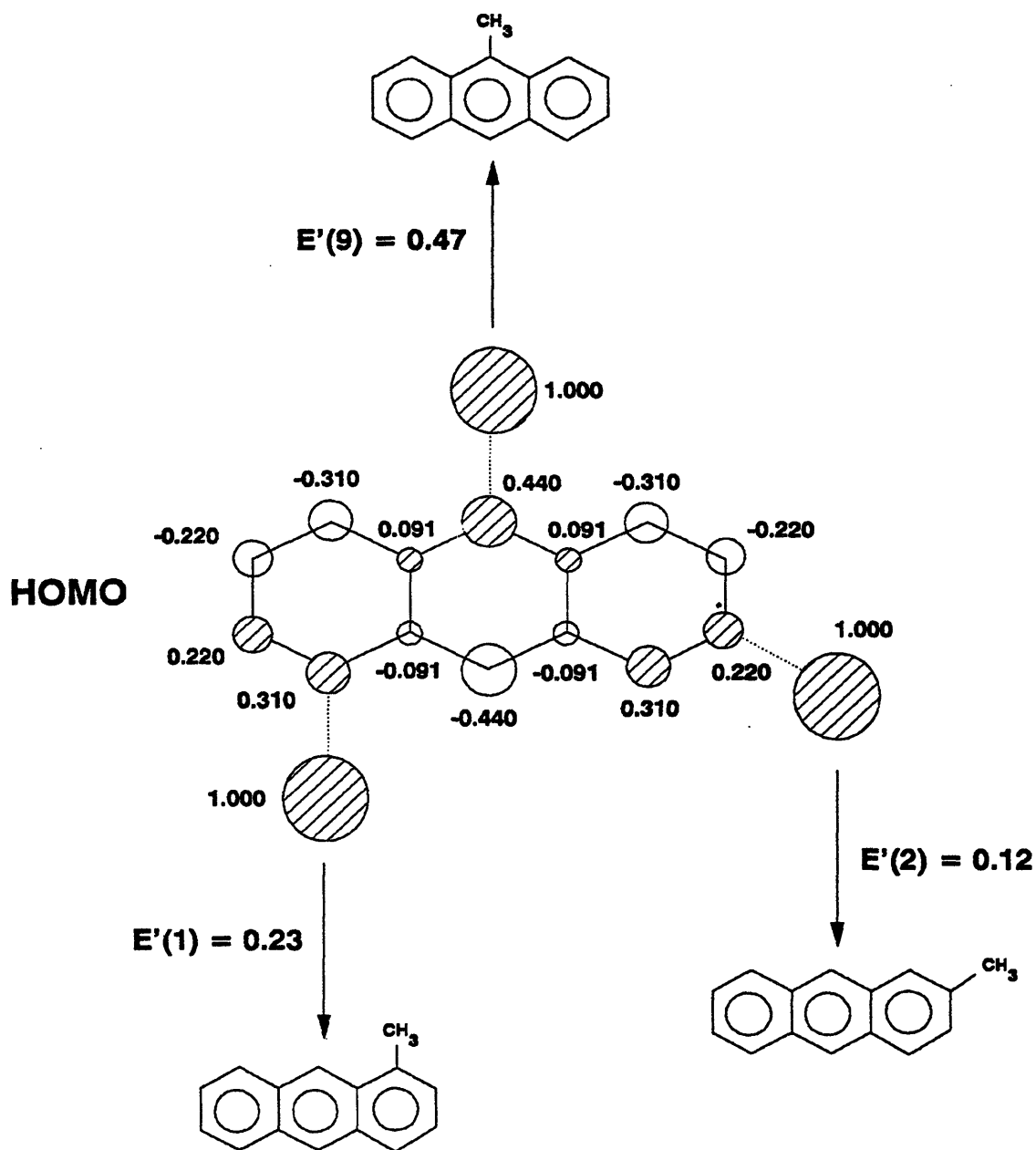
Figure 1.34: Estimation of isomer periselectivity by FMO theory using Hückel MOs for addition of methyl radical to anthracene to form 9-, 2- and 1-methylanthracene.

112

magnitude as the ratio of methyl affinities obtained from the minor methylated product ratios in the present experiments at much higher temperatures, T ~ 350°C.

1.10 Conclusions

1. 9,10-dimethylanthracene (910DMA) was thermolyzed at temperatures from 315 - 409°C initial concentrations from 0.082 - 2.47 mol/l, and fractional conversions, X, from 0.05 - 0.99. All gaseous and up to 19 liquid thermolysis products were assayed by GC and certain heavy products were also detected and identified by GC/MS. The experiments provided, for the first time, quantitative experimental information concerning 910DMA thermolysis kinetics and reaction pathways.

2. 910DMA thermolysis kinetics were found, overall, to be of 3/2 order in substrate with activation energy ~45 kcal/mol. Arrhenius parameters for the thermolysis were $[\log_{10} A, E^*] = [11.1 \pm 0.1, 44.6 \pm 2.1]$.

3. Three primary parallel pathways were identified for 910DMA thermolysis, namely: (P1) Hydrogenation, to 9,10-dihydro-9,10-dimethylanthracene (DHDMA), (P2) Demethylation to 9-methylanthracene (9MA), and (P3) Methylation, to 1,9,10-trimethylanthracene (and other isomers, TMA). This pathway triad secondarily operates upon the primary products, forming 9,10-dihydro-9-methylanthracene (DHMA), a host of dimethylanthracenes (1,9-, 1,10-, 2,9- and 3,9-isomers), and anthracene (ANT), as well as minor amounts of 9,10-dihydroanthracene and 1- and 2-methylanthracenes (1MA, 2MA).

113

4. A 10-elementary step free-radical mechanism was formulated for the early stages of 910DMA thermolysis. Initiation occurs by substrate disproportionation, to form respectively dehydrogenated and hydrogenated radicals, 910DMA* and HDMA*. Of these, HDMA* propagates the reaction. It can either abstract H from substrate or undergo β-scission, controlling the pathway ratio P1/P2. The methyl radical formed by β-scission of HDMA* can subsequently either abstract H from substrate or add to it, setting the pathway ratio P2/P3. Termination occurs by pure- and cross-combination of the 910DMA* and HDMA* radicals.

5. The preceding mechanism served as the platform for the quantitative numerical simulation and modelling of 910DMA thermolysis kinetics and product selectivities. Thermochemical and kinetic parameters required for the model were derived from first principles and the system of stiff differential conservation relations comprising the model was numerically solved with an appropriately stable computer code called ACUCHEM (Braun, 1988). A sensitivity analysis was performed to estimate the inherent uncertainties in model predictions. An optimized model was finally developed to best-fit the experimental observations. At T = 355°C with $[910DMA]_o$ = 0.82 mol/l, the optimized model was able to match within a factor of 2 the observed substrate decay half-life, the product selectivities of 9MA, DHDMA, TMA and dimers, and the product ratios R[DHDMA/9MA] and R[TMA/9MA].

6. The relative amounts of minor methylated products formed during 910DMA thermolyses were modelled as arising from periselective methyl radical

attack on an arene ring position, governed by the single-center FMO stabilization energy. This approach predicted the relative abundances of both the minor dimethylanthracene isomers (2,9- + 3,9-)DMA/(1,9- + 1,10-)DMA as well as the minor methylanthracene isomers 2MA/1MA.

Chapter 2.

Introduction

2.1 Objectives

The objective of this thesis is to build an experimental and theoretical framework that will help delineate the role of thermal reaction pathways in thermolysis and incineration of petroleum-, coal- and wood-derived materials, particularly their contribution to the structure and toxicity of the products that are ultimately emitted into the environment from such processes.

2.2 Background

The burning of natural resources, such as petroleum, coal and wood, has contributed to the environmental toxicity problem. Understanding how the thermal reaction pathways that operate during the thermolysis and incineration of fuel-derived materials contribute to the structure and toxicity of the products that are ultimately emitted into the environment could help control these processes and reduce the toxic emissions. One of the problems that arises in delineating these reaction pathways is the complexity of the starting materials. For this reason, simple model substrates have been chosen for this study to mimic the chemical moieties that participate in pyrolytic reactions. Emphasis is placed on multiply methylated acenes, that model the simplest petroleum asphaltenes as well as the alkyl-aromatic moieties in coal and wood. Multiply methylated anthracenes are also particularly interesting because they thermally decompose to intermediates that are potentially far more toxic than either the original substrate or the final product.

2.3 Previous Work

Several workers have previously studied the pyrolysis of aromatic and alkylaromatic molecules. Of these, the works particularly relevant to the present investigation include those of Schaefgen (1955), Badger (1965), Klein (1980), Pomerantz et al. (1980), Pope (1987), Wornat (1988), Savage and Klein (1987a,

1987b, 1988a, 1988b, 1989a, 1989b), Savage et al. (1985, 1989), and Smith and Savage (1991a&b).

Schaefgen (1955) studied the pyrolysis of p-xylene by vaporizing it through a hot quartz tube with products collected in a series of cooled traps. Pyrolysis temperatures ranged from 795-900°C, with residence times of 0.1-0.3 seconds. Gas products consisted principally of hydrogen and methane, with smaller amounts of ethylene and propylene. The main liquid product was toluene, but smaller amount of other aromatic hydrocarbons were also present. The chief solid products were qualitatively identified as 1,2-di-(p-tolyl)ethane, cyclo-di-p-xylylene, and cyclo-tri-p-xylylene. In addition to theses products, very small amounts of an alkyl substituted *trans*-stilbene (probably p,p'-dimethyl-*trans*-stilbene), and a substituted anthracene (probably 2,6-dimethylanthracene) were isolated as a mixture. Figure 2.1 lists possible reactions during the pyrolysis of p-xylene, as proposed by the author. Initiation involved scission of either a benzylic C-H bond or a phenyl C-C bond, with subsequent abstraction of a methyl or hydrogen from the p-xylene. Propagation and chain transfer steps involving these radicals led to the products methane, hydrogen, toluene, p-xylene and poly-p-xlylyene. Termination steps led to solid products.

Badger (1965) conducted a systematic study of the vapor phase pyrolytic behavior of a host of hydrocarbons, including n-decane, 2,2,4-trimethylpentane, propylene, 2-butene, benzene, naphthalene, anthracene, phenanthrene, pyrene, styrene, indene, toluene, ethylbenzene, propylbenzene, butylbenzene, tetralin, and

119
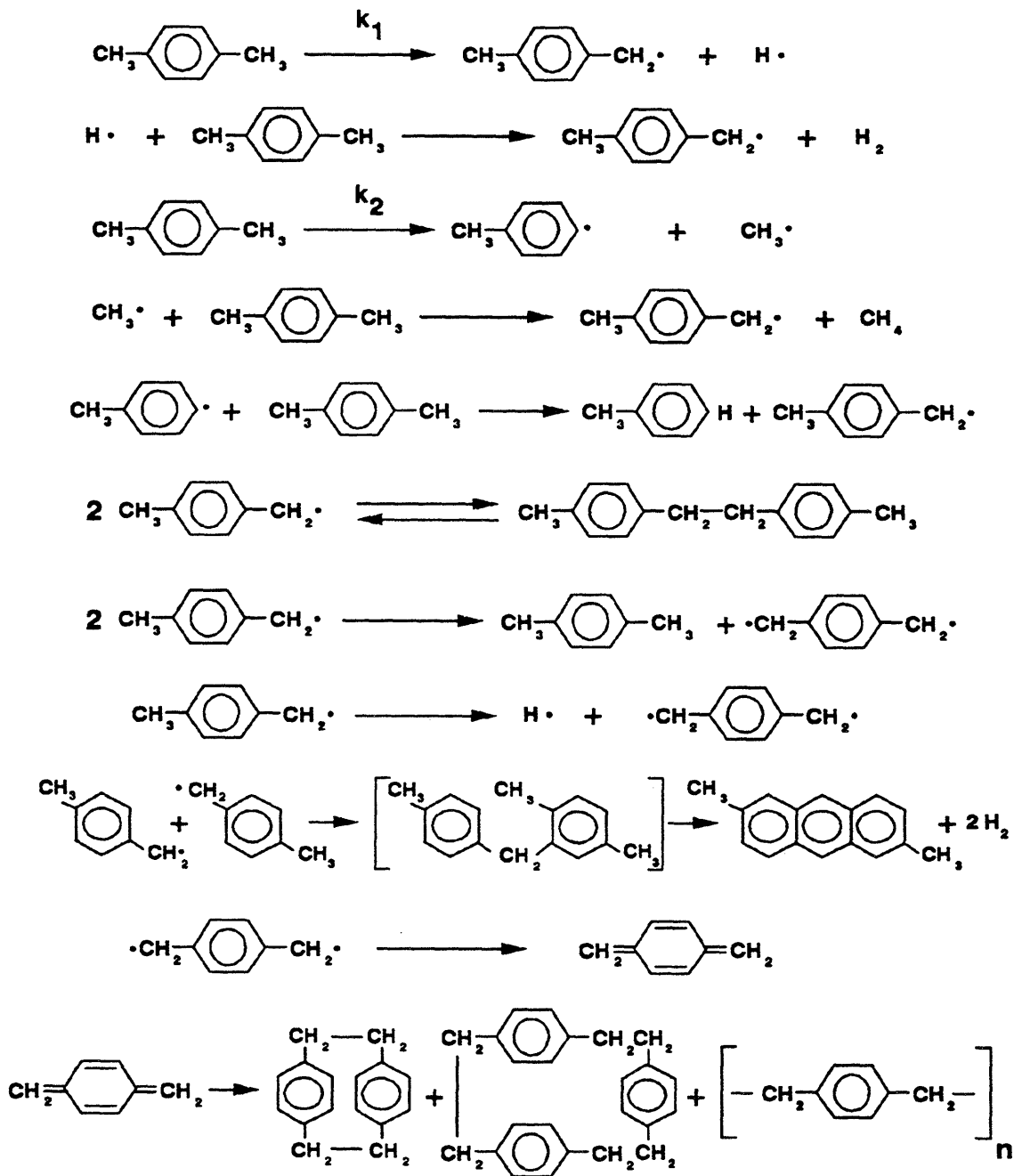
Figure 2.1: Reactions during *p*-xylene pyrolysis (Schaefgen 1955).

α,ω-diphenylalkanes. Pyrolysis temperatures ranged from 700°C (typically) to 1200°C, with residence times of up to 8 minutes. The major products of aromatic compound pyrolysis were bi-aryls, and the products of bi-aryl cyclodehydrogenation. Badger proposed the pyrolysis pathways shown in Figure 2.2 for naphthalene. These involve the initial abstraction of a hydrogen atom from the aromatic substrate to form aryl radicals, which combine to form various bi-aryls, that, in turn, dehydrogenate to condensed products. An increase in pyrolysis temperature increased conversion of the pyrolyzed species and favored production of the more highly condensed products of cyclodehydrogenation. Pyrolysis under very severe conditions (950°C for 30 min) led to formation of solid carbon and aliphatic gases, particularly CH_4 and C_2H_6. For a given reaction severity, alkylated aromatics achieved higher conversions and higher yields of solid carbon and aliphatic gases than their unalkylated counterparts, which was attributed to the weaker carbon-hydrogen and carbon-carbon bonds on the alkyl side chains that more readily underwent fission to form primary and secondary radicals. Table 2.1 lists the major products of alkylbenzene pyrolysis at 700°C from Badger and Spotswood (1960). The yields of higher polycyclic hydrocarbons varied with the nature of the aliphatic side chain. In butylbenzene, for example, there were
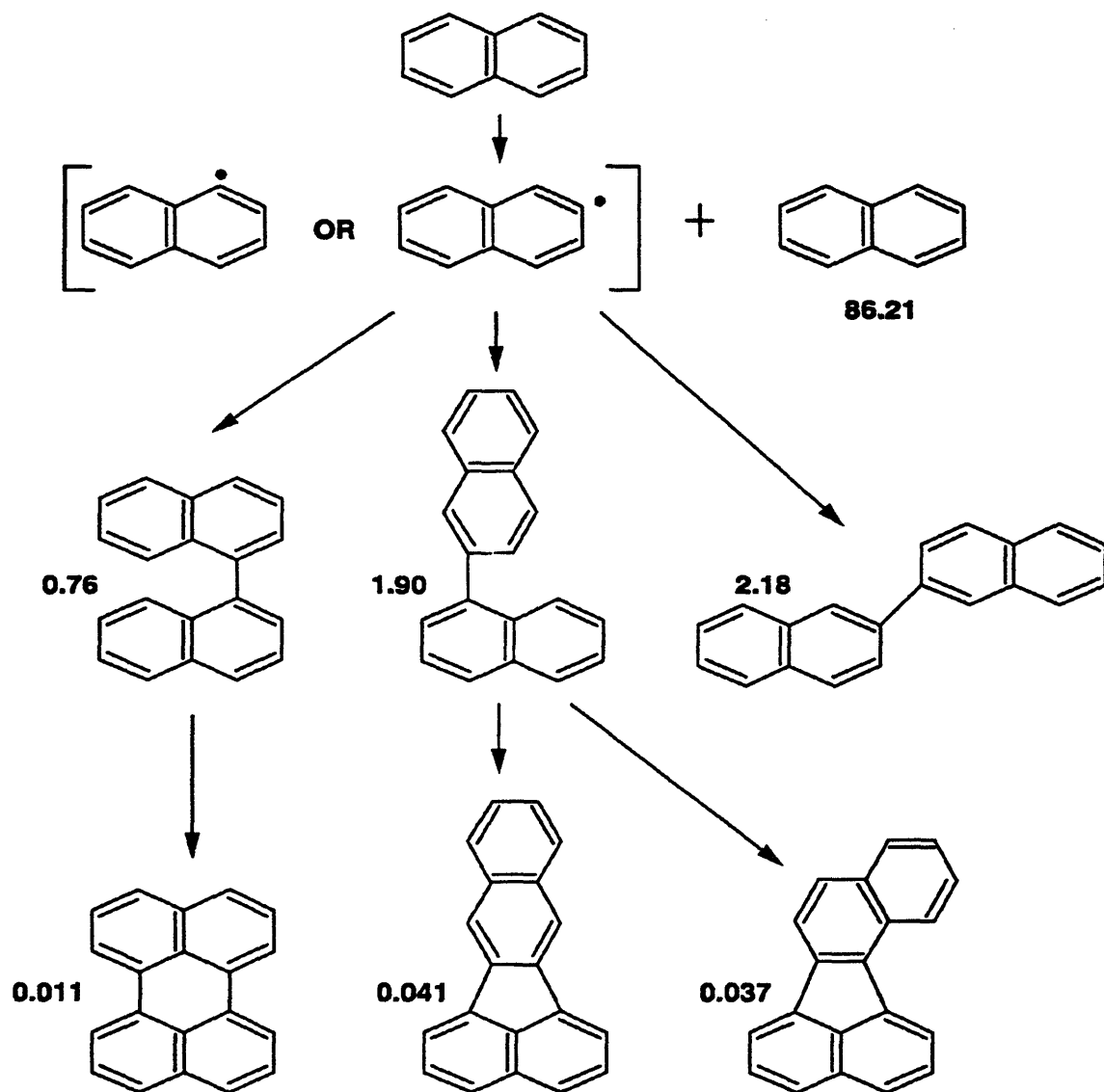
Figure 2.2: Badger (1965) pyrolysis pathway for naphthalene at 700°C (boldface numbers besides product structure indicate weight percentages in tar).

122

Table 2.1

MAJOR PRODUCTS FROM THE PYROLYSIS
OF ALKYLBENZENES AT 700°C[1]

PRODUCT	TOLUENE	ETHYL-BENZENE	PROPYL-BENZENE	BUTYL-BENZENE
		YIELD (% OF TAR FORMED)		
ANTHRACENE	0.009	0.88	0.73	0.93
BENZ[A]ANTHRACENE	0.014	0.46	0.62	0.19
BENZENE	2.54	34.8	14.6	31.1
1,2-BENZOFLUORENE	0.007	0.42	0.85	0.57
2,3-BENZOFLUORENE	0.017	0.79	1.79	0.96
BENZO[A]PYRENE	0.002	0.065	0.17	0.92
CHRYSENE	0.03	2.20	0.96	1.82
BIBENZYL	1.00	2.20	3.20	0.37
4,4'-DIMETHYLBIPHENYL	0.99			
2,2'-BINAPHTHYL		0.45	0.48	0.76
BIPHENYL	0.27	3.11	1.61	2.80
ETHYLBENZENE		0.76	0.75	0.24
FLUORANTHENE	trace	0.34	0.67	1.07
INDENE		0.41	1.31	1.10
NAPHTHALENE	0.042	4.54	3.43	21.0
PHENANTHRENE	0.12	14.3	14.0	13.5
2-PHENYLNAPHTHALENE		0.47	1.20	0.13
PYRENE	trace	0.33	0.21	2.0
STYRENE	0.11	9.9	14.7	2.7
TOLUENE	93.5	21.6	33.0	7.5

[1] adapted from Badger (1965)

four carbon-carbon bonds that would be expected to break as shown by Equation

(2.1):

$$C_6H_5CH_2CH_2CH_2CH_3 \rightarrow \begin{array}{l} \rightarrow C_6H_5\bullet + CH_3CH_2CH_2CH_2\bullet \\ \rightarrow C_6H_5CH_2\bullet + CH_3CH_2CH_2\bullet \\ \\ \rightarrow C_6H_5CH_2CH_2\bullet + CH_3CH_2\bullet \\ \rightarrow C_6H_5CH_2CH_2CH_2\bullet + CH_3\bullet \end{array} \qquad (2.1)$$
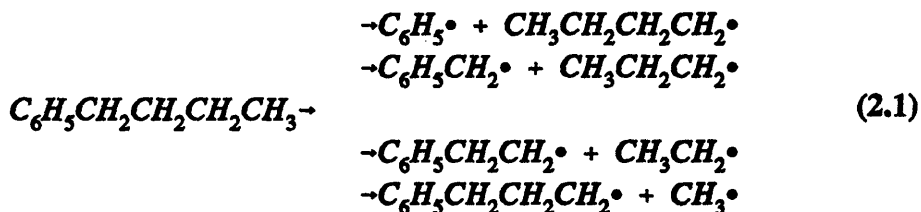
The alkyl radicals would lose hydrogen to give alkenes; the phenethyl radical would

give styrene, and the phenylpropyl radical would possibly lead to some methylstyrene.

The various radicals could also abstract hydrogen; especially from the α-carbon atom

of butylbenzene, the phenyl radical would give benzene, and the phenylmethyl radical

would give toluene. The heavy products were formed by two radicals combining

followed by "cyclodehydrogenation"; such as two benzyl radicals interacting to give

bibenzyl which then cyclodehydrogenated to give phenanthrene. Naphthalene was

formed by the cyclization of radicals formed by dehydrogenation of the alkyl side

chain.

Klein (1981) studied model pathways in lignin thermolysis. Lignin, a natural

phenolic polymer, is a major component of biomass, accounting for up to a third of

wood by weight. Klein selected 20 model compound pyrolysis substrates to mimic

the reactive functional groups present in whole-lignin. The most significant model

compounds were phenethyl phenyl ether (PPE), which depicted the most prevalent

lignin interunit linkage; guaiacol, model of the predominant aromatic methoxy

substituents; and saliganol and cinnamyl alcohol, models of important propanoid side chains. Reaction conditions and major products are shown in Figure 2.3 for two model compounds. Detailed pathway and kinetic analyses and determination of reaction Arrhenius parameters provided mechanistic insights into the model compound pyrolyses. Several pericyclic reaction mechanisms, not mentioned previously in the lignin pyrolysis literature, were suggested. In particular, Figure 2.3 shows how PPE likely pyrolyses via a concerted retro-ene mechanism, whereas guaiacol may eliminate methane by concerted group transfers.

Pomerantz et al. (1983) pyrolyzed 9-methylanthracene (9MA) at 400°C with concentrations of 0.16 and 0.20 mol/l for 3 and 24 hours as part of his work on the thermal extrusion of one-carbon species from molecules and free radicals. Anthracene was the major decomposition product with other products including 1-methylanthracene (1MA), 2-methylanthracene (2MA), and 9,10-dihydroanthracene. They suggested that the 1MA and 2MA were formed by some type of intermolecular process since when the pressure in the reaction was doubled, the ratio of 9MA:(1MA+2MA) changed from about 1:1 to about 1:5.

Pope (1987) studied 9,10-dimethylanthracene (DMA) decompositions over a temperature range of 300-380°C, concentration range of 2.0-3.8 mol/l and reaction times of 900-10800 seconds as part of his work on the kinetics and mechanism of thermal hydrogen transfer reactions between aromatic and hydroaromatic hydrocarbons. The principal liquid phase products were the demethylation product

125

**PHENETHYL
PHENYL ETHER**

T = 300-550°C

1-240 MINUTES

GUAIACOL

T = 250-535°C

2-10 MINUTES
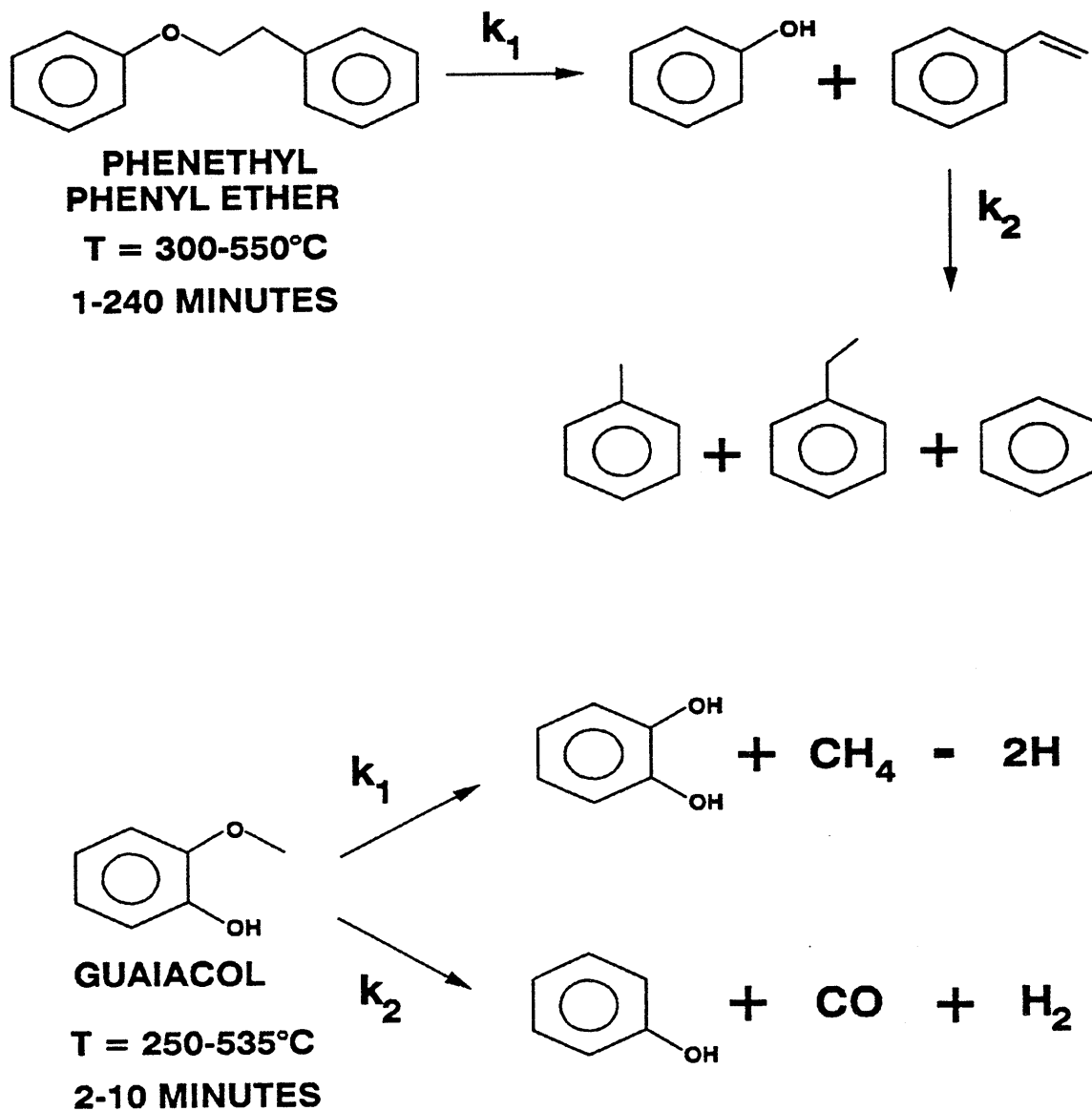
Figure 2.3: Klein's (1981) pathways for thermolysis of phenethyl phenyl ether and guaiacol.

9-methylanthracene (9MA), the methylation product trimethylanthracene (TMA), and

the hydrogenation products cis- and trans-9,10-dihydrodimethylanthracene (DHDMA)

with an apparent second order (in DMA) rate constant for DMA decomposition, log

k_{DMA} = (9.8 ± 1.4) - (42.7 ±4.0)/θ. Pope proposed a 9-step elementary free radical

mechanism for the decomposition of DMA, with initiation by molecular

disproportionation of DMA, and termination by radical recombination that was

consistent with the observed products, rate expressions, and features of the

concentration histories. Kinetics parameters for each elementary reaction were used

in the conservation equations for the molecular and radical species to calculate their

concentration histories, starting from known experimental initial conditions.

Arrhenius relations for the elementary reactions were estimated "a priori" from

analogous reactions by assuming Evans-Polanyi relationships between the enthalpy

of reaction and the activation energy, and by adjusting the pre-exponential factors

according to the reaction path degeneracy. Model results were able to simulate the

main features of the experimental observations.

The pyrolysis products of coal were determined by Wornat (1988) as part of

the effort on Health Effects of Fossil Fuels (Sarofim, Longwell, and Wornat; 1987).

Wornat pyrolyzed 44-53 μm particles of Pittsburgh Seam high-volatile bituminous

coal between temperatures of 1125-1473 K and holding times of 0.25-0.75 seconds.

Since PACs from coal pyrolysis contain so many individual species, many of them

isomeric, it was not always feasible to identify and quantify each species. Instead,

Wornat described the compositional changes of the PACs in terms of two structural characteristics: the degree of functional group substitution and the aromatic ring number distribution. In general, among these coal-derived samples, PACs with functional group substituents decayed much more rapidly than did their unsubstituted counterparts. Identification of the functional groups present at various stages of PAC conversion suggested the following order of PAC reactivity:

hydroxy- and/or amino-substituted PAC > alkyl- and ether-substituted PAC

> unsubstituted PAC and PAC with carbonyl groups.

Ring number analyses on the substituted and unsubstituted PAC fractions of the coal pyrolysis samples revealed that for each ring number group, the substituted PAC underwent more drastic depletion than the unsubstituted PAC as pyrolysis conditions became more severe. Wornat noted the importance of unsubstituted PACs, in regard to both their dominance at high temperatures and their high toxicity, and also showed that a host of substituted PACs and hetero-atom containing PACs were produced at the lower temperatures, especially during the early stages of pyrolysis. Figure 2.4 shows representative coal pyrolysis data at three temperatures.

Savage et al. (1985) and Savage and Klein (1987b, 1988a, 1988b, 1989a) studied asphaltene reaction pathways and presented the results in a series of five papers that include: 1) thermolysis; 2) pyrolysis of n-pentadecylbenzene; 3) effect of reaction environment; 4) pyrolysis of n-tridecylcyclohexane and 2-ethyltetralin; and 5) chemical and mathematical modeling. The first paper, thermolysis, identified
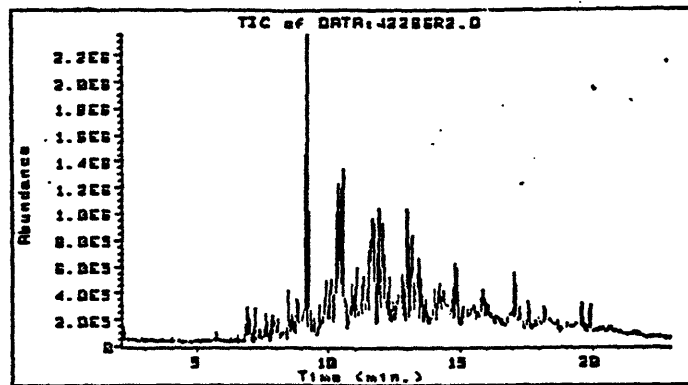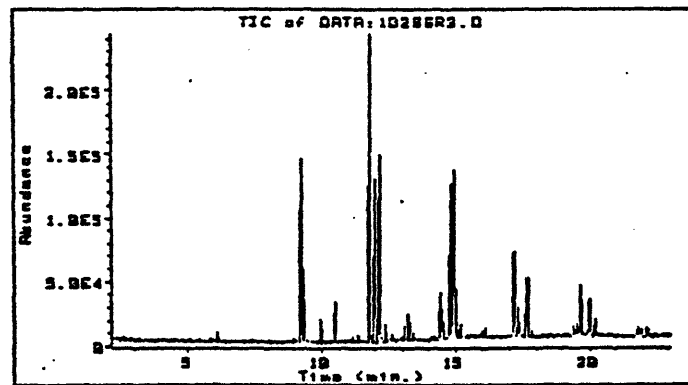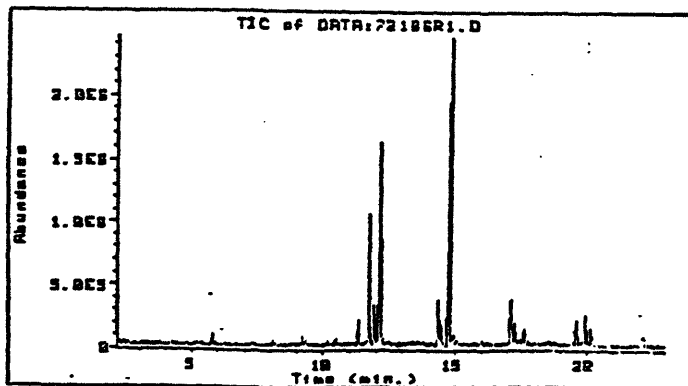
Figure 2.4: GC traces of Wornat's coal pyrolysis data at 1100, 1273 and 1390 K.

products fractions of petroleum asphaltenes pyrolyzed at temperatures ranging from 350 to 565°C for times from 5 to 150 minutes. Asphaltene pyrolysis included primary reactions to its aromatic core, maltene, and gas product fractions. Components in each of these product fractions underwent secondary degradation to lighter products, gas, and char. The third paper dealt with the effect of reaction environment. Asphaltenes were subjected to pyrolysis and hydropyrolysis, both neat and in solvents, and catalytic hydroprocessing. Thermal reactions in the absence of an effective hydrogen donor lead to high asphaltene conversions and high yields of coke. In the presence to a hydrogen donor, asphaltene was converted more slowly but also more selectively to maltenes, with the ultimate yield of coke expected to be comparable to that from neat pyrolysis. Addition of a hydrotreating catalyst produced intermediate reaction rates and maintained high selectivities to maltenes, even at high conversions. The final paper combined chemical and mathematical modelling for the pyrolysis of a generic, fully hydrocarbon asphaltene by combining model-compound-deduced thermolysis kinetics and pathways with asphaltene structural information.

The second paper in the series dealt with the pyrolysis of n-pentadecylbenzene (PDB), a representative model of the alkyl-aromatic moieties likely present in asphaltenes. The reactions, pathways, kinetics and mechanisms were probed via the thermolysis at temperatures from 375 to 450°C with batch holding times from 10 to 180 minutes with initial PDB concentrations from 0.0043 to 2.3 mol/l. The primary

reaction pathway led to two major product pairs, toluene plus 1-tetradecane and styrene plus n-tridecane, respectively. A complete series of n-alkanes, α-olefins, phenylalkanes, and phenylolefins was also formed in lesser yields. The top panel of Figure 2.5 shows the PDB thermolysis pathways. PDB thermolysis was demonstrably first-order (1.08), and associated Arrhenius parameter of [E* (kcal/mol), log A (s^{-1})] = [55.45, 14.04] were determined. Three possible PDB mechanisms were proposed: 1) a six-center, intramolecular retro-ene reaction between the ring and the alkyl chain, 2) a four-center, intramolecular reaction of the alkyl chain, or 3) an intermolecular free-radical reaction, as shown on the bottom of Figure 2.5. Reaction of tetralin-d_{12} indicated that the operative PDB thermolysis mechanism was entirely free-radical. This free-radical mechanism in conjunction with possible combinations of bond energies and reaction kinetics permitted rationalization of the observed product spectrum.

The fourth paper dealt with the pyrolysis of n-tridecylcyclohexane (TDC) and 2-ethyltetralin (2ET), which modeled thermal reactions of the alkylnaphthenic and alkylhydroaromatic moieties likely present in petroleum asphaltenes, at temperatures from 375 to 450°C with batch holding times from 10 to 180 minutes. TDC pyrolyzed to the major product pairs cyclohexane plus 1-tridecane and methylenecyclohexane plus n-dodecane with cyclohexane, methylcyclohexane, and n-tridecane also formed as minor products. 2ET pyrolyzed to 1,2-dihydronaphthalene (dialin) and 2-
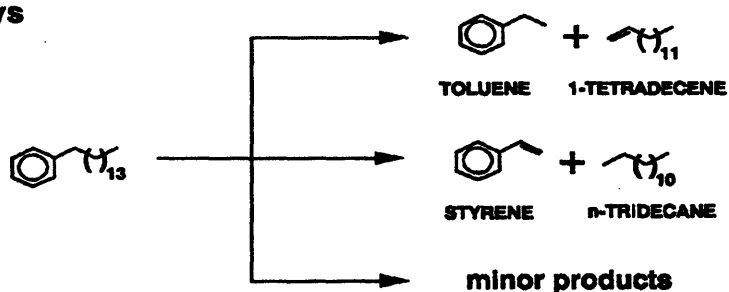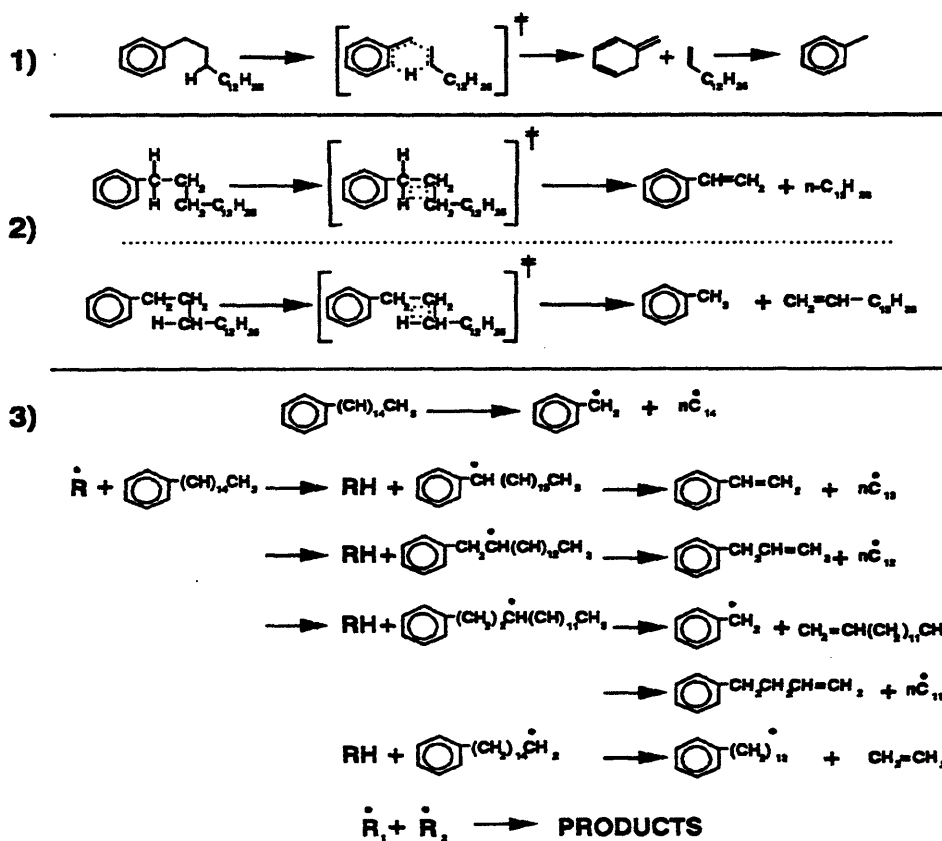
Figure 2.5: *n*-pentadecylbenene (PDB) thermolysis pathways (A) and three possible mechanisms (B), adapted from Savage and Klein (1987b).

ethyldialins as major primary products. Secondary reactions of these primary products led to naphthalene, tetralin, and 2-ethylnaphthalene, as shown in Figure 2.6. The pyrolysis of both compounds were consistent with free-radical reaction mechanisms in which the dominant reactions resulted in dealkylation near or at the ring, the opening of which being minor. The saturated ring did dehydrogenate, however, and significant yields of aromatics (e.g., 30% naphthalene from 2ET) were observed at the more severe conditions, indicating that once formed, aromatic rings did not hydrogenate under these reaction conditions.

Savage and Klein (1987a) added tetralin-d_{12} to the liquid-phase thermolyses of 1-phenyldodecane (PDD) at 400°C with batch holding times of 30 to 240 minutes to discriminate between molecular mechanisms and stepwise free-radical mechanisms. The incorporation of a deuterium label into the major pyrolysis product, toluene, proved that free-radical steps were kinetically significant since an intramolecular mechanism would have proceeded independently of the added tetralin and yielded only protonated products. Both thermolysis mechanisms are shown in Figure 2.7. The results of these pyrolyses of PDD in tetralin-d_{12} when plotted as deuterium incorporated (DI) vs. 1/R demonstrated that at infinite dilution of PDD in tetralin-d_{12} (R→∞), all toluene was formed with a deuterium label (DI→1.0), suggesting that PDD thermolysis was entirely free-radical, and the molecular mechanism was not kinetically significant under these conditions. This free-radical pathway also accounted for formation of other major products; styrene, n-decane and 1-undecene.

**RING-OPENING
PRODUCTS**

2-ETHYLDIALIN

2-ETHYLNAPHTHALENE

DIALIN

NAPHTHALENE
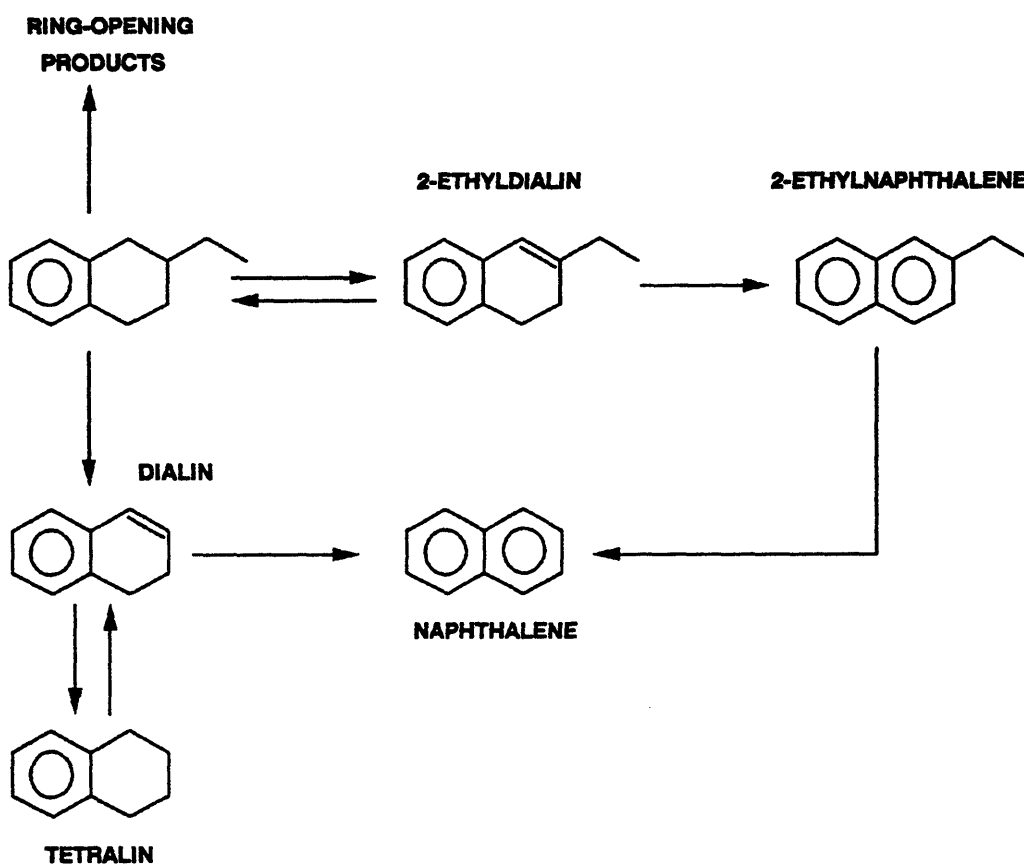
TETRALIN

Figure 2.6: 2-ethyltetralin (2ET) thermolysis pathways (adapted from Savage and Klein, 1988b).

134

MOLECULAR MECHANISM
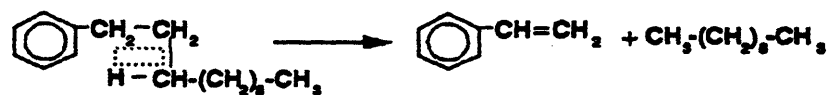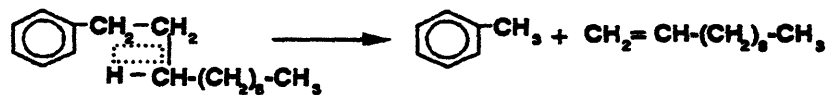
FREE-RADICAL MECHANISM
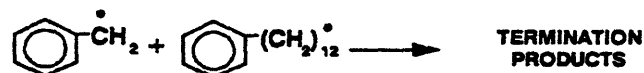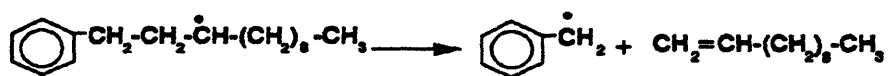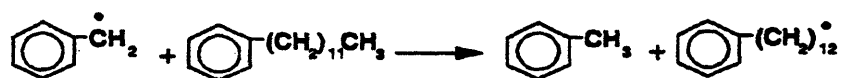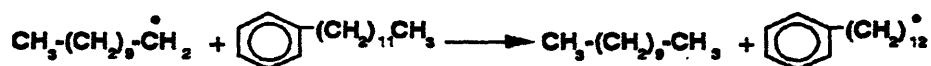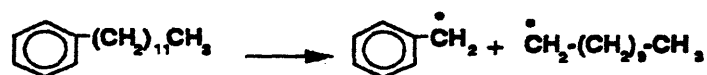
Figure 2.7: 1-phenyldodecane (PDD) thermolysis mechanisms: molecular vs. free radical (adapted from Savage and Klein, 1987a).

Savage and Klein (1989b) used the pyrolysis of *n*-pentadecylbenzene (PDB) to develop a general methodology for the formulation of an analytical rate expression for the reaction of a single substrate to a complex product spectrum. The methodology organized reaction products into pairs that form from closed-chain sequences, and allowed chain transfer by both μ and β radicals to determine quantitative product selectivities. Initiation steps and termination by all possible combinations of μ and β radicals provided quantitative reaction rates. These steps are illustrated in Figure 2.8 where μ and β denote substrate-derived radicals that respectively decomposed unimolecularly and reacted bimolecularly in the propagation steps that transformed R in to the stable products βH and Q. PDB pyrolysis was modeled as three coupled parallel chains that led to the product pairs toluene plus 1-tetradecene, styrene plus tridecane, and minor products, as shown in the pathway on the top of Figure 2.5. Estimates of the rate constants for each elementary step allowed comparison with experimental data on the concentration dependence of a pseudo-first-order rate constant and product selectivities. A critical reactant concentration R_c served as a criterion for determining the significance of chain transfer by μ radicals. At $R > R_c$ these chain transfer steps dramatically influenced product selectivities and the global first-order rate constant. Qualitative agreement between the model and the experiments was always good, and quantitative agreement was excellent at high PDB concentrations.

$$R \rightarrow 2\beta \quad (\alpha_1) \quad \textit{Initiation}$$

$$\beta_1 + R \rightarrow \beta_1 H + \mu_1 \quad (k_{11})$$

$$\mu_1 \rightarrow \beta_1 + Q_1 \quad (k_{\mu_1})$$

Chain Transfer   *Chain Transfer*

$\beta_1 + R \rightarrow \beta_1 H + \mu_2 \quad (k_{12})$ $\beta_2 + R \rightarrow \beta_2 H + \mu_1 \quad (k_{21})$

$\mu_1 + R \rightarrow R + \mu_2 \quad (k_{12}')$ $\mu_2 + R \rightarrow R + \mu_1 \quad (k_{21}')$

$$\beta_2 + R \rightarrow \beta_2 H + \mu_2 \quad (k_{22})$$

$$\mu_2 \rightarrow \beta_2 + Q_2 \quad (k_{\mu_2})$$

$\beta_2 + R \rightarrow \beta_2 H + \mu_3 \quad (k_{23})$ $\beta_3 + R \rightarrow \beta_3 H + \mu_2 \quad (k_{32})$

$\mu_2 + R \rightarrow R + \mu_3 \quad (k_{23}')$ $\mu_3 + R \rightarrow R + \mu_2 \quad (k_{32}')$

$$\beta_3 + R \rightarrow \beta_3 H + \mu_3 \quad (k_{33})$$

$$\mu_3 \rightarrow \beta_3 + Q_3 \quad (k_{\mu_3})$$

$\beta_3 + R \rightarrow \beta_3 H + \mu_1 \quad (k_{31})$ $\beta_1 + R \rightarrow \beta_1 H + \mu_3 \quad (k_{13})$

$\mu_3 + R \rightarrow R + \mu_1 \quad (k_{31}')$ $\mu_1 + R \rightarrow R + \mu_3 \quad (k_{13}')$

Termination

$$\beta_i + \beta_j \rightarrow \quad (\omega_{ij})$$

$$\mu_i + \beta_j \rightarrow \quad (\omega_{ij}')$$

$$\mu_i + \mu_j \rightarrow \quad (\omega_{ij}'')$$

β_1	*Benzyl radical*	μ_1	γ-*PBD radical*
β_2	*Tridecyl radical*	μ_2	α-*PBD radical*
β_3	*Other non-PBD radicals*	μ_3	*Other PBD radicals*
$\beta_1 H$	*Toluene*	Q_1	*1-Tetradecane*
$\beta_2 H$	*Tridecane*	Q_2	*Styrene*
$\beta_3 H$	*Minor products*	Q_3	*Minor products*

Figure 2.8:   Free-radical mechanism for pentadecylbenzene (PDB) pyrolysis.

Savage et al. (1989) pyrolyzed 1-dodecylpyrene (DDP) at 375-425°C with batch holding times of 10-180 minutes. Major products at low conversions were 1-methylpyrene, 1-undecene, 1-ethylpyrene and n-decane. At higher conversions, pyrene and n-dodecane were the major products. Minor products included a series of n-alkanes, α-olefins, and alkyl-substituted pyrenes, as shown in Figure 2.9. The variations of the products' molar yields with substrate conversion suggested that the reaction pathways operative at low DDP conversions were analogous to those observed in alkylbenzene pyrolysis, pathway 1 in Figure 2.9. However, a different pathway, pathway 2 in Figure 2.9, involving facile and apparently autocatalytic cleavage of the strong aryl-alkyl C-C bond was dominant at moderate and high DDP conversions. The kinetics of DDP disappearance was also consistent with autocatalytic decomposition. These results suggested that thermal cleavage of aryl-alkyl C-C bonds in heavy hydrocarbon resources such as petroleum residua, asphaltenes, and coal might be more prevalent than previously thought.

Smith and Savage (1991a) continued the study by pyrolyzing 1-dodecylpyrene (DDP) at concentrations between 0.0007 and 0.47 mol/l in a benzene diluent at temperatures between 375 to 450°C with batch holding times from 10 to 1050 minutes. They reported product yields and selectivities as functions of both conversion and initial concentration. DDP pyrolysis at low conversion (<25%) and low initial concentrations (<0.14 M) yielded primary products analogous to those observed for alkylbenzene pyrolysis, whereas experiments at higher conversions and
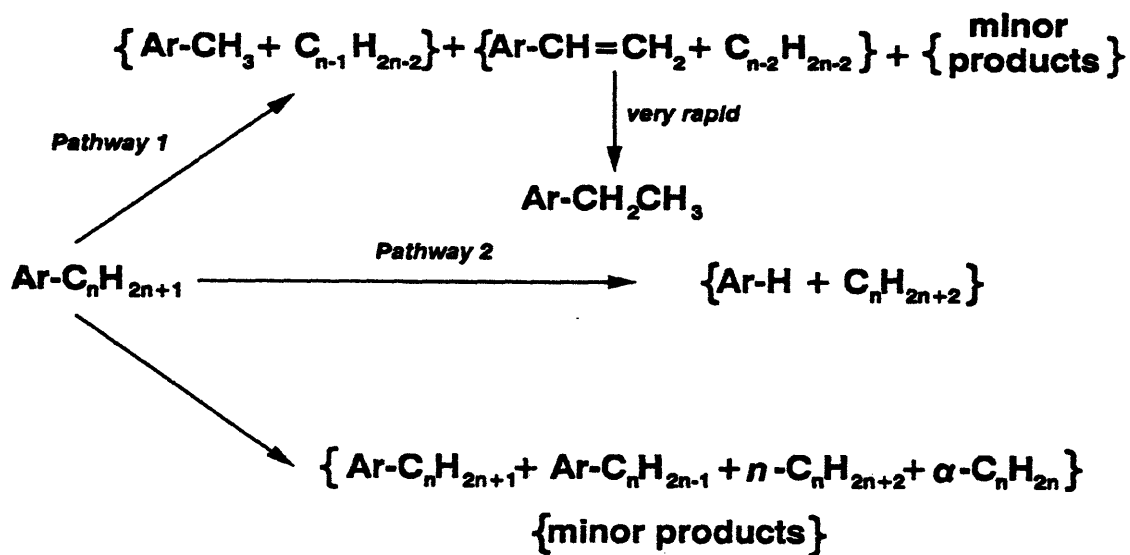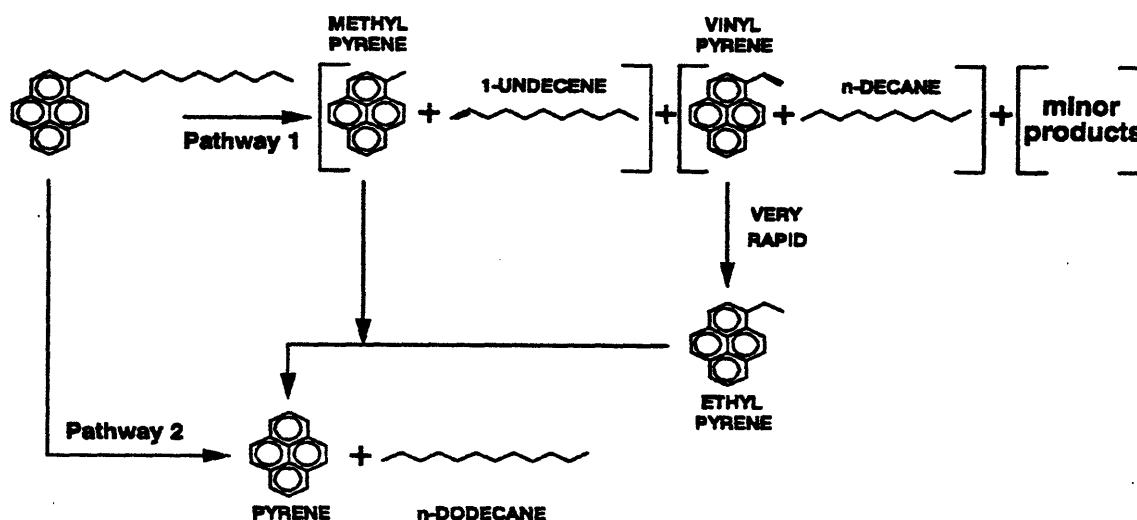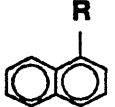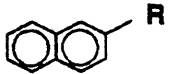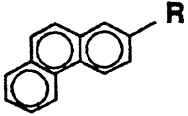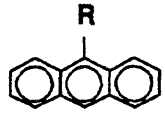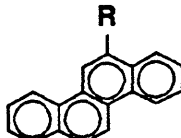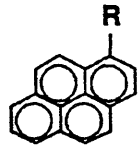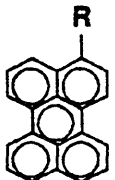
Figure 2.9: 1-dodecylpyrene (DDP) pyrolysis pathway (top, Savage et.al., 1989) and general pyrolysis network for alkyl-substituted polycyclic aromatic hydrocarbons (bottom, Smith and Savage, 1991b).

concentrations yielded *n*-dodecane and pyrene as the major products through the cleavage of the strong aryl-alkyl C-C bond, again as in Figure 2.9. Kinetic analysis showed that this concentration-dependant behavior could be modeled by using the rate law previously derived for alkylbenzene pyrolysis plus an addition term accounting for the apparently autocatalytic decomposition of the strong aryl-alkyl bond. Pyrolyses of DDP with a hydrogen-transfer molecule, 1,6-dimethylnaphthalene, showed that a selective hydrogenolysis mechanism was likely responsible for cleavage of the aryl-alkyl C-C bond.

In order to better understand pathways for polycyclic aromatics, Smith and Savage (1991b) pyrolyzed a family of alkyl-substituted polycyclic aromatic hydrocarbons at temperatures between 350°C and 425°C with batch holding times from 10 to 500 minutes. A general pyrolysis network was deduced for these compounds, and it comprised two major and one minor parallel pathway. The bottom panel of Figure 2.9 shows the general pyrolysis network. The first major pathway resulted in products analogous to the major products observed from alkylbenzene pyrolysis, shown in the top panel of Figure 2.5. The second major pathway led to products via the cleavage of the strong aryl-alkyl C-C bond. The third pathway led to small amounts of products, presumably through cyclization and condensation reactions. The importance of aryl-alkyl C-C bond cleavage during the pyrolysis of polycyclic alkylaromatics depended primarily on the localization energy at the specific point of substitution. The occurrence of aryl-alkyl C-C bond cleavage

was independent of the number of rings, the length of the alkyl chain, and the type of condensation of the aromatic nucleus. A quantitative correlation exists between the Dewar reactivity number, which can be calculated from perturbation molecular orbital theory, and the rate of aryl-alkyl C-C bond cleavage during the pyrolysis of *n*-alkylarenes. Structures, abbreviations, alkyl chain length, Dewar numbers and pseudo-first-order rate constants for the compounds used in the study are shown in Table 2.2. This correlation provided a link between the structure and the reactivity of polycyclic *n*-alkylaromatics and suggested that the mechanism responsible for the aryl-alkyl C-C bond cleavage was moderately selective. The difference in the relative importance of pathways 1 and 2 suggested that three different categories existed for compounds. Pathway 1 dominated for compounds in the first category, whose Dewar reactivity numbers were greater than 1.81. Both pathways 1 and 2 were important for compounds in the second category, whose Dewar reactivity numbers were between 1.51 and 1.67. Pathway 2 was dominant for compounds in the third category, whose Dewar reactivity numbers were less than 1.33. Figure 2.10 compares the literature data in a plot of log of pseudo-first-order rate constant versus Dewar reactivity number for the decomposition of methylated polycyclic aromatics to the parent aromatic. The upper set of data (▵ points and solid line) represents Smith and Savage's (1991) overall pseudo-first-order rate constants at 400°C. These data were then corrected for the initial concentration differences, assuming second order kinetics and the corrected rate was then multiplied by the selectivity to the parent

Table 2.2

ALKYLAROMATIC PYROLYSES(data from literature)[1]				
Model Compounds	Name	Alkyl Chain Length	Dewar Number	k_{eff}@400°C (10^4 sec^{-1})
	DDB	12	2.31	1.1 ± 0.27
	BN	4	2.12	0.33 ± 0.10
	UDN,DD	11,12	1.81	0.47 ± 0.22
	DDH	12	2.18	0.55 ± 0.28
	DDA	12	1.26	17 ± 4.3
	OC	8	1.67	0.93 ± 0.02
	DDP	12	1.51	2.7 ± 0.7
	HP	6	1.33	3.2 ± 1.5

[1] adapted from Smith and Savage (1991b)
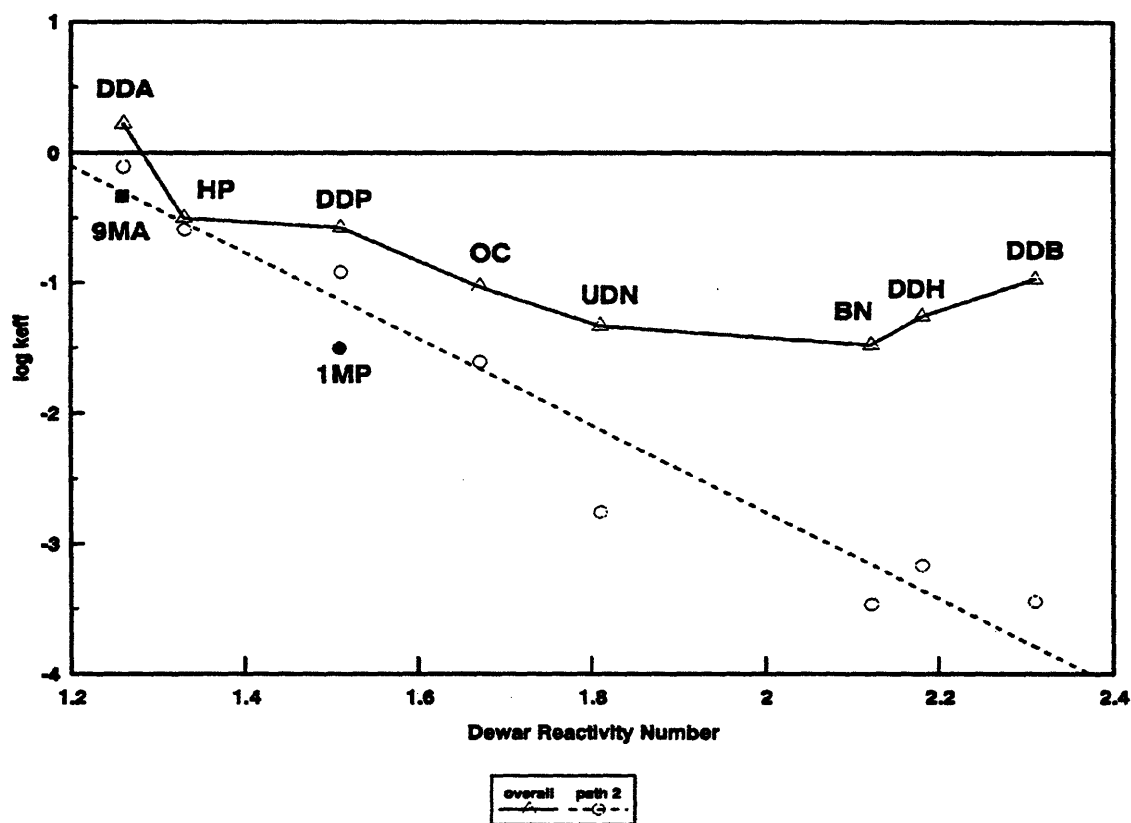
Figure 2.10: Comparison of effective first order rate constant (log k_{eff}) versus Dewar reactivity number for alkylaromatic pyrolysis (A) overall decomposition rates and (B) rate of pathway 2.

aromatic. The resultant values represent the pseudo-first order rates of path 2 of Smith and Savage (1991b) and are shown in Figure 2.10 as the lower sets of data (O points and dashed line). These are best fit by a line of slope -3.3±0.6 with intercept of 5.7±0.7. This slope corresponds to a Hückel resonance parameter of $|2\beta| \sim 10$ kcal/mole. Also on this graph are the data of Pomerantz (● point) for 9-methylanthracene at 400°C and Savage and Smith for 1-methylpyrene (■ point) at 400°C.

2.4 Present Approach

Previous experimental work shows a complex reaction network exists for alkyl-substituted polycyclic aromatic hydrocarbon pyrolysis. The reaction network can be delineated by analyzing one pathway at a time. This work investigates the importance of pathway 2 in the generalized pyrolysis network of Figure 2.9 by studying methyl-substituted acenes, which are the limiting case of alkyl-substituted polycyclic aromatic hydrocarbons.

The present investigation comprises three related aspects:

First, chemical modelling was used to select simple substrates that mimic both the chemical moieties found in the original complex materials to be pyrolyzed, as well as subsidiary moieties that might arise from secondary reactions during

thermolysis. The model substrates chosen included unsubstituted polycyclic aromatic hydrocarbons and their methyl-substituted analogs. These are shown in Figure 2.11, respectively, 1,4-dimethylnaphthalene (14DMN), 9,10-dimethylanthracene (910DMA) and 9-methylanthracene (9MA). Two and three ring compounds were chosen to mimic aromatic character in multi-ring compounds. Methyl substituents were chosen because they are the simplest electron donating substituent found in coal and wood, and are the smallest methyl substituents in asphaltenes. Dimethylanthracene was also chosen for the interesting fact that its decomposition product, methylanthracene, is far more toxic than the substrate itself. And 9-methylanthracene was chosen to represent an intermediate moiety that arises during thermolysis.

Second, thermal pathways available to the model substrates were experimentally established by studying their thermolysis in batch reactors designed to span the range of conditions encountered during the early stages of incineration. Reactor operations encompassed temperatures from 370 to 550°C and residence times from 150 to 115200 seconds to simulate various severities of thermolysis. Product analyses included gaseous and liquid reaction products.

Third, theoretical interpretation of the thermolysis data will focus on development of quantitative chemical mechanisms for all major pathways observed. From the nature of the substrates and the conditions of their thermolysis, both free-radical mechanisms and thermally-allowed concerted mechanisms seem likely to be
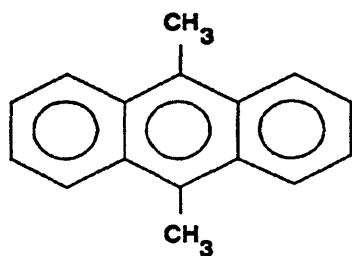
9,10-DIMETHYLANTHRACENE
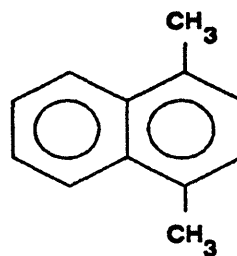
1,4-DIMETHYLNAPHTHALENE
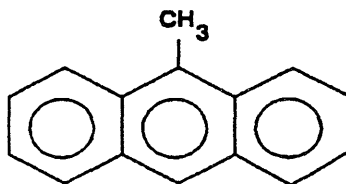
9-METHYLANTHRACENE

Figure 2.11: Models compounds used in the present work.

important. Both these mechanisms appear amenable to analysis by frontier molecular orbital (FMO) theory (Fukui, 1975). It was hoped that FMO theory might offer a theoretical basis for correlation and wide generalization of the experimental results obtained from the model substrates.

Chapter 3.

Frontier Molecular Orbital Theory

A portion of the present work is devoted to developing relationships between Frontier Molecular Orbital (FMO) theory and the observed reaction kinetics, as well as experimentally observed relative abundances of pyrolysis products. Background concerning FMO theory and the molecular orbital methods actually used in the present work is given in this chapter.

3.1 Transition States, Perturbation Theory and Chemical Reactivity

In approaching the problem of chemical reactivity, it is easiest to imagine two molecules which are about to combine with each other in a simple, one-step reaction.

149

The energies of the starting materials and possible products are frequently fairly well known, as in Figure 3.1, therefore the problem in assessing reactivity lies in estimating the energies of the transition states. Although both ends of the reaction path can affect the transition state, the Hammond postulate states that transition states for exothermic reactions are reactant-like, and for endothermic reactions are product-like (Hammond, 1955). For exothermic reactions, perturbation theory (Dewar, 1975) can be used to estimate the slope of an early path along the reaction coordinate leading up to the transition state, the steeper slope leading to the higher-energy transition state, as shown in Figure 3.1.

Two reacting molecules perturb each other's orbitals, as shown in Figure 3.2. As the molecules approach each other, the highest occupied molecular orbital (HOMO) of the molecule on the right and the HOMO of the molecule on the left can combine in both a bonding and an antibonding sense. These new molecular orbitals will then be an approximation of the two orbitals of the transition state. The formation of the bonding orbital is exothermic (E_1) but the formation of the antibonding orbital is endothermic (E_2) because two electrons must go into it. For all combinations of fully occupied orbitals, $|E_2| > |E_1|$, that is, the occupied-occupied MO interaction is destabilizing because the energy needed for the antibonding combination is greater than that gained from the bonding combination. Combinations of unfilled orbitals with other unfilled orbitals will have no effect on the energy of the system because no electrons will be placed in these orbitals.
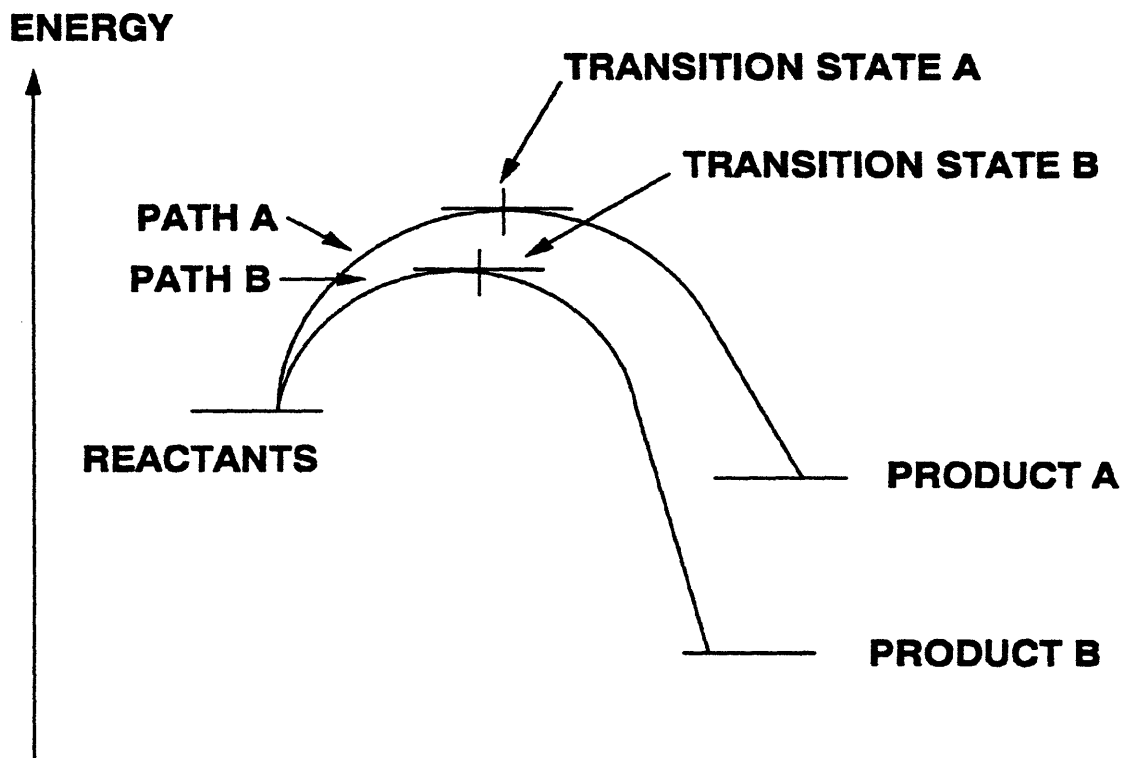
ENERGY

Figure 3.1: The energy along two possible reaction coordinates (adapted from Fleming, 1976).
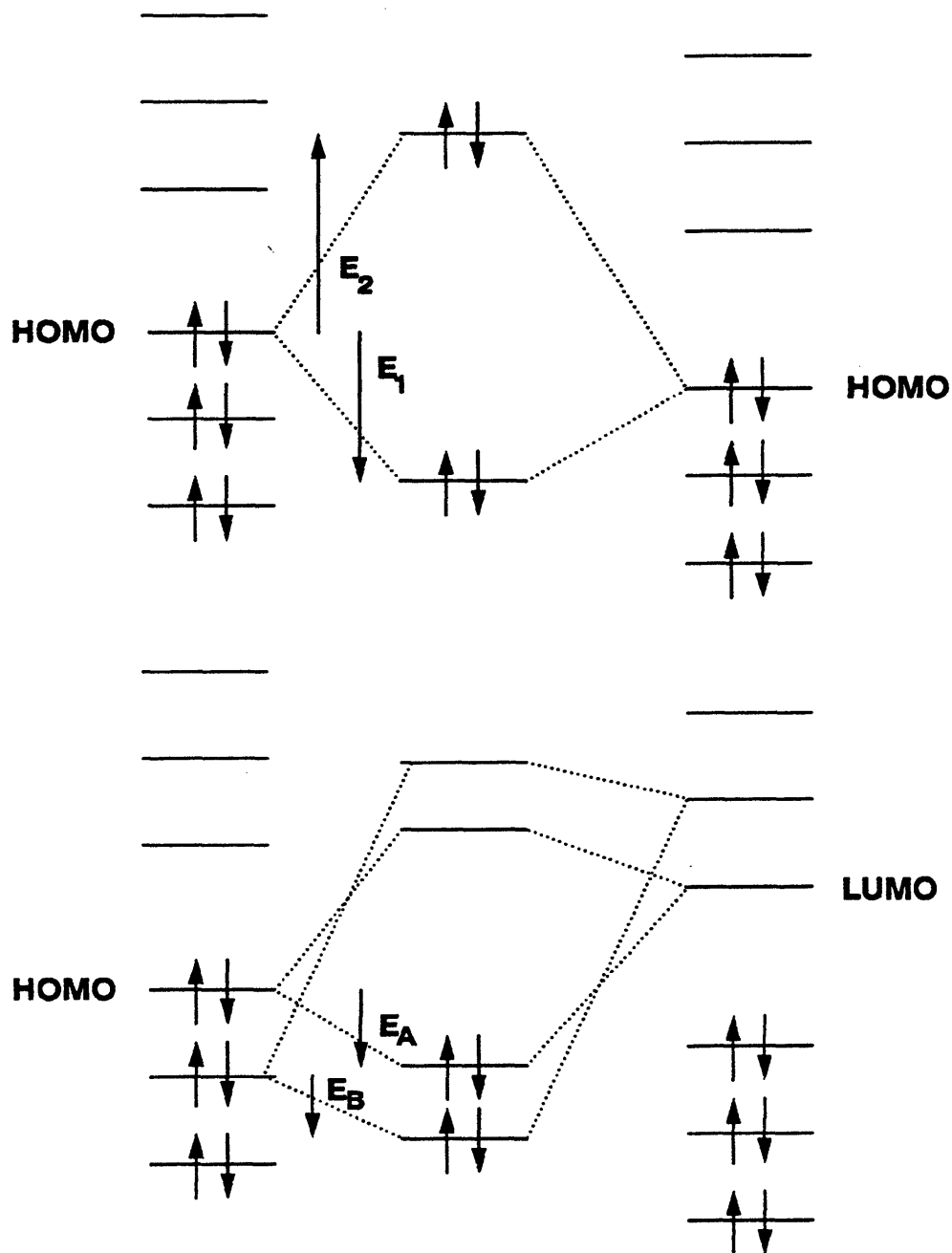
Figure 3.2: The interaction of the HOMO of a molecule with the HOMO of another (top) and the interaction of the HOMO of a molecule with the LUMO of another (bottom) (adapted from Fleming, 1976).

Interactions between filled orbitals and unfilled orbitals have an important energy-lowering effect. Figure 3.2 shows the case where the energy-lowering bonding combination is as usual, yet the rise in energy of the antibonding combination as no affect on the actual energy of the system because no electrons go into that orbital. Figure 3.2 also shows that the interaction of the HOMO of the left hand molecule and the LUMO of the right hand molecule leads to the largest drop in energy $(2E_A > 2E_B)$. Interactions of other occupied orbitals with other unoccupied orbitals is less effective, because the closer the interacting orbitals are in energy, the larger is the "splitting" of their levels. This is why the interactions of the HOMO/LUMO pair of orbitals, called "Frontier Orbitals" by Fukui, is the most important. The other occupied/unoccupied orbital interactions also contribute to the energy of the interaction, thereby lowering the energy of the transition state, but their contributions are smaller than that of the dominant HOMO/LUMO interaction.

The HOMO/HOMO interactions are large compared with the HOMO/LUMO interactions; in Figure 3.2, both E_1 and E_2 are much larger then E_A. This is because the HOMO/HOMO interactions (first-order interactions) are between orbitals of comparable energy, whereas the HOMO of one molecule is usually well separated in energy from the LUMO of another molecule (second-order interactions). Although the bonding (E_1) and antibonding (E_2) interactions cancel each other out somewhat, there is always a large net antibonding interaction. These first-order interactions give rise to a large part of the activation energy for the

reaction. The second-order interactions, even though entirely bonding in character, reduce the activation energy but are relatively small. The HOMO/LUMO interaction is the largest of the second-order interactions.

3.2 Frontier Molecular Orbital (FMO) Theory

Frontier Molecular Orbital (FMO) theory is a simplification of the molecular orbital interaction energy of the reactants, ΔE_{MO}, which is given by the generalized perturbation (GP) equation, presented in the following form by Fleming (1976):

$$\Delta E_{MO} = -\sum_{ab}(q_a+q_b)\beta_{ab}S_{ab} + \frac{\sum_{t<u}(Q_tQ_r)}{\epsilon R_{tu}} + \frac{\sum_r^{occ}\sum_s^{unocc}-\sum_s^{occ}\sum_r^{unocc}2(\sum\beta_{ab}c_{ra}c_{sb})^2}{E_r-E_s} \quad (3.1)$$

In the GP equation, t and u refer to the interacting atoms, a and b are atomic orbitals (AO's) located on t and u respectively, and r and s are molecular orbitals (MO's) associated with the molecules containing atoms t and u. The variables in the GP equation are defined as follows:

q_a = electron density in AO a

β_{ab} = resonance integral between AO's a and b

S_{ab} = overlap integral between AO's a and b

Q_t = total charge on atom t

R_{tu} = distance between atoms t and u

ϵ = dielectric constant

c_{ra} = LCAO-MO coefficient of AO a in MO r

E_r = energy of MO r

The derivation of this equation involves many approximations and assumptions that cannot be fully explained here (see Fleming, 1976). It is valid only because the overlap integral, S, will be small for p-orbitals. As hybridized orbitals approach, there is an initial gain in bonding which slows up as the front lobe of one orbital begins to overlap the back lobe of the other. This is the form of the integral S, as shown in Figure 3.3, which reaches a maximum value of 0.27 at a distance of 1.74A (for a C-C pσ-bond) and then rapidly falls off. Therefore, any reasonable estimate of the distance between atoms of the transition state will make S small. The integral β is roughly proportional to S, so the third term of the GP equation is the second-order term. Third and higher-order terms can be neglected, since S is always small.

The three terms in the GP equation have the following significance. The first term represents the first-order closed-shell repulsion term, and comes from the interaction of filled orbitals of the one molecule with the filled orbitals of another. This is a positive, or destabilizing, contribution to ΔE_{MO}. The second term represents Coulombic repulsion or attraction. This term, which contains total charge, Q, on each atom, is important when charged species, e.g. ions or polar molecules, react. This term can be a stabilizing or destabilizing contribution to ΔE_{MO} depending on the charges involved. Finally, the third term represents electronic interaction between all the filled orbitals with all the empty orbitals of the correct symmetry. It is the

155
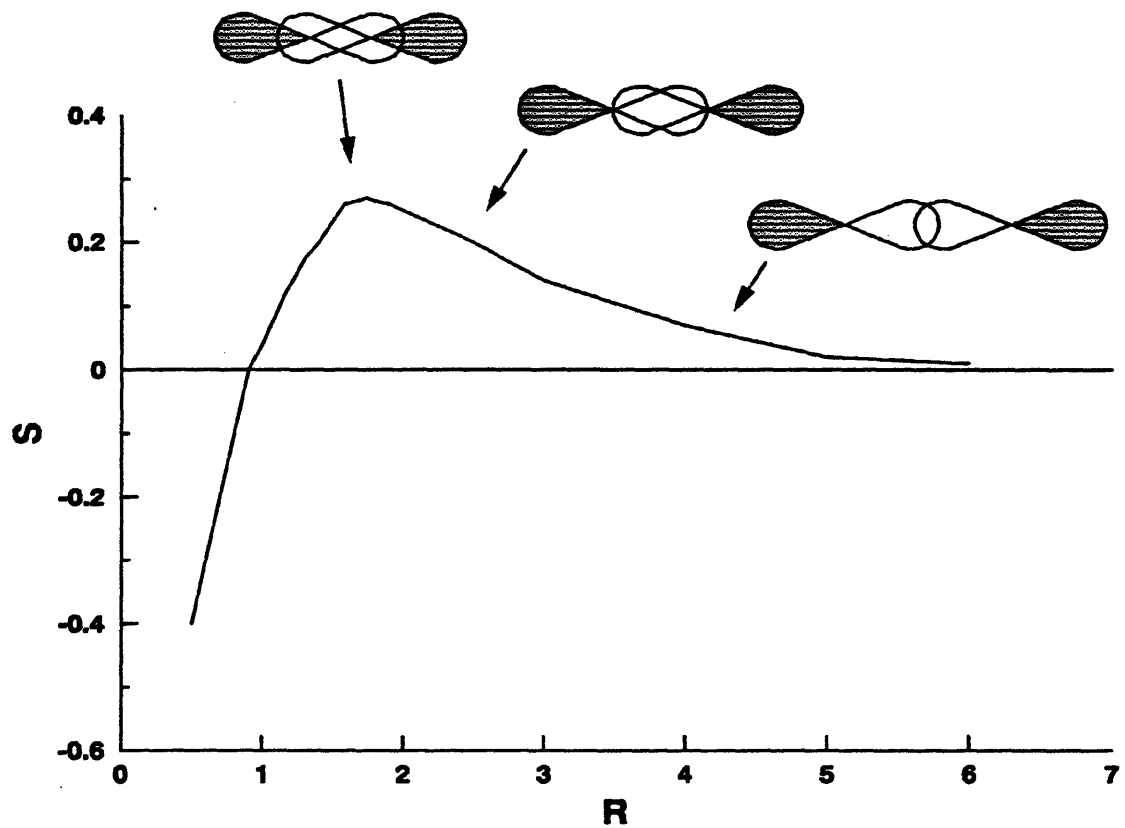
Figure 3.3: The function S (overlap integral) with distance R for a $2p\sigma$-$2p\sigma$ C-C bond (adapted from Fleming, 1976).

second-order perturbation term. This is always a negative, that is a stabilizing, contribution to ΔE_{MO}.

FMO theory is related to kinetics through the Arrhenius' relation:

$$\log k = \log A - \frac{E^*}{\theta} \qquad (3.2)$$

where:

A   = Arrhenius pre-exponential factor, units of k

E^* = activation energy (kcal/mol)

θ = scaled temperature = 0.004573 T

T   = temperature (K)

The activation energy E^* is essentially the enthalpy difference between the transition state and the substrates, while log A is related to the entropy difference between these states. For a family of reactions with similar transition state geometries, log A is roughly constant and so their relative rates depend entirely on the relative activation energies.

In general, the observed activation energy comprises both thermodynamic and electronic barriers. Thermodynamic barriers are dominant for highly endothermic reactions while electronic barriers become dominant for thermoneutral and exothermic reactions. The electronic barriers of the activation energy are addressed by FMO theory.

FMO Theory (Fukui 1975) states that observed activation energy is the result of two types of electronic interactions between the orbitals of molecules A and B:

$$E^* = E_{(REP)} + E_{(FMO)} \tag{3.3}$$

where:

E(REP) = E(occ-occ), the summed energy of interaction between occupied orbitals in both molecules. This term is always positive, because it is a repulsive term, and represents the physical manifestation of Pauli's exclusion principle.

E(FMO) = E(occ-unocc), the summed energy of interaction between an occupied orbital in one molecule and an unoccupied orbital in the other. This term is inherently negative since it is stabilizing and represents a form of Mulliken's covalent bonding energy.

The two terms above correspond to the first and the third terms of the GP equation 3.1. The second ionic term is zero in our case because two neutral molecules are interacting. Of the two terms above, E(REP) is relatively insensitive to the details of the interacting MOs and is relatively constant within a given class of reactions. Thus the second term, E(FMO), which is highly dependent upon the details of the interacting MOs, controls the activation energy.

The mode of orbital interaction in a cyclo-addition reaction is shown in Figure 3.4. Molecule A (called the diene) and molecule B (called the dienophile)
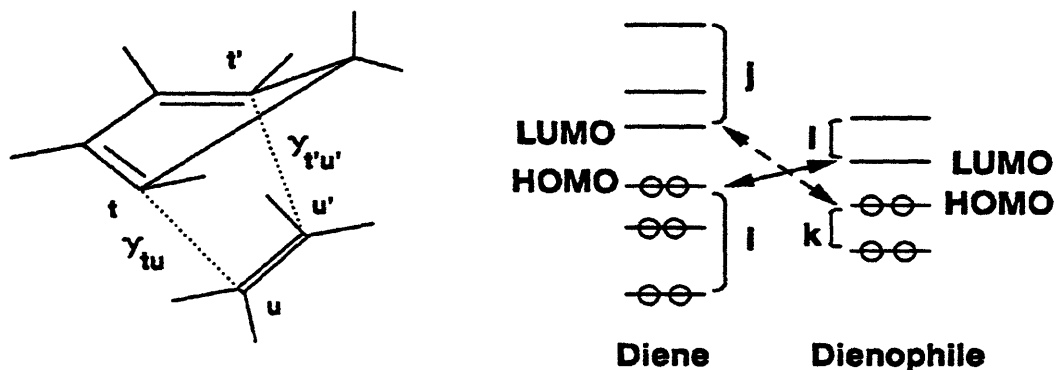
$$\Delta E = 2 \sum_{l}^{occ} \sum_{l}^{uno} \frac{(c_t^{(l)} c_u^{(l)} \gamma_{tu} + c_{t'}^{(l)} c_{u'}^{(l)} \gamma_{t'u'})^2}{E_{al} - E_{bl}}$$

$$+ 2 \sum_{k}^{occ} \sum_{j}^{uno} \frac{(c_t^{(j)} c_u^{(k)} \gamma_{tu} + c_{t'}^{(j)} c_{u'}^{(k)} \gamma_{t'u'})^2}{E_{bk} - E_{aj}}$$

$$\Delta E \cong 2 \; \frac{(c_t^{(HO)} c_u^{(LU)} \gamma_{tu} + c_{t'}^{(HO)} c_{u'}^{(LU)} \gamma_{t'u'})^2}{E_{a,HO} - E_{b,LU}}$$

Figure 3.4: The mode of orbital interactions in cyclo-addition and the stabilization energy E(FMO) (from Fujimoto and Fukui, 1974).

159

interact and eventually form bonds at each of two "centers", respectively involving the atom pairs (t,u) and (t',u'). The energy levels of the occupied and unoccupied MOs of both molecules are depicted to the right of Figure 3.4, with the highest occupied and the lowest unoccupied molecular levels marked HOMO and LUMO; these latter are called "Frontier Orbitals". The interaction energy ΔE_{rs} between an occupied MO r of A and an unoccupied MO s of B is of the form:

$$\Delta E_{rs} = \frac{2(C_{tr}C_{us}\gamma_{tu} + C_{t'r}C_{u's}\gamma_{t'u'})^2}{E_{(A,r)} - E_{(B,s)}} \tag{3.4}$$

where:

C_{tr} = coefficient of occupied MO r at atom t in molecule A

C_{us} = coefficient of unoccupied MO s at atom u in molecule B

γ_{tu} = resonance integral of new t-u bond being formed (kcal/mol)

$C_{t'r}$ = coefficient of occupied MO r at atom t' in molecule A

$C_{u's}$ = coefficient of unoccupied MO s at atom u' in molecule B

$\gamma_{t'u'}$ = resonance integral of new t'-u' bond being formed (kcal/mol)

$E_{(A,r)}$ = energy of occupied MO r in molecule A (kcal/mol)

$E_{(B,s)}$ = energy of unoccupied MO s in molecule B (kcal/mol)

Each occupied MO r of A will interact with all the unoccupied MOs s of B; thus the above expression must be summed over all s for each r and then over all r to provide $\Delta E(A_{occ}-B_{unocc})$. Similarly, each of the occupied MOs k of B will interact with all the unoccupied MOs j of A; thus an expression analogous to the above must

be summed over all k and j to provide $\Delta E(B_{occ}-A_{unocc})$. The sum of these two terms

is E(FMO), corresponding to the full expression in Figure 3.4.

Since each term in the full expression for E(FMO) has the form of the above

equation, it is apparent that the terms with the lowest denominators will make the

greatest contributions. Thus E(FMO) will be dominated by interactions between the

pairs of orbitals with the smallest energy separations. These are the two Frontier

Orbital pairs, namely A(HOMO)↔B(LUMO) and B(HOMO)↔A(LUMO), connected

by the arrows in Figure 3.4. Fukui has further postulated that once the interaction

between these pairs commences, electron delocalization further diminishes their

energy separations, reinforcing their dominance. The full summations for E(FMO)

thus reduce to two terms:

$$\Delta E(FMO) = \frac{2\gamma^2(C_{t(HO)}C_{u(LU)}+C_{t'(HO)}C_{u'(LU)})^2}{E_{(A,HO)}-E_{(B,LU)}} + \frac{2\gamma^2(C_{t(LU)}C_{u(HO)}+C_{t'(LU)}C_{u'(HO)})^2}{E_{(B,HO)}-E_{(A,LU)}} \quad (3.5)$$

where:

$\gamma_{tu} = \gamma_{t'u'}$ = resonance integral of new bonds being formed (kcal/mol)

$C_{t(HO/LU)}$ = coefficient of HOMO or LUMO at atom t in molecule A

$C_{u(HO/LU)}$ = coefficient of HOMO or LUMO at atom u in molecule B

$C_{t'(HO/LU)}$ = coefficient of HOMO or LUMO at atom t' in molecule A

$C_{u'(HO/LU)}$ = coefficient of HOMO or LUMO at atom u' in molecule B

$E_{(A,HO/LU)}$ = energy of HOMO or LUMO in molecule A (kcal/mol)

$E_{(B,HO/LU)}$ = energy of HOMO or LUMO in molecule B (kcal/mol)

The resonance integrals γ_{tu} and $\gamma_{t'u'}$ strictly depend upon the extent to which the new bonds are formed at the transition state. It is usually assumed that both bonds form simultaneously with equal resonance integrals whose value γ is constant, which is characteristic of the transition state alone for a family of reactions.

Dual-center FMO theory is essentially based on the above equation. Frequently, the contribution from one of the frontier orbital pairs is significantly larger than that for the other. In such a case, E(FMO) collapses to a single term corresponding to the dominant FMO interaction.

Similar logic is applied to a radical reacting with a molecule. Since radicals have one unpaired electron, they have a singly occupied molecular orbital (SOMO) that interacts with both the HOMO and the LUMO of the molecule. ΔE(FMO) will not collapse to a single term in this case since both of the frontier orbital pairs interact with the SOMO. The expression for ΔE(FMO) is as follows:

$$\Delta E(FMO) \;=\; \frac{\gamma^2 (C_{t(HO)} C_{u(SO)})^2}{E_{(A,HO)} - E_{(B,SO)}} \;+\; \frac{\gamma^2 (C_{t(LU)} C_{u(SO)})^2}{E_{(B,SO)} - E_{(A,LU)}} \tag{3.6}$$

where:

γ = resonance integral of new bonds being formed (kcal/mol)

$C_{t(HO/LU)}$ = coefficient of HOMO of LUMO at atom t in molecule A

$C_{u(SO)}$ = coefficient of SOMO at atom u in molecule B

$E_{(A,HO/LU)}$ = energy of HOMO or LUMO in molecule A (kcal/mol)

$E_{(B,SO)}$ = energy of SOMO in molecule B (kcal/mol)

Applications of FMO theory require some understanding of the covalent bonding in molecules. The electron system of a molecule is described by molecular orbitals (MO) that are linear combinations of atomic p-orbitals (LCAO). MOs are predicted by computer programs that make assumptions to simplify Schrödinger's equation for the system. The resulting eigenvalues and eigenvectors respectively provide the energies and coefficients of the MOs. These values can be used in the FMO expressions, such as Equations 3.5 and 3.6, to evaluate $\Delta E(FMO)$. Two examples of FMO theory applied to the coal pyrolysis data of Wornat (1988) are considered next, with Hückel MOs.

3.3 Analysis of Coal Pyrolysis Data

Representative GC-MS data from the coal pyrolysis study of Wornat (1988) were shown in Figure 2.4. These data were obtained from pyrolysis at temperatures from 1100 to 1500 K at residence times from 2 to 6 seconds. The products that were most abundant, and could be detected over the widest temperature range, are listed in Table 3.1. The 23 unsubstituted PACs form 9 groups, which distributed themselves rather uniquely into mass number groups that differed by increments of either 24 or 50, closely corresponding to acetylene (C2) and diacetylene (C4) increments. The last two columns respectively indicate the relative abundance of each product at T = 1378 K with respect to both the overall most abundant product

Table 3.1

POLYCYCLIC AROMATIC COMPOUNDS OBSERVED IN COAL PYROLYSIS AT 1378 K[1]

ID#	Group#	Mass	Compound	Area relative to pyrene	Area relative to group
1	1	152	acenaphthylene	44	
2	2	178	phenanthrene	540	1.000
3	2	178	anthracene	220	0.408
4	3	202	fluoranthene	849	1.000
5	3	202	acephenanthrylene	454	0.535
6	3	202	pyrene	1000	1.178
7	4	216	benzo[a]fluorene	44	0.671
8	4	216	benzo[b]fluorene	66	1.000
9	5	226	benzo[ghi]fluoranthene	182	0.330
10	5	226	benzo[c]phenanthrene	115	0.209
11	5	226	cyclopenta[cd]pyrene	553	1.000
12	6	228	benz[a]anthracene	936	1.000
13	6	228	chrysene		
14	6	228	triphenylene	50	0.053
15	7	252	benzo[j,b]fluoranthene	493	1.000
16	7	252	benzo[k,a]fluoranthene	156	0.316
17	7	252	benzo[e]pyrene	90	0.362
18	7	252	benzo[a]pyrene	248	1.000
19	7	252	perylene	47	0.188
20	8	276	indeno[123cd]pyrene	162	0.866
21	8	276	benzo[ghi]perylene	187	1.000
22	8	276	dibenzo[def,mno]chrysene	72	0.385
23	9	300	coronene	36	

[1] data from Wornat (1988)   164

(pyrene) and a characteristically abundant product within a group (e.g. phenanthrene in Group 2).

Within each group of Table 3.1, it is interesting to assess how closely the observed isomer distribution corresponds to its equilibrium distribution at the reaction temperature T = 1378 K. Thermodynamic data required for the equilibrium calculations are available for each of the first 6 entries in Table 3.1 (Pedley et. al., 1986). In Group 2, the ratio of [Anthracene/Phenanthrene] calculated at equilibrium is 0.064, almost an order of magnitude smaller than the observed ratio of 0.41. In Group 3, the ratio of [Acephenanthrylene/Benzofluorene] calculated at equilibrium is 0.035, an order of magnitude higher than the observed ratio of 0.54. Also, the ratio of [Pyrene/Fluoranthene] calculated at equilibrium is 1660, three orders of magnitude higher than the observed ratio of 1.18. In all these cases, the respective isomer pairs are far from equilibrated, which means that they must be forming (and disappearing) under kinetic control.

Although the chemical mechanism of PAC growth or destruction is not certain, the relatively high temperatures involved in this case, as well as the structures of the PAC substrates, are such that both free-radical and concerted molecular reactions are likely to be important. If we presume that the rate-determining step in acetylene addition is concerted, then the formation of higher PACs becomes theoretically analogous to pericyclic cyclo-addition reactions, for which dual-center FMO theory can be applied.

165

To illustrate the application of dual-center FMO theory, two examples pertaining to C16 PACs are chosen. These were among the most abundant observed products (Group 3 in Table 3.1). All computations were made with Hückel MO parameters, obtained from the compilation of Coulson and Streitwieser (1960). Only the one-term FMO equation is used, recast for use with Hückel MO such that ΔE_{FMO} became a non-dimensional FMO stabilization energy E'(FMO):

$$E'(FMO) = \frac{-\Delta E(FMO)}{\frac{-2\gamma^2}{\beta}} = \frac{(C_r(HO)C_u(LU) + C_u(HO)C_r(LU))^2}{X_{(B,LU)} - X_{(A,HO)}} \tag{3.7}$$

where X = Hückel non-dimensionalized energy of the orbital. Higher values of the non-dimensional E'(FMO) physically correspond to more negative $\Delta E(FMO)$, hence lower activation energy E^* and higher rate constant k.

Example 1 illustrates the application of FMO theory to predict the relative reaction rates of separate substrates A with a common B. The two cases, labelled (R1) and (R2), are treated in Figure 3.5, which show the relevant chemical structures, MO parameters, and FMO calculations. In both cases, the dominant FMO interaction is between the HOMO of the PAC and the LUMO of C2 acetylene. Evidently, both reactions are symmetry allowed, because the MO coefficient products at both centers have the same signatures. However, pyrene has a higher-lying HOMO, and hence exhibits a lesser HOMO-LUMO energy separation than fluoranthene. The quantity 1/[X(LU)-X(HO)] is thus larger for pyrene than for
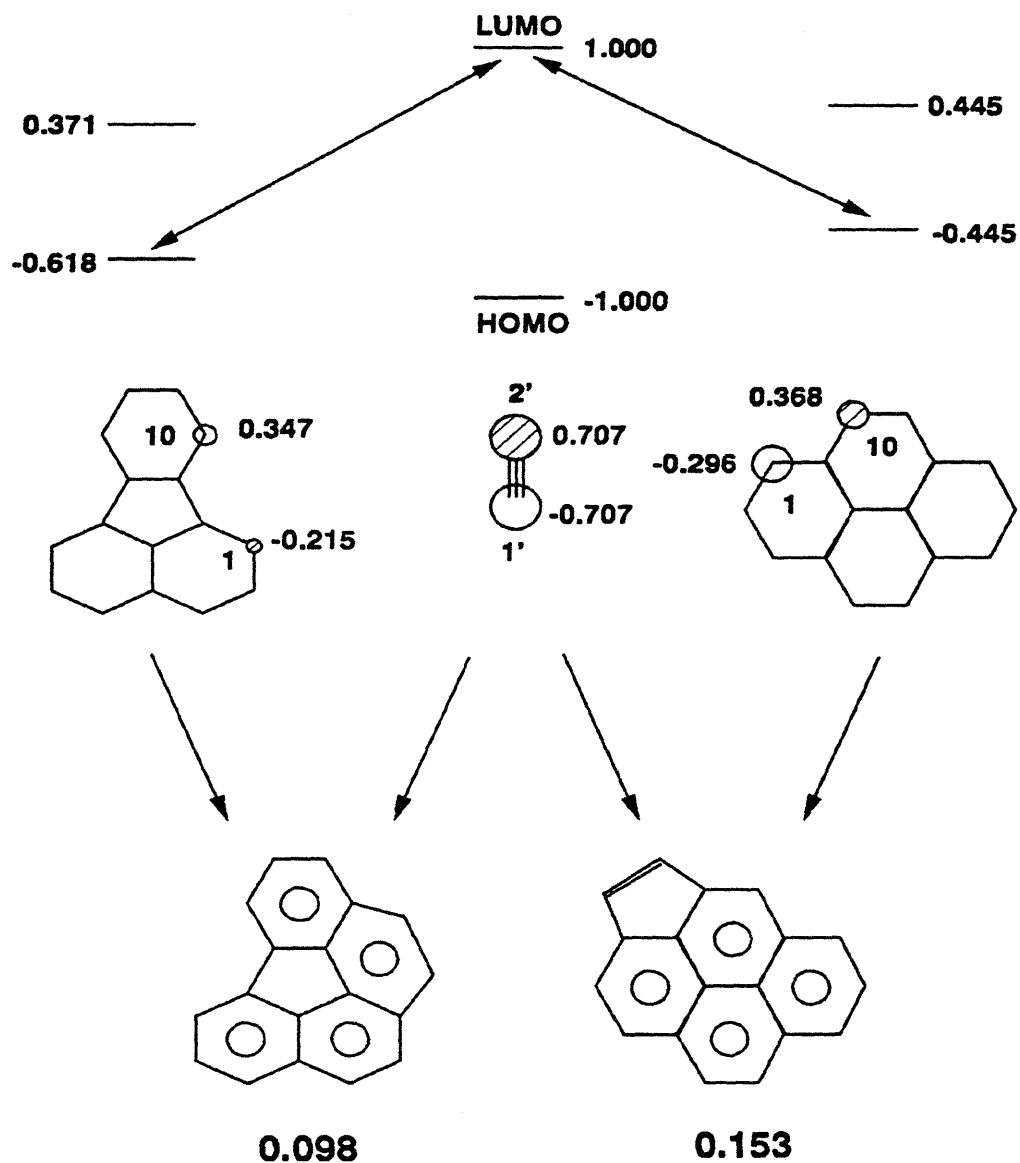
Figure 3.5: Estimation of relative reaction rates by FMO theory: addition of C2 acetylene to C16 PACs fluoranthene and pyrene to form C18 PACs benzo[ghi]fluoranthene and cyclopenta[cd]pyrene.

167

fluoranthene, which is the main reason why E'(FMO)pyrene > E'(FMO)fluoranthene. In this very simple fashion, reaction (R2) is predicted to be faster than (R1).

Inspection of the experimental data in Table 3.1 shows that the observed substrate ratio (Pyrene/Fluoranthene) $\approx$ 1 whereas the observed product ratio (Cyclopenta[cd]pyrene/Benzo[ghi]fluoranthene) $\approx$ 3. Allowing for statistical factors, which include reaction path degeneracies of 4 and 2 for (R1) and (R2) respectively, the data imply that the intrinsic rate of (R2) is about 1.5 times as fast as that of (R1). Evidently, example 1 indicates a qualitative accord between the theoretical FMO predictions and the observed product ratios.

Example 2 illustrates the use of FMO theory to predict "Periselectivity" of isomers when one substrate A adds to another B with multiple reaction sites. Figure 3.6 is an "Orbital Interaction Diagram" for the system comprising C4 Acetylene A and C12 PAC Acenaphthylene B, with energy as ordinate and the molecules confined to separate columns. The two occupied and two unoccupied MOs of A are shown to the right while the six occupied and six unoccupied MOs of B are shown to the left, with the HOMOs and LUMOs duly noted. The pair of Frontier Orbital interactions are indicated by two-headed arrow between their levels, the dominant interaction A(HO) $\leftrightarrow$ B(LU) denoted by the solid arrow.
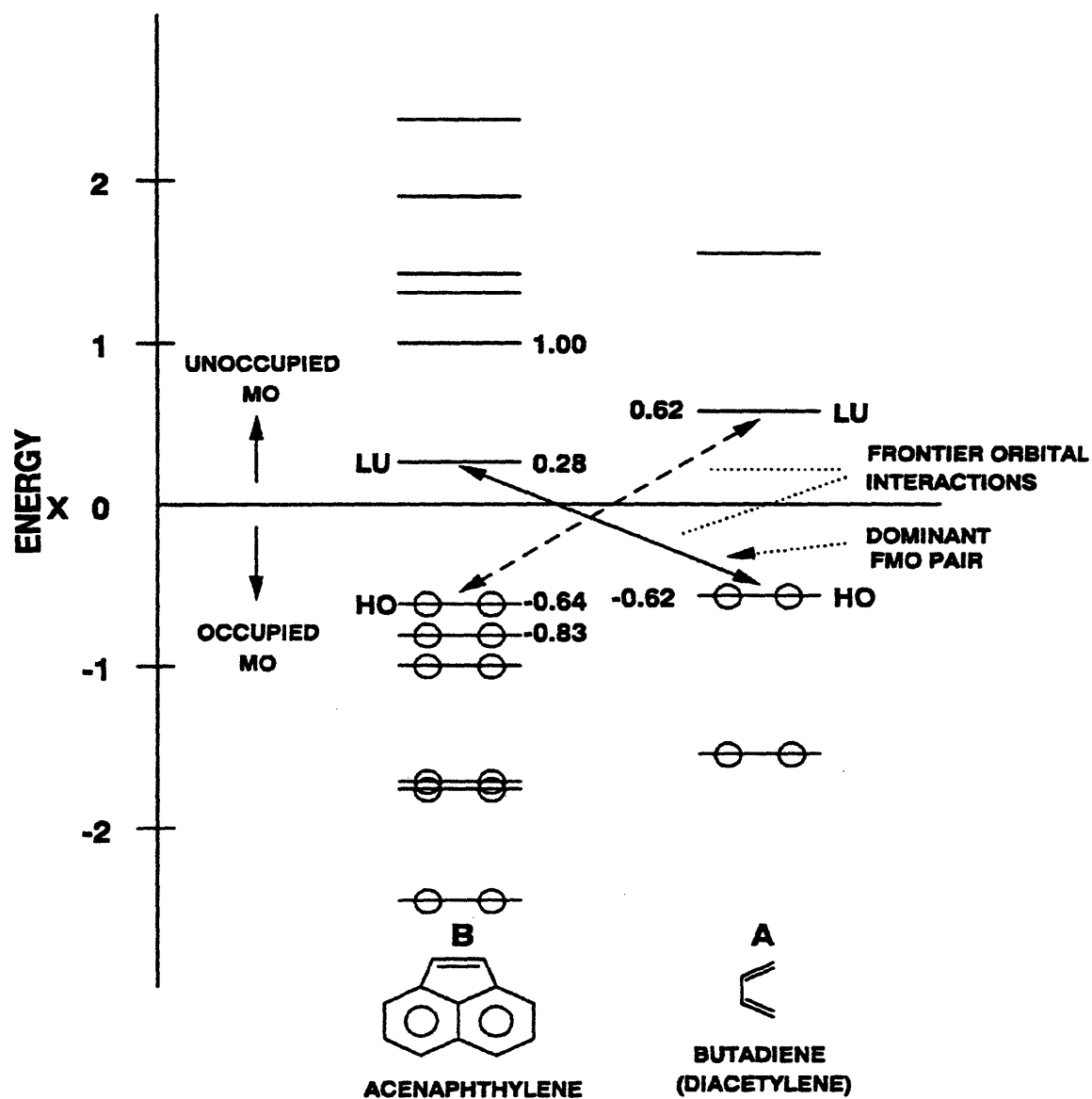
Figure 3.6: Frontier orbital interaction diagram - Example 2: addition of C4 acetylene to C12 PAC acenaphthylene to form C16 PACs fluoranthene, acephenanthrylene and aceanthrylene.

169

The dominant FMO interaction fixes the denominator of the $\Delta E(FMO)$ expression, but since B possesses multiple reaction sites, the numerator can take several different values. This is illustrated in Figure 3.7, a "Periselectivity Diagram", indicating three possible reactive orientations of A around the periphery of B. These will, respectively, lead to the isomeric products Fluoranthene, Acephenanthrylene, and Aceanthrylene, by reactions labelled (R1), (R2), and (R3). Superimposed on the skeletons of both molecules are circles that denote, by their size and shading, both the magnitudes and signatures of the coefficients of the interacting MOs. By inspection of the signatures of these interacting coefficient pairs it can be verified that (R1) and (R2) are both Symmetry Allowed while (R3) is Symmetry Forbidden. The same inspection will also make it apparent that the sum of the coefficient products, hence the numerator of the $\Delta E(FMO)$ expression, and the expression itself, will be in the order (R1) > (R2) > > (R3). The actual numerical values of E'(FMO) are quoted to the right of each reaction label. In this way, FMO theory predicts that the relative isomer formation rates from Acenaphthylene and a C4 Acetylene fragment will be in the order: Fluoranthene > Acephenanthrylene > > Aceanthrylene.

Experimental data in Table 3.1 (Group 3) show the observed relative amounts of the C16 isomers to be Fluoranthene : Acephenanthrylene : Aceanthrylene are 1.00 : 0.54 : <0.05 (not detected). Accounting for statistical factors, which include a reaction path degeneracy of 1:2:2, the observed relative rates of the intrinsic
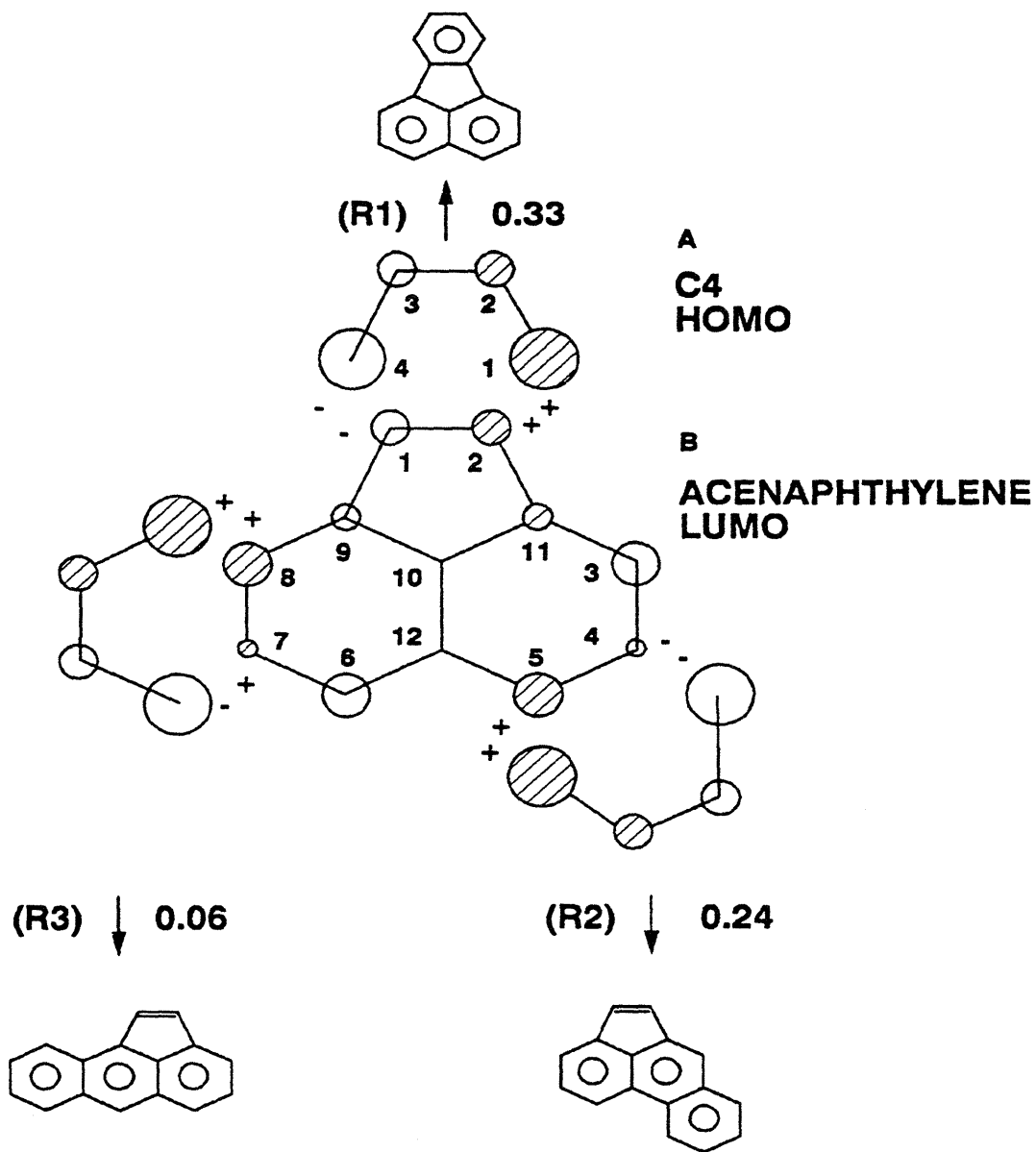
Figure 3.7: Estimation of isomer periselectivity by FMO theory - Example 2: addition on C4 acetylene to C12 acenaphthylene to from C16 PACs fluoranthene, acephenanthrylene, and aceanthrylene.

171

formation reactions are 1.00 : 0.27 : <0.02, in the order (R1) > (R2) >> (R3). Example 2 thus shows qualitative agreement between the theoretically predicted and experimentally observed C16 PAC isomer distributions.

3.4 Molecular Orbital Calculations

The previous two examples of FMO theory used Hückel coefficients and energy levels. While being satisfactory for this initial analysis of polycyclic aromatic reactivity and periselectivity, Hückel methods fail when applied to substituted aromatics. Accurate molecular orbital energies and coefficients necessary for FMO calculations are available from a variety of modern computational chemistry sources. Over the past two decades, computational chemistry has evolved along three main branches: molecular mechanics (MM), semiempirical, and ab initio or Gaussian methods. Each branch has certain advantages over the other two. Molecular mechanics is most effective for studying the conformations of macromolecules. Some MM methods are also as accurate as the best ab initio methods, particularly for hydrocarbons. MM methods are usually parameterized only for ground state systems; as a result they are unable to adequately represent the geometries involved in bond making-bond breaking processes. Ab initio methods most accurately calculate electronic properties of small molecules, including transition states and excited states, while the drawback to this high level work is the cost in terms of computer resources. Semiempirical methods lie somewhere in the middle between MM and ab initio

methods. Like molecular mechanics methods, they use experimentally determined parameters; like ab initio methods, they are basically quantum mechanical in nature, with the main difference between semiempirical and ab initio methods being the extensive use of approximations in the semiempirical approach. This allows semiempirical methods to avoid the need to evaluate the large number of terms used in ab initio work, while the use of experimental data to determine parameters to be used in these approximations result in chemically useful accuracy.

Table 3.2 shows the four classes of semiempirical molecular orbital methods which differ by what are considered valence electrons and how electron-electron interactions are calculated (Harris, 1992). Hückel and extended Hückel MO theory, which is a slightly more rigorous MO treatment, are both based on an "one-electron" approximation, where interactions between electrons in different molecular orbitals are ignored. These theories only deal with pi electrons. Other MO theories take electron-electron repulsion into account by considering the interaction between an electron in a given orbital and the mean field of the other electrons in the molecule. This approach is known as the self-consistent field (SCF) method, and involves an iterative process in which the orbitals are improved from cycle to cycle until the electronic energy reaches a minimum value and the orbitals no longer change. This situation is described as "self-consistent". Semiempirical MO methods use SCF theory for their calculations. Figure 3.8 helps illustrate the relations between the MO calculation methods considered below.

Table 3.2

VALENCE ELECTRONS CONSIDERED

	π-electron theory	π and σ-electron theory
ELECTRON INTERACTIONS CONSIDERED — One Electron Treatment	Hückel	Extended Hückel
Two Electron Treatment	Pariser-Parr-Pople	CNDO - INDO - MINDO - MNDO (including AM1 and PM3)

```
                                    ┌─────────────┐
                                    │ MNDO        │
                                    │ P arametric │        ┌──────────────┐
                                    │ Method      │        │ AB INITIO    │
                                    │ Number/3    │        │              │
                                    └──────┬──────┘        │ rigorous, non-│
                                           │               │ parametrized │
                                    ┌──────┴──────┐        │ MO method    │
      ┌──────────────┐             │ A ustin     │         └──────┬───────┘
      │ Modified     │             │ Model       │                │
      │ I ntermediate│             │ 1           │                │
      │ N eglect of  │             └──────┬──────┘                │
      │ D ifferential│                    │                       │
      │ O verlap/3   │             ┌──────┴──────┐                │
      └──────┬───────┘             │ Modified    │                │
             │                     │ N eglect of │                │
      ┌──────┴───────┐             │ D iatomic   │                │
      │ I ntermediate│             │ Overlap     │                │
      │ N eglect of  │             └──────┬──────┘                │
      │ D ifferential│                    │                       │
      │ O verlap     │             ┌──────┴──────┐                │
      └──────┬───────┘             │ N eglect of │                │
             │                     │ D iatomic   │                │
 ┌──────────┐│                     │ D ifferential│               │
 │ EXTENDED ││                     │ O verlap    │                │
 │ HÜCKEL   ││                     └──────┬──────┘                │
 └────┬─────┘└──────┐      ┌──────────────┴┐                      │
      │      ┌──────┴──────┤ Complete      │                      │
 ┌────┴─────┐│            │ N eglect of   │                      │
 │ HÜCKEL   ││            │ D ifferential │                      │
 │ no electron-│          │ O verlap      │                      │
 │ electron │            └───────┬────────┘                      │
 │ Interaction│                  │                               │
 └────┬─────┘                    │                               │
      │                          │                               │
──────┴──────────────────────────┴───────────────────────────────┴────
```

SCHRÖDINGER EQUATION

Figure 3.8: Molecular orbital methods.

175

A historic view of semiempirical theory starts with the Hückel calculations. Initial work employed the simplest "Hückel MOs", readily available from compilations of Coulson and Streitwieser (1960). Hückel MOs are most useful for relative comparisons between unsubstituted hydrocarbon pi-orbital systems, wherein the underlying quantum mechanical parameters remain reasonably constant. In such cases, Hückel MOs provided adequate numerical values of MO coefficients but their values of the corresponding energy levels are rather less satisfactory. Because the denominator of the FMO expression is sensitive to their magnitudes, it is important to employ accurate MO energies in FMO calculations. Thus, more sophisticated MO calculations than Hückel's are required for the proper application of FMO theory.

The first two-electron interacting semiempirical MO methods considered are CNDO, INDO, and NDDO, which were developed by J. A. Pople. The simplest, CNDO (Complete Neglect of Differential Overlap), assumes the atomic orbitals to be spherically symmetrical when evaluating electron repulsion integrals. The direction of the p-orbitals is included only via the one-electron resonance integrals, the sizes of which depend on the orientation and distances of the orbitals and on a constant assigned to each type of bond. CNDO ignored most of the integrals used in ab initio calculations and approximated, by these simple expressions, those integrals that were retained. The second version of CNDO (CNDO/2) corrected the fact that two neutral molecules separated by a distance of several Angstroms were attracted to each other. The next stage, the INDO (Intermediate Neglect of

Differential Overlap) approximation, includes one-center repulsion integrals between atomic orbitals on the same atom. This meant that different spin states on radicals could now be represented. None of the earlier methods could represent the repulsion between two lone pairs of electrons. NDDO (Neglect of Diatomic Differential Overlap) was the first in which the direction of the atomic orbitals was considered in calculating the repulsion integrals, therefore allowing repulsion between lone electron pairs. In this case all two-electron two-center integrals involving charge clouds arising from pairs of atoms were retained. None of these programs, however, included geometry optimization which meant a good estimate of the experimental geometry was needed. Furthermore, since the parameters were optimized for specific problems, the methods could be applied only to very small classes of systems.

The next evolution MINDO/3 was a significant improvement over previous methods in that the parameters used in the approximations had been carefully optimized. The basic form of the equations was similar to those in INDO, only in MINDO/3 the origin of the parameters was different. Rather than use atomic spectral data to define certain integrals, they were made adjustable parameters. MINDO/3 had several of these parameters, which were adjusted to give the best fit to experimental data for molecules. Geometries could also be optimized, therefore requiring the supplied geometry did not need to be very accurate. The core-core interactions were also changed. In earlier methods, core-electron attraction was set

177

equal to the electron-electron repulsion, therefore making hydrogen atoms in triplet hydrogen repel each other at all distances. To correct this in MINDO/3, the core-core repulsion term was made a function of the electron-electron repulsion integral. Examination of the MINDO/3 core-core repulsion function showed that as the distance R_{AB} increased, the function rapidly approached the classical point-charge form. MINDO/3 had limitations, especially in calculating heats of formations. The ΔH_f errors were large, averaging 11.0 kcal/mol for 138 compounds (Stewart 1991b), and some amines were predicted to have planar structures. Furthermore, extending MINDO/3 to new elements was difficult; in addition to the atomic parameters, two diatomic parameters for each element that had already been parameterized were necessary.

Since MINDO/3 was based on the INDO approximation, which could not represent lone-pair lone-pair interactions; MINDO/3 had difficulty with systems which contained lone pairs. MNDO, modified neglect of diatomic overlap, was the next program developed and was based on the NDDO approximation. As with MINDO/3, the core-core repulsion term was made a function of the electron-electron repulsion integral. The parameters used in MNDO were obtained using experimental data on 34 compounds. The parameters were optimized to reproduce observed heats of formation, dipole moments, ionization potentials, and molecular geometries. MNDO used entirely monatomic parameters for the resonance integral and core-core repulsion, instead of diatomic parameters which had limited extending

MINDO/3 to new elements. MNDO was further expanded to included parameters for many atoms, while various limitations became apparent. MNDO produced a spurious repulsion that became apparent at just outside chemical bonding distances, which was manifested by MNDO's inability to reproduce the hydrogen bond in the water dimer and by the unexpectedly large heat of formation of neopentane.

The inability to reproduce hydrogen bonding disallowed application of MNDO to the study of biologically interesting systems. Reparameterization was not the answer, since no terms existed within MNDO that could correct for the excessive repulsion at van der Waals' distances. Instead, each atom was assigned a number of spherical Gaussians that were intended to mimic the correlation effects. Three parameters were added to the core-core term, thereby increasing the number of parameters from the original seven to between 13 to 16 per atom. After further refinement, AM1 (Austin Model 1) reproduced the hydrogen bond and fully optimized the water dimer geometry.

In progressing for CNDO to MINDO/3 to MNDO and AM1, most parameters were changed from depending on atomic spectra to depending on molecular data. In MNDO and AM1 only the two-electron one-center integrals were still based on atomic spectra. In obtaining the parameters for MINDO/3, MNDO, and AM1, considerable chemical intuition had been used, but a large increase in speed resulted from automating the optimization process. This new process employed first- and second-derivatives of all calculated values for reference data to speed the

optimization. By increasing the speed of optimization, development of a new method changed from deriving parameters to assembling reference data and constructing new approximations. The new method, in addition to optimizing the seven parameters of MNDO and the two AM1-type Gaussians, optimized all one-center two-electron integrals, meaning all parameters were derived from molecular data. This method was called MNDO-PM3 to indicate the third parameterization of MNDO, with AM1 being the second. In PM3 the parameters were optimized using an automatic optimization routine that used a large set of reference molecular data which allowed 12 elements to be optimized simultaneously.

These four distinct two-electron methods, MNDO, MINDO/3, AM1 and MNDO-PM3, are available within MOPAC, which is a general-purpose, semiempirical molecular orbital program for the study of chemical reactions involving molecules, ions and linear polymers. The programs implements the semiempirical Hamiltonians for each of the four methods and combines the calculation of vibrational spectra, thermodynamic quantities, isotopic substitute effects, and force calculations in a fully integrated program. Within the electronic part of the calculation, molecular and localized orbitals, excited states up to sextets, chemical bond indices, and charges are computed. A transition-state location routine and two transition-state optimizing routines are available for studying chemical reactions, and also both intrinsic and dynamic reaction coordinates can be calculated (Stewart, 1990a).

The four distinct methods available within MOPAC: MINDO/3, MNDO, AM1, and PM3; have roughly the same structure and have many features in common. They are all self-consistent field (SCF) methods that take into account electrostatic repulsion and exchange stabilization with all calculated integrals evaluated by approximate means. They all use a restricted basis set of one s and three p orbitals (p_x, p_y and p_z) per atom and ignore overlap integrals in the secular equation. Thus, instead of solving:

$$|H-ES|=0 \qquad (3.8)$$

where H is the secular determinant, S is the overlap matrix, and E is the set of eigenvalues, the expression:

$$|H-E|=0 \qquad (3.9)$$

is solved. These approximations considerably simplify quantum mechanical calculations on larger systems of chemical interest. Since computational methods are only models, there is no advantage in rigorously solving Schrödinger's equation for a large system if that system has had to be abbreviated in order to make the calculations tractable. Thus, semiempirical methods are accurate enough to have useful predictive powers while being fast enough to allow large systems to be studied.

All four semiempirical methods within MOPAC contain sets of parameters. For MINDO/3 atomic and diatomic parameters exist, while MNDO, AM1 and PM3 use only single-atom parameters. Elements parameterized at the MNDO level

include H, Li, Be, B, C, N, O, F, Al, Si, P, S, Cl, Ge, Br, Sn, Hg, Pb, and I; whereas

PM3 includes H, C, N, O, F, Al, Si, P, S, Cl, Br, and I. Not all parameters are

optimized for all methods. In Table 3.3, parameters optimized for a given method

are indicated by *, a + indicates that the value of the parameter was obtained from

experiment (not optimized) and where neither symbol is given, the associated

parameter is not used in that method. All four semiempirical methods within

MOPAC also use two experimentally determined constants per atom: the atomic

mass of the most abundant isotope and the heat of atomization.

Stewart (1990a) includes tables which illustrate the relative accuracy of three

semiempirical methods: MNDO, AM1 and MNDO-PM3, on such factors as heat of

formation, molecular geometries, dipole moments and ionization potentials.

Reference geometry data was taken from many sources, mainly X-ray and microwave

structures. Average ΔH_f errors are 13.8 (MNDO), 1.2 (AM1) and 0.3 kcal/mol

(PM3), while average dipole errors are 0.45 (MNDO), 0.35 (AM1) and 0.38D (PM3)

and average ionization errors are 0.78 (MNDO), 0.61 (AM1) and 0.57 eV (PM3).

Table 3.4 compares experimental and derived ΔH_f°, show in subsequent Chapters 5,

6 and 7, with values calculated from both AM1 and PM3. His general comments on

these methods include the fact that MNDO predicts sterically crowded molecules to

be too unstable, in contrast, four-membered rings are predicted to be too stable.

This trends are largely corrected in both AM1 and PM3. AM1 does better for

hydrocarbons than the statistics indicate. The largest error in the hydrocarbons,

Table 3.3

PARAMETERS USED IN SEMIEMPIRICAL ORBITAL METHODS[1]

PARAMETER	DESCRIPTION	MINDO/3	MNDO	AM1	PM3
U_s and U_p	s and p atomic orbital one-electron one-center integrals	+	*	*	*
β_s and β_p	s and p atomic one-electron two-center resonance integral terms		*	*	*
I_s	s atomic orbital ionization potential for two-center resonance integral term	+			
I_p	p atomic orbital ionization potential for two-center resonance integral term	+			
β_{AB}	diatomic two-center one-electron resonance integral multiplier	*			
ξ_s	s-type Slater atomic orbital exponent	*	*	*	*
ξ_p	p-type Slater atomic orbital exponent	*	*	*	*
α_A	atom A core-core repulsion term		*	*	*
α_{AB}	atoms A and B core-core repulsion term	*			
G_{ss}	s-s atomic orbital one-center two-electron repulsion integral	+	+	+	*
G_{sp}	s-p atomic orbital one-center two-electron repulsion integral	+	+	+	*
G_{pp}	p-p atomic orbital one-center two-electron repulsion integral	+	+	+	*
G_{p2}	p-p' atomic orbital one-center two-electron repulsion integral	+	+	+	*
H_{sp}	s-p atomic orbital one-center two-electron exchange integral	+	+	+	*
K_{nA} or a_{nA}	Gaussian multiplier for nth Gaussian of atom A			*	*
L_{nA} or b_{nA}	Gaussian exponent multiplier for nth Gaussian of atom A			*	*
M_{nA} or c_{nA}	radius of center of nth Gaussian of atom A			*	*

[1] adapted from Stewart (1990a)

Table 3.4

COMPARISON OF ENTHAPLIES OF FORMATION FROM EXPERIMENT AND SEMIEMPIRICAL METHODS FOR MULTIPLY-METHYLATED ACENES

MULTIPLY-METHYLATED ACENE	EXPERIMENTAL VALUE (kcal/mol)	AM1 VALUE (kcal/mol)	PM3 VALUE (kcal/mol)
Naphthalene	35.9	40.6	40.7
1-Methylnaphthalene	27.2	33.9	32.1
2-Methylnaphthalene	26.4	32.9	31.2
1,4-Dimethylnaphthalene	19.7	27.4	23.6
Anthracene	55.2	62.9	61.7
1-Methylanthracene	46.5	56.3	53.1
2-Methylanthracene	45.7	55.1	52.1
9-Methylanthracene	47.0	59.0	54.6
9,10-Dimethylanthracene	38.8	55.2	48.1

bicyclobutane, is over 10 kcal/mol larger than any other error.

The final step beyond semiempirical methods is ab initio molecular orbital theory. The term ab initio implies a rigorous, nonparametrized molecular orbital treatment derived from first principles, although in practice, a number of simplifying assumptions are made. The calculations are more complete, and therefore more expensive in terms of computer time, than semiempirical methods.

3.5 Comparison of Molecular Orbital Methods

Although Stewart (1990a) provided tables to illustrate the accuracy of each method for average ΔH_f errors, dipole errors and ionization energies, we chose to concentrate of the differences in the calculated to the experimental ionization potentials and electron affinities for substituted and unsubstituted polycyclic aromatic hydrocarbons. Ionization potentials and electron affinities were chosen since these values are directly used in the FMO expression. Ionization potentials are calculated in these methods using Koopmans' theorem, which states that for closed-shell systems the ionization potential is the negative of the corresponding molecular orbital eigenvalue. To determine how the different semiempirical calculation methods for the MO parameters influence the values of E'(FMO), an error analysis was performed using the addition of *cis*-butadiene to acenaphthylene using values from Hückel, MNDO and AM1 methods. The full two-term non-dimensionalized

185

expression, $E'(FMO) = -\Delta E(FMO)/2\gamma^2$, was differentiated with respect to each variable in the expression. The relevant equations are shown in Figure 3.9. As a basis, experimental ionization potentials and electron affinities and average values of coefficients from the three methods considered were used to compute $\Delta E'(FMO)$. For the coefficients, the deltas were the absolute value of the difference of the absolute values of the average value for the MO coefficients minus the absolute value of the coefficients of the considered method. For the energies, the deltas were the differences between the energy of the method being considered minus the experimental ionization potential or electron affinity. Figure 3.10 shows how the cis-butadiene molecule can add to the acenaphthylene to yield either fluoranthene, aceanthrylene or acephenanthrylene and the values for $E'(FMO)$ and the errors as a percent of the $E'(FMO)$ calculated with Hückel, MNDO, and AM1 methods. These calculations show that errors in the MO energy levels led to much larger errors in $E'(FMO)$ than errors in the MO coefficients since the errors in the Hückel energy levels were much larger than the MOPAC energy level errors. From this comparison, it is concluded that the semiempirical methods available within MOPAC were best for estimating the MO parameters needed for our $E(FMO)$ calculations.

To determine which semiempirical method would be used, we compared the calculated ionization potentials and electron affinities from AM1 and PM3 to the experimental values for a variety of substituted and unsubstituted hydrocarbons ranging in ring size from benzene to perylene and including both methyl and

$$E'(FMO) = \frac{\Delta E}{\gamma^2} = \frac{(C_t^{HO}C_u^{LU}+C_{t'}^{HO}C_{u'}^{LU})^2}{E_A^{HO}-E_B^{LU}} + \frac{(C_t^{LU}C_u^{HO}+C_{t'}^{LU}C_{u'}^{HO})^2}{E_B^{HO}-E_A^{LU}}$$

DIFFERENTIATING:

$$\Delta E'(FMO) = \frac{\partial E'(FMO)}{\partial C_t^{HO}}|\Delta C_t^{HO}| + \frac{\partial E'(FMO)}{\partial C_u^{LU}}|\Delta C_u^{LU}| + \frac{\partial E'(FMO)}{\partial C_t^{LU}}|\Delta C_t^{LU}| +$$

$$\frac{\partial E'(FMO)}{\partial C_u^{HO}}|\Delta C_u^{HO}| + \frac{\partial E'(FMO)}{\partial C_{t'}^{HO}}|\Delta C_{t'}^{HO}| + \frac{\partial E'(FMO)}{\partial C_{u'}^{LU}}|\Delta C_{u'}^{LU}| +$$

$$\frac{\partial E'(FMO)}{\partial C_{t'}^{LU}}|\Delta C_{t'}^{LU}| + \frac{\partial E'(FMO)}{\partial C_{u'}^{HO}}|\Delta C_{u'}^{HO}| + \frac{\partial E'(FMO)}{\partial E_B^{LU}}|\Delta E_B^{LU}| +$$

$$\frac{\partial E'(FMO)}{\partial E_A^{HO}}|\Delta E_A^{HO}| + \frac{\partial E'(FMO)}{\partial E_A^{LU}}|\Delta E_A^{LU}| + \frac{\partial E'(FMO)}{\partial E_B^{HO}}|\Delta E_B^{HO}|$$

WHERE:

$$\frac{\partial E'(FMO)}{\partial C_t^{HO}} = \frac{2(C_t^{HO}C_u^{LU}+C_{t'}^{HO}C_{u'}^{LU})C_u^{LU}}{E_A^{HO}-E_B^{LU}} \qquad \frac{\partial E'(FMO)}{\partial C_{t'}^{LU}} = \frac{2(C_t^{LU}C_u^{HO}+C_{t'}^{LU}C_{u'}^{HO})C_{u'}^{HO}}{E_B^{HO}-E_A^{LU}}$$

$$\frac{\partial E'(FMO)}{\partial C_u^{LU}} = \frac{2(C_t^{HO}C_u^{LU}+C_{t'}^{HO}C_{u'}^{LU})C_t^{HO}}{E_A^{HO}-E_B^{LU}} \qquad \frac{\partial E'(FMO)}{\partial C_{u'}^{HO}} = \frac{2(C_t^{LU}C_u^{HO}+C_{t'}^{LU}C_{u'}^{HO})C_{t'}^{LU}}{E_B^{HO}-E_A^{LU}}$$

$$\frac{\partial E'(FMO)}{\partial C_t^{LU}} = \frac{2(C_t^{LU}C_u^{HO}+C_{t'}^{LU}C_{u'}^{HO})C_u^{HO}}{E_B^{HO}-E_A^{LU}} \qquad \frac{\partial E'(FMO)}{\partial E_B^{LU}} = \frac{(C_t^{HO}C_u^{LU}+C_{t'}^{HO}C_{u'}^{LU})^2}{(E_A^{HO}-E_B^{LU})^2}$$

$$\frac{\partial E'(FMO)}{\partial C_u^{HO}} = \frac{2(C_t^{LU}C_u^{HO}+C_{t'}^{LU}C_{u'}^{HO})C_t^{LU}}{E_B^{HO}-E_A^{LU}} \qquad \frac{\partial E'(FMO)}{\partial E_A^{HO}} = \frac{-(C_t^{HO}C_u^{LU}+C_{t'}^{HO}C_{u'}^{LU})^2}{(E_A^{HO}-E_B^{LU})^2}$$

$$\frac{\partial E'(FMO)}{\partial C_{t'}^{HO}} = \frac{2(C_t^{HO}C_u^{LU}+C_{t'}^{HO}C_{u'}^{LU})C_{u'}^{LU}}{E_A^{HO}-E_B^{LU}} \qquad \frac{\partial E'(FMO)}{\partial E_A^{LU}} = \frac{(C_t^{LU}C_u^{HO}+C_{t'}^{LU}C_{u'}^{HO})^2}{(E_B^{HO}-E_A^{LU})^2}$$

$$\frac{\partial E'(FMO)}{\partial C_{u'}^{LU}} = \frac{2(C_t^{LU}C_u^{HO}+C_{t'}^{LU}C_{u'}^{HO})C_{t'}^{HO}}{E_A^{HO}-E_B^{LU}} \qquad \frac{\partial E'(FMO)}{\partial E_B^{HO}} = \frac{-(C_t^{LU}C_u^{HO}+C_{t'}^{LU}C_{u'}^{HO})^2}{(E_B^{HO}-E_A^{LU})^2}$$

Figure 3.9: Equations used in error analysis of FMO expression.

187

FLUORANTHENE

BASIS = 0.05430

	Huckel	MNDO	AM1
E'(FMO)	0.03384	0.05012	0.05040
ΔE'(FMO)	0.02046	0.00417	0.00390
%error	37.69	7.70	7.19

ACEANTHRYLENE

BASIS = 0.00217

	Huckel	MNDO	AM1
E'(FMO)	0.00187	0.00232	0.00146
ΔE'(FMO)	0.00029	0.00015	-0.00071
%error	0.55	-0.27	1.31

ACEPHENANTHRYLENE

BASIS = 0.01516

	Huckel	MNDO	AM1
E'(FMO)	0.01016	0.01462	0.01564
ΔE'(FMO)	0.00500	0.00053	-0.00048
%error	9.21	0.99	-0.89
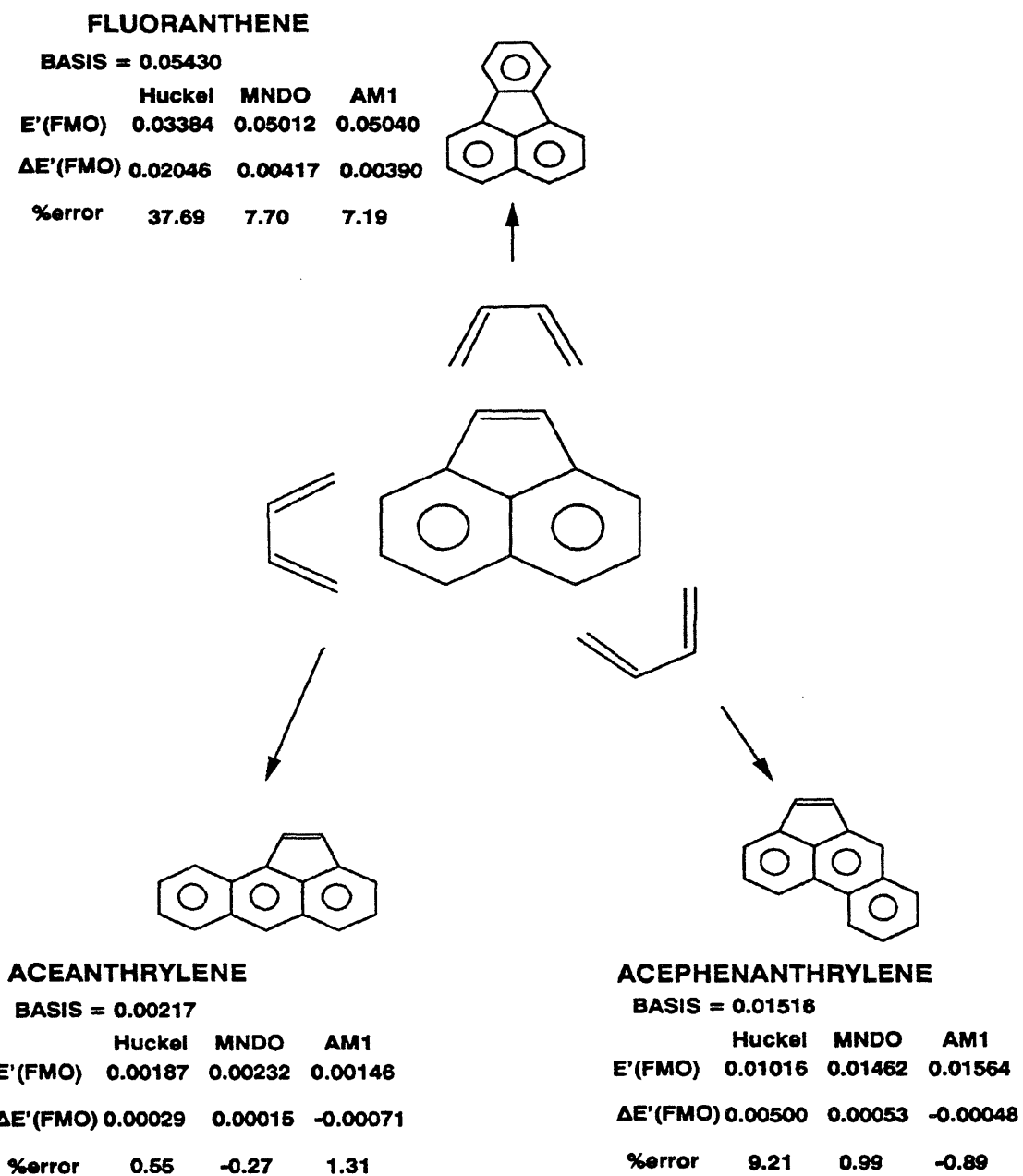
Figure 3.10: E'(FMO) values and errors for semiempirical molecular orbital methods.

dimethyl substitution. The comparison included only compounds that had experimentally determined ionization potentials and electron affinities available. After speaking with Dr. Stewart (1992), he suggested either AM1 or PM3 be used and that we compare methods for the our class of molecules. His comparison of six aromatic compounds gave average errors of 0.55 eV for MNDO, 0.49 eV for AM1 and 0.65 eV for PM3 (Stewart 1991b).

Figure 3.11 shows the comparison of AM1 calculated ionization potentials (top) and electron affinities (bottom) with the experimental values. Experimental values for the ionization potentials are from Lias et. al. (1988) and for electron affinities are from Wojnarovtis and Foldiak (1981). Only the parent of a group of methyl substituted molecules is labeled. Linear regression of the ionization potential data yielded a line of slope 0.771 ± 0.061 and intercept 2.534 ± 0.168 at the 90% confidence limit, whereas linear regression of the electron affinity data yielded a line of slope 1.740 ± 0.229 and intercept -0.040 ± 0.104 again at the 90% confidence limit. Figure 3.12 shows the comparison of PM3 calculated ionization potentials (top) and electron affinities (bottom) with the experimental values. Again only the parent of a group of methyl substituted molecules is labeled. Linear regression of the ionization potentials yielded a line of slope 0.759 ± 0.173 and intercept of 2.740 ± 0.175 at the 90% confidence limit, whereas linear regression of the electron affinity data yielded a line of slope 1.698 ± 0.231 and intercept 0.101 ± 0.105 again
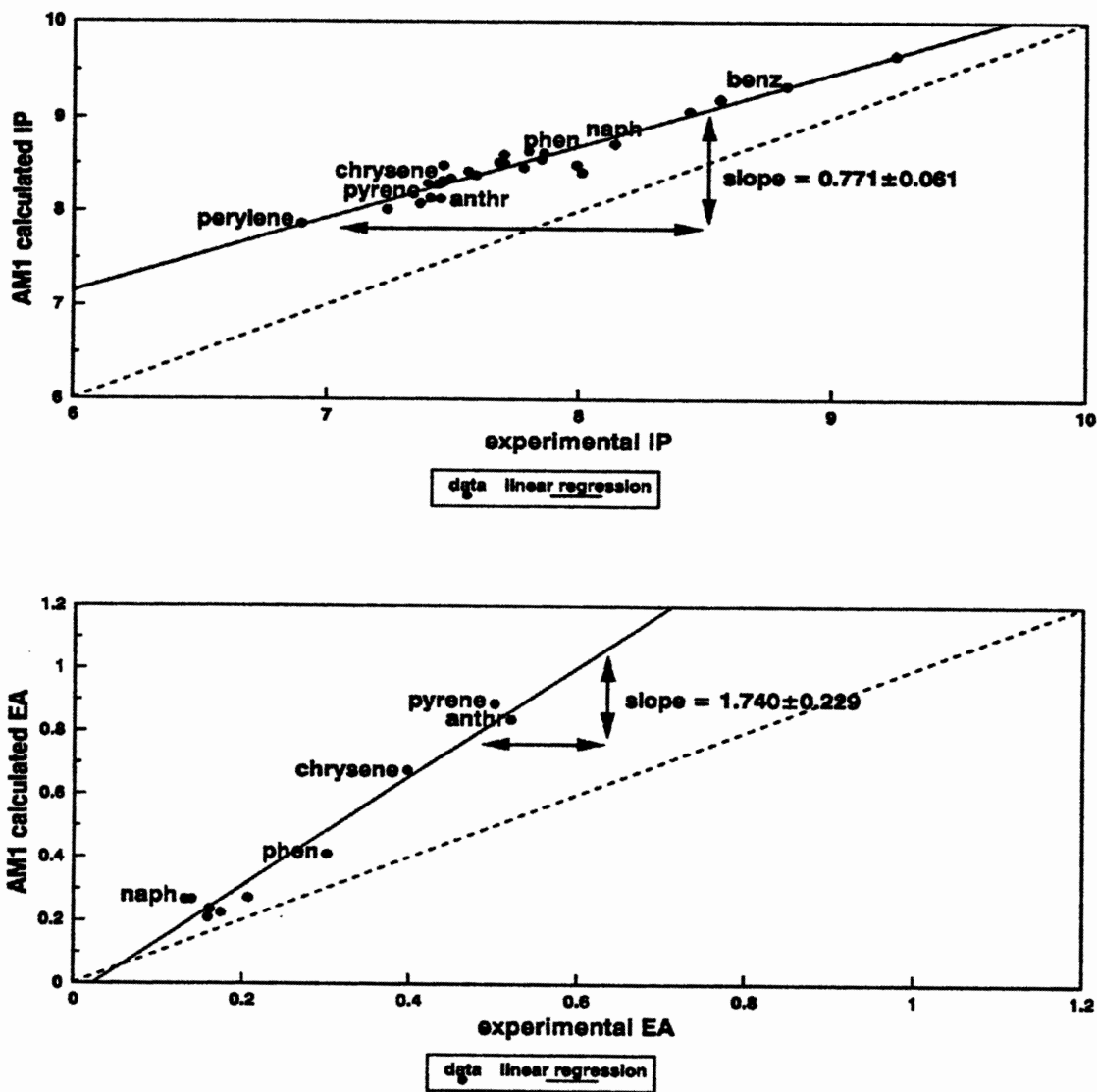
Figure 3.11: Comparison of AM1 ionization potentials (top) and electron affinities (bottom) to experimental values.

190
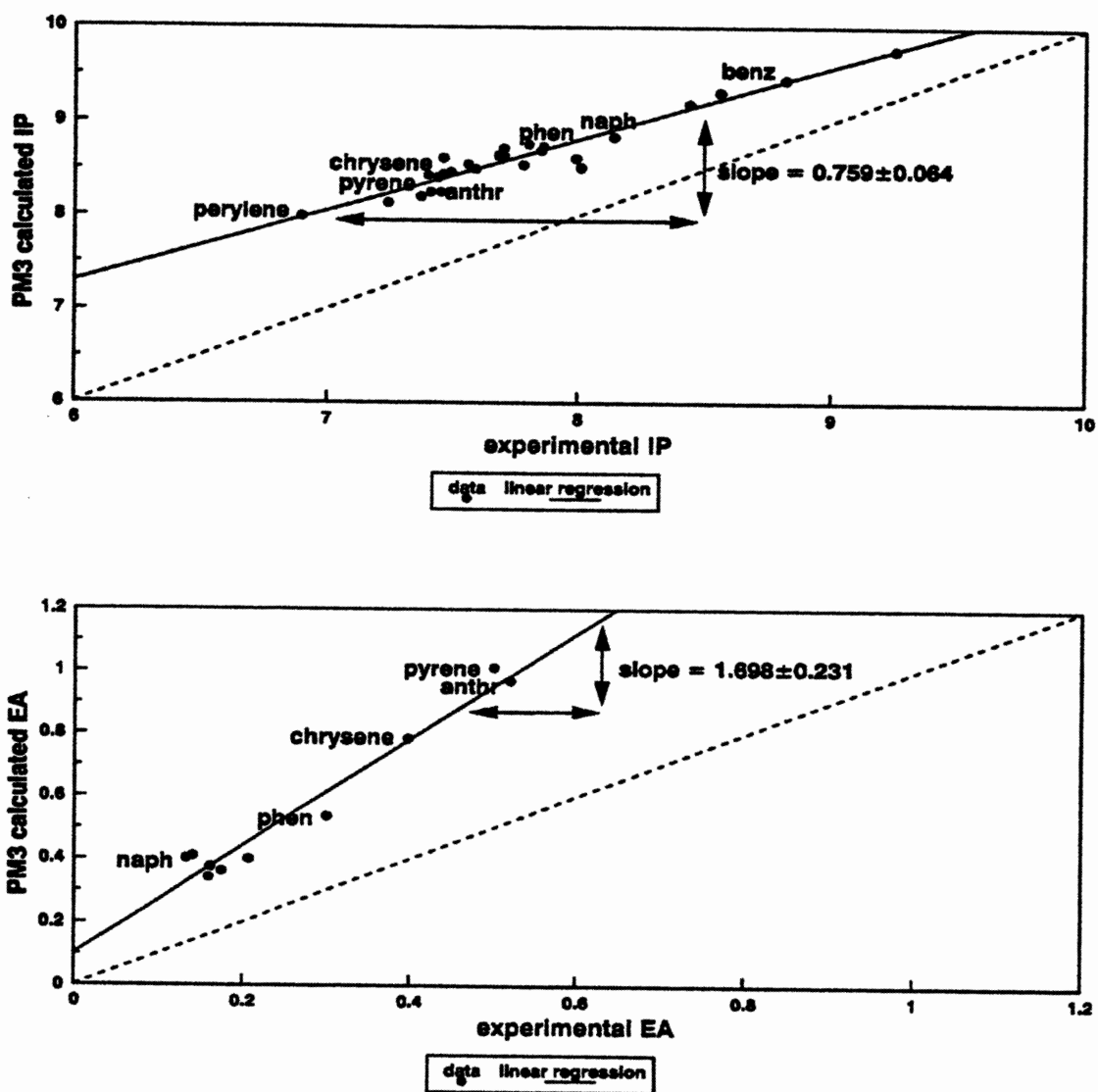
Figure 3.12: Comparison of PM3 ionization potentials (top) and electron affinities (bottom) with experimental values.

at the 90% confidence limit. The slopes and the intercepts of these lines for these

methods are very close. Figure 3.13 compares the electron densities of the HOMO

and LUMO energy levels of anthracene by AM1 and PM3 methods. Again, there

is very little difference between the two methods. Table 3.5 compares experimental

properties with values calculated from both AM1 and PM3. Both methods give close

values to experimental ΔH_r°, electron affinities, ionization potentials and bond

lengths with very little difference between them. PM3 was chosen in the present

work on account of its being the latest evolution of these methods.
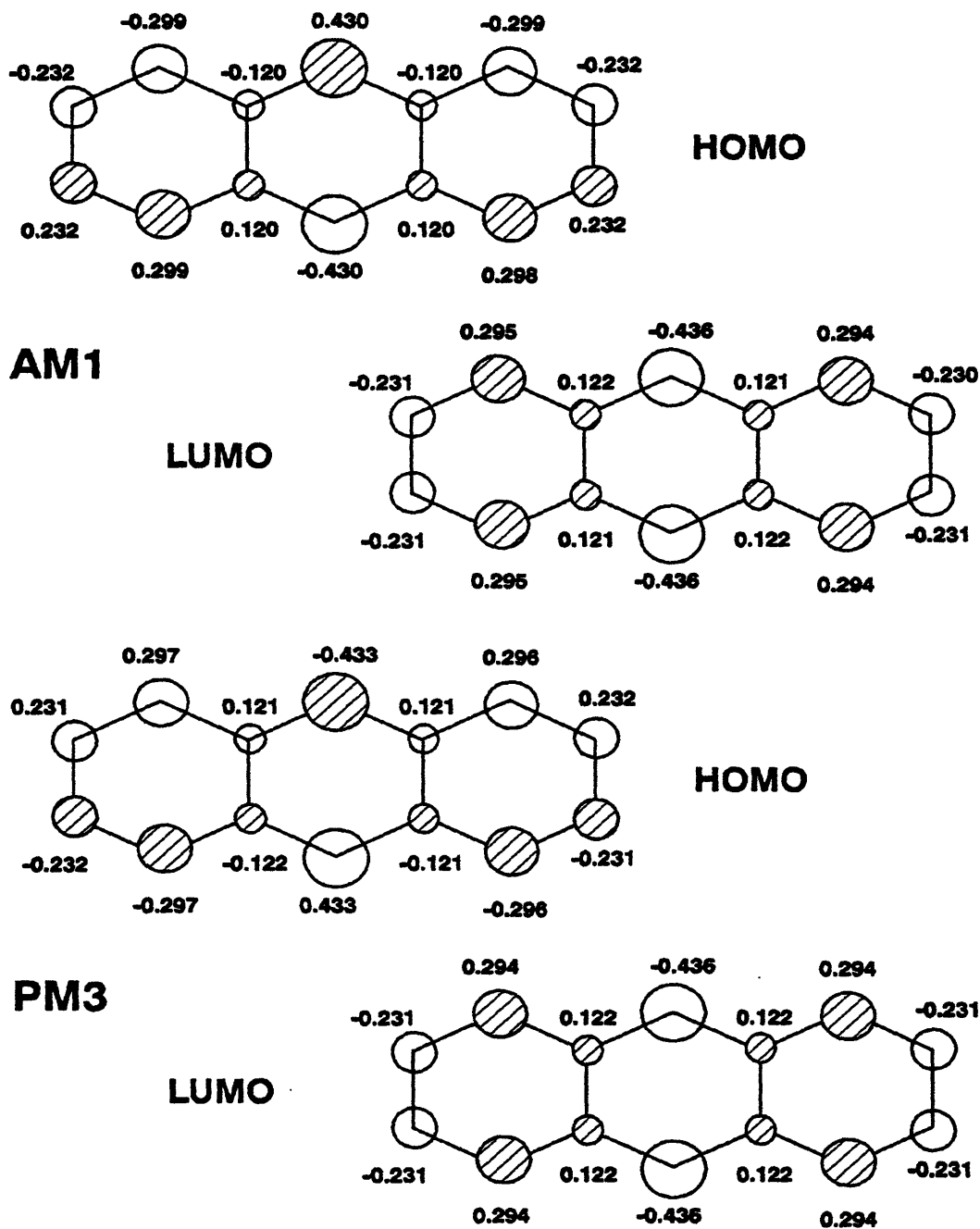
Figure 3.13: Comparison of the electron densities of the HOMO and LUMO levels of anthracene by AM1 and PM3.

Table 3.5

COMPARISON OF EXPERIMENTAL WITH SEMIEMPIRICAL CALCULATED VALUES FOR ANTHRACENE

PROPERTY	EXPERIMENTAL VALUE	AM1 VALUE	PM3 VALUE
Heat of Formation[1] (kcal/mol)	55.44 ± 1.1	62.94	61.66
Ionization Potentials[2]: 1st (eV)	7.41	8.13	8.25
Second	8.54	9.19	9.27
Third	9.19	9.85	9.91
Fourth	10.54	11.10	11.08
Electron Affinity[3] (eV)	0.52	0.84	0.97
Bond Lengths[4]: C1-C2 (Å)	1.375	1.364	1.360
C2-C3	1.418	1.426	1.426
C3-C4	1.375	1.365	1.360
C4-C12	1.444	1.432	1.433
C5-C6	1.375	1.365	1.360
C6-C7	1.418	1.425	1.425
C7-C8	1.375	1.364	1.360
C8-C14	1.444	1.434	1.433
C9-C11	1.405	1.399	1.400
C9-C14	1.405	1.399	1.397
C10-C12	1.405	1.399	1.400
C10-C13	1.405	1.399	1.400
C11-C12	1.433	1.428	1.421
C13-C14	1.433	1.428	1.421

[1] Cox and Pilcher (1970)

[2] Dias (1987)

[3] Wojnarovtis and Foldiak (1981)
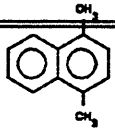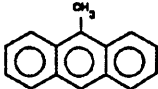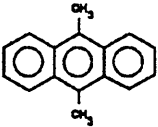
[4] Mason (1964)

Chapter 4.

Experimental Procedures

Table 4.1 is a summary detailing the range of operating conditions for the experimental thermolysis. Listed are the model compound, structure, temperature, batch holding time and concentration range studied and the temperature at which the light gas analysis was performed. These studies provided kinetic measurements and mechanics interpretations of the core and peripheral reactions.

Table 4.1

EXPERIMENTAL GRID FOR MODEL COMPOUND THERMOLYSIS

Compound	Structure	Temperature Range (°C)	Holding Times (sec)	Concentration (moles/liter)	Temperature of Light Gas Analysis (°C)
1,4-dimethyl-naphthalene		370-550	150-115200	0.081-2.07	450
9-methyl-anthracene		315-409	450-57600	0.082-2.06	370
9,10-dimethyl-anthracene		315-409	450-57600	0.082-2.47	335 and 370

196

4.1 Chemicals and Experimental Apparatus

4.1.1 Chemicals

All chemicals were purchased commercially from Aldrich Chemical Company and have the nominal purities given in Table 4.2. All chemicals were used at their purchased level of purity. *Cis-* and *trans*-dihydrodimethylanthracene were synthesized by Pope (1987). A mixture of 99% *cis* and 1% *trans* was used for matching retention times. Response factors were not calculated for the *cis-* and *trans*-dihydrodimethylanthracene since the compounds' purities were not known. The methylene chloride solvent used was either omnisolv glass distilled from EM Science or CHromAR HPLC from Malinckrodt.

4.1.2 Liquid and Gas Reactors

Previous work by Klein (1981), Bass (1982) and Pope (1987) led to the choice of tubing bomb reactor. This batch reactor was easy to use, minimized consumption of scarce and costly chemicals, and provided adequate time versus conversion data. The major limitation of the batch system was the exclusion of very small residence time thermolysis due to human reflex and reactor heat-up times.

The liquid's reactor was constructed of a Swagelok 1/4" 316 stainless steel port connector (cat. #SS-401-PC) with a 1/4" 316 stainless steel cap (cat. #SS-400-C) at

Table 4.2

PURITIES AND RESPONSE FACTORS FOR STANDARDS

COMPOUND	PURITY	RESPONSE FACTOR
Biphenyl	99%	1.0000
Naphthalene	99%	0.7818 ± 0.0233
1-Methylnaphthalene	99%	1.0364 ± 0.0099
2-Methylnaphthalene	97%	0.9068 ± 0.0323
2,6-Dimethylnaphthalene	99%	0.9930 ± 0.0384
1,3-Dimethylnaphthalene	96%	1.1398 ± 0.0432
1,2-Dimethylnaphthalene	98%	1.0991 ± 0.0414
1,4-Dimethylnaphthalene	95%	1.0510 ± 0.0188
Anthracene	99.9%	1.1904 ± 0.0463
Phenanthrene	98+%	1.1642 ± 0.0440
1-Methylanthracene	99%	1.2027 ± 0.0518
2-Methylanthracene	97%	1.2062 ± 0.0423
9-Methylanthracene	98%	1.2586 ± 0.0360
9,10-Dimethylanthracene	99%	1.3239 ± 0.0363

both ends. Copper wire suspends the reactors at an equal depth from a unistrut

frame that rests atop the sand bath. The volume of the reactor was calculated from

the dimensions shown in Figure 4.1. The depressions in the caps were approximated

as cones of base b/2 and height a. The total volume of the reactor was the volume

of the port connector, which was calculated as the volume of a cylinder, plus the

depression in the caps:

$$V = \frac{\pi b^2 c}{4} + \frac{2\pi b^2 a}{12} \qquad (4.1)$$

The reactant concentration was calculated as the number of moles of substrate

loaded divided by the reactor volume. Appendix B shows the calculations for the

estimation of the state properties for the model compounds and biphenyl diluent.

The techniques for determining the state properties of reaction mixtures within the

reactor were taken from Bass (1982) and Reid et.al. (1987). These properties were

such that over the temperature range of interest (315-550°C) 0.3 g of reactant

provides a predominance of material in the liquid phase as well as a healthy safety

margin against failure of the vessel.

The tubing bomb type reactor was modified to analyze for light gases.

Figure 4.1 shows the apparatus used for the analysis. Slightly different configurations

were used for the anthracene and naphthalene compounds. For the anthracene

compounds, an 1/8" diameter piece of stainless steel tubing (length = 5 3/4") was

connected to the tubing bomb reactor (1/4" port connector) with a union reducer
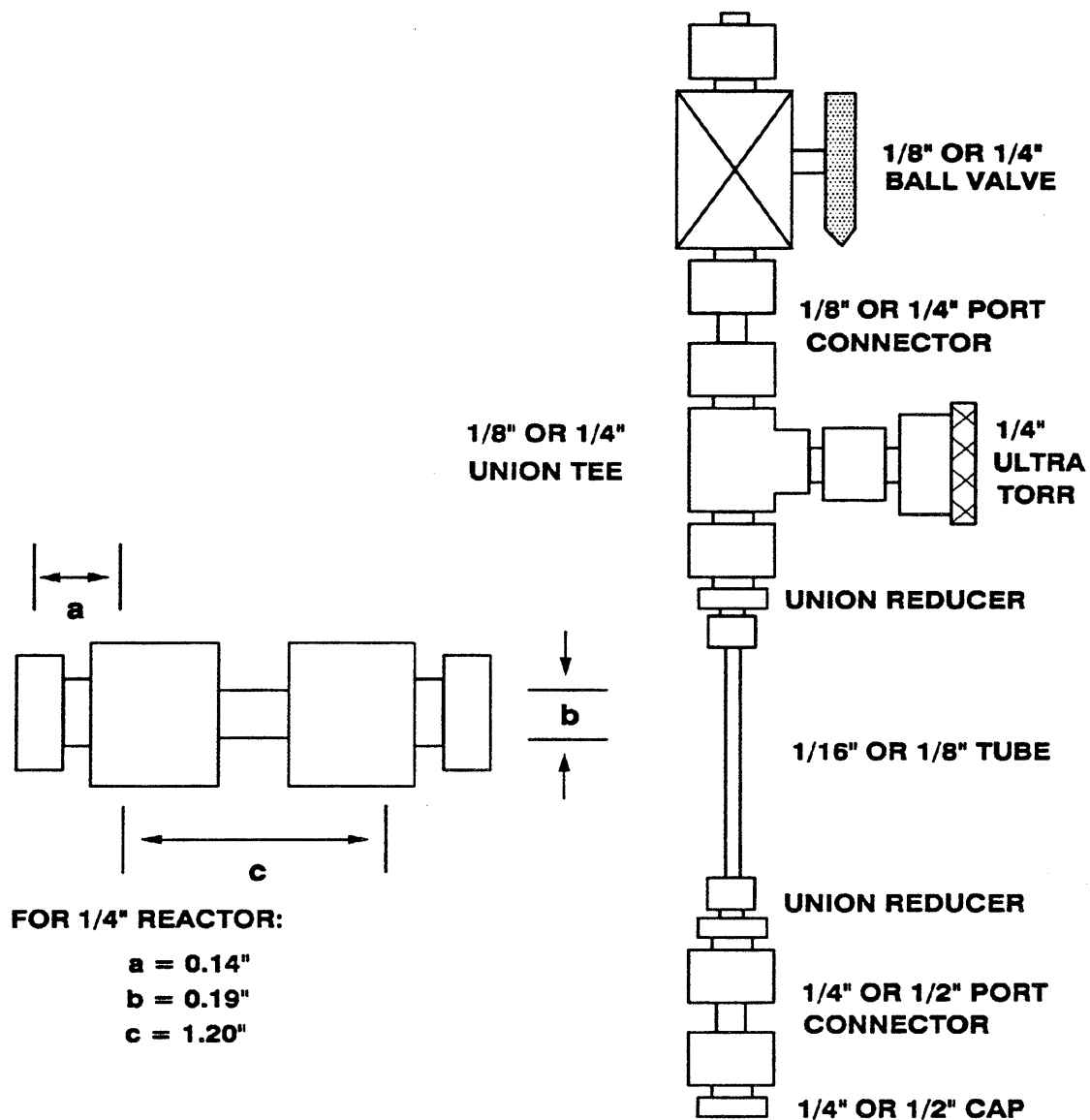
Figure 4.1: Dimensions used to calculate liquid reactor volume and modifications for light gas analysis.

(cat. #SS-400-6-2). A 1/4" union tee (cat. #SS-400-3) was placed at the other end of the tube with another union reducer. A 1/4" port connector off the union tee connected a 1/4" ultra torr fitting (cat. #SS-4-UT-A-4) equipped with a 9.5 mm thermogreen LB-2 septum through where the gas samples were taken. Another 1/4" port connector off the top of the union tee joined a 1/4" stainless steel ball value (cat. #SS-42S4), which allowed nitrogen to purge the reactor vessel. Nitrogen also served as an internal standard in the light gas analysis. The volume of the apparatus, 4.0 cm^3, was calculated from internal measurements of the Swagelok parts given in the manufacturer's catalog. Although the reactor volume for the gas analysis was approximately seven times the volume of the tubing bomb, Appendix B shows that over the range of reaction temperatures both 9-methylanthracene and 9,10-dimethylanthracene are primarily in the liquid phase, therefore indicating that the reaction took place in the 65% of the reactor volume submerged in the sand bath. The same amount of biphenyl and anthracene substrate was used in both the tubing bombs and the light gas apparatus.

For the naphthalene compound, Appendix B shows at T = 450°C most of the substrate is in the gas phase. Therefore, the apparatus was modified so a larger volume of the reactor was in the sand bath. A 1/2" port connector (#SS-811-PC) tubing bomb reactor was connected to a 1/16" piece of stainless steel tube with a union reducer (#SS-810-6-2). Another union reducer joined the tube to a 1/8" union tee (#SS-200-3). A 1/8" port connector (#SS-201-PC) off the union tee connected

a 1/4" ultra torr fitting (cat. #SS-4-UT-A-4) equipped with a 9.5 mm thermogreen

LB-2 septum though where the gas samples were taken. A 1/8" port connector off

the top of the union tee was attached to a 1/8" stainless steel ball value (cat. #SS-

41S2), which again allowed nitrogen to purge the reactor vessel. The volume of the

apparatus, 5.0 cm^3, was calculated from internal measurements of the Swagelok parts

given in the manufacturer's catalog. The larger port connector increases the amount

of reactor submerged in the sand bath to 85%. The amount of 1,4-

dimethylnaphthalene was increased corresponding to the appropriate increase in

reactor volume, while the amount of biphenyl used remained the same.

4.1.3. Sand Bath and Temperature Control

A Techne Fluidised Sand Bath Model SBS-4 coupled with Techne

Temperature Controller Model TC4B was used for the thermolysis reactions. The

sand bath temperature capabilities ranged from ambient to 600°C and thus provided

a wide range of temperatures for thermolysis. Although the temperature was set

using the controller, a thermocouple was placed in the sand bath at the same depth

as the reactors to insure accurate temperatures and maintain isothermal conditions

throughout the runs. An Omega Model 650 Thermocouple Thermometer displayed

the temperature in the sand bath around the reactors for the duration of the runs.

Over a sixteen hour run, the sand bath temperature only fluctuated by ± 1°C. Heat-

up and cool-down times were estimated at approximately 30 seconds by Bass (1982), therefore negligible for runs longer than 3 minutes.

4.2 Experimental Procedure

The full experimental grid was run for each model compounds, as summarized in Table 4.1. The following sections describe the protocol for analysis of the liquid products alone and the liquid and gaseous products together.

4.2.1 Liquid Product Protocol

Seven reactors were run simultaneously in the Techne sand bath. These reactors spanned the chosen reaction times for a given concentration and temperature. Each reactor was cleaned with methylene chloride, rinsed with acetone and the soaked in methylene chloride and allowed to air dry. The reactors were charged on a Mettler balance (model AE100). The biphenyl was added first followed by the species to be thermolyzed. The reactors were then sealed without any inert involved. It was shown that conversions remained relatively constant for a given reaction time and temperature with and without a nitrogen purge by comparing the results to the runs with the light gas analysis for the anthracene cases.

The reactors were then draped over a small unistrut frame that sits on top of the sand bath. A 16" piece of copper wire wrapped tightly around the body of the reactor suspended the reactors 8" from the unistrut frame into the sand bath. All

203

reactors were plunged into the sand bath simultaneously with the temperature set 2-3°C higher than desired for the run. The bath returned to the run temperature within a minute.

When the reaction had proceeded for the desired time, the reactors were removed from the sand bath and quenched in a beaker of ice water. After two or three minutes of quenching, the reactors were removed, wiped dry, the exterior rinsed with acetone and then methylene chloride and opened. The contents were removed with methylene chloride and the reactor was washed repeatedly to insure complete extraction. The products were then diluted up to 100 ml with methylene chloride making sure the solids dissolve as solvent was increased. Three 0.5 μl sample were injected into the GC.

4.2.2 Light Gas Product and Liquid Product Protocol

Similarly to the liquid analysis, six reactors were run simultaneously in the sand bath. Again, each tubing bomb reactor was cleaned with methylene chloride, rinsed with acetone and the soaked in methylene chloride and allowed to air dry. The tube, tee and ball valve were rinsed with acetone and then methylene chloride and allowed to air dry. A new septum was placed in the ultra torr before each run. The reactors were again charged on a Mettler balance (model AE100). In these reactors, the species to be thermolyzed was added before the biphenyl. The tubing bombs were then connected to the tube, tee and ball valve while a small amount of

N_2 was flowing through the apparatus. Once the port connector was tightly sealed, N_2 was allowed to purge the air out of the apparatus through the ultra torr fitting. After five minutes of purging, the ultra torr was tightened and the ball valve closed. Once the purge was removed and a cap placed on the exposed end of the ball valve, the reactor was brought back to atmospherical pressure by a quick opening and closing of the ball valve. This procedure is outlined in Figure 4.2.

The reactors were then draped over a small unistrut frame that sat on top on the sand bath. This frame was designed to hold the reactors vertically while allowing the tubing bombs to remain at the same 8" depth in the sand bath that the reactors were in the liquid runs. Again, all reactors were plunged into the sand bath simultaneously with the temperature set 2-3°C higher than desired for the run. The bath returned to the run temperature within a minute.

When the reaction had proceeded for the desired time, the reactor was then removed from the sand bath and quenched in a beaker of ice water, making sure the entire length of the reactor was cooled. After two or three minutes of quenching, three gas samples of 100μl each were taken through the septum in the ultra torr fitting and run consecutively on the GC. Once the gas analysis was complete, the reactor exterior was rinsed with acetone followed by methylene chloride and then opened. The contents were removed with methylene chloride and the reactor was washed repeatedly to insure complete extraction. The products were then diluted up

N$_2$

valve open

valve closed

Fill reactor with
DMA and BIP

Attach top part and
purge with nitrogen
while ultra torr fitting
is loose

Tighten ultra torr fitting
then close ball valve
Vent ball valve quickly
to bring back to
atmospheric pressure
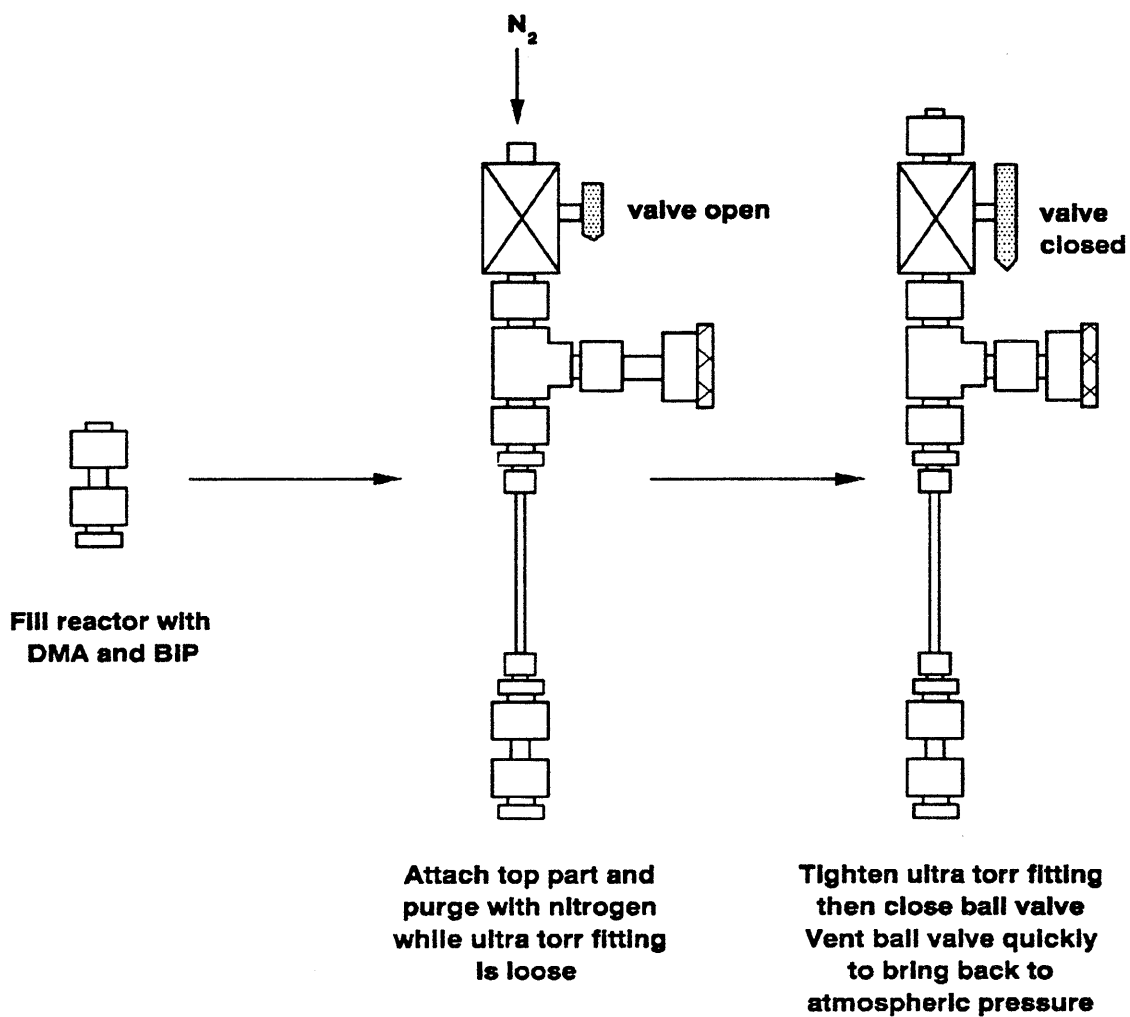
Figure 4.2: Procedure for loading light gas reactors.

to 100 ml with methylene chloride making sure the solids dissolve as solvent was increased. Three 0.5 μl sample were injected into the GC.

4.3 Identification and Analysis of Thermolysis Products

All liquids and gaseous thermolysis products were identified and analyzed. Gas chromatography was the main vehicle for analysis, with gas chromatography/mass spectrometry and liquid chromatography used to identify the heavy components that would not elute on the GC. Gas chromatography/mass spectrometry was also used to identify products for which standards were not available.

4.3.1 Gas Chromatography

All thermolysis products were identified and analyzed by a Hewlett-Packard 5890 Series II Gas Chromatograph (GC) equipped with flame ionization (FID) and thermal conductivity (TCD) detectors and on-column and split/splitless injectors. The GC was controlled and the data was gathered by a Hewlett-Packard Vectra ES12 running the HP3365 Chemstation software package. Identification of some products was made by matching retention times to known standards.

4.3.1.1 Liquid Products

Concentrations of liquid products were calculated using response factors with an internal standard in each run. Biphenyl, the internal standard, was shown to be inert in runs up to 550°C and times up to 16 hours, therefore it was assumed that all the biphenyl put into the reactor was recovered after thermolysis. Absolute area/g counts for biphenyl were checked in each run to ensure complete extraction of products form the reactor and that biphenyl was truly inert.

The liquid products were analyzed using a HP-101 (Methyl Silicone Fluid) 25m x 0.2mm x 0.2μm film thickness column in the on-column injector and FID. Column flow rate was 0.5 ml/min of He carrier. The temperature program used in these runs was 80°C for 2 minutes followed by 7°C/min ramp to 250°C for 10 minutes. The injector was programmed at the same rate, but with a final temperature of 240°C for only 5 minutes to help speed up cool down time for the injector. The detector temperature was 320°C with air flow rate of 400±20 ml/min, H_2 flow rate of 30±1 ml/min and He make-up flow rate of 20±1 ml/min. Under these conditions with this column, polyaromatic hydrocarbons up to corene are eluted.

Response factors relative to biphenyl were calculated for all the chemicals shown in Table 4.2. Nine standards of varying concentrations of each chemical were prepared and analyzed. Each standard was run five times. Five different HP-101 columns were also used throughout the experiments. The above values were the

average of all 45 GC runs. Product concentrations were calculated using experimentally determined response factors with biphenyl as the internal standard. Response factors for each compound, i, were calculated as shown in Equation (4.2).

$$RF_i = \frac{area_i * X_i}{area_{(BIP)} * X_{(BIP)}} * RF_{(BIP)} \qquad (4.2)$$

where: X_i = mole fraction of compound i

RF_{BIP} = 1.000

For compounds not available commercially, response factors were estimated based on molecular weight by dividing the mass of carbon in the compound to the mass of carbon in biphenyl. Equation (4.3) shows how concentrations were calculated for each product species, i.

$$moles_i = \frac{area_i}{RF_i} * \frac{area_{BIP}}{moles_{BIP}} \qquad (4.3)$$

The biphenyl was assumed to be at the concentration put into the reactor initially. This assumption was checked for each run by calculating the area per gram of biphenyl placed in the reactors. Average area per grams values for biphenyl were determined from a series of standards.

All runs were integrated with an area reject value of 500, but only peaks with area greater than 1000 were quantified. A standard of anthracene and biphenyl was used to test the linearity of the peak area down to area counts of 900. The concentrations used were the same as in the 0.82 mol/l thermolysis runs. The initial

0.82 mol/l standard gave a peak area of approximately 1500000 counts for anthracene and 5300000 counts for biphenyl. This standard was then progressively diluted by steps of 2.5 and 10 up to 1526 and 1000 times the initial concentration. Each dilution was injected into the GC. From these GC runs, Figure 4.3 displays a doubly logarithmic plot of the area of the anthracene peak and the moles of the anthracene peak calculated from the area of the biphenyl peak and RRF for anthracene versus the moles of anthracene determined from dilution of the initial standard. These lines yield slopes of 1.006 ± 0.010 and 1.009 ± 0.007, respectively, for the area and moles calculated from RRF, indicating a linear relationship between peak area and concentration over four decades in both peak areas and concentrations.

4.3.1.2 Gas Products

Concentrations of the gas products were calculated from absolute area/μl counts for the gases using the nitrogen purge gas as an internal standard. The gases were analyzed on a 12ft 80/100 mesh HayeSep Q packed column with a split/splitless injector modified for a packed column and the TCD. Column flow rate was 35 ml/min of He carrier. The temperature program used in these runs was 38°C for 2 minutes followed by 15°C/min ramp to 150°C for 10 minutes. The detector temperature was 300°C with He reference flow rate of ±1 ml/min. The injector temperature was held at 250°C. Product concentrations were calculated from
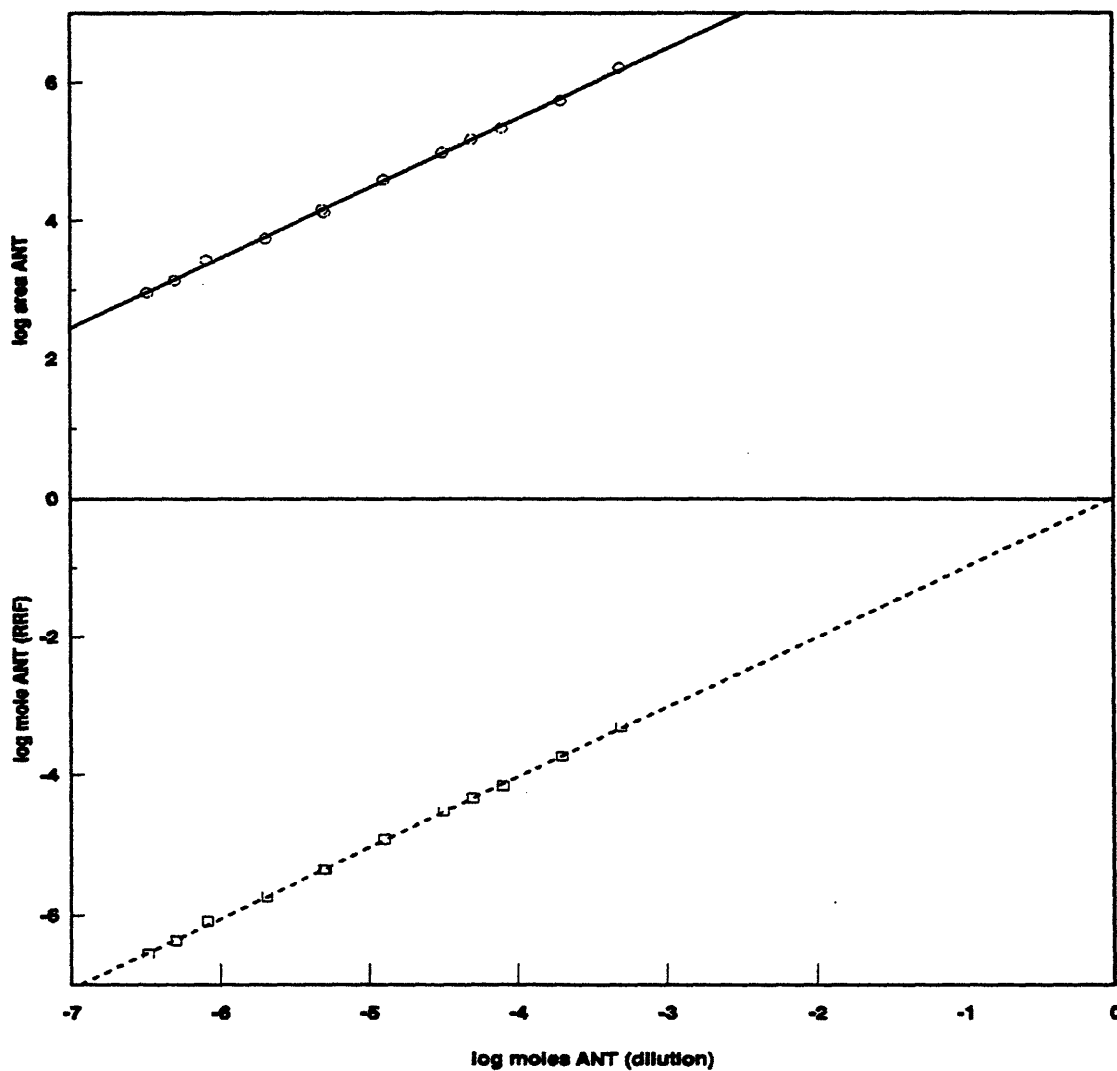
Figure 4.3: Showing linearity of GC area count versus concentration: log area
ANT peak and log moles$_{RRF}$ ANT versus log moles$_{dil}$ ANT.

dividing area counts by mole fractions using the nitrogen purge gas as an internal standard. The nitrogen concentration was calculated from the ideal gas law using the volume of the gas apparatus. It was assumed that this concentration remained the same throughout the reaction time. Mole fractions, X, for each compound, i, were calculated from area counts, weight factors in a TCD and molecular weight for the compound as shown in Equation (4.4).

$$X_i = \frac{area_i * WF_i}{MW_i} \qquad (4.4)$$

The concentration of the products were then calculated from the mole fractions for the species as shown in Equation (4.5).

$$moles_i = \frac{X_i}{X_{N_2}} * moles_{N_2} \qquad (4.5)$$

Figure 4.4 displays the GC of a standard used for light gas identification. The standard mixture was 49% H_2, 20% CO_2, 25% CO, 3% CH_4, 2% C_2H_6 and 1% C_3H_8. Although the standard did not contain N_2, it eluted at the same time as CO_2, which was determined by injection of N_2 with the same temperature program.
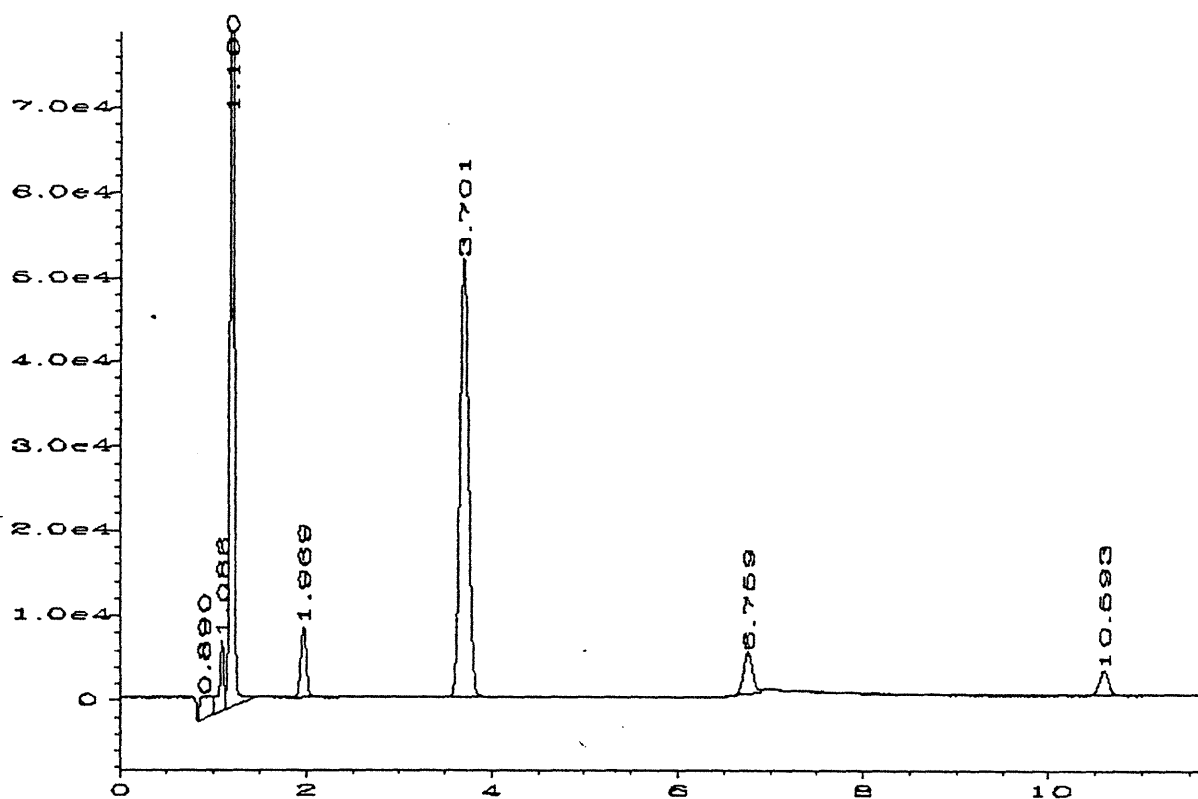
RETENTION TIME	COMPOUND
1.086	H_2
1.190	CO
1.969	CH_4
3.701	CO_2
6.759	C_2H_6
10.593	C_3H_8

Figure 4.4: GC of light gases standard.

213

4.3.2 Gas Chromatography/Mass Spectrometry

Three sets of product spectrums representing a low, medium and high conversion run were analyzed for each model compound on a gas chromatograph/mass spectrometer. These runs were performed in the absence of biphenyl and at an initial concentration of 0.82 mol/l. The anthracene runs were at 370°C while the naphthalene run was at 450°C. These samples were then concentrated between 2 and 5 times for GC/MS analysis.

4.3.2.1 Methylated Anthracene and Naphthalene Products

The methylated anthracene and naphthalene thermolysis products were analyzed on a Hewlett-Packard 5890 Gas Chromatograph (GC) equipped with a 5970 Series Mass Selective Detector. The GC was controlled and the data was gathered by a Hewlett-Packard 59970 GC/MS Workstation. A J&W DB-5 Durabond FSOT 30m x 0.25mm x 0.1μm film thickness column was used in the analysis. The temperature program used in these runs was 40°C for 0 minutes followed by 10°C/min ramp to 280°C for 40 minutes. The injector was held at 250°C while the detector temperature was held at 280°C. Under these conditions with this column, polyaromatic hydrocarbons of masses up to 300 a.m.u. should be detected.

The mass of each peak was verified with the mass spectrometer. From the mass, a tentative identity was given to most peaks. In cases where the identity of the peak was still unknown, a comparison to a reference MS library was performed. For

the methyl- and dimethylanthracene thermolyses, the library offered little assistance since the only fragmentation pattern on file were those for anthracene and the three methylanthracene. The only dimethylanthracene isomer cataloged was 9,10-dimethylanthracene. In the case of 1,4-dimethylnaphthalene, naphthalene, the methylnaphthalenes, almost all of the dimethylnaphthalene isomers and even some trimethylnaphthalene isomers were cataloged and available for matching against peaks in the spectrum. If an identity could not be found, the peak was labelled unknown (UNK) followed by the mass (eg. UNK210). Although the columns were not the same in both GCs, they were both fused-silica columns that eluted polyaromatic hydrocarbons in the same order.

Figure 4.5 shows the GCs from the 910DMA thermolysis at 370°C for three conversions; 0.24, 0.55 and 0.99, with the peaks identified by GC/MS labelled. Peaks with * next to them were identified by injections of standards. All other peaks were identified by determining their mass on the GC/MS and correlating their retention time to times for known peaks. The top chromatogram in Figure 4.5 contains a relatively small number of peaks. The largest peak, #27, is the substrate 9,10-dimethylanthracene, identified by matching retention time to a known standard. The next largest peak, #17, is 9-methylanthracene, which was identified by both matching retention time to a known standard and matching the fragmentation pattern to the MS library. The third largest peak, #33, is a trimethylanthracene. Trimethylanthracenes were assigned based on mass determined by GC/MS alone.

215

1 = Dihydroanthracene (DHA) *
2 = Dihydromethylanthracene (DHMA)
3 = cis-9,10-dihydro-9,10-dimethylanthracene
    (cDHDMA) *
4 = Unknown mass of 182 (UNK182)
5 = DHMA
6 = trans-9,10-dihydro-9,10-dimethylanthracene
    (tDHDMA) *
7 = Anthracene (ANT) *
8 = DHMA
9 = DHDMA
10 = Unknown mass of 222 (UNK222)
11 = Unknown mass of 222 (UNK222)
12 = Unknown mass of 196 (UNK196)
13 = Unknown mass of 196 (UNK196)
14 = 2-Methylanthracene (2MA) *
15 = 1-Methylanthracene (1MA) *
16 = DHDMA
17 = 9-Methylanthracene (9MA) *
18 = Unknown mass of 210 (UNK210)
19 = Dimethylanthracene (DMA)
20 = Dimethylanthracene (DMA)
21 = Dimethylanthracene (DMA)
22 = Dimethylanthracene (DMA)
23 = Dimethylanthracene (DMA)
24 = 2,9-&3,9-Dimethylanthracene (29&39DMA)
25 = 1,9-Dimethylanthracene (19DMA)
26 = 1,10-Dimethylanthracene (110DMA)
27 = 9,10-Dimethylanthracene (910DMA)*
28 = Trimethylanthracene (TMA)
29 = Trimethylanthracene (TMA)
30 = Trimethylanthracene (TMA)
31 = Trimethylanthracene (TMA)
32 = Trimethylanthracene (TMA)
33 = Trimethylanthracene (TMA)
34 = Trimethylanthracene (TMA)
35 = Trimethylanthracene (TMA)
36 = Tetramethylanthracene
37 = Tetramethylanthracene
38 = Tetramethylanthracene

Figure 4.5: Gas chromatograms of 910DMA thermolysis with identification of peaks from GC/MS.

216

There were no trimethylanthracenes available in the MS library for further isomer identification. All three peaks after 910DMA, #28, #33 and #35, were trimethylanthracenes based on the mass determined by the GC/MS. Peaks #3 and #6 were *cis*- and *trans*-9,10-dihydro-9,10-dimethylanthracenes (DHDMA) based on the mass (= 208) determined by the GC/MS and matching retention times to synthesized standards. The other hydrogenated species were assigned by GC/MS mass identification. They eluted at much earlier times than their saturated counterparts, and had much smaller differences in retention times. Care had to be given that the parent ion's mass (M^+) was determined correctly since these species readily lost a methyl group, which led to a very large peak at $M^+ - 14$ that could have easily been misidentified as the mass. This was aided by generating ion chromatograms at masses of 180, 194 and 208 and following the evolution of peaks. Ion chromatograms are GC chromatograms that show peak at a desired mass. Dihydroanthracene was also identified by a match against the GC/MS library and matching retention time to that of the known standard. Peak #7 was anthracene (ANT) and peak #15 was 1-methylanthracene (1MA), which were both identified by matching retention time to a known standard and matching the fragmentation pattern to the MS library. Peak #26 had a mass of 206, which corresponded to a dimethylanthracene.

The middle chromatogram in Figure 4.5 shows in increase in area for all the peaks of the top chromatogram and the appearance of several more peaks. All the

217

peaks after 910DMA, #28 - #38, were trimethylanthracenes based on the mass determined by the GC/MS. Peak #14 was 2-methylanthracene (2MA) based on matching retention time to a known standard and matching the fragmentation pattern to the MS library. Peaks #16, #19, and #24-#26 were dimethylanthracenes, based on the mass of 206 determined by the MS. Peaks #24 -#26 were identified as 2,9&3,9-dimethylanthracene (29&39DMA), 1,9-dimethylanthracene (19DMA) and 1,10-dimethylanthracene (110DMA), respectively, using their retention times differences, elution order, and peak areas by analogy to the methylanthracene isomers which were all commercially available and by comparison to the dimethylnaphthalene isomers retention indices and boiling points given in Table 4.3. Figure 4.6 displays the elution order and boiling points for the methylanthracenes and dimethylnaphthalenes that were used in the identification of the dimethylanthracenes. Peaks #2 and #5 were identified by GC/MS as dihydromethylanthracenes (mass = 194). Peak #10 and #11 were identified at dihydrotrimethylanthracene by GC/MS (mass = 222). Peak #9 was another dihydrodimethylanthracene, as identified by GC/MS mass of 208.

The bottom chromatogram of Figure 4.5 displays products at the highest conversion. While some new peaks have appeared, many of the peaks on the previous two chromatograms have decreased in area or totally vanished. The largest peak is #7, which is ANT. Many of the trimethylanthracenes (#28 - #38) have vanished. Peaks #20 - #23 have appeared and were identified as more

1,7-DIMETHYLNAPHTHALENE
I = 240.66

2,9-DIMETHYLANTHRACENE

2-METHYLANTHRACENE
I = 321.57

1,6-DIMETHYLNAPHTHALENE
I = 240.72

3,9-DIMETHYLANTHRACENE

1,5-DIMETHYLNAPHTHALENE
I = 244.98

1,9-DIMETHYLANTHRACENE

1-METHYLANTHRACENE
I = 323.33

1,8-DIMETHYLNAPHTHALENE
I = 249.52

1,10-DIMETHYLANTHRACENE

9-METHYLANTHRACENE
I = 329.13
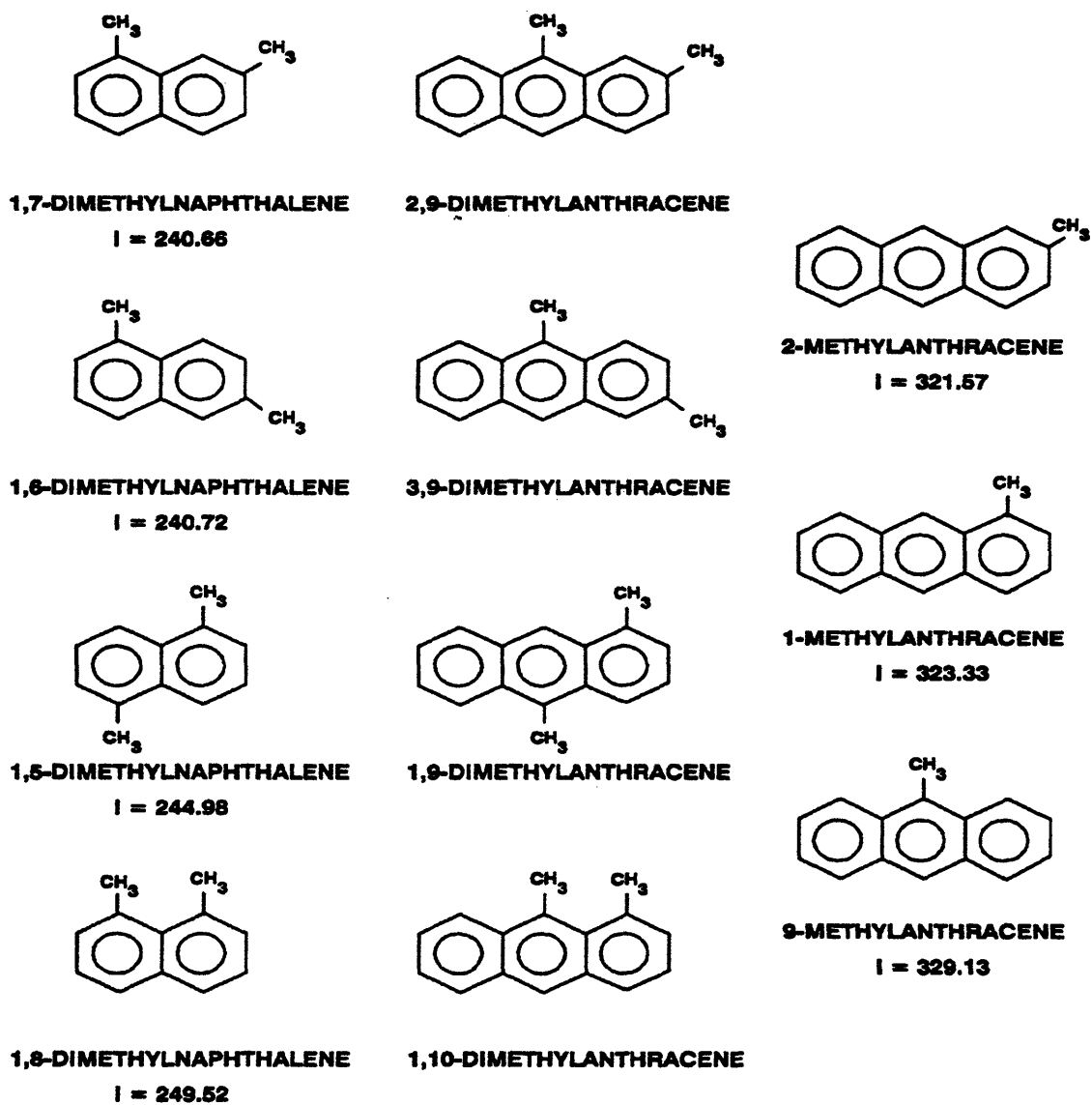
Figure 4.6: Identification of 1,10-; 1,9- and 29&39-dimethylanthracene isomers by comparison to the methylanthracenes and dimethylnaphthalenes.

dimethylanthracenes (mass = 206) by GC/MS. Peak #12 and #13 correspond to a mass of 196, which could possibly be tetrahydromethylanthracenes, but are left labelled UNK196. Peak #8 is another dihydrodimethylanthracene (mass = 206). Peak #4 was identified with a mass of 182 and matched the library as a tetrahydrophenanthrene. Since there is no evidence of phenanthrene in these runs, it could possibly be tetrahydroanthracene, but is left labelled UNK182. Peak #1 is dihydroanthracene, and was determined by a match against the GC/MS library.

Figure 4.7 shows the GCs from the 9MA thermolysis at 370°C for three conversions; 0.22, 0.39 and 0.82, with the peaks identified by GC/MS labelled using the same numbers as in the 910DMA thermolysis peaks. Once again, peaks with * next to them were identified by injections of standards. All other peaks were identified by determining their mass on the GC/MS, correlating their retention time to times for known peaks and by comparison to the 910DMA case. The 9MA thermolysis has essentially the same compounds as in the 910DMA thermolysis, with the exception of some of the trimethylanthracenes and dihydrodimethylanthracenes. Comparison of the 9MA and 910DMA thermolyses assisted in identification of some peaks in the 910DMA thermolysis, especially the hydrogenated species. Once again, ion chromatograms at masses of 180, 194 and 208 were generated and the evolution of peaks was monitored for identification of the hydrogenated species.

The top chromatogram in Figure 4.7 had a relatively small number of peaks. The largest peak, #17, is the substrate 9-methylanthracene. The next largest peak

2 = Dihydromethylanthracene (DHMA)

4 = Unknown mass of 182 (UNK182)

7 = Anthracene (ANT) *

8 = DHMA

9 = DHDMA

14 = 2-Methylanthracene (2MA) *

15 = 1-Methylanthracene (1MA) *

16 = DHDMA

17 = 9-Methylanthracene (9MA) *

19 = Dimethylanthracene (DMA)

20 = Dimethylanthracene (DMA)

21 = Dimethylanthracene (DMA)

22 = Dimethylanthracene (DMA)

23 = Dimethylanthracene (DMA)

24 = 2,9-&3,9-Dimethylanthracene (29&39DMA)

25 = 1,9-Dimethylanthracene (19DMA)

26 = 1,10-Dimethylanthracene (110DMA)

27 = 9,10-Dimethylanthracene (910DMA)*

28 = Trimethylanthracene (TMA)

31 = Trimethylanthracene (TMA)

33 = Trimethylanthracene (TMA)

Figure 4.7: Gas chromatograms of 9MA thermolysis with identification of peaks from GC/MS (* indicate where standards were available for identification).

221

is #7, anthracene. Third largest is #27, 9,10-dimethylanthracene. These peaks were again identified by matching retention times to those of known standards. 29&39DMA, 19DMA, and 110DMA, #24 - #26 respectively, have also appeared, which again were identified by mass of 206 from the GC/MS and by analogy to the methylanthracene isomers. The 1MA and 2MA have formed but are not resolvable, as seen by #14 and #15. Peak #19 is another dimethylanthracene with mass of 206 from the MS. Peak #2 is a dihydromethylanthracene, as determined by mass 194 on the GC/MS.

The middle chromatogram in Figure 4.7 has the same peaks as in the top chromatogram with their areas slightly increased and the addition of two more peaks. Peaks #28 and #33 are trimethylanthracenes, as identified by mass 220 on the GC/MS.

The bottom chromatogram in Figure 4.7 several more peaks than the top two spectrums. Once again, #17 9-methylanthracene and #7 anthracene are the dominant peaks in the chromatogram. The peaks #14 and #15, 2MA and 1MA respectively, are now resolved and have increased in area. More dimethylanthracenes, #16 and #19 - #27, have appeared although the 29&39DMA, 19DMA, 110DMA, and 910DMA have all decreased in area. These peaks were once again identified by mass = 206 on the GC/MS. Beside #2, another dihydromethylanthracene has arisen, #8. Peak #9 is a dihydrodimethylanthracene. These two peak were identified by parent ion mass and also using the ion

chromatograms of masses 194 and 208. Peak #4 had a mass of 182, same as in the DMA runs, and once again matched the library best as a tetrahydrophenanthrene. Since no phenanthrene was detected in this thermolysis either, this peak again remains as UNK182. Peak #1 was identified as dihydroanthracene by the mass of 180, a match against the MS library and comparison of retention time to the known standard.

Figure 4.8 shows the GCs from the DMN thermolysis at 450°C for three conversions; 0.40, 0.62 and 0.97, with the peaks identified by GC/MS labelled and peaks with * next to them were identified by injections of standards. Identification of the dimethylnaphthalene isomers was also aided by using their experimental boiling points and gas chromatographic polycyclic aromatic hydrocarbon (PAH) retention index (I). White (1986) gives both experimental boiling points and retention indices for 48 planar PAH including the naphthalene, methyl-, dimethyl- and trimethylnaphthalenes, anthracene, and the methylanthracenes, as shown in Table 4.3. All the dimethylnaphthalenes were commercially available as standards and were run for retention time and order. The elution order matched White's boiling point and retention index values. Peaks were assign masses from the GC/MS and then matched against the MS library for possible identification, but final determination was based upon comparison of retention time and retention order to known standards.

1 = Naphthalene (NAPH) *

2 = 2-Methylnaphthalene (2MN) *

3 = 1-Methylnaphthalene (1MN) *

4 = Dimethylnaphthalene (DMN)

5 = 2,6-Dimethylnaphthalene (26DMN) *

6 = 1,3-Dimethylnaphthalene (13DMN) *

7 = 1,4-Dimethylnaphthalene (14DMN) *

8 = 1,2-Dimethylnaphthalene (12DMN) *

9 = 1,4,5-Trimethylnaphthalene (145TMN)

10 = TMN

11 = TMN

12 = 1,4,6-Trimethylnaphthalene (146TMN)

13 = TMN

14 = TMN

15 = TMN
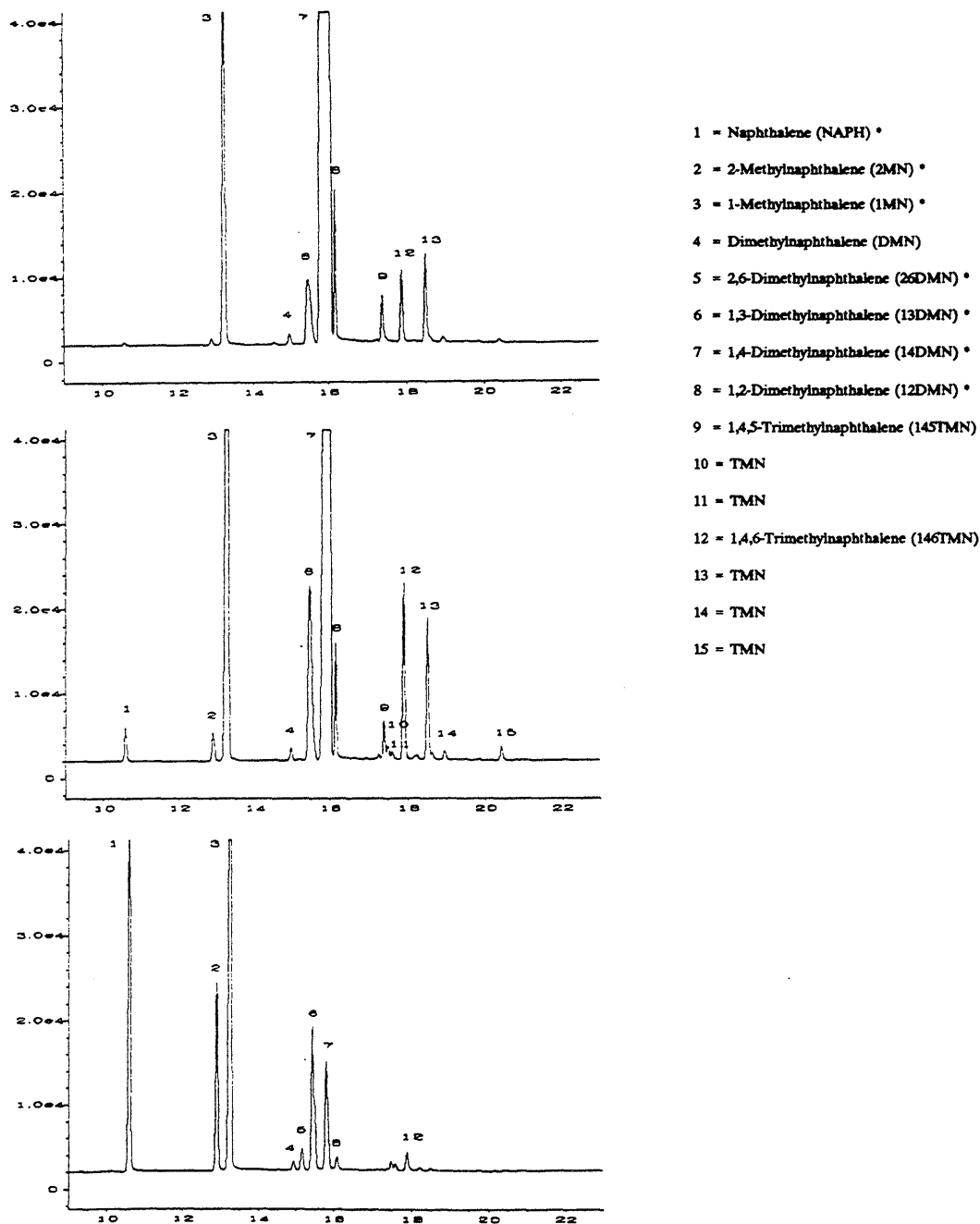
Figure 4.8:   Gas chromatograms of 14DMN thermolysis with identification of peaks from GC/MS (* indicate where standards were available for identification).

224

Table 4.3

Retention Indices (I) and Boiling Points of Planar PAH[1]

Planar PAH	Experimental I	Boiling Point (K)
naphthalene	200.00	491
2-methylnaphthalene	218.14	514
1-methylnaphthalene	221.04	518
2-ethylnaphthalene	236.08	531
1-ethylnaphthalene	236.56	532
2,6-dimethylnaphthalene	237.58	535
2,7-dimethylnaphthalene	237.71	535
1,3-dimethylnaphthalene	240.25	538
1,7-dimethylnaphthalene	240.66	536
1,6-dimethylnaphthalene	240.72	539
2,3-dimethylnaphthalene	243.55	541
1,4-dimethylnaphthalene	243.57	541
1,5-dimethylnaphthalene	244.98	542
1,2-dimethylnaphthalene	246.49	544
1,8-dimethylnaphthalene	249.52	
2,3,6-trimethylnaphthalene	263.31	559
2,3,5-trimethylnaphthalene	265.90	558
anthracene	301.69	613
2-methylanthracene	321.57	632
1-methylanthracene	323.33	636
9-methylanthracene	329.13	
9,10-dimethylanthracene	355.49	

[1] from White 1986

The top chromatogram in Figure 4.8 represents the lowest conversion run. The largest peak in the chromatogram, #7, is 1,4-dimethylnaphthalene (14DMN), which was identified by a comparison of retention time to that of a known standard and matching against the MS library. The second largest peak, #3, is 1-methylnaphthalene (1MN), which was identified in the same manner as 14DMN. Peaks #4, #6 and #8 were also dimethylnaphthalenes, as identified by mass 156 on the MS. Matches against the MS library led to an elution order for the peak that was not possible. Comparison of retention time and order to know standards led to identification of 1,3-dimethylnaphthalene (13DMN) for #6 and 1,2-dimethylnaphthalene (12DMN) for #8. Peak #4 did not match a retention time for any dimethylnaphthalene, in fact all the dimethylnaphthalenes eluted at times greater than peak #4. The MS library matched the fragmentation pattern up to 1-ethylnaphthalene, which also has a mass of 156. Peak #9, #12 and #13 were identified as trimethylnaphthalenes with a mass of 170. Peak #9 matched the library as 1,4,5-trimethylnaphthalene (145TMN) while peak #12 matched best as 1,4,6-trimethylnaphthalene (146TMN). Peak #13 did not have a match as a specific TMN against the library.

The middle chromatogram in Figure 4.8 represents a medium range conversion run. All of the same peaks are present with greater areas and there are also some new peaks. Peaks #1 and #2 were identified as naphthalene and 2-methylnaphthalene, respectively, by matching both retention time to a known

226

standard and matching the MS library. Several other trimethylnaphthalenes, #10, #11, #14 and #15, also appeared.

The middle chromatogram in Figure 4.8 represents a high conversion run. There is only one new peak in this chromatogram. Peak #5 was identified as 2,6-dimethylnaphthalene by mass 156 determined by GC/MS and matching retention time and elution order to the known standards. Most of the trimethylnaphthalenes have vanished at this high conversion. The dominant species are #1, naphthalene, and #3, 1-methylnaphthalene.

Peak #4 in Figure 4.8 buried beneath biphenyl and methylbiphenyl (phenyltoluenes) in the actual runs. The methylbiphenyls were identified by running a sample on the GC/MS that contained biphenyl. This run contained all three methylated biphenyls in small quantities. The 3- and 4-phenyltoluenes eluted in between the dimethyl and trimethylnaphthalenes and did not interfere with any peaks. The biphenyl and 2-phenyltoluene eluted in between the methyl and the dimethylnaphthalenes, burying peak #4. In the actual runs, the biphenyl area used for calculating retention factors was the sum of the areas for the biphenyl and the three methyltoluenes.

4.3.2.2 Heavy Anthracene and Naphthalene Products

Heavy thermolysis products, defined as dimers of the methylanthracenes and methylnaphthalenes, were analyzed on a Hewlett-Packard 5890 Gas Chromatograph

(GC) equipped with a 5971A Series Mass Selective Detector (MSD). A HP-1 12m x 0.2mm x 0.33μm film thickness column was used in the analysis. The temperature program used in these runs was 70°C for 1.5 minutes followed by 10°C/min ramp to 310°C for 4 minutes. The injector was held at 250°C while the detector temperature was held at 280°C. Scans were made for masses between 100 and 500 a.m.u.s. Only the lowest conversion thermolysis runs were analyzed on this instrument since these heavy products would also decompose with increasing reaction time, therefore at lower conversions, the amounts of the heavy products should be at a maximum.

For 910DMA, ion chromatograms were generated for masses of 408 - 412, 394 - 398, 380 - 384, 366 - 370 and 352 - 356 on the HP 5970 MSD to check for heavy dimer products. None were found at any of the conversions for the 910DMA thermolyses. One explanation for the lack of heavy products detected is that these analysis only ran 40 minutes and the heavy products could have eluted at times greater than 40 minutes. When the X = 0.24 sample was run on HP 5971A MSD, one large peak is detected at t ~ 29.5 min, with several smaller peaks in front of it, as shown in the upper panel of Figure 4.9. The fragmentation pattern and structure of the peak at 29.5 minutes are shown in the lower panel of Figure 4.9. The mass of 410 is two times the 910DMA mass minus two. This structure shown on the fragmentation pattern was deduced from the small molecular ion at 410 and large fragment peak at 205, which is indicative of alkyl-substituted aromatics cleavage at the bond beta to the ring, giving the resonance-stabilized benzyl ion. For this
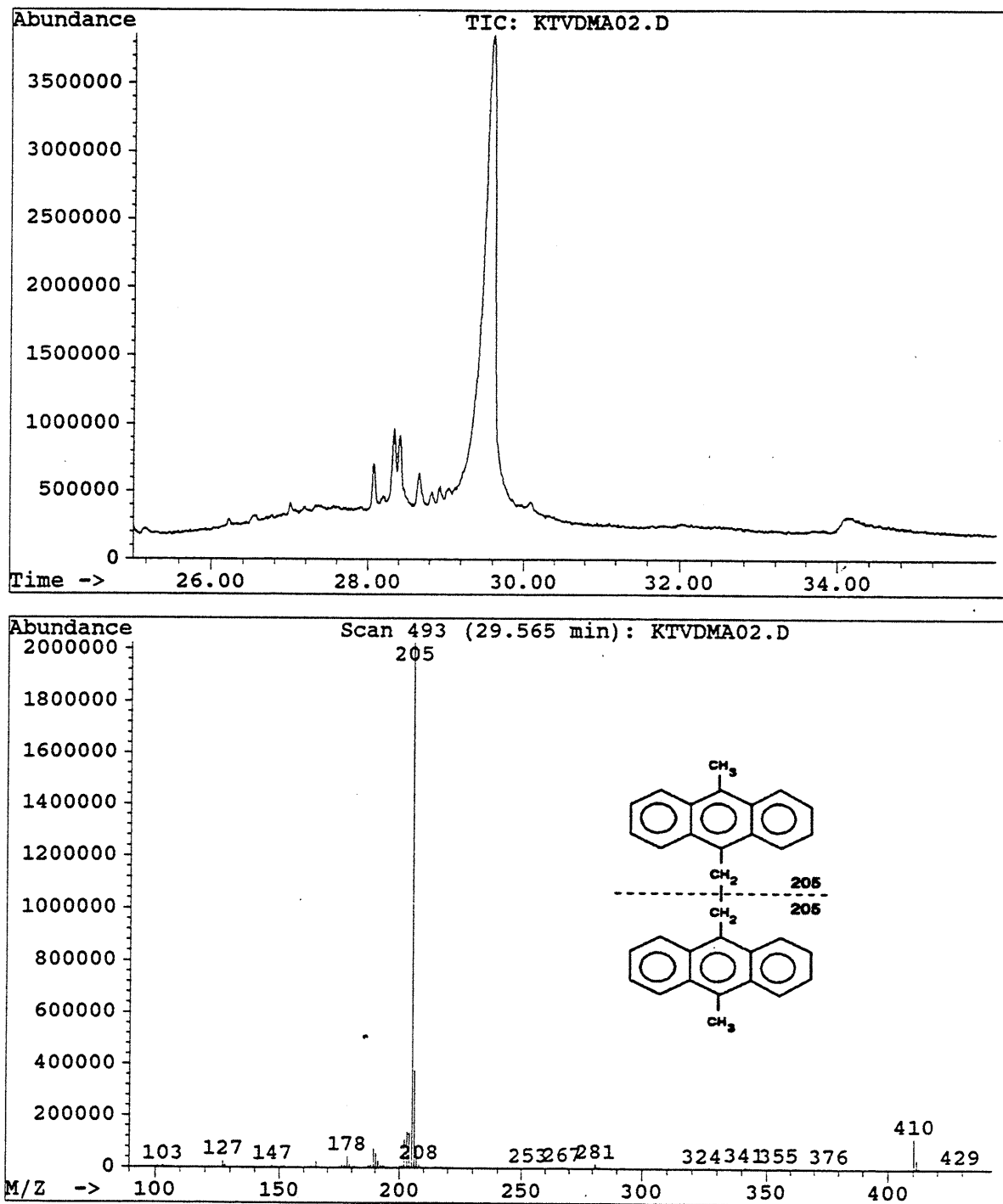
Figure 4.9: Gas chromatogram, fragmentation pattern and structure of X = 0.24
910DMA thermolysis.

structure, the bond beta to both rings, as shown by the dotted lines on the structure, is the alkyl C-C bond, which yields a fragment of mass 205. Although the methyl groups as placed in the 10 position on both aromatic rings, this information cannot be deduced for the fragmentation pattern. This orientation was assigned based on the information that the substrate was 9,10 methyl substituted. Figure 4.10 displays the fragmentation patterns for the peaks at t = 28.1 and 28.3 minutes formed at X = 0.24 during 910DMA thermolysis. The upper panel of Figure 4.10 shows a small molecular ion at mass of 412, with large fragments at 206, 191 and 176. This pattern is representative of an alkyl-substituted aromatic, which is shown on the fragmentation pattern. The large fragment at 206 is generated by cleavage of the bond beta to the aromatic ring, as shown by the dotted line on the structure, which is the same fragment for beta cleavage to either ring. The fragments at 191 and 176 arise from loss of one and two methyl groups, respectively, from the 206 fragment. The lower panel of Figure 4.10 shows a small molecular ion of mass 396, with a large fragment at mass 205 and another fragment at mass 191; again indicative of an alkyl-substituted aromatic structure. The structure shown on the fragmentation pattern can explain the fragmentation seen. Cleavage of the beta bond to the ring with no methyl substitution yields the fragment of mass 205 while cleavage of the bond beta to the ring with the methyl substituent yields the fragment of mass 191, as indicated by the dotted lines on the structure. Figure 4.11 displays the fragmentation patterns for the peak at t = 28.4 minutes formed at X = 0.24 during 910DMA thermolysis.
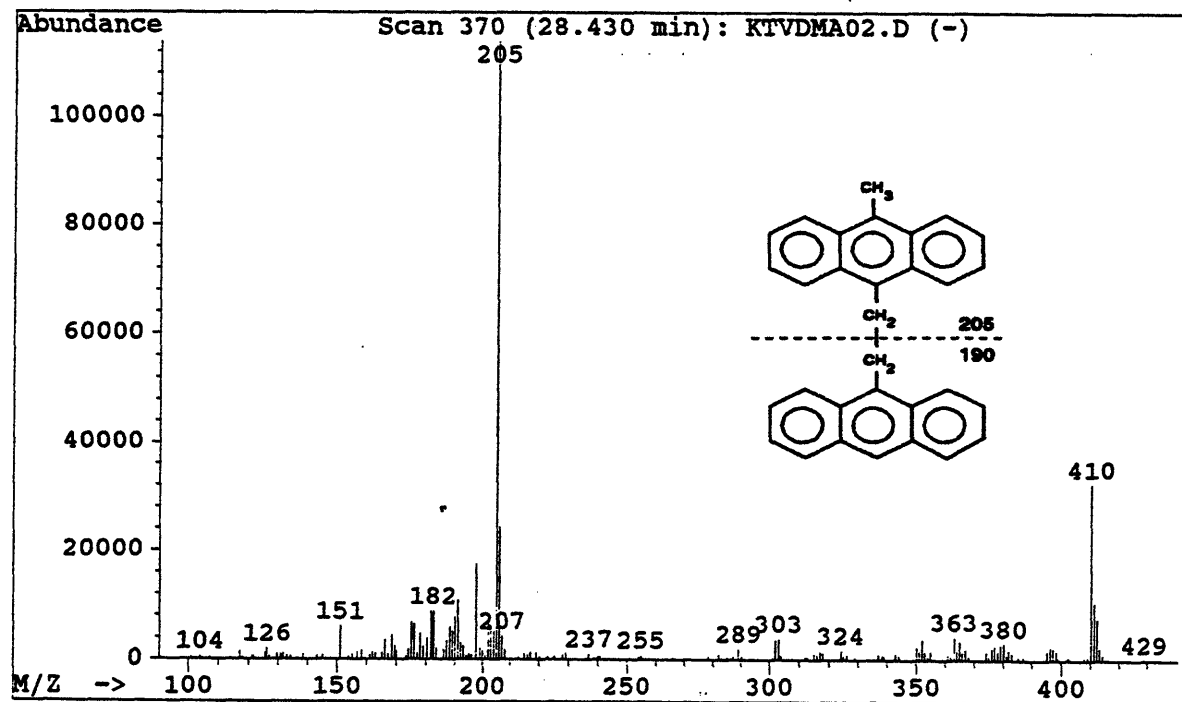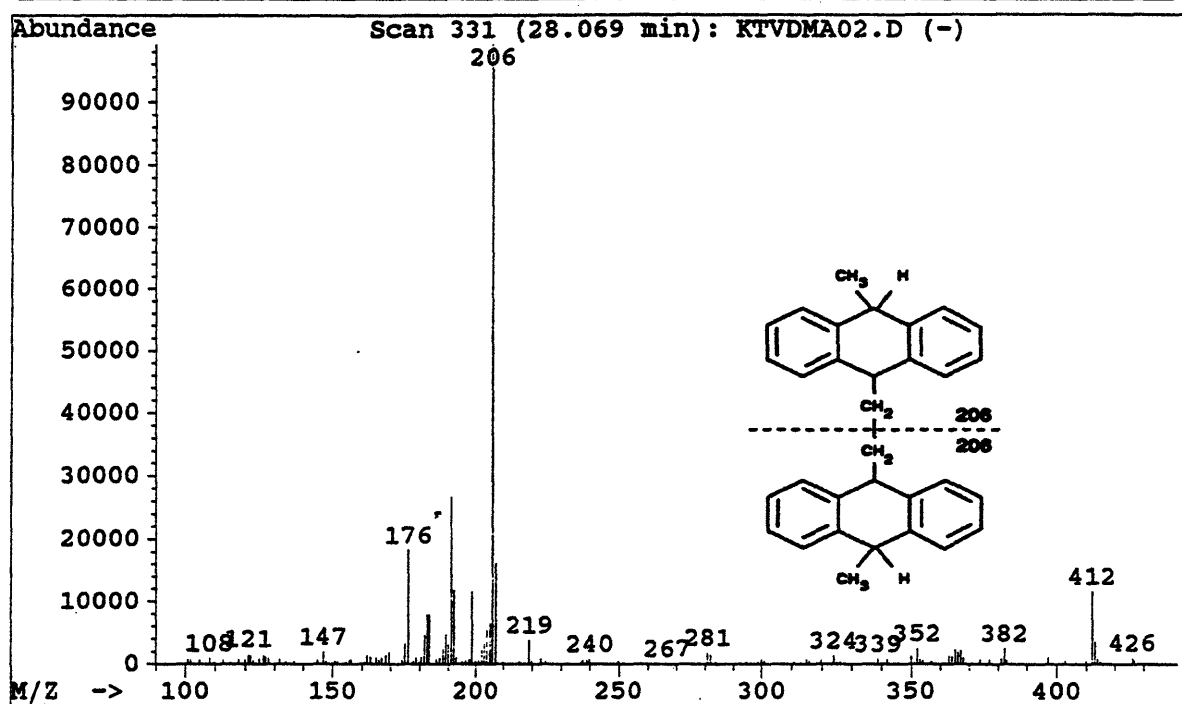
Figure 4.10: Fragmentation patterns and structures for peaks at t = 28.1 and 28.3 minutes from X = 0.24 910DMA thermolysis.
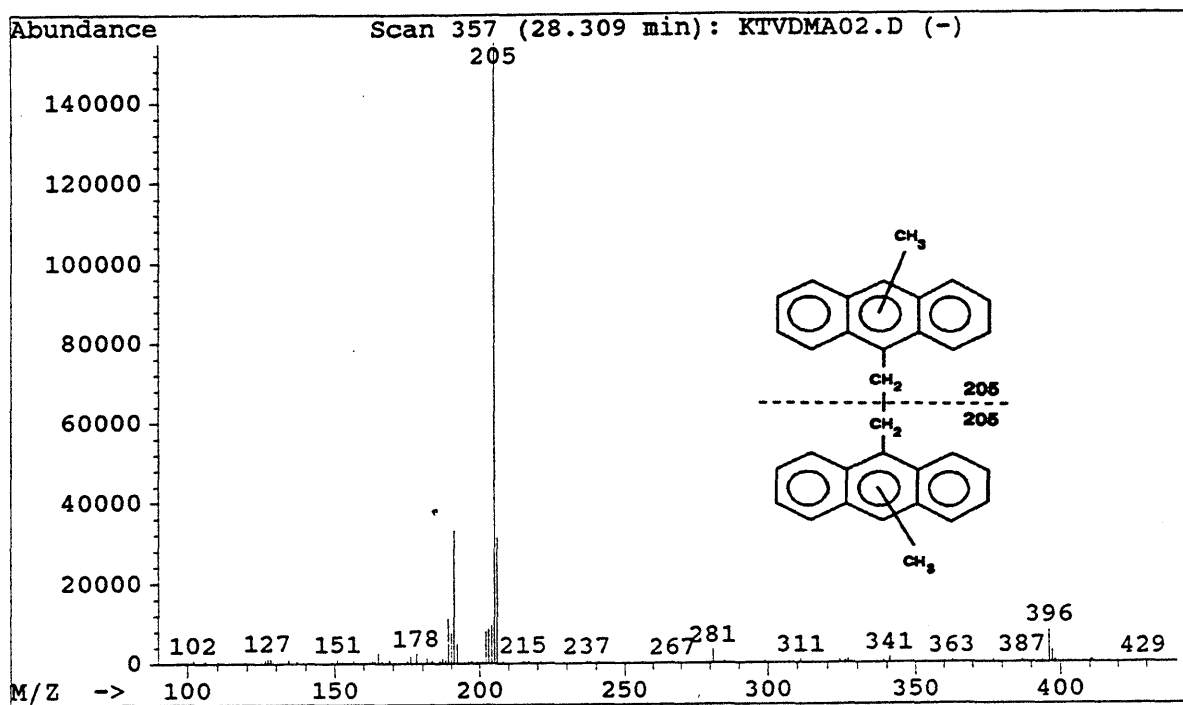
Figure 4.11: Fragmentation pattern and structure of the peak at t = 28.4 minutes formed in 910DMA thermolysis with X = 0.24.

This fragmentation pattern also exhibits alkyl-substituted aromatic features of the small molecular ion at mass 410 and the large fragment ion at mass 205. This pattern is similar to the fragmentation pattern on the bottom of Figure 4.9 meaning that this peak corresponds to a different methyl substituted, although it is impossible to know where the methyl group are on the molecular. The structure on the fragmentation pattern in Figure 4.11 shows the general features of the molecule, with the dotted lines indicating the cleavage of the beta bonds to the aromatic rings which led to the large fragment at mass 205.

For 9MA, ion chromatograms were also generated for masses of 394 - 398, 380 - 384, 366 - 370 and 352 - 356 on the HP 5970 MSD to check for heavy products. At X = 0.82, no peaks were detected at any of these masses. At X = 0.38, species were detected at a mass range of 380 - 384, which corresponded to twice the 9MA mass (192). Figure 4.12 shows the gas chromatogram, fragmentation patterns and structures for the two peaks with mass of 382. Although fragmentation pattern for both peak are indicative of alkyl-substituted aromatics with small molecular ion and large fragment peaks, their structures can be deduced from the difference in the fragment masses. The peak at t ~ 27 minutes can only generate fragments with masses of 191 when cleavage occurs beta to either ring, as shown by the dotted lines on the structure. The peak at t ~ 33.6 minutes can generate fragments with mass 205 or mass 191, depending on which bond is cleaved beta relative to the rings, as shown by the dotted lines on the structure in Figure 4.12. At X = 0.22, species were

233
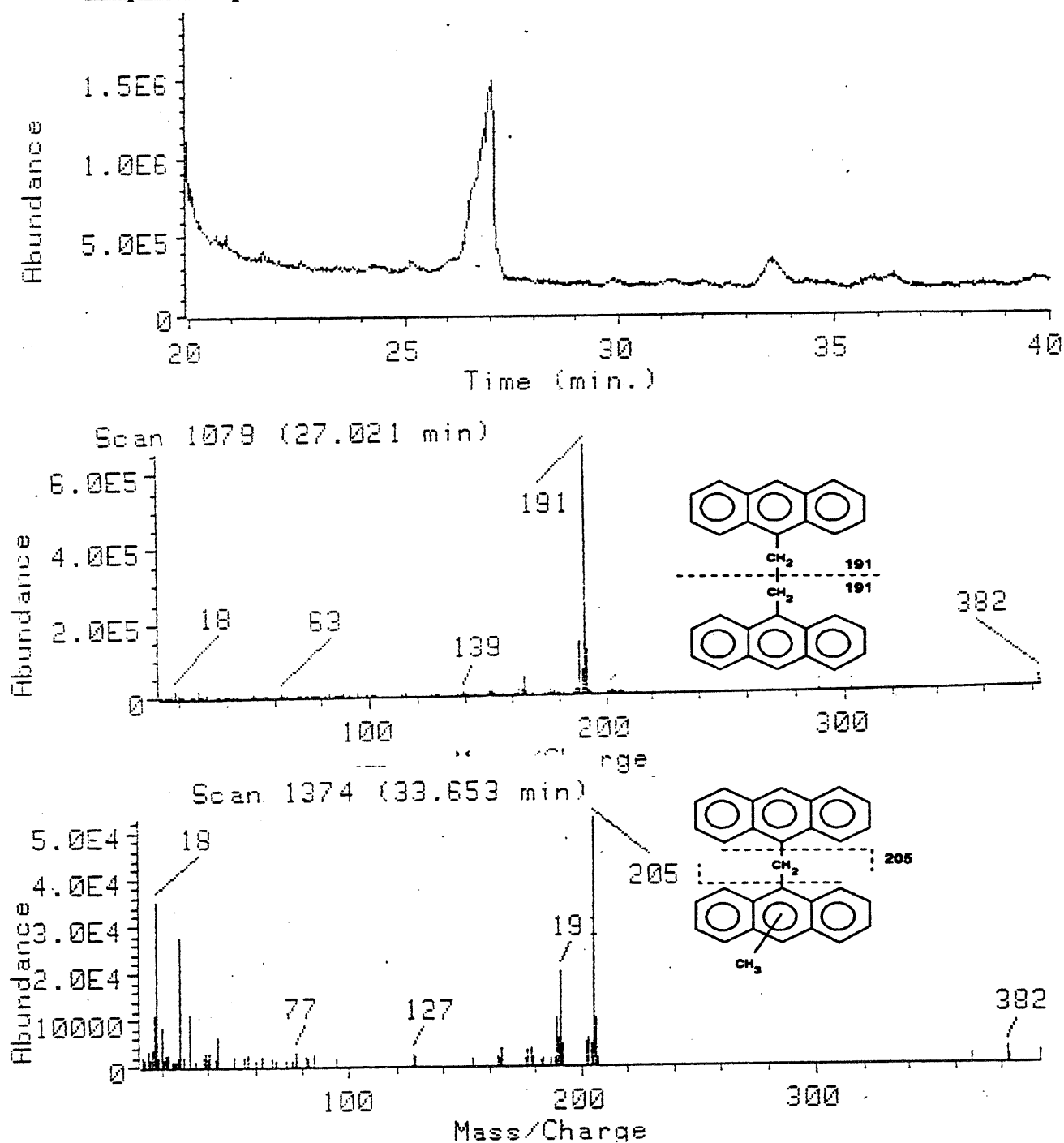
Figure 4.12: Gas chromatogram (top) and fragmentation patterns of peaks with retention times of 27.0 (middle) and 33.7 minutes (bottom) from 9MA thermolysis with X = 0.38.

also detected at mass range of 380 - 384. The first peak with mass 382 had the same fragmentation pattern as the peak at t ~ 27 minutes at X = 0.38. Unfortunately, this run was stopped shortly following this peak, therefore a possible peak similar to the peak at t ~ 33.5 minutes at X = 0.38 was not detected. The X = 0.22 sample was also analyzed on HP 5971A MSD. Figure 4.13 shows the gas chromatogram, fragmentation pattern and structure for the X = 0.22 9MA thermolysis. One large peak is detected on the chromatogram at approximately 27.4 minutes with several smaller peaks following. The fragmentation pattern and possible structure of the peak at t ~ 27.4 minutes are also shown in Figure 4.13. This fragmentation pattern appears to be identical to the first peak detected by the HP 5970 MSD. The structure is indicative of an alkyl-substituted aromatic; small molecular ion and large fragment ions. Cleavage of the bond beta to either ring leads to the fragment of mass 191, as shown by the dotted lines on the structure.

For 14DMN thermolysis, the heavy products have a much lower mass (310) than in the anthracene thermolyses (412), therefore there were readily detectable on either MSD and both gave similar peak area and elution order in the gas chromatograms from both instruments. The discussion of the heavy products with be using the HP 5971A MSD. Figure 4.14 shows the chromatogram of the heavy products formed during 14DMN thermolysis with X = 0.40 in the upper panel and the fragmentation pattern and structure of the peak at t = 22 minutes in the lower panel. Fragmentation pattern of only the largest peaks with be discussed, but the
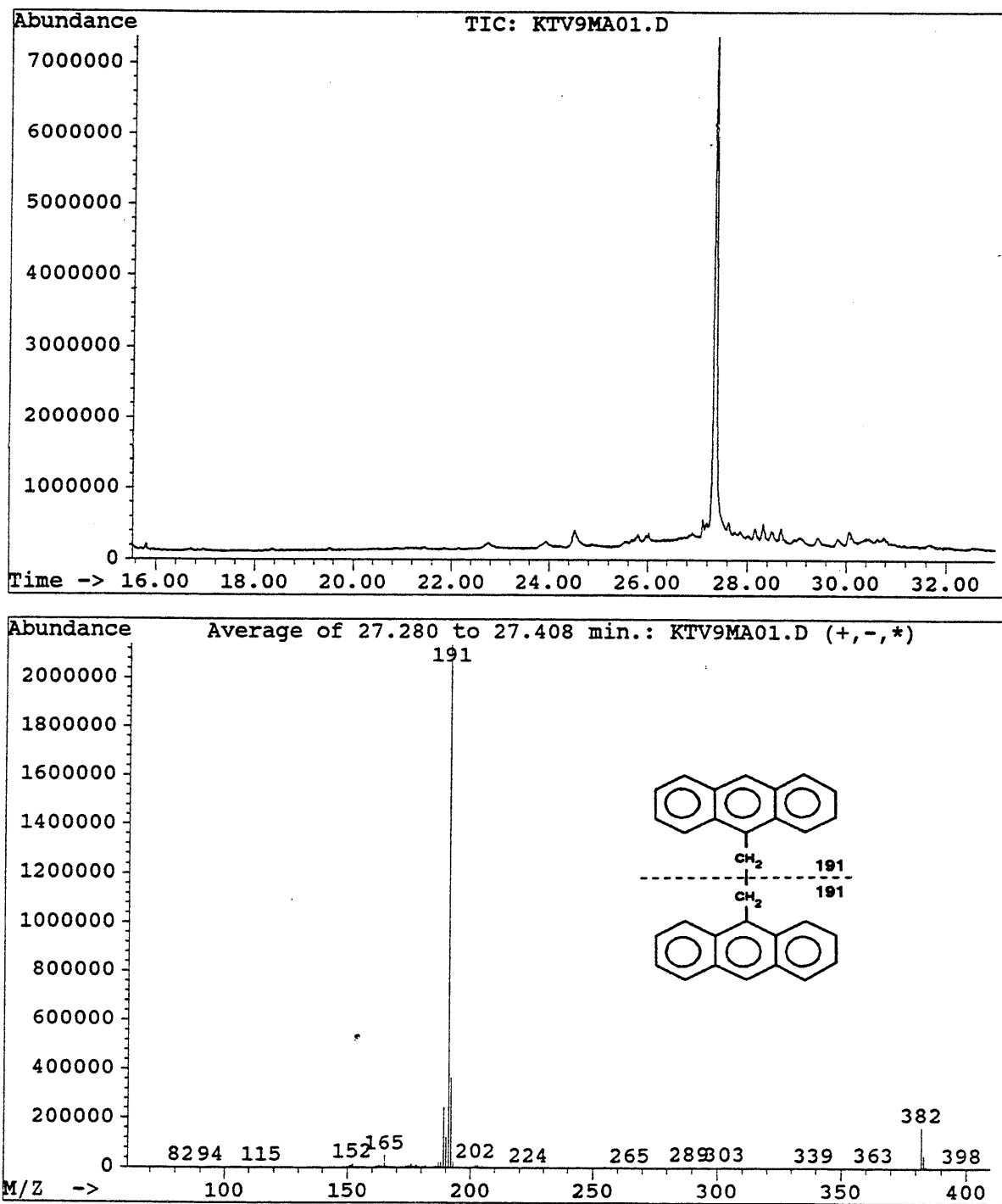
Figure 4.13: Gas chromatogram (top), fragmentation pattern and structure (bottom) from 9MA thermolysis with X = 0.22.
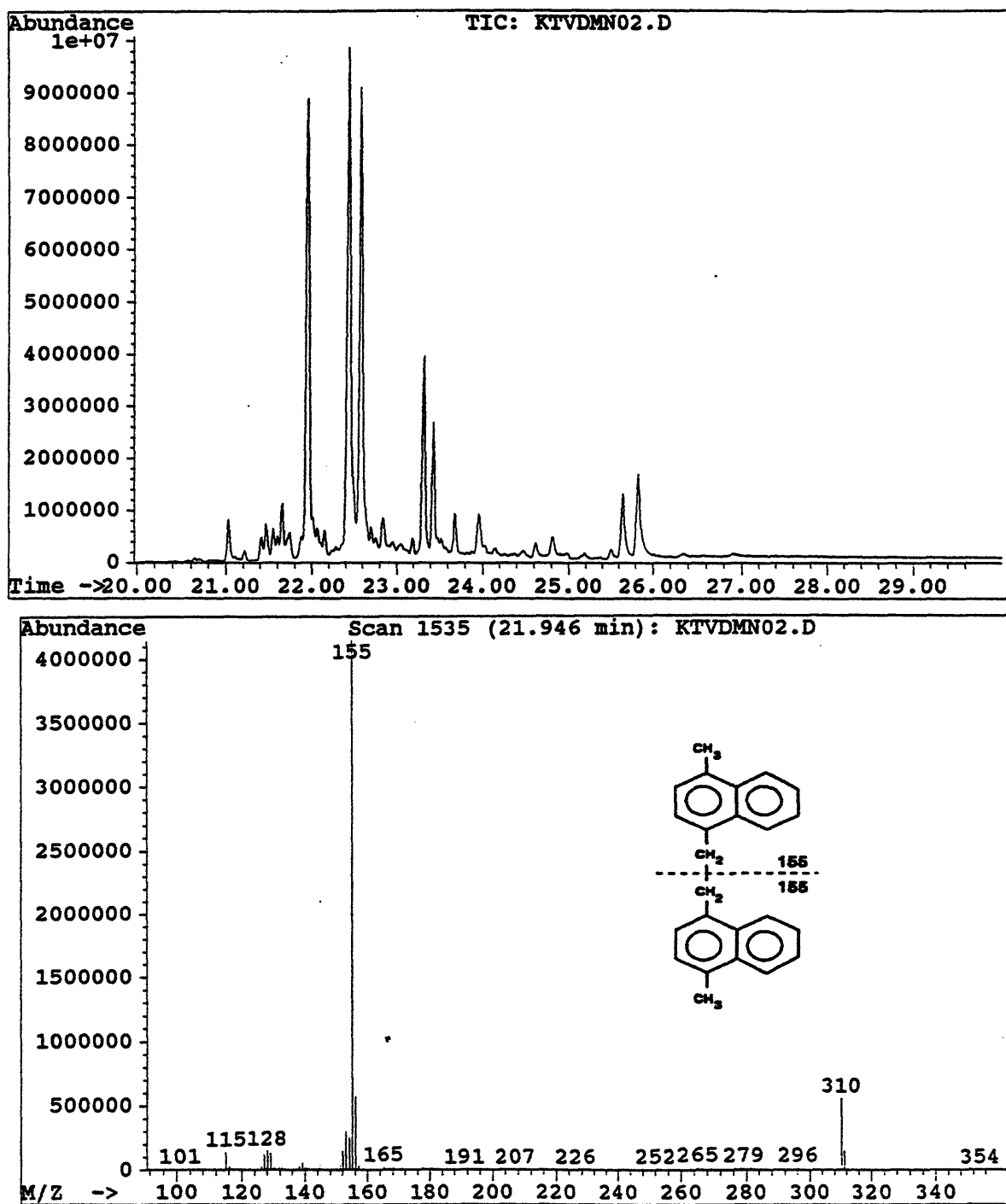
Figure 4.14: GC chromatogram (top) from the GC/MS showing the heavy products formed during 14DMN thermolysis with X = 0.40 and fragmentation pattern and structure for the peak at t = 22 minutes (bottom).

masses with be given of all peaks in the chromatogram. The first group of peaks, retention times 21 - 21.8 minutes, had masses of 296. Three large peaks appeared between 22 and 226 minutes and had masses of 310. The lower panel of Figure 4.14 and Figure 4.15 shows the fragmentation patterns of the peaks with mass of 310. In the lower panel of Figure 4.14, the peak at t C 22 minutes is representative of an alkyl-substituted aromatic; a small molecular ion and large fragment peaks. The lone large fragment at mass of 155 signifies there are two methyl groups between the aromatic rings, meaning cleavage of the bond beta to either ring yields a fragment of mass 155, as shown by the dotted lines on the structure. The peak at t ~ 22.4 minutes, shown in the upper panel of Figure 4.15, has a fragmentation pattern indicative of aromatic compounds; large molecular ion with very little fragmentation peaks. The peaks at masses 295, 280 and 265 demonstrate loss of successive methyl groups from the parent ion. Positions of the methyl groups cannot be deduced from fragmentation patterns, therefore the structure shown on the fragmentation is a representative one. The lower panel of Figure 4.15 is the fragmentation pattern for the peak at t = 22.6 minutes. This fragmentation pattern has features of both an alkyl-substituted aromatic and an aromatic compound. The large molecular ion at 310 with large fragments at 295, 280 and 265, which indicate successive loss of methyl from the parent ion, are suggestive of an aromatic structure. The large fragment at mass 168 is indicative of an alkyl-substituted aromatic that could readily fragment. The difficulty in interpreting this pattern is that the fragment at mass 168 cannot
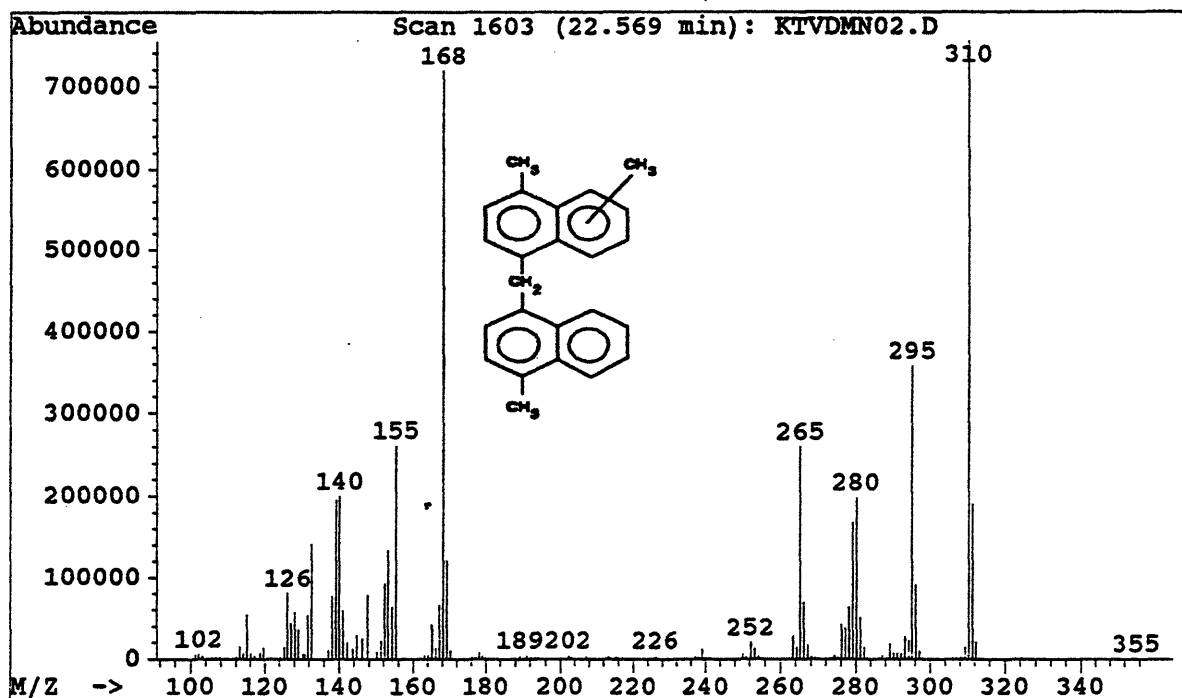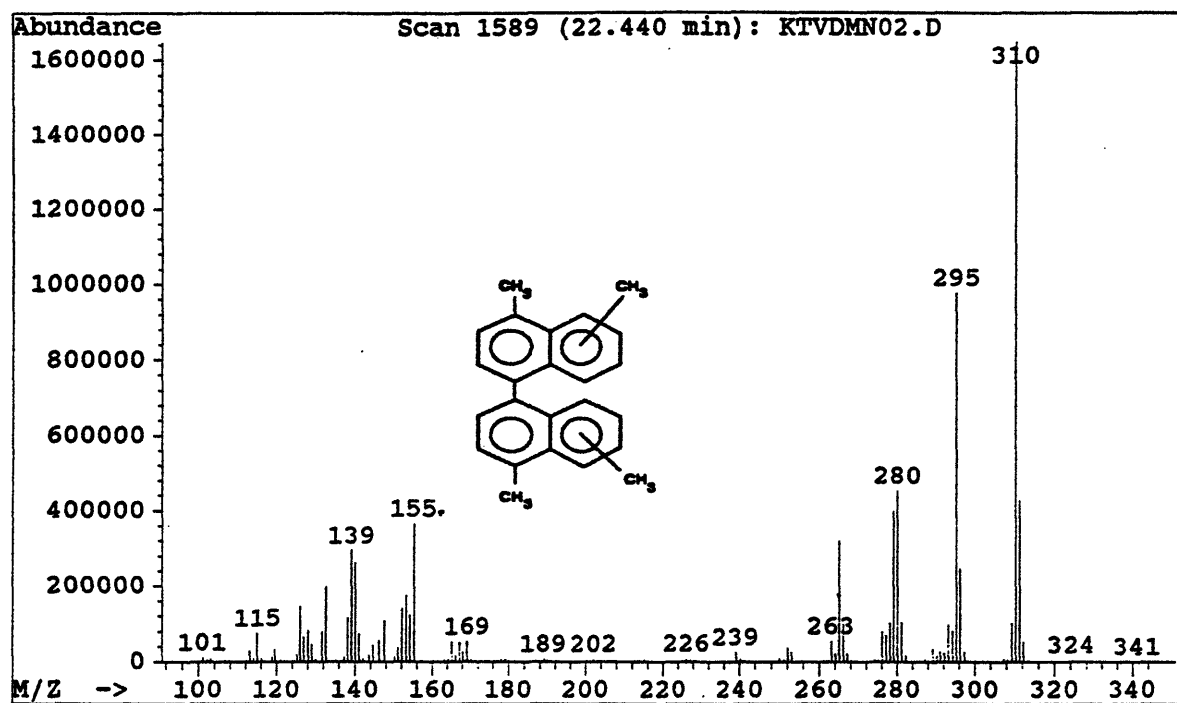
Figure 4.15: Fragmentation patterns and structures of peaks at t = 22.4 (top) and 22.6 minutes (bottom) formed during 14DMN thermolysis with X = 0.40.

239

easily be explained. If the molecular ion of mass 310 fragmented as an alkyl-substituted aromatic, the fragment would have an odd mass of 169. The mass of 168 indicates that a neutral species of mass 142 was lost from the molecular ion or a hydrogen transfer took place with the fragment of mass 169. A possible structure is shown on the fragmentation pattern that explains the large molecular ion and subsequent peaks from loss of successive methyl groups. It is not clear how this molecule could generate the fragment with mass of 168.

The two large peaks between 23.2 and 23.5 minutes had masses of 324. Figure 4.16 displays the fragmentation patterns and structures for the peaks of mass 324. The top fragmentation pattern in Figure 4.16 for the peak at t ~ 23.2 minutes is indicative of an alkyl-substituted aromatic and an aromatic compound; a large fragment at mass 168 and a large molecular ion with large fragments at successive losses of methyl groups. This compound is the same that was seen at t = 22.6 minutes with the addition of another methyl group. A structure is shown on the fragmentation pattern that would explain the aromatic features, but is not obvious how a fragment of mass 168 would be generated. The bottom fragmentation pattern in Figure 4.16 for the peak at t ~ 23.5 minutes is indicative of an aromatic compound; large molecular ion and very little fragmentation. The fragments at masses 309 and 293 correspond to loss of a methyl group. The representative structure without exact placement of the methyl groups is shown on the fragmentation pattern.
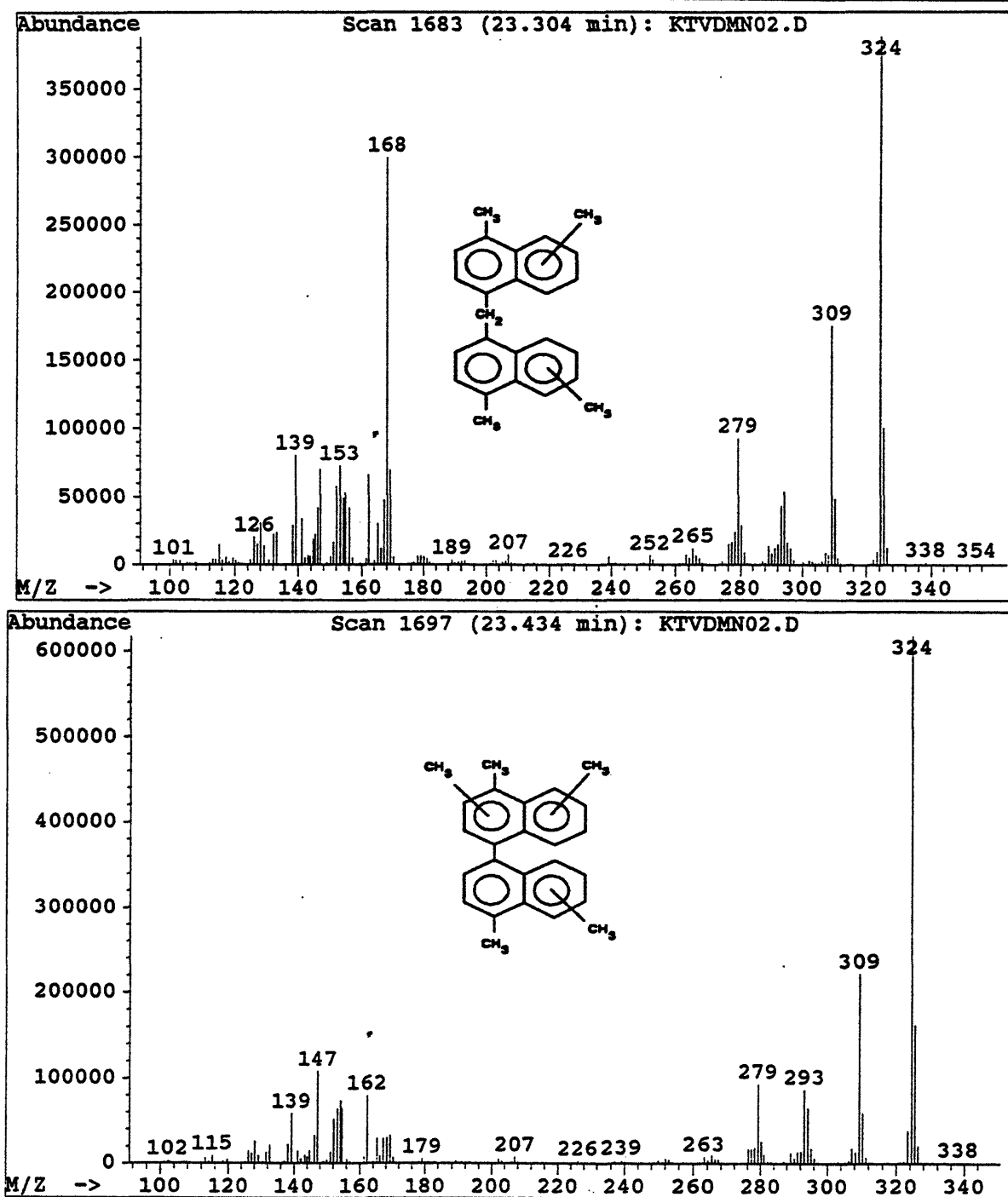
Figure 4.16: Fragmentation patterns and structures for peaks at t = 23.2 (top) and 23.5 minutes (bottom) formed during 14DMN thermolysis with X = 0.40.

The two large peaks between 23.7 and 24 minutes had masses of 338. Figure 4.17 displays the fragmentation patterns and structures for the peaks of mass 338. The upper panel of Figure 4.17 displays the fragmentation pattern of the peak at t = 23.7 minutes, which is indicative of an aromatic structure. The molecular ion is very small with a mass of 338 while large fragments at masses of 310, 295, 280, 265 and 324 are generated by successive losses of methyl groups. The structure on the fragmentation pattern arbitrarily places 3 methyls on each naphthalene rings, although this is not necessarily correct. It cannot be determined where or how many methyls are on each ring, but it must be taken into consideration that loss of 2 methyl groups generated the largest fragment (mass = 310). The lower panel of Figure 4.17 displays the fragmentation pattern of the peak at t = 24 minutes, which is also indicative of an aromatic structure. The molecular ion is small with a mass of 338 while large fragments at masses of 324, 308, 293, 278 and 263 are generated by successive losses of methyl groups. As in the upper panel, the structure on the fragmentation pattern arbitrarily places 4 methyls and 2 methyls on the naphthalene rings. It must be taken into consideration that the largest fragment has a mass of 293.

The two larger peaks at times greater than 25 minutes, t = 25.6 and 25.8 minutes, have masses of 306. Figure 4.18 displays the fragmentation patterns and structures for the peaks of mass 306. The upper panel of Figure 4.18 displays the fragmentation pattern of the peak at t = 25.6 minutes, which is indicative of an
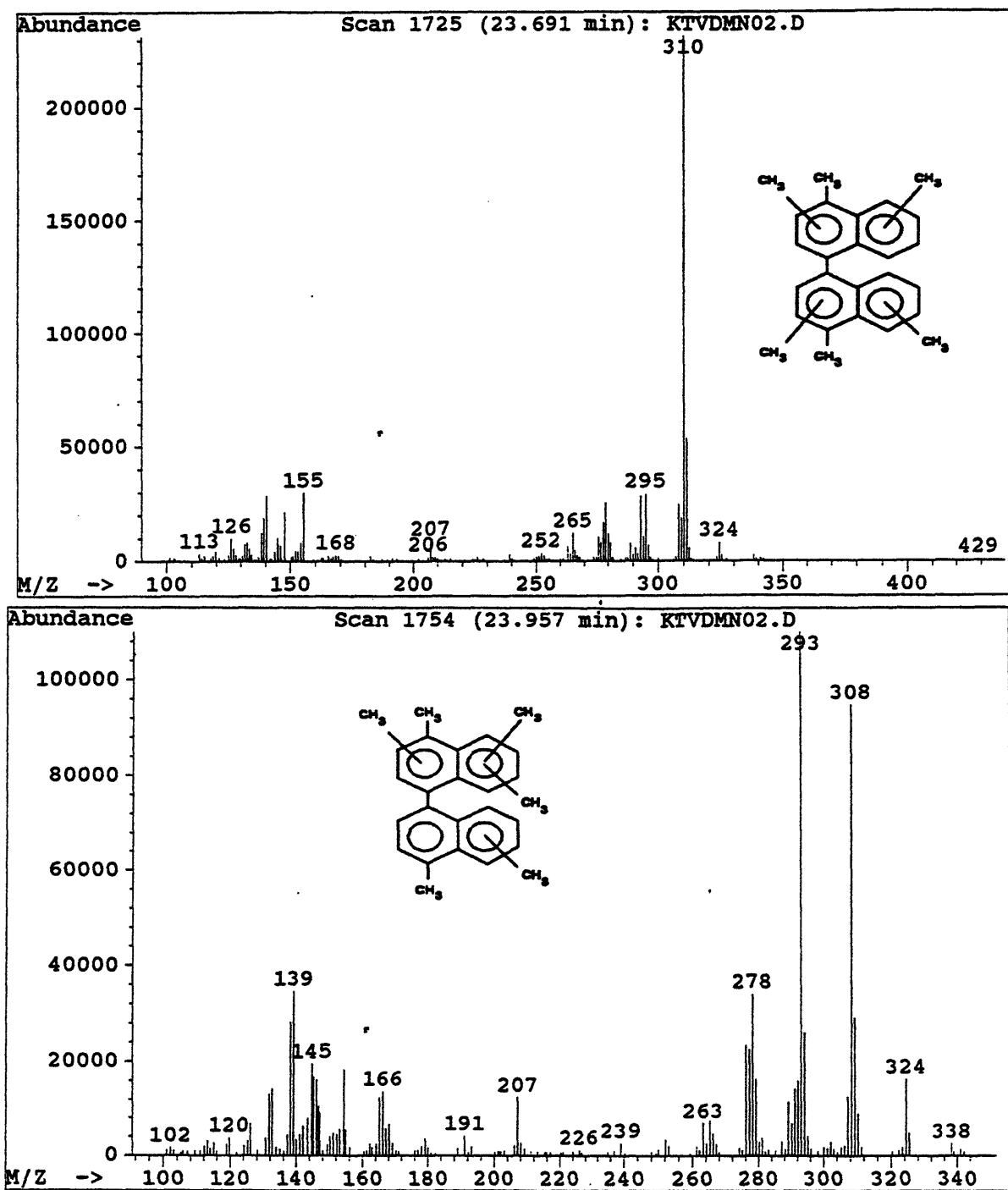
Figure 4.17: Fragmentation pattern and structures for peaks at t = 23.7 (top) and 24.0 (bottom) minutes formed during 14DMN thermolysis with X = 0.40.
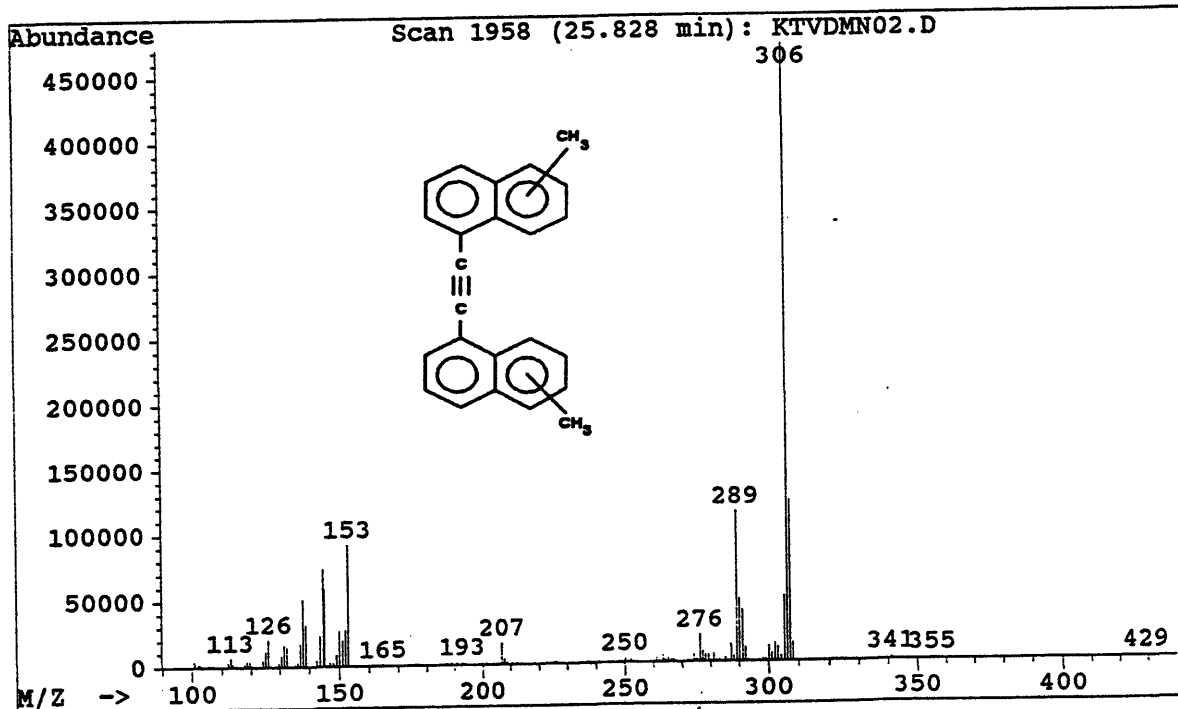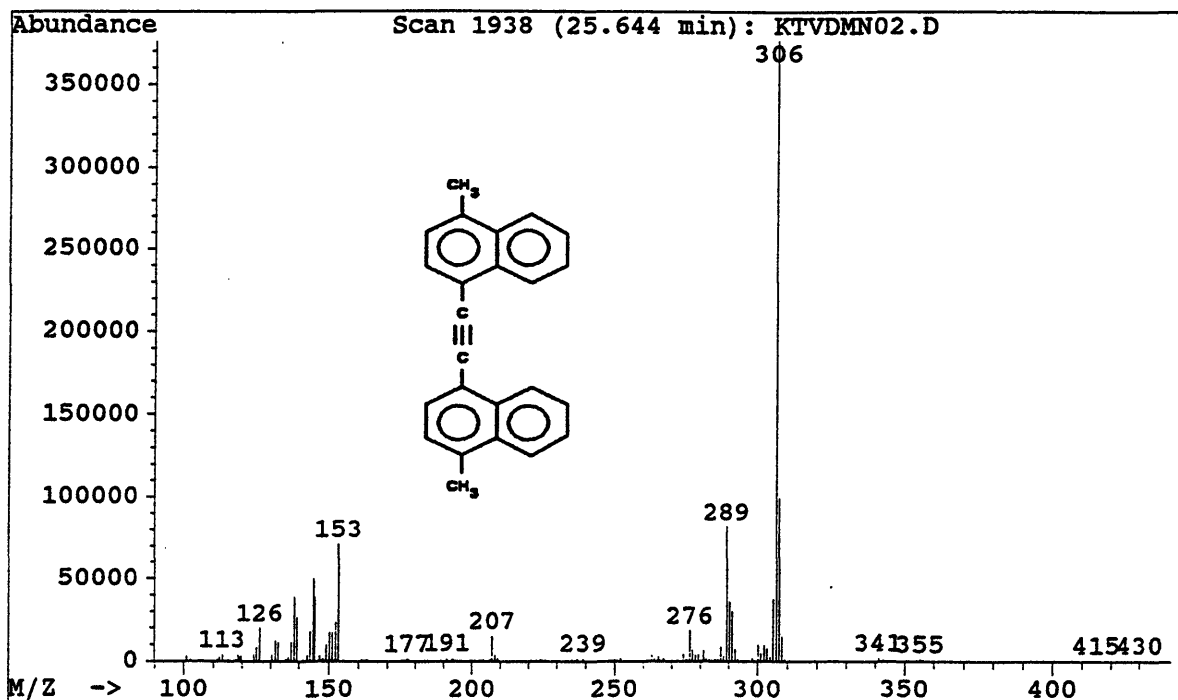
Figure 4.18: Fragmentation pattern and structures for peaks at t = 25.6 and 25.8 minutes formed during 14DMN thermolysis with X = 0.40.

aromatic structure with the large molecular ion and small fragment peaks. A possible structure is shown on the fragmentation pattern. While this compound has a mass of 306, it cannot fully explain the fragments seen, especially the loss of 17 a.m.u. from the molecular ion. The lower panel of Figure 4.18 displays the fragmentation pattern of the peak at t = 25.8 minutes, which is also indicative of an aromatic structure with the large molecular ion and small fragment peaks. The same structure as the upper panel is shown since the fragmentation pattern are almost identical. Although their fragmentation patterns are not shown, the two peaks at t = 24.6 and 24.8 minutes have a mass of 308, which corresponds to the addition of 2 hydrogen to the mass of 306.

4.3.3 Liquid Chromatography

The thermolysis products were analyzed on a Hewlett-Packard 1090 Liquid Chromatograph (LC) equipped with a diode array detector. The LC was controlled and the data was gathered by a Hewlett-Packard 79994A LC ChemStation. A reverse phase Vydac column was used in the analysis. The program used in these runs was acetonitrile/H_2O (40:60) for 40 minutes followed by 100% acetonitrile for 40 minutes followed by 100% dichloromethane for 25 minutes at a flow rate of 1 ml/min.

Liquid chromatography (LC) was performed on the medium and high conversion runs of 910DMA and 9MA that were used for the GC/MS analysis. The

anthracene species were chosen since only a few dimers were identified by GC/MS and standards of 9,9'-, 1,2'- and 1,1'-bianthryl had previously been run on the LC. A standard of anthracene, 1-methylanthracene, 2-methylanthracene, 9-methylanthracene and 9,10-dimethylanthracene was also run as a basis of comparison of retention times. Figure 4.19 shows the liquid chromatogram from the current anthracene standards run for retention time and a table comparing retention times to those previously run.

A Ultraviolet/Visible (UV/VIS) spectrum was generated for each peak of the LC and then compared to a reference library. Unlike GC and GC/MS, retention times vary slightly from run to run and cannot be used alone as a method of identification, but matches to UV/VIS spectrum library were almost perfect. The problem with the methylated anthracenes is that all UV/VIS spectrums a very similar for all methyl-substituted anthracenes. Positional isomers of the methyl anthracenes are indistinguishable by UV/VIS, and addition of a methyl group does yield a red shift (a shift to longer wavelengths), but it is so small that positive identification is impossible. Identification of the peaks was based on matches to the library of standards with shifts in the retention times considered between the previously run anthracenes' standard and the current anthracenes' standard.

While identification of specific peaks was impossible, the LC did reveal that there were numerous species in these thermolysis runs. The current retention times for the anthracene standards show that the dimethylated species elute by ~ 25
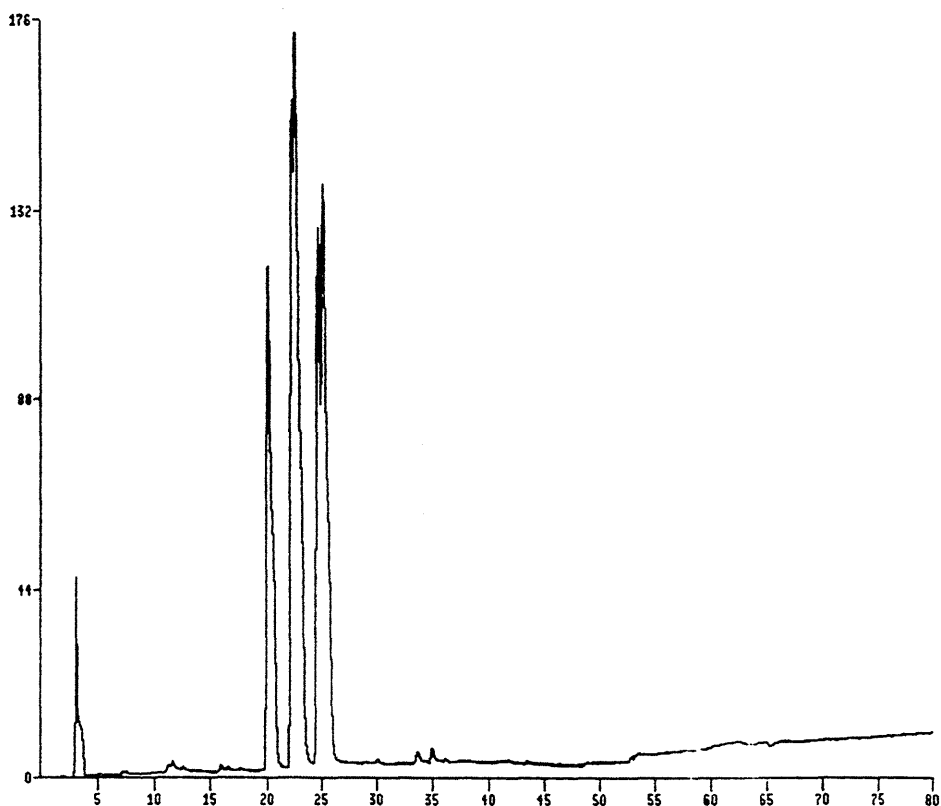
COMPOUND	CURRENT RETENTION TIME (min)	PREVIOUS RETENTION TIME (min)
ANTHRACENE	20.1	18.9
1-METHYLANTHRACENE	22.3	16.5
2-METHYLANTHRACENE	25.1	20.0
9-METHYLANTHRACENE	22.6	17.6
9,10-DIMETHYLANTHRACENE	24.7	19.2
1,2'-BIANTHRYL		35.2
2,2'-BIANTHRYL		50.4
9,9'-BIANTHRYL		26.3

Figure 4.19: Liquid chromatogram of anthracene standards run for retention time and table of these retention times with times of previously run anthracene standards.

247

minutes, therefore the peaks that elute after 25 minutes could be heavy thermolysis products, as shown in Figure 4.20 for 9MA thermolysis and Figure 4.21 for 910DMA thermolysis. The table in the lower panel of Figure 4.19 also shows that the bianthryls eluted after 25 minutes. Taking the shifts in retention time into consideration, it can be estimated that 1,2'-, 1,1'- and 9,9'-bianthryl elute around 40, 55 and 31 minutes, respectively. Methylation of the bianthryl species would shirt these retention times to slightly greater values. Figure 4.20 and Figure 4.21 shows that there are peaks that could correspond to the retention times of these methylated bianthryl species.
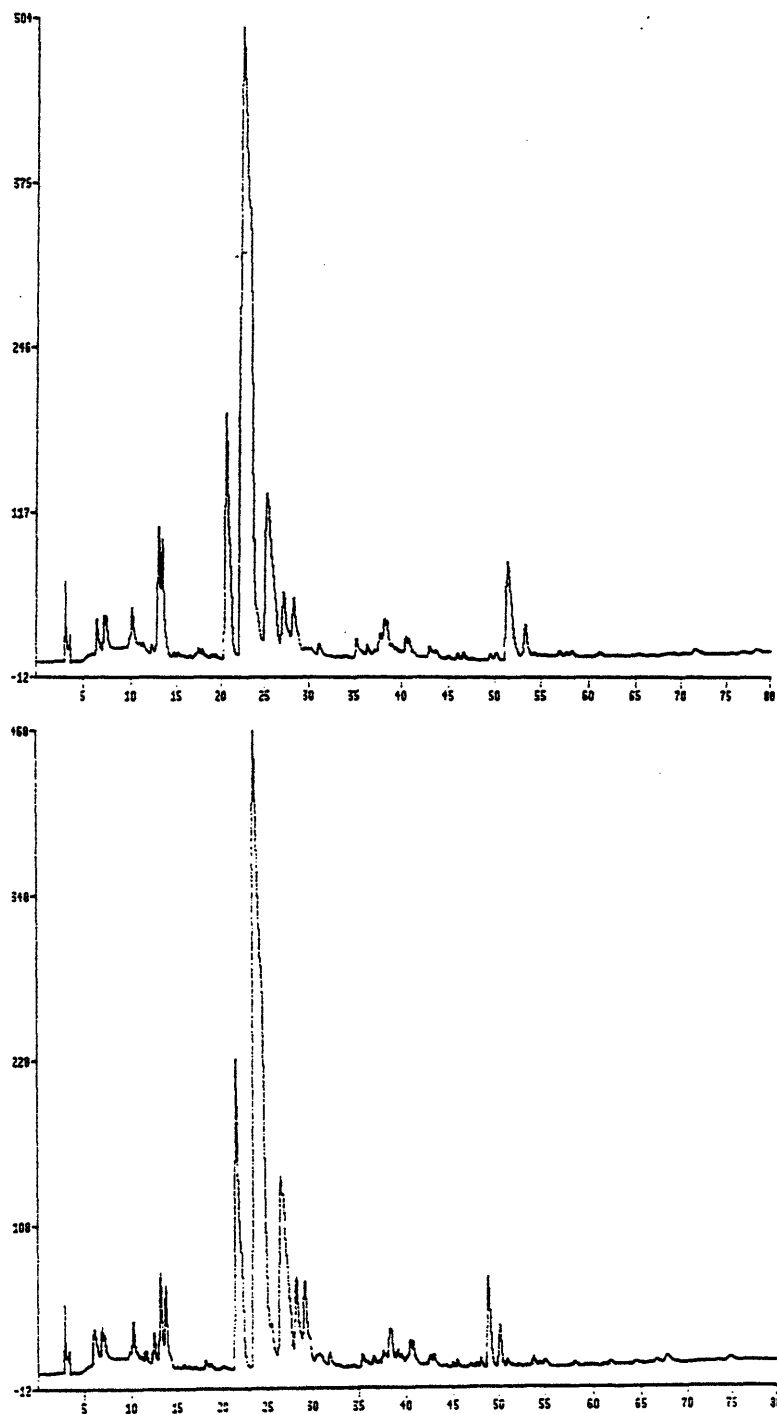
Figure 4.20: Liquid chromatograms for 9MA thermolysis with X = 0.39 (top) and X = 0.82 (bottom).

249
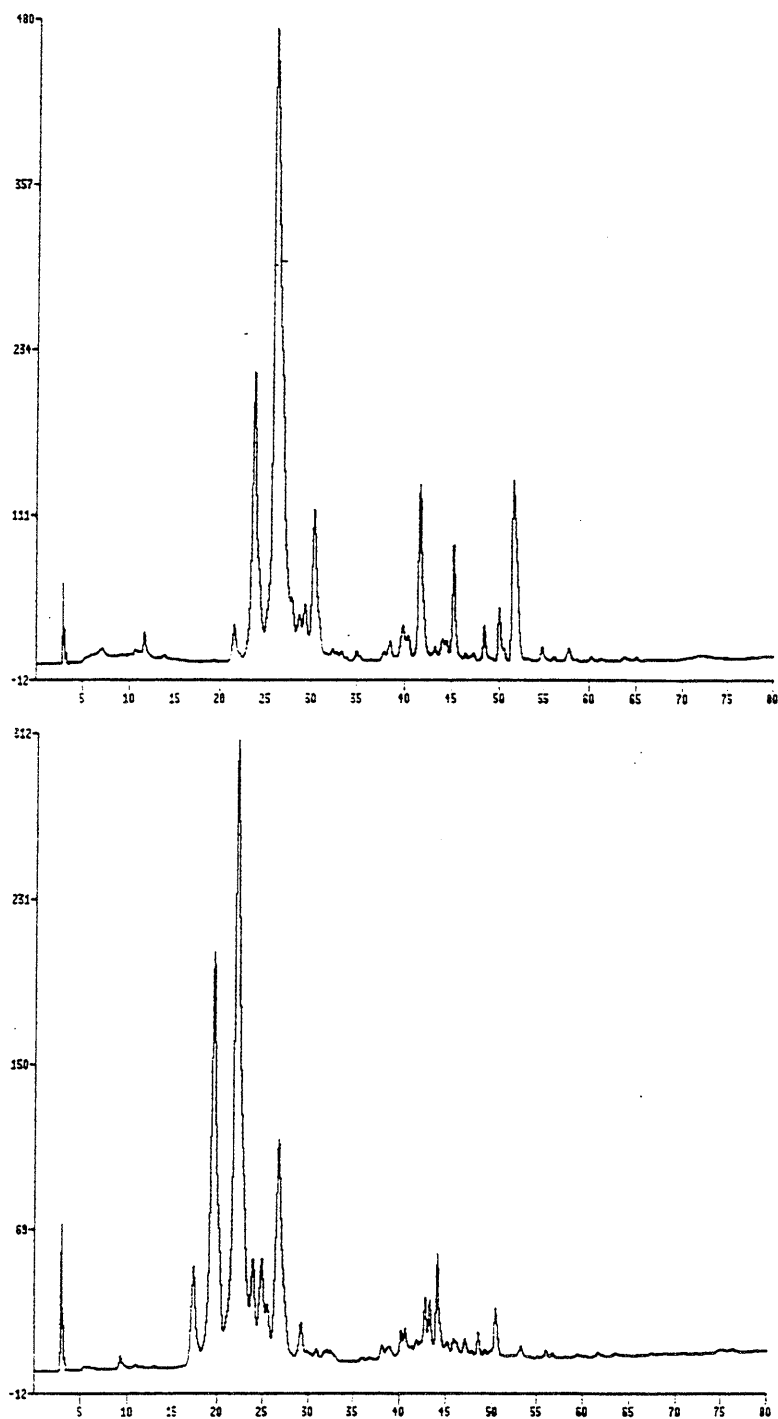
Figure 4.21: Liquid chromatograms for 910DMA thermolysis with X = 0.55 (top) and X = 0.99 (bottom).

250

Chapter 5.

9,10-Dimethylanthracene Thermolysis

9,10-dimethylanthracene (910DMA) was thermolyzed at temperatures between 315 and 409°C, initial concentrations from 0.082 to 2.47 mol/l, and batch holding times from 450 to 57600 seconds. Figure 5.1 illustrates this experimental grid which, including replication, comprised 212 individual runs. Liquid reaction products were analyzed in every experiment and gaseous products were also analyzed in experiments with $[910DMA]_o$ = 0.82 mol/l and temperatures of 335 and 370°C. The product histories and selectivity diagrams of the individual runs were used to infer 910DMA thermolysis pathways. Reaction kinetics were determined from concentration scans at a fixed temperature, T = 335°C, which led to reaction order,
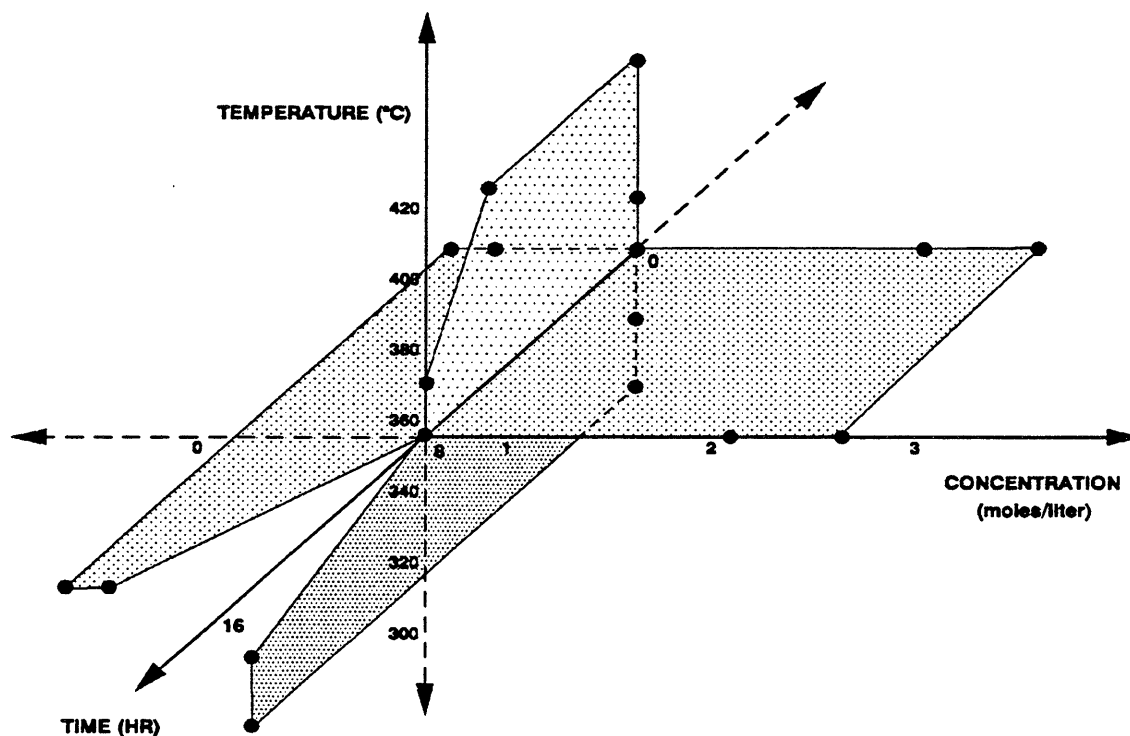
Figure 5.1: Grid for 910DMA thermolysis experiments.

and temperature scans at fixed initial concentrations, $[910DMA]_o = 0.82$ mol/l, which led to the activation parameters. An overall free radical mechanism was proposed to account for 9,10-dimethylanthracene decomposition. Both the kinetics of the system and the observed product histories were modelled. Finally frontier molecular orbital theory was used to interpret the kinetics and minor product distributions.

5.1 Experimental Results

5.1.1 A Representative Example

Product formation histories and a corresponding selectivity diagram were derived from each set of experiments at a fixed temperature and constant initial 910DMA concentration. Figure 5.2, T = 370°C and $[910DMA]_o = 0.82$ mol/l, shows the histories of the major liquid and gaseous products (top) and minor liquid products (bottom). The plot uses arithmetic coordinates of absolute substrate amounts J in the reactor in moles, versus reaction holding time t in seconds, with the appropriate, different, ordinal scales in the upper and lower panels; all data refer to fixed reactor volume $V = 0.60$ cm^3. In the upper panel of Figure 5.2, the substrate 910DMA, symbol O, is seen to decay continuously from an initial $J = 4.9E\text{-}04$ moles to $J = 6.6E\text{-}05$ moles at $t = 28800$ s, the latter corresponding to a substrate fractional conversion $X = 0.867$; the decay half-life is $t^* \sim 9900$ s. The principal product, 9-methylanthracene, abbreviated 9MA with symbol ◻, increases from 0 initially to a maximum value $J = 1.3E\text{-}04$ moles at $t = 14400$ s and then decreases
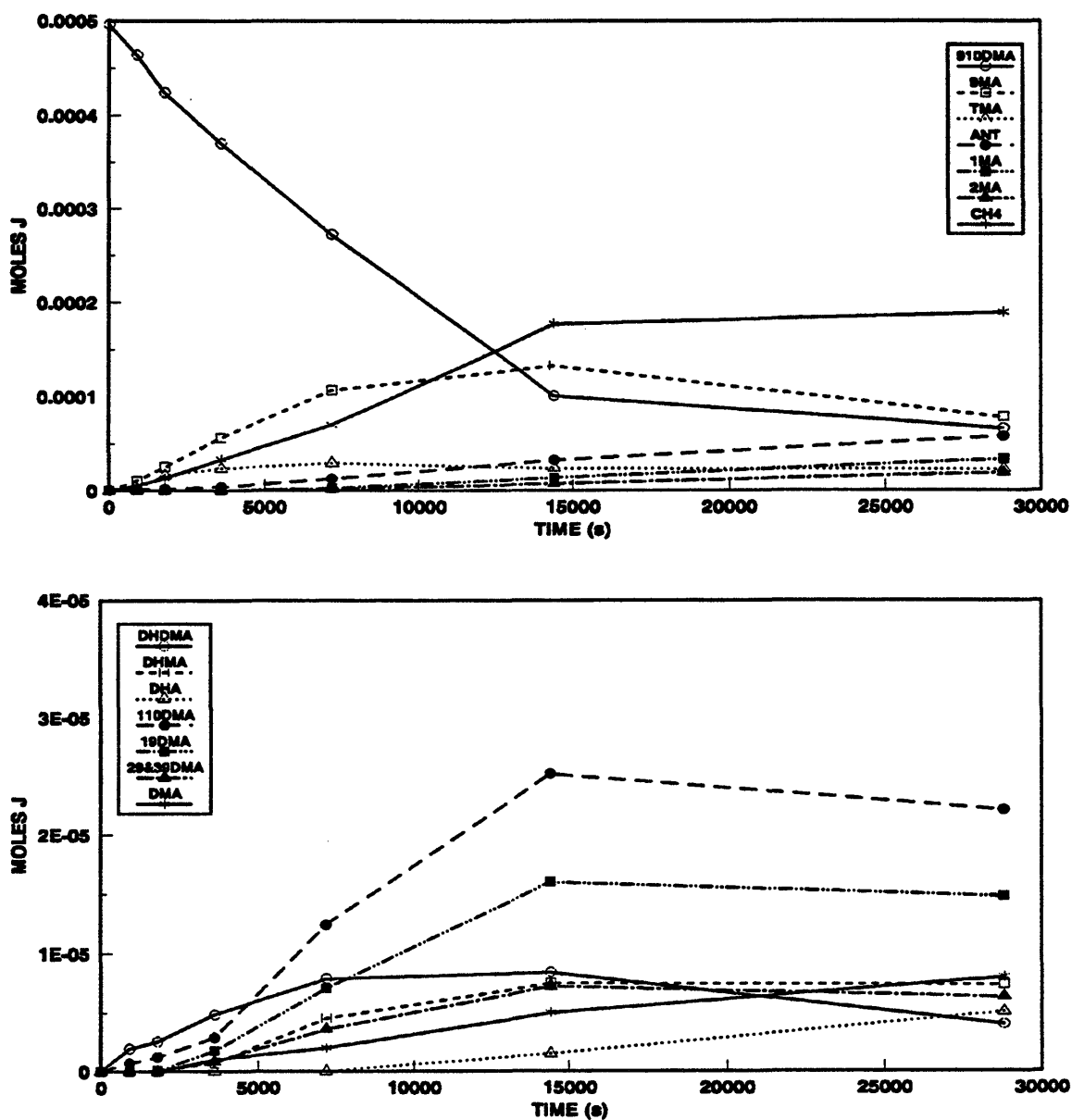
Figure 5.2: Product histories for 910DMA thermolysis at 370°C with $[910DMA]_0$ = 0.82 mol/l: major products (top) and minor products (bottom).

to J = 7.8E-05 moles at t= 28800 s. The sum of several trimethylanthracenes, abbreviated TMA with symbol ▲, grow from 0 initially to J = 2.3E-05 moles at t= 3000 s, then maintains a plateau with shallow maximum J = 2.9E-05 moles at t = 7200 s, after which they decay slowly with increasing time to J = 2.3E-05 moles at t = 28800 s. Anthracene, abbreviated ANT with symbol •, appears first at t = 900 s with J = 1.1E-05 moles, and then rises monotonically with increasing reaction time to J = 5.8E-05 moles at t = 28800 s. The 1-methylanthracene, abbreviated 1MA with symbol ■, and 2-methylanthracene, abbreviated 2MA with symbol ▲, respectively, appear at t = 7200 s and t = 14400 s with J = 2.9E-06 and 1.4E-06 moles, well after the first appearance of anthracene. Both 1MA and 2MA grow monotonically with increasing time, to respectively, J = 3.3E-05 and J = 1.9E-05 moles at t = 28800 s, with 1MA the predominant of the two species. The gaseous product methane, abbreviated CH4 with symbol *, increases monotonically from 0 initially to J = 1.8E-04 moles at t = 14400 s, followed by a slight increase to J = 1.9E-04 moles at t = 28800 s; surpassing the major liquid product 9MA for t > 10000 s. The substrate and major product histories in the present graph depict a classical sequential reaction series A(910DMA) → B(9MA) → C(ANT).

The bottom panel of Figure 5.2 shows the histories of several minor liquid products that are formed during 910DMA thermolysis, including the hydrogenated dimethylanthracene, methylanthracene, and anthracene species as well as the 1,10-, 1,9-, and 2,9-&3,9-dimethylanthracene, and other dimethylanthracene isomers. Data

labelled DHDMA, symbol o, represent the sum of four dihydrodimethylanthracene species actually detected (seen earlier Figure 4.3), of which *cis*- and *trans*-9,10-dihydro-9,10-dimethylanthracenes are most abundant. The DHDMAs first appear at t = 900 s with J = 1.9E-06 moles, reach a maximum value J = 8.4E-06 moles at t = 14400 s and then slowly decay to J = 4.0E-06 moles at t = 28800 s. Data labelled DHMA, symbol ▢, represent the sum of three dihydromethylanthracene species, of which one, likely 9,10-dihydromethylanthracene, is most abundant. The DHMAs first appear at t = 1800 s with J = 8.6E-08 moles, reach a maximum J ~ 7.5E-06 moles at t = 14000 s, and then remain at this level up to the longest t = 28800 s. 9,10-dihydroanthracene, abbreviated DHA with symbol ▵, first appears at t = 14400 s with J = 1.5E-06 moles and increase to amount J = 5.1E-06 moles at t = 28800 s. Of the dimethylanthracene isomers, in order of abundance, the 1,10-dimethylanthracene, abbreviated 110DMA with symbol •, first appears at t = 900 s with J = 6.7E-07 moles, grows to a maximum J = 2.5E-05 moles at t = 14400 s, and then decays slightly to J = 2.2E-05 moles at t = 28800 s. 1,9-dimethylanthracene, abbreviated 19DMA with symbol •, first appears at t = 3600 s with J = 1.7E-06 moles, grows to a maximum J = 1.6E-05 moles at t = 14400 s, and then decays slightly to J = 1.5E-05 moles at t = 28800 s. 2,9&3,9-dimethylanthracenes, abbreviated 29&39DMA with symbol ▴, first appear at t = 3600 s with J = 8.4E-08 moles, increase to a maximum J = 7.2E-06 moles at t = 14400 s and then decrease slightly to J = 6.3E-06 moles at t = 28800 s. DMA isomers other than those

256

previously mentioned, abbreviated DMA with symbol *, first appear at t = 3600 s

with J = 1.3E-06 moles and then increase monotonically to J = 8.3E-06 moles at t

= 28800 s. It is noteworthy that 110DMA appears at t ~ 900 s and 19DMA,

29&39DMA and other DMAs all appear at t ~ 3600 s, subsequent to the appearance

of 9MA at t < 900 s.

The data in Figure 5.2 are displayed as selectivity diagrams in Figure 5.3,

using ordinates of selectivity, S, defined as moles of product formed divided by moles

of substrate 910DMA reacted, and an abscissae of substrate 910DMA fractional

conversion, X. The upper and lower panels of Figure 5.3 respectively display the

major liquid and gaseous product selectivities and the minor liquid product

selectivities obtained for 910DMA thermolysis at T = 370°C and [910DMA]$_o$ = 0.82

mol/l. In the upper panel of Figure 5.3, the selectivity to 9MA, symbol □, is S ~

0.33 at X = 0.06 and 0.15, then increases slowly to exhibit a shallow maximum S =

0.48 at X = 0.45, before declining, at first slowly to S ~ 0.34 at X = 0.80, then

sharply to S = 0.19 at X = 0.87. Selectivity to TMA, symbol ▲, is S = 0.042 at X =

0.06, increases sharply to S = 0.22 at X = 0.15, and then declines steadily to S =

0.052 at X = 0.87. ANT, symbol •, appears with S = 0.033 at X = 0.06, declines

slightly to S = 0.027 at X = 0.25 and then increases steadily to S = 0.082 at X = 0.8,

after which it increases more steeply to S = 0.13 at X = 0.87. At low conversions,

X < 0.10, identification of peaks is difficult since ANT, *cis*-DHDMA and a DHMA

elute only 0.2 s apart, as shown in Figure 4.5. When concentrations of these species
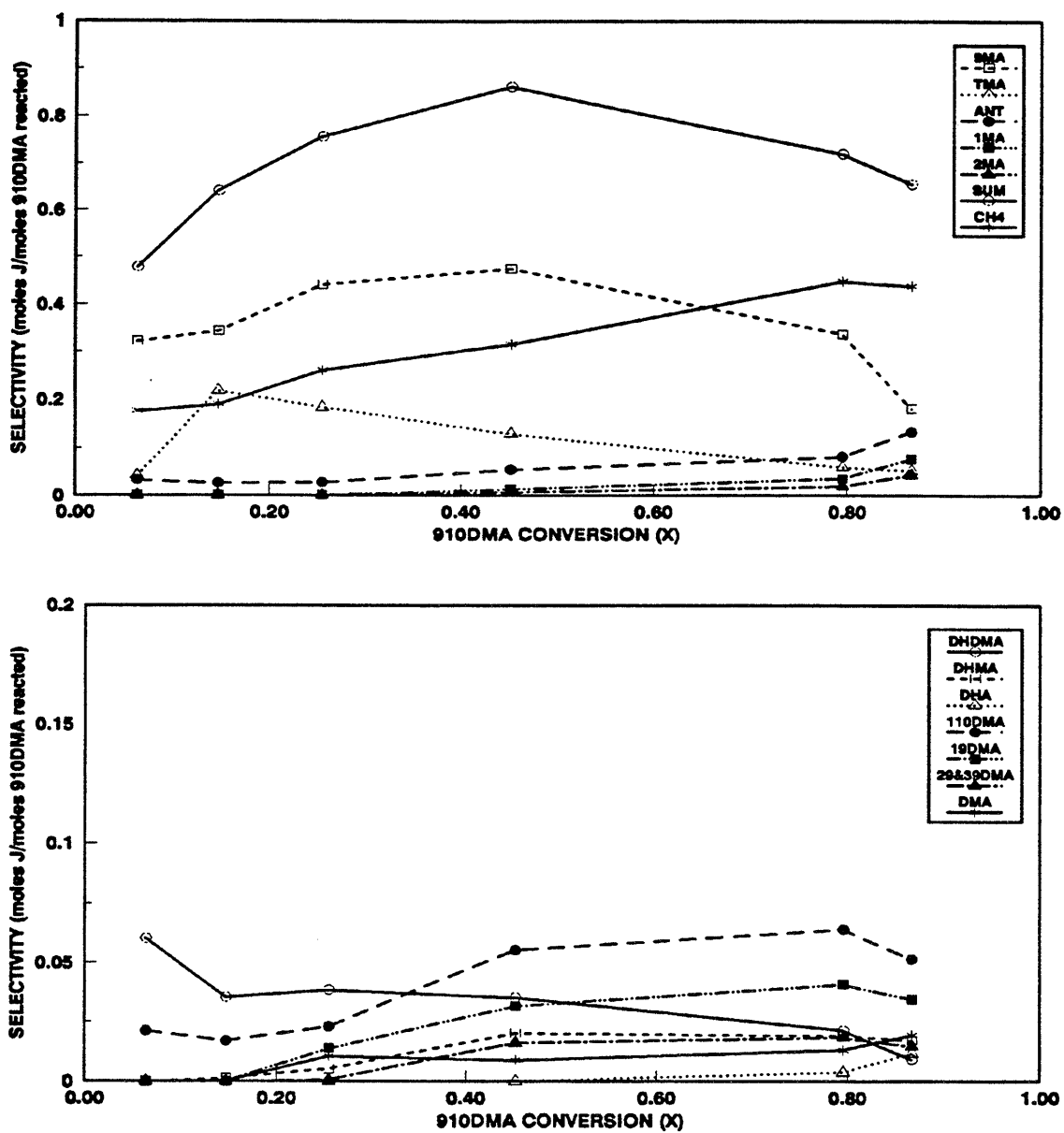
Figure 5.3: Selectivity diagram for 910DMA thermolysis at 370°C with [910DMA]$_o$ = 0.82 mol/l: major products (top) and minor products (bottom).

are small, as in the low conversion runs, it is difficult to discern between ANT, *cis*-DHDMA and DHMA peaks. Although much care was given to correctly identify all peaks, there are most likely some peaks misidentified, especially at the low conversions. The isomers 1MA, symbol ■, and 2MA, symbol ▲, start with S = 0.013 and 0.0062, respectively, at X = 0.45, rise slowly to S = 0.035 and 0.019 by X = 0.80, and then rise more quickly to S = 0.077 and 0.043 by X = 0.87. The sum of the selectivities of all identified products, Σ, abbreviated SUM with symbol ○, increases from Σ = 0.48 at X = 0.06 to Σ = 0.86 at X = 0.45 and then declines slightly to Σ = 0.66 at X = 0.87; over a wide range of 910DMA conversions, 0.2 < X < 0.9, the selectivity sum is roughly constant, at Σ = 0.75 ± 0.08. The selectivity to methane, symbol *, is S = 0.20 at X = 0.15 and 0.25, then increases slowly to S = 0.45 at X = 0.80, and then remains roughly constant to X = 0.87.

In the bottom panel of Figure 5.3, showing minor liquid product selectivities, DHDMA, symbol ○, exhibits a maximum S = 0.060 at X = 0.06, drops to S = 0.030 ± 0.005 for 0.15 < X < 0.80 and then decreases to S = 0.0093 at X = 0.87. DHMA selectivity, symbol ▢, is S = 0.0012 at X = 0.15 and rises to S = 0.018 ± 0.002 for 0.45 < X < 0.87. DHA, symbol △, appears first at X = 0.80 with S = 0.0038 and increases to S = 0.012 at X = 0.87. Selectivities of the dimethylanthracene isomers, 110DMA, symbol •, and 19DMA, symbol ■, both increase monotonically, from S = 0.02 and 0, respectively, for X < 0.15 to S = 0.055 and 0.031 at X = 0.45, after which they exhibit a maximum S = 0.064 and 0.041 at X = 0.80 before declining to

259

S = 0.051 and 0.034 at X = 0.87. 110DMA selectivity at low conversions may be attributed to the fact that the 910DMA substrate was 99% pure, with a 1% 9MA impurity. Methylation of this 9MA impurity may lead to the amounts of 110DMA seen at low conversions. 29&39DMA, symbol ▲, appears at X = 0.25 with S = 0.001 and rises to S = 0.016 ± 0.002 for 0.45 < X < 0.87. Other DMA selectivity, symbol *, is S = 0.011 ± 0.002 for 0.25 < X < 0.80 and then increases to S = 0.019 at X = 0.87.

The preceding selectivity diagrams show that 9MA, CH4, and TMA, with respective S ~ 0.35, 0.20, and 0.20, as well as DHDMA and ANT, with S ~ 0.03 and 0.03, are among the earliest products observed during 910DMA thermolysis. The pair of minor products 110DMA and 19DMA are observed well after the appearance of 9MA, suggesting that they were from methylation of 9MA, rather than from isomerization of the substrate 910DMA. Similarly, 1MA and 2MA are observed well after the appearance of ANT, suggesting that they likely arise from the methylation of ANT, rather than from isomerization of 9MA. Finally, the hydrogenated products DHMA and DHA both arise subsequent to the appearance of the respective parents, 9MA and ANT.

Reaction pathways corresponding to the product histories and selectivities can now be elaborated as a basic demethylation sequence A(910DMA) → B(9MA) → C(ANT), with competing, parallel, hydrogenation and methylation pathways at each stage. For example, at the first stage, A(910DMA) → H_2A(DHDMA) and

A(910DMA) → MeA(TMA), followed by B(9MA) → H₂B(DHMA) and B(9MA) →

MeB(110DMA and 19DMA) at the second and C(ANT) → H₂C(DHA) and C(ANT)

→ MeC(1MA and 2MA) at the third stage.

All subsequent 910DMA results are discussed using the plots and symbols

presented in the preceding example.

5.1.2. Effect of Initial 9,10-Dimethylanthracene Concentration

Initial 9,10-dimethylanthracene concentration was varied in four steps from

0.082 to 2.47 mol/l at fixed reaction temperature T = 355°C; these experiments are

represented by the horizontal plane of the grid in Figure 5.1.

Figure 5.4 shows substrate and product histories at T = 355°C and $[910DMA]_o$

= 0.082 mol/l. In the upper panel, the moles of substrate 910DMA decrease from

the initial J = 4.9E-05 moles to J = 2.2E-05 moles; the decay half-life is t^* ~ 59000

s. The amounts of 9MA and TMA products increase monotonically from 0 initially

to, respectively, J = 1.8E-05 and 1.5E-06 moles at t = 57600 s. ANT is first detected

at t = 28800 s with J = 5.0E-07 moles and reaches J = 1.6E-06 moles by t = 57600

s. A small amount of 1MA, J = 8.6E-07 moles, appears at the longest time, t =

57600 s. In the lower panel of Figure 5.4, DHDMA appears at t = 1800 s with J =

3.2E-07 moles and remains roughly constant at J = 4.0 ± 1.0E-07 moles to t = 57600

s. 110DMA is first detected at t = 28800 s with J = 4.6E-07 moles and grows to J

= 1.3E-06 moles by t = 57600 s. 19DMA and 29&39DMA are only detected at the
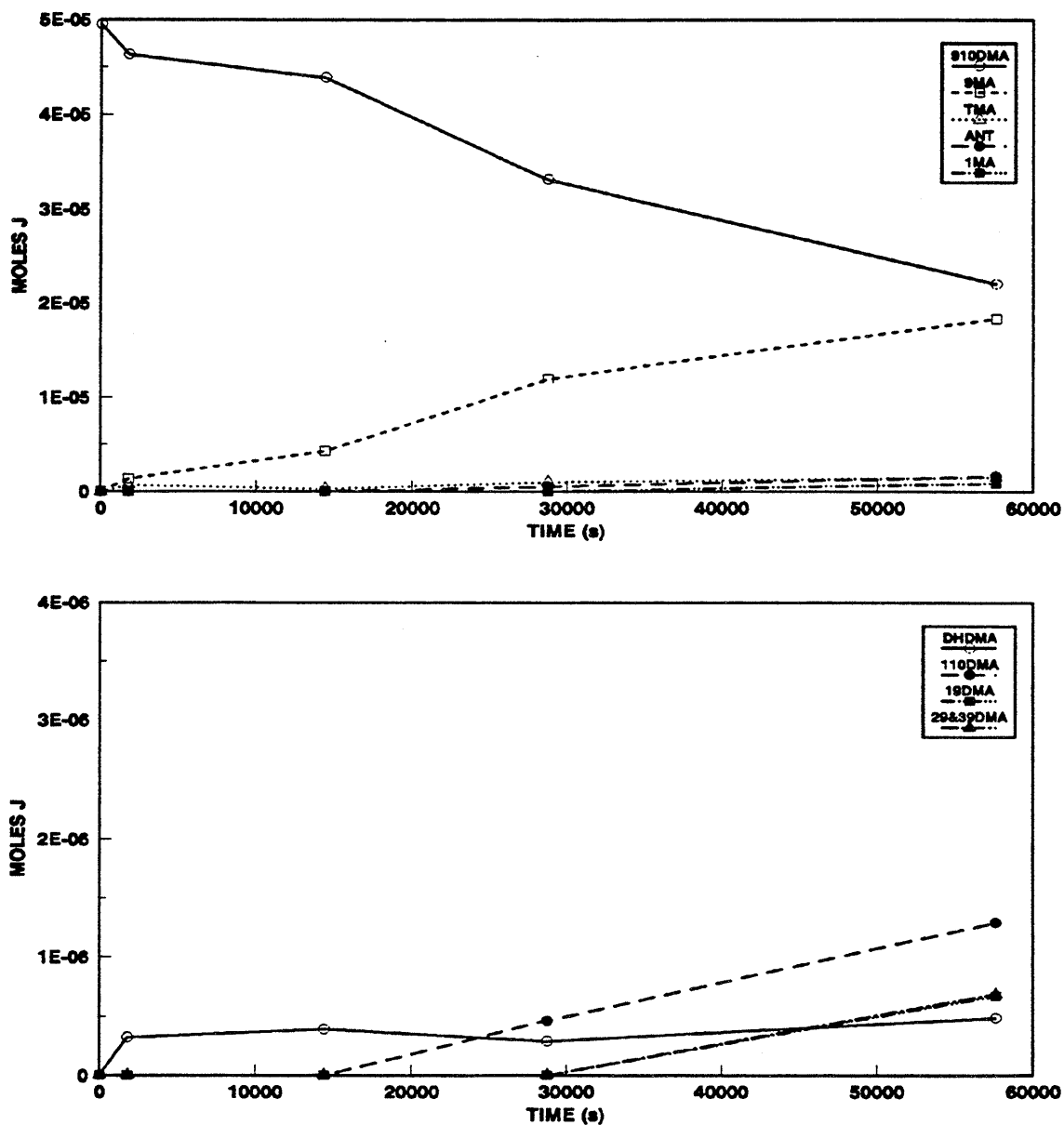
Figure 5.4: Product histories for 910DMA thermolysis at 355°C with [910DMA]$_o$ = 0.082 mol/l: major products (top) and minor products (bottom).

longest time t = 57600 s with J = 6.7E-07 and 6.9E-07 moles, respectively.

Figure 5.5 is a selectivity diagram corresponding to the data in Figure 5.4. In the upper panel, the selectivity to 9MA is S = 0.37 at X = 0.07, but increases abruptly to S = 0.68 ± 0.03 for 0.12 < X < 0.56. TMA selectivity is S = 0.19 at X = 0.07 and decreases abruptly to S = 0.05 ± 0.01 for 0.12 < X < 0.56. ANT appears with S = 0.029 at X = 0.34 and increases to S = 0.057 at X = 0.56. 1MA is only detected at X = 0.56 with selectivity S = 0.030. The selectivity sum is Σ = 0.65 at X = 0.07 and then remains roughly constant at Σ = 0.86 ± 0.04 for 0.12 < X < 0.56. In the lower panel of Figure 5.5, DHDMA selectivity is a maximum of S = 0.089 at X = 0.07, which decreases sharply to S = 0.017 by X = 0.34 after which it remains relatively constant up to X = 0.56. 110DMA selectivity is 0.027 at X = 0.34 and rises to S = 0.045 by X = 0.56. 19DMA and 29&39DMA are only detected at X = 0.56 with selectivities, respectively, S = 0.023 and 0.024.

Figure 5.6 shows the substrate and product histories at T = 355°C and [910DMA]$_o$ = 0.25 mol/l. In the upper panel, the moles of substrate 910DMA decay from the initial J = 1.5E-04 moles to J = 6.4E-05 moles at t = 57600 s; the decay half-life is t* ~ 44000 s. 9MA product grows monotonically from J = 0 initially to J = 4.9E-05 moles at t = 57600 s. TMA is first detected at t = 7200 s with J = 1.7E-06 moles and increases to J = 6.8E-06 moles by t = 57600 s. ANT first appears at t = 28800 s with J = 1.6E-06 moles and increases to J = 4.4E-06 moles at t = 57600 s; 1MA and 2MA are only detected at the highest t = 57600 s, with,
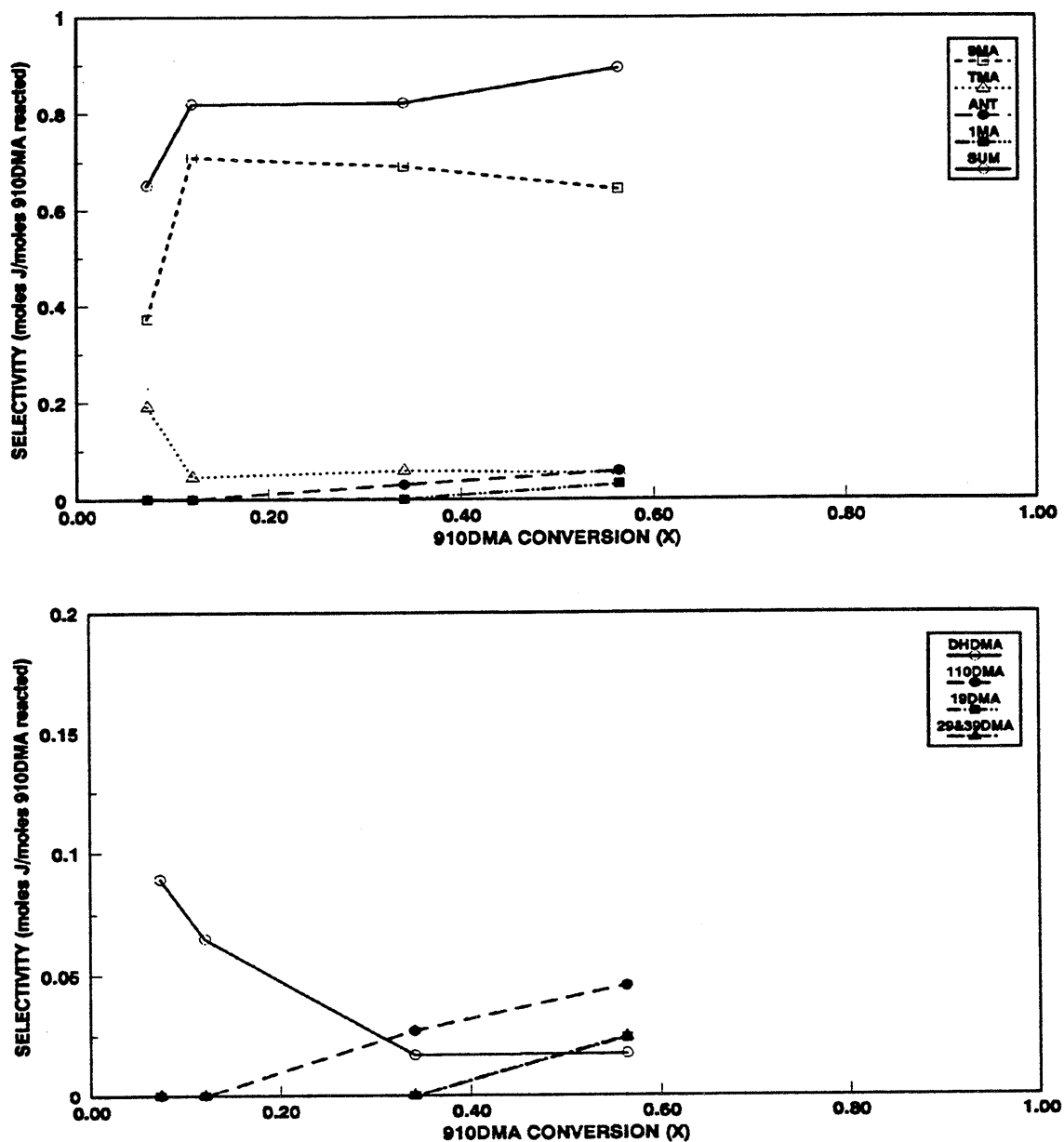
Figure 5.5: Selectivity diagram for 910DMA thermolysis at T = 355°C with [910DMA]$_o$ = 0.082 mol/l: major products (top) and minor products (bottom).
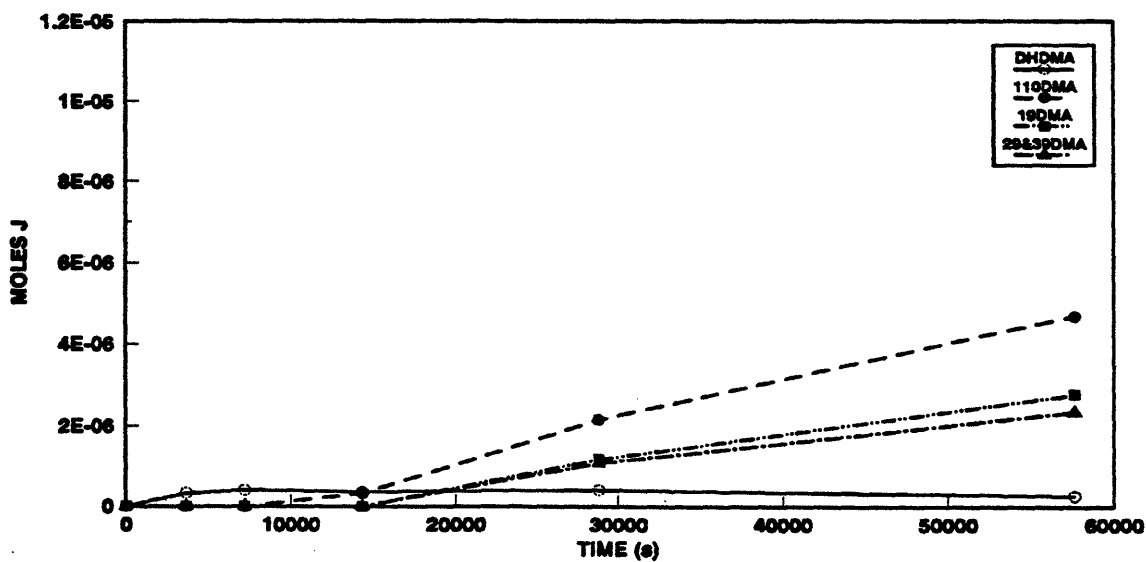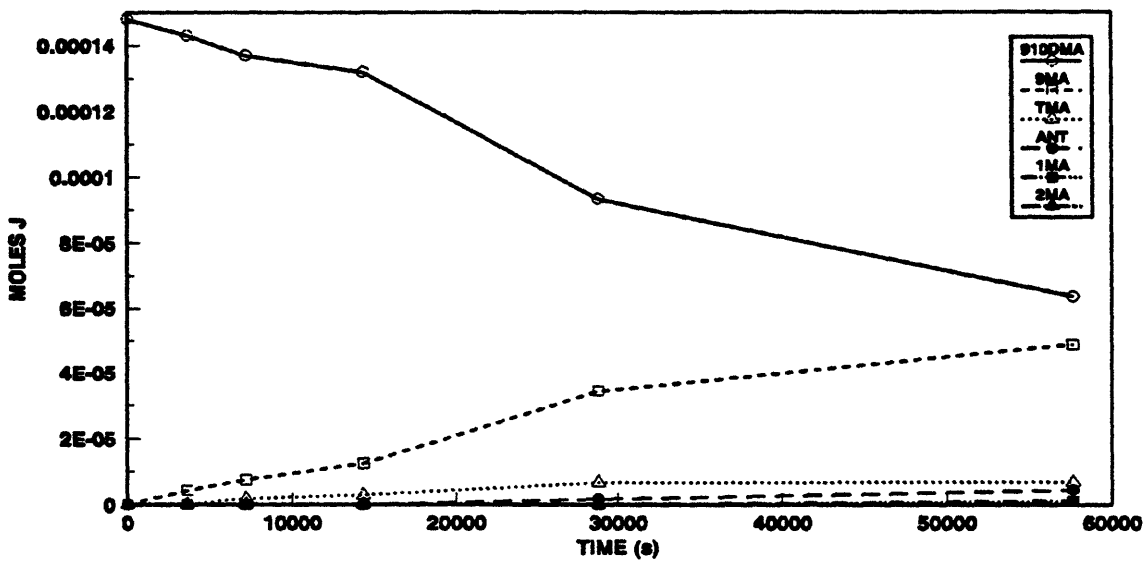
Figure 5.6: Product histories for 910DMA thermolysis at 355°C with $[910DMA]_o$ = 0.25 mol/l: major products (top) and minor products (bottom).

respectively, J = 1.1E-06 and 4.8E-07 moles. In the lower panel of Figure 5.6, DHDMA is first detected at t = 3600 s with J = 3.1E-07 moles and remains roughly constant at J = 3.2 ± 0.7E-07 moles to t = 57600 s. 110DMA is detected at t = 14400 s with J = 3.2E-07 moles and increases to J = 4.7E-06 moles at t = 57600 s. 19DMA and 29&39DMA are detected at t = 28800 s with, respectively, J = 1.2E-06 and 1.1E-06 moles and rise to J = 2.8E-06 and 2.3E-06 moles at t = 57600 s.

Figure 5.7 is a selectivity diagram corresponding to the data in Figure 5.6. In the upper panel of Figure 5.7, 9MA selectivity is S = 0.66 ± 0.04 for 0.07 < X < 0.37, then decreases slightly to S = 0.56 at the highest X = 0.58. TMA appears with S ~ 0.16 at X = 0.07 and decreases monotonically to S = 0.078 at X = 0.58. ANT appears with S = 0.029 at X = 0.37 and increases to S = 0.051 at X = 0.58. 1MA and 2MA are only detected at X = 0.58 with selectivity S = 0.013 and 0.0056, respectively. The selectivity sum decreases from Σ = 1.1 at X = 0.03 to Σ = 0.87 ± 0.03 for 0.07 < X < 0.58. In the lower panel of Figure 5.7, DHDMA appears with maximum S = 0.078 at X = 0.03 and decreases sharply to S = 0.0029 by X = 0.58. 110DMA appears at X = 0.12 with S = 0.018 and increases to S = 0.054 at X = 0.58. 19DMA and 29&39DMA appear at X = 0.37 with S = 0.021 and 0.019, respectively, and increase to S = 0.032 and 0.027 at X = 0.58.

Figure 5.8 shows the substrate and product histories at T = 355°C and [910DMA]$_o$ = 0.82 mol/l. In the upper panel of Figure 5.8, 910DMA is seen to decay from J = 4.9E-04 moles initially to J = 1.6E-04 moles at t = 28800 s; the half-
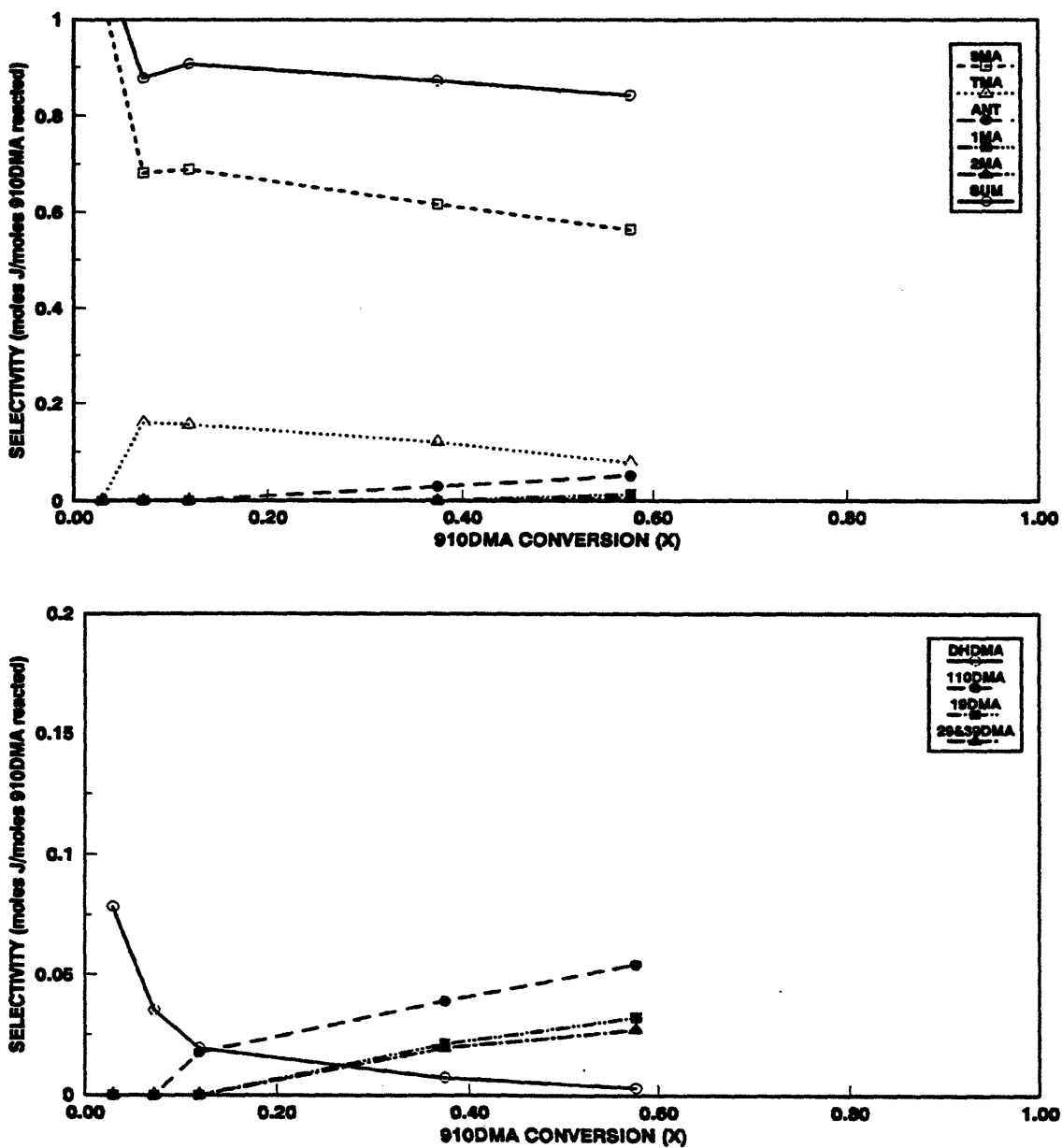
Figure 5.7: Selectivity diagrams for 910DMA thermolysis at 355°C with [910DMA]$_0$ = 0.25 mol/l: major products (top) and minor products (bottom).
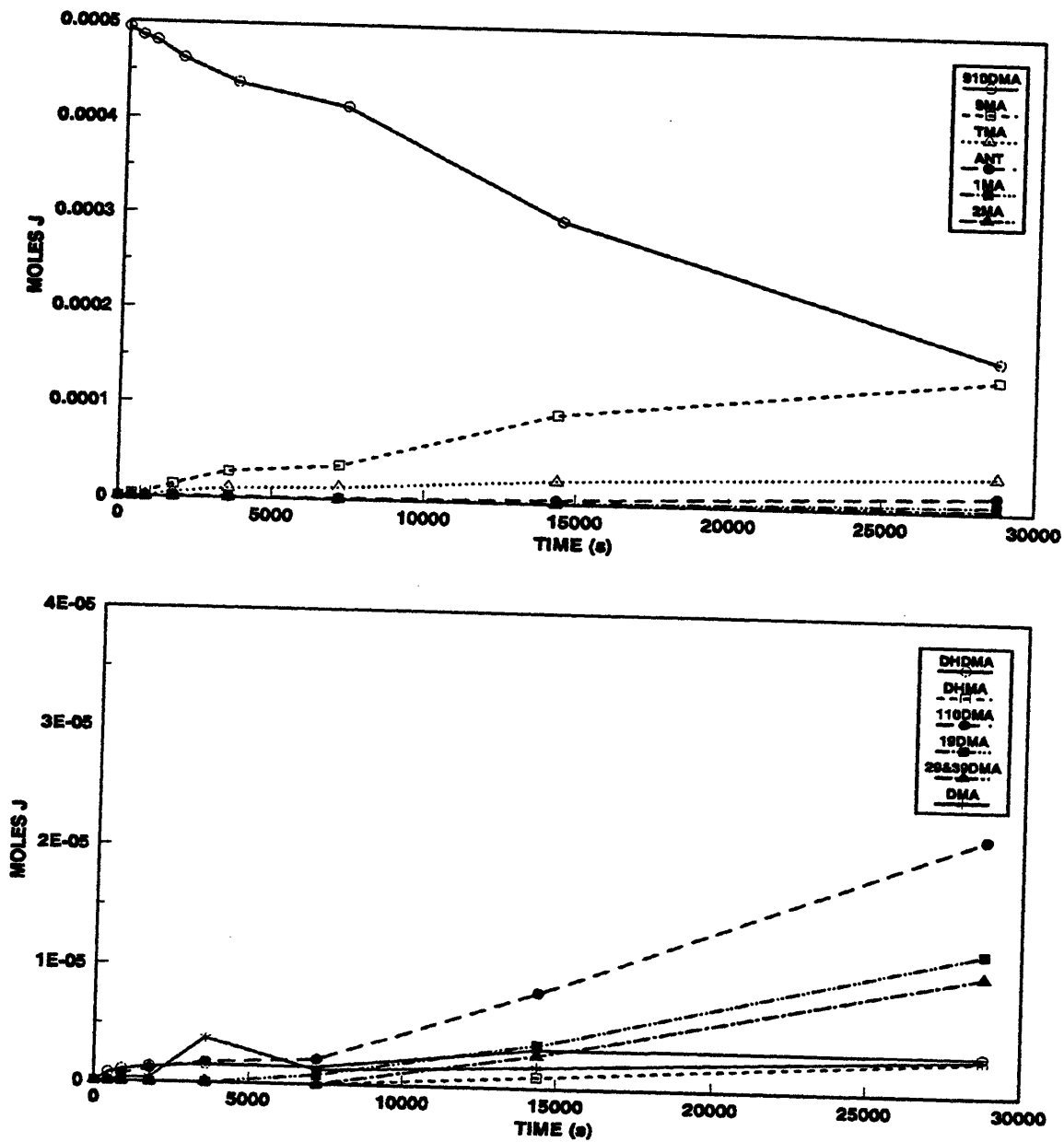
Figure 5.8: Products histories for 910DMA thermolysis at 355°C with $[910DMA]_o$ = 0.82 mol/l: major products (top) and minor products (bottom).

life t* ~ 22000 s. 9MA increases almost linearly from 0 initially to J = 9.3E-05

moles at t = 14400 s and then more slowly to J = 1.4E-04 moles at t = 28800 s.

The TMAs increase from J ~ 0 at t = 450 s to J = 3.7E-05 moles at t = 28800 s.

ANT is first detected at t = 450 s with J = 6.7E-07 moles and increases to J = 1.7E-

05 moles at t = 28800 s. 1MA and 2MA are detected at, respectively, t = 1800 and

14400 s with J = 3.8E-07 and 7.1E-07 moles and grow monotonically to J = 7.2E-06

and 2.9E-06 moles at t = 28800 s. In the lower panel of Figure 5.8, the

hydrogenated product DHDMA is detected at t = 450 s with J = 6.9E-07 moles,

rises to J = 1.3E-06 moles at t= 1800 s and then to J = 3.4E-06 moles at t = 28800

s. DHMA is detected at t = 14400 s with J = 9.3E-07 moles and reaches J = 3.0E-

06 moles at t = 28800 s. 110DMA is detected at t = 900 s with J = 6.2E-07 moles

and grows monotonically to J = 2.2E-05 moles at t = 28800 s. 19DMA and

29&39DMA are detected at, respectively, t = 7200 and 14400 s with J = 7.7E-07 and

2.8E-06 moles and thereafter increase to J = 1.2E-05 and 1.0E-05 moles by t =

28800 s. Other DMAs are detected at t = 900 s with J = 3.3E-07 moles and then

remain at J = 2.5 ± 1.3E-06 moles for 3600 < t < 28800 s.

Figure 5.9 is a selectivity diagram corresponding to the data in Figure 5.8.

In the upper panel of Figure 5.9, 9MA selectivity is initially S = 0.32 at X = 0.02,

after which it remains relatively constant at S = 0.45 ± 0.05 for 0.07 < X < 0.68.

TMA is detected with S = 0.030 at X = 0.03 and increases to S = 0.15 ± 0.04 for

0.07 < X < 0.68. ANT selectivity at X = 0.02 is S = 0.074, decreases to S = 0.013
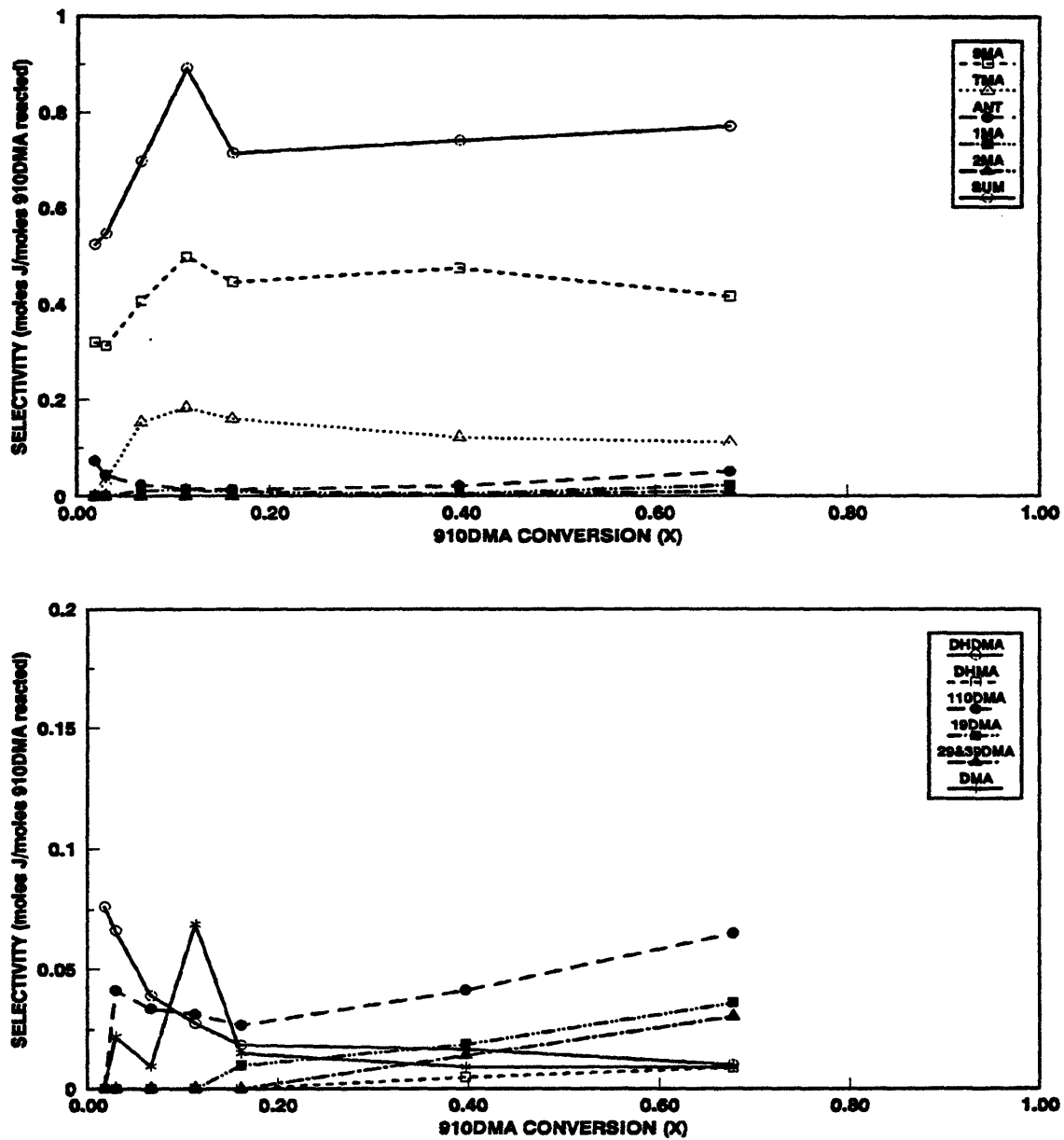
Figure 5.9: Selectivity diagram for 910DMA thermolysis at 355°C with [910DMA]$_o$ = 0.82 mol/l: major products (top) and minor products (bottom).

270

by $X = 0.16$ and then increases monotonically to $S = 0.050$ at $X = 0.68$. 1MA selectivity is $S = 0.012$ at $X = 0.07$, decreases to $S = 0.0055$ at $X = 0.40$ and then increases to $S = 0.022$ at $X = 0.68$. 2MA is detected at $X = 0.40$ with $S = 0.0036$ and rises to $S = 0.0087$ at $X = 0.68$. The selectivity sum increases from $\Sigma = 0.52$ at $X = 0.02$ to $\Sigma = 0.75 \pm 0.10$ for $0.16 < X < 0.68$. In the lower panel of Figure 5.9, DHDMA selectivity is a maximum of $S = 0.076$ at $X = 0.02$ and decreases sharply to $S = 0.010$ by $X = 0.68$. DHMA shows $S = 0.0070 \pm 0.0020$ for $0.40 < X < 0.68$. 110DMA selectivity is 0.041 at $X = 0.03$, decreases slightly to $S = 0.027$ by $X = 0.16$ and then grows monotonically to $S = 0.065$ at $X = 0.68$. 19DMA and 29&39DMA selectivities at, respectively, $X = 0.16$ and 0.40 are $S = 0.0098$ and 0.014, rising to $S = 0.036$ and 0.030 at $X = 0.68$. Other DMA's selectivity is $S = 0.02$ at $X = 0.022$ and remains roughly constant at $S = 0.012 \pm 0.003$ for $0.16 < X < 0.68$.

Figure 5.10 shows substrate and product at $T = 355°C$ and $[910DMA]_o = 2.06$ mol/l. In the upper panel of Figure 5.10, the moles of substrate 910DMA decay from $J = 1.2E-03$ moles initially to $J = 2.2E-04$ moles at $t = 28800$ s; the decay half-life is $t^* \sim 10000$ s. 9MA and TMA both appear at the earliest time of $t = 450$ s with, respectively, $J = 4.7E-05$ and $1.3E-05$ moles, grow monotonically but with decreasing slope to $J = 3.3E-04$ and $1.1E-04$ moles at $t = 14400$ s and then to $J = 3.4E-04$ and $1.1E-04$ moles at $t = 28800$ s. ANT also appears at $t = 450$ s with $J = 4.7E-06$ moles and rises monotonically to $J = 8.2E-05$ moles at $t = 28800$ s. The
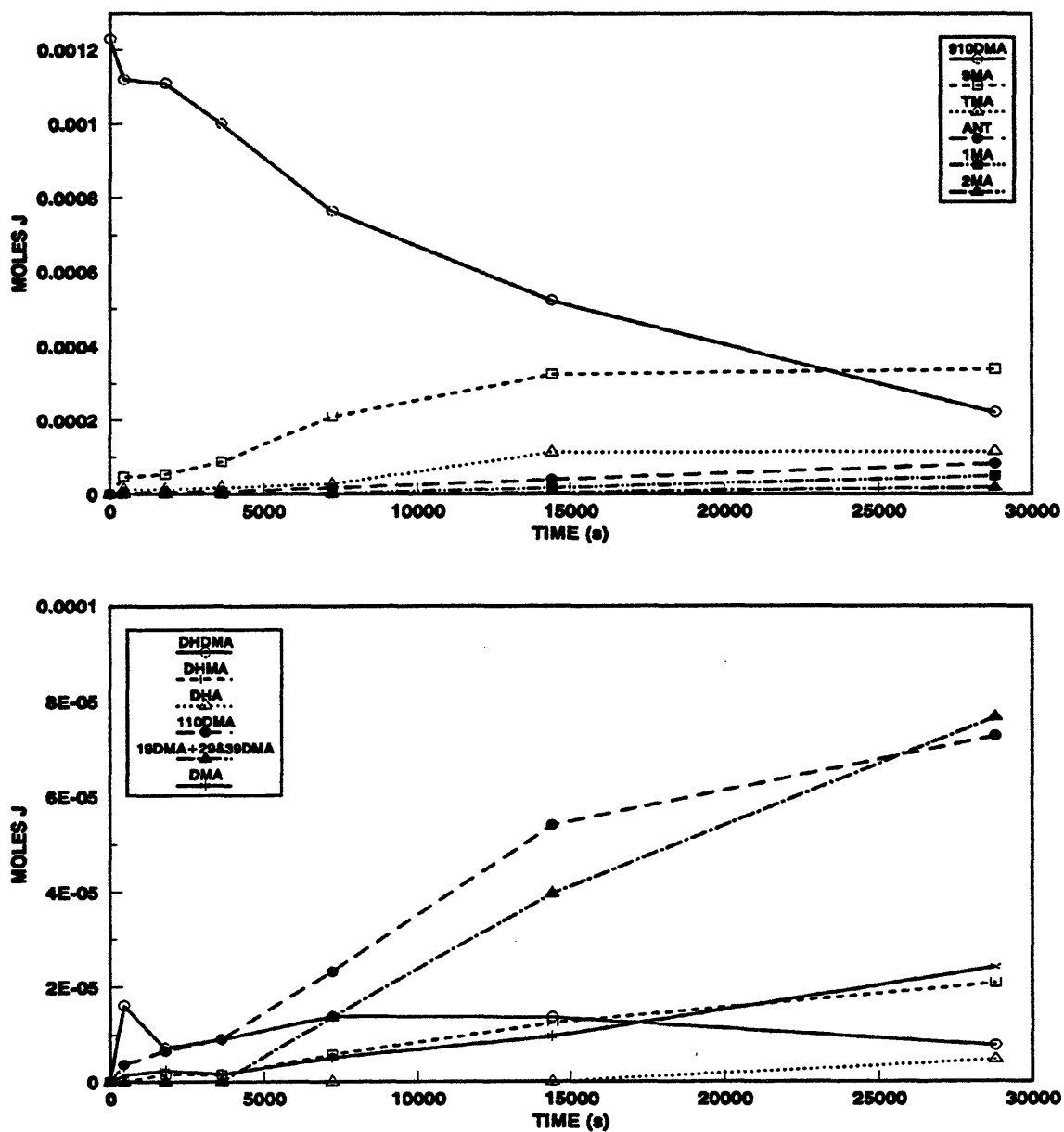
Figure 5.10: Product histories for 910DMA thermolysis at 355°C with [910DMA]$_o$ = 2.06 mol/l: major products (top) and minor products (bottom).

1MA and 2MA, respectively, are detected at t = 1800 and 7200 s with J = 2.2E-06 and 1.9E-06 moles and rise to J = 4.9E-05 and 1.8E-05 moles at t = 28800 s. In the lower panel of Figure 5.10, DHDMA appears at t = 450 s with J = 1.6E-05 moles after which its amount remains roughly constant at J = 1.1 ± 0.3E-05 moles for 1800 < t < 28800 s. DHMA appears at t = 1800 s with J = 1.6E-06 moles and then rises monotonically to J = 2.1E-05 moles at t = 28800 s. DHA is only detected at the highest time t = 28800 s with J = 4.7E-06 moles. 110DMA is detected at t = 450 s with J ~ 3.7E-07 moles, rises monotonically but with decreasing slope to J ~ 5.4E-05 moles at t = 14400 s and then to J = 7.3E-05 moles at t = 28800 s. 19DMA and 29&39DMA are detected at t = 7200 s with J = 1.4E-05 moles and grow to J = 7.7E-05 moles by t = 28800 s, but are not separately resolved as this high initial concentration. Other DMAs appear at t = 450 s with J = 1.4E-06 moles and grow slowly to J = 2.4E-05 moles at t = 28800 s.

Figure 5.11 is a selectivity diagram corresponding to the data in Figure 5.10. In the upper panel of Figure 5.11, 9MA selectivity is roughly constant at S ~ 0.40 ± 0.05 for 0.10 < X < 0.82. TMA is detected with S = 0.12 at X = 0.10 and then fluctuates between S = 0.11 ± 0.05 over the range of 0.10 < X < 0.82. ANT selectivity is roughly constant at S = 0.040 ± 0.008 for 0.10 < X < 0.60, and then increases to S = 0.081 at X = 0.82. 1MA and 2MA appear, respectively, with S = 0.017 and 0.0041 at X = 0.10 and 0.38 and rise slowly to S = 0.049 and 0.018 at X = 0.82. The selectivity sum is roughly constant at Σ = 0.75 ± 0.15 for 0.10 < X <

273
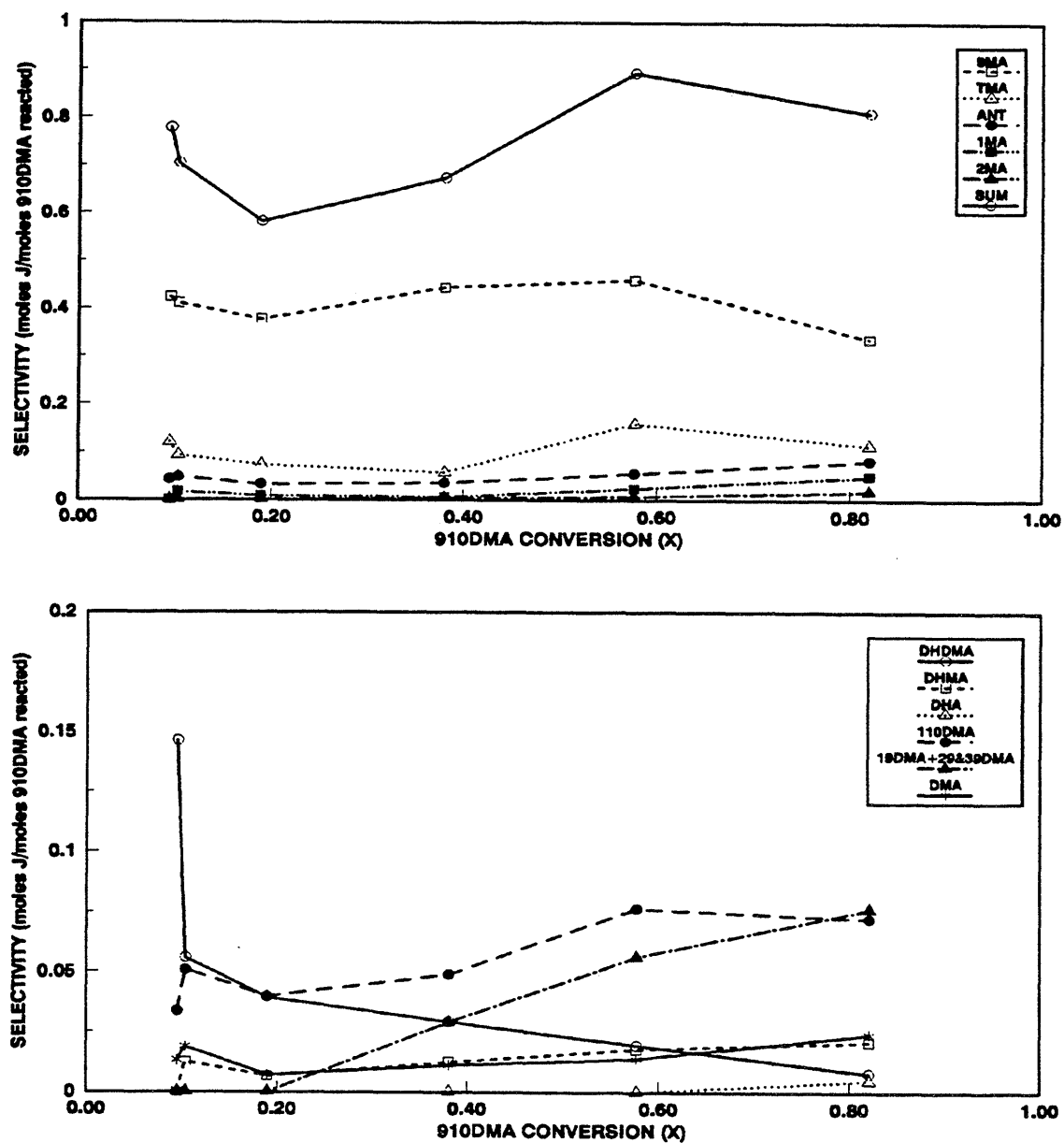
Figure 5.11: Selectivity diagrams for 910DMA thermolysis at 355°C with $[910DMA]_o$ = 2.06 mol/l: major products (top) and minor products (bottom).

0.82. In the lower panel of Figure 5.11, DHDMA selectivity is 0.15 at X = 0.09 followed by a sharp drop to S = 0.056 at X = 0.10 and a decline to S = 0.0077 at X = 0.82. DHMA selectivity is 0.010 ± 0.004 for 0.10 < X < 0.38, followed by a slight increase to S = 0.021 at X = 0.82. DHA selectivity is 0.0047 at X = 0.82. 110DMA selectivity is 0.043 ± 0.008 for 0.09 < X < 0.38, which then increases to S = 0.073 ± 0.002 for 0.58 < X < 0.82. 19DMA and 29&39DMA selectivity at X = 0.38 is 0.029, rising to S = 0.076 at X = 0.82. Other DMA isomer's selectivity is S = 0.015 ± 0.005 for 0.09 < X < 0.82.

Figure 5.12 shows the substrate and product histories at T = 355°C and [910DMA]$_o$ = 2.47 mol/l. In the upper panel of Figure 5.12, 910DMA is seen to decay from J = 1.5E-03 moles initially to J = 3.1E-04 moles at t = 28800 s; the decay half-life t* ~ 12000 s. 9MA increases almost linearly from 0 initially to J ~ 4.0E-04 moles at t = 14400 s and then increases more slowly to J = 4.5E-04 moles at t = 28800 s. The TMAs increase from J ~ 0 initially to J = 1.3E-04 moles at t = 14400 s, and more slowly to J = 1.5E-04 moles at t = 28800 s. ANT is detected with J = 2.2E-06 moles at t = 450 s and increases monotonically to J = 1.1E-04 moles at t = 28800 s. 1MA and 2MA are detected, respectively, at t = 7200 and 14400 s with J = 2.3E-06 and 5.6E-06 moles and monotonically increase to J = 5.5E-05 and 2.7E-05 moles at t = 28800 s. In the lower panel of Figure 5.12, DHDMA is detected with J = 6.0E-06 moles at t = 450 s, increases almost linearly to J = 2.2E-05 moles at t = 14400 s, after which it slowly declines to J = 1.7E-05 moles at

275
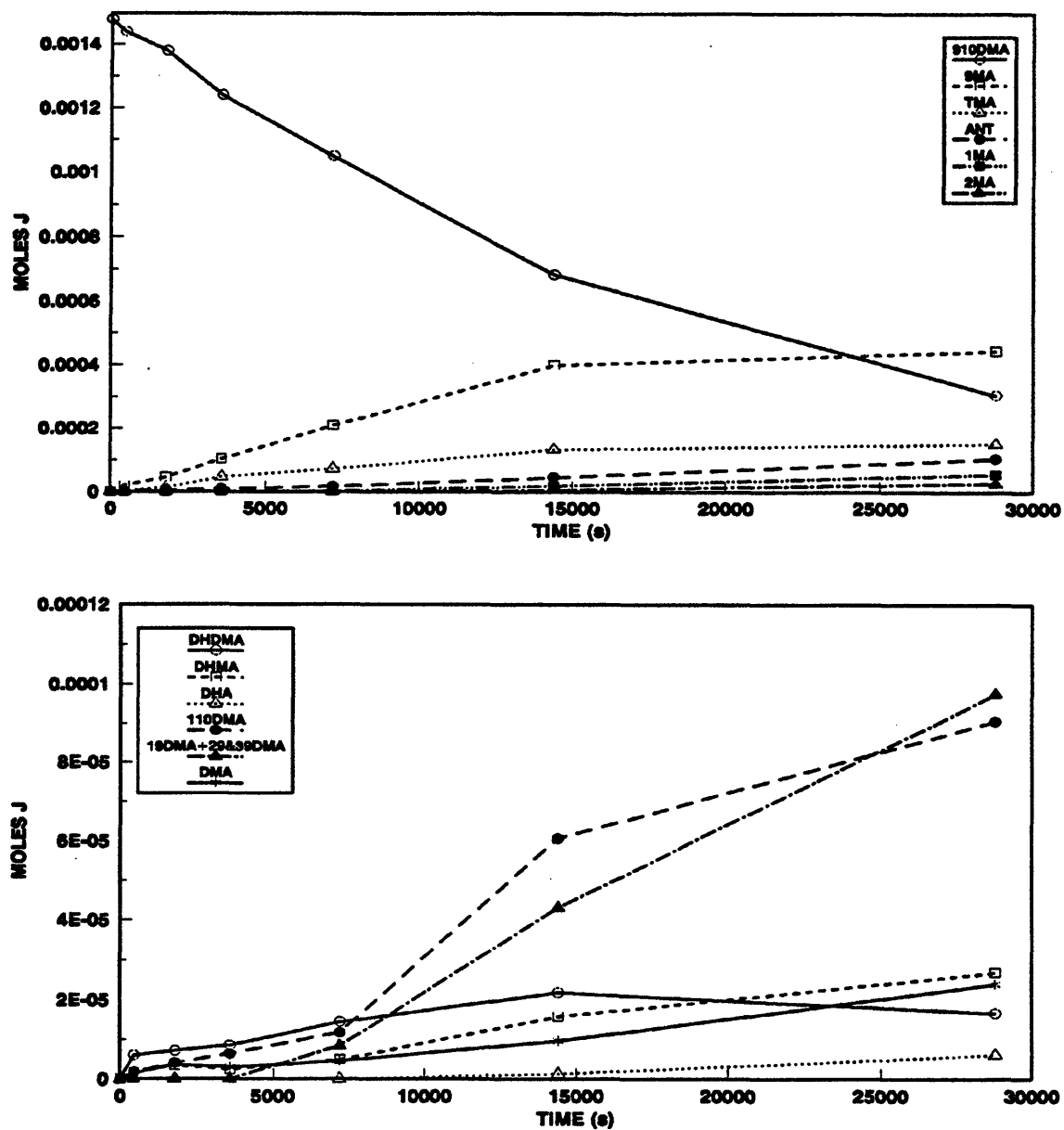
Figure 5.12: Products histories for 910DMA thermolysis at 355°C with [910DMA]$_o$ = 2.47 mol/l: major products (top) and minor products (bottom).

t = 28800 s. DHMA is also detected at t = 450 s with J = 1.8E-06, remains roughly constant at J = 3.7 ± 1.3E-06 moles for 900 < t < 7200 s, and then rises to J = 2.7E-05 moles at t = 28800 s. DHA is detected at t = 14400 s with J = 1.3E-06 moles and rises to J = 6.2E-06 moles at t = 28800 s. 110DMA rises linearly from 0 initially to J = 1.2E-05 moles at t = 7200 s, then increases more rapidly to J ~ 6.1E-05 moles at t = 14400 s and then to J = 9.1E-05 moles at t = 28800 s. 19DMA and 29&39DMA are detected together with J = 8.4E-06 moles at t = 7200 s and then increase linearly to J = 9.8E-05 moles at t = 28800 s. Other DMA isomers are detected with J = 1.5E-06 moles at t = 450 s and grow to J = 2.4E-05 moles at t = 28800 s.

Figure 5.13 is a selectivity diagram corresponding to the data in Figure 5.12. In the upper panel of Figure 5.13, 9MA selectivity is roughly constant at S = 0.45 ± 0.05 for 0.03 < X < 0.60, and then declines slightly to S = 0.38 at X = 0.79. TMA is detected with S = 0.045 at X = 0.03, but remains roughly constant at S = 0.17 ± 0.03 for 0.08 < X < 0.79. ANT selectivity is roughly constant at S = 0.047 ± 0.013 for 0.02 < X < 0.60, and then increases to S = 0.089 at X = 0.79. 1MA and 2MA appear, respectively, with S = 0.0054 and 0.0071 at X = 0.29 and 0.54 and then rise to S = 0.047 and 0.023 at X = 0.79. The selectivity sum remains roughly constant at Σ = 0.85 ± 0.15 over the range 0.02 < X < 0.79; it starts at Σ = 0.96 for X = 0.02, drops to Σ = 0.72 by X = 0.17 and rises back to Σ = 0.97 at X = 0.54. In the lower panel of Figure 5.13, DHDMA selectivity is 0.15 at X = 0.02 followed by a
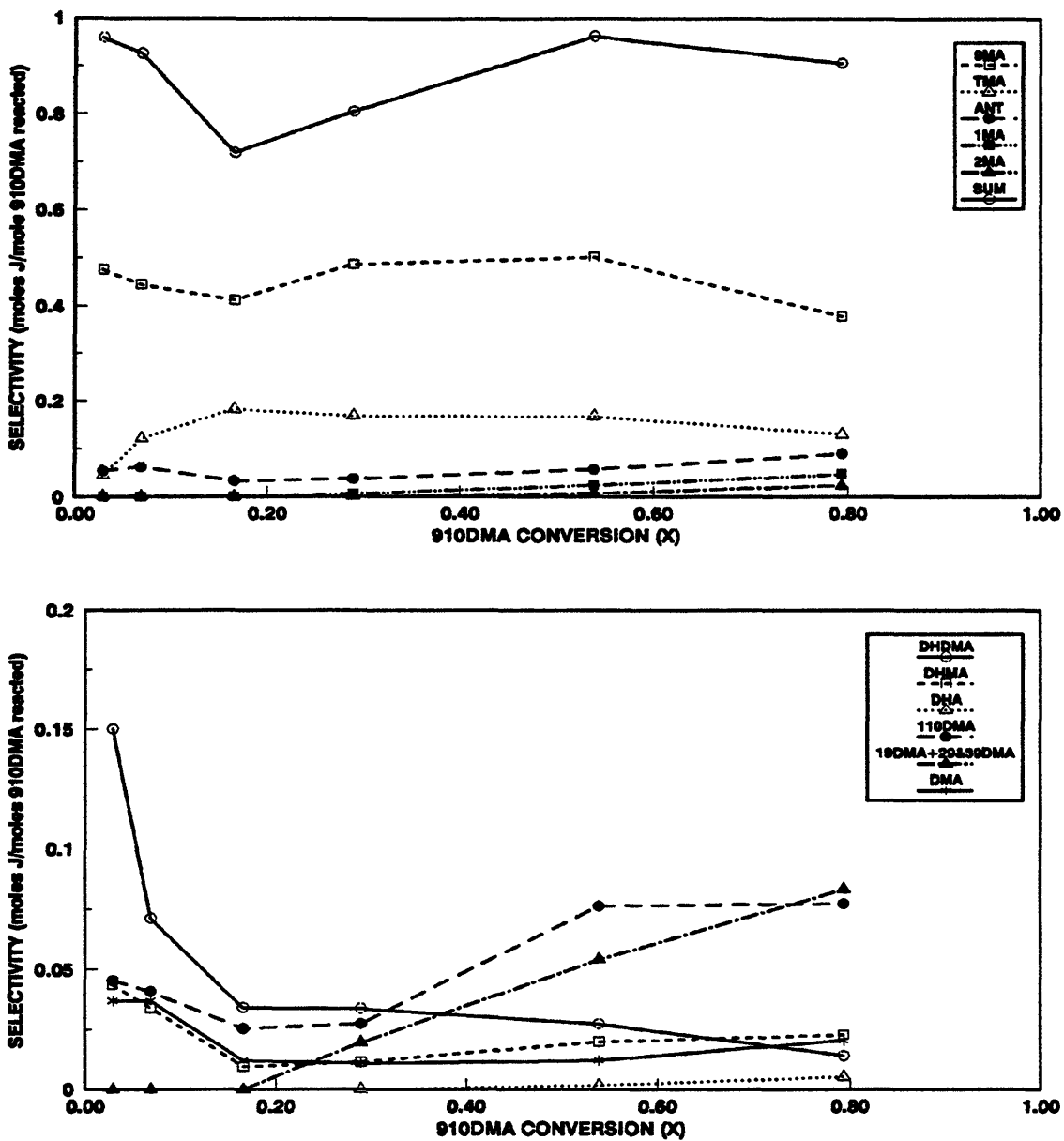
Figure 5.13: Selectivity diagrams for 910DMA thermolysis at 355°C with [910DMA]$_o$ = 2.47 mol/l: major products (top) and minor products (bottom).

sharp drop to S = 0.071 at X = 0.07, and further declines to S = 0.014 at X = 0.79.

DHMA selectivity is 0.044 at X = 0.02 but then remains relatively constant at S =

0.012 ± 0.005 for 0.17 < X < 0.79. DHA selectivity S = 0.0017 at X = 0.54 and

increases to S = 0.0053 at X = 0.79. 110DMA selectivity is 0.035 ± 0.010 for 0.02

< X < 0.29 and then rises to S = 0.077 for 0.53 < X < 0.79. 19DMA and

29&39DMA selectivity at X = 0.29 is 0.020, rising to S = 0.083 at X = 0.79. Other

DMA isomer's selectivity is S = 0.037 at X = 0.02 and 0.05, then remains at S =

0.015 ± 0.005 for 0.17 < X < 0.79.

5.1.3 Summary of Concentration Effects

Increasing initial substrate concentration from $[910DMA]_o$ = 0.082 to 2.47

mol/l at fixed T = 355°C influences both the reaction kinetics and product

selectivities, as respectively summarized in Table 5.1 and Table 5.2. Note that values

in the tables are the averages over all runs, including replication and are therefore

not precisely identical to those seen in the preceding figures. Part (a) of Table 5.1

shows that the substrate decay half-life t^* decreased about 5-fold, from 59000 to

12000 s, as initial concentration $[910DMA]_o$ increased 30-fold, from 0.082 to 2.47

mol/l. Figure 5.14, a doubly logarithmic plot of t^* versus $[910DMA]_o$, shows that the

Table 5.1

EFFECT OF INITIAL 910DMA CONCENTRATION ON KINETIC PARAMETERS AT T = 355°C

Part		[910DMA]$_o$ (mol/l)				
		0.082	0.25	0.82	2.06	2.47
a	Half-life t^*, s	59067 ± 10243[1]	43665 ± 2661	21912 ± 2743	10084 ± 1132	11891 ± 1723
b	[9MA/910DMA]$_{tmax1}$				1.52	1.47
	t_{max1}/t^*				2.86	2.42
c	[DHDMA/910DMA]$_{tmax2}$	0.012	0.004	0.011	0.017	0.029
	t_{max2}/t^*	0.24	0.66	0.65	0.71	1.21

[1]   ± = standard deviation of the average half-life

Table 5.2

EFFECT OF INITIAL 910DMA CONCENTRATION ON PRODUCT SELECTIVITIES AT T = 355°C

Part	Selectivity S of:	Conversion X Range:	[910DMA]$_o$ (mol/l)				
			0.082	0.25	0.82	2.06	2.47
a	9MA	0.1 - 0.8	0.65	0.51	0.48	0.46	0.45
	TMA	0.1 - 0.8	0.04	0.07	0.11	0.12	0.16
b	DHDMA	0.06 ± 0.02	0.089	0.078	0.076	0.081	0.076
		0.56 ± 0.02	0.017	0.003	0.012	0.019	0.024
	DHMA	0.56 ± 0.02	ND	ND	0.009	0.018	0.021
	DHA	0.8	ND	ND	ND	0.007	0.005
c	ANT	0.56 ± 0.02	0.057	0.051	0.054	0.055	0.051
	1MA	0.56 ± 0.02	0.030	0.013	0.015	0.023	0.020
	2MA	0.56 ± 0.02	ND	0.006	0.007	0.007	0.008
	110DMA	0.56 ± 0.02	0.045	0.054	0.061	0.076	0.064
	19DMA	0.56 ± 0.02	0.024	0.032	0.036	0.056[1]	0.059[1]
	29&39DMA	0.56 ± 0.02	0.024	0.027	0.030		
	DMA	0.56 ± 0.02	ND	ND	0.009	0.014	0.011

[1] Selectivity for 19DMA & 29&39DMA combined; these peaks are not resolvable on GC for [910DMA]$_o$ = 2.07 and 2.47 mol/l

Figure 5.14: Decay half-life t^* for varying initial concentrations $[910DMA]_o$ at fixed $T = 355°C$.

data adhere to a line:

$$\log t^* = -0.528 \log[910DMA]_o + 4.25 \qquad (5.1)$$

The slope of this line, $\sim -1/2$, implies that 910DMA decomposition is 3/2 order in substrate. Also, the intercept of the line shows the rate constant at $T = 355°C$ to be $\log k_1 = -4.34$, by reference to the integrated 3/2-order rate expression:

$$\frac{1}{[910DMA]_t^{1/2}} - \frac{1}{[910DMA]_o^{1/2}} = \frac{k_1 t}{2} \qquad (5.2)$$

Product histories at the highest $[910DMA]_o = 2.06$ and 2.47 mol/l, shown in Figure 5.10 and Figure 5.12, also provide an indication of the relative kinetics of the sequential reactions:

$$910DMA \xrightarrow{k_1} 9MA \xrightarrow{k_2} ANT \qquad (5.3)$$

If 9MA is presumed to have attained its maximum concentration $[9MA]_{max}$ at the longest times t_{max1} in both figures, then, as shown in part (b) of Table 5.1, the ratios $[9MA/910DMA]t_{max1} \sim 1.5$ and $[t_{max1}/t^*] \sim 2.6$ both imply that 9MA decomposes more slowly than 910DMA. If both decompositions are presumed to be of the same 3/2 order in their respective substrates, then we can estimate the rate constant ratio $(k_1/k_2) = [9MA/910DMA]_{tmax1}^{3/2} \sim 1.8$. Logic analogous to the preceding can also be applied to the hydrogenated product DHDMA, which is seen reach a shallow

maximum at approximately 14400 s in Figure 5.6, Figure 5.8, Figure 5.2, Figure 5.10 and Figure 5.12, to suggest a series:

$$910DMA \xrightarrow{k_3} DHDMA \xrightarrow{k_4} products \tag{5.4}$$

Using the maximum DHDMA concentration, $[DHDMA/910DMA]_{tmax2}$ remains roughly constant while $[t_{max2}/t^*]$ increases with increasing $[910DMA]_o$, as shown in part (c) of Table 5.1. $[DHDMA/910DMA]_{tmax2} \sim 0.015$ for $0.082 < [910DMA]_o < 2.06$ mol/l and $[DHDMA/910DMA]_{tmax2} = 0.029$ for $[910DMA]_o = 2.47$ mol/l while $[t_{max2}/t^*] = 0.24$ at $[910DMA]_o = 0.082$ mol/l and increases to $[t_{max2}/t^*] = 1.21$ at $[910DMA]_o = 2.47$ mol/l. Both suggest that DHDMA decomposes faster than it forms from 910DMA, i.e., $k_4/k_3 > 1$, and that k_4 is of lower order than k_3.

Turning to product selectivities, summarized in Table 5.2, both 9MA and TMA selectivities were roughly independent of conversion over the ranges $0.1 < X < 0.8$ at all initial concentrations, as shown in part (a) of Table 5.2. The absolute values of S(9MA) declined somewhat with increasing $[910DMA]_o$, from $S \sim 0.65$ at $[910DMA]_o = 0.082$ mol/l to $S \sim 0.45$ for $0.82 < [910DMA]_o < 2.47$ mol/l, while S(TMA) increased somewhat with increasing $[910DMA]_o$, from $S \sim 0.04$ at $[910DMA]_o = 0.082$ mol/l to $S \sim 0.11$ at $[910DMA]_o = 0.82$ mol/l to $S \sim 0.16$ at $[910DMA]_o = 2.47$ mol/l. The hydrogenated species DHDMA selectivity was essentially highest at the lowest conversions and then declined, in some cases precipitously, with increasing X, as shown in part (b) of Table 5.2. For all

[910DMA]$_o$, S(DHDMA) ~ 0.08 at X = 0.06 ± 0.02 decreased to S ~ 0.015 at X = 0.56 ± 0.02. Of the other hydrogenated species, DHMA was detected at the highest [910DMA]$_o$ = [0.82, 2.06, 2.47 mol/l] with S(DHMA) ~ [0.009, 0.018, 0.021] at X = 0.56 ± 0.02. DHA was only detected at the highest [910DMA]$_o$ = 2.06 and 2.47 mol/l, and then only at the highest conversion, with S(DHA) ~ 0.006 at X = 0.80. ANT, methylanthracene and other minor dimethylanthracene selectivities increased monotonically from 0 as conversions increased for all initial concentrations, as shown in part (c) of Table 5.2. At X = 0.56 ± 0.02 for all initial concentrations, S(ANT) = 0.053 ± 0.003. The minor methylated species all exhibited analogous behavior in regard to their selectivities. Among monomethylated species, S(1MA) and S(2MA) generally increased with increasing X at all [910DMA]$_o$, with S(1MA) > S(2MA) always and both always < S(ANT) at any X. S(1MA) = 0.020 ± 0.010 at X = 0.56 ± 0.02 for all [910DMA]$_o$ and S(2MA) = 0.007 ± 0.001 at X = 0.56 ± 0.02 for 0.25 < [910DMA]$_o$ < 2.47 mol/l. Of the dimethylated species, the order of abundance was generally S(110DMA) > S(19DMA) > S(29&39DMA) > S(other DMAs), with each of these always < S(9MA) at any X; also, dimethylated species selectivities generally increased with increasing X at all [910DMA]$_o$. The absolute values of S(110DMA), S(19DMA), S(29&39DMA) and S(other DMAs) increased somewhat with increasing [910DMA]$_o$. At X = 0.56 ± 0.02, S(110DMA) rose from 0.045 at [910DMA]$_o$ = 0.082 mol/l to S(110DMA) ~ 0.061 at [910DMA]$_o$ = 0.82 mol/l to S(110DMA) ~ 0.070 ± 0.006 at [910DMA]$_o$ = 2.06 and 2.47 mol/l. At X

= 0.56 ± 0.02, S(19DMA) and S(29&39DMA) rose from 0.024 each at $[910DMA]_o$

= 0.082 mol/l to 0.036 and 0.030, respectively, at $[910DMA]_o$ = 0.82 mol/l. For

$[910DMA]_o$ = 2.06 and 2.47 mol/l, 19DMA and 29&39DMA were not separately

resolved on the GC. Other DMAs were only detected at the higher $[910DMA]_o$ >

0.82 mol/l. At X = 0.56 ± 0.02, S(DMA) rose from 0.009 at $[910DMA]_o$ = 0.82

mol/l to S(DMA) = 0.012 ± 0.002 at $[910DMA]_o$ = 2.06 and 2.47 mol/l.

Finally, Figure 5.15, Figure 5.16 and Figure 5.17 depict the variation of certain

product ratios, namely R[ANT/9MA], R[(Σ minor DMAs)/9MA] and

R[(1MA+2MA)/ANT], versus 910DMA conversion X at all initial substrate

concentrations. In Figure 5.15 it is seen that, for X > 0.15, the ratio of ANT to

9MA, R[ANT/9MA], is essentially a function of conversion only, with data for all

initial concentrations, 0.082 < $[910DMA]_o$ < 2.47 mol/l, lying on roughly the same

curve. This relationship implicitly describes the kinetics of 910DMA demethylation

under the present conditions. For X < 0.15, the amount of ANT formed was below

the detection limits of the GC at $[910DMA]_o$ = 0.082 and 0.25 mol/l. For X < 0.15

and $[910DMA]_o$ = 0.82, 2.06 and 2.47 mol/l, the species identified as ANT may

actually be *cis*-DHDMA of DHMA, as noted in the representative example.

Figure 5.15 reinforces this possibility since the trend in the R[ANT/9MA] vs. X for

X < 0.15 is the same trend as for R[DHDMA/9MA] vs. X for X < 0.15 (shown

later, Figure 5.41). In Figure 5.16 it is seen that, for X > 0.15, the ratio of minor

dimethylated species to 9MA, R[Σ minor DMA/9MA], is essentially a function of
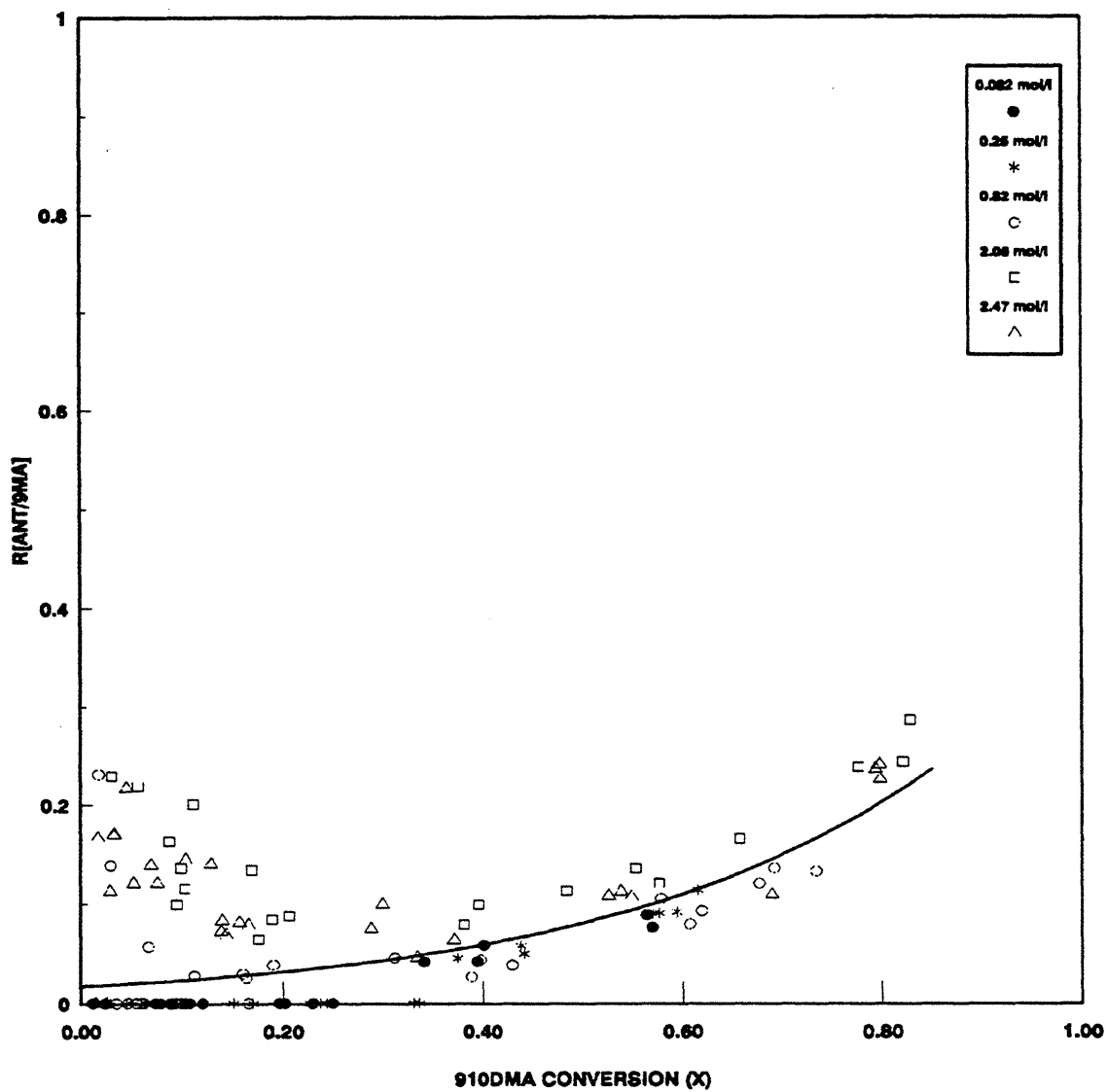
Figure 5.15: Ratio of moles ANT to moles 9MA produced vs. 910DMA conversion (X) for varying $[910DMA]_o$ at fixed T = 355°C.

287
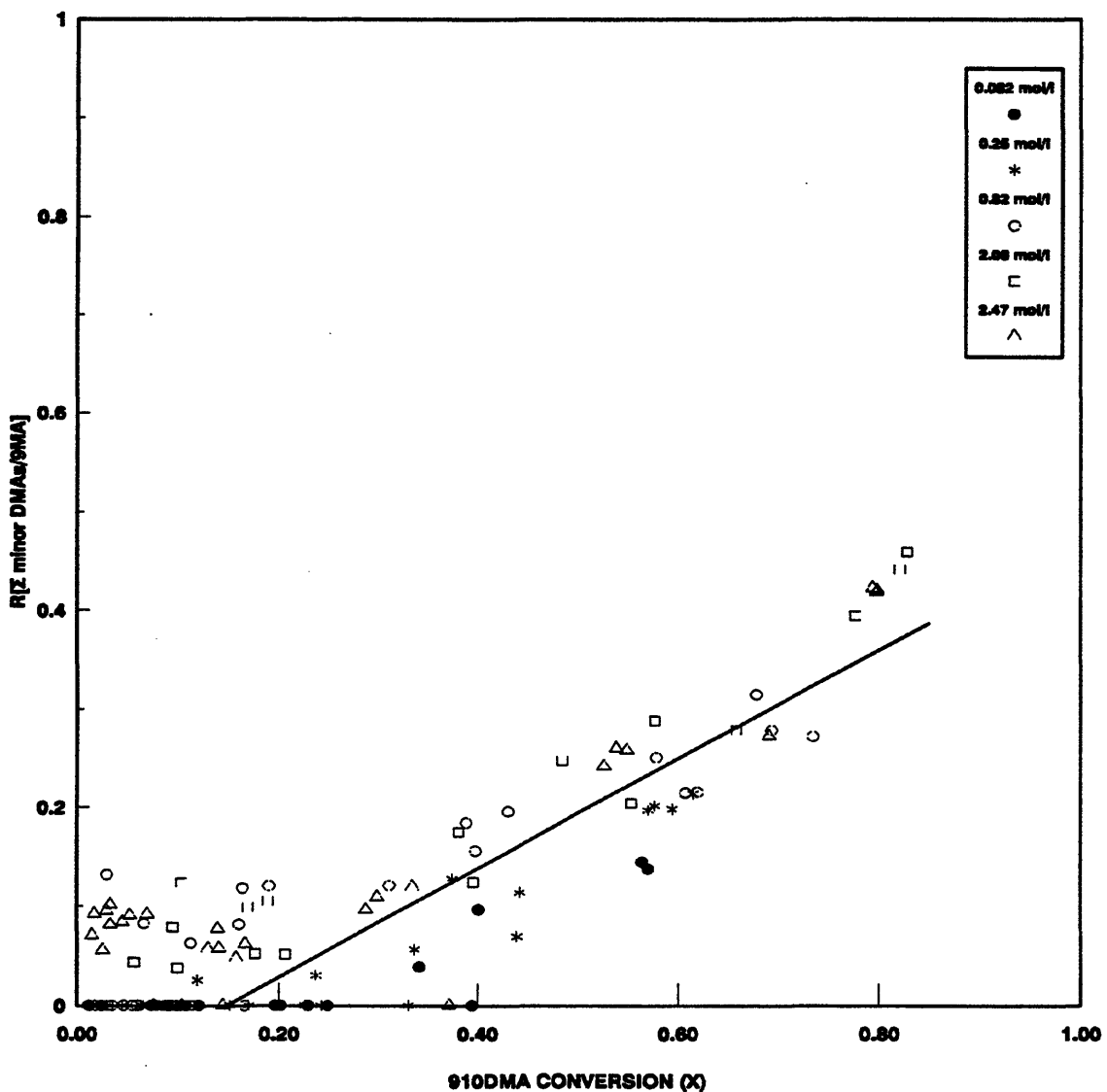
Figure 5.16: Ratio of moles Σ minor DMAs to moles 9MA produced vs. 910DMA conversion (X) for varying [910DMA]$_0$ at fixed T = 355°C.
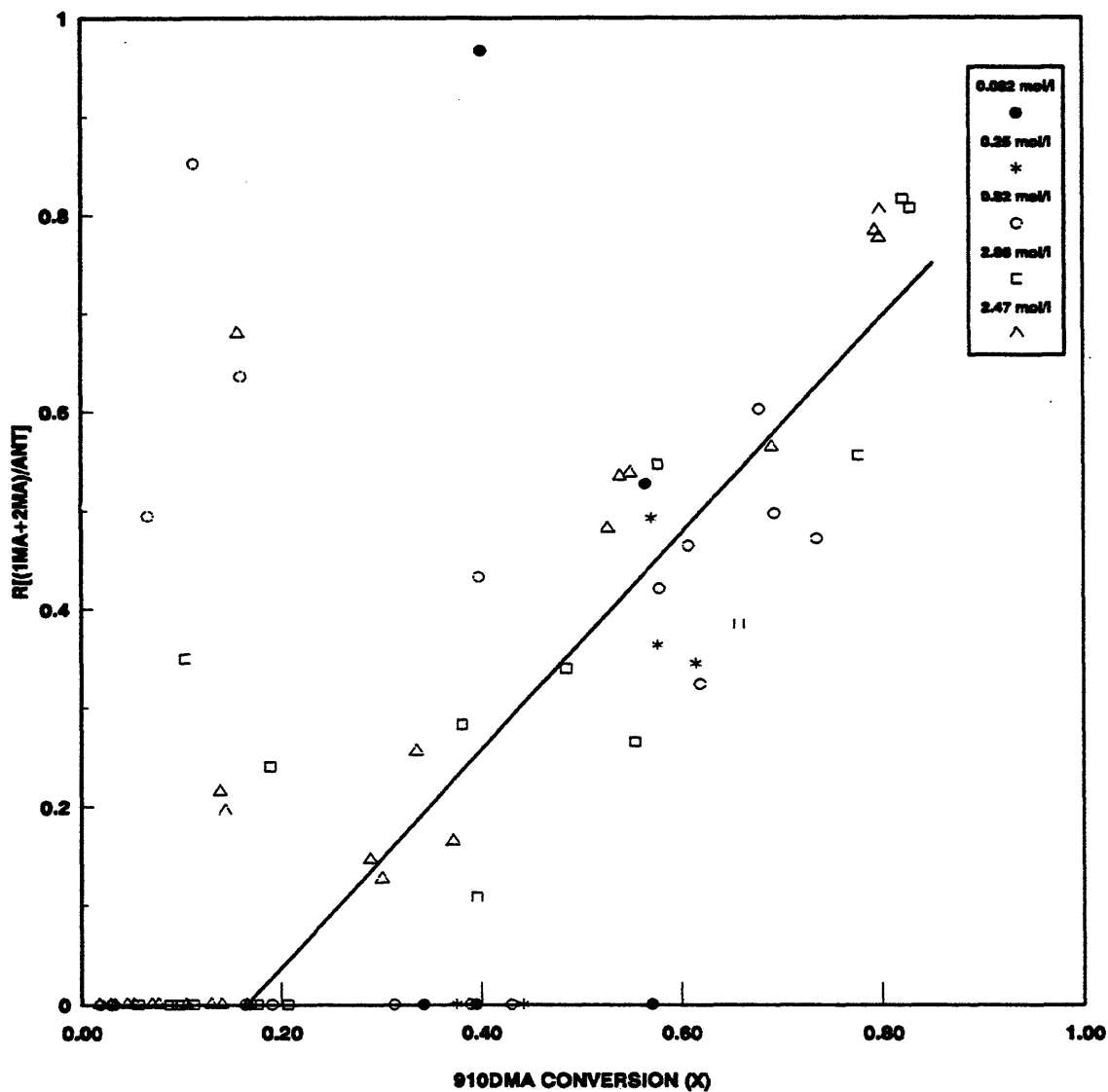
Figure 5.17: Ratio of moles 1MA and 2MA to moles ANT produced vs. 910DMA conversion (X) for varying [910DMA]$_o$ at fixed T = 355°C.

conversion only, with data for all initial concentrations, 0.082 < $[910DMA]_o$ < 2.47

mol/l, lying on roughly the same curve. Implicit in this latter relationship are the

kinetics of 9MA methylation during thermolysis of the 910DMA substrate under the

present conditions. Similarly, Figure 5.17 shows that, for X > 0.15, the ratio of

monomethylated species to ANT, R[(1MA+2MA)/ANT], is essentially a function of

conversion only, with data for all initial concentrations, 0.082 < $[910DMA]_o$ < 2.47

mol/l, lying on roughly the same curve. This latter relationship implicitly describes

the kinetics of ANT methylation during thermolysis of the 910DMA substrate under

the present conditions.

5.1.4. Effect of Temperature

Reaction temperature was varied from 315 to 409°C at a fixed initial

concentration of $[910DMA]_o$ = 0.82 M, with these experiments represented by the

vertical plane of the grid in Figure 5.1.

Figure 5.18 shows substrate and product histories at T = 315°C and

$[910DMA]_o$ = 0.82 M. In the upper panel of Figure 5.18, the moles of substrate

910DMA decay from the initial J = 5.0E-04 moles to J ~ 4.4E-04 moles at t =

57600 s; the decay half-life t^* ~ 300,000 s. 9MA grows monotonically from 0 initially

to J = 2.6E-05 moles at t = 57600 s. TMA and ANT are first detected at t = 7200

and 3600 s with J = 3.8E-07 and 3.3E-07 moles, respectively, and increase to J =

9.7E-06 and 1.7E-06 moles at t = 57600 s. In the lower panel of Figure 5.18,
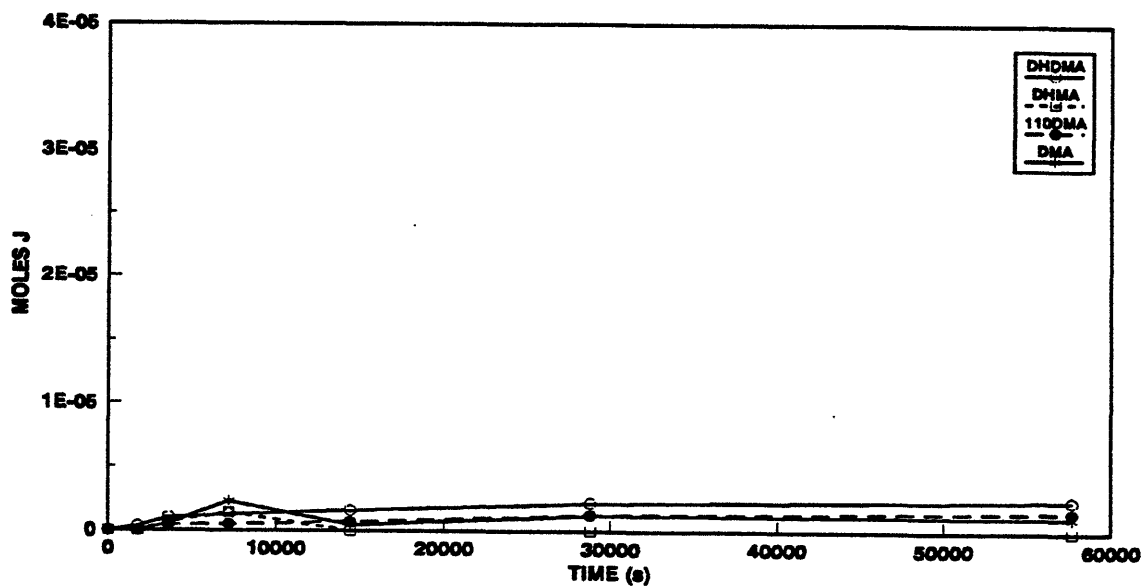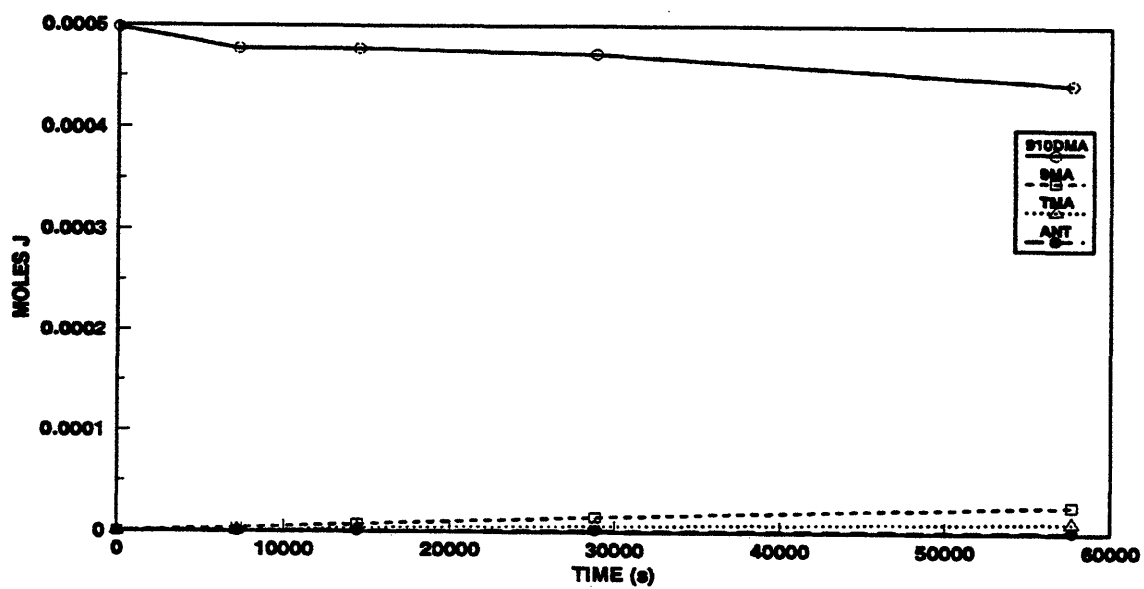
Figure 5.18: Product histories for 910DMA thermolysis at 315°C with $[910DMA]_o$ = 0.82 mol/l: major products (top) and minor products (bottom).

291

DHDMA was detected at t = 7200 s with J = 1.2E-06 moles and increases slightly to J = 2.4E-06 moles by t = 57600 s. DHMA is only detected at t = 7200 s with J = 1.4E-06 moles. 110DMA appears at t = 7200 s with J = 4.2E-07 moles and increases to J = 1.5E-06 moles at t = 57600 s. Other DMAs arise at t = 7200 s with J = 2.3E-06 moles and remain at J ~ 1.1E-06 moles to t = 57600 s.

Figure 5.19 is a selectivity diagram corresponding the data in Figure 5.18. In the upper panel, 9MA selectivity is S = 0.17 at X = 0.037, but increases abruptly to S ~ 0.57 ± 0.03 for 0.05 < X < 0.10. TMA appears with S = 0.20 ± 0.03 for 0.04 < X < 0.10. ANT selectivity is S = 0.042 ± 0.02 for 0.037 < X < 0.10. The selectivity sum increases from Σ = 0.55 at X = 0.037 to Σ ~ 0.85 for 0.05 < X < 0.10. In the lower panel of Figure 5.19, DHDMA selectivity is S = 0.064 at X = 0.037, increases to a maximum S = 0.090 at X = 0.05 and then declines to S = 0.048 by X = 0.10. DHMA is only detected at X = 0.037 with S = 0.072. 110DMA appears at X = 0.037 with S = 0.026 and exhibits S = 0.040 for 0.05 < X < 0.10. DMA selectivity is S = 0.12 at X = 0.037 and S = 0.035 for 0.05 < X < 0.10.

Figure 5.20 shows substrate and product histories at T = 335°C and [910DMA]$_o$ = 0.82 M. In the upper panel of Figure 5.20, the moles of substrate 910DMA decay from J = 4.9E-04 moles initially to J = 2.6E-04 moles at t = 57600 s, the decay half-life t* ~ 62000 s. 9MA increases monotonically but with decreasing slope from 0 initially to J = 7.9E-05 moles at t = 28800 s, and then to J = 1.1E-04 moles at t = 57600 s. TMA increases from J = 3.8E-07 moles at t = 1800 s to J =
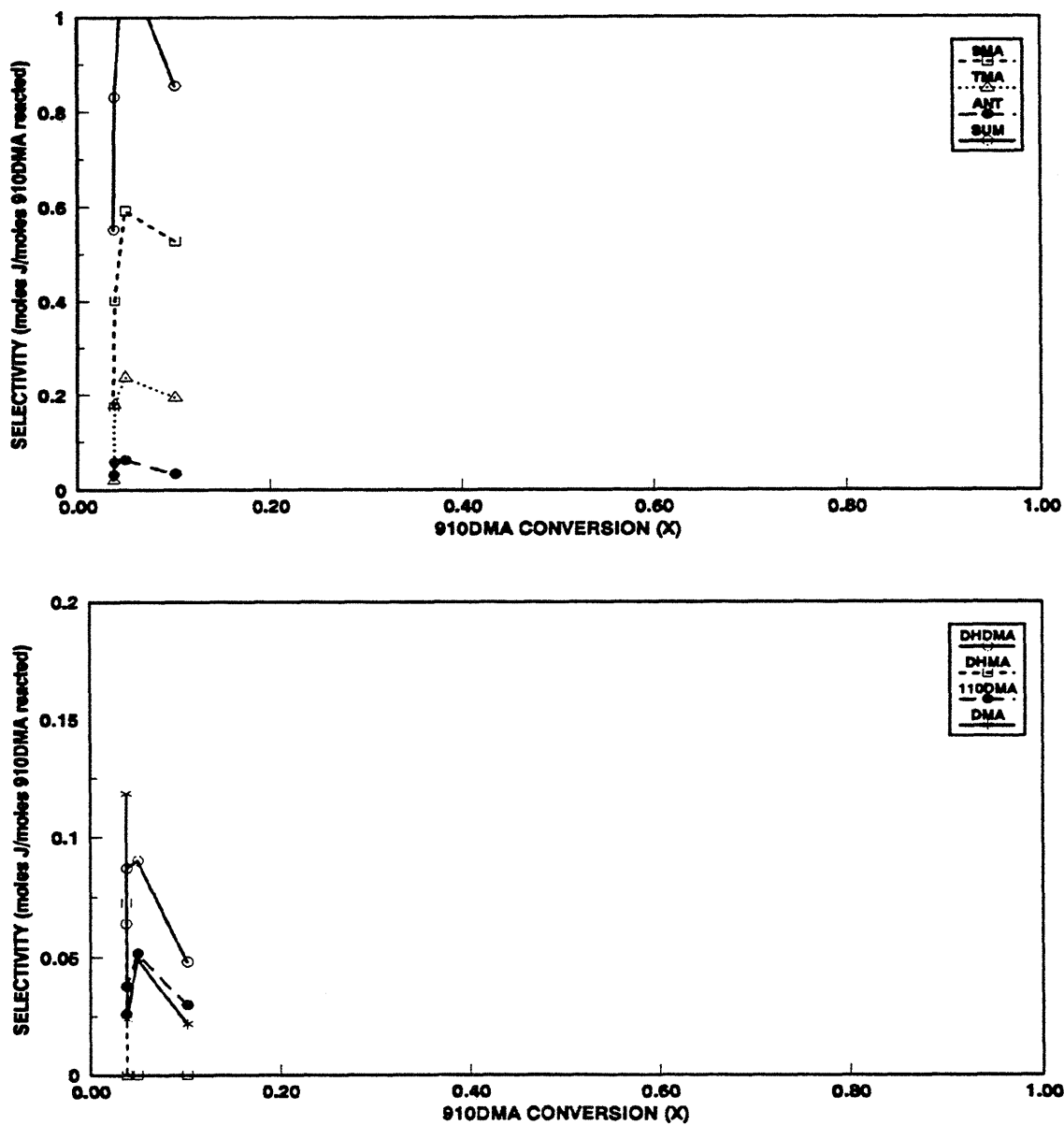
Figure 5.19: Selectivity diagrams for 910DMA thermolysis at 315°C with [910DMA]$_o$ = 0.82 mol/l: major products (top) and minor products (bottom).
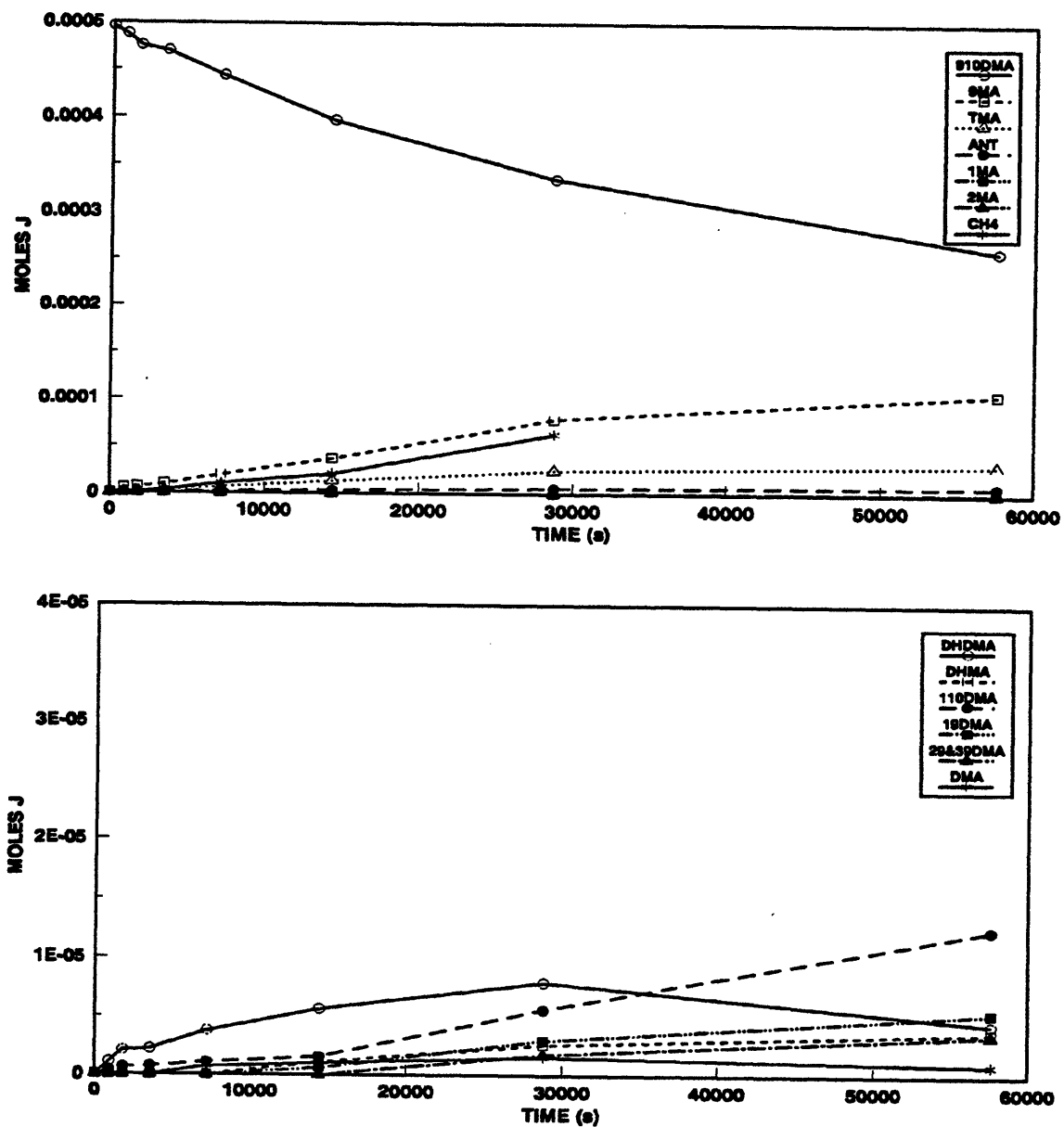
Figure 5.20: Product histories for 910DMA thermolysis at 335°C with $[910DMA]_o$ = 0.82 mol/l: major products (top) and minor products (bottom).

3.1E-05 moles at t = 57600 s. ANT is first detected at t = 900 s with J = 4.0E-07 moles and increases to J = 7.9E-06 moles at t = 57600 s. 1MA and 2MA are detected at the t = 28800 s with J = 3.6E-07 and 2.8E-07 moles, respectively, and increase to J = 1.7E-06 and 6.0E-07 moles at t = 57600 s. CH4 increases almost linearly from 0 initially to J = 2.1E-05 moles at t= 14400 s, and then more quickly to J = 6.3E-05 moles at t = 28800 s. In the lower panel of Figure 5.20, DHDMA first appears at t = 900 s with J = 1.1E-06 moles, reaches a maximum J = 7.9E-06 moles at t = 28800 s, and declines to J = 4.4E-06 moles at t = 57600 s. DHMA appears at t = 14400 s with J = 1.1E-06 moles and increases to J = 3.7E-06 moles by t = 57600 s. 110DMA, 19DMA and 29&39DMA first appear at t = 900, 14400 and 28800 s, respectively, with J = 3.5E-07, 6.1E-07 and 1.8E-06 moles and increase monotonically to J = 1.2E-05, 5.3E-06 and 3.5E-06 moles at t = 57600 s. Other DMAs are detected at t = 7200 s with J = 6.6E-07 moles, and remain approximately constant at J = 1.2 ± 0.3E-06 moles for 14400 < t < 57600 s.

Figure 5.21 is a selectivity diagram corresponding to the data in Figure 5.20. In the upper panel of Figure 5.21, 9MA selectivity is S = 0.69 at X = 0.015, sharply declines to S = 0.35 for 0.038 < X < 0.20, and then increases to S = 0.47 ± 0.02 for 0.32 < X < 0.48. TMA appears with S = 0.020 at X = 0.038 and increases to S = 0.13 ± 0.03 for 0.05 < X < 0.48. ANT arises at X = 0.015 with S = 0.056 and remains roughly constant at S = 0.039 ± 0.005 for 0.038 < X < 0.48. 1MA and 2MA appear at X = 0.32 with S = 0.0022 and 0.0018 and increase to S = 0.0072 and
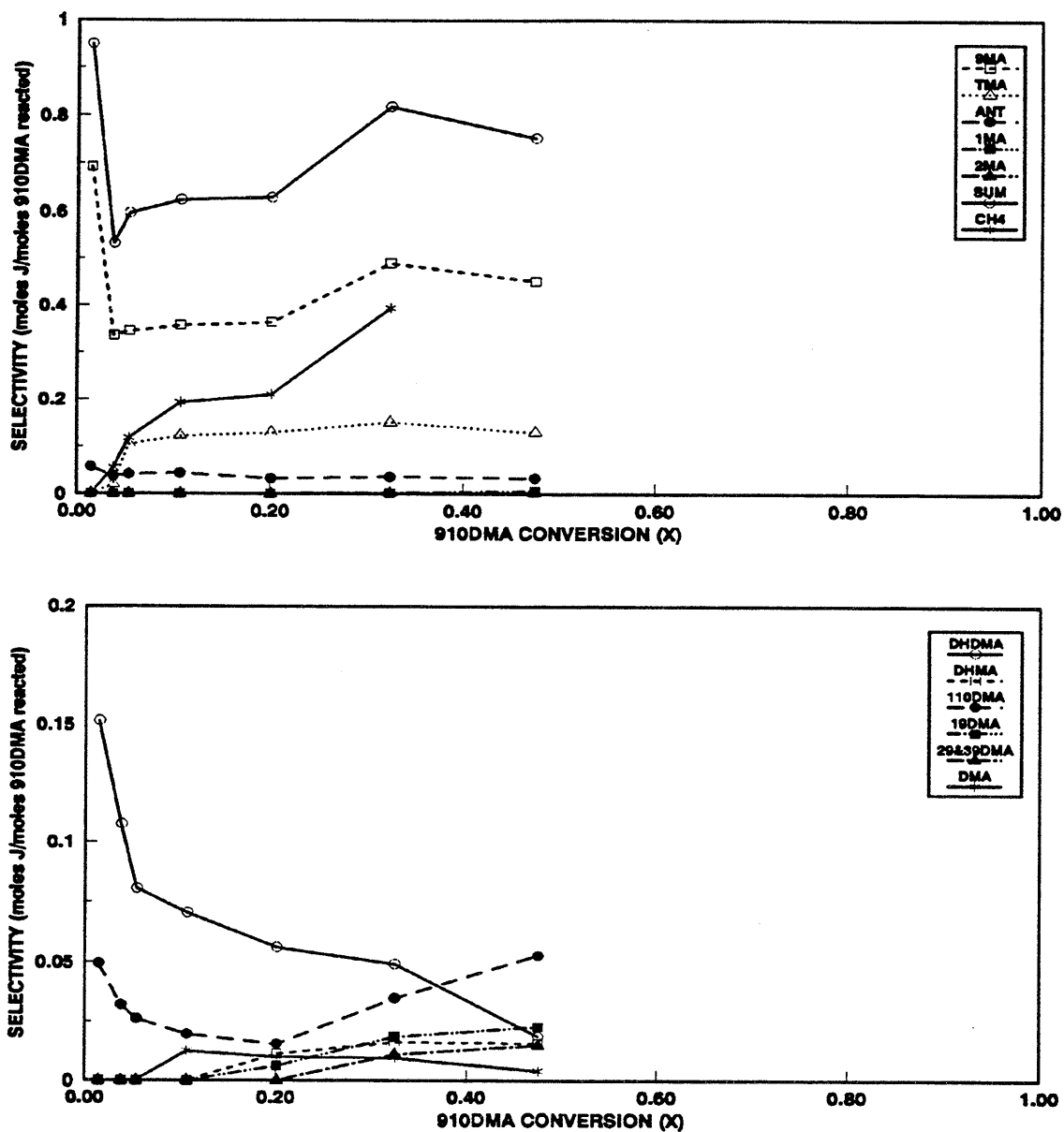
Figure 5.21: Selectivity diagrams for 910DMA thermolysis at 335°C with [910DMA]$_o$ = 0.82 mol/l: major products (top) and minor products (bottom).

0.0025 at X = 0.48. CH4 appears at X = 0.038 with S = 0.054, increases to S = 0.20 for 0.10 < X < 0.20, and sharply rises to S = 0.39 at X = 0.32. The selectivity sum fluctuates between Σ = 0.95 at X = 0.015 and Σ = 0.53 at X = 0.038 at low conversions, then rises to Σ = 0.61 ± 0.02 for 0.05 < X < 0.20 and to Σ = 0.78 ± 0.03 for 0.32 < X < 0.48. In the lower panel of Figure 5.21, DHDMA appears with maximum S = 0.15 at X = 0.015, declines sharply to S = 0.081 at X = 0.05 and then more slowly to S = 0.019 at X = 0.48. DHMA is detected with S = 0.013 ± 0.003 for 0.20 < X < 0.48. 110DMA is detected with S = 0.049 at X = 0.015, decreases to S = 0.015 at X = 0.20 and then increases to S = 0.053 at X = 0.48. 19DMA and 29&39DMA appear at X = 0.20 and 0.32 with, respectively, S = 0.0061 and 0.011, followed by a increase to S = 0.023 and 0.015 at X = 0.48. Other DMAs appear at X = 0.11 with S = 0.012 and decrease slightly to S = 0.004 at X = 0.48.

Figure 5.8, earlier described in Section 5.1.2 on the effect of varying initial 910DMA concentration, shows substrate and product histories at T = 355°C and [910DMA]$_o$ = 0.82 M. Figure 5.9, also in Section 5.1.2, is a selectivity diagram corresponding to the data in Figure 5.8.

Figure 5.2, earlier described in Section 5.1.1 as the representative example, shows substrate and product histories at T = 370°C and [910DMA]$_o$ = 0.82 M.

Figure 5.3, also in Section 5.1.1, is a selectivity diagram corresponding to the data in Figure 5.2.

Figure 5.22 shows substrate and product histories at T = 409°C and $[910DMA]_o$ = 0.82 M. In the upper panel of Figure 5.22, the moles of substrate 910DMA decay from J = 4.9E-04 moles initially to J = 5.0E-05 moles at t = 3600 s, and then, more slowly, to J = 1.7E-06 moles at t = 21600 s; the decay half-life t^* ~ 1300 s. 9MA increases from 0 initially to a maximum J = 1.6E-04 moles at 1800 < t < 3600 s, followed by a decline to J = 2.9E-05 moles at t = 10800 s and to J = 1.0E-05 moles at t = 21600 s. TMA increases from 0 initially to a maximum J = 3.3E-05 moles at t = 1800 s and declines slowly to J = 7.8E-06 moles at t = 21600 s. ANT first appears at t = 450 s with J = 1.3E-06 moles, rises steadily to J = 1.2E-04 moles at t = 7200 s, and then more slowly to J = 1.4E-04 moles at t = 21600 s. 1MA and 2MA are first detected at t = 450 and 1800 s with J = 3.4E-07 and 1.9E-06 moles, respectively, rise to J = 5.8E-05 and 3.7E-05 moles at t = 7200 s, and then to J = 7.3E-05 and 4.8E-05 moles at t = 21600 s. In the lower panel of Figure 5.22, DHDMA is detected at t = 450 s with J = 4.2E-07 moles, remains roughly constant at J ~ 1.3E-4 moles for 900 < t < 1800 s and then decays to J = 0 by t = 7200 s. DHMA appears at t = 900 s with J = 6.7E-07 moles, remains roughly constant at J = 1.8 ± 0.7E-06 moles for 3600 < t < 10800 s and decays to J = 4.5E-07 moles by t = 21600 s. DHA first appears at t = 3600 s with J = 1.0E-06 moles and increases monotonically to J = 8.9E-06 moles at t = 21600 s. 110DMA is first detected at t

298
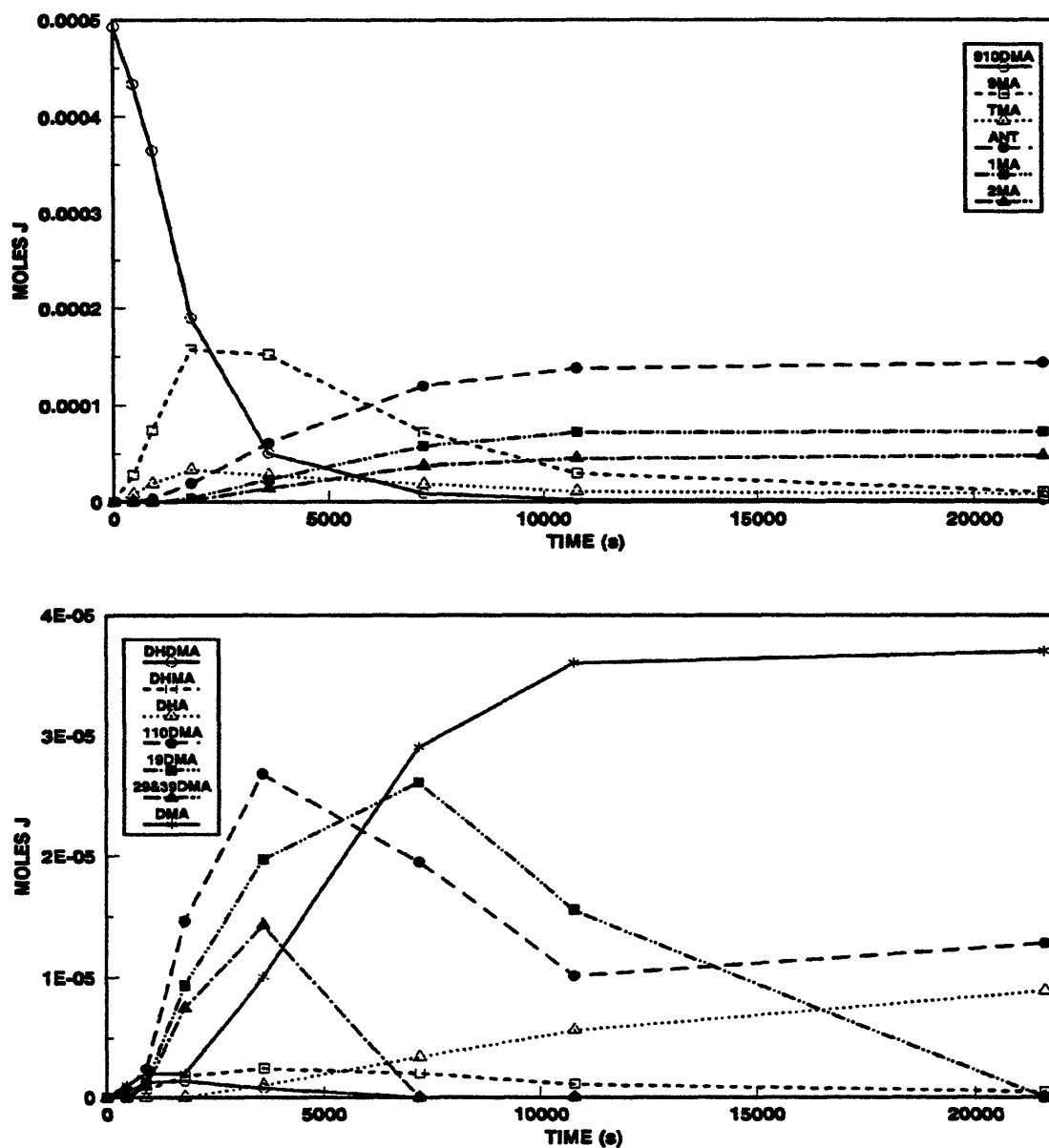
Figure 5.22: Product histories for 910DMA thermolysis at 409°C with [910DMA]$_o$ = 0.82 mol/l: major products (top) and minor products (bottom).

= 450 s with J = 7.6E-07 moles, rises rapidly to a maximum J = 2.7E-05 moles at t = 3600 s and then declines to J = 1.1E-05 moles at t = 10800 and 21600 s. 19DMA first arises with J = 1.2E-06 moles at t = 900 s, rises quickly to J = 2.0E-05 moles at t = 3600 s, attains a maximum J = 2.6E-05 moles at = 7200 s and then declines to J = 0 by t = 21600 s. 29&39DMA are detected at t = 900 s with J = 9.2E-07 moles, increase to J = 1.4E-05 moles at t = 3600 s, and abruptly decline to J = 0 at t = 7200 s. Other DMAs appear with J = 1.1E-06 moles at t = 450 s, rise to J = 2.6E-06 moles at t = 900 s, then increase steeply to J = 3.7E-05 moles at t = 10800 s and remain at this level until t = 21600 s.

Figure 5.23 is a selectivity diagram corresponding to the data in Figure 5.22. In the upper panel of Figure 5.23, 9MA selectivity is S = 0.46 at X = 0.12, rises to S = 0.56 at X = 0.27, then slowly decreases to S = 0.34 at X = 0.90, after which it declines abruptly to S = 0.021 at X = 0.997. TMA selectivity is S = 0.13 at X = 0.12 and 0.27, decreases slowly to S = 0.061 at X = 0.90, after which it drops further to S = 0.016 at X = 0.997. ANT appears with S = 0.022 at X = 0.12, grows monotonically with increasing slope to S = 0.14 at X = 0.90, and then to S = 0.29 at X = 0.997. 1MA and 2MA appear with, respectively, S = 0.0057 and 0.0063 at X = 0.012 and 0.62, grow monotonically to S = 0.051 and 0.031 at X = 0.90, and rise sharply to S = 0.15 and 0.10 at X = 0.997. The selectivity sum increases from Σ = 0.65 at X = 0.12 to Σ = 0.80 ± 0.02 for 0.27 < X < 0.98, and drops to Σ = 0.70 by X = 0.997. In the lower panel of Figure 5.23, DHDMA selectivity is S = 0.0070 at
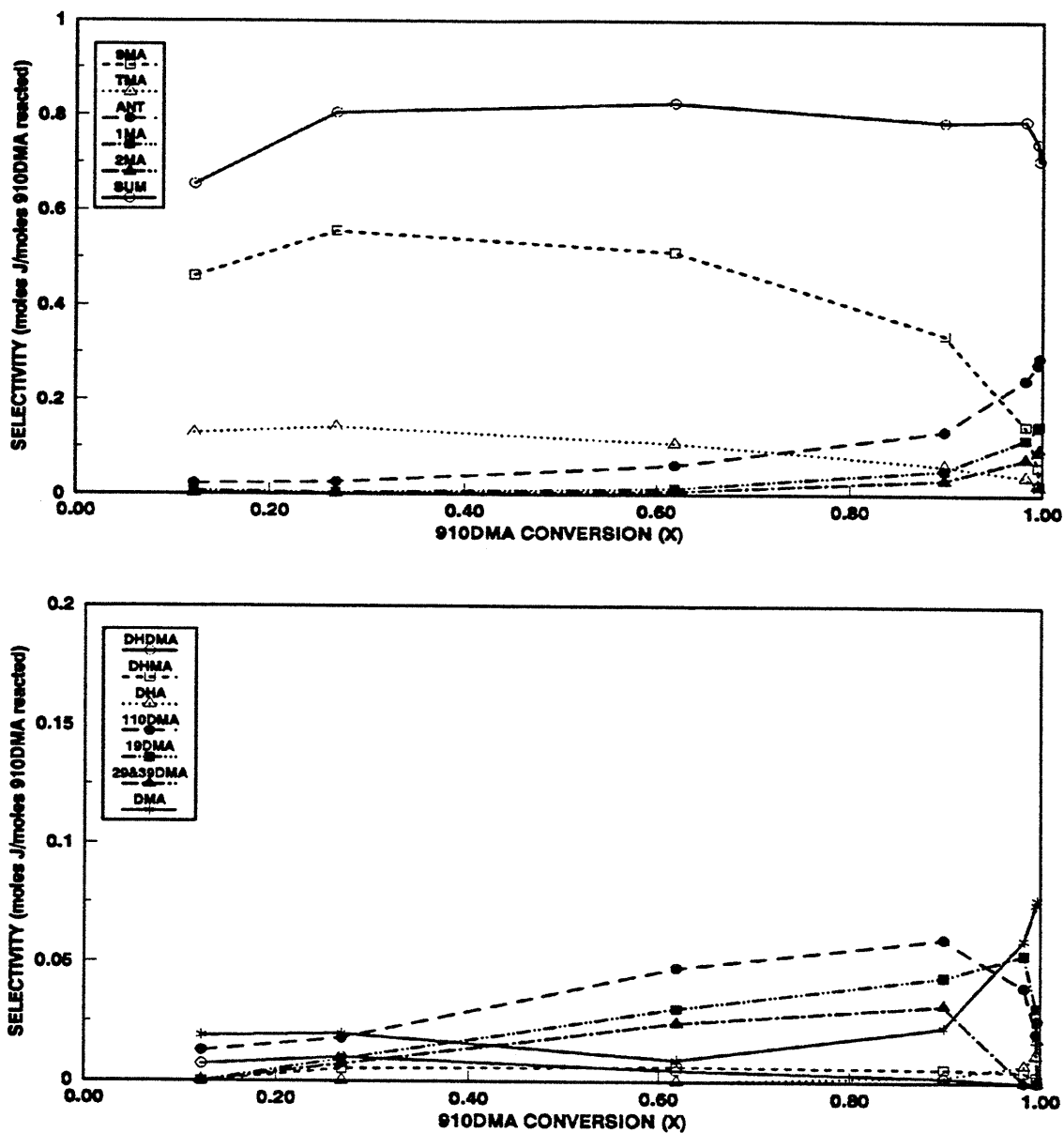
Figure 5.23: Selectivity diagrams for 910DMA thermolysis at 409°C with [910DMA]$_o$ = 0.82 mol/l: major products (top) and minor products (bottom).

X = 0.12 and drops to S = 0 by X = 0.90. DHMA has selectivity S = 0.0050 ±

0.0008 for 0.12 < X < 0.98 and then declines to S ~ 0 by X = 0.997. DHA appears

at X = 0.90 with S = 0.0022 and rises to S = 0.018 at X = 0.997. 110DMA is first

detected at X = 0.12 with S = 0.013, rises monotonically to a maximum S = 0.060

at X = 0.90, and then drops abruptly to S = 0.026 at X = 0.997. 19DMA is detected

with selectivity S = 0.0091 at X = 0.27, which rises to a maximum S = 0.053 at X

= 0.98, and drops abruptly to S = 0.031 by X = 0.995. 29&39DMA appear at X =

0.27 with S = 0.0068, reach a maximum S = 0.032 at X = 0.90, and drop to S = 0

by X = 0.98. Selectivity of the other DMAs is S = 0.016 ± 0.07 for 0.12 < X <

0.90, then rises sharply to S = 0.077 at X = 0.977.

5.1.5 Summary of Temperature Effects

Increasing temperature from T = 315 to 409°C at fixed $[910DMA]_o$ = 0.82

mol/l influences both the reaction kinetics and product selectivities, as summarized

in Table 5.3 and Table 5.4. Note that values in the tables are the averages over all

runs, including replication, and are therefore not precisely identical to those seen in

the preceding figures. Part (a) of Table 5.3 shows the substrate decay half-life t^*

decreased about 230-fold, from 300000 to 1300 s, as reaction temperature T

increased ~ 100°C, from 315 to 409°C. Figure 5.24, a plot of log t^* vs. $1/\theta$, where

302

Table 5.3

EFFECT OF TEMPERATURE ON

KINETIC PARAMETERS WITH $[910DMA]_o$ = 0.82 mol/l

Part		Temperature (°C)				
		315	335	355	370	409
a	Half-life t^*, s	300000^1 $\pm$ 100000^2	62069 $\pm$ 574	21912 $\pm$ 2743	9905 $\pm$ 1350	1311 $\pm$ 201
b	$[9MA/910DMA]_{tmax1}$				1.41	1.30
	t_{max1}/t^*				1.45	1.50
c	$[DHDMA/910DMA]_{tmax2}$	0.005	0.025	0.011	0.026	0.007
	t_{max2}/t^*	0.19	0.46	0.65	0.73	1.37

[1]   Half-life calculated using X at longest t and integrated 3/2 order rate expression: $t^* = 0.41421t / [(1/(1-X)^{½}) - 1]$

[2] $\pm$ = standard deviation of the average half-life

Table 5.4

	Selectivity	Conversion	Temperature (°C)				
Part	S of:	X Range:	315[1]	335[2]	355	370	409
a	9MA	0.1 - 0.8	0.52	0.43	0.47	0.42	0.45
	TMA	0.1 - 0.8	0.20	0.12	0.11	0.11	0.11
b	DHDMA	0.06	0.053	0.041	0.048	0.060	0.007[3]
		0.56 ± 0.02	0.049	0.019	0.012	0.011	0.004
	DHMA	0.56 ± 0.02	0.017	0.011	0.009	0.008	0.006
	DHA	0.95	ND	ND	0.001[4]	0.010	0.010
c	ANT	0.56 ± 0.02	0.034	0.033	0.054	0.055	0.061
	1MA	0.56 ± 0.02	ND	0.007	0.015	0.013	0.012
	2MA	0.56 ± 0.02	ND	0.003	0.007	0.006	0.006
	110DMA	0.56 ± 0.02	0.035	0.054	0.061	0.055	0.048
		0.85 ± 0.05				0.064	0.060
		0.91 ± 0.05				0.051	0.040
	19DMA	0.56 ± 0.02	0.006	0.024	0.036	0.031	0.030
		0.85 ± 0.05				0.041	0.044
		0.91 ± 0.05				0.034	0.031
	29&39DMA	0.56 ± 0.02	ND	0.016	0.031	0.030	0.024
		0.85 ± 0.05				0.035	0.032
		0.91 ± 0.05				0.008	0
	DMA	0.56 ± 0.02	0.022	0.009	0.009	0.012	0.015
		0.91 ± 0.05				0.039	0.069

[1] For T = 315°C, all data at X = 0.10 except DHDMA at X = 0.06

[2] For T = 335°C, all data at X = 0.46 except DHDMA at X = 0.06

[3] This point at X = 0.12, the lowest conversion at T = 409°C

[4] This point at X = 0.68, the highest conversion at T = 355°C

Figure 5.24: Decay half-life t^* for varying temperatures with fixed $[910DMA]_o$ = 0.82 mol/l.

$\theta = 4.573 \times 10^{-3} T$ in Kelvins, shows that the data adhere to a line:

$$\log t^* = -10.7 + \frac{43.1}{\theta} \qquad (5.5)$$

for T = 335 - 409°C. The slope of this line, 43.1, is equal to the activation energy in kcal/mol of the overall reaction; also, for 3/2 order decomposition, the intercept of the line provides a pre-exponential factor of -10.7. Thus 910DMA thermolysis is 3/2 order in substrate with Arrhenius parameters $(\log_{10} A, E^*) = (-10.6, 43.1)$.

Product histories at the highest temperatures T = 370 and 409°C, shown in Figure 5.2 and Figure 5.22, also provide an indication of the relative kinetics of the sequential reactions 910DMA → 9MA → ANT earlier shown in Equation (5.3). 9MA attained its maximum concentration $[9MA]_{max}$ at t_{max1} in both figures, then, as shown in part (b) of Table 5.3, the ratios $[9MA/910DMA]_{tmax1} \sim 1.4$ and $[t_{max1}/t^*] \sim 1.5$ both imply that 9MA decomposes more slowly than 910DMA. If both decompositions are presumed to be of the same 3/2 order in their respective substrates, then we can estimate the rate constant ratio $(k_1/k_2) = [9MA/910DMA]_{tmax1}^{3/2} \sim 1.7$ for the range 370 < T < 409°C. This is similar to the estimate of $(k_1/k_2) \sim 1.8$ earlier obtained from results at fixed T = 355°C and varying initial substrate concentrations. Logic analogous to the preceding can also be applied to the hydrogenated product DHDMA, which is seen to maximize at early times in Figure 5.18, Figure 5.20, Figure 5.8, Figure 5.2 and Figure 5.22. Using the maximum DHDMA concentration at each temperature, $[DHDMA/910DMA]_{tmax2}$

remains roughly constant while $[t_{max2}/t^*]$ increases with increasing temperature, as shown in part (c) of Table 5.3. $[DHDMA/910DMA]_{tmax2} \sim 0.015 \pm 0.010$ for $315 < T < 409°C$ while $[t_{max2}/t^*] = 0.19$ at $T = 315°C$ and increases to $[t_{max2}/t^*] = 1.37$ at $T = 409°C$. Both again suggest that DHDMA decomposes faster than it forms from 910DMA, i.e., $k_4/k_3 > 1$ in the reaction series shown in Equation (5.4), which is in agreement with the earlier results obtained at fixed $T = 355°C$ and varying substrate concentrations. This does also suggest that k_4 is less activated than k_3.

Turning to product selectivities, summarized in Table 5.4, both 9MA and TMA selectivities were roughly independent of conversion over the ranges $0.1 < X < 0.8$ at temperatures of $315 < T < 409°C$, as shown in part (a) of Table 5.4. The absolute values of S(9MA) and S(TMA) remained essentially constant at S(9MA) $\sim$ 0.47 ± 0.05 and S(TMA) $\sim 0.15 \pm 0.05$ over the entire range of temperatures, 315 $< T < 409°C$. The hydrogenated species DHDMA selectivity was essentially highest at the lowest conversions and then declined with increasing X, more steeply at the lower temperatures, as shown in part (b) of Table 5.4. Thus S(DHDMA) ~ 0.050 ± 0.010 at $X = 0.06$ for $315 < T < 370°C$ and then decreased to S(DHDMA) $=$ 0.019 at $X = 0.46$ for $T = 335°C$ and S(DHDMA) $= 0.017$ and 0.009 at $X = 0.56$ ± 0.02 for $T = 355$ and $370°C$. Of the other hydrogenated species, DHMA was detected at all temperatures, with S(DHMA) $= 0.017$ at $X = 0.10$ for $T = 315°C$, S(DHMA) $= 0.011$ at $X = 0.46$ for $T = 335°C$ and S(DHMA) $\sim 0.010 \pm 0.005$ at $X = 0.56 \pm 0.02$ for $355 < T < 409°C$. DHA was only detected at the higher $T =$

[355, 370, 409°C] with S(DHA) ~ 0.001 at X = 0.68 for T = 355°C and with

S(DHA) ~ 0.010 at X = 0.95 for T = 370 and 409°C. ANT, 1MA and 2MA

selectivities increased monotonically from 0 as conversions increased for all

temperatures, as shown in part (c) of Table 5.4. S(ANT) = 0.057 ± 0.004 at X =

0.56 ± 0.02 for 355 < T < 409°C, S(ANT) = 0.033 at X = 0.46 at T = 335°C and

S(ANT) = 0.034 at X = 0.10 at T = 315°C. Among monomethylated species,

S(1MA) and S(2MA) generally increased with increasing X at all temperatures, with

S(1MA) > S(2MA) always and both always < S(ANT) at any X. Absolute S(1MA)

and S(2MA) = 0.013 and 0.006, respectively, at X = 0.56 ± 0.03 for 355 < T <

409°C and S(1MA) and S(2MA) = 0.007 and 0.003 at X = 0.46 for T < 335°C. For

the minor dimethylanthracenes at all temperatures; 1,10-, 1,9- and 2,9-&3,9-DMA;

selectivities increased monotonically from 0 as conversions increased and for 0 < X

< 0.85, maximized at X ~ 0.85 , and then decreased for X > 0.85 at T = 370 and

409°C, as shown in part (c) of Table 5.4. The other minor dimethylanthracene,

DMA, selectivities remained roughly constant from 0.10 < X < 0.85 and increased

at X > 0.85 for T = 370 and 409°C, also shown in part (c) of Table 5.4. Of the

dimethylated species, the order of abundance was generally S(110DMA) >

S(19DMA) > S(29&39DMA) > S(other DMAs) for X < 0.85, with each of these

always < S(9MA) at any X, while at X > 0.85, S(other DMAs) > S(110DMA) >

S(19DMA) > S(29&39DMA). The absolute values of S(110DMA), S(19DMA) and

S(29&39DMA) decreased somewhat with increasing temperature for all X < 0.85.

S(110DMA) = 0.061 at X = 0.56 ± 0.02 for T = 355°C and decreased to

S(110DMA) = 0.048 at X = 0.56 ± 0.02 for T = 409°C. S(19DMA) and

S(29&39DMA) = 0.036 and 0.031, respectively, at X = 0.56 ± 0.02 for T = 355°C

and decreased to S(19DMA) and S(29&39DMA) = 0.030 and 0.024 at X = 0.56 ±

0.02 for T = 409°C. The absolute values of S(110DMA), S(19DMA) and

S(29&39DMA) reached a maximum at X ~ 0.85 and decreased as X → 1 at the

higher T = 370 and 409°C. S(110DMA) = 0.064 and 0.060 at X = 0.85 ± 0.05 for

T = 370 and 409°C, respectively, and decreased to S(110DMA) = 0.051 and 0.040

at X = 0.91 ± 0.05. S(19DMA) = 0.041 and 0.053 at X = 0.85 ± 0.05 for T = 370

and 409°C, respectively, and decreased to S(19DMA) = 0.034 and 0.031 at X = 0.91

± 0.05. S(29&39DMA) = 0.018 and 0.032 at X = 0.85 ± 0.05 for T = 370 and

409°C, respectively, and decreased to S(19DMA) = 0.015 and 0 at X = 0.91 ± 0.05.

The absolute value of S(DMA) remained roughly constant for 0.10 < X < 0.85 at

all temperatures. S(DMA) = 0.12 ± 0.03 at X = 0.56 ± 0.02 for 355 < T < 409°C

and X = 0.46 for T = 335°C and S(DMA) = 0.022 at X = 0.10 for T = 315°C. The

absolute value of S(DMA) increased at X > 0.85 for T = 370 and 409°C; with

S(DMA) = 0.039 and 0.069 at X = 0.91 ± 0.05 for T = 370 and 409°C, respectively.

Finally, Figure 5.25, Figure 5.26 and Figure 5.27 depict the variation of certain

product ratios, namely R[ANT/9MA], R[(Σ minor DMAs)/9MA] and R[(1MA +

2MA)/ANT], versus 910DMA conversion X at all temperatures. In Figure 5.25 it

is seen that, for X > 0.15 and all experiments, the ratio of ANT to 9MA,
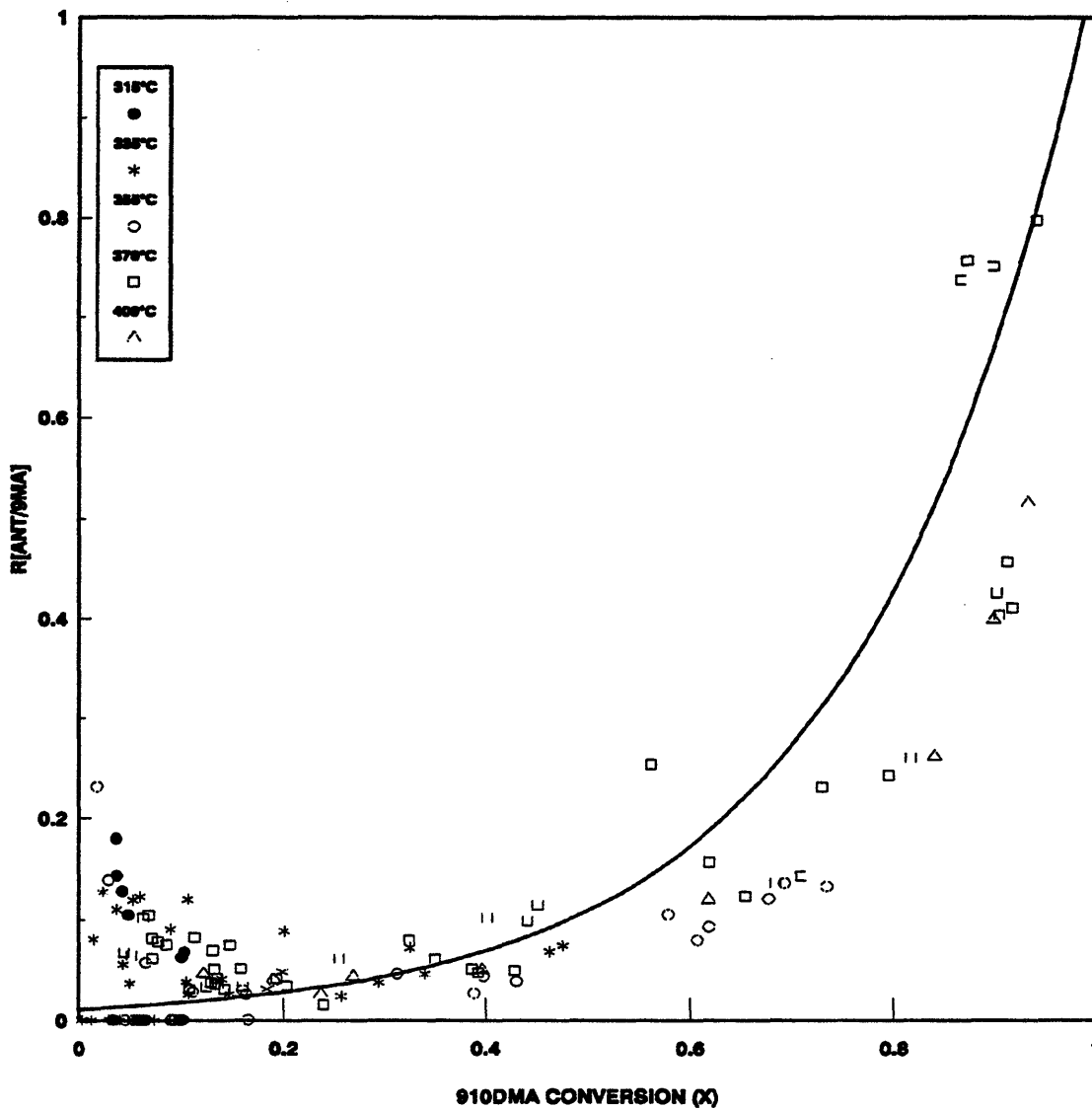
Figure 5.25: Ratio of moles ANT to moles 9MA produced vs. 910DMA conversion (X) for varying temperatures with fixed $[910DMA]_o$ = 0.82 mol/l.
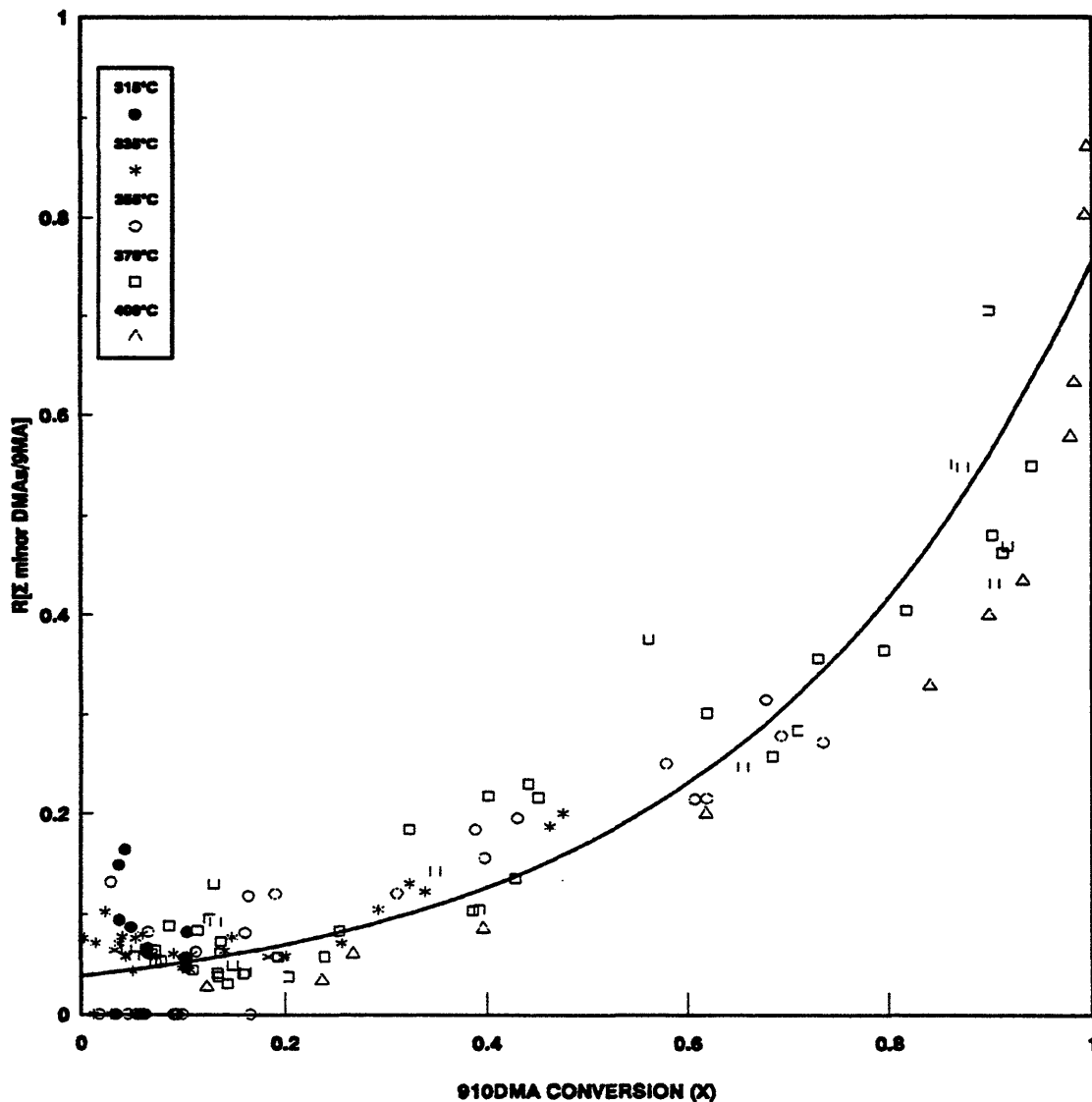
Figure 5.26: Ratio of moles Σ minor DMAs to moles 9MA produced vs. 910DMA conversion (X) for varying temperatures with fixed $[910DMA]_o = 0.82$ mol/l.
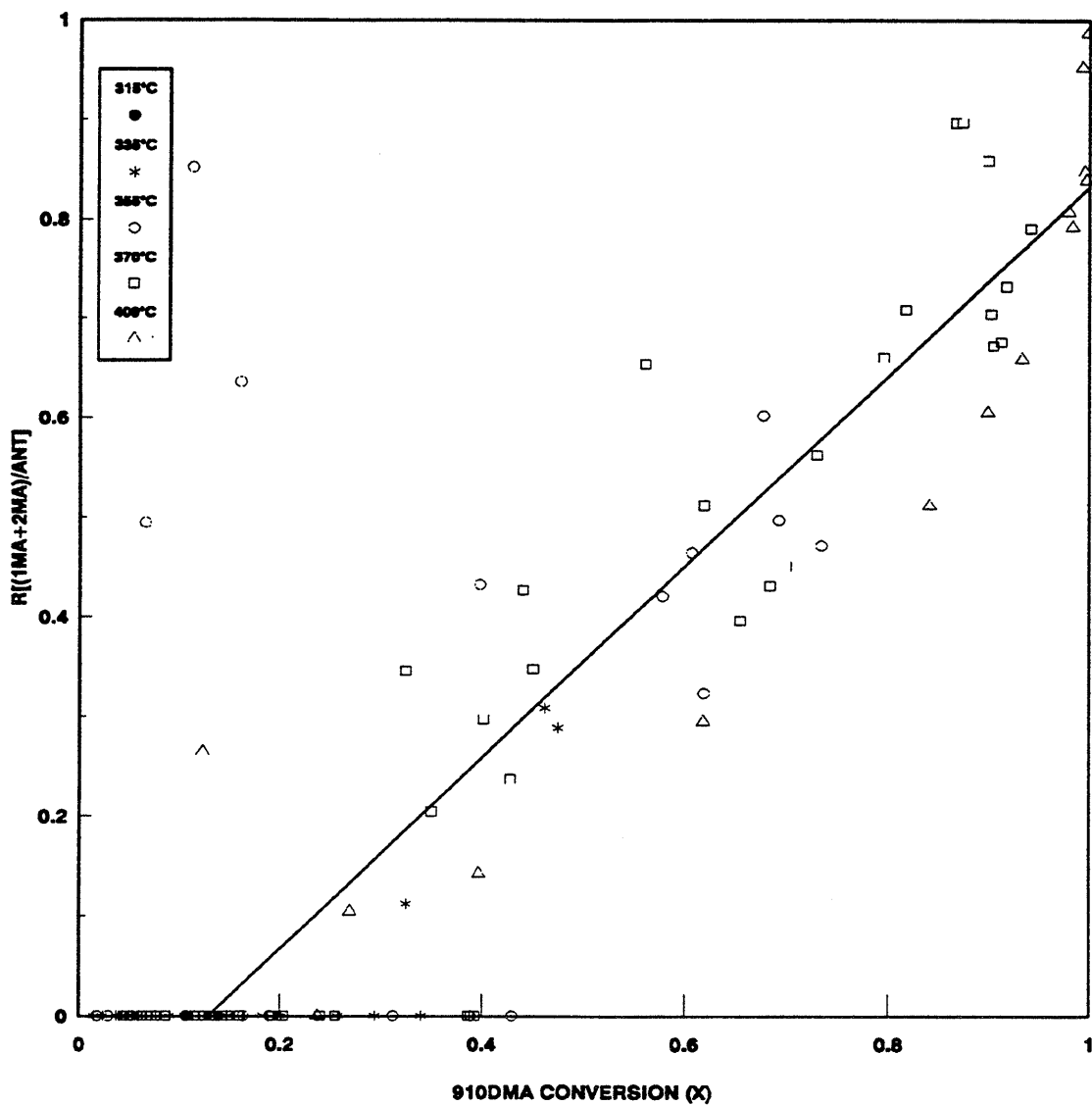
Figure 5.27: Ratio of moles 1MA and 2MA to moles ANT produced vs. 910DMA conversion (X) for varying temperatures with fixed $[910DMA]_o = 0.82$ mol/l.

R[ANT/9MA], is essentially a function of conversion only, with data for all temperatures, 315 < T < 409°C, lying on roughly the same curve. This relationship implicitly describes the kinetics of 910DMA demethylation under the present conditions. For X < 0.15, the explanation is the same as in the varying initial concentration case that there could possibly be misidentified *cis*-DHDMA or DHMA called ANT. In Figure 5.26 it is seen that, for X > 0.15 and all experiments, the ratio of minor dimethylated species to 9MA, R[Σ minor DMA/9MA], is essentially a function of conversion only, with data for all temperatures, 315 < T < 409°C, lying on roughly the same curve. Implicit in this latter relationship are the kinetics of 9MA methylation during thermolysis of the 910DMA substrate under the present conditions. Figure 5.27 shows that, for X > 0.15 and all experiments, the ratio of monomethylated species to ANT, R[(1MA+2MA)/ANT], is essentially a function of conversion only, with data for all temperatures, 315 < T < 409°C, lying on roughly the same curve. This latter relationship implicitly describes the kinetics of ANT methylation during thermolysis of the 910DMA substrate under the present conditions.

5.2 Kinetics

The kinetics of the experimental thermolyses were analyzed to derive reaction order and activation parameters. Reaction order was obtained from data at initial concentrations 0.082 mol/l < [910DMA]$_o$ < 2.47 mol/l at a fixed T = 355°C, while

313

activation parameters were derived from data at temperatures 315°C < T < 409°C

at fixed $[910DMA]_o = 0.82$ mol/l. Both effective first order rate constants, k_{eff}, and

the true rate constants, k, were employed to ascertain reaction order and activation

parameters.

5.2.1 Reaction Order

The order of reaction for overall 910DMA decay was formally examined in

the series of experiments at constant temperature T = 355°C with initial 910DMA

substrate concentrations ranging from 0.082 and 2.47 mol/l.

5.2.1.1 Apparent First Order Rate Constants, k_{eff}

The effective first order rate constant k_{eff}, units 1/s, is defined by Equation

(5.6):

$$k_{eff} = \frac{-\ln(1-X)}{t} \qquad (5.6)$$

where X is the fractional conversion at holding time t, Equation (5.7):

$$X = 1 - \frac{[910DMA]_t}{[910DMA]_o} \qquad (5.7)$$

with $[910DMA]_o$ and [910DMA] the respective concentrations of 910DMA at times

0 and t. Effective first order rate constants were calculated at each point, for all

runs. At each T and $[910DMA]_o$, values of log k_{eff} were averaged over intervals of

fractional conversion, respectively 0 - 0.1, 0.1 - 0.2, 0.2 - 0.4, 0.4 - 0.6, 0.6 - 0.8, and

0.8 - 1.0. The average log k_{eff} over each of the chosen conversion intervals are shown

as horizontal lines with vertical error bars in Figure 5.28, Figure 5.29 and Figure 5.30.

As a representative example, the upper panel of Figure 5.28 refers to 910DMA

thermolysis at T = 355°C and $[910DMA]_o$ = 0.082 mol/l. In each of the four

conversion intervals, values of the average log k_{eff} are ~ -4.9 ± 0.1. The uncertainty

associated with log k_{eff} is seen to diminish greatly with increasing conversion, the

error bars spanning 1.0, 0.4, 0.3 and 0.05 units of log k_{eff} in the conversion intervals

of 0 - 0.1, 0.1 - 0.2, 0.2 - 0.4 and 0.4 - 0.6, as seen on line 3 of Table 5.5. Table 5.5

summarizes the average log k_{eff}, error of the average log k_{eff} and error for each

conversion range for all $[910DMA]_o$ and temperatures. The lower panel of

Figure 5.28 refers to 910DMA thermolysis at T = 355°C and $[910DMA]_o$ = 0.25

mol/l, the upper and lower panels of Figure 5.29 refer to 910DMA thermolysis at T

= 355°C and $[910DMA]_o$ = 0.82 mol/l and $[910DMA]_o$ = 2.06 mol/l, respectively,

and Figure 5.30 refers to 910DMA thermolysis at T = 355°C and $[910DMA]_o$ = 2.47

mol/l, while lines 4 - 7 of Table 5.5 summarize the average log k_{eff}, error in the

average log k_{eff} and errors for each conversion range. It can be seen in Table 5.5

that the uncertainty associated with log k_{eff} diminishes with increasing conversion for

all $[910DMA]_o$, the error bars ranging from 0.67 - 1.03, 0.24 - 0.69, 0.08 - 0.30, 0 -

0.19 and 0 - 0.15 units of log k_{eff} in the conversion intervals of 0 - 0.1, 0.1 - 0.2, 0.2 -

0.4, 0.4 - 0.6 and 0.6 - 0.8.
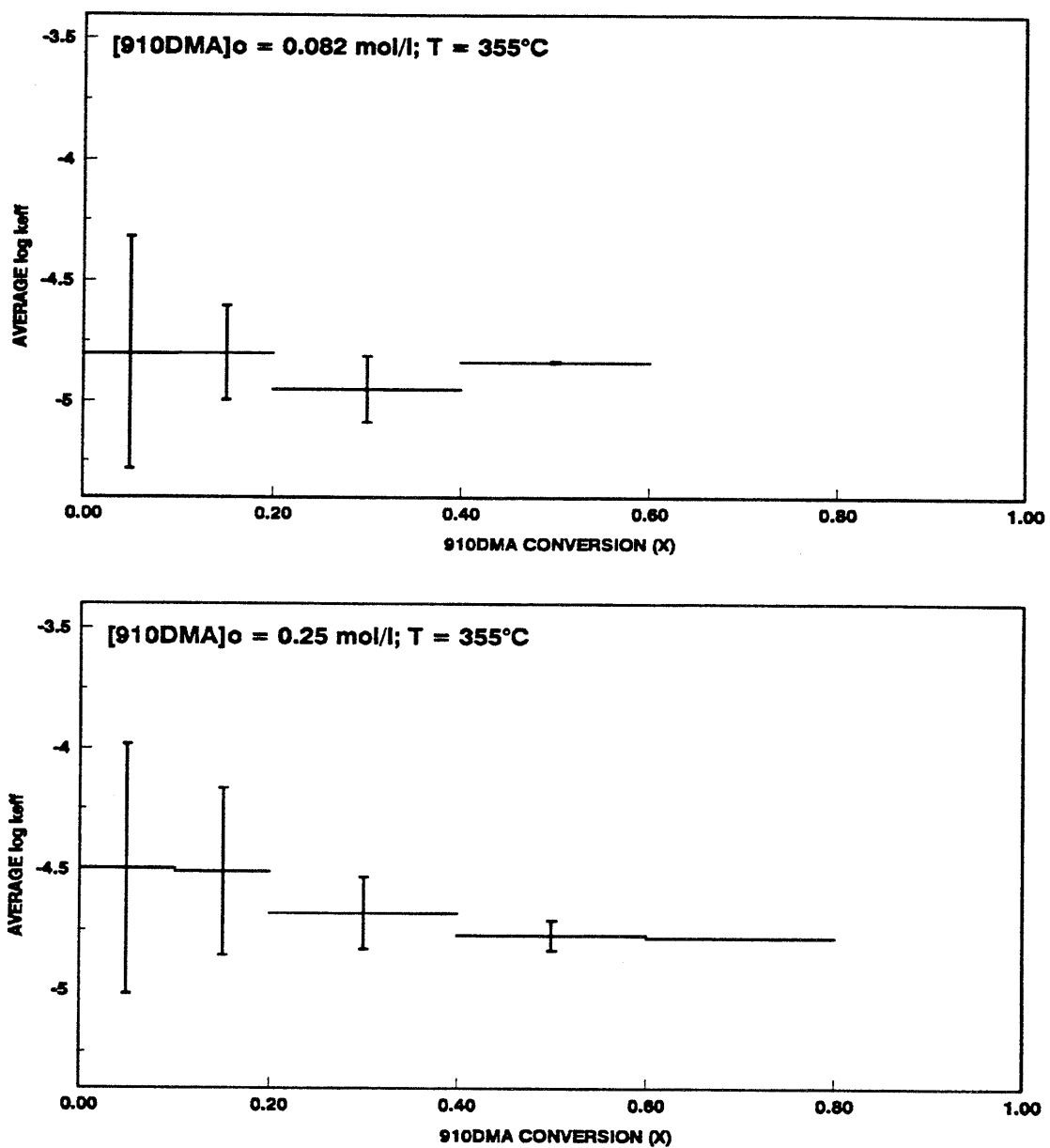
Figure 5.28: Average log k_{eff} vs. 910DMA conversion at T = 355°C for $[910DMA]_o$ = 0.082 (top) and 0.25 mol/l (bottom).

316
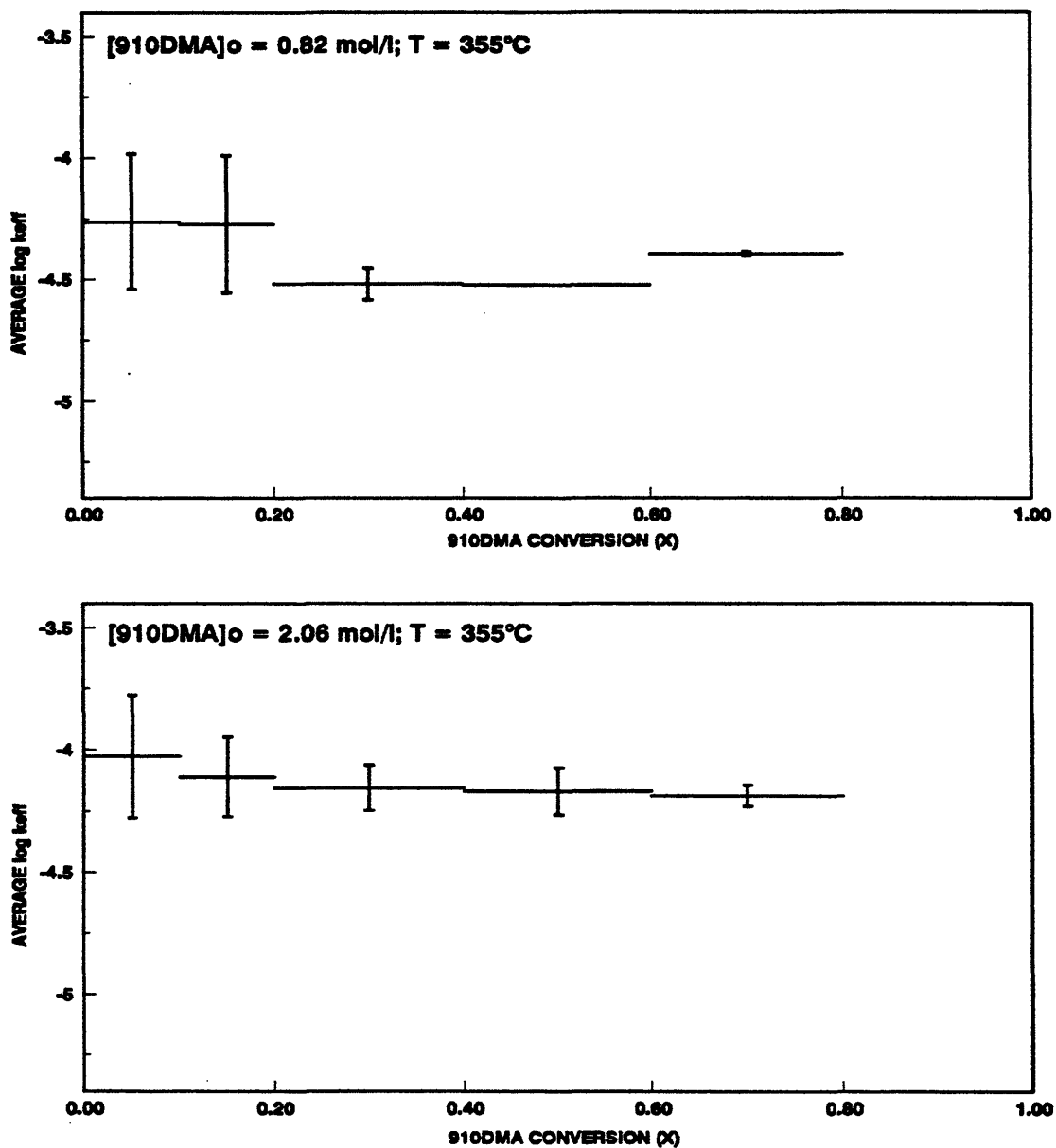
Figure 5.29: Average log k_{eff} vs. 910DMA conversion at T = 355°C for [910DMA]$_o$ = 0.82 (top) and 2.06 mol/l (bottom).
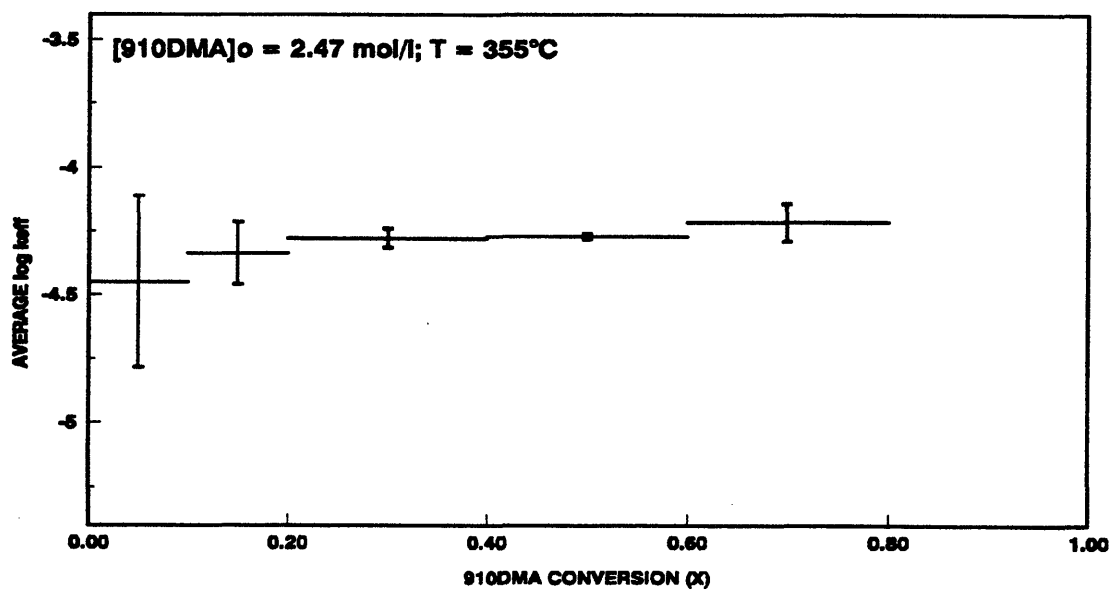
Figure 5.30: Average log k_{eff} vs. 910DMA conversion at T = 355°C for $[910DMA]_o$ = 2.47 mol/l.

Table 5.5

AVERAGE log k_{eff} AND ASSOCIATED UNCERTAINTIES FOR 910DMA THERMOLYSIS

T °C	[910DMA]$_o$ mol/l	$<k_{eff}>$ ± error	Conversion intervals and associated uncertainties in log k_{eff}					
			0-0.1	0.1-0.2	0.2-0.4	0.4-0.6	0.6-0.8	0.8-1.0
315	0.82	-5.07 ± 0.54	1.06	0.30				
335	0.82	-4.85 ± 0.26	0.62	0.38	0.12	0.02		
355	0.082	-4.84 ± 0.33	0.96	0.39	0.27	0.01		
355	0.25	-4.60 ± 0.37	1.03	0.69	0.30	0.12	0	
355	0.82	-4.31 ± 0.26	0.55	0.56	0.13	0	0.02	
355	2.06	-4.12 ± 0.18	0.52	0.32	0.19	0.19	0.09	
355	2.47	-4.35 ± 0.24	0.67	0.24	0.08	0.02	0.15	
370	0.82	-4.12 ± 0.16	0.41	0.42	0.13	0.12	0.15	0.15
409	0.82	-3.32 ± 0.18		0	0.21		0	0.42

The order of 910DMA decomposition at T = 355°C was determined by plotting the log k_{eff} vs log $[910DMA]_0$ as shown in Figure 5.31, the upper panel of which shows data for all X while the lower panel shows data for X < 0.4. The low conversion data, X < 0.4, approximately represent the limit X → 0. It can be demonstrated that for a reaction rate expression:

$$r = k[910DMA]^\alpha \qquad (5.8)$$

with rate constant k and reaction order α, the apparent first order rate constant at low conversions, X → 0, is:

$$k_{eff} = k[910DMA]_0^{\alpha - 1} \qquad (5.9)$$

Consequently, a plot of log k_{eff} versus log $[910DMA]_0$ should exhibit slope (α - 1) and intercept log k. In Figure 5.31, regression of log k_{eff} vs. log $[910DMA]_0$ for all conversions gives α - 1 = 0.40 ± 0.05 and log k = -4.37 ± 0.30, while regression of the low conversion data gives α - 1 = 0.38 ± 0.06 and log k = -4.36 ± 0.34, both results implying that 910DMA thermolysis is close to 3/2 order with respect to the substrate. This accords with the 3/2 order inferred from the variation of 910DMA decomposition half-lifes with varying $[910DMA]_0$ in Section 5.1.3.
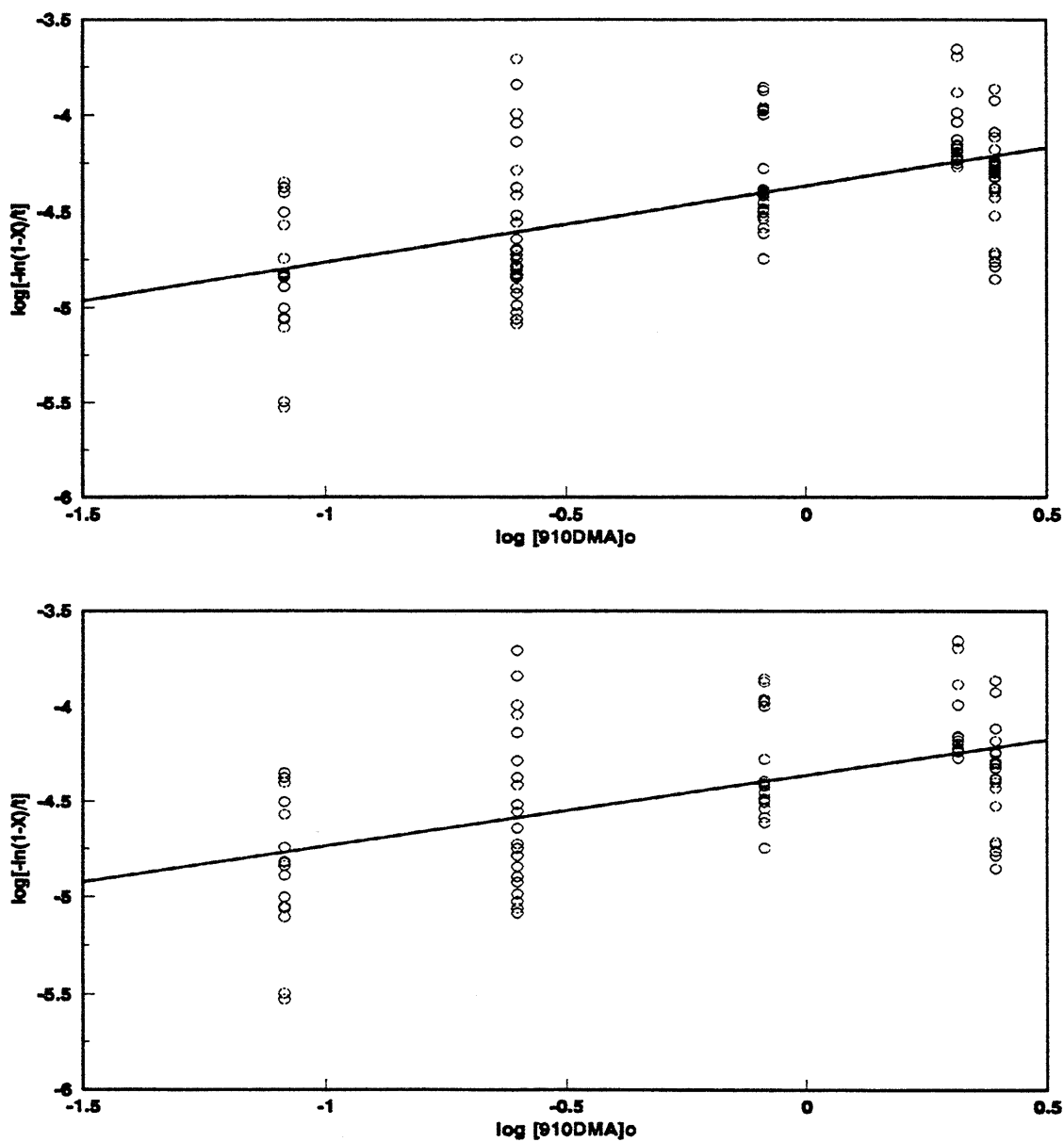
Figure 5.31: Determination of reaction order for 910DMA thermolysis from log [910DMA]$_o$ vs. log k_{eff}: all X (top) and only X < 0.4 (bottom).

321

5.2.1.2 True Rate Constants, $k_{3/2}$

The 3/2 order rate expression:

$$r = k_{3/2}[910DMA]^{3/2} \qquad (5.10)$$

integrated with respect to time reads:

$$\frac{1}{[910DMA]_t^{1/2}} - \frac{1}{[910DMA]_o^{1/2}} = \frac{k_{3/2}\ t}{2} \qquad (5.11)$$

Thus, a plot of $1/[910DMA]_t^{1/2}$ versus time should be linear, with slope $k_{3/2}/2$ and intercept $1/[910DMA]_o^{1/2}$. Figure 5.32 shows the present data for 910DMA thermolysis at T = 355°C on coordinates of $1/[910DMA]^{1/2}$ versus t. Data at all $[910DMA]_o$ and all conversions are plotted on the graph, but at each $[910DMA]_o$, only the low conversion results, X < 0.4, were regressed, with the corresponding best-fit lines indicated in the figure. The light dashed-dotted diagonal line in the figure is the locus of times and concentrations at which X = 0.4. The best-fit regressed lines are roughly parallel, with slopes, that is $(k_{3/2}/2)$ = [1.70E-05, 1.53E-05, 1.66E-05, 2.49E-05, 1.86E-05] for $[910DMA]_o$ = [0.082, 0.25, 0.82, 2.06, 2.47 mol/l] respectively. It is noteworthy that the individual slopes vary by less than a factor of 2 over a 30-fold range of initial concentrations, reinforcing the validity of the chosen 3/2 order. Figure 5.33, a plot of $2(1/[910DMA]_t^{1/2} - 1/[910DMA]_o^{1/2})$ versus time, superimposes all the $[910DMA]_o$ data onto a single line of slope $k_{3/2}$, passing through

322
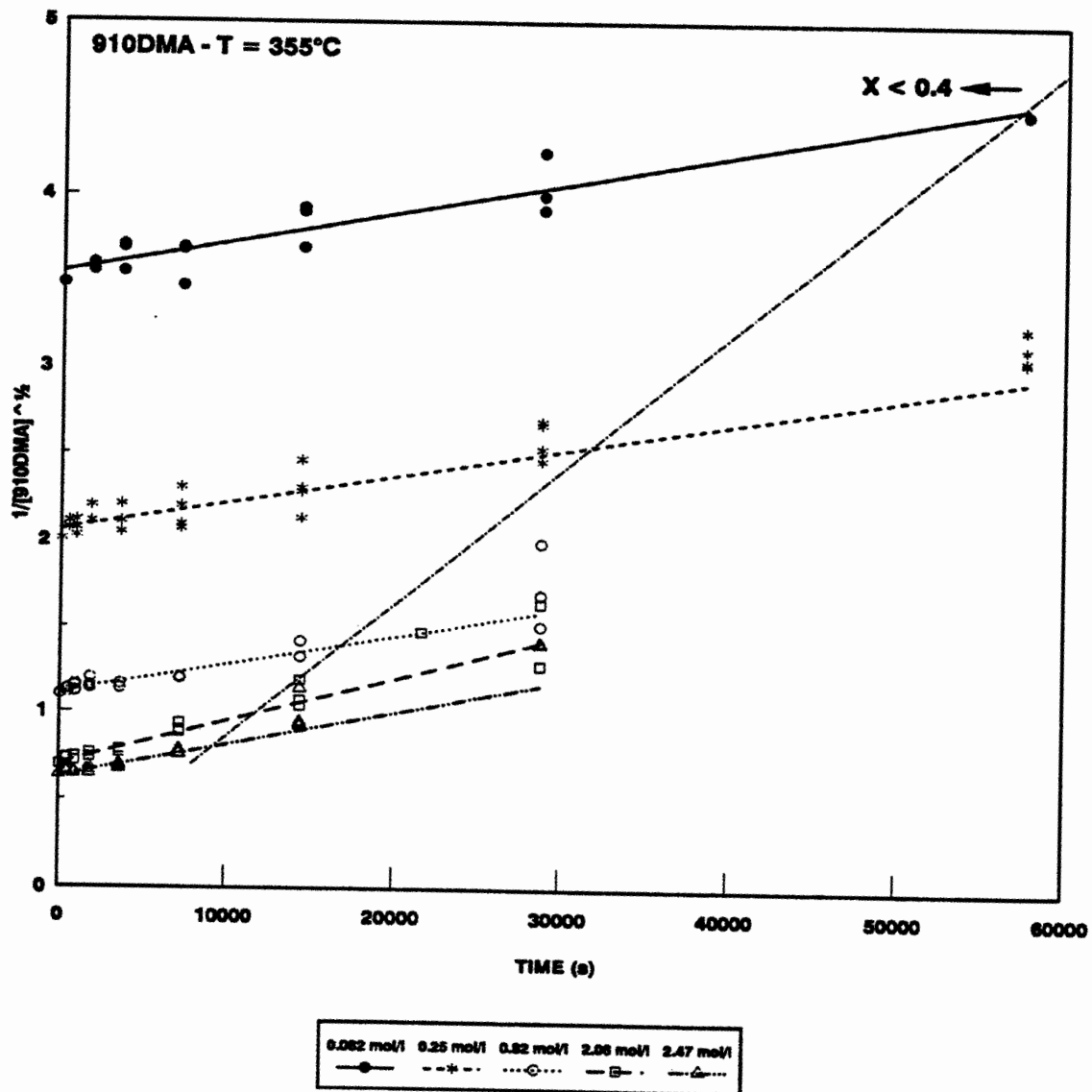
Figure 5.32: 3/2 order plot, $1/[910DMA]_t^{1/2}$ vs. t, for 910DMA thermolysis with varying $[910DMA]_o$ at fixed T = 355°C.
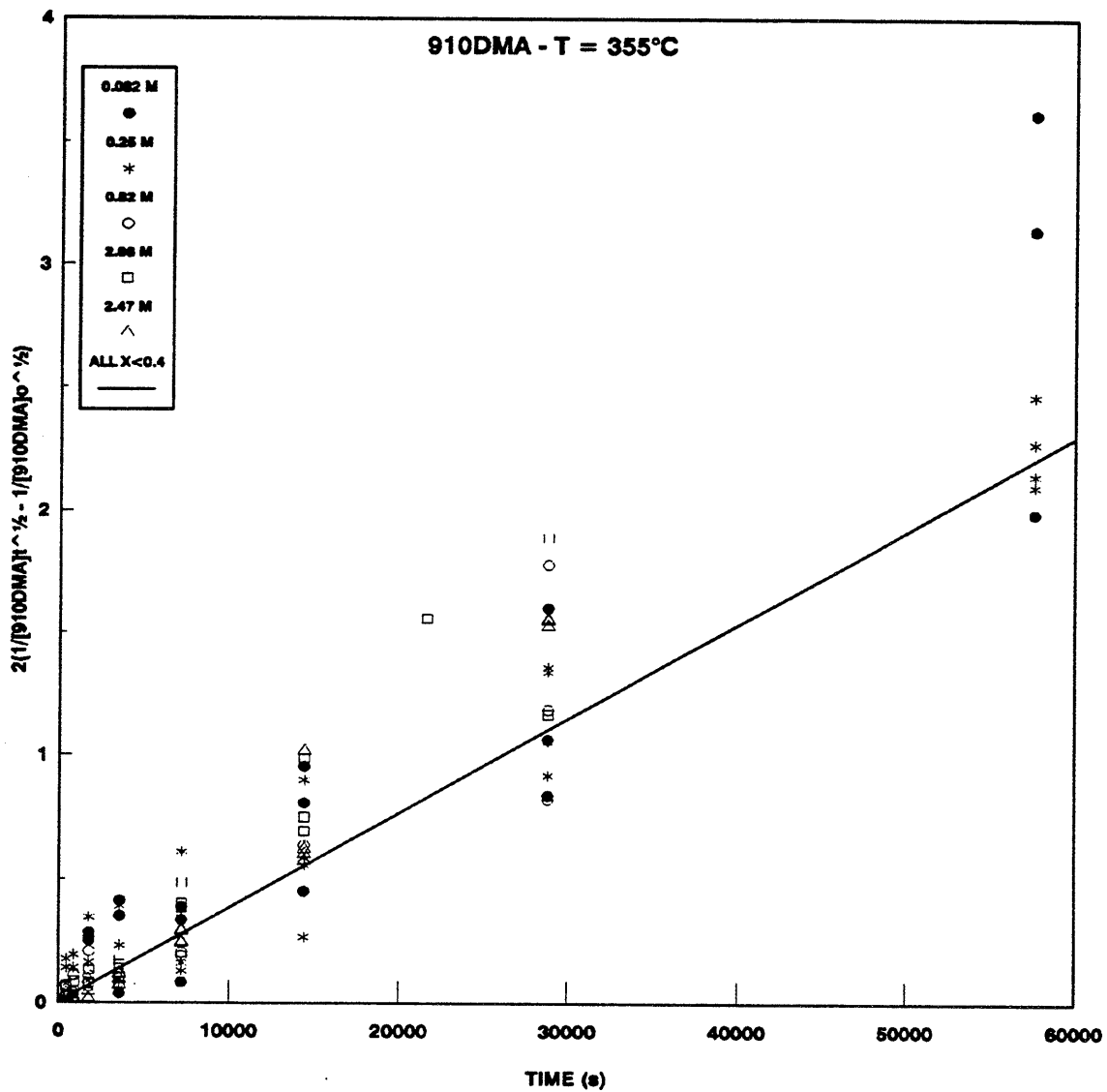
Figure 5.33: Plot of the integrated 3/2 order rate expression for 910DMA thermolysis with varying $[910DMA]_0$ at fixed T = 355°C.

the origin. From regression of all the data at low conversions, $X < 0.4$, we obtain $\langle k_{3/2} \rangle = (3.83 \pm 0.13)\text{E-05}$ for $0.082 < [910DMA]_o < 2.47$ mol/l at $T = 355°C$.

5.2.2 Activation Parameters

Thermolyses of 910DMA at fixed $[910DMA]_o = 0.82$ mol/l and varying temperatures from 315 - 409°C revealed the activation parameters associated with both the effective first order and true 3/2 order rate constants.

Effective first order rate constants were calculated at each point, for all runs. At each T and $[910DMA]_o$, values of log k_{eff} were averaged over intervals of fractional conversion, respectively 0 - 0.1, 0.1 - 0.2, 0.2 - 0.4, 0.4 - 0.6, 0.6 - 0.8, and 0.8 - 1.0. The average log k_{eff} over each of the chosen conversion intervals are shown as horizontal lines with vertical error bars in Figure 5.34 and Figure 5.35. The upper panel of Figure 5.34 refers to 910DMA thermolysis at $T = 315°C$ and $[910DMA]_o = 0.82$ mol/l. In each of the two conversion intervals, values of the average log k_{eff} are ~ -5.3 ± 0.3. The uncertainty associated with log k_{eff} is seen to diminish with increasing conversion, the error bars spanning 1.1 and 0.3 units of log k_{eff} in the conversion intervals of 0 - 0.1 and 0.1 - 0.2, as shown on line 1 of Table 5.5. The lower panel of Figure 5.34 refers to 910DMA thermolysis at $T = 335°C$ and $[910DMA]_o = 0.82$ mol/l, the upper panel of Figure 5.29 refers to 910DMA thermolysis at $T = 355°C$ and $[910DMA]_o = 0.82$ mol/l and the upper and lower panels of Figure 5.35 refer to 910DMA thermolysis at $T = 370°C$ and 409°C,
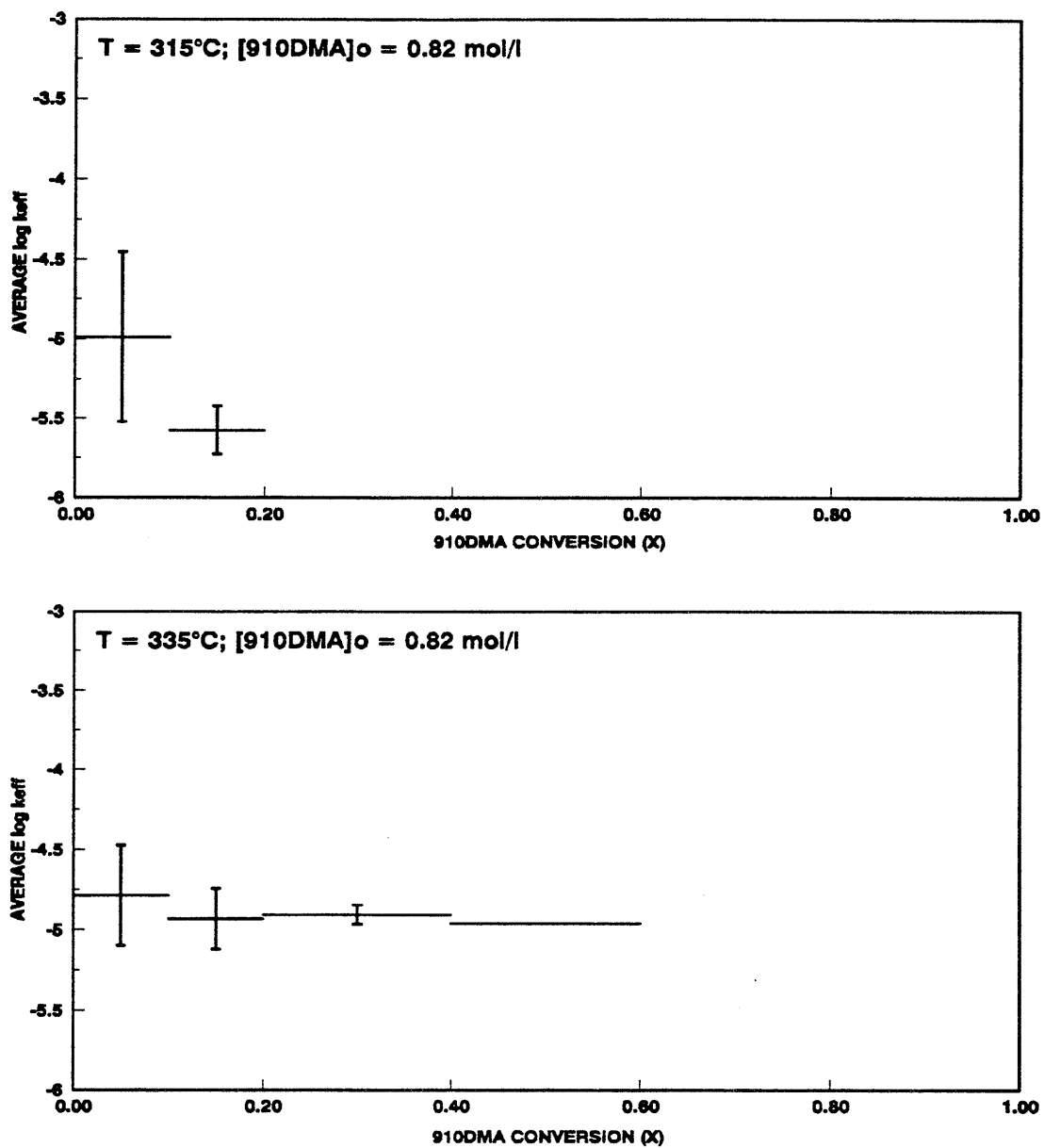
Figure 5.34: Average log k_{eff} vs. 910DMA conversion at $[910DMA]_o$ = 0.82 mol/1 for T = 315°C (top) and T = 335°C (bottom).
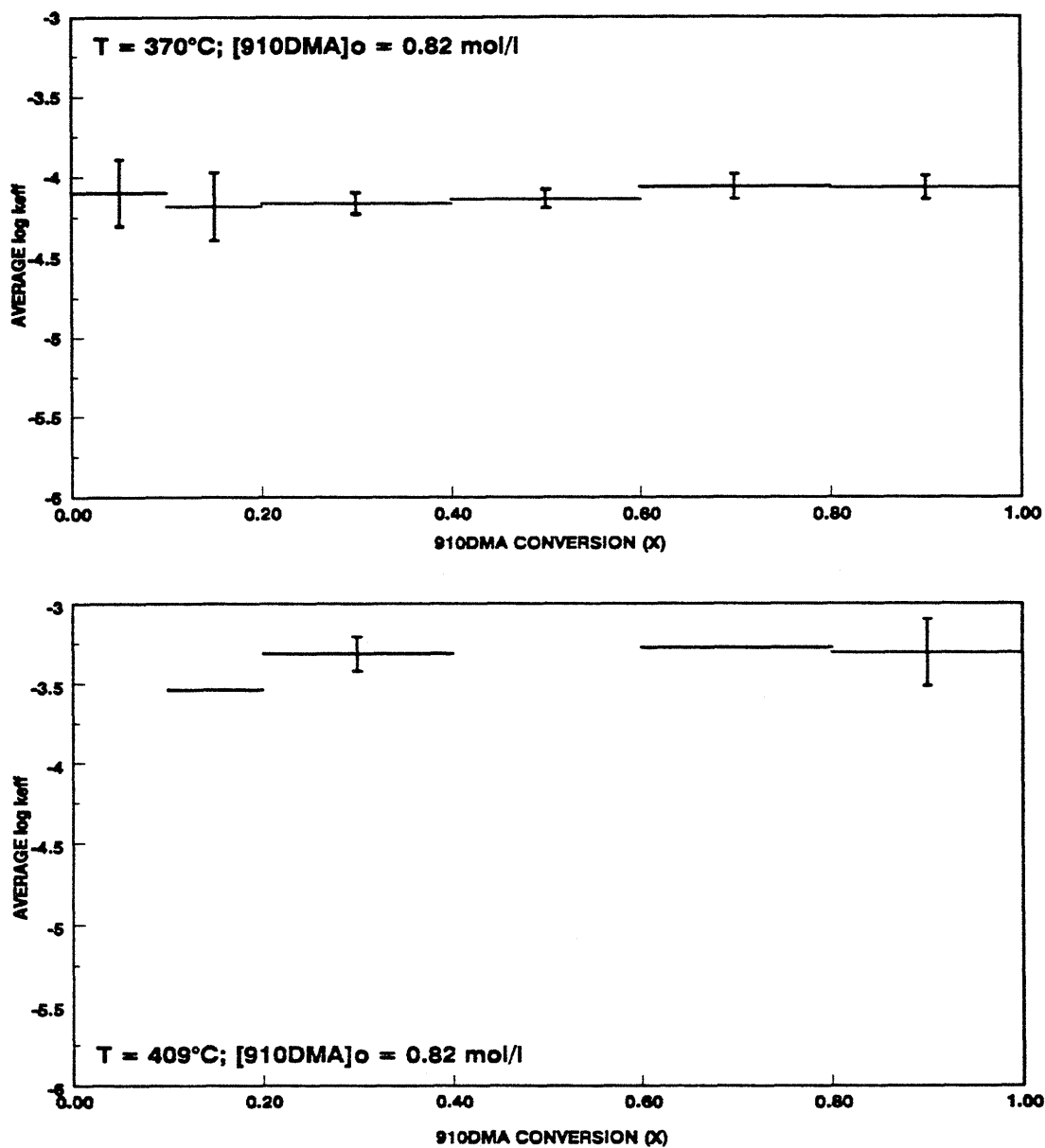
Figure 5.35: Average log k_{eff} vs. 910DMA conversion at $[910DMA]_o = 0.82$ mol/l for T = 370°C (top) and T = 409°C (bottom).

327

respectively, at $[910DMA]_o$ = 0.82 mol/l with the respective average and errors summarized on lines 2, 5, 8 and 9 of Table 5.5.

Figure 5.36 is a plot of the integrated 3/2 rate expression, $2(1/[910DMA]_t^{1/2} - 1/[910DMA]_o^{1/2})$ versus time, for 910DMA thermolysis at fixed $[910DMA]_o$ = 0.82 mol/l and varying reaction temperatures, 315 < T °C < 409. At each temperature, lines are drawn to represent the best-fits at low conversions, X < 0.4. The slopes of these lines provide the rate constants $<k_{3/2}>$ = [2.50E-06, 1.36E-05, 3.62E-05, 7.81E-05, 5.49E-04] at each thermolysis temperature T = [315, 335, 355, 370, 409°C].

The variation of rate constants k_{eff} and $k_{3/2}$ with temperature is respectively shown in Figure 5.37 and Figure 5.38, using Arrhenius coordinates of $log_{10}k$ versus $1/\theta$, where θ = $4.573x10^{-3}$ T in Kelvins; on these coordinates, an Arrhenius relation of form:

$$log_{10} k = log_{10} A - \frac{E^*}{\theta}$$

(5.12)

is described by a straight line of slope equal to activation energy E^* in kcal/mol and intercept $log_{10}A$, where the pre-exponential factor A has units of the rate constant. The upper and lower panels of Figure 5.37 depict Arrhenius diagrams for the effective first order rate constant, k_{eff}, the upper panel derived from data over all conversions and the lower panel derived from low conversion data at X < 0.4. The hollow circles represent the average $log k_{eff}$ and the error bars are the standard deviation from these averages. The error bars are relatively the same size for the
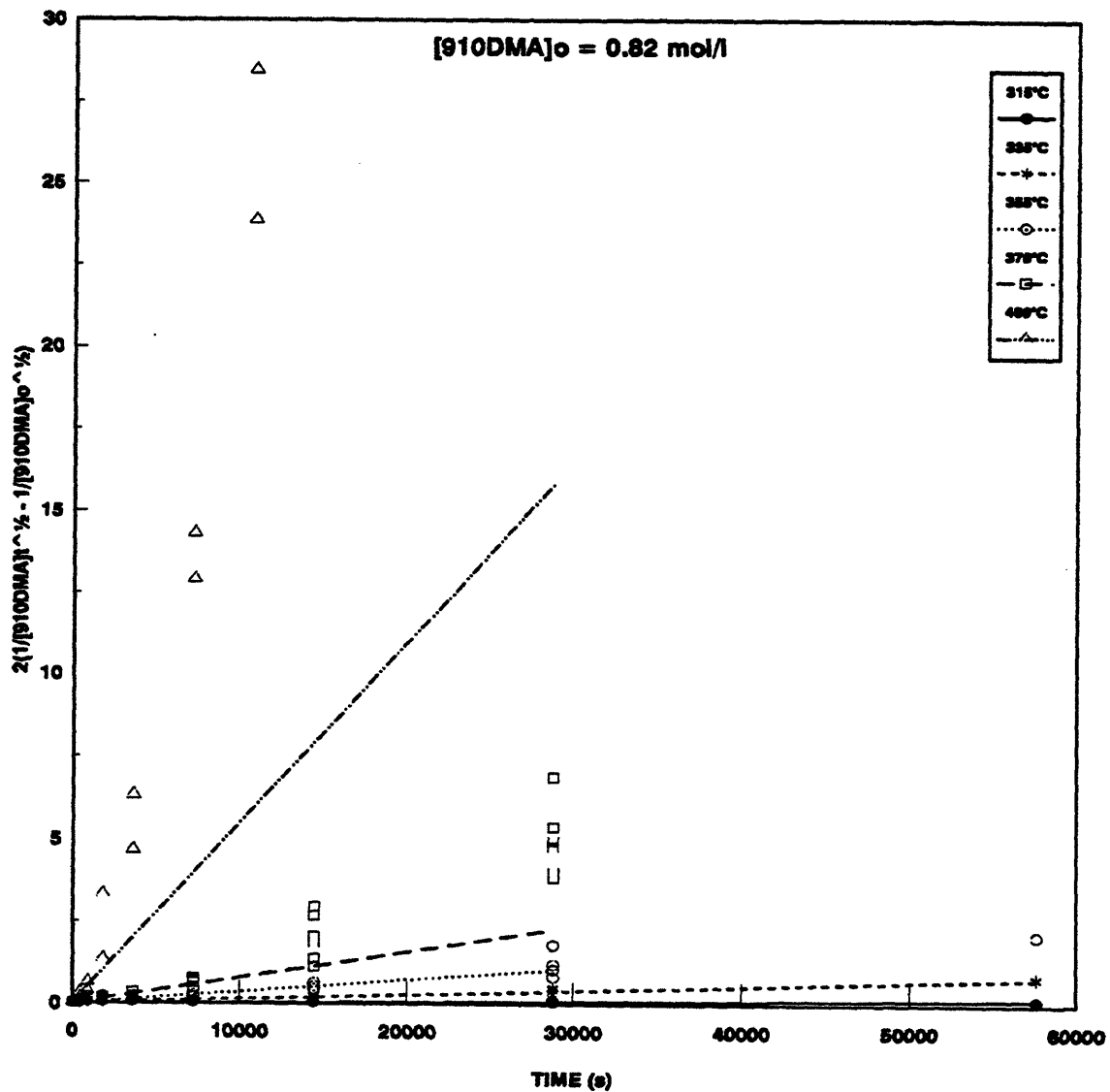
Figure 5.36: Plot of the integrated 3/2 order rate expression for 910DMA thermolysis with varying temperature with fixed $[910DMA]_o$ = 0.82 mol/l.
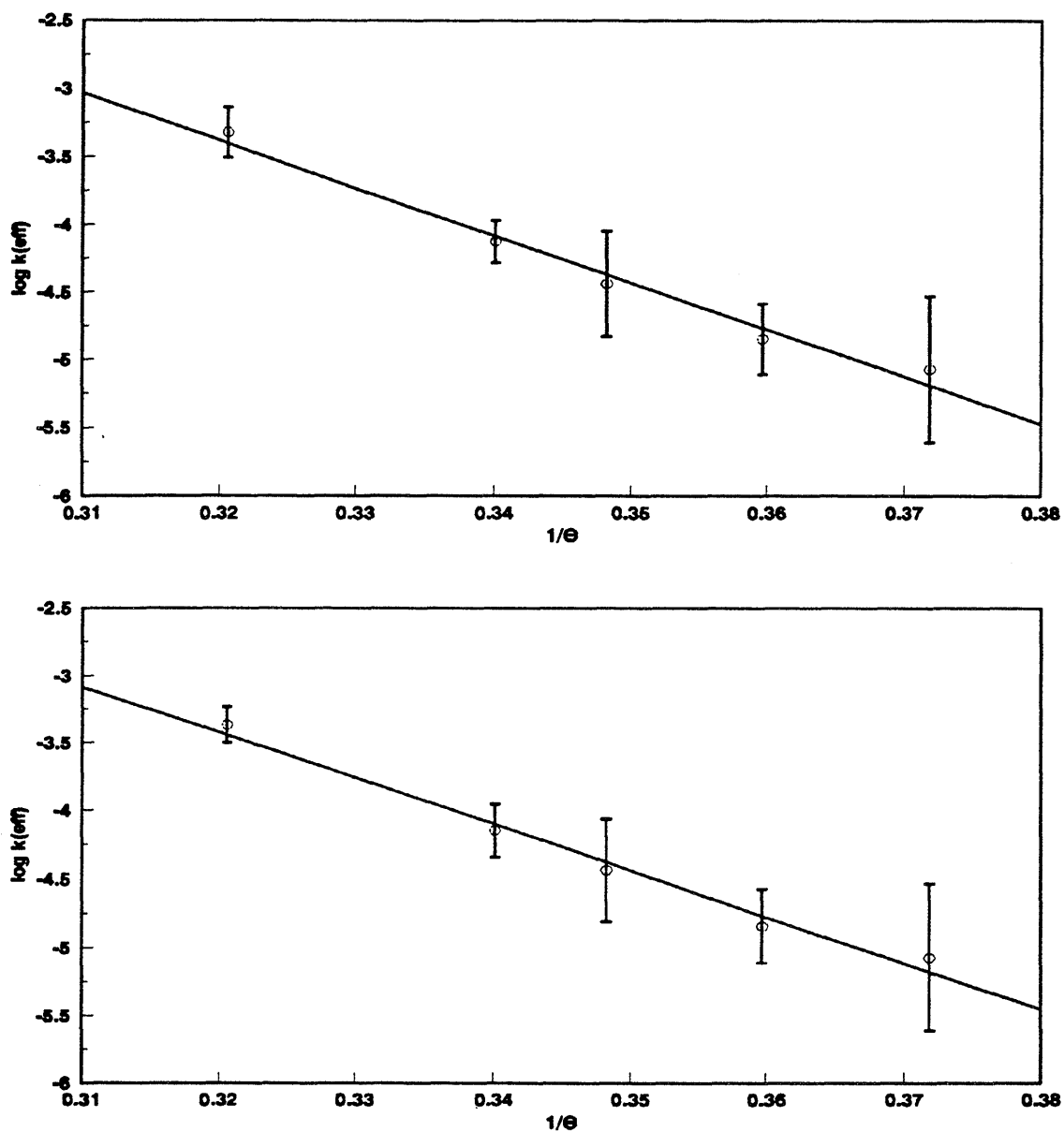
Figure 5.37: Arrhenius plot for k_{eff} for all conversions (top) and for $X < 0.4$ (bottom) with $[910DMA]_o = 0.82$ mol/l at $T = 355°C$.
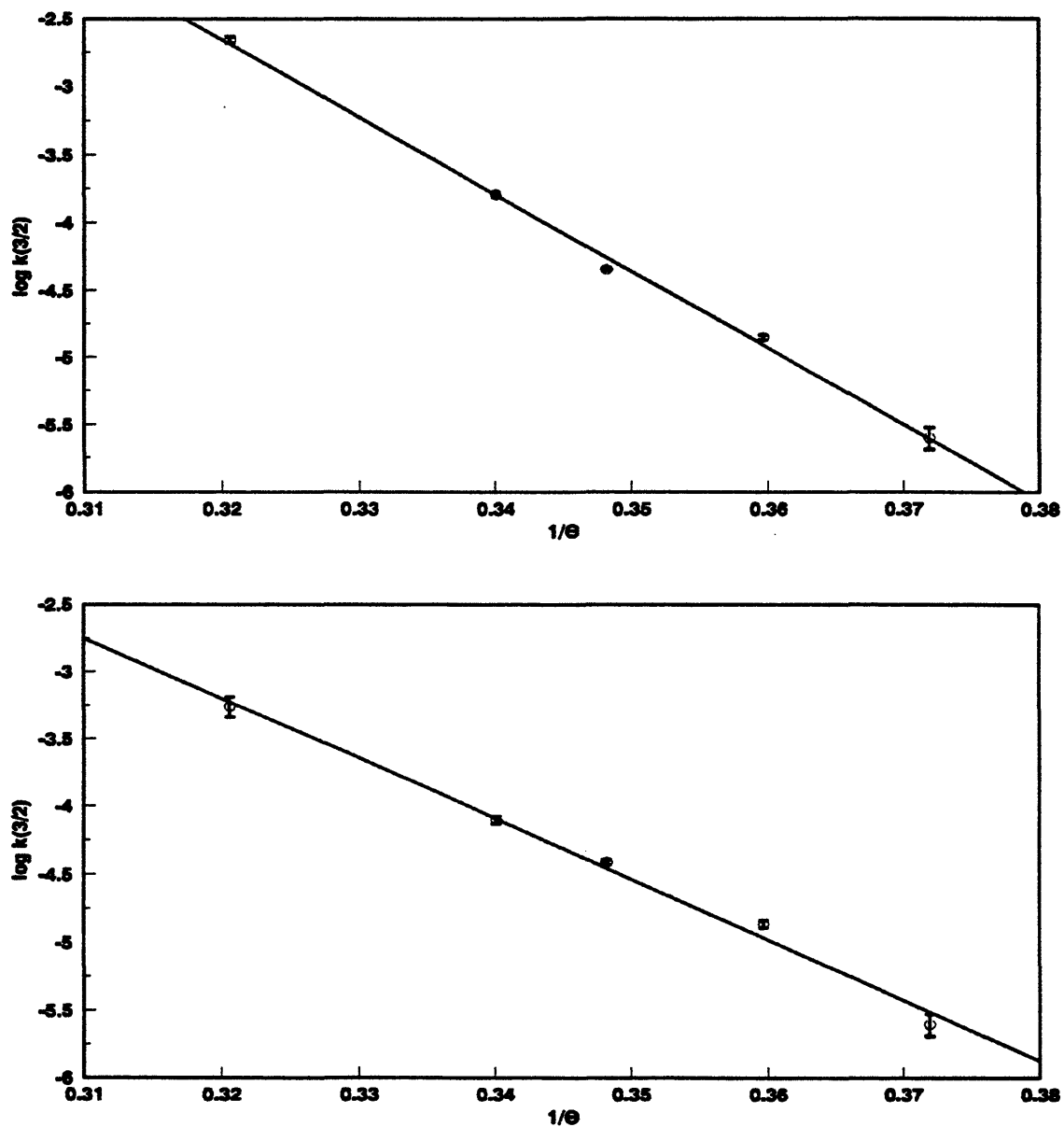
Figure 5.38: Arrhenius plot for $k_{3/2}$ for all conversions (top) and for $X < 0.4$ (bottom) with $[910DMA]_o = 0.82$ mol/l at $T = 355°C$.

average log k_{eff} using all conversions and the low conversion data at X < 0.4 because most of the scatter in the data is at X < 0.2, as seen in Table 5.5. The best-fit Arrhenius parameters $[\log_{10}$ A (s^{-1}), E^* (kcal/mol)$]$ = $[7.79 \pm 0.11, 34.9 \pm 2.8]$ for the average k_{eff} using all conversions and $[\log_{10}$ A (s^{-1}), E^* (kcal/mol)$]$ = $[7.42 \pm 0.10, 33.9 \pm 2.5]$ for the average k_{eff} using X < 0.4.

The upper and lower panels of Figure 5.38 depict Arrhenius diagrams for the 3/2 order rate constant, $k_{3/2}$, the upper panel using data over all conversions and the lower panel using only low conversion data at X < 0.4. The hollow circles represent the slope of the integrated 3/2 rate expression versus time while the error bars are the standard errors of these slopes. The error bars for these data are much smaller than those for log k_{eff} in the previous figure, implying a better fit. The best-fit Arrhenius parameters $[\log_{10}$ A $(l^{1/2}/mol^{1/2}$ s$)$, E^* (kcal/mol)$]$ = $[15.6 \pm 0.06, 56.9 \pm 1.6]$ for $k_{3/2}$ using all conversions and $[\log_{10}$ A $(l^{1/2}/mol^{1/2}$ s$)$, E^* (kcal/mol)$]$ = $[11.1 \pm 0.08, 44.6 \pm 2.1]$ for $k_{3/2}$ with X < 0.4. The two sets of activation parameters $(\log_{10}$ A, $E^*)$ for $k_{3/2}$ differ due to the pronounced curvature of the integrated 3/2 rate expression at long times at the higher temperatures, T = 370 and 409°C, as seen in Figure 5.36. For this reason, the parameters derived from data at X < 0.4 are the more reliable. Also, for comparison, regression of the half-lifes t^* at varying temperatures in Section 5.1.5 gave Arrhenius parameters $[\log_{10}$ A (s^{-1}), E^* (kcal/mol)$]$ = $[10.6 \pm 0.03, 43.1 \pm 1.0]$ for $k_{3/2}$.

5.2.3 Summary of Kinetics

Table 5.6 summarizes the kinetic parameters for 910DMA thermolysis as determined from the k_{eff} for the low conversion data at $X < 0.4$, the 3/2 order rate expression for the low conversion data at $X < 0.4$ and the half-lifes at fixed $[910DMA]_0$ while varying temperature. Analysis of both the k_{eff} and t^* data led to approximately 3/2 order 910DMA decomposition kinetics. The activation parameters ($\log_{10} A$, E^*) obtained from the 3/2 order rate expression were similar to those derived from the half-life data, while $\log_{10} A$ and E^* obtained from the k_{eff} regression data were both appreciably lower then the corresponding parameters in the former sets.

5.3 Reaction Pathways

Pathways for the thermolysis of 910DMA deduced from the results over the experimental grid are summarized in Figure 5.39. Three primary pathways operate in parallel upon the original 910DMA substrate, namely: (P1) hydrogenation to *cis*- and *trans*-9,10-dihydro-9,10-dimethylanthracene, (P2) demethylation to 9-methylanthracene, and (P3) methylation to 1,9,10-trimethylanthracene and other TMA isomers. The main demethylation sequence, shown bold, cascades from 910DMA to 9MA to ANT. The primary demethylation product 9MA is secondarily operated upon by a pathway triad analogous to the preceding primary triad, eventually forming 9,10-dihydro-9-methylanthracene, a host of dimethylanthracenes

Table 5.6

SUMMARY OF KINETICS
FOR 910DMA THERMOLYSIS

	Order	$\log_{10} A$	E^*	log k (355°C)
k_{eff} (X < 0.4)	1.38 ± 0.06	7.42 ± 0.10	33.9 ± 2.5	-4.38
3/2 order rate expression (X < 0.4)	3/2	11.1 ± 0.08	44.6 ± 2.1	-4.43
t^*	1.53 ± 0.06	10.6 ± 0.03	43.1 ± 1.0	-4.41
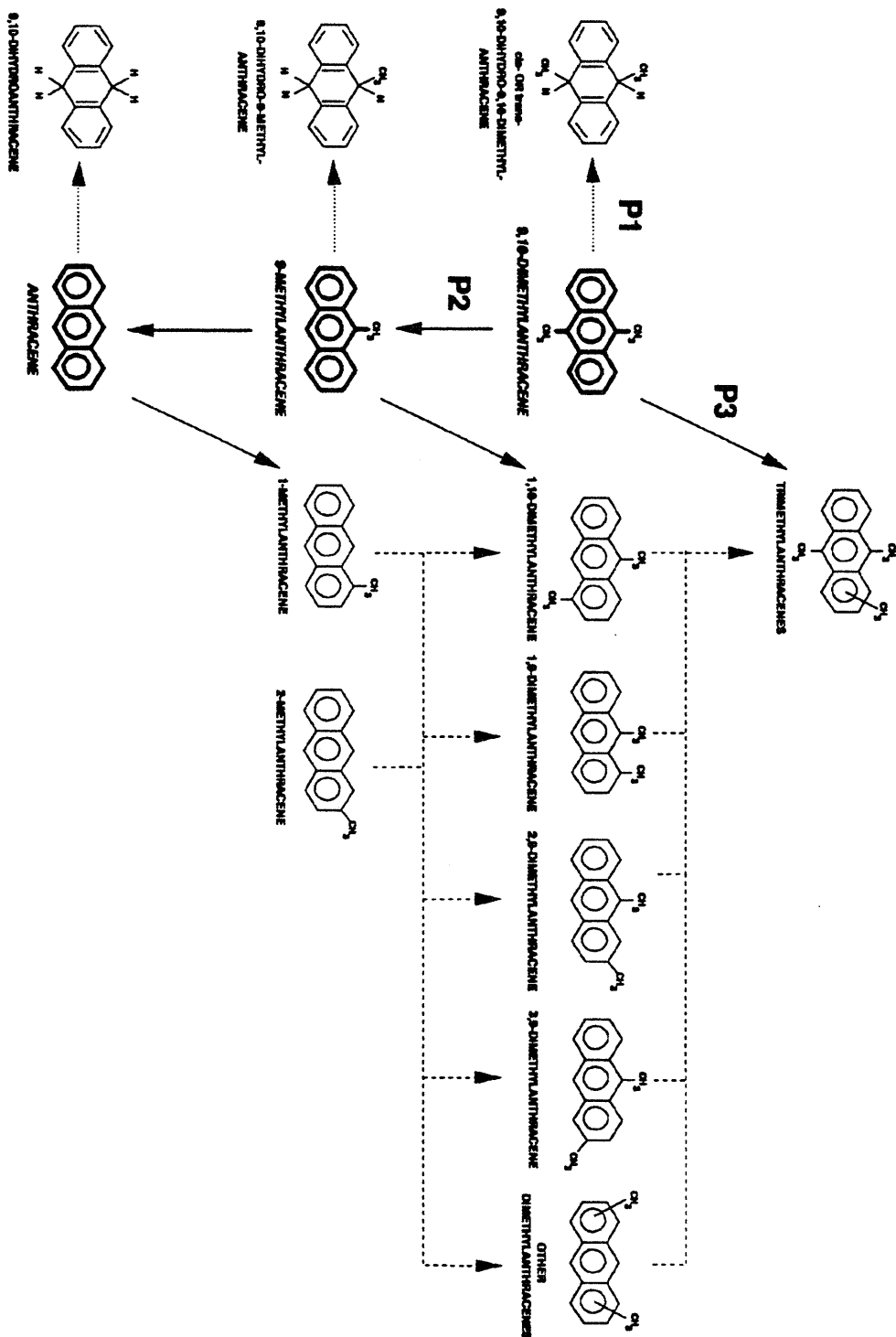
Figure 5.39: 910DMA primary decomposition pathways.

(1,9-, 1,10-, 2,9-&3,9- and others) and anthracene. And at the highest substrate conversions, even the terminal demethylation product ANT suffers hydrogenation and methylation, as witnessed by the appearance of the minor products DHA, 1MA and 2MA. Neither 910DMA nor 9MA isomerize to their positional isomers, since the latter (methylated) species do not arise prior to the appearance of their demethylated precursor. Thus, 1,9-, 1,10- and other DMAs rise after 9MA, while 1MA and 2MA arise after ANT.

Figure 5.40 summarizes secondary and termination pathways deduced from the results over the experimental grid. The main demethylation sequence is shown again in bold. The primary demethylation product of 910DMA, 9MA, is associated with methane gas. The primary methylation product of 910DMA, TMA, is secondarily operated upon by a pathway triad analogous to the primary triads, forming dihydrotrimethylanthracenes (UNK222 in Section 4.3.2.1) and tetramethylanthracenes. Hydrogenated products formed by the primary product triads acting upon 910DMA, 9MA and ANT are further hydrogenated to yield tetrahydrogenated products (UNK182 and UNK210 in Section 4.3.2.1). Termination products included both pure- and cross-termination species related to 910DMA and DHDMA. Among these, the DMAD dimer was detected for the 910DMA substrate (mass 410 in Section 4.3.2.2) and the cross-termination products were detected for the 9MA substrate.
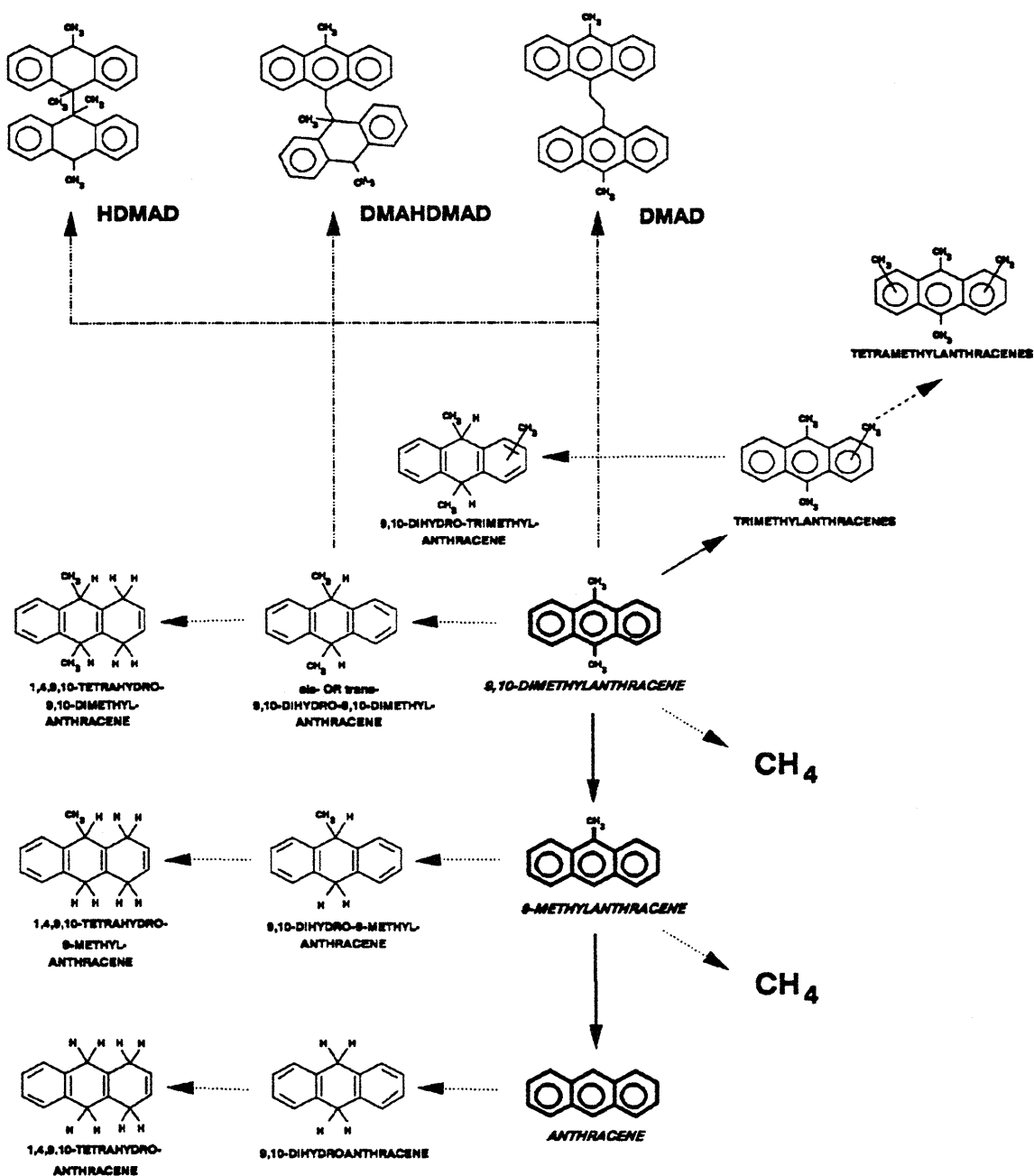
Figure 5.40: 910DMA secondary decomposition pathways.

337

The relative importance of primary pathways (P1 - P3) in Figure 5.39 is shown in Figure 5.41, Figure 5.42 and Figure 5.43, which depict the variation of certain primary product ratios R, namely R[DHDMA/9MA], R[TMA/9MA] and R[CH4/9MA], versus conversion X at all initial substrate concentrations and temperatures.

R[DHDMA/9MA] measures the ratio of hydrogenation (P1) to demethylation (P2) pathways. The upper panel of Figure 5.41 shows that, for all initial 910DMA concentrations, R[DHDMA/9MA] ~ 0.4 at the lowest concentrations, X → 0, and then drops rapidly to 0.04 ± 0.02 for X > 0.20. The lower panel of Figure 5.41 shows that, at all temperatures, R[DHDMA/9MA] ~ 0.4 for X → 0 and then drops rapidly to a level of 0.04 ± 0.04 for X > 0.20.

R[TMA/9MA] measures the ratio of methylation (P3) to demethylation (P2) while R[CH4/9MA] measures the ratio of methane gas formed (roughly P2 - P3) relative to demethylation (P2). The upper panel of Figure 5.42 shows that R[TMA/9MA] is a weak function of initial concentration, with R[TMA/9MA] = $[0.09 \pm 0.02, 0.16 \pm 0.05, 0.23 \pm 0.09, 0.23 \pm 0.08, 0.29 \pm 0.10]$ for $[910DMA]_0$ = [0.082, 0.25, 0.82, 2.06, 2.47 mol/l] for X > 0.20. The lower panel of Figure 5.42 shows that R[TMA/9MA] is essentially independent of temperature, with R[TMA/9MA] = 0.24 ± 0.10 for X > 0.20 at all temperatures. Figure 5.43 shows that R[CH4/9MA] = 0.63 ± 0.08 for X > 0.20 at T = 355 and 370°C and $[910DMA]_0$ = 0.82 mol/l. Taken together, the data in the lower panel of Figure 5.42
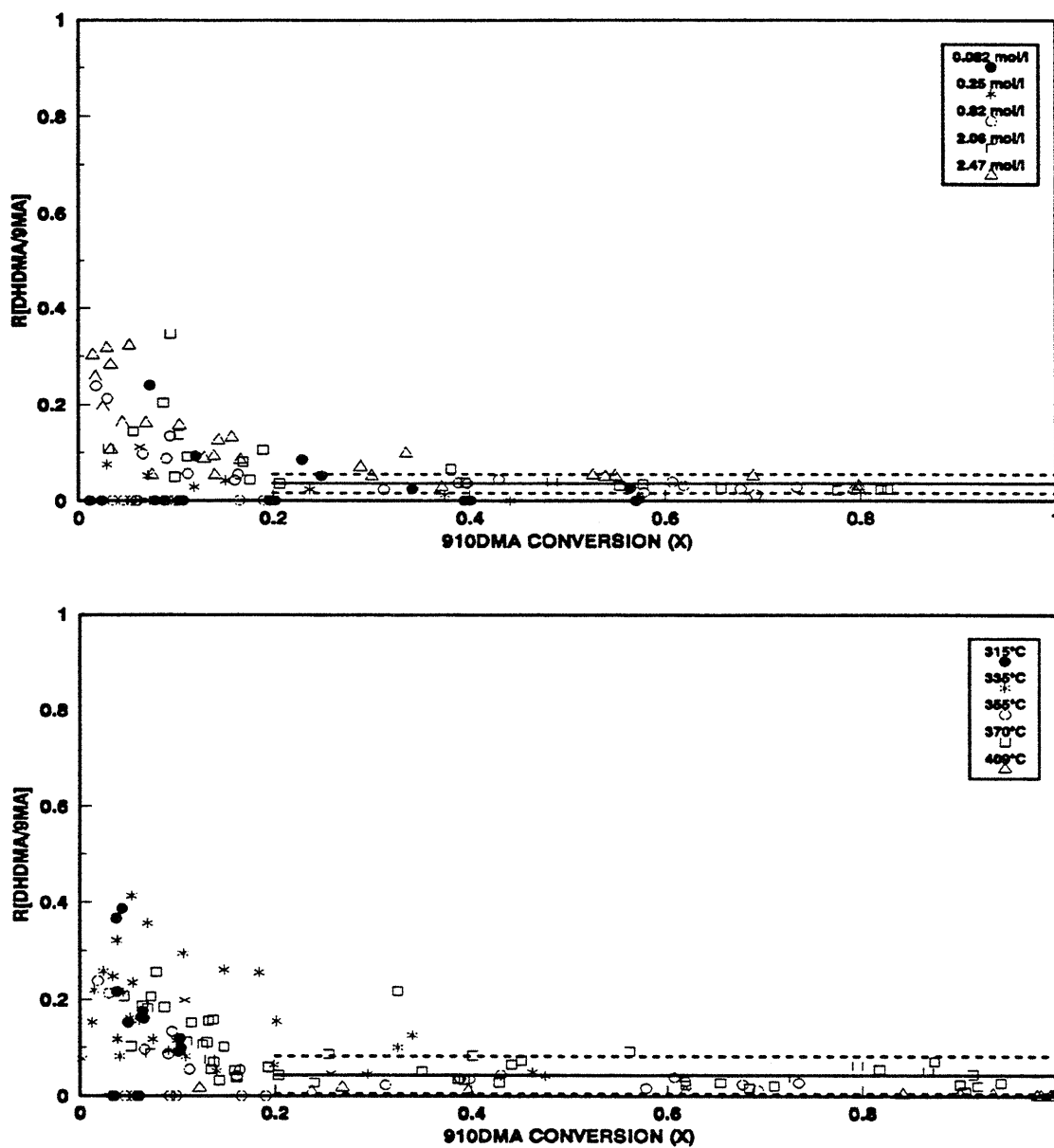
Figure 5.41: Ratio moles DHDMA to moles 9MA produced vs. 910DMA conversion (X) for varying [910DMA]$_o$ at T = 355°C (top) and for varying T with [910DMA]$_o$ = 0.82 mol/l (bottom).
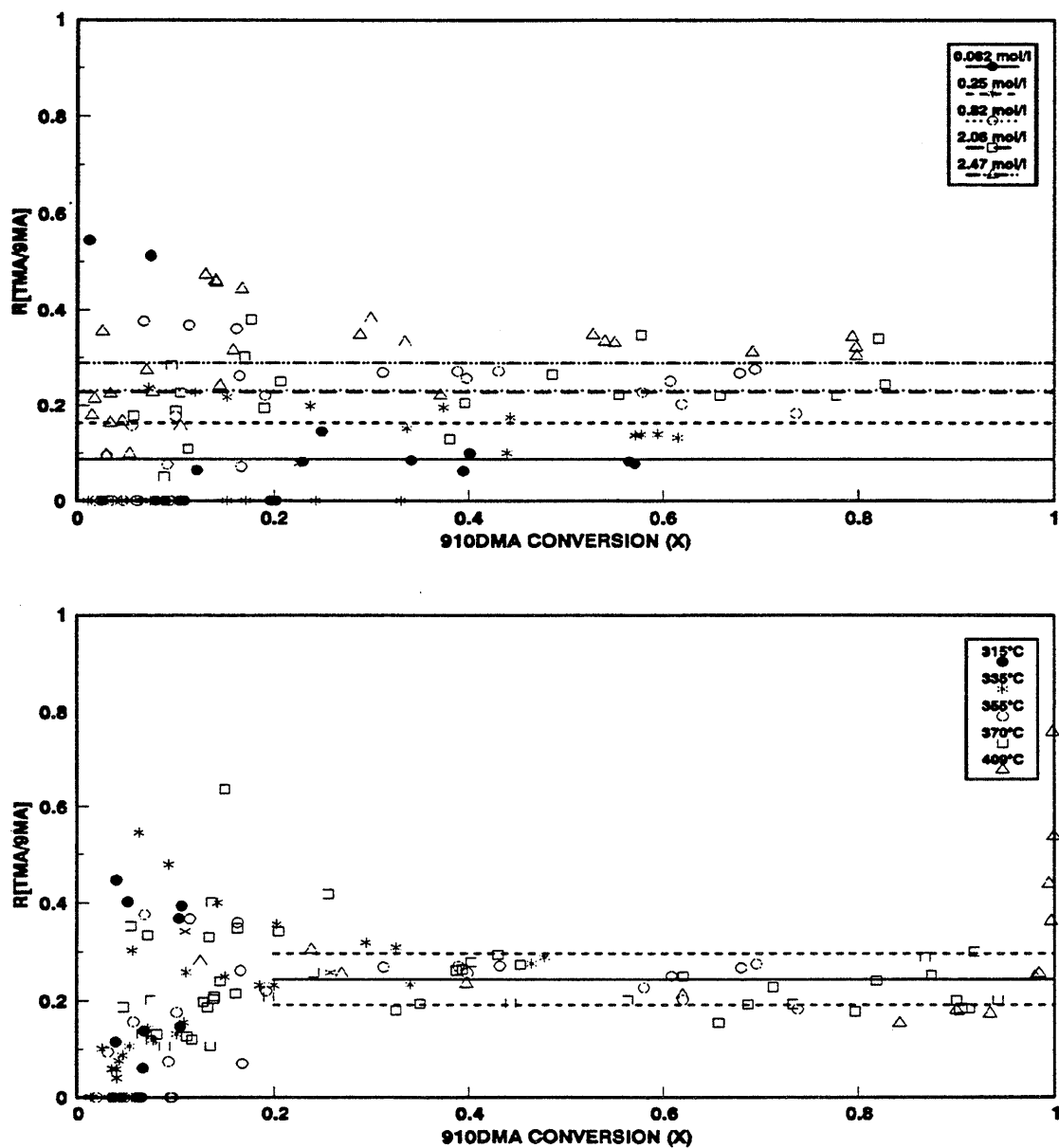
Figure 5.42: Ratio of moles TMA to moles 9MA produced vs. 910DMA conversion (X) for varying [910DMA]$_o$ at T = 355°C (top) and for varying T with [910DMA]$_o$ = 0.82 mol/l (bottom).

340
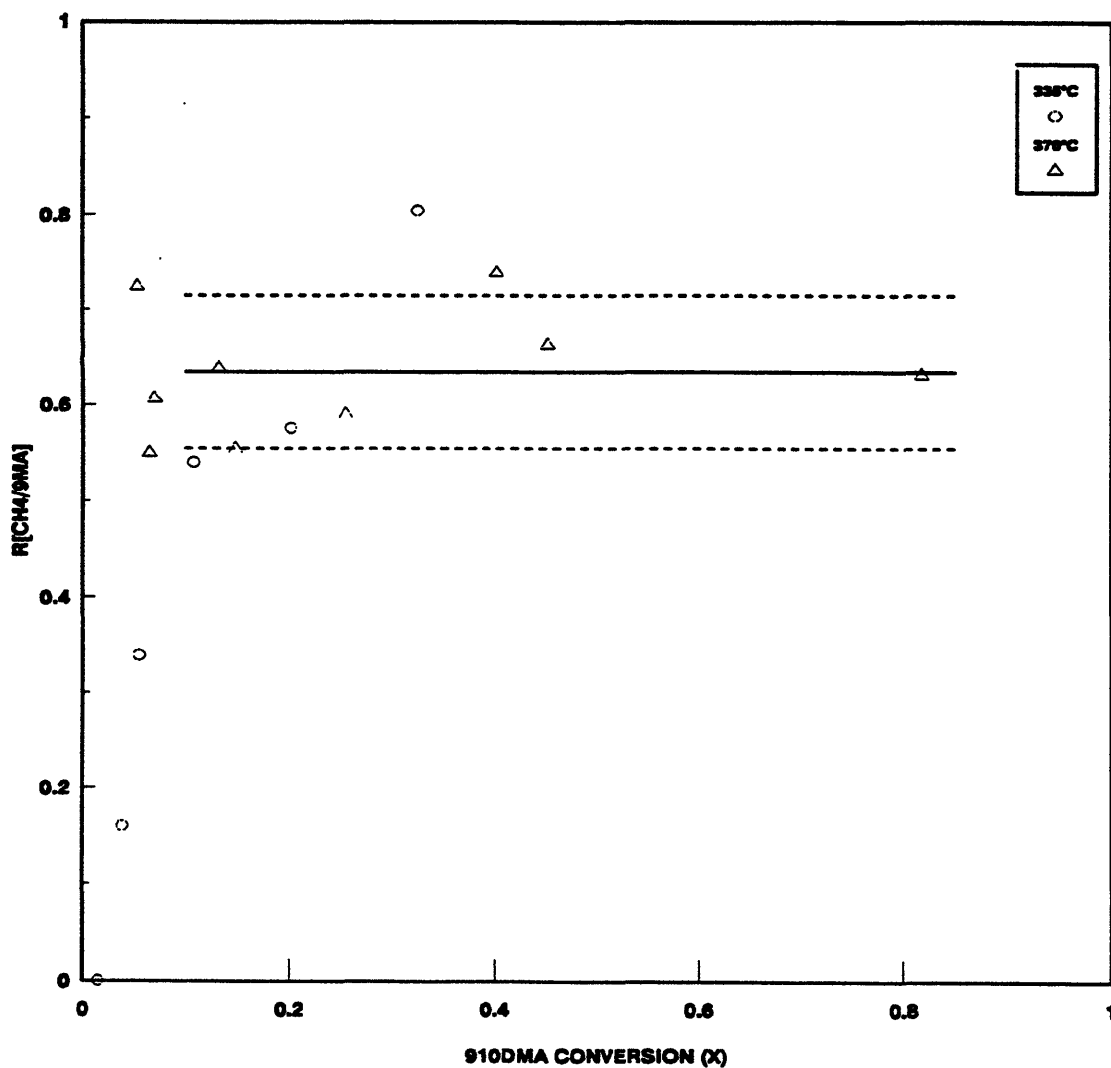
Figure 5.43: Ratio of moles CH4 to moles 9MA produced vs. 910DMA conversion (X) for varying T with $[910DMA]_o$ = 0.82 mol/l.

and in Figure 5.43 show that the sum of the ratios R[TMA/9MA] + R[CH4/9MA]

~ 0.87 is close to unity, accounting for the methyl radicals implicitly formed in the

demethylation pathway P2. It is also noteworthy that, under the present experimental

conditions, ~ 2/3 of the methyl radicals formed by P2 are quenched by hydrogen

abstraction, forming methane gas, while ~ 1/3 add to the 910DMA substrate,

eventually appearing as TMAs.

5.4 Mechanism and Modelling

A possible mechanism for the early stages of 910DMA thermolysis, that is

consistent with the present pathway and kinetic observations and accounts for all the

products observed during the initial stages of 910DMA thermolysis at low

conversions, was devised. Thermochemical and activation parameters were then

assigned from first principles for each elementary reaction and its reverse. An

algebraic steady state analysis was performed on the 910DMA mechanism to provide

an independent check on numerical results of computer calculations. The

mechanistic scheme and rate constants provided a platform for quantitative modelling

of 910DMA thermolysis kinetics and product selectivities. A sensitivity analysis was

performed to demonstrate how the errors of the estimated thermochemical and

activation parameters affected the model results. These activation parameters were

then adjusted within the limits of the errors to provide the best fit to the

experimental results.

5.4.1 Mechanism

A possible mechanism of 910DMA thermolysis is summarized in Figure 5.44, as an elementary step "graph". This is constructed such that the substrate and all stable molecular products are arrayed in the bottom row while unstable radical intermediates (the transition states) are arrayed in the top row. Reaction "nodes", arrayed in the middle row, connect the individual species in the bottom and top rows with arrows indicating the initial direction of reaction (all reactions are, of course, reversible). Initiation reactions are denoted by solid interconnecting lines, propagation (product forming) reactions by various kinds of dashed lines and termination reactions by dotted lines. Also, the substrate 910DMA is shown with heavy borders in the middle of the bottom row, with light (propagation) products to its right and heavy (termination) products, mostly dimers, to its left.

The free-radical cycle is initiated by the substrate 910DMA undergoing bimolecular disproportionation (R1), an intermolecular hydrogen transfer reaction, to form the respectively dehydrogenated and hydrogenated radical species 910DMA* and HDMA*. Of these, the latter can either abstract hydrogen from 910DMA substrate by (R2), to form DHDMA products (*cis-* and *trans-* not distinguished), or undergo a β-scission type of radical decomposition by (R3), forming 9MA product and a methyl radical CH_3^*. The CH_3^* can either abstract H from 910DMA substrate by (R4), to form methane product, or add to the 910DMA substrate by (R5), to form the trimethyl radical HTMA1*. The latter can then abstract H from substrate

Figure 5.44: Elementary step graph of 910DMA thermolysis mechanism.

910DMA via (R6) to form the observed 2910TMA product. Finally, the radical mechanism is terminated by the species 910DMA* and HDMA* engaging in both pure- and cross-combination, (R7-R9), to form various dimeric products. HDMA* radical can also terminate by disproportionation, (R10), to form 910DMA and DHDMA. Figure 5.45 displays the ten elementary steps that correspond to the "graph" in Figure 5.44 and the primary triad acting upon 910DMA in the pathway Figure 5.39.

5.4.2 Stoichiometric Limits

The proposed mechanism exhibits certain stoichiometric limits. Consider three cases: 1) R1, R2 and R7 only; 2) R1, R3, R4 and R7; and 3) R1, R3, R5, R6 and R8 only. The first case, R1, R2 and R7 only, produces no 9MA, TMA, or CH4 and gives the overall reaction:

$$3 \ 910DMA \rightarrow DHDMA + DMAD \tag{5.13}$$

This case yields S(DHDMA) = 0.33, S(9MA) = 0, S(CH4) = 0, S(TMA) = 0 and S(HVY) = 0.33. The second case, R1, R3, R4 and R7 only, produces no DHDMA or CH4 and gives the overall reaction:

$$3 \ 910DMA \rightarrow 9MA + CH_4 + DMAD \tag{5.14}$$
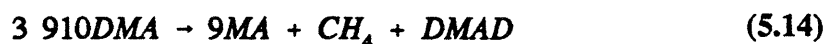
This case yields S(DHDMA) = 0, S(9MA) = 0.33, S(CH4) = 0.33, S(TMA) = 0 and S(HVY) = 0.33. The third case, R1, R3, R5, R6 and R8 only, produces no DHDMA
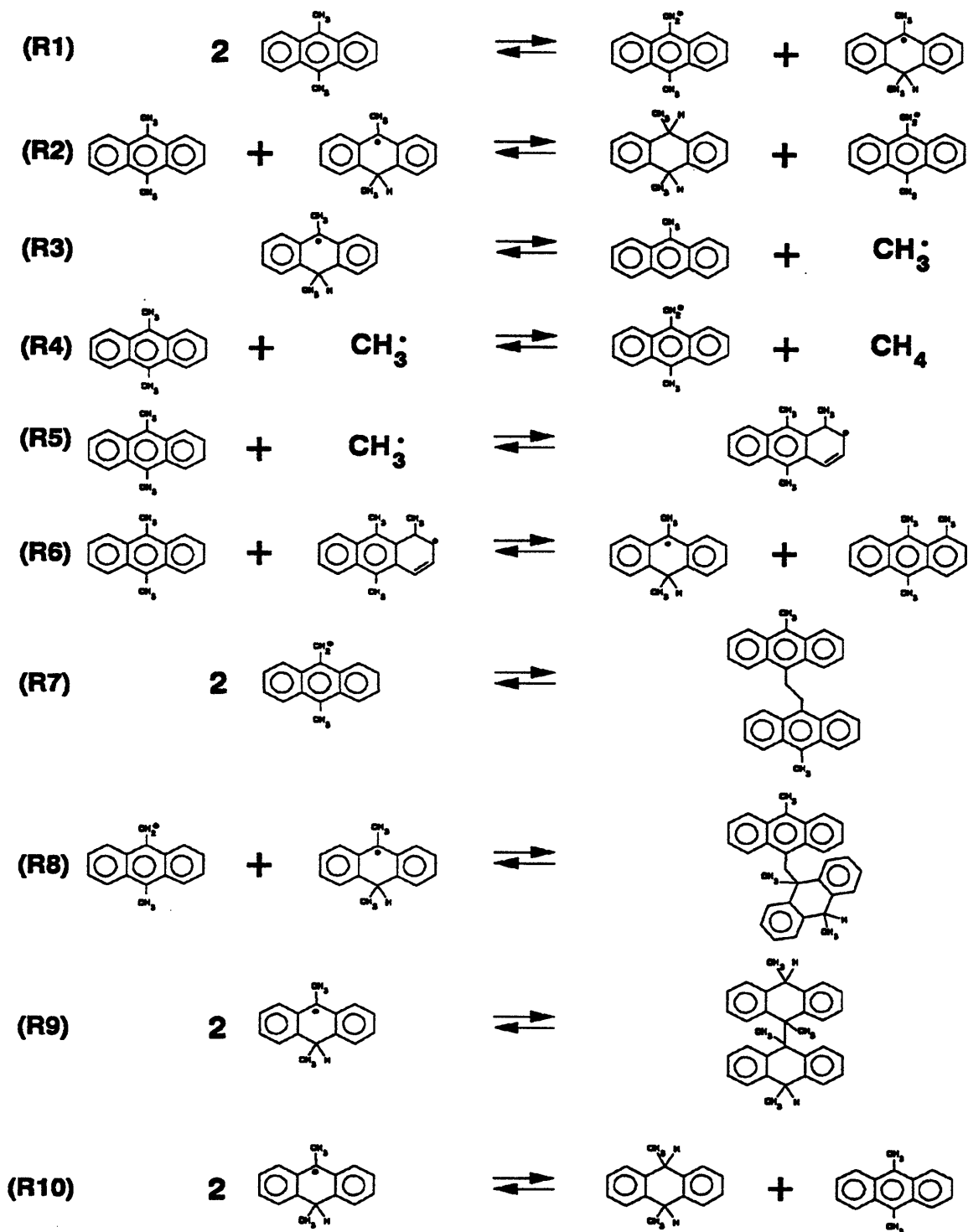
Figure 5.45: Elementary steps for the 910DMA thermolysis mechanism.

or CH4 and yields the overall reaction:

$$3 \ 910DMA \rightarrow 9MA + TMA + DMAHDMAD \qquad (5.15)$$

This case yields S(DHDMA) = 0, S(9MA) = 0.33, S(CH4) = 0, S(TMA) = 0.33 and

S(HVY) = 0.33. The mechanism thus restricts the maximum selectivities of each of

DHDMA, 9MA, TMA and heavies to 1/3.

5.4.3 Thermochemical Property Estimation

In order to derive kinetic parameters for the 910DMA mechanism, values of

the thermochemical property ΔH°_{f298}, the enthalpy of formation, were required for

all participating chemical species. Values of ΔH°_{f} for all stable species Table 5.7 are

listed in and for all radical species in Table 5.8. Each table lists the species, the

ΔH°_{f}, the source, remarks about how the ΔH°_{f} was estimated, and the error associated

with the experimental or estimated ΔH°_{f}. The upper portion of each table, above the

dashed line, lists experimental values, and their errors, for species that were used as

a basis for the present derivations, which are list below the dotted line. Data for the

basis species are from a variety of sources, including Benson (1977), abbreviated

Benson1; Shaw, Golden and Benson (1977), abbreviated ShGB; Benson et al. (1969),

abbreviated Benson2; Pedley (1976); Stein, Golden and Benson (1977), abbreviated

StGB; Stull (1969); Structure and Property Experimental (Stein et al., 1991),

abbreviated SPX; and Structure and Property Estimation (Stein et al., 1991),

abbreviated SPE. The enthalpy of formation in the tables for the species of interest

Table 5.7

ENTHALPIES OF FORMATION OF STABLE SPECIES
IN 910DMA THERMOLYSIS MECHANISM

Species	ΔH_f° (kcal/mol)	Source	Remarks	Error in ΔH_f°
ANT	55.2	Pedley		± 0.5
DHA	38.2	Pedley		± 1.1
NAP	35.9	Pedley		± 0.4
1MN	27.2	StGB		± 0.5
2MN	26.4	StGB		± 0.6
18DMN	26.0	Pedley		± 0.4
17DMN	19.6	Stull		± 0.5
14CHD[1]	25.9	ShGB		± 0.5
36DM-14CHD[2]	11.3	ShGB		± 1.0
910DMA	38.8	est	ANT + 2 (1MN - NAP) + 2 *gauche* alkene[3]	± 1.0
9MA	47.0	est	ANT + (1MN - NAP) + *gauche* alkene	± 0.8
2910TMA	28.3	est	910DMA + (2MN - NAP)	± 1.3
1910TMA	35.7	est	2910TMA + (18DMN - 17DMN)	± 1.4
cDHDMA	23.0	est	avg DHDMA = DHA + (36DM-14CHD - 14CHD) = 23.6	± 1.6
tDHDMA	24.3	est	cis & trans estimated from eqlbrm. value (Pope 1987)	± 1.6
CH4	-17.8	Benson1		± 0.1
DMAD	83.2	SPE		± 3.0
DMAHDMAD	68.6	est	interpolated from DMAD & HDMAD	± 3.0
HDMAD	53.9	SPE		± 3.0

[1]   14CHD = 1,4-cyclohexadiene

[2]   36DM-14CHD = 3,6-dimethyl-1,4-cyclohexadiene

[3]   *gauche* alkene interaction = 0.5 kcal/mol (Benson 1976)

348

Table 5.8

ENTHALPIES OF FORMATION OF RADICAL SPECIES IN 910DMA THERMOLYSIS MECHANISM

Species	$\Delta H_f°$ (kcal/mol)	Source	Remarks	Error in $\Delta H_f°$
H*	52.1	Benson1		± 0.1
DHA*	68.1	est	$D_oC\text{-}H(DPM)^1$ - $\Delta H_f°(H^*)$ + $\Delta H_f°(DHA)$	± 2.3
12DHN	30.2	Benson2		± 2.0
14DHN	32.9	ShGB		± 2.0
14DHA	49.7	ShGB		± 2.0
cyclohexane (CHX)	-29.5	ShGB		± 0.2
methylcyclohexane (MeCHX)	-37.0	Benson2		± 0.4
3-methyl-1,2-dihydroanthracene (3Me-12DHA)	39.5	est	14DHA + (12DHN - 14DHN) + (MeCHX - CHX)	± 3.5
3Me-12DHA*	71.4	est	$D_oC\text{-}H(14DHA)^2$ - $\Delta H_f°(H^*)$ + $\Delta H_f°(3Me\text{-}12DHA)$	± 4.0
CH3*	34.8	Benson1		± 0.1
910DMA*	68.7	est	$D_oC\text{-}H(9MA)^3$ - $\Delta H_f°(H^*)$ + $\Delta H_f°(910DMA)$	± 2.3
HDMA*	52.3	est	DHA* + (avgDHDMA - DHA) + $(D_oC\text{-}H(CUM)^4 - D_oC\text{-}H(ETBZ)^4)$ + 2 *gauche* alkene	± 3.7
HTMA1*	55.0	est	3Me-12DHA* + (910DMA - ANT)	± 4.2
HTMA2*	58.4	est	HTMA1* + $(D_oC\text{-}H(14DMN)^5$ - $D_oC\text{-}H(12DMN)^5)$ + (18DMN - 17DMN)	± 5.1

[1] $D_oC\text{-}H(diphenylmethane)$ = 82.0 ± 2.0 kcal/mol (Bordwell et.al. 1988)

[2] $D_oC\text{-}H(1,4\text{-}dihydroanthracene)$ = 84.0 ± 2.0 kcal/mol (NMBO estimate)

[3] $D_oC\text{-}H(9MA)$ = 82.0 ± 2.0 kcal/mol (Stein and Brown 1991)

[4] $D_oC\text{-}H(cummene)$ = 82.5 ± 1.5 kcal/mol and $D_oC\text{-}H(ethylbenzene)$ = 84.7 ± 1.5 kcal/mol (S & PX)

[5] $D_oC\text{-}H(14DHN)$ = 81.0 ± 2.0 kcal/mol and $D_oC\text{-}H(12DHN)$ = 84.0 ± 2.0 kcal/mol (NBMO estimate)

were derived using a "macro" group additivity technique, starting with a basis molecule that was as large and as structurally similar to the desired species. Other basis species were then added and subtracted from the starting species to account for structural differences between it and the desired species. These methods are illustrated for the stable species 9MA and the radical species HDMA* in Figure 5.46. Finally, Table 5.9 details the relationships between ΔH°_f for each of the species in the 910DMA mechanism and the basis set of species, corrections and bond strengths.

Table 5.10 compares the best estimates from the present "macro" group additivity technique to values from THERM, an automated thermodynamic property estimation program for radicals and molecules using Benson's group additivity method by Ritter and Bozzelli (1990). The last two columns in Table 5.10 provide results from a second, alternative, "macro" estimate using the present methods. From Table 5.10 it is seen that, for all species, our best estimates for ΔH°_f differ from THERM, and for our alternate estimates, by amounts comparable to the errors stated in Table 5.7 and Figure 5.45. Some confidence can therefore be placed upon the present ΔH°_f estimates.

5.4.4 Kinetic Parameter Estimation

Arrhenius expressions, of the form $\log_{10} k = \log_{10} A - E^*/\theta$, with rate constant k and pre-exponential factor A in units of $(l\ mol^{-\frac{1}{2}}\ s^{-\frac{1}{2}})$ and activation energy E^* in kcal/mol, were generated for each elementary step R1 - R10 of the 910DMA
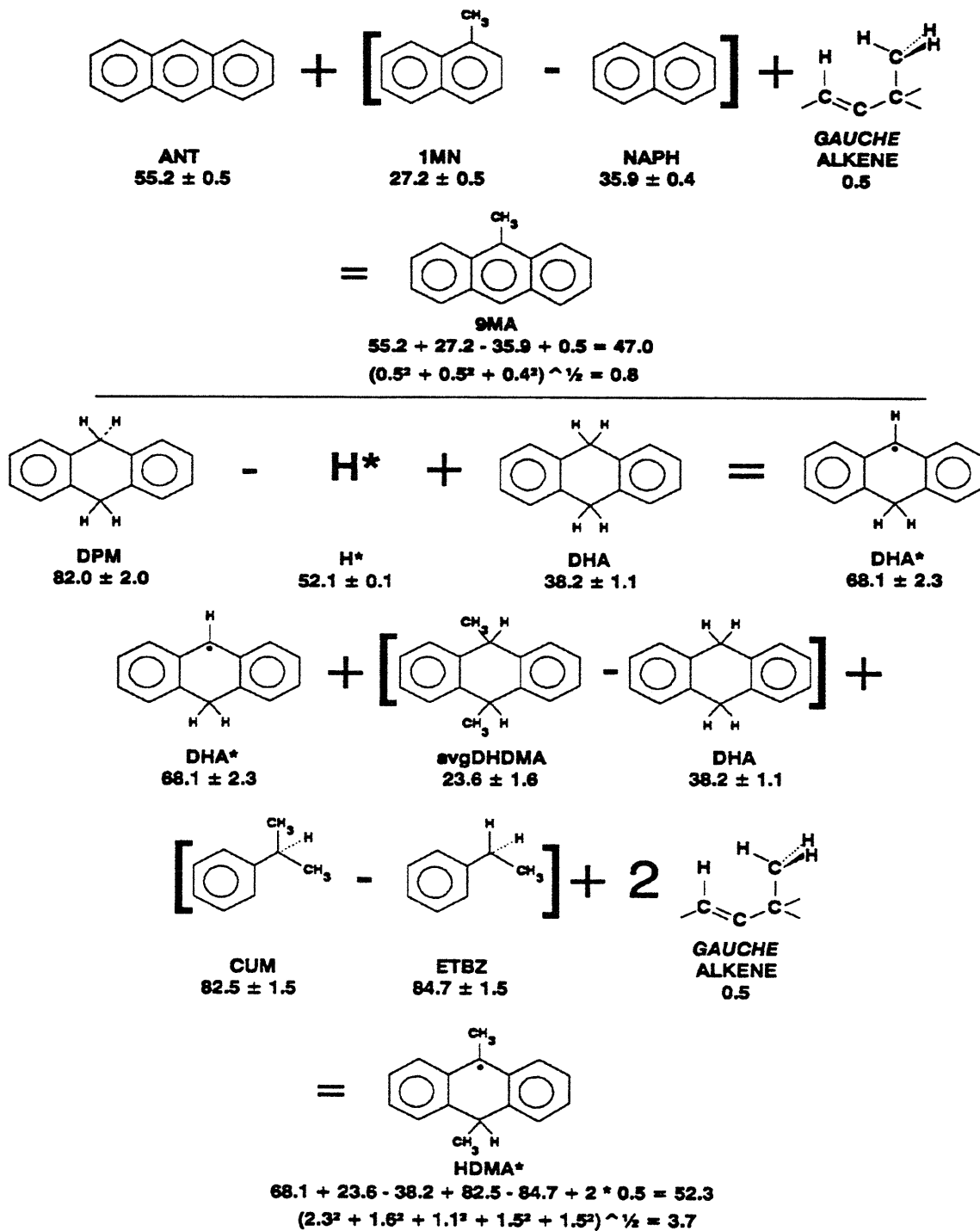
Figure 5.46: Example of the "macro" group additivity technique used to estimate enthalpies of formation for stable and radical species, and errors associated with the estimations.

351

Table 5.9

ΔHf	Species	ANT	DHA	CHD	36DM-14CHD	CHX	MeCHX	NAP	12DHN	14DHN	1MN	2MN	17DMN	18DMN	14DHA	gauche alkene	DoC-H(ETBZ*)	DoC-H(CUM*)	DoC-H(12DHN)	DoC-H(14DH-N)	DoC-H(DPM)	DoC-H(14DHA)	DoC-H(9MA)
38.8±1.0	910DMA	*				2*		2*									2*						
47.0±0.8	9MA	*				*		*									*						
28.3±1.3	2910TMA	*				2*		2*	*								2*						
35.7±1.4	1910TMA	*				2*		2*	*	*	*						2*						
23.0±1.6	cDHDMA		*	*	*																		
24.3±1.6	tDHDMA		*	*	*																		
23.6±1.6	DHDMA		*	*	*																		
30.7±1.2	DHMA		*			*	*																
68.7±2.3	910DMA*	*				2*		2*									2*						*
52.3±3.7	HDMA*		*	*	*												*	*	*			*	
55.0±4.2	HTMA1*				*	*		2*	*	*		2*		*			2*					*	
58.4±5.1	HTMA2*				*	*		2*	*	*		2*	*	*	*		2*		*	*		*	
76.9±2.2	9MA*	*				*		*															*
60.8±2.3	HMA10*		*			*	*															*	
59.6±3.1	HMA9*		*			*	*										*	*	*			*	
	ΔHf	55.2±0.5	38.2±1.1	25.9±0.5	11.3±1.0	-29.5±0.2	-37.0±0.4	35.9±0.4	30.2±2.0	32.9±2.0	27.2±0.5	26.4±0.6	19.8±0.5	26.0±0.5	49.7±2.0	0.5	84.7±1.5	82.5±1.5	84.0±2.0	81.0±2.0	82.0±2.0	84.0±2.0	82.0±2.0

Table 5.10

COMPARISON OF ΔH°_f FOR SPECIES IN 910DMA THERMOLYSIS MECHANISM

| Species | ΔH°_f (kcal/mol) from: | | | |
	Best Estimate	THERM	2nd "Macro" Estimate	Remarks on 2nd Macro Estimate
910DMA	38.8	38.2	40.0	ANT + (14DMN[1] - NAP) + 2 *gauche* alkene
9MA	47.0	45.2		
2910TMA	28.3	30.2	29.5	ANT + (14DMN - NAP) + (2MN - NAPH)
1910TMA	35.7	35.2	37.1	ANT + (18DMN - NAP) + (1MN - NAP) + *gauche* alkene
cDHDMA	23.0	25.4	23.5	DHA + (c14DM-CHX[2] - CHX)
tDHDMA	24.3	26.2	25.4	DHA + (t14DM-CHX[3] - CHX)
DMAD	83.2	83.1		
DMAHDMAD	68.6	70.0		
HDMAD	53.9	52.0		
910DMA*	68.7	67.9		
HDMA*	52.3	55.1	52.9	DHA* + (cDHDMA - DHA)
HTMA1*	55.0	53.5	57.5	3Me-12DHA*[4] + (910DMA - ANT)
HTMA2*	58.4	58.1	60.9	HTMA1* + (D°C-H(14DMN) - D°C-H(12DMN)) + (18DMN - 17DMN)

[1] 14DMN = 1,4-dimethylnaphthalene, ΔH_f° = 19.7 kcal/mol (Stull)

[2] c14DM-CHX = *cis*-1,4-dimethylcyclohexane, ΔH_f° = -42.2 kcal/mol (Benson2)

[3] t14DM-CHX = *cis*-1,4-dimethylcyclohexane, ΔH_f° = -44.1 kcal/mol (Benson2)

[4] 3Me-12DHA = ANT + (12DMN - NAPH) + (MeCHX - CHX) = 42.0 kcal/mol; 3Me-12DHA* = D₀C-H(14DHA) - ΔH_f°(H*) + ΔH_f°(3Me-12DHA) = 73.9 kcal/mol

353

thermolysis mechanism, Figure 5.45. These expressions, and information regarding their deviation, are summarized in Table 5.11, as follows. Each elementary reaction was clarified according to type (column 2), using standard free-radical reaction notation. Next, kinetic data reported in the literature for that type of reaction was analyzed to ascertain its activation parameters. Of these, $\log_{10} A$ was decomposed into an intrinsic portion, $\log_{10} A_{int}$ (column 3) and a reaction path degeneracy, rpd (column 4), with $\log_{10} A = \log_{10} A_{int} + \log_{10} (rpd)$. The activation energy E^* was determined by an Evans-Polanyi expression (column 5), of form $E^* = E_o + \alpha \Delta H^\circ_r$. Values of the enthalpy of reaction ΔH°_r (column 6), derived from the data of Section 5.4.3, then led to E^* (column 7). Final Arrhenius expressions are summarized in column 8 of Table 5.11.

Specific remarks concerning individual elementary steps and reaction types are elaborated below:

(R1) Benson (1976) estimated $\log A_{int} = 9.0 \pm 1.0$ and $E^* = \Delta H_r^\circ$ for molecular disproportionation of small hydrocarbon molecules into radicals. Stein (1981) estimates $\log A_{int} = 8.1$ for stabilized hydrocarbon radicals. Billmers et al. (1986) report $\log A_{int} = 8.7 \pm 0.14$ for molecular disproportionation of 9,10-dihydroanthracene and 2-ethylanthracene. From these, we have chosen $\log A_{int} = 8.5 \pm 0.5$ and $E^* = \Delta H^\circ_r$ to represent molecular disproportionation to radicals. Also, for k_1, rpd = 3 x 2 x 2 x 2 = 24 because each methyl group contains three hydrogen atoms, there are two methyl groups on each 910DMA, each 910DMA has two sites

354

Table 5.11

ARRHENIUS EXPRESSIONS FOR ELEMENTARY STEPS OF 910DMA THERMOLYSIS MECHANISM

	Type of Reaction	$\log_{10} A_{int}$ l mol^{-1} s^{-1}	rpd	Evans-Polanyi Relation: $E^* =$	ΔH_r° kcal/mol	E^* kcal/mol	Arrhenius Expression: $\log_{10} k =$
R1	molecular disproportionation	8.5	24	ΔH_r°	43.4	43.4	9.9 - 43.4/θ
R-1	radical disproportionation	8.5	1	0	-43.4	0	8.5
R2	H-abstraction	8.1	6	17.5 + ΔH_r°/2	1.2	18.1	8.9 - 18.1/θ
R-2	H-abstraction	8.1	2	17.5 + ΔH_r°/2	-1.2	16.9	8.4 - 16.9/θ
R3	methyl scission	13.5	1	2.1 + ΔH_r°	29.5	31.6	13.5 - 31.6/θ
R-3	CH3* addition	8.3	1	2.1	-29.5	2.1	8.3 - 2.1/θ
R4	H-abstraction	8.1	6	17.5 + ΔH_r°/2	-22.7	6.2	8.9 - 6.2/θ
R-4	H-abstraction	8.1	4	17.5 + ΔH_r°/2	22.7	28.9	8.7 - 28.9/θ
R5	CH3* addition	8.3	4	5.1	-18.6	5.1	8.9 - 5.1/θ
R-5	methyl scission	13.5	1	5.1 + ΔH_r°	18.6	23.7	13.5 - 23.7/θ
R6	radical H transfer	8.1	2	17.5 + ΔH_r°/2	-13.2	10.9	8.4 - 10.9/θ
R-6	radical H transfer	8.1	1	17.5 + ΔH_r°/2	13.2	24.1	8.1 - 24.1/θ
R7	radical combination	9.3	1	0	-54.2	0	9.3
R-7	homolytic dissociation	15.5	1	ΔH_r°	54.2	54.2	15.5 - 54.2/θ
R8	radical combination	9.3	1	0	-52.4	0	9.3
R-8	homolytic dissociation	15.5	1	ΔH_r°	52.4	52.4	15.5 - 52.4/θ
R9	radical combination	9.3	1	0	-50.7	0	9.3
R-9	homolytic dissociation	15.5	1	ΔH_r°	50.7	50.7	15.5 - 50.7/θ
R10	radical disproportionation	8.5	1	0	-42.2	0	8.5
R-10	molecular disproportionation	8.5	4	ΔH_r°	42.2	42.2	9.1 - 42.2/θ

355

for hydrogenation (9 and 10), and each of the two 910DMA can serve as either hydrogen donor or acceptor.

(R-1) Radical disproportionation is estimated to have the same $\log A_{int} = 8.5 \pm 0.5$ as molecular disproportionation, with activation energy $E^* = 0$. For k_{-1}, rpd = 1.

(R2) H-abstraction by a hydrocarbon radicals has been correlated by Kerr (1973), who provides $\log A_{int} = 7.7$ and $E_o = 12.7$ kcal/mol for $C_2H_5^*$ and $\log A_{int} = 8.2$ and $E_o = 14.3$ kcal/mol for CH_3^*, and by Benson (1976), who quotes $\log A_{int} = 8.2$ and $E_o = 14.6$ kcal/mol for CH_3^*. Also, Ingold (1973) reported on CH_3^* abstracting hydrogen from toluene with $\log A_{int} = 8.1$ and $E^* = 9.5$ kcal/mol, from which the corresponding Evans-Polanyi relation, with a slope α of 0.5 and $\Delta H^\circ_r = -16.0$ kcal/mol yields $E_o = 17.5$ kcal/mol. Figure 5.47 shows the Evans-Polanyi plot for CH3* and C2H5* abstracting hydrogen. We use Ingolds' results, $\log A_{int} = 8.1$ and $E^* = 17.5 + \Delta H^\circ_r/2$, as the basis for all H-abstraction kinetics.

(R-2) Since the microscopic reverse of an H-abstraction is another H-abstraction, the same parameters apply to R-2 as were used for R2.

(R3) Methyl scissions, a particular type of β-scission reaction, typically have $\log A = 13.5$ and $E^* = 7 + \Delta H^\circ_r$ (Kerr 1983, Dean 1985). For (R3), the value of $E_o = 7$ kcal/mol has been adjusted, as explained below for (R-3), to $E_o = 2.1$ kcal/mol.

(R-3) Holt and Kerr (1977) provide Arrhenius parameters of $\log A_{int} = 8.3$ and $E^* = 7.6$ kcal/mol for CH3* addition to benzene. The activation energy for the addition of a methyl radical to 9MA will be less than that for the addition to benzene
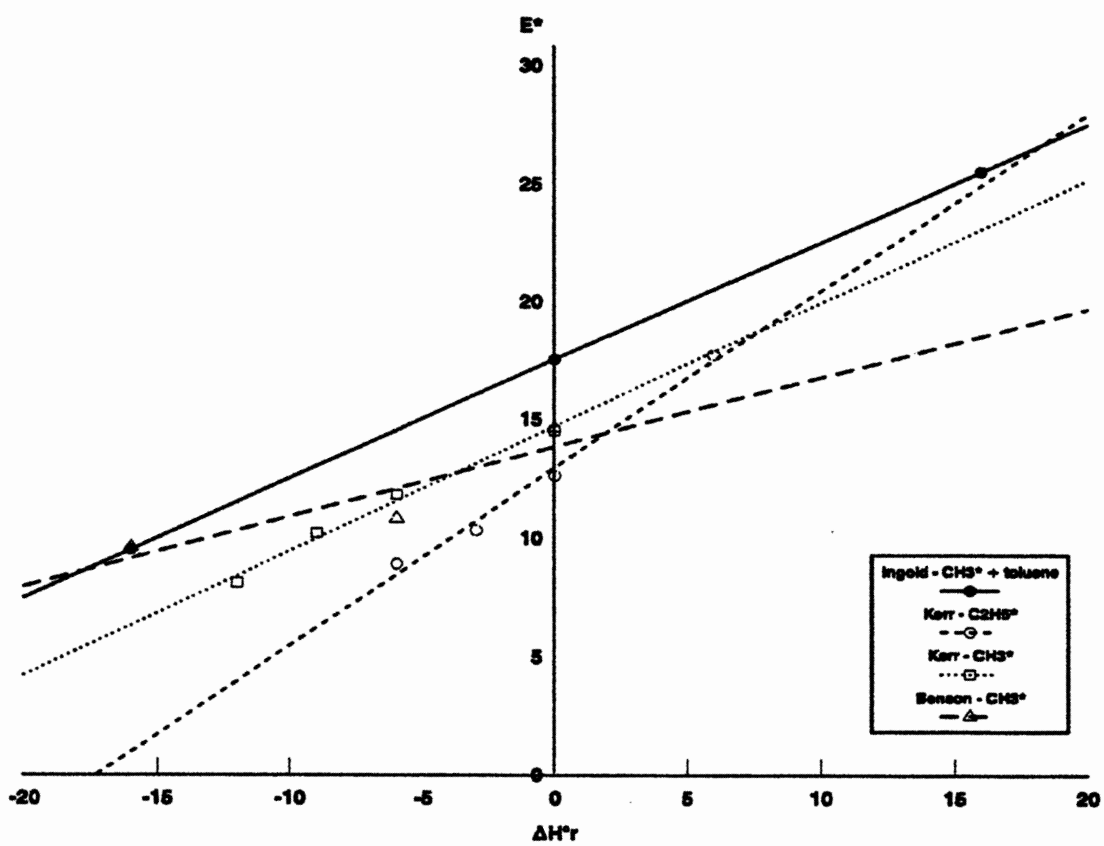
Figure 5.47: Evans-polanyi plot for H-abstraction by CH3* and C2H5*.

357

because of the lower localization energy in 9MA. This adjustment was estimated from Stephani and Szwarc (1962) who found that at 85°C the rate of methyl addition to anthracene was 2460 times faster than the rate of methyl addition to benzene. Assuming equal pre-exponential factors, the rate difference corresponds to a difference in activation energy of 5.5 kcal/mol. Thus $E^* = 2.1$ for CH3* addition to 9MA; this is also the value of E_0 in the Evans-Polanyi relation for the reverse methyl scission reaction (R3).

(R4 and R-4) These are H-abstractions, treated in the same manner as (R2 and R-2). (R5 and R-5) These are analogous to (R-3 and R3) discussed above with the difference that in (R5) the required adjustment of the activation energy was estimated from Stephani and Szwarc (1962) who found that at 85°C the rate of methyl addition to naphthalene was 33 times faster than the rate of methyl addition to benzene; this corresponds to an activation energy difference of 2.5 kcal/mol. Thus, $E^* = 5.1$ for (R5), and this is also E_0 for (R-5). Also, for k_5, rpd = 4 (pi bonds).

(R6 and R-6) These radical hydrogen transfer (RHT) reactions, wherein a hydrogen atom differ somewhat from the conventional H-abstraction, wherein the H-atom transfers from a molecule to a radical. Billmers et al. (1986) estimated log A = 8.2 + log rpd and E_0 = 18.3 kcal/mol for a thermoneutral H transfer at 350°C from a 9-hydroanthryl radical to 2-ethylanthracene. We directly apply the H-abstraction relations, developed for R2 and R-2, to the present RHTs R6 and R-6.

(R7) Ingold (1973) quotes radical combination rates of log k = 9.3 for two benzyl (also two cumyl) radicals. Benson (1976) has log k = 9.5 for two *t*-butyl radicals, and Miller and Stein (1981) give log k = 9.5 for two α-1,2-diphenylethyl radicals. Since radical combinations are unactivated, that is, $E^* = 0$, we choose log A = 9.3 for all pure benzyl radical combinations.

(R-7) For homolytic dissociation into stabilized radicals, Benson (1976) estimated log A = 15.5 ± 0.5 and $E^* = \Delta H_r^\circ$. Miller and Stein (1981) used log A = 15.9 and $E^* = \Delta H_r^\circ = 57.5$ kcal/mol for 1,2,3,4-tetraphenylbutane dissociating into two α-1,2-diphenylethyl radicals. We adopt Benson's parameters.

(R8 and R-8) Radical combination and homolytic dissociation analogous to (R7 and R-7) except that R8 is a cross-combination, so the $k_8 = 2\, k_7 k_9$ and log $k_8 = 9.6$.

(R9 and R-9) Radical combination and homolytic dissociation also analogous to (R7 and R-7).

(R10 and R-10) Radical and molecular disproportionations are analogous to (R1 and R-1).

5.4.5 Modelling

The 910DMA thermolysis mechanism devised in Figure 5.44 combined with the Arrhenius expressions derived for each elementary step in Table 5.11 provided a mechanistic kinetic model of 910DMA thermolysis, valid at low conversions, over the entire initial concentration and temperature ranges of the present experiments.

Results of this mechanistic model, and comparisons between these and experimental results, are detailed in this section. Most model calculations were made at the center of the experimental grid, where $[910DMA]_o = 0.82$ mol/l and T = 355°C. Selected calculations were also made at the four corners of the grid, for $[910DMA]_o = 0.082$ and 2.47 mol/l at T = 355°C and at T = 315 and 409°C for $[910DMA]_o = 0.82$ mol/l. The scheme of calculations was as follows. First an algebraic analysis was performed, to estimate the pseudo-steady-state radical concentrations at selected low conversions; these served to verify the validity of subsequent numerical solutions. Next, full numerical solutions were obtained for the model 910DMA thermolysis mechanism, using a computer code ("ACUCHEM", Braun et al., 1988) for solving the system of simultaneous differential equations for the conservation of all species. The calculated product histories, selectivities and product ratios were compared with experimental values. A sensitivity analysis of the model was performed at the central point of the experimental grid, by separately perturbing selected elementary step kinetics over their estimated uncertainty limits. Based on this, a set of "optimized" kinetic parameters were derived to best-fit the model to experimental observations.

5.4.5.1 Algebraic Analysis

The pseudo-steady-state approximation is applied to the radical species, whereby the rate of change in the concentration of all radical species is deemed to

be ~ 0. In our case, this yields four algebraic equations, one for each radical species, as shown in Figure 5.48. When added together, these equations provide an expression equating the rate of initiation LHS to the rate of termination RHS. Given the concentrations of stable species, and all rate constants, the foregoing system of algebraic equations can be solved (e.g. by successive approximations) to provide the concentrations of all radicals species. Results for the solution at $[910DMA]_o = 0.82$ mol/l and $T = 355°C$ at initial conditions of $X = 0$, where substrate is the only stable species, are given in column 2 of Table 5.12. It is seen that 910DMA* and HDMA* are the most prevalent radicals, with concentrations respectively 4.5E-08 and 6.7E-09 mol/l. These results can further be used to calculate instantaneous rates of formation for all products at $X = 0$, based on which it is possible to estimate the amounts of all species at an adjacent (low) conversions, say $X = 0.05$. Here the pseudo-steady-state calculations can be repeated with the new stable species concentrations, to provide a new set of radical concentrations. Column 3 of Table 5.12 shows results obtained in this manner at $X = 0.10$. It is seen the 910DMA* and HDMA* remain the dominant radical species, but their concentrations, respectively 9.1E-8 and 5.3E-9 mol/l differ somewhat from the values at $X = 0$.

The final two columns of Table 5.12 show radical and stable species concentrations calculated (see below) during the full numerical solution for $[910DMA]_o = 0.82$ mol/l and $T = 355°C$ at conversions respectively $X \rightarrow 0$ (very low)

$$\frac{d[910DMA*]}{dt} = k_1[910DMA]^2 - k_{-1}[HDMA*][910DMA*] + k_2[910DMA][HDMA*]$$

$$- k_{-2}[DHDMA][910DMA*] + k_4[910DMA][CH3*] - k_{-4}[910DMA*][CH4]$$

$$- 2k_7[910DMA*]^2 + 2k_{-7}[DMAD] - k_8[910DMA*][HDMA*]$$

$$+ k_{-8}[DMAHDMAD] = 0$$

$$\frac{d[HDMA*]}{dt} = k_1[910DMA]^2 - k_{-1}[HDMA*][910DMA*] - k_2[910DMA][HDMA*]$$

$$+ k_{-2}[DHDMA][910DMA*] - k_3[HDMA*] + k_{-3}[9MA][CH3*]$$

$$+ k_6[HTMA*][910DMA] - k_{-6}[TMA][HDMA*] - k_8[910DMA*][HDMA*]$$

$$+ k_{-8}[DMAHDMAD] - 2k_9[HDMA*]^2 + 2k_{-9}[HDMAD]$$

$$- 2k_{10}[HDMA*] + 2k_{-10}[910DMA][DHDMA] = 0$$

$$\frac{d[CH3*]}{dt} = k_3[HDMA*] - k_{-3}[9MA][CH3*] - k_4[910DMA][CH3*]$$

$$+ k_{-4}[CH4][910DMA*] - k_5[910DMA][CH3*] + k_{-5}[HTMA*] = 0$$

$$\frac{d[HTMA*]}{dt} = k_5[910DMA][CH3*] - k_{-5}[HTMA*] - k_6[910DMA][HTMA*]$$

$$+ k_{-6}[TMA][HDMA*] = 0$$

ADDING TOGETHER:

$$k_1[910DMA]^2 + k_{-7}[DMAD] + k_{-8}[DMAHDMAD] + k_{-9}[HDMAD] + k_{-10}[910DMA][DHDMA]$$

$$= k_7[910DMA*]^2 \left(1 + \frac{(k_{-1} + k_8)[HDMA*]}{k_7[910DMA*]} + \frac{(k_9 + k_{10})[HDMA*]^2}{k_7[910DMA*]^2}\right)$$

Figure 5.48: Steady-state expression for the radical species in the 910DMA mechanism.

Table 5.12

COMPARISON OF PSEUDO-STEADY-STATE AND FULL NUMERICAL SOLUTION RESULTS FOR 910DMA THERMOLYSIS WITH [910DMA]$_o$ = 0.82 mol/l AND T = 355°C

Species	Pseudo-Steady-State		Numerical Solution	
	X = 0	X = 0.10	X → 0	X = 0.10
910DMA*	4.49E-08[1]	9.10E-08	4.17E-08	8.28E-08
HDMA*	6.71E-09	5.28E-09	6.11E-09	6.97E-09
CH3*	5.43E-13	3.04E-13	3.08E-13	3.64E-13
HTMA*	3.23E-11	1.31E-11	1.60E-11	1.73E-11
910DMA	8.20E-01	7.38E-01	8.20E-01	7.36E-01
9MA	0	1.56E-02	1.92E-05	1.49E-02
DHDMA	0	1.59E-02	1.99E-05	1.40E-02
CH4	0	1.57E-02	1.39E-05	1.09E-02
TMA	0	6.14E-02	5.26E-06	3.95E-03
DMAD	0	3.36E-02	3.45E-05	2.50E-02
DMAHDMAD	0	0	5.03E-06	6.27E-03
HDMAD	0	0	7.19E-07	1.38E-05

[1] Values in table are species concentrations in mol/l

and X = 0.10. The numerical solution also shows 910DMA* and HDMA* to be the dominant radical species at both conversions. Also, the concentrations of all species, both radical and stable, calculated by the numerical solution agree quite closely , to within a factor of 2 or better, with corresponding results obtained from the pseudo-steady-state algebraic solution. This bolsters our confidence in the fidelity of the numerical solution results.

5.4.5.2 Numerical Solutions and Comparison with Experiments

Conservation relations derived from the mechanistic model of 910DMA thermolysis and using the rate constants of Section 5.4.4 were numerically integrated using a computer program called ACUCHEM (Braun et al., 1988). This is a program that numerically solves a system of differential equations that describe the temporal behavior of a spatially homogeneous, isothermal, multicomponent chemical reaction system. To perform integrations in a reliable and efficient manner, ACUCHEM uses a suite of subroutines called DDRIV which are designed to solve general systems of nonlinear ordinary differential equations. It has options that solve for the solution of "stiff" or "nonstiff" equations, but always uses the former, as appropriate for kinetics problems. DDRIV uses variable order, variable step methods of the "linear multivalue" type, meaning it automatically adapts its integration step size, including the initial step as well as the integration formula order to the problem. The integration methods are implicit, and require the use of a

Jacobian matrix, which is formed exactly by ACUCHEM. The user's integration tolerance governs the error control mechanism which in turn controls the step size strategy. We used the recommended integration tolerance of 0.001, which controls the integration step size. Errors are measured on a per step basis. Thus, there is no guarantee that cumulative errors will not be significantly larger, but Braun et. al. (1988) stated that for stable problems, this very rarely occurs. DDRIV is derived from method described by Gear (1971).

Initial conditions $[910DMA]_o$ and T were chosen to match experimental initial conditions, rate constants for each elementary step at the given T were set and the program then generated results for all species concentrations versus time. By invoking both program options for the concentration versus time output, either 50 equispaced points over a designated time range or specific times at which to print concentrations, it was verified the concentration versus time profile for all species was independent of the nominal time interval chosen. Representative results at $[910DMA]_o$ = 0.82 mol/l and T = 355°C, obtained by using both of these options, are shown in Figure 5.49 and Figure 5.50. Comparisons between the upper and lower panels of Figure 5.49, which show concentration histories respectively calculated at 50 equispaced times and at the experimental times, show no significant differences for any of the four radical species, 910DMA*, HDMA*, CH3*, and HTMA*, for $[910DMA]_o$ = 0.82 mol/l and T = 355°C. This figures also shows that the radical concentrations do not vary significantly with time, that is the psuedo-
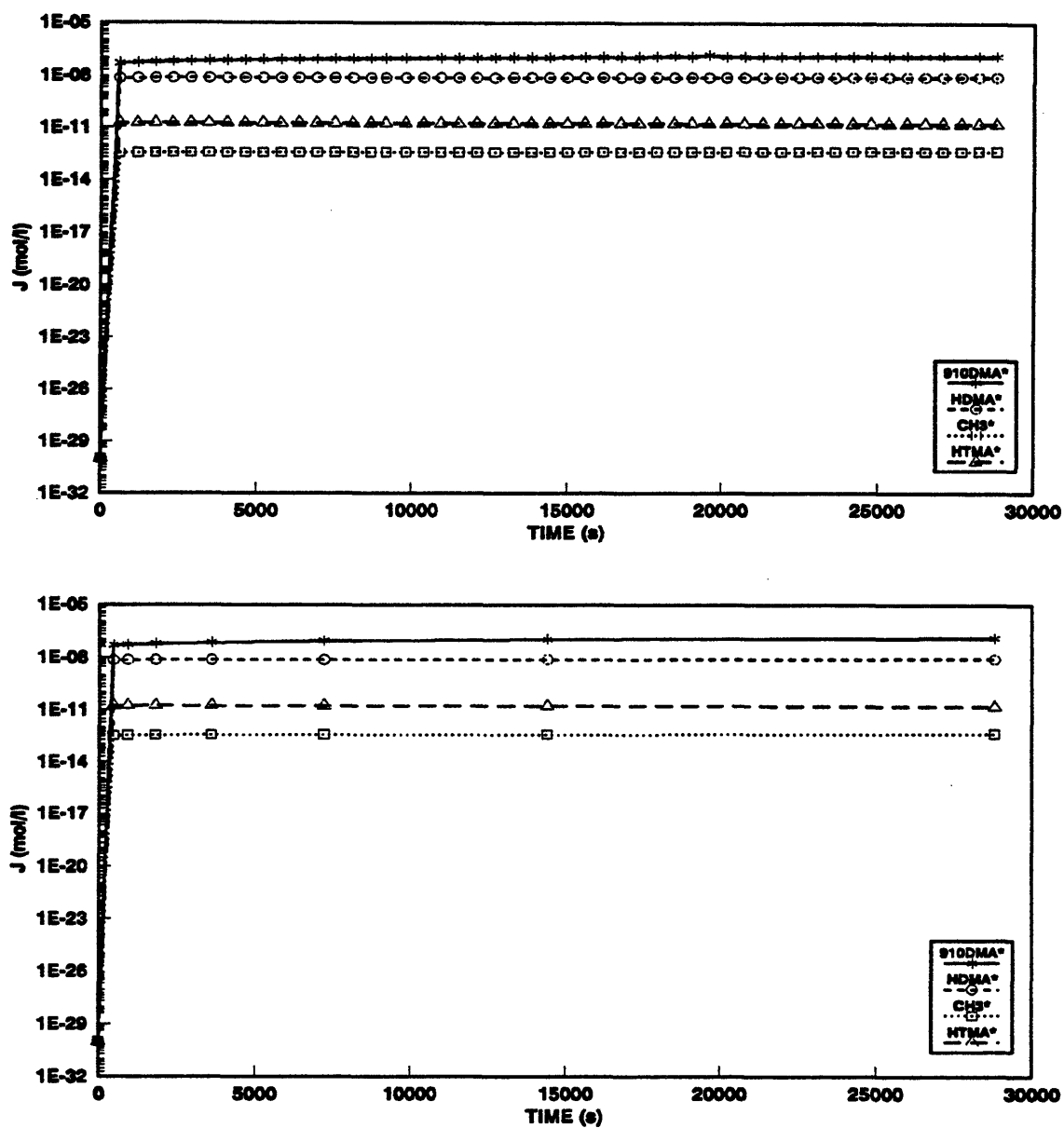
Figure 5.49: Comparison of ACUCHEM outputs from 50 equispaced points over the time range from the experiments (top) and times corresponding to experiments (bottom) for $[910DMA]_o$ = 0.82 mol/l and T = 355°C.
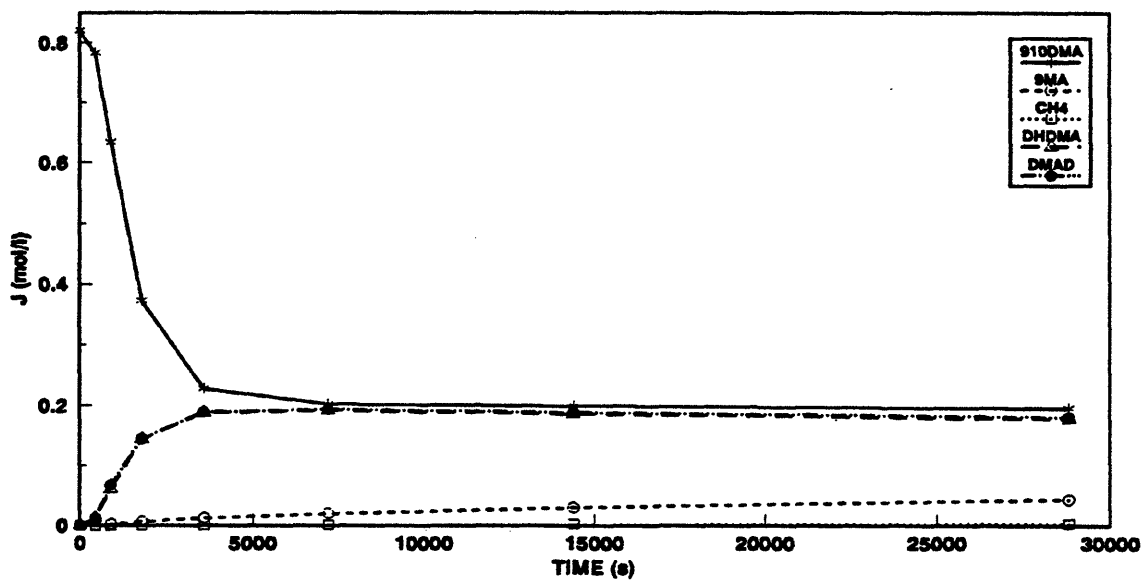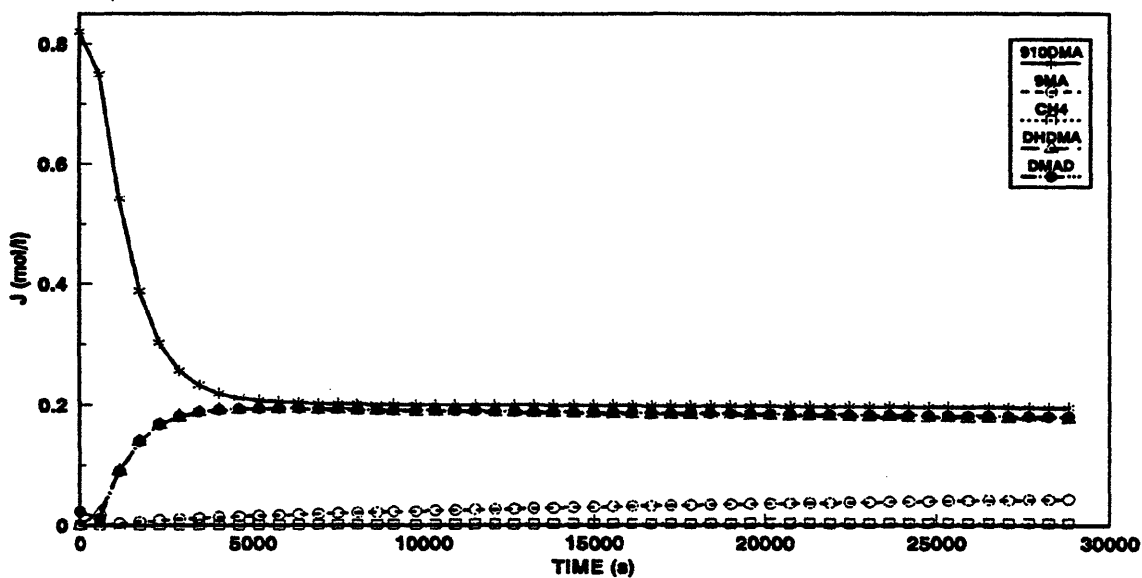
Figure 5.50: Comparison of ACUCHEM outputs from 50 equispaced points over the time range from the experiments (top) and times corresponding to experiments (bottom) for $[910DMA]_o$ = 0.82 mol/l and T = 355°C.

367

steady-state approximation is valid. Comparisons between the upper and lower panels of Figure 5.50, which show concentration histories respectively calculated at 50 equispaced times and at the experimental times, show no significant differences for any of the five major species, 910DMA, 9MA, CH4, DHDMA and DMAD, for $[910DMA]_o = 0.82$ mol/l and T = 355°C.

5.4.5.2.1 Detailed Calculations at T = 355°C for $[910DMA]_o = 0.82$ mol/l

Table 5.13 and Table 5.14 detail our numerical solution of the model at the central point, T = 355°C and $[910DMA]_o = 0.82$ mol/l, of the experimental grid. Columns 2-4 of Table 5.13 show Arrhenius expressions, with pre-exponential factor A (l mol^{-1} s^{-1} units), activation energy E* in kcal/mol and rate constant k (l mol^{-1} s^{-1} units), for each elementary step R1 - R10 of the 910DMA thermolysis mechanism (columns 2-4). The radical and stable species concentrations generated by the numerical solution were then used with the rate constants to ascertain the rate, in mol l^{-1} s^{-1}, of each forward and reverse reaction in the 910DMA thermolysis mechanism at two conversions X = 0.001 (limit X ~ 0) and X = 0.31, as shown in the last two columns of Table 5.13. The rates of the elementary reactions were then used to calculate the rates of radical and stable species formation at X = 0.001 and X = 0.31 as shown in columns 3 and 5 respectively of Table 5.14. The elementary reactions that contribute to the formation of each radical and stable species are listed in column 2 of Table 5.14, while those reactions that make the major contributions

Table 5.13

ARRHENIUS EXPRESSIONS, RATE CONSTANTS AND RATES OF ELEMENTARY STEPS IN THE MODEL 910DMA THERMOLYSIS AT T = 355°C WITH [910DMA]$_o$ = 0.82 mol/l

			k	Rate, r(mol/l s), at Conversion (X)	
	$\log_{10} A$	E^*	(T = 355°C)	0.001	0.31
R1	9.9	43.4	6.13E-06	4.12E-06	1.98E-06
R-1	8.5	0	3.16E+06	8.27E-08	3.26E-07
R2	8.9	18.1	3.96E+02	2.01E-06	1.80E-06
R-2	8.4	16.9	3.28E+02	1.39E-09	1.42E-06
R3	13.5	31.6	3.14E+02	1.95E-06	2.51E-06
R-3	8.3	2.1	3.70E+07	1.12E-09	8.40E-07
R4	8.9	6.2	5.51E+06	1.41E-06	1.31E-06
R-4	8.7	28.9	4.33E-02	1.28E-13	2.29E-10
R5	8.9	5.1	1.33E+07	3.41E-06	3.16E-06
R-5	13.5	23.7	1.77E+05	2.87E-06	2.80E-06
R6	8.4	10.9	4.02E+04	5.35E-07	3.61E-07
R-6	8.1	24.1	5.11E-01	8.39E-14	5.39E-11
R7	9.3	0	2.00E+09	3.55E-06	3.32E-05
R-7	15.5	54.2	4.24E-04	7.35E-08	3.16E-05
R8	9.3	0	2.00E+09	5.22E-07	2.06E-06
R-8	15.5	52.4	1.79E-06	4.42E-08	2.05E-06
R9	9.3	0	2.00E+09	7.67E-08	1.27E-07
R-9	15.5	50.7	7.01E-03	2.24E-08	1.28E-07
R10	8.5	0	3.16E+08	1.22E-08	2.02E-08
R-10	9.1	42.2	2.54E-06	2.09E-10	4.84E-08

Table 5.14

CALCULATED RATES OF FORMATION OF RADICAL AND STABLE SPECIES AT X = 0.001 AND 0.31 AT T = 355°C WITH [910DMA]$_o$ = 0.82 mol/l

	CONTRIBUTING REACTIONS	r (mol/l s) at X = 0.001	Major Contribution	r (mol/l s) at X = 0.31	Major Contribution
r(910DMA*)	R1 - R-1 + R2 - R-2 + R4 - R-4 - 2R7 + 2R-7 - R8 + R-8	2.0E-08		1.3E-07	
r(HDMA*)	R1 - R-1 - R2 + R-2 - R3 + R-3 + R6 - R-6 - R8 + R-8 - 2R9 + 2R-9 - 2R10 + 2R-10	7.5E-09		1.4E-08	
r(CH3*)	R3 - R-3 - R4 + R-4 - R5 + R-5	-6.9E-09		-8.1E-09	
r(HTMA*)	R5 - R-5 - R6 + R-6	5.2E-09		5.1E-09	
r(910DMA)	-2R1 + 2R-1 - R2 + R-2 - R4 + R-4 - R5 + R-5 - R6 + R-6 + R10 - R-10	-1.3E-05	R1, R2, R4, R5, R-5	-6.1E-06	R1, R2, R-2, R4, R5, R-5
r(9MA)	R3 - R-3	1.9E-06	R3	1.7E-06	R3
r(TMA)	R6 - R-6	5.3E-07	R6	3.6E-07	R6
r(CH4)	R4 - R-4	1.4E-06	R4	1.3E-06	R4
r(DHDMA)	R2 - R-2 + R10 - R-10	2.0E-06	R2	3.5E-07	R2, R-2
r(DMAD)	R7 - R-7	3.5E-06	R7	1.6E-06	R7, R-7
r(DMAHDMAD)	R8 - R-8	4.8E-07	R8	8.7E-09	R8, R-8
r(HDMAD)	R9 - R-9	5.4E-08	R9	-1.2E-10	R9, R-9

370

to the formation of the stable species at the low and high conversions are noted columns 4 and 6. It is seen that the rate of destruction of 910DMA is dominated by R1 (4.12E-06), R2 (2.01E-06), R4 (1.41E-06), R5 (3.41E-06) and R-5 (2.87E-06) at X = 0.001 and by R1 (1.98E-06), R2 (1.80E-06), R-2 (1.42E-06), R4 (1.31E-06), R5 (3.16E-06) and R-5 (2.80E-06) at X = 0.31. The rate of formation of 9MA is controlled by R3 (1.85E-06 and 2.51E-06, respectively) at both X = 0.001 and X = 0.31, whereas the rate formation of CH4 and TMA are controlled by R4 (1.41E-06 and 1.31E-06) and R6 (5.35E-07 and 3.61E-07), respectively, at both low and high conversions. The rate of formation of DHDMA is the sum of R2, R-2, R10 and R-10, but R2 (2.01E-06) is the major contribution to the rate of formation of DHDMA at X = 0.001 and R2 (1.80E-06) and R-2 (1.42E-06) are the major contributions at X = 0.31. The rates of dimer formation, r(DMAD), r(DMAHDMAD), and r(HDMAD), are controlled by the respective termination reactions, R7 (3.55E-06), R8 (5.22E-07) and R9 (7.67E-08) at low conversions, whereas at X = 0.31, the dimer formation rates are controlled by R7 (3.32E-05) and R-7 (3.16E-05), R8 (2.06E-06) and R-8 (2.05E-06) and R9 (1.27E-07) and R-9 (1.28E-07). Figure 5.51 graphically depicts the elementary reaction traffic during 910DMA thermolysis at X → 0, with the thicker arrows denoting reactions with the greater net (forward - backward) rates. Figure 5.52 presents a similar depiction of reaction traffic at X = 0.31.

Figure 5.53 compares the substrate and product histories (upper panel) and product selectivities (lower panel) as obtained from numerical solution of the
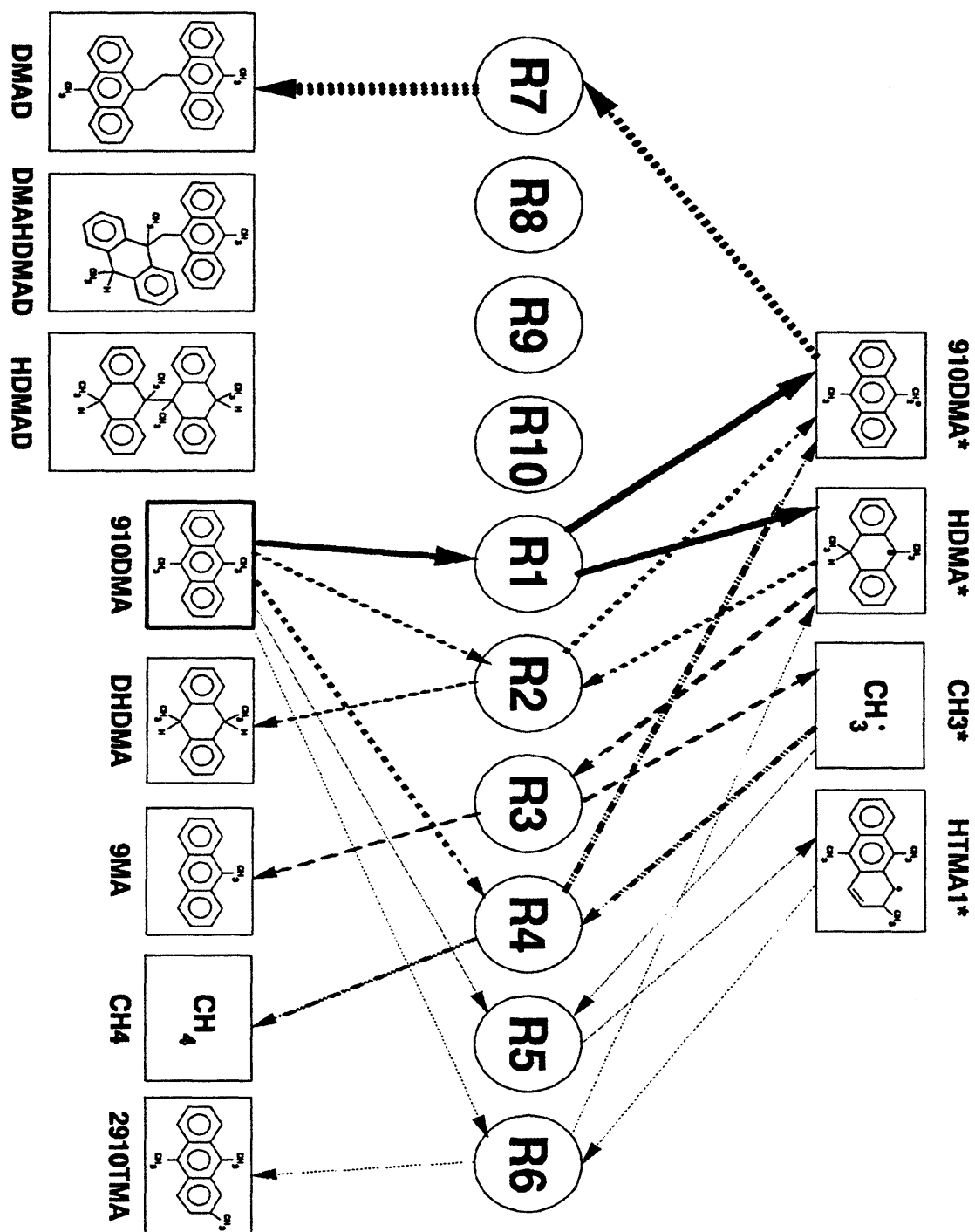
Figure 5.51: Relative elementary reaction rate traffic at T = 355°C and with [910DMA]$_o$ = 0.82 mol/l for X → 0.
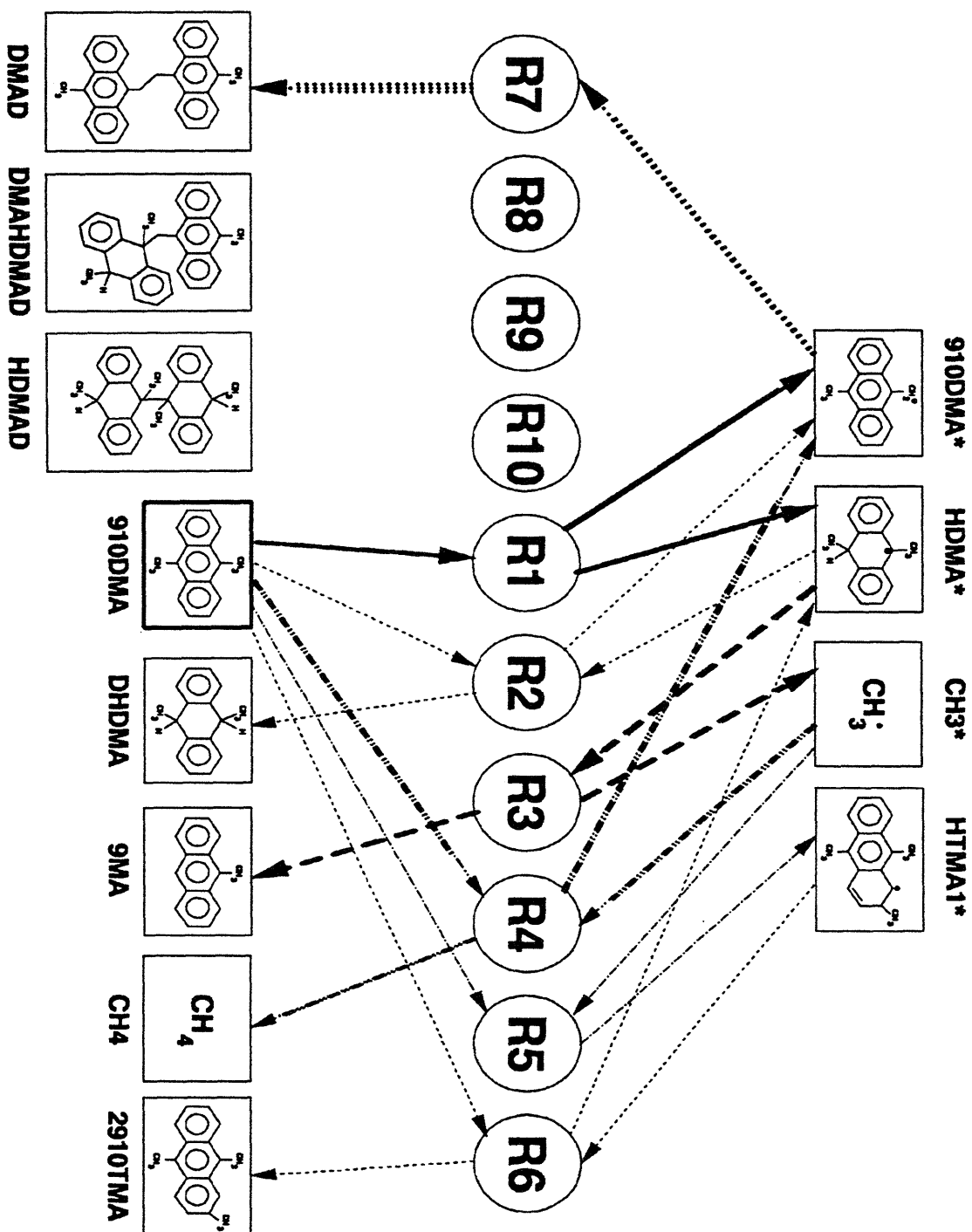
Figure 5.52: Relative elementary reaction rate traffic at T = 355°C and with [910DMA]$_o$ = 0.82 mol/l for X = 0.31.
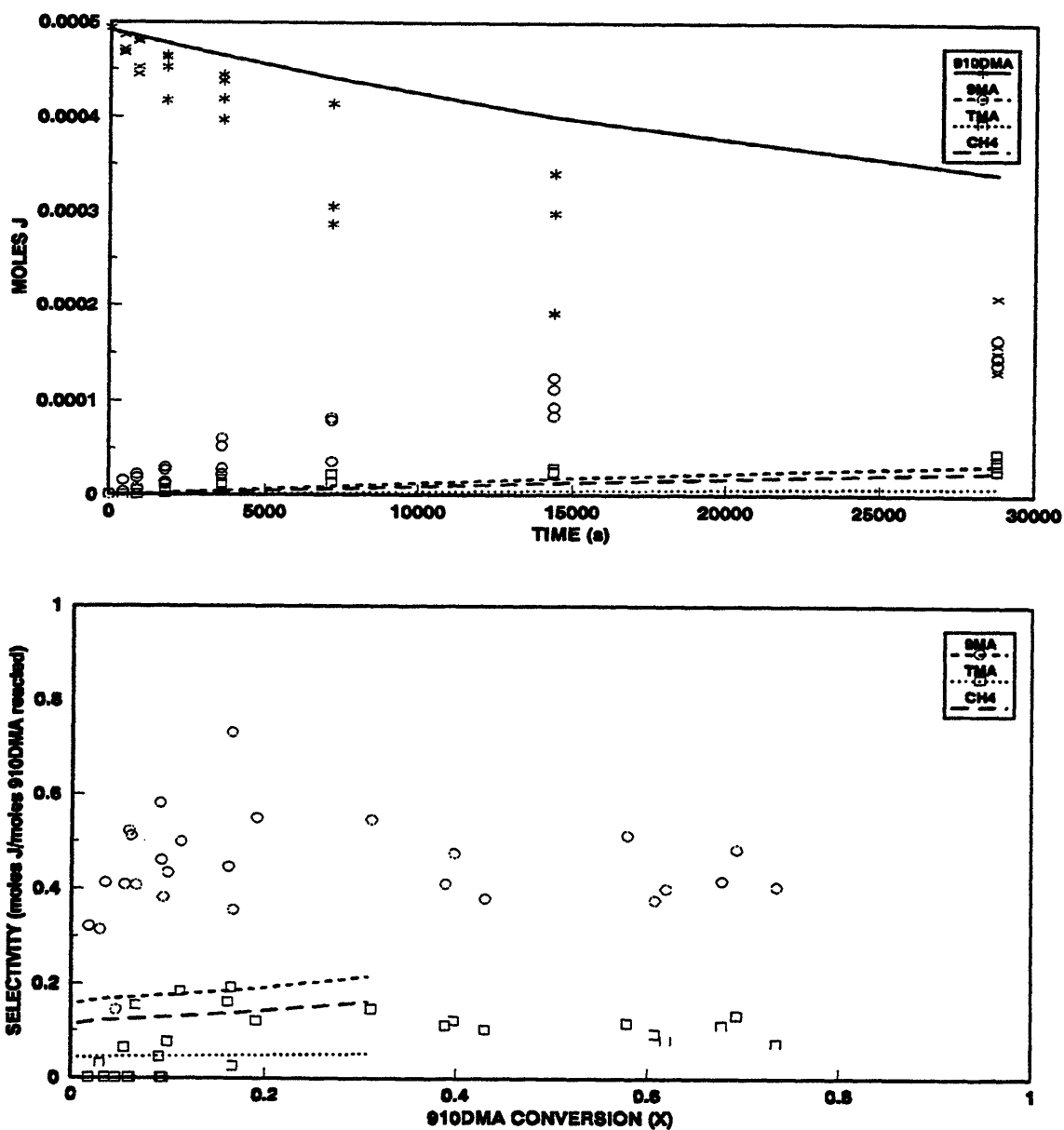
Figure 5.53: Product histories (top) and selectivity diagram (bottom) comparing model results (lines) to experimental data (symbols) for 910DMA, 9MA, TMA and CH4 at T = 355°C with [910DMA]$_o$ = 0.82 mol/l.

thermolysis model to the experimental data for 910DMA, 9MA, TMA and CH4 at the center of the experimental grid, [910DMA]o = 0.82 mol/l and T = 355°C. In the upper panel of Figure 5.53, the model is seen to predict 910DMA decay, the solid line, that is too slow compared to the experimental observations, shown as asterisks. The model half-life, t^*, is 2.6-fold slower than the experimental. The upper panel of Figure 5.53 also shows that the absolute amounts of 9MA, the short-dashed line versus the circles, and of TMA, the dotted line versus the squares, formed by the model are both lower than observed in the experiments. However, the model predicts the relative amounts of 9MA > CH4 > TMA and the sum of CH4 plus TMA equal to the 9MA produced, both of which accord with the experiment. The lower panel of Figure 5.53 shows that the selectivities S(9MA) and S(TMA) from the model are respectively 2.5 and 2.2-fold too low compared to the average values of S(9MA) and S(TMA) observed from the experiments between 0.1 < X < 0.8.

Figure 5.54 continues the comparison between model (solid line) and experimental (circles) product histories and selectivities for DHDMA product. In the upper panel of this figure, the model is seen to predict DHDMA amounts generally higher than experimentally observed, the more so at the longer times. In the lower panel of Figure 5.54, a selectivity diagram, we see that, relative to experiments,
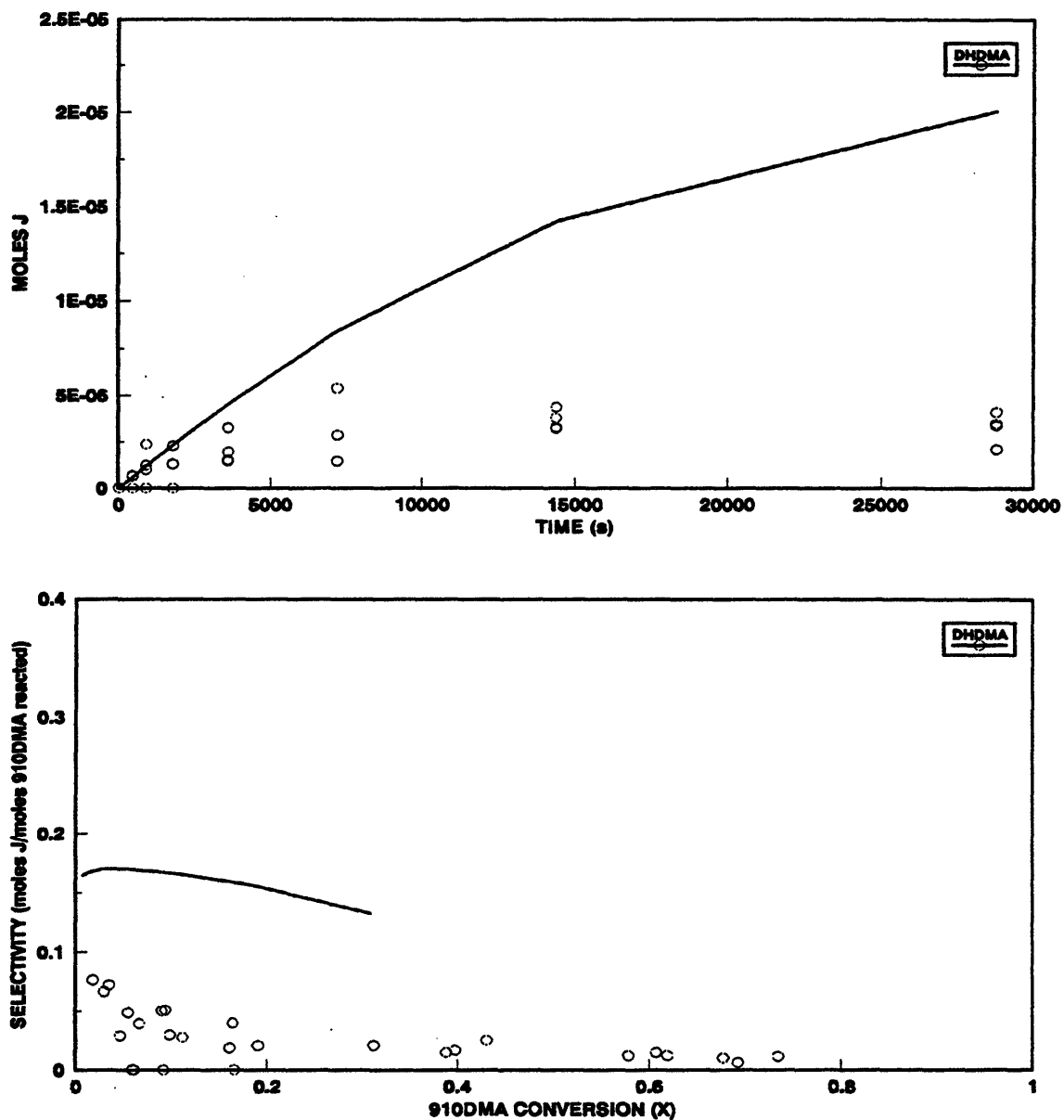
Figure 5.54: Product histories (top) and selectivity diagram (bottom) comparing model results (lines) to experimental data (symbols) for DHDMA at T = 355°C with $[910DMA]_0$ = 0.82 mol/l.

S(DHDMA) from the model is 1.8-fold too high at low conversions, $X \sim 0.06$, and 3.7-fold too high for $X > 0.2$.

Figure 5.55 compares the model calculation (lines) to the experimental data (solid circles) for heavies (DMAD, DMAHDMAD and HDMAD). Since these heavies were not specifically assayed, the moles of heavies produced in the experiments were calculated by subtracting the sum of the selectivities of detected species (Σ) from 1, multiplying this result by the concentration of 910DMA converted and then dividing by two since the heavies were essentially dimers of 910DMA. In the upper panel of Figure 5.55, the model is seen to predict heavies production comparable to the experiments at shorter times, but produces more dimer than seen in the experiments at long times. Also, the model predicts the dominant heavy dimer to be DMAD, which was the only dimer detected in the experiments by GC/MS, in Figure 4.9. The lower panel of Figure 5.55 shows that the dimer selectivity S(DMAD) ~ 0.3 calculated from the model is close to the experimental S(HVY) $\sim$ 0.25 at low $X < 0.1$, but whereas the S(HVY) in the experiments decreases to ~ 0.1 with increasing conversion, S(DMAD) from the model remains roughly constant at S(DMAD) ~ 0.3. For $X > 0.2$, S(DMAD) is 2.8-fold higher than the experimental S(HVY).

Finally, Figure 5.56 compares the product ratios R[DHDMA/9MA] and R[TMA/9MA] as functions of 910DMA conversion (X) derived from the model (lines) to those observed experimentally (symbols). In the upper panel of

377
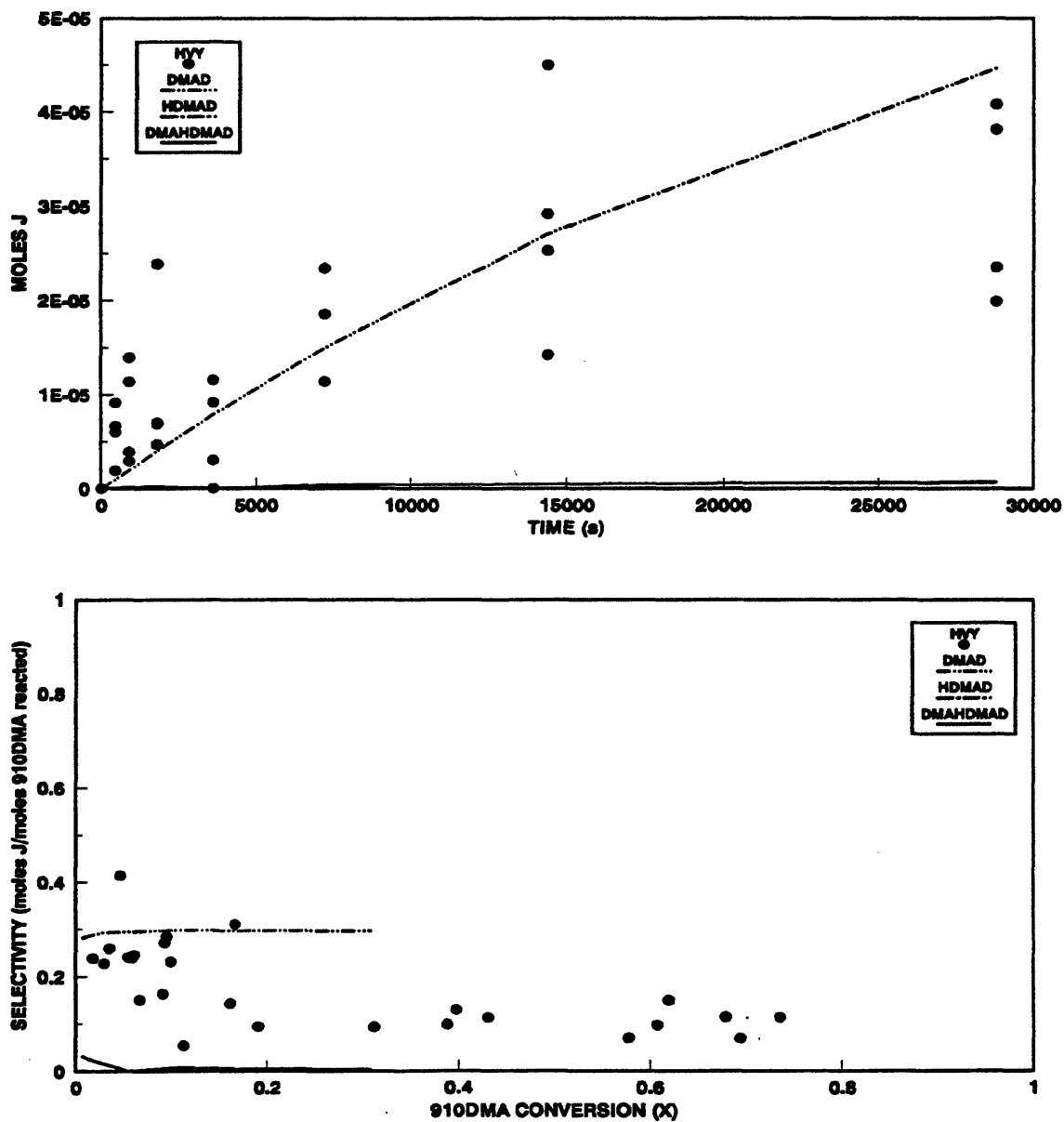
Figure 5.55: Product histories (top) and selectivity diagram (bottom) comparing model results (lines) to experimental data (symbols) for heavies at T = 355°C with $[910DMA]_o$ = 0.82 mol/l.
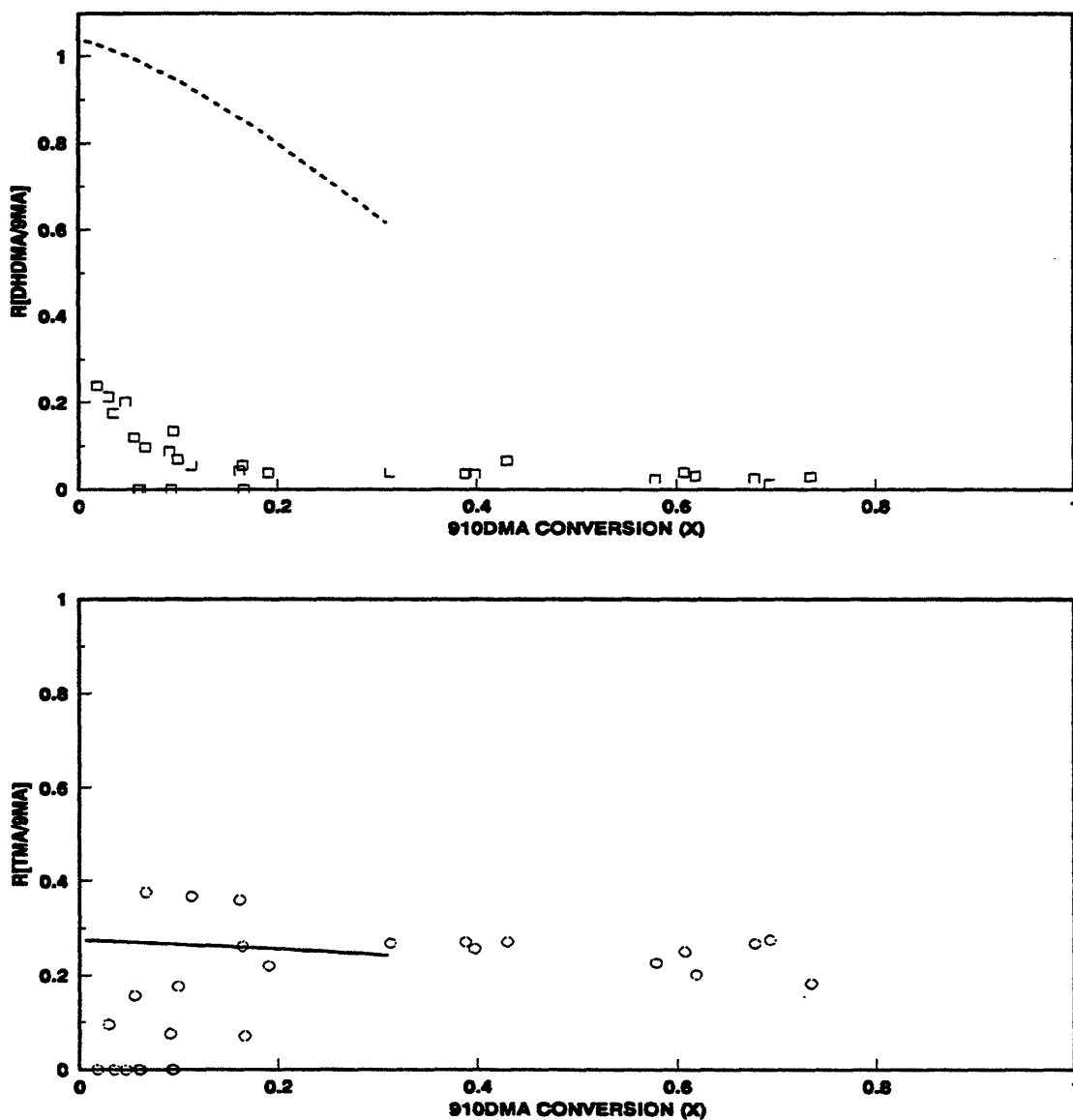
Figure 5.56: Ratio of moles DHDMA to moles 9MA produced vs. 910DMA conversion (top) and ratio of moles TMA to moles 9MA produced vs. 910DMA conversion (bottom) at T = 355°C with $[910DMA]_o$ = 0.82 mol/l.

379

Figure 5.56, the model is seen to predict R[DHDMA/9MA] about 4-fold higher than experimental at low conversions, X ~ 0.05, and almost 10-fold higher than experimental for X > 0.2. In the lower panel of Figure 5.56, the model is seen to predict R[TMA/9MA] approximately equal to that experimentally observed at all conversions 0 < X < 0.3.

5.4.5.2.2 Model Results at All T and [910DMA]$_o$

Table 5.15 compares with experiments the 910DMA decay half-life, major product selectivities and product ratios obtained from numerical solutions of the 910DMA thermolysis model for varying initial concentrations at fixed T = 355°C, while Table 5.16 compares experimental and model results for varying temperature at fixed [910DMA]$_o$ = 0.82 mol/l.

In parts (a) of Table 5.15 and Table 5.16 and in the corresponding Figure 5.57 and Figure 5.58, the model is seen to predict 910DMA decay half-lifes t^* too long, that is, decay kinetics too slow, compared to the experimental observations at all initial concentrations and temperatures. From part (a) of Table 5.15, as [910DMA]$_o$ increases from 0.082 to 2.47 mol/l at T = 355°C, the ratio of model to experimental half-lifes R[mod/exp] decreases from 9.3 to 2.1, indicating that the model decay is of higher order in [910DMA]$_o$ than experimental. Figure 5.57, a log-log plot of t^* vs. [910DMA]$_o$, shows that the model (hollow points, dashed line) yields a slope -0.93, implying ~ 2 order, versus the experimental (solid points, solid line) data that yield

380

Table 5.15

COMPARISON OF MODEL TO EXPERIMENTAL DATA
AT T = 355°C FOR VARYING [910DMA]$_o$

Part	X:			[910DMA]$_o$ (mol/l)		
---	---	---	---	0.082	0.82	2.47
a	Half-life		exp	59067	21912	11891
	t* (s)		mod	551693	57258	24448
			R[mod/exp]	9.34	2.61	2.06
b	S(9MA)	0.1-0.8	exp	0.65	0.48	0.45
			mod	0.31	0.19	0.10
			R[mod/exp]	0.48	0.40	0.22
	S(TMA)	0.1-0.8	exp	0.04	0.11	0.16
			mod	0.013	0.049	0.043
			R[mod/exp]	0.32	0.45	0.27
c	S(DHDMA)	0.06	exp	0.10	0.09	0.15
		0.06	mod	0.029	0.17	0.24
			R[mod/exp]	0.29	1.89	1.60
		0.2-0.85	exp	0.021	0.014	0.024
			mod	0.028	0.13	0.17
			R[mod/exp]	1.33	9.29	7.08
d	S(HVY)	0.2-0.85	exp	0.12	0.10	0.10
			mod	0.32	0.28	0.28
			R[mod/exp]	2.70	2.80	2.80
e	R[DHDMA/9MA]	0.06	exp	0.24	0.24	0.37
		0.06	mod	0.10	1.00	2.91
			R[mod/exp]	0.42	4.17	7.86
		0.2-0.85	exp	0.035	0.035	0.035
			mod	0.091	0.62	0.91
			R[mod/exp]	2.60	17.7	26.0
f	R[TMA/9MA]	0.1-0.8	exp	0.086	0.23	0.29
			mod	0.042	0.27	0.46
			R[mod/exp]	0.48	1.17	1.59

Table 5.16

COMPARISON OF MODEL TO EXPERIMENTAL DATA WITH $[910DMA]_o$ = 0.82 mol/l FOR VARYING T

Part	X:			Temperature (°C)		
				315[1]	355	409
a	Half-life		exp	300000	21912	1311
	t^* (s)		mod	570077	57258	4992
			R[mod/exp]	1.90	2.61	3.81
b	S(9MA)	0.1-0.8	exp	0.52	0.48	0.45
			mod	0.11	0.19	0.25
			R[mod/exp]	0.21	0.40	0.56
	S(TMA)	0.1-0.8	exp	0.20	0.11	0.11
			mod	0.046	0.049	0.034
			R[mod/exp]	0.23	0.45	0.31
c	S(DHDMA)	0.06	exp	0.090	0.10	ND
		0.06	mod	0.21	0.16	0.098
			R[mod/exp]	2.22	1.60	-
		0.2-1.0	exp	0.05	0.014	< 0.01
			mod	0.23	0.13	0.0019
			R[mod/exp]	4.60	9.29	-
d	S(HVY)	0.2-1.0	exp	0.060	0.10	0.10
			mod	0.28	0.28	0.30
			R[mod/exp]	4.67	2.80	3.00
e	R[DHDMA/9MA]	0.06	exp	0.39	0.24	ND
		0.06	mod	2.16	1.00	0.44
			R[mod/exp]	5.54	4.17	-
		0.2-1.0	exp	0.044	0.044	0.044
			mod	1.98	0.62	0.046
			R[mod/exp]	45.0	14.1	1.05
f	R[TMA/9MA]	0.1-0.8	exp	0.24	0.24	0.24
			mod	0.41	0.27	0.15
			R[mod/exp]	1.71	1.13	0.63

[1] For T = 315°C, maximum X_{exp} = 0.10 compared with maximum X_{mod} = 0.08

[2] ND = not detected

382
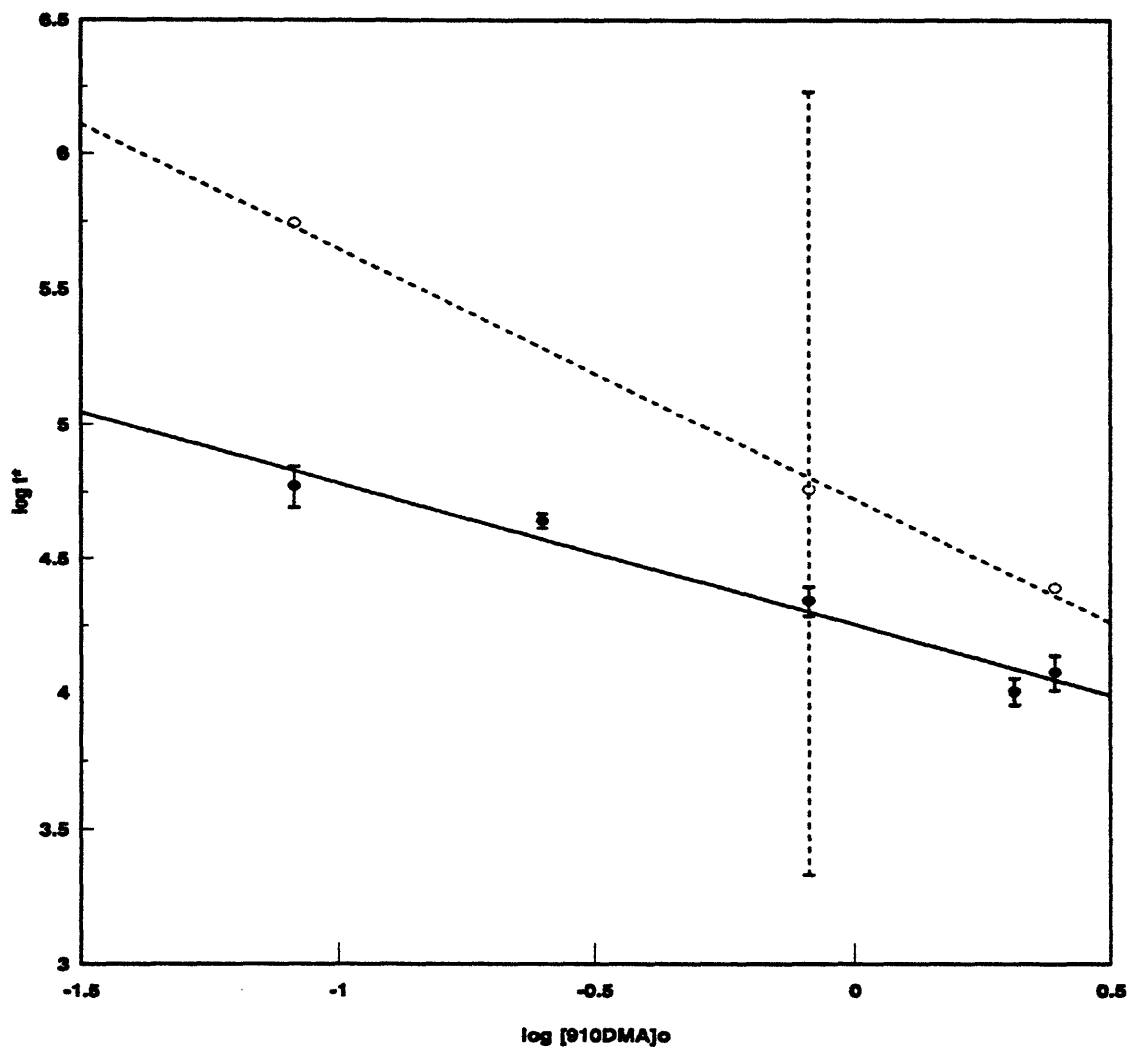
Figure 5.57: Decay half-life t^*_{exp} (solid line & circles) and t^*_{mod} (dashed line, circles; vertical line-error band from sensitivity analysis) for varying $[910DMA]_o$ at fixed T=355°C.

383
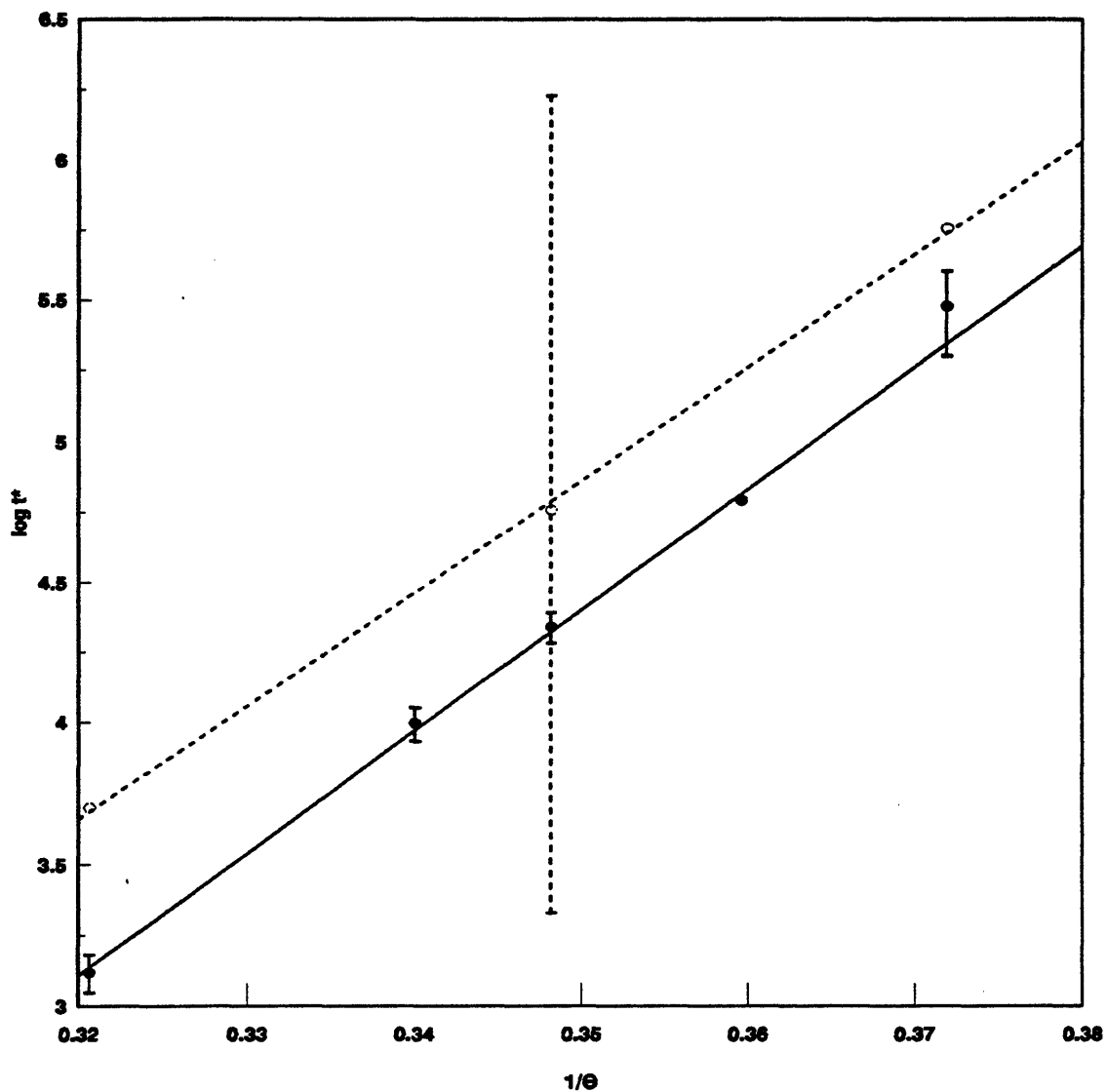
Figure 5.58: Decay half-life t^*_{exp} (solid line, circles) and t^*_{mod} (dashed line, hollow circles, vertical dashed line indicates error band) for varying T with fixed $[910DMA]_o = 0.82$ mol/l.

a slope of -0.53, implying 1½ order decomposition kinetics. From part (a) of Table 5.16, increasing temperature from 315 to 409°C increases the R[mod/exp] from 1.9 to 3.8, indicating that the model 910DMA decay is slightly less activated than the experiments. This is also borne out by Figure 5.58, a semi-log plot of t^* vs. $1/\theta$, wherein the model (hollow points, dashed line) yields an activation energy 40.1 kcal/mol versus the experimental (solid points, solid lines) data that provided E^* ~ 43.1 kcal/mol. It should be noted that the vertical lines in both Figure 5.57 and Figure 5.58 represent results of a sensitivity analysis of the present 910DMA thermolysis model at T = 355°C and $[910DMA]_o$ = 0.82 mol/l that are discussed in a subsequent section.

Parts (b) of Table 5.15 and Table 5.16, refer to the selectivities of 9MA and TMA products for 0.1 < X < 0.8. As initial concentrations increase from 0.082 to 2.47 mol/l, model calculations show S(9MA) decreasing from 0.31 to 0.10 while S(TMA) increases from 0.013 to ~ 0.045. Both S(9MA) and S(TMA) predicted by the model are lower than experimental, with respective ratios R[mod/exp] decreasing from 0.48 to 0.22 for 9MA and remaining roughly constant at 0.38 ± 0.05 for TMA. With increasing temperatures from 315 to 409°C, the model calculations show S(9MA) increasing from 0.11 to 0.25 while S(TMA) decreases slightly from 0.046 to 0.034. Both S(9MA) and S(TMA) from the model are lower than experimental, with respective ratios R[mod/exp] increasing from 0.21 to 0.56 for 9MA and remaining roughly constant at 0.34 ± 0.11 for TMA. Figure 5.59 graphically depicts the results
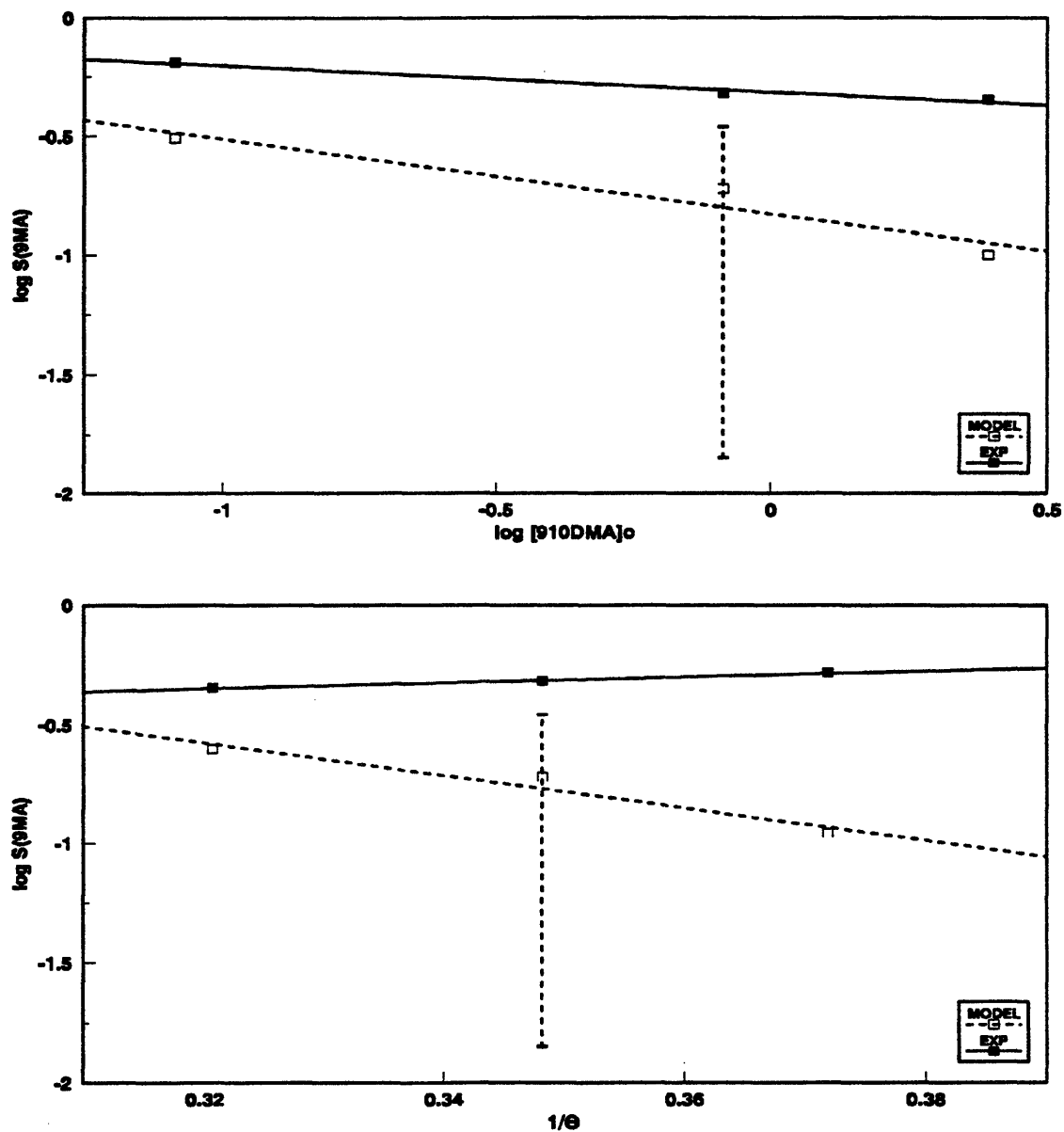
Figure 5.59: Comparison of experiment (solid squares) and model (squares) S(9MA) for varying $[910DMA]_o$ at fixed T = 355°C (top) and varying T with fixed $[910DMA]_o$ = 0.82 mol/l (bottom).

for S(9MA) on log-log coordinates of S(9MA) vs. $[910DMA]_o$ (upper panel) and semi-log coordinates of S(9MA) vs. $1/\theta$ (lower panel). In the upper panel, it is seen that the model S(9MA) decreases more strongly, slope -0.31, than in the experiments, slope -0.11; thus the model exhibits an order for 9MA formation that is less than that for 910DMA decay by more than that observed experimentally. Also, in the lower panel of Figure 5.59, the model S(9MA) decreases more strongly with increasing $1/\theta$, that is decreasing temperature, slope -6.88, than in the experiments which show S(9MA) essentially independent of temperature, slope 1.22; thus the model predicts 9MA formation to be more activated than 910DMA decay by ~ 7 kcal/mol whereas the experiments show 910DMA decay to be more activated than 9MA formation by ~ 1 kcal/mol. The vertical dashed lines in both upper and lower panels of Figure 5.59 are results of a sensitivity analysis discussed in a subsequent section.

Parts (c) of Table 5.15 and Table 5.16 show the selectivities of DHDMA product, at both low (X ~ 0.06) and high (X > 0.2) conversions. At low conversions, in Table 5.15, as $[910DMA]_o$ increases from 0.082 to 2.47 mol/l, S(DHDMA) from the model increases from 0.029 to 0.24 with its ratio R[mod/exp] increasing from 0.29 to ~ 1.8; in Table 5.16, as T increases from 315 to 409°C, S(DHDMA) from the model decreases from 0.21 to 0.10, with R[mod/exp] decreasing slightly from 2.2 at T = 315°C to 1.6 at T = 355°C (there were no reliable experimental values for S(DHDMA) at T = 409°C). Thus it is seen that, at low conversions, the DHDMA selectivities predicted by the model are essentially the same as those observed

experimentally; from the ratios R[mod/exp], the dependence of S(DHDMA) on [910DMA]$_o$ predicted by the model exceeds that observed experimentally. While the dependence of S(DHDMA) on T of the model is essentially the same as experimental over a limited range $315 < T < 355°C$. At high conversions, in Table 5.15, as [910DMA]$_o$ increases from 0.082 to 2.47 mol/l, S(DHDMA) from the model increases from 0.028 to 0.17 with its ratio R[mod/exp] increasing from 1.33 to 7.1; in Table 5.16, as T increases from 315 to 409°C, S(DHDMA) from the model decreases from 0.23 to 0.002, with R[mod/exp] increasing from 4.6 at T = 315°C to 9.3 at T = 355°C (the experimental value for S(DHDMA) at T = 409°C is < 0.01). Thus it is seen that, at high conversions, the DHDMA selectivities predicted by the model are appreciably higher than those observed experimentally, with ratios R[mod/exp] up to 10 at the lower T and higher [910DMA]$_o$.

Parts (d) of Table 5.15 and Table 5.16, refer to the selectivities of heavy products (sum of DMAD, DMAHDMAD and HDMAD) for $0.2 < X < 0.85$. As initial concentrations increase from 0.082 to 2.47 mol/l, model calculations show S(HVY) decreasing from 0.32 to 0.28. S(HVY) predicted by the model are higher than experimental, with respective ratios R[mod/exp] remaining roughly constant at 2.75 ± 0.05. With increasing temperatures from 315 to 409°C, the model calculations show S(HVY) increasing from 0.28 to 0.30. S(HVY) from the model are higher than experimental, with ratios R[mod/exp] increasing from 4.70 at T = 315°C to 10 ± 2.5 at T = 355 and 409°C. Thus it is seen that the HVY selectivities predicted by the

model are higher than those observed experimentally; from the ratios R[mod/exp], the dependence of S(HVY) is essentially the same as experimental for all [910DMA]$_o$. While the dependence of S(HVY) on T predicted by the model exceeds that observed experimentally, more so at the higher T.

Parts (e) of Table 5.15 and Table 5.16 show the ratio of DHDMA product to 9MA product, at both low (X ~ 0.06) and high (X > 0.2) conversions. At low conversions, in Table 5.15, as [910DMA]$_o$ increases from 0.082 to 2.47 mol/l, R[DHDMA/9MA] from the model increases from 0.10 to 2.9 with its ratio R[mod/exp] increasing from 0.42 to 7.9; in Table 5.16, as T increases from 315 to 409°C, R[DHDMA/9MA] from the model decreases from 2.2 to 0.44, with R[mod/exp] decreasing slightly from 5.5 at T = 315°C to 4.3 at T = 355°C (there were no reliable experimental values for DHDMA at T = 409°C). Thus it is seen that, at low conversions, the R[DHDMA/9MA] predicted by the model are lower those observed experimentally at the lowest [910DMA]$_o$ and as [910DMA]$_o$ > 0.82 mol/l, become higher than those observed experimentally; from the ratios R[mod/exp], the dependence of R[DHDMA/9MA] on [910DMA]$_o$ predicted by the model exceeds that observed experimentally. While the dependence of R[DHDMA/9MA] on T of the model is essentially the same as experimental over a limited range 315 < T < 355°C. At high conversions, in Table 5.15, as [910DMA]$_o$ increases from 0.082 to 2.47 mol/l, R[DHDMA/9MA] from the model increases from 0.091 to 0.91 with its ratio R[mod/exp] increasing from 2.6 to 26.0; in

Table 5.16, as T increases from 315 to 409°C, R[DHDMA/9MA] from the model

decreases from 2.0 to 0.046, with R[mod/exp] decreasing from 45.0 to 1.1. Thus it

is seen that, at high conversions, the R[DHDMA/9MA] predicted by the model are

appreciably higher than those observed experimentally, with ratios R[mod/exp] up

to 26 at the higher [910DMA]$_o$ and up to 45 at the lower T. Figure 5.60 graphically

depicts the results for R[DHDMA/9MA] on log-log coordinates of

R[DHDMA/9MA] vs. [910DMA]$_o$ (upper panel) and semi-log coordinates of

R[DHDMA/9MA] vs. 1/θ (lower panel). In the upper panel, it is seen that, at low

conversions, the model R[DHDMA/9MA] increases more strongly, slope 0.99, than

in the experiments, slope 0.11; thus the model exhibits an order for DHDMA

formation that is higher than that for 9MA formation by more than that observed

experimentally. At high conversions, the model R[DHDMA/9MA] increases more

strongly, slope 0.78, than in the experiments which show R[DHDMA/9MA]

essentially independent of initial concentration, slope 0; thus the model exhibits again

exhibits an order for DHDMA formation that is higher than that for 9MA formation

whereas experiments show DHDMA and 9MA formation to be about the same

order. Also, in the lower panel of Figure 5.60, at low conversions, the model

R[DHDMA/9MA] increases more strongly with increasing 1/θ, that is decreasing

temperature, slope 13.4, than in the experiments, slope 8.9; thus the model predicts

9MA formation to be more activated than DHDMA formation by ~ 13 kcal/mol

whereas the experiments show 9MA formation to be more activated than DHDMA
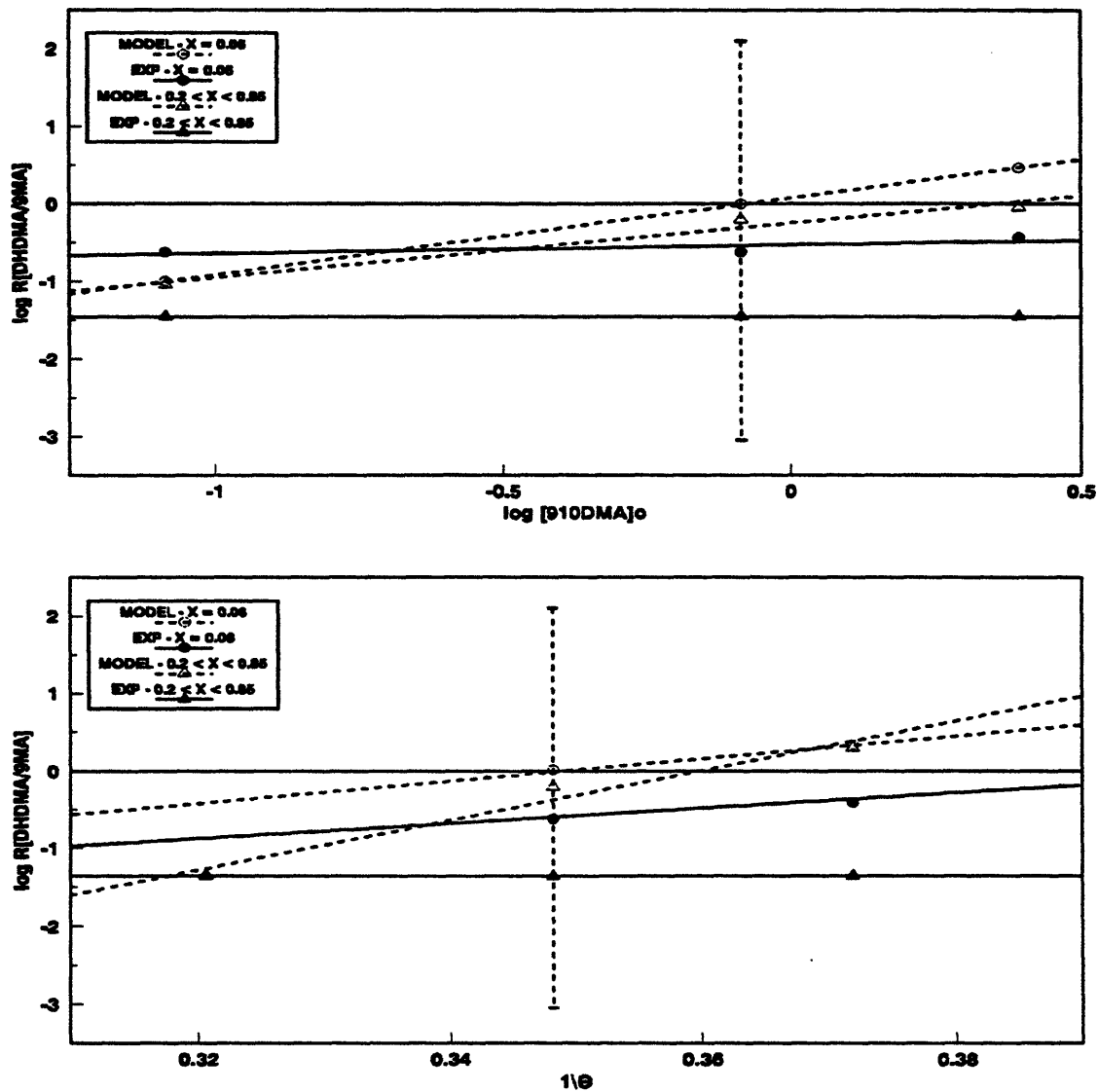
Figure 5.60: Comparison of experiment (solid symbols) and model (hollow) R[DHDMA/9MA] for varying $[910DMA]_o$ at fixed $T=355°C$(top) and varying T with fixed $[910DMA]_o=0.82$ mol/l(bottom).

formation by ~ 9 kcal/mol. At high conversions, the model R[DHDMA/9MA] increases more strongly, slope 32.1, than in the experiments which show R[DHDMA/9MA] essentially independent of temperature, slope 0; thus the model exhibits DHDMA formation to be more activated than 9MA formation by ~ 32 kcal/mol whereas the experiments show DHDMA and 9MA formation to be about equally activated. The vertical dashed lines in both upper and lower panels of Figure 5.60 are results of a sensitivity analysis discussed in a subsequent section.

Finally, parts (f) of Table 5.15 and Table 5.16, refer to the ratio of TMA product to 9MA product for 0.1 < X < 0.8. As initial concentrations increase from 0.082 to 2.47 mol/l, model calculations show R[TMA/9MA] increasing from 0.042 to 0.46 with its ratio R[mod/exp] increasing from 0.48 to 1.6. With increasing temperatures from 315 to 409°C, the model calculations show R[TMA/9MA] decreasing from 0.41 to 0.15 with its ratio R[mod/exp] decreasing from 1.7 to 0.63. Figure 5.61 graphically depicts the results for R[TMA/9MA] on log-log coordinates of R[TMA/9MA] vs. $[910DMA]_o$ (upper panel) and semi-log coordinates of R[TMA/9MA] vs. $1/\theta$ (lower panel). In the upper panel, it is seen that the model R[TMA/9MA] increases more strongly, slope 0.72, than in the experiments, slope 0.37; thus the model exhibits an order for TMA formation that is slightly higher than that for 9MA formation by more than that observed experimentally. Also, in the lower panel of Figure 5.61, the model R[TMA/9MA] increases more strongly with increasing $1/\theta$, that is decreasing temperature, slope 8.5, than in the experiments
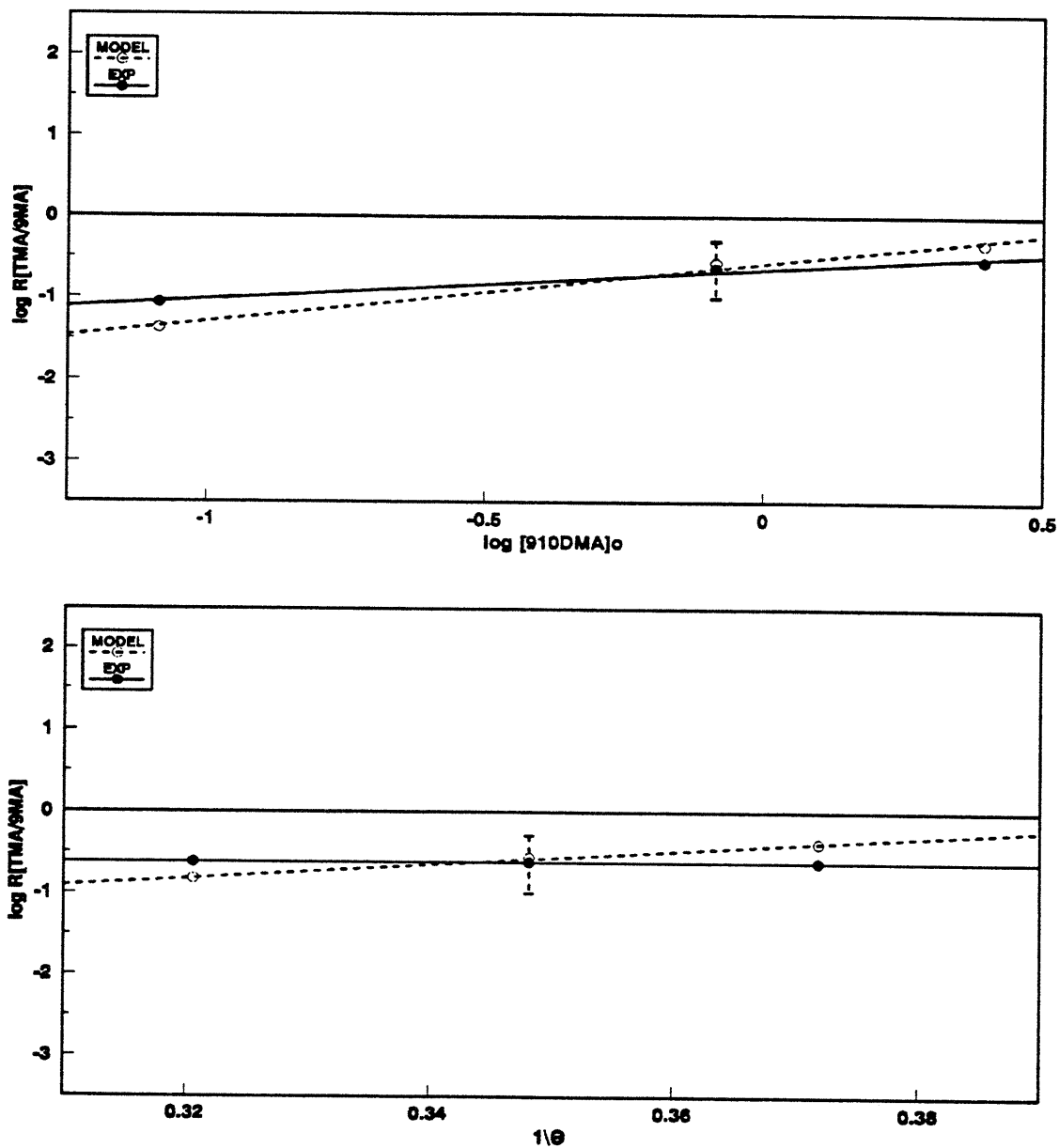
Figure 5.61: Comparison of experiment (solid circles) and model (circles) R[TMA/9MA] for varying [910DMA]$_o$ at fixed T=355°C(top) and varying T with fixed [910DMA]$_o$=0.82 mol/l(bottom).

which show R[TMA/9MA] independent of temperature, slope 0; thus the model predicts 9MA formation to be more activated than TMA formation by ~ 8.5 kcal/mol whereas the experiments show both TMA and 9MA formation to be about equally activated. The vertical dashed lines in both upper and lower panels of Figure 5.61 are results of a sensitivity analysis discussed in a subsequent section.

5.4.5.3 Sensitivity Analysis

The sensitivity of our 910DMA thermolysis model was analyzed at the central point of the 910DMA experimental grid, T = 355°C and $[910DMA]_o$ = 0.82 mol/l, by separately perturbing the kinetics of selected elementary steps over their estimated uncertainty limits. From Table 5.7 and Table 5.8, the inherent errors in ΔH°_f are between 1 - 3 kcal/mol for stable species and 2 - 5 kcal/mol for radicals. These errors in ΔH°_f translate into errors of ± 2 - 5 kcal/mol for ΔH°_r which propagate through the Evans-Polanyi relations of Table 5.11 into errors of ± 2 - 5 kcal/mol for E^*; when coupled with a θ ~ 3, which corresponds to the temperatures of the present experiments, these lead to errors of ±0.7 - 1.7 in $\log_{10} k$. The errors in the $\log_{10} A$ estimates are, at most, ± 0.5, which translate directly to errors of ±0.5 in $\log_{10} k$. Thus, in general, the calculated rate constants of the elementary steps are beset more by errors in their E^* than in their $\log_{10} A$. For this reason, the sensitivity analysis was performed by separately perturbing the E^* of selected elementary reactions over the inherent errors in their ΔH°_r to show their effects on 910DMA decay half-life t^*,

9MA selectivity S(9MA), and the primary product ratios R[DHDMA/9MA] and R[TMA/9MA]. Results of the sensitivity analysis are summarized in Table 5.17.

In our 910DMA thermolysis model, the destruction of substrate is affected by numerous elementary steps, of which, as shown in Table 5.13 and Table 5.14, R1 is the most important at both low and high conversions. The sensitivity of 910DMA half-life, t^*, was thus examined by perturbing E^*_1, the activation energy of R1, by $\pm$ 4.4 kcal/mol, which is the inherent error in $\Delta H^°_{R1}$, using the Evans-Polanyi relation $E^*_1 = \Delta H^°_{R1}$. Results of t^* sensitivity to the preceding perturbations are given in the last 3 columns of row 1 in Table 5.17 and were graphically depicted by the vertical dashed lines in Figure 5.57 and Figure 5.58. Two noteworthy conclusions arise from perusal of the results. First, the variation in t^*_{mod} on account of the inherent errors in the estimated rate constants is large enough to exceed the span of t^*_{exp} variations by changes in $[910DMA]_0$ and T. Second, at T = 355°C and $[910DMA]_0$ = 0.82 mol/l, the 2.5-fold difference between t^*_{mod} and t^*_{exp} is well within the 30-fold uncertainty in t^*_{mod}.

The formation of 9MA is affected by R3 the most important at both low and high conversions. The sensitivity of selectivity to 9MA, S(9MA), was thus examined by perturbing E^*_3, the activation energy of R3, by $\pm$ 3.7 kcal/mol, which is the inherent error in $\Delta H^°_{R3}$, using the Evans-Polanyi relation $E^*_3 = 2.1 + \Delta H^°_{R3}$. Results of S(9MA) sensitivity to the preceding perturbations are given in the last 3 columns of row 2 in Table 5.17 and were graphically depicted by the vertical dashed lines in

Table 5.17

	RESULTS OF SENSITIVITY ANALYSIS AT T = 355°C WITH $[910DMA]_o$ = 0.82 mol/l					
Parameter	Dominant	Inherent Error	Perturbation in	Results		
	Reaction(s)	in ΔH°_r (kcal/mol)	$E^\bullet$ (kcal/mol)	+Perturbation	0	-Perturbation
910DMA half-life, $t^\bullet$	R1	± 4.4	± 4.4	1700000	57258	2137
Selectivity to 9MA, S(9MA)	R3	± 3.7	± 3.7	0.014	0.16	0.345
Ratio of moles of DHDMA to moles of 9MA produced, R[DHDMA/9MA]	R2	± 4.7	± 2.35	+R2, +R3 $3.35^1, 0.83^2$ +R2, -R3	$1.00^1,$ 0.62^2	-R2, -R3 $0.34, 0.32$ -R2, +R3
	R3	± 3.7	± 3.7	0.0076, 0.0009		126, 95
Ratio of moles of TMA to moles of 9MA produced, R[TMA/9MA]	R4	± 2.5	± 1.25	0.50	0.27	0.12
	R5		0			

[1] R[DHDMA/9MA] at X = 0.06

[2] R[DHDMA/9MA] at X > 0.20

Figure 5.59. Two noteworthy conclusions arise from perusal of the results. First, the variation in t^*_{mod} on account of the inherent errors in the estimated rate constants is large enough to exceed the span of t^*_{exp} variations by changes in $[910DMA]_o$ and T. Second, at T = 355°C and $[910DMA]_o$ = 0.82 mol/l, the 2.5-fold difference between t^*_{mod} and t^*_{exp} is well within the 30-fold uncertainty in t^*_{mod}.

The formation of DHDMA and 9MA are affected by both R2 and R3 at both low and high conversions. The sensitivity of the ratio of moles of DHDMA to moles of 9MA produced, R[DHDMA/9MA], was thus examined by perturbing E^*_2 and E^*_3, the activation energy of R2 and R3, by ± 2.35 and ± 3.7 kcal/mol respectively, which are the inherent errors in $\Delta H°_{R2}/2$ and $\Delta H°_{R3}$, using the respective Evans-Polanyi relations E^*_2 = 17.5 + $\Delta H°_{R2}/2$ and E^*_3 = 2.1 + $\Delta H°_{R3}$. Results of R[DHDMA/9MA] sensitivity to the preceding perturbations are given in the last 3 columns of rows 3 and 4 in Table 5.17 and were graphically depicted by the vertical dashed lines in Figure 5.60. Two noteworthy conclusions arise from perusal of the results. First, the variation in R[DHDMA/9MA]$_{mod}$ on account of the inherent errors in the estimated rate constants is large enough to exceed the span of R[DHDMA/9MA]$_{exp}$ variations by changes in $[910DMA]_o$ and T at both low and high conversions. Second, at T = 355°C and $[910DMA]_o$ = 0.82 mol/l, the 4.2-fold difference between R[DHDMA/9MA]$_{mod}$ and R[DHDMA/9MA]$_{exp}$ at X = 0.06 and the 18-fold difference between R[DHDMA/9MA]$_{mod}$ and R[DHDMA/9MA]$_{exp}$ at 0.2 < X < 0.85 are well within the 100000-fold uncertainty in R[DHDMA/9MA]$_{mod}$.

The formation of TMA and 9MA is affected by R4 and R5 at both low and high conversions. The sensitivity of the ratio of moles of TMA to moles of 9MA produced, R[TMA/9MA], was thus examined by perturbing E^*_4, the activation energy of R4, by $\pm$ 1.25 kcal/mol, which is the inherent error in $\Delta H^\circ_{R4}/2$, using the Evans-Polanyi relation $E^*_4 = 17.5 + \Delta H^\circ_{R4}/2$. The activation energy of R5, E^*_5, was not affected by errors in ΔH°_{R5}. Results of R[TMA/9MA] sensitivity to the preceding perturbations are given in the last 3 columns of row 5 in Table 5.17 and were graphically depicted by the vertical dashed lines in Figure 5.61. Two noteworthy conclusions arise from perusal of the results. First, the variation in R[TMA/9MA]$_{mod}$ on account of the inherent errors in the estimated rate constants is large enough to exceed the span of R[TMA/9MA]$_{exp}$ variations by changes in [910DMA]$_o$ and T. Second, at T = 355°C and [910DMA]$_o$ = 0.82 mol/l, the 1.2-fold difference between R[TMA/9MA]$_{mod}$ and R[TMA/9MA]$_{exp}$ is well within the 4.2-fold uncertainty in R[TMA/9MA]$_{mod}$.

5.4.5.4 Optimized Model

The preceding comparisons between model and experimental results, along with the sensitivity analysis, permitted the deviation of optimized parameters for the model of 910DMA thermolysis, to best-fit the experimental data at T = 355°C and [910DMA]$_o$ = 0.82 mol/l. The best-fit arose by subtracting 1.2 kcal/mol from E^*_1, adding 1.2 kcal/mol to E^*_2, subtracting 1.2 kcal/mol from E^*_{-2}, and subtracting 1.2

kcal/mol from E^{*}_{3}. It can be verified by reference to Table 5.17 that all of those adjustments to the E^{*} were within their inherent error-limits. Figure 5.62 compares the substrate and product histories (upper panel) and product selectivities (lower panel) as obtained from the numerical solution to the thermolysis model to the experimental data for 910DMA, 9MA, TMA and CH4 at the center of the experimental grid, $[910DMA]_{o}$ = 0.82 mol/l and T = 355°C. In the upper panel of Figure 5.62, the model is seen to predict 910DMA decay, the solid line, within the experimental observations, shown as asterisks. The t^{*}_{mod} = 25429 s whereas the t^{*}_{exp} = 21912 s. The upper panel of Figure 5.62 also shown that the absolute amounts of 9MA, the short-dashed line versus the circles, and of TMA, the dotted line versus the squares, formed by the model are both lower than observed in the experiments. The lower panel of Figure 5.62 is a selectivity diagram for the present case of $[910DMA]_{o}$ = 0.82 mol/l and T = 355°C. S(9MA) and S(TMA) from the model are respectively 1.7 and 1.4-fold too low compared to the average values of S(9MA) and S(TMA) observed from the experiments between 0.1 < X < 0.8. The mechanism as the upper limit of 0.33 for S(9MA), as shown in Section 5.4.2, therefore the optimized model generates S(9MA) very close to the maximum limit.

Figure 5.63 continues the comparison between the optimized model (lines) and experimental (circle) product histories and selectivities for DHDMA product. In the upper panel of Figure 5.63, the model is seen to predict DHDMA within the experimentally data. In the lower panel of Figure 5.63, a selectivity diagram, we see
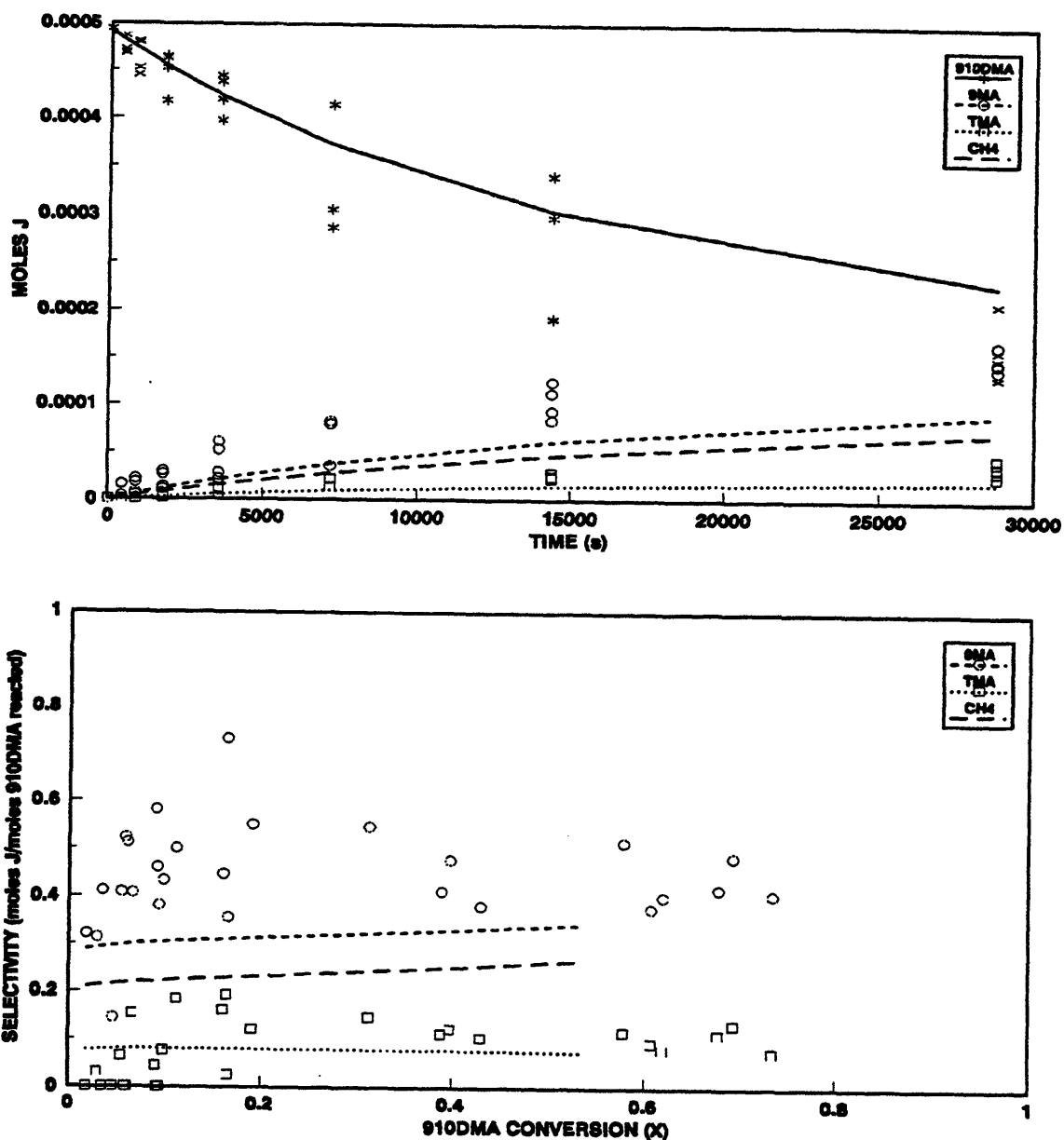
Figure 5.62: Product histories (top) and selectivity diagram (bottom) comparing optimized model (lines) to experimental data (symbols) for 910DMA, 9MA, TMA and CH4 at T = 355°C with $[910DMA]_o$ = 0.82 mol/l.
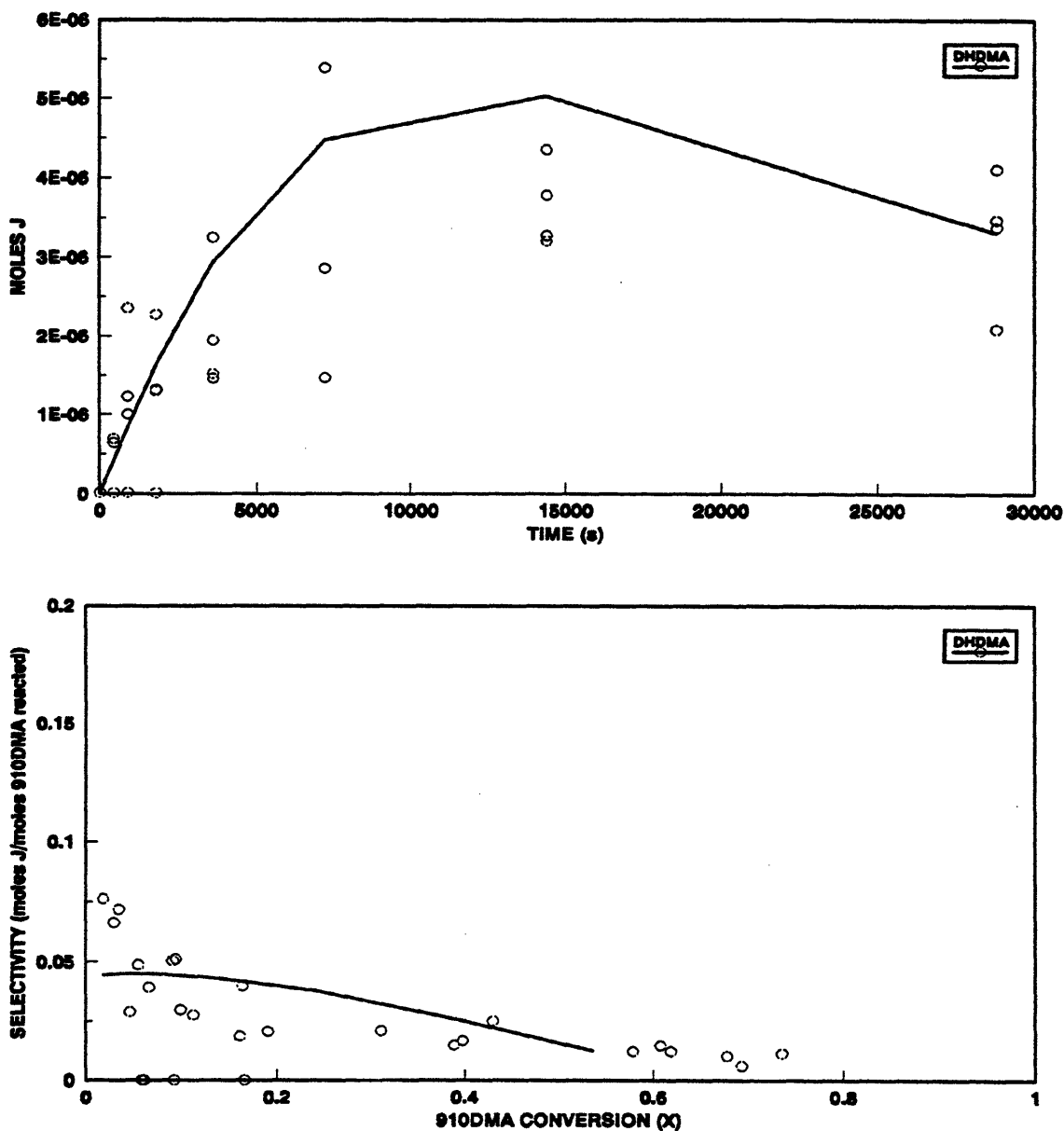
Figure 5.63: Product histories (top) and selectivity diagram (bottom) comparing optimized model results (lines) to experimental data (symbols) for DHDMA at $T = 355°C$ with $[910DMA]_0 = 0.82$ mol/l.

401

that, relative to the experiments, S(DHDMA) from the model has the correct values at low and high conversions, but the slope of the line does not correspond to the trend of the experimental data.

Figure 5.64 compares the model calculations (lines) to the experimental data (solid circles) for heavies (DMAD, DMAHDMAD and HDMAD). In the upper panel of Figure 5.64, the model predicts heavies production comparable to the experiments at shorter times, but at long times produces more dimer than seen in the experiments. The lower panel of Figure 5.64 shows the dimer selectivity S(DMAD) ~ 0.27 calculated from the model is close to the experimental S(HVY) ~ 0.25 at low X < 0.1, but whereas the S(HVY) in the experiments decreases to ~0.01 with increasing conversion, X > 0.2, S(DMAD) from the model remains roughly constant at S(DMAD) ~ 0.27.

Finally, Figure 5.65 compares the product ratios R[DHDMA/9MA] and R[TMA/9MA] as functions of 910DMA conversion (X) derived from the optimized model (lines) to those observed experimentally (symbols). In the upper panel of Figure 5.65, the model is seen to predict R[DHDMA/9MA] comparable to the experimental values at low and high conversions, but the slope of the line does not correspond to the observed experimental data. In the lower panel of Figure 5.65, the model is seen to predict R[TMA/9MA] approximately equal to that experimentally observed at all conversions 0 < X < 0.54.
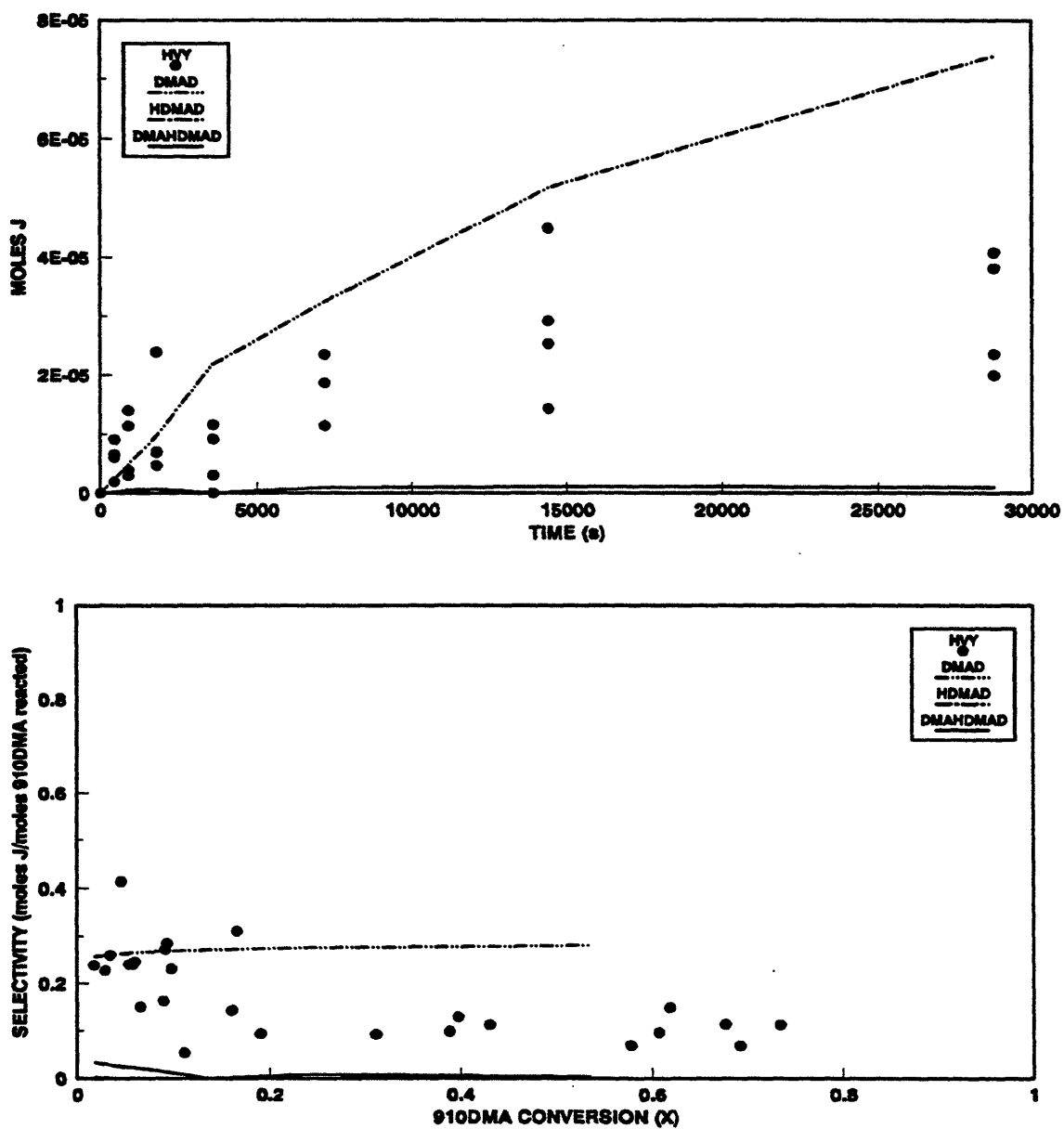
Figure 5.64: Product histories (top) and selectivity diagram (bottom) comparing optimized model results (lines) to experimental data (symbols) for heavies at T = 355°C with $[910DMA]_o$ = 0.82 mol/l.
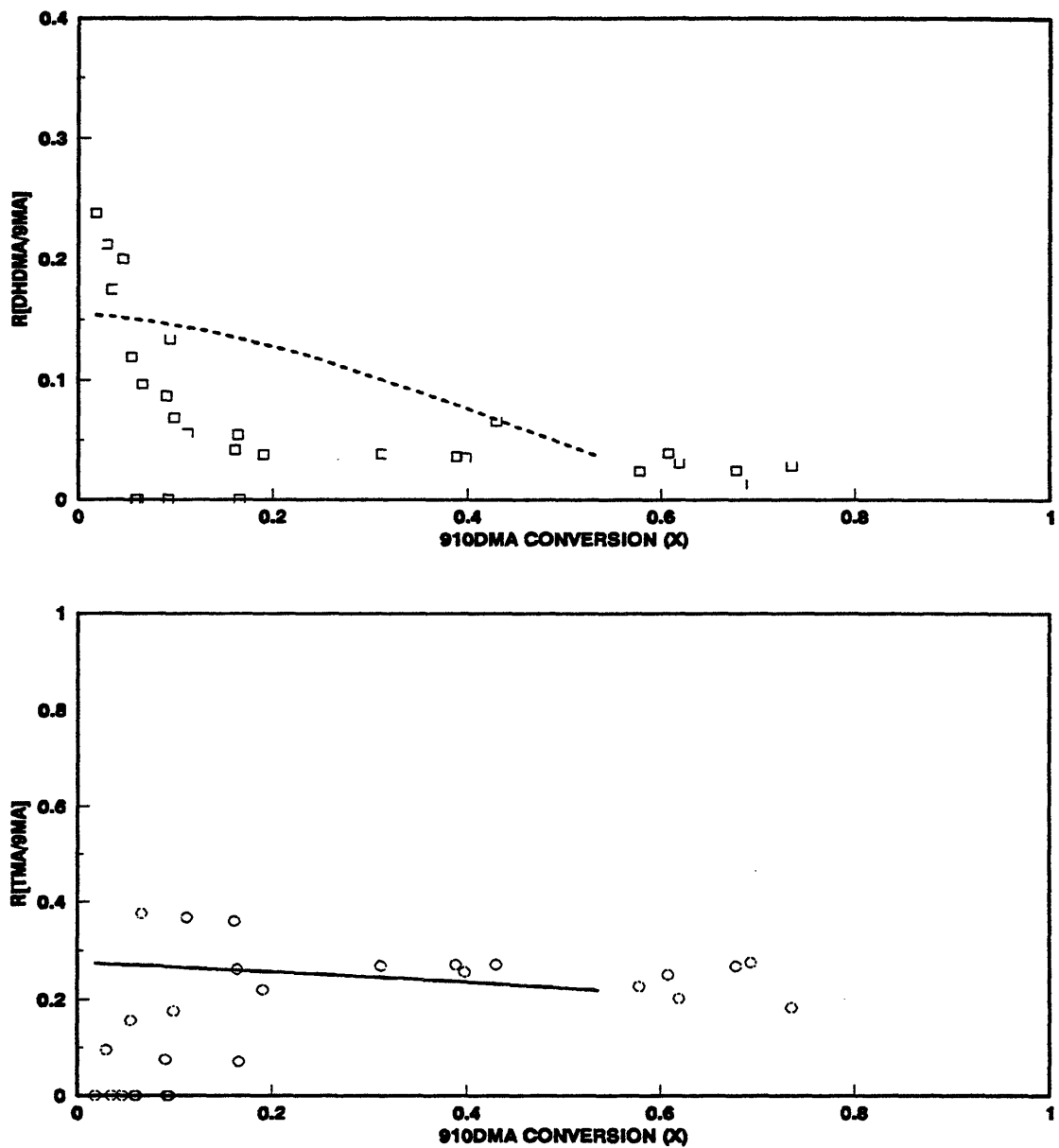
Figure 5.65: R[DHDMA/9MA] (top) and R[TMA/9MA] (bottom) comparing optimized model results (lines) to experimental data (symbols) at T = 355°C with $[910DMA]_o$ = 0.82 mol/l.

5.5 Minor Methylated Products

The observed formations of dimethylanthracene isomers 1,9-, 1,10-, 2,9- and 3,9-DMA from 9MA and of methylanthracene isomers 1MA and 2MA from ANT during 910DMA thermolysis at high severities invite interpretation by frontier orbital theory, as examples of periselective methyl radical attack on the aromatic anthracene nucleus.

5.5.1 Observed Product Ratios

Figure 5.66 and Figure 5.67, respectively, shows the ratios of (2,9- + 3,9-)DMA/(1,9- + 1,10-)DMA and of 2MA/1MA obtained as functions of 910DMA conversion during the present experiments. In the upper panel of Figure 5.66, it is seen that, at constant T = 355°C and 0.082 < [910DMA]$_o$ < 0.82 mol/l, the ratio R[(2,9- + 3,9-)DMA/(1,9- + 1,10-)DMA] = 0.29 ± 0.07 for 0.3 < X < 0.7. In the lower panel of Figure 5.66, R[(2,9- + 3,9-)DMA/(1,9- + 1,10-)DMA] = 0.24 ± 0.06 for 0.3 < X < 0.98 at [910DMA]$_o$ = 0.82 mol/l and all temperatures for 315 - 409°C. In the upper panel of Figure 5.67, it is seen that, at constant T = 355° and 0.25 < [910DMA]$_o$ < 2.47 mol/l, the ratio R[2MA/1MA] = 0.49 ± 0.12 for 0.4 < X < 0.8. In the lower panel of Figure 5.67, R[2MA/1MA] = 0.51 ± 0.15 for 0.4 < X < 0.99 at [910DMA]$_o$ = 0.82 mol/l and T > 335°C. The ratios R[(2,9- + 3,9-)DMA/(1,9- + 1,10-)DMA] and R[2MA/1MA] can both be viewed as the relative methyl
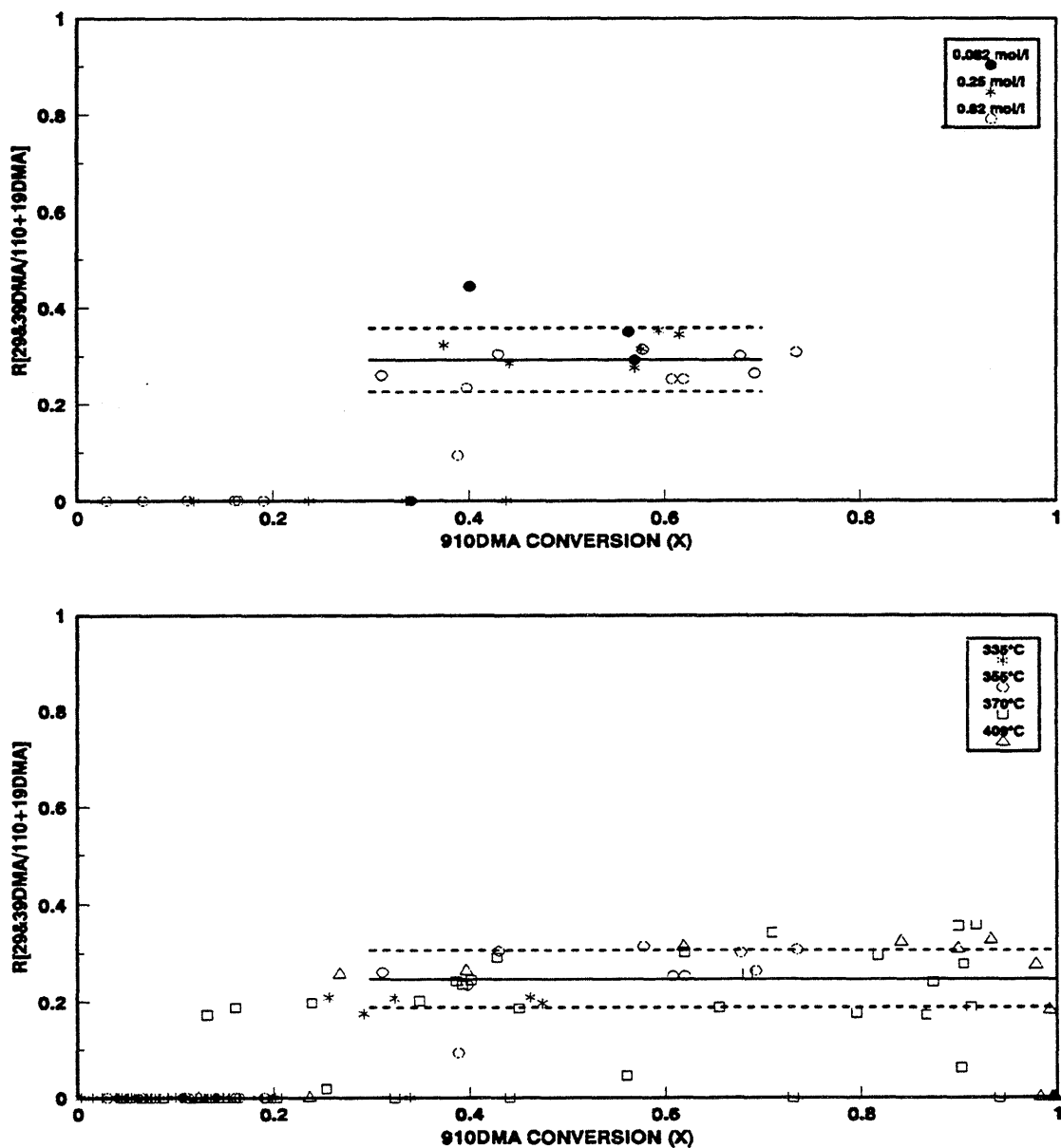
Figure 5.66: Ratio of moles (2,9-+3,9-)DMA/moles (1,9-+1,10-)DMA vs. 910DMA conversion for varying [910DMA]$_o$ at T = 355°C(top) and for varying T with [910DMA]$_o$ = 0.82 mol/l(bottom).
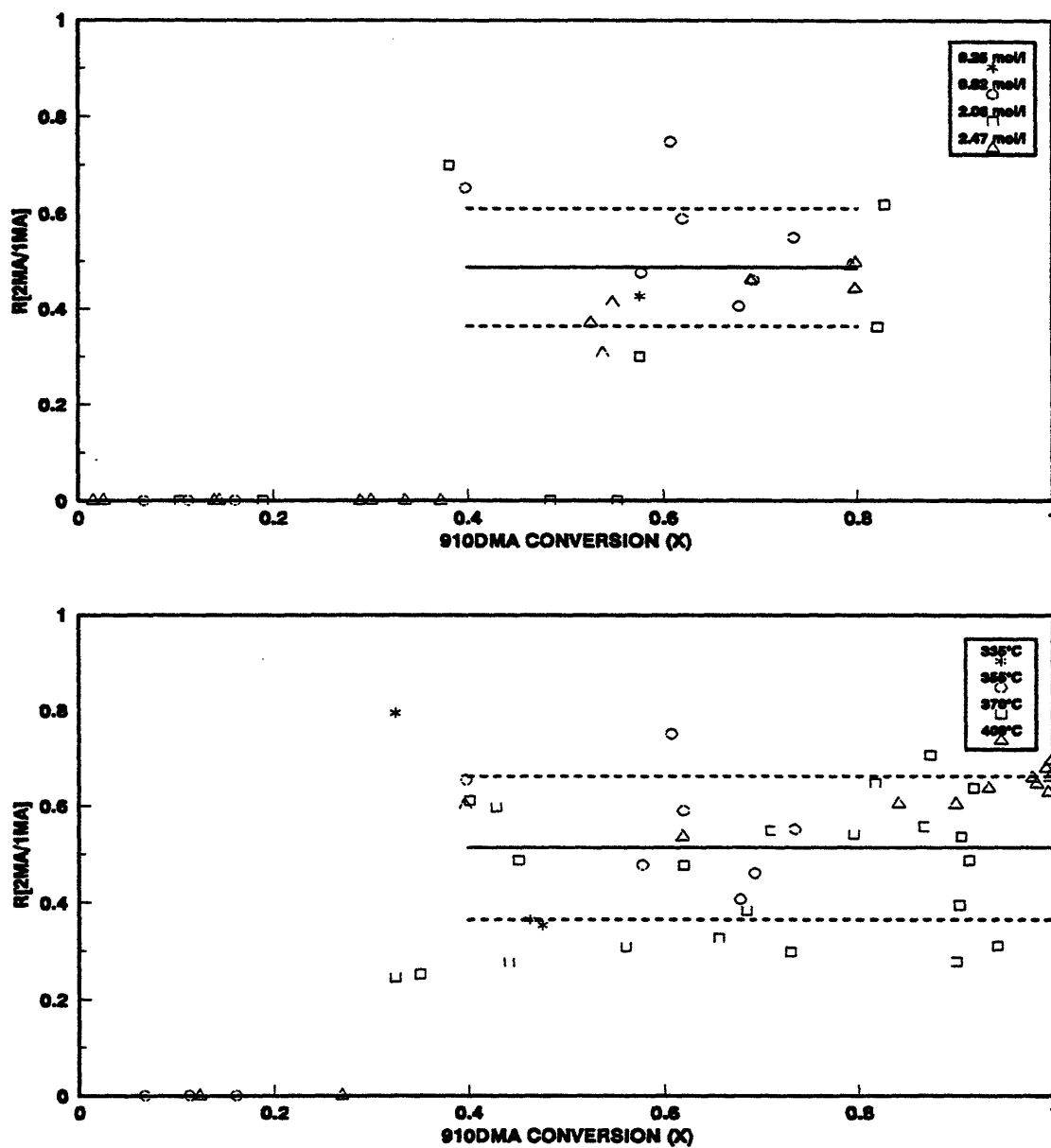
Figure 5.67: Ratio of moles 2MA to moles 1MA produced vs. 910DMA conversion for varying $[910DMA]_0$ at fixed $T = 355°C$ (top) and for varying T with fixed $[910DMA]_0$ (bottom).

407

affinities of positions 1 and 2 on the periphery of the anthracene ring, with methyl attack at position 2 less favored than at position 1 by a factor of 2 to 4.

5.5.2 Frontier Molecular Orbital Treatment using Hückel MOs

Using Equation (3.6) for the interaction between the frontier orbitals of a radical and a molecule, the favorable, non-dimensional FMO stabilization energy $E'(t)$ is given by the interaction between the singly-occupied MO (SOMO) of the $CH3^*$ radical and the highest-occupied and lowest-unoccupied MOs (HOMO and LUMO) of the ANT at position t:

$$E'(t) = \frac{\Delta E(FMO)}{\frac{\gamma^2}{\beta}} = \frac{c_{t,HO}^2}{-X_{HO}} + \frac{c_{t,LU}^2}{X_{LU}} = \frac{2c_{t,HO}^2}{-X_{HO}} \qquad (5.16)$$

where:

c_t =   MO coefficient at position t

$X_{HO\,or\,LU}$ =   nondimensionalized Hückel MO energy and the subscripts HO and LU refer to the frontier orbitals.

Figure 5.68 is an orbital interaction diagram for the system comprising ANT and $CH3^*$, with energy as ordinate and the molecules confined to separate columns. Equation (5.16) reduces to one term because, in the Hückel approximation, alternate hydrocarbons such as ANT have $X_{LU} = -X_{HO}$ and radical such as $CH3^*$ have $X_{SO} = 0$. The dominant FMO interaction fixes the denominator of Equation (5.16), but
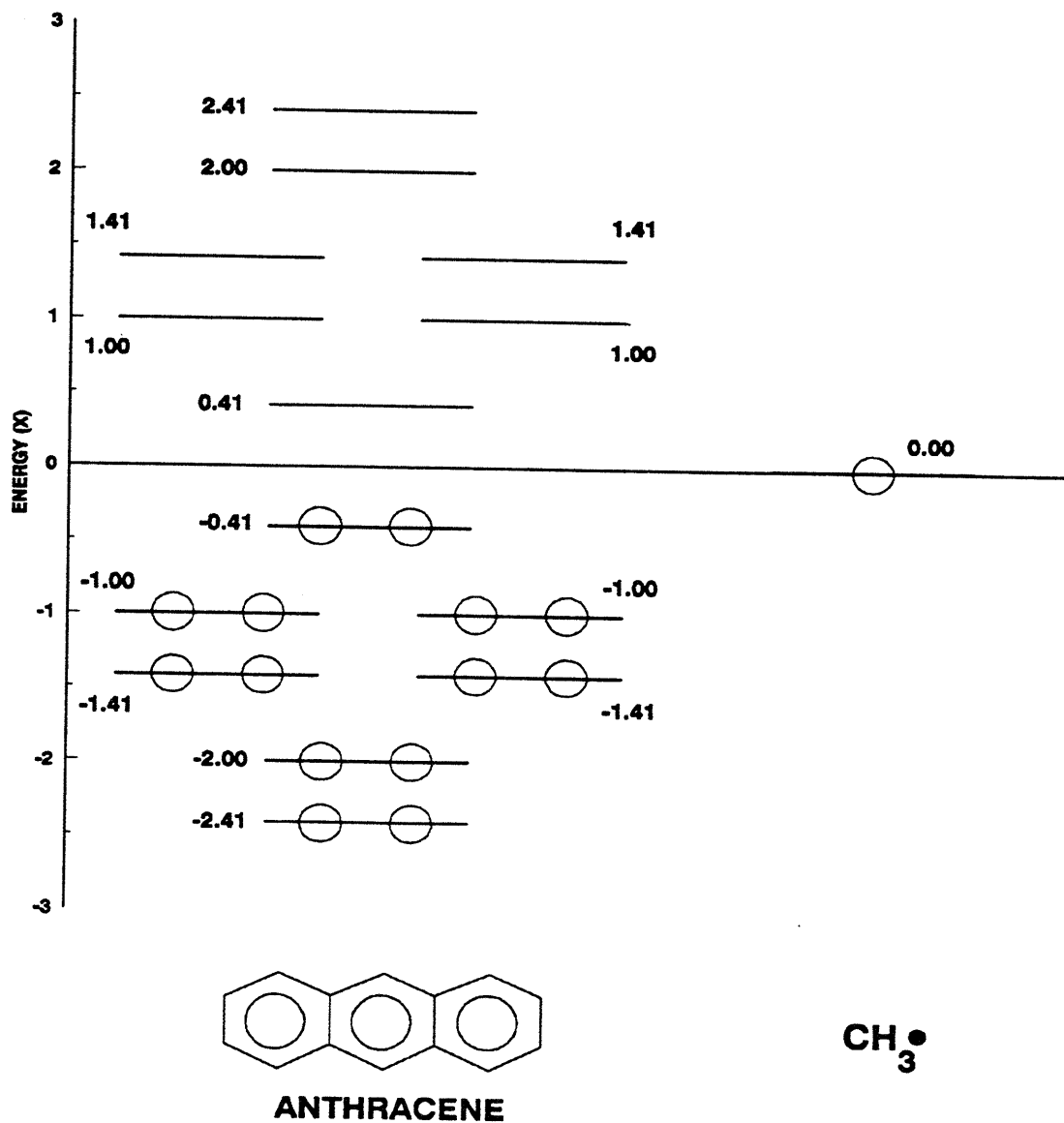
Figure 5.68: Frontier orbital interaction diagram for addition of methyl radical to anthracene using Hückel MOs.

since ANT possesses multiple reaction sites, the numerator can take several different values. Frontier orbital coefficients from the Hückel MOs of CH3* and ANT are shown in Figure 5.69, a "periselectivity diagram" that indicates the three possible sites at which CH3* can add to ANT. For ANT positions t = (2,1,9), the respective E'(t) = (0.12, 0.23, 0.47); that is, FMO theory predicts CH3* attack favored in the order of positions 2 < 1 < 9. The predicted inequality between positions 2 and 1 of the ANT nucleus accords with the experimentally observed minor product ratios R[2MA/1MA] ~ 0.5 for methylation of ANT.

5.5.2 Frontier Molecular Orbital Treatment using PM3 MOs

Figure 5.70 and Figure 5.71 are orbital interaction diagrams for the respective systems comprising ANT and CH3* and 9MA and CH3*, both with energies obtained from PM3 MO calculations. In Figure 5.70 (also Figure 5.71) it is seen that the SOMO of CH3* does not lie between the LUMO and the HOMO of ANT but possesses an energy such that $E_{SO} << E_{LU}$ and $E_{SO} \sim E_{HO}$. Thus, the SOMO-LUMO interaction remains a second order perturbation, whereas SOMO-HOMO interaction is now a first order perturbation of a much larger magnitude. For interactions between orbitals of roughly the same energy (degenerate) the total change in energy, ΔE_1, is the sum of the one-electron energies calculated by
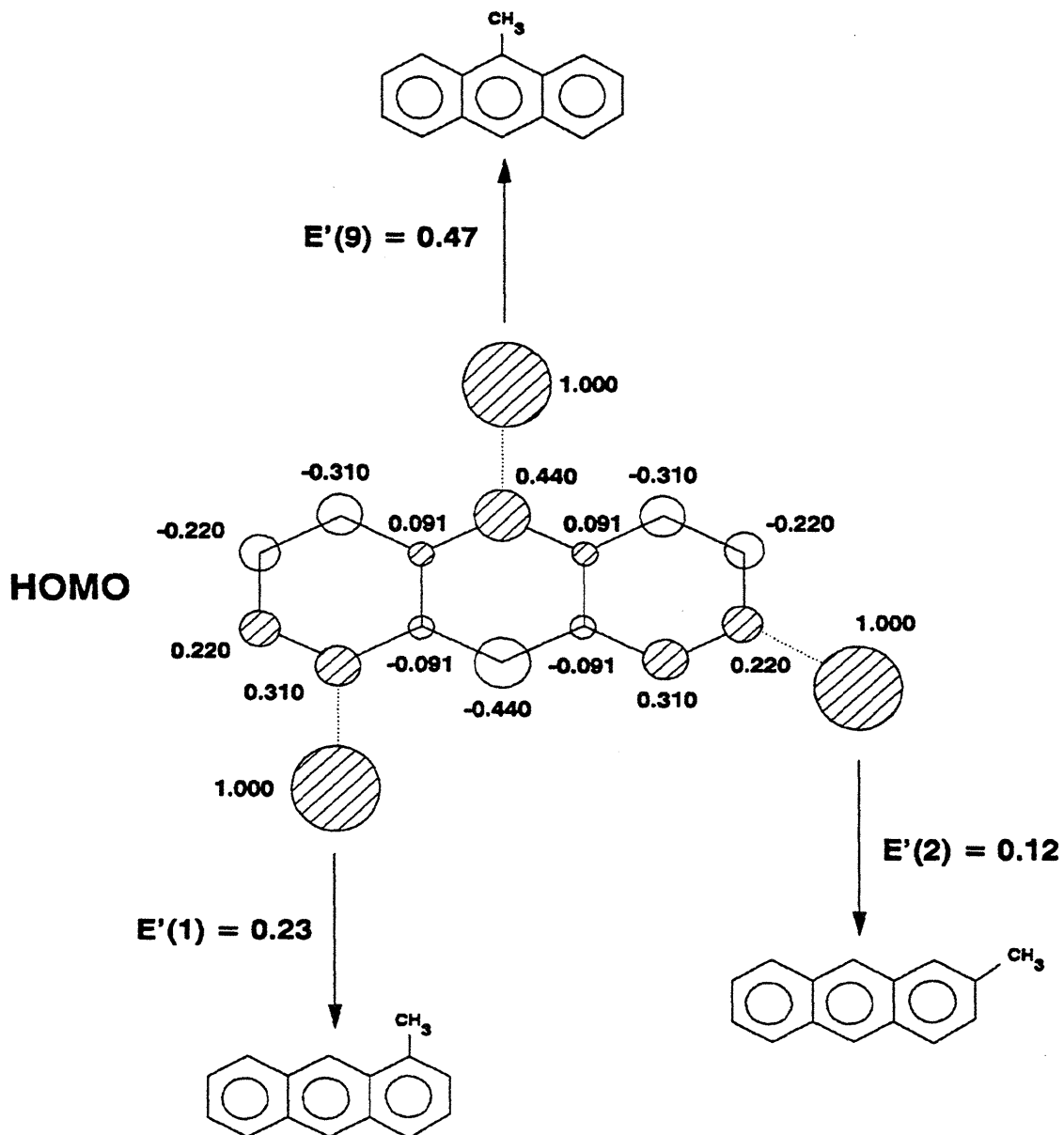
Figure 5.69: Estimation of isomer periselectivity by FMO theory using Hückel MOs for addition of methyl radical to anthracene to form 9-, 2- and 1-methylanthracene.

411
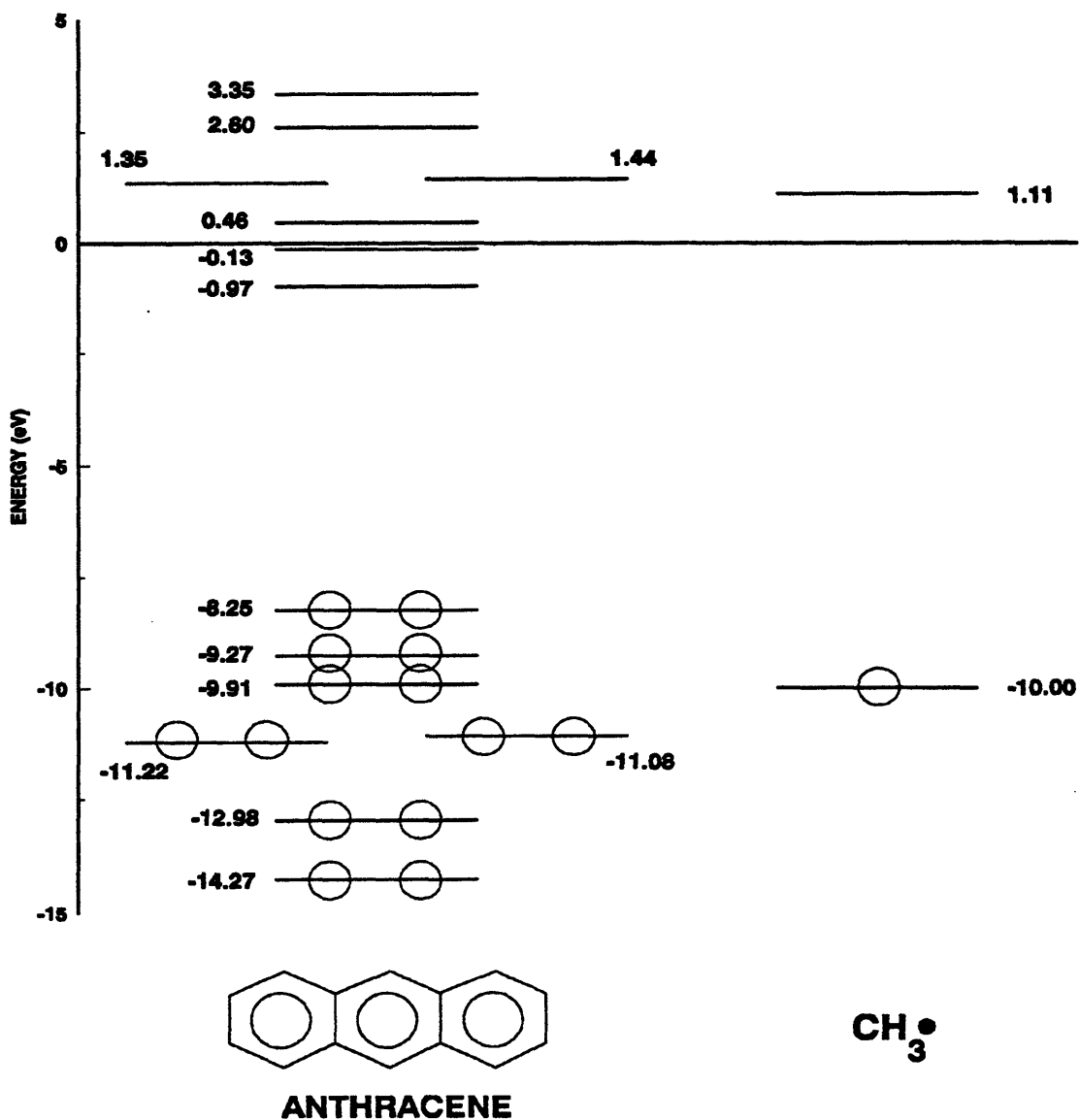
Figure 5.70: Frontier orbital interaction diagram for addition of methyl radical to anthracene using the PM3 MOs.
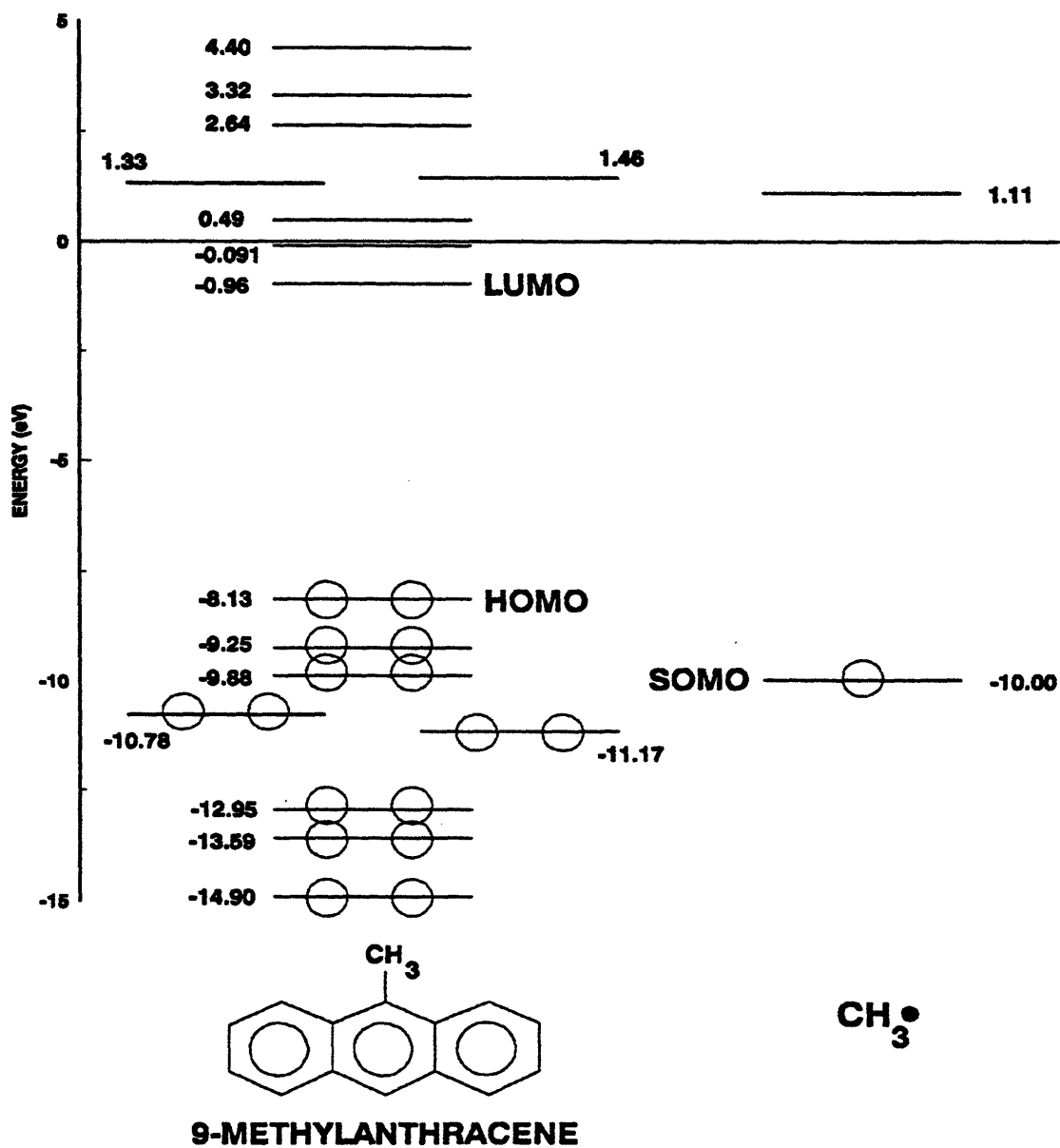
Figure 5.71: Frontier orbital interaction diagram for addition of methyl radical to 9-methylanthracene using the PM3 MOs.

413

first-order perturbation theory (Hudson, 1974):

$$\Delta E_1 = \sum_t^{occ} C_t C_{u(SO)} \gamma_{tu} \qquad (5.17)$$

where:

C_t = coefficient of occupied MO at atom t in molecule A

$C_{u(SO)}$ = coefficient of SOMO at atom u in molecule B

γ_{tu} = resonance integral between AO's t and u

Table 5.18 lists the C_t from PM3 calculations for all the occupied levels of ANT and 9MA. If the HOMO is believed to be the "stereo-directing" occupied MO (Klopman, 1974), then the full summation for ΔE_1 reduces to one term, corresponding to the SOMO-HOMO interaction. Using only the HOMO in Equation (5.17), the favorable, non-dimensional first order FMO stabilization energy E"(t) is:

$$E''(t) = \frac{\Delta E_1}{\gamma} = C_{t(HO)} C_{u(SO)} \qquad (5.18)$$

The second-order SOMO-LUMO interaction is neglected relative to the larger first order SO-HO interaction. Figure 5.72 gives the values for the energies E (eV) and coefficients C_t for the ANT and 9MA HOMOs and LUMOs, as well as the E and C_t for the CH3* SOMO from the PM3 calculations. Figure 5.73 is a periselectivity diagram indicating the three possible sites at which CH3* can add to ANT and the corresponding E"(t) at each position. For ANT positions t = (2,1,9), the respective E"(t) = (0.23, 0.29, 0.43); that is, FMO theory predicts CH3* attack favored in the order of positions 2 < 1 < 9. The predicted inequality between positions 2 and 1

414

Table 5.18

COEFFICIENTS FROM PM3 MO CALCULATION OF ANTHRACENE AND 9-METHYLANTHRACENE

MO	ENERGY (eV)	$C_{(10)}$	$C_{(3)}$	$C_{(4)}$
ANT - 7 - HOMO	-8.25	-0.433	0.231	0.294
ANT - 6	-9.27	0.001	-0.297	-0.016
ANT - 5	-9.91	0.000	0.246	0.403
ANT - 4	-11.08	-0.391	-0.144	-0.281
ANT - 3	-11.22	0.254	-0.381	-0.190
ANT - 2	-12.98	-0.000	-0.319	-0.296
ANT - 1	-14.27	-0.307	-0.174	-0.218
9MA - 7 - HOMO	-8.13	-0.439	0.221	0.286
9MA - 6	-9.25	0.001	0.291	0.010
9MA - 5	-9.88	-0.002	0.243	0.397
9MA - 4	-10.78	-0.223	-0.273	-0.331
9MA - 3	-11.17	0.387	-0.303	-0.074
9MA - 2	-12.95	0.011	-0.311	-0.286
9MA - 1	-13.59	-0.286	-0.194	-0.228

ANT

E(HO) = -8.25

E(LU) = -0.97

9MA

E(HO) = -8.13

E(LU) = -0.96

CH3*

E(SO) = -10.00

Figure 5.72: Values of coefficients C_t and energies E from PM3 calculations of anthracene, 9-methylanthracene and methyl radical.

416
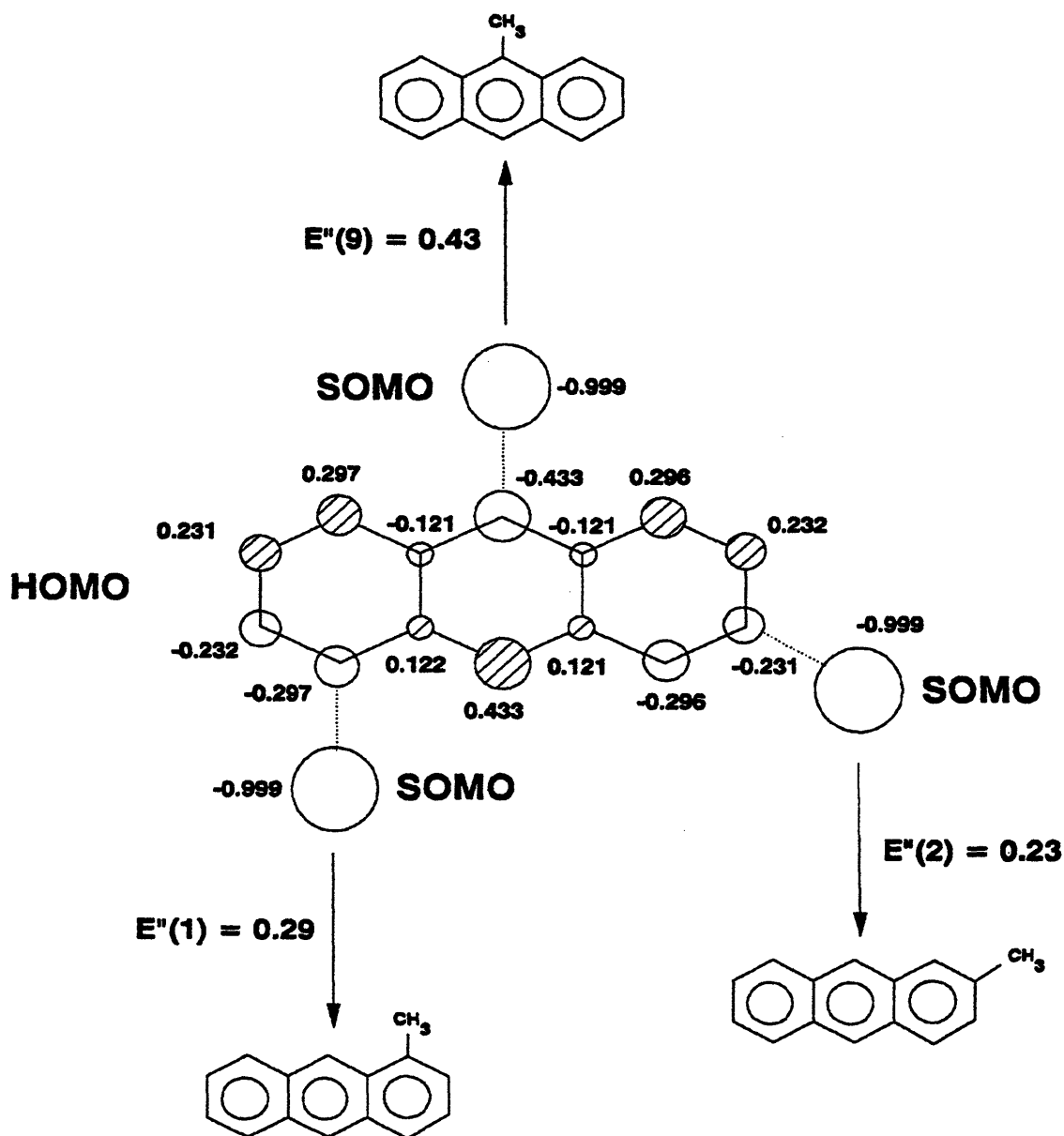
Figure 5.73: Estimation of isomer periselectivity by FMO theory using PM3 MOs for addition of methyl radical to anthracene to form 9-, 2- and 1-methylanthracene.

417

of ANT is in accord with the experimentally observed R[2MA/1MA] ~ 0.5.

Figure 5.74 is a periselectivity diagram indicating the five possible sites at which

CH3* can add to 9MA and the corresponding values of E"(t) at each position. For

9MA positions t = (2,3,1,4,10), the respective E'(t) = (0.22, 0.23, 0.28, 0.28, 0.44);

that is, FMO theory predicts CH3* attack favored in the order of positions (2, 3) <

(1, 4) < 9. Methyl attack at position 2 leads to 2,9-DMA, at position 3 to 3,9-DMA,

at position 1 to 1,9-DMA, at position 4 to 1,10-DMA and at position 10 to 9,10-

DMA. The predicted inequality between positions (2, 3) and (1, 4) accords with the

experimentally observed ratio R[(2,9- + 3,9-)DMA/(1,9- + 1,10-)DMA] ~ 0.25.

Finally, it is worth noting that in free-radical phenylation of ANT at T = 30°C,

Dickerman (1973) reported relative phenyl affinities at position (2,1,9) in the ratio

(0.28, 1.00, 14.32), that is, position 2 was less favored than position 1 by a factor of

3.5. The ratio of phenyl affinities at ANT positions 1 and 2 is of roughly the same

magnitude as the ratio of methyl affinities obtained from the minor methylated

product ratios in the present experiments.

5.6 Summary

9,10-dimethylanthracene (910DMA) was thermolyzed over the range: T = 315

- 409°C, [910DMA]$_o$ = 0.082 - 2.47 mol/l and t = 450 - 57600 s, which lead to X =

0.05 - 0.99. Products seen in the 910DMA thermolysis included: 9-methylanthracene

(9MA), trimethylanthracenes (TMAs), dihydro-dimethylanthracenes (DHDMA),
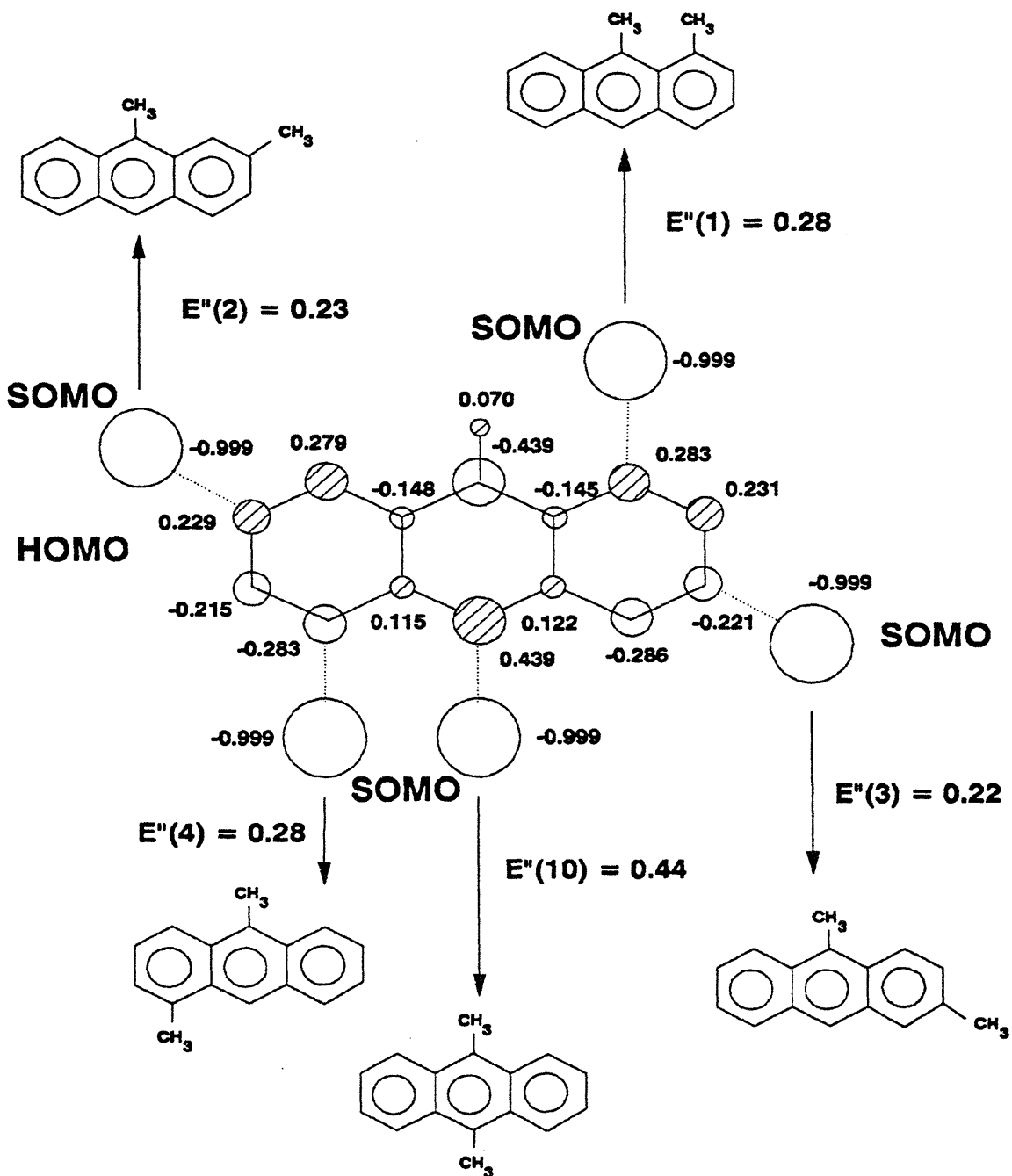
Figure 5.74: Estimation of isomer periselectivity by FMO theory using PM3 MOs for addition of methyl radical to 9-methylanthracene to form 1,10-, 1,9-, 2,9- and 3,9-dimethylanthracene.

419

dihydromethylanthracenes (DHMA), dihydroanthracene (DHA), anthracene (ANT), 1-methylanthracene (1MA), 2-methylanthracene (2MA), 1,10-dimethylanthracene (110DMA), 1,9-dimethylanthracene (19DMA), 2,9&3,9-dimethylanthracene (29&39DMA), other dimethylanthracenes (other DMAs), heavy (dimer) products, dihydro-trimethylanthracenes (DHTMA), and methane (CH4). The substrate and major product histories depict a classical sequential reaction series A(910DMA) → B(9MA) → C(ANT), with competing, parallel, hydrogenation and methylation pathways at each stage. S(9MA) and S(TMA) were roughly independent of conversions at all [910DMA]$_o$ and T. Absolute values of S(9MA) declined somewhat while S(TMA) increased somewhat with increasing [910DMA]$_o$ at fixed T = 355°C, whereas absolute values of S(9MA) and S(TMA) remained essentially constant with increasing T at fixed [910DMA]$_o$. S(DHDMA) was essentially highest at the lowest conversion and declined precipitously with increasing X at all [910DMA]$_o$ and T. DHMA and DHA were only detected at [910DMA]$_o$ > 0.25 mol/l and all T and increased monotonically from zero as conversions increased. ANT, 1MA and 2MA selectivities increased monotonically from zero as conversions increased for all [910DMA]$_o$ and T, with S(1MA) > S(2MA) always and both always < S(ANT) at any X. 110DMA, 19DMA and 29&39DMA selectivities also increased monotonically from zero as conversions increased and approached X ~ 0.85 for all [910DMA]$_o$ and T, and then decreased for X > 0.85 at T = 355°C. The other minor DMAs selectivity remained roughly constant for X < 0.85 for all T, and then increased for

X > 0.85. Of the dimethylated species, S(110DMA) > S(19DMA) > S(29&39DMA) > S(other DMAs) for X < 0.85 and each always < S(9MA) at any X, while at X > 0.85, S(other DMAs) > S(110DMA) > S(19DMA) > S(29&39DMA). Absolute values of S(110DMA), S(19DMA) and S(29&39DMA) increased somewhat with increasing $[910DMA]_0$ and decreased somewhat with increasing T for all X < 0.85, while absolute values of S(110DMA), S(19DMA) and S(29&39DMA) decreased as X → 1. Absolute values of S(other DMA) remained roughly constant for X < 0.85 and increased at X > 0.85.

The kinetics of the 910DMA experimental thermolyses were analyzed to derive reaction order and activation parameters. Reaction order for overall 910DMA decay was determined from k_{eff}, the effective first order rate constants, and 910DMA decay half-life, t^*, in the series of experiments at constant T = 355°C with $[910DMA]_0$ ranging from 0.082 to 2.47 mol/l. Analysis of both led to approximately 3/2 order 910DMA decomposition kinetics, with k_{eff} yielding 1.38 ± 0.06 and t^* yielding 1.53 ± 0.06. Thermolysis of 910DMA at fixed $[910DMA]_0$ = 0.82 mol/l and varying temperature from 315 - 409°C revealed the activation parameters associated with both the effective first order and true 3/2 order rate constants. The best-fit Arrhenius parameters $[\log_{10} A \ (s^{-1}), E^* \ (kcal/mol)]$ = [7.42 ± 0.10, 33.9 ± 2.5] for the average k_{eff} and $[\log_{10} A \ (l^{1/2}/mol^{1/2} \ s), E^* \ (kcal/mol)]$ = [11.1 ± 0.08, 44.6 ± 2.1] for $k_{3/2}$ with low conversion data, X < 0.4. Regression of the half-lifes t^* at varying

temperatures gave Arrhenius parameters $[\log_{10} A\ (s^{-1}), E^*\ (kcal/mol)] = [10.1 \pm 0.03,$

$43.1 \pm 1.0]$ for $k_{3/2}$.

Three primary reaction pathways operate in parallel upon 910DMA substrate:

(P1) Hydrogenation to *cis*- and *trans*-9,10-dihydro-9,10-dimethylanthracene, (P2)

Demethylation to 9-methylanthracene, and (P3) Methylation to 1,9,10-

trimethylanthracene and other TMA isomers. The primary demethylation product

9MA and the primary methylation product TMA are secondary operated upon by a

pathway triad analogous to the preceding primary triad, eventually forming 9,10-

dihydro-9-methylanthracene and dihydrotrimethylanthracene, a host of

dimethylanthracenes and dimethylanthracenes, and anthracene and reforming

910DMA substrate. And at the highest substrate conversions, even the terminal

demethylation product ANT suffers hydrogenation and methylation, as witnessed by

the appearance of the minor products DHA, 1MA and 2MA. Neither 910DMA or

9MA isomerize to their positional isomers, since the methylated species do not arise

until after the demethylated compound appears. Hydrogenated products formed by

the primary triads are further hydrogenated to yield tetrahydrogenated products.

Terminated products include both pure- and cross-termination of 910DMA and

DHDMA radicals.

A possible mechanism for the early stages of 910DMA thermolysis, that is

consistent with the present pathway and kinetic observations and accounts for all the

products observed during the initial stages of 910DMA thermolysis at low

conversions, was devised and is summarized as follows: The free-radical cycle is initiated by the substrate 910DMA undergoing bimolecular disproportionation, an intermolecular hydrogen transfer reaction, to form the respectively dehydrogenated and hydrogenated radical species 910DMA* and HDMA*. Of these, the latter can either abstract hydrogen from 910DMA substrate to form DHDMA products or undergo a β-scission type of radical decomposition forming 9MA product and a methyl radical CH_3*. The CH_3* can either abstract H from 910DMA substrate to form methane product, or add to the 910DMA substrate to form the trimethyl radical HTMA1*. The latter can then abstract H from substrate 910DMA to form the observed 2910TMA product. Finally, the radical mechanism is terminated by the species 910DMA* and HDMA* engaging in both pure- and cross-combination to form various dimeric products. HDMA* radical can also terminate by disproportionation to form 910DMA and DHDMA. The proposed mechanism exhibits certain stoichiometric limits and thus restricts the maximum selectivities of each of DHDMA, 9MA, TMA and heavies to 1/3.

Thermochemical and activation parameters were then assigned from first principles for each elementary reaction and its reverse in the mechanism. In order to derive kinetic parameters for the mechanism, values of the enthalpy of formation, ΔH°_f, were required for all participating chemical species. Where experimental values were unavailable, enthalpies of formation were derived using a "macro" group additivity technique, which started with a basis molecule that was as large and as

structurally similar to the desired product and then added and subtracted other basis species from the starting species to account for structural differences between it and the desired species. Arrhenius expressions were generated for each elementary step of the 910DMA thermolysis mechanism from kinetic data reported in the literature for that type of reaction, which was analyzed to ascertain its activation parameters, including $\log_{10} A$, which was decomposed into an intrinsic portion, $\log_{10} A_{int}$, and a reaction path degeneracy, rpd, with $\log_{10} A = \log_{10} A_{int} + rpd$. The activation energy E^* was determined by an Evans-Polanyi expression of form $E^* = E_o + \alpha\Delta H^o_r$. An algebraic steady state analysis was performed on the 910DMA mechanism to provide an independent check on numerical results of computer calculations, which agreed quite closely to within a factor of 2 or better. Conservation relations derived from the mechanistic model of 910DMA thermolysis and using the estimated rate constants were numerically integrated using a computer program called ACUCHEM.

Substrate and product histories and product selectivities as obtained from the numerical solution of the thermolysis model were compared to the experimental data for 910DMA, 9MA, TMA, CH4, DHDMA, heavies and product ratios R[DHDMA/9MA] and R[TMA/9MA] at the center of the experimental grid, $[910DMA]_o = 0.82$ mol/l and T = 355°C. The model is seen to predict 910DMA decay too slow, S(9MA) and S(TMA) are respectively 2.5 and 2.2-fold too low, S(DHDMA) is 1.8-fold too low at low conversions (X ~ 0.06) and 3.7-fold too high for X > 0.2, S(HVY) (sum of DMAD, DMAHDMAD and HDMAD) is comparable

at low X < 0.1 and 2.8-fold higher at X > 0.2, R[DHDMA/9MA] about 4-fold higher at low conversions and almost 10-fold higher for X > 0.2, and R[TMA/9MA] approximately equal to that experimentally observed.

910DMA decay half-life, major product selectivities and product ratios obtained from numerical solutions were compared with the experimental observations for varying $[910DMA]_o$ at fixed T = 355°C and for varying T at fixed $[910DMA]_o$ = 0.82 mol/l. The model predicted t^* too long, that is, decay kinetics too slow, compared to the experimental observations at all $[910DMA]_o$ and T with the model yielding a slope -0.93, implying ~ 2 order, versus the experimental data that yielded a slope of -0.53, implying 1½ order decomposition kinetics, and the model yielded an E^* = 40.1 kcal/mol versus the experimental data that provided E^* = 43.1 kcal/mol. The model predicted S(9MA) and S(TMA) too low at all $[910DMA]_o$ and T, S(DHDMA) too high for $[910DMA]_o$ > 0.082 mol/l and all T and too low for $[910DMA]_o$ = 0.082 mol/l at low (X ~ 0.06) conversions and too high for all $[910DMA]_o$ and T at high (X > 0.2) conversions , S(HVY) too high at all $[910DMA]_o$ and T, R[DHDMA/9MA] too high for $[910DMA]_o$ > 0.082 mol/l and all T and too low for $[910DMA]_o$ = 0.082 mol/l at low (X ~ 0.06) conversions and too high for all $[910DMA]_o$ and T at high (0.2 < X < 0.85) conversions, and R[TMA/9MA] too high at $[910DMA]_o$ > 0.082 mol/l and all T and too low at $[910DMA]_o$ = 0.082 mol/l.

A sensitivity analysis was performed to demonstrate how the errors of the estimated thermochemical and activation parameters affected the model results at the central point of the 910DMA experimental grid by separately perturbing the E^* of selected elementary reactions over the inherent errors in the ΔH°_r to show their effects on t^*, S(9MA), R[DHDMA/9MA] and R[TMA/9MA]. The variations of t^*_{mod}, R[DHDMA/9MA]$_{mod}$ and R[TMA/9MA]$_{mod}$ on account of the inherent errors in the estimated rate constants were large enough to exceed the span of experimental variations by changes in [910DMA]$_o$ at T = 355°C and in T at [910DMA]$_o$ = 0.82 mol/l. The variation in 9MA$_{mod}$ was not large enough to exceed the span of S(9MA)$_{exp}$ variations by changes in [910DMA]$_o$ and T due to the stoichiometric limit on S(9MA) but the 2.5-fold difference between t^*_{mod} and t^*_{exp} is well within the 30-fold uncertainty in t^*_{mod}.

These activation parameters were then adjusted within the limits of the errors to provide the best fit to the experimental results. Results as obtained from the optimized numerical solution were compared to the thermolysis model to the experimental data for 910DMA, 9MA, TMA, CH4, DHDMA, heavies, R[DHDMA/9MA] and R[TMA/9MA] at the center of the experimental grid. The model predicted 910DMA decay within the experimental observations, S(9MA) and S(TMA) are respectively 1.7 and 1.4-fold too low compared to the experimental observations (the mechanism as the upper limit of 0.33 for S(9MA) which was lower than the experimental values of S(9MA)), S(DHDMA) and R[DHDMA/9MA] had

426

the correct values at low and high conversions but the slope of the line did not correspond to the experimental data, S(HVY) was comparable at low X and 2.7-fold too high at X > 0.2, and R[TMA/9MA] was approximately equal to that experimentally observed at all conversions.

The observed formations of dimethylanthracene isomers 1,9-, 1,10-, 2,9- and 3,9-DMA from 9MA and of methylanthracene isomers 1MA and 2MA from ANT during 910DMA thermolysis at high severities invited interpretation by frontier orbital theory, as examples of periselective methyl radical attack on the aromatic anthracene nucleus. The ratios R[(2,9- + 3,9-)DMA/(1,9- + 1,10-)DMA] and R[2MA/1MA] can both be viewed as the relative methyl affinities of positions 1 and 2 on the periphery of the anthracene ring, with methyl attack at position 2 less favored than at position 1 by a factor of 2 to 4 as seen experimentally.

For ANT positions 2, 1 and 9, FMO theory using both Hückel and PM3 MO calculations predicts CH3* attack favored in the order of positions 2 < 1 < 9, which accords with the experimentally observed minor product ratios R[2MA/1MA] ~ 0.5 for methylation of ANT. For 9MA positions 2, 3, 1, 4 and 10, FMO theory using PM3 MO calculations predicts CH3* attack favored in the order of positions (2, 3) < (1, 4) < 9. Methyl attack at position 2 leads to 2,9-DMA, at position 3 to 3,9-DMA, at position 1 to 1,9-DMA, at position 4 to 1,10-DMA and at position 10 to 9,10-DMA. The predicted inequality between positions (2, 3) and (1, 4) accords with the experimentally observed ratio R[(2,9- + 3,9-)DMA/(1,9- + 1,10-)DMA] ~ 0.25.

5516.52

Chapter 6.

9-Methylanthracene Thermolysis

9-methylanthracene (9MA) was thermolyzed at temperatures between 315 and

409°C, initial concentrations from 0.082 to 2.08 mol/l, and batch holding times from

450 to 57600 seconds. Figure 6.1 illustrates this experimental grid which, including

replication, comprised 115 individual runs. Liquid reaction products were analyzed

in every experiment and gaseous products were also analyzed in experiments with

$[9MA]_o$ = 0.82 mol/l and a temperature of 370°C. The product histories and

selectivity diagrams of the individual runs were used to infer 9MA thermolysis

pathways. Reaction kinetics were determined from concentration scans at a fixed

temperature, T = 370°C, which led to reaction order, and temperature scans at fixed
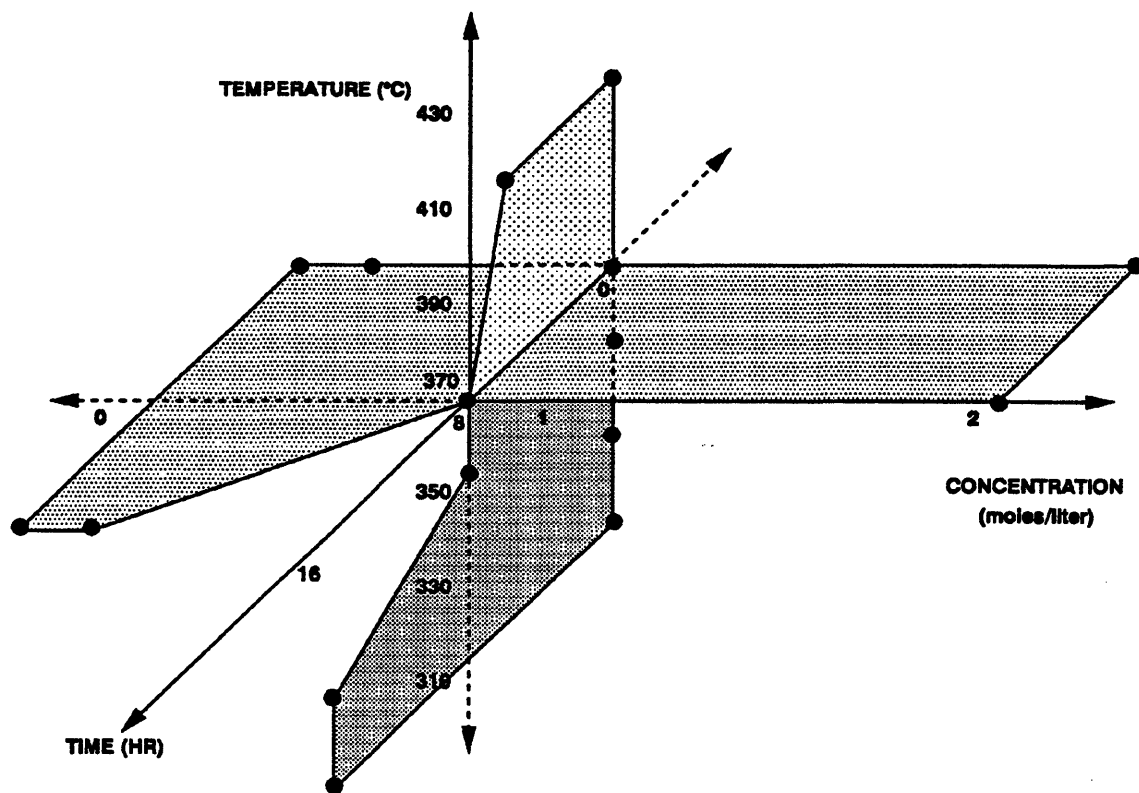
Figure 6.1: Grid for 9MA thermolysis experiments.

430

initial concentration, $[9MA]_o$ = 0.82 mol/l, which led to activation parameters. An overall free-radical mechanism was proposed to account for 9-methylanthracene decomposition. Both the kinetics of the system and the observed product histories were modelled. Finally frontier molecular orbital theory was used to interpret the kinetics and minor product distributions.

6.1 Experimental Results

6.1.1 A Representative Example

Product formation histories and a corresponding selectivity diagram were derived from each set of experiments at a fixed temperature and constant initial 9MA concentration. Figure 6.2, T = 370°C and $[9MA]_o$ = 0.82 mol/l, shows the histories of the major liquid and gaseous products (top) and minor liquid products (bottom). The plot uses arithmetic coordinates of absolute substrate amounts J in the reactor in moles, versus reaction holding time t in seconds, with the appropriate, different, ordinal scales in the upper and lower panels; all data refer to fixed reactor volume V = 0.60 cm³. In the upper panel of Figure 6.2, the substrate 9MA, symbol □, is seen to decay continuously from an initial J = 4.9E-04 moles to J = 2.0E-04 moles at t = 28800 s, the latter corresponding to a substrate fractional conversion X = 0.60; the decay half-life is t^* ~ 23400 s. The principal product, anthracene, abbreviated ANT with symbol •, increases from 0 initially to J = 1.2E-04 moles at t = 28800 s. The sum of all dimethylanthracenes, abbreviated ALL DMAs with symbol o, grow
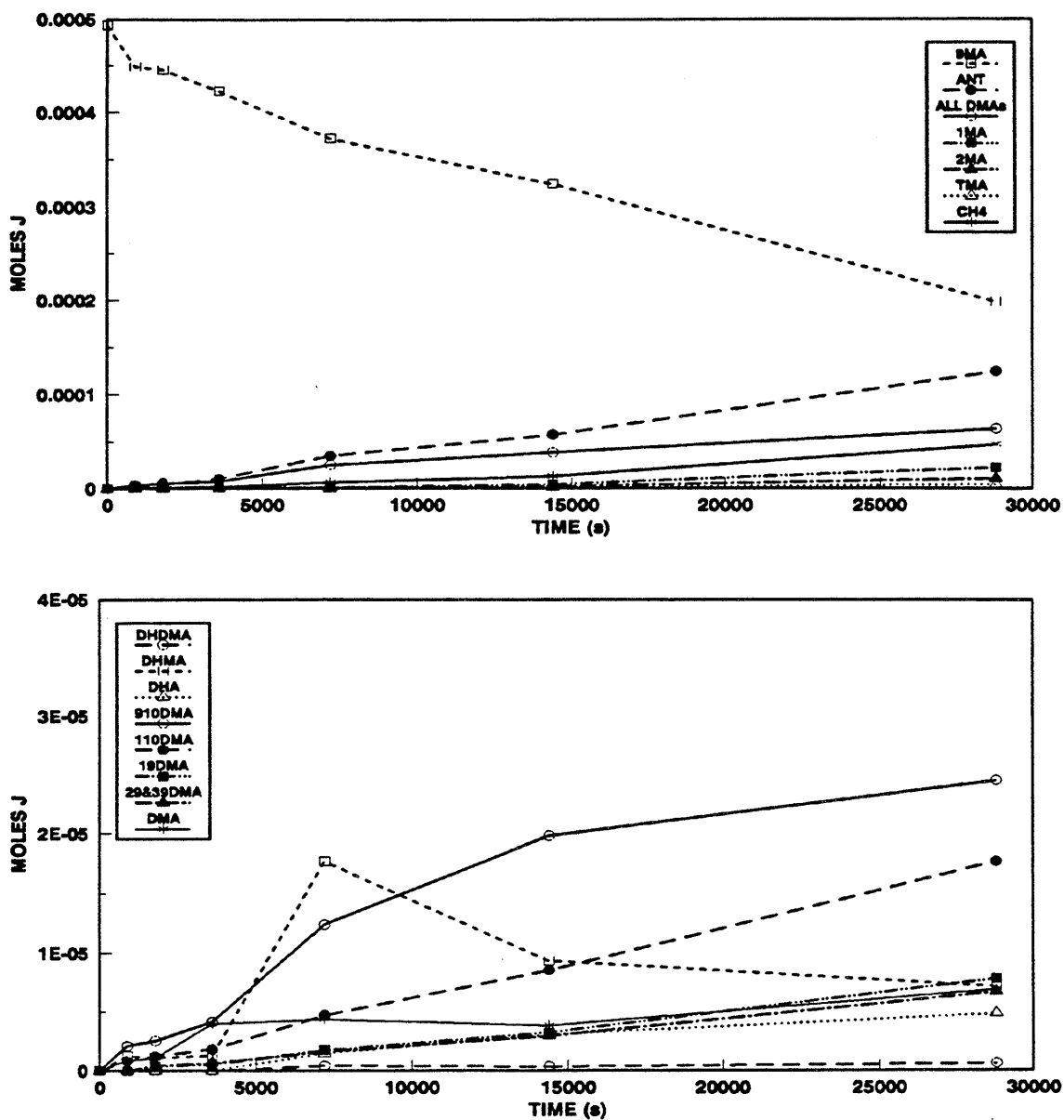
Figure 6.2: Product histories for 9MA thermolysis at 370°C with $[9MA]_o$ = 0.82 mol/l: major products (top) and minor products (bottom).

432

from 0 initially to J = 2.5E-5 moles at t = 7200 s, and then rise more slowly to J = 6.0E-05 moles at t = 28800 s. The 1-methylanthracene, abbreviated 1MA with symbol ■, and 2-methylanthracene, abbreviated 2MA with symbol ▲, respectively, appear at t = 900 and 7200 s with J = 1.9E-06 and 5.47E-07 moles, respectively, well after the first appearance of anthracene. 1MA is present as a 2% impurity in the 9MA substrate and therefore is detected at the shortest times in all experiments. The amount of 1MA detected at the shorter times remains relatively constant until the time 2MA is detected, and then increases. Both 1MA and 2MA grow monotonically with increasing time, to respectively, J = 2.2E-05 and 1.1E-05 moles at t = 28800 s, with 1MA the predominant of the two species. The sum of several trimethylanthracenes, abbreviated TMA with symbol ▵, appears first at t = 14400 s with J = 1.2E-06 and rises to J = 4.3E-06 moles at t = 28800 s. The gaseous product methane, abbreviated CH4 with symbol *, increases monotonically from 0 initially to J = 4.7E-05 moles at t = 28800 s. The substrate and major product histories in the present graph depict a classical parallel reaction series B(9MA) → A(910DMA) and B(9MA) → C(ANT).

The bottom panel of Figure 6.2 shows the histories of several minor liquid products that are formed during 9MA thermolysis, including the hydrogenated methylanthracene, anthracene, and dimethylanthracene species and the 1,10-, 1,9-, and 2,9-&3,9-dimethylanthracenes, and other dimethylanthracene isomers. Results labelled DHDMA, symbol ○, represent the *cis*-9,10-dihydro-9,10-dimethylanthracenes,

433

which was the only DHDMA detected of the four types that were identified in Section 4.3. The DHDMA appears at t = 7200 s with J = 4.1E-07 moles and rises slightly to J = 6.0E-07 moles at t = 28800 s. Results labelled DHMA, symbol □, represent the sum of three dihydromethylanthracene species, of which one, likely 9,10-dihydromethylanthracene, is most abundant. The DHMA appears at t = 900 s with J = 1.2E-06 moles, reaches a maximum J = 1.8E-05 moles at t = 72000 s, and then decreases to J = 7.1E-06 moles by the longest t = 28800 s. 9,10-dihydroanthracene, abbreviated DHA with symbol ▵, appears at t = 7200 s with J = 1.5E-06 moles and increases to amount J = 4.7E-06 moles at t = 28800 s. Of the dimethylanthracene isomers, in order of abundance, the 9,10-dimethylanthracene, abbreviated 910DMA with symbol ○, first appears at t = 900 s with J = 2.1E-06 moles and grows monotonically, but with decreasing slope to J = 2.5E-05 moles at t = 28800 s. 1,10-dimethylanthracene, abbreviated 110DMA with symbol •, appears at t = 900 s with J = 8.0E-07 moles and grows to J = 1.8E-05 moles at t = 28800 s. 1,9-dimethylanthracene, abbreviated 19DMA with symbol •, and 2,9&3,9-dimethylanthracenes, abbreviated 29&39DMA with symbol ▲, arise at t = 1800 s with, respectively, J = 3.4E-07 and 4.4E-07 moles and increase monotonically to J = 7.8E-06 and 6.7E-06 moles at t = 28800 s. DMA isomers other than those previously mentioned, abbreviated DMA with symbol *, first appear at t = 900 s with J = 8.7E-07 moles and rise to J = 5.3 ± 1.5E-06 moles for 7200 < t < 28800 s.

The data in Figure 6.2 are displayed as selectivity diagrams in Figure 6.3,

434
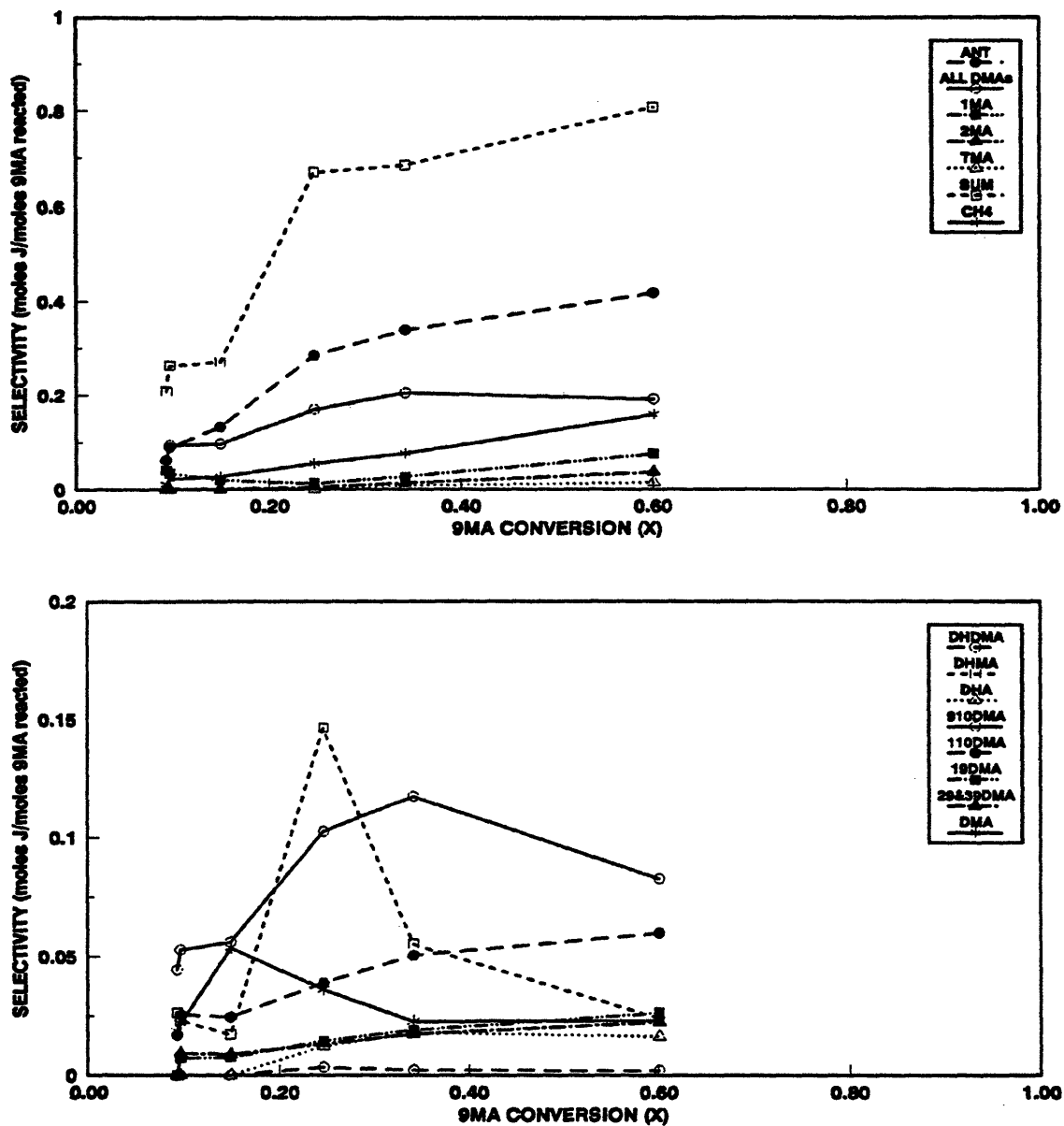
Figure 6.3: Selectivity diagram for 9MA thermolysis at 370°C with $[9MA]_o$ = 0.82 mol/l: major products (top) and minor products (bottom).

435

using ordinates of selectivity, S, defined as moles of product formed divided by moles

of substrate 9MA reacted, and an abscissae of substrate 9MA fractional conversion,

X. The upper and lower panels of Figure 6.3 respectively display the major liquid

and gaseous product selectivities and the minor liquid product selectivities obtained

for 9MA thermolysis at T = 370°C and $[9MA]_o$ = 0.82 mol/l. In the upper panel of

Figure 6.3, the selectivity to ANT, symbol •, is S = 0.061 at X = 0.093, then

increases monotonically but with decreasing slope to S = 0.42 at X = 0.60. The

selectivity to ALL DMAs, symbol o, appears with S = 0.061 at X = 0.093 and

increases to S = 0.18 ± 0.02 for 0.25 < X < 0.60. The isomer 1MA, symbol ■, starts

with S = 0.040 at X = 0.093, decreases slightly to S = 0.012 by X = 0.25 and then

rises to S = 0.075 by X = 0.60. The isomer 2MA, symbol ▲, appears with S =

0.0045 at X = 0.25 and increases to S = 0.036 at X = 0.60. Selectivity to TMA,

symbol △, is S = 0.0073 at X = 0.34 and increases to S = 0.014 at X = 0.60. The

sum of the selectivities of all identified products, Σ, abbreviated SUM with symbol

▫, increases sharply from Σ = 0.21 at X = 0.09 to Σ ~ 0.74 ± 0.07 for 0.25 < X <

0.60. The selectivity to methane, symbol *, is S = 0.010 at X = 0.093 and increases

to S = 0.16 at X = 0.60.

In the bottom panel of Figure 6.3, showing minor liquid product selectivities,

DHDMA, symbol o, appears at X = 0.25 and remains roughly constant at S =

0.0027 ± 0.0007 for 0.25 < X < 0.60. DHMA selectivity, symbol ▫, is S ~ 0.022 ±

0.005 for 0.09 < X < 0.15, rises sharply to S = 0.15 at X = 0.25 followed by a slow

decline to S = 0.024 at X = 0.60. DHA, symbol △, appears at X = 0.25 with S = 0.012 and increases to S = 0.017 for 0.34 < X < 0.60. 910DMA appears at X = 0.093 with S = 0.044, increases to maximum S = 0.12 at X = 0.34 and then decreases to S = 0.082 at X = 0.60. Selectivities of the dimethylanthracene isomers, 110DMA, symbol •, and 19DMA, symbol ■, both increase from S = 0.017 and 0, respectively, for X = 0.09 to S = 0.060 and 0.026 at X = 0.60. 29&39DMA selectivity, symbol ▲, increases from S = 0.0091 at X =0.10 to S = 0.022 at X = 0.60. Other DMA selectivity, symbol *, is S = 0.020 ± 0.003 for 0.093 < X < 0.60.

The preceding selectivity diagrams show that ANT, CH4, and ALL DMAs, with respective S ~ 0.35, 0.20, and 0.20, as well as DHMA, with S = 0.04, are among the earliest products observed during 9MA thermolysis. The pair of minor products 1MA and 2MA are observed well after the appearance of ANT, suggesting that they were from methylation of ANT, rather than from isomerization of the substrate 9MA. Finally, the hydrogenated products DHDMA and DHA both arise subsequent to the appearance of the parents, ALL DMAs and ANT.

Reaction pathways corresponding to the product histories and selectivities can now be elaborated as a basic demethylation and methylation sequence B(9MA) → C(ANT) and B(9MA) → A(910DMA), with competing, parallel, hydrogenation and methylation pathways at each stage. For example, at the first stage, B(9MA) → H_2B(DHMA) and B(9MA) → MeB(910DMA, 110DMA, 19DMA and 29&39DMA), followed by A(910DMA) → H_2A(DHDMA) and A(910DMA) → MeA(TMA) and

437

C(ANT) → H_2C(DHA) and C(ANT) → MeC(1MA and 2MA).

All subsequent 9MA results are discussed using the plots and symbols presented in the preceding example.

6.1.2. Effect of Initial 9-Methylanthracene Concentration

Initial 9-methylanthracene concentration was varied in three steps from 0.082 to 2.06 mol/l at fixed reaction temperature T = 370°C; this is represented by the horizontal plane of the experimental grid in Figure 6.1.

Figure 6.4 shows substrate and product histories at T = 370°C and $[9MA]_o$ = 0.082 mol/l. In the upper panel of Figure 6.4, the moles of substrate 9MA decrease from the initial J = 4.9E-05 moles to J = 2.7E-05 moles at t = 57600 s; the decay half-life is t^* ~ 70500 s. The amount of ANT increases monotonically but with decreasing slope from 0 initially to J = 7.4E-06 moles at t = 28800 s and then to J = 1.0E-05 moles at t = 57600 s. ALL DMAs are detected with J = 3.7E-07 moles at t = 7200 s and increase to J = 3.1E-06 moles at t = 57600 s. A small amount of 1MA, J = 8.0E-07 moles is detected at the longest t = 57600 s. In the lower panel of Figure 6.4, 910DMA is detected at t = 7200 s with J = 3.7E-07 moles, increases to J = 2.1E-06 moles at t = 28800 s and then rises slower to J = 2.4E-06 moles at t = 57600 s. 110DMA is detected at t = 14400 s with J = 4.5E-07 moles and increases slightly to J = 7.9E-07 moles at t = 57600 s.

Figure 6.5 is a selectivity diagram corresponding to the data in Figure 6.4.
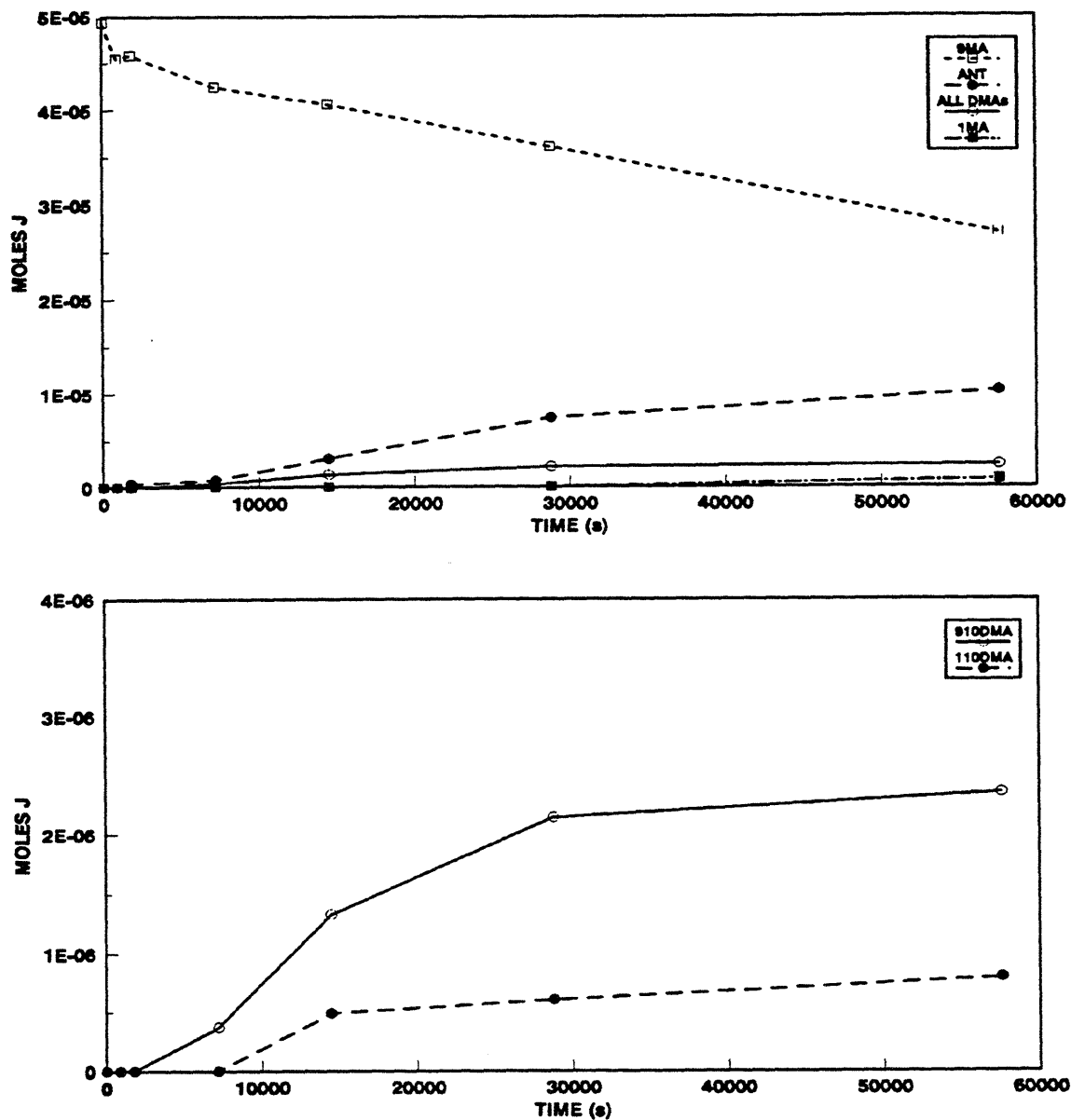
Figure 6.4: Product histories for 9MA thermolysis at 370°C with $[9MA]_o$ = 0.082 mol/l: major products (top) and minor products (bottom).

439
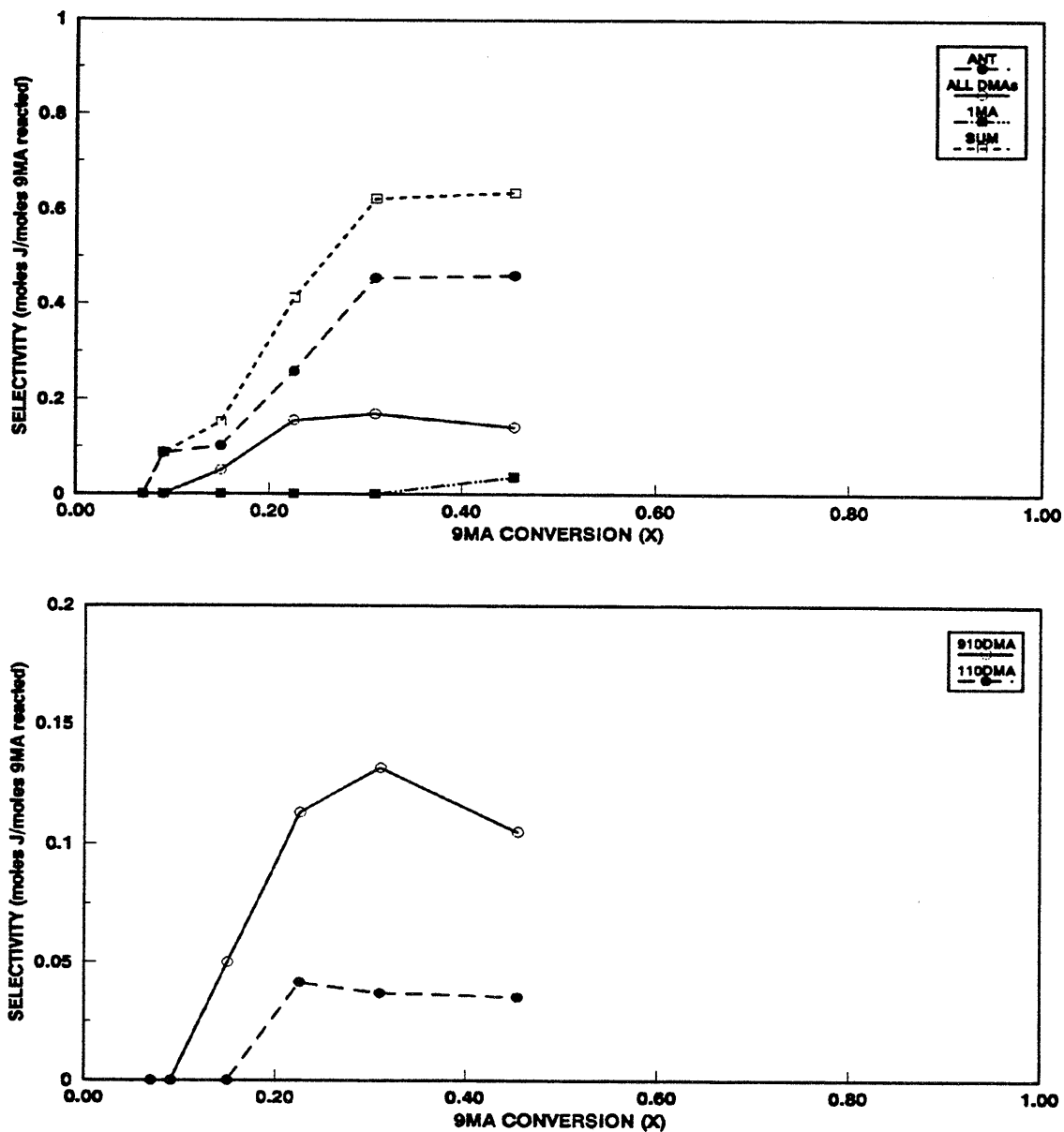
Figure 6.5: Selectivity diagram for 9MA thermolysis at 370°C with $[9MA]_o = 0.082$ mol/l: major products (top) and minor products (bottom).

440

The upper panel of Figure 6.5, the selectivity to ANT is S = 0.086 at X = 0.091 and increases to S = 0.46 for 0.31 < X < 0.45. ALL DMAs are detected at X = 0.15 with S = 0.050 and remain roughly constant with S = 0.15 ± 0.01 over 0.23 < X < 0.45. 1MA selectivity is S = 0.036 at X = 0.45. The selectivities sum is Σ = 0.086 at X = 0.091, rises sharply and then remains roughly constant at Σ = 0.62 ± 0.01 for 0.31 < X < 0.45. In the lower panel of Figure 6.5, 910DMA selectivity is S = 0.050 at X = 0.15, rises to S = 0.13 at X = 0.31 and then declines to S = 0.10 at X = 0.45. 110DMA is detected with S = 0.041 at X = 0.23 and remains roughly constant to X = 0.45.

Figure 6.6 shows the substrate and product histories at T = 370°C and [9MA]$_o$ = 0.25 mol/l. In the upper panel of Figure 6.6, the moles of substrate 9MA decay from the initial J = 1.5E-04 moles to J = 8.0E-05 moles at t = 14400 s followed by a shallower decline to J = 5.8E-05 moles at t = 57600 s; the decay half-life is t* = 31000 s. ANT product grows from 0 initially to J = 2.7E-06 moles at t = 14400 s and rises slower to J = 4.4E-04 moles at t = 57600 s. ALL DMAs are first detected at t = 1800 s with J = 2.9E-06 moles and increase to J = 1.4 ± 0.1E-05 moles for 14400 < t < 57600 s. 1MA is detected at t = 900 s with J = 2.6E-07 moles and increases to J = 7.5E-06 moles at t = 57600 s. 2MA is detected at t = 14400 s with J = 8.6E-07 moles and rises monotonically to J = 2.3E-06 moles at t= 57600 s. TMA is only detected at the longest time t = 57600 s with J = 4.3E-07 moles. In the lower panel of Figure 6.6, DHMA is detected with J = 8.7E-07 moles at t =

441
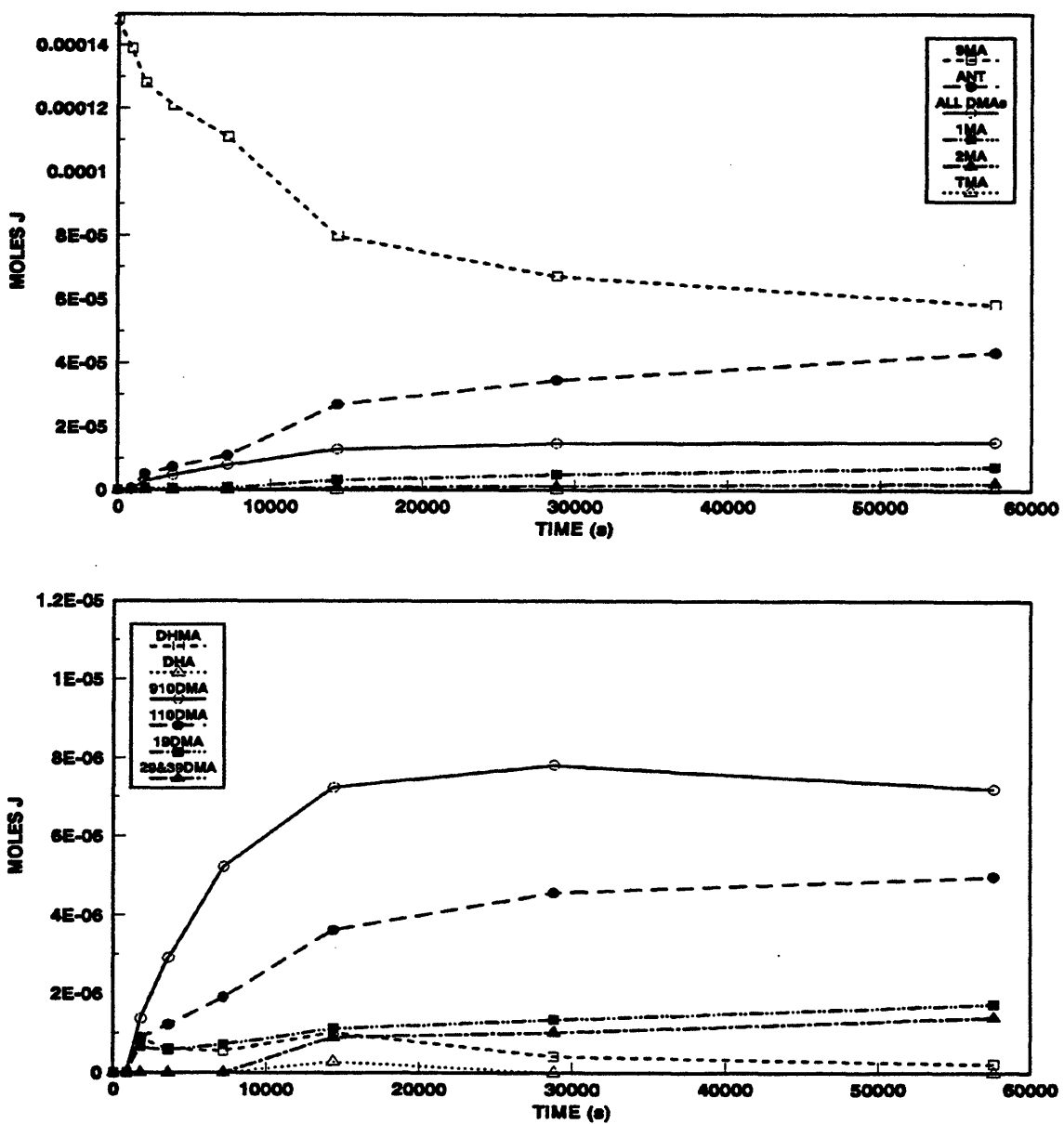
Figure 6.6: Product histories for 9MA thermolysis at 370°C with [9MA]$_o$ = 0.25 mol/l: major products (top) and minor products (bottom).

442

1800 s, rises to a shallow maximum of J = 1.0E-06 moles at t = 14400s, and then declines to J = 2.2E-07 moles at t = 57600 s. DHA is only detected at t = 14400 s with J = 2.8E-07 moles. 910DMA is detected at t = 1800 s with J = 1.4E-06 moles, increases to J = 7.2E-06 moles at t = 14400 s where its remains roughly constant up to t = 57600 s. 110DMA is detected at t = 1800 s with J = 8.8E-07 moles, rises to J = 4.6E-06 moles at t = 28800 s and remains constant up to t = 57600 s. 19DMA is detected at t = 1800 s with J = 6.4E-07 moles and increases slightly to J = 1.7E-06 moles at t = 57600 s. 29&39DMA are detected at t = 14400 s with J = 9.0E-07 moles and rises to J = 1.4E-06 moles at t = 57600 s.

Figure 6.7 is a selectivity diagram corresponding to the data in Figure 6.6. In the upper panel of Figure 6.7, ANT exhibits selectivity S = 0.062 at X = 0.055, increases to S = 0.27 at X = 0.18, grows slower to S = 0.42 at X = 0.55, and more steeply increases to S = 0.49 at X = 0.60. ALL DMAs appear with S = 0.13 at X = 0.15, increase to maximum S = 0.22 at X = 0.25 and then decline to S = 0.16 at X = 0.60. 1MA appears with S = 0.033 at X = 0.055, remains roughly constant at X = 0.030 ± 0.010 for 0.06 < X < 0.47 and then increases to S = 0.085 at X = 0.60. 2MA is detected at X = 0.47 with selectivity S = 0.012 and climbs to S = 0.026 at X = 0.60. The selectivity sum increases sharply from Σ = 0.095 at X = 0.06 to Σ = 0.55 at X = 0.25, followed by a slower increase to Σ = 0.68 at X = 0.55 which is followed by an increase to Σ = 0.78 at X = 0.60. In the lower panel of Figure 6.7, DHMA selectivity appears with a maximum S = 0.038 at X = 0.15 and then declines

443
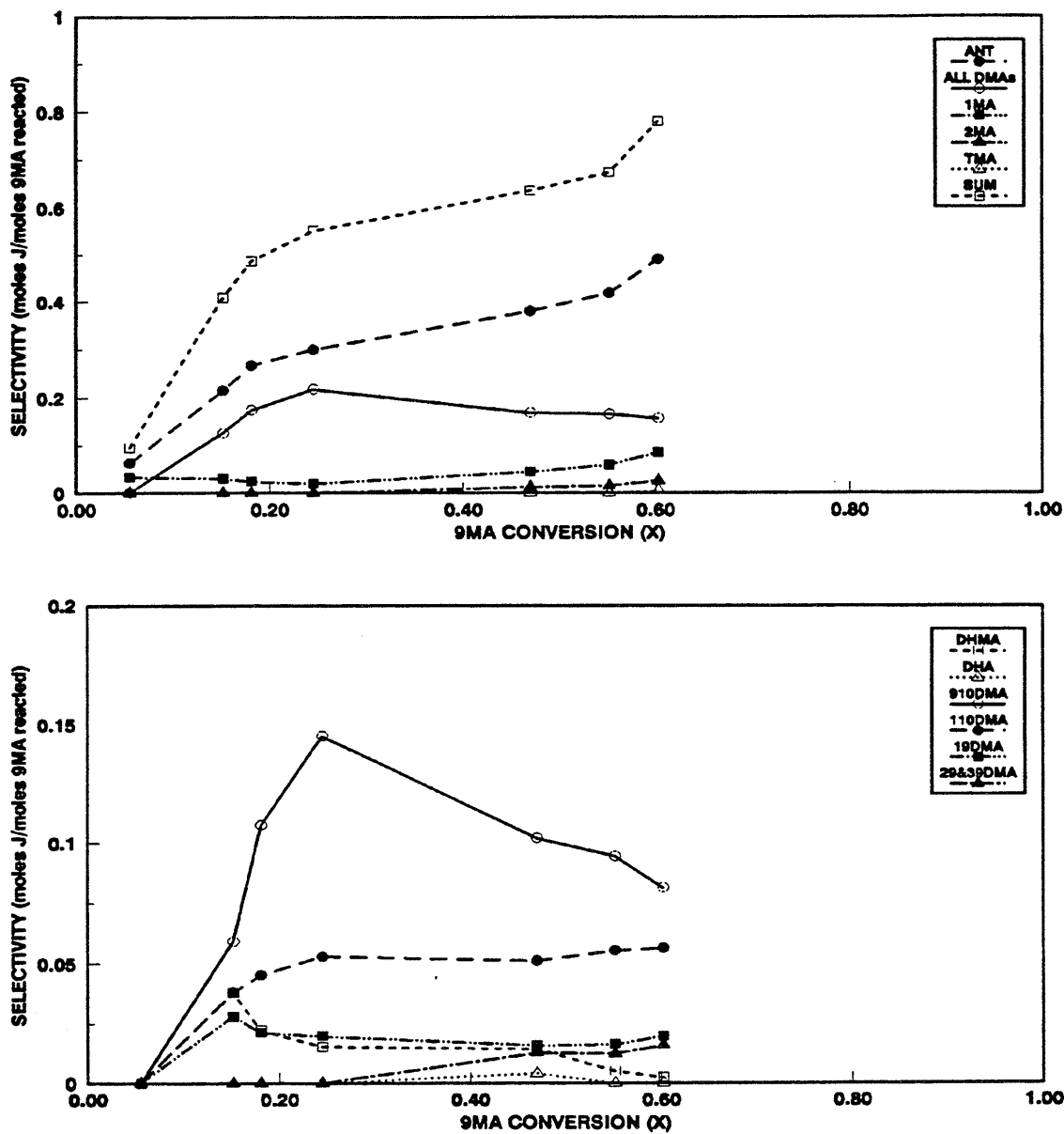
Figure 6.7: Selectivity diagrams for 9MA thermolysis at 370°C with [9MA]$_o$ = 0.25 mol\l: major products (top) and minor products (bottom).

to S = 0.0024 at X = 0.60. DHA selectivity at X = 0.47 is S = 0.0040. 910DMA

emerges at X = 0.15 with S = 0.059, increases to S = 0.15 at X = 0.25 and slowly

declines to S = 0.081 by X = 0.60. 110DMA appears at X = 0.15 with S = 0.038

and maintains S = 0.050 ± 0.006 over 0.24 < X < 0.60. 19DMA appears at X =

0.15 with S = 0.028 and remains roughly constant at S = 0.018 ± 0.003 over 0.18 <

X < 0.60. 29&39DMA appear at X = 0.47 with S = 0.13 and remain roughly

constant up to X = 0.60.

Figure 6.8 shows substrate and product at T = 370°C and $[9MA]_o$ = 2.06

mol/l. In the upper panel of Figure 6.8, the moles of substrate 9MA decay from J

= 1.2E-03 moles initially to J = 3.4E-04 moles at t = 28800 s; the decay half-life is

t^* ~ 12500 s. ANT appears at the earliest time of t = 450 s with J = 6.8E-06 moles

and grows monotonically but with decreasing slope to J = 3.8E-04 moles at t =

28800 s. The sum of ALL DMAs is J = 1.1E-05 moles at t = 450 s, grows to a

maximum J = 1.5E-04 moles at t = 14400 s and then declines slightly to J = 1.4E-04

moles at t = 28800 s. 1MA is also detected at t = 450 s with J = 6.5E-06 moles and

rises monotonically J = 9.8E-05 moles at t = 28800 s. 2MA is detected at t = 900

s with J = 2.7E-07 moles and rises to J = 4.7E-05 moles at t = 28800 s. TMA is

detected with J = 8.8E-07 moles at t = 1800 s and grows to J = 1.0E-05 moles by

t = 28800 s. In the lower panel of Figure 6.8, DHMA appears at t = 450 s with J

= 4.0E-06 moles, grows to maximum J = 1.6E-05 moles at t = 14400 s and then

declines slightly to J = 1.5E-05 moles at t = 28800 s. DHA appears at t = 3600 s
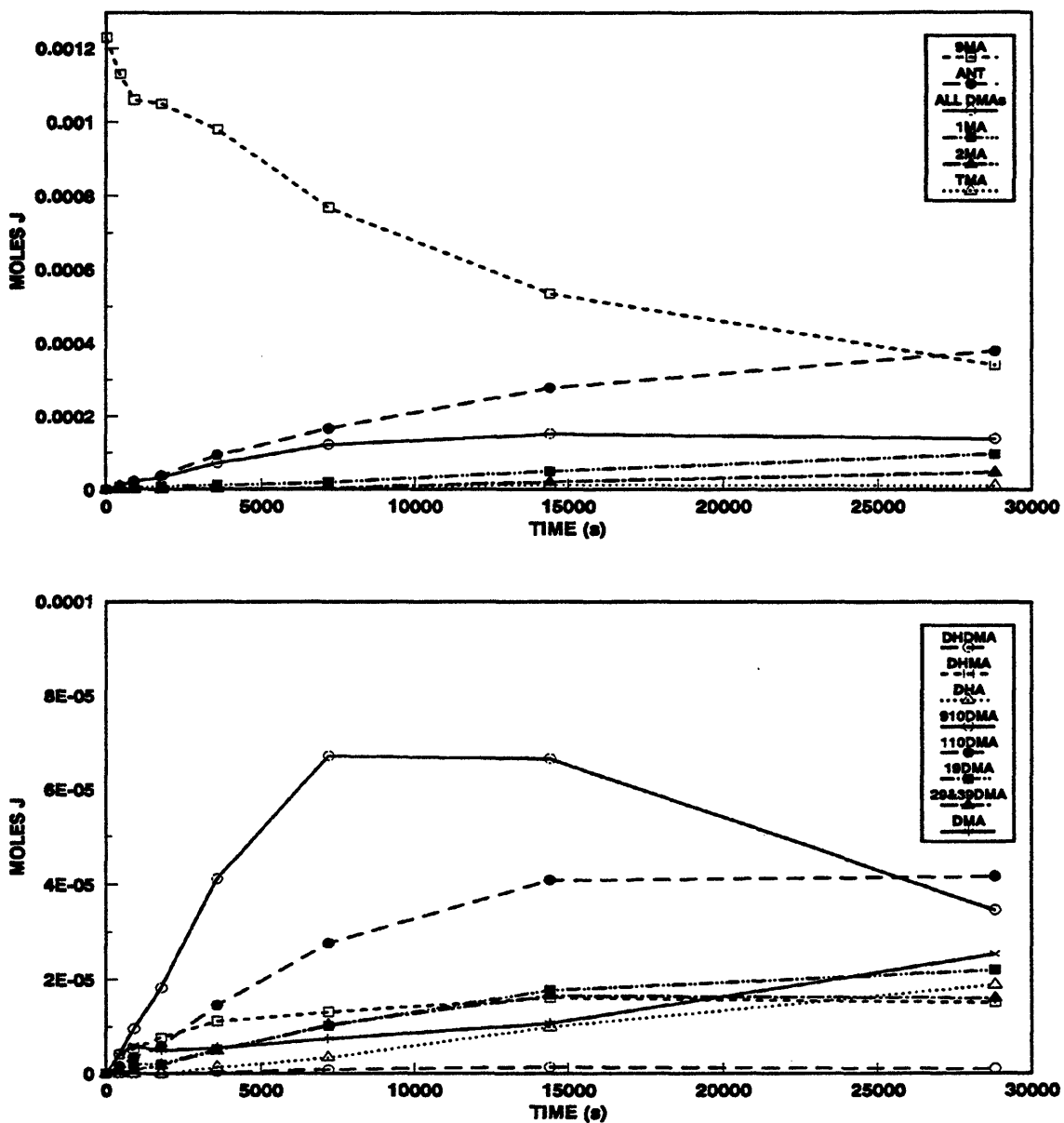
Figure 6.8: Product histories for 9MA thermolysis at 370°C with [9MA]$_o$ = 2.06 mol/l: major products (top) and minor products (bottom).

446

with J = 1.3E-06 moles and then rises monotonically to J = 1.9E-05 moles at t = 28800 s. 910DMA is detected at t = 450 s with J = 4.2E-06 moles, rises to maximum J = 6.7E-05 moles for 7200 < t < 14400 s, and then declines to J = 3.9E-05 moles at t = 28800 s. 110DMA, 19DMA and 29&39DMA are each detected at t = 450 s with J = 1.6E-06, 9.6E-07 and 2.7E-07 moles, respectively, rise monotonically but decreasing slope to J = 4.1E-05, 1.8E-05 and 1.6E-05 moles at t = 14400 s and then to J = 4.2E-05, 2.2E-05 and 1.6E-05 moles at t = 28800 s. Other DMA isomers appear at t = 450 s with J = 4.0E-06 moles, remain roughly constant at J = 5.0 ± 1.0E-06 moles for 450 < t < 7200 s, and then increase to J = 2.5E-05 moles at t = 28800 s.

Figure 6.9 is a selectivity diagram corresponding to the data in Figure 6.8. In the upper panel of Figure 6.9, ANT selectivity is S = 0.068 at X = 0.083, and then remains at S = 0.39 ± 0.04 for 0.21 < X < 0.72. ALL DMAs are detected with S = 0.11 at X = 0.083, increases to a maximum of S = 0.27 at X = 0.21, then decreases to S = 0.16 at X = 0.72. 1MA selectivity is roughly constant at S = 0.052 ± 0.014 for 0.083 < X < 0.38 and then increases to S = 0.11 at X = 0.72. 2MA appears with S = 0.0015 at X = 0.14 and increases monotonically to S = 0.053 at X = 0.72. TMA appears with S = 0.0049 at X = 0.15, rises to S = 0.018 at X = 0.57 ant then declines to S = 0.012 at X = 0.72. The selectivity sum is Σ = 0.29 at X = 0.083 rises and remains roughly constant Σ = 0.76 ± 0.05 for 0.21 < X < 0.72. The bottom graph of Figure 6.9 shows the selectivity of other minor liquid products.
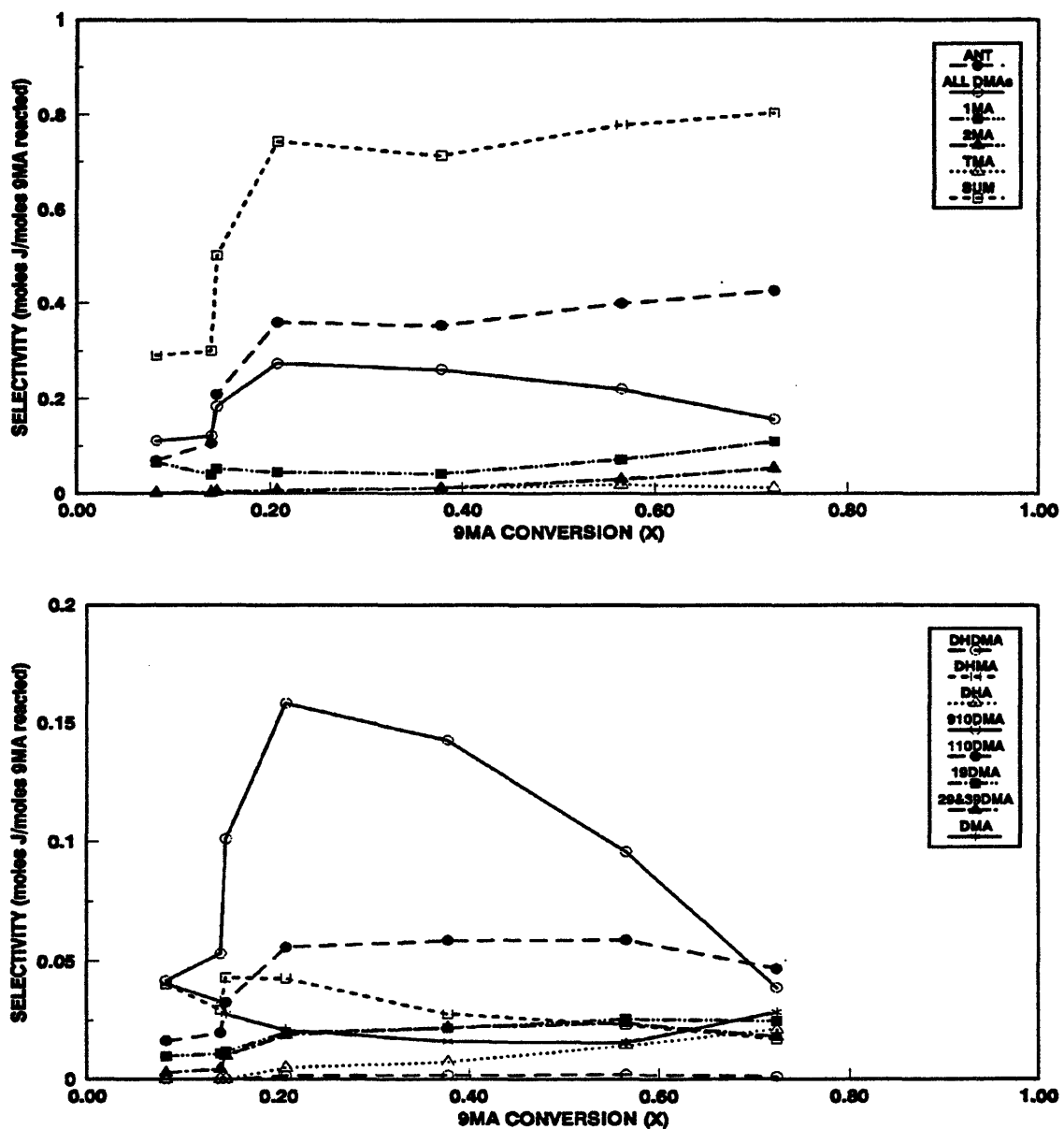
Figure 6.9: Selectivity diagrams for 9MA thermolysis at 370°C with $[9MA]_o = 2.06$ mol/l: major products (top) and minor products (bottom).

448

DHDMA is detected at $X = 0.21$ with $S = 0.0015$ and remains constant with $S = 0.0015 \pm 0.0004$ for $0.21 < X < 0.72$. DHMA selectivity is $S = 0.040$ at $X = 0.083$, increases to $S = 0.043$ at $X = 0.15$, and then declines to $S = 0.017$ at $X = 0.72$. DHA selectivity is 0.0048 at $X = 0.21$ and grows monotonically to $S = 0.021$ at $X = 0.72$. 910DMA selectivity is $S = 0.042$ at $X = 0.083$, rose sharply to $S = 0.16$ at $X = 0.21$ and then declines to $S = 0.04$ by $X = 0.71$. 110DMA selectivity increases from $S = 0.016$ at $X = 0.083$ to $S = 0.055 \pm 0.006$ for $0.21 < X < 0.72$. 19DMA and 29&39DMA appear with $S = 0.0096$ and 0.0027, respectively, at $X = 0.083$ and increase to $S = 0.023 \pm 0.003$ and 0.021 ± 0.003 for $0.21 < X < 0.72$. Selectivity to the other DMAs is approximately constant at $S = 0.020 \pm 0.010$ for $0.083 < X < 0.72$.

6.1.3 Summary of Concentration Effects

Increasing initial substrate concentration from $[9MA]_o = 0.082$ to 2.06 mol/l at fixed $T = 370°C$ influences both the reaction kinetics and product selectivities, as respectively summarized in Table 6.1 and Table 6.2. Note that values in the tables are the averages over all runs, including replication and are therefore not precisely identical to those seen in the preceding figures. Part (a) of Table 6.1 shows that the substrate decay half-life t^* decreased about 6-fold, from 70477 to 12494 s, as initial concentration $[9MA]_o$ increased 25-fold, from 0.082 to 2.06 mol/l. Figure 6.10, a

Table 6.1

		\[9MA\]$_o$ (mol/l)			
Part		0.082	0.25	0.82	2.06
a	Half-life t^*, s	70477[1] $\pm$ 4401[2]	31288 $\pm$ 10085	23430 $\pm$ 748	12494 $\pm$ 318
b	\[DHMA/9MA\]$_{t=14400}$	ND	0.013	0.013	0.028
	$t = 14400/t^*$		0.46	1.23	1.15

EFFECT OF INITIAL 9MA CONCENTRATION ON KINETIC PARAMETERS AT T = 370°C

[1] Half-life calculated using X at longest t and integrated 3/2 order rate expression: $t^* = 0.41421t / [(1/(1-X)^{\frac{1}{2}}) - 1]$

[2] $\pm$ = standard deviation of the average half-life

Table 6.2

EFFECT OF INITIAL 9MA CONCENTRATION ON PRODUCT SELECTIVITIES AT T = 370°C

Part	Selectivity S of:	Conversion X Range:	[9MA]$_o$ (mol/l) 0.082	0.25	0.82	2.06
a	ANT	0.2 - 0.75	0.41	0.39	0.37	0.37
	ALL DMAs	0.2 - 0.75	0.14	0.20	0.22	0.22
b	DHMA	0.15 ± 0.01	ND	0.038	0.031	0.054
		0.40 ± 0.03	ND	0.003	0.014	0.028
	DHA	0.40 ± 0.03	ND	ND	0.004	0.007
	DHDMA	0.65 ± 0.05	ND	ND	0.002	0.001
c	1MA	0.40 ± 0.03	0.036	0.045	0.043	0.041
	2MA	0.40 ± 0.03	ND	0.007	0.012	0.011
	910DMA	0.25 ± 0.05	0.131	0.173	0.168	0.162
		0.40 ± 0.03	0.107	0.156	0.144	0.142
	110DMA	0.2 - 0.6	0.034[1]	0.056	0.056	0.055
	19DMA	0.2 - 0.6	ND	0.019	0.021	0.023
	29&39DMA	0.2 - 0.6	ND	0.014	0.019	0.020
	other DMAs	0.2 - 0.6	ND	ND	0.015	0.018

[1] For [9MA]$_o$ = 0.082 mol/l, S(110DMA) over range 0.2 < X < 0.4

451
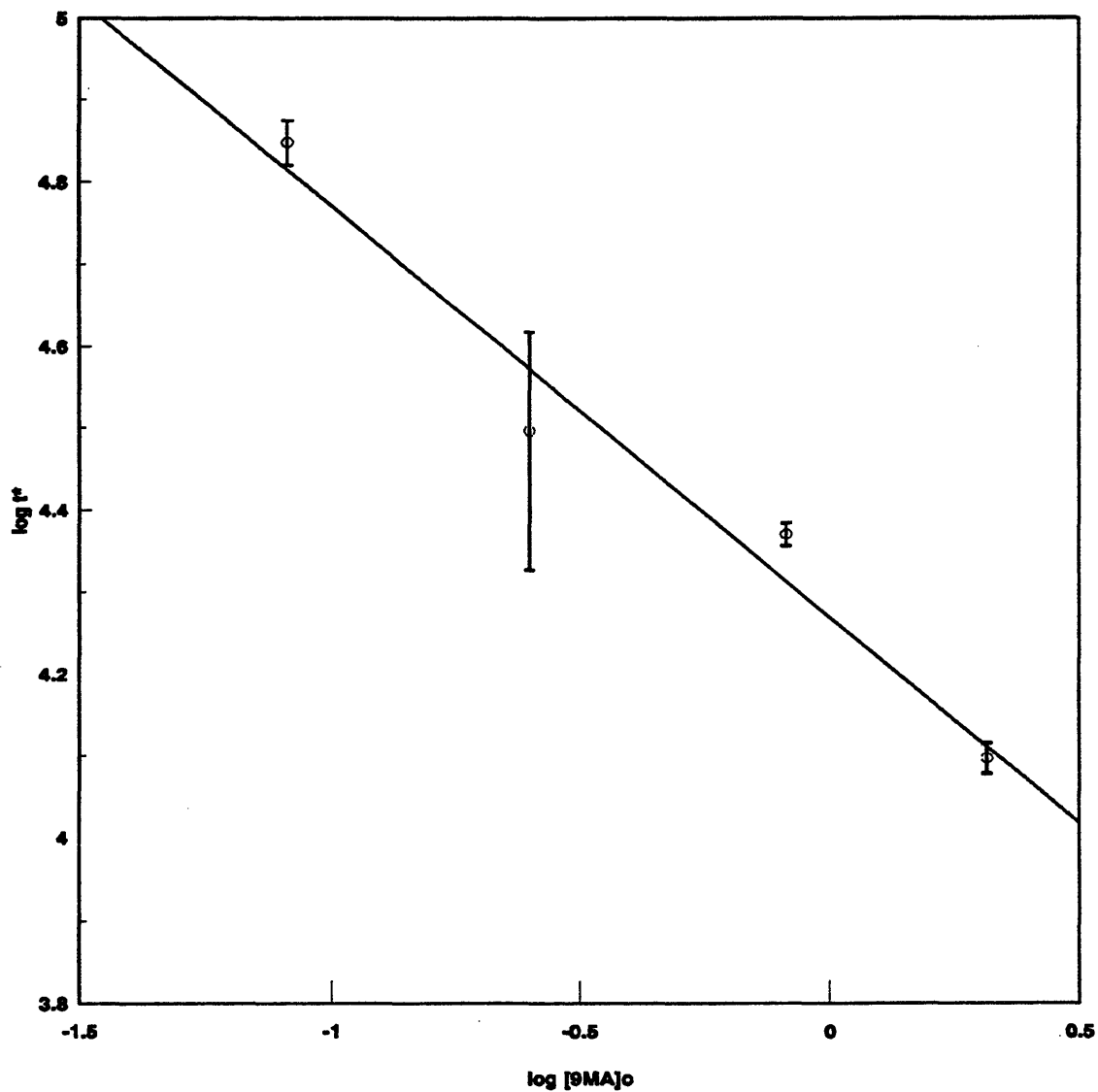
Figure 6.10: Decay half-life t^* for varying initial concentrations $[9MA]_o$ at fixed T
= 370°C.

doubly logarithmic plot of t^* vs. $[9MA]_o$, shows that the data adhere to a line:

$$\log t^* = -0.502 \ \log[9MA]_o + 4.27 \qquad (6.1)$$

The slope of this line, $\sim -1/2$, implies that 9MA decomposition is 3/2 order in substrate. Also, the intercept of the line shows the rate constant at T = 370°C to be $\log k_2 = -4.35$, by reference to the integrated 3/2-order rate expression:

$$\frac{1}{[9MA]_t^{1/2}} - \frac{1}{[9MA]_o^{1/2}} = \frac{k_2 \, t}{2} \qquad (6.2)$$

Product histories at $[9MA]_o$ = 0.25, 0.82 and 2.06 mol/l, shown in Figure 6.6, Figure 6.2 and Figure 6.8, also provide an indication of the relative kinetics of the parallel reactions:

$$9MA \ \overset{k_3}{\rightarrow} \ DHMA \ \overset{k_4}{\rightarrow} \ products \qquad (6.3)$$

DHMA attains a shallow maximum concentration $[DHMA]_{max}$ at t = 14400 s in the figures, then, as shown in part (b) of Table 6.1, $[DHMA/9MA]_{t=14400}$ remains roughly constant while $[t = 14400/t^*]$ increases with increasing [9MA]o. $[DHMA/9MA]_{t=14400}$ $\sim$ 0.013 for 0.25 < $[9MA]_o$ < 0.82 mol/l and $[DHMA/9MA]_{t=14400}$ = 0.028 for $[9MA]_o$ = 2.06 mol/l while $[t=14400/t^*]$ = 0.46 at $[9MA]_o$ = 0.25 mol/l and increases to $[t=14400/t^*]$ = 1.19 ± 0.04 at $[9MA]_o$ = 0.82 and 2.06 mol/l. Both suggest that DHMA decomposes faster than it forms from 9MA, i.e., $k_4/k_3 > 1$, and that k_4 is of lower order than k_3.

453

Turning to product selectivities, summarized in Table 6.2, both ANT and sum of ALL DMAs selectivities were roughly independent of conversion over the ranges $0.2 < X < 0.75$ at all initial concentrations, as shown in part (a) of Table 6.2. The absolute values of S(ANT) and S(ALL DMAs) remained somewhat constant with increasing $[9MA]_o$ at $S = 0.38 \pm 0.03$ and 0.18 ± 0.04, respectively. The hydrogenated species DHMA selectivity was essentially highest at the lowest conversions and then declined, in some cases precipitously, with increasing X, as shown in part (b) of Table 6.2. For all $[9MA]_o > 0.25$ mol/l, the absolute S(DHMA) increased with increasing $[9MA]_o$ at both $X = 0.15 \pm 0.01$ and $X = 0.40 \pm 0.03$. S(DHMA) = 0.038 at $X = 0.15 \pm 0.01$ for $[9MA]_o = 0.25$ mol/l increases to S(DHMA) = 0.054 at $X = 0.15 \pm 0.01$ for $[9MA]_o = 2.06$ mol/l, while S(DHMA) = 0.003 at $X = 0.40 \pm 0.03$ for $[9MA]_o = 0.25$ mol/l increases to S(DHMA) = 0.028 at $X = 0.40 \pm 0.03$ at $[9MA]_o = 2.06$ mol/l. Of the other hydrogenated species, DHA was detected at the highest $[9MA]_o = 0.82$ and 2.06 mol/l with S(DHA) ~ 0.004 and 0.007, respectively, at $X = 0.40 \pm 0.03$. DHDMA was detected at the highest $[9MA]_o = 0.82$ and 2.06 mol/l, and then only at the highest conversion, with S(DHDMA) = 0.002 and 0.001, respectively, at $X = 0.65 \pm 0.05$. Methylanthracene selectivities increased monotonically from 0 as conversions increased for all initial concentrations, as shown in part (c) of Table 6.2. S(1MA) and S(2MA) generally increased with increasing X at all $[9MA]_o$, with S(1MA) > S(2MA) always and both always < S(ANT) at any $X > 0.10$. S(1MA) was sometimes

greater than S(ANT) for X < 0.10 due to the impurity of 1MA in the 9MA substrate. S(1MA) = 0.040 ± 0.005 at X = 0.40 ± 0.03 for all $[9MA]_o$ and S(2MA) = 0.007 ± 0.003 at X = 0.40 ± 0.03 for 0.25 < $[9MA]_o$ < 2.06 mol/l. 910DMA selectivity increase monotonically from 0 to a maximum at X ~ 0.25 for all $[9MA]_o$ > 0.25 mol/l and then declined monotonically with increasing conversion for all initial concentrations, as shown in part (c) of Table 6.2. S(910DMA) = 0.131 at X = 0.30 for $[9MA]_o$ = 0.082 mol/l and S(910DMA) = 0.167 ± 0.005 at X = 0.25 ± 0.05 for $[9MA]_o$ > 0.25 mol/l. S(910DMA) decreased to 0.107 at X = 0.40 ± 0.03 at $[9MA]_o$ = 0.082 mol/l and 0.149 ± 0.007 at X = 0.40 ± 0.03 for $[9MA]_o$ > 0.25 mol/l. The other dimethylanthracene, 110DMA, 19DMA, 29&39DMA and other DMA, selectivities generally remained constant as conversions increased for all initial concentrations, as shown in part (c) of Table 6.2. Of the dimethylated species, the order of abundance was generally S(910DMA) > S(110DMA) > S(19DMA) > S(29&39DMA) > S(other DMAs) at X < 0.60. The absolute values of S(110DMA), S(19DMA), S(29&39DMA) and S(DMA) remained roughly constant with increasing $[9MA]_o$. S(110DMA) = 0.034 for 0.2 < X < 0.4 at $[9MA]_o$ = 0.082 mol/l and S(110DMA) = 0.055 for 0.2 < X < 0.6 for 0.25 < $[9MA]_o$ < 2.06 mol/l. S(19DMA) = 0.021 ± 0.002 for 0.2 < X < 0.6 for 0.25 < $[9MA]_o$ < 2.06 mol/l. S(29&39DMA) = 0.017 ± 0.003 for 0.2 < X < 0.6 for 0.25 < $[9MA]_o$ < 2.06 mol/l. S(DMA) = 0.016 ± 0.002 for 0.2 < X < 0.6 for 0.82 < $[9MA]_o$ < 2.06 mol/l.

Finally, Figure 6.11 depicts the variation of product ratio
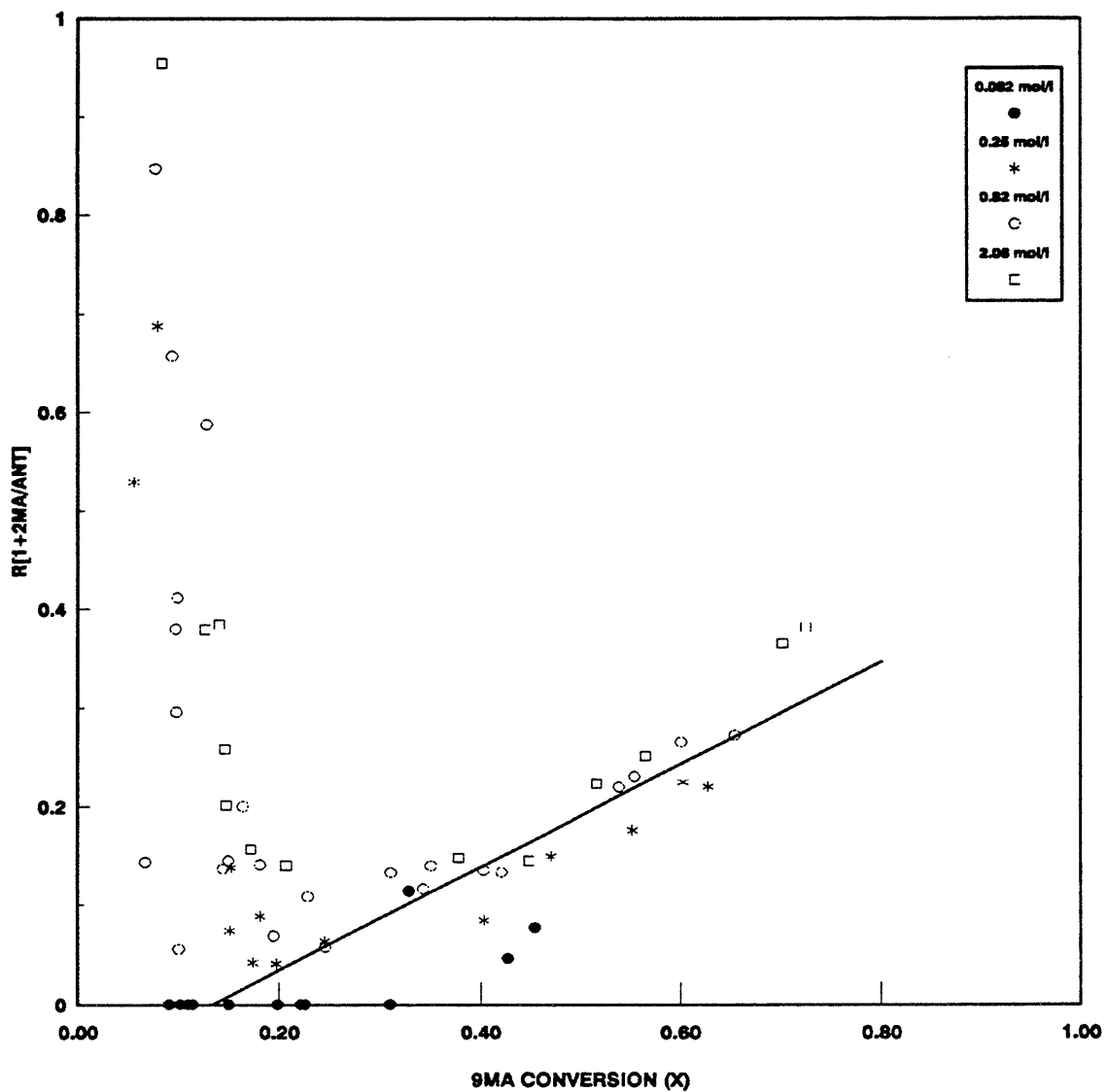
Figure 6.11: Ratio of moles 1MA and 2MA to moles ANT produced vs. 9MA conversion (X) for varying [9MA]$_o$ at fixed T = 370°C.

R[(1MA+2MA)/ANT] versus 9MA conversion X at all initial substrate concentrations. In Figure 6.11, it is seen that, for all experiments at X > 0.15, the ratio of monomethylated species to ANT, R[(1MA+2MA)/ANT], is essentially a function of conversion only, with data for all initial concentrations, $0.082 < [9MA]_o < 2.06$ mol/l, lying on roughly the same curve. At X < 0.15, the R[(1MA+2MA)/ANT] is as large as 1 due to the 1% 1MA impurity in the 9MA substrate. At these low conversions, there is very little ANT formed, therefore the 1MA impurity is accentuated when divided by the small amount of ANT. This relationship implicitly describes the kinetics of ANT methylation during thermolysis of the 9MA substrate under the present conditions.

6.1.4. Effect of Temperature

Reaction temperature was varied from 315 to 409°C at a fixed initial concentration of $[9MA]_o = 0.82$ M, with these experiments represented by the vertical plane of the grid in Figure 6.1.

Figure 6.12 shows substrate and product histories at T = 315°C and $[9MA]_o = 0.82$ M. In the upper panel of Figure 6.12, the moles of substrate 9MA decay from the initial J = 4.9E-04 moles to J = 4.3E-04 moles at t = 57600 s; the decay half-life $t^* \sim 390,000$ s. ANT grows monotonically from 0 initially to J = 6.1E-06 moles at t = 57600 s. ALL DMAs are first detected at t = 7200 s with J = 1.1E-06 moles and increase to J = 5.9E-06 moles at t = 57600 s. 1MA remains roughly
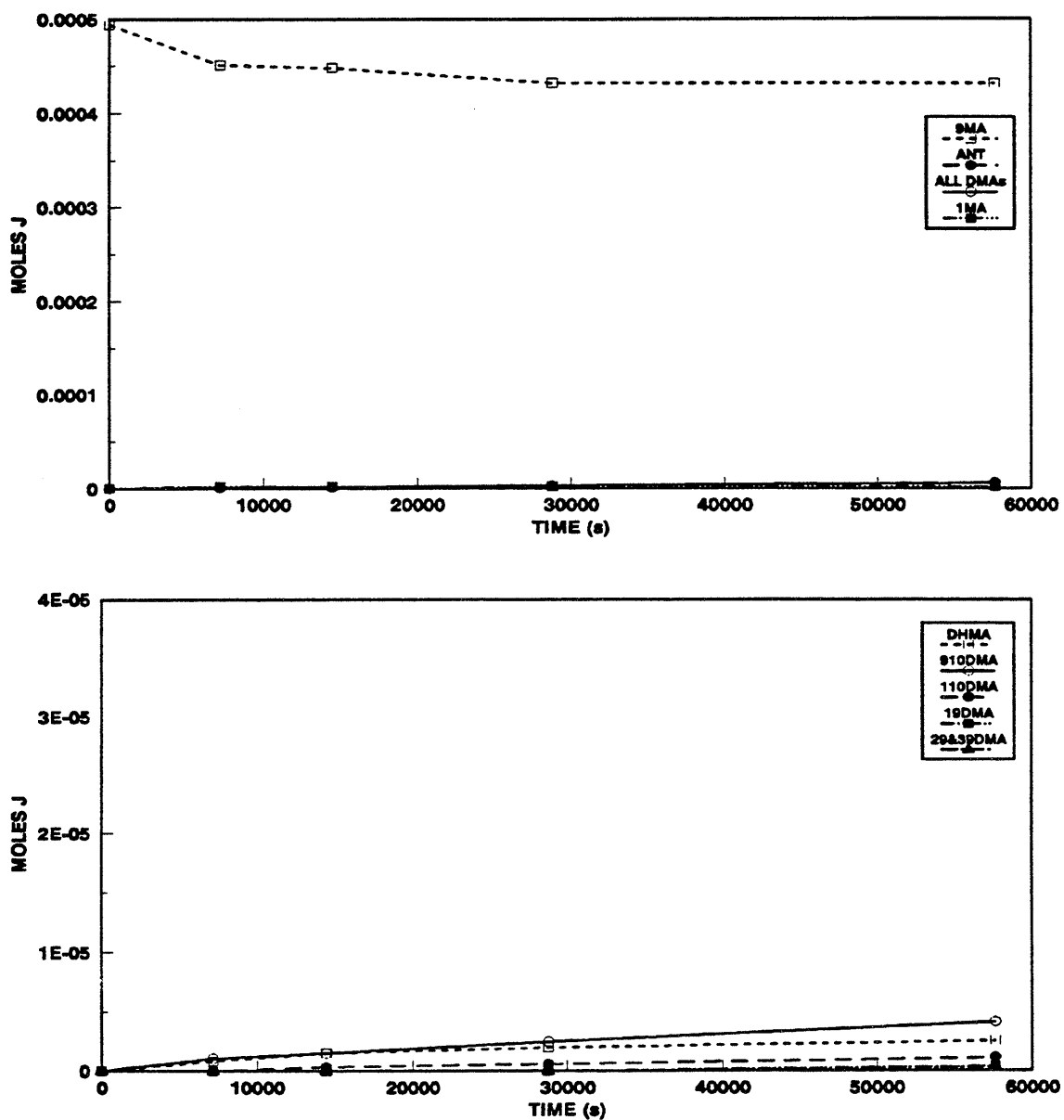
Figure 6.12: Product histories for 9MA thermolysis at 315°C with $[9MA]_o$ = 0.82 mol/l: major products (top) and minor products (bottom).

constant at J = 2.2 ± 0.2E-06 moles for 7200 < t < 57600 s. In the lower panel of Figure 6.12, DHMA was detected at t = 7200 s with J = 8.3E-07 moles and increases to J = 2.5E-06 moles by t = 57600 s. 910DMA is detected at t = 7200 s with J = 1.2E-06 moles and increases to J = 4.1E-06 moles at t = 57600 s. 110DMA appears at t = 14400 s with J = 3.5E-07 moles and increases to J = 1.1E-06 moles at t = 57600 s. 19DMA and 29&39DMA arise only at the longest time t = 57600 s with J = 4.0E-07 and 3.1E-07 moles, respectively.

Figure 6.13 is a selectivity diagram corresponding the data in Figure 6.12. In the upper panel of Figure 6.13, ANT and ALL DMAs selectivity is S = 0.019 and 0.025, respectively, at X = 0.086 and increases to S = 0.091 and 0.088 at X = 0.13. 1MA selectivity decreases from S = 0.058 at X < 0.086 to S = 0.030 at X = 0.13. The selectivity sum increases from Σ = 0.12 at X = 0.086 to Σ = 0.25 at X = 0.13. In the lower panel of Figure 6.13, DHMA selectivity is S = 0.020 at X = 0.086, increases to S = 0.033 at X = 0.093 and remains roughly constant to X = 0.13. 910DMA is detected at X = 0.086 with S = 0.025 and increases sharply to S = 0.061 at X = 0.13. 110DMA appears at X = 0.093 with S = 0.0075 and increases to S = 0.017 at X = 0.13. 19DMA and 29&39DMA are only detected at X = 0.13 with S = 0.0060 and 0.0046, respectively.

Figure 6.14 shows substrate and product histories at T = 335°C and $[9MA]_0$ = 0.82 M. In the upper panel of Figure 6.14, the moles of substrate 9MA decay from J = 4.9E-04 moles initially to J = 3.8E-04 moles at t = 57600 s, the decay half-
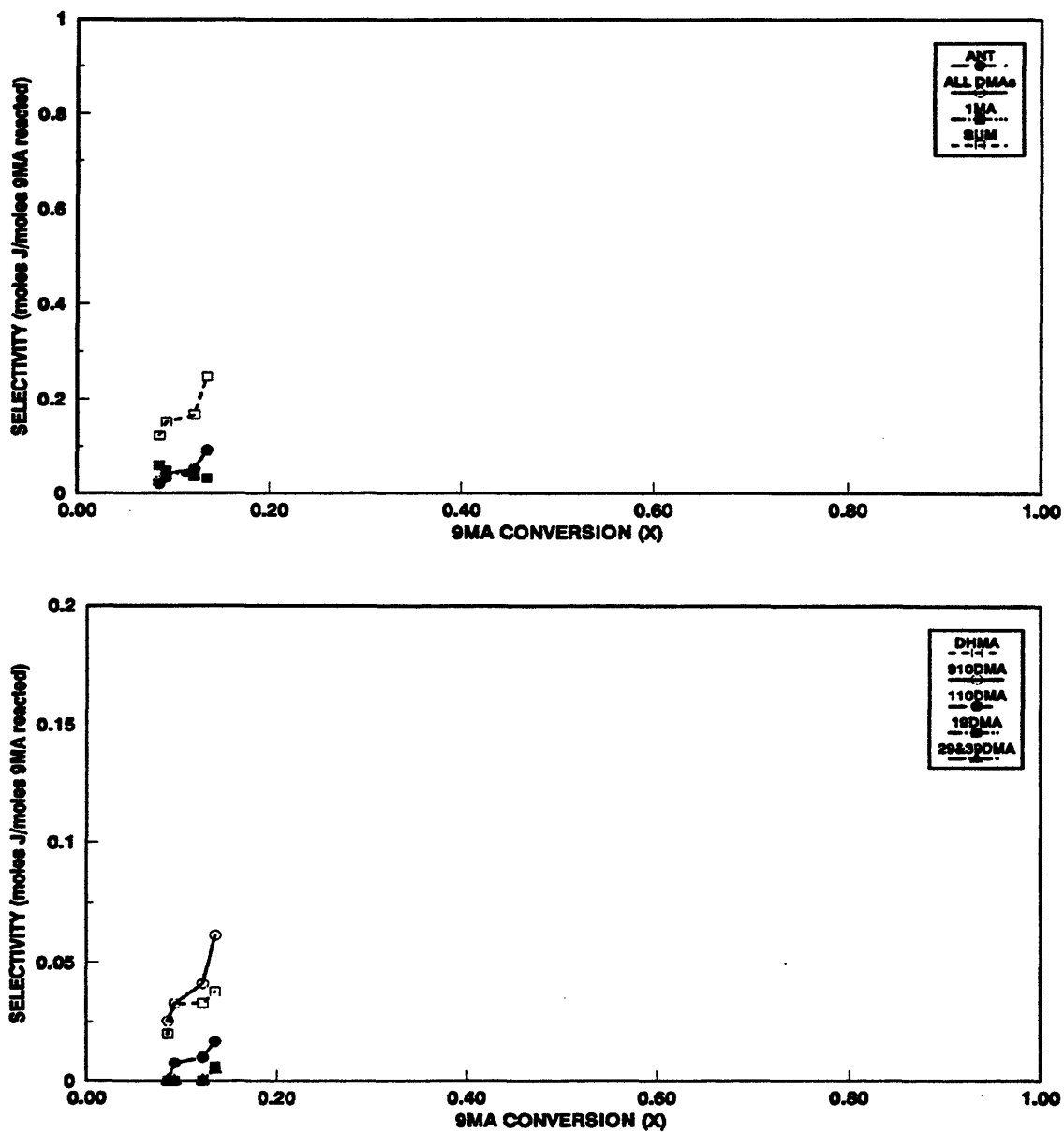
Figure 6.13: Selectivity diagrams for 9MA thermolysis at 315°C with $[9MA]_o$ = 0.82 mol/l: major products (top) and minor products (bottom).
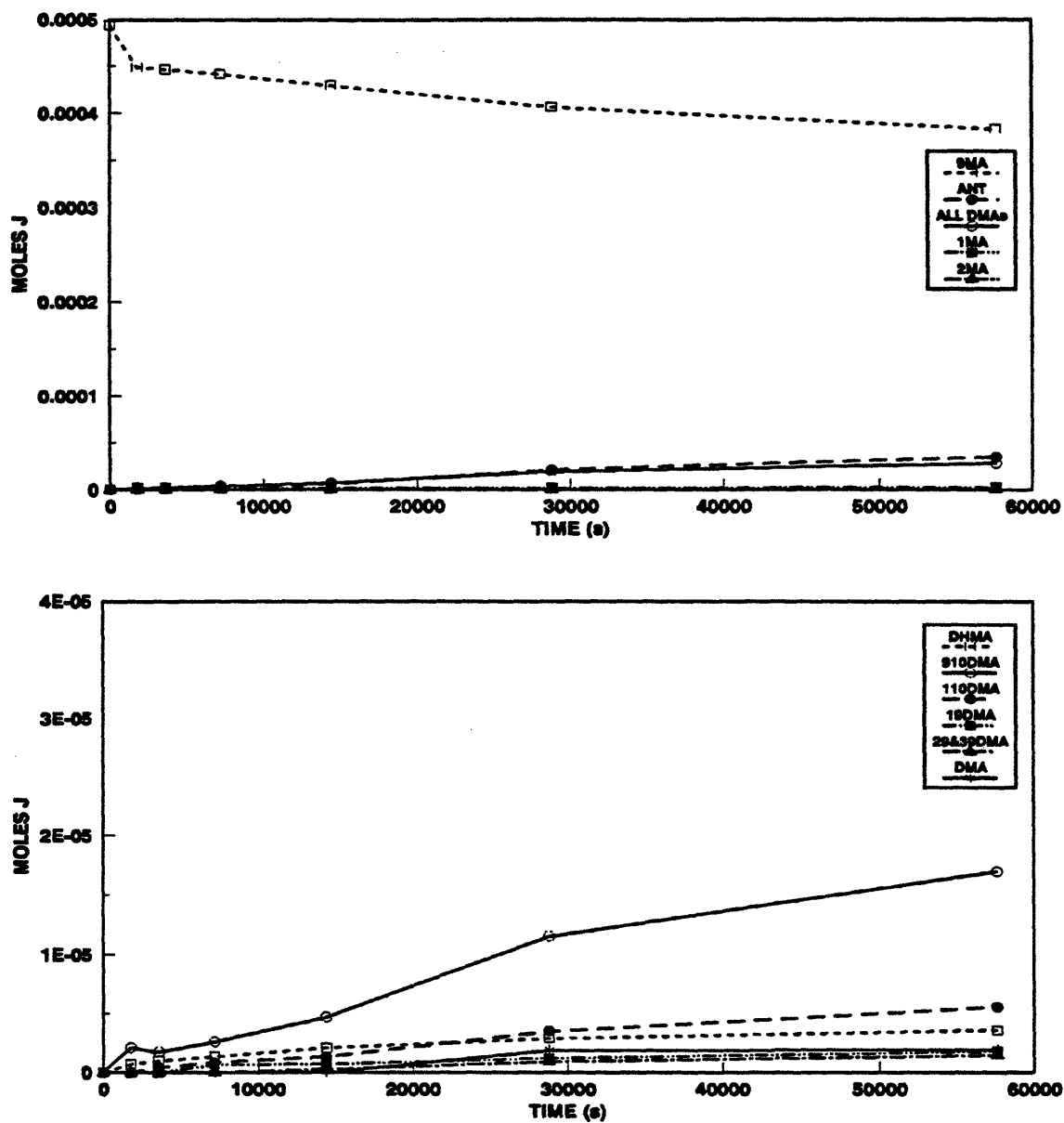
Figure 6.14: Product histories for 9MA thermolysis at 335°C with $[9MA]_o = 0.82$ mol/l: major products (top) and minor products (bottom).

life t* ~ 180000 s. ANT increases monotonically from 0 initially to J = 3.5E-05

moles at t = 57600 s. ALL DMAs increase from J = 2.1E-06 moles at t = 1800 s

to J = 2.8E-05 moles at t = 57600 s. 1MA is first detected at t = 1800 s with J =

2.10E-06 moles and remains roughly constant at J = 2.1 ± 0.3E-06 moles for 1800

< t < 57600 s. 2MA is detected at the longest t = 57600 s with J = 4.6E-07 moles.

In the lower panel of Figure 6.14, DHMA appears at t = 1800 s with J = 7.0E-07

moles and increases to J = 3.6E-06 moles at t = 57600 s. 910DMA appears at t =

1800 s with J = 2.1E-06 moles and increases monotonically but with decreasing slope

to J = 1.7E-05 moles at t = 57600 s. 110DMA appears at t = 3600 s with J = 4.3E-

07 moles and increases monotonically to J = 5.6E-06 moles at t = 57600 s. 19DMA

and 29&39DMA appear with J = 6.6E-07 and 2.9E-07 moles, respectively, at t =

7200 and 14400 s and increase to J = 1.8E-06 and 1.5E-06 moles at t = 57600.

Other DMAs are detected at t = 28800 s with J = 1.9E-06 moles, and remain

approximately constant up to t = 57600 s.

Figure 6.15 is a selectivity diagram corresponding to the data in Figure 6.14.

In the upper panel of Figure 6.15, ANT selectivity is S = 0.011 at X = 0.092 and

increases to S = 0.30 at X = 0.23. ALL DMAs appear with S = 0.047 at X = 0.092

and increase to S = 0.24 at X = 0.23. 1MA declines from S = 0.046 at X = 0.092

to S = 0.021 at X = 0.23. 2MA appears at X = 0.23 with S = 0.0041. The

selectivity sum is Σ = 0.12 at X = 0.092 and increases sharply to Σ = 0.24 at X =

0.23. In the lower panel of Figure 6.15, DHMA appears with S = 0.015 at X =
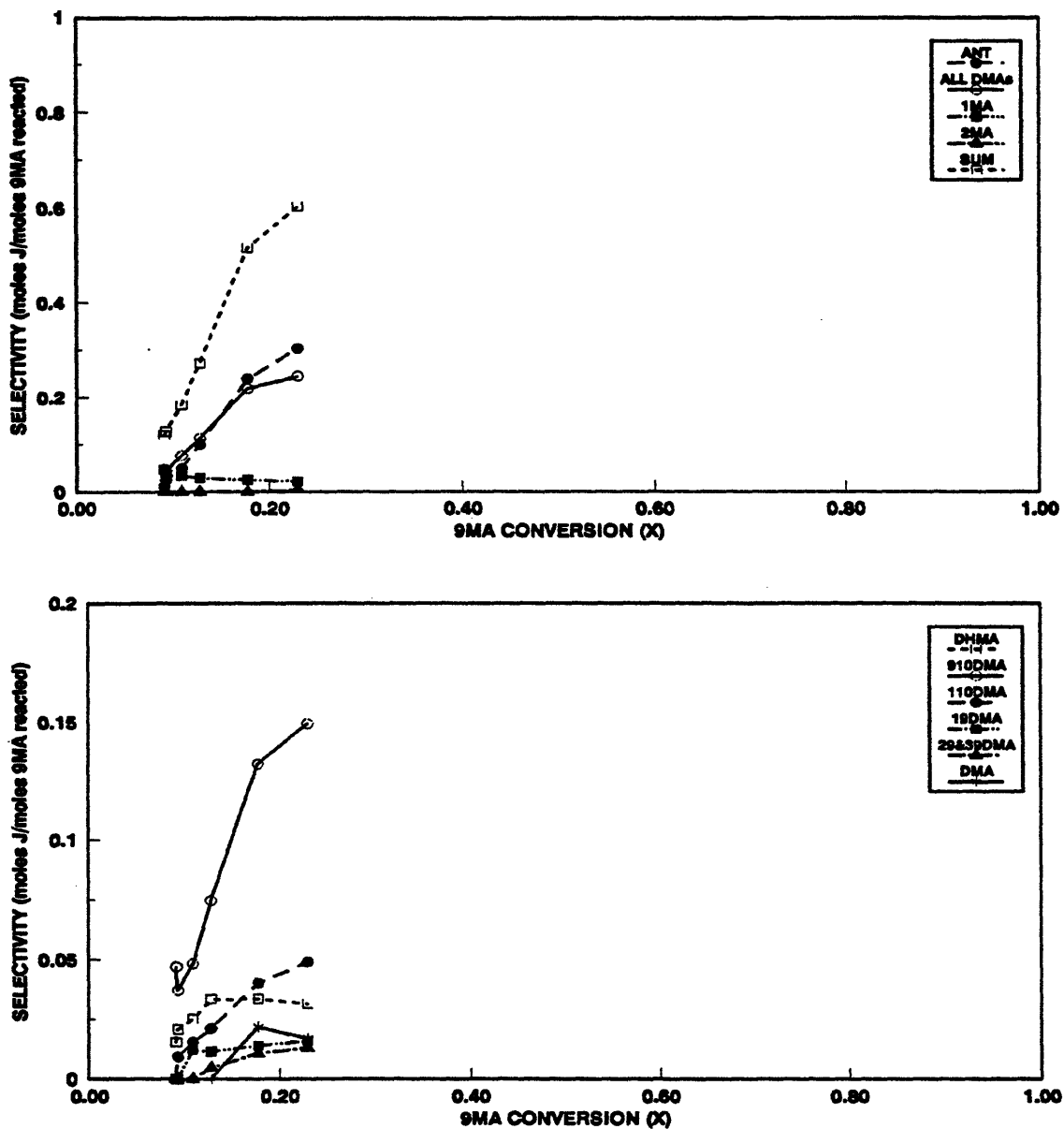
Figure 6.15: Selectivity diagrams for 9MA thermolysis at 335°C with $[9MA]_o$ = 0.82 mol/l: major products (top) and minor products (bottom).

0.092, increases to maximum S = 0.033 at X = 0.13 and remains roughly constant

at S = 0.033 up to X = 0.23. 910DMA is detected with S = 0.047 at X = 0.23 and

increases to S = 0.15 at X = 0.23. 110DMA is detected with S = 0.0092 at X =

0.094 and increases to S = 0.044 ± 0.004 for 0.18 < X < 0.23. 19DMA and

29&39DMA appear at X = 0.11 and 0.13 with, respectively, S = 0.012 and 0.0047

and remain roughly constant at S = 0.015 ± 0.001 and 0.012 ± 0.001 for 0.18 < X

< 0.23. Other DMAs appear at X = 0.18 with S = 0.022 and remain roughly

constant at S = 0.017 up to X = 0.23.

Figure 6.16 shows substrate and product histories at T = 355°C and $[9MA]_o$

= 0.82 M. In the upper panel of Figure 6.16, the moles of substrate 9MA decay

from J = 4.9E-04 moles initially to J = 3.5E-04 moles at t = 28800 s, the decay half-

life t^* ~ 58700 s. ANT increases monotonically from 0 initially to J = 5.6E-05 moles

at t = 28800 s. ALL DMAs increase from J = 1.6E-06 moles at t = 450 s to J =

4.4E-05 moles at t = 28800 s. 1MA is detected at t = 450 s with J = 5.6E-07 moles

and remains roughly constant at J = 5.3 ± 0.9E-07 moles for 450 < t < 14400 s and

then increases to J = 3.1E-06 moles at t = 28800 s. 2MA is detected at t = 14400

s with J = 1.1E-06 moles and remains at this level up to t = 28800 s. TMAs are

detected at the longest t = 28800 s with J = 7.5E-07 moles. In the lower panel of

Figure 6.16, DHMA appears at t = 450 s with J = 7.6E-07 moles, increases to J =

3.2E-06 moles at t = 14400 s and remains roughly constant up to t = 28800 s. DHA

is detected at t = 14400 s with J = 2.9E-07 moles and increases to J = 5.8E-07
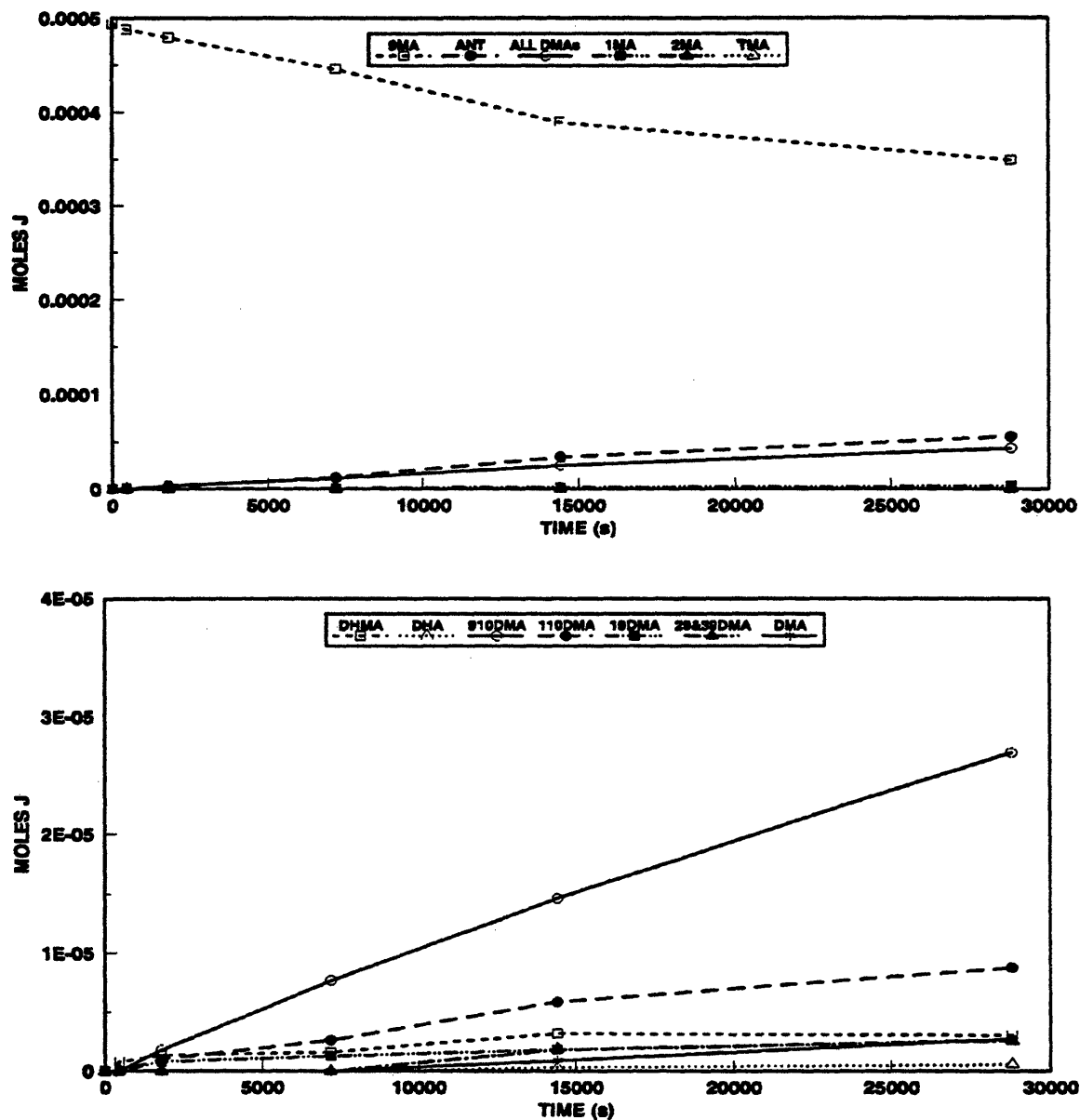
Figure 6.16: Product histories for 9MA thermolysis at 355°C with $[9MA]_o$ = 0.82 mol/l: major products (top) and minor products (bottom).

465

moles at t = 28800 s. 910DMA appears at t = 450 s with J = 1.8E-06 moles and increases to J = 2.7E-05 moles at t = 28800 s. 110DMA appears at t = 1800 s with J = 1.0E-06 moles and increases monotonically to J = 8.8E-06 moles at t = 28800 s. 19DMA and 29&39DMA appear with J = 7.9E-07 and 1.8E-06 moles, respectively, at t = 1800 and 14400 s and increase to J = 2.6E-06 moles each at t = 28800 s. Other DMAs are detected at t = 14400 s with J = 9.0E-07 moles and increase to J = 2.7E-06 moles at t = 28800 s.

Figure 6.17 is a selectivity diagram corresponding to the data in Figure 6.16. In the upper panel of Figure 6.17, ANT selectivity is S = 0.074 at X = 0.015, increases sharply to S = 0.25 at X = 0.099 and then rises more slowly to S = 0.38 at X = 0.29. ALL DMAs appear with S = 0.21 at X = 0.033, remain roughly constant at S = 0.22 ± 0.02 for 0.033 < X < 0.21 and increase to S = 0.28 at X = 0.29. 1MA declines from S = 0.070 at X = 0.033 to S = 0.012 at X = 0.099 and then rises slightly to S = 0.021 at X = 0.29. 2MA appears at X = 0.21 with S = 0.010 and remains constant up to X = 0.29. TMA selectivity at the highest X = 0.29 is S = 0.0052. The selectivity sum is Σ = 0.24 at X = 0.033, increases to Σ = 0.53 at X = 0.099 followed by an increase to Σ = 0.75 at X = 0.29; over the range 0.099 < X < 0.29, the selectivity sum is roughly constant at Σ = 0.64 ± 0.10. In the lower panel of Figure 6.17, DHMA appears with maximum S = 0.094 at X = 0.015 and decreases sharply to S = 0.032 at X = 0.099 and remains roughly at S = 0.026 ± 0.005 for 0.099 < X < 0.29. DHA is detected with S = 0.0087 at X = 0.21 and
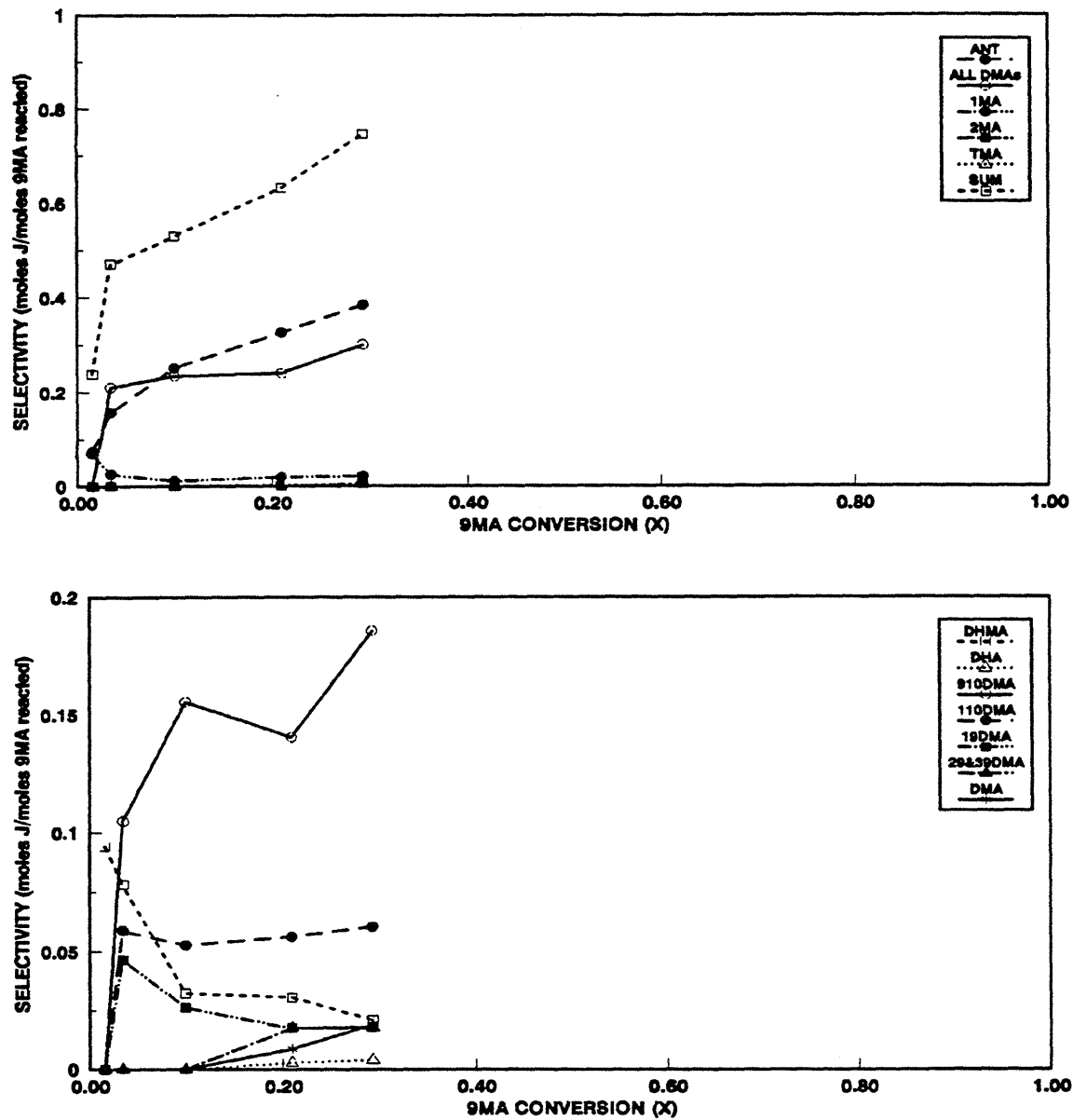
Figure 6.17: Selectivity diagrams for 9MA thermolysis at 355°C with $[9MA]_o$ = 0.82 mol/l: major products (top) and minor products (bottom).

467

increases to $S = 0.019$ at $X = 0.29$. 910DMA is detected with $S = 0.10$ at $X = 0.015$

and increases to $S = 0.19$ at $X = 0.29$. 110DMA is detected with $S = 0.052$ at $X = 0.011$ and remains roughly constant at $S = 0.054 \pm 0.007$ for $0.015 < X < 0.29$.

19DMA appears at $X = 0.033$ with $S = 0.046$, decreases slightly to $S = 0.026$ at $X = 0.099$ and the remains roughly constant at $S = 0.018$ for $0.21 < X < 0.29$.

29&39DMA appear at $X = 0.21$ with $S = 0.17$ and remain at this level up to $X = 0.29$. Other DMAs appear at $X = 0.21$ with $S = 0.0087$ and increase slightly to $S = 0.018$ at $X = 0.29$.

Figure 6.2, earlier described in Section 6.1.1 as the representative example, shows substrate and product histories at $T = 370°C$ and $[9MA]_0 = 0.82$ M. Figure 6.3, also in Section 6.1.1, is a selectivity diagram corresponding to the data in Figure 6.2.

Figure 6.18 shows substrate and product histories at $T = 409°C$ and $[9MA]_0 = 0.82$ M. In the upper panel of Figure 6.18, the moles of substrate 9MA decay from $J = 4.9E\text{-}04$ moles initially to $J = 2.8E\text{-}05$ moles at $t = 21600$ s; the decay half-life $t^* \sim 2800$ s. ANT increases monotonically with decreasing slope from 0 initially to $J = 2.0E\text{-}04$ moles at $t = 21600$ s. ALL DMAs increase from 0 initially to a maximum $J = 6.3E\text{-}05$ moles at $t = 7200$ s and decline slowly to $J = 4.9E\text{-}05$ moles at $t = 21600$ s. 1MA appears at $t = 450$ s with $J = 1.7E\text{-}06$ moles and rises monotonically to $J = 8.2E\text{-}05$ moles at $t = 21600$ s. 2MA is detected at $t = 1800$ s with $J = 1.2E\text{-}06$ moles and increases to $J = 3.5E\text{-}05$ moles at $t = 21600$ s. TMAs
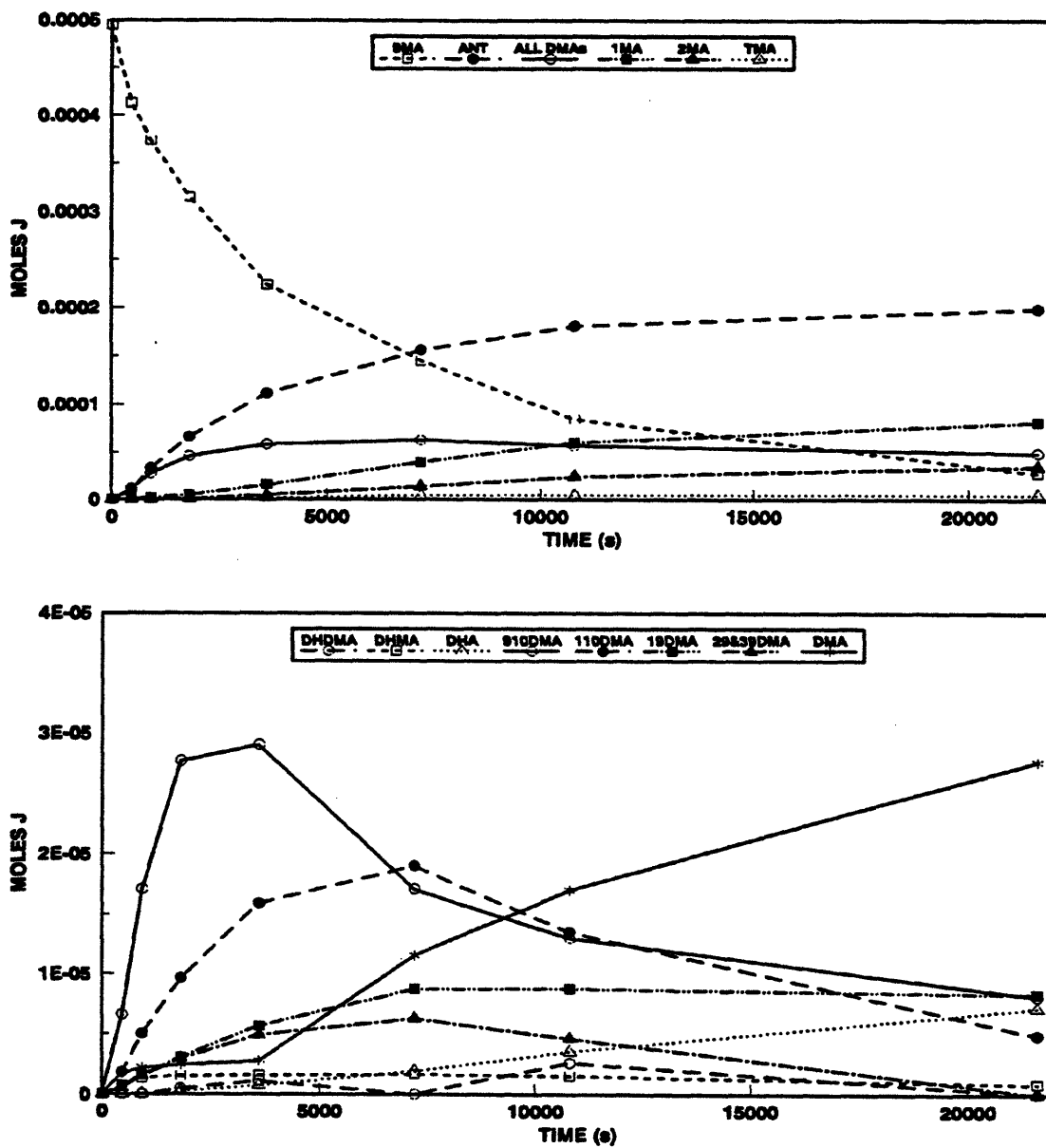
Figure 6.18: Product histories for 9MA thermolysis at 409°C with $[9MA]_o = 0.82$ mol/l: major products (top) and minor products (bottom).

are detected at t = 1800 s with J = 2.5E-07 moles and increase slightly to J = 4.9E-06 moles at t = 21600 s. In the lower panel of Figure 6.18, DHDMA is detected at t = 1800 s with J = 4.6E-07 moles, increases to maximum J = 2.6E-06 moles at t = 10800 s and then decays to J = 0 by t = 21600 s. DHMA appears at t = 450 s with J = 6.0E-07 moles, increases to maximum J = 1.7E-06 moles at t = 7200 s and decays to J = 8.6E-07 moles by t = 21600 s. DHA first appears at t = 1800 s with J = 2.5E-07 moles and increases monotonically to J = 7.1E-06 moles at t = 21600 s. 910DMA increases sharply from 0 initially to maximum J = 2.9E-05 moles at t = 3600 s and then decays, sharply to J = 1.7E-05 moles at t = 7200s followed by a slower decay to J = 8.1E-06 moles at t = 21600 s. 110DMA is first detected at t = 450 s with J = 1.8E-06 moles, rises to a maximum J = 1.9E-05 moles at t = 7200 s and then declines to J = 4.9E-06 moles at t = 21600 s. 19DMA arises with J = 7.2E-07 moles at t = 450 s, rises to J = 8.7E-06 moles at t = 7200 s, and remains roughly constant at J = 8.5 ± 0.2E-06 moles for 7200 < t < 21600 s. 29&39DMA are detected at t = 450 s with J = 5.0E-07 moles, increase to maximum J = 6.3E-06 moles at t = 7200 s, and decrease to J = 0 at t = 21600 s. Other DMAs appear with J = 1.7E-06 moles at t = 450 s, increase to J = 2.7E-06 moles at t = 3600 s and then rise monotonically to J = 2.8E-05 moles at t = 21600 s.

Figure 6.19 is a selectivity diagram corresponding to the data in Figure 6.18. In the upper panel of Figure 6.19, ANT selectivity is S = 0.11 at X = 0.17 and rises to S = 0.41 ± 0.03 for 0.36 < X < 0.94. ALL DMAs selectivity is S = 0.13 at X =
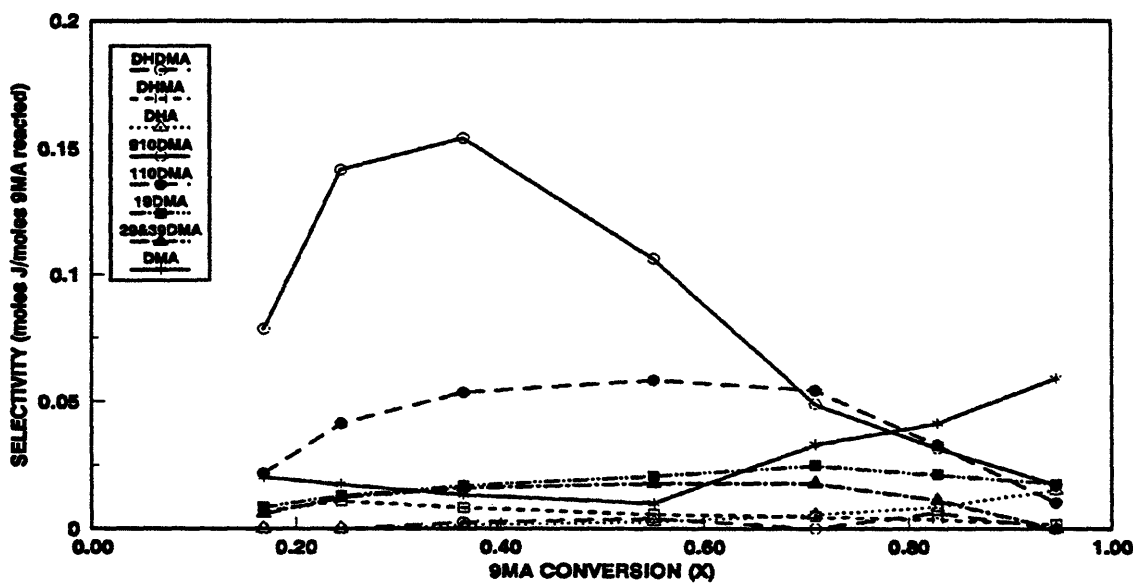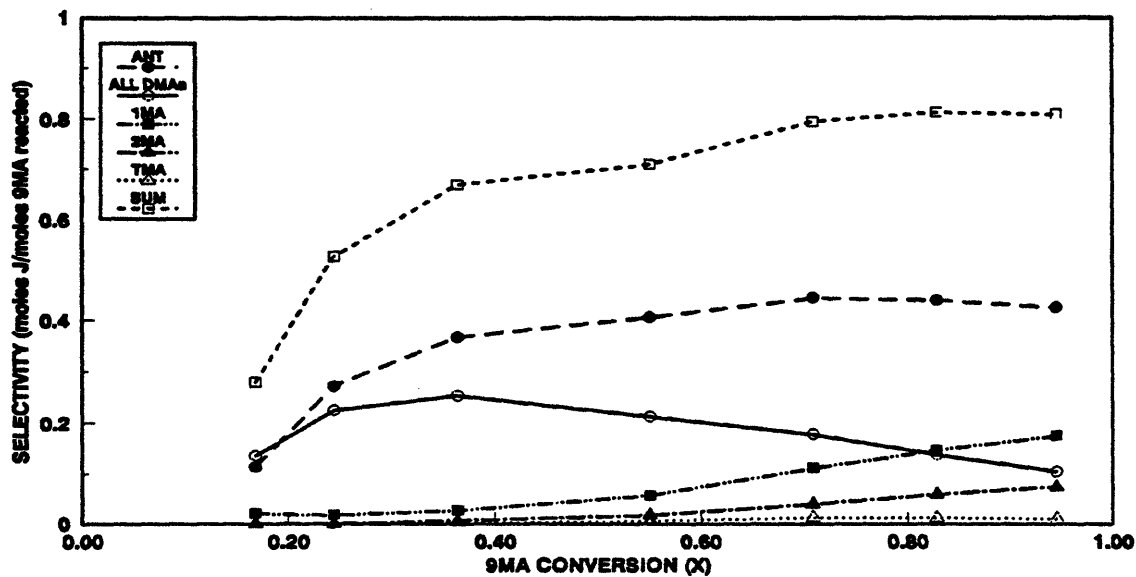
Figure 6.19: Selectivity diagrams for 9MA thermolysis at 409°C with $[9MA]_o$ = 0.82 mol/l: major products (top) and minor products (bottom).

471

0.17, increases to maximum S = 0.25 at X = 0.36, and then declines to S = 0.10 at

X = 0.94. 1MA appears with S = 0.021 at X = 0.17, remains roughly constant up

to X = 0.36 and then grows monotonically to S = 0.18 at X = 0.94. 2MA appear

at X = 0.36 with S = 0.0064 and grows monotonically to S = 0.074 at X = 0.94.

TMA selectivity at X = 0.36 is S = 0.0029, rises to S = 0.012 at X = 0.71 and

remains roughly at S = 0.11 up to X = 0.94. The selectivity sum increases from Σ

= 0.28 at X = 0.17 to Σ = 0.74 ± 0.07 for 0.37 < X < 0.94. In the lower panel of

Figure 6.19, DHDMA selectivity is S = 0.0040 for 0.37 < X < 0.83. DHMA

selectivity S = 0.0071 at X = 0.17, increases to maximum S = 0.011 at X = 0.24 and

then declines to S = 0.0018 by X = 0.94. DHA appears at X = 0.36 with S =

0.0014 and rises to S = 0.015 at X = 0.94. 910DMA selectivity at X = 0.17 is S =

0.078, increases to maximum S = 0.15 at X = 0.36 and then decreases monotonically

to S = 0.017 at X = 0.94. 110DMA is detected at X = 0.17 with S = 0.022, rises to

a shallow maximum S = 0.05 at X = 0.36, and then declines to S = 0.010 at X =

0.94. 19DMA is detected with selectivity S = 0.0085 at X = 0.17, which rises to a

shallow maximum S = 0.025 at X = 0.71, and decreases slightly to S = 0.018 by X

= 0.94. 29&39DMA appear at X = 0.17 with S = 0.0060, reach a maximum S =

0.018 at X = 0.83, and drop to S = 0 by X = 0.94. Selectivity of the other DMAs

is S = 0.015 ± 0.05 for 0.17 < X < 0.55 and then rises to S = 0.059 at X = 0.94.

6.1.5 Summary of Temperature Effects

Increasing temperature from T = 315 to 409°C at fixed $[9MA]_0$ = 0.82 mol/l influences both the reaction kinetics and product selectivities, as respectively summarized in Table 6.3 and Table 6.4. Note that values in the tables are the averages over all runs, including replication, and are therefore not precisely identical to those seen in the preceding figures. Part (a) of Table 6.3 shows the substrate decay half-life t^* decreased about 140-fold, from 390000 to 2800 s, as reaction temperature T increased ~ 100°C, from 315 to 409°C. Figure 6.20, a plot of log t^* vs. $1/\theta$, where $\theta = 4.573 \times 10^{-3}T$ in Kelvins, shows that the data adhere to a line:

$$\log t^* = -10.7 + \frac{43.1}{\theta} \qquad (6.4)$$

for T = 335 - 409°C. The slope of this line, 46.4, is equal to the activation energy in kcal/mol of the overall reaction; also, for 3/2 order decomposition, the intercept of the line provides a pre-exponential factor of -11.4. Thus 9MA thermolysis is 3/2 order in substrate with Arrhenius parameters $(\log_{10} A, E^*)$ = (-11.4, 46.4).

The hydrogenated product DHMA, which is seen to maximize at early times with increasing temperature in Figure 6.12, Figure 6.14, Figure 6.16, Figure 6.2 and Figure 6.18, suggests a series as shown in Equation (6.3). Using the maximum DHMA concentration at each temperature, $[DHMA/9MA]_{tmax}$ remains roughly constant while $[t_{max}/t^*]$ increases with increasing temperature, as shown in part (c) of Table 6.3. $[DHMA/9MA]_{tmax}$ ~ 0.009 ± 0.003 for 315 < T < 409°C while

Table 6.3

EFFECT OF TEMPERATURE ON
KINETIC PARAMETERS WITH [9MA]$_o$ = 0.82 mol/l

Part		Temperature (°C)				
		315	335	355	370	409
a	Half-life t^*, s	388859[1] ± 70000[2]	179066[1] ± 24438	58695[1] ± 5200	23430 ± 748	2827 ± 318
b	[DHMA/9MA]$_{tmax}$	0.006	0.009	0.009	0.013	0.012
	t_{max}/t^*	0.15	0.32	0.37	1.23	2.55

[1] Half-life calculated using X at longest t and integrated 3/2 order rate expression: $t^* = 0.41421t / [(1/(1-X)^{\frac{1}{2}}) - 1]$

[2] ± = standard deviation of the average half-life

Table 6.4

EFFECT OF TEMPERATURE ON
PRODUCT SELECTIVITIES WITH $[9MA]_0$ = 0.82 mol/l

Part	Selectivity S of:	Conversion X Range:	Temperature (°C)				
			315[1]	335[2]	355[3]	370	409
a	ANT	0.2 - 1.0	ND	0.30	0.35	0.37	0.39
	ALL DMAs	0.2 - 1.0	ND	0.24	0.26	0.22	0.19
b	DHMA	0.15 ± 0.02	0.038	0.034	0.028	0.031	0.012
		0.40 ± 0.03	ND	0.029	0.018	0.014	0.007
	DHA	0.40 ± 0.03	ND	ND	0.003	0.004	0.003
	DHDMA	0.65 ± 0.05	ND	ND	ND	0.002	0.006
c	1MA	0.40 ± 0.03	ND	0.021	0.028	0.043	0.029
	2MA	0.40 ± 0.03	ND	0.004	0.007	0.012	0.009
	910DMA	0.25 ± 0.05	0.061	0.145	0.185	0.168	0.150
		0.40 ± 0.03	ND	ND	ND	0.144	0.125
	110DMA	0.2 - 0.6	0.017	0.051	0.058	0.056	0.048
		0.95					0.005
	19DMA	0.2 - 0.6	0.006	0.016	0.018	0.021	0.016
		0.95					0.010
	29&39DMA	0.2 - 0.6	0.005	0.013	0.016	0.019	0.014
		0.95					0
	other DMAs	0.2 - 0.6	ND	ND	0.014	0.015	0.015
		0.95					0.043

[1] For T = 315°C, all data at X = 0.13

[2] For T = 335°C, all data at X = 0.24 except DHMA at X = 0.15

[3] For T = 355°C, all data at X = 0.29 except DHMA at X = 0.15
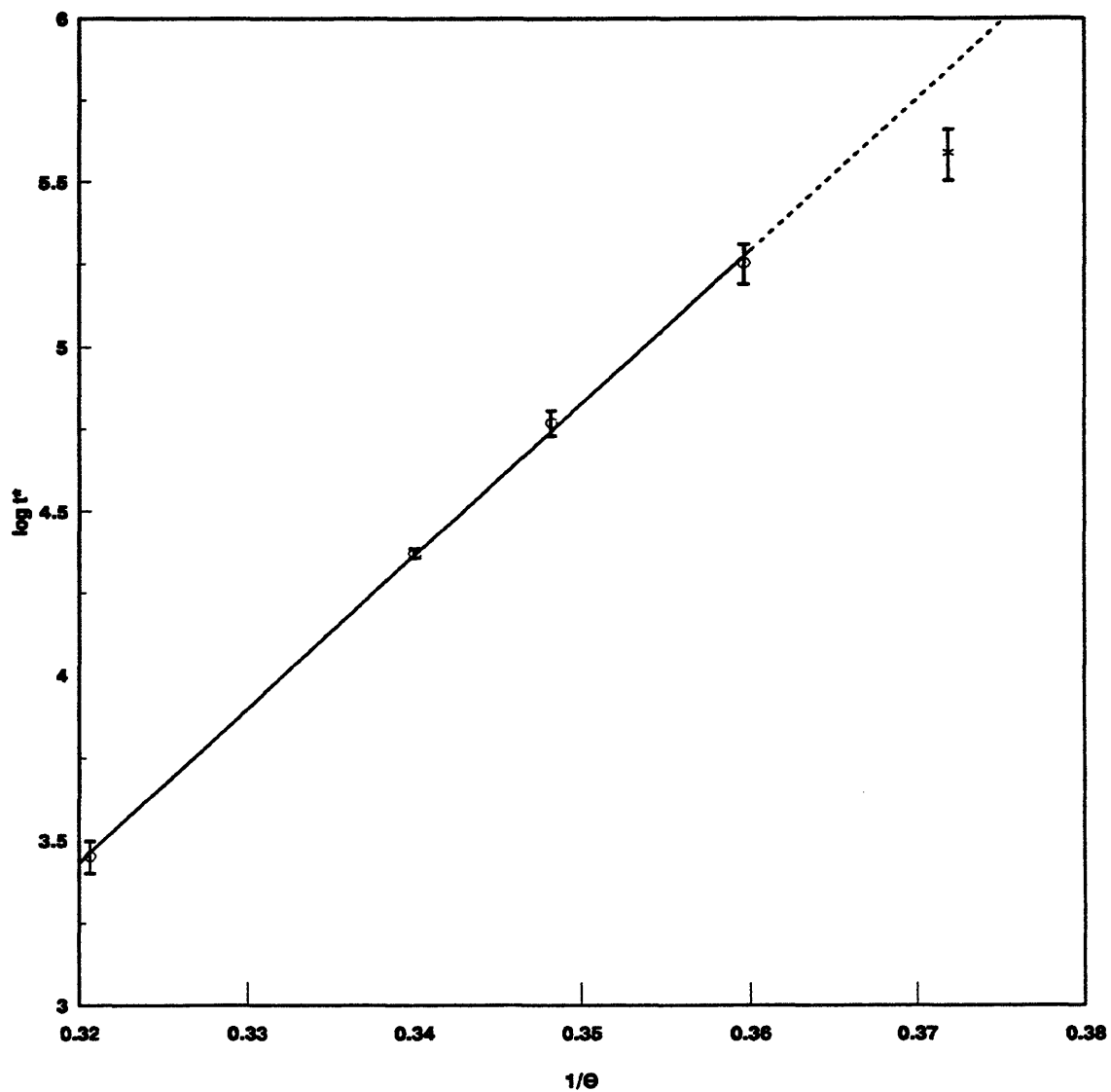
Figure 6.20: Decay half-life t^* for varying temperatures with fixed $[9MA]_o = 0.82$ mol/l.

$[t_{max}/t^*] = 0.15$ at $T = 315°C$ and increases to $[t_{max}/t^*] = 2.55$ at $T = 409°C$. Both again suggest that DHMA decomposes faster than it forms from 9MA, i.e., $k_4/k_3 > 1$, which is in agreement with the earlier results obtained at fixed $T = 355°C$ and varying substrate concentrations. It also suggest that k_4 is less activated than k_3.

Turning to product selectivities, summarized in Table 6.4, both ANT and ALL DMAs selectivities were roughly independent of conversion over the ranges $0.2 < X < 0.6$ at temperatures, as shown in part (a) of Table 6.4. The absolute values of S(ANT) and S(ALL DMAs) remained essentially constant at $S(ANT) = 0.34 \pm 0.05$ and $S(ALL\ DMAs) = 0.22 \pm 0.04$ over the range of temperatures, $335 < T < 409°C$. The values at $T = 335$ and $355°C$ only included data between $0.20 - 0.24$ and $0.20 - 0.29$, respectively, and therefore may account for the fact that the S(ANT) is slightly lower than at $T = 370$ and $409°C$ while the S(ALL DMAs) is slightly higher than at $T = 370$ and $409°C$. The hydrogenated species DHMA selectivity was essentially highest at $X \sim 0.20$ and then declined with increasing X, as shown in part (b) of Table 6.4. Thus $S(DHMA) = 0.033 \pm 0.005$ at $X = 0.15 \pm 0.02$ for $315 < T < 370°C$ and $S(DHMA) = 0.012$ at $X = 0.15 \pm 0.02$ at $T = 409°C$, and then decreased to $S(DHMA) = 0.029$ at $X = 0.24$ for $T = 335°C$, $S(DHMA) = 0.018$ at $X = 0.29$ at $T = 355°C$ and $S(DHMA) = 0.010 \pm 0.004$ at $X = 0.40 \pm 0.03$ for $T = 370$ and $409°C$. Of the other hydrogenated species, $S(DHA) = 0.0035 \pm 0.0005$ at $X = 0.40 \pm 0.03$ for $355 < T < 409°C$. DHDMA was detected with $S(DHDMA) = 0.004 \pm 0.002$ at $X = 0.65 \pm 0.05$ only at the higher $T = 370$ and $409°C$. 1MA and 2MA

selectivities increased monotonically from 0 as conversions increased for all temperatures, as shown in part (c) of Table 6.4, with S(1MA) > S(2MA) always at any X. Absolute S(1MA) and S(2MA) = 0.021 and 0.004, respectively, at X = 0.24 for T = 335°C, S(1MA) and S(2MA) = 0.028 and 0.007 at X = 0.29 for T = 355°C, and S(1MA) and S(2MA) = 0.036 ± 0.007 and 0.011 ± 0.002 at X = 0.40 ± 0.03 for 370 < T < 409°C. 910DMA selectivity increased monotonically from 0 to a maximum at X ~ 0.20 for all temperatures and then monotonically declined with increasing conversion for T > 370°C, as shown in part (c) of Table 6.4. S(910DMA) = 0.061 at X = 0.13 for T = 315°C and S(910DMA) = 0.165 ± 0.020 at X = 0.25 ± 0.05 for T > 335°C. S(910DMA) decreased to 0.135 ± 0.010 at X = 0.40 ± 0.03 for T = 370 and 409°C. The other dimethylanthracene; 1,10-, 1,9-, 2,9-&3,9-DMA and other DMAs; selectivities remained roughly constant over 0.20 < X < 0.60 for all temperatures, and then decreased at X > 0.60 for T = 409°C, as shown in part (c) of Table 6.4. Of the dimethylated species, the order of abundance was generally S(110DMA) > S(19DMA) > S(29&39DMA) > S(other DMAs) for X < 0.60, with each of these < S(910DMA) at X < 0.60. S(110DMA) = 0.017 at X = 0.13 for T = 315°C and S(110DMA) = 0.053 ± 0.005 for 0.2 < X < 0.6 for T > 335°C. S(19DMA) = 0.006 at X = 0.13 for T = 315°C and S(19DMA) = 0.019 ± 0.003 for 0.2 < X < 0.6 for T > 335°C. S(29&39DMA) = 0.005 at X = 0.13 for T = 315°C and S(29&39DMA) = 0.016 ± 0.003 for 0.2 <X < 0.6 for T > 335°C. S(other DMAs) = 0.0145 ± 0.0005 for 0.2 <X < 0.6 for T > 355°C. The S(110DMA),

S(19DMA) and S(29&39DMA) decreased with increasing conversion for X > 0.60

as X → 1 while the S(DMAs) increased with increasing conversion for X > 0.6 as X

→ 1 at the highest T = 409°C, as shown in part (c) of Table 6.4. S(110DMA) =

0.005 at X = 0.95 for T = 409°C. S(19DMA) = 0.010 at X = 0.95 for T = 409°C.

S(29&39DMA) = 0 at X = 0.95 for T = 409°C. S(other DMAs) = 0.043 at X =

0.95 for T = 409°C.

Finally, Figure 6.21 depicts the variation of product ratio

R[(1MA+2MA)/ANT] versus 9MA conversion X at all temperatures. In

Figure 6.21, it is seen that, for X > 0.15 and all experiments, the ratio of

monomethylated species to ANT, R[(1MA+2MA)/ANT], is essentially a function of

conversion only, with data for all temperatures, 315 < T < 409°C, lying on roughly

the same curve. For X < 0.15, the 1MA impurity in the 9MA substrate again is

accentuated by the small amount of ANT formed at low conversions. This

relationship implicitly describes the kinetics of ANT methylation during thermolysis

of the 9MA substrate under the present conditions.

6.2 Kinetics

The kinetics of the experimental thermolyses were analyzed to derive reaction

order and activation parameters. Reaction order was obtained from data at initial

concentrations 0.082 mol/l < [9MA]$_o$ < 2.06 mol/l at a fixed T = 370°C, while

activation parameters were derived from data at temperatures 315°C < T < 409°C

479
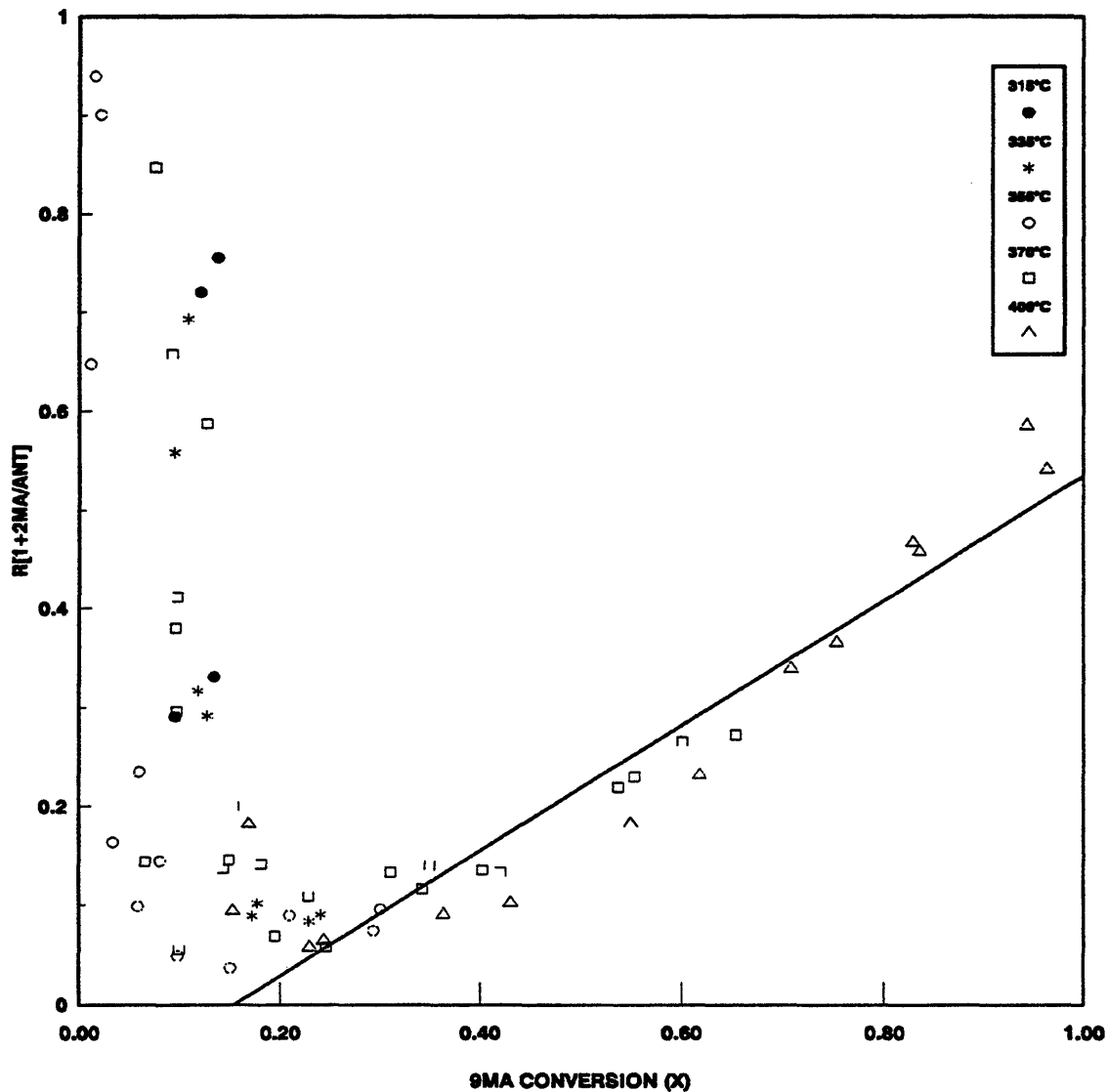
Figure 6.21: Ratio of moles 1MA and 2MA to moles ANT produced vs. 9MA conversion (X) for varying temperatures with fixed $[9MA]_o$ = 0.82 mol/l.

at fixed $[9MA]_o = 0.82$ mol/l. Both effective first order rate constants, k_{eff}, and the true rate constants, k, were employed to ascertain reaction order and activation parameters

6.2.1 Reaction Order

The order of reaction for overall 9MA decay was formally examined in the series of experiments at constant temperature $T = 370°C$ with initial 9MA substrate concentrations ranging from 0.082 and 2.06 mol/l.

6.2.1.1 Apparent First Order Rate Constants, k_{eff}

The effective first order rate constant k_{eff}, units 1/s, is defined by Equation (6.5):

$$(6.5) \quad k_{eff} = \frac{-\ln(1-X)}{t}$$

where X is the fractional conversion at holding time t, Equation (6.6):

$$X = 1 - \frac{[9MA]_t}{[9MA]_o} \qquad (6.6)$$

with $[9MA]_o$ and $[9MA]_t$ the respective concentrations of 9MA at times 0 and t. Effective first order rate constants were calculated at each point, for all runs. At each T and $[9MA]_o$, values of log k_{eff} were averaged over intervals of fractional conversion, respectively 0 - 0.1, 0.1 - 0.2, 0.2 - 0.4, 0.4 - 0.6, 0.6 - 0.8, and 0.8 - 1.0.

481

The average log k_{eff} over each of the chosen conversion intervals are shown as horizontal lines with vertical error bars in Figure 6.22 and Figure 6.23. As a representative example, the upper panel of Figure 6.22 refers to 9MA thermolysis at $T = 370°C$ and $[9MA]_o = 0.082$ mol/l. In each of the four conversion intervals, values of the average log k_{eff} are $\sim -4.4 \pm 0.5$. The uncertainty associated with log k_{eff} is seen to diminish greatly with increasing conversion, the error bars spanning 0.4, 0.7, 1.2 and 0.03 units of log k_{eff} in the conversion intervals of 0 - 0.1, 0.1 - 0.2, 0.2 - 0.4 and 0.4 - 0.6, as seen on line 3 of Table 6.5. Table 6.5 summarizes the average log k_{eff}, error of the average log k_{eff} and error for each conversion range for all $[9MA]_o$ and temperatures. The lower panel of Figure 6.22 refers to 9MA thermolysis at $T = 370°C$ and $[9MA]_o = 0.25$ mol/l and the upper and lower panels of Figure 6.23 refer to 9MA thermolysis at $T = 370°C$ and $[9MA]_o = 0.82$ mol/l and $[9MA]_o = 2.06$ mol/l, respectively, while lines 4 - 7 of Table 6.5 summarize the average log k_{eff}, error in the average log k_{eff} and errors for each conversion range. It can be seen in Table 6.5 that the uncertainty associated with log k_{eff} diminishes with increasing conversion for all $[9MA]_o$, the error bars ranging from 0.42 - 0.65, 0 - 1.10, 0 - 1.24, 0.04 - 0.32, 0.02 - 0.18 and 0.08 units of log k_{eff} in the conversion intervals of 0 - 0.1, 0.1 - 0.2, 0.2 - 0.4, 0.4 - 0.6, 0.6 - 0.8 and 0.8 - 1.0.

The order of 9MA decomposition at $T = 370°C$ was determined by plotting the log k_{eff} vs log $[9MA]_o$ as shown in Figure 6.24, the upper panel of which shows data for all X while the lower panel shows data for $X < 0.4$. The low conversion
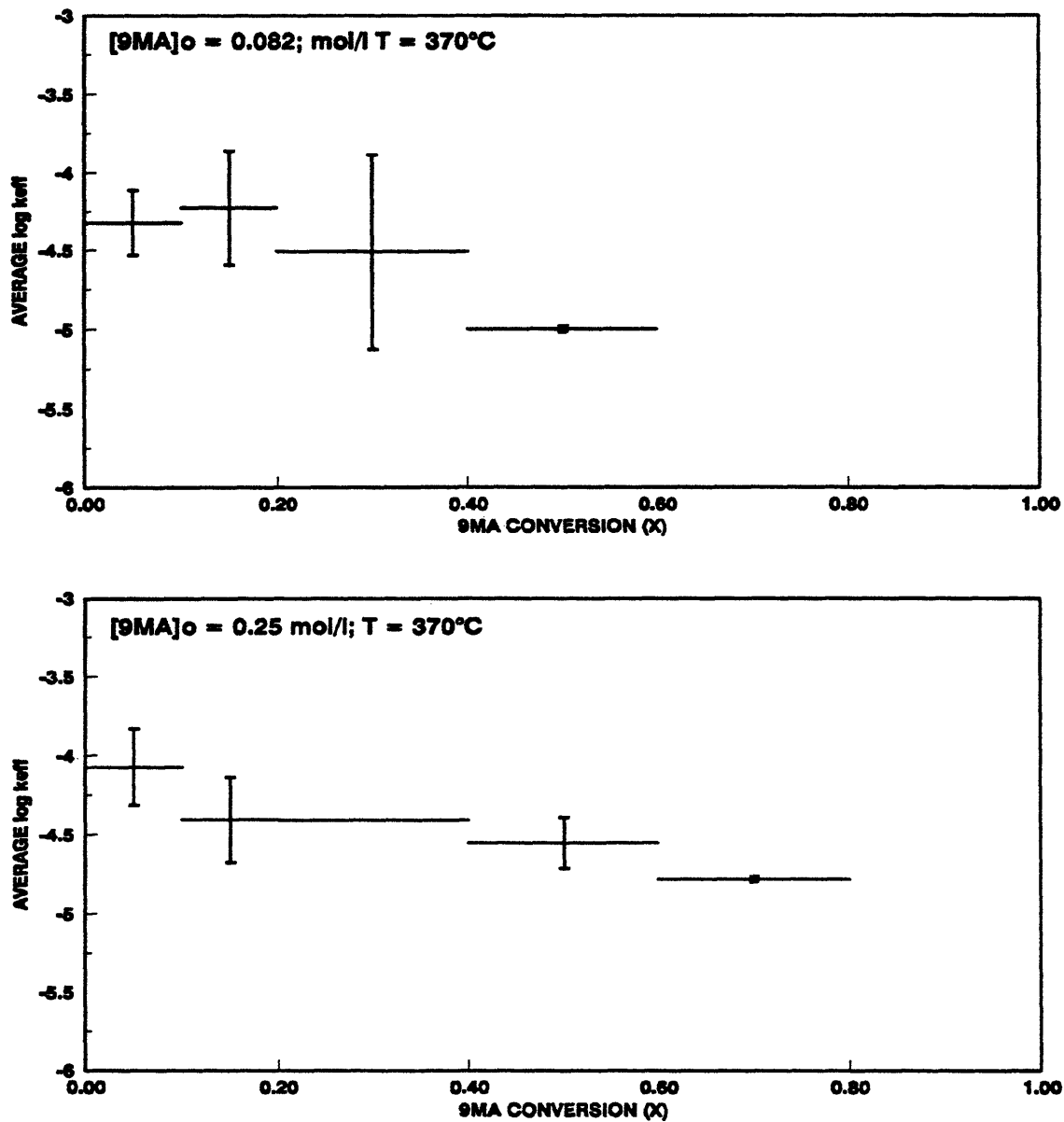
Figure 6.22: Average log k_{eff} vs. 9MA conversion at T = 370°C for $[9MA]_o$ = 0.082 (top) and 0.25 mol/l (bottom).

483
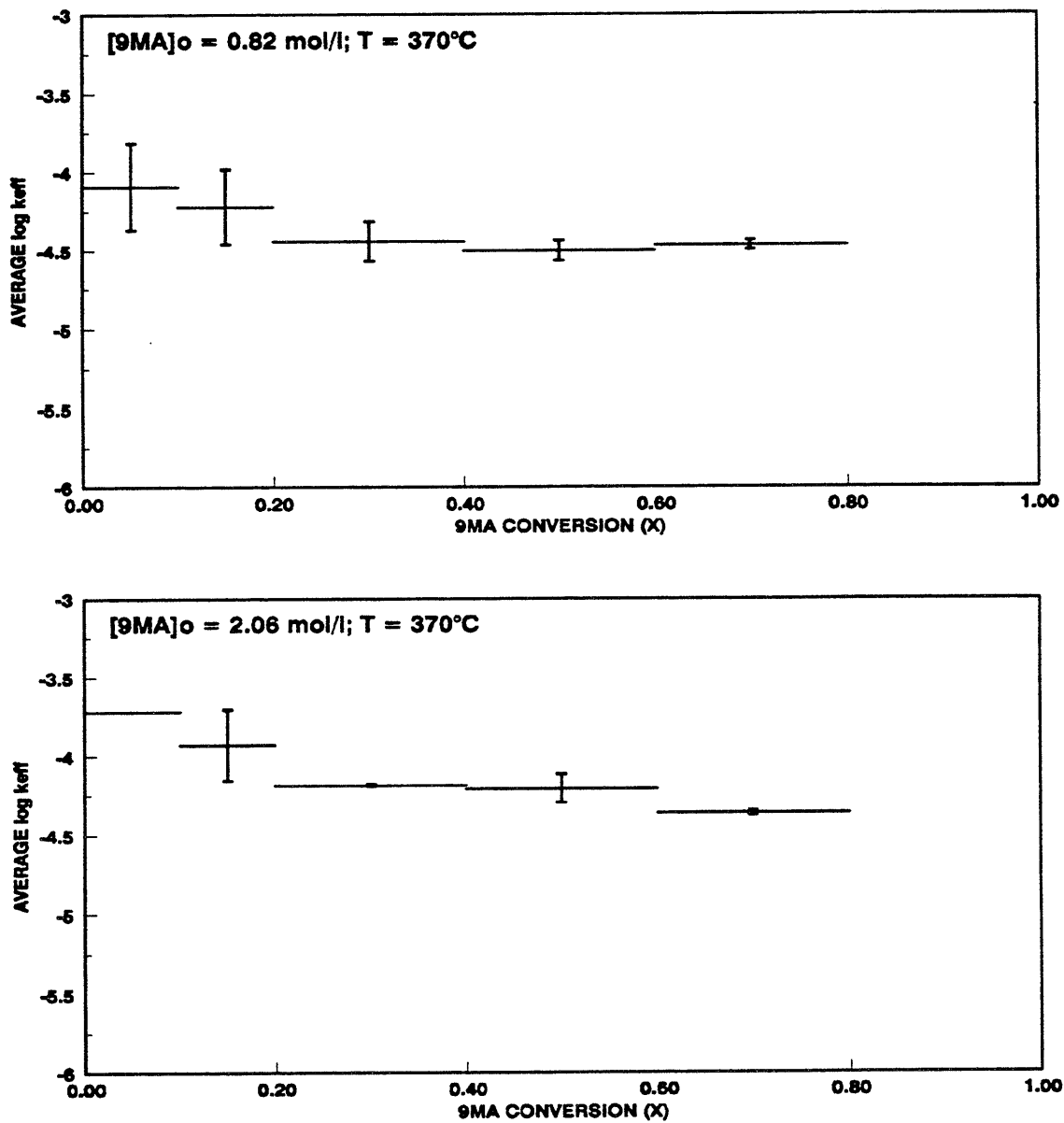
Figure 6.23: Average log k_{eff} vs. 9MA conversion at T = 370°C for $[9MA]_o$ = 0.82 (top) and 2.06 mol/l (bottom).

Table 6.5

AVERAGE log k_{eff} AND ASSOCIATED UNCERTAINTIES FOR 9MA THERMOLYSIS

T	[9MA]$_o$		Conversion intervals and associated uncertainties in log k_{eff}					
°C	mol/l	<k_{eff}> ± error	0 - 0.1	0.1 - 0.2	0.2 - 0.4	0.4 - 0.6	0.6 - 0.8	0.8 - 1.0
315	0.82	-4.93 ± 0.53	0.69	1.10				
335	0.82	-4.86 ± 0.37	0.45	0.28	0.03			
355	0.82	-4.75 ± 0.26	0.57	0	0.12			
370	0.082	-4.43 ± 0.49	0.42	0.74	1.24	0.04		
370	0.25	-4.42 ± 0.30	0.48	0.54	0	0.32	0.02	
370	0.82	-4.28 ± 0.27	0.56	0.48	0.26	0.12	0.06	
370	2.06	-4.07 ± 0.24	0	0.46	0.01	0.18	0.02	
409	0.82	-3.64 ± 0.15		0.05	0.08	0.15	0.16	0.08
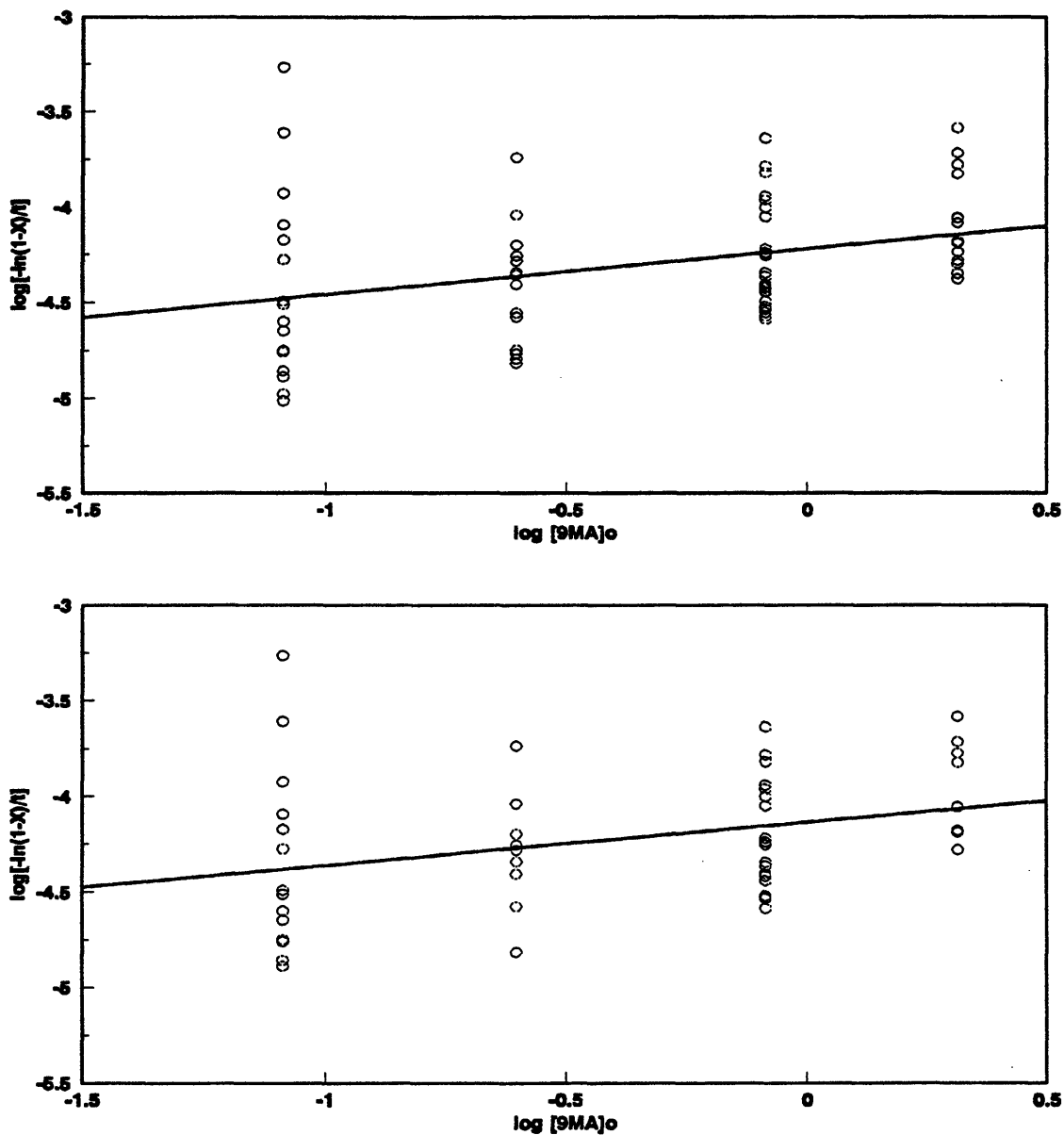
Figure 6.24: Determination of reaction order for 9MA thermolysis from log $[9MA]_o$ vs. log k_{eff}: all X (top) and only X < 0.4 (bottom).

486

data, $X < 0.4$, approximately represent the limit $X \to 0$. It can be demonstrated that for a reaction rate expression:

$$r = k[9MA]^\alpha \qquad (6.7)$$

with rate constant k and reaction order α, the apparent first order rate constant at low conversions, $X \to 0$, is:

$$k_{eff} = k[9MA]_o^{\alpha - 1} \qquad (6.8)$$

Consequently, a plot of log k_{eff} versus log $[9MA]_o$ should exhibit slope $(\alpha - 1)$ and intercept log k. In Figure 6.24, regression of log k_{eff} vs. log $[9MA]_o$ for all conversions gives $\alpha - 1 = 0.24 \pm 0.08$ and log k = -4.22 $\pm$ 0.34, while regression of the low conversion data gives $\alpha - 1 = 0.22 \pm 0.09$ and log k = -4.14 $\pm$ 0.35, both results implying that 9MA thermolysis is close to 3/2 order with respect to the substrate. This accords with the 3/2 order inferred from the variation of 9MA decomposition half-lifes with varying $[9MA]_o$ in Section 6.1.2.

6.2.1.2 True Rate Constants, $k_{3/2}$

The 3/2 order rate expression:

$$r = k_{3/2}[9MA]^{3/2} \qquad (6.9)$$

integrated with respect to time reads:

$$\frac{1}{[9MA]_t^{1/2}} - \frac{1}{[9MA]_o^{1/2}} = \frac{k_{3/2}\ t}{2} \qquad (6.10)$$

Thus, a plot of $1/[9MA]_t^{1/2}$ versus time should be linear, with slope $k_{3/2}/2$ and intercept $1/[9MA]_o^{1/2}$. Figure 6.25 shows the present data for 9MA thermolysis at T = 370°C on coordinates of $1/[9MA]_t^{1/2}$ versus t. Data at all $[9MA]_o$ and all conversions are plotted on the graph, but at each $[9MA]_o$, only the low conversion results, X < 0.4, were regressed, with the corresponding best-fit lines indicated in the figure. The light dashed-dotted diagonal line in the figure is the locus of times and concentrations at which X = 0.4. The best-fit regressed lines are roughly parallel, with slopes, that is $(k_{3/2}/2)$ = [1.81E-05, 1.59E-05, 1.54E-05, 2.13E-05] for $[9MA]_o$ = [0.082, 0.25, 0.82, 2.06 mol/l] respectively. It is noteworthy that the individual slopes vary by less than a factor of 1.4 over a 25-fold range of initial concentrations, reinforcing the validity of the chosen 3/2 order. Figure 6.26, a plot of $2(1/[9MA]_t^{1/2}$ - $1/[9MA]_o^{1/2})$ versus time, superimposes all the $[9MA]_o$ data onto a single line of slope $k_{3/2}$, passing through the origin. From regression of all the data at low conversions, X < 0.4, we obtain $\langle k_{3/2}\rangle$ = (5.28 ± 0.35)E-05 for 0.082 < $[9MA]_o$ < 2.06 mol/l at T = 370°C.
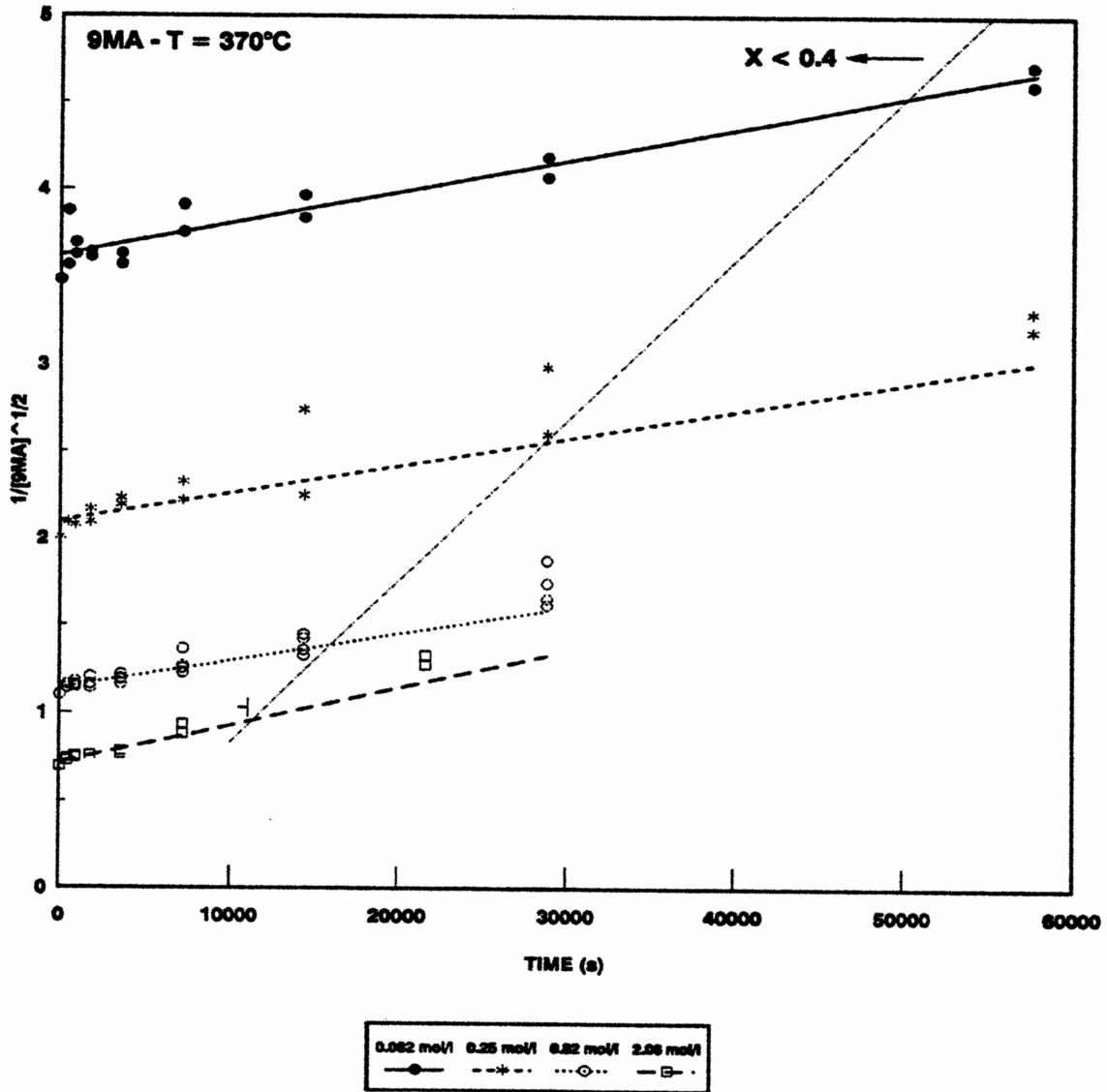
Figure 6.25: 3/2 order plot, $1/[9MA]_t^{1/2}$ vs. t, for 9MA thermolysis with varying $[9MA]_o$ at fixed T = 370°C.

489

Figure 6.26: Plot of the integrated 3/2 order rate expression for 9MA thermolysis with varying $[9MA]_0$ at fixed T = 370°C.

6.2.2 Activation Parameters

Thermolysis of 9MA at fixed $[9MA]_o$ = 0.82 mol/l and varying temperatures from 315 - 409°C revealed the activation parameters associated with both the effective first order and true 3/2 order rate constants.

Effective first order rate constants were calculated at each point, for all runs. At each T and $[9MA]_o$, values of log k_{eff} were averaged over intervals of fractional conversion, respectively 0 - 0.1, 0.1 - 0.2, 0.2 - 0.4, 0.4 - 0.6, 0.6 - 0.8, and 0.8 - 1.0. The average log k_{eff} over each of the chosen conversion intervals are shown as horizontal lines with vertical error bars in Figure 6.27 and Figure 6.28. The upper panel of Figure 6.27 refers to 9MA thermolysis at T = 315°C and $[9MA]_o$ = 0.82 mol/l. In each of the two conversion intervals, values of the average log k_{eff} are ~ - 4.9 ± 0.5. The uncertainty associated with log k_{eff} is seen to diminish with increasing conversion, the error bars spanning 0.69 and 1.10 units of log k_{eff} in the conversion intervals of 0 - 0.1 and 0.1 - 0.2, as shown on line 1 of Table 6.5. The lower panel of Figure 6.27 refers to 9MA thermolysis at T = 335°C and $[9MA]_o$ = 0.82 mol/l, the upper panel of Figure 6.28 refers to 9MA thermolysis at T = 355°C and $[9MA]_o$ = 0.82 mol/l, the upper panel of Figure 6.23 refers to 9DMA thermolysis at T = 370°C and $[9MA]_o$ = 0.82 mol/l and the lower panel of Figure 6.28 refers to 9MA thermolysis at T = 409°C and $[9MA]_o$ = 0.82 mol/l with the respective average and errors summarized on lines 2, 3, 6 and 8 of Table 6.5.

Figure 6.29 is a plot of the integrated 3/2 rate expression, $2(1/[9MA]_t^{1/2}$ -
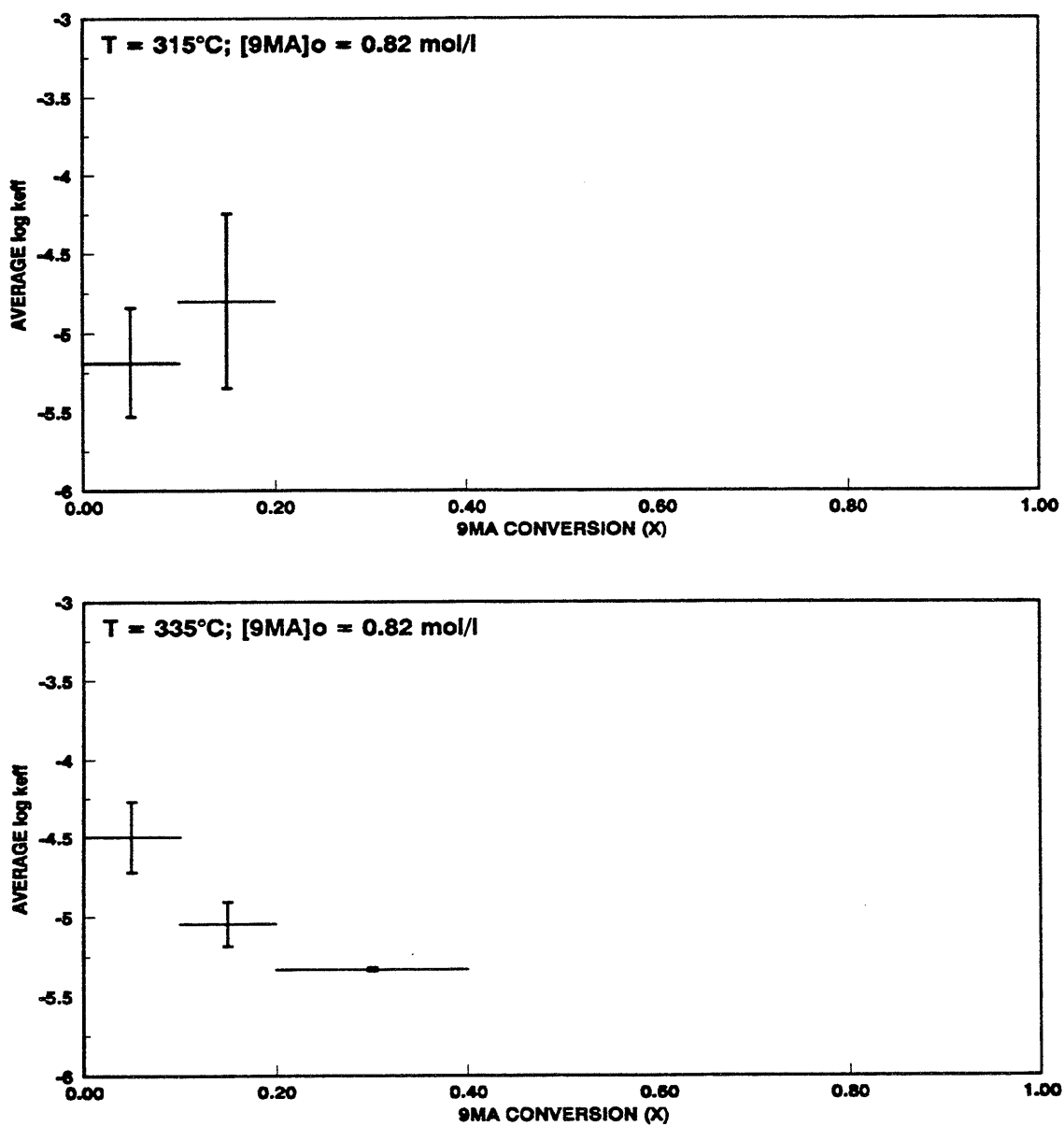
Figure 6.27: Average log k_{eff} vs. 9MA conversion at $[9MA]_o$ = 0.82 mol/l for T = 315°C (top) and T = 335°C (bottom).
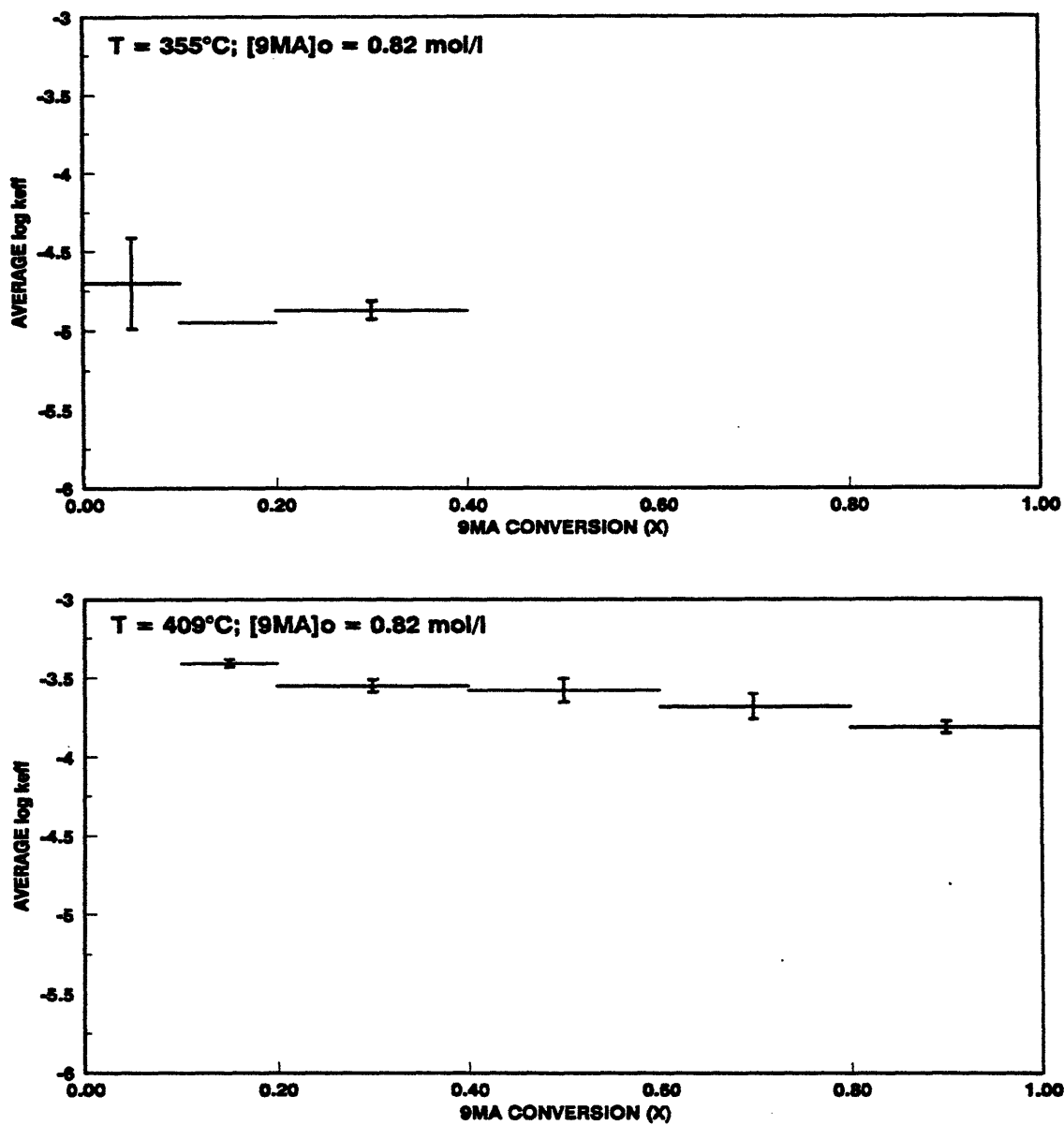
Figure 6.28: Average log k_{eff} vs. 9MA conversion at $[9MA]_o$ = 0.82 mol/l for T = 355°C (top) and T = 409°C (bottom).

493
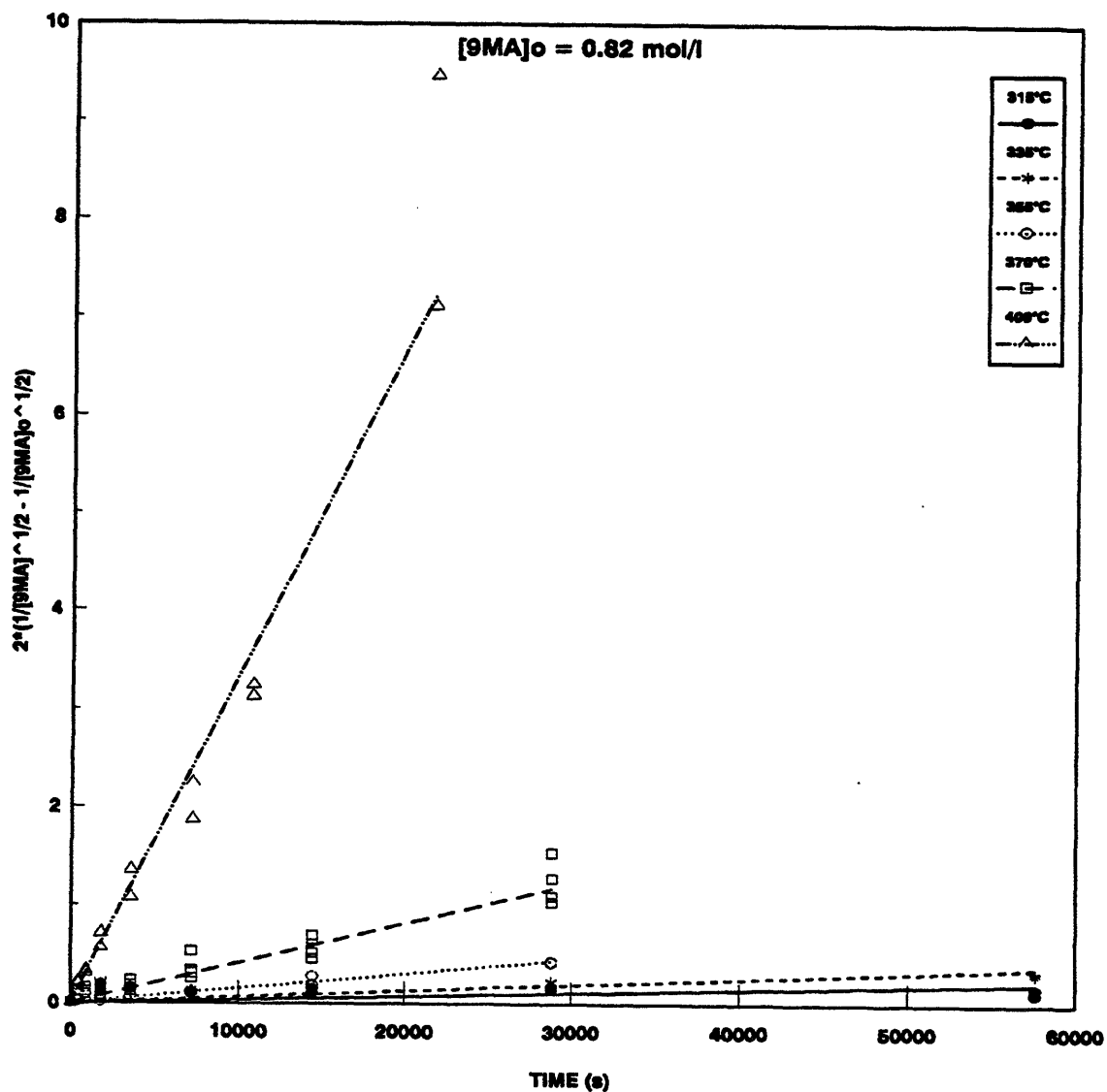
Figure 6.29: Plot of the integrated 3/2 order rate expression for 9MA thermolysis with varying temperature with $[9MA]_o = 0.82$ mol/l.

$1/[9MA]_o^{1/2}$) versus time, for 9MA thermolysis at fixed $[9MA]_o$ = 0.82 mol/l and varying reaction temperatures, 315 < T °C < 409. At each temperature, lines are drawn to represent the best-fits at low conversions, X < 0.4. The slopes of these lines provide the rate constants $<k_{3/2}>$ = [3.63E-06, 6.37E-06, 1.51E-05, 4.07E-05, 3.34E-04] at each thermolysis temperature T = [315, 335, 355, 370, 409°C].

The variation of rate constants k_{eff} and $k_{3/2}$ with temperature is respectively shown in Figure 6.30 and Figure 6.31, using Arrhenius coordinates of $\log_{10}k$ versus $1/\theta$, where θ = 4.573×10^{-3} T in Kelvins; on these coordinates, an Arrhenius relation of form:

$$\log_{10} k = \log_{10} A - \frac{E^*}{\theta} \qquad (6.11)$$

is described by a straight line of slope equal to activation energy E^* in kcal/mol and intercept $\log_{10} A$, where the pre-exponential factor A has units of the rate constant. The upper and lower panels of Figure 6.30 depict Arrhenius diagrams for the effective first order rate constant, k_{eff}, the upper panel derived from data over all conversions and the lower panel derived from low conversion data at X < 0.4. The hollow circles represent the average log k_{eff} and the error bars are the standard deviations from these averages. The error bars are relatively the same size for log k_{eff} using all conversions and the low conversions data at X < 0.4 because most of the scatter in the data is at X < 0.2, as seen in Table 6.5. The best-fit Arrhenius parameters [$\log_{10} A$ (s^{-1}), E^* (kcal/mol)] = [4.61 ± 0.20, 26.2 ± 5.2] for k_{eff} using all
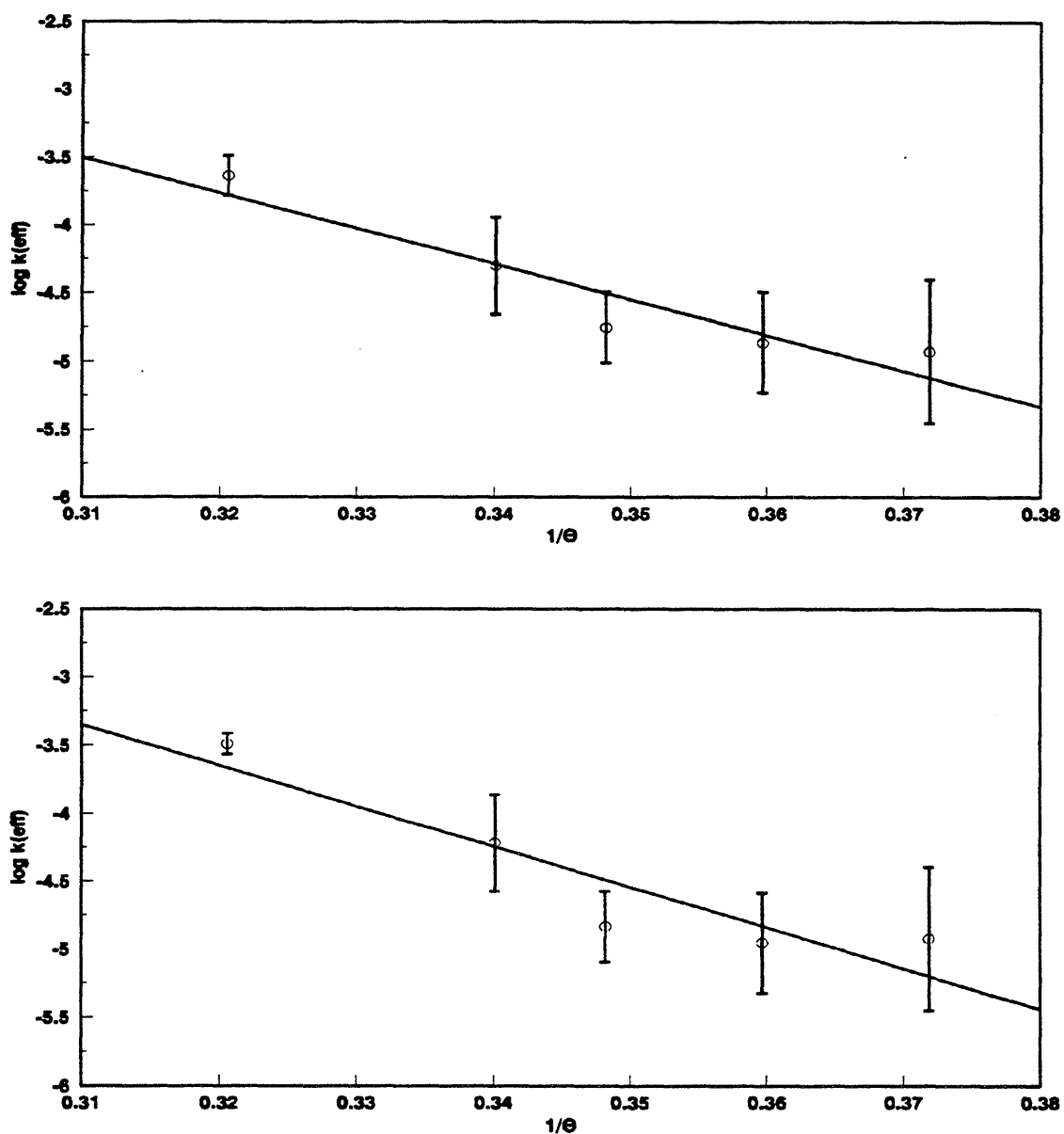
Figure 6.30: Arrhenius plot for k_{eff} for all conversions (top) and for X < 0.4 (bottom) with $[9MA]_o$ = 0.82 mol/l at T = 370°C.
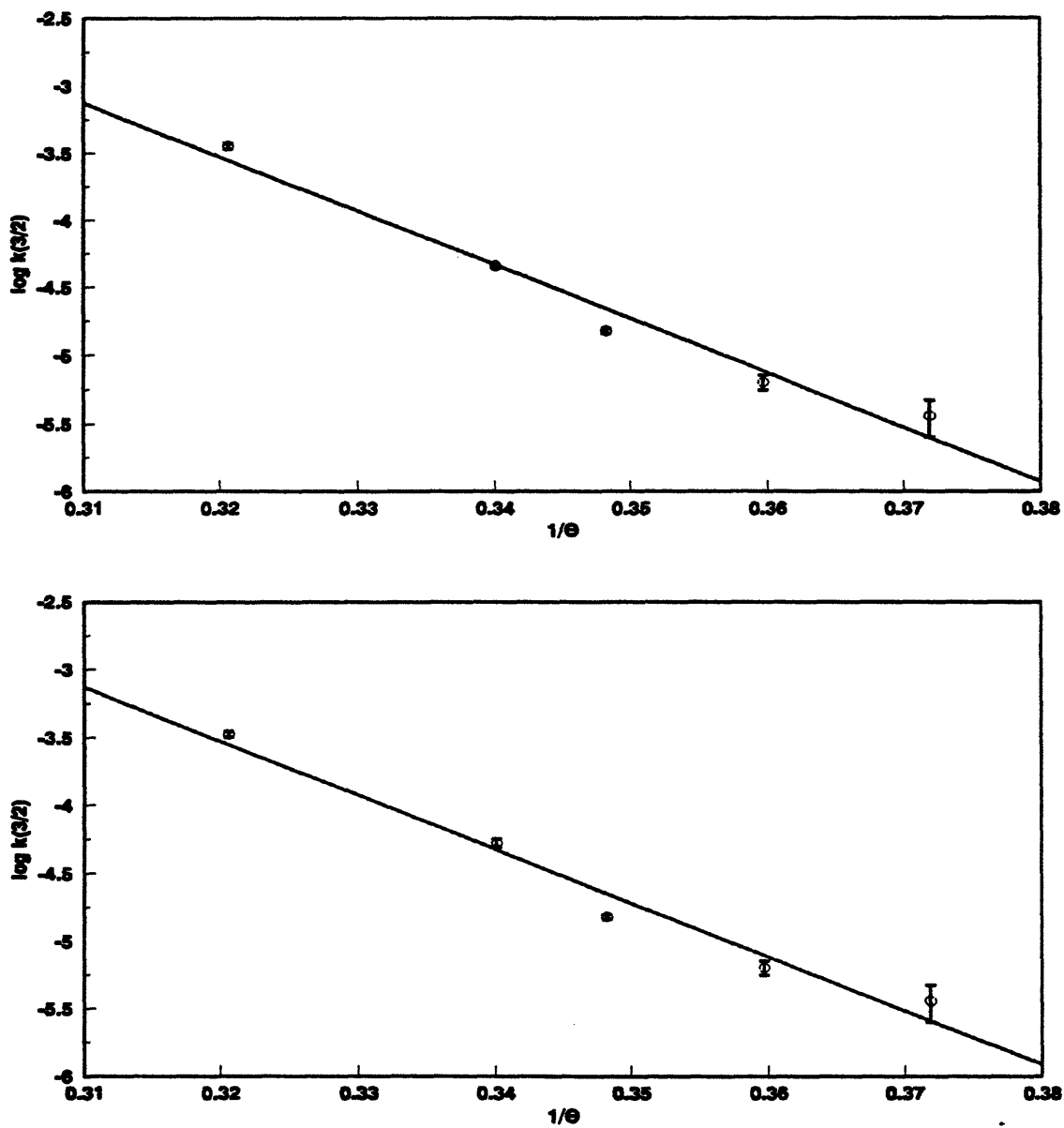
Figure 6.31: Arrhenius plot for $k_{3/2}$ for all conversions (top) and for $X < 0.4$ (bottom) with $[9MA]_o = 0.82$ mol/l at $T = 370°C$.

conversions and $[\log_{10} A \ (s^{-1}), E^* \ (kcal/mol)] = [5.92 \pm 0.28, 29.9 \pm 7.3]$ for k_{eff} using $X < 0.4$.

The upper and lower panels of Figure 6.31 depict Arrhenius diagrams for the 3/2 order rate constant, $k_{3/2}$, the upper panel using data over all conversions and the lower panel using only low conversion data at $X < 0.4$. The hollow circles represent the slope of the integrated 3/2 rate expression versus time while the error bars are the standard errors of these slopes. The error bars for these data are much smaller than those for $\log k_{eff}$ in the previous figure, implying a better fit. The best-fit Arrhenius parameters $[\log_{10} A \ (s^{-1}), E^* \ (kcal/mol)] = [9.3 \pm 0.16, 40.0 \pm 3.9]$ for $k_{3/2}$ using all conversions and $[\log_{10} A \ (l^{\frac{1}{2}}/(mol^{\frac{1}{2}} \ s)), E^* \ (kcal/mol)] = [9.2 \pm 0.15, 39.7 \pm 3.9]$ for $k_{3/2}$ with $X < 0.4$. Regression of the half-lifes t^* at varying temperatures in Section 6.1.3 gave Arrhenius parameters $[\log_{10} A \ (s^{-1}), E^* \ (kcal/mol)] = [11.4 \pm 0.03, 46.4 \pm 0.9]$ for $k_{3/2}$.

6.2.3 Summary of Kinetics

Table 6.6 summarizes the kinetic parameters for 9MA thermolysis as determined from the k_{eff} for the low conversion data at $X < 0.4$, the 3/2 order rate expression for the low conversion data at $X < 0.4$ and the half-lifes at fixed $[9MA]_0$ while varying temperature. Analysis of both the k_{eff} and t^* data led to approximately 3/2 order 9MA decomposition kinetics. The activation parameters $(\log_{10} A, E^*)$ obtained from the 3/2 order rate expression were similar to those derived from the

Table 6.6

SUMMARY OF KINETICS **FOR 9MA THERMOLYSIS**				
	Order	$\log_{10} A$	E^*	$\log_{10} k$ $(370^\circ C)$
k_{eff} (X < 0.4)	1.22 ± 0.09	5.92 ± 0.28	29.9 ± 7.3	-4.25
3/2 order rate expression (X < 0.4)	3/2	9.2 ± 0.15	39.7 ± 3.9	-4.30
t^*	1.50 ± 0.07	11.4 ± 0.03	46.4 ± 0.09	-4.38

half-life data, while $\log_{10} A$ and E^* obtained from the k_{eff} regression data were both appreciably lower than the corresponding parameters in the former sets.

6.3 Reaction Pathways

Pathways for the thermolysis of 9MA deduced from the results over the experimental grid are summarized in Figure 6.32. Three primary pathways operate in parallel upon the original 9MA substrate, namely: (P1) Hydrogenation to 9,10-dihydro-9-methylanthracene, (P2) Demethylation to anthracene, and (P3) Methylation to 9,10-dimethylanthracene and other DMA isomers. The main sequence, shown bold, displays the parallel pathways to 910DMA and ANT from 9MA. The primary methylation product 910DMA is secondarily operated upon by a pathway triad analogous to the preceding primary triad, eventually forming cis- and trans-9,10-dihydro-9,10-dimethylanthracene, trimethylanthracenes and regenerating the substrate 9MA. The primary demethylation product ANT suffers hydrogenation and methylation, as witnessed by the appearance of the minor products DHA, 1MA and 2MA. 9MA does not isomerize to its positional isomers 1MA and 2MA, since the latter species do not arise prior to the appearance of their demethylated precursor ANT.

Figure 6.33 summarizes secondary and termination pathways deduced from the results over the experimental grid. The parallel sequence of methylation and demethylation is shown again in bold. The primary demethylation product of 9MA,
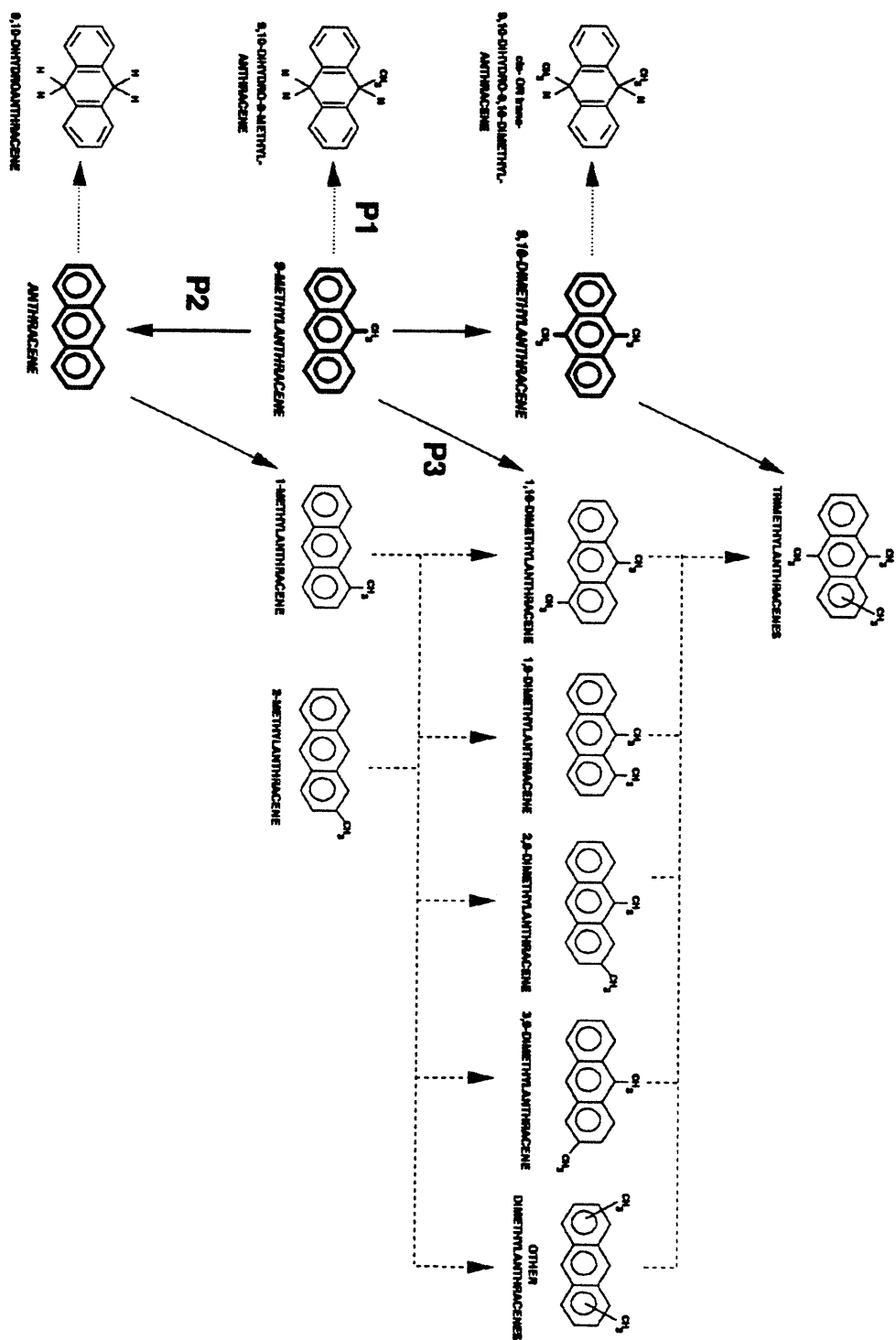
Figure 6.32: 9MA primary decomposition pathways.

501
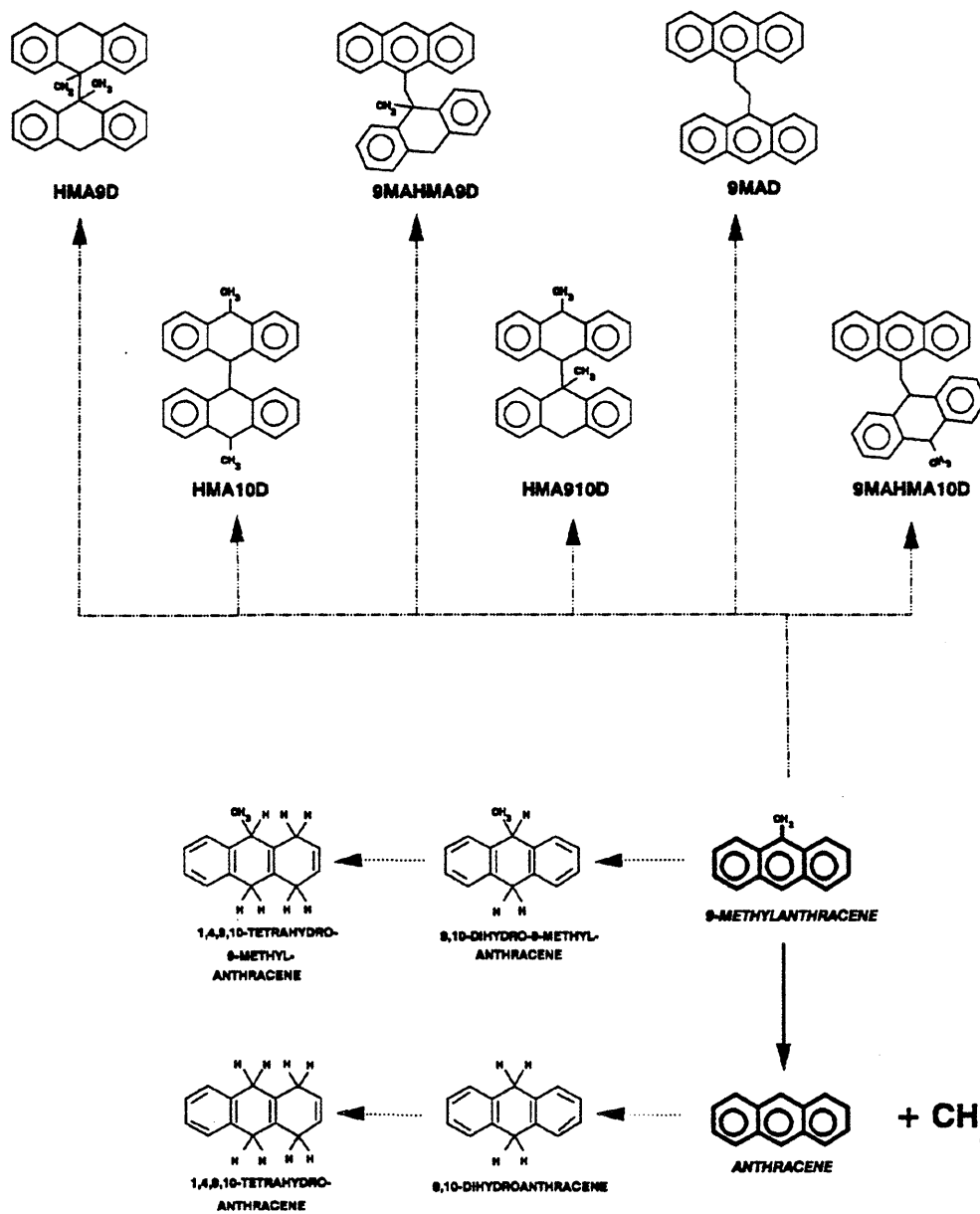
Figure 6.33: 9MA secondary decomposition pathways.

ANT, is associated with methane gas. Hydrogenated products formed by the primary pathway triads acting upon 910DMA, 9MA and ANT are further hydrogenated to yield tetrahydrogenated products (UNK182, UNK196 and UNK210 in Section 4.3.2.1). Termination products included both pure- and cross-termination species related to 9MA and DHMA. Among these, the 9MAD dimer was detected for the 9MA substrate (mass 382 in Section 4.3.2.2) and the cross-termination products seen for the 910DMA thermolysis.

The relative importance of primary pathways (P1 - P3) in Figure 6.32 is shown in Figure 6.34, Figure 6.35 and Figure 6.36 which depict the variation of certain primary product ratios R, namely R[DHMA/ANT], R[ΣDMAs/ANT] and R[CH_4/ANT], versus conversion X at all initial substrate concentrations and temperatures.

R[DHMA/ANT] measures the ratio of hydrogenation (P1) to demethylation (P2) pathways. The upper panel of Figure 6.34 shows that, for all initial 9MA concentrations, R[DHMA/ANT] ~ 0.70 and drops rapidly to a level of 0.051 ± 0.027 at 0.20 < X < 0.75. The lower panel of Figure 6.34 shows that, for all temperatures, R[DHMA/ANT] also starts at a maximum of approximately 0.90 and drops rapidly to a level of 0.047 ± 0.040 at 0.20 < X < 1.0.

R[ΣDMAs/ANT] measures the ratio of methylation (P3) to demethylation (P2) pathways while R[CH4/ANT] measures the ratio of methane gas formed (roughly P2 - P3) relative to demethylation (P2). The upper panel of Figure 6.35

503
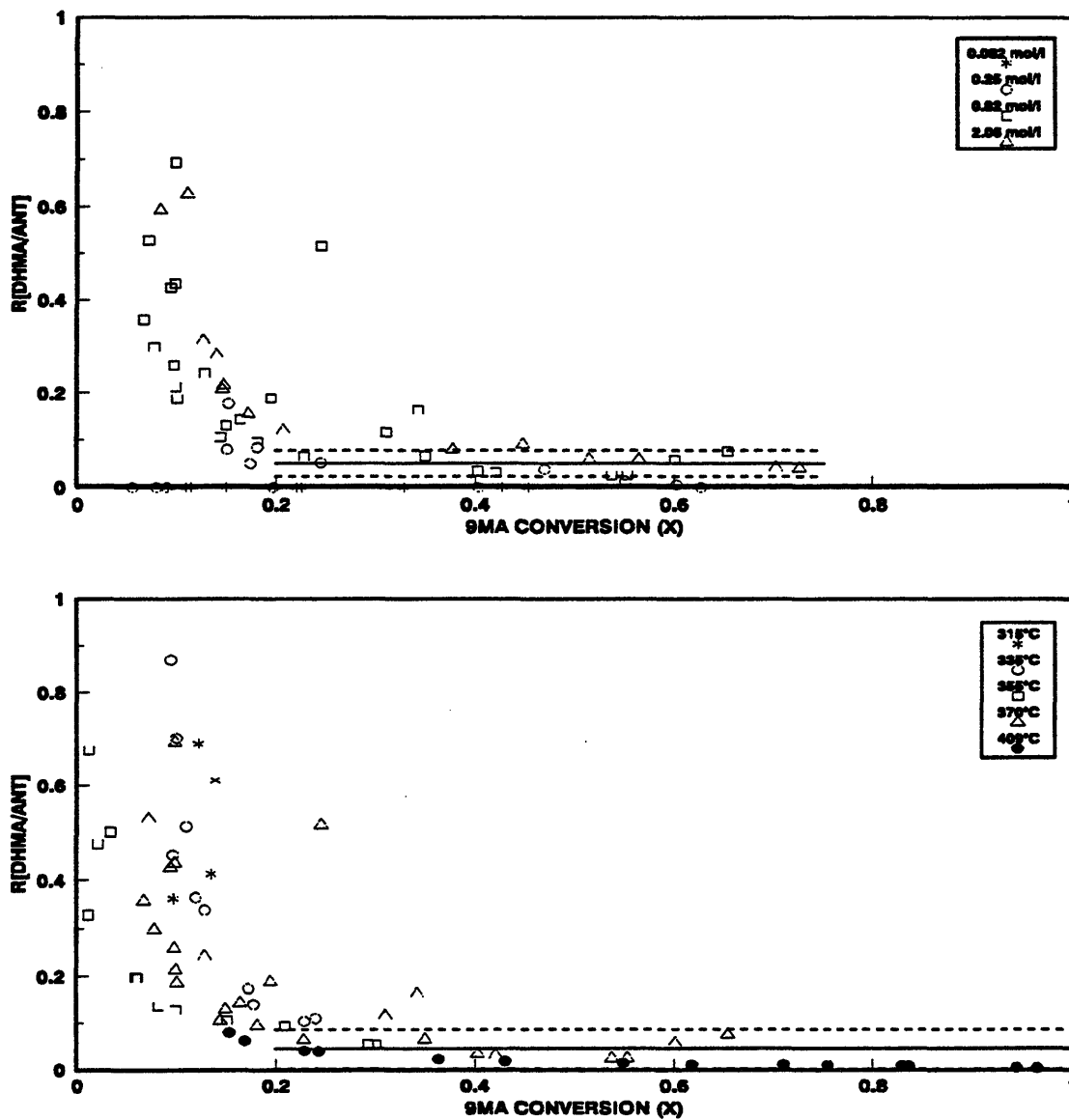
Figure 6.34: Ratio of moles DHMA to moles ANT produced vs. 9MA conversion (X) for varying $[9MA]_o$ at fixed $T = 370°C$(top) and for varying T with fixed $[9MA]_o = 0.82$ mol/l (bottom).

504
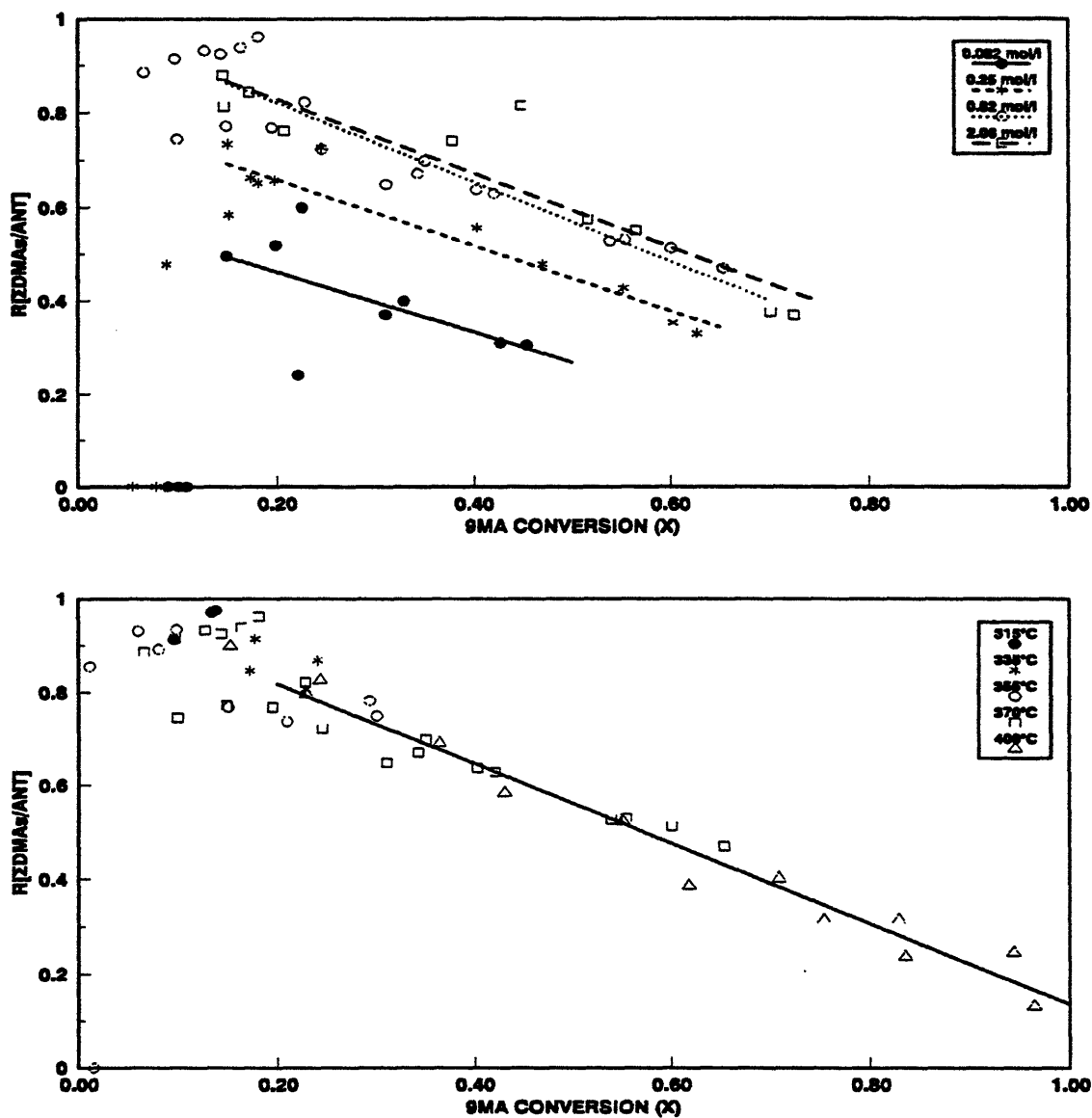
Figure 6.35: Ratio of moles Σ DMAs to moles ANT produced vs. 9MA conversion (X) for varying [9MA]$_o$ at fixed T = 370°C (top) and for varying T with fixed [9MA]$_o$ = 0.82 mol/l (bottom).

505
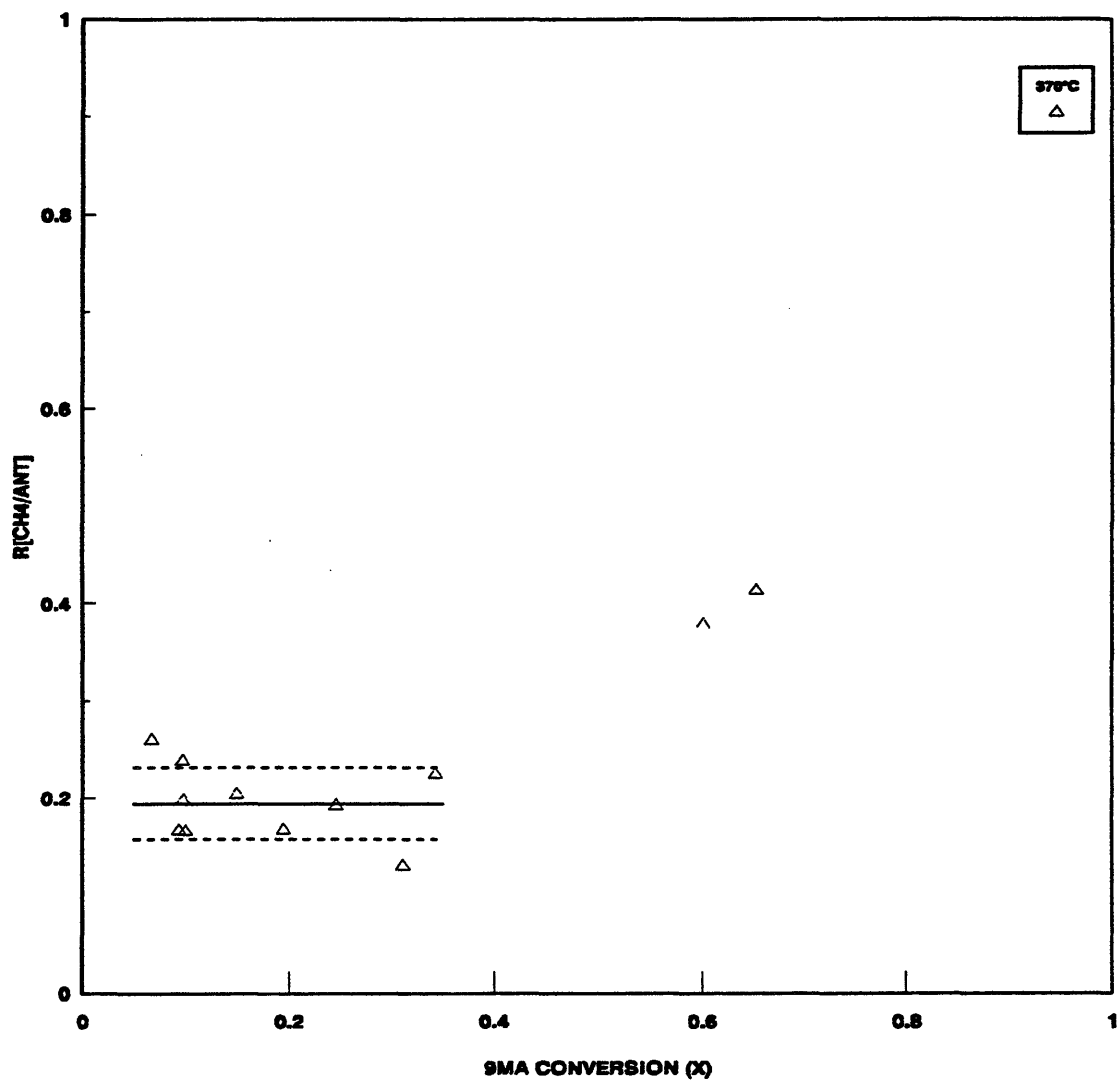
Figure 6.36: Ratio of moles CH_4 to moles ANT formed vs. 9MA conversion (X) for varying $[9MA]_o$ at fixed T = 370°C (top) and for varying T with fixed $[9MA]_o$ = 0.82 mol/l (bottom).

506

shows that R[ΣDMAs/ANT] is a weak function of initial concentration, with the

slopes = [-0.65, -0.69, -0.84, -0.78] and intercepts = [0.59, 0.80, 0.99, 0.99] for [9MA]$_0$

= [0.082, 0.25, 0.82, 2.06 mol/l] for 0.15 < X < [0.50, 0.65, 0.70, 0.75]. The lower

panel of Figure 6.35 shows that R[ΣDMAs/ANT] is essentially independent of

temperature, with the slope = -0.85 and intercept = 0.99 for 0.20 < X < 1.0 at all

temperatures. Figure 6.36 shows that R[CH_4/ANT] = 0.19 ± 0.04 for 0.05 < X <

0.35 at T = 370°C. Taken together, the data in the lower panel of Figure 6.35 and

in Figure 6.36 show that the sum of the ratios R[ΣDMAs/ANT] + R[CH4/ANT] ~

1.0 is close to unity at X = 0.25, accounting for the methyl radicals implicitly formed

in the demethylation pathway P2. It is also noteworthy that, under the present

experiment conditions, ~ 1/5 of the methyl radicals formed by P2 are quenched by

hydrogen abstraction, forming methane gas, while ~ 4/5 add to the 9MA substrate,

eventually appearing as DMAs.

6.4 Mechanism and Modelling

A possible mechanism for the early stages of 9MA thermolysis, that is

consistent with the present pathway and kinetic observations and accounts for all the

products observed during the initial stages of 9MA thermolysis at low conversions,

was devised. Thermochemical and activation parameters were then assigned from

first principles for each elementary reaction and its reverse. An algebraic steady

state analysis was performed on the 9MA mechanism to provide an independent

507

check on numerical results of computer calculations. The mechanistic scheme and rate constants provided a platform for quantitative modelling of 9MA thermolysis kinetics and product selectivities. A sensitivity analysis was performed to demonstrate how the errors of the estimated thermochemical and activation parameters affected the model results. These activation parameters were then adjusted within the limits of the errors to provide the best fit to the experimental results.

6.4.1 Mechanism

A possible mechanism of 9MA thermolysis is summarized in Figure 6.37, as an elementary step "graph". This is constructed such that the substrate and all stable molecular products are arrayed in the bottom row while unstable radical intermediates (the transition states) are arrayed in the top row. Reaction "nodes", arrayed in the middle row, connect the individual species in the bottom and top rows with arrows indicating the initial direction of reaction (all reactions are, of course, reversible). Initiation reactions are denoted by solid interconnecting lines, propagation (product forming) reactions by various kinds of dashed lines and termination reactions by dotted lines. Also, the substrate 9MA is shown with heavy borders in the middle of the bottom row, with light (propagation) products to its right and heavy (termination) products, mostly dimers, to its left.

The free-radical cycle is initiated by the substrate 9MA undergoing
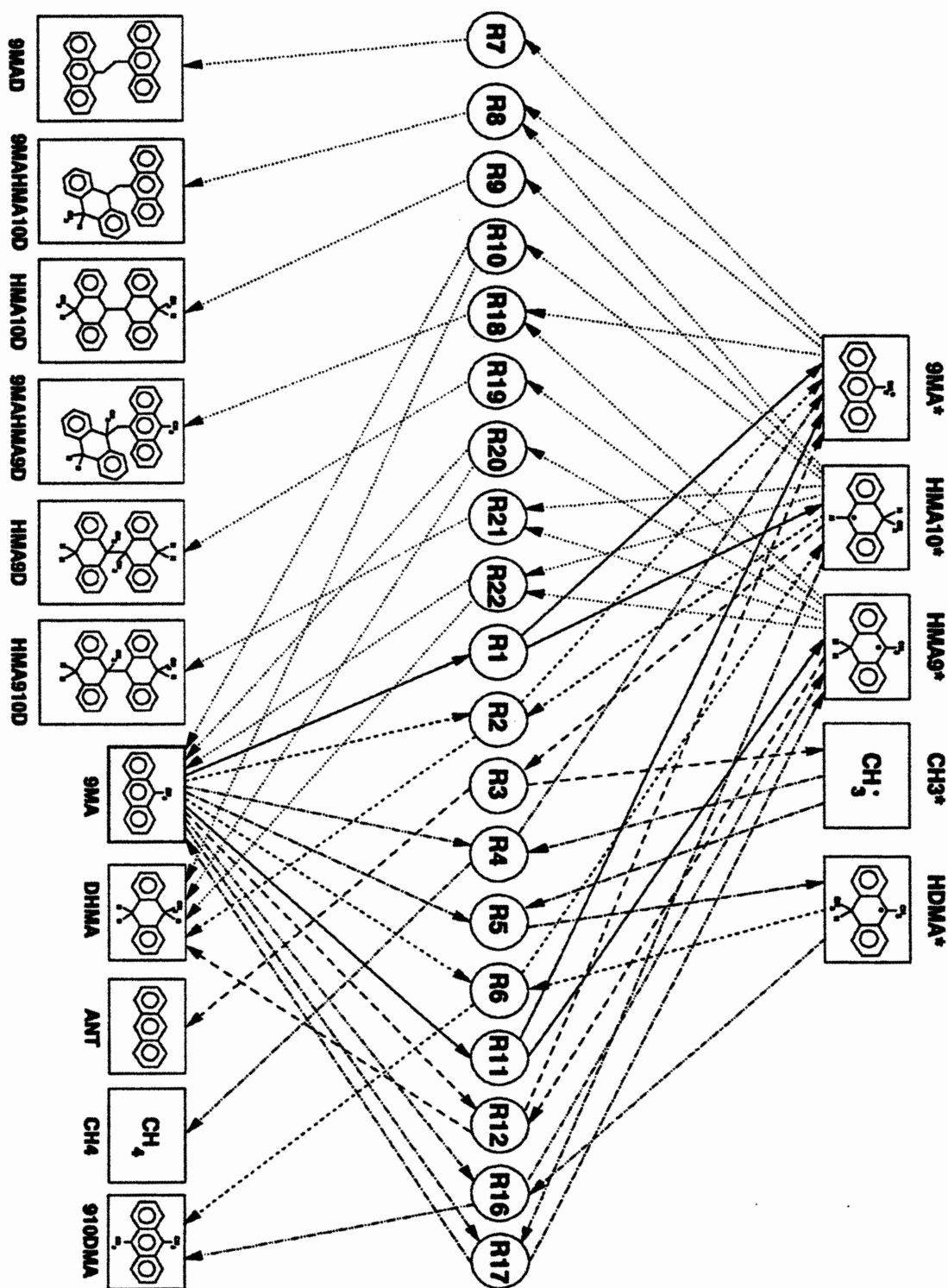
Figure 6.37: Elementary step graph of 9MA thermolysis mechanism.

509

bimolecular disproportionation (R1) and (R11), an intermolecular hydrogen transfer reaction, to form the respectively dehydrogenated and hydrogenated radical species 9MA*, HMA10* and HMA9*. Of these, HMA10* and HMA9* can either abstract hydrogen from 9MA substrate by (R2) and (R12), to form DHMA products, or HMA10* undergoes a ß-scission type of radical decomposition by (R3), forming ANT product and a methyl radical CH_3*. The CH_3* can either abstract H from 9MA substrate by (R4), to form methane product, or add to the 9MA substrate by (R5), to form the dimethyl radical HDMA*. The latter can then abstract H from substrate 9MA via (R6) or (R16) to form the observed 910DMA product and either HMA10* or HMA9*. HMA10* can also abstract H from substrate 9MA via (R16) to form the HMA9* and regenerate a molecule of 9MA. Finally, the radical mechanism is terminated by the species 9MA*, HMA10* and HMA9* engaging in both pure- and cross-combination, (R7-R9), (R18-R19) and (R21), to form various dimeric products. HMA9* and HMA10* radicals can also terminate by pure- or cross-disproportionation, (R10), (R20) and R(22) to form 9MA and DHMA. Figure 6.38 and Figure 6.39 display the 19 elementary steps that correspond to the "graph" in Figure 6.37 and the primary triad acting upon 9MA in the pathway Figure 6.32.

6.4.2 Stoichiometric Limits

The proposed mechanism exhibits certain stoichiometric limits. Consider three: 1) R1, R2, R11, R12, and R7 only; 2) R1, R3, R4, R11, R17 and R7 only; and
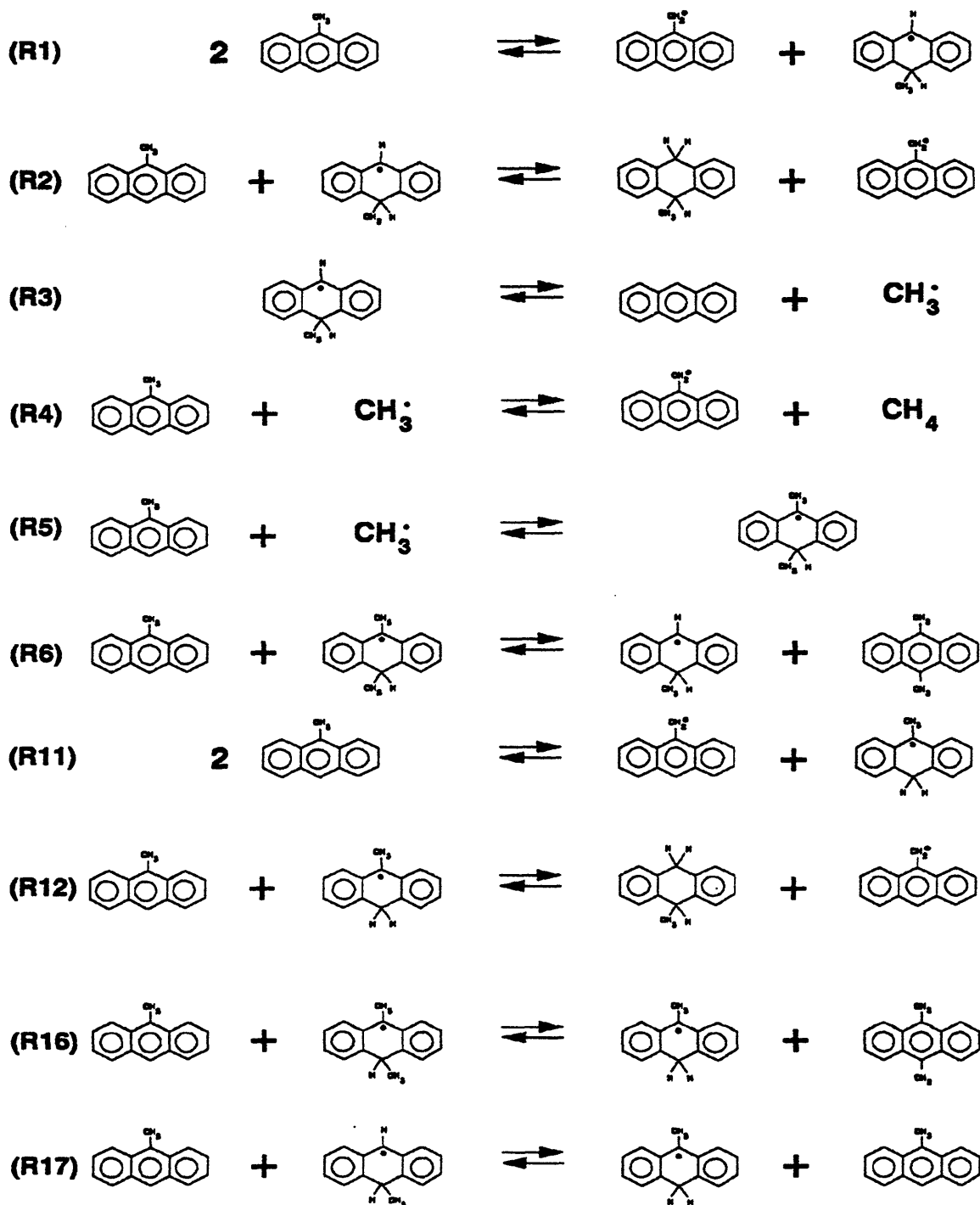
Figure 6.38: Elementary reactions for initiation and propagation steps in 9MA decomposition.

511

(R7)

(R8)

(R9)

(R10)

(R18)

(R19)

(R20)

(R21)

(R22)
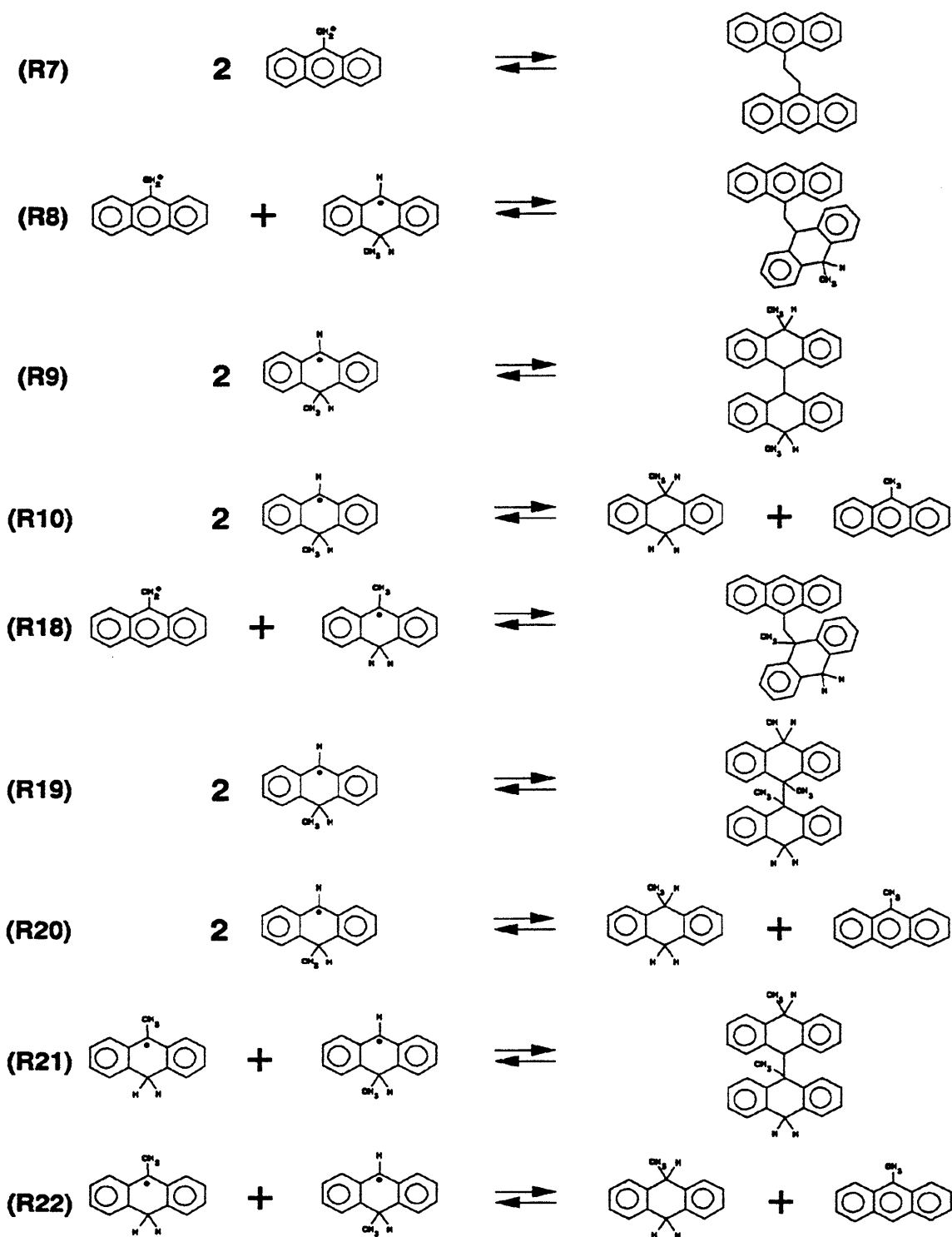
Figure 6.39: Elementary reactions for the terminations steps in 9MA decomposition.

512

3) R1, R3, R5, R6, R11, R16 and R8 only. The first case, R1, R2, R11, R12 and R7 only, produces no ANT, 910DMA or CH4 and gives the overall reaction:

$$3 \; 9MA \rightarrow DHMA + 9MAD \tag{6.12}$$

This case yields S(DHMA) = 0.33, S(ANT) = 0, S(CH4) = 0, S(910DMA) = 0 and S(HVY) = 0.33. The second case, R1, R3, R4, R11, R17 and R7 only, produces no DHMA or 910DMA and gives the overall reaction:

$$3 \; 9MA \rightarrow ANT + CH4 + 9MAD \tag{6.13}$$

In this case, it is assumed the HMA9* radicals are converted to HMA10* radicals via R17. This case yields S(DHMA) = 0, S(ANT) = 0.33, S(CH4) = 0.33, S(910DMA) = 0 and S(HVY) = 0.33. The third case, R1, R3, R5, R6, R11, R16 and R8 only, produces no DHMA or CH4 and gives the overall reaction:

$$3 \; 910DMA \rightarrow DHDMA + DMAD \tag{6.14}$$

This case yields S(DHMA) = 0, S(ANT) = 0.33, S(CH4) = 0, S(910DMA) = 0.33 and S(HVY) = 0.33. The mechanism thus restricts the maximum of each DHMA, ANT, CH4, 910DMA and heavies to 1/3.

6.4.3 Thermochemical Property Estimation

In order to derive kinetic parameters for the 9MA mechanism, values of the thermochemical property the enthalpy of formation, $\Delta H_f^{\circ}{}_{298}$, were required for all

participating chemicals species. Values of ΔH°_f for all stable species are listed in Table 6.7 and for all radical species in Table 6.8. Each table lists the species, the ΔH°_f, the source, remarks about how the ΔH°_f was estimated, and the error associated with the experimental or estimated ΔH°_f. The upper portion of each table, above the dashed lines, lists experimental values, and their errors, for species that were used as a basis for the present derivations, which are listed below the dotted line. Data for the basis species are from a variety of sources, including Benson (1977), abbreviated Benson1; Shaw, Golden and Benson (1977), abbreviated ShGB; Benson et al. (1969), abbreviated Benson2; Pedley (1976); Stein, Golden and Benson (1977), abbreviated StGB; Stull (1969); Structure and Property Experimental (Stein et al., 1991), abbreviated SPX; and Structure and Property Estimation (Stein et al., 1991), abbreviated SPE. The enthalpies of formation in the tables for the species of present interest were again derived using a "macro" group additivity technique, starting with a basis molecule that was as large and as structurally similar to the desired species. Other basis species were then added and subtracted from the starting species to account for structural differences between it and the desired species. Finally, Table 5.9 details the relationships between ΔH°_f for each species in the 9MA mechanism and the basis set of species, corrections and bond strengths.

Table 6.9 compares the best estimates from the present "macro" additivity technique to values from THERM, an automated thermodynamic property estimation program for radicals and molecules using Benson's group additivity method by Ritter

Table 6.7

ENTHALPY OF FORMATION OF STABLE SPECIES
IN 9MA THERMOLYSIS MECHANISM

Species	ΔH°_f (kcal/mol)	Source	Remarks	Error in ΔH°_f
DHA	38.2	Pedley		± 1.1
NAP	35.9	Pedley		± 0.4
1MN	27.2	StGB		± 0.5
2MN	26.4	StGB		± 0.6
CHX[1]	-29.5	ShGB		± 0.2
MeCHX[2]	-37.0	Benson		± 0.4
9MA	47.0	est	ANT + (1MN - NAP) + *gauche* alkene	± 0.8
ANT	55.2	Pedley		± 0.5
910DMA	38.8	est	ANT + 2 (1MN - NAP) + 2 *gauche* alkene[3]	± 1.2
DHMA	30.7	est	DHA + (Me-CHX - CHX)	± 1.2
CH4	-17.8	Benson		± 0.1
H2	0	Benson		± 0.1
9MAD	99.1	SPE		± 3.0
9MAHMA10D	84.3	SPE		± 3.0
HMA10D	69.5	SPE		± 3.0
9MAHMA9D	83.7	SPE		± 3.0
HMA9D	68.3	SPE		± 3.0
HMA910D	68.9	est	interpolated from HMA9D & HMA10D	± 3.0

[1]   CHX = cyclohexane

[2]   Me-CHX = methylcyclohexane

[3]   *gauche* alkene interaction = 0.5 kcal/mol (Benson 1976)

Table 6.8

ENTHALPIES OF FORMATION OF RADICAL SPECIES IN 9MA THERMOLYSIS MECHANISM

Species	ΔH°_f (kcal/mol)	Source	Remarks	Error in ΔH°_f
DHA*	68.1	est	$D_oC\text{-}H(DPM)^1 - \Delta H_f^\circ(H^*) + \Delta H_f^\circ(DHA)$	± 2.3
14CHD[2]	25.9	ShGB		± 0.5
36DM-14CHD[3]	11.3	ShGB		± 1.0
avgDHDMA	23.6	est	DHA + (36DM-14CHD - 14CHD)	± 1.6
H*	52.1	Benson		± 0.1
CH3*	34.8	Benson		± 0.1
9MA*	76.9	est	$D_oC\text{-}H(9MA)^4 - \Delta H_f^\circ(H^*) + \Delta H_f^\circ(9MA)$	± 2.2
HMA10*	60.8	est	$D_oC\text{-}H(DPM) - \Delta H_f^\circ(H^*) + \Delta H_f^\circ(DHMA)$	± 2.3
HMA9*	59.6	est	HMA10* + ($D_oC\text{-}H(CUM)^5 - D_o(ETBZ)^5$) + 2 *gauche* alkene	± 3.1
HDMA*	52.3	est	DHA* + (avgDHDMA - DHA) + ($D_oC\text{-}H(CUM) - D_oC\text{-}H(ETBZ)$) + 2 *gauche* alkene	± 3.7

[1] $D_oC\text{-}H(\text{diphenylmethane}) = 82.0 \pm 2.0$ kcal/mol (Bordwell et.al. 1988)

[2]   14CHD = 1,4-cyclohexadiene

[3]   36Me-14CHX = 3,6-dimethyl-1,4-cyclohexadiene

[4] $D_oC\text{-}H(9MA) = 82.0 \pm 2.0$ kcal/mol (Stein and Brown 1991)

[5] $D_oC\text{-}H(\text{cummene}) = 82.5 \pm 1.5$ kcal/mol and $D_oC\text{-}H(\text{ethylbenzene}) = 84.7 \pm 1.5$ kcal/mol (S & PX)

Table 6.9

COMPARISON OF $\Delta H°_f$ FOR SPECIES IN 9MA THERMOLYSIS MECHANISM

Species	$\Delta H°_f$ (kcal/mol) from:			
	Best Estimate	THERM	2nd "Macro" Estimate	Remarks on 2nd Macro Estimate
9MA	47.0	45.2		
910DMA	38.8	38.2	40.0	ANT + (14DMN[1] - NAP) + 2 *gauche* alkene
ANT	55.2	52.2		
DHMA	30.7	31.9		
9MAD	99.1	99.1		
9MAHMA10D	84.3	85.3		
HMA10D	69.5	72.8		
9MAHMA9D	83.7	87.5		
HMA9D	68.3	68.3		
HMA910D	68.9	70.5		
9MA*	76.9	74.9		
HMA10*	60.8	61.6		
HMA9*	59.6	60.8	59.7	$D_oC-H(DPE)^2 - \Delta H_f°(H^*)$ + $\Delta H_f°(DHMA)$ + 2 *gauche* alkene
HDMA*	52.3	55.1	60.4	DHA* + (cDHDMA - (DHA + (MeCHX - CHX)))

[1]   14CHD = 1,4-cyclohexadiene

[2] D_oC-H(1,1-diphenylethane) = 80.1 kcal/mol (Rossi et.al., 1984)

and Bozzelli (1990). The last two columns in Table 6.9 provide results from a second, alternative, "macro" estimate using the present method. From Table 6.9 it is seen that, for all species, our best estimates for ΔH°_f differ from THERM, and from our alternate estimate, by amounts comparable to the errors stated in Table 6.7. Some confidence can therefore be placed upon the present ΔH°_f estimates.

6.4.4 Kinetic Parameter Estimation

Arrhenius expressions, of the form $\log_{10} k = \log_{10} A - E^*/\theta$, with rate constant k and pre-exponential factor A in units of ($l\ mol^{-1}\ s^{-1}$) and activation energy E^* in kcal/mol were generated for each elementary step R1 - R22 of the 9MA thermolysis mechanism, Figure 6.38 and Figure 6.39. These expressions, and information regarding their deviation, are summarized in Table 6.10 and Table 6.11, as follows. Each elementary reaction was classified according to type (column 2), using free-radical reaction notation. Next, kinetic data reported in the literature for that type of reaction was analyzed to ascertain its activation parameters. Of these, $\log_{10} A$ was decomposed into an intrinsic portion, $\log_{10} A_{int}$ (column 3) and a reaction path degeneracy, rpd (column 4), with $\log_{10} A = \log_{10} A_{int} + \log_{10}$ (rpd). The activation energy E^* was described by an Evans-Polanyi expression (column 5), of form $E^* = E_0 + \alpha \Delta H^{\circ}_r$. Values of the enthalpy of reaction ΔH°_r (column 6), derived from the data of Section 6.4.3, then led to E^* (column 7). Final Arrhenius expressions are summarized in column 8 of Table 6.10 and Table 6.11.

Table 6.10

	ARRHENIUS EXPRESSIONS FOR ELEMENTARY STEPS OF 9MA THERMOLYSIS MECHANISM						
	Type of Reaction	$\log_{10} A_{int}$ l mol⁻¹ s⁻¹	rpd	Evans-Polanyi Relation: $E^* =$	ΔH°_r kcal/mol	E^* kcal/mol	Arrhenius Expression: $\log_{10} k =$
R1	molecular disproportionation	8.5	6	ΔH_r°	43.7	43.7	9.3 - 43.7/θ
R-1	radical disproportionation	8.5	1	0	-43.7	0	8.5
R2	H-abstraction	8.1	3	$17.5 + \Delta H_r^\circ/2$	-0.2	17.4	8.6 - 17.4/θ
R-2	H-abstraction	8.1	2	$17.5 + \Delta H_r^\circ/2$	0.2	17.6	8.4 - 17.6/θ
R3	methyl scission	13.5	1	$2.1 + \Delta H_r^\circ$	29.2	31.3	13.5 - 31.3/θ
R-3	CH3* addition	8.3	2	2.1	-29.2	2.1	8.6 - 2.1/θ
R4	H-abstraction	8.1	3	$17.5 + \Delta H_r^\circ/2$	-22.7	6.2	8.6 - 6.2/θ
R-4	H-abstraction	8.1	4	$17.5 + \Delta H_r^\circ/2$	22.7	28.9	8.7 - 28.9/θ
R5	CH3* addition	8.3	1	2.1	-29.5	2.1	8.3 - 2.1/θ
R-5	methyl scission	13.5	1	$2.1 + \Delta H_r^\circ$	29.5	31.6	13.5 - 31.6/θ
R6	radical H transfer	8.1	1	$17.5 + \Delta H_r^\circ/2$	0.3	17.65	8.1 - 17.7/θ
R-6	radical H transfer	8.1	1	$17.5 + \Delta H_r^\circ/2$	-0.3	17.35	8.1 - 17.4/θ
R7	radical combination	9.3	1	0	-54.7	0	9.3
R-7	homolytic dissociation	15.5	1	ΔH_r°	54.7	54.7	15.5 - 54.7/θ
R8	radical combination	9.3	1	0	-53.4	0	9.3
R-8	homolytic dissociation	15.5	1	ΔH_r°	53.4	53.4	15.5 - 53.4/θ
R9	radical combination	9.3	1	0	-52.1	0	9.3
R-9	homolytic dissociation	15.5	1	ΔH_r°	52.1	52.1	15.5 - 52.1/θ
R10	radical disproportionation	8.5	1	0	-43.9	0	8.5
R-10	molecular disproportionation	8.5	2	ΔH_r°	43.9	43.9	8.8 - 43.9/θ

Table 6.11

ARRHENIUS EXPRESSIONS FOR ELEMENTARY STEPS OF 9MA THERMOLYSIS MECHANISM (continued)

	Type of Reaction	$\log_{10} A_{int}$ l mol^{-1} s^{-1}	rpd	Evans-Polanyi Relation: E* =	$\Delta H_r°$ kcal/mol	E* kcal/mol	Arrhenius Expression: $\log_{10}$ k =
R11	molecular disproportionation	8.5	6	$\Delta H°_r$	42.5	42.5	9.3 - 42.5/θ
R-11	radical disproportionation	8.5	1	0	-42.5	0	8.5
R12	H-abstraction	8.1	3	17.5 + $\Delta H°_r$/2	1.0	18.0	8.6 - 18.0/θ
R-12	H-abstraction	8.1	1	17.5 + $\Delta H°_r$/2	-1.0	17.0	8.1 - 17.0/θ
R16	radical H transfer	8.1	1	17.5 + $\Delta H°_r$/2	-0.9	17.05	8.1 - 17.1/θ
R-16	radical H transfer	8.1	2	17.5 + $\Delta H°_r$/2	0.9	17.95	8.4 - 18.0/θ
R17	radical H transfer	8.1	1	17.5 + $\Delta H°_r$/2	-1.2	16.9	8.1 - 16.9/θ
R-17	radical H transfer	8.1	2	17.5 + $\Delta H°_r$/2	1.2	18.1	8.4 - 18.1/θ
R18	radical combination	9.3	1	0	-52.8	0	9.3
R-18	homolytic dissociation	15.5	1	$\Delta H°_r$	52.8	52.8	15.5 - 52.8/θ
R19	radical combination	9.3	1	0	-50.9	0	9.3
R-19	homolytic dissociation	15.5	1	$\Delta H°_r$	50.9	50.9	15.5 - 50.9/θ
R20	radical disproportionation	8.5	1	0	-41.5	0	8.5
R-20	molecular disproportionation	8.5	1	$\Delta H°_r$	41.5	41.5	9.1 - 41.5/θ
R21	radical combination	9.3	1	0	-51.5	0	9.3
R-21	homolytic dissociation	15.5	1	$\Delta H°_r$	51.5	51.5	15.5 - 51.5/θ
R22	radical disproportionation	8.5	1	0	-42.7	0	8.5 - 42.7/θ
R-22	molecular disproportionation	8.5	2	$\Delta H°_r$	42.7	42.7	8.8 - 42.7/θ

Specific remarks concerning the kinetics of individual elementary steps and reaction types are elaborated below:

(R1) Benson (1976) estimated log A_{int} = 9.0 ± 1.0 and E^* = ΔH°_r for molecular disproportionation of small hydrocarbon molecules into radicals. Stein (1981) estimates log A_{int} = 8.1 for stabilized hydrocarbon radicals. Billmers et.al. (1986) report log A_{int} = 8.7 ± 0.14 for molecular disproportionation of 9,10-dihydroanthracene and 2-ethylanthracene. From these, we have chosen log A_{int} = 8.5 ± 0.5 and E^* = ΔH°_r to represent molecular disproportionation to radicals. Also, for k_1, rpd = 2 x 3 = 6 because each methyl group contains three hydrogen atoms and each of the two 9MA can serve as either hydrogen donor or acceptor.

(R-1) Radical disproportionation is estimated to have the same k_1 with log A_{int} = 8.5 ± 0.5 as molecular disproportionation, with activation energy E^* = 0.

(R2) H-abstraction by hydrocarbon radicals has been correlated by Kerr (1973), who provides log A_{int} = 7.7 and E_o = 12.7 kcal/mol for $C_2H_5^*$ and log A_{int} = 8.2 and E_o = 14.3 kcal/mol for CH_3^*, and by Benson (1976), who quotes log A_{int} = 8.2 and E_o = 14.6 kcal/mol for CH_3^*. Also, Ingold (1973) reported on CH_3^* abstracting hydrogen from toluene with log A_{int} = 8.1 and E^* = 9.5 kcal/mol, from which the corresponding Evans-Polanyi relation with a slope α of 0.5 and ΔH°_r = -16.0 kcal/mol yields E_o = 17.5 kcal/mol. We use Ingolds results, log A_{int} = 8.1 and E^* = 17.5 + $\Delta H^\circ_r/2$ as the basis for all H-abstraction kinetics.

(R-2) Since the microscopic reverse of an H-abstraction is another H-abstraction,

the same parameters apply to R-2 as were used for R2.

(R3) Methyl scissions, a particular type of β-scission reaction, typically have log A

= 13.5 and E^* = 7 + ΔH°_r (Kerr 1983, Dean 1985). For (R3), the value of E_0 = 7

kcal/mol has been adjusted, as explained below for (R-3), to E_0 = 2.1 kcal/mol.

(R-3) Holt and Kerr (1977) provide Arrhenius parameters of log A_{int} = 8.3 and E^*

= 7.6 kcal/mol for CH3* addition to benzene. The activation energy for the

addition of a methyl radical to 9MA will be less than that for the addition to benzene

because of the lower localization energy in 9MA. This adjustment was estimated

from Stephani and Szwarc (1962) who found that at 85°C the rate of methyl addition

to anthracene was 2460 times faster than the rate of methyl addition to benzene.

Assuming equal pre-exponential factors, the rate difference corresponds to a

difference in activation energy of 5.5 kcal/mol. Thus E^* = 2.1 for CH3* addition to

9MA; this is also the value of E_0 in the Evans-Polanyi relation for the reverse methyl

scission reaction (R3).

(R4 and R-4) These are H-abstractions, related in the same manner as (R2

and R-2).

(R5 and R-5) These are analogous to (R-3 and R3) discussed above.

(R6 and R-6) These radical hydrogen transfer (RHT) reactions, wherein a hydrogen

atom transfers from a radical to a molecule, differ somewhat from the conventional

H-abstraction, wherein the H-atom transfers from a molecule to a radical. Definite

kinetic data are lacking for RHTs. Billmers et.al. (1986) estimated log A = 8.2 +

log rpd and E_o = 18.3 kcal/mol for a thermoneutral H transfer at 350°C from a 9-hydroanthryl radical to 2-ethylanthracene. We directly apply the H-abstraction relations, developed for R2 and R-2, to the present RHTs R6 and R-6.

(R7) Ingold (1973) quotes radical recombination rates of log k = 9.3 for two benzyl (also two cumyl) radicals. Benson (1976) has log k = 9.5 for two *t*-butyl radicals, and Miller and Stein (1981) give log k = 9.5 for two α-1,2-diphenylethyl radicals. Since radical combinations are unactivated, that is, E^* = 0, we choose log A = 9.3 for all pure benzyl radical combinations.

(R-7) For homolytic dissociation into stabilized radicals, Benson (1976) estimated log A = 15.5 ± 0.5 and E^* = ΔH°_r. Miller and Stein (1981) used log A = 15.9 and E^* = ΔH°_r = 57.5 kcal/mol for 1,2,3,4-tetraphenylbutane dissociating into two α-1,2-diphenylethyl radicals. We adopt Benson's parameters.

(R8 and R-8) Radical combination and homolytic dissociation are analogous to (R7 and R-7) except that R8 is a cross-combination, so that $k_8 = 2(k_7 k_9)^{1/2}$ and log k_8 = 9.6.

(R9 and R-9) Radical combination and homolytic dissociation are analogous to (R7 and R-7).

(R10 and R-10) Radical and molecular disproportionations are analogous to (R1 and R-1).

(R11 and R-11) Molecular and radical disproportionations are analogous to (R1 and R-1).

(R12 and R-12) H-abstractions are analogous to (R2 and R-2).

(R16 and R-16) Radical hydrogen transfers are analogous to (R6 and R-6).

(R17 and R-17) H-abstractions are analogous to (R2 and R-2).

(R18 and R-18) Radical recombination and homolytic dissociation are analogous to (R8 and R-8).

(R19 and R-19) Radical recombination and homolytic dissociation are analogous to (R9 and R-9).

(R20 and R-20) Radical and molecular disproportionations are analogous to (R1 and R-1).

(R21 and R-21) Radical recombination and homolytic dissociation are analogous to (R9 and R-9).

(R22 and R-22) Radical and molecular disproportionations are analogous to (R1 and R-1).

6.4.5 Modelling

The 9MA thermolysis mechanism devised in Figure 6.38 and Figure 6.39 combined with the Arrhenius expressions derived for each elementary step in Table 6.10 and Table 6.11 provided a mechanistic kinetic model of 9MA thermolysis, valid at low conversions, over the entire initial concentration and temperature ranges of the present experiments. Results of the mechanistic model, and comparisons between these and experimental results, are detailed in this section. Most model

calculations were made at the center of the experimental grid, where $[9MA]_o = 0.82$ mol/l and T = 370°C. Selected calculations were also made at the four corners of the grid, for $[9MA]_o = 0.082$ and 2.06 mol/l at T = 370°C and at T = 315 and 409°C for $[9MA]_o = 0.82$ mol/l. First an algebraic analysis was performed, to estimate the pseudo-steady-state radical concentrations ar selected low conversions; these served to verify the validity of subsequent numerical solutions. Next, full numerical solutions were obtained for the model 9MA thermolysis mechanism, using a computer code ("ACUCHEM", Braun et al., 1988) for solving the system of simultaneous differential equations for the conversion of all species. The calculated product histories, selectivities and product ratios were compared with experimental values. A sensitivity analysis of the model was performed at the central point of the experimental grid, by separately perturbing selected elementary step kinetics over their uncertainty limits. Based on this, a set of "optimized" kinetic parameters were derived to best-fit the model to experimental data.

6.4.5.1 Algebraic Analysis

The pseudo-steady-state approximation is applied to the radical species, whereby the rate of change in the concentration of all radical species is deemed to be ~ 0. In our case, this yields five algebraic equations, one for each radical species, as shown in Figure 6.40. When added together, these equations provide an expression equating the rate of initiation LHS to the rate of termination RHS.

$$\frac{d[9MA*]}{dt} = k_1[9MA]^2 - k_{-1}[HMA10*][9MA*] + k_2[9MA][HMA10*]$$

$$- k_{-2}[DHMA][9MA*] + k_4[9MA][CH3*] - k_{-4}[9MA*][CH4]$$

$$- 2k_7[9MA*]^2 + 2k_{-7}[9MAD] - k_8[9MA*][HMA10*]$$

$$+ k_{-8}[9MAHMA10D] + k_{11}[9MA]^2 - k_{-11}[9MA*][HMA9*]$$

$$+ k_{12}[9MA][HMA9*] - k_{-12}[HDMA][9MA*] + k_{18}[9MA*][HMA9*]$$

$$- k_{-18}[9MAHMA9D] = 0$$

$$\frac{d[HMA10*]}{dt} = k_1[9MA]^2 - k_{-1}[HMA10*][9MA*] - k_2[9MA][HMA10*]$$

$$+ k_{-2}[DHMA][9MA*] - k_3[HMA10*] + k_{-3}[ANT][CH3*]$$

$$+ k_6[HDMA*][9MA] - k_{-6}[910DMA][HMA10*] - k_8[9MA*][HMA10*]$$

$$+ k_{-8}[9MAHMA10D] - 2k_9[HMA10*]^2 + 2k_{-9}[HMA10D]$$

$$- 2k_{10}[HMA10*]^2 + 2k_{-10}[9MA][DHMA] - k_{17}[9MA][HMA10*]$$

$$+ k_{-17}[9MA][HMA9*] - k_{21}[HMA9*][HMA10*] + k_{-21}[HMA910D]$$

$$- k_{22}[HMA9*][HMA10*] + k_{-22}[9MA][DHMA] = 0$$

$$\frac{d[HMA9*]}{dt} = k_{11}[9MA]^2 - k_{-11}[9MA*][HMA9*] - k_{12}[9MA][HMA9*]$$

$$+ k_{-12}[HDMA][9MA*] + k_{16}[9MA][HDMA*] - k_{-16}[910DMA][HMA9*]$$

$$+ k_{17}[9MA][HMA10*] - k_{-17}[9MA][HMA9*] - k_{18}[9MA*][HMA9*]$$

$$+ k_{-18}[9MAHMA9D] - 2k_{19}[HMA9*]^2 + 2k_{-19}[HMA9D]$$

$$- 2k_{20}[HMA9*]^2 + 2k_{-20}[9MA][HDMA] - k_{21}[HMA9*][HMA10*]$$

$$+ k_{-21}[HMA910D] - k_{22}[HMA9*][HMA10*] + k_{-22}[9MA][DHMA] = 0$$

$$\frac{d[CH3*]}{dt} = k_3[HMA10*] - k_{-3}[ANT][CH3*] - k_4[9MA][CH3*]$$

$$+ k_{-4}[CH4][9MA*] - k_5[9MA][CH3*] + k_{-5}[HDMA*] = 0$$

$$\frac{d[HTMA*]}{dt} = k_5[9MA][CH3*] - k_{-5}[HDMA*] - k_6[9MA][HDMA*]$$

$$+ k_{-6}[910DMA][HMA10*] - k_{16}[9MA][HDMA*] + k_{-16}[910DMA][HMA9*] = 0$$

ADDING TOGETHER:

$$(k_1 + k_{11})[9MA]^2 + k_{-7}[9MAD] + k_{-8}[9MAHMA10D] + k_{-18}[9MAHMA9D] + k_{-9}[HMA10D]$$

$$+ k_{-19}[HMA9D] + k_{-21}[HMA910D] + (k_{-10} + k_{-20} + k_{-22})[9MA][DHMA]$$

$$= [9MA*]^2 \left(k_7 + \frac{(k_9 + k_{10})[HMA10*]^2}{[9DMA*]^2} + \frac{(k_{19} + k_{20})[HMA9*]^2}{[9MA*]^2} \right.$$

$$\left. + \frac{(k_{-1} + k_8)[HMA10*]}{[9MA*]} + \frac{(k_{-11} + k_{18})[HMA9*]}{[9MA*]} + \frac{(k_{21} + k_{22})[HMA9*][HMA10*]}{[9MA*]^2} \right)$$

Figure 6.40: Steady-state expression for the radical species in the 9MA mechanism.

Given the concentrations of stable species, and all rate constants, the foregoing system of algebraic equations can be solved (e.g. by successive approximations) to provide the concentrations of all radical species. Results for the solution at $[9MA]_0$ = 0.82 mol/l and T = 370°C at initial conditions of X → 0, where substrate is the only stable species, are given in column 2 of Table 6.12. It is seen that 9MA*, HMA10* and HMA9* are the most prevalent radicals, with concentrations respectively 3.56E-08, 2.36E-09 and 9.41E-09 mol/l. These results can further be used to calculate instantaneous rates of formation for all products at X = 0, based on which it is possible to estimate the amounts of all species at an adjacent (low) conversion, say X = 0.05. Here the pseudo-steady-state calculations can be repeated with the new stable species concentrations, to provide a new set of radical concentrations. Column 3 of Table 6.12 shows results obtained in this manner at X = 0.10. It is seen that the 9MA*, HMA10* and HMA9* remain the dominant radical species, but their concentrations, respectively 3.20E-08, 2.43E-09 and 9.59E-09 mol/l differ somewhat from the values at X → 0.

The final two columns of Table 6.12 radical and stable species concentrations calculated (see below) during the full numerical solution for $[9MA]_0$ = 0.82 mol/l and T = 370°C at conversions respectively X → 0 (very low) and X = 0.10. The numerical solution also shows 9MA*, HMA10* and HMA9* to be the dominate radical species at both conversions. Also, the concentrations of all species, both radical and stable, calculated by the numerical solution agree quite closely, to within

527

Table 6.12

COMPARISON OF PSEUDO-STEADY-STATE AND FULL NUMERICAL SOLUTION RESULTS FOR 9MA THERMOLYSIS AT $[9MA]_o$ = 0.82 mol/l AND T = 370°C

Species	Steady-State		ACUCHEM Model	
	X → 0	X = 0.10	X → 0	X = 0.09
9MA*	3.56E-08[1]	3.20E-08	4.99E-08	9.77E-08
HMA10*	2.36E-09	2.43E-09	2.94E-09	4.06E-09
HMA9*	9.41E-09	9.59E-09	1.19E-08	1.64E-08
CH3*	4.74E-14	5.36E-14	1.66E-13	2.49E-13
HDMA*	2.75E-09	2.90E-09	6.27E-09	8.88E-09
9MA	8.20E-01	7.38E-01	8.19E-01	7.48E-01
ANT	0	7.97E-03	1.03E-04	9.25E-03
DHMA	0	1.77E-02	2.02E-04	1.63E-02
CH4	0	4.37E-03	2.14E-05	1.98E-03
910DMA	0	1.59E-03	8.17E-05	7.27E-03
9MAD	0	7.83E-03	2.36E-04	1.84E-02
9MAHMA10D	0	2.04E-04	1.34E-05	3.41E-04
9MAHMA9D	0	4.99E-04	5.20E-05	8.85E-04
HMA9D	0	3.05E-05	9.36E-06	3.46E-05
HMA10D	0	5.10E-06	7.16E-07	5.36E-06
HMA910D	0	1.25E-05	2.65E-06	1.37E-05

[1]   Values in table are species concentration in mol/l

a factor of 4 or better, with corresponding results obtained from the pseudo-steady-state algebraic solution. This bolsters our confidence in the fidelity of the numerical solution results.

6.4.5.2 Numerical Solutions and Comparison with Experiments

Conservation relations derived from the mechanistic model of 9MA thermolysis and using the rate constants of Section 6.4.4 were numerically integrated using ACUCHEM (Braun et. al. 1988). Initial conditions ($[9MA]_o$) were chosen to match experimental initial conditions. Concentration versus time data was generated for each $[9MA]_o$ and T.

6.4.5.2.1 Detailed Calculations at T = 370°C for $[9MA]_o$ = 0.82 mol/l

Table 6.13, Table 6.14, Table 6.15 and Table 6.16 detail our numerical solution of the model at the central point, T = 370°C and $[9MA]_o$ = 0.82 mol/l, of the experimental grid. Columns 2-4 of Table 6.13 and Table 6.14 show Arrhenius expressions, with pre-exponential factor A ($1 \text{ mol}^{-1} \text{ s}^{-1}$ units), activation energy E^* in kcal/mol and rate constant k ($1 \text{ mol}^{-1} \text{ s}^{-1}$ units), for each elementary step R1 - R22 of the 9MA thermolysis mechanism. The radical and stable species concentrations generated by the numerical solution were then used with the rate constants to ascertain the rate, in mol $l^{-1} \text{ s}^{-1}$, of each forward and reverse reaction in the 9MA thermolysis mechanism at two conversions X = 0.001 (limit X ~ 0) and X = 0.41,

529

Table 6.13

**ARRHENIUS EXPRESSIONS, RATE CONSTANTS AND
RATES OF ELEMENTARY STEPS IN THE MODEL 9MA
THERMOLYSIS AT T = 370°C AND [9MA]$_o$ = 0.82 mol/l**

	$\log_{10} A$	E^*	k (T = 370°C)	Rate, r(mol/l s), at Conversion (X) 0.001	0.41
R1	9.3	43.7	2.74E-06	1.84E-06	6.42E-07
R-1	8.5	0	3.18E+08	4.64E-08	4.25E-07
R2	8.6	17.4	4.81E+02	1.16E-06	1.90E-06
R-2	8.5	17.6	3.27E+02	3.29E-09	2.49E-06
R3	13.5	31.3	7.17E+02	2.11E-06	5.86E-06
R-3	8.6	2.1	7.69E+07	1.31E-09	3.30E-06
R4	8.6	6.2	3.22E+06	4.38E-07	7.93E-07
R-4	8.7	28.9	7.74E-02	8.25E-14	2.77E-10
R5	8.3	2.1	3.85E+07	5.23E-06	9.47E-06
R-5	13.5	31.6	5.67E+02	3.55E-06	7.69E-06
R6	8.1	17.7	1.25E+02	6.43E-07	8.22E-07
R-6	8.1	17.4	1.58E+02	3.80E-11	8.10E-08
R11	9.3	42.5	7.02E-06	4.71E-06	1.64E-06
R-11	8.5	0	3.16E+02	1.88E-07	1.19E-06
R12	8.6	18.0	3.01E+02	2.94E-06	3.33E-06
R-12	8.4	17.0	4.15E+02	4.18E-09	3.16E-06
R16	8.1	17.1	2.00E+02	1.03E-06	1.31E-06
R-16	8.4	18.0	1.97E+02	1.93E-10	2.83E-07
R17	8.1	16.9	2.25E+02	5.42E-07	8.90E-07
R-17	8.4	18.1	1.76E+02	1.72E-06	1.95E-06

Table 6.14

ARRHENIUS EXPRESSIONS, RATE CONSTANTS AND RATES OF ELEMENTARY STEPS IN THE MODEL 9MA THERMOLYSIS AT T = 370°C AND [9MA]$_0$ = 0.82 mol/l

| | $\log_{10} A$ | E^* | k (T = 370°C) | Rate, r(mol/l s), at Conversion (X) | |
				X = 0.001	X = 0.41
R7	9.3	0	2.00E+09	4.96E-06	5.41E-05
R-7	15.5	54.7	7.89E-04	1.86E-07	5.37E-05
R8	9.3	0	2.00E+09	2.92E-07	2.68E-06
R-8	15.5	53.4	2.18E-03	2.92E-08	2.68E-06
R9	9.3	0	2.00E+09	1.72E-08	1.33E-07
R-9	15.5	52.1	6.05E-03	4.33E-09	1.33E-07
R10	8.5	0	3.16E+08	2.73E-09	2.11E-08
R-10	8.8	43.9	7.42E-07	1.22E-10	1.66E-08
R18	9.3	0	2.00E+09	1.19E-06	7.53E-06
R-18	15.5	52.8	3.50E-03	1.82E-07	7.53E-06
R19	9.3	0	2.00E+09	2.84E-07	1.05E-06
R-19	15.5	50.9	1.55E-02	1.45E-07	1.05E-06
R20	8.5	0	3.16E+08	4.50E-08	1.66E-07
R-20	8.5	41.5	2.43E-06	4.02E-10	5.44E-08
R21	9.3	0	2.00E+09	7.00E-08	3.74E-07
R-21	15.5	51.5	9.67E-03	2.56E-08	3.74E-07
R22	8.5	0	3.16E+08	1.11E-08	5.92E-08
R-22	8.8	42.7	1.90E-06	3.13E-10	4.24E-08

Table 6.15

CALCULATED RATES OF FORMATION OF RADICAL SPECIES AT X = 0.001 AND 0.41 AT T = 370°C WITH [9MA]$_0$ = 0.82 mol/l

	CONTRIBUTING REACTIONS	r (mol/l s) at X=0.001	Major Contribution	r (mol/l s) at X=0.41	Major Contribution
r(9MA*)	R1 - R-1 + R2 - R-2 + R4 - R-4 - 2R7 + 2R-7 - R8 + R-8 + R11 - R-11 + R12 - R-12 - R18 + R-18	3.1E-08		3.4E-07	
r(HMA10*)	R1 - R-1 - R2 + R-2 - R3 + R-3 + R6 - R-6 - R8 + R-8 - 2R9 + 2R-9 - 2R10 + 2R-10 - R17 + R-17 - R21 + R-21 - R22 + R-22	-6.7E-10		9.7E-09	
r(HMA9*)	R11 - R-11 - R12 + R-12 + R16 - R-16 + R17 - R-17 - R18 + R-18 - 2R19 + 2R-19 - 2R20 + 2R-20 - R21 + R-21 - R22 + R-22	3.3E-08		1.4E-07	
r(CH3*)	R3 - R-3 - R4 + R-4 - R5 + R-5	-8.2E-09		-1.6E-08	
r(HDMA*)	R5 - R-5 - R6 + R-6 - R16 + R-16	4.5E-09		1.1E-08	

Table 6.16

	CONTRIBUTING REACTIONS	r (mol/l s) at X=0.001	Major Contribution	r (mol/l s) at X=0.41	Major Contribution
		CALCULATED RATES OF FORMATION OF STABLE SPECIES AT X = 0.001 AND 0.41 AT T = 370°C WITH [9MA]$_o$ = 0.82 mol/l			
r(9MA)	-2R1 + 2R-1 - R2 + R-2 - R4 + R-4 - R5 + R-5 - R6 + R-6 + R10 - R-10 + 2R11 + 2R-11 - R12 + R-12 + R20 - R20 + R22 - R-20	-2.0E-05	R1, R2, R5, R-5, R11, R12	-5.1E-06	R1, R2, R-2, R5, R-5, R11, R12, R-12
r(ANT)	R3 - R-3	2.1E-06	R3	2.6E-06	R3, R-3
r(910DMA)	R6 - R-6 + R6 - R-16	1.7E-06	R6, R16	1.8E-06	R6, R16, R-16
r(CH4)	R4 - R-4	4.4E-07	R4	7.9E-07	R4
r(DHMA)	R2 - R-2 + R10 - R-10 + R12 - R-12 + R20 - R-20 + R22 - R-22	4.2E-06	R2, R12	-2.7E-07	R2, R-2, R12, R-12
r(9MAD)	R7 - R-7	4.8E-06	R7	3.6E-07	R7, R-7
r(9MAHMA9D)	R18 - R-18	1.0E-06	R18	-7.9E-09	R18, R-18
r(9MAHMA10D)	R8 - R-8	2.6E-07	R8	4.3E-10	R8, R-8
r(HMA9D)	R19 - R-19	1.4E-07	R19, R-19	-1.9E-09	R19, R-19
r(HMA10D)	R9 - R-9	1.3E-08	R9	3.9E-11	R9, R-9
r(HMA910D)	R21 - R-21	4.4E-08	R21	-9.2E-10	R21, R-21

533

as shown in the last two columns of Table 6.13 and Table 6.14. The rates of the elementary reactions were then used to calculate the rates of radical and stable species formation at $X = 0.001$ and $X = 0.41$ as shown in column 3 and 5 respectively of Table 6.13 and Table 6.14. The elementary reaction that contribute to the formation of each radical and stable species are listed in column 2 of Table 6.15 and Table 6.16, while those reactions that make the major contributions to the formation of the stable species at the low and high conversions are noted in columns 4 and 6. It is seen that the rate of destruction of 9MA is dominated by R1 (1.84E-06), R2 (1.16E-06), R5 (5.23E-06), R-5 (3.55E-06), R11 (4.71E-06) and R12 (2.94E-06) at $X = 0.001$ and R1 (6.42E-07), R2 (1.90E-06), R-2 (2.49E-06), R5 (9.47E-06), R-5 (7.69E-06), R11 (1.64E-06), R12 (3.33E-06) and R-12 (3.16E-06) at $X = 0.41$. The rate of formation of ANT is dominated by R3 (2.11E-06) at $X = 0.001$ and by R3 (5.86E-06) and R-3 (3.30E-06) at $X = 0.42$, whereas the rate of formation of CH4 is controlled by R4 (4.38E-07 and 7.93E-07) at both $X = 0.001$ and 0.41. The rate of formation of 910DMA is the sum of R6 (6.43E-07) and R16 (1.03E-06) at $X = 0.01$ and the sum of R6 (8.22E-07), R16 (1.31E-06) and R-16 (2.83E-07) at $X = 0.41$. The rate of formation of DHMA is the sum of R2 (1.16E-06) and R12 (2.94E-06) at $X = 0.001$ and the sum of R2 (1.90E-06), R-2 (2.49E-06), R12 (3.33E-06) and R-12 (3.16E-06) at $X = 0.41$. The rates of dimer formation; r(9MAD), r(9MAHMA9D), r(9MAHMA10D), r(HMA9D), r(HMA10D) and r(HMA910D); are controlled by the respective termination reactions; R7 (4.96E-06),

534

R18 (1.19E-06), R8 (2.92E-07), R19 (2.84E-07) and R-19 (1.45E-07), R9 (1.72E-08) and R21 (7.00E-08), whereas at X = 0.41, the dimer formation rates are controlled by R7 (5.41E-05) and R-7 (5.37E-07); R18 (7.53E-06) and R-18 (7.53E-06); R8 (2.68E-06) and R-8 (2.68E-06); R19 (1.05E-06) and R-19 (1.05E-06); R9 (1.33E-07) and R-9 (1.33E-07); and R21 (3.74E-07) and R-21 (3.74E-07). Figure 6.41 graphically depicts the elementary reaction rate traffic during 9MA thermolysis at X → 0, with the thicker arrows denoting reactions with the greater net (forward - backward) rates. Figure 6.42 presents a similar depiction of reaction traffic at X = 0.41.

Figure 6.43 compares the substrate and product histories (upper panel) and product selectivities (lower panel) as obtained from numerical solution of the thermolysis model to the experimental data for 9MA, ANT, 910DMA and CH4 at the center of the experimental grid, $[9MA]_0$ = 0.82 mol/l and T = 370°C. In the upper panel of Figure 6.43, the model is seen to predict 9MA decay, the solid line, that is too slow compared to the experimental observations, shown as asterisks. The model half-life, t^*, is 1.7-fold slower than the experimental. The upper panel of Figure 6.43 also shows that the absolute amounts of ANT, the short-dashed line versus the circles, and of 910DMA, the dotted line versus the squares, formed by the model are both lower than observed in the experiments. However, the model predicts the relative amounts of ANT > 910DMA > CH4 and the sum of CH4 plus 910DMA equal to the ANT product, both of which accord with the experiment. The

535
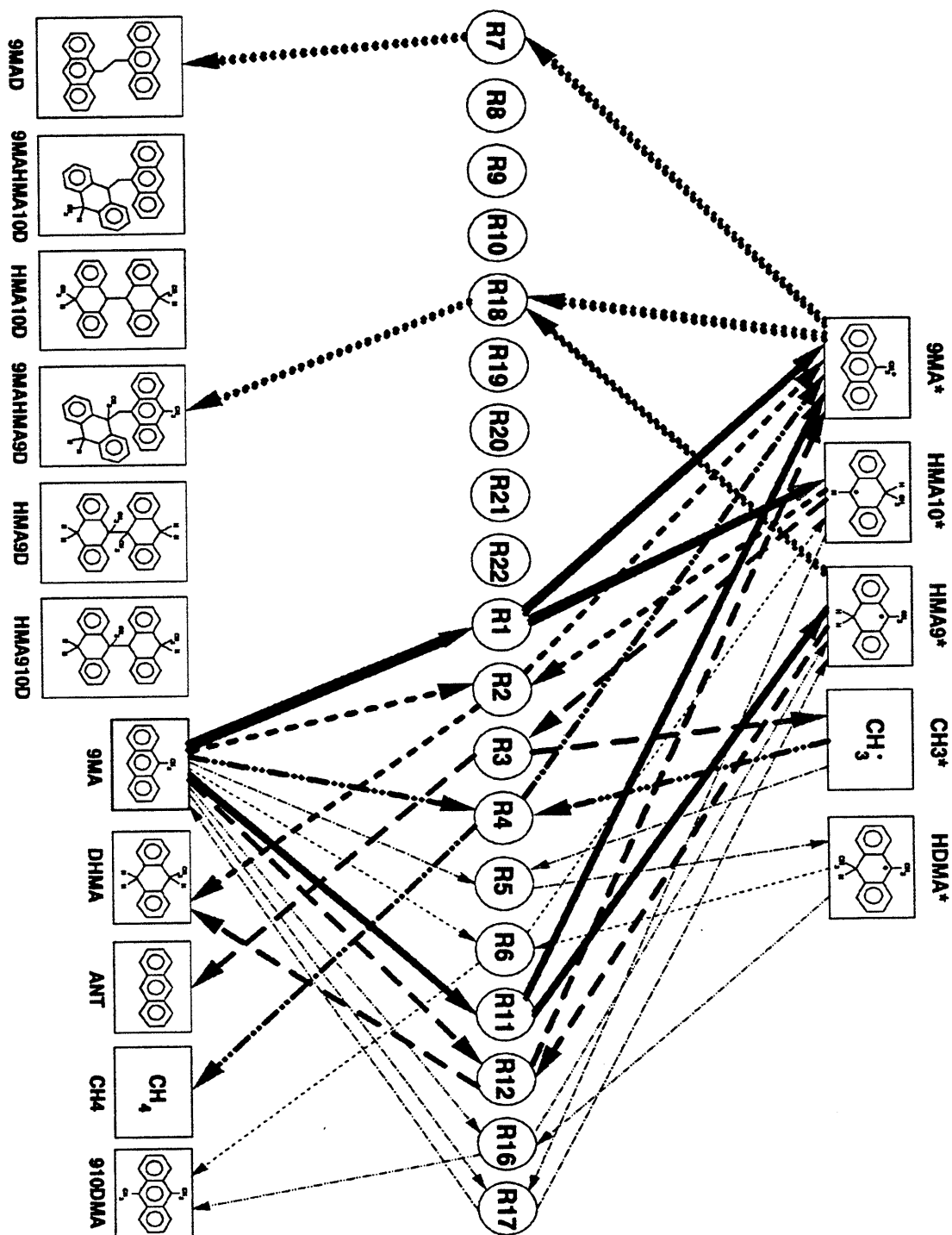
Figure 6.41: Relative elementary reaction rate traffic at T = 370°C and [9MA]₀ = 0.82 mol/l for X → 0.
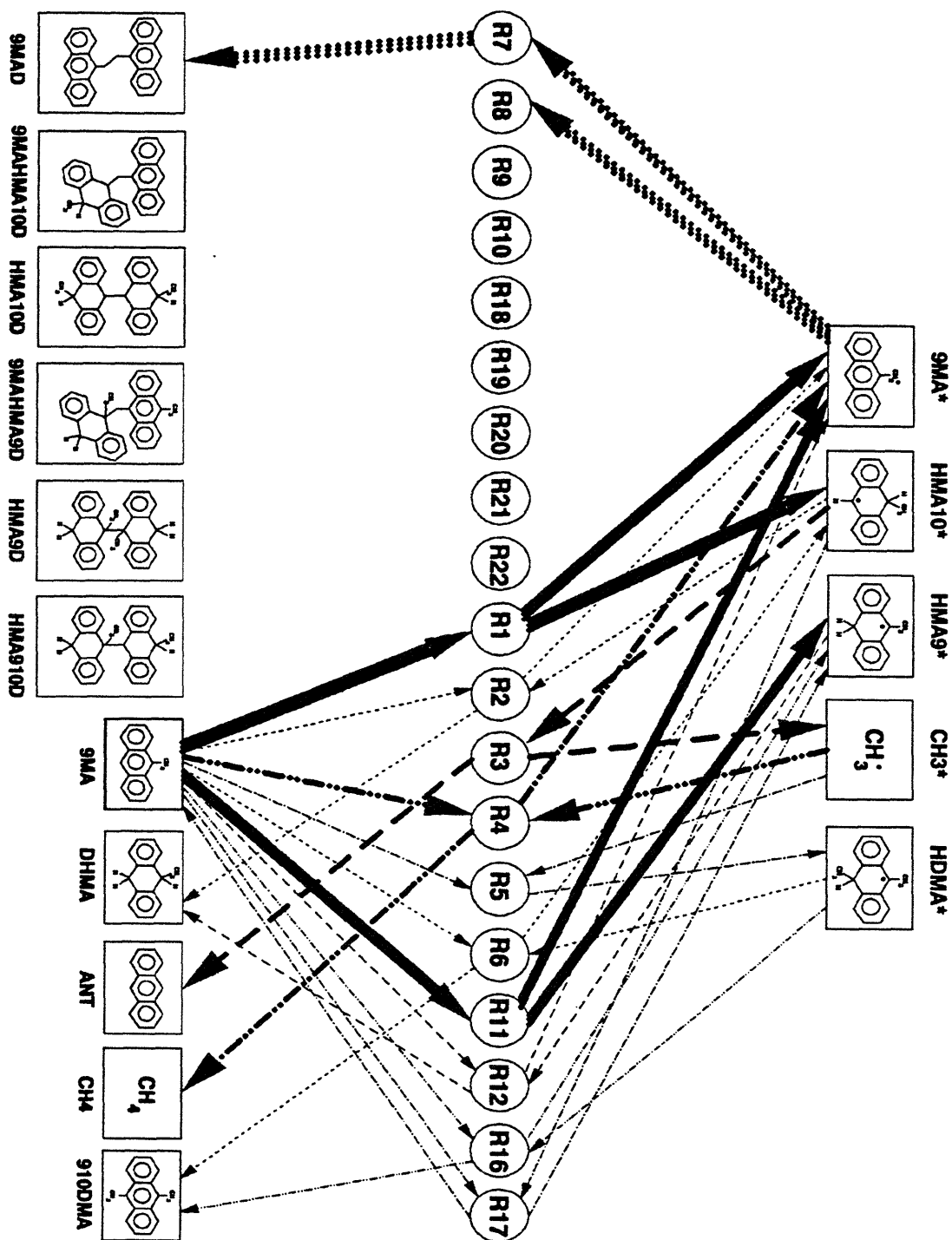
Figure 6.42: Relative elementary reaction rate traffic at T = 370°C and [9MA]$_o$ = 0.82 mol/l for X = 0.41.
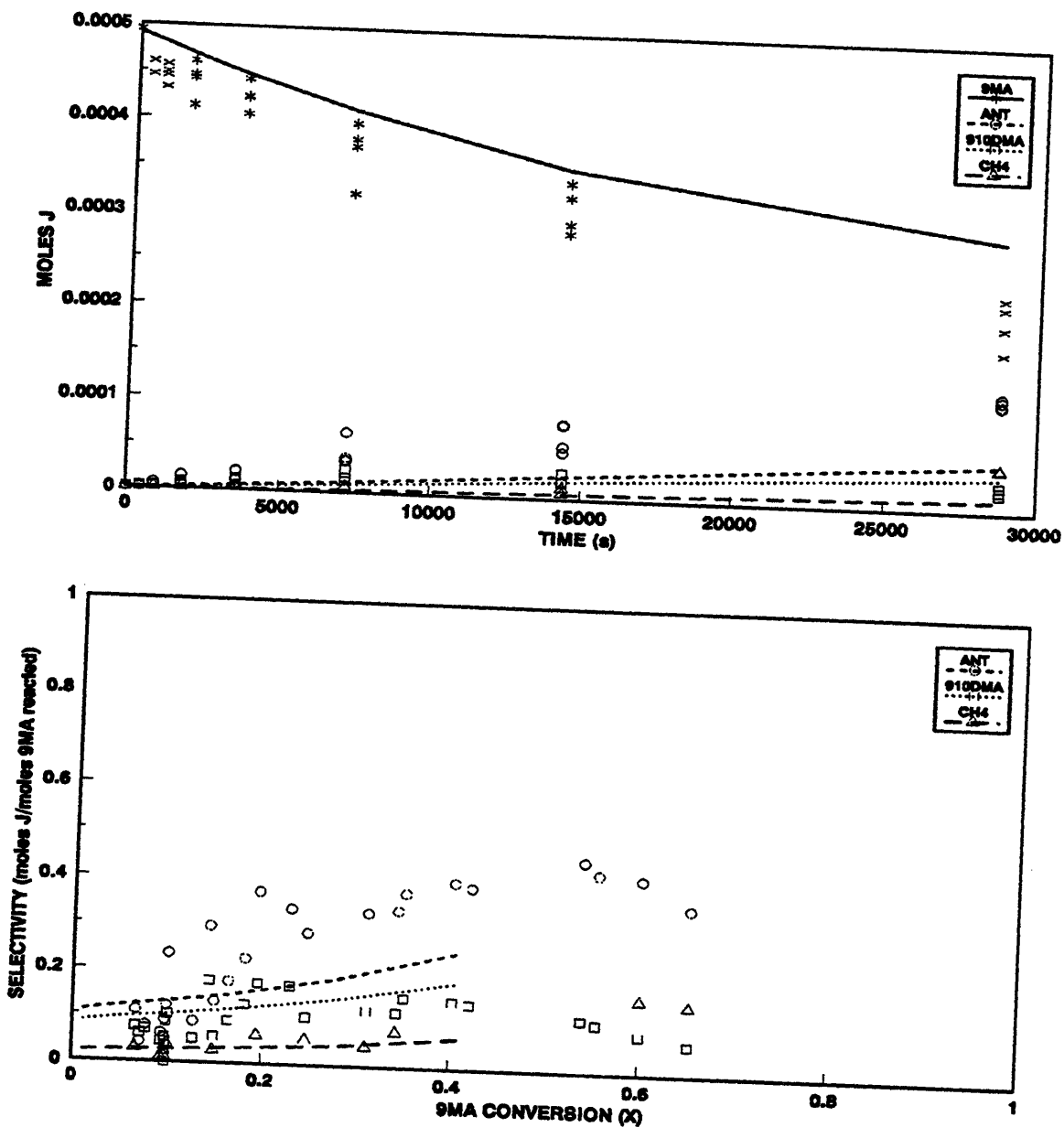
Figure 6.43: Product histories (top) and selectivity diagram (bottom) comparing model results (lines) to experimental data (symbols) for 9MA, ANT, 910DMA and CH4 at T = 370°C with $[9MA]_o$ = 0.82 mol/l.

lower panel of Figure 6.43 shows that the selectivities S(ANT) and S(910DMA) from the model are respectively 2.2 and 1.3-fold low compared to the average values of S(9MA) and S(TMA) observed from the experiments between $0.2 < X < 0.75$.

Figure 6.44 continues the comparison between model (solid line) and experimental (circles) product histories and selectivities for DHMA product. In the upper panel of this figure, the model is seen to predict DHMA amounts generally higher than experimentally observed, the more so at the longer times. In the lower panel of Figure 6.44, a selectivity diagram, we see that, relative to experiments, S(DHMA) from the model is 6.8-fold too high at low conversions, $X \sim 0.15$, and 10-fold too high for $X = 0.40$.

Figure 6.45 compares the model calculation (lines) to the experimental data (solid circles) for heavies (9MAD, 9MAHMA9D, 9MAHMA10D, HMA9D, HMA10D and HMA910D). Since these heavies were not specifically assayed, the moles of heavies produced in the experiments were calculated by subtracting the sum of the selectivities of detected species (Σ) from 1, multiplying this result by the concentration of 9MA converted and dividing by two since the heavies were essentially dimers of 9MA. In the upper panel of Figure 6.45, the model predicts heavies production comparable to the experiments at shorter times, but produces more dimer than seen in the experiments at long times. Also, the model predicts the dominant heavy dimer to be 9MAD, which was the only dimer detected in the experiments by GC/MS, in Figures 4.12 and 4.13. The lower panel of Figure 6.45
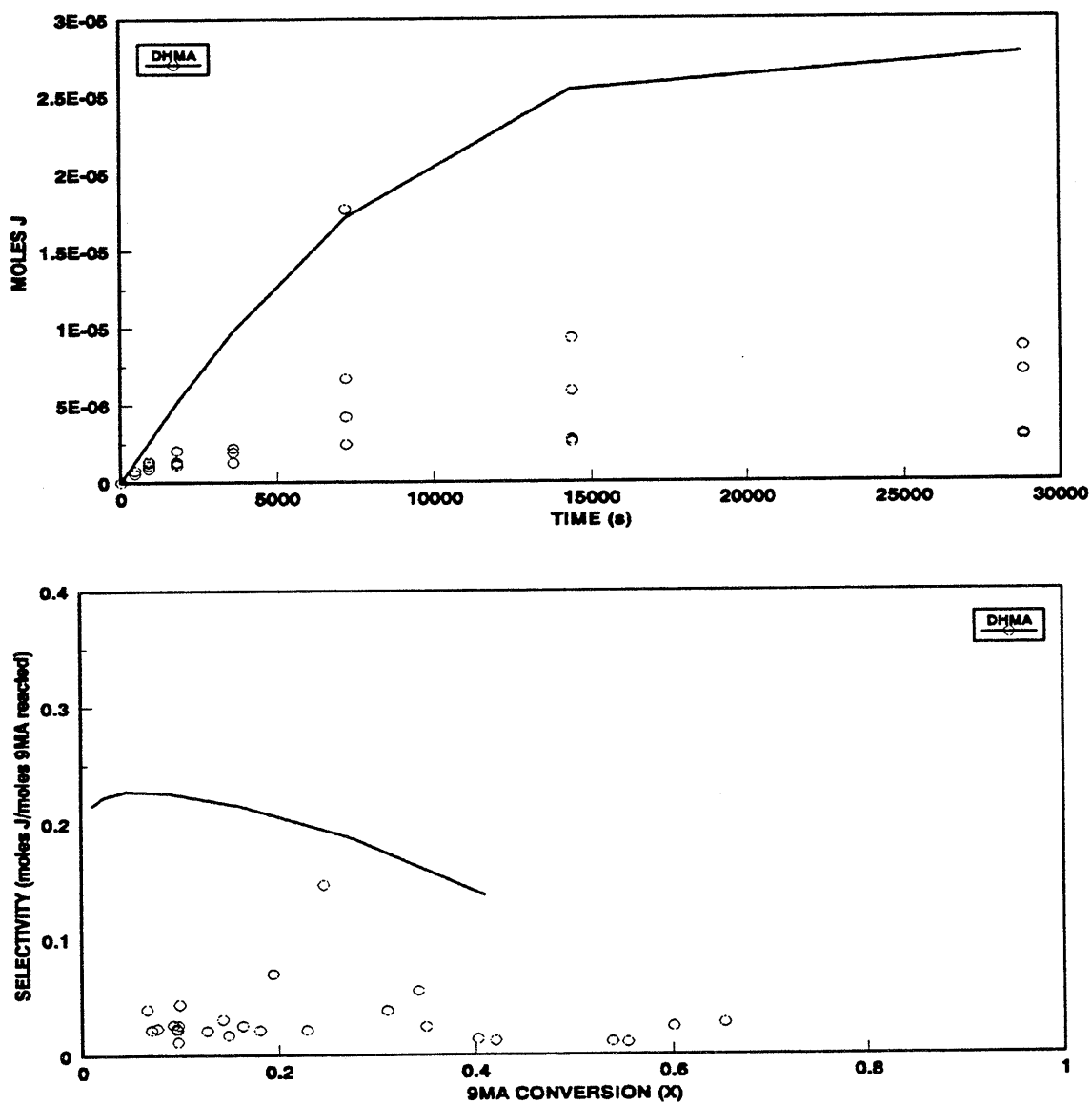
Figure 6.44: Product histories (top) and selectivity diagram (bottom) comparing model results (lines) to experimental data (symbols) for DHMA at T = 370°C with $[9MA]_o$ = 0.82 mol/l.
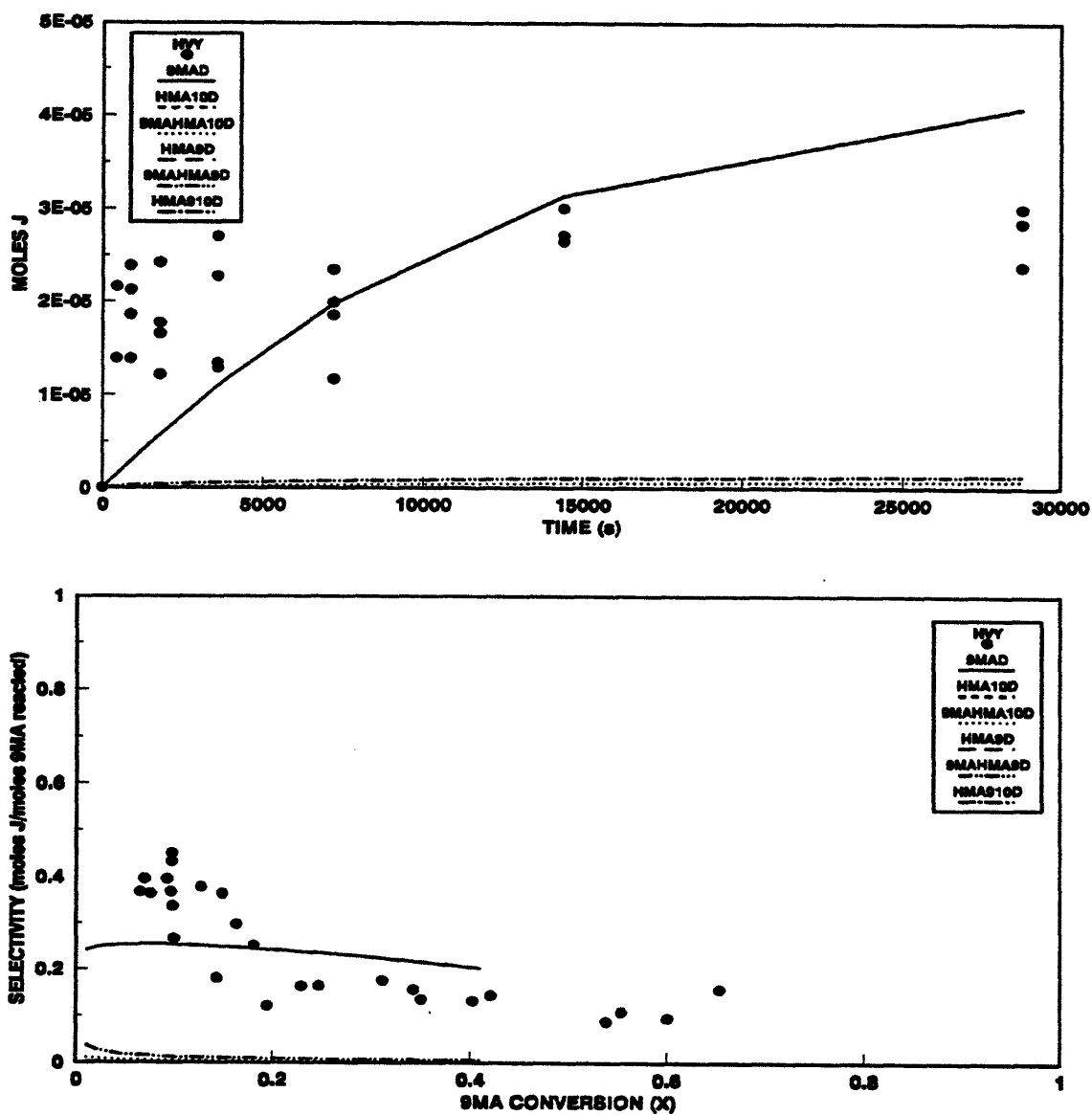
Figure 6.45: Product histories (top) and selectivity diagram (bottom) comparing model results (lines) to experimental data (symbols) for heavies at T = 370°C with $[9MA]_0$ = 0.82 mol/l.

541

shows that the dimer selectivity S(9MAD) ~ 0.20 calculated from the model is close

to the experimental S(HVY) ~ 0.40 at low X < 0.1, but whereas the S(HVY) in the

experiments decreases to ~ 0.15 with increasing conversion, S(9MAD) from the

model remains roughly constant at S(9MAD) ~ 0.20. For 0.2 < X < 0.75, S(9MAD)

is 1.7-fold higher than the experimental S(HVY).

Finally, Figure 6.46 compares the product ratios R[DHMA/ANT] and

R[910DMA/ANT] as functions of 9MA conversion (X) derived from the model

(lines) to those observed experimentally (symbols). In the upper panel of

Figure 6.46, the model is seen to predict R[DHMA/ANT] about 4.5-fold higher than

experimental at low conversions, X ~ 0.06, and almost 11-fold higher than

experimental for 0.2 < X < 0.75. In the lower panel of Figure 6.46 shows that the

R[910DMA/ANT] ~ 0.80 calculated from the model is close to the experimental

R[910DMA/ANT] ~ 0.90 at low X ~ 0.06, but whereas the R[910DMA/ANT] in

the experiments decreases to ~ 0.20 with increasing conversion, R[910DMA/ANT]

from the model remains roughly constant at R[910DMA/ANT] ~ 0.80.

6.4.5.2.2 Model Results at All T and [9MA]$_0$

Table 6.17 compares with experiments the 9MA decay half-life, major product

selectivities and product ratios obtained from numerical solutions of the 9MA

thermolysis model for varying initial concentrations at fixed T = 370°C, while

Table 6.18 compares experimental and model results for varying temperature at fixed
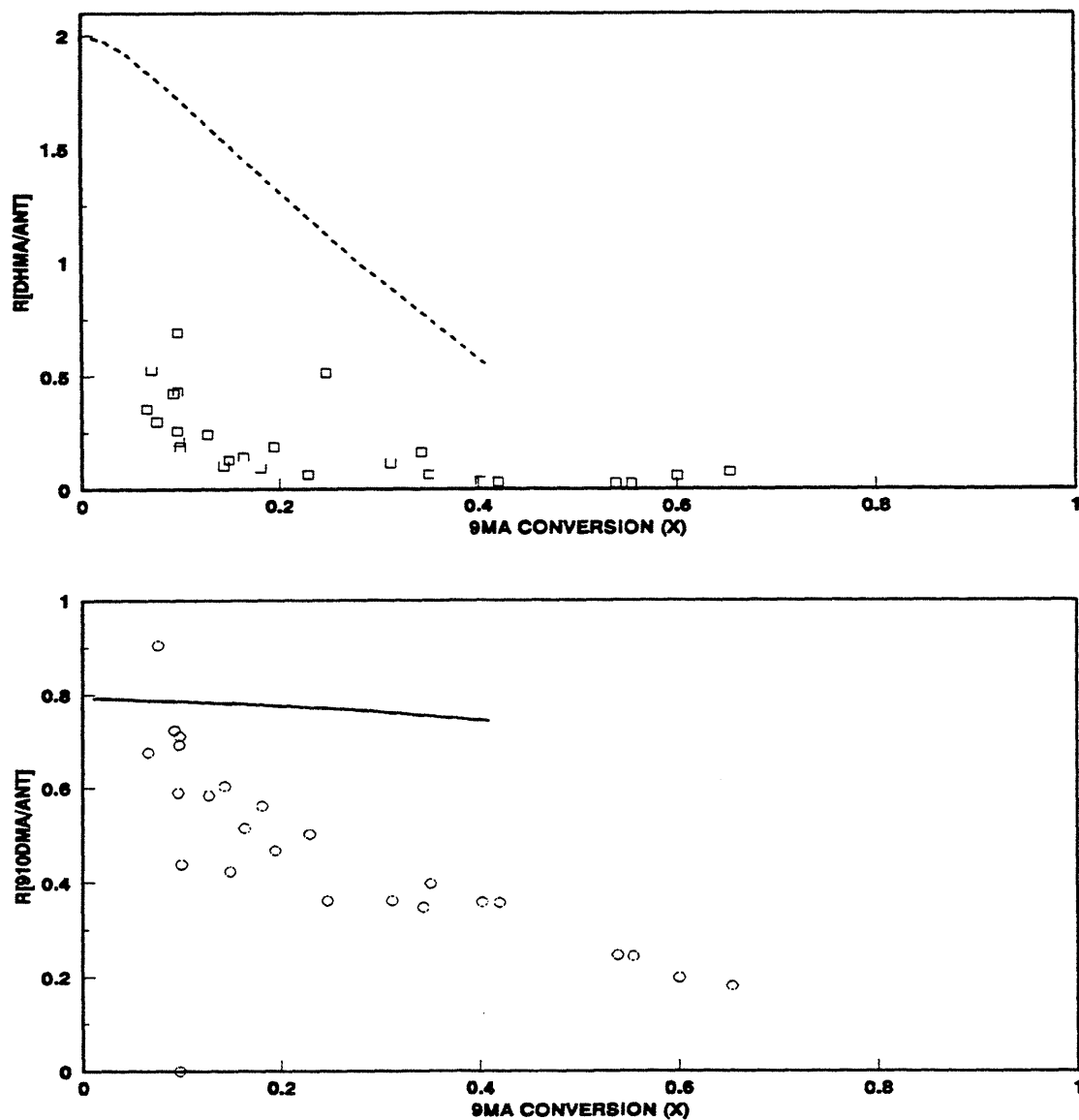
Figure 6.46: Ratio of moles DHMA to moles ANT produced vs. 9MA conversion (top) and ratio of moles 910DMA to moles ANT produced vs. 9MA conversion (bottom) at T = 370°C with $[9MA]_o$ = 0.82 mol/l.

Table 6.17

COMPARISON OF MODEL TO EXPERIMENTAL DATA FOR AT T = 370°C FOR VARYING [9MA]ₒ

Part	X·		[9MA]$_o$ (mol/l)		
			0.082[1]	0.82	2.06
a	Half-life	exp	70477	23430	12494
	t* (s)	mod	357738	38995	21101
		R[mod/exp]	5.08	1.66	1.69
b	S(ANT)	0.2-0.75	exp	0.41	0.37	0.37
		mod	0.24	0.17	0.089
		R[mod/exp]	0.59	0.46	0.24
	S(910DMA)	0.25 exp	0.13	0.17	0.16
		0.25 mod	0.081	0.13	0.077
		R[mod/exp]	0.62	0.76	0.48
c	S(DHMA)	0.15 exp	ND	0.031	0.054
		0.15 mod	0.11	0.21	0.25
		R[mod/exp]	-	6.77	4.63
		0.40 exp	ND	0.014	0.028
		0.40 mod	-	0.14	0.19
		R[mod/exp]	-	10.0	6.79
d	S(HVY)	0.2-0.75 exp	0.24	0.13	0.10
		mod	0.28	0.23	0.22
		R[mod/exp]	1.17	1.77	2.20
e	R[DHMA/ANT]	0.06 exp	ND	0.43	0.59
		0.06 mod	0.85	1.92	3.76
		R[mod/exp]	-	4.47	6.37
		0.2-0.75 exp	ND	0.051	0.051
		mod	0.47	0.55	0.51
		R[mod/exp]	-	10.8	10.0
f	R[910DMA/ANT]	0.06 exp	0.50	0.69	0.65
		0.06 mod	0.34	0.79	0.86
		R[mod/exp]	0.68	1.14	1.32
		0.40 exp	0.20	0.36	0.41
		0.40 mod	0.33	0.74	0.84
		R[mod/exp]	1.65	2.06	2.05

[1]   For [9MA]$_o$ = 0.082 mol/l, maximum X_{mod} = 0.12

Vikki J. Vlastnik

Table 6.18

COMPARISON OF MODEL TO EXPERIMENTAL DATA AT $[9MA]_0 = 0.82$ mol/l FOR VARYING TEMPERATURES

Part	X:		Temperature (°C) 315[1]	370	409
a	Half-life	exp	388859	23430	2827
	t^* (s)	mod	781530	38995	7914
		R[mod/exp]	2.01	1.66	2.80
b	S(ANT)	0.2-0.75	exp	ND	0.37	0.39
		mod	0.066	0.17	0.20
		R[mod/exp]	-	0.46	0.51
	S(910DMA)	0.25 exp	ND	0.17	0.15
		0.25 mod	0.059	0.13	0.12
		R[mod/exp]	-	0.76	0.80
c	S(DHMA)	0.15 exp	0.038	0.028	0.012
		0.15 mod	0.27	0.21	0.19
		R[mod/exp]	7.11	7.50	15.8
		0.40 exp	ND	0.018	0.007
		0.40 mod	-	0.14	0.09
		R[mod/exp]	-	7.78	12.9
d	S(HVY)	0.2-1.0 exp	ND	0.14	0.15
		mod	0.24	0.24	0.25
		R[mod/exp]	-	1.71	1.67
e	R[DHMA/ANT]	0.06 exp	ND	0.43	0.08
		0.06 mod	4.05	1.92	1.26
		R[mod/exp]	-	4.47	15.8
		0.2-1.0 exp	ND	0.047	0.047
		mod	-	0.55	0.031
		R[mod/exp]	-	11.7	0.66
f	R[910DMA/ANT]	0.06 exp	ND	0.69	0.65
		0.06 mod	0.90	0.79	0.66
		R[mod/exp]	-	1.14	1.02
		0.40 exp	ND	0.36	0.35
		0.40 mod	-	0.74	0.59
		R[mod/exp]	-	2.06	1.69

[1] For T = 315°C, maximum X_{mod} = 0.059

545

$[9MA]_o = 0.82$ mol/l.

In parts (a) of Table 6.17 and Table 6.18 in the corresponding Figure 6.47 and Figure 6.48, the model is seen to predict 9MA decay half-lifes t^* too long, that is, decay kinetics too slow, compared to the experimental observations at all initial concentrations and temperatures. From part (a) of Table 6.17, as $[9MA]_o$ increases for 0.082 to 2.06 mol/l at T = 370°C, the ratio of model to experimental half-lifes R[mod/exp] decreases from 5.1 to 1.7, indicating that the model decay of higher order in $[9MA]_o$ than experimental. Figure 6.47, a log-log plot of t^* vs. $[9MA]_o$, shows that the model (hollow points, dashed line) yields a slope of -0.89, implying ~ 2 order, versus the experimental (solid points, solid line) data that yield a slope of -0.50, implying 1½ order decomposition kinetics. From part (a) of Table 6.18, increasing temperature from 315 to 409°C increases the R[mod/exp] from 2.0 to 2.8, indicating that the model 9MA decay is slightly less activated than the experiments. This is also borne out by Figure 6.48, a semi-log plot of t^* vs. $1/\theta$, wherein the model (hollow points, dashed line) yields an activation energy of 39.1 mol/l versus the experimental (solid points, solid line) data that provided $E^* \sim 46.4$ kcal/mol. It should be noted that the vertical lines in both Figure 6.47 and Figure 6.48 represent results of a sensitivity analysis of the present 9MA thermolysis model at T = 370°C and $[9MA]_o = 0.82$ mol/l that are discussed in a subsequent section.

In parts (b) of Table 6.17 and Table 6.18 refer to the selectivities of ANT product for 0.2 < X < 0.75 and 910DMA product at X = 0.25. As initial
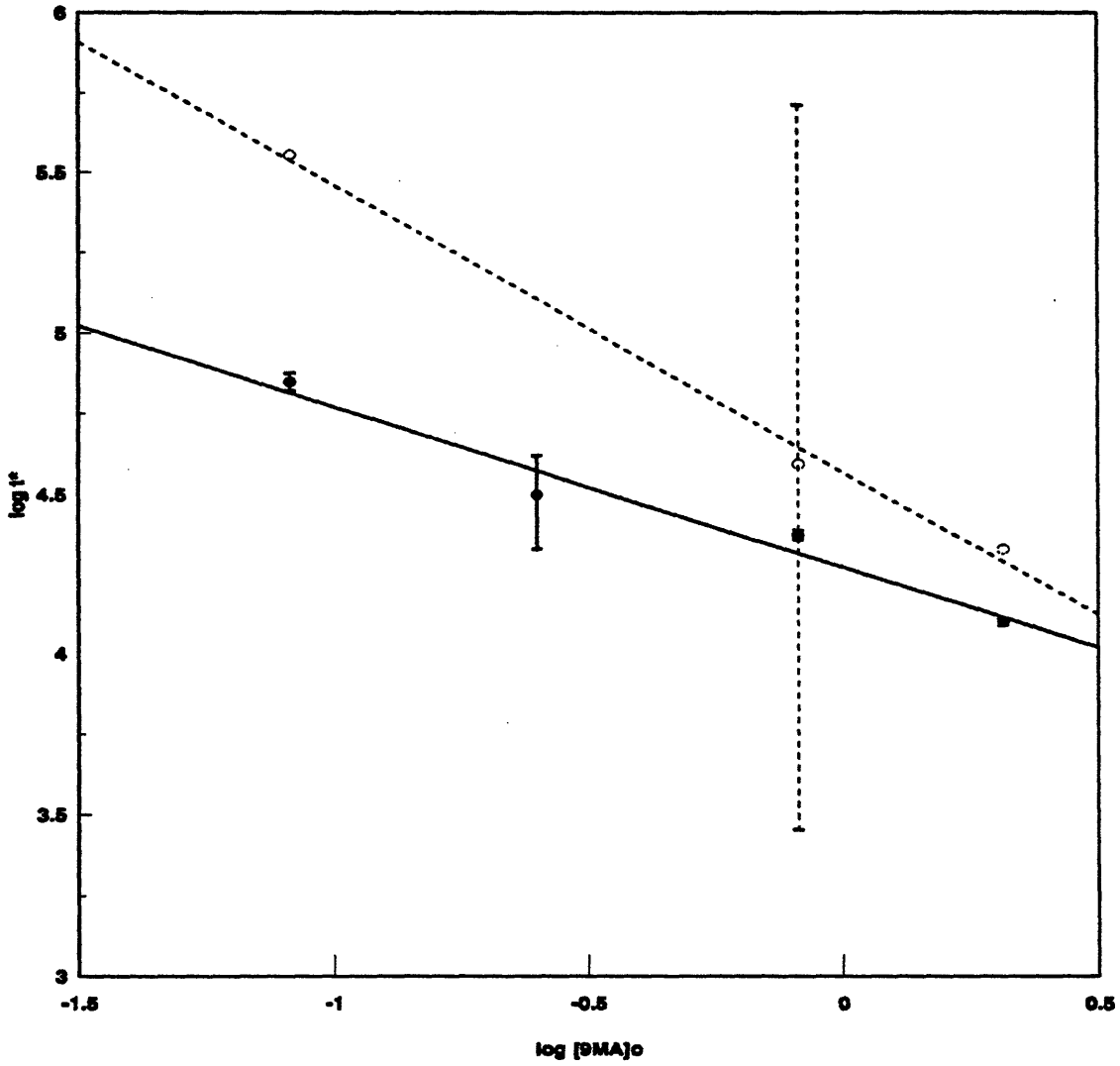
Figure 6.47: Decay half-life t^*_{exp} (solid line & symbols) and t^*_{mod} (dashed line, hollow symbols, vertical lines - error band from sensitivity analysis) at fixed T.
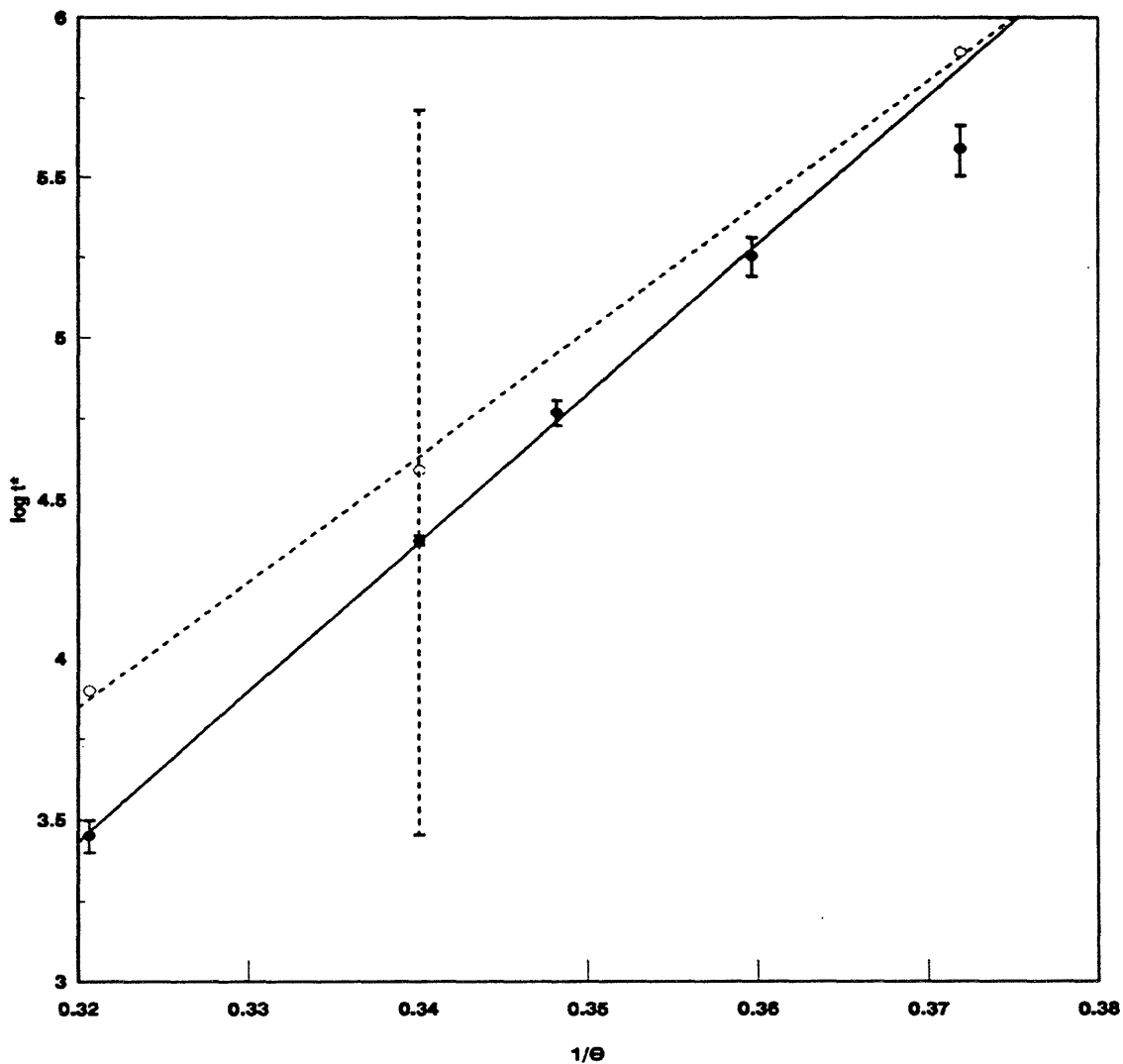
Figure 6.48: Decay half-life t^*_{exp} (solid line & symbols) and t^*_{mod} (dashed line, hollow symbols, vertical lines-error band from sensitivity analysis) with fixed $[9MA]_o$.

concentrations increase for 0.082 to 2.06 mol/l, model calculations show S(ANT) decreasing for 0.24 to 0.09 while S(910DMA) remains roughly constant at 0.10 ± 0.03. Both S(ANT) and S(910DMA) predicted by the model are lower than experimental, with respective ratios R[mod/exp] decreasing from 0.59 to 0.24 for ANT and remaining roughly constant at 0.62 ± 0.14 for 910DMA. With increasing temperatures from 315 to 409°C, the model calculations show S(ANT) increases from 0.07 to 0.20 while S(910DMA) increases from 0.06 to 0.12. Both S(ANT) and S(910DMA) from the model are lower than experimental, with the respective R[mod/exp] increasing slightly from 0.46 to 0.51 for ANT and increasing slightly from 0.76 to 0.80 for 910DMA. Figure 6.49 graphically depicts the results for S(ANT) on log-log coordinates of S(ANT) vs. [9MA]$_o$ (upper panel) and semi-log coordinates of S(9MA) vs. $1/\theta$ (lower panel). In the upper panel, it is seen that the model S(ANT) decreases more strongly, slope -0.28, than in the experiments, slope -0.03; thus the model exhibits an order for ANT formation that is less than that for 9MA decay by more than that observed experimentally. Also, in the lower panel of Figure 6.49, the model S(ANT) decreases more strongly with increasing $1/\theta$, that is decreasing temperature, slope -3.63, than in the experiments which show S(ANT) essentially independent of temperature, slope -1.18; thus the model predicts ANT formation to be more activated than 9MA decay by ~ 4 kcal/mol whereas the experiments show ANT formation to be more activated than 9MA decay by ~ 1 kcal/mol. The vertical

549
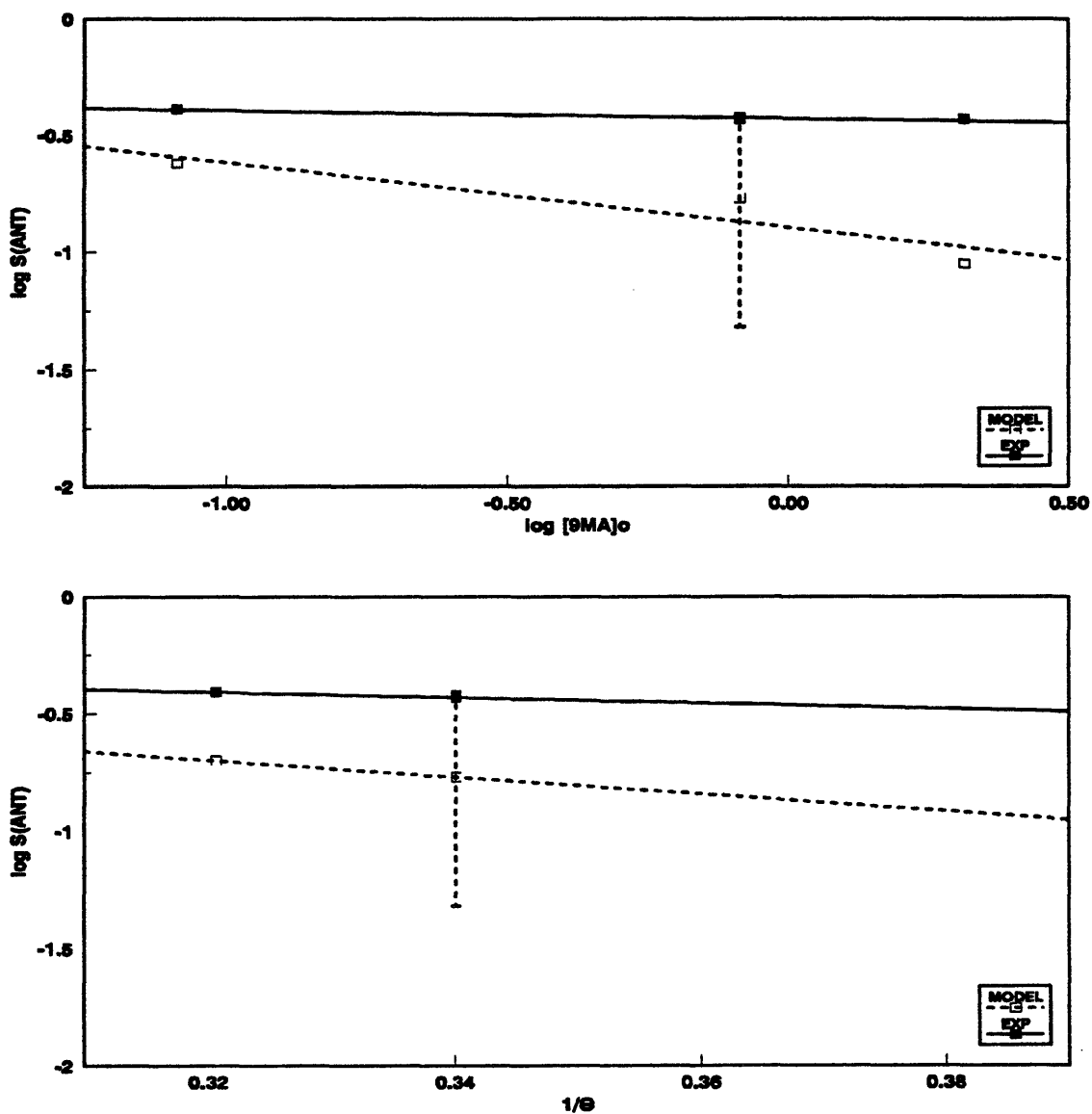
Figure 6.49: Comparison of experimental (solid squares) and model (squares) S(ANT) for varying $[9MA]_o$ at fixed $T = 370°C$ (top) and for varying T with fixed $[9MA]_o = 0.82$ mol/l.

dashed lines in both the upper and lower panels of Figure 6.49 are results of a sensitivity analysis discussed in a subsequent section.

In parts (c) of Table 6.17 and Table 6.18 show the selectivities of DHMA product, at both low (X ~ 0.15) and high (X = 0.40) conversions. At low conversions, in Table 6.17, as $[9MA]_o$ increases from 0.082 to 2.06 mol/l, S(DHMA) from the model increases from 0.11 to 0.25 with its ratio R[mod/exp] decreasing slightly from 6.8 at $[9MA]_o$ = 0.82 mol/l to 4.6 at $[9MA]_o$ = 2.06 mol/l (there were no reliable experimental values for S(DHMA) at $[9MA]_o$ = 0.082 mol/l); in Table 6.18, as temperature increases from 315 to 409°C, S(DHMA) from the model decreases from 0.27 to 0.19, with R[mod/exp] increasing from 7.1 to 15.8. Thus it is seen that, at low conversions, the DHMA selectivities predicted by the model are appreciably higher than those observed experimentally, with ratios of R[mod/exp] up to 16 at the higher T and lower $[9MA]_o$. At higher conversions, X = 0.40, in Table 6.17, as $[9MA]_o$ increases from 0.82 to 2.06 mol/l, S(DHMA) from the model increases from 0.14 to 0.19 with its ratio R[mod/exp] decreasing from 10.0 to 6.8 (there were no reliable experimental values for S(DHMA) at $[9MA]_o$ = 0.082 mol/l and the maximum X_{mod} = 0.12); in Table 6.18, as T increases from 315 to 409°C, S(DHMA) from the model decreases from 0.14 to 0.09, with R[mod/exp] increasing from 7.8 to 12.9 (there were no reliable experimental values for S(DHMA) at T = 315°C and the maximum X_{mod} = 0.06). Thus it is seen that, at high conversions, the DHMA selectivities predicted by the model are appreciably higher than those

observed experimentally, with ratios of R[mod/exp] up to 12 at the higher T and lower $[9MA]_o$.

In parts (d) of Table 6.17 and Table 6.18 refer to the selectivities of heavy products (sum of 9MAD, 9MAHMA10D, 9MAHMA9D, HMA9D, HMA10D and HMA910D) for 0.2 < X < 0.75. As initial concentrations increase from 0.082 to 2.06 mol/l, model calculations show S(HVY) decreasing from 0.28 to 0.22. S(HVY) predicted by the model are higher then experimental, with respective ratios R[mod/exp] increasing from 1.2 to 2.2. With increasing temperatures from 315 to 409°C, the model calculations show S(HVY) remaining roughly constant at 0.24. S(HVY) from the model are higher than experimental, with ratios R[mod/exp] remaining roughly constant at 1.7 for T = 370 and 409°C. Thus it is seen that the HVY selectivities predicted by the model are higher than those observed experimentally; from the ratios R[mod/exp], the dependence of S(HVY) on $[9MA]_o$ predicted by the model exceeds that observed experimentally, more so at higher $[9MA]_o$. While the dependence of S(HVY) is essentially the same as experimental for all T.

In parts (e) of Table 6.17 and Table 6.18 show the ratio of DHMA product to ANT product, at both low (X ~ 0.06) and high (0.2 < X < 0.75) conversions. At low conversions, in Table 6.17, as $[9MA]_o$ increases from 0.082 to 2.06 mol/l, R[DHMA/ANT] from the model increases from 0.85 to 3.8 with its ratio R[mod/exp] increasing from 4.5 at $[9MA]_o$ = 9.82 mol/l to 6.4 at $[9MA]_o$ = 2.06

mol/l (there were no reliable experimental values for DHMA at $[9MA]_o$ = 0.082

mol/l); in Table 6.18, as T increases from 315 to 409°C, R[DHMA/ANT] decreases

from 4.1 to 1.3, with R[mod/exp] increasing from 4.5 at T = 370°C to 15.8 at T =

409°C (there were no reliable experimental values for DHMA at T = 315°C). Thus

it is seen that, at low conversions, the R[DHMA/ANT] predicted by the model are

higher than those observed experimentally, with ratios R[mod/exp] up to 6 at the

higher $[9MA]_o$ and up to 16 at the higher T. At high conversions, in Table 6.17, as

$[9MA]_o$ increases from 0.082 to 2.06 mol/l, R[DHMA/ANT] from the model remains

roughly constant at 0.51 ± 0.04, with its ratio R[mod/exp] remaining roughly constant

at 10.4 ± 0.4 for $[9MA]_o$ = 0.82 and 2.06 mol/l (there were no reliable experimental

values for DHMA at $[9MA]_o$ = 0.082 mol/l); in Table 6.18, as T increases from 370

to 409°C, R[DHMA/ANT] from the model decreases from 0.55 to 0.031, with

R[mod/exp] decreasing from 12 to 0.7. Thus it is seen that, at high conversions, the

R[DHMA/ANT] predicted by the model are appreciably higher than those observed

experimentally, with ratios R[mod/exp] up to 11 at the higher $[9MA]_o$ and up to 12

at the lower T. Figure 6.50 graphically depicts the results for R[DHMA/ANT] on

log-log coordinates of R[DHMA/ANT] versus $[9MA]_o$ (upper panel) and semi-log

coordinates of R[DHMA/ANT] versus 1/θ (lower panel). In the upper panel, it is

seen that, at low conversions, the model R[DHMA/ANT] increases more strongly,

slope 0.44, than in the experiments, slope 0.34; thus the model exhibits an order for

DHMA formation that is slightly higher than that for ANT formation by more than
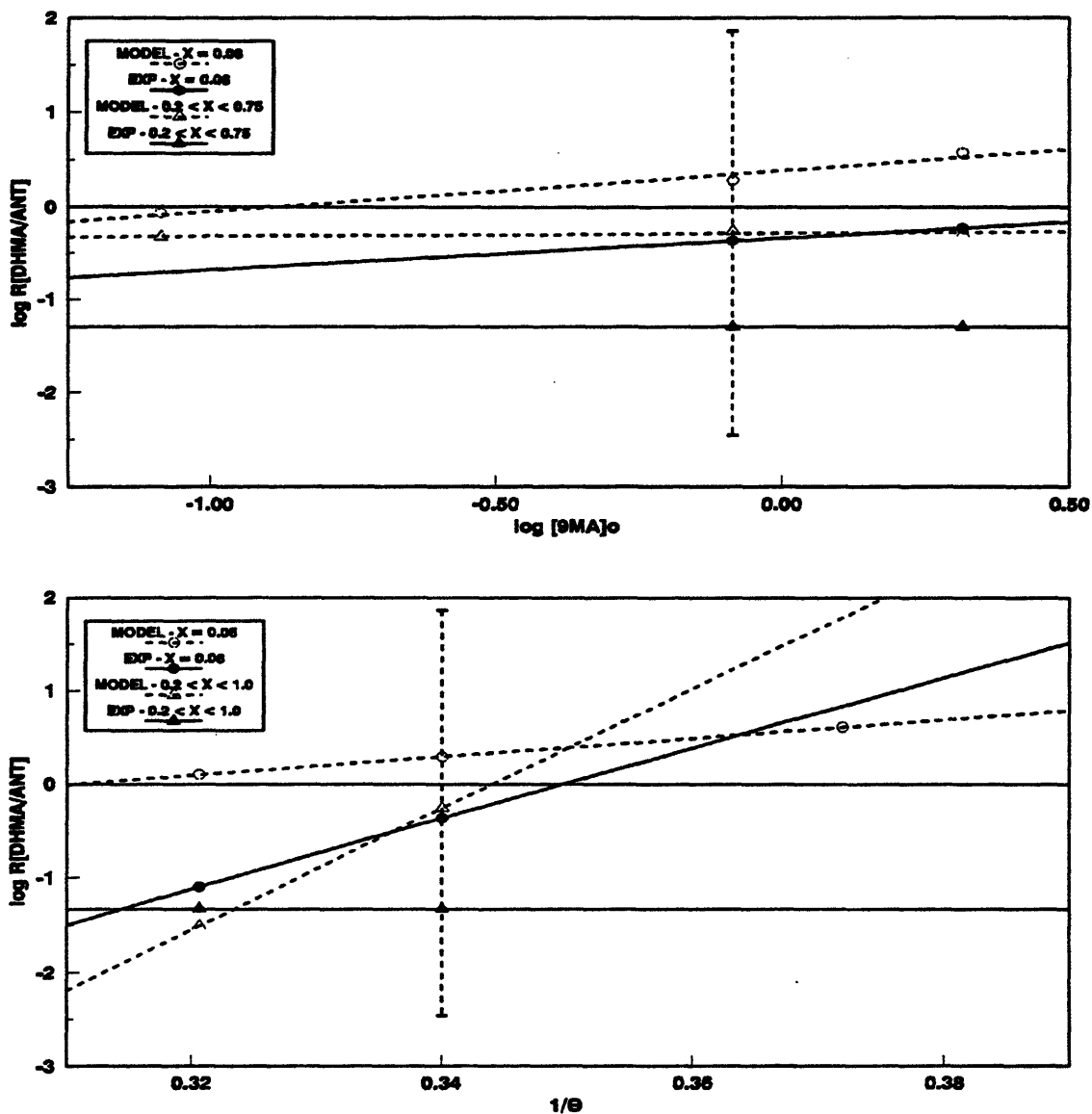
Figure 6.50: Comparison of experiment (solid symbols) and model (hollow symbols) R[DHMA/ANT] for varying [9MA]$_o$ at fixed T = 370°C (top) and for varying T with fixed [9MA]$_o$ = 0.82 mol/l.

observed experimentally. At high conversions, the model R[DHMA/ANT] increases more strongly, slope 0.03, than in the experiments which show R[DHMA/ANT] essentially independent of initial concentration, slope 0; thus the model exhibits an order for DHMA formation that is slightly higher than that for ANT formation whereas the experiments show both DHMA and ANT formation to be approximately the same order. Also, in the lower panel of Figure 6.50, at low conversions, the model R[DHMA/ANT] increases more weakly with increasing $1/\theta$, that is decreasing temperature, slope 9.9, than in the experiments, slope 38; thus the model predicts ANT formation to be more activated than DHMA formation by $\sim$ 10 kcal/mol whereas the experiments show ANT formation to be more activated than DHMA formation by $\sim$ 40 kcal/mol. At high conversions, the model R[DHMA/ANT] increases more strongly, slope 64, than in the experiments which show R[DHMA/ANT] essentially independent of initial concentration, slope 0. The vertical dashed lines in both upper and lower panels of Figure 6.50 are results of a sensitivity analysis discussed in a subsequent section.

Finally, in parts (f) of Table 6.16 and Table 6.17 show the ratio of 910DMA product to ANT product, at both low (X $\sim$ 0.06) and high (X = 0.40) conversions. At low conversions, in Table 6.16, as $[9MA]_o$ increases from 0.082 to 2.06 mol/l, R[910DMA/ANT] from the model increases from 0.34 to 0.86 with its ratio R[mod/exp] increasing from 0.68 to 1.32; in Table 6.17, as T increases from 315 to 409°C, R[910DMA/ANT] decreases from 0.90 to 0.66, with R[mod/exp] remaining

roughly constant at 1.08 ± 0.06 for T = 370 and 409°C (there were no reliable experimental values for 910DMA at T = 315°C). Thus it is seen that, at low conversions, the R[910DMA/ANT] predicted by the model are approximately equal to those observed experimentally, with ratios R[mod/exp] of 1.0 ± 0.3 at all [9MA]$_o$ and approximately 1.1 at all T. At high conversions, in Table 6.16, as [9MA]$_o$ increases from 0.082 to 2.06 mol/l, R[910DMA/ANT] from the model increases from 0.33 to 0.84 with its ratio R[mod/exp] remaining roughly constant at 1.85 ± 0.20; in Table 6.17, as T increases from 370 to 409°C, R[910DMA/ANT] from the model decreases from 0.74 to 0.59 with R[mod/exp] remaining roughly constant at 1.9 ± 0.2 for T = 370 and 409°C (there were no reliable experimental values for 910DMA at T = 315°C). Thus it is seen that, at high conversions, the R[910DMA/ANT] predicted by the model are higher than those observed experimentally, with ratios R[mod/exp] of approximately 1.9 at all [9MA]$_o$ and T. Figure 6.51 graphically depicts the results for R[910DMA/ANT] on log-log coordinates of R[910DMA/ANT] versus [9MA]$_o$ (upper panel) and semi-log coordinates of R[910DMA/ANT] versus 1/θ (lower panel). In the upper panel, it is seen that, at low conversions, the model R[910DMA/ANT] increases more strongly, slope 0.30, than in the experiments which show R[910DMA/ANT] essentially independent of initial concentration, slope 0.09; thus the model exhibits 910DMA formation that is greater than that for ANT formation by more than that observed experimentally. At high conversions, the model R[910DMA/ANT] increases more strongly, slope 0.30, than in the
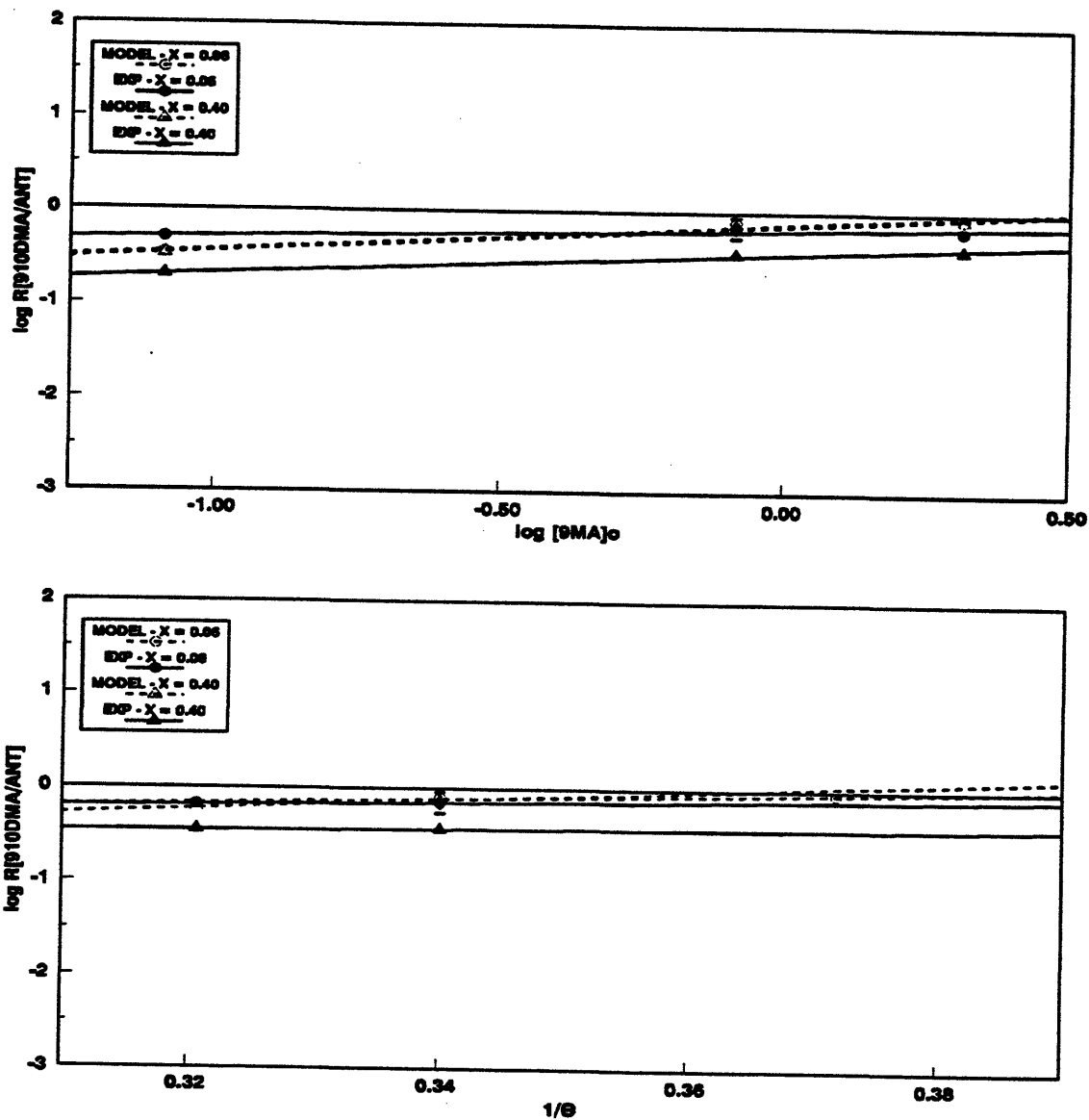
Figure 6.51: Comparison of experimental (solid symbols) and model (hollow symbols) R[910DMA/ANT] for varying [9MA]$_o$ at fixed T (top) and for varying T with fixed [9MA]$_o$ (bottom).

experiments, slope 0.23; thus the model exhibits 910DMA formation that is greater than that for ANT formation by more than that observed experimentally. Also, in the lower panel of Figure 6.51, at low conversions, the model R[910DMA/ANT] increases more strongly with increasing $1/\theta$, that is decreasing temperature, slope 2.5, than in the experiments, slope 1.3; thus the model predicts ANT formation to be more activated than 910DMA formation by $\sim$ 2.5 kcal/mol whereas the experiments show ANT formation to be more activated than 910DMA formation by $\sim$ 1 kcal/mol. At high conversions, the model R[910DMA/ANT] increases more strongly, slope 5,1, than in the experiments, slope 0.6. The vertical dashed lines in both upper and lower panels of Figure 6.51 are results of a sensitivity analysis discussed in a subsequent section.

6.4.5.3 Sensitivity Analysis

The sensitivity of our 9MA thermolysis model was analyzed at the central point of the 9MA experimental grid, T = 370°C and $[9MA]_0$ = 0.82 mol/l, by separately perturbing the kinetics of selected elementary steps over their estimated uncertainty limits. From Table 6.7 and Table 6.8, the inherent errors in ΔH°_f are between 0.5 - 3 kcal/mol for stable species and 2 - 4 kcal/mol for radicals. These errors in ΔH°_f translate into errors of $\pm$ 2 - 4 kcal/mol for ΔH°_r which propagate through Evans-Polanyi relations of Table 6.10 and Table 6.11 into errors of $\pm$ 2 - 5 kcal/mol for E^*; when coupled with a $\theta \sim$ 3, which corresponds to the temperatures

558

of the experiments, these lead to errors of $\pm$ 0.7 - 1.3 in $\log_{10}$ k. The errors in the $\log_{10}$ A estimates are, at most, $\pm$ 0.5, which translate directly to errors of $\pm$ 0.5 in $\log_{10}$ k. Thus, in general, the calculated rate constants of the elementary steps are beset more by errors in their E^* than in their $\log_{10}$ A. For this reason, the sensitivity analysis was performed by separately perturbing the E^* of selected elementary reactions over the inherent errors in their ΔH°_r to show their effects on 9MA half-life t^*, ANT selectivity S(ANT), and the primary product ratios R[DHMA/ANT] and R[910DMA/9MA]. Results of the sensitivity analysis are summarized in Table 6.19.

In our 9MA thermolysis model, the destruction of substrate is affected by numerous elementary steps, of which, as shown in Table 6.13, Table 6.14, Table 6.15 and Table 6.16, R1 and R11 are the most important at both low and high conversions. The sensitivity of 9MA half-life, t^*, was thus examined by perturbing E^*_1, the activation energy of R1, by $\pm$ 3.4 kcal/mol, and E^*_{11}, the activation energy of R11, by $\pm$ 4.0 kcal/mol, which are the inherent error in ΔH°_{R1} and ΔH°_{R11}, using the Evans-Polanyi relations $E^*_1 = \Delta H^\circ_{R1}$ and $E^*_{11} = \Delta H^\circ_{R11}$. Results of t^* sensitivity to the preceding perturbations are given in the last 3 columns of rows 1 - 2 in Table 6.19 and were graphically depicted by the vertical dashed lines in Figure 6.47 and Figure 6.48. Two noteworthy conclusions arise from perusal of the results. First, the variation in t^*_{mod} on account of the inherent errors in the estimated rate constants is large enough to exceed the span of t^*_{exp} variations by changes in [9MA]$_o$ and T.

Table 6.19

RESULTS OF SENSITIVITY ANALYSIS AT
$T = 370°C$ AND $[9MA]_o = 0.82$ mol/l

Parameter	Dominant Reaction(s)	Inherent Error in $\Delta H°_r$ (kcal/mol)	Perturbation in E^* (kcal/mol)	Results +Perturbation	0	-Perturbation
9MA half-life, t*	R1	± 3.4	± 3.4	+R1, +R11		-R1, -R11
	R11	± 4.0	± 4.0	512586	21883	2836
Selectivity to	R3	± 2.4	± 2.4	+R3, -R17		-R3, +R17
ANT, S(ANT)	R17	± 3.9	± 1.95	0.01	0.17	0.30
Ratio of moles of	R2	± 3.5	± 1.75	+R2, +R12 +R3, -R17		-R2, -R12 +R3, -R17
DHMA to moles	R12	± 4.1	± 2.05	9.7^1, 1.3^2	1.9^1,	73, 29
of ANT produced,	R3	± 2.4	± 2.4	+R2, +R12 -R3, +R17	0.55^2	-R2, -R12 -R3, +R17
R[DHMA/ANT]	R17	± 3.9	± 1.95	0.08, 0.004		1.4, 0.84
Ratio of moles of 910DMA to moles	R4	± 2.5	± 1.25	0.90^3,	0.79^3,	0.60,
of ANT produced,	R5		0	0.87^4	0.74^4	0.54
R[910DMA/ANT]						

[1] R[DHMA/ANT] at X = 0.06

[2] R[DHMA/ANT] at X > 0.20

[3] R[910DMA/ANT] at X = 0.06

[2] R[910DMA/ANT] at X = 0.40

Second, at $T = 370°C$ and $[9MA]_o = 0.82$ mol/l, the 1.7-fold difference between t^*_{mod} and t^*_{exp} is well within the 180-fold uncertainty in t^*_{mod}.

The formation of ANT is most affected by R3 and R17 the most at both low and high conversions. The sensitivity of selectivity to ANT, S(ANT), was thus examined by perturbing E^*_3, the activation energy of R3, by $\pm$ 2.4 kcal/mol and E^*_{17}, the activation energy of R17, by $\pm$ 1.95 kcal/mol, which are the respective inherent errors in $\Delta H°_{R3}$ and $\Delta H°_{R17}$, using the respective Evans-Polanyi relations $E^*_3 = 2.1 + \Delta H°_{R3}$ and $E^*_{17} = 17.5 + \Delta H°_{R17}/2$. Results of S(ANT) sensitivity to the preceding perturbations are given in the last 3 columns of rows 3 - 4 in Table 6.19 and were graphically depicted by the vertical dashed lines in Figure 6.49. Two noteworthy conclusions arise from perusal of the results. First, the variation in S(ANT) on account of the inherent errors in the estimated rate constants is large enough to exceed the span of $S(ANT)_{exp}$ variations by changes in $[9MA]_o$ and T, even though the mechanism limits S(ANT) to 0.33. Second, at $T = 370°C$ and $[9MA]_o = 0.82$ mol/l, the 2.2-fold difference between $S(ANT)_{mod}$ and $S(ANT)_{exp}$ is well within the 30-fold uncertainty in $S(ANT)_{mod}$.

The formation of DHMA and ANT are affected by R2, R12, R3 and R17 at both low and high conversions. The sensitivity of the ratio of moles of DHMA to moles of ANT produced, R[DHMA/ANT], was thus examined by perturbing E^*_2, E^*_{12}, E^*_3 and E^*_{17}, the activation energy of R2, R12, R3 and R17, by $\pm$ 1.75, $\pm$ 2.05, $\pm$ 2.4 and $\pm$ 1.95 kcal/mol respectively, which are the inherent errors in $\Delta H°_{R2}/2$,

$\Delta H^{\circ}_{R12}/2$, ΔH°_{R3} and $\Delta H^{\circ}_{R17}/2$, using the respective Evans-Polanyi relations $E^{*}_{2} = 17.5 + \Delta H^{\circ}_{R2}/2$, $E^{*}_{12} = 17.5 + \Delta H^{\circ}_{R12}/2$, $E^{*}_{3} = 2.1 + \Delta H^{\circ}_{R3}$ and $E^{*}_{17} = 17.5 + \Delta H^{\circ}_{R17}/2$. Results of R[DHMA/ANT] sensitivity to the preceding perturbations are given in the last 3 columns of rows 5 - 9 in Table 6.19 and were graphically depicted by the vertical dashed lines in Figure 6.50. Two noteworthy conclusions arise from perusal of the results. First, the variation in R[DHMA/ANT] on account of the inherent errors in the estimated rate constants is large enough to exceed the span of R[DHMA/ANT]$_{exp}$ variations by changes in [9MA]$_{o}$ and T. Second, at T = 370°C and [9MA]$_{o}$ = 0.82 mol/l, the 12-fold difference between R[DHMA/ANT]$_{mod}$ and R[DHMA/ANT]$_{exp}$ is well within the 21000-fold uncertainty in R[DHMA/ANT]$_{mod}$.

The sensitivity of 910DMA and ANT are affected by R4 and R15 at both low and high conversions. The sensitivity of the ratio of moles of 910DMA to moles of ANT produced, R[910DMA/ANT], was thus examined by perturbing E^{*}_{4} and E^{*}_{5}, the activation energy of R4 and R5, by ± 1.65 and 0 kcal/mol respectively, which are the inherent errors in $\Delta H^{\circ}_{R4}/2$ and ΔH°_{R5}, using the respective Evans-Polanyi relations $E^{*}_{4} = 17.5 + \Delta H^{\circ}_{R4}/2$ and $E^{*}_{5} = 2.1$. Results of R[910DMA/ANT] sensitivity to the preceding perturbations are given in the last 3 columns of rows 10 - 14 in Table 6.19 and were graphically depicted by the vertical dashed lines in Figure 6.51. Two noteworthy conclusions arise from perusal of the results. First, the variation in R[910DMA/ANT] on account of the inherent errors in the estimated rate constants is large enough to exceed the span of R[910DMA/ANT]$_{exp}$ variations by changes in

$[9MA]_o$ and T. Second, at T = 370°C and $[9MA]_o$ = 0.82 mol/l, the 2-fold difference between $R[910DMA/ANT]_{mod}$ and $R[910DMA/ANT]_{exp}$ is well within the 1.7-fold uncertainty in $R[910DMA/ANT]_{mod}$.

6.4.5.4 Optimized Model

The preceding comparisons between model and experimental results, along with the sensitivity analysis, permitted the deviation of optimized parameters for the model of 9MA thermolysis, to best-fit experimental data at $[9MA]_o$ = 0.82 mol/l and T = 370°C. The best-fit arose from subtracting 0.4 kcal/mol from E^* in R1, adding 2.2 kcal/mol to E^* in R2, subtracting 2.2 kcal/mol from E^* in R-2, subtracting 1.5 kcal/mol from E^* in R3, subtracting 0.4 kcal/mol from E^* in R11, adding 2.2 kcal/mol to E^* in R12, subtracting 2.2 kcal/mol from E^* in R-12, adding 2.0 kcal/mol to E^* in R17 and subtracting 2.0 kcal/mol from E^* in R17. It can be verified by reference to Table 6.19 that all of those adjustments to the E^* were within their inherent error-limits. Figure 6.52 compares the substrate and product histories (upper panel) and product selectivities (lower panel) as obtained from the numerical solution to the thermolysis model to the experimental data for 9MA, ANT, 910DMA and CH4 at the center of the experimental grid, $[9MA]_o$ = 0.82 mol/l and T = 370°C. In the upper panel of Figure 6.52, the model is seen to predict 9MA decay, the solid line, within the experimental observations, shown as asterisks. The t^*_{mod} = 21883 s whereas the t^*_{exp} = 23430 s. The upper panel of Figure 6.52 also shows that
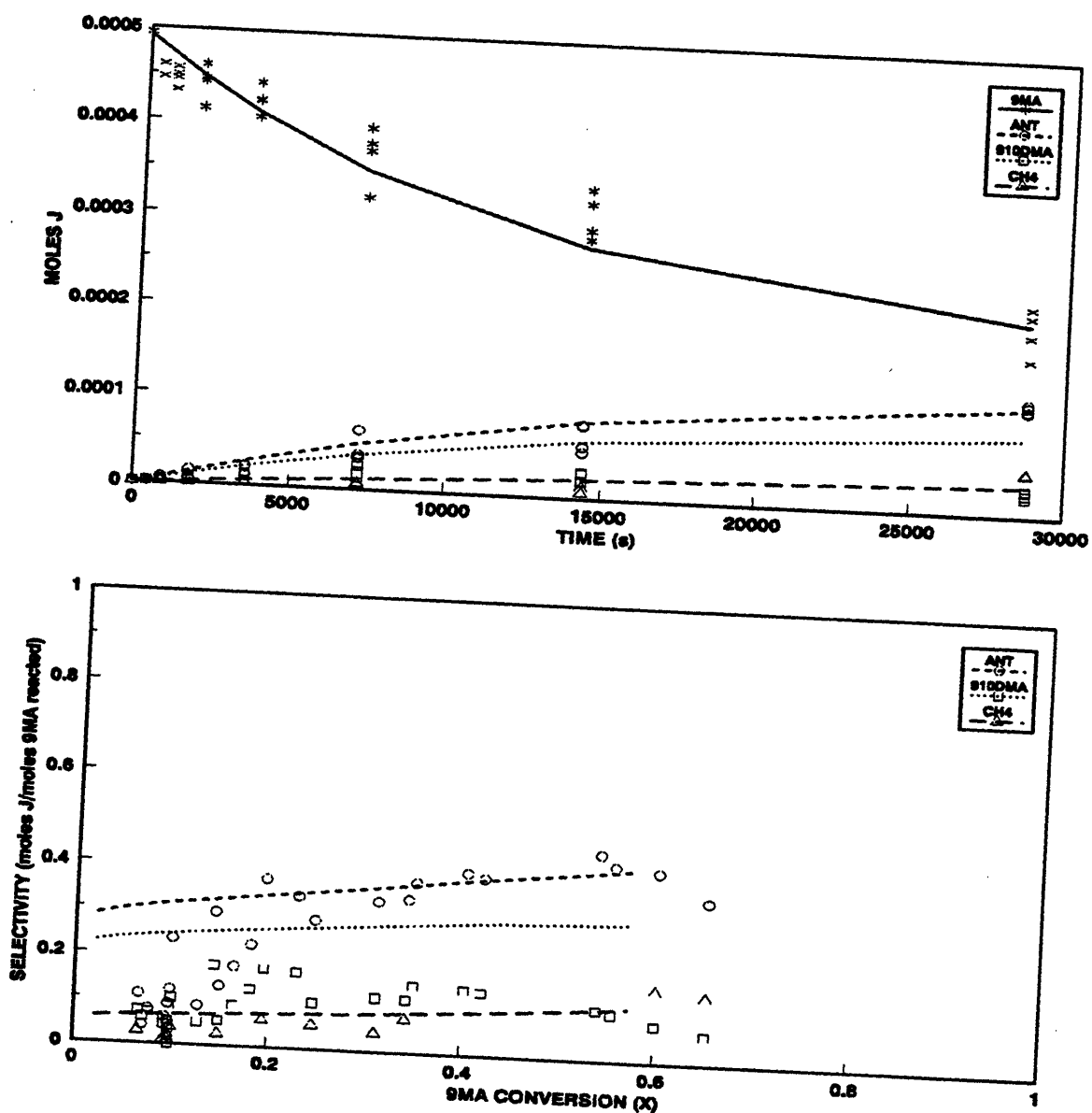
Figure 6.52: Product histories (top) and selectivity diagram (bottom) comparing optimized model (lines) to experimental data (symbols) for 9MA, ANT, 910DMA and CH4 at T = 370°C with $[9MA]_o$ = 0.82 mol/l.

the absolute amounts of ANT, the short-dashed lines versus the circles, and of 910DMA, the dotted line versus the squares, formed by the model are both lower than observed in the experiments. The lower panel of Figure 6.52 shows that the selectivity S(ANT) from the model 1.3-fold too low compared to the average values of S(ANT) observed from experiments between $0.2 < X < 0.75$ and S(910DMA) from the model is 1.6-fold too high compared to the S(910DMA) observed from experiments at $X = 0.25$. The model as the upper limit of 0.33 for S(ANT), as shown in Section 6.4.1, therefore the optimized model gives S(ANT) very close to the maximum limit.

Figure 6.53 continues the comparison between the optimized model (lines) and experimental (circles) product histories and selectivities for DHMA product. In the upper panel of Figure 6.53, the model is seen to predict DHMA within the experimental data. In the lower panel of Figure 6.53, a selectivity diagram, wee see that, relative to experiments, S(DHMA) from the model has the correct values at low and high conversions, but the slope of the line does not correspond to the trend of the experimental data.

Figure 6.54 compares the model calculation (lines) to the experimental data (solid circles) for heavies (9MAD, 9MAHMA9D, 9MAHMA10D, HMA9D, HMA10D and HMA910D). In the upper panel of Figure 6.54, the model predicts heavies production comparable to the experiments at shorter times, but as long times, produces more dimer than seen in the experiments. The lower panel of Figure 6.54
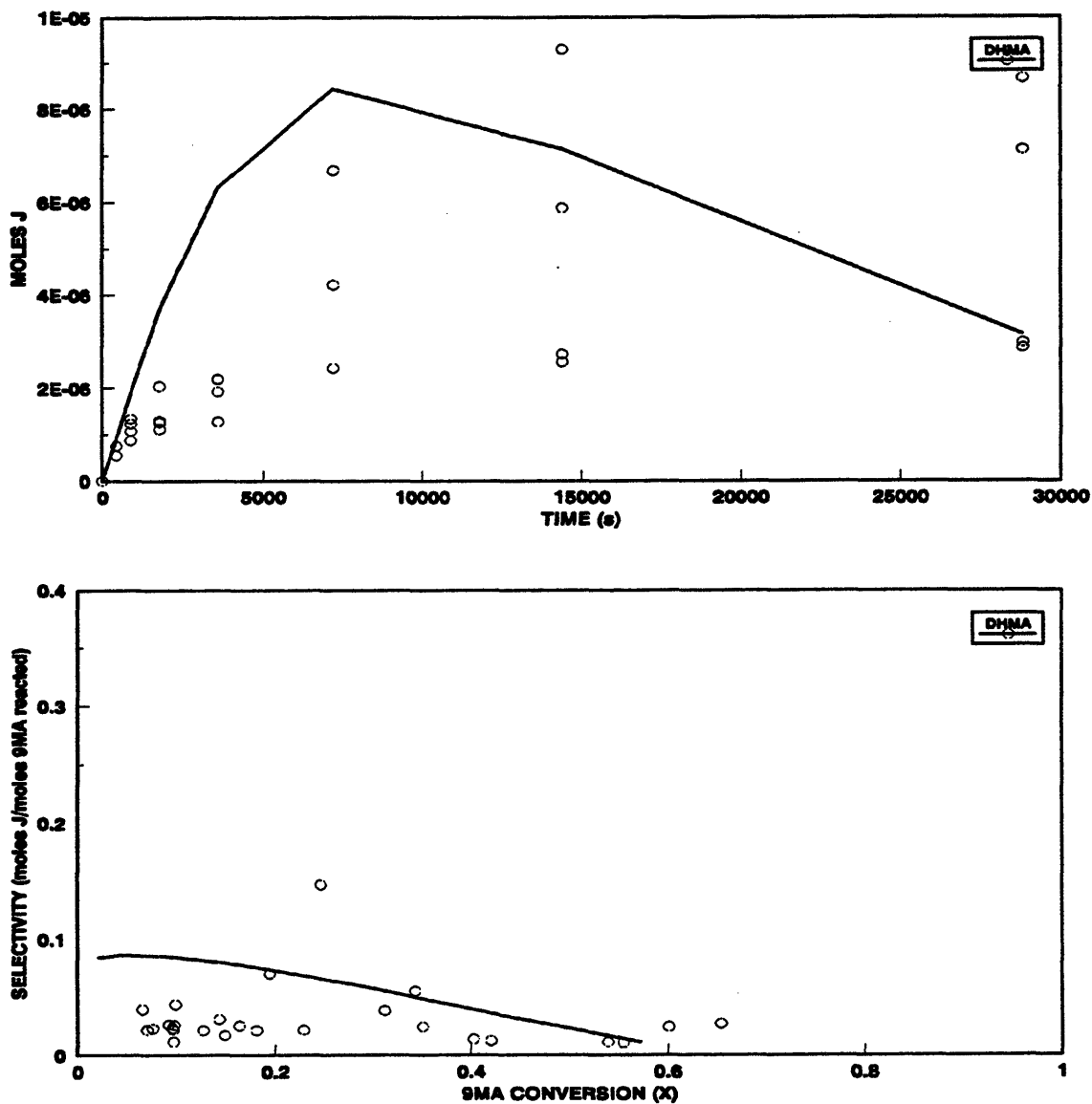
Figure 6.53: Product histories (top) and selectivity diagram (bottom) comparing optimized model results (lines) to experimental data (symbols) for DHMA at T = 370°C with $[9MA]_0$ = 0.82 mol/l.
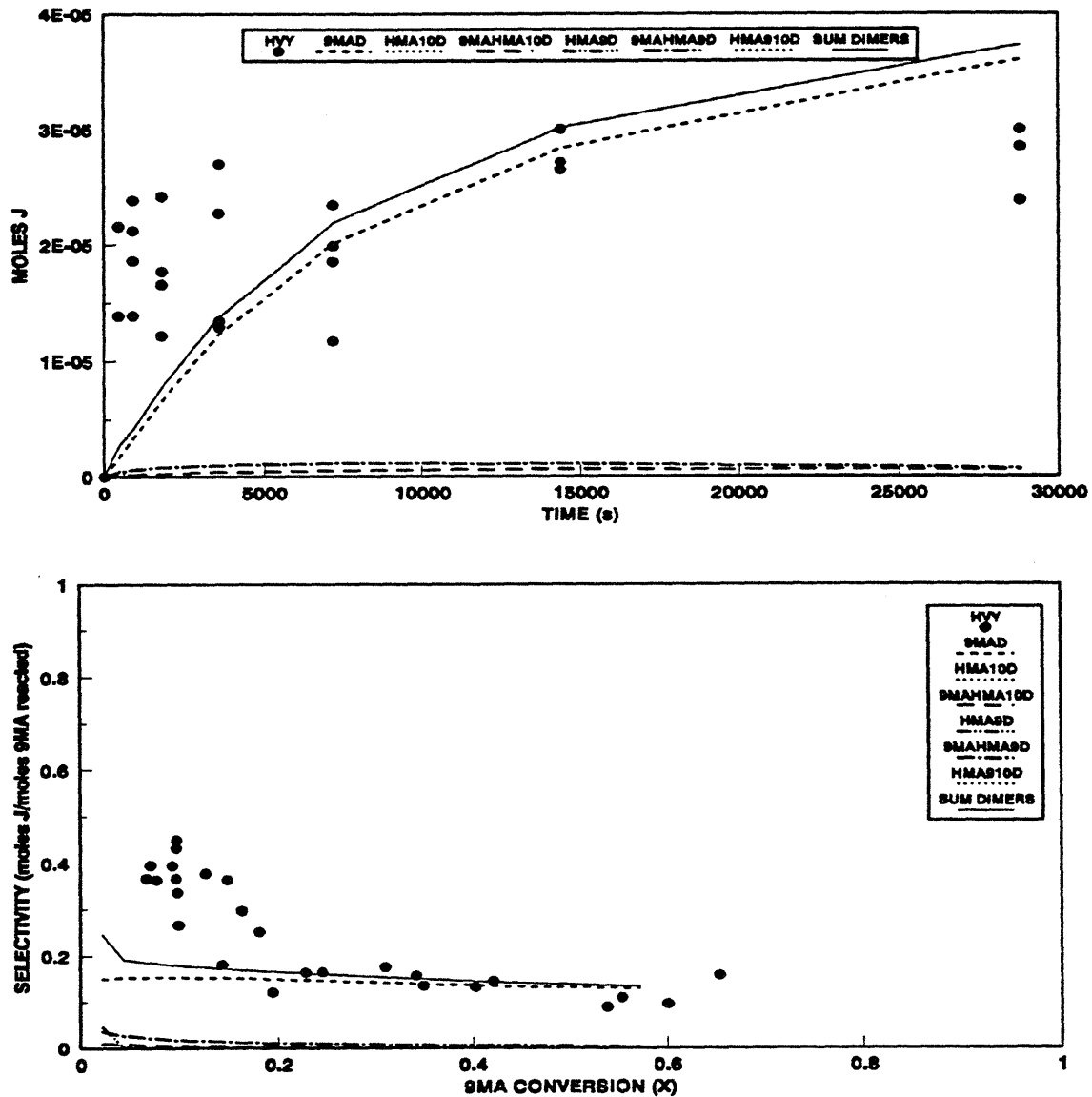
Figure 6.54: Product histories (top) and selectivity diagram (bottom) comparing optimized model (lines) to experimental data (symbols) for heavies at T = 370°C with $[9MA]_o$ = 0.82 mol/l.

shows the dimer selectivity $S(9MAD) \sim 0.15$ calculated from the model is close to the experimental $S(HVY) \sim 0.40$ at low $X < 0.1$, but whereas the $S(HVY)$ in the experiments decreases to ~ 0.15 with increasing conversion, $X > 0.2$, $S(9MAD)$ from the model remains roughly constant at $S(9MAD) \sim 0.14$.

Finally, Figure 6.55 compares the product ratios $R[DHMA/ANT]$ and $R[910DMA/ANT]$ as functions of 9MA conversion (X) derived from the optimized model (lines) to those observed experimentally (symbols). In the upper panel of Figure 6.55, the model is seen to predict $R[DHMA/ANT]$ comparable to the experimental values at $X > 0.1$, but the values at $X < 0.1$ and the slope of the line does not correspond to the observed experimental data. In the lower panel of Figure 6.55, the model is seen to predict $R[910DMA/ANT]$ comparable to the experimental values at low conversions, $X < 0.1$, but whereas the $R[910DMA/ANT]$ in the experiments decreases to 0.36 by $X = 0.40$, $R[910DMA/ANT]$ from the model decreases to $R[910DMA/ANT] = 0.75$ at $X = 0.40$.

6.5 Minor Methylated Products

The observed formations of methylanthracene isomers 1MA and 2MA from ANT and of dimethylanthracene isomers 1,9-, 1,10-, 2,9- and 3,9-DMA from 9MA during 9MA thermolysis at high severities invite interpretation by frontier orbital theory, as examples of periselective methyl radical attack on the aromatic anthracene nucleus.
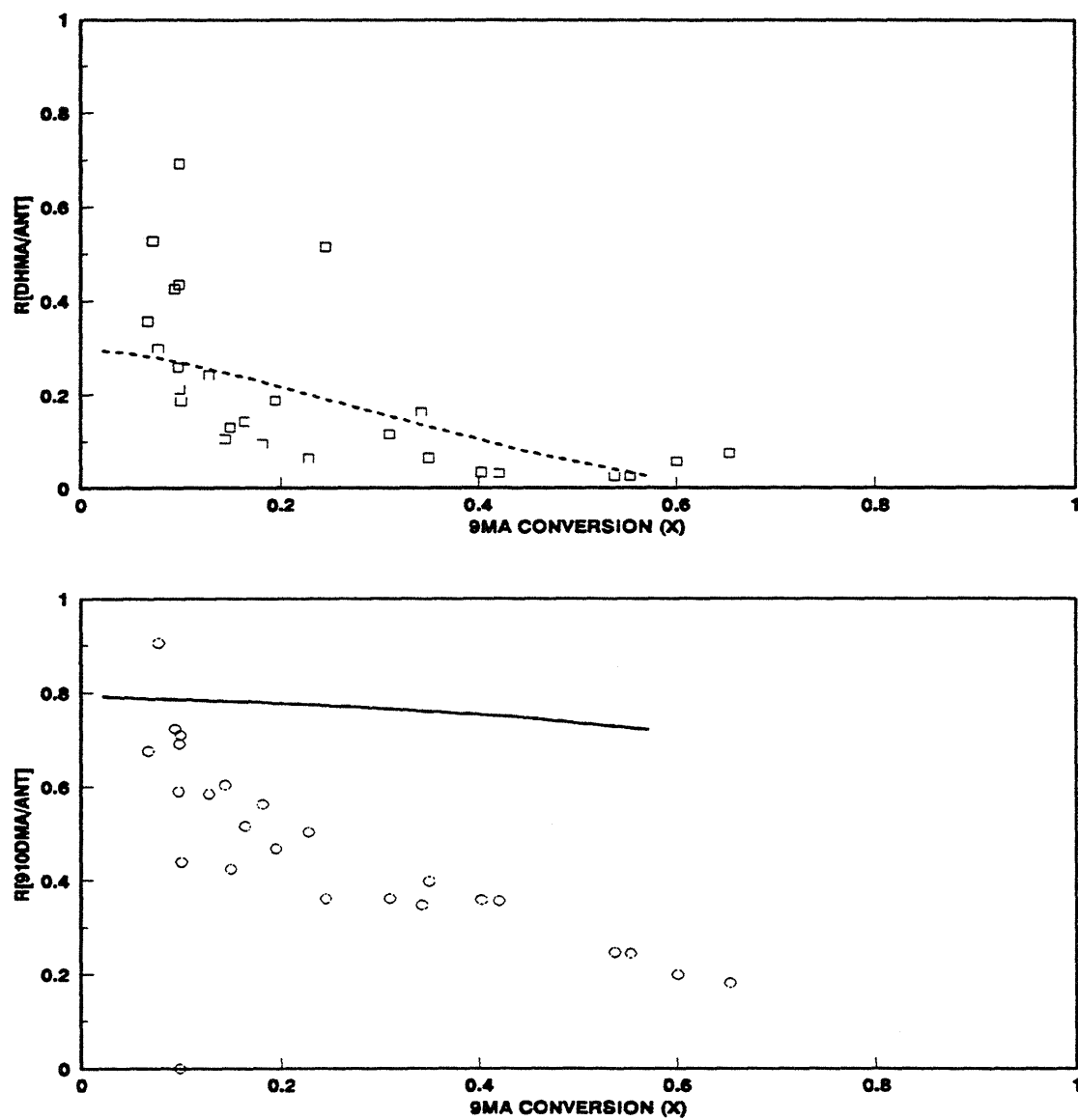
Figure 6.55: R[DHDMA/9MA] (top) and R[TMA/9MA] (bottom) comparing optimized model results (lines) to experimental data (symbols) at T = 370°C with [9MA]$_o$ = 0.82 mol/l.

569

6.5.1 Observed Product Ratios

Figure 6.56 and Figure 6.57, respectively, show the ratios of 2MA/1MA and of (2,9- + 3,9-)DMA/(1,9- + 1,10-)DMA obtained as functions of 9MA conversion during the present experiments. In the upper panel of Figure 6.56, it is seen that, at constant T = 370° and $0.25 < [9MA]_o < 2.06$ mol/l, the ratio R[2MA/1MA] = 0.36 ± 0.11 for $0.2 < X < 0.8$. In the lower panel of Figure 6.56, R[2MA/1MA] = 0.38 ± 0.19 for $0.2 < X < 0.99$ at $[9MA]_o = 0.82$ mol/l and T > 335°C. In the upper panel of Figure 6.57, it is seen that, at constant T = 370°C and $0.082 < [9MA]_o < 2.06$ mol/l, the ratio R[(2,9- + 3,9-)DMA/(1,9- + 1,10-)DMA] = 0.23 ± 0.05 for $0.1 < X < 0.75$. In the lower panel of Figure 6.57, R[(2,9- + 3,9-)DMA/(1,9- + 1,10-)DMA] = 0.22 ± 0.04 for $0.1 < X < 0.85$ at $[9MA]_o = 0.82$ mol/l and all temperatures for 315 - 409°C. The ratios R[(2,9- + 3,9-)DMA/(1,9- + 1,10-)DMA] and R[2MA/1MA] can both be viewed as the relative methyl affinities of positions 1 and 2 on the periphery of the anthracene ring, with methyl attack at position 2 less favored than at position 1 by a factor of 5 to 3.

Figure 6.58 and Figure 6.59, respectively, shows the ratios of (2,9- + 3,9-)DMA/910DMA and of (1,10- + 1,9-)DMA/910DMA obtained as functions of 9MA conversion during the present experiments. In the upper panel of Figure 6.58, it is seen that, at constant T = 370° and $0.25 < [9MA]_o < 2.06$ mol/l, the ratio R[(2,9- + 3,9-)DMA/910DMA] = 0.13 ± 0.05 for $0.1 < X < 0.6$. In the lower panel of Figure 6.58, R[(2,9- + 3,9-)DMA/910DMA] = 0.11 ± 0.04 for $0.1 < X < 0.6$ at
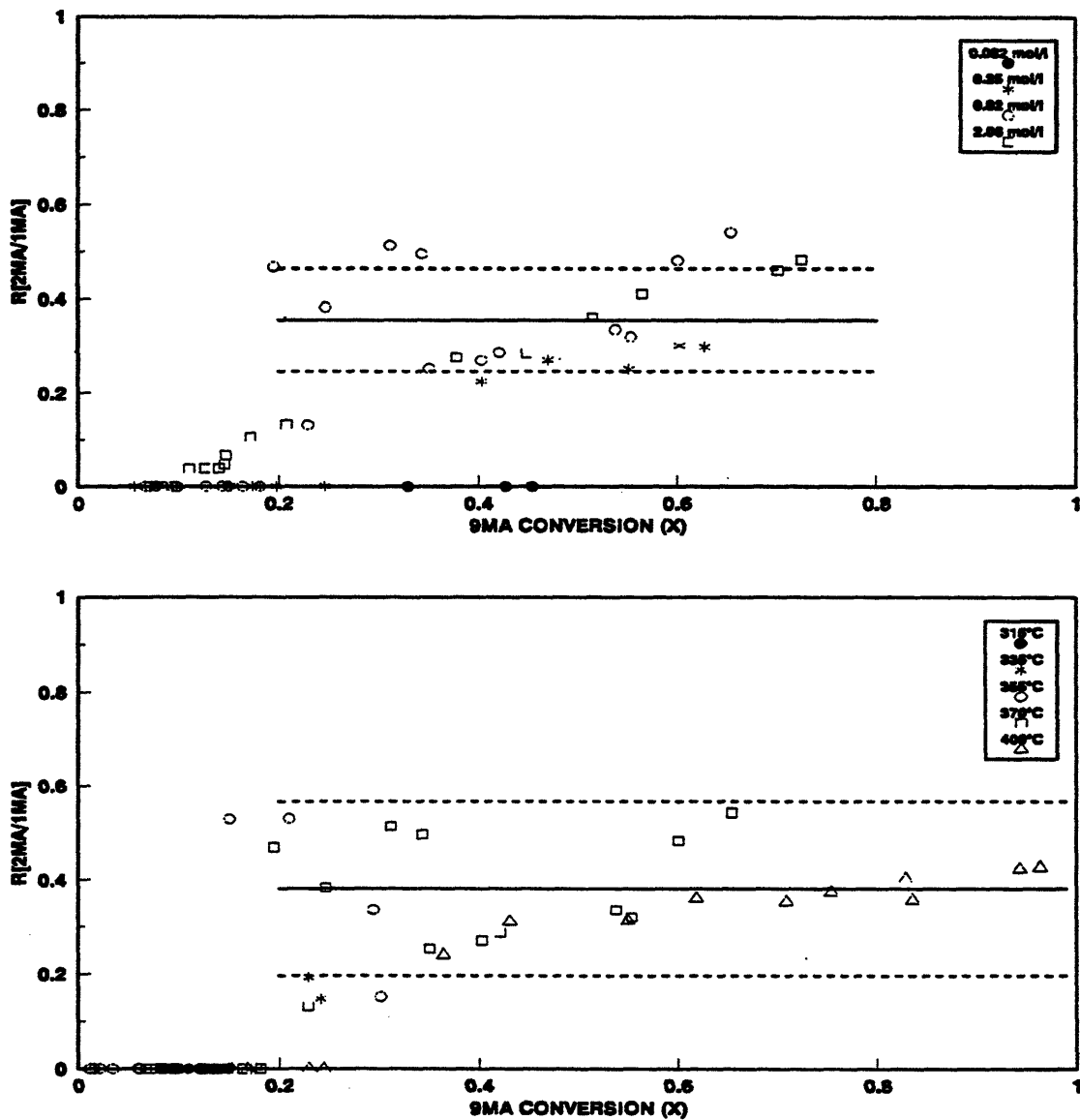
Figure 6.56: Ratio of moles 2MA to moles 1MA produced vs. 9MA conversion (X) for varying $[9MA]_0$ at T = 370°C (top) and for varying T with $[9MA]_0$ = 0.82 mol/l (bottom).

571
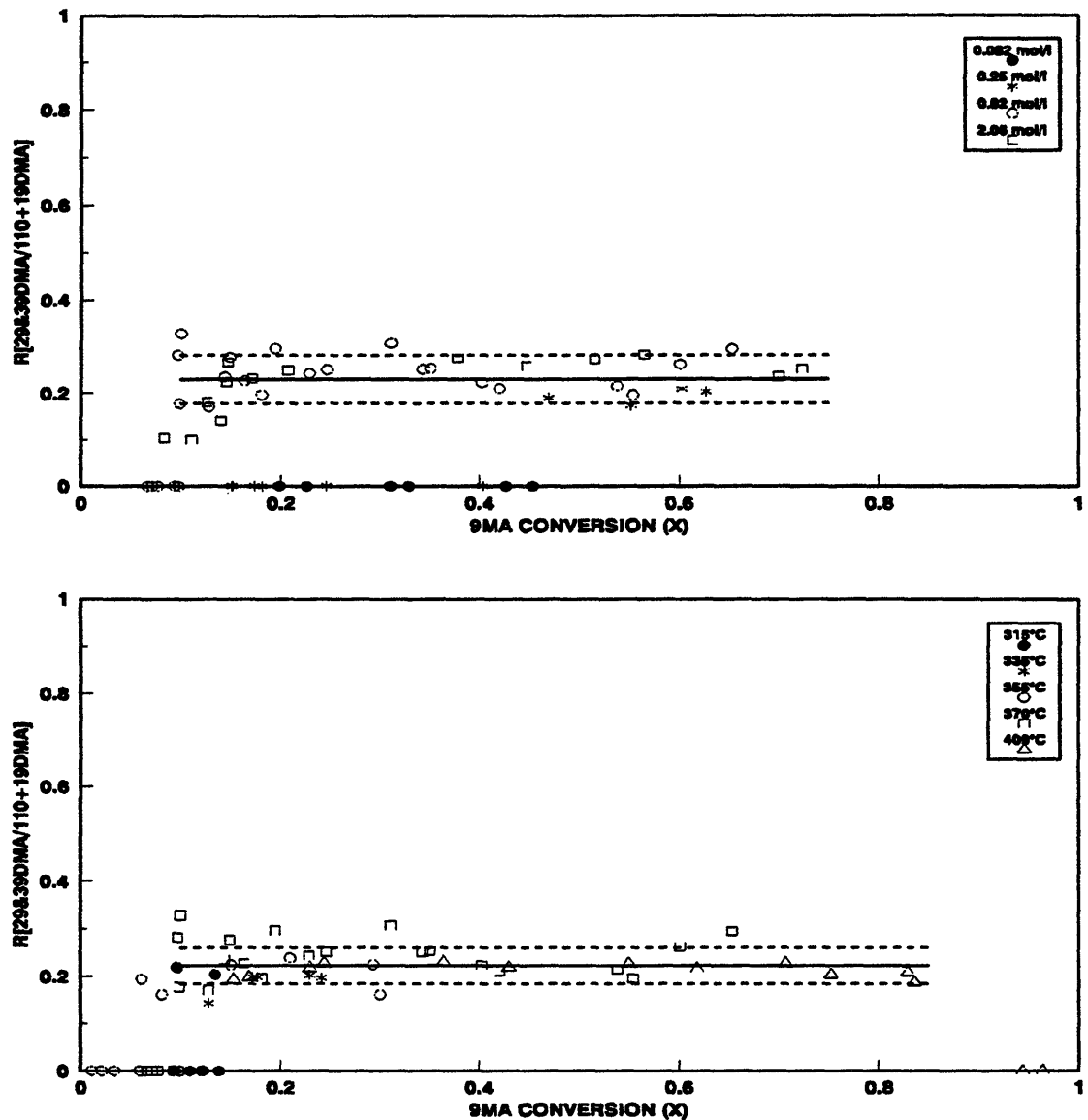
Figure 6.57: Ratio of moles (2,9-+3,9-)DMA/moles (1,9-+1,10-)DMA vs. 910DMA conversion(X) for varying [9MA]$_0$ at T = 370°C(top) and for varying T with [9MA]$_0$ = 0.82 mol/l(bottom).

572
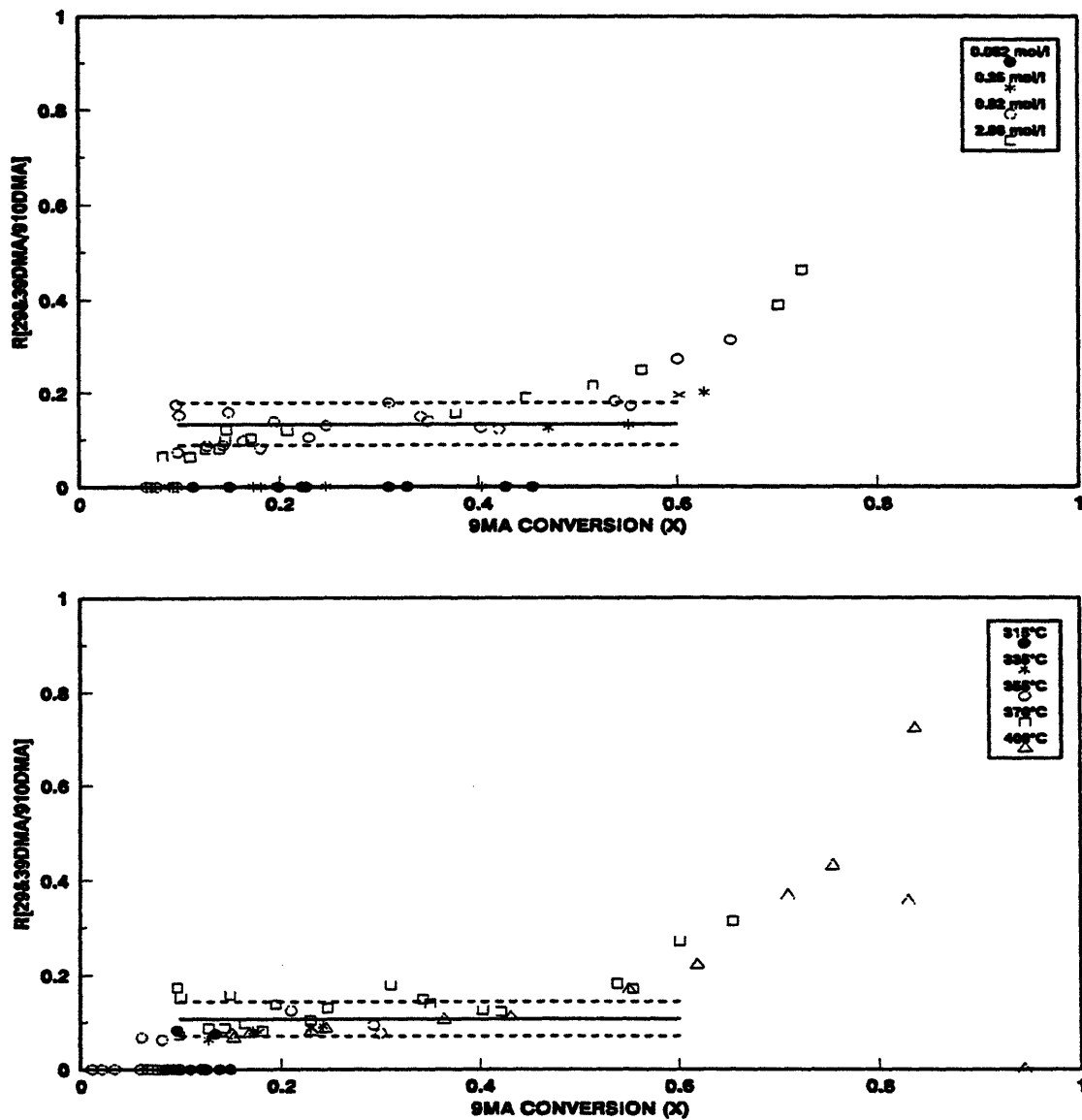
Figure 6.58: Ratio of moles (2,9-&3,9-)DMA to moles 910DMA produced vs. 9MA conversion (X) for varying [9MA]$_o$ at T = 370°C (top) and for varying T with [9MA]$_o$ = 0.82 mol/l (bottom).

573
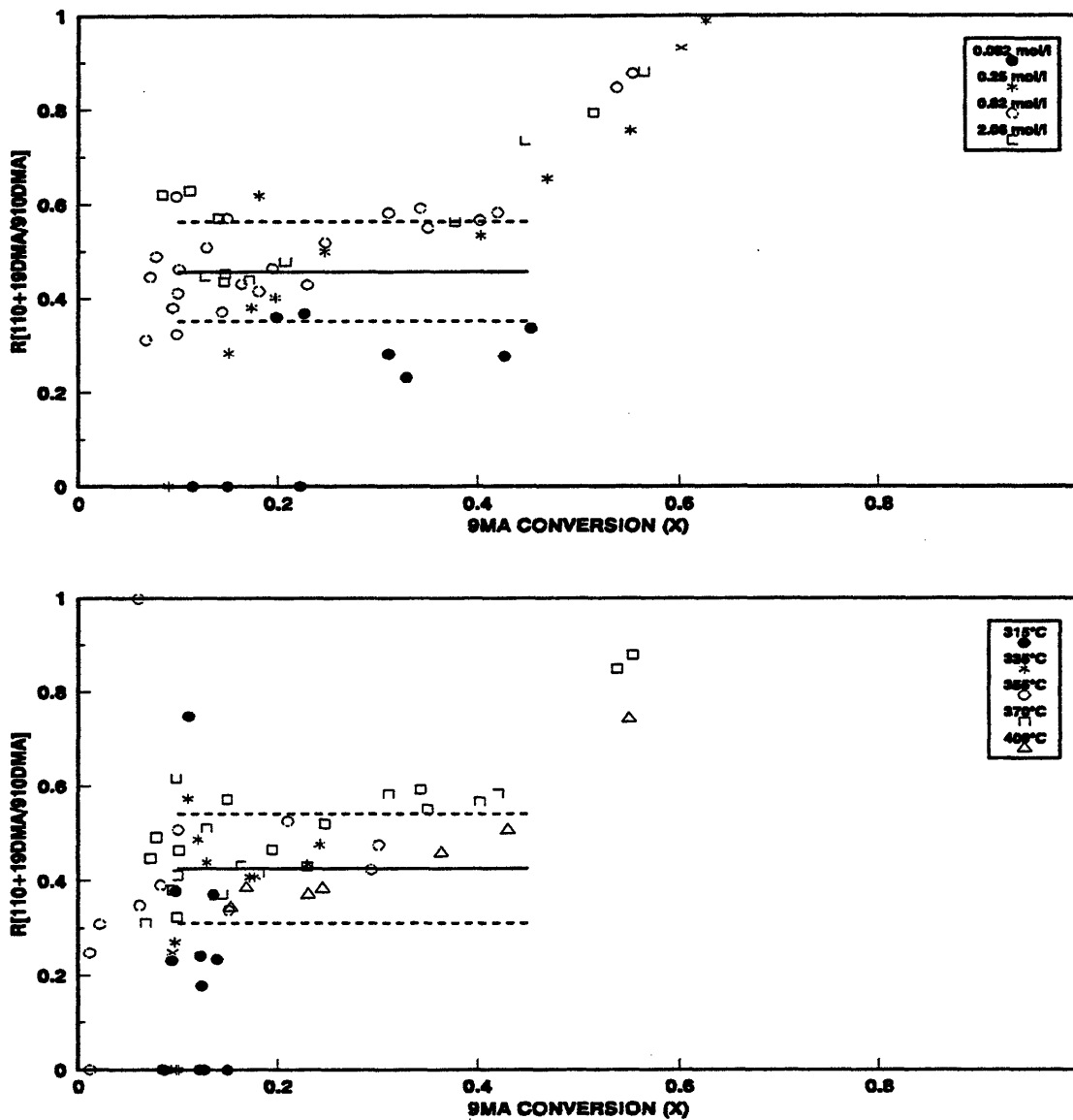
Figure 6.59: Ratio of moles (1,10-+1,9-)DMA to moles 910DMA vs. 9MA conversion (X) for varying $[9MA]_o$ at T = 370°C (top) and for varying T with $[9MA]_o$ = 0.82 mol/l (bottom).

574

$[9MA]_o$ = 0.82 mol/l and all temperatures for 315 - 409°C. In the upper panel of

Figure 6.59, it is seen that, at constant T = 370°C and 0.082 < $[9MA]_o$ < 2.06 mol/l,

the ratio R[(1,10- + 1,9-)DMA/910DMA] = 0.46 ± 0.11 for 0.1 < X < 0.45. In the

lower panel of Figure 6.59, R[(1,10- + 1,9-)DMA/910DMA] = 0.43 ± 0.11 for 0.1

< X < 0.45 at $[9MA]_o$ = 0.82 mol/l and all temperatures for 315 - 409°C. The

ratios R[(2,9- + 3,9-)DMA/910DMA] and R[(1,10- + 1,9-)DMA/910DMA] can

respectively be viewed as the relative methyl affinities of positions 2 and 9 and

positions 1 and 9 on the periphery of the anthracene ring, with methyl attack at

position 2 less favored than at position 9 and methyl attack at position 1 less favored

than at position 9.

6.5.2 Frontier Molecular Orbital Treatment using Hückel MOs

Using Equation (3.6) for the interaction between the frontier orbitals of a

radical and a molecule, the favorable, non-dimensional FMO stabilization energy

E'(t) is given by the interaction between the singly-occupied MO (SOMO) of the

CH3* radical and the highest-occupied and lowest-unoccupied MOs (HOMO and

LUMO) of the ANT at position t:

$$E'(t) = \frac{\Delta E(FMO)}{\frac{\gamma^2}{\beta}} = \frac{c_{t,HO}^2}{-X_{HO}} + \frac{c_{t,LU}^2}{X_{LU}} = \frac{2c_{t,HO}^2}{-X_{HO}} \tag{6.15}$$

where:

c_t =   MO coefficient at position t

X_{HOorLU} =   nondimensionalized Hückel MO energy and the subscripts HO and LU

refer to the frontier orbitals.

Figure 6.60 is an orbital interaction diagram for the system comprising ANT and CH3*, with energy as ordinate and the molecules confined to separate columns. Equation (6.15) reduces to one term because, in the Hückel approximation, alternate hydrocarbons such as ANT have $X_{LU} = -X_{HO}$ and radical such as CH3* have $X_{SO} = 0$. The dominant FMO interaction fixes the denominator of Equation (6.15), but since ANT possesses multiple reaction sites, the numerator can take several different values. Frontier orbital coefficients from the Hückel MOs of CH3* and ANT are shown in Figure 6.61, a "periselectivity diagram" that indicates the three possible sites at which CH3* can add to ANT. For ANT positions t = (2,1,9), the respective E'(t) = (0.12, 0.23, 0.47); that is, FMO theory predicts CH3* attack favored in the order of positions 2 < 1 < 9. The predicted inequality between positions 2 and 1 of the ANT nucleus accords with the experimentally observed minor product ratios R[2MA/1MA] ~ 0.4 for methylation of ANT.

6.5.3 Frontier Molecular Orbital Treatment using PM3 MOs

Figure 6.62 and Figure 6.63 are orbital interaction diagrams for the respective systems comprising ANT and CH3* and 9MA and CH3*, both with energies obtained
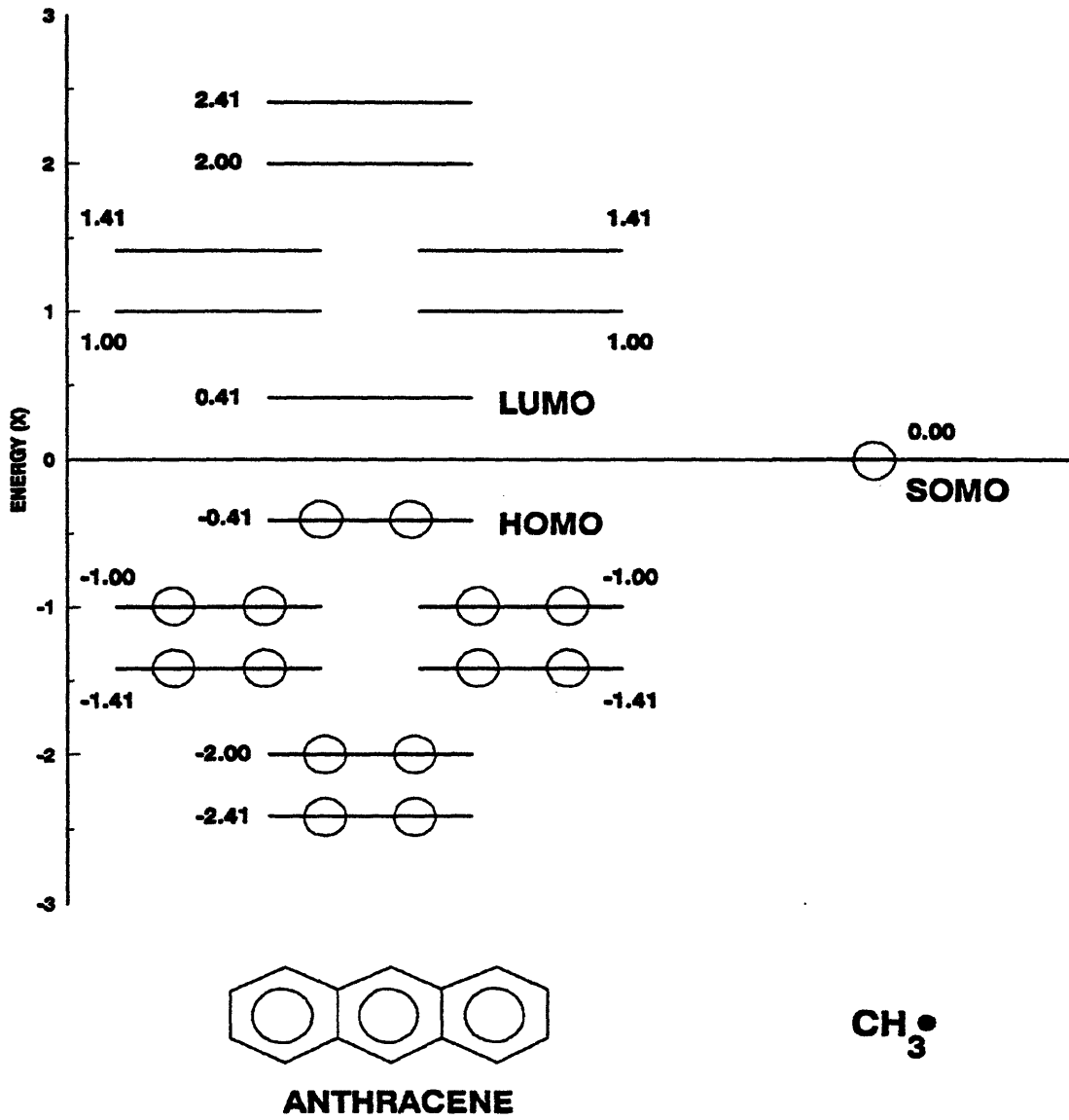
Figure 6.60: Frontier orbital interaction diagram for addition of methyl radical to anthracene using Hückel MOs.
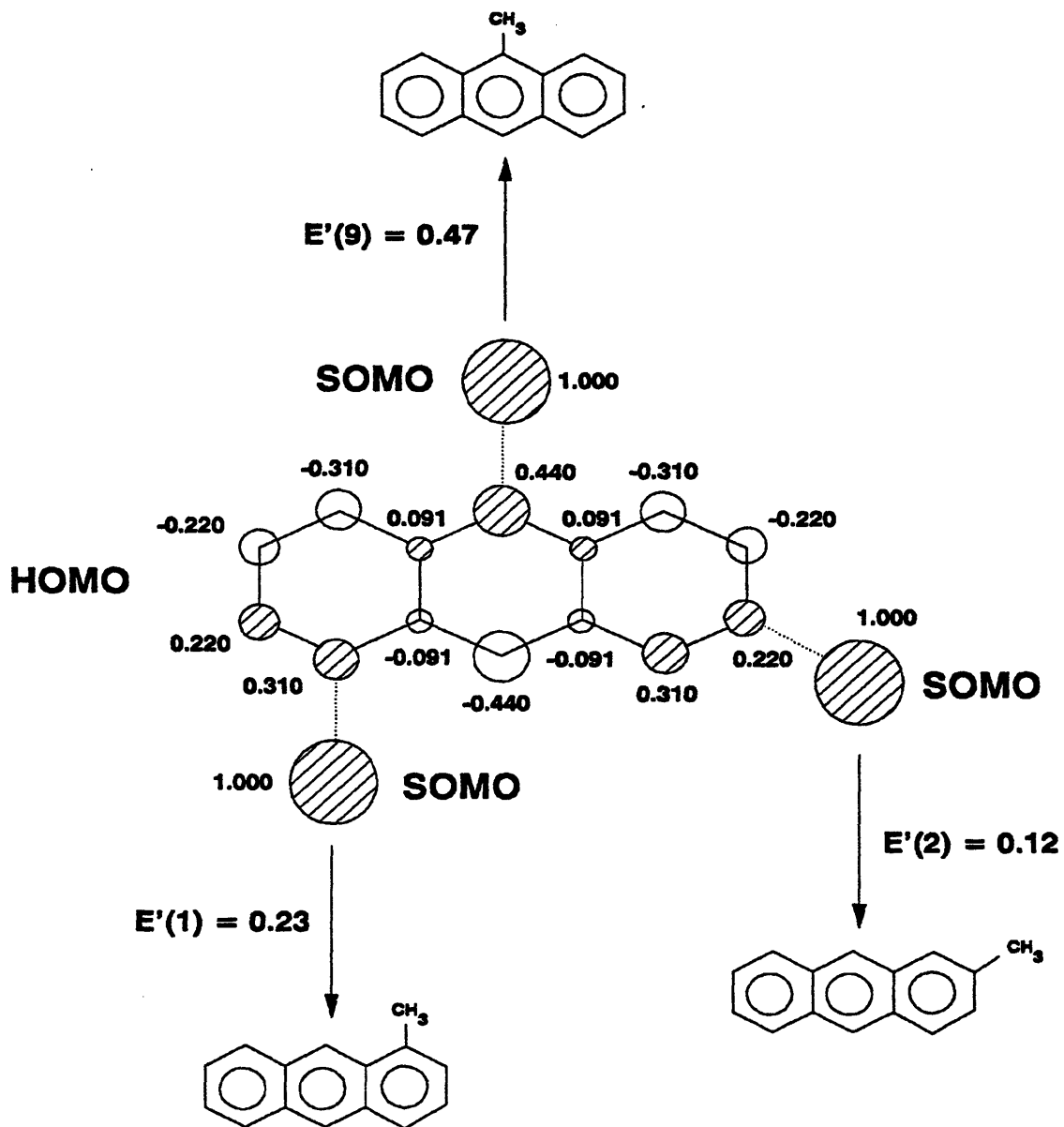
Figure 6.61: Estimation of isomer periselectivity by FMO theory using Hückel MOs for addition of methyl radical to anthracene to form 9-, 2- and 1-methylanthracene.

578
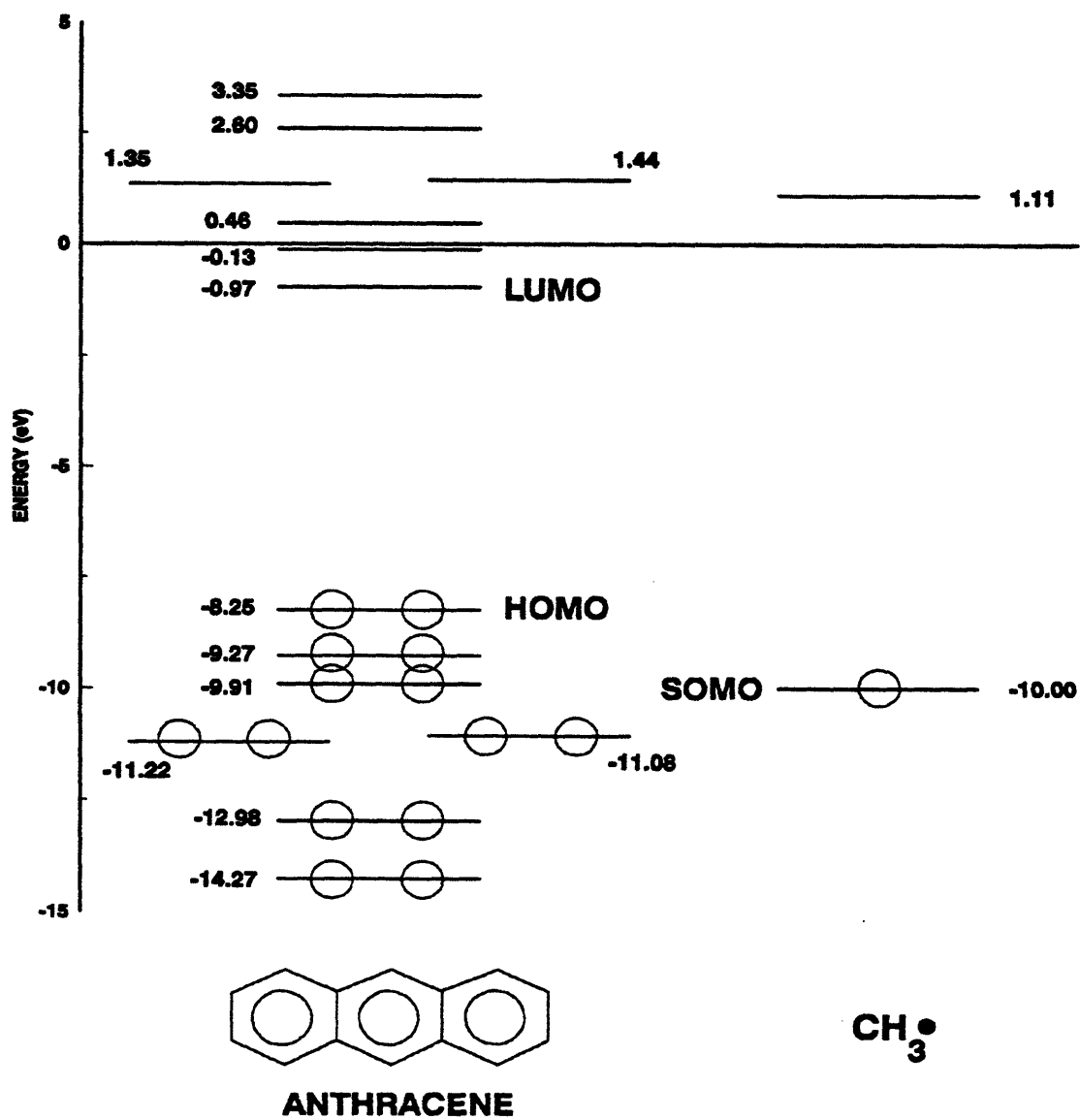
Figure 6.62: Frontier orbital interaction diagram for addition of methyl radical to anthracene using the PM3 MOs.

579
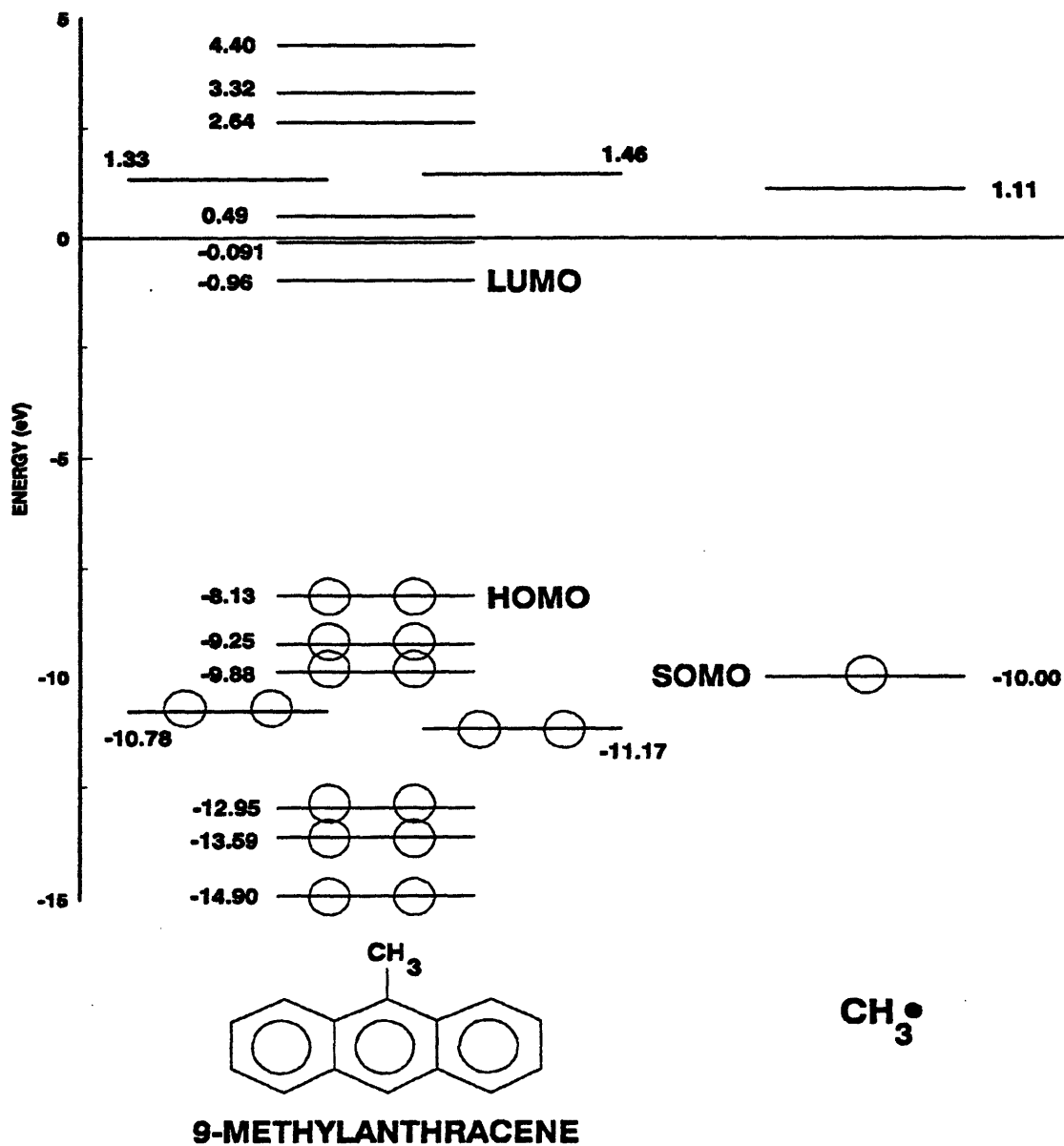
Figure 6.63: Frontier orbital interaction diagram for addition of methyl radical to 9-methylanthracene using the PM3 MOs.

from PM3 MO calculations. In Figure 6.62 (also Figure 6.63) it is seen that the SOMO of CH3* does not lie between the LUMO and the HOMO of ANT but possesses an energy such that $E_{SO} << E_{LU}$ and $E_{SO} \sim E_{HO}$. Thus, the SOMO-LUMO interaction remains a second order perturbation, whereas SOMO-HUMO interaction is now a first order perturbation of a much larger magnitude. For interactions between orbitals of roughly the same energy (degenerate) the total change in energy, ΔE_1, is the sum of the one-electron energies calculated by first-order perturbation theory (Hudson, 1974):

$$\Delta E_1 = \sum_t^{occ} C_t C_{u(SO)} \gamma_{tu} \qquad (6.16)$$

where:

C_t = coefficient of occupied MO at atom t in molecule A

$C_{u(SO)}$ = coefficient of SOMO at atom u in molecule B

γ_{tu} = resonance integral between AO's t and u

Table 6.20 lists the C_t from PM3 calculations for all the occupied levels of ANT and 9MA. If the HOMO is believed to be the "stereo-directing" occupied MO (Klopman, 1974), then the full summation for ΔE_1 reduces to one term, corresponding to the SOMO-HOMO interaction. Using only the HOMO in Equation (6.16), the favorable, non-dimensional first order FMO stabilization energy $E''(t)$ is:

$$E''(t) = \frac{\Delta E_1}{\gamma} = C_{x(HO)} C_{u(SO)} \qquad (6.17)$$

Table 6.20

COEFFICIENTS FROM PM3 MO CALCULATION OF ANTHRACENE AND 9-METHYLANTHRACENE

MO	ENERGY (eV)	$C_{(10)}$	$C_{(3)}$	$C_{(4)}$
ANT - 7 - HOMO	-8.25	-0.433	0.231	0.294
ANT - 6	-9.27	0.001	-0.297	-0.016
ANT - 5	-9.91	0.000	0.246	0.403
ANT - 4	-11.08	-0.391	-0.144	-0.281
ANT - 3	-11.22	0.254	-0.381	-0.190
ANT - 2	-12.98	-0.000	-0.319	-0.296
ANT - 1	-14.27	-0.307	-0.174	-0.218
9MA - 7 - HOMO	-8.13	-0.439	0.221	0.286
9MA - 6	-9.25	0.001	0.291	0.010
9MA - 5	-9.88	-0.002	0.243	0.397
9MA - 4	-10.78	-0.223	-0.273	-0.331
9MA - 3	-11.17	0.387	-0.303	-0.074
9MA - 2	-12.95	0.011	-0.311	-0.286
9MA - 1	-13.59	-0.286	-0.194	-0.228

The second-order SOMO-LUMO interaction is neglected relative to the larger first order SO-HO interaction. Figure 6.64 gives the values for the energies E (eV) and coefficients C_t for the ANT and 9MA HOMOs and LUMOs, as well as the E and C_t for the CH3* SOMO from the PM3 calculations. Figure 6.65 is a periselectivity diagram indicating the three possible sites at which CH3* can add to ANT and the corresponding E"(t) at each position. For ANT positions t = (2,1,9), the respective E"(t) = (0.23, 0.29, 0.43); that is, FMO theory predicts CH3* attack favored in the order of positions 2 < 1 < 9. The predicted inequality between positions 2 and 1 of ANT is in accord with the experimentally observed R[2MA/1MA] ~ 0.4. Figure 6.66 is a periselectivity diagram indicating the five possible sites at which CH3* can add to 9MA and the corresponding values of E"(t) at each position. For 9MA positions t = (2,3,1,4,10), the respective E"(t) = (0.22, 0.23, 0.28, 0.28, 0.44); that is, FMO theory predicts CH3* attack favored in the order of positions (2, 3) < (1, 4) < 9. Methyl attack at position 2 leads to 2,9-DMA, at position 3 to 3,9-DMA, at position 1 to 1,9-DMA, at position 4 to 1,10-DMA and at position 10 to 9,10-DMA. The predicted inequality between positions (2, 3), (1, 4) and (10) accords with the experimentally observed ratios R[(2,9- + 3,9-)DMA/(1,9- + 1,10-)DMA] ~ 0.25, R[(2,9- + 3,9-)DMA/910DMA] ~ 0.12 and R[(1,10- + 1,9-)DMA/910DMA] ~ 0.45.

Finally, it is worth noting that in free-radical phenylation of ANT at T = 30°C, Dickerman (1973) reported relative phenyl affinities at position (2,1,9) in the ratio (0.28, 1.00, 14.32), that is, position 2 was less favored than position 1 by a factor of

583

ANT

E(HO) = -8.25

E(LU) = -0.97

9MA

E(HO) = -8.13

E(LU) = -0.96

CH3*

E(SO) = -10.00
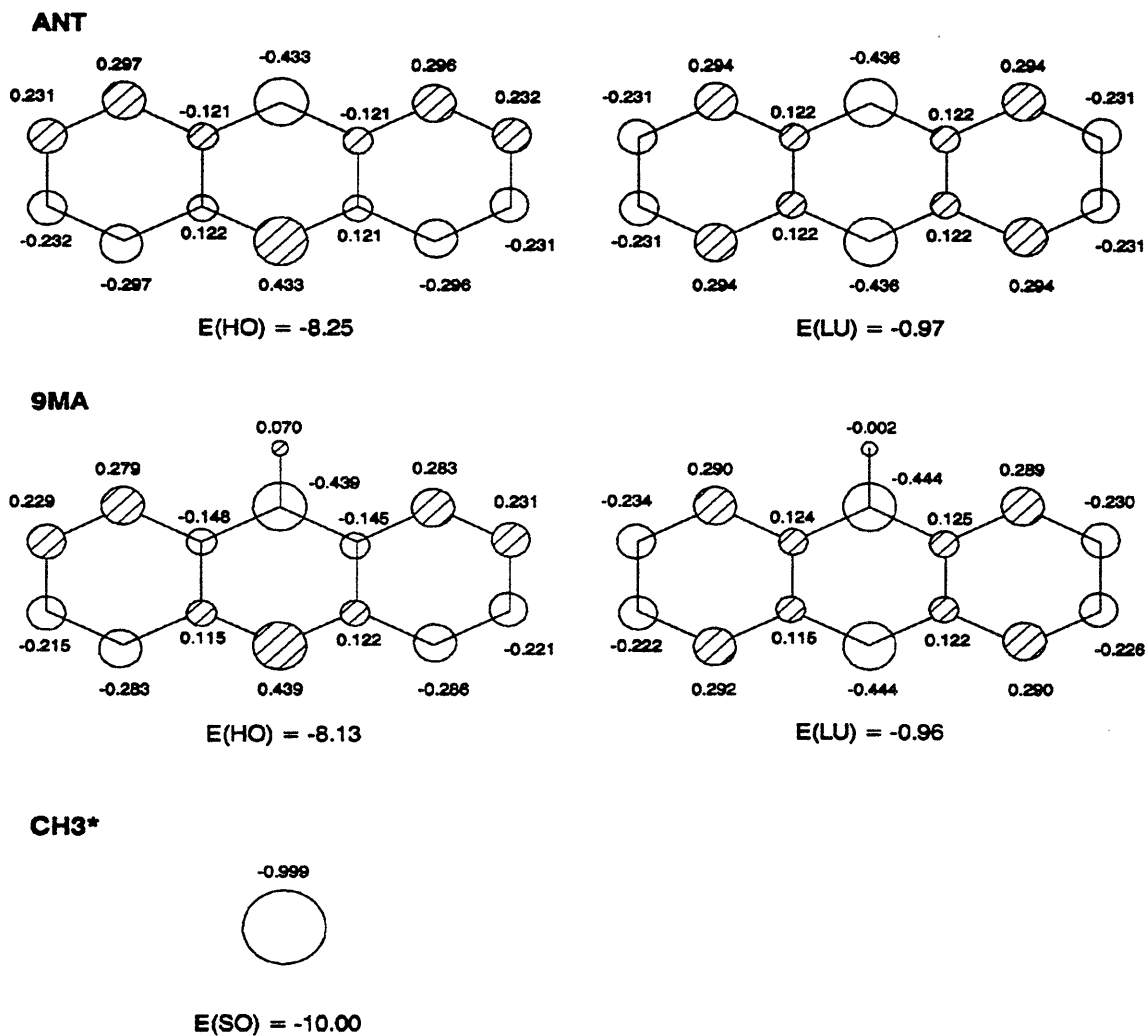
Figure 6.64: Values of coefficients C_t and energies E from PM3 calculations of anthracene, 9-methylanthracene and methyl radical.
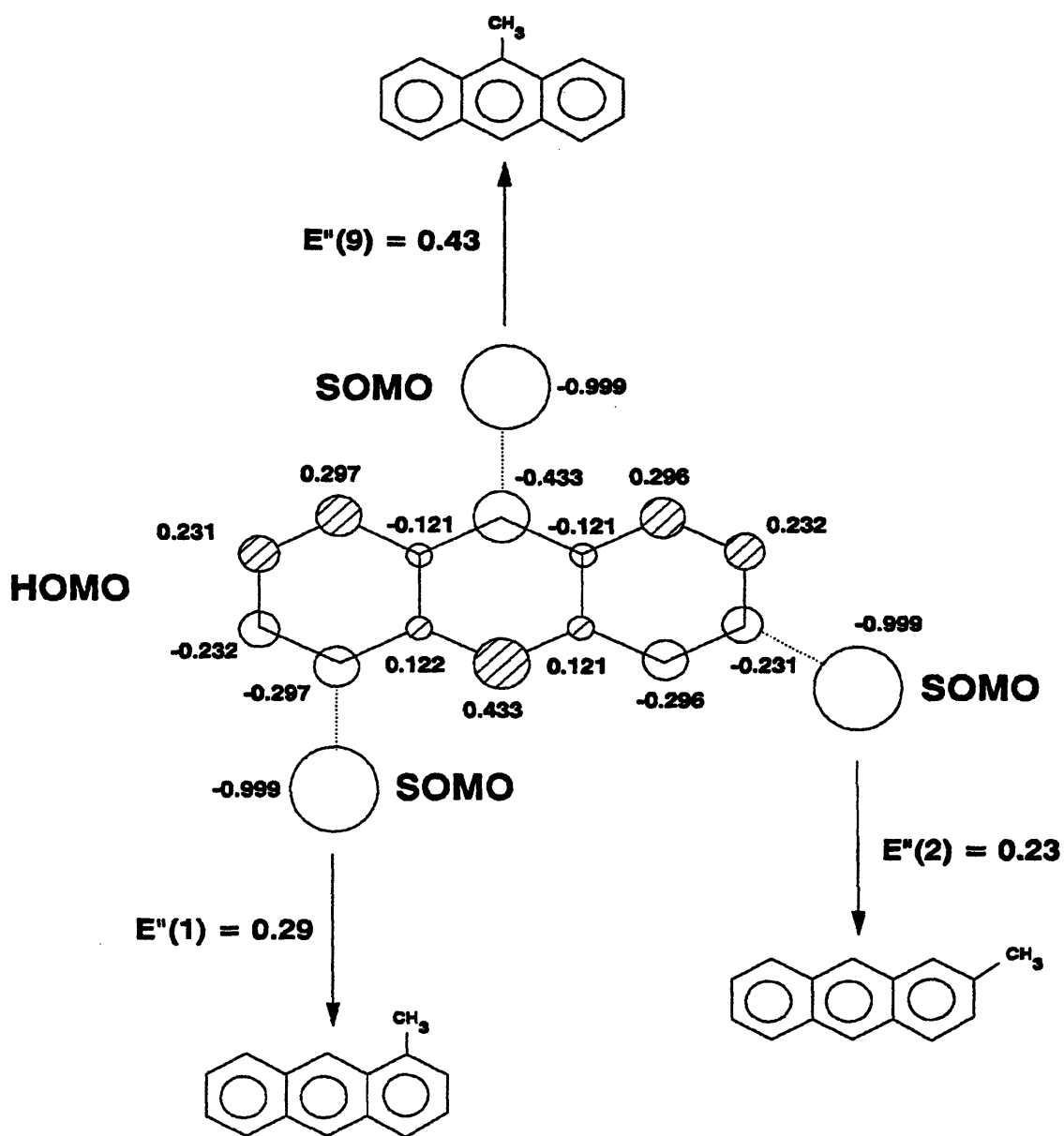
Figure 6.65: Estimation of isomer periselectivity by FMO theory using PM3 MOs for addition of methyl radical to anthracene to form 9-, 2- and 1-methylanthracene.

585
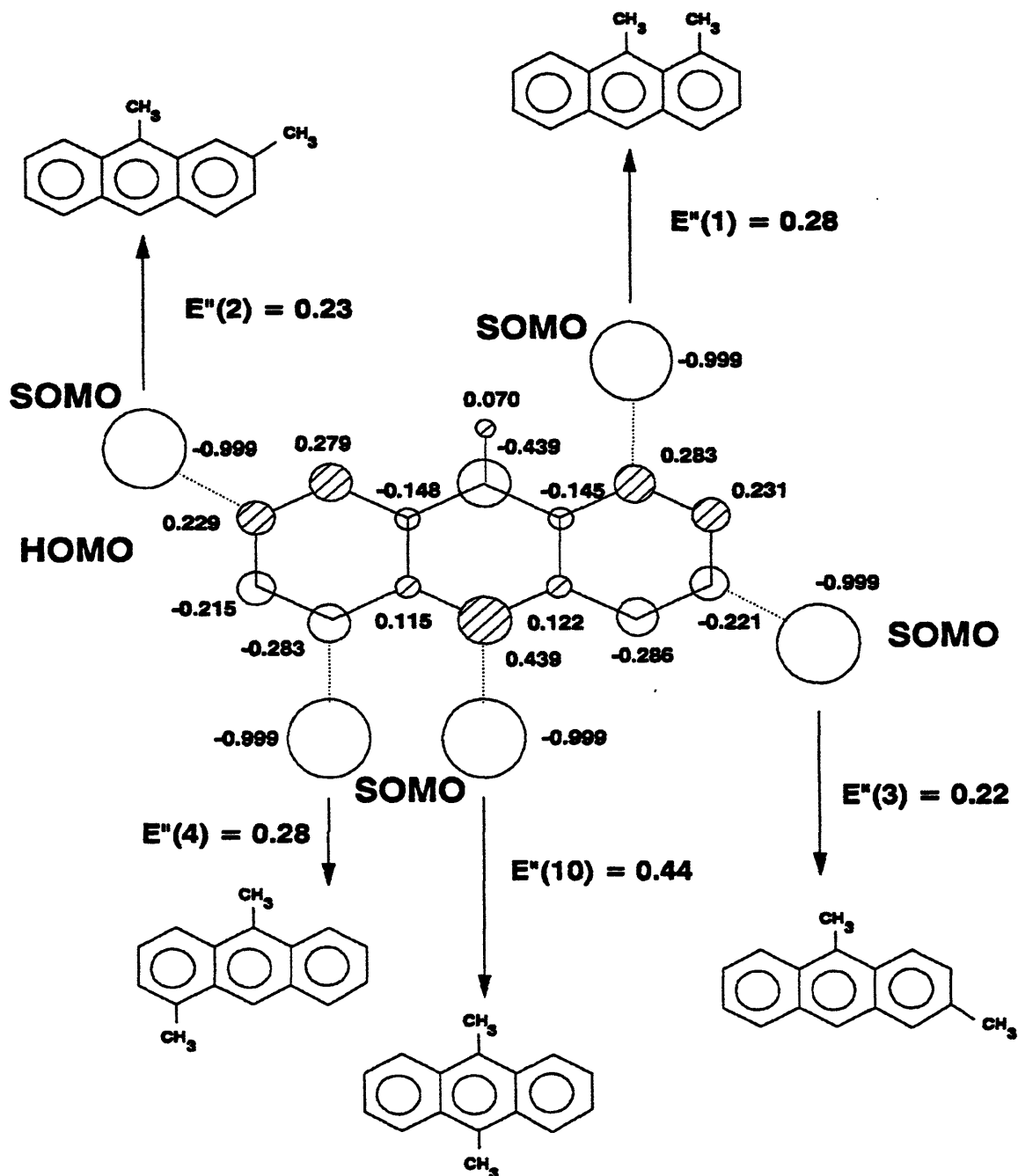
Figure 6.66: Estimation of isomer periselectivity by FMO theory using PM3 MOs for addition of methyl radical to 9-methylanthracene to form 1,10-, 1,9-, 2,9- and 3,9-dimethylanthracene.

3.5. The ratio of phenyl affinities at ANT positions 1 and 2 is of roughly the same magnitude as the ratio of methyl affinities obtained from the minor methylated product ratios in the present experiments.

6.6 Summary

9-methylanthracene (9MA) was thermolyzed over the range: $T = 315 - 409°C$, $[9MA]_o = 0.082 - 2.06$ mol/l and $t = 450 - 57600$ s, which lead to $X = 0.05 - 0.99$. Products seen in the 9MA thermolysis included: anthracene (ANT), 9,10-dimethylanthracene (910DMA), dihydro-methylanthracenes (DHMA), dihydro-dimethylanthracenes (DHDMA), dihydroanthracene (DHA), 1-methylanthracene (1MA), 2-methylanthracene (2MA), 1,10-dimethylanthracene (110DMA), 1,9-dimethylanthracene (19DMA), 2,9&3,9-dimethylanthracene (29&39DMA), other dimethylanthracenes (other DMAs), trimethylanthracenes (TMAs), heavy (dimer) products, and methane (CH4). The substrate and major product histories depict a classical parallel reaction series B(9MA) → C(ANT) and B(9MA) → A(910DMA), with competing, parallel, hydrogenation and methylation pathways at each stage. S(ANT) and S(DMAs) were roughly independent of conversions at all $[9MA]_o$ and T. Absolute values of S(ANT) and S(ALL DMAs) remained somewhat constant with increasing $[9MA]_o$ at fixed T and with increasing T at fixed $[9MA]_o$. S(DHMA) was essentially highest at the lowest conversion and declined precipitously with increasing X at all $[9MA]_o$ and T. DHDMA and DHA were only detected at $[9MA]_o > 0.25$

mol/l and all T and increased monotonically from zero as conversions increased. ANT, 1MA and 2MA selectivities increased monotonically from zero as conversions increased for all $[9MA]_o$ and T, with S(1MA) > S(2MA) always and both always < S(ANT) at any X. 910DMA selectivity increased monotonically from zero to a maximum at X ~ 0.25 for all $[9MA]_o$ and T, and then declined monotonically with increasing conversion for all $[9MA]_o$ and T. 110DMA, 19DMA and 29&39DMA selectivities also increased monotonically from zero as conversions increased and approached X ~ 0.85 for all $[9MA]_o$ and T, and then decreased for X > 0.85 at T = 355°C. The other minor DMAs selectivity remained roughly constant for X < 0.85 for all T, and then increased for X > 0.85. Of the dimethylated species, S(910DMA) > S(110DMA) > S(19DMA) > S(29&39DMA) > S(other DMAs) for X < 0.60 and each always < S(9MA) at any X. Absolute values of S(110DMA), S(19DMA) and S(29&39DMA) increased somewhat with increasing $[9MA]_o$ and decreased somewhat with increasing T for all X < 0.60, while absolute values of S(110DMA), S(19DMA) and S(29&39DMA) decreased as X → 1. Absolute values of S(other DMA) remained roughly constant for X < 0.60 and increased at X > 0.60.

The kinetics of the 9MA experimental thermolyses were analyzed to derive reaction order and activation parameters. Reaction order for overall 9MA decay was determined from k_{eff}, the effective first order rate constants, and 9MA decay half-life, t^*, in the series of experiments at constant T = 370°C with $[9MA]_o$ ranging from 0.082 to 2.06 mol/l. Analysis of both led to approximately 3/2 order 9MA

decomposition kinetics, with k_{eff} yielding 1.22 ± 0.09 and t^* yielding 1.50 ± 0.07.

Thermolysis of 9MA at fixed $[9MA]_o = 0.82$ mol/l and varying temperature from 315 - 409°C revealed the activation parameters associated with both the effective first order and true 3/2 order rate constants. The best-fit Arrhenius parameters $[\log_{10} A$ (s^{-1}), E^* (kcal/mol)] = $[5.92 \pm 0.28, 29.9 \pm 7.3]$ for the average k_{eff} and $[\log_{10} A$ $(l^{\frac{1}{2}}/mol^{\frac{1}{2}}$ s), E^* (kcal/mol)] = $[9.2 \pm 0.15, 39.7 \pm 3.9]$ for $k_{3/2}$ with low conversion data, X < 0.4. Regression of the half-lifes t^* at varying temperatures gave Arrhenius parameters $[\log_{10} A$ (s^{-1}), E^* (kcal/mol)] = $[11.4 \pm 0.03, 46.4 \pm 0.09]$ for $k_{3/2}$.

Three primary reaction pathways operate in parallel upon 9MA substrate: (P1) Hydrogenation to 9,10-dihydro-9-methylanthracene, (P2) Demethylation to anthracene, and (P3) Methylation to 9,10-dimethylanthracene and other DMA isomers. The primary methylation product 910DMA is secondary operated upon by a pathway triad analogous to the preceding primary triad, eventually forming 9,10-dihydro-9,10-dimethylanthracene, trimethylanthracenes and reforming 9MA substrate. The primary demethylation product ANT suffers hydrogenation and methylation, as witnessed by the appearance of the minor products DHA, 1MA and 2MA. 9MA does not isomerize to their positional isomers 1MA and 2MA, since the methylated species do not arise until after the demethylated compound appears. Terminated products include both pure- and cross-termination of 9MA and DHMA radicals.

A possible mechanism for the early stages of 9MA thermolysis, that is consistent with the present pathway and kinetic observations and accounts for all the

products observed during the initial stages of 9MA thermolysis at low conversions, was devised and is summarized as follows: The free-radical cycle is initiated by the substrate 9MA undergoing bimolecular disproportionation, an intermolecular hydrogen transfer reaction, to form the respectively dehydrogenated and hydrogenated radical species 9MA*, HMA9* and HMA10*. Of these, HMA9* and HMA10* can either abstract hydrogen from 9MA substrate to form DHMA products or HMA10* can undergo a β-scission type of radical decomposition forming ANT product and a methyl radical CH_3*. The CH_3* can either abstract H from 9MA substrate to form methane product, or add to the 9MA substrate to form the dimethyl radical HDMA*. The latter can then abstract H from substrate 9MA to form the observed 910DMA product and either HMA9* and HMA10*. Finally, the radical mechanism is terminated by the species 9MA*, HMA9* and HMA10* engaging in both pure- and cross-combination to form various dimeric products. HMA9* and HMA10* radicals can also terminate by disproportionation to form 9MA and DHMA. The proposed mechanism exhibits certain stoichiometric limits and thus restricts the maximum selectivities of each of DHMA, ANT, 910DMA and heavies to 1/3.

Thermochemical and activation parameters were then assigned from first principles for each elementary reaction and its reverse in the mechanism. In order to derive kinetic parameters for the mechanism, values of the enthalpy of formation, ΔH°_f, were required for all participating chemical species. Where experimental

590

values were unavailable, enthalpies of formation were derived using a "macro" group additivity technique, which started with a basis molecule that was as large and as structurally similar to the desired product and then added and subtracted other basis species from the starting species to account for structural differences between it and the desired species. Arrhenius expressions were generated for each elementary step of the 9MA thermolysis mechanism from kinetic data reported in the literature for that type of reaction, which was analyzed to ascertain its activation parameters, including $\log_{10} A$, which was decomposed into an intrinsic portion, $\log_{10} A_{int}$, and a reaction path degeneracy, rpd, with $\log_{10} A = \log_{10} A_{int} + rpd$. The activation energy E^* was determined by an Evans-Polanyi expression of form $E^* = E_o + \alpha\Delta H^{\circ}_r$. An algebraic steady state analysis was performed on the 9MA mechanism to provide an independent check on numerical results of computer calculations, which agreed quite closely to within a factor of 4 or better. Conservation relations derived from the mechanistic model of 9MA thermolysis and using the estimated rate constants were numerically integrated using a computer program called ACUCHEM.

Substrate and product histories and product selectivities as obtained from the numerical solution of the thermolysis model were compared to the experimental data for 9MA, 910DMA, ANT, CH4, DHMA, heavies and product ratios R[DHMA/ANT] and R[910DMA/ANT] at the center of the experimental grid, $[9MA]_o = 0.82$ mol/l and T = 370°C. The model is seen to predict 9MA decay too slow, S(ANT) and S(910DMA) are respectively 2.2 and 1.3-fold too low, S(DHMA) is 6.8-fold too low

at low conversions (X ~ 0.15) and 10-fold too high for X = 0.40, S(HVY) (sum of

9MAD, 9MAHMA9D, 9MAHMA10D, HMA9D, HMA10D and HMA910D) is

comparable at low X < 0.1 and 1.7-fold higher at X > 0.20, R[DHMA/ANT] about

4.5-fold higher at low conversions and almost 11-fold higher for X > 0.20, and

R[910DMA/ANT] is comparable at low X < 0.10 and 4-fold higher at X = 0.40.

9MA decay half-life, major product selectivities and product ratios obtained

from numerical solutions were compared with the experimental observations for

varying $[9MA]_o$ at fixed T = 370°C and for varying T at fixed $[9MA]_o$ = 0.82 mol/l.

The model predicted t^* too long, that is, decay kinetics too slow, compared to the

experimental observations at all $[9MA]_o$ and T with the model yielding a slope -0.89,

implying ~ 2 order, versus the experimental data that yielded a slope of -0.53,

implying 1½ order decomposition kinetics, and the model yielded an E^* = 39.1

kcal/mol versus the experimental data that provided E^* = 46.4 kcal/mol. The model

predicted S(ANT) and S(910DMA) too low at all $[9MA]_o$ and T, S(DHMA) too high

at $[9MA]_o$ and T at low (X ~ 0.15) conversions and too high for all $[9MA]_o$ and T

at high (X = 0.40) conversions , S(HVY) too high at all $[9MA]_o$ and T,

R[DHMA/ANT] too high at all $[9MA]_o$ and T at low (X ~ 0.06) conversions and too

high for all $[9MA]_o$ and T at high (0.20 < X < 1.0) conversions, and

R[910DMA/ANT] too high at all $[9MA]_o$ and T at low (X ~ 0.06) conversions and

too high for all $[9MA]_o$ and T at high (X = 0.40) conversions.

A sensitivity analysis was performed to demonstrate how the errors of the

estimated thermochemical and activation parameters affected the model results at the central point of the 9MA experimental grid by separately perturbing the E^* of selected elementary reactions over the inherent errors in the ΔH°_r to show their effects on t^*, S(ANT), R[DHMA/ANT] and R[910DMA/ANT]. The variations of t^*_{mod}, R[DHMA/ANT]$_{mod}$ and R[910DMA/ANT]$_{mod}$ on account of the inherent errors in the estimated rate constants were large enough to exceed the span of experimental variations by changes in [9MA]$_o$ at $T = 370°C$ and in T at [9MA]$_o$ = 0.82 mol/l. The variation in ANT$_{mod}$ was not large enough to exceed the span of S(ANT)$_{exp}$ variations by changes in [9MA]$_o$ and T due to the stoichiometric limit on S(ANT) but the 2.2-fold difference between t^*_{mod} and t^*_{exp} is well within the 30-fold uncertainty in t^*_{mod}.

These activation parameters were then adjusted within the limits of the errors to provide the best fit to the experimental results. Results as obtained from the optimized numerical solution were compared to the thermolysis model to the experimental data for 9MA, ANT, 910DMA, CH4, DHMA, heavies, R[DHMA/ANT] and R[910DMA/ANT] at the center of the experimental grid. The model predicted 9MA decay within the experimental observations, S(ANT) and S(910DMA) are respectively 1.3 and 1.6-fold too low compared to the experimental observations (the mechanism as the upper limit of 0.33 for S(ANT) which was lower than the experimental values of S(ANT)), S(DHMA) and R[DHMA/ANT] had the correct values at low and high conversions but the slope of the line did not

593

correspond to the experimental data, S(HVY) was too 3-fold low at low X and comparable at X > 0.2, and R[910DMA/ANT] was approximately equal to that experimentally observed at low conversions and 3-fold too low at X = 0.40.

The observed formations of dimethylanthracene isomers 1,9-, 1,10-, 2,9- and 3,9-DMA from 9MA and of methylanthracene isomers 1MA and 2MA from ANT during 9MA thermolysis at high severities invited interpretation by frontier orbital theory, as examples of periselective methyl radical attack on the aromatic anthracene nucleus. The ratios R[(2,9- + 3,9-)DMA/(1,9- + 1,10-)DMA] and R[2MA/1MA] can both be viewed as the relative methyl affinities of positions 1 and 2 on the periphery of the anthracene ring, with methyl attack at position 2 less favored than at position 1 by a factor of 2 to 4 as seen experimentally.

For ANT positions 2, 1 and 9, FMO theory using both Hückel and PM3 MO calculations predicts CH3* attack favored in the order of positions 2 < 1 < 9, which accords with the experimentally observed minor product ratios R[2MA/1MA] ~ 0.4 for methylation of ANT. For 9MA positions 2, 3, 1, 4 and 10, FMO theory using PM3 MO calculations predicts CH3* attack favored in the order of positions (2, 3) < (1, 4) < 9. Methyl attack at position 2 leads to 2,9-DMA, at position 3 to 3,9-DMA, at position 1 to 1,9-DMA, at position 4 to 1,10-DMA and at position 10 to 9,10-DMA. The predicted inequality between positions (2, 3) and (1, 4) accords with the experimentally observed ratio R[(2,9- + 3,9-)DMA/(1,9- + 1,10-)DMA] ~ 0.23.

594

Chapter 7.

1,4-Dimethylnaphthalene Thermolysis

1,4-dimethylnaphthalene (14DMN) was thermolyzed at temperatures between 370 and 550°C, initial concentrations from 0.081 to 2.07 mol/l, and batch holding times from 150 to 115200 seconds. Figure 7.1 illustrates this experimental grid which, including replication, comprised 100 individual runs. Liquid reaction products were analyzed in every experiment and gaseous products were also analyzed in experiments with $[14DMN]_o$ = 0.87 mol/l and a temperature of 450°C. The product histories and selectivity diagrams of the individual runs were used to infer 14DMN thermolysis pathways. Reaction kinetics were determined from concentration scans at a fixed temperature, T = 450°C, which led to reaction order, and temperature
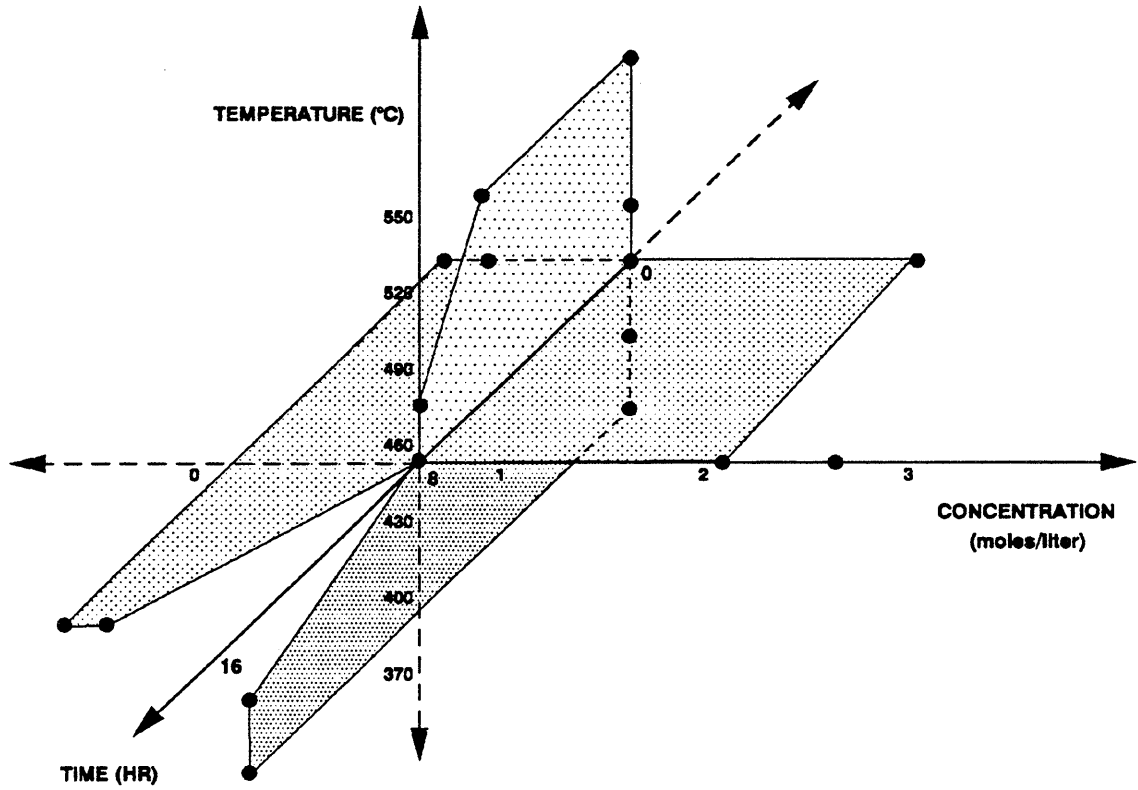
Figure 7.1: Grid for 14DMN thermolysis experiments.

596

scans at fixed initial concentration, $[14DMN]_o = 0.87$ mol/l, which led to activation parameters. An overall free-radical mechanism was proposed to account for 1,4-dimethylnaphthalene decomposition. Both the kinetics of the system and the observed product histories were modelled. Finally frontier molecular orbital theory was used to interpret the kinetics and minor product distributions.

7.1 Experimental Results

7.1.1 A Representative Example

Product formation histories and a corresponding selectivity diagram were derived from each set of experiments at a fixed temperature and constant initial 14DMN concentration. Figure 7.2, T = 450°C and $[14DMN]_o = 0.87$ mol/l, shows the histories of the major liquid products (top) and minor liquid products (bottom). The plot uses arithmetic coordinates of absolute substrate amounts J in the reactor in moles, versus reaction holding time t in seconds, with the appropriate, different, ordinal scales in the upper and lower panels; all data refer to fixed reactor volume $V = 0.60$ cm³. In the upper panel of Figure 7.2, the substrate 14DMN, symbol o, is seen to decay continuously from an initial J = 5.2E-04 moles to J = 1.0E-04 moles at t = 28800 s, the latter corresponding to a substrate fractional conversion X = 0.80; the decay half-life is $t^* \sim 17600$ s. The principal product, 1-methylnaphthalene, abbreviated 1MN with symbol ▢ increases from 0 initially to J = 2.2E-04 moles at t = 28800 s. The sum of all trimethylnaphthalenes, abbreviated ALL TMNs with

597
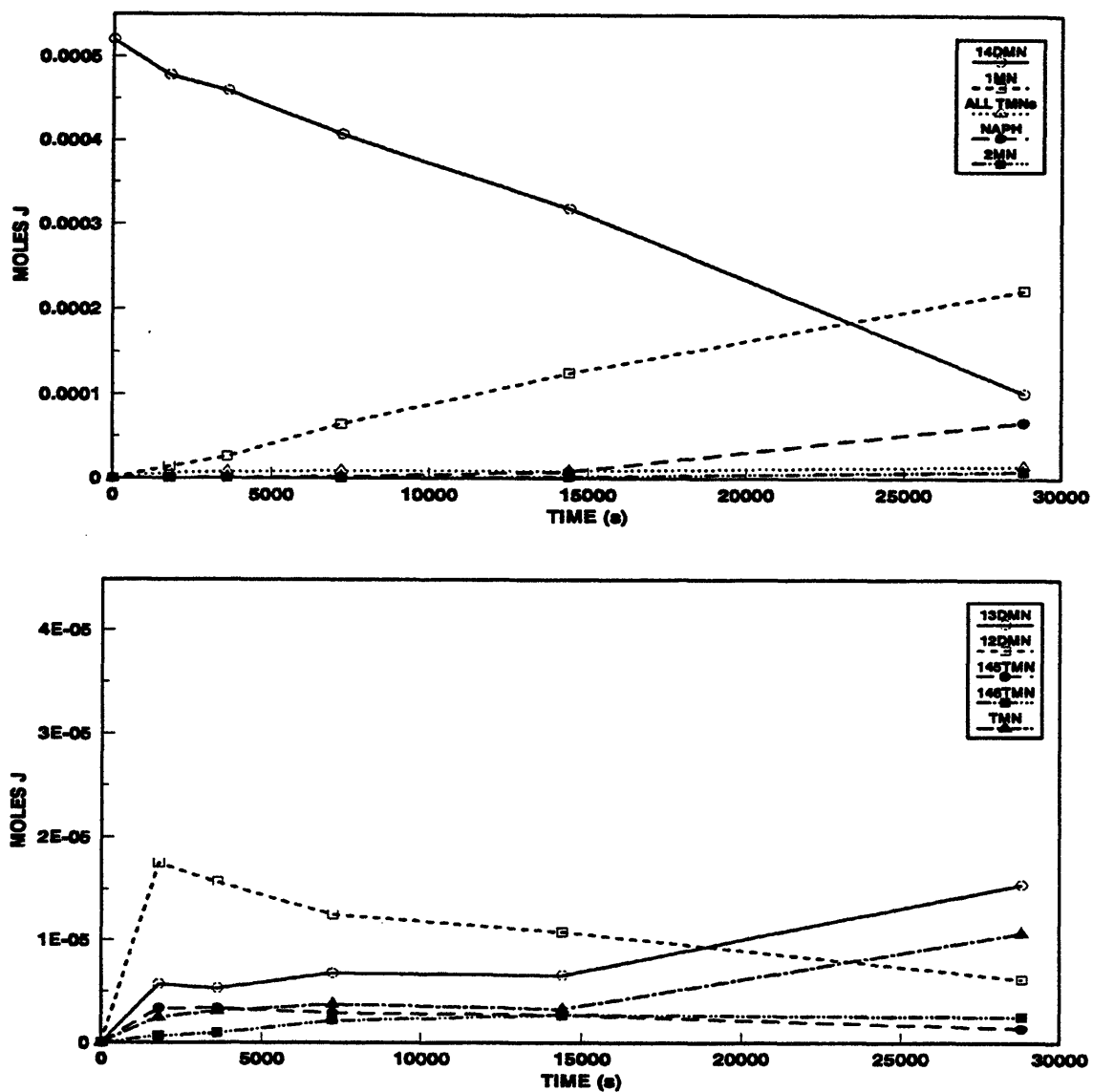
Figure 7.2: Product histories for 14DMN thermolysis at 450°C with [14DMN]$_o$ = 0.87 mol/l: major products (top) and minor products (bottom).

598

symbol Δ, grow from 0 initially to J = 1.5E-05 moles at t = 28800 s. The naphthalene, abbreviated NAP with symbol •, appears at t = 1800 s with J = 3.6E-07 moles, increases slowly to J = 7.9E-06 moles at t = 14400 s and then rising more quickly to J = 6.7E-05 moles at t = 28800 moles. The 2-methylnaphthalene, abbreviated 2MN with symbol ■, appears at t = 3600 s with J = 3.5E-07 moles, well after the first appearance of naphthalene, and increases to J = 8.7E-06 moles at t = 28800 s. The gaseous product methane was detected during the 14DMN thermolysis, but were not quantified. The substrate and major product histories in the present graph depict a classical series reaction series A(14DMN) → B(1MN) → C(NAP).

The bottom panel of Figure 7.2 shows the histories of several minor liquid products that are formed during 14DMN thermolysis, including dimethylnaphthalene and trimethylnaphthalenes isomers. Unlike with the dimethylanthracene isomers, of which some were discernable, the dimethylnaphthalene isomers elute very close to each other, as shown in Table 4.3. Some of the isomers actual co-elute; such as, 2,6-dimethylnaphthalene and 2,7-dimethylnaphthalene; 1,3-dimethylnaphthalene, 1,7-dimethylnaphthalene, and 1,6-dimethylnaphthalene; and 2,3-dimethylnaphthalene and 1,4-dimethylnaphthalene. After the 2,3-dimethylnaphthalene and 1,4-dimethylnaphthalene elute, the order of elution is 1,5-dimethylnaphthalene, 1,2-dimethylnaphthalene and 1,8-dimethylnaphthalene. Although 1,4-dimethylnaphthalene and 1,5-dimethylnaphthalene eluted sequentially, their boiling points are sufficiently close enough that resolution is not possible. The group of

isomers, 1,3-dimethylnaphthalene, 1,7-dimethylnaphthalene, and 1,6-dimethylnaphthalene, will be called 1,3-dimethylnaphthalene throughout the chapter, abbreviated 13DMN with symbol $\circ$, and appears at t = 1800 s with J = 5.7E-06 moles, remains roughly constant at J = 5.9 $\pm$ 0.6E-06 moles up to t = 14400 s and then rises to J = 1.6E-05 moles at t = 28800 s. 1,2-dimethylnaphthalene, abbreviated 12DMN with symbol $\square$, another of the dimethylnaphthalene isomers, arises at t = 1800 s with maximum J = 1.8E-05 moles and decreases to J = 6.2E-06 moles by the longest t = 28800 s. 1,4,5-trimethylnaphthalene, abbreviated 145TMN with symbol $\bullet$, one of the trimethylnaphthalenes identified by GC/MS, appears at t = 1800 s with maximum J = 3.4E-06 moles and decreases to amount J = 1.4E-06 moles at t = 28800 s. 1,4,6-trimethylnaphthalene, abbreviated 146TMN with symbol $\blacksquare$, another of the trimethylnaphthalene isomers identified by GC/MS, arises at t = 1800 s with J = 6.5E-07 moles, grows monotonically to a shallow maximum J = 2.7E-06 moles at t = 14400 s, and then decreases slightly to J = 2.6E-06 moles at t = 28800 s. Other TMN isomers other than those previously mentioned, abbreviated TMN with symbol $\blacktriangle$, appear at t = 1800 s with J = 2.5E-06 moles, increases slightly to J = 3.3E-06 moles at t = 14400 s and then increases sharper to J = 1.1E-05 moles at t = 28800 s.

The data in Figure 7.2 are displayed as selectivity diagrams in Figure 7.3, using ordinates of selectivity, S, defined as moles of product formed divided by moles of substrate 14DMN reacted, and an abscissae of substrate 14DMN fractional
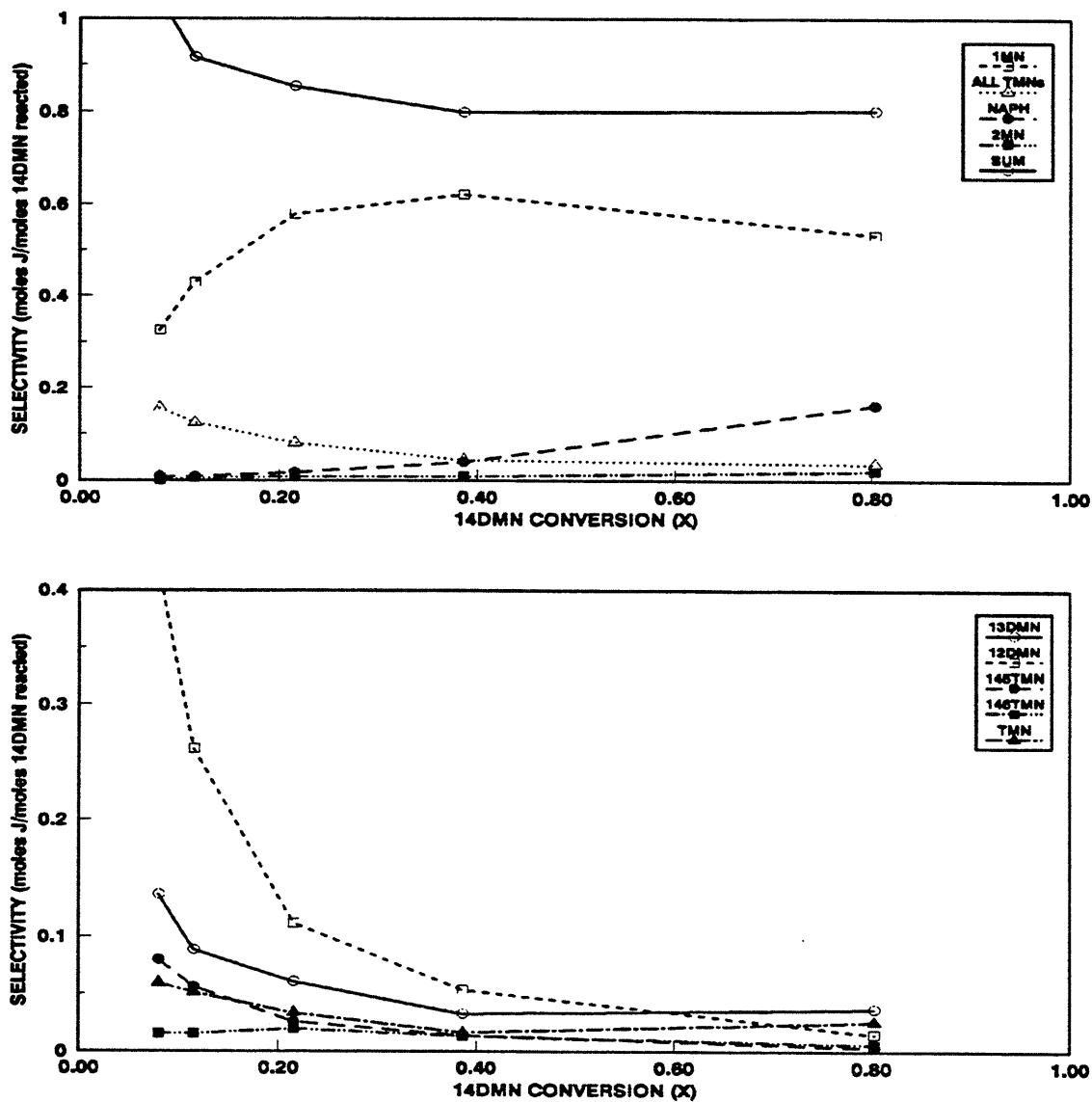
Figure 7.3: Selectivity diagram for 14DMN thermolysis at 450°C with [14DMN]$_o$ = 0.87 mol/l: major products (top) and minor products (bottom).

conversion, X. The upper and lower panels of Figure 7.3 respectively display the major liquid product selectivities and the minor liquid product selectivities obtained for 14DMN thermolysis at T = 450°C and $[14DMN]_o$ = 0.87 mol/l. In the upper panel of Figure 7.3, the selectivity to 1MN, symbol □, is S = 0.33 at X = 0.081, then increases slightly S = 0.58 ± 0.05 for 0.22 < X < 0.80. The 14DMN used in the thermolysis was 95% pure, with major impurities of 12DMN, 1MN, and 13DMN. This impurity gave the high initial selectivities seen for the impurities. For 1MN, more 1MN is formed as the 14DMN decomposed, therefore the overall increase in S(1MN) is seen. The selectivity to ALL TMNs, symbol ▲, appears with maximum S = 0.15 at X = 0.081 and decreases to S = 0.035 at X = 0.80. NAP, symbol •, starts with S = 0.0085 at X = 0.081 and rises to S = 0.16 by X = 0.80. The isomer 2MN, symbol ■, appears with S = 0.0058 at X = 0.12 and increases to S = 0.021 at X = 0.80. The sum of the selectivities of all identified products, Σ, abbreviated SUM with symbol ○, decreases sharply from Σ ~ 1 at X = 0.081 to Σ = 0.83 ± 0.03 for 0.22 < X < 0.80. The impurities in the 14DMN substrate contributed to an initial selectivity sum greater than 1.

In the bottom panel of Figure 7.3, showing minor liquid product selectivities, 13DMN, symbol ○, appears at X = 0.081 with maximum S = 0.14, decreases slowly to S = 0.061 at X = 0.22 and then remains roughly constant at S = 0.037 to X = 0.80. 12DMN selectivity, symbol □, appears at X = 0.081 with maximum S = 0.42, decreases sharply to S = 0.11 at X = 0.22 and then decreases slower to S = 0.015

at X = 0.80. Once again, the 13DMN and 12DMN impurities in the 14DMN substrate contributed to the high selectivities at low X. The overall decrease in S(13DMN) and S(12DMN) indicated that these compounds decayed faster than they were formed. 145TMN, symbol •, appears at X = 0.081 with S = 0.08 and decreases to S = 0.0034 at X = 0.80. 146TMN, symbol ■, appears with S = 0.017 ± 0.003 for 0.081 < X < 39 and then decreases to S = 0.0061 at X = 0.80. Other TMN selectivity, symbol ▲, is S = 0.059 at X = 0.081 and decreases to S = 0.021 ± 0.005 for 0.39 < X < 0.80.

The preceding selectivity diagrams show that 1MN and ALL TMNs, with respective S ~ 0.60 and 0.10, as well as NAP with S = 0.01, are among the earliest products observed during 14DMN thermolysis. Due to the impurities of 1MN, 13DMN and 12DMN in the substrate 14DMN, it was not apparent that the pair of minor products 13DMN and 12DMN were observed after the appearance of 1MN, suggesting that they were from methylation of 1MN, rather than from isomerization of the substrate 14DMN, but 2MN was observed only after the appearance of NAP, suggesting it arises from the methylation of NAP, rather than from isomerization of 1MN. Therefore, it can be expected that other DMNs arose of methylation of the monomethylnaphthalenes instead of isomerization of the 14DMN, 13DMN and 12DMN that were present for the start of the thermolysis.

Reaction pathways corresponding to the product histories and selectivities can now be elaborated as a basic demethylation sequence A(14DMN) → B(1MN) →

603

C(NAP), with competing, parallel methylation pathways at each stage. For example, at the first stage, A(14DMN) → MeA(TMN), followed by B(1MN) → MeB(12DMN and 13DMN) at the second and C(NAP) → MeC(1MN and 2MN) at the third step.

All subsequent 14DMN results are discussed using the plots and symbols presented in the preceding example.

7.1.2. Effect of Initial 1,4-Dimethylnaphthalene Concentration

Initial 1,4-dimethylnaphthalene concentration was varied in three steps from 0.081 to 2.07 mol/l at fixed reaction temperature T = 450°C; this is represented by the horizontal plane of the experimental grid in Figure 7.1.

Figure 7.4 shows substrate and product histories at T = 450°C and $[14DMN]_0$ = 0.081 mol/l. In the upper panel of Figure 7.4, the moles of substrate 14DMN decrease from the initial J = 4.9E-05 moles to J = 3.1E-05 moles at t = 57600 s; the decay half-life is t^* ~ 115000 s. The amount of 1MN increases monotonically but with decreasing slope from 0 initially to J = 8.0E-06 moles at t = 28800 s and then to J = 1.3E-05 moles at t = 57600 s. A small amount of NAP, J = 1.2E-06 moles is detected at the longest t = 57600 s. In the lower panel of Figure 7.4, 13DMN is detected at t = 7200 s with J = 1.5E-06 moles and increases monotonically to J = 3.5E-06 moles at t = 57600 s. 12DMN is detected at t = 3600 s with J = 1.1E-06 moles, increases to J = 2.3E-03 moles at t = 7200 s, remains at this level until t =
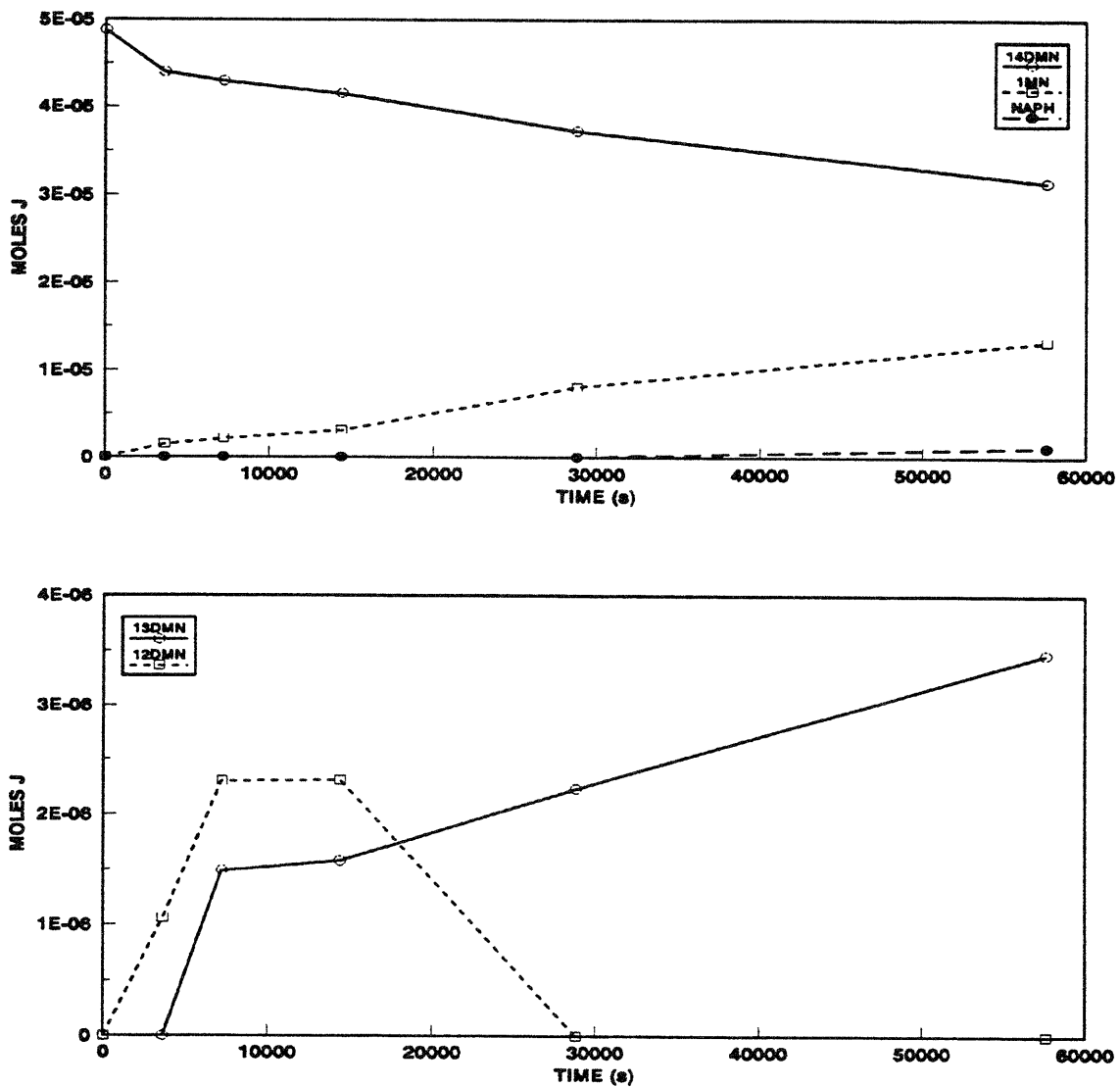
Figure 7.4: Product histories for 14DMN thermolysis at 450°C with $[14DMN]_o$ = 0.081 mol/l: major products (top) and minor products (bottom).

14400 s and then decreases to J = 0 at t = 28800 s.

Figure 7.5 is a selectivity diagram corresponding to the data in Figure 7.4. The upper panel of Figure 7.5, the selectivity to 1MN is S = 0.31 at X = 0.099, increases to S = 0.70 at X = 0.24 and rises slower to S = 0.76 at X = 0.36. NAP selectivity is S = 0.067 at X = 0.36. The selectivities sum is Σ = 0.53 at X = 0.099, rises sharply and then remains roughly constant at Σ = 0.96 ± 0.07 for 0.12 < X < 0.36. In the lower panel of Figure 7.5, 13DMN selectivity is S = 0.26 at X = 0.12, which then decreases and remains roughly constant at S = 0.21 ± 0.02 for 0.15 < X < 0.36. 12DMN is detected with S = 0.22 at X = 0.099, remains roughly constant at S = 0.36 ± 0.04 for 0.12 < X < 0.15 and then declines to S = 0 by X = 0.24.

Figure 7.6 shows the substrate and product histories at T = 450°C and $[14DMN]_o$ = 0.24 mol/l. In the upper panel of Figure 7.6, the moles of substrate 14DMN decay monotonically from the initial J = 1.5E-04 moles to J = 7.5E-05 moles at t = 57600 s; the decay half-life is t^* = 51000 s. The 1MN product grows from 0 initially to J = 4.9E-05 moles at t = 57600 s. ALL TMNs are first detected at t = 7200 s with J = 9.4E-07 moles and decrease to J = 5.3 ± 0.6E-07 moles for 14400 < t < 57600 s. NAP is detected at t = 28800 s with J = 1.4E-06 moles and increases to J = 5.9E-06 moles at t = 57600 s. 2MN is detected at t = 14400 s with J = 3.3E-07 moles and rises monotonically to J = 8.3E-06 moles at t= 57600 s. In the lower panel of Figure 7.6, 13DMN is detected with J = 1.6E-06 moles at t = 3600 s and rises slowly to J = 3.5E-06 moles at t = 57600 s. 12DMN is detected at
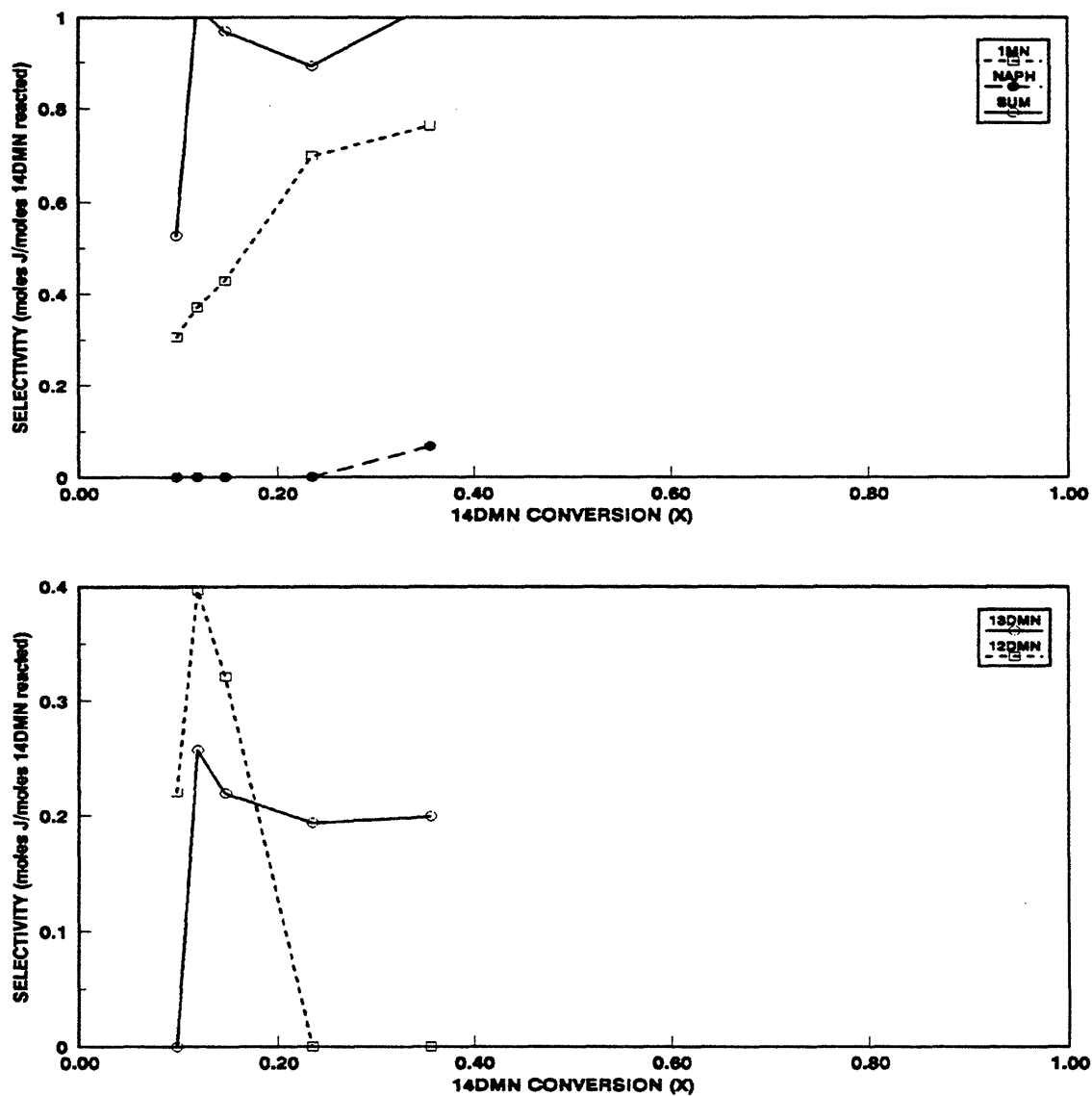
Figure 7.5: Selectivity diagram for 14DMN thermolysis at 450°C with [14DMN]$_o$ = 0.081 mol/l: major products (top) and minor products (bottom).

607
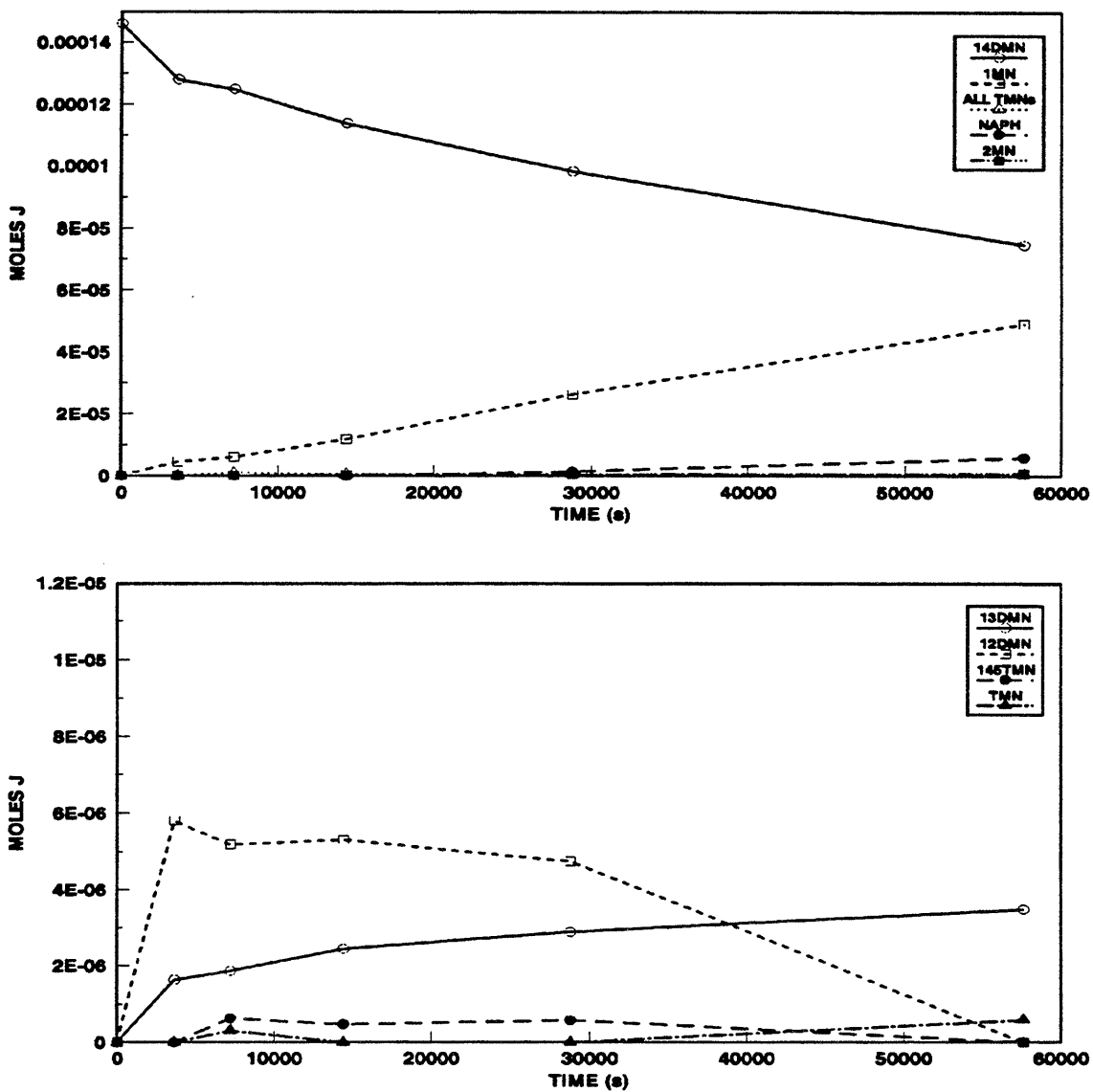
Figure 7.6: Product histories for 14DMN thermolysis at 450°C with $[14DMN]_o$ = 0.24 mol/l: major products (top) and minor products (bottom).

t = 3600 s with J = 5.8E-06 moles, decreases slowly to J = 4.8E-06 moles at t = 28800 s and then more rapidly to J = 0 by t = 57600 s. 145TMN is detected at t = 7200 s with J = 6.3E-07 moles, remains roughly constant with J = 5.6 ± 0.07E-07 moles for 7200 < t < 28800 s and declines to J = 0 at t = 57600 s. TMN is detected at t = 7200 s with J = 3.1E-07 moles, decreases to J = 0 for 14400 < t < 28800 s and reappears with J = 5.7E-07 moles at t = 57600 s.

Figure 7.7 is a selectivity diagram corresponding to the data in Figure 7.6. In the upper panel of Figure 7.7, 1MN exhibits selectivity S = 0.25 at X = 0.13 and increases to S = 0.69 at X = 0.49. ALL TMNs appear with S = 0.045 at X = 0.14 and decrease to S = 0.0082 at X = 0.49. NAP appears with S = 0.030 at X = 0.33 and increases to S = 0.083 at X = 0.49. 2MN is detected at X = 0.22 with selectivity S = 0.010 and climbs to S = 0.012 at X = 0.49. The selectivity sum remains roughly constant at Σ = 0.65 ± 0.02 for 0.13 < X < 0.22 followed by an increase to Σ = 0.84 at X = 0.49. In the lower panel of Figure 7.7, 13DMN selectivity appears with a maximum S = 0.090 at X = 0.13 and then declines to S = 0.049 at X = 0.49. 12DMN selectivity at X = 0.13 a maximum of S = 0.32, which decreases to S = 0.10 at X = 0.33 and then to S = 0 at X = 0.49. 145TMN emerges at X = 0.14 with S = 0.030, decreases to S = 0.012 at X = 0.33 and then to S = 0
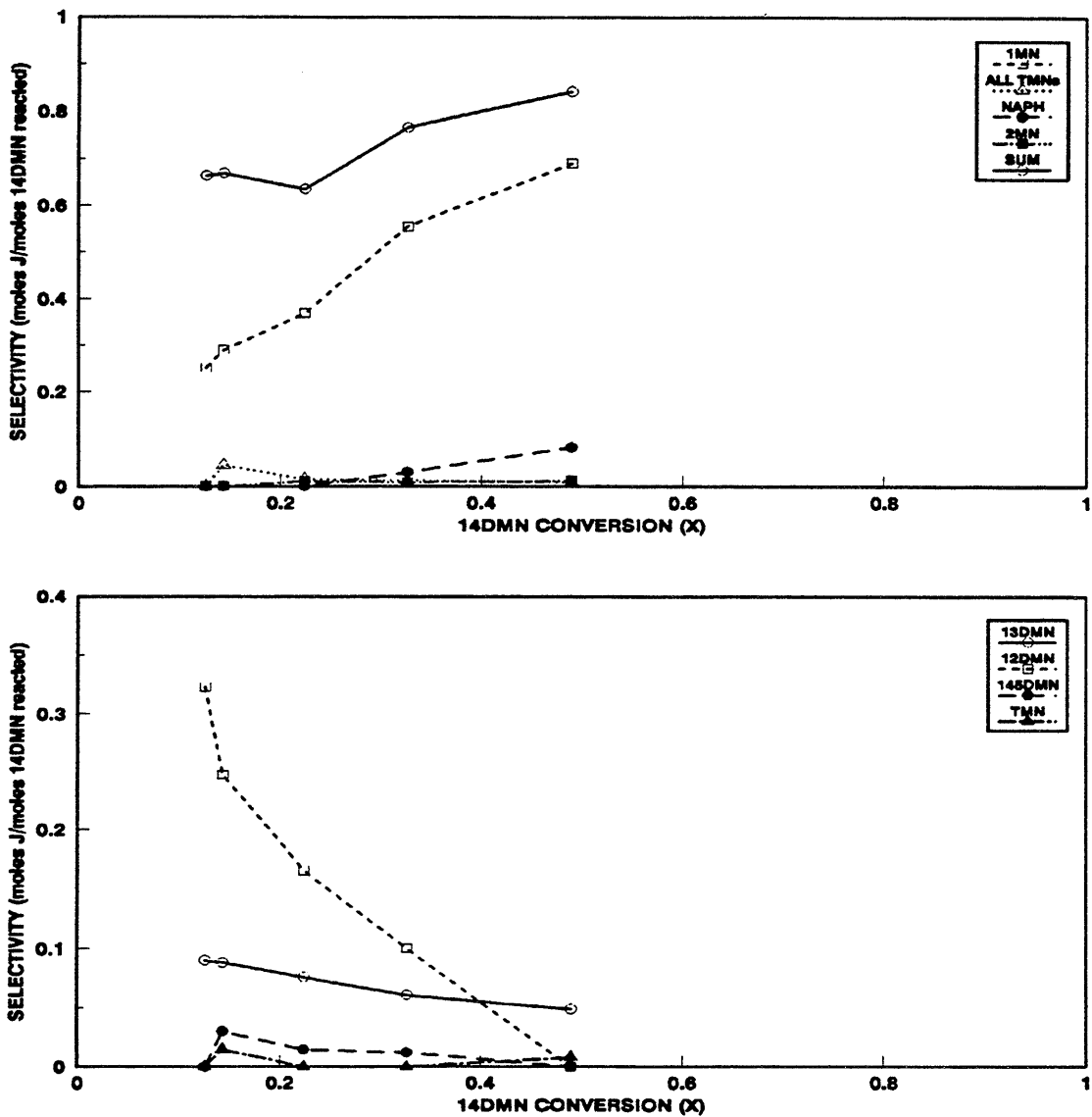
Figure 7.7: Selectivity diagrams for 14DMN thermolysis at 450°C with [14DMN]$_o$ = 0.24 mol/l: major products (top) and minor products (bottom).

by X = 0.49. Other TMN selectivity at X = 0.14 is S = 0.015 and at X = 0.49 is S = 0.0082.

Figure 7.8 shows substrate and product at T = 450°C and $[14DMN]_o$ = 2.07 mol/l. In the upper panel of Figure 7.8, the moles of substrate 14DMN decay from J = 1.2E-03 moles initially to J = 4.0E-04 moles at t = 7200 s, and then more slowly to J = 8.7E-05 moles at t = 28800 s; the decay half-life is t* ~ 5000 s. 1MN appears at the earliest time of t = 1800 s with J = 9.8E-05 moles, grows to a shallow maximum of J = 4.0E-04 moles at t = 14400 s and then declines to J = 3.8E-04 moles at t = 57600 s. The sum of ALL TMNs is J = 3.5E-05 moles at t = 1800 s, grows to a maximum J = 7.0E-05 moles at t = 7200 s and then declines to J = 4.3E-05 moles at t = 28800 s. NAP is also detected at t = 1800 s with J = 1.3E-06 moles and rises monotonically to J = 2.3E-04 moles at t = 28800 s. 2MN is detected at t = 1800 s with J = 1.5E-06 moles and rises to J = 7.5E-05 moles at t = 28800 s. In the lower panel of Figure 7.8, 13DMN appears at t = 1800 s with J = 2.6E-05 moles, grows to maximum J = 8.6 ± 0.3E-05 moles for 7200 < t < 14400 s and then declines slightly to J = 7.5E-05 moles at t = 28800 s. 12DMN appears at t = 1800 s with J = 1.7E-05 moles and decreases monotonically to J = 8.5E-06 moles at t = 28800 s. 2,6-dimethylnaphthalene, abbreviated 26DMN with symbol ▲, is detected at t = 3600 s with J = 1.7E-06 moles and rises to J = 9.6E-06 moles at t = 28800 s. 145TMN is detected at t = 1800 s with J = 5.8E-06 moles, rises to maximum J = 6.4E-06 moles at t = 3600 s and then decreases to J = 3.3 ± 0.5E-06 moles for
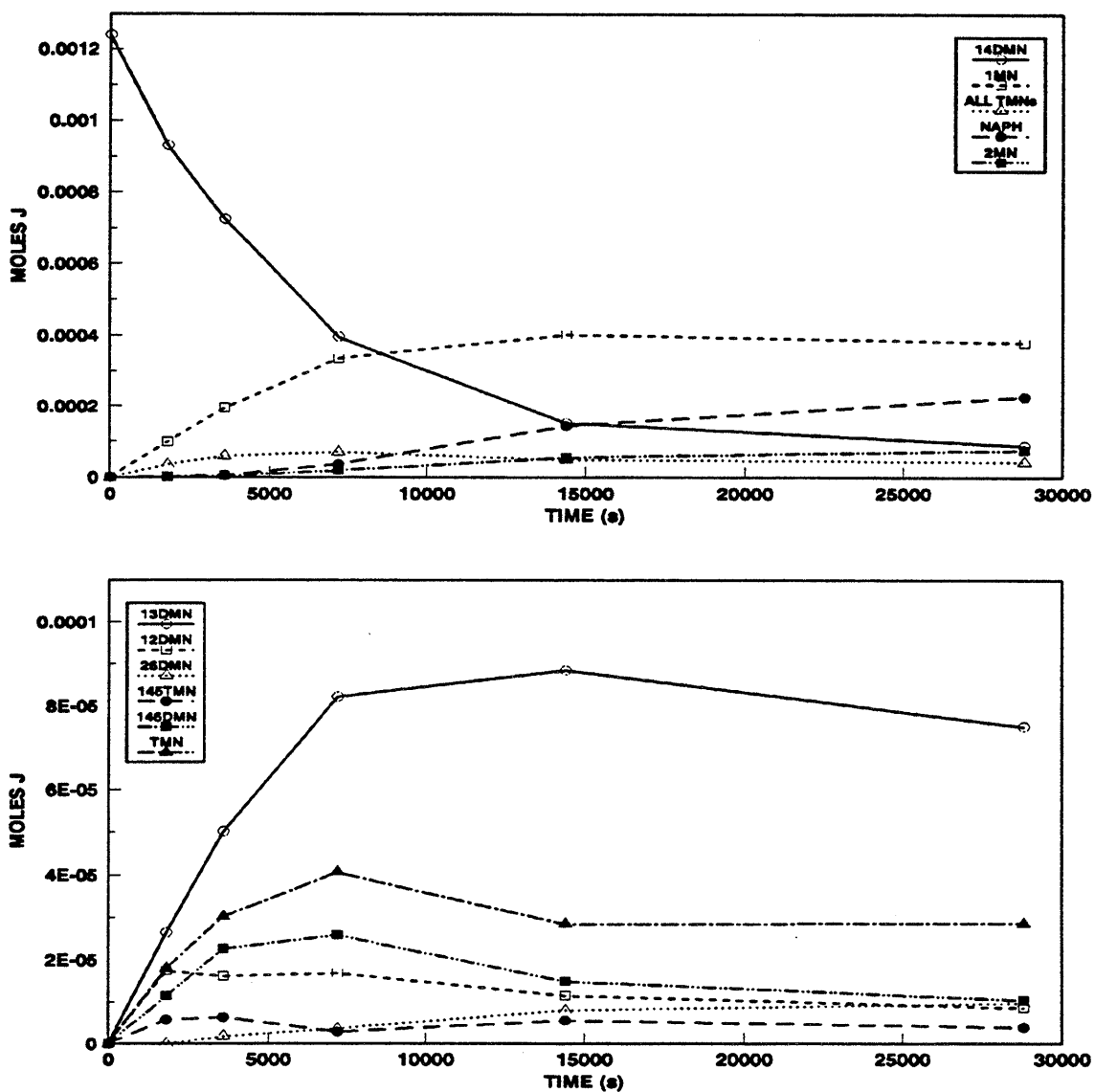
Figure 7.8: Product histories for 14DMN thermolysis at 450°C with $[14DMN]_o$ = 2.07 mol/l: major products (top) and minor products (bottom).

7200 < t < 28800 s. 146TMN appears at t = 1800 s with J = 1.1E-05 moles, increase to maximum J = 2.6E-05 moles at t = 7200 s, and then decreases to J = 1.0E-05 moles at t = 28800 s. TMN appears at t = 1800 s with J = 1.8E-05 moles, grows to maximum J = 4.1E-05 moles at t = 7200 s, declines to J = 2.9E-06 moles at t = 14400 s, and remains roughly constant up to t = 28800 s.

Figure 7.9 is a selectivity diagram corresponding to the data in Figure 7.8. In the upper panel of Figure 7.9, 1MN selectivity is S = 0.32 at X = 0.25 and remains roughly constant at S = 0.36 ± 0.04 for 0.25 < X < 0.93. ALL TMNs are detected with S = 0.11 at X = 0.25, remain at this level up to X = 0.41 and the decrease to S = 0.037 at X = 0.93. NAP selectivity is S = 0.0042 at X = 0.25, increases slowly to S = 0.043 at X = 0.68 and then increases sharper to S = 0.20 at X = 0.93. 2MN appears with S = 0.0050 at X = 0.25 and increases monotonically to S = 0.065 at X = 0.93. The selectivity sum is Σ = 0.58 at X = 0.25 rises slightly and remains roughly constant Σ = 0.68 ± 0.03 for 0.41 < X < 0.93. In the lower panel of Figure 7.9, 13DMN is detected at X = 0.25 with S = 0.085, remains constant with S = 0.097 ± 0.001 for 0.41 < X < 0.68 and then declines to S = 0.065 at X = 0.93. 12DMN selectivity is S = 0.056 at X = 0.25 and decreases monotonically to S = 0.0074 at X = 0.93. 26DMN selectivity is S = 0.0034 at X = 0.41 and grows monotonically to S = 0.0083 at X = 0.93. 145TMN selectivity is a maximum S = 0.019 at X = 0.25 and declines to S = 0.0034 by X = 0.93. 146TMN selectivity increases from S = 0.037 at X = 0.25 to S = 0.044 at X = 0.41 and then decreases
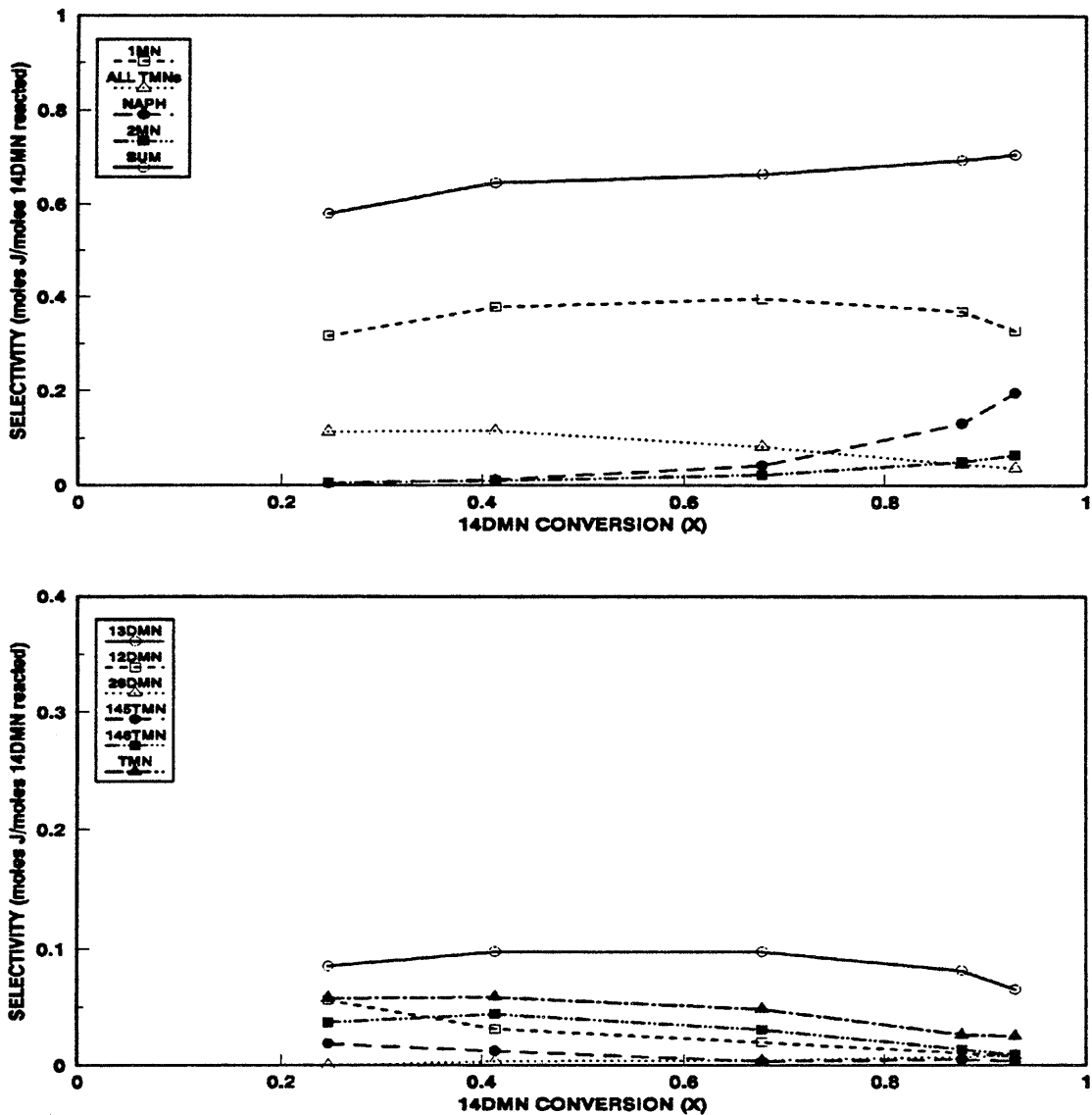
Figure 7.9:   Selectivity diagrams for 14DMN thermolysis at 450°C with [14DMN]$_o$ = 2.07 mol/l: major products (top) and minor products (bottom).

to S = 0.0090 at X = 0.93. TMN appears with S = 0.058 at both X = 0.25 and 0.41 and decreases to S = 0.025 at X = 0.93.

7.1.3 Summary of Concentration Effects

Increasing initial substrate concentration from $[14DMN]_o$ = 0.081 to 2.07 mol/l at fixed T = 450°C influences both the reaction kinetics and product selectivities, as summarized in Table 7.1 and Table 7.2. Note that values in the tables are the averages over all runs, including replication and are therefore not precisely identical to those seen in the preceding figures. Part (a) of Table 7.1 shows that the substrate decay half-life t^* decreased about 22-fold, from 115000 to 5000 s, as initial concentration $[14DMN]_o$ increased 25-fold, from 0.081 to 2.07 mol/l. Figure 7.10, a doubly logarithmic plot of t^* vs. $[14DMN]_o$, shows that the data adhere to a line:

$$\log t^* = -1.05 \log[14DMN]_o + 4.09 \tag{7.1}$$

for $[14DMN]_o$ = 0.24 - 2.07 mol/l. The slope of this line, ~ -1.05, implies that 14DMN decomposition is 2nd order in substrate. Also, the intercept of the line shows the rate constant at T = 450°C to be $\log k_2$ = -4.08, by reference to the

Table 7.1

EFFECT OF INITIAL 14DMN CONCENTRATION ON KINETIC PARAMETERS AT T = 450°C

Part		$[14DMN]_o$ (mol/l)			
		0.081	0.24	0.87	2.07
a	Half-life t^*, s	115293^1 $\pm$ 26078^2	50877 $\pm$ 8901	17572 $\pm$ 744	5111 $\pm$ 362
b	$[1MN/14DMN]_{tmax}$				2.64
	t_{max}/t^*				2.82

[1]   Half-life calculated using X at longest t and integrated 2nd order rate expression: $t^* = t(1-X)/X$

[2] $\pm$ = standard deviation of the average half-life

Table 7.2

EFFECT OF INITIAL 14DMN CONCENTRATION ON PRODUCT SELECTIVITIES AT T = 450°C

Part	Selectivity S of:	Conversion X Range:	[14DMN]$_o$ (mol/l)			
			0.081[1]	0.24	0.87	2.07
a	1MN	0.2 - 0.8	0.74	0.62	0.60	0.36
	ALL TMNs	0.2 - 0.8	ND	0.012	0.052	0.099
b	NAP	0.35 ± 0.03	0.067	0.038	0.039	0.009
	2MN	0.35 ± 0.03	ND	0.007	0.009	0.007
	13DMN	0.10 ± 0.02	0.26	0.09	0.14	ND
		0.2 - 0.8	0.20	0.056	0.043	0.084
	12DMN	0.10 ± 0.02	0.40	0.32	0.42	ND
		0.2 - 0.8	0	0.069	0.043	0.037
	26DMN	0.2 - 0.8	ND	ND	ND	0.003
	145TMN	0.10 ± 0.02	ND	0.039	0.080	ND
		0.2 - 0.8	ND	0.012	0.017	0.013
	146TMN	0.10 ± 0.02	ND	ND	0.032	ND
		0.2 - 0.8	ND	0.007	0.015	0.036
	other TMNs	0.10 ± 0.02	ND	0.022	0.059	ND
		0.2 - 0.8	ND	0.010	0.021	0.050

[1] For [14DMN]$_o$ = 0.081 mol/l, range for X = 0.20 - 0.35
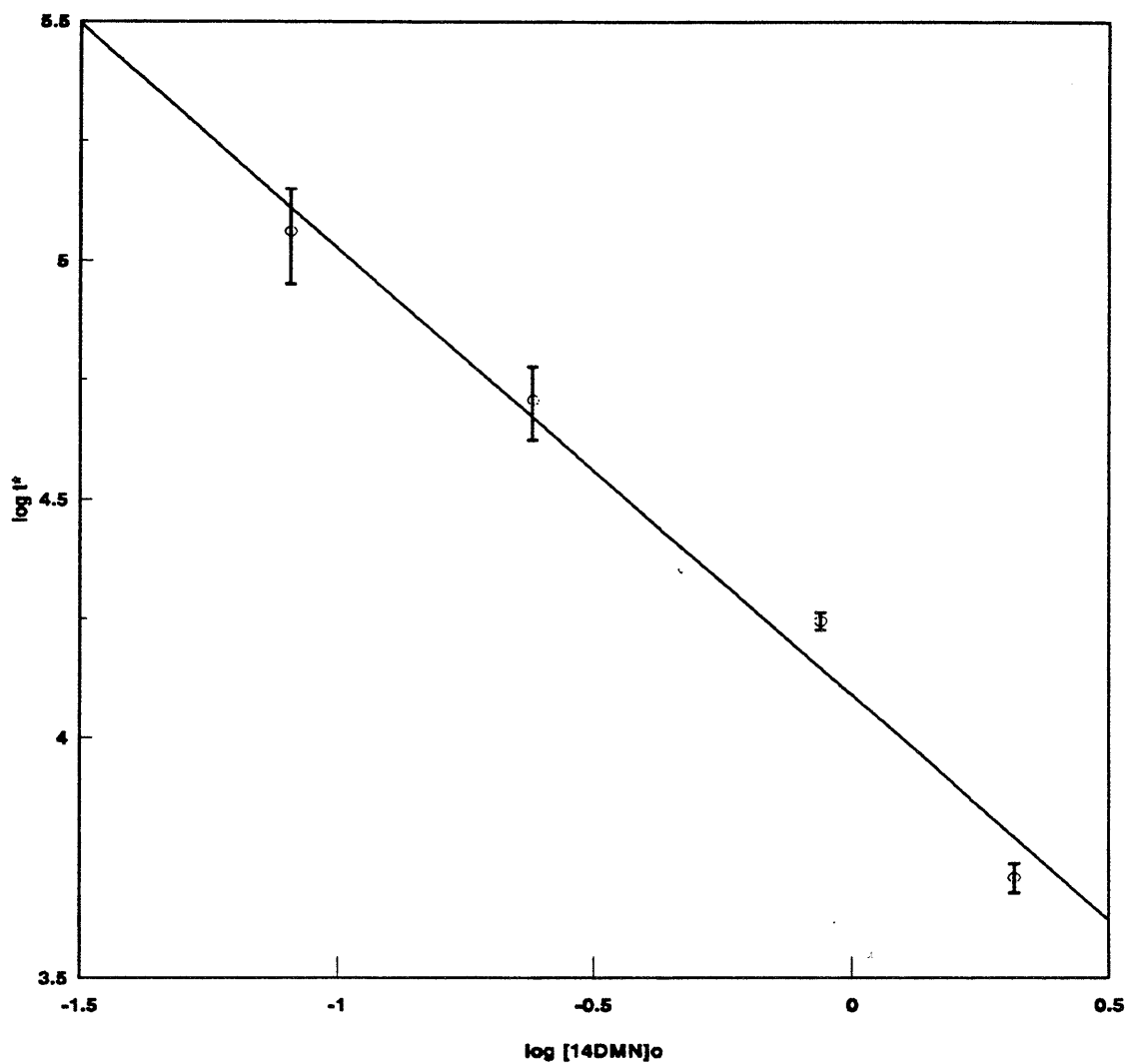
Figure 7.10: Decay half-life t^* for varying initial concentrations $[14DMN]_o$ at fixed $T = 450°C$.

integrated 2nd-order rate expression:

$$\frac{1}{[14DMN]_t} - \frac{1}{[14DMN]_o} = k_2\, t \tag{7.2}$$

Product histories at $[14DMN]_o = 2.07$ mol/l, shown in Figure 7.8, also provide an indication of the relative kinetics of the parallel reactions:

$$14DMN \xrightarrow{k_1} 1MN \xrightarrow{k_2} NAP \tag{7.3}$$

If 1MN attains its maximum concentration $[1MN]_{max}$ at time t_{max} in the figure, then, as shown in part (b) of Table 7.1, the ratio $[1MN/14DMN]t_{max} \sim 2.6$ and $[t_{max}/t^*] \sim 2.8$ both imply that 1MN decomposes more slowly than 14DMN. If both decompositions are presumed to be of the same 2nd order in their respective substrates, then we can estimate the rate constant ratio $(k_1/k_2) = [1MN/14DMN]_{tmax}^2 \sim 10.2$.

Turning to product selectivities, summarized in Table 7.2, both 1MN and sum of ALL TMNs selectivities were roughly independent of conversion over the ranges $0.2 < X < 0.8$ at all initial concentrations, as shown in part (a) of Table 7.2. The absolute values of S(1MN) decreased with increasing $[14DMN]_o$, from $S \sim 0.74$ at $[14DMN]_o = 0.081$ mol/l to $S \sim 0.36$ at $[14DMN]_o = 2.07$ mol/l, while S(ALL TMNs) increased with increasing $[14DMN]_o$, from $S \sim 0.012$ at $[14DMN]_o = 0.24$ mol/l to $S \sim 0.099$ at $[14DMN]_o = 2.07$ mol/l. Naphthalene and 2MN selectivities increased monotonically from 0 as conversions increased for all initial concentrations,

as shown in part (b) of Table 7.2. S(NAP) and S(2MN) generally increased with increasing X at all $[14DMN]_0$, with S(NAP) > S(2MN) always. S(NAP) decreased from 0.067 to 0.009 at X = 0.35 ± 0.03 for $[14DMN]_0$ increasing from 0.081 to 2.07 mol/l. S(2MN) = 0.008 ± 0.001 at X = 0.35 ± 0.03 for 0.24 < $[14DMN]_0$ < 2.07 mol/l. The other dimethylnaphthalenes, 13DMN and 12DMN, selectivities generally started at their maximum values at low conversions, decreased sharply by X ~ 0.20 and then slowly declined for all initial concentrations, as shown in part (b) of Table 7.2, while 26DMN only appeared at the highest [14DMN] = 2.07 mol/l. Of the dimethylated species, the order of abundance was generally S(12DMN) > S(13DMN) > S(26DMN). The absolute values of S(13DMN), S(12DMN), and S(26DMN) remained roughly constant with increasing $[14DMN]_0$ for 0.2 < X < 0.8. S(13DMN) = 0.17 ± 0.08 at X = 0.10 ± 0.02 for 0.081 < $[14DMN]_0$ < 0.87 mol/l and decreases to S(13DMN) = 0.20 for 0.2 < X < 0.35 for $[14DMN]_0$ = 0.081 mol/l and S(13DMN) = 0.064 ± 0.020 for 0.2 < X < 0.8 for 0.24 < $[14DMN]_0$ < 2.07 mol/l. S(12DMN) = 0.37 ± 0.05 at X = 0.10 ± 0.02 for 0.081 < $[14DMN]_0$ < 0.87 mol/l and decreases to S(12DMN) = 0 for 0.2 < X < 0.35 for $[14DMN]_0$ = 0.081 mol/l and S(12DMN) = 0.053 ± 0.016 for 0.2 < X < 0.8 for 0.24 < $[14DMN]_0$ < 2.07 mol/l. S(26DMN) = 0.003 for 0.2 < X < 0.8 for $[14DMN]_0$ = 2.07 mol/l. The trimethylnaphthalenes, 145TMN, 146TMN and other TMNs, selectivities generally started at their maximum values at low conversions, decreased sharply by X ~ 0.20 and then slowly declined for all initial concentrations, as shown in part (b) of

Table 7.2. Of the trimethylated species, the order of abundance was generally S(TMN) > S(146TMN) > S(145TMN). The absolute values of S(146TMN), S(145TMN), and S(TMN) remained roughly constant with increasing $[14DMN]_o$ for $0.2 < X < 0.8$. S(146TMN) = 0.032 at X = 0.10 ± 0.02 for $[14DMN]_o$ = 0.87 mol/l and decreases to S(146TMN) = 0.022 ± 0.015 for $0.2 < X < 0.8$ for $0.24 < [14DMN]_o < 2.07$ mol/l. S(145TMN) = 0.060 ± 0.020 at X = 0.10 ± 0.02 for $0.24 < [14DMN]_o < 0.87$ mol/l and decreases to S(145TMN) = 0.015 ± 0.003 for $0.2 < X < 0.8$ for $0.24 < [14DMN]_o < 2.07$ mol/l. S(TMN) = 0.041 ± 0.019 for $0.2 < X < 0.8$ for $0.24 < [14DMN]_o < 0.87$ mol/l and decreases to S(TMN) = 0.030 ± 0.020 for $0.2 < X < 0.8$ for $0.24 < [14DMN]_o < 2.07$ mol/l.

Finally, Figure 7.11, Figure 7.12 and Figure 7.13 depict the variation of certain product ratios, namely R[NAP/1MN], R[Σ minor DMNs/1MN] and R[2MN/NAP], versus 14DMN conversion X at all initial substrate concentrations. In Figure 7.11, it is seen that for all experiments, the ratio of NAP to 1MN, R[NAP/1MN], is essentially a function of conversion only, with data for all initial concentrations, $0.081 < [14DMN]_o < 2.07$ mol/l, lying on roughly the same curve. This curve shows an exponential relationship that implicitly describes the kinetics of 14DMN demethylation under the present conditions. In Figure 7.12, it is seen that, for all experiments at X < 0.20, the ratio of minor dimethylated species to 1MN, R[Σminor DMNs/1MN], is essentially a function of conversion only, with data for all initial concentrations, $0.081 < [14DMN]_o < 2.07$ mol/l, lying on roughly the same curve.
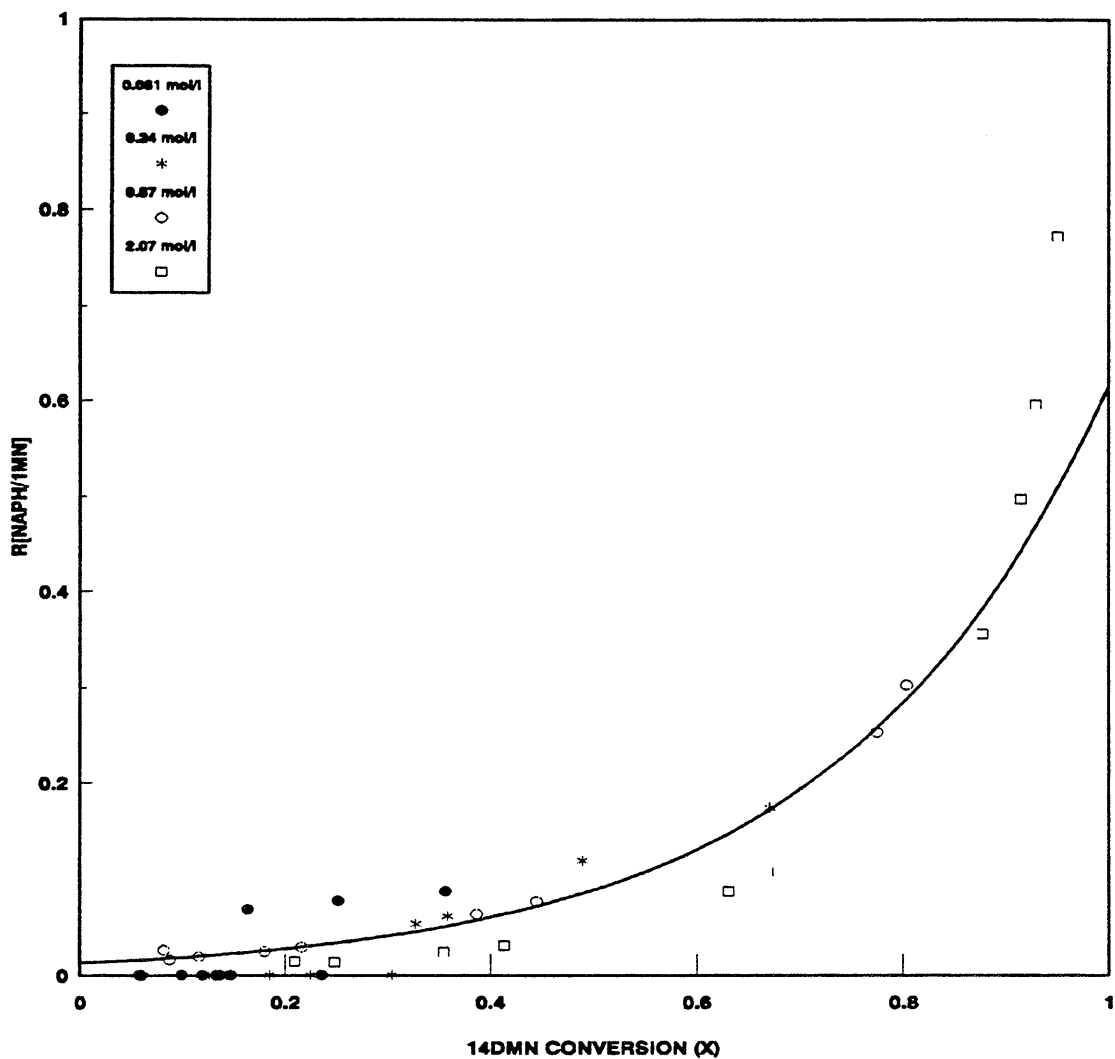
Figure 7.11: Ratio of moles NAP to moles 1MN produced vs. 14DMN conversion (X) for varying $[14DMN]_o$ at fixed T = 450°C.

622
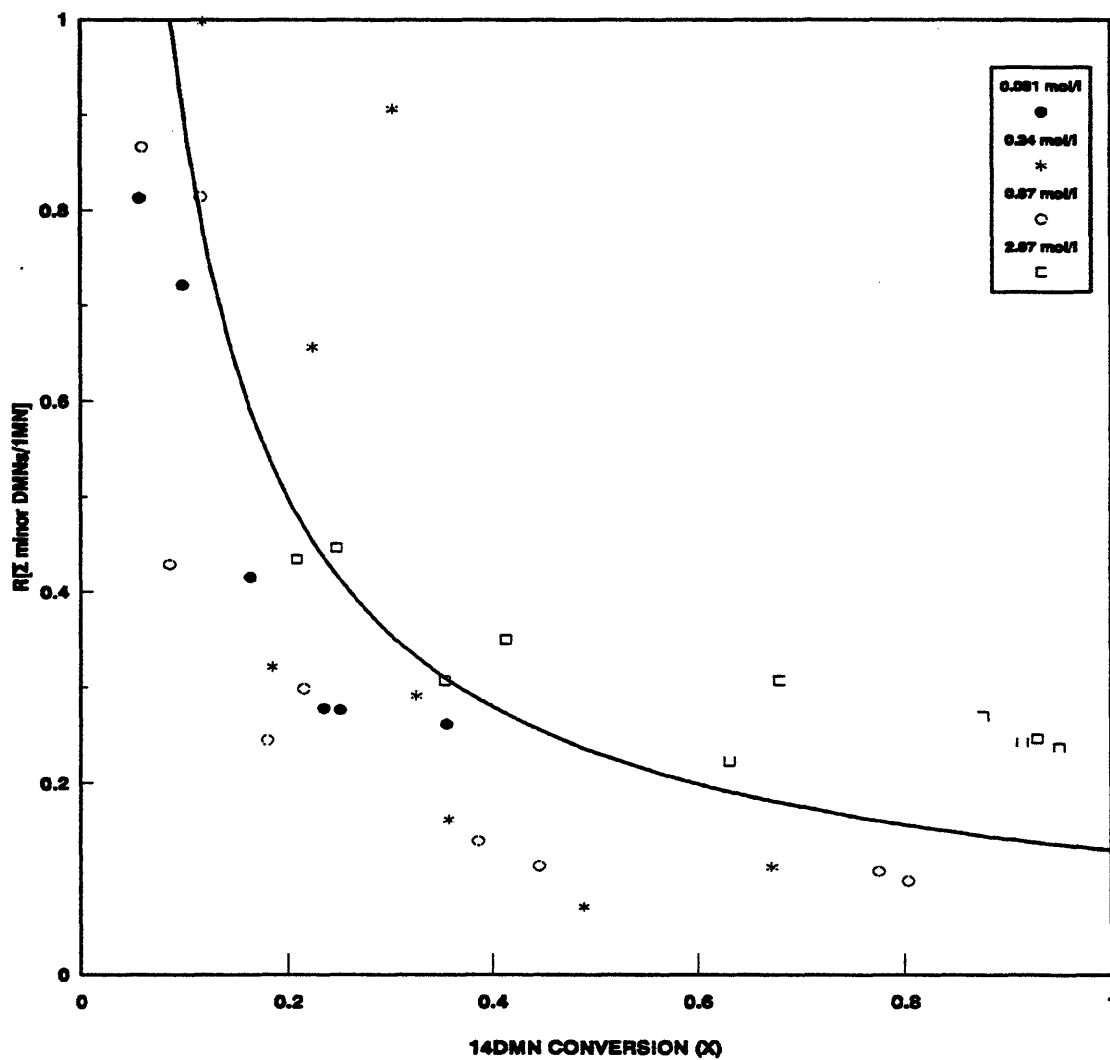
Figure 7.12: Ratio of moles Σ minor DMNs to moles 1MN produced vs. 14DMN conversion (X) for varying $[14DMN]_o$ at fixed T = 450°C.

623
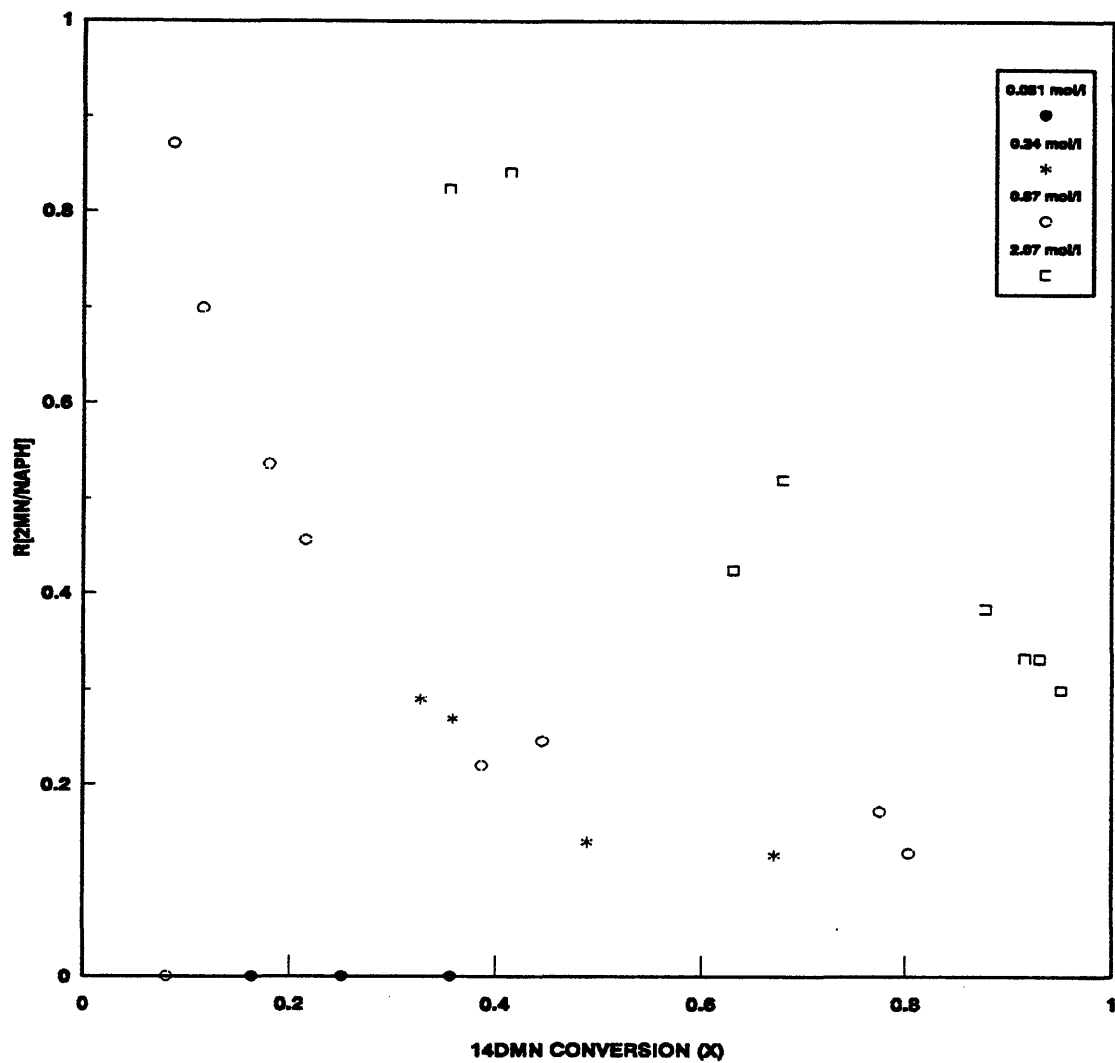
Figure 7.13: Ratio of moles 2MN to moles NAP produced vs. 14DMN conversion (X) for varying $[14DMN]_o$ at fixed T = 450°C.

At X < 0.20, the impurities of 1MN, 13DMN and 12DMN from the 14DMN substrate disallow consideration of the R[Σminor DMNs/1MN] yet by X = 0.20, the levels should have attained the same level as if the initial impurities did not exist. Implicit in this relationship are the kinetics of 1MN methylation during thermolysis of the 14DMN substrate under the present conditions. Similarly, Figure 7.13 shows that for all experiments, the ratio of monomethylated species 2MN to NAP, R[2MN/NAP], is essentially a function of conversion only, with data for initial concentrations, 0.081 < $[14DMN]_o$ < 0.87 mol/l, lying on roughly the same curve and the $[14DMN]_o$ = 2.07 mol/l lying on a different curve. These curves are both exponential relationships that implicitly describes the kinetics of NAP methylation during thermolysis of the 14DMN substrate under the present conditions.

7.1.4. Effect of Temperature

Temperature was varied from 370 to 550°C at a fixed initial concentration of $[14DMN]_o$ = 0.87 M, with these experiments represented by the vertical plane of the grid in Figure 7.1.

Figure 7.14 shows substrate and product histories at T = 370°C and $[14DMN]_o$ = 0.87 M. In the upper panel of Figure 7.14, the moles of substrate 14DMN decay from the initial J = 5.2E-04 moles to J = 4.4E-04 moles at t = 115200 s; the decay half-life t^* ∼ 530000 s. 1MN grows monotonically from 0 initially to J = 2.6E-05 moles at t = 115200 s. ALL TMNs are first detected at t = 7200 s with J = 4.5E-06
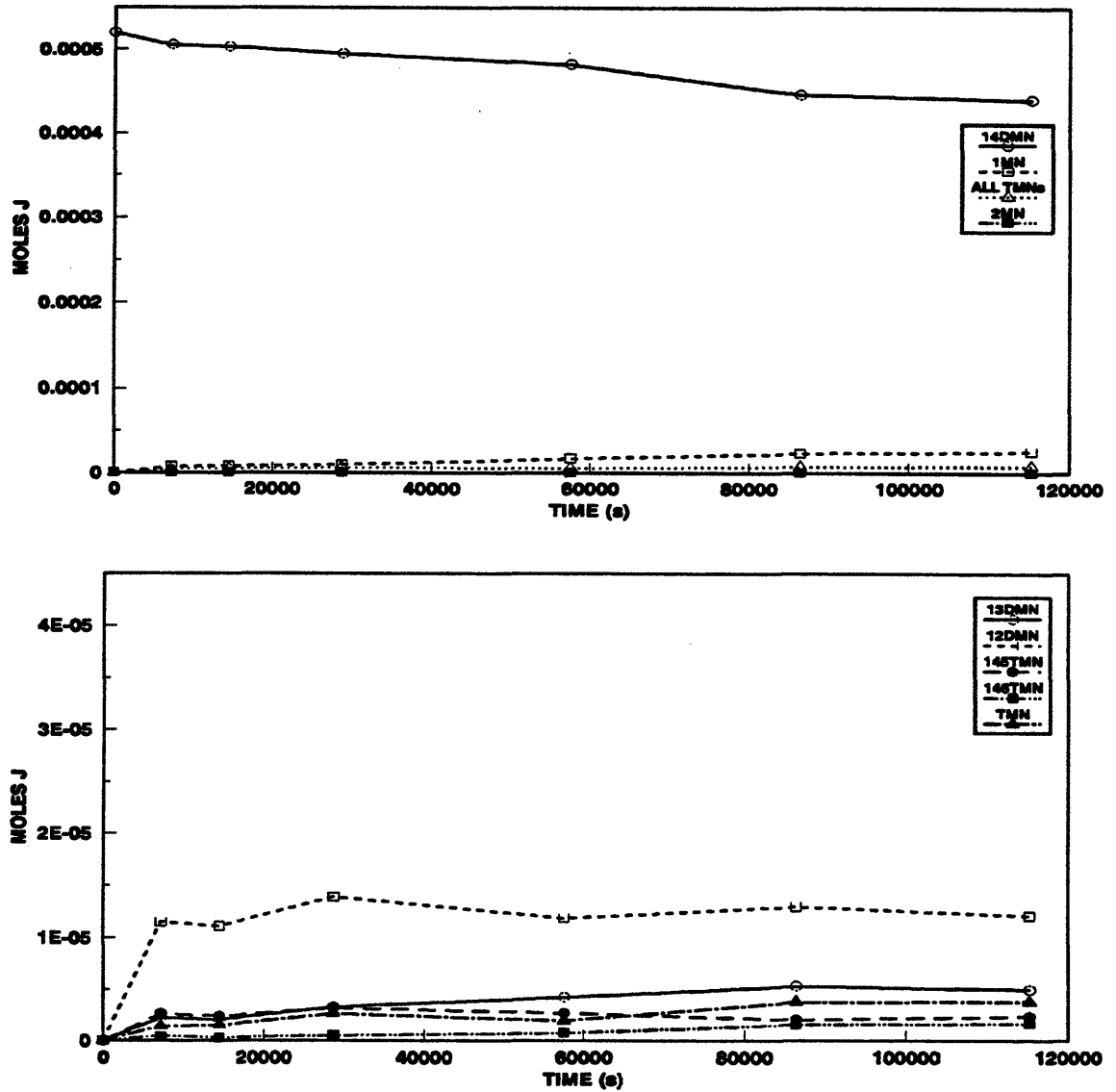
Figure 7.14: Product histories for 14DMN thermolysis at 370°C with [14DMN]$_o$ = 0.87 mol/l: major products (top) and minor products (bottom).

moles and increase to J = 7.9E-06 moles at t = 115200 s. 2MN is only detect at the

longest t = 115200 s with J = 3.42E-07 moles. In the lower panel of Figure 7.14,

13DMN is detected at t = 7200 s with J = 2.2E-06 moles and increases slightly to

J = 5.0E-06 moles by t = 115200 s. 12DMN is detected at t = 7200 s with J = 1.2E-

05 moles and remains roughly constant at J = 1.3 ± 0.01E-05 moles for 7200 < t <

115200 s. 145TMN appears at t = 7200 s with J = 2.6E-06 moles and remains

roughly constant at J = 2.6 ± 0.6E-06 moles for 7200 < t < 115200 s. 146TMN

arises at t = 7200 s with J = 4.6E-07 moles and increases to J = 1.7E-06 moles at

t = 115200 s. TMN is detected at t = 7200 s with J = 1.4E-06 moles and increases

to J = 3.8E-06 moles at t = 115200 s.

Figure 7.15 is a selectivity diagram corresponding the data in Figure 7.14. In

the upper panel of Figure 7.15, 1MN and ALL TMNs selectivities are S = 0.49 and

0.30, respectively, at X = 0.030 and decrease to S = 0.32 and 0.010 at X = 0.15.

2MN selectivity is S = 0.0043 at X = 0.15. The selectivity sum decreases from Σ ~

1 at X = 0.030 to Σ = 0.64 at X = 0.15. In the lower panel of Figure 7.15, 13DMN

selectivity is S = 0.15 at X = 0.030 and decreases to S = 0.063 at X = 0.15.

12DMN is detected at X = 0.030 with S = 0.77 and decreases sharply to S = 0.15

at X = 0.15. 145TMN appears at X = 0.030 with S = 0.18 and decreases to S =

0.030 at X = 0.15. 146TMN is detected at X = 0.030 with S = 0.031, decreases and

remains roughly constant at S = 0.020 ± 0.002 for 0.033 < X < 0.15. TMN arises
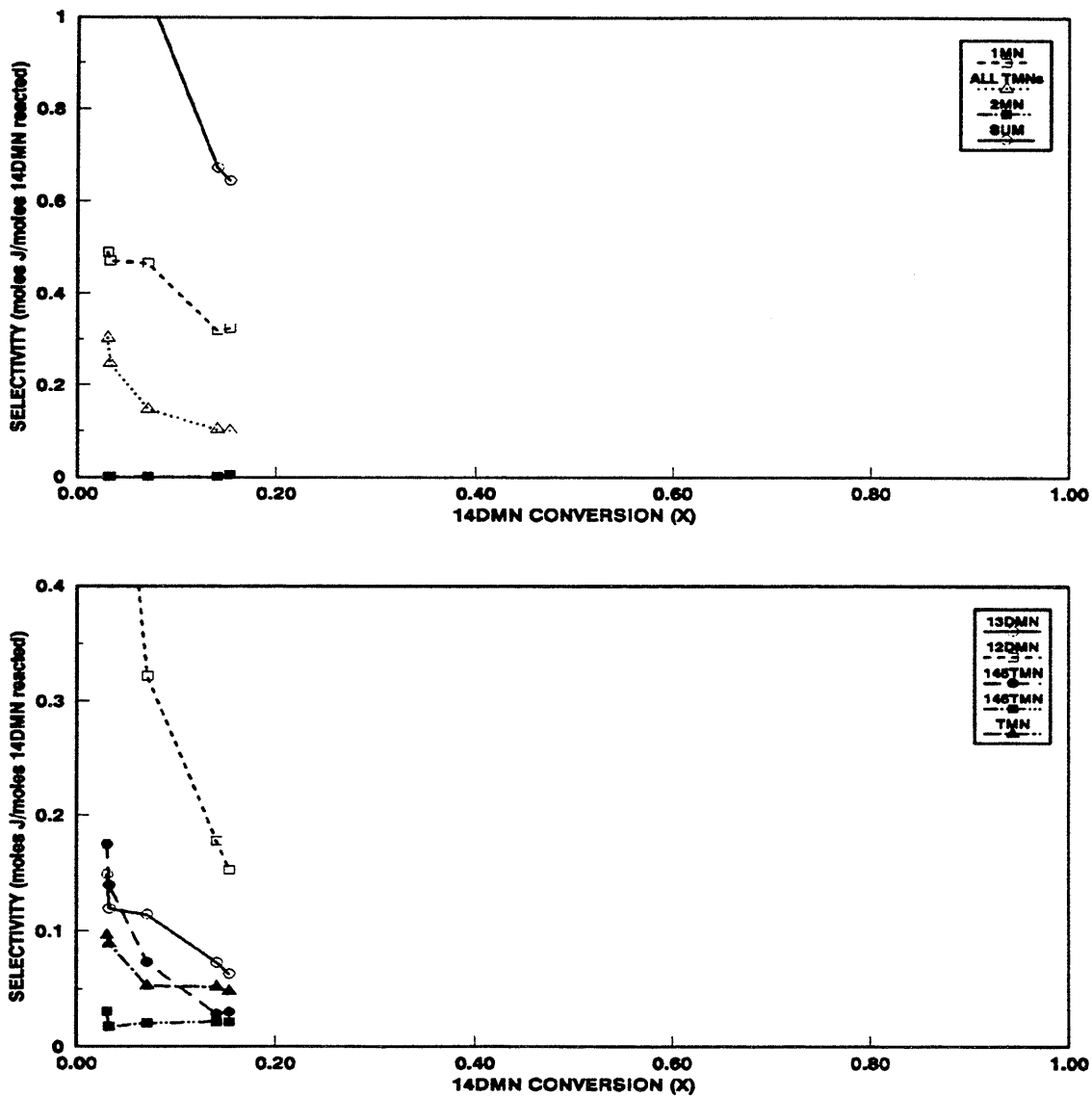
Figure 7.15: Selectivity diagrams for 14DMN thermolysis at 370°C with $[14DMN]_o$ = 0.87 mol/l: major products (top) and minor products (bottom).

at X = 0.030 with S = 0.096, decreases and remains roughly constant at S = 0.050 ± 0.002 for 0.071 < X < 0.15.

Figure 7.16 shows substrate and product histories at T = 409°C and [14DMN]$_0$ = 0.87 M. In the upper panel of Figure 7.16, the moles of substrate 14DMN decay from J = 5.2E-04 moles initially to J = 3.0E-04 moles at t = 57600 s, the decay half-life t* ~ 71500 s. 1MN increases monotonically from 0 initially to J = 1.2E-04 moles at t = 57600 s. ALL TMNs increase from J = 5.3E-06 moles at t = 3600 s to J = 2.5E-05 moles at t = 57600 s. NAP and 2MN are first detected at t = 14400 s with J = 5.1E-07 and 4.3E-07 moles, respectively, and increase to J = 7.2E-06 and 2.9E-06 moles at t = 57600 s. In the lower panel of Figure 7.16, 13DMN appears at t = 3600 s with J = 4.9E-06 moles and increases to J = 2.0E-05 moles at t = 57600 s. 12DMN appears at t = 3600 s with J = 1.4E-05 moles, decreases to J = 7.3E-06 moles at t =14400 s and remains roughly constant at J = 7.8 ± 0.5E-06 moles for 14400 < t < 57600 s. 26DMN is detected only at the longest t = 57600 s with J = 2.9E-06 moles. 145TMN appears at t = 3600 s with J = 2.4E-06 moles and remains roughly constant at J = 2.5 ± 0.4E-06 moles for 3600 < t < 57600 s. 146TMN appears with J = 5.3E-07 moles at t = 3600 s and increases to J = 9.0E-06 moles at t = 57600. Other TMNs are detected at t = 3600 s with J = 2.3E-06 moles and increase to J = 1.4E-05 moles at t = 57600 s.

Figure 7.17 is a selectivity diagram corresponding to the data in Figure 7.16. In the upper panel of Figure 7.17, 1MN selectivity is S = 0.35 at X = 0.060,
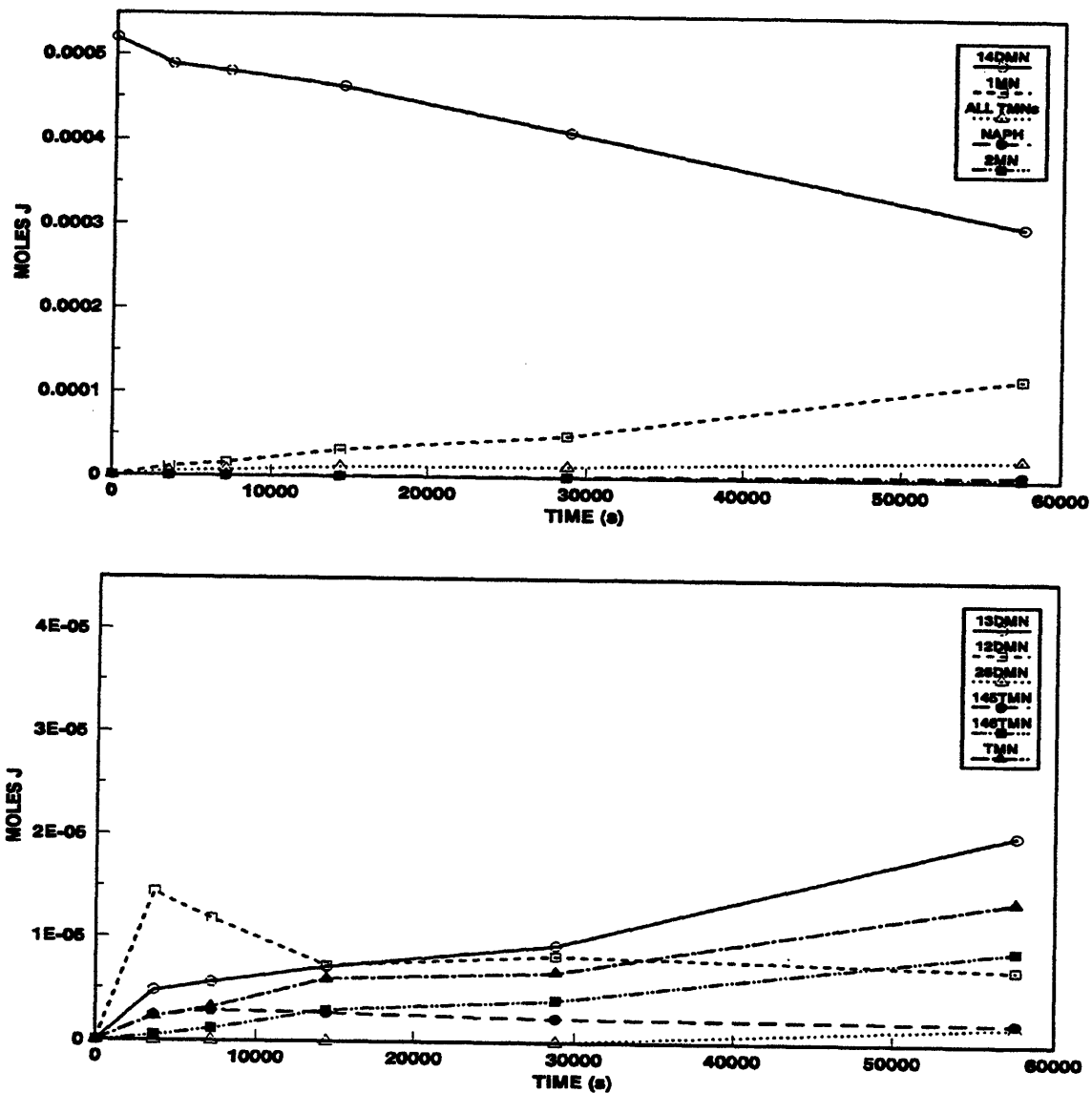
Figure 7.16: Product histories for 14DMN thermolysis at 409°C with $[14DMN]_o$ = 0.87 mol/l: major products (top) and minor products (bottom).
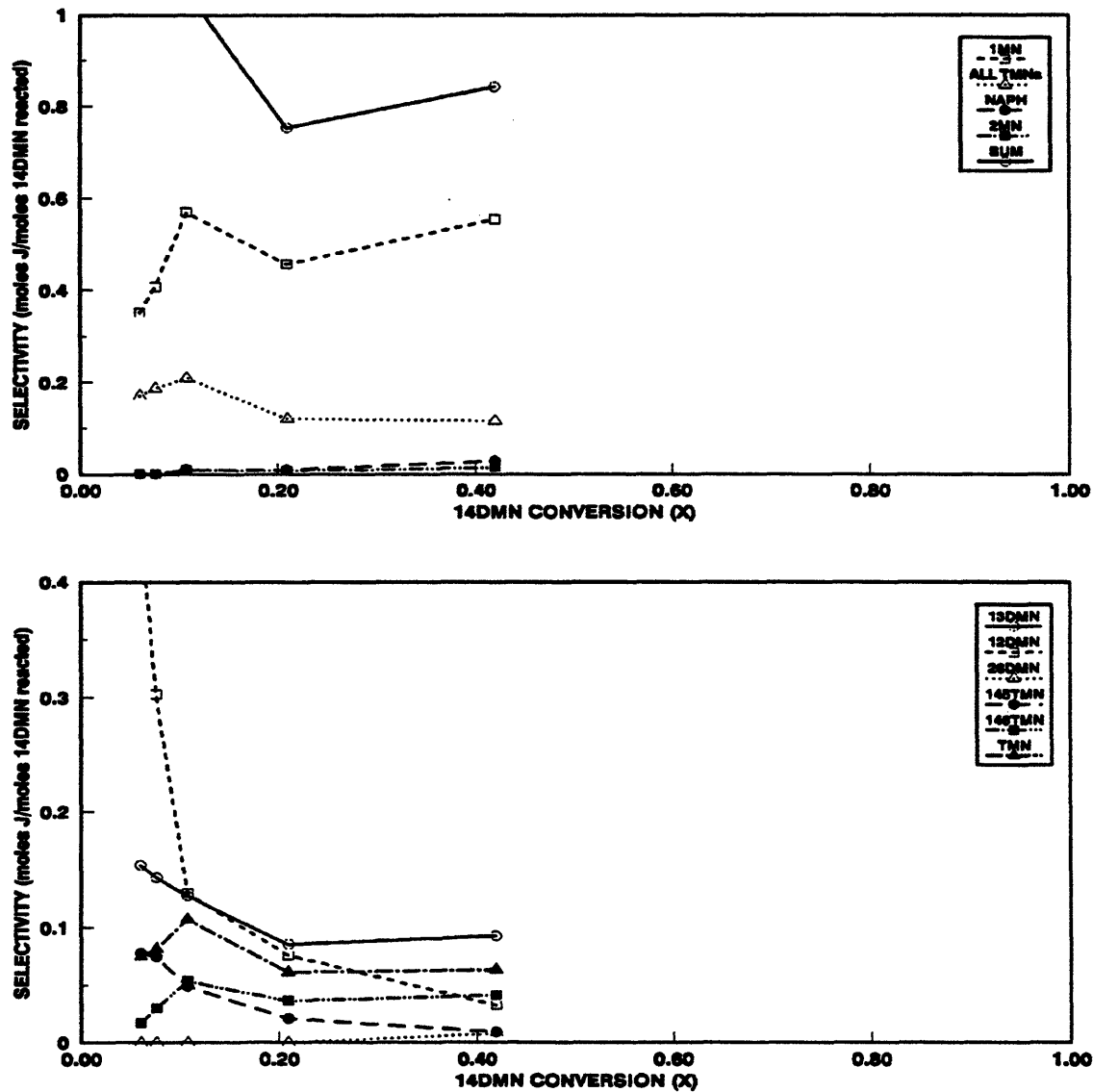
Figure 7.17: Selectivity diagrams for 14DMN thermolysis at 409°C with [14DMN]$_o$ = 0.87 mol/l: major products (top) and minor products (bottom).

increases and remains roughly constant at S = 0.51 ± 0.06 for 0.11 < X < 0.42. ALL TMNs appear with S = 0.17 at X = 0.060, increase slightly to S = 0.21 at X = 0.11 and decline to S = 0.12 for 0.21 < X < 0.42. NAP increases from S = 0.0090 at X = 0.11 to S = 0.028 at X = 0.42. 2MN appears at X = 0.11 with S = 0.0077 and increases to S = 0.013 to X = 0.42. The selectivity sum is a maximum Σ = 1.1 at X = 0.060, decreases sharply to Σ = 0.75 at X = 0.21 and remains constant up to X = 0.42. In the lower panel of Figure 7.17, 13DMN appears with S = 0.15 at X = 0.060, decreases to S = 0.085 at X = 0.21 and remains roughly constant at S = 0.092 up to X = 0.42. 12DMN is detected with S = 0.47 at X = 0.060, decreases sharply to S = 0.13 at X = 0.11 and then slower to S = 0.033 at X = 0.42. 26DMN selectivity S = 0.0079 at X = 0.42. 145TMN is detected with S = 0.078 at X = 0.060 and decreases to S = 0.0094 at X = 0.42. 146TMN appears at X = 0.060 with S = 0.017, decreases and remains roughly constant at S = 0.042 ± 0.012 for 0.076 < X < 0.42. Other TMNs appear at X = 0.060 with S = 0.075 and remain roughly constant at S = 0.081 ± 0.020 up to X = 0.42.

Figure 7.2, which was in Section 7.1.1 as the representative example, shows substrate and product histories at T = 450°C and $[14DMN]_o$ = 0.87 M. Figure 7.3, also in Section 7.1.1, is a selectivity diagram corresponding to the data in Figure 7.2. As with the previous case, refer to Section 7.1.1 for the description of both figures.

Figure 7.18 shows substrate and product histories at T = 500°C and $[14DMN]_o$ = 0.87 M. In the upper panel of Figure 7.18, the moles of substrate 14DMN decay
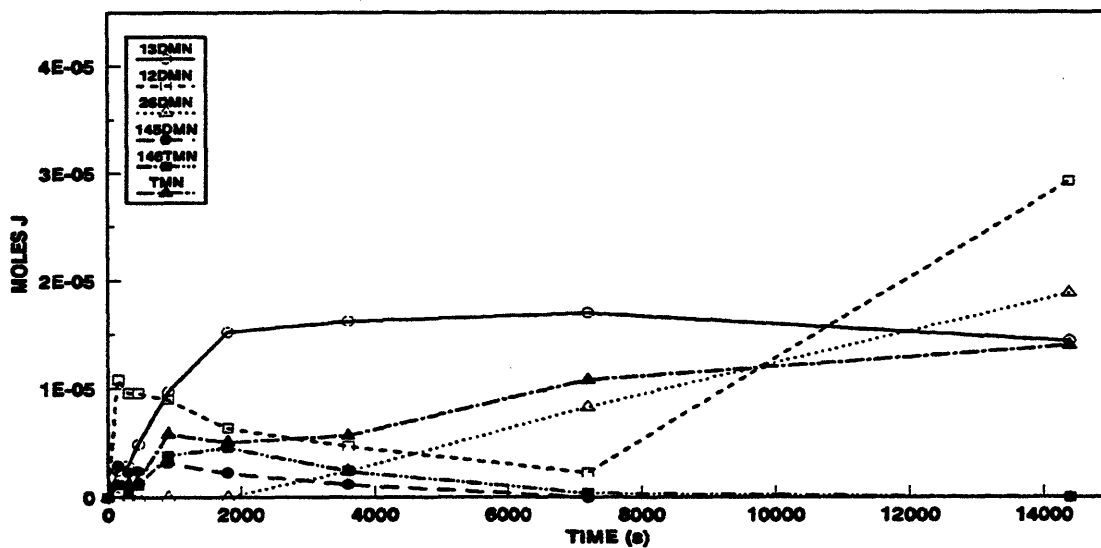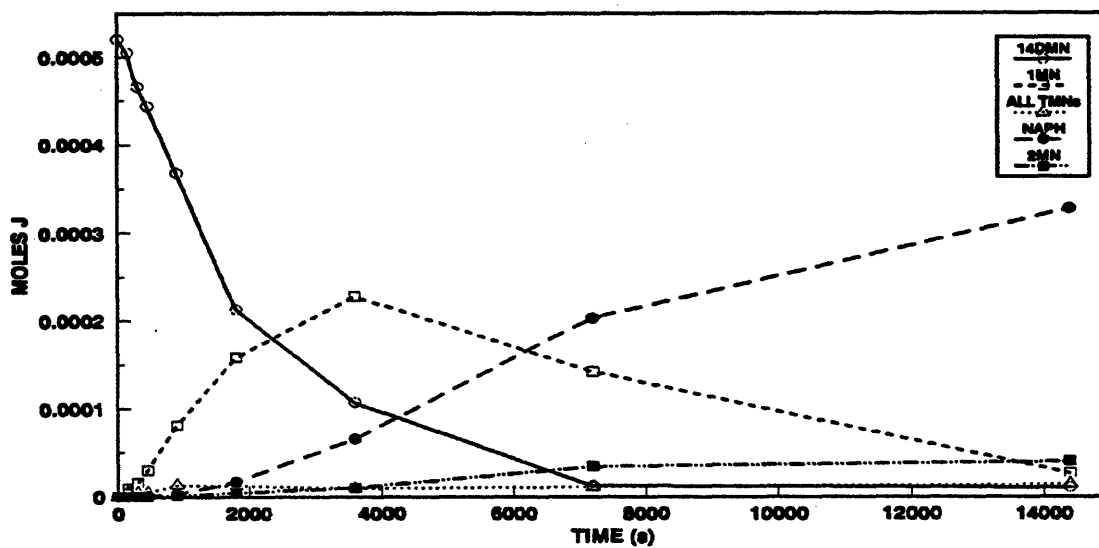
Figure 7.18: Product histories for 14DMN thermolysis at 500°C with $[14DMN]_o = 0.87$ mol/l: major products (top) and minor products (bottom).

from J = 5.2E-04 moles initially to J = 1.0E-05 moles at t = 14400 s, the decay half-life t* ~ 1800 s. 1MN increases from 0 initially to J = 2.3E-04 moles at t = 7200 s, and then decreases monotonically to J = 2.6E-05 moles at t = 28800 s. ALL TMNs are detected at t = 150 s with J = 5.2E-06 moles and remains roughly constant at J = 1.1 ± 0.3E-06 moles for 450 < t < 14400 s. NAP increases monotonically from J = 5.1E-07 moles at t = 300 s to J = 3.3E-04 moles at t = 14400 s. 2MN is detected at t = 450 s with J = 4.4E-07 moles and increases to J = 4.0E-05 moles t = 14400 s. In the lower panel of Figure 7.18, 13DMN appears at t = 150 s with J = 2.4E-06 moles, sharply increases to J = 9.7E-06 moles at t = 900 s and remains roughly constant at J = 1.3 ± 0.4E-05 moles up to t = 28800 s. 12DMN is detected at t = 150 s with maximum J = 1.1E-05 moles and increases to J = 2.9E-06 moles at t = 14400 s. 26DMN appears at t = 3600 s with J = 2.4E-06 moles and increases to J = 1.9E-05 moles at t = 14400 s. 145DMN appears with J = 2.8 ± 0.4E-06 moles for 150 < t < 900 s, decreases to J = 0 at t = 7200 s. 146DMN appears with J = 1.2E-06 moles at t = 150 s, increases to J = 4.6E-06 moles at t = 1800 s, and decreases to J = 0 at t = 14400 s. Other TMNs are detected at t = 150 s with J = 1.1E-06 moles, increase and remain roughly constant at J = 5.4 ± 0.4E-06 moles for 900 < t < 3600 s, and increases to J = 1.4E-05 moles at t = 14400 s.

Figure 7.19 is a selectivity diagram corresponding to the data in Figure 7.18. In the upper panel of Figure 7.19, 1MN selectivity is S = 0.63 at X = 0.029, decreases slightly, then remains roughly constant at S = 0.53 ± 0.02 for 0.15 < X <
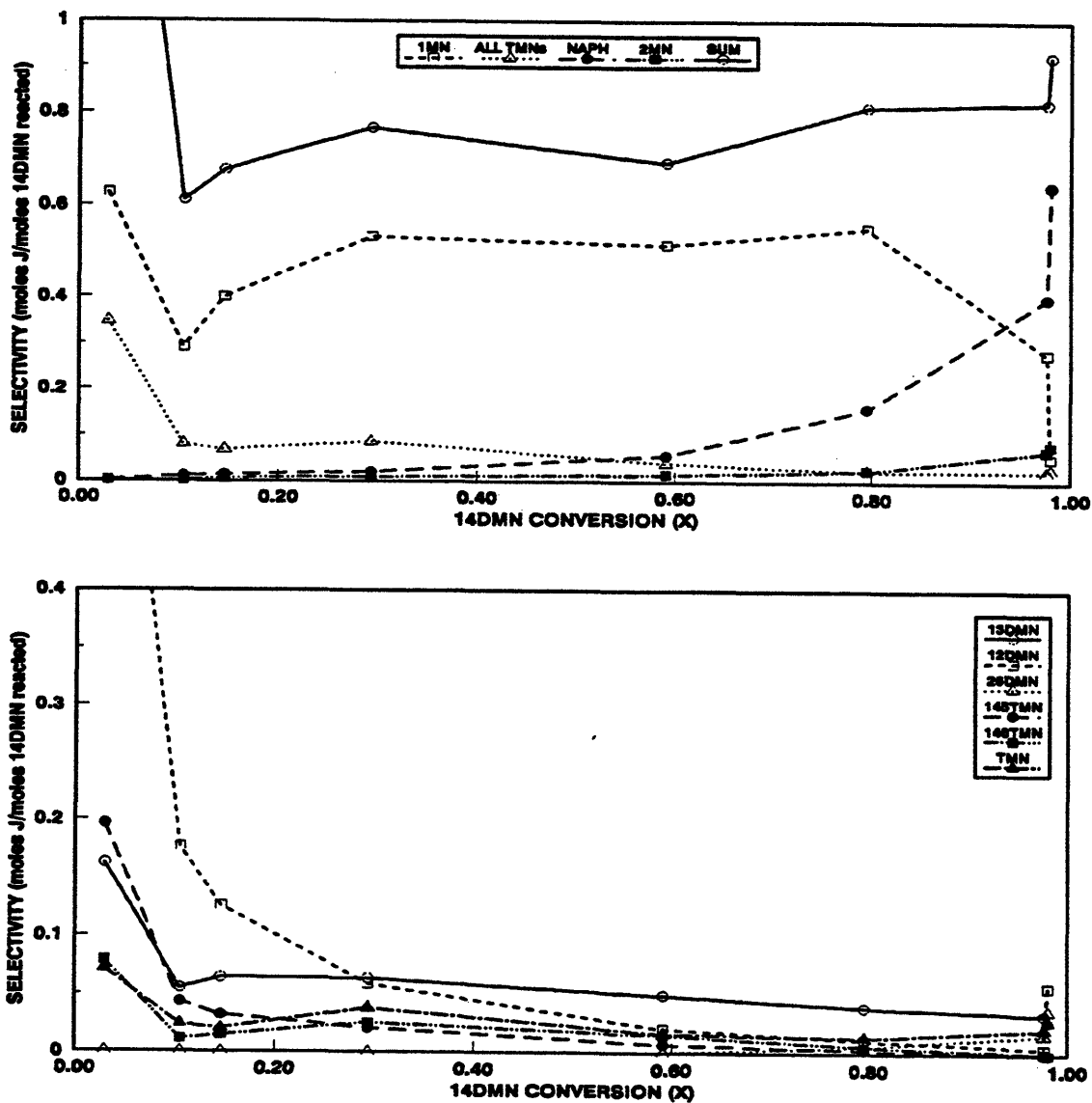
Figure 7.19: Selectivity diagrams for 14DMN thermolysis at 500°C with [14DMN]$_o$ = 0.87 mol/l: major products (top) and minor products (bottom).

635

0.80 and then decreases to S = 0.052 at X = 0.98. ALL TMNs appear with S = 0.35 at X = 0.029, decrease sharply, then remain roughly constant at S = 0.076 ± 0.009 for 0.11 < X < 0.29 and then decrease to S = 0.025 ± 0.003 for 0.80 < X < 0.98. NAP increases monotonically from S = 0.0094 at X = 0.11 to S = 0.055 at X = 0.59 and then rises sharply to S = 0.40 at X = 0.98. 2MN appears at X = 0.15 with S = 0.0057 and increases monotonically to S = 0.079 at X = 0.98. The selectivity sum is roughly constant at Σ = 0.71 ± 0.10 for 0.11 < X < 0.98. In the lower panel of Figure 7.19, 13DMN appears with maximum S = 0.16 at X = 0.029, decreases sharply to S = 0.055 at X = 0.11 and then decreases slightly to S = 0.028 at X = 0.98. 12DMN is detected with maximum S = 0.72 at X = 0.029, decreases sharply to S = 0.059 at X = 0.29 and then decreases to S = 0.0045 at X = 0.98. 26DMN is detected with S = 0.0059 at X = 0.80 and increases to S = 0.037 at X = 0.98. 145TMN is detected with maximum S = 0.20 at X = 0.029, drops sharply to S = 0.043 at X = 0.11 and decreases to S = 0 at X = 0.98. 146TMN appears at X = 0.029 with maximum S = 0.079, decreases and remains roughly constant at S = 0.018 ± 0.007 for 0.11 < X < 0.59, and then decreases to S = 0 at X = 0.98. Other TMNs appear at X = 0.029 with maximum S = 0.071 and decreases the remains roughly constant at S = 0.025 ± 0.013 for 0.11 < X < 0.98.

Figure 7.20 shows substrate and product histories at T = 550°C and [14DMN]$_0$ = 0.87 M. In the upper panel of Figure 7.20, the moles of substrate 14DMN decays from J = 5.2E-04 moles initially to J = 1.4E-05 moles at t = 1800 s and then to J
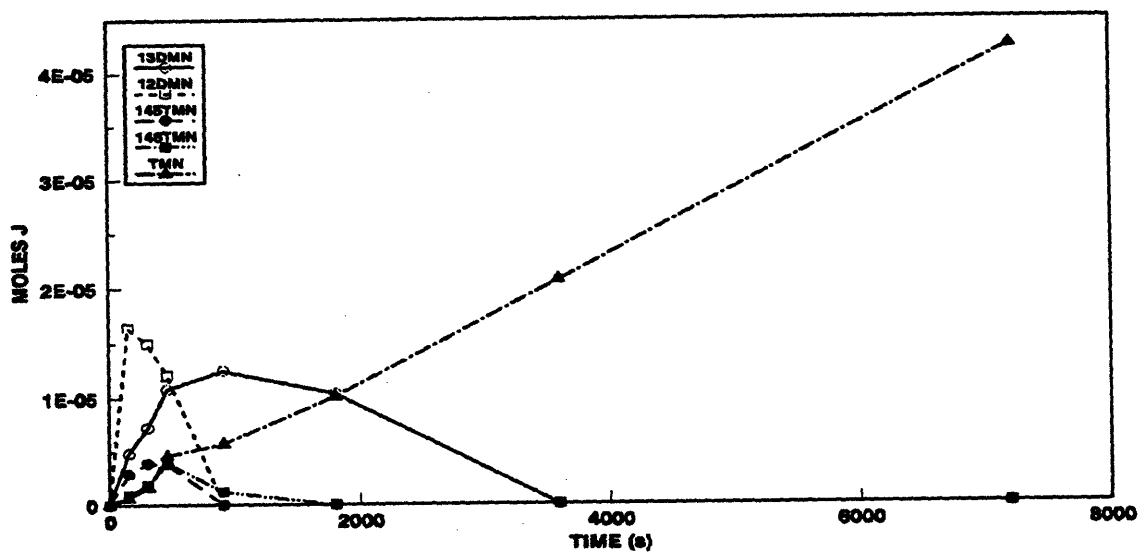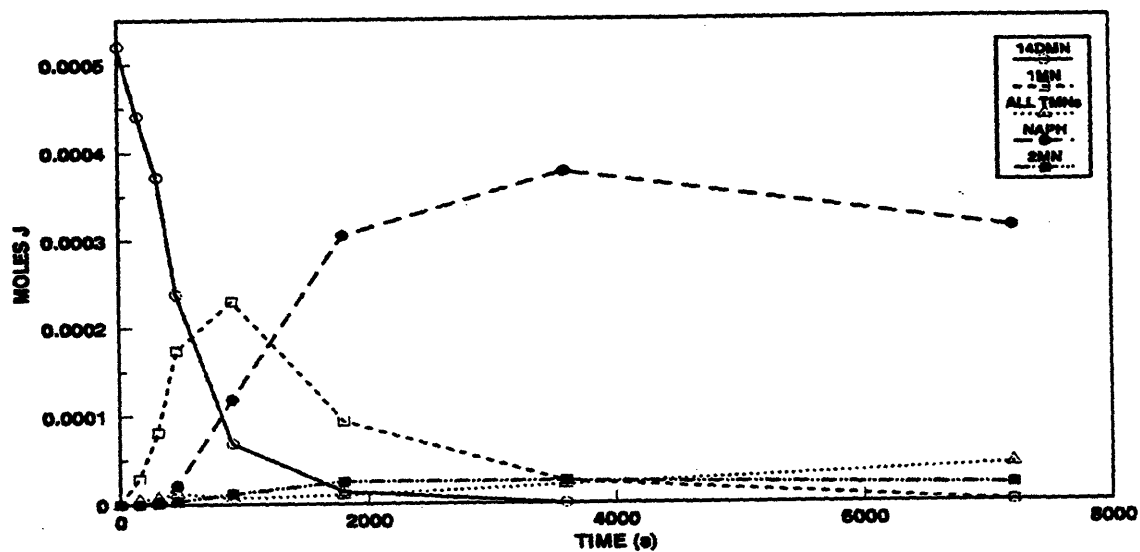
Figure 7.20: Product histories for 14DMN thermolysis at 550°C with $[14DMN]_0$ = 0.87 mol/l: major products (top) and minor products (bottom).

= 0 at t = 3600 s; the decay half-life t* ~ 500 s. 1MN increases from 0 initially to maximum J = 2.3E-04 at t = 900 s and then decreases, sharply at first, to J = 2.5E-05 moles at J = 3600 s before going to J = 0 at t = 7200 s. ALL TMNs increase monotonically from 0 initially to J = 4.2E-05 moles at t = 3600 s. NAP appears at t = 300 s with J = 3.0E-06 moles, rises monotonically to J = 3.0E-04 moles at t = 1800 s, and remains roughly constant at this level to t = 7200 s. 2MN is detected at t = 150 s with J = 3.7E-07 moles, increases monotonically to J = 2.5E-05 moles at t = 1800 s and remains roughly up to t = 7200 s. In the lower panel of Figure 7.20, 13DMN is detected at t = 150 s with J = 4.8E-06 moles, increases to maximum J = 1.3E-05 moles at t = 900 s and then decays to J = 0 by t = 3600 s. 12DMN appears at t = 150 s with maximum J = 1.6E-05 moles and decays to J = 0 by t = 900 s. 145TMN appears at t = 150 s with J = 2.9E-06 moles, increases to maximum J = 3.9E-06 moles at t = 300 s and then decays to J = 0 to t = 900 s. 146TMN increases from 0 initially to maximum J = 3.9E-06 moles at t = 450 s and then decays to J = 0 at t = 1800 s. Other TMNs increase monotonically from 0 initially to J = 4.2E-05 moles at t = 7200 s.

Figure 7.21 is a selectivity diagram corresponding to the data in Figure 7.20. In the upper panel of Figure 7.21, 1MN selectivity is S = 0.37 at X = 0.15, increases and remains roughly constant at S = 0.51 ± 0.05 for 0.29 < X < 0.87, and then declines to S = 0.049 at X = 0.97. ALL TMNs selectivity is S = 0.056 at X = 0.15, declines to S = 0.015 at X = 0.54 and then increases to S = 0.081 at X = 1.0. NAP
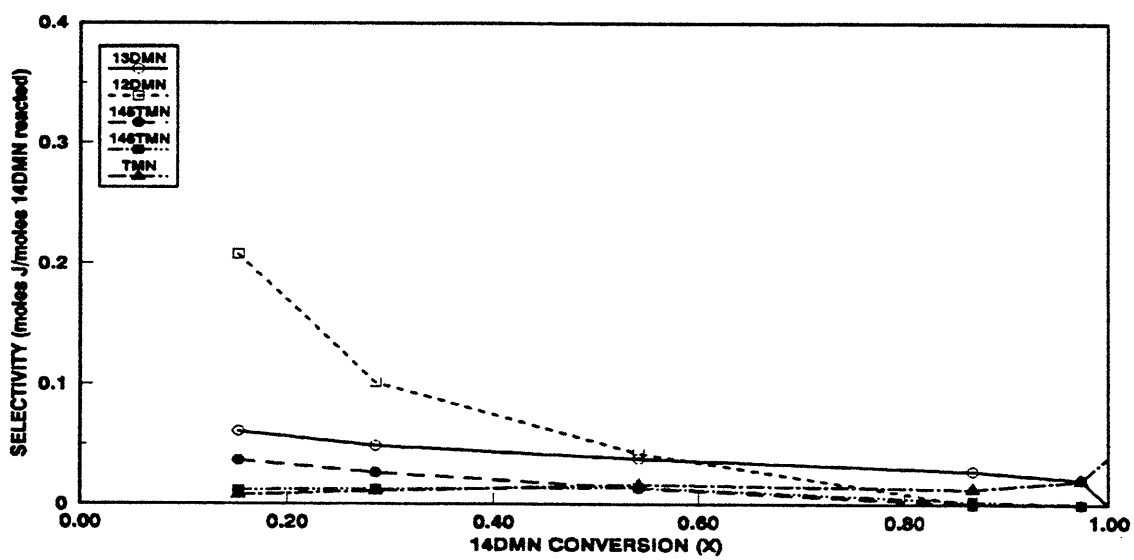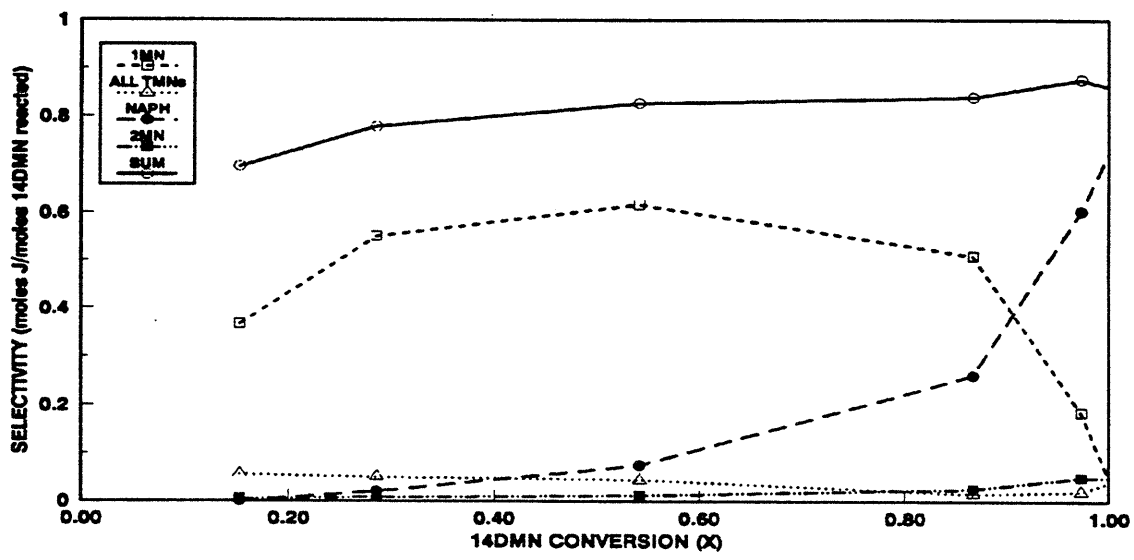
Figure 7.21: Selectivity diagrams for 14DMN thermolysis at 550°C with [14DMN]$_o$ = 0.87 mol/l: major products (top) and minor products (bottom).

appears with S = 0.020 at X = 0.29, increases monotonically to S = 0.26 at X = 0.54 and then increases sharply to S = 0.73 at X = 1.0. 2MN appears at X = 0.15 with S = 0.0047 and increases monotonically to S = 0.049 at X = 1.0. The selectivity sum remains at Σ = 0.79 ± 0.09 for 0.15 < X < 1.0. In the lower panel of Figure 7.21, 13DMN selectivity decreases from maximum S = 0.061 at X = 0.15 to S = 0 at X = 1.0. 12DMN selectivity is a maximum S = 0.21 at X = 0.15 and declines quickly to S = 0 by X = 0.87. 145TMN appears at X = 0.15 with maximum S = 0.037 and decreases to S = 0 at X = 0.87. 146TMN selectivity is S = 0.013 ± 0.001 for 0.15 < X < 0.54 and decreases to S = 0 at X = 0.87. Selectivity of the other TMNs is S = 0.0075 at X = 0.15 and rises to S = 0.082 at X = 1.0.

7.1.5 Summary of Temperature Effects

Increasing temperature from T = 370 to 550°C at fixed $[14DMN]_o$ = 0.87 mol/l influences both the reaction kinetics and product selectivities, as summarized in Table 7.3 and Table 7.4. Note that values in the tables are the averages over all runs, including replication, and are therefore not precisely identical to those seen in the preceding figures. Part (a) of Table 7.3 shows the substrate decay half-life t^* decreased about 1100-fold, from 530000 to 500 s, as reaction temperature T increased ~ 200°C, from 370 to 550°C. Figure 7.22, a plot of log t^* vs. $1/\theta$, where

Table 7.3

EFFECT OF TEMPERATURE ON KINETIC PARAMETERS WITH $[14DMN]_o$ = 0.87 mol/l					
	Temperature (°C)				
Part	370	409	450	500	550
a Half-life t^*, s	529486[1] ± 62109[2]	71454[1] ± 4457	17572 ± 744	1763 ± 224	484 ± 42
b $[1MN/14DMN]_{tmax}$				3.06	3.35
t_{max}/t^*				2.04	1.86

[1]   Half-life calculated using X at longest t and integrated 2nd order rate expression: $t^* = t(1-X)/X$

[2]   ± = standard deviation of the average half-life

Table 7.4

EFFECT OF TEMPERATURE ON

PRODUCT SELECTIVITIES WITH [14DMN]$_o$ = 0.87 mol/l

Part	Selectivity S of:	Conversion X Range:	Temperature (°C)				
			370	409[1]	450	500	550
a	1MN	0.2 - 0.8	0.32	0.53	0.60	0.54	0.60
	ALL TMNs	0.2 - 0.8	0.10	0.12	0.052	0.054	0.049
b	NAP	0.35 ± 0.03	ND	0.023	0.039	0.020	0.029
	2MN	0.35 ± 0.03	ND	0.010	0.009	0.009	0.008
	13DMN	0.10 ± 0.02	0.11	0.14	0.14	0.077	0.061
		0.2 - 1.0	ND	0.093	0.043	0.060	0.048
	12DMN	0.10 ± 0.02	0.32	0.30	0.42	0.18	0.21
		0.2 - 1.0	ND	0.034	0.043	0.038	0.079
	26DMN	0.2 - 0.6	ND	0.009	ND	0.003	ND
	145TMN	0.10 ± 0.02	0.073	0.075	0.080	0.043	0.037
		0.2 - 1.0	ND	0.009	0.017	0.012	0.021
	146TMN	0.10 ± 0.02	0.020	0.030	0.032	0.011	0.012
		0.2 - 1.0	ND	0.041	0.015	0.018	0.014
	other TMNs	0.10 ± 0.02	0.053	0.081	0.059	0.024	0.008
		0.2 - 1.0	ND	0.065	0.021	0.024	0.014

[1] For T = 409°C, range for 0.20 < X < 0.42
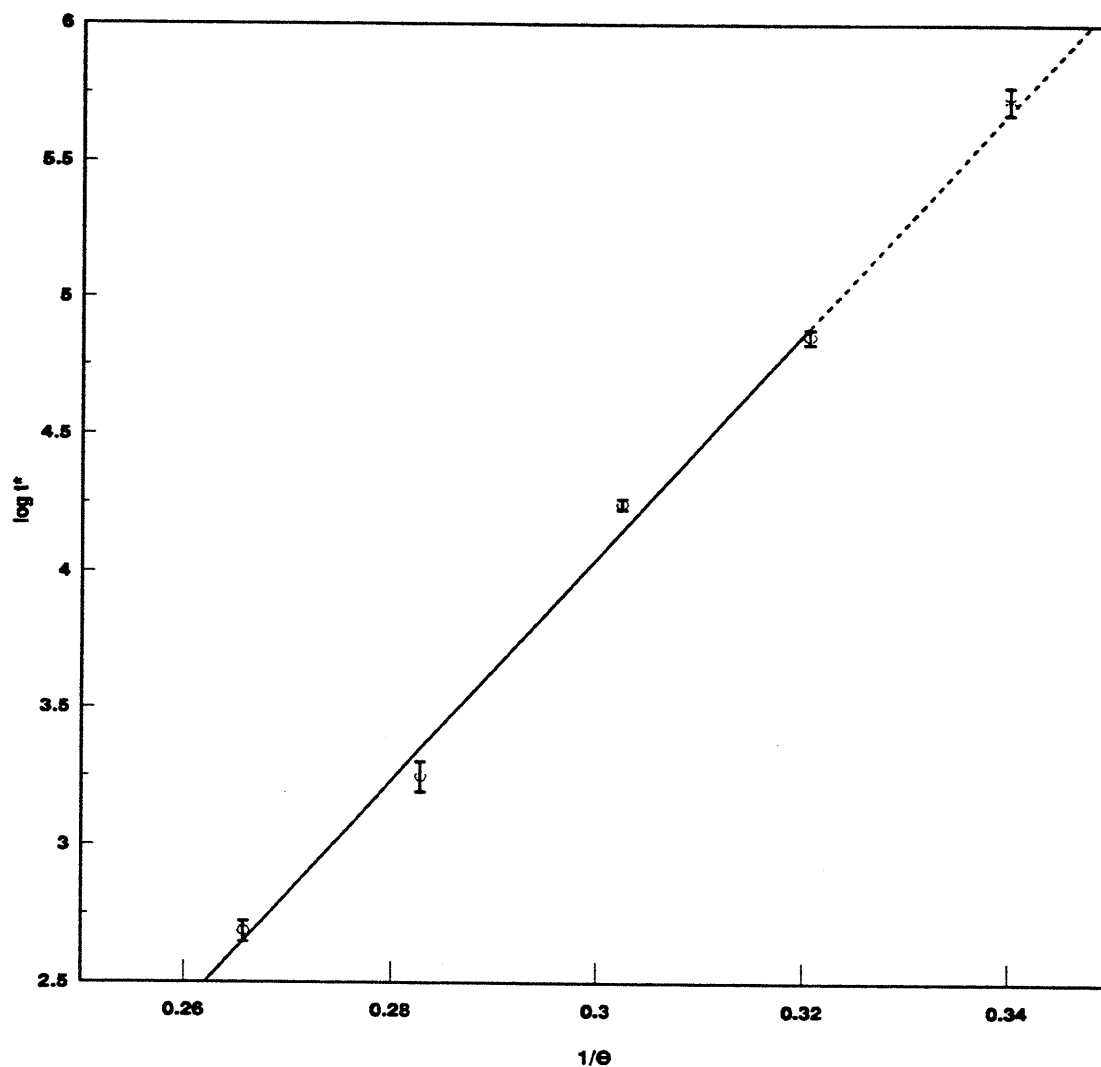
Figure 7.22:   Decay half-life t^* for varying temperatures with fixed $[14DMN]_o = 0.87$ mol/l.

θ = $4.573 \times 10^{-3}T$ in Kelvins, shows that the data adhere to a line:

$$\log t^* = -8.53 + \frac{42.0}{\theta} \qquad (7.4)$$

for T = 409 - 550°C. The slope of this line, 42.0, is equal to the activation energy in kcal/mol of the overall reaction; also, for 2nd order decomposition, the intercept of the line provides a pre-exponential factor of -8.5. Thus 14DMN thermolysis is 3/2 order in substrate with Arrhenius parameters ($\log_{10} A$, E^*) = (-8.5, 42.0).

Product histories at the highest temperatures T = 500 and 550°C, shown in Figure 7.18 and Figure 7.20, also provide an indication of the relative kinetics of the sequential reactions as shown in (7.3). 1MN attained its maximum concentration $[1MN]_{max}$ at t_{max} in both figures, then, as shown in part (b) of Table 7.3, the ratios $[1MN/14DMN]_{tmax} \sim 3.2$ and $[t_{max}/t^*] \sim 1.95$ both imply that 1MN decomposes more slowly than 14DMN. If both decompositions are presumed to be of the same 2nd order in their respective substrates, then we can estimate the rate constant ratio (k_1/k_2) = $[1MN/14DMN]_{tmax}^2 \sim 10.3$ for the range 500 < T < 550°C. This is similar to the estimate of $(k_1/k_2) \sim 10.2$ earlier obtained from results at fixed T = 450°C and varying initial substrate concentrations.

Turning to product selectivities, summarized in Table 7.4, both 1MN and ALL TMNs selectivities were roughly independent of conversion over the ranges 0.2 < X < 0.8 at temperatures, as shown in part (a) of Table 7.4. The absolute values of S(1MN) and S(ALL TMNs) remained essentially constant at S(1MN) = 0.57 $\pm$ 0.04

and S(ALL TMNs) = 0.08 ± 0.04 over the range of temperatures, 370 < T < 550°C.

Naphthalene and 2MN selectivities increased monotonically from 0 as conversions

increased for all initial concentrations, as shown in part (b) of Table 7.4. S(NAP)

and S(2MN) generally increased with increasing X at all $[14DMN]_o$, with S(NAP) >

S(2MN) always. S(NAP) remained roughly constant at 0.030 ± 0.010 at X = 0.35

± 0.03 for temperature increasing from 409 to 550°C. S(2MN) = 0.009 ± 0.001 at

X = 0.35 ± 0.03 for 409 < T < 550°C. The other dimethylnaphthalenes, 13DMN

and 12DMN, selectivities generally started at their maximum values at low

conversions, decreased sharply by X ~ 0.20 and then slowly declined for all initial

concentrations, as shown in part (b) of Table 7.4, while 26DMN only appeared at T

= 409 and 500°C. Of the dimethylated species, the order of abundance was generally

S(12DMN) > S(13DMN) > S(26DMN). The absolute values of S(13DMN),

S(12DMN), and S(26DMN) remained roughly constant with increasing $[14DMN]_o$ for

0.2 < X < 1.0. S(13DMN) = 0.010 ± 0.004 at X = 0.10 ± 0.02 for 370 < T <

550°C and decreases to S(13DMN) = 0.093 for 0.2 < X < 0.42 for T = 409°C and

S(13DMN) = 0.051 ± 0.009 for 0.2 < X < 1.0 for 450 < T < 550°C. S(12DMN)

= 0.30 ± 0.12 at X = 0.10 ± 0.02 for 370 < $_T$ < 550°C and decreases to S(12DMN)

= 0.057 ± 0.023 for 0.2 < X < 1.0 for 409 < T < 550°C. S(26DMN) = 0.006 ±

0.003 for 0.2 < X < 1.0 for T = 409 and 500°C. The trimethylnaphthalenes,

145TMN, 146TMN and other TMNs, selectivities generally started at their maximum

values at low conversions, decreased sharply by X ~ 0.20 and then slowly declined

for all initial concentrations, as shown in part (b) of Table 7.4. Of the trimethylated species, the order of abundance was generally S(TMN) > S(146TMN) > S(145TMN). The absolute values of S(146TMN) and S(145TMN) remained roughly constant with increasing [14DMN]$_o$ for $0.2 < X < 1.0$. S(146TMN) = 0.021 ± 0.010 at X = 0.10 ± 0.02 for $370 < T < 550°C$ and decreases to S(146TMN) = 0.041 for $0.2 < X < 0.42$ for T = 409°C and S(146TMN) = 0.016 ± 0.002 for $0.2 < X < 1.0$ for $450 < T < 550°C$. S(145TMN) = 0.059 ± 0.021 at X = 0.10 ± 0.02 for $370 < T < 550°C$ and decreases to S(145TMN) = 0.015 ± 0.006 for $0.2 < X < 1.0$ for $409 < T < 550°C$. The absolute values of S(TMN) somewhat decrease with increasing T at X = 0.10 ± 0.02, with S(TMN) = [0.053, 0.081, 0.059, 0.024, 0.008] for T = [370, 409, 450, 500, 550°C]. The absolute values of S(TMN) also decrease with increasing T at $0.2 < X < 1.0$, with S(TMN) = [0.065, 0.021, 0.024, 0.014] for T = [409, 450, 500, 550°C].

Finally, Figure 7.23, Figure 7.24 and Figure 7.25 depict the variation of certain product ratios, namely R[NAP/1MN], R[Σ minor DMNs/1MN] and R[2MN/NAP], versus 14DMN conversion X at all temperatures. In Figure 7.23 it is seen that for all experiments, the ratio of NAP to 1MN, R[NAP/1MN], is essentially a function of conversion only, with data for all temperatures, $370 < T < 550°C$, lying on roughly the same curve. This curve shows an exponential relationship that implicitly describes the kinetics of 14DMN demethylation under the present conditions. In Figure 7.24 it is seen that, for X > 0.20 and all experiments, the ratio of
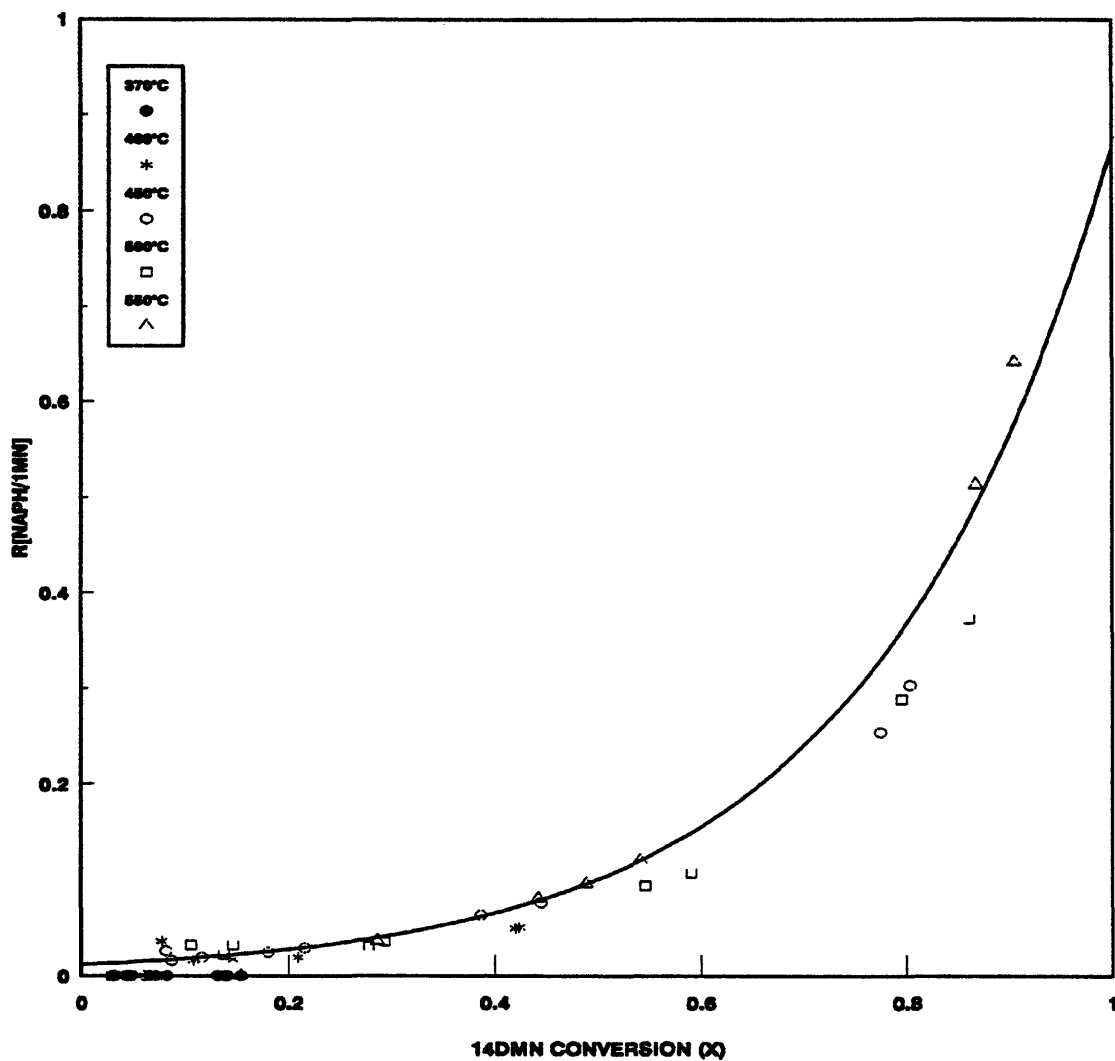
Figure 7.23: Ratio of moles NAP to moles 1MN produced vs. 14DMN conversion (X) for varying T with fixed $[14DMN]_o$ = 0.87 mol/l.
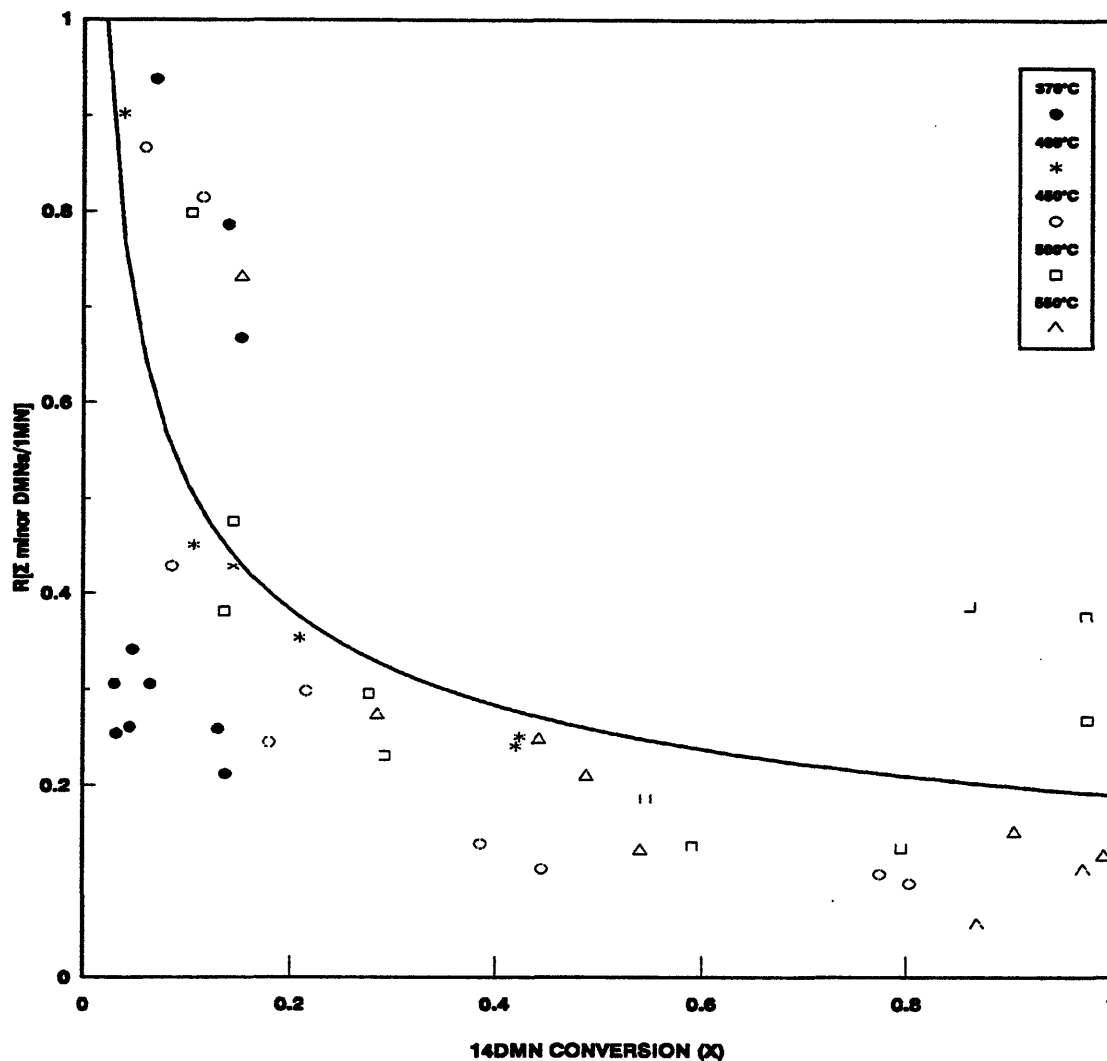
Figure 7.24: Ratio of moles Σ DMNs to moles 1MN produced vs. 14DMN conversion (X) for varying T with fixed $[14DMN]_o$ = 0.87 mol/l.
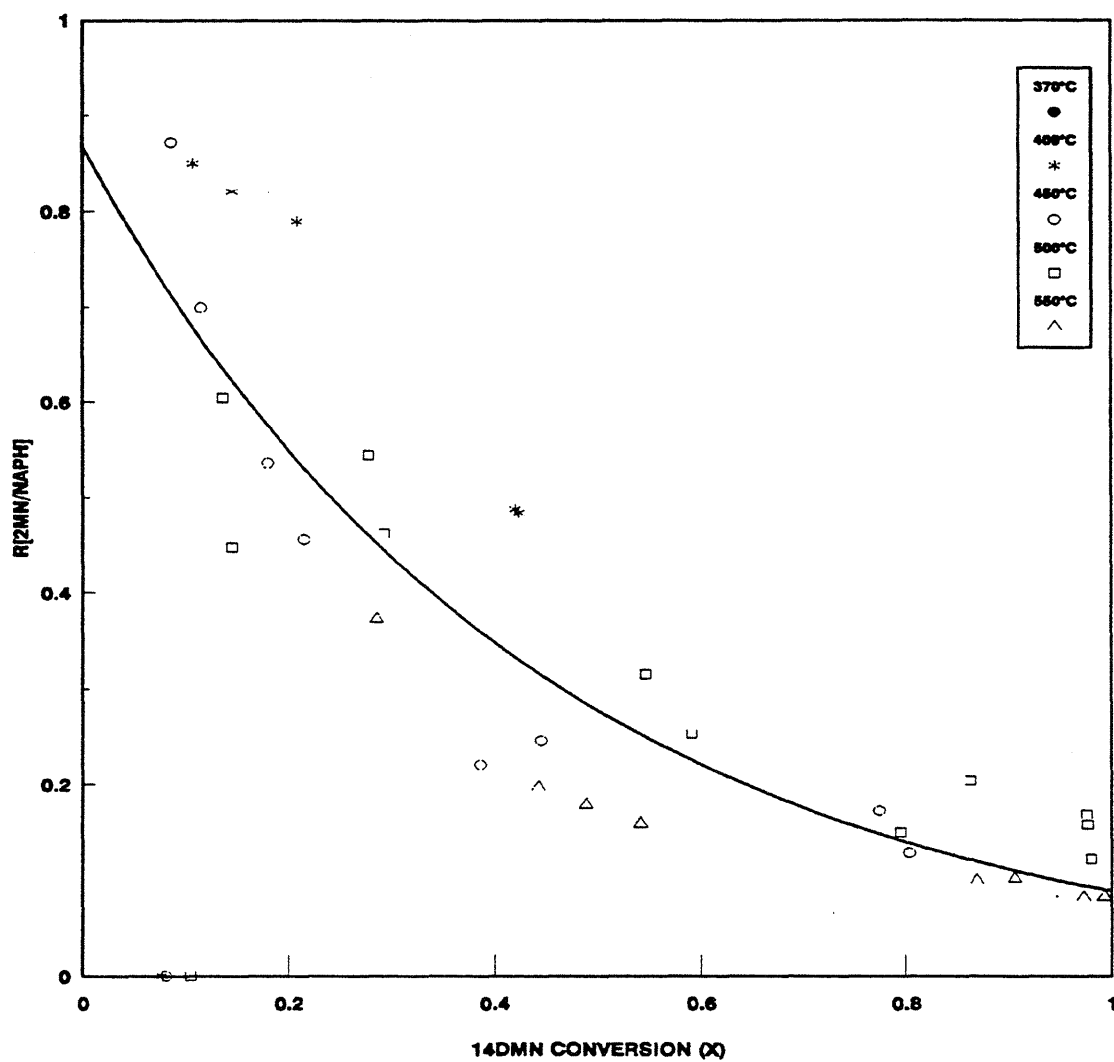
Figure 7.25: Ratio of moles 2MN to moles NAP produced vs. 14DMN conversion (X) for varying T with fixed $[14DMN]_o = 0.87$ mol/l.

dimethylated naphthalene species to 1MN, $R[\Sigma DMNs/1MN]$, is essentially a function of conversion only, with data for all temperatures, $370 < T < 550°C$, lying on roughly the same curve. Once again, the impurities of 1MN, 13DMN and 12DMN in the 14DMN substrate disallow the data at $X < 0.20$. Implicit in this linear relationship are the kinetics of 1MN methylation during thermolysis of the 14DMN substrate under the present conditions. Figure 7.25 shows that for all experiments, the ratio of monomethylated species to NAP, $R[2MN/NAP]$, is essentially a function of conversion only, with data for all temperatures, $370 < T < 550°C$, lying on roughly the same curve. This exponential relationship implicitly describes the kinetics of NAP methylation during thermolysis of the 14DMN substrate under the present conditions.

7.2 Kinetics

The kinetics of the experimental thermolyses were analyzed to derive reaction order and activation parameters. Reaction order was obtained from data at initial concentrations $0.081 \text{ mol/l} < [14DMN]_o < 2.07 \text{ mol/l}$ at a fixed $T = 450°C$, while activation parameters were derived from data at temperatures $370°C < T < 550°C$ at fixed $[14DMN]_o = 0.87 \text{ mol/l}$. Both effective first order rate constants, k_{eff}, and the true rate constants, k, were employed to ascertain reaction order and activation parameters.

7.2.1 Reaction Order

The order of reaction for overall 14DMN decay was formally examined in the series of experiments at constant temperature T = 450°C with initial 14DMN substrate concentrations ranging from 0.081 to 2.07 mol/l.

7.2.1.1 Apparent First Order Rate Constants, k_{eff}

The effective first order rate constant k_{eff}, units 1/s, is defined by Equation (7.5):

$$k_{eff} = \frac{-\ln(1-X)}{t} \tag{7.5}$$

where X is the fractional conversion at holding time t, Equation (7.6):

$$X = 1 - \frac{[14DMN]_t}{[14DMN]_o} \tag{7.6}$$

with $[14DMN]_o$ and $[14DMN]_t$ the respective concentrations of 14DMN at times 0 and t. Effective first order rate constants were calculated at each point, for all runs. At each T and $[14DMN]_o$, values of log k_{eff} were averaged over intervals of fractional conversion, respectively 0 - 0.1, 0.1 - 0.2, 0.2 - 0.4, 0.4 - 0.6, 0.6 - 0.8, and 0.8 - 1.0. The average log k_{eff} over each of the chosen conversion intervals are shown as horizontal lines with vertical error bars in Figure 7.26 and Figure 7.27. As a representative example, the upper panel of Figure 7.26 refers to 14DMN thermolysis at T = 450°C and $[14DMN]_o$ = 0.081 mol/l. In each of the four conversion intervals,

651
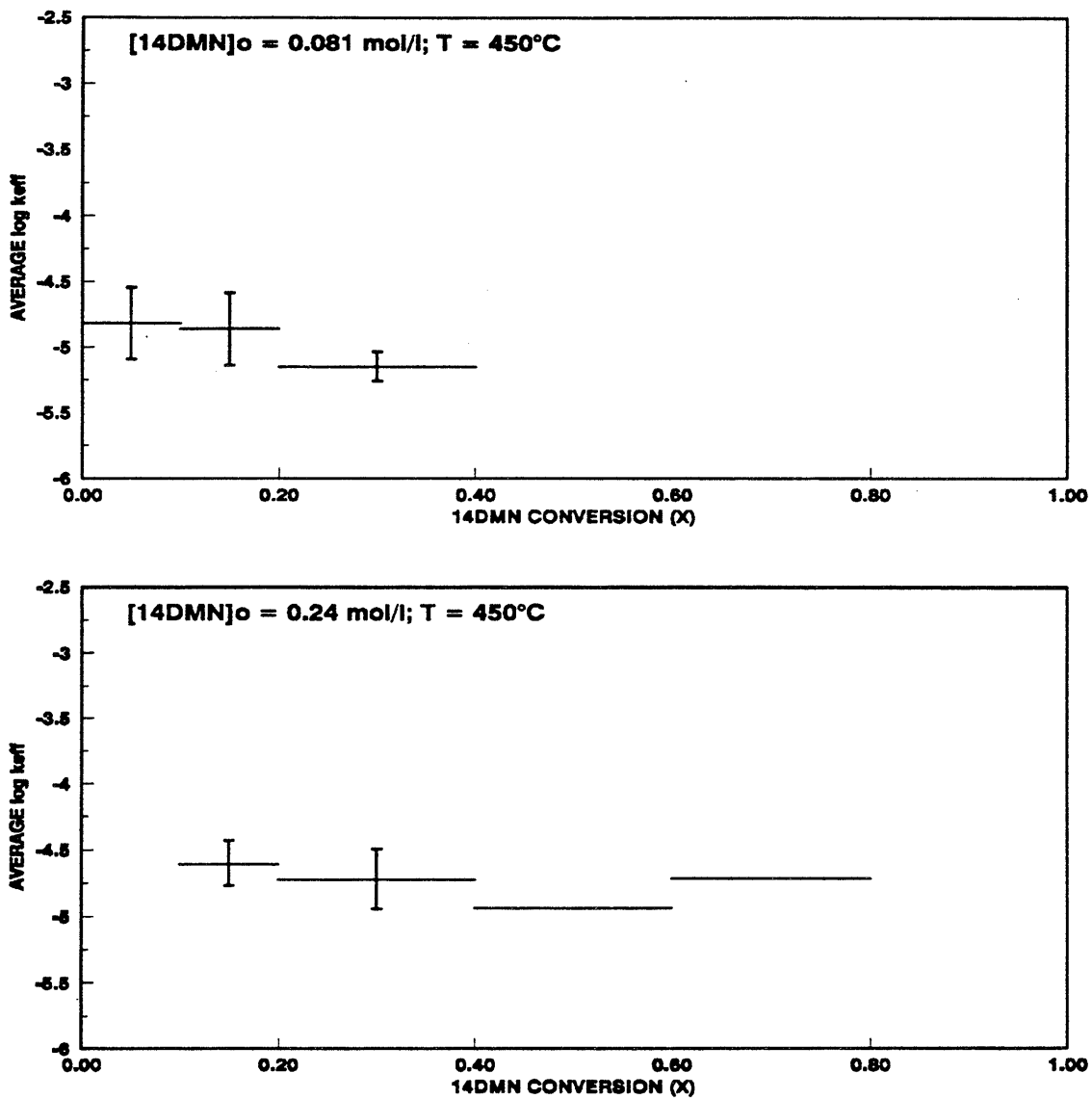
Figure 7.26: Average log k_{eff} vs. 14DMN conversion at T = 450°C for $[14DMN]_o$ = 0.081 (top) and 0.24 mol/l (bottom).
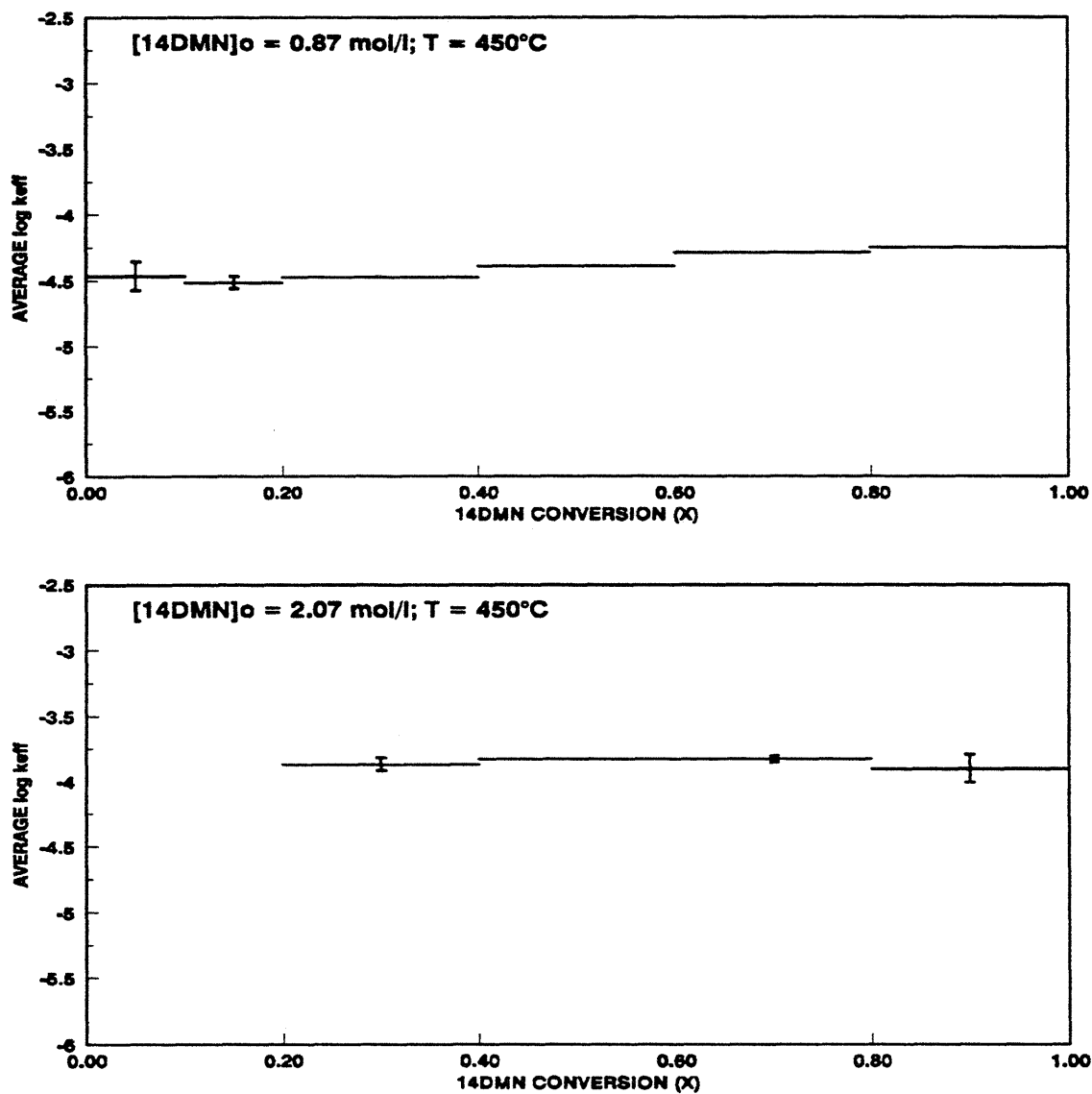
Figure 7.27: Average log k_{eff} vs. 14DMN conversion at T = 450°C for $[14DMN]_o$ = 0.87 (top) and 2.07 mol/l (bottom).

values of the average log k_{eff} are $\sim$ -4.9 $\pm$ 0.3. The uncertainty associated with log k_{eff} is seen to diminish greatly with increasing conversion, the error bars spanning 0.5, 0.6 and 0.2 units of log k_{eff} in the conversion intervals of 0 - 0.1, 0.1 - 0.2 and 0.2 - 0.4, as seen on line 3 of Table 7.5. Table 7.5 summarizes the average log k_{eff}, error of the average log k_{eff} and error for each conversion range for all $[14DMN]_o$ and temperatures. The lower panel of Figure 7.26 refers to 14DMN thermolysis at T = 450°C and $[14DMN]_o$ = 0.24 mol/l and the upper and lower panels of Figure 7.27 refer to 14DMN thermolysis at T = 450°C and $[14DMN]_o$ = 0.87 mol/l and $[14DMN]_o$ = 2.07 mol/l, respectively, while lines 4 - 7 of Table 7.5 summarize the average log k_{eff}, error in the average log k_{eff} and errors for each conversion range. It can be seen in Table 7.5 that the uncertainty associated with log k_{eff} diminishes with increasing conversion for all $[14DMN]_o$, the error bars ranging from 0.22, 0.09 - 0.34, 0 - 0.45, 0, 0 - 0.06 and 0 - 0.22 units of log k_{eff} in the conversion intervals of 0 - 0.1, 0.1 - 0.2, 0.2 - 0.4, 0.4 - 0.6, 0.6 - 0.8 and 0.8 - 1.0.

The order of 14DMN decomposition at T = 450°C was determined by plotting the average log k_{eff} vs log $[14DMN]_o$ as shown in Figure 7.28, the upper panel of which shows data for all X while the lower panel shows data for X < 0.4. The low conversion data, X < 0.4, approximately represent the limit X $\rightarrow$ 0. It can be

Table 7.5

AVERAGE log k_{eff} FOR 14DMN THERMOLYSIS

T °C	[14DMN]$_o$ mol/l	$<k_{eff}> \pm$ error	0 - 0.1	0.1 - 0.2	0.2 - 0.4	0.4 - 0.6	0.6 - 0.8	0.8 - 1.0
					Conversion interval			
370	0.87	-5.55±0.40	0.81	0.10				
409	0.87	-5.01±0.13	0.17	0.16	0	0		
450	0.081	-4.94±0.28	0.55	0.55	0.22			
450	0.24	-4.68±0.20	0.34	0.45	0	0		
450	0.87	-4.42±0.11	0.22	0.09	0	0	0	0
450	2.07	-3.87±0.08			0.10	0	0.06	0.22
500	0.87	-3.43±0.16	0	0.32	0.03	0.05	0	0.25
550	0.87	-2.78±0.13		0	0	0.10		0.09
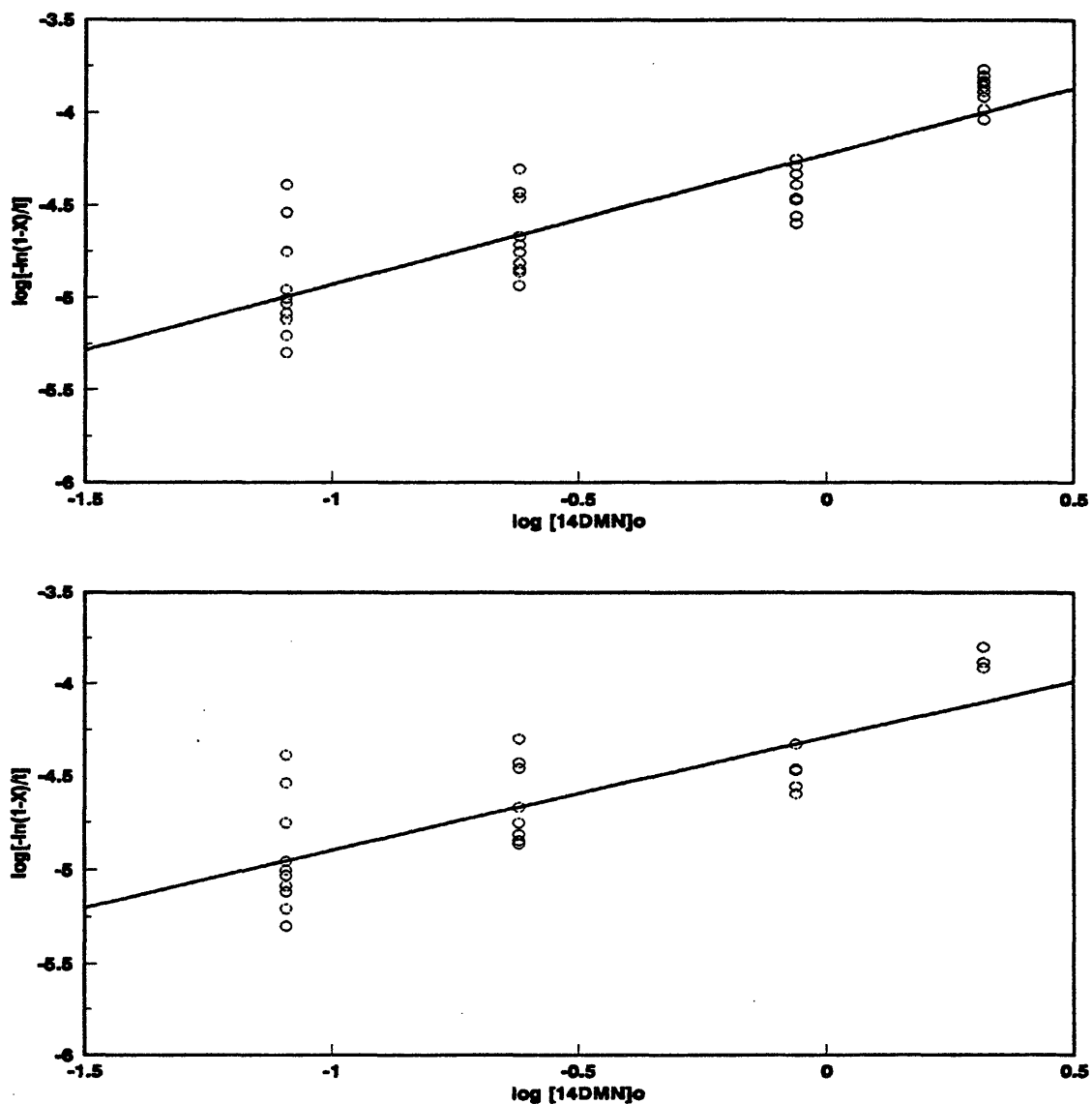
Figure 7.28: Determination of reaction order for 14DMN thermolysis from log [14DMN]$_o$ vs. log k$_{eff}$: all X (top) and only X < 0.4 (bottom).

demonstrated that for a reaction rate expression:

$$r = k[14DMN]^{\alpha} \qquad (7.7)$$

with rate constant k and reaction order α, the apparent first order rate constant at low conversions, $X \rightarrow 0$, is:

$$k_{eff} = k[14DMN]_o^{\alpha - 1} \qquad (7.8)$$

Consequently, a plot of log k_{eff} versus log $[14DMN]_o$ should exhibit slope (α - 1) and intercept log k. In Figure 7.28, regression of log k_{eff} vs. log $[14DMN]_o$ for all conversions gives α - 1 = 0.71 ± 0.06 and log k = -4.22 ± 0.22, while regression of the low conversion data gives α - 1 = 0.60 ± 0.09 and log k = -4.29 ± 0.24, both results implying that 14DMN thermolysis is close to 2nd order with respect to the substrate. This accords with the 2nd order inferred from the variation of 14DMN decomposition half-lifes with varying $[14DMN]_o$ in Section 7.1.2.

7.2.1.2 True Rate Constants, k_2

The 2nd order rate expression:

$$r = k_2[14DMN]^2 \qquad (7.9)$$

integrated with respect to time reads:

$$\frac{1}{[14DMN]_t} - \frac{1}{[14DMN]_o} = k_2 t \qquad (7.10)$$

Thus, a plot of $1/[14DMN]_t$ versus time should be linear, with slope k_2 and intercept $1/[14DMN]_o$. Figure 7.29 shows the present data for 14DMN thermolysis at T = 450°C on coordinates of $1/[14DMN]_t$ versus t. Data at all $[14DMN]_o$ and all conversions are plotted on the graph, but at each $[14DMN]_o$, only the low conversion results, X < 0.4, were regressed, with the corresponding best-fit lines indicated in the figure. The light dashed-dotted diagonal line in the figure is the locus of times and concentrations at which X = 0.4. The best-fit regressed lines are roughly parallel, with slopes, that is k_2 = [8.16E-05, 6.45E-05, 4.92E-05, 7.44E-05] for $[14DMN]_o$ = [0.081, 0.24, 0.87, 2.07 mol/l] respectively. It is noteworthy that the individual slopes vary by less than a factor of 2.0 over a 20-fold range of initial concentrations, reinforcing the validity of the chosen 2nd order. Figure 7.30, a plot of $1/[14DMN]_t$ - $1/[14DMN]_o$ versus time, superimposes all the $[14DMN]_o$ data onto a single line of slope k_2, passing through the origin. From regression of all the data at low conversions, X < 0.4, we obtain $\langle k_2 \rangle$ = (9.51 ± 0.63)E-05 for 0.081 < $[14DMN]_o$ < 2.07 mol/l at T = 450°C.
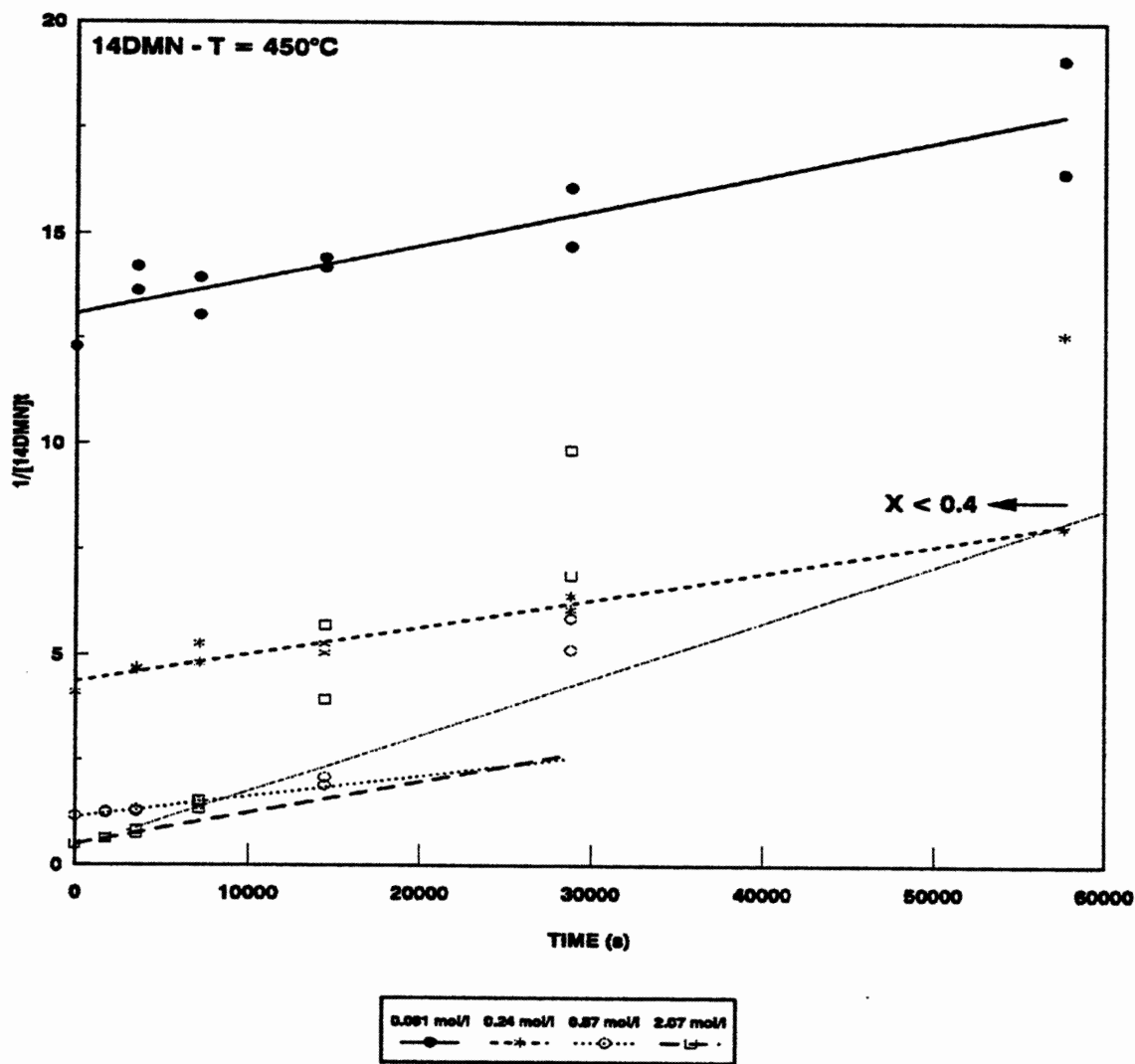
Figure 7.29: 2nd order plot, $1/[14DMN]_t$ vs. t, for 14DMN thermolysis with varying $[14DMN]_o$ at fixed $T = 450°C$.
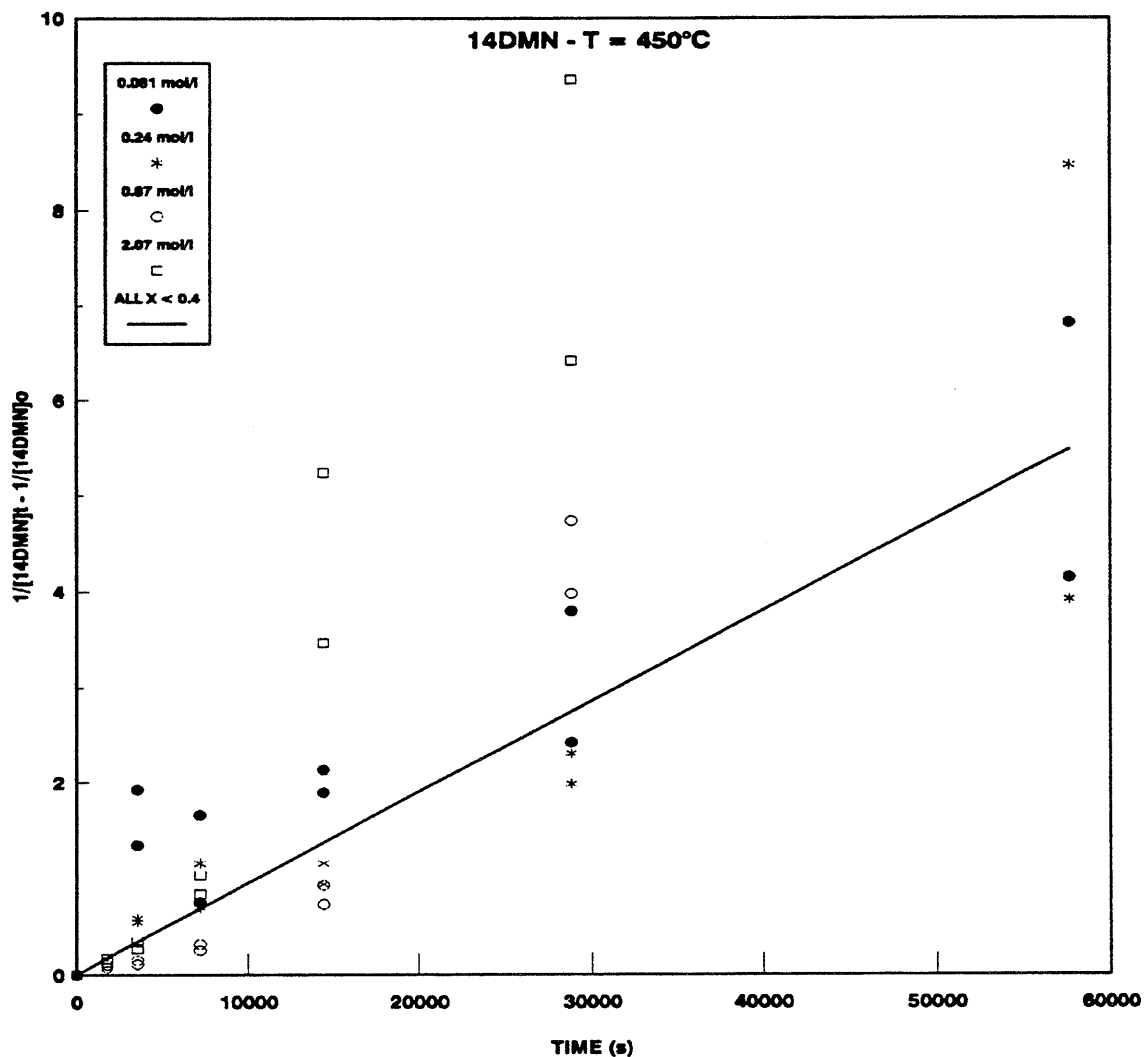
Figure 7.30: Plot of the integrated 2nd order rate expression for 14DMN thermolysis with varying $[14DMN]_o$ at fixed T = 450°C.

7.2.2 Activation Parameters

Thermolyses of 14DMN at fixed $[14DMN]_0 = 0.87$ mol/l and varying temperatures from 370 - 550°C revealed the activation parameters associated with both the effective first order and true 2nd order rate constants.

Effective first order rate constants were calculated at each point, for all runs. At each T and $[14DMN]_0$, values of log k_{eff} were averaged over intervals of fractional conversion, respectively 0 - 0.1, 0.1 - 0.2, 0.2 - 0.4, 0.4 - 0.6, 0.6 - 0.8, and 0.8 - 1.0. The average log k_{eff} over each of the chosen conversion intervals are shown as horizontal lines with vertical error bars in Figure 7.31 and Figure 7.32. The upper panel of Figure 7.31 refers to 14DMN thermolysis at T = 370°C and $[14DMN]_0 = 0.87$ mol/l. In each of the two conversion intervals, values of the average log k_{eff} are ~ -5.5 ± 0.4. The uncertainty associated with log k_{eff} is seen to diminish with increasing conversion, the error bars spanning 0.81 and 0.10 units of log k_{eff} in the conversion intervals of 0 - 0.1 and 0.1 - 0.2, as shown on line 1 of Table 7.5. The lower panel of Figure 7.31 refers to 14DMN thermolysis at T = 409°C and $[14DMN]_0 = 0.87$ mol/l, the upper panel of Figure 7.27 refers to 14DMN thermolysis at T = 450°C and $[14DMN]_0 = 0.87$ mol/l, the upper panel of Figure 7.32 refers to 14DMN thermolysis at T = 500°C and $[14DMN]_0 = 0.87$ mol/l and the lower panel of Figure 7.32 refers to 14DMN thermolysis at T = 550°C and $[14DMN]_0 = 0.87$
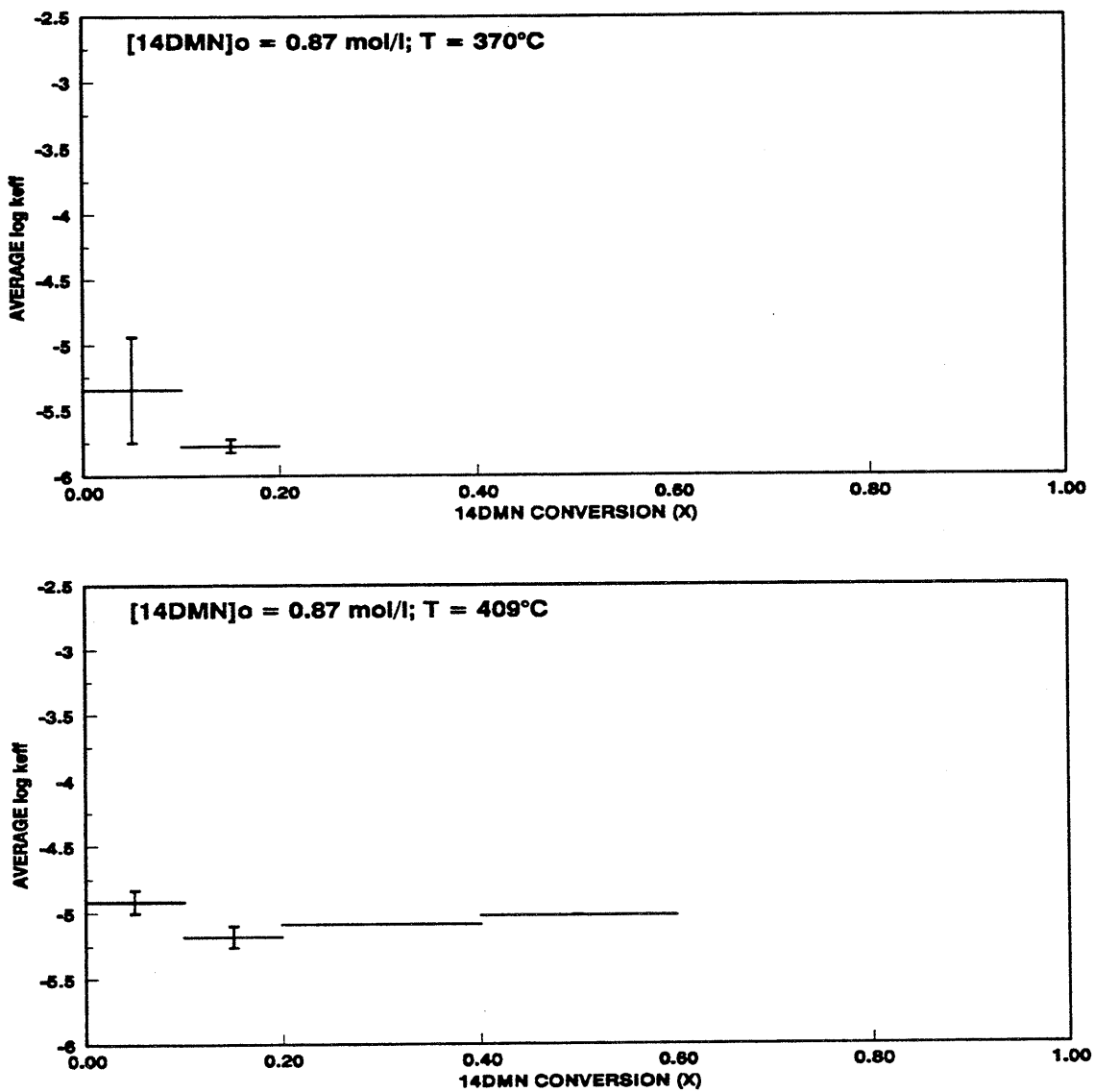
Figure 7.31: Average log k_{eff} vs. 14DMN conversion at $[14DMN]_o = 0.87$ mol/l for $T = 370°C$ (top) and $T = 409°C$ (bottom).
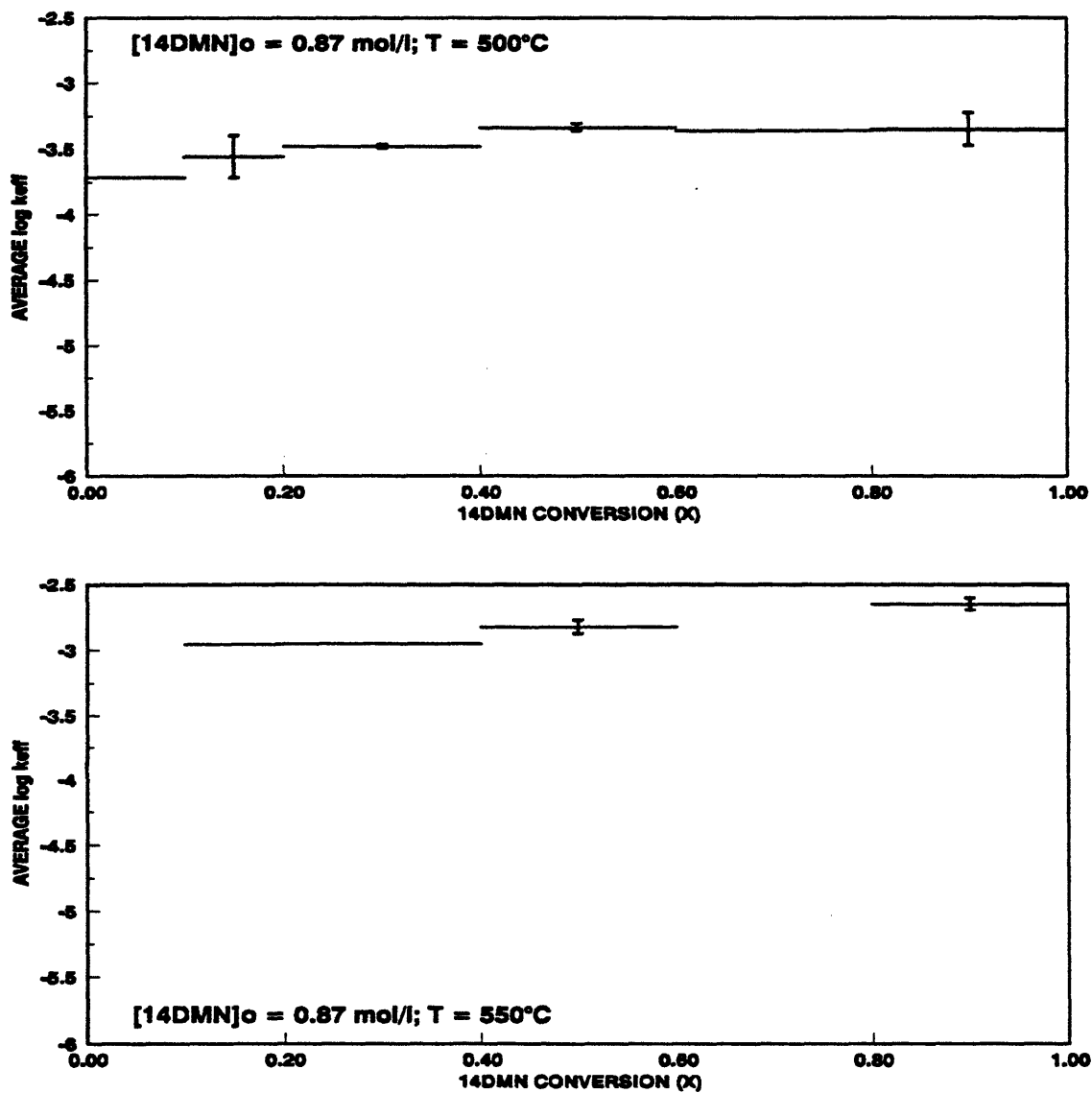
Figure 7.32: Average log k_{eff} vs. 14DMN conversion at $[14DMN]_o$ = 0.87 mol/l for T = 500°C (top) and T = 550°C (bottom).

663

mol/l with the respective average and errors summarized on lines 2, 3, 6 and 8 of Table 7.5.

Figure 7.33 is a plot of the integrated 2nd order rate expression, $1/[14DMN]_t$ - $1/[14DMN]_o$ versus time, for 14DMN thermolysis at fixed $[14DMN]_o = 0.87$ mol/l and varying reaction temperatures, $370 < T\ °C < 550$. At each temperature, lines are drawn to represent the best-fits at low conversions, $X < 0.4$. The slopes of these lines provide the rate constants $<k_2> = $ [1.81E-06, 9.17E-06, 4.60E-05, 4.10E-04, 1.50E-03] at each thermolysis temperature $T = $ [370, 409, 450, 500, 550°C].

The variation of rate constants k_{eff} and k_2 with temperature is respectively shown in Figure 7.34 and Figure 7.35, using Arrhenius coordinates of $\log_{10} k$ versus $1/\theta$, where $\theta = 4.573 \times 10^{-3}$ T in Kelvins; on these coordinates, an Arrhenius relation of form:

$$\log_{10} k = \log_{10} A - \frac{E^*}{\theta} \qquad (7.11)$$

is described by a straight line of slope equal to activation energy E^* in kcal/mol and intercept $\log_{10} A$, where the pre-exponential factor A has units of the rate constant. The upper and lower panels of Figure 7.34 depict Arrhenius diagrams for the effective first order rate constant, k_{eff}, the upper panel derived from data over all conversions and the lower panel derived from low conversion data at $X < 0.4$. The best-fit Arrhenius parameters $[\log_{10} A\ (s^{-1}), E^*\ (kcal/mol)] = $ [7.30 ± 0.15, 38.2 ±
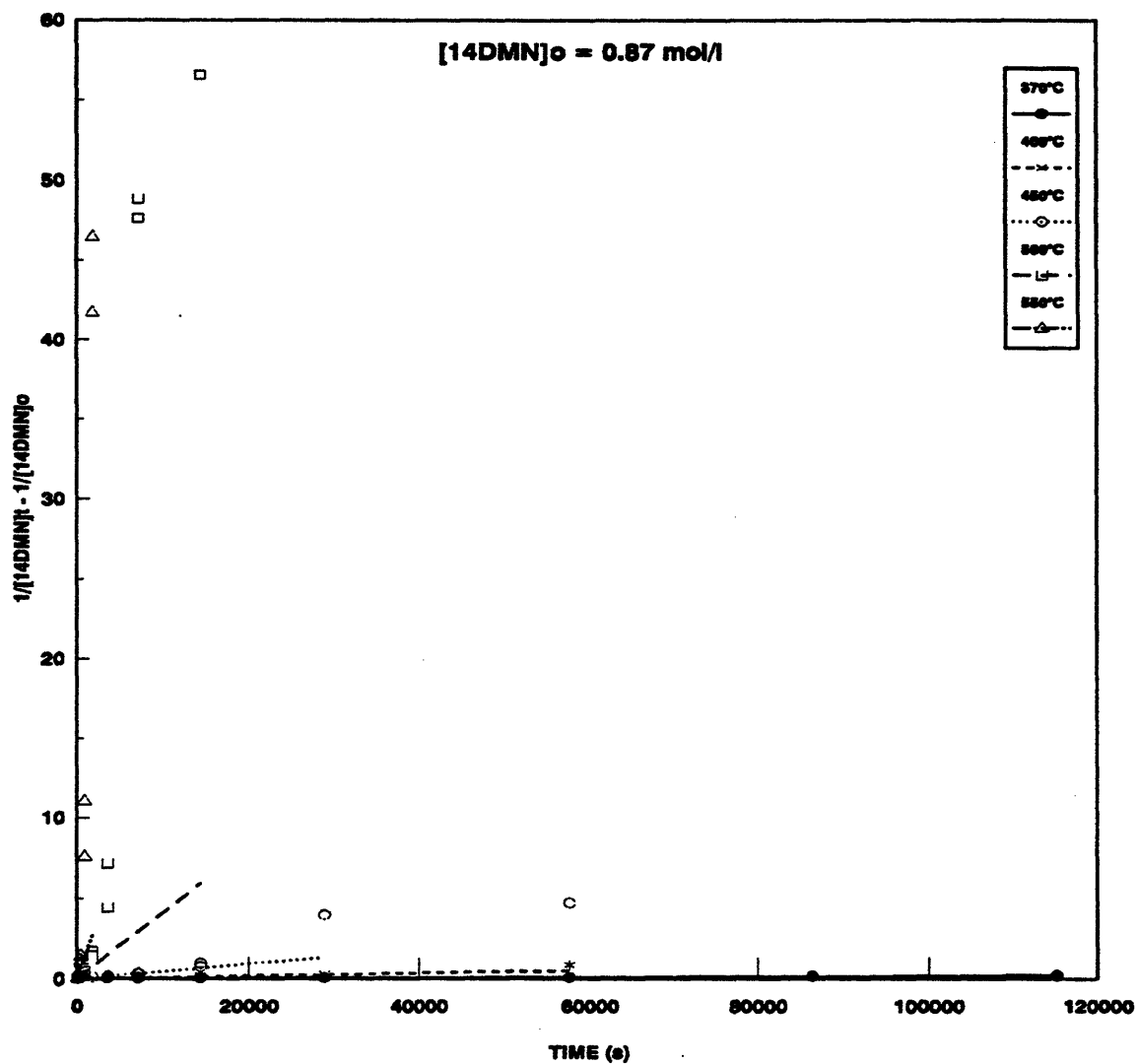
Figure 7.33: Plot of the integrated 2nd order rate expression for 14DMN thermolysis for varying T with fixed [14DMN]$_o$ = 0.87 mol/l.

665
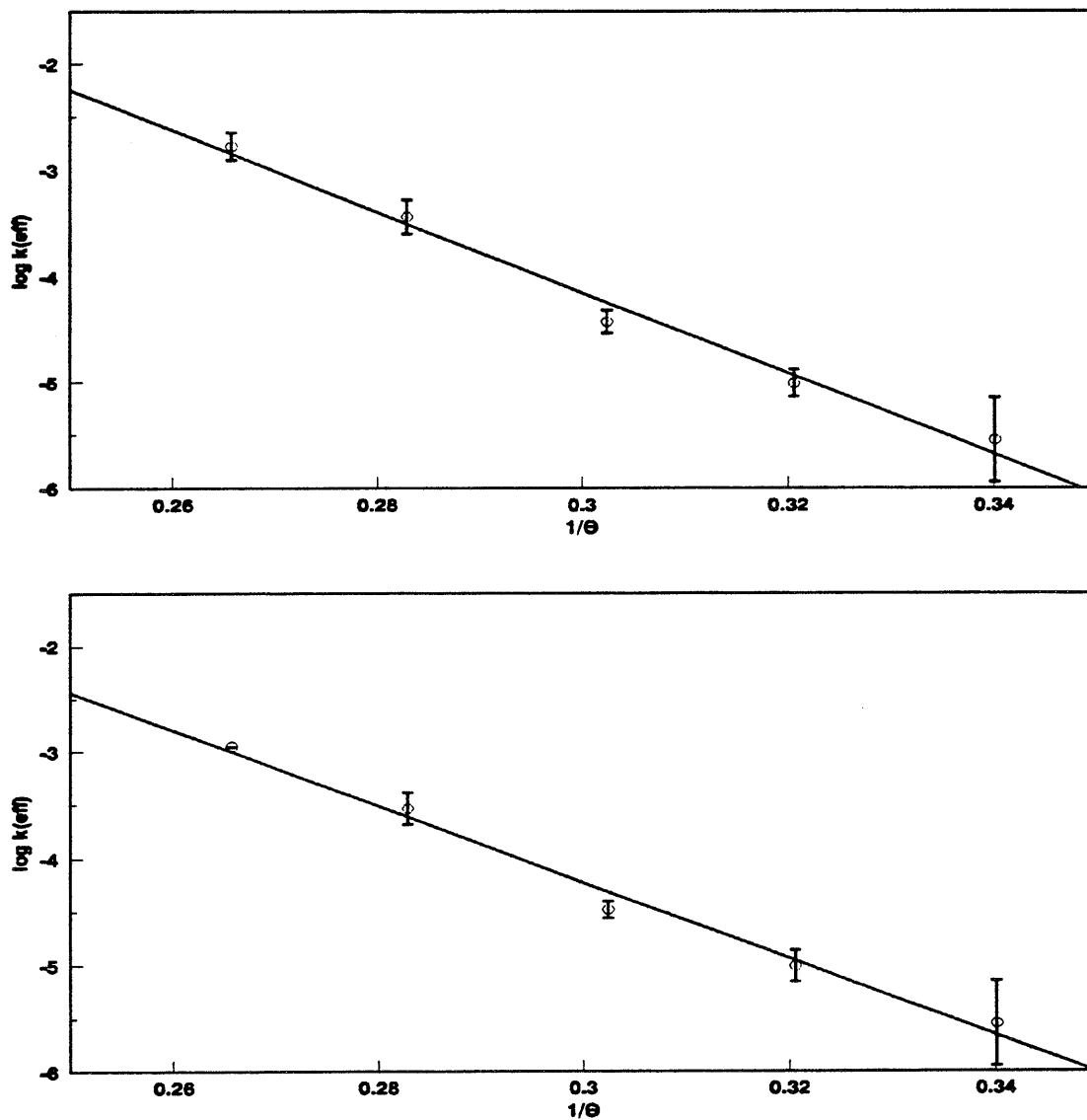
Figure 7.34: Arrhenius plot for k_{eff} for all conversions (top) and for $X < 0.4$ (bottom) with $[14DMN]_o = 0.87$ mol/l at $T = 450°C$.
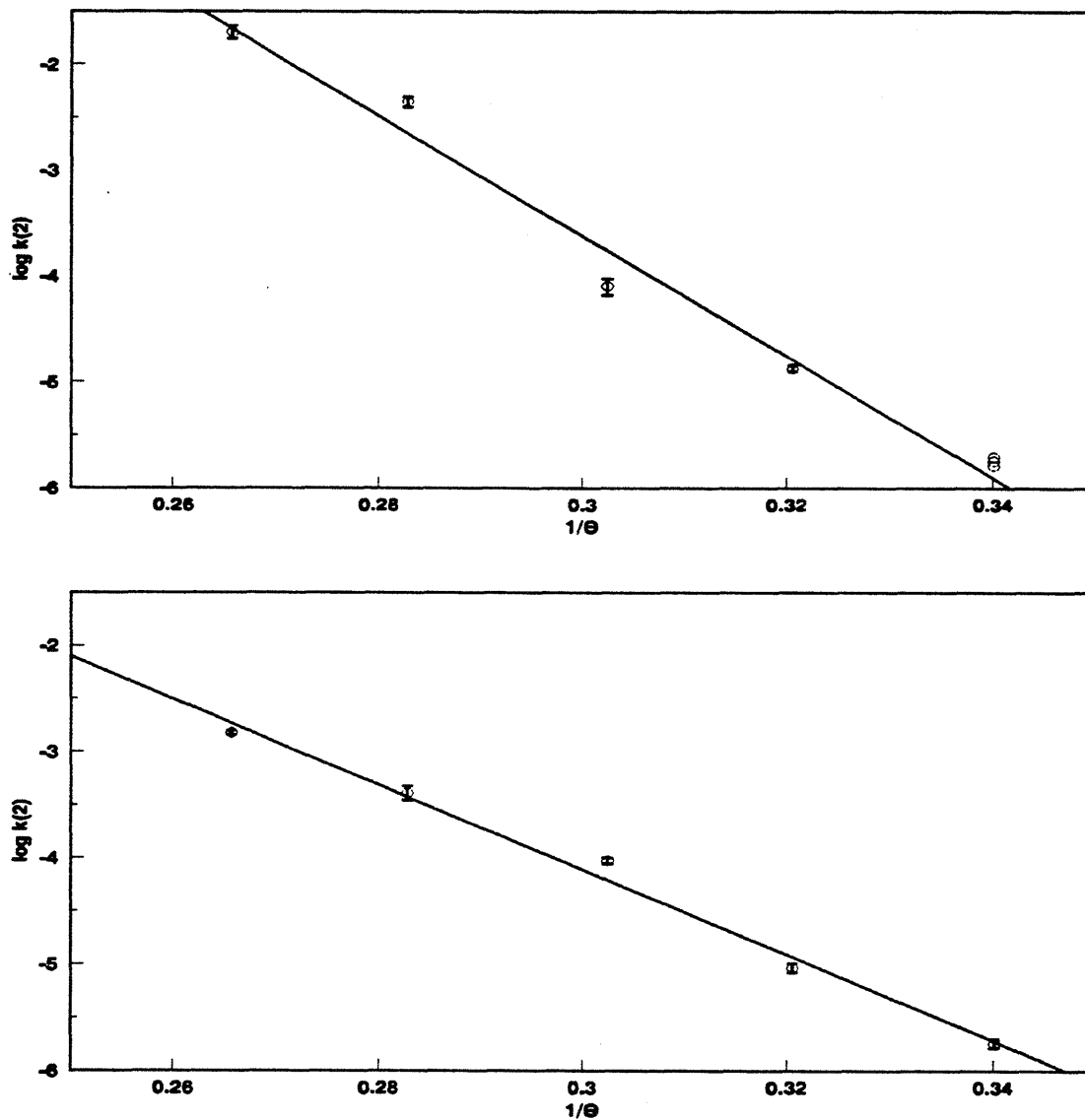
Figure 7.35: Arrhenius plot for $k_{3/2}$ for all conversions (top) and for X < 0.4 (bottom) with $[14DMN]_o$ = 0.87 mol/l at T = 450°C.

2.5] for k_{eff} using all conversions and [$\log_{10} A$ (s^{-1}), E* (kcal/mol)] = [6.50 ± 0.13, 35.7 ± 2.2] for k_{eff} using X < 0.4.

The upper and lower panels of Figure 7.35 depict Arrhenius diagrams for the 2nd order rate constant, k_2, the upper panel using data over all conversions and the lower panel using only low conversion data at X < 0.4. The best-fit Arrhenius parameters [$\log_{10} A$ (s^{-1}), E* (kcal/mol)] = [13.5 ± 0.21, 57.0 ± 3.6] for k_2 using all conversions and [$\log_{10} A$ (l$^{\frac{1}{2}}$/(mol$^{\frac{1}{2}}$ s)), E* (kcal/mol)] = [7.94 ± 0.14, 40.1 ± 2.3] for k_2 with X < 0.4. Regression of the half-lifes t* at varying temperatures in Section 7.1.3 gave Arrhenius parameters [$\log_{10} A$ (s^{-1}), E* (kcal/mol)] = [8.53 ± 0.09, 42.0 ± 1.6] for k_2.

7.2.3 Summary of Kinetics

Table 7.6 summarizes the kinetic parameters for 14DMN thermolysis as determined from the k_{eff} for the low conversion data at X < 0.4, the 2nd order rate expression for the low conversion data at X < 0.4 and the half-lifes at fixed [14DMN]$_0$ while varying temperature. The k_{eff} and t* analysis led to a 2nd order. The activation parameters $\log_{10} A$ and E* from the t* and 2nd order rate expression regression were comparable, while the $\log_{10} A$ and E* from the k_{eff} regression were somewhat lower.

Table 7.6

Summary of Kinetics for 14DMN Thermolysis				
	Order	$\log_{10} A$	E^*	log k (450°C)
k_{eff} (X < 0.4)	1.60 ± 0.09	6.50 ± 0.13	35.7 ± 2.2	-4.30
2nd order rate expression (X < 0.4)	2	7.94 ± 0.14	40.1 ± 2.3	-4.19
t^*	2.05 ± 0.16	8.53 ± 0.09	42.0 ± 1.6	-4.17

7.3 Reaction Pathways

Pathways for the thermolysis of 14DMN deduced from the results over the experimental grid are summarized in Figure 7.36. Three primary pathways operate in parallel upon the original 14DMN substrate, namely: (P1) Hydrogenation to *cis*- and *trans*-1,4-dihydro-1,4-dimethylnaphthalene, (P2) Demethylation to 1-methylnaphthalene, and (P3) Methylation to 1,4,5-trimethylnaphthalene, 1,4,6-trimethylnaphthalene and other TMN isomers. The main demethylation sequence, shown bold, cascades from 14DMN to 1MN to NAP. The primary demethylation product 1MN is secondarily operated upon by a pathway triad analogous to the preceding primary triad, eventually forming 1,4-dihydro-1-methylnaphthalene, a host of dimethylnaphthalenes (1,3-, 1,2- and 2,6-) and naphthalene. And at the highest substrate conversions, even the terminal demethylation product NAP suffers hydrogenation and methylation, as witnessed by the appearance of the minor products DHN and 2MN. Neither 14DMN or 1MN isomerize to their positional isomers, since the latter (methylated) species do not arise prior to the appearance of their demethylated precursor. Thus, the 1,3-, 1,2-, 2,6- and other DMNs rise after 1MN, while 2MN arises after NAP.

Figure 7.37 summarizes secondary and termination pathways deduced from the results over the experimental grid. The main demethylation sequence is shown again in bold. The primary demethylation product of 14DMN, 1MN, is associated with methane gas. The primary methylation products of 14DMN, 145TMN and
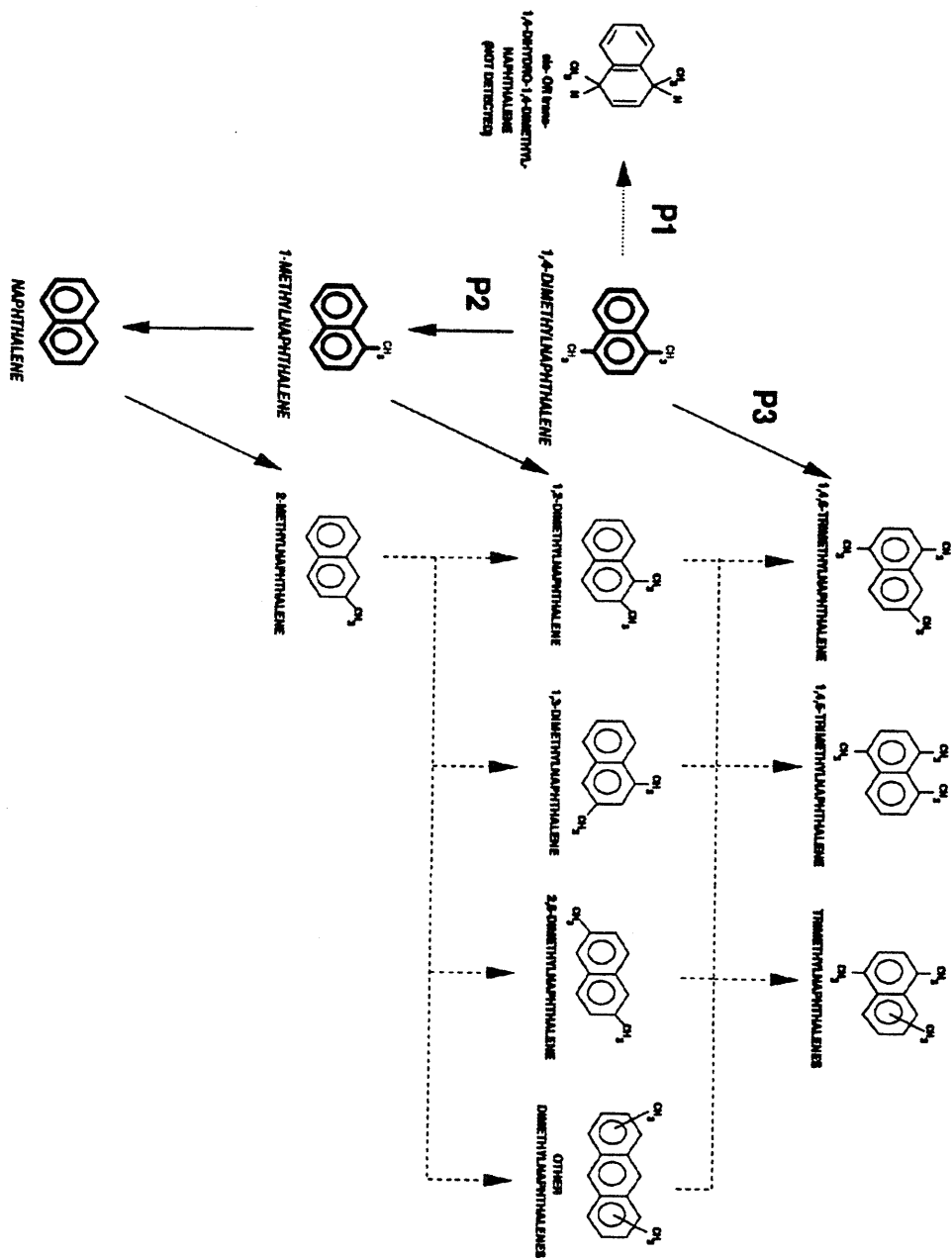
Figure 7.36: 14DMN primary decomposition pathways.
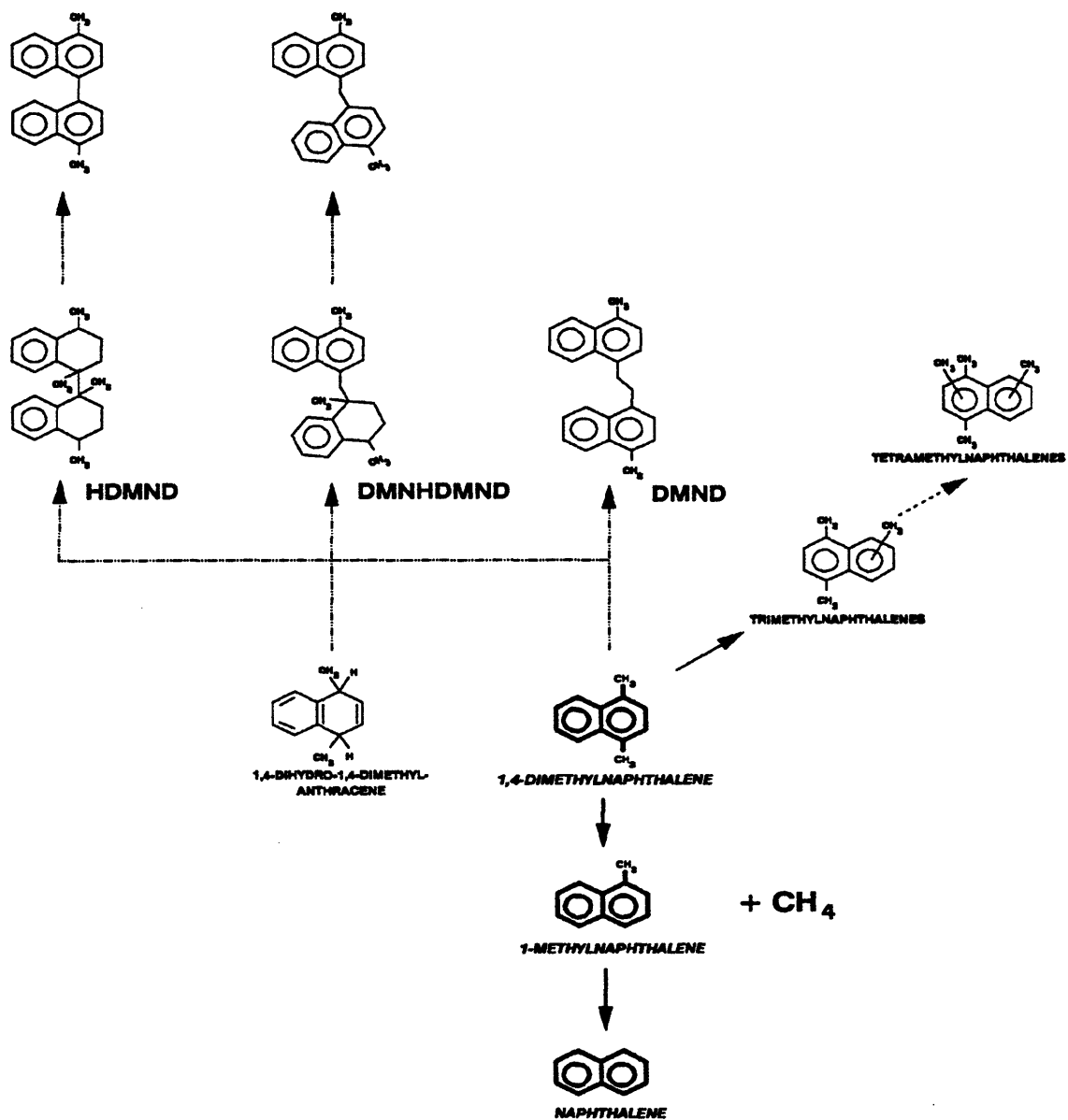
Figure 7.37: 14DMN secondary decomposition pathways.

145TMN, is secondarily operated upon by a pathway triad analogous to the primary triads, forming dihydrotrimethylnaphthalenes, tetramethylnaphthalenes (UNK182 in Section 4.3.2.1), and a multitude of dimethylnaphthalenes. Termination products include both pure- and cross-termination of 14DMN and 1MN radicals.

The relative importance of primary pathways (P1 - P3) in Figure 7.36 is shown in Figure 7.38, which depict the variation of certain primary product ratios R[TMN/1MN] versus conversion X at all initial substrate concentrations and temperatures.

R[DHDMN/1MN] measures the ratio of hydrogenation (P1) to demethylation (P2) pathways. R[DHDMN/1MN] was zero for all conversion since there was no DHDMN detected at any initial concentrations or temperatures.

R[TMN/1MN] measures the ratio of methylation (P3) to demethylation (P2) while R[CH4/1MN] measures the ratio of methane gas formed (roughly P2 - P3) relative to demethylation (P2). The upper panel of Figure 7.38 shows that R[TMN/1MN] has a power dependence on conversion for $0.24 < [14DMN]_o < 0.87$ mol/l and a weak function of conversion for $[14DMN]_o = 2.07$ mol/l, with R[TMN/1MN] $= 0.056 \, X^{-1.14}$ for $[14DMN]_o = [0.24, 0.87 \, mol/l]$ and slope of -0.37 and intercept of 0.44 for $[14DMN]_o = 2.07$ mol/l. The lower panel of Figure 7.38 shows that R[TMN/1MN] has a power dependence on conversion for all temperatures, with R[TMN/1MN] $= 0.051 \, X^{-0.76}$ for $0 < X < 0.95$. Although CH4 was detected, it was not quantified, therefore the R[CH4/1MN] was not available.
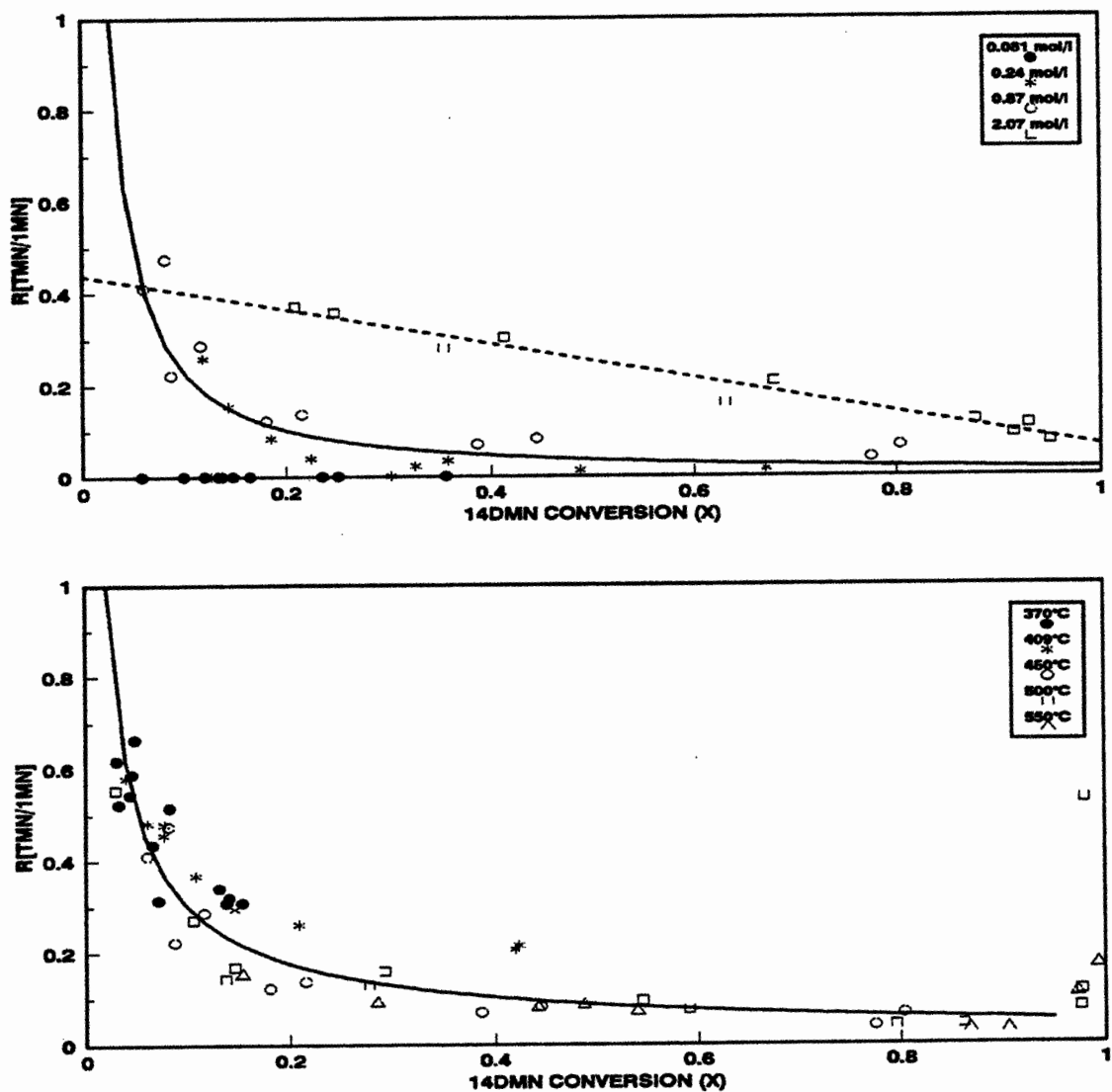
Figure 7.38: Ratio of moles TMN to moles 1MN produced vs. 14DMN conversion (X) for varying $[14DMN]_o$ at fixed T = 450°C (top) and for varying T with fixed $[14DMN]_o$ = 0.87 mol/l (bottom).

674

7.4 Mechanism and Modelling

A possible mechanism for the early stages of 14DMN thermolysis, that is consistent with the present pathway and kinetic observations and accounts for all the products observed during the initial stages of 14DMN thermolysis at low conversions, is enumerated. Thermochemical and activation parameters were assigned from first principles for each elementary reaction and its reverse. An algebraic steady state analysis was performed on the 14DMN mechanism to provide an independent check on numerical computer calculations. The mechanistic scheme and rate constants provided a platform for quantitative modelling of 14DMN thermolysis kinetics and product selectivities. A sensitivity analysis was performed to demonstrate how the errors of the estimated thermochemical and activation affected the model results. These activated parameters were then adjusted within the limits of the errors to provide the best fit to the experimental results.

7.4.1 Mechanism

A possible mechanism of 14DMN thermolysis is summarized in Figure 7.39, as an elementary step "graph". This is constructed such that the substrate and all stable molecular products are arrayed in the bottom row while unstable radical intermediates (the transition states) are arrayed in the top row. Reaction "nodes", arrayed in the middle row, connect the individual species in the bottom and top rows
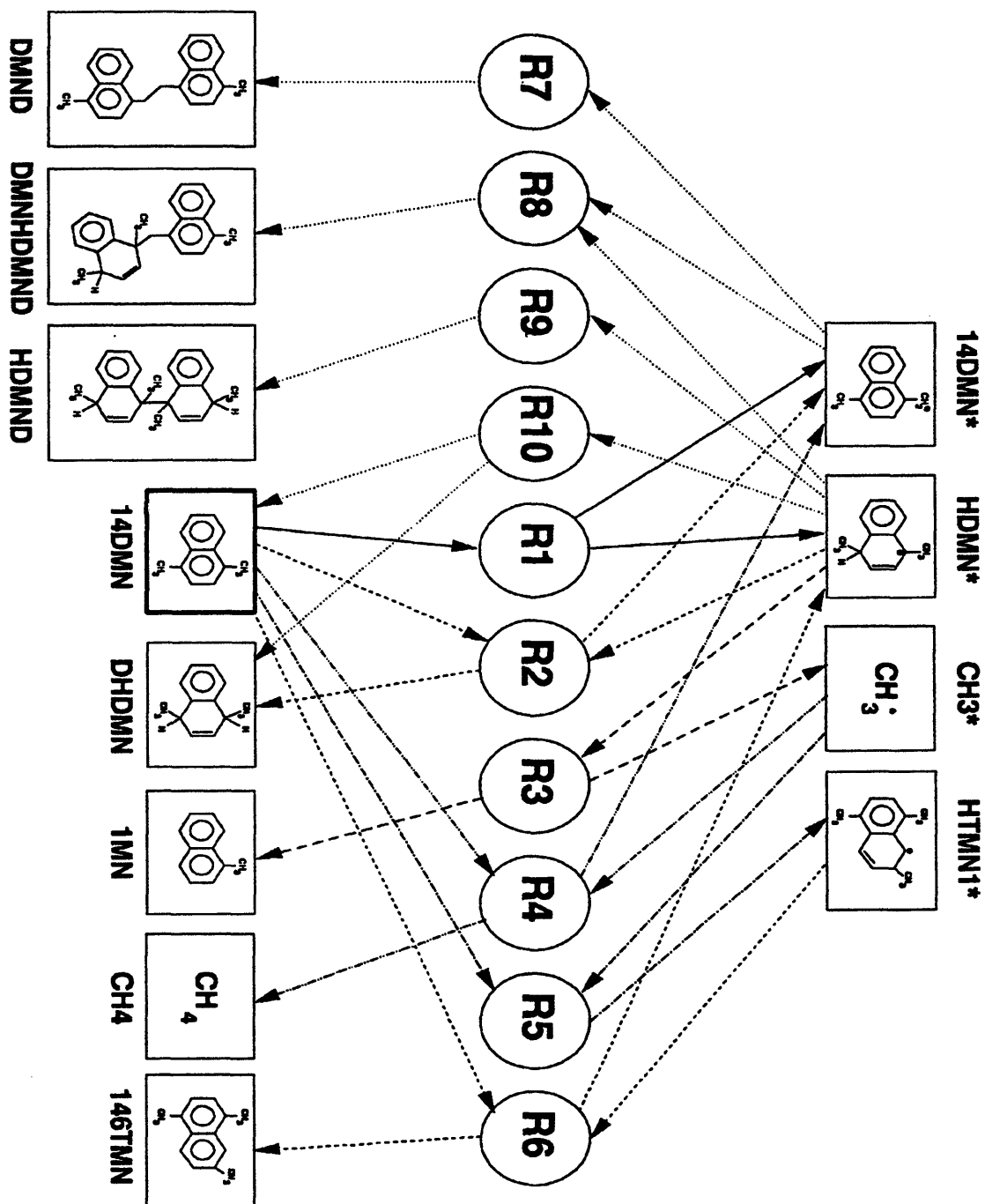
Figure 7.39: Elementary step graph of 14DMN thermolysis mechanism.

with arrows indicating the initial direction of reaction (all reactions are, of course, reversible). Initiation reactions are denoted by solid interconnecting lines, propagation (product forming) reactions by various kinds of dashed lines and termination reactions by dotted lines. Also, the substrate 14DMN is shown with heavy borders in the middle of the bottom row, with light (propagation) products to its right and heavy (termination) products, mostly dimers, to its left.

The free-radical cycle is initiated by the substrate 14DMN undergoing bimolecular disproportionation (R1), an intermolecular hydrogen transfer reaction, to form the respectively dehydrogenated and hydrogenated radical species 14DMN* and HDMN*. Of these, the latter can either abstract hydrogen from 14DMN substrate by (R2), to form DHDMN products (*cis-* or *trans-* not distinguished), or undergo a 6-scission type of radical decomposition by (R3), forming 1MN product and a methyl radical CH_3^*. The CH_3^* can either abstracted H from 14DMN substrate by (R4), to form methane product, or add to the 14DMN substrate by (R5), to form the trimethyl radical HTMN*. The latter can then abstract H from substrate 14DMN via (R6) to form the observed 145TMN or 146TMN product. Finally, the radical mechanism is terminated by the species 14DMN* and HDMN* engaging in both pure- and cross-combination, (R7-R9), to form various dimeric products. HDMN* radical can also terminate by disproportionation, (R10), to form 14DMN and DHDMN. Figure 7.40 displays the ten elementary steps that correspond to the "graph" in Figure 7.39 and the primary triad acting upon 14DMN in Figure 7.36.
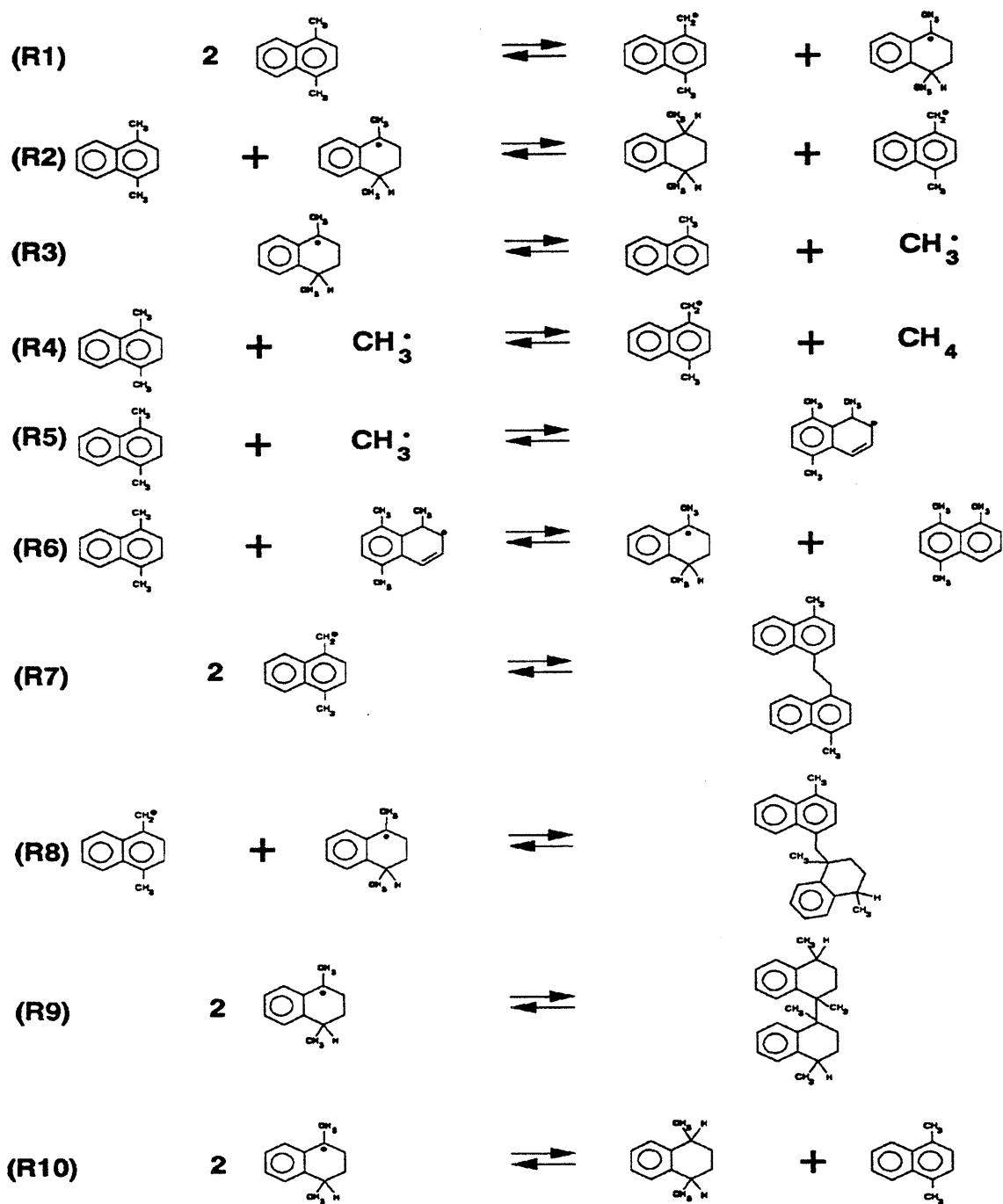
Figure 7.40: Elementary steps in 14DMN decomposition.

7.4.2 Stoichiometric Limits

The proposed mechanism exhibits certain stoichiometric limits. Consider three cases: 1) R1, R2 and R7 only; 2) R1, R3, R4 and R7; and 3) R1, R3, R5, R6 and R8 only. The first case, R1, R2 and R7 only, produces no 1MN, TMN, or CH4 and gives the overall reaction:

$$3 \ 14DMN \rightarrow DHDMN + DMND \qquad (7.12)$$

This case yields S(DHDMN) = 0.33, S(1MN) = 0, S(CH4) = 0, S(TMN) = 0 and S(HVY) = 0.33. The second case, R1, R3, R4 and R7 only, produces no DHDMN or CH4 and gives the overall reaction:

$$3 \ 14DMN \rightarrow 1MN + CH_4 + DMND \qquad (7.13)$$

This case yields S(DHDMN) = 0, S(1MN) = 0.33, S(CH4) = 0.33, S(TMN) = 0 and S(HVY) = 0.33. The third case, R1, R3, R5, R6 and R8 only, produces no DHDMN or CH4 and yields the overall reaction:

$$3 \ 14DMN \rightarrow 1MN + TMN + DMNHDMND \qquad (7.14)$$

This case yields S(DHDMN) = 0, S(1MN) = 0.33, S(CH4) = 0, S(TMN) = 0.33 and S(HVY) = 0.33. The mechanism thus restricts the maximum selectivities of each of DHDMN, 1MN, TMN and heavies to 1/3.

7.4.3 Thermochemical Property Estimation

In order to derive kinetic parameters for 14DMN mechanism, values of thermochemical property $\Delta H_f^{\circ}{}_{298}$, the enthalpy of formation, were required for all participating chemical species. Values of ΔH°_f for all species Table 7.7 are listed in and for all radical species in Table 7.8. Each table lists the species, the ΔH°_f, the source, remarks about how the ΔH°_f was estimated, and the error associated with the experimental or estimated ΔH°_f. The upper portion of each table, above the dashed line, lists experimental values, and their errors, for species that were used as a basis for the present derivations, which are list below the dotted line. Data for the basis species are from a variety of sources, including Benson (1977), abbreviated Benson1; Shaw, Golden and Benson (1977), abbreviated ShGB; Benson et. al. (1969), abbreviated Benson2; Pedley (1976); Stein, Golden and Benson (1977), abbreviated StGB; Stull (1969); Structure and Property Experimental (Stein et al., 1991), abbreviated SPX; and Structure and Property Estimation (Stein et al., 1991), abbreviated SPE. The enthalpy of formation in the tables for the species of interest were derived using a "macro" group additivity technique, starting with a basis molecule that was as large and as structurally similar to the desired species. Other basis species were then added and subtracted from the starting species to account for structural differences between it and the desired species. Finally, Table 5.9 details the relationships between ΔH°_f for each of the species in the 910DMA mechanism

Table 7.7

THERMOCHEMICAL PROPERTIES FOR STABLE SPECIES IN 14DMN THERMOLYSIS MECHANISM

Species	ΔH_f° (kcal/mol)	Source	Remarks	Error in ΔH_f°
12DHN	30.2	Benson2		± 2.0
14DHN	32.9	ShGB		± 2.0
2MN	26.4	StGB		± 0.6
18DMN	26.0	Pedley		± 0.4
17DMN	19.6	Stull		± 0.5
14CHD[1]	25.9	ShGB		± 0.5
36DM-14CHD[2]	11.3	ShGB		± 1.0
14DMN	19.7	Stull		± 0.5
1MN	27.2	StGB		± 0.5
NAPH	35.9	Pedley		± 0.4
146TMN	10.2	est	14DMN + (2MN - NAPH)	± 0.9
145TMN	16.6	est	146TMN + (18DMN - 17DMN)	± 1.1
avgDHDMN	18.3	est	14DHN + (36DM-14CHD - 14CHD)	± 2.3
CH4	-17.9	Pedley		± 0.1
DMND	56.0	calc		± 3.0
DMNHDMND	49.3	calc		± 3.0
HDMND	46.0	calc		± 3.0

Table 7.8

THERMOCHEMICAL PROPERTIES FOR RADICAL SPECIES IN 14DMN THERMOLYSIS MECHANISM

Species	ΔH_f° (kcal/mol)	Source	Remarks	Error in ΔH_f°
H*	52.1	Benson1		± 0.1
NAPH1*	62.1	est	$D_oC\text{-}H(12DHN)^1 - \Delta H_f^\circ(H^*) + \Delta H_f^\circ(12DHN)$	± 2.8
NAPH2*	59.1	est	$D_oC\text{-}H(14DHN)^2 - \Delta H_f^\circ(H^*) + \Delta H_f^\circ(12DHN)$	± 2.8
cyclohexane (CHX)	-29.5	ShGB		± 0.2
methylcyclohexane (MeCHX)	-37.0	Benson2		± 0.4
3-methyl-1,2-dihydronaphthalene (3Me-12DHN)	22.7	est	12DHN + (MeCHX - CHX)	± 2.0
3Me-12DHN*	54.6	est	$D_oC\text{-}H(12DHN)^1 - \Delta H_f^\circ(H^*) + \Delta H_f^\circ(3Me\text{-}12DHN)$	± 2.9
CH3*	34.8	Benson1		± 0.1
14DMN*	53.7	est	$D_oC\text{-}H(1MN)^3 - \Delta H_f^\circ(H^*) + \Delta H_f^\circ(14DMN)$	± 2.2
HDMN*	42.3	est	NAPH2* + (avgDHDMN - 14DHN) + ($D_oC\text{-}H(CUM)^4 - D_oC\text{-}H(ETBZ)^4$)	± 4.7
HTMN2*	38.4	est	3Me-12DHN* + (14DMN - NAPH)	± 2.9
HTMN1*	41.8	est	HTMN2* + ($D_oC\text{-}H(14DHN)^2 - D_oC\text{-}H(12DHN)^1$) + (18DMN - 17DMN)	± 4.1

[1] $D_oC\text{-}H(12DHN) = 84.0 \pm 2.0$ kcal/mol (NMBO estimate)

[2] $D_oC\text{-}H(14DHN) = 81.0 \pm 2.0$ kcal/mol (NMBO estimate)

[3] $D_oC\text{-}H(1MN) = 86.1 \pm 1.0$ kcal/mol (Stein and Brown 1990)

[4] $D_oC\text{-}H(cummene) = 82.5 \pm 1.5$ kcal/mol and $D_oC\text{-}H(ethylbenzene) = 84.7 \pm 1.5$ kcal/mol (S & PX)

Table 7.9

		NAP	14CHD	36DM-14CHD	CHX	MeCHX	12DHN	14DHN	1MN	2MN	14DMN	17DMN	18DMN	DoC-H(ETBZ*)	DoC-H(CUM*)	DoC-H(12DHN)	DoC-H(14DHN)	DoC-H(1MN)
		35.9±0.4	25.9±0.5	11.3±1.0	-29.5±0.2	-37.0±0.4	30.2±2.0	32.9±2.0	27.2±0.5	26.4±0.6	19.7±0.5	19.6±0.5	26.0±0.5	84.7±1.5	82.5±1.5	84.0±2.0	81.0±2.0	86.1±1.0
19.7±0.5	14DMN										*							
27.2±0.5	1MN								*									
10.2±0.9	146TMN	*								*	*							
16.6±1.1	145TMN	*								*	*	*	*					
18.3±2.3	avg DHDMN		*	*				*										
53.7±2.2	14DMN*										*						*	
42.3±4.7	HDMN*		*	*			*	*			*			*	*		*	
41.8±4.1	HTMN1*	*			*	*	*				*	*	*			*	*	
38.4±2.9	HTMN2*	*			*	*	*				*							

683

and the basis set of species, corrections and bond strengths.

Table 7.10 compares the best estimates from the present "macro" group additivity technique to values from THERM, an automated thermodynamic property estimation program for radicals and molecules using Benson's group additivity method by Ritter and Bozzelli (1990). The last two columns in Table 7.10 provide results from a second, alternative, "macro" estimate using the present methods. From Table 7.10 it is seen that, for all species, our best estimates for ΔH°_f differ from THERM, and for our alternate estimates, by amounts comparable to the errors stated in Table 7.7 and Table 7.8. Some confidence can therefore be placed upon the present ΔH°_f estimates.

7.4.4 Kinetic Parameter Estimation

Arrhenius expressions, of the form $\log_{10} k = \log_{10} A - E^*/\theta$, with rate constant k and pre-exponential factor A in units of ($l \; mol^{-\frac{1}{2}} \; s^{-\frac{1}{2}}$) and activation energy E^* in kcal/mol, were generated for each elementary step R1 - R10 of the 14DMN thermolysis mechanism, Figure 7.40. These expressions, and information regarding their deviation, are summarized in Table 7.11, as follows. Each elementary reaction was clarified according to type (column 2), using standard free-radical reaction notation. Next, kinetic data reported in the literature for that type of reaction was analyzed to ascertain its activation parameters. Of these, $\log_{10} A$ was decomposed into an intrinsic portion, $\log_{10} A_{int}$ (column 3) and a reaction path degeneracy, rpd

Table 7.10

COMPARISON OF $\Delta H_f°$ FOR SPECIES
IN 14DMN THERMOLYSIS MECHANISM

Species	$\Delta H_f°$ (kcal/mol) from:			
	Best Estimate	THERM	Other Method	Remarks on Other Methods
14DMN	19.7	21.0		
1MN	27.2	28.5		
NAPH	35.9	36.0		
146TMN	10.2	13.0	10.9	17DMN + (2MN - NAPH)
145TMN	16.6	18.0	17.3	18DMN + (1MN - NAPH)
cDHDMN		17.4	20.2	14DHN + (c14DM-CHX[1] - CHX)
tDHDMN		18.2	15.6	14DHN + (t14DM-CHX[2] - CHX)
DMND	56.0	51.7		
DMNHDMND	49.3	48.5		
HDMND	46.0	45.4		
14DMN*	53.7	54.9		
HDMN*	42.3	47.1		NAPH* + (cDHDMA - (14DHN + (MeCHX - CHX)))
HTMN1*	38.4	43.5		
HTMN2*	41.8	42.1		

[1]   c14DM-CHX = *cis*-1,4-dimethylcyclohexane, $\Delta H_f°$ = -42.2 kcal/mol (Benson2)

[2]   t14DM-CHX = *cis*-1,4-dimethylcyclohexane, $\Delta H_f°$ = -44.1 kcal/mol (Benson2)

Table 7.11

	Type of Reaction	$\log_{10} A_{int}$ l mol^{-1} s^{-1}	rpd	Evans-Polanyi Relation: $E^* =$	ΔH_r° kcal/mol	E^* kcal/mol	Arrhenius Expression: $\log_{10} k =$
	ARRHENIUS EXPRESSIONS FOR ELEMENTARY STEPS OF 14DMN THERMOLYSIS MECHANISM						
R1	molecular disproportionation	9.0	24	ΔH_r°	56.6	56.6	9.9 - 56.6/θ
R-1	radical disproportionation	8.5	1	0	-56.6	0	8.5
R2	H-abstraction	8.1	6	17.5 + ΔH_r°/2	10.0	22.5	8.9 - 22.5/θ
R-2	H-abstraction	8.1	2	17.5 + ΔH_r°/2	-10.0	12.5	8.4 - 12.5/θ
R3	methyl scission	13.5	1	5.1 + ΔH_r°	19.7	24.8	13.5 - 24.8/θ
R-3	CH3* addition	8.3	1	5.1	-19.7	5.1	8.3 - 5.1/θ
R4	H-abstraction	8.1	6	17.5 + ΔH_r°/2	-18.6	8.2	8.9 - 8.2/θ
R-4	H-abstraction	8.1	4	17.5 + ΔH_r°/2	18.6	26.8	8.7 - 26.8/θ
R5	CH3* addition	8.3	4	5.1	-16.1	5.1	8.9 - 5.1/θ
R-5	methyl scission	13.5	1	5.1 + ΔH_r°	16.1	21.1	13.5 - 21.1/θ
R6	radical H transfer	8.1	2	17.5 + ΔH_r°/2	-5.6	14.7	8.4 - 14.7/θ
R-6	radical H transfer	8.1	1	17.5 + ΔH_r°/2	5.6	20.3	8.1 - 20.3/θ
R7	radical combination	9.3	1	0	-55.7	0	9.3
R-7	homolytic dissociation	15.5	1	ΔH_r°	55.7	55.7	15.5 - 55.7/θ
R8	radical combination	9.3	1	0	-47.5	0	9.3
R-8	homolytic dissociation	15.5	1	ΔH_r°	47.5	47.5	15.5 - 47.5/θ
R9	radical combination	9.3	1	0	-39.2	0	9.3
R-9	homolytic dissociation	15.5	1	ΔH_r°	39.2	39.2	15.5 - 39.2/θ
R10	radical disproportionation	8.5	1	0	-46.6	0	8.5
R-10	molecular disproportionation	8.5	4	ΔH_r°	46.6	46.6	9.1 - 46.6/θ

(column 4), with $\log_{10} A = \log_{10} A_{int} + \log_{10}$ (rpd). The activation energy E^* was determined by an Evans-Polanyi expression (column 5), of form $E^* = E_o + \alpha \Delta H^\circ_r$. Values of the enthalpy of reaction ΔH°_r (column 6), derived from the data of Section 5.4.3, then led to E^* (column 7). Final Arrhenius expressions are summarized in column 8 of Table 7.11.

Specific remarks concerning individual elementary steps and reaction types are elaborated below:

(R1) Benson (1976) estimated $\log A_{int} = 9.0 \pm 1.0$ and $E^* = \Delta H_r^\circ$ for molecular disproportionation of small hydrocarbon molecules into radicals. Stein (1981) estimates $\log A_{int} = 8.1$ for stabilized hydrocarbon radicals. Billmers et.al. (1986) report $\log A_{int} = 8.7 \pm 0.14$ for molecular disproportionation of 9,10-dihydroanthracene and 2-ethylanthracene. From these, we have chosen $\log A_{int} = 8.5 \pm 0.5$ and $E^* = \Delta H^\circ_r$ to represent molecular disproportionation to radicals. Also, for k_1, rpd $= 3 \times 2 \times 2 \times 2 = 24$ because each methyl group contains three hydrogen atoms, there are two methyl groups on each 14DMN, each 14DMN has two sites for hydrogenation (9 and 10), and each of the two 14DMN can serve as either hydrogen donor or acceptor.

(R-1) Radical disproportionation is estimated to have the same $\log A_{int} = 8.5 \pm 0.5$ as molecular disproportionation, with activation energy $E^* = 0$. For k_{-1}, rpd $= 1$.

(R2) H-abstraction by a hydrocarbon radicals has been correlated by Kerr (1973), who provides $\log A_{int} = 7.7$ and $E_o = 12.7$ kcal/mol for $C_2H_5^*$ and $\log A_{int} = 8.2$

and E_o = 14.3 kcal/mol for CH_3^*, and by Benson (1976), who quotes log A_{int} = 8.2

and E_o = 14.6 kcal/mol for CH_3^*. Also, Ingold (1973) reported on CH_3^* abstracting

hydrogen from toluene with log A_{int} = 8.1 and E^* = 9.5 kcal/mol, from which the

corresponding Evans-Polanyi relation, with a slope α of 0.5 and ΔH°_r = -16.0

kcal/mol yields E_o = 17.5 kcal/mol. We use Ingolds' results, log A_{int} = 8.1 and E^*

= 17.5 + $\Delta H^{\circ}_r/2$, as the basis for all H-abstraction kinetics.

(R-2) Since the microscopic reverse of an H-abstraction is another H-abstraction,

the same parameters apply to R-2 as were used for R2.

(R3) Methyl scissions, a particular type of β-scission reaction, typically have log A

= 13.5 and E^* = 7 + ΔH°_r (Kerr 1983, Dean 1985). For (R3), the value of E_o = 7

kcal/mol has been adjusted, as explained below for (R-3), to E_o = 5.1 kcal/mol.

(R-3) Holt and Kerr (1977) provide Arrhenius parameters of log A_{int} = 8.3 and E^*

= 7.6 kcal/mol for CH3* addition to benzene. The activation energy for the

addition of a methyl radical to 1MN will be less than that for the addition to benzene

because of the lower localization energy in 1MN. This adjustment was estimated

from Stephani and Szwarc (1962) who found that at 85°C the rate of methyl addition

to naphthalene was 33 times faster than the rate of methyl addition to benzene.

Assuming equal pre-exponential factors, the rate difference corresponds to a

difference in activation energy of 2.5 kcal/mol. Thus E^* = 5.1 for CH3* addition to

1MN; this is also the value of E_o in the Evans-Polanyi relation for the reverse methyl

scission reaction (R3).

(R4 and R-4) These are H-abstractions, treated in the same manner as (R2 and R-2).

(R5 and R-5) These are analogous to (R-3 and R3) with rpd = 4 (pi bonds).

(R6 and R-6) These radical hydrogen transfer (RHT) reactions, wherein a hydrogen atom differ somewhat from the conventional H-abstraction, wherein the H-atom transfers from a molecule to a radical. Billmers et.al. (1986) estimated $\log A = 8.2 + \log$ rpd and $E_o = 18.3$ kcal/mol for a thermoneutral H transfer at 350°C from a 9-hydroanthryl radical to 2-ethylanthracene. We directly apply the H-abstraction relations, developed for R2 and R-2, to the present RHTs R6 and R-6.

(R7) Ingold (1973) quotes radical combination rates of $\log k = 9.3$ for two benzyl (also two cumyl) radicals. Benson (1976) has $\log k = 9.5$ for two t-butyl radicals, and Miller and Stein (1981) give $\log k = 9.5$ for two α-1,2-diphenylethyl radicals. Since radical combinations are unactivated, that is, $E^* = 0$, we choose $\log A = 9.3$ for all pure benzyl radical combinations.

(R-7) For homolytic dissociation into stabilized radicals, Benson (1976) estimated $\log A = 15.5 \pm 0.5$ and $E^* = \Delta H_r^\circ$. Miller and Stein (1981) used $\log A = 15.9$ and $E^* = \Delta H_r^\circ = 57.5$ kcal/mol for 1,2,3,4-tetraphenylbutane dissociating into two α-1,2-diphenylethyl radicals. We adopt Benson's parameters.

(R8 and R-8) Radical combination and homolytic dissociation analogous to (R7 and R-7) except that R8 is a cross-combination, so the $k_8 = 2 k_7 k_9$ and $\log k_8 = 9.6$.

(R9 and R-9) Radical combination and homolytic dissociation are also analogous to (R7 and R-7).

(R10 and R-10) Radical and molecular disproportionations are analogous to (R1 and R-1).

7.4.5 Modelling

The 14DMN thermolysis mechanism devised in Figure 7.40 combined with the Arrhenius expressions derived for each elementary step in Table 7.11 provided a mechanistic kinetic model of 14DMN thermolysis, valid at low conversions, over the entire initial concentration and temperature ranges of the present experiments. Results of this mechanistic model, and comparisons between these and experimental results, are detailed in this section. Most model calculations were made at the center of the experimental grid, where $[14DMN]_o = 0.87$ mol/l and T = 450°C. Selected calculations were also made at the four corners of the grid, for $[14DMN]_o = 0.081$ and 2.07 mol/l at T = 450°C and at T = 370 and 550°C for $[14DMN]_o = 0.87$ mol/l. The scheme of calculations was as follows. First an algebraic analysis was performed, to estimate the pseudo-steady-state radical concentrations at selected low conversions; these served to verify the validity of subsequent numerical solutions. Next, full numerical solutions were obtained for the model 14DMN thermolysis mechanism, using a computer code ("ACUCHEM", Braun et. al. 1988) for solving the system of simultaneous differential equations for the conservation of all species. The calculated product histories, selectivities and product ratios were compared with experimental values. A sensitivity analysis of the model was performed at the central

point of the experimental grid, by separately perturbing selected elementary step kinetics over their estimated uncertainty limits. Based on this, a set of "optimized" kinetic parameters were derived to best-fit the model to experimental observations.

7.4.5.1 Algebraic Analysis

The pseudo-steady-state approximation is applied to the radical species, whereby the rate of change in the concentration of all radical species is deemed to be ~ 0. In our case, this yields four algebraic equations, one for each radical species, as shown in Figure 7.41. When added together, these equations provide an expression equating the rate of initiation LHS to the rate of termination RHS. Given the concentrations of stable species, and all rate constants, the foregoing system of algebraic equations can be solved (e.g. by successive approximations) to provide the concentrations of all radicals species. Results for the solution at $[14DMN]_o = 0.87$ mol/l and $T = 450°C$ at initial conditions of $X = 0$, where substrate is the only stable species, are given in column 2 of Table 7.12. It is seen that 14DMN* is the most prevalent radicals, with concentration 4.8E-08 mol/l; and HDMN* being the second most prevalent radical with a much lower concentration of 4.6E-14 mol/l. These results can further be used to calculate instantaneous rates of formation for all products at $X = 0$, based on which it is possible to estimate the amounts of all species at an adjacent (low) conversions, say $X = 0.05$. Here the pseudo-steady-state calculations can be repeated with the new stable species

$$\frac{d[14DMN*]}{dt} = k_1[14DMN]^2 - k_{-1}[HDMN*][14DMN*] + k_2[14DMN][HDMN*]$$

$$- k_{-2}[DHDMN][14DMN*] + k_4[14DMN][CH3*] - k_{-4}[14DMN*][CH4]$$

$$- 2k_7[14DMN*]^2 + 2k_{-7}[DMND] - k_8[14DMN*][HDMN*]$$

$$+ k_{-8}[DMNHDMND] = 0$$

$$\frac{d[HDMN*]}{dt} = k_1[14DMN]^2 - k_{-1}[HDMN*][14DMN*] - k_2[14DMN][HDMN*]$$

$$+ k_{-2}[DHDMN][14DMN*] - k_3[HDMN*] + k_{-3}[1MN][CH3*]$$

$$+ k_6[HTMN*][14DMN] - k_{-6}[TMN][HDMN*] - k_8[14DMN*][HDMN*]$$

$$+ k_{-8}[DMNHDMND] - 2k_9[HDMN*]^2 + 2k_{-9}[HDMND]$$

$$- 2k_{10}[HDMN*] + 2k_{-10}[14DMN][DHDMN] = 0$$

$$\frac{d[CH3*]}{dt} = k_3[HDMN*] - k_{-3}[1MN][CH3*] - k_4[14DMN][CH3*]$$

$$+ k_{-4}[CH4][14DMN*] - k_5[14DMN][CH3*] + k_{-5}[HTMN*] = 0$$

$$\frac{d[HTMN*]}{dt} = k_5[14DMN][CH3*] - k_{-5}[HTMN*] - k_6[14DMN][HTMN*]$$

$$+ k_{-6}[TMN][HDMN*] = 0$$

ADDING TOGETHER:

$$k_1[14DMN]^2 + k_{-7}[DMND] + k_{-8}[DMNHDMND] + k_{-9}[HDMND] + k_{-10}[14DMN][DHDMN]$$

$$= k_7[14DMN*]^2 \left(1 + \frac{(k_{-1} + k_8)[HDMN*]}{k_7[14DMN*]} + \frac{(k_9 + k_{10})[HDMN*]^2}{k_7[14DMN*]^2}\right)$$

Table 7.12

COMPARISON OF PSEUDO-STEADY-STATE AND FULL NUMERICAL SOLUTION RESULTS FOR 14DMN THERMOLYSIS AT T = 450°C WITH $[14DMN]_0$ = 0.87 mol/l

Species	Pseudo-Steady-State		Numerical Solution	
	X = 0	X = 0.10	X → 0	X = 0.10
14DMN*	4.79E-08[1]	1.30E-07	8.61E-09	8.40E-07
HDMN*	4.60E-14	5.07E-13	4.60E-14	4.95E-14
CH3*	2.00E-14	2.44E-13	2.00E-14	6.86E-14
HTMN*	2.00E-14	3.32E-13	3.02E-14	9.25E-14
14DMN	8.70E-01	7.38E-01	8.70E-01	7.36E-01
1MN	0	7.40E-04	2.30E-06	3.17E-02
DHDMN	0	1.53E-08	2.46E-10	1.36E-10
CH4	0	7.36E-04	2.29E-06	3.14E-02
TMN	0	3.77E-06	1.18E-08	3.13E-04
DMND	0	7.36E-04	2.28E-06	3.14E-02
DMNHDMND	0	3.42E-08	5.83E-14	6.11E-12
HDMND	0	1.24E-14	9.63E-22	1.11E-21

[1]   Values in table are species concentrations in mol/l

concentrations, to provide a new set of radical concentrations. Column 3 of Table 7.12 shows results obtained in this manner at X = 0.10. It is seen the 14DMN* remains the dominant radical species but its concentration 1.30E-07 mol/l differed somewhat from the values at X = 0, while HDMN* remained the second most prevalent species, again with a much lower concentration, 5.07E-13 mol/l.

The final two columns of Table 7.12 show radical and stable species concentrations calculated (see below) during the full numerical solution for $[14DMN]_o$ = 0.87 mol/l and T = 450°C at conversions respectively X → 0 (very low) and X = 0.10. The numerical solution also show 14DMN* to be the dominant radical species and HDMN* second most prevalent at both conversions. Also, the concentrations of all species, both radical and stable, calculated by the numerical solution agree quite closely, to within a factor of 2 or better, with corresponding results obtained from the pseudo-steady-state algebraic solution at low conversions. At X = 0.10, the radical concentrations agree within an order of magnitude, and the stable species agree within 2 orders of magnitude for the dominant species; 1MN, CH4, TMN and DMND. Although these estimates do not agree as well as the two previous cases, 2-fold for 910DMA and 4-fold for 9MA, this still bolsters our confidence in the fidelity of the numerical solution results.

7.4.5.2 Numerical Solutions and Comparison with Experiments

Conservation relations derived from the mechanistic model of 14DMN thermolysis and using the rate constants of Section 7.4.4 were numerically integrated using a computer program called ACUCHEM (Braun et. al. 1988). Initial conditions $[14DMN]_o$ and T were chosen to match experimental initial conditions. Concentration versus time data was generated for each $[14DMN]_o$ and T.

7.4.5.2.1 Detailed Calculations at T = 450°C for $[14DMN]_o$ = 0.87 mol/l

Table 7.13 and Table 7.14 detail our numerical solution of the model at the central point, T = 450°C and $[14DMN]_o$ = 0.87 mol/l, of the experimental grid. Columns 2-4 of Table 7.13 show Arrhenius expressions, with pre-exponential factor A ($l\ mol^{-1}\ s^{-1}$ units), activation energy E^* in kcal/mol and rate constant k ($l\ mol^{-1}\ s^{-1}$ units), for each elementary step R1 - R10 of the 14DMN thermolysis mechanism (columns 2-4). The radical and stable species concentrations generated by the numerical solution were then used with the rate constants to ascertain the rate, in mol $l^{-1}\ s^{-1}$, of each forward and reverse reaction in the 14DMN thermolysis mechanism at two conversions X = 0.001 (limit X ~ 0) and X = 0.32, as shown in the last two columns of Table 7.13. The rates of the elementary reactions were then used to calculate the rates of radical and stable species formation at X = 0.001 and X = 0.32 as shown in columns 3 and 5 respectively of Table 7.14. The elementary reactions that contribute to the formation of each radical and stable species are listed

695

Table 7.13

ARRHENIUS EXPRESSIONS, RATE CONSTANTS AND RATES OF ELEMENTARY STEPS IN THE MODEL 14DMN THERMOLYSIS AT T = 450°C WITH [14DMN]$_o$ = 0.87 mol/l					
			k	**Rate, r(mol/l s), at Conversion (X)**	
	log$_{10}$ A	**E***	**(T = 450°C)**	**0.001**	**0.32**
R1	9.9	56.6	6.04E-08	4.57E-08	2.13E-08
R-1	8.5	0	3.16E+06	1.25E-13	9.11E-11
R2	8.9	22.5	1.24E+02	4.98E-12	1.50E-11
R-2	8.4	12.5	4.16E+04	8.83E-14	1.49E-11
R3	13.5	24.8	9.98E+05	4.59E-08	2.02E-07
R-3	8.3	5.1	5.72E+06	2.63E-13	1.79E-07
R4	8.9	8.2	2.63E+06	4.57E-08	5.25E-07
R-4	8.7	26.8	3.93E+00	7.73E-14	5.06E-07
R5	8.9	5.1	2.28E+07	3.96E-07	4.55E-06
R-5	13.5	21.1	1.31E+07	3.97E-07	4.56E-06
R6	8.4	14.7	8.99E+03	2.37E-10	1.85E-09
R-6	8.1	20.3	9.12E+01	4.97E-20	5.67E-14
R7	9.3	0	2.00E+09	1.48E-07	4.04E-03
R-7	15.5	55.7	4.50E-02	1.03E-07	4.08E-03
R8	9.3	0	2.00E+09	7.91E-13	5.75E-10
R-8	15.5	47.5	1.36E+01	7.92E-13	5.76E-10
R9	9.3	0	2.00E+09	4.23E-18	8.18E-17
R-9	15.5	39.2	4.40E+03	4.24E-18	8.21E-17
R10	8.5	0	3.16E+08	6.70E-19	1.30E-17
R-10	9.1	46.6	1.01E-05	2.17E-15	1.51E-15

Table 7.14

CALCULATED RATES OF FORMATION OF RADICAL AND STABLE SPECIES AT X = 0.001 AND 0.32 AT T = 450°C WITH [14DMN]$_o$ = 0.87 mol/l

	CONTRIBUTING REACTIONS	r (mol/l s) at X = 0.001	Major Contribution	r (mol/l s) at X = 0.32	Major Contribution
r(14DMN*)	R1 - R-1 + R2 - R-2 + R4 - R-4 - 2R7 + 2R-7 - R8 + R-8	8.0E-10		7.0E-05	
r(HDMN*)	R1 - R-1 - R2 + R-2 - R3 + R-3 + R6 - R-6 - R8 + R-8 - 2R9 + 2R-9 - 2R10 + 2R-10	3.8E-12		5.6E-11	
r(CH3*)	R3 - R-3 - R4 + R-4 - R5 + R-5	1.2E-09		1.6E-08	
r(HTMN*)	R5 - R-5 - R6 + R-6	-1.2E-09		-1.4E-08	
r(14DMN)	-2R1 + 2R-1 - R2 + R-2 - R4 + R-4 - R5 + R-5 - R6 + R-6 + R10 - R-10	-1.4E-07	R1, R4, R5, R-5	-5.1E-08	R1, R4, R-4, R5, R-5
r(1MN)	R3 - R-3	4.6E-08	R3	2.3E-08	R3, R-3
r(TMN)	R6 - R-6	2.4E-10	R6	1.9E-09	R6
r(CH4)	R4 - R-4	4.6E-08	R4	1.9E-08	R4, R-4
r(DHDMN)	R2 - R-2 + R10 - R-10	4.9E-12	R2	3.9E-14	R2, R-2
r(DMND)	R7 - R-7	4.5E-08	R7, R-7	-3.5E-05	R7, R-7
r(DMNHDMND)	R8 - R-8	-1.1E-15	R8, R-8	-1.4E-12	R8, R-8
r(HDMND)	R9 - R-9	-1.3E-20	R9, R-9	-2.6E-19	R9, R-9

in column 2 of Table 7.14, while those reactions that make the major contributions to the formation of the stable species at the low and high conversions are noted columns 4 and 6. It is seen that the rate of destruction of 14DMN is dominated by R1 (4.57E-08), R4 (4.57E-08), R5 (3.96E-07) and R-5 (3.97E-07) at X = 0.001 and by R1 (2.13E-08), R4 (5.25E-07), R-4 (5.06E-07), R5 (4.55E-06) and R-5 (4.56E-06) at X = 0.32. The rate of formation of 1MN is controlled by R3 (4.59E-08) at X = 0.001 and by R3 (2.02E-07) and R-3 (1.79E-07) at X = 0.32, whereas the rate formation of CH4 is controlled by R4 (4.57E-08) at low conversion and by R4 (5.25E-07) and R-4 (5.06E-07) at X = 0.32. The rate of formation of TMN is controlled by both R6 (respectively, 2.37E-10 and 1.85E-09) at X = 0.001 and 0.32. The rate of formation of DHDMN is the sum of R2, R-2, R10 and R-10, but R2 (4.98E-12) is the major contribution to the rate of formation of DHDMN at X = 0.001 and R2 (1.50E-11) and R-2 (1.49E-11) are the major contributions at X = 0.32. The rates of dimer formation, r(DMND), r(DMNHDMND), and r(HDMND), are controlled by respective termination reactions. The rate of formation of DMND is the sum of both R7 (respectively, 1.48E-07 and 4.04E-03) and R-7 (respectively, 1.03E-07 and 4.08E-03) at X = 0.001 and 0.32. The rate of formation of DMNHDMND is the sum of both R8 (respectively, 7.91E-13 and 5.75E-10) and R-8 (respectively, 7.92E-13 and 5.76E-10) at X = 0.001 and 0.32. The rate of formation of HDMND is the sum of both R9 (respectively, 4.23E-18 and 8.18E-17) and R-9 (respectively, 4.24E-18 and 8.21E-17) at X = 0.001 and 0.32. Figure 7.42 graphically
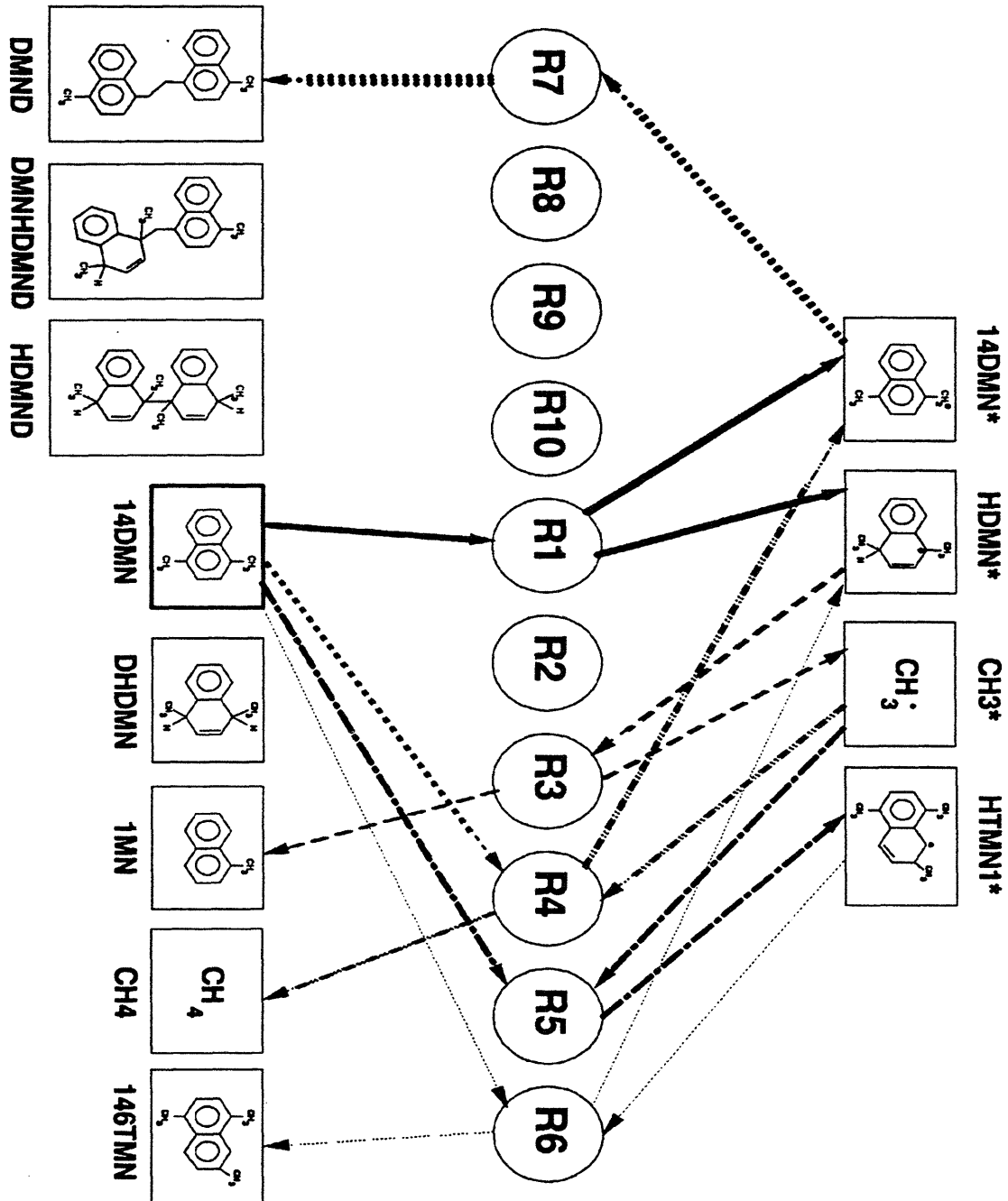
Figure 7.42: Relative elementary reaction rate traffic at T = 450°C and $[14DMN]_o$ = 0.87 mol/l for X → 0.

depicts the elementary reaction traffic during 14DMN thermolysis at $X \to 0$, with the thicker arrows denoting reactions with the greater net (forward - backward) rates. Figure 7.43 presents a similar depiction of reaction traffic at $X = 0.32$.

Figure 7.44 compares the substrate and product histories (upper panel) and product selectivities (lower panel) as obtained from numerical solution of the thermolysis model to the experimental data for 14DMN, 1MN, TMN and CH4 at the center of the experimental grid, $[14DMN]_o = 0.87$ mol/l and $T = 450°C$. In the upper panel of Figure 7.44, the model is seen to predict 14DMN decay, the solid line, that is too slow compared to the experimental observations, shown as asterisks. The model half-life, t^*, is 300-fold lower than the experimental. The upper panel of Figure 7.44 also shows that the absolute amounts of 1MN, the short-dashed line versus the circles, and of TMN, the dotted line versus the squares, formed by the model are both much lower than observed in the experiments. However, the model predicts the relative amounts of 1MN > CH4 > TMN and the sum of CH4 plus TMN equal to the 1MN produced. The lower panel of Figure 7.44 shows that the selectivities S(1MN) and S(TMN) from the model are respectively 1.8 and 29-fold too low compared to the average values of S(1MN) and S(TMN) observed from the experiments between $0.2 < X < 0.8$.

Figure 7.45 displays the model (solid line) product histories and selectivities for DHDMN product. In the upper panel of this figure, the model is seen to predict DHDMN amounts that maximize at low times and decrease with increasing time.
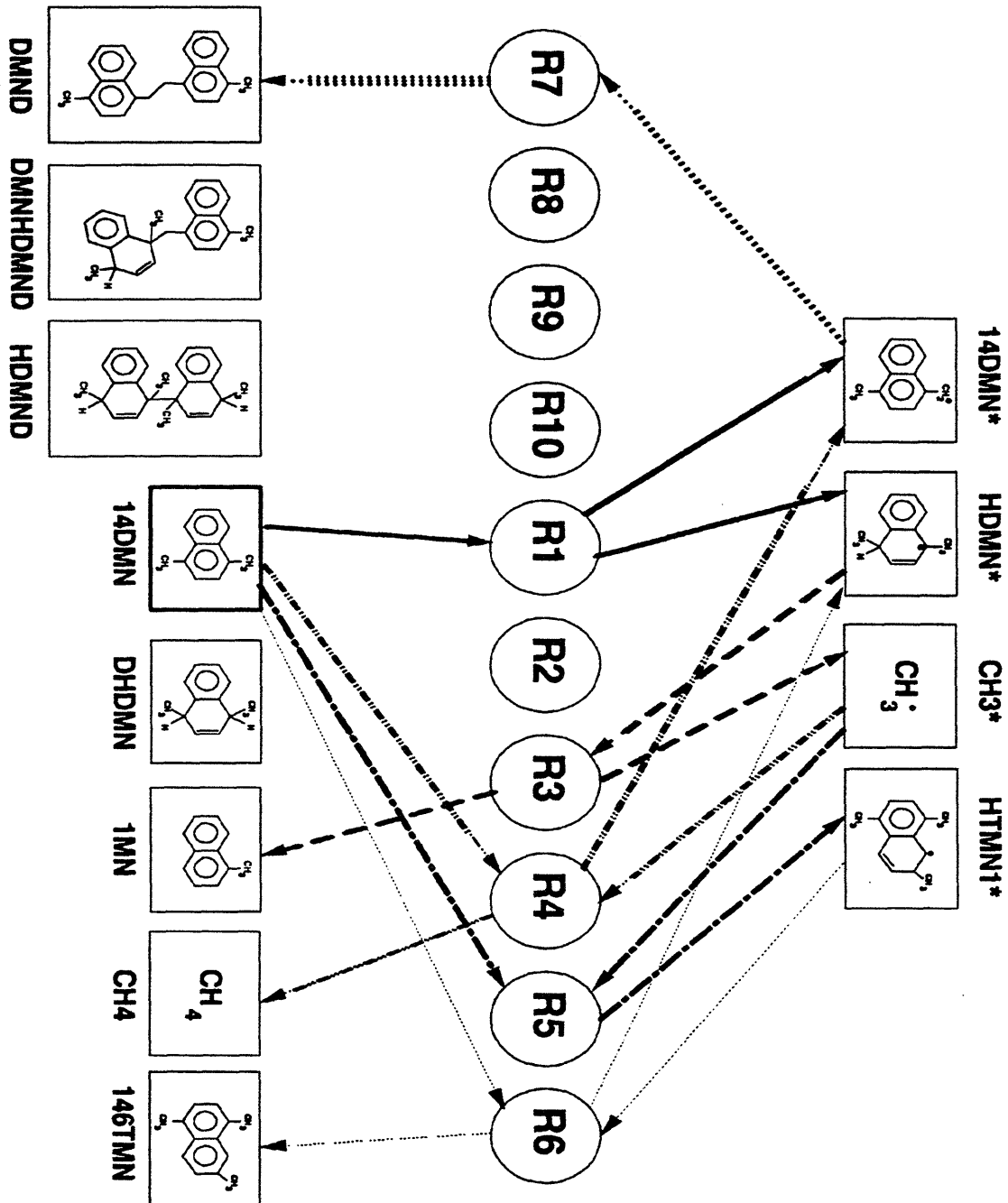
Figure 7.43: Relative elementary reaction rate traffic at T = 450°C and [14DMN]$_o$ = 0.87 mol/l for X = 0.32.
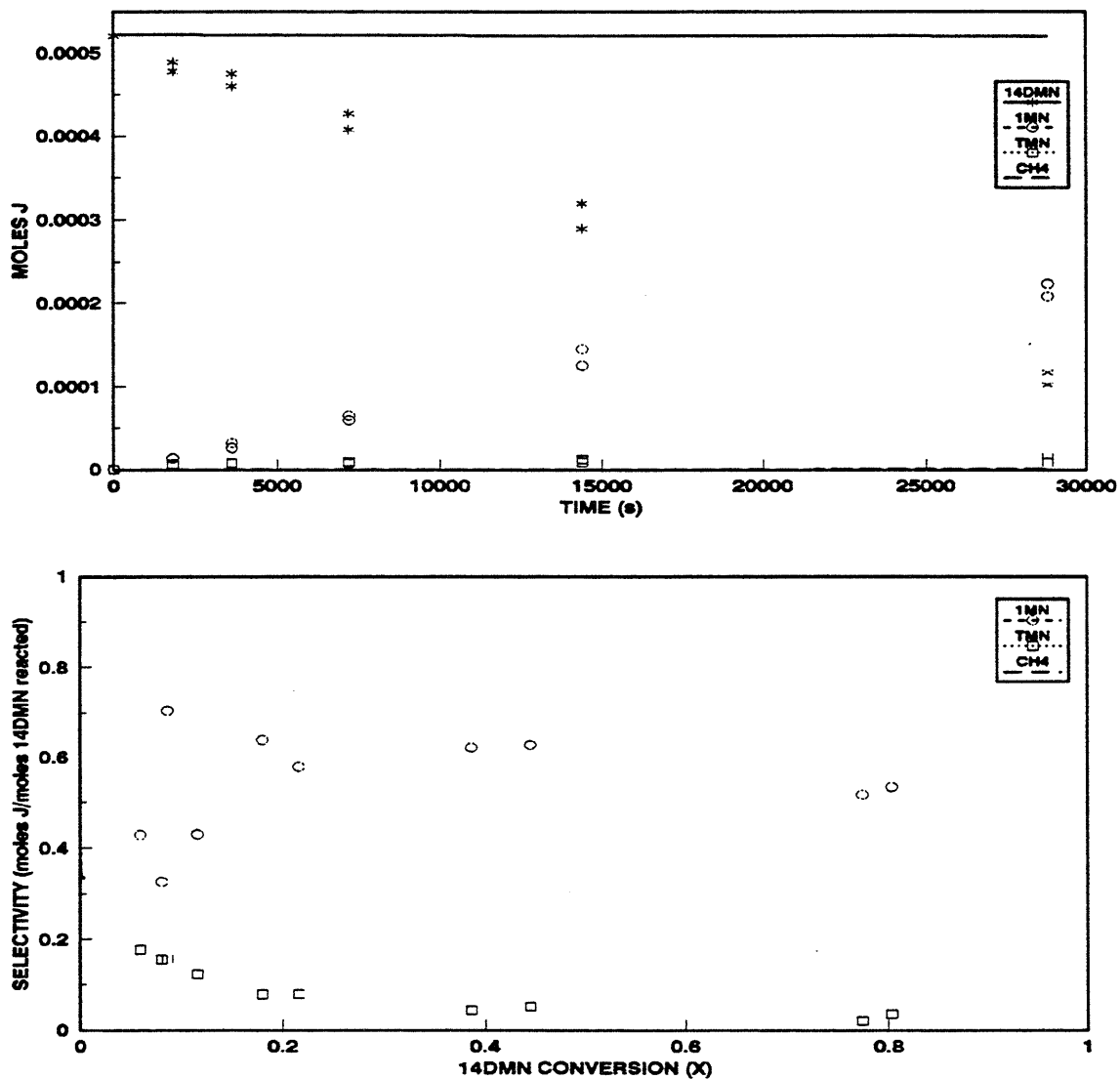
Figure 7.44: Product histories (top) and selectivity diagram (bottom) comparing model results (lines) to experimental data (symbols) for 14DMN, 1MN, TMN and CH4 at T = 450°C with $[14DMN]_o$ = 0.87 mol/l.
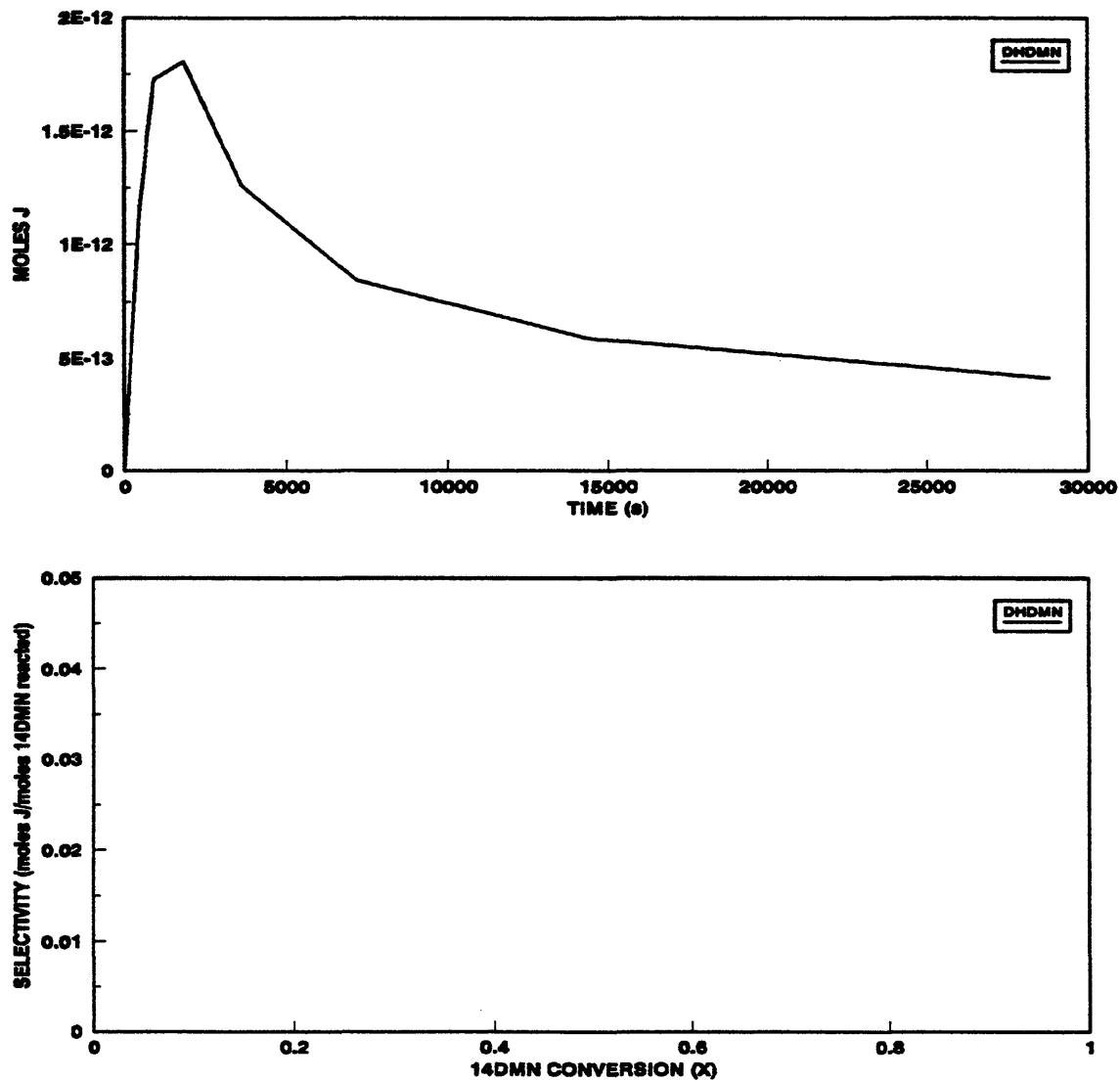
Figure 7.45: Product histories (top) and selectivity diagram (bottom) of model results (lines) for DHDMN at T = 450°C with [14DMN]$_o$ = 0.87 mol/l.

The amounts that were predicted by the model were very low at all times. That was no DHDMN experimentally observed. In the lower panel of Figure 7.45, a selectivity diagram, we see that S(DHDMA) from the model so low that it is not visible at X ~ 0.06 or X > 0.2.

Figure 7.46 compares the model calculation (lines) to the experimental data (solid circles) for heavies (DMND, DMNHDMND and HDMND). Since these heavies were not specifically assayed, the moles of heavies produced in the experiments were calculated by subtracting the sum of the selectivities of detected species (Σ) from 1, multiplying this result by the concentration of 14DMN converted and then dividing by two since the heavies were essentially dimers of 14DMN. In the upper panel of Figure 7.46, the model predicts heavies production lower than experiments at all times, more so at long times. Also, the model predicts the dominant heavy dimer to be DMND, which was the only dimer detected in the experiments by GC/MS, in Figures 4.14 - 4.17. The lower panel of Figure 7.46 shows that the dimer selectivity S(DMAD) ~ 0.33 calculated from the model is greater than the experimental S(HVY) ~ 0.05 at low X < 0.1. S(DMND) from the model remains roughly constant at S(DMND) ~ 0.33, whereas for 0.20 < X < 0.85, the model predicts S(DMND) 3.4-fold greater then S(HVY).

Finally, Figure 7.47 compares the product ratio R[TMN/1MN] as a function of 14DMN conversion (X) derived from the model (line) to those observed experimentally (symbol). The model is seen to predict R[TMA/9MA] approximately

704
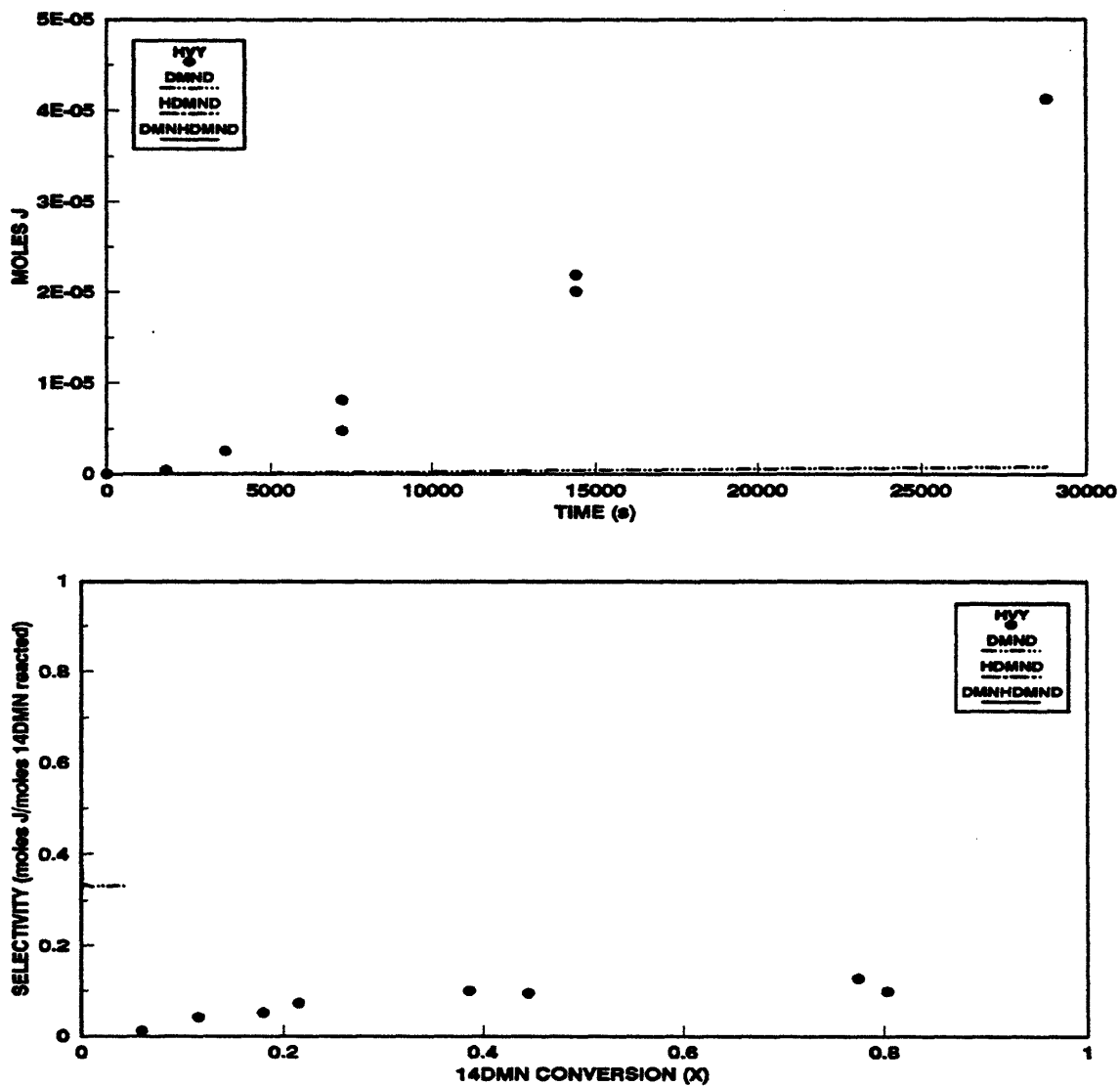
Figure 7.46: Product histories (top) and selectivity diagram (bottom) comparing model results (lines) to experimental data (symbols) for heavies at T = 450°C with $[14DMN]_o$ = 0.87 mol/l.
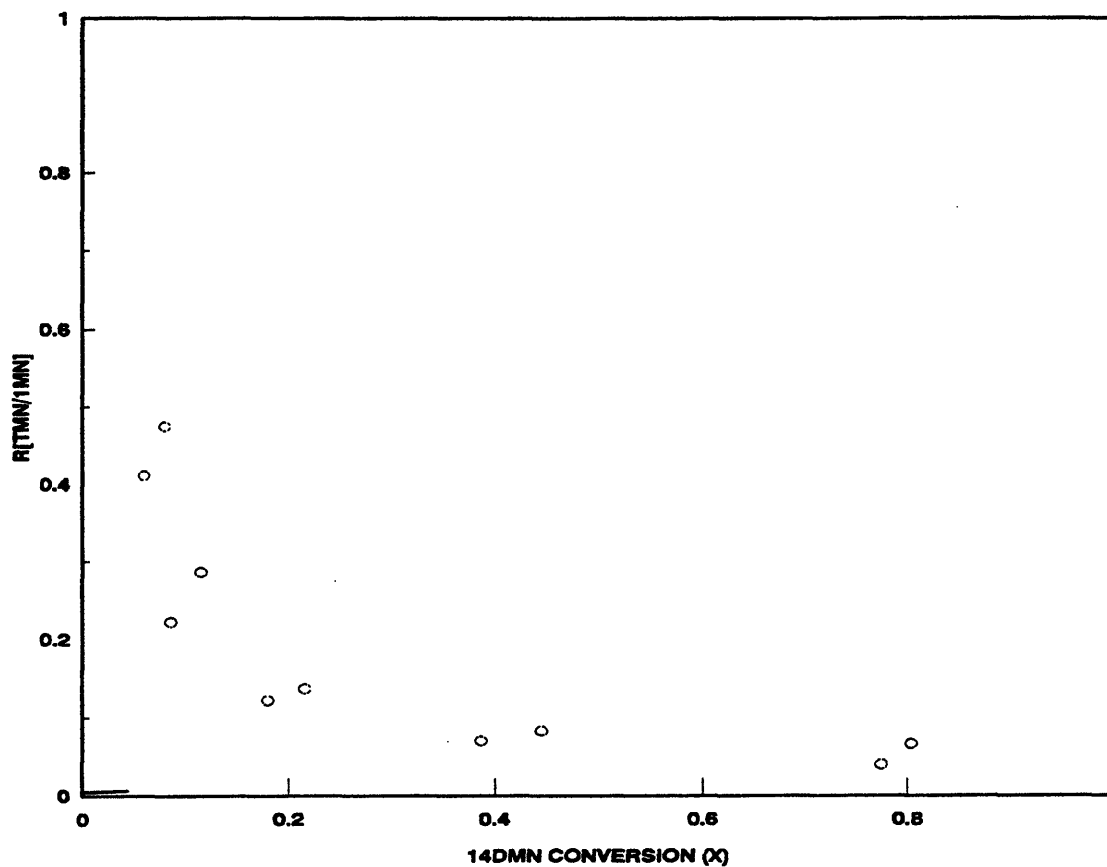
Figure 7.47: Ratio of moles TMN to moles 1MN produced vs. 14DMN conversion (X) comparing model results (line) to experimental data (symbol) for T = 450°C with $[14DMN]_0$ = 0.87 mol/l.

706

79-fold lower than experimentally observed at X ~ 0.05. Experimentally, the R[TMN/1MN] decreased from a maximum value of 0.41 at low X to approximately 0.07 at X = 0.80, whereas the model increases with increasing conversions from initial values of 0.005.

7.4.5.2.2 Model Results at All T and $[14DMN]_o$

Table 7.15 compares with experiments the 14DMN decay half-life, major product selectivities and product ratios obtained from numerical solutions of the 14DMN thermolysis model for varying initial concentrations at fixed T = 450°C, while Table 7.16 compares experimental and model results for varying temperature at fixed $[14DMN]_o$ = 0.87 mol/l.

In parts (a) of Table 7.15 and Table 7.16 and in the corresponding Figure 7.48 and Figure 7.49, the model is seen to predict 14DMN decay half-lifes t* too long, that is, decay kinetics too slow, compared to the experimental observations at all initial concentrations and temperatures. From part (a) of Table 7.15, as $[14DMN]_o$ increases from 0.081 to 2.07 mol/l at T = 450°C, the ratio of model to experimental half-lifes R[mod/exp] decreases from 626 to 298 for 0.081 to 0.87 and then increases to 522 for 2.07 mol/l, indicating that the model decay is of higher order in $[14DMN]_o$ than experimental. Figure 7.48, a log-log plot of t* vs. $[14DMN]_o$, shows that the model (hollow points, dashed line) yields a slope -1.04, implying ~ 2 order, versus the experimental (solid points, solid line) data that yield a slope of -1.05, also

707

Table 7.15

COMPARISON OF MODEL TO EXPERIMENTAL DATA
AT T = 450°C FOR VARYING [14DMN]$_o$

Part		X:		[14DMN]$_o$ (mol/l) 0.081	0.87	2.07
a	Half-life		exp	115293	17572	5111
	t* (s)		mod	72162514	5242327	2666618
			R[mod/exp]	626	298	522
b	S(1MN)	0.2-0.8	exp	0.74	0.60	0.36
			mod	0.33	0.33	0.34
			R[mod/exp]	0.45	0.55	0.94
	S(TMN)	0.2-0.8	exp	ND	0.052	0.099
			mod	0.0002	0.0018	0.0043
			R[mod/exp]	-	0.035	0.043
c	S(DHDMN)		exp	ND	ND	ND
		0.01	mod	0.000001	0.000001	~ 0
			R[mod/exp]	-	-	-
d	S(HVY)	0.2-0.85	exp	0.053	0.099	0.19
			mod	0.33	0.34	0.33
			R[mod/exp]	6.2	3.4	1.7
e	R[TMN/1MN]	0.05	exp	ND	0.41	ND
			mod	0.0010	0.0052	0.014
			R[mod/exp]	-	0.013	-
		0.8	exp	ND	0.066	0.091
			mod	0.47	0.38	0.33
			R[mod/exp]	-	5.8	3.6

Table 7.16

COMPARISON OF MODEL TO EXPERIMENTAL DATA WITH [14DMN] = 0.87 mol/l FOR VARYING T					
			Temperature (°C)		
Part	X:		370	450	550
a	Half-life	exp	529486	17572	484
	t^* (s)	mod	375796800	5242327	47423
		R[mod/exp]	708	298	98
b	S(1MN) 0.2-0.8	exp	0.32	0.60	0.60
		mod	0.39	0.33	0.33
		R[mod/exp]	1.22	0.55	0.55
	S(TMN) 0.2-0.8	exp	0.10	0.052	0.049
		mod	0.0046	0.0018	0.0010
		R[mod/exp]	0.046	0.035	0.020
c	S(DHDMN)	exp	ND	ND	ND
	0.01	mod	0.000013	0.000001	~ 0
		R[mod/exp]	-	-	-
d	S(HVY) 0.2-0.85	exp	0.060	0.099	0.10
		mod	0.39	0.34	0.33
		R[mod/exp]	6.5	3.4	3.3
e	R[TMN/1MN] 0.05	exp	0.54	0.41	ND
	0.05	mod	0.011	0.0052	0.0031
		R[mod/exp]	0.020	0.013	-
	0.80	exp	-	0.066	0.044
		mod	0.37	0.38	0.38
		R[mod/exp]	-	5.8	8.6

[1]   ND = not detected

709
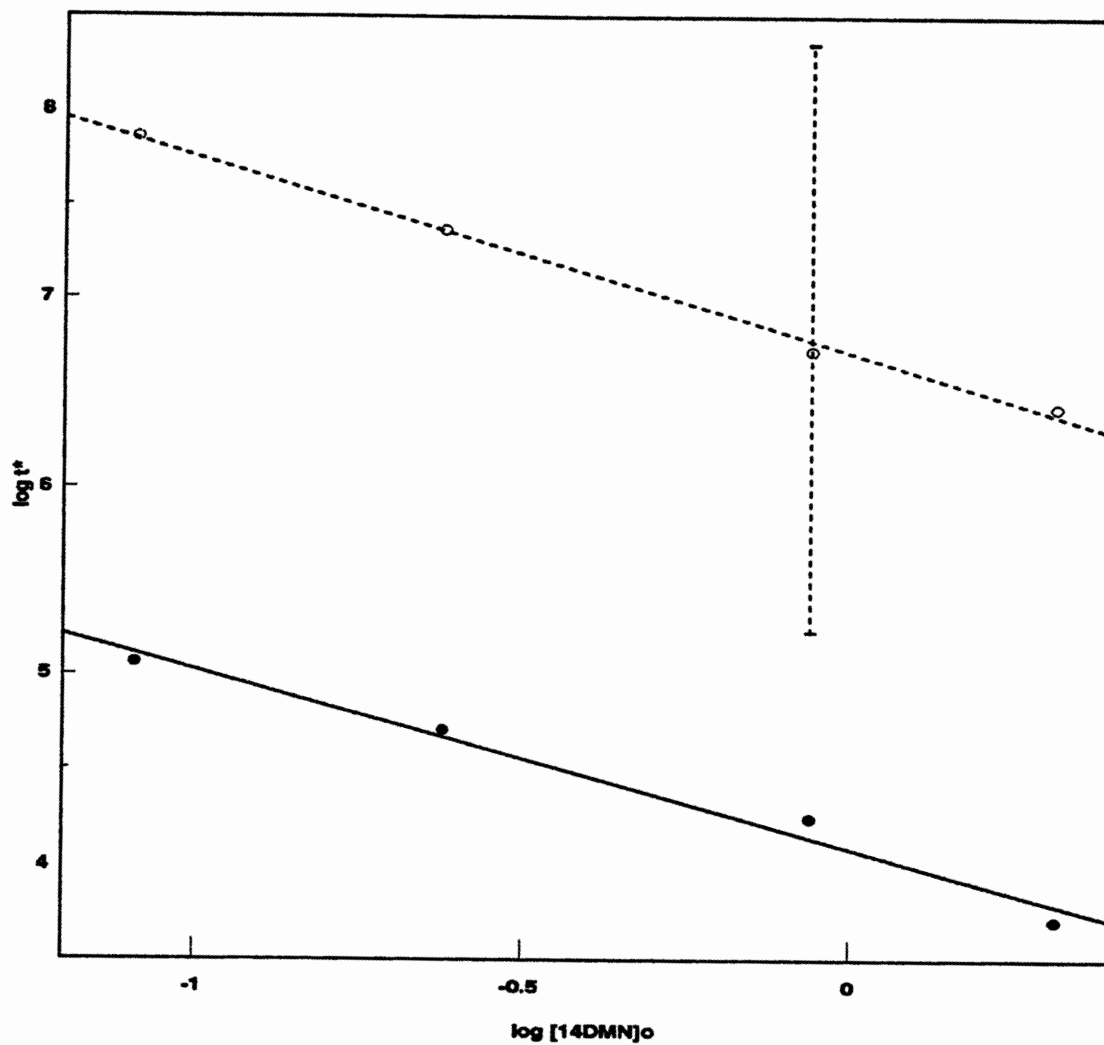
Figure 7.48: Decay half-life t^*_{exp} (solid line, circles) and t^*_{mod} (dashed line, hollow circles, vertical dashed lines-error band from sensitivity analysis) for varying $[14DMN]_o$.
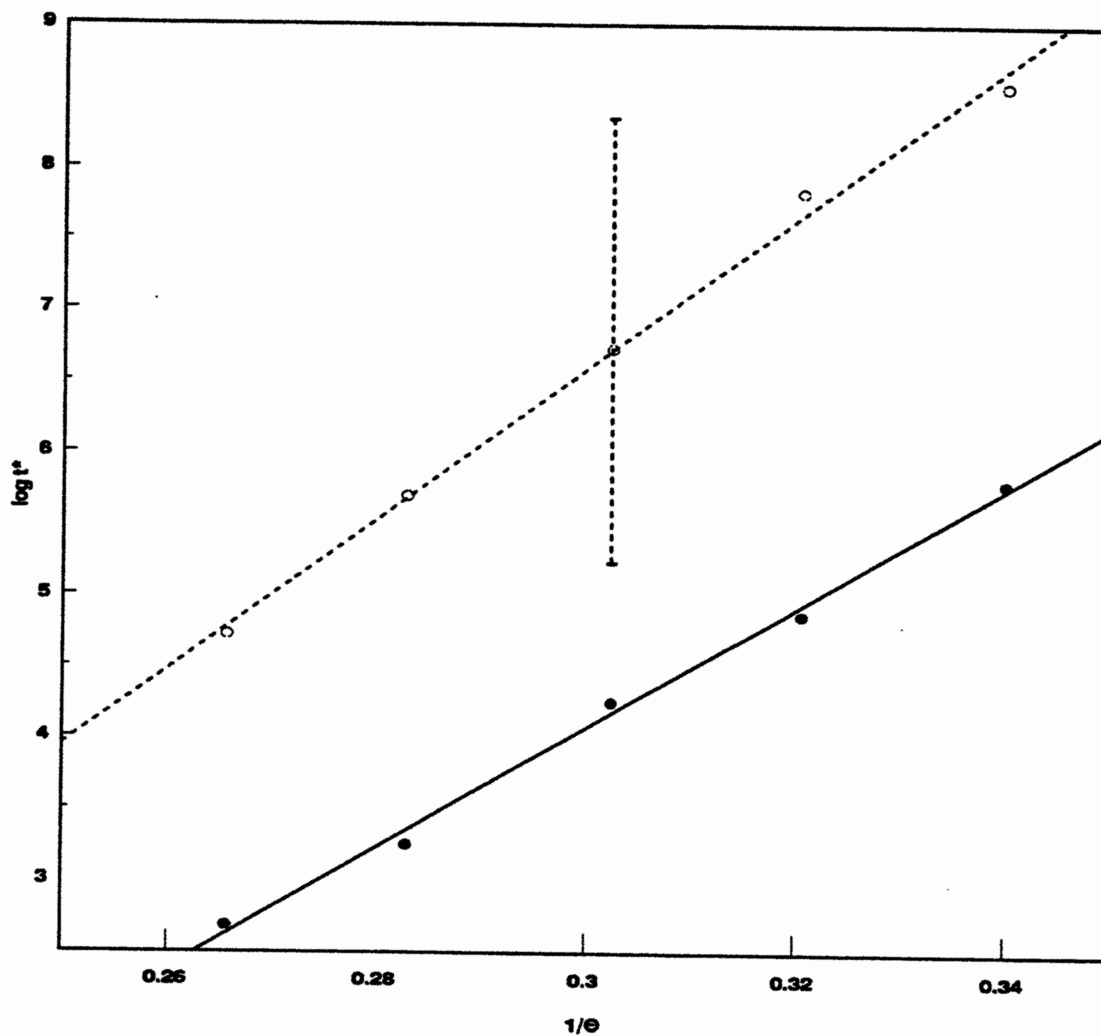
Figure 7.49: Decay half-life t^*_{exp} (solid line, circles) and t^*_{mod} (dashed line, hollow circles, vertical dashed line - error band) for varying T with fixed $[14DMN]_o = 0.87$ mol/l.

implying 2 order decomposition kinetics. From part (a) of Table 7.16, increasing

temperature from 370 to 550°C decreases the R[mod/exp] from 708 to 98, indicating

that the model 14DMN decay is slightly more activated than the experiments. This

is also borne out by Figure 7.49, a semi-log plot of t^* vs. $1/\theta$, wherein the model

(hollow points, dashed line) yields an activation energy 52.7 kcal/mol versus the

experimental (solid points, solid lines) data that provided $E^* \sim 42.0$ kcal/mol. It

should be noted that the vertical lines in both Figure 7.48 and Figure 7.49 represent

results of a sensitivity analysis of the present 14DMN thermolysis model at T =

450°C and $[14DMN]_o = 0.87$ mol/l that are discussed in a subsequent section.

Parts (b) of Table 7.15 and Table 7.16, refer to the selectivities of 1MN and

TMN products for $0.2 < X < 0.8$. As initial concentrations increase from 0.081 to

2.07 mol/l, model calculations show S(1MN) remaining roughly constant at 0.33 while

S(TMN) increases from 0.0002 to 0.0043. Both S(1MN) and S(TMN) predicted by

the model are lower than experimental, with respective ratios R[mod/exp] increasing

from 0.45 to 0.94 for 1MN and increasing from 0.038 to 0.043 for TMN. With

increasing temperatures from 370 to 550°C, the model calculations show S(1MN)

decreasing from 0.39 to 0.33 while S(TMN) decreases from 0.0046 to 0.0010. Both

S(1MN) and S(TMN) from the model are lower than experimental, with respective

ratios R[mod/exp] decreasing from 1.22 to 0.55 for 1MN and decreasing from 0.046

to 0.020 for TMN. Figure 7.50 graphically depicts the results for S(1MN) on log-log

coordinates of S(1MN) vs. $[14DMN]_o$ (upper panel) and semi-log coordinates of
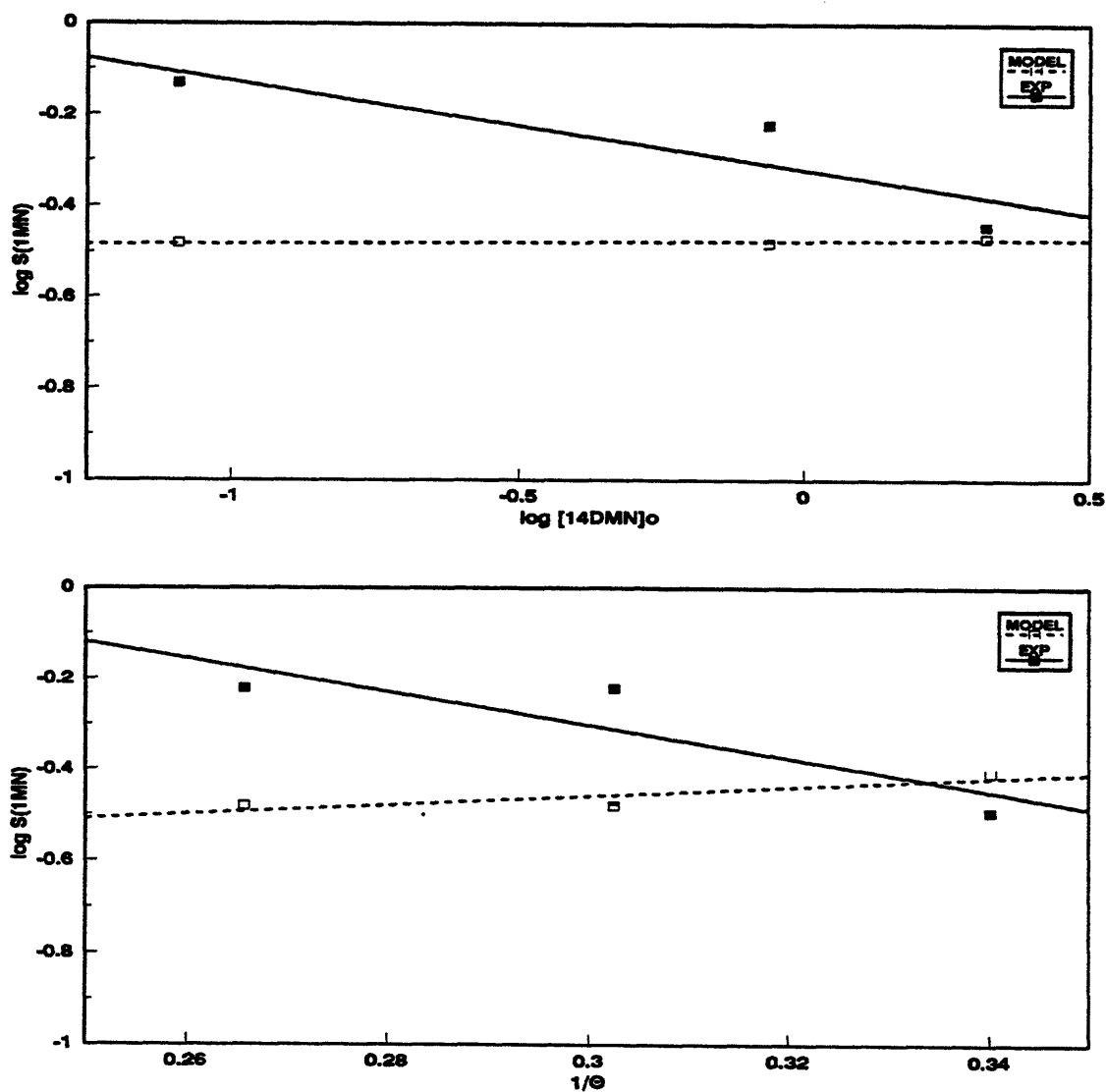
Figure 7.50: Comparison of experiments (solid squares) and model (squares) S(1MN) for varying [14DMN]$_o$ at fixed T = 450°C(top) and for varying T with fixed [14DMN]$_o$ = 0.87 mol/l(bottom).

S(1MN) vs. $1/\theta$ (lower panel). In the upper panel, it is seen that the model S(1MN) in essentially independent of concentration, slope 0.007, whereas in the experiments the slope is -0.19; thus the model exhibits an order for 1MN formation that is more than that for 14DMN decay whereas the experiments show an order for 1MN formation that is less than that for 14DMN decay. Also, in the lower panel of Figure 7.50, the model S(1MN) decreases more weakly with increasing $1/\theta$, that is decreasing temperature, slope 0.98, than in the experiments, slope -3.68; thus the model predicts 14DMN decay to be more activated the 1MN formation by $\sim$ 1 kcal/mol whereas the experiments predicts 1MN formation to be more activated than 14DMN decay by $\sim$ 4 kcal/mol. The vertical dashed lines in both upper and lower panels of Figure 7.50 are results of a sensitivity analysis discussed in a subsequent section.

Parts (c) of Table 7.15 and Table 7.16, show the selectivities of DHDMN product at low conversion, X = 0.01. In Table 7.15, as $[14DMN]_o$ increases from 0.081 to 2.07 mol/l, S(DHDMN) from the model decreases slightly from 0.000001 to $\sim$ 0 whereas no DHDMN was detected at any initial concentration; in Table 7.16, as T increases from 370 to 550°C, S(DHDMN) from the model decreases from 0.000013 to $\sim$ 0, again with no detectable values for DHDMN at any T. Thus it is seen that, at low conversions, the DHDMN selectivities predicted by the model are essentially greater those observed experimentally for all $[14DMN]_o$ and T.

Parts (d) of Table 7.15 and Table 7.16, refer to the selectivities of heavy products (sum of DMND, DMNHDMND and HDMND) for $0.2 < X < 0.85$. As initial concentrations increase from 0.081 to 2.07 mol/l, model calculations show S(HVY) remaining roughly constant at 0.33. S(HVY) predicted by the model are lower than experimental, with respective ratios R[mod/exp] decreasing from 6.2 to 1.7. With increasing temperatures from 370 to 550°C, the model calculations show S(HVY) decreasing from 0.39 to 0.33. S(HVY) from the model are lower than experimental, with ratios R[mod/exp] decreasing from 6.5 to 3.3. Thus it is seen that the HVY selectivities predicted by the model are higher than those observed experimentally; from the ratios R[mod/exp], the dependence of S(HVY) on $[14DMN]_o$ and T predicted by the model exceeds that observed experimentally, more so at the lower $[14DMN]_o$ and T.

Finally, parts (e) of Table 7.15 and Table 7.16 refer to the ratio of TMN product to 1MN product, at both low ($X \sim 0.05$) and high ($X = 0.80$) conversions. At low conversions, in Table 7.15, as initial concentrations increase from 0.081 to 2.07 mol/l, model calculations show R[TMN/1MN] increasing from 0.0010 to 0.014. R[mod/exp] = 0.013 for $[14DMN]_o$ = 0.87 mol/l, but no comparison to initial concentrations could be made since there was no TMN detected at $[14DMN]_o$ = 0.081 mol/l and $X < 0.15$ where not studied for $[14DMN]_o$ = 2.07 mol/l. At low conversions, in Table 7.16, with increasing temperatures from 370 to 550°C, the model calculations show R[TMN/1MN] decreasing from 0.011 to 0.0031 with its ratio

R[mod/exp] decreasing from 0.020 at T = 370°C to 0.013 at T = 450°C. Thus it is seen that, at low conversions, the R[TMN/1MN] predicted by the model are lower than those observed experimentally at all [14DMN]$_o$ and T; from the ratios R[mod/exp], the dependence of R[TMN/1MN] on [14DMN]$_o$ and T predicted by the model exceeds that observed experimentally. At high conversions, in Table 7.15, as initial concentrations increase from 0.081 to 2.07 mol/l, model calculations show R[TMN/1MN] decreasing from 0.47 to 0.33 with its ratio R[mod/exp] decreasing from 5.8 to 3.6 for [14DMN]$_o$ > 0.87 mol/l. At high conversions, in Table 7.16, with increasing temperatures from 370 to 550°C, the model calculations show R[TMN/1MN] remaining roughly constant at 0.38 with its ratio R[mod/exp] increasing from 5.8 to 8.6 for T > 450°C. Thus it is seen that, at high conversions, the R[TMN/1MN] predicted by the model are higher than those observed experimentally at all [14DMN]$_o$ and T; from the ratios R[mod/exp], the dependence of R[TMN/1MN] on [14DMN]$_o$ and T predicted by the model exceeds that observed experimentally. Figure 7.51 graphically depicts the results for R[TMN/1MN] on log-log coordinates of R[TMN/1MN] vs. [14DMN]$_o$ (upper panel) and semi-log coordinates of R[TMN/1MN] vs. 1/θ (lower panel). In the upper panel, it is seen that, at low conversions, the model R[TMN/1MN] has slope 0.75, whereas the experiments only detected TMN at [14DMN]$_o$ = 0.87 mol/l. At high conversions, the model R[TMN/1MN] increases more strongly, slope 7.40, than in the experiments, slope 1.09; thus the model exhibits an order for 1MN formation that is
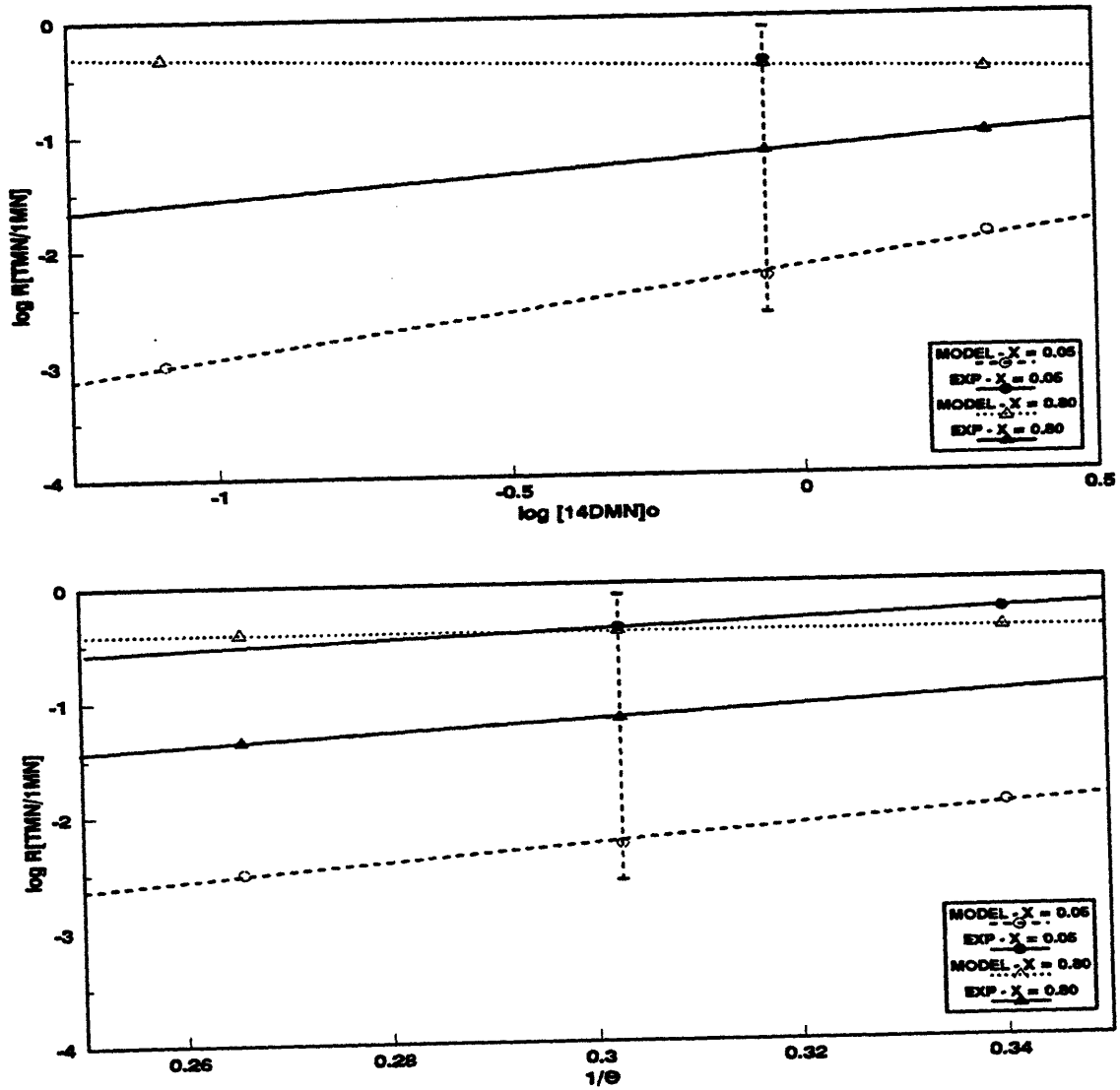
Figure 7.51: Comparison of experiments (solid symbols) and model (symbols) R[TMN/1MN] for varying [14DMN]$_o$ at fixed T=450°C(top) and varying T with fixed [14DMN]$_o$ = 0.87 mol/l(bottom).

more than that for TMN formation by more than observed experimentally. Also, in the lower panel of Figure 7.51, the model R[TMN/1MN] and the experimental R[TMN/1MN] are approximately the same with increasing $1/\theta$, that is decreasing temperature, model slope -0.10 and experimental slope -0.16; thus the model and experiments predict 1MN formation to be more activated than TMN formation by ~ 0.2 kcal/mol. At high conversions, the model R[TMN/1MN] decreases more strongly, slope -0.16, than in the experiments, slope 0.13. The vertical dashed lines in both upper and lower panels of Figure 7.51 are results of a sensitivity analysis discussed in a subsequent section.

7.4.5.3 Sensitivity Analysis

The sensitivity of our 14DMN thermolysis model was analyzed at the central point of the 14DMN experimental grid, T = 450°C and $[14DMN]_o$ = 0.87 mol/l, by separately perturbing the kinetics of selected elementary steps over their estimated uncertainty limits. From Table 7.7 and Table 7.8, the inherent errors in ΔH°_f are between 1 - 3 kcal/mol for stable species and 2 - 5 kcal/mol for radicals. These errors in ΔH°_f translate into errors of ± 2 - 5 kcal/mol for ΔH°_r which propagate through the Evans-Polanyi relations of Table 7.11 into errors of ± 2 - 5 kcal/mol for E^*; when coupled with a θ ~ 3, which corresponds to the temperatures of the present experiments, these lead to errors of ± 0.7 - 1.7 in $\log_{10} k$. The errors in the $\log_{10} A$ estimates are, at most, ± 0.5, which translate directly to errors of ± 0.5 in $\log_{10} k$.

718

Thus, in general, the calculated rate constants of the elementary steps are beset more by errors in their E^* than in their $\log_{10} A$. For this reason, the sensitivity analysis was performed by separately perturbing the E^* of selected elementary reactions over the inherent errors in their ΔH°_r to show their effects on 14DMN decay half-life t^*, 1MN selectivity S(1MN), and the primary product ratio R[TMN/1MN]. Results of the sensitivity analysis are summarized in Table 7.17.

In our 14DMN thermolysis model, the destruction of substrate is affected by numerous elementary steps, of which, as shown in Table 7.13 and Table 7.14, R1 is the most important at both low and high conversions. The sensitivity of 14DMN half-life, t^*, was thus examined by perturbing E^*_1, the activation energy of R1, by $\pm$ 5.2 kcal/mol, which is the inherent error in ΔH°_{R1}, using the Evans-Polanyi relation $E^*_1 = \Delta H^{\circ}_{R1}$. Results of t^* sensitivity to the preceding perturbations are given in the last 3 columns of row 1 in Table 7.17 and were graphically depicted by the vertical dashed lines in Figure 7.48 and Figure 7.49. The variation in t^*_{mod} on account of the inherent errors in the estimated rate constants is not large enough to exceed the span of t^*_{exp} variations by changes in [14DMN]$_o$ and T. At T = 450°C and [14DMN]$_o$ = 0.87 mol/l, the 300-fold difference between t^*_{mod} and t^*_{exp} is not within the 1330-fold uncertainty in t^*_{mod}. All values of t^*_{mod} were considerably higher than t^*_{exp}.

The formation of 1MN is affected by R3 the most important at both low and high conversions. The sensitivity of selectivity to 1MN, S(1MN), was thus examined by perturbing E^*_3, the activation energy of R3, by $\pm$ 4.7 kcal/mol, which is the

719

Table 7.17

RESULTS OF SENSITIVITY ANALYSIS AT
T = 450°C WITH [14DMN]$_o$ = 0.87 mol/l

Parameter	Dominant Reaction(s)	Inherent Error in ΔH°_r (kcal/mol)	Perturbation in E^* (kcal/mol)	Results +Perturbation	Results 0	Results -Perturbation
14DMN half-life, t^*	R1	± 5.2	± 5.2	224991709	17572	169236
Selectivity to 1MN, S(1MN)	R3	± 4.7	± 4.7	0.33	0.60	0.33
Ratio of moles of TMN to moles of 1MN produced, R[TMN/1MN]	R4	± 2.3	± 1.65	0.017[1], 0.78[2]	0.41[1], 0.066[2]	0.0025, 0.056
	R5	0	0			

[1] R[TMN/1MN] at X = 0.05

[2] R[TMN/1MN] at X = 0.80

inherent error in ΔH°_{R3}, using the Evans-Polanyi relation $E^{*}_3 = 2.1 + \Delta H^{\circ}_{R3}$. Results

of S(1MN) sensitivity to the preceding perturbations are given in the last 3 columns

of row 2 in Table 7.17 and were graphically depicted by the vertical dashed lines in

Figure 7.50, which is essentially non existent since both perturbations gave S(1MN)

= 0.33. The variation in t^{*}_{mod} on account of the inherent errors in the estimated rate

constants is not large enough to exceed the span of t^{*}_{exp} variations by changes in

[14DMN]$_o$ and T. At T = 450°C and [14DMN]$_o$ = 0.87 mol/l, the 1.8-fold difference

between t^{*}_{mod} and t^{*}_{exp} is not within the uncertainty in t^{*}_{mod}.

The formation of TMN and 1MN is affected by R4 and R5 at both low and

high conversions. The sensitivity of the ratio of moles of TMN to moles of 1MN

produced, R[TMN/1MN], was thus examined by perturbing E^{*}_4, the activation energy

of R4, by ± 1.65 kcal/mol, which is the inherent error in $\Delta H^{\circ}_{R4}/2$, using the Evans-

Polanyi relation $E^{*}_4 = 17.5 + \Delta H^{\circ}_{R4}/2$. The activation energy of R5, E^{*}_5, was not

affected by errors in ΔH°_{R5}. Results of R[TMN/1MN] sensitivity to the preceding

perturbations are given in the last 3 columns of row 3 in Table 7.17 and were

graphically depicted by the vertical dashed lines in Figure 7.51. Two noteworthy

conclusions arise from perusal of the results. First, the variation in R[TMN/1MN]$_{mod}$

on account of the inherent errors in the estimated rate constants is large enough to

exceed the span of R[TMN/1MN]$_{exp}$ variations by changes in [14DMN]$_o$ and T at

both low and high conversions. Second, at T = 450°C and [14DMN]$_o$ = 0.82 mol/l,

the 77 and 5.8-fold differences between R[TMN/1MN]$_{mod}$ and R[TMN/1MN]$_{exp}$ at

low and high conversions are well within the 315-fold uncertainty in $R[TMN/1MN]_{mod}$.

7.4.5.4 Optimized Model

The preceding comparisons between model and experimental results, along with the sensitivity analysis, permitted the deviation of optimized parameters for the model of 14DMN thermolysis, to best-fit the experimental data at T = 450°C and $[14DMN]_o$ = 0.87 mol/l. The best-fit arose by subtracting 5.2 kcal/mol from E^*_1, subtracting 2.85 kcal/mol to E^*_2, adding 2.85 kcal/mol from E^*_{-2}, subtracting 4.7 kcal/mol from E^*_3, adding 1.65 kcal/mol to E^*_4 and subtracting 1.65 kcal/mol from E^*_{-4}. It can be verified by reference to Table 7.17 that only adjustments to the E^* of R2 and R3 were within their inherent error-limits, while the E^* of R1 and R4 were within 2 times their inherent error-limits. Figure 7.52 compares the substrate and product histories (upper panel) and product selectivities (lower panel) as obtained from the numerical solution to the thermolysis model to the experimental data for 14DMN, 1MN, TMN and CH4 at the center of the experimental grid, $[14DMN]_o$ = 0.87 mol/l and T = 450°C. In the upper panel of Figure 7.52, the model is seen to predict 14DMN decay, the solid line, that is too slow compared to the experimental observations, shown as asterisks. The model half-life, t^*, is 9.5-fold lower than the experimental the model is slower than the experiments; the t^*_{mod} = 167603 s whereas the t^*_{exp} = 17572 s. The upper panel of Figure 7.52 also shown that the absolute
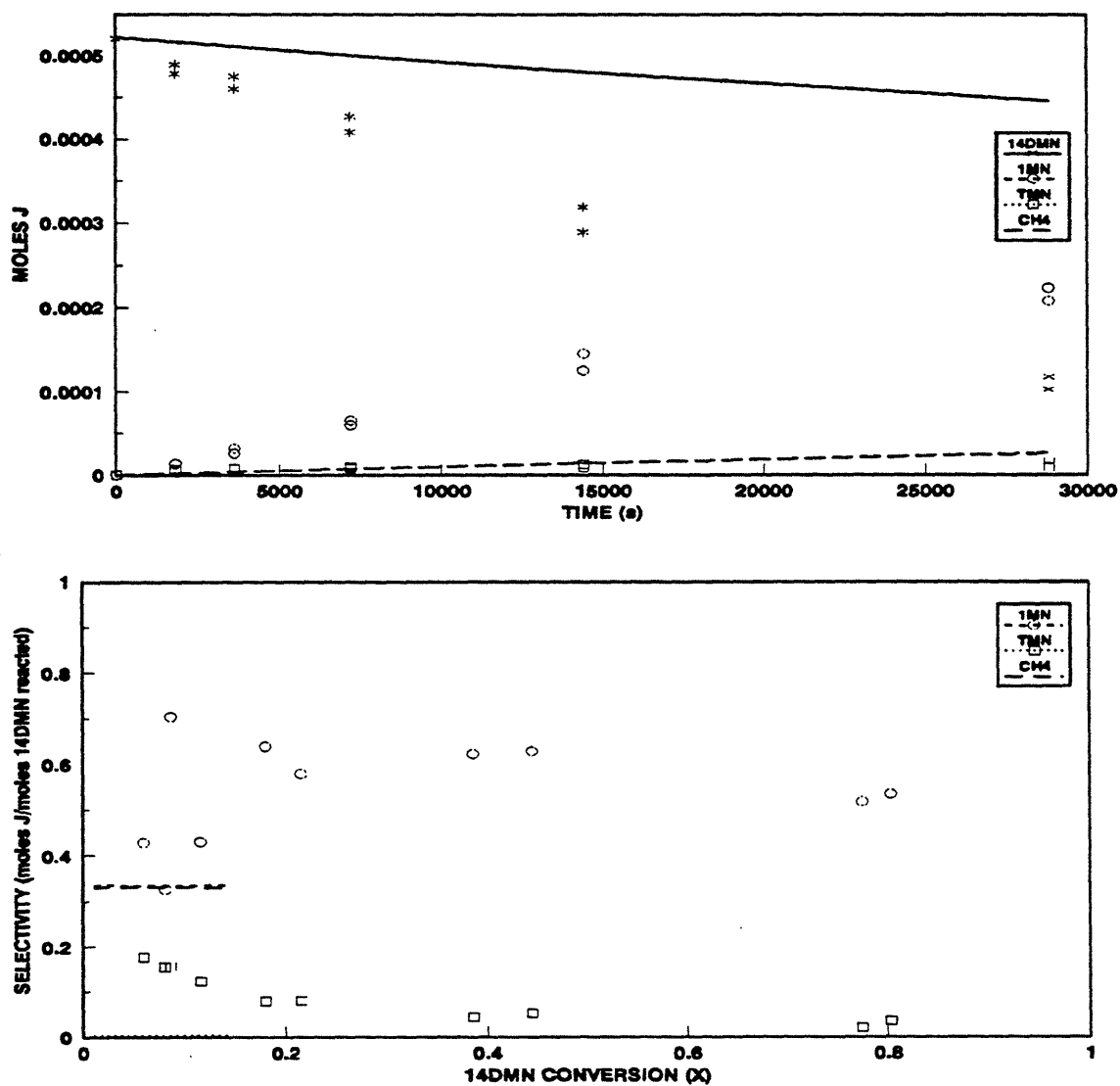
Figure 7.52: Product histories (top) and selectivity diagram (bottom) comparing optimized model (lines) to experimental data (symbols) for 14DMN, 1MN, TMN and CH4 at T = 450°C with $[14DMN]_o$ = 0.87 mol/l.

amounts of 1MN, the short-dashed line versus the circles, formed by the model are lower than observed in the experiments, more so at longer times, and of TMN, the dotted line versus the squares, formed by the model within the experimental observations, more so at longer times. The lower panel of Figure 7.52 is a selectivity diagram for the present case of $[14DMN]_o = 0.87$ mol/l and T = 450°C. S(1MN) and S(TMN) from the model are respectively 1.8 and 6.5-fold too low compared to the average values of S(1MN) and S(TMN) observed from the experiments between $0.2 < X < 0.8$. The mechanism as the upper limit of 0.33 for S(1MN), as shown in Section 7.4.2, therefore the optimized model generates S(1MN) at the maximum limit.

Figure 7.53 shows the optimized model (lines) product histories and selectivities for DHDMN product. There was no DHDMN detected in the experiments. In the upper panel of Figure 7.53, the optimized model is seen to predict DHDMN amounts greater than in the ethical model, of order 1E-09 versus 2E-12 moles. The trend of the DHDMN formation is also different, the ethical model started with DHDMN at a maximum and then decayed with increasing time whereas in the optimized model, the DHDMN starts at its lowest value and increases with increasing time. In the lower panel of Figure 7.53, a selectivity diagram, we see
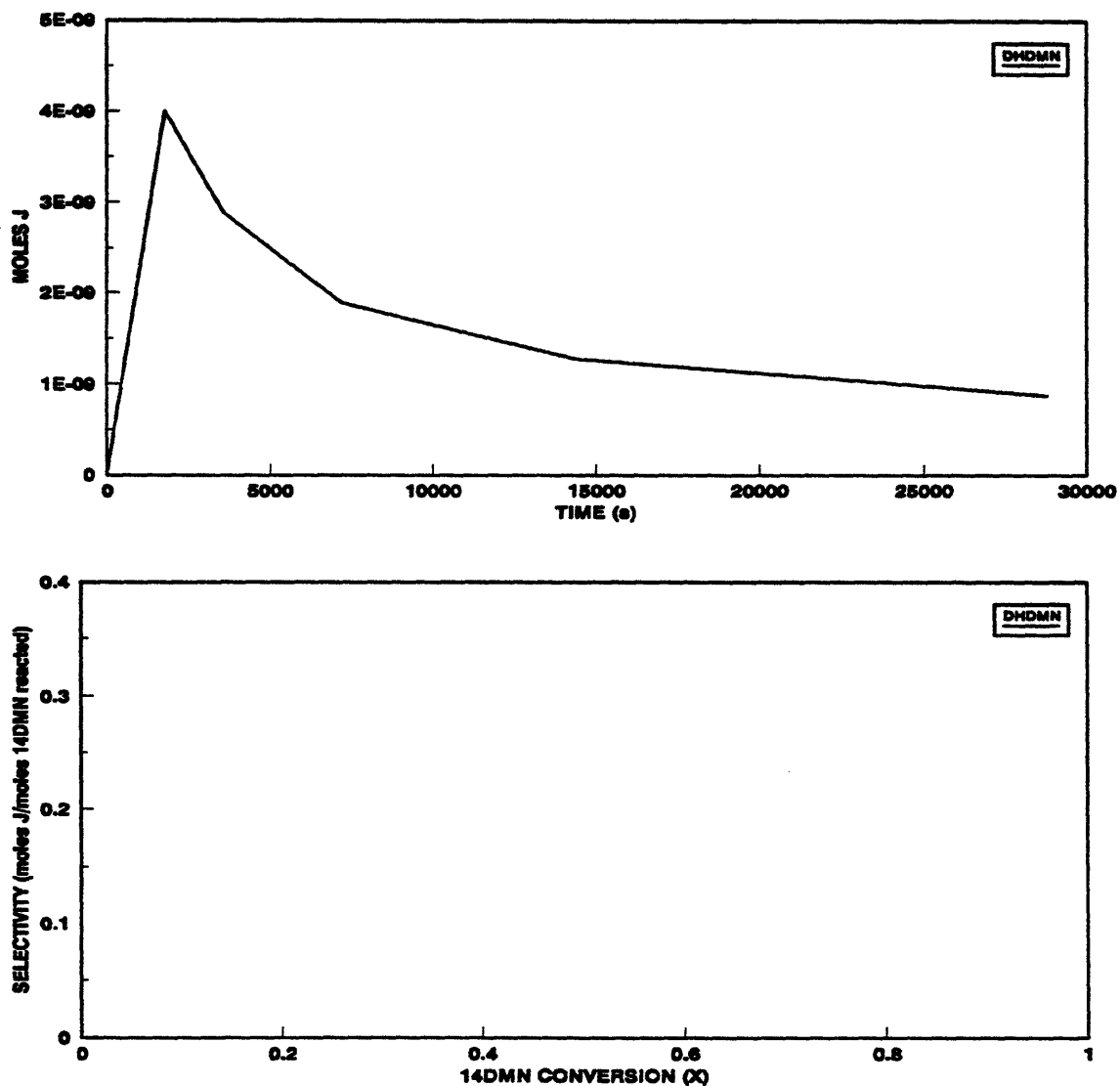
Figure 7.53: Product histories (top) and selectivity diagram (bottom) from optimized model results (lines) for DHDMN at T = 450°C with $[14DMN]_o$ = 0.87 mol/l.

that S(DHDMN) from the model appeared with maximum 0.0007 and decreased with increasing X.

Figure 7.54 compares the model calculations (lines) to the experimental data (solid circles) for heavies (DMND, DMNHDMND and HDMND). In the upper panel of Figure 7.54, the model predicts heavies production slightly less than the experiments at all times. The lower panel of Figure 7.54 shows the dimer selectivity remains roughly constant at S(DMAD) ~ 0.33 for all X while the experimental heavies selectivity remains roughly constant at ~ 0.10 for 0.2 < X < 0.8.

Finally, Figure 7.55 compares the product ratio R[TMN/1MN] as functions of 14DMN conversion (X) derived from the optimized model (lines) to those observed experimentally (symbols). In Figure 7.55, the model is seen to predict R[TMN/1MN] 37-fold lower than the experimental values at low conversions and 2.8-fold higher than the experimental values at high conversions. The trend predicted by the model is opposite of what was seen experimentally. In the experiments, R[TMN/1MN] started at a maximum and decreased with increasing conversion, whereas the model started at the minimum and rose with increasing conversion.

7.5 Minor Methylated Products

The observed formations of trimethylnaphthalene isomers 1,4,5- and 1,4,6-TMN from 14DMN, of dimethylnaphthalene isomers 1,2- and 1,3-dimethylnaphthalene from 1MN, and of methylnaphthalene isomers 1MN and 2MN
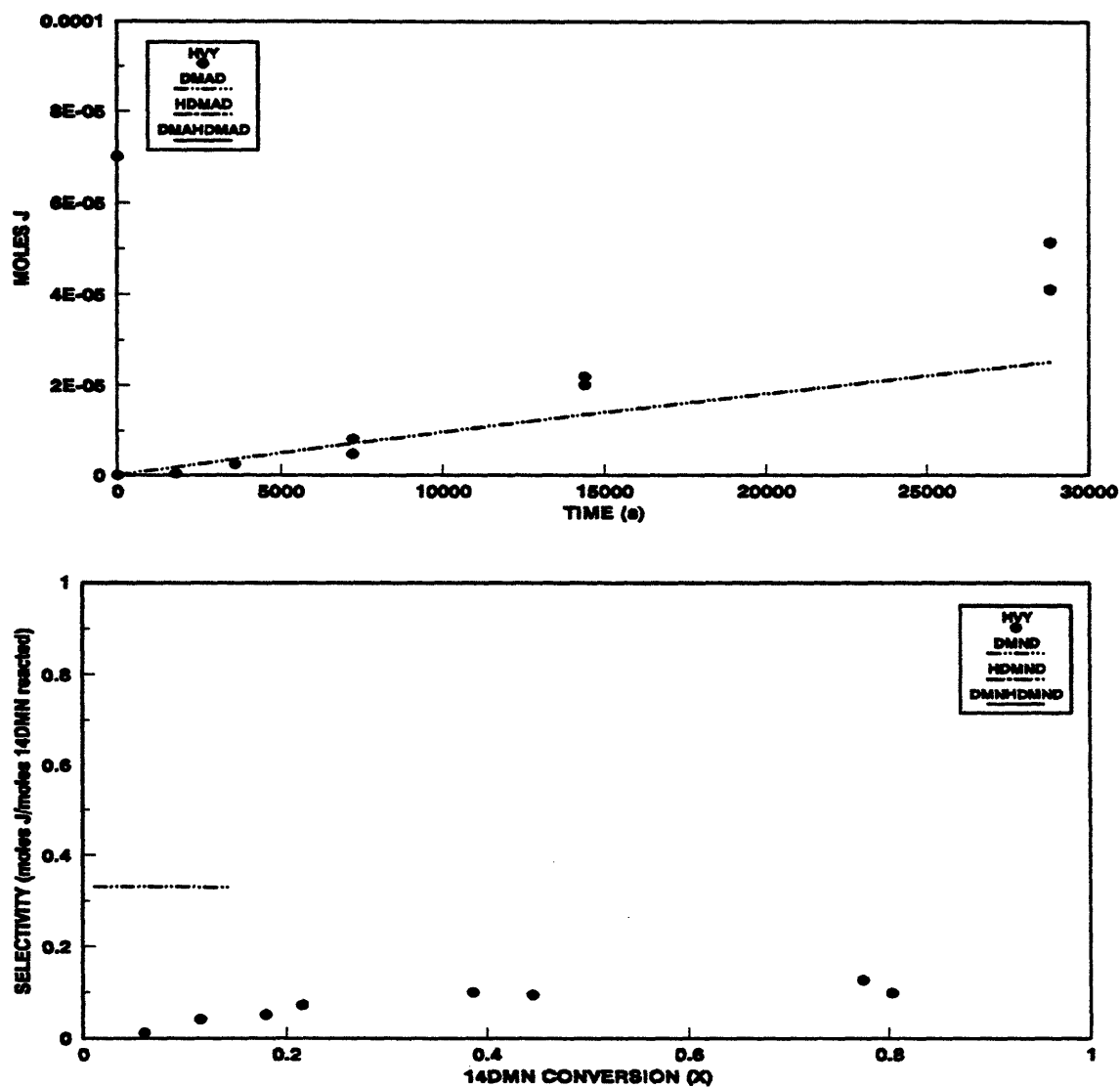
Figure 7.54: Product histories (top) and selectivity diagram (bottom) comparing optimized model results (lines) to experimental data (symbols) for heavies at T = 450°C with $[14DMN]_o$ = 0.87 mol/l.

727
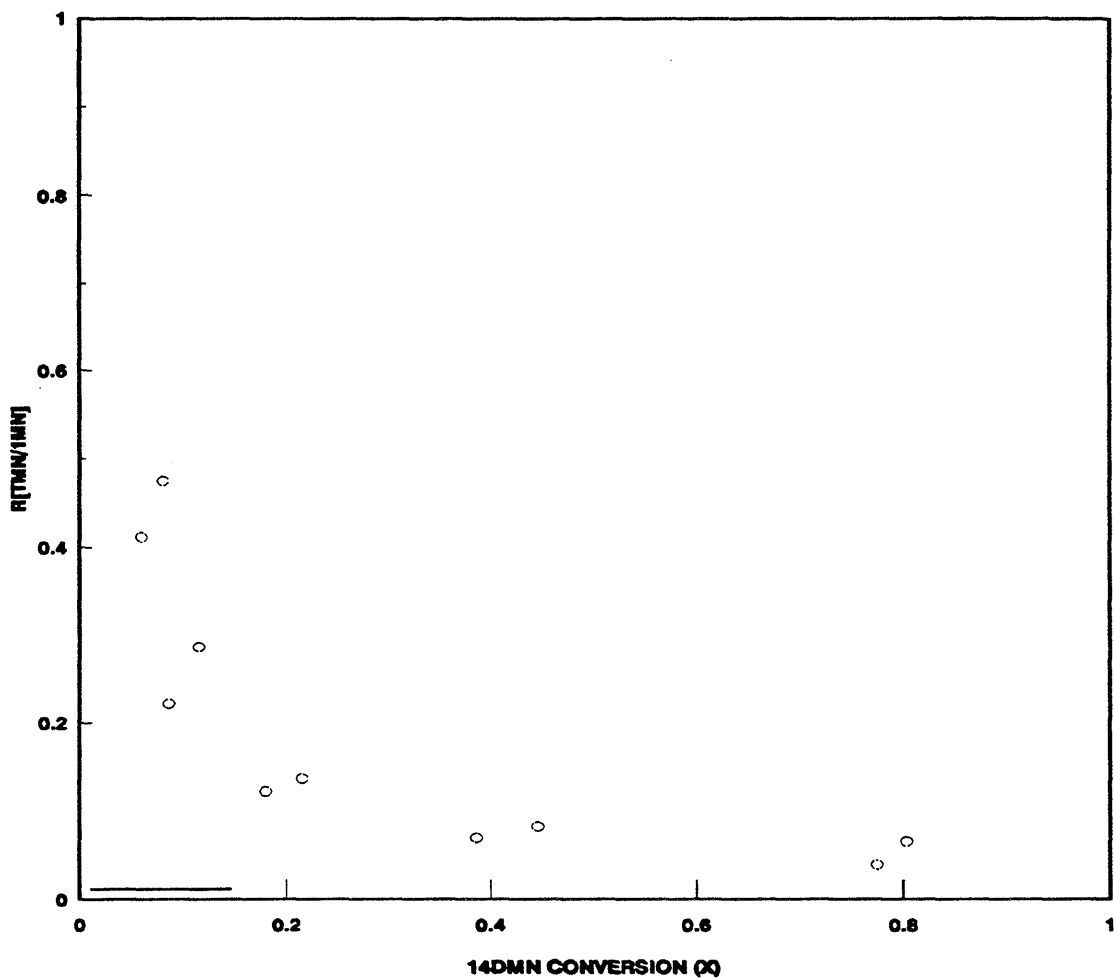
Figure 7.55: R[TMN/1MN] comparing optimized model results (lines) to experimental data (symbols) at T = 450°C with [14DMN]$_o$ = 0.87 mol/l.

728

from NAP during 14DMN thermolysis at high severities invite interpretation by frontier orbital theory, as examples of periselective methyl radical attack on the aromatic naphthalene nucleus. Due to the rapid decay of 1,4,5-TMN once it was formed, the ratio of 1,4,6-TMN/1,4,5-TMN was not representative of methylation at 2 positions. The dimethylnaphthalene isomer ratio could not be calculated due to the previously mentioned co-elution of the dimethylnaphthalene isomers. The ratio 2MN/1MN is not a constant function of conversion because 1MN is also formed by 14DMN decomposition as well as NAP methylation.

7.6 Summary

1,4-dimethylnaphthalene (14DMN) was thermolyzed over the range: T = 370 - 550°C, $[14DMN]_o$ = 0.081 - 2.07 mol/l and t = 150 - 115200 s, which lead to X = 0.05 - 0.99. Products seen in the 14DMN thermolysis included: 1-methylnaphthalene (1MN), 1,4,5-trimethylnaphthalene(145TMN), 1,4,6-trimethylnaphthalene(146TMN), trimethylnaphthalenes (TMNs), naphthalene (NAP), 2-methylnaphthalene (2MN), 1,3-dimethylnaphthalene (13DMN), 1,2-dimethylnaphthalene (12DMN), 2,6-dimethylnaphthalene (26DMN), heavy (dimer) products and methane (CH4). The substrate and major product histories depict a classical sequential reaction series A(14DMN) → B(1MN) → C(NAP), with competing, parallel, hydrogenation and methylation pathways at each stage. S(1MN) and S(ALL TMNs) were roughly independent of conversions at all $[14DMN]_o$ and T. Absolute values of S(1MN)

declined somewhat while S(ALL TMNs) increased somewhat with increasing [14DMN]$_o$ at fixed T = 450°C, whereas absolute values of S(1MN) and S(ALL TMNs) remained essentially constant with increasing T at fixed [14DMN]$_o$. NAP and 2MN selectivities increased monotonically from zero as conversions increased for all [14DMN]$_o$ and T, with S(NAP) > S(2MA) always. 13DMN and 12DMN selectivities started at maximum values at low conversions, decreased sharply by X ~ 0.20 and then slowly declined for all [14DMN]$_o$ and T. Of the dimethylated species, the order of abundance was generally S(13DMN) > S(12DMN) > S(26DMN). Absolute values of S(13DMN), S(12DMN) and S(26DMN) remained roughly constant with increasing [14DMN]$_o$ and T. 146TMN, 145TMN and TMN selectivities started at maximum values at low conversions, decreased sharply by X ~ 0.20 and then slowly declined for all [14DMN]$_o$ and T. Of the trimethylated species, the order of abundance was generally S(TMN) > S(146TMN) > S(145TMN). Absolute values of S(146TMN), S(T1MN) and S(TMN) remained roughly constant with increasing [14DMN]$_o$ and T.

The kinetics of the 14DMN experimental thermolyses were analyzed to derive reaction order and activation parameters. Reaction order for overall 14DMN decay was determined from k_{eff}, the effective first order rate constants, and 14DMN decay half-life, t^*, in the series of experiments at constant T = 450°C with [14DMN]$_o$ ranging from 0.081 to 2.07 mol/l. Analysis of both led to approximately 2nd order 14DMN decomposition kinetics, with k_{eff} yielding 1.60 ± 0.09 and t^* yielding 2.05 ±

0.16. Thermolysis of 14DMN at fixed $[14DMN]_o$ = 0.87 mol/l and varying temperature from 370 - 550°C revealed the activation parameters associated with both the effective first order and true 2nd order rate constants. The best-fit Arrhenius parameters $[\log_{10} A \ (s^{-1}), E^* \ (kcal/mol)]$ = [6.50 ± 0.13, 35.7 ± 2.2] for the average k_{eff} and $[\log_{10} A \ (1/mol \ s), E^* \ (kcal/mol)]$ = [7.97 ± 0.14, 40.1 ± 2.3] for k_2 with low conversion data, X < 0.4. Regression of the half-lifes t^* at varying temperatures gave Arrhenius parameters $[\log_{10} A \ (s^{-1}), E^* \ (kcal/mol)]$ = [8.53 ± 0.09, 42.0 ± 1.6] for k_2.

Three primary reaction pathways operate in parallel upon 14DMN substrate: (P1) Hydrogenation to *cis*- and *trans*-9,10-dihydro-9,10-dimethylnaphthalene, (P2) Demethylation to 1-methylnaphthalene, and (P3) Methylation to 1,4,5-trimethylnaphthalene, 1,4,6-trimethylnaphthalene and other TMA isomers. The primary demethylation product 1MN and the primary methylation product TMN are secondary operated upon by a pathway triad analogous to the preceding primary triad, eventually forming a host of dimethylanthracenes and dimethylanthracenes, and naphthalene and reforming 14DMN substrate. And at the highest substrate conversions, even the terminal demethylation product NAP suffers methylation, as witnessed by the appearance of the minor product 2MN. Neither 14DMN or 1MN isomerize to their positional isomers, since the methylated species do not arise until after the demethylated compound appears. Terminated products include both pure- and cross-termination of 14DMN and DHDMN radicals.

A possible mechanism for the early stages of 14DMN thermolysis, that is consistent with the present pathway and kinetic observations and accounts for all the products observed during the initial stages of 14DMN thermolysis at low conversions, was devised and is summarized as follows: The free-radical cycle is initiated by the substrate 14DMN undergoing bimolecular disproportionation, an intermolecular hydrogen transfer reaction, to form the respectively dehydrogenated and hydrogenated radical species 14DMN* and HDMN*. Of these, the latter can either abstract hydrogen from 14DMN substrate to form DHDMN products or undergo a β-scission type of radical decomposition forming 1MN product and a methyl radical CH_3*. The CH_3* can either abstract H from 14DMN substrate to form methane product, or add to the 14DMN substrate to form the trimethyl radical HTMN1*. The latter can then abstract H from substrate 14DMN to form the observed 146TMN product. Finally, the radical mechanism is terminated by the species 14DMN* and HDMN* engaging in both pure- and cross-combination to form various dimeric products. HDMN* radical can also terminate by disproportionation to form 14DMN and DHDMN. The proposed mechanism exhibits certain stoichiometric limits and thus restricts the maximum selectivities of each of DHDMN, 1MN, TMN and heavies to 1/3.

Thermochemical and activation parameters were then assigned from first principles for each elementary reaction and its reverse in the mechanism. In order to derive kinetic parameters for the mechanism, values of the enthalpy of formation,

ΔH°_{f}, were required for all participating chemical species. Where experimental values were unavailable, enthalpies of formation were derived using a "macro" group additivity technique, which started with a basis molecule that was as large and as structurally similar to the desired product and then added and subtracted other basis species from the starting species to account for structural differences between it and the desired species. Arrhenius expressions were generated for each elementary step of the 14DMN thermolysis mechanism from kinetic data reported in the literature for that type of reaction, which was analyzed to ascertain its activation parameters, including $\log_{10} A$, which was decomposed into an intrinsic portion, $\log_{10} A_{int}$, and a reaction path degeneracy, rpd, with $\log_{10} A = \log_{10} A_{int} + rpd$. The activation energy E^{*} was determined by an Evans-Polanyi expression of form $E^{*} = E_{o} + \alpha \Delta H^{\circ}_{r}$. An algebraic steady state analysis was performed on the 14DMN mechanism to provide an independent check on numerical results of computer calculations, which agreed closely to within a factor of 4 or better. Conservation relations derived from the mechanistic model of 14DMN thermolysis and using the estimated rate constants were numerically integrated using a computer program called ACUCHEM.

Substrate and product histories and product selectivities as obtained from the numerical solution of the thermolysis model were compared to the experimental data for 14DMN, 1MN, TMN, CH4, DHDMN, heavies and product ratio R[TMN/1MN] at the center of the experimental grid, $[14DMN]_{o} = 0.87$ mol/l and T = 450°C. The model is seen to predict 14DMN decay too slow, S(1MN) and S(TMN) are

respectively 1.8 and 29-fold too low, S(DHDMA) is below GC detection limits, which agreed with experiments, S(HVY) (sum of DMND, DMNHDMND and HDMND) is comparable at low X < 0.1 and 3.4-fold higher at X > 0.2, and R[TMN/1MN] 79-fold too low at low conversions X ~ 0.05, with the slope of opposite sign as experimentally observed.

14DMN decay half-life, major product selectivities and product ratios obtained from numerical solutions were compared with the experimental observations for varying [14DMN]$_o$ at fixed T = 450°C and for varying T at fixed [14DMN]$_o$ = 0.87 mol/l. The model predicted t* too long, that is, decay kinetics too slow, compared to the experimental observations at all [14DMN]$_o$ and T with the model yielding a slope -1.04, implying ~ 2 order, versus the experimental data that yielded a slope of - 1.60, implying 2nd order decomposition kinetics, and the model yielded an E* = 52.7 kcal/mol versus the experimental data that provided E* = 42.0 kcal/mol. The model predicted S(1MN) and S(TMN) too low at all [14DMN]$_o$ and T, S(HVY) too high for all [14DMN]$_o$ and T at low conversion and too low for all [14DMN]$_o$ and T at high conversions.

A sensitivity analysis was performed to demonstrate how the errors of the estimated thermochemical and activation parameters affected the model results at the central point of the 14DMN experimental grid by separately perturbing the E* of selected elementary reactions over the inherent errors in the ΔH°_r to show their effects on t*, S(1MN) and R[TMN/1MN]. The variations of t$^*_{mod}$ and

R[TMN/1MN]$_{mod}$ on account of the inherent errors in the estimated rate constants were large enough to exceed the span of experimental variations by changes in [14DMN]$_o$ at T = 450°C and in T with [14DMN]$_o$ = 0.87 mol/l. The variation in 1MN$_{mod}$ was not large enough to exceed the span of S(1MN)$_{exp}$ variations by changes in [14DMN]$_o$ and T due to the stoichiometric limit on S(1MN) and the hugh difference between t$^*_{mod}$ and t$^*_{exp}$ is not within the 300-fold uncertainty in t$^*_{mod}$.

These activation parameters were then adjusted to the limits of the errors to provide the best fit to the experimental results. Results as obtained from the optimized numerical solution were compared to the thermolysis model to the experimental data for 14DMN, 1MN, TMN, CH4, DHDMN, heavies, and R[TMN/1MN] at the center of the experimental grid. The model predicted 14DMN decay toss slow, S(1MN) and S(TMN) are respectively 1.8 and 6.5-fold too low compared to the experimental observations (the mechanism as the upper limit of 0.33 for S(1MN)), S(DHDMA) very low that corresponded to the experimental data, S(HVY) was comparable at low X and 3-fold too high at X > 0.2, and R[TMA/9MA] was 37-too low at low conversions, 3-fold too high at high conversions and a slope of opposite sign as the experimental trend.

Chapter 8.

Discussion

This discussion section is divided into seven parts. The first section will compare the decomposition kinetics of the three multiply methylated acene substrates, 910DMA, 9MA and 14DMN. The second section will consider with the generalized pathways and mechanisms developed for methylated acene thermolysis. The third part will compare experimental selectivity and product ratio results at T = 370°C and initial concentrations of ~ 0.85 mol/l for all substrates. The fourth part of the chapter will consider the numerical solutions based on the model pathways and mechanism. The predictions of the numerical solutions will be compared to the experimental and theoretical kinetics, stoichiometric limits, product

selectivities and product ratios. The limitations and strengths of the simulations will be derived from this discussion. The fifth section combines of the models separately developed for 910DMA and 9MA thermolyses and compares their joint results to experimental observations for 910DMA at high conversions. The sixth part of the chapter correlates the experimental minor product data in terms of aromatic reactivities as predicted by frontier molecular orbital theory. The seventh and final part compares the present multiply-methylated acene decomposition results with data previously reported in the literature for related aromatic species.

8.1 Comparison of Multiply-Methylated Acene Thermolysis Kinetics

This section will compare the kinetics experimentally derived from each of the three multiply-methylated acene thermolyses as well as the kinetics associated with the modelling of each thermolysis by the "macro" group additivity method. The relevant orders, activation parameters, and rate constants are summarized in Table 8.1. In all cases, orders were obtained from data at varying initial concentrations at fixed temperature, while activation parameters were derived from data at varying temperatures for fixed initial concentrations. For each substrate, two sets of experimental results are quoted, respectively based on the true rate constants and on substrate decay half-lifes, as well as two sets of model results, respectively based on the original "macro" group additivity-bond model and on the optimized model. Order and activation parameters for model results are based upon the

Table 8.1

SUMMARY OF EXPERIMENTAL AND MODEL KINETICS FOR MULTIPLY METHYLATED ACENE THERMOLYSIS

Compound		Order	$\log_{10}$ A	E^*	$\log_{10}$ k
910DMA	k_{true} (X < 0.4)	3/2	11.1 ± 0.08	44.6 ± 2.1	-4.43 (T = 355°C)
	t^*	1.53 ± 0.06	10.6 ± 0.03	43.1 ± 1.0	-4.41 (T = 355°C)
	"macro" additivity	2	9.9 ± 0.05	43.4 ± 4.4	-5.21 (T = 355°C)
	optimized model	2	9.9	42.2	-4.79 (T = 355°C)
9MA	k_{true} (X < 0.4)	3/2	9.2 ± 0.15	39.7 ± 3.9	-4.30 (T = 370°C)
	t^*	1.50 ± 0.07	11.4 ± 0.03	46.4 ± 0.09	-4.28 (T = 370°C)
	"macro" additivity	2	9.3 ± 0.05	43.7 ± 3.4	-5.56 (T = 370°C)
	optimized model	2	9.3	43.3	-5.43 (T = 370°C)
14DMN	k_{true} (X < 0.4)	2	7.94 ± 0.14	40.1 ± 2.3	-4.19 (T = 450°C)
	t^*	2.05 ± 0.16	8.52 ± 0.09	42.0 ± 1.6	-4.17 (T = 450°C)
	"macro" additivity	2	9.9 ± 0.05	56.6 ± 5.2	-7.2 (T = 450°C)
	optimized model	2	9.9	48.6	-4.80 (T = 450°C)

initiation reaction, wherein two methylated acenes disproportionate by an intermolecular hydrogen transfer reaction forming a dehydrogenated benzyl acene radical and a hydrogenated acene radical species. Table 8.1 display reaction order (column 3) and Arrhenius parameters, pre-exponential factor A (column 4) in units appropriate to the reaction order and activation energy E^* (column 5) in kcal/mol, and rate constant k (column 6) also in units appropriate to reaction order.

For 910DMA and 14DMN, the orders and Arrhenius parameters derived from k_{true} and from t^* were similar. For 9MA, reaction orders derived from k_{true} and from t^* were approximately equal, but the Arrhenius parameters derived from k_{true} were both lower than derived from t^*, although the $\log_{10} k$ values were comparable. Turning to the model parameters, associated with the initiation reaction common to all mechanisms, it is seen that the model order is always 2, which accords with the experimentally observed order for 14DMN but is higher than the observed 3/2 orders for 910DMA and 9MA. Arrhenius parameters obtained from the 910DMA and 9MA models are in reasonable accord with the corresponding experimental values but the 14DMN model Arrhenius parameters [9.9, 56.6] are much higher than the experimentally observed values [~8.3, ~41] for 14DMN. Since reaction orders generally differed for each of the model compounds, substrate decay half-lifes were used to compare their thermolysis kinetics. Figure 8.1 displays $\log t^*$ versus log initial concentration over the full range of initial concentrations at fixed T = 355°C for 910DMA, T = 370°C for 9MA and T = 450°C for 14DMN, respectively. The
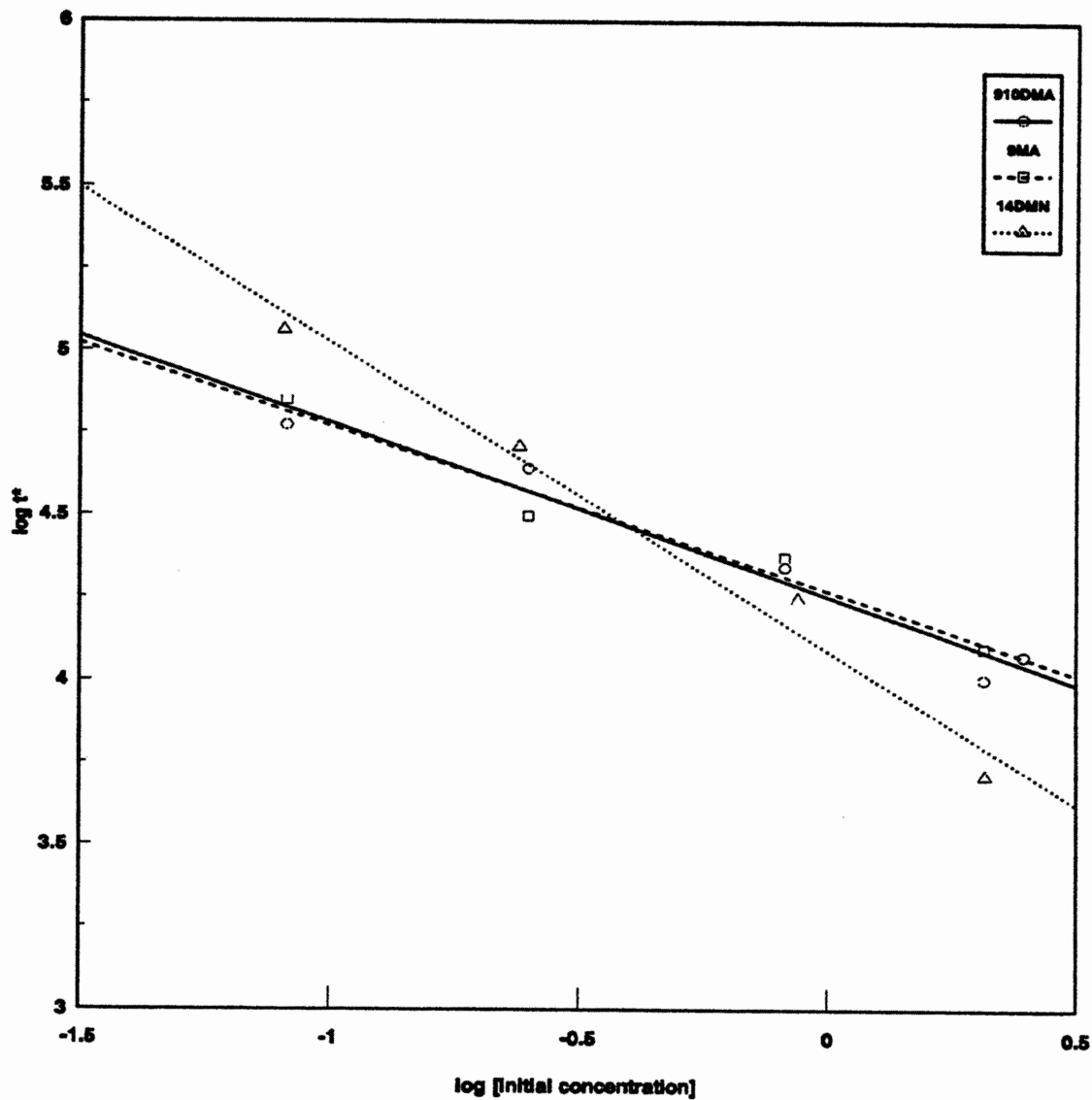
Figure 8.1: Decay half-life t* for varying initial concentrations of multiply-methylated acenes at T = 355°C for 910DMA, T = 370°C for 9MA and T = 450°C for 14DMN.

experiments traverse considerable ranges of initial concentrations, ~ 2.5 decades for

9MA and 14DMN and ~ 3 decades of 910DMA, over which the reaction orders were

3/2 for 910DMA and 9MA and 2nd for 14DMN. Figure 8.2 uses Arrhenius related

coordinates of log t^* versus the reciprocal of a scaled absolute temperature, $1/\theta$,

where $\theta = 0.004573 * T$ in K, over the full range of temperatures at fixed initial

concentrations ~ 0.85 mol/l. The experiments traverse considerable ranges of rate

constants, ~ 2 decades for 910DMA and 9MA and ~ 3 decades of 14DMN, over

which the apparent activation energies are respectively $E^*_{app} \approx 43$, 46 and 42

kcal/mol. Thermolysis of 14DMN is evidently much slower than that of 910DMA

and 9MA; at fixed T = 409°C, $[1/\theta] = 0.32$, the ratio of $t^*(910DMA)/t^*(14DMN)$

~ 0.018 and $t^*(9MA)/t^*(14DMN)$ ~ 0.040. These fifty-fold and twenty-five-fold

slower rates seem theoretically related to the endothermicity of the elementary

initiation step of the thermolyses. As seen in Table 8.1, the model E^* predicted for

the initiation reaction by the "macro" group additivity method is 56.6 kcal/mol for the

naphthalene aromatic system of 14DMN which is larger than the 43.4 kcal/mol for

the anthracene system of 910DMA; however the models predict that $-(E^*_{14DMN} -$

$E^*_{910DMA})/\theta \approx -4 = 0.0001$, that is 14DMN initiation should be ten-thousand fold

slower than 910DMA initiation whereas the experiments show the overall kinetics of

14DMN decomposition only 50-fold slower than that of 910DMA.
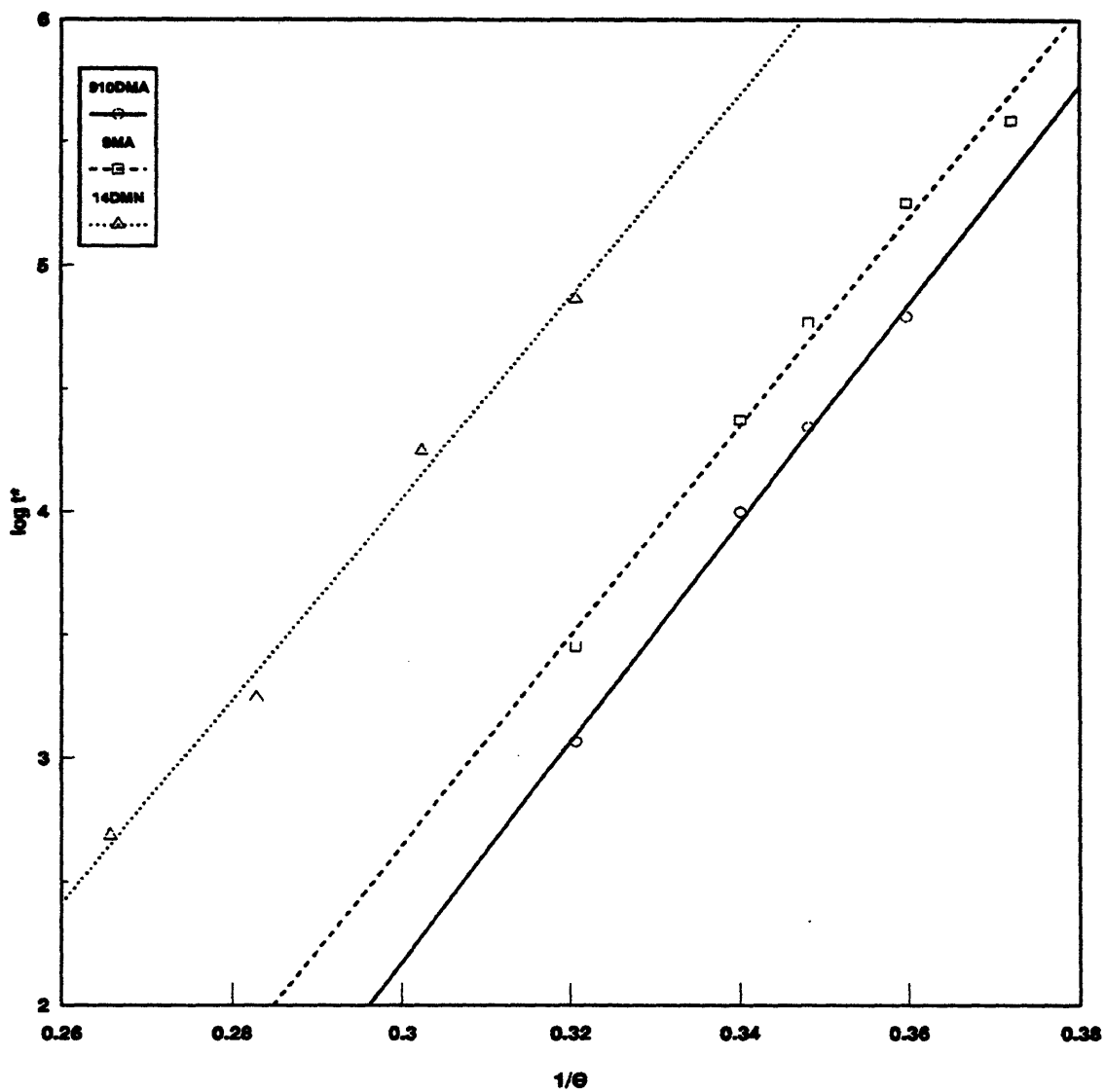
Figure 8.2: Decay half-life t^* for varying temperatures with fixed initial concentrations ~ 0.85 mol/l.

8.2 Generalized Multiply-Methylated Acene Pathway and Mechanism

A generalized pathway for the thermolysis of a multiple (X-)methyl acene, deduced from the present experiments, is presented in Figure 8.3. Three primary pathways operate in parallel upon the original X-methyl acene, where X indicates the original number of methyl groups, namely: (P1) Hydrogenation to the dihydro-X-methyl acene, (P2) Demethylation to the (X - 1) methyl acene, and (P3) Methylation to the (X + 1) methyl acene. Also, as shown in Figure 8.3, the demethylated acene products are associated with methane gas. Termination products include both pure- and cross-termination species related to the multiply methylated and hydrogenated acenes.

Figure 8.4 displays the main sequential decomposition from X methylated acene to (X - 1) methylated acene, eventually reaching the parent acene. The primary methylation and demethylation products are secondarily operated upon by a pathway triad analogous to the preceding primary triad, whereas the secondary products are also operated upon by a pathway triad analogous to the primary pathway triad. X and (X - 1) methyl acenes do not isomerize to their positional isomers, since the position isomers do not arise prior to the appearance of their demethylated precursor.

Table 8.2 shows which compounds in the generalized multiply methylated acene pathways were detected in each of the model compound thermolysis. With the methylated anthracenes, 9,10-dimethylanthracene (910DMA) and 9-methylanthracene
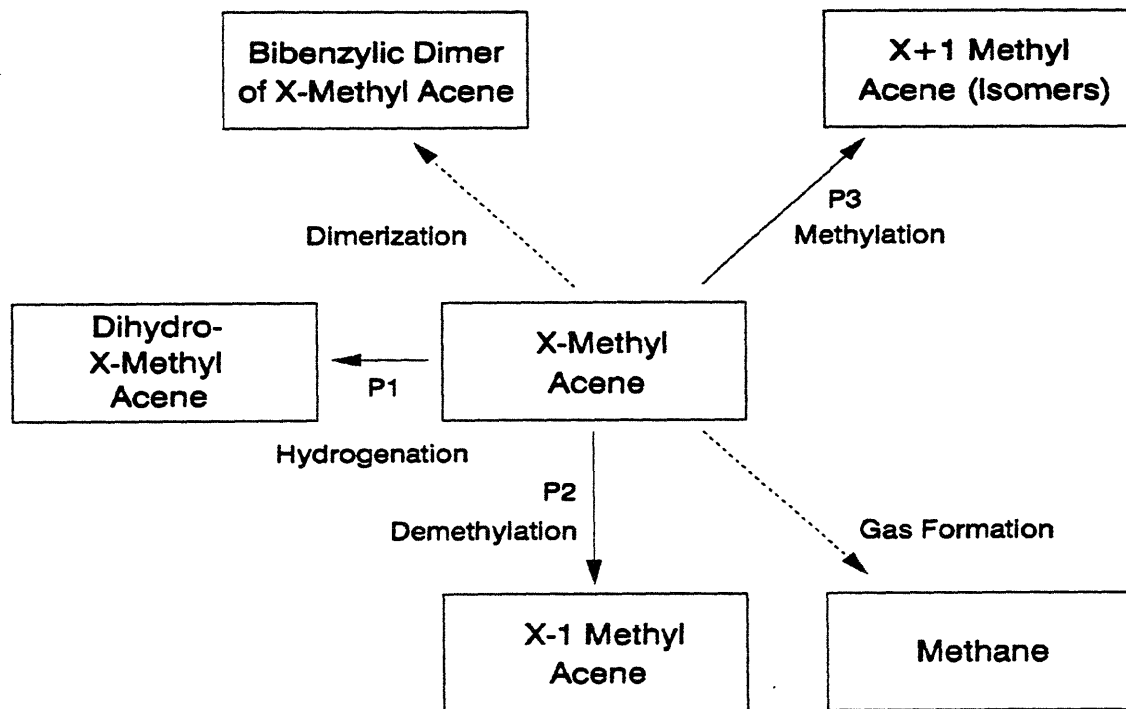
Figure 8.3: Generalized decomposition pathway for X-methyl acenes.

From previous figure
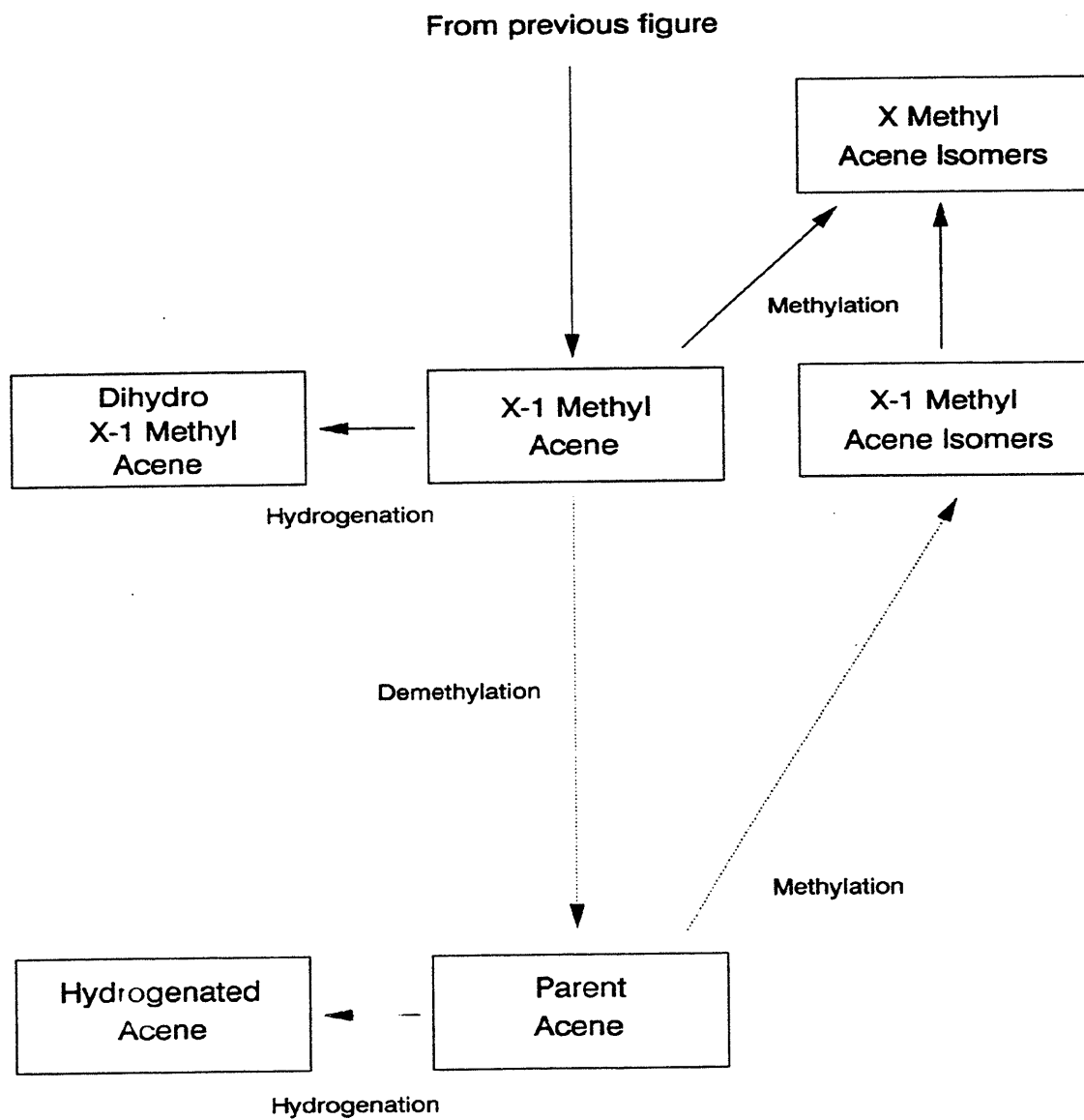
Figure 8.4: Secondary generalized decomposition pathway for X-methyl acenes.

Table 8.2

COMPOUNDS DETECTED IN
MULTIPLY-METHYLATED ACENE THERMOLYSES

Compound	910DMA	9MA	14DMN
Tetramethyl Acenes	X		X
Trimethyl Acenes	X	X	X
Dimethyl Acenes	X	X	X
Methyl Acenes	X	X	X
Parent Acene	X	X	X
Hydrogenated-trimethyl Acene	X		
Hydrogenated-dimethyl Acene	X	X	
Dihydrogenated-dimethyl acene	X		
Hydrogenated-methyl Acene	X	X	
Dihydrogenated-methyl Acene	X	X	
Hydrogenated Parent Acene	X	X	
Dihydrogenated Parent Acene	X	X	
Methane	X	X	X
Methylated Acene Dimer	X	X	X
Methylated-Hydrogenated Acene Dimer	X		
Hydrogenated Acene Dimer	X		

(9MA), all three primary pathway; hydrogenation, demethylation, and methylation; products were detected. For 910DMA, hydrogenation products included both dihydro- and tetrahydro-products of the parent methylated acene and both of the two subsequent sequential demethylation acene products and hydrogenation products of the primary methyl acene product. For 9MA, hydrogenation products included both dihydro- and tetrahydro-products of the parent methylated acene and the subsequent sequential demethylation acene product and hydrogenation products of the primary methyl acene product. Demethylation products down to the parent anthracene were detected for both 910DMA and 9MA. Methylation products up to tetramethylanthracene was detected for 910DMA and up to trimethylanthracene for 9MA. Methane production was quantified for both 910DMA and 9MA thermolyses. Termination products in the 910DMA thermolysis included both pure- and cross-termination possibilities, whereas in the 9MA experiments, only the pure-termination of the dimethyl acene was detected; no hydrogenated-methylated products were detected.

With the methylated naphthalenes, 1,4-dimethylnaphthalene (14DMN), only the demethylation and methylation pathway products were detected. This does not indicate the hydrogenation pathway did not occur with the methylated naphthalene, but only that the hydrogenated product amounts lay below our experimental detection limits; it is possible that hydrogenated 14DMN species reacted as quickly as they were formed therefore none was detected. Demethylation products down to

the parent naphthalene and methylation products up to trimethylnaphthalene were detected in 14DMN thermolyses. Methane was also detected during 14DMN thermolysis, but it could not be quantified. Termination products in the 14DMN thermolysis included only the pure-termination of the methylated acenes; no hydrogenated-methylated products were detected.

8.3 Comparison of Experimental Product Selectivities and Product Ratios

Table 8.3 displays experimental results in terms of substrate decay half-life, product selectivities and product ratios at T = 370°C and initial concentrations of ~ 0.85 mol/l. In part (a) of Table 8.3, the substrate decay half-lifes, t^*, for the experimental results increase as one goes from 910DMA to 9MA to 14DMN, indicating $E^*_{14DMN} > E^*_{9MA} > E^*_{910DMA}$, which agrees with the data shown in Table 8.1.

Part (b) of Table 8.3 refers to the selectivities of the major demethylated, methylated, hydrogenated and heavy products. The major demethylated product of 910DMA was 9MA, of 9MA was ANT, and of 14DMN was 1MN. Selectivity of the demethylated products decreased when going from 910DMA to 9MA to 14DMN; S(9MA) = 0.42, S(ANT) = 0.37 and S(1MN) = 0.32. The major methylated product of 910DMA was all TMAs, 9MA was all DMAs, and 14DMN was all TMNs. Selectivity to methylated products was higher for 9MA, than for 910DMA and 14DMN, S(TMAs) = 0.10, S(DMAs) = 0.22 and S(TMNs) = 0.10. This trend was

Table 8.3

COMPARISON OF EXPERIMENTAL SELECTIVITY AND PRODUCT RATIO RESULTS FOR 910DMA, 9MA AND 14DMN AT T =370°C AND INITIAL CONCENTRATIONS OF ~ 0.85 mol/l

Part:		Conversion X Range:	910DMA	9MA	14DMN
a	Substrate Decay Half-Life, t^* (s)		9900	23400	529000
b	Selectivity to:				
	demethylated product	0.2 - 1.0	S(9MA) = 0.42	S(ANT) = 0.37	S(1MN) = 0.32
	methylated product	0.2 - 1.0	S(TMAs) = 0.10	S(DMAs) = 0.22	S(TMNs) = 0.10
	hydrogenated product	~ 0.05	S(DHDMA) = 0.060	S(DHMA) = 0.031	S(DHDMN) = 0
		0.48 ± 0.08	0.011	0.014	0
	heavy products	0.2 - 1.0	0.15	0.13	0.060
c	Product ratios of:				
	hydrogenated/ demethylated products	0.06	R[DHDMA/9MA] 0.21	R[DHMA/ANT] 0.43	R[DHDMN/1MN] 0
		0.2 - 1.0	0.044	0.051	0
	methylated/ demethylated products	~ 0.05	R[TMA/9MA] 0.35	R[DMA/ANT] 0.69	R[TMN/1MN] 0.54
		0.40	0.28	0.36	-

true for all initial concentrations and temperatures. It can be explained by the fact that 9MA has a highly reactive site (position #10) available for methyl radical attack, whereas the 910DMA and 14DMN only have less reactive positions (#1 and #2) available for methyl radical attack. The major hydrogenated products of 910DMA were DHDMAs and of 9MA were DHMAs. Hydrogenated products DHDMNs of 14DMN were not detected at any initial concentration or temperature. Selectivity to the 910DMA and 9MA hydrogenated products started out at maximum value, ~ 0.045 ± 0.015 at X ~ 0.05, dropped rapidly by X = 0.20 and remained roughly constant at ~ 0.01 over 0.2 < X < 1.0. The heavy products of all substrates include methyl acene dimers, methyl-hydrogenated acene dimers and hydrogenated acene dimers. The dominant dimer in all cases was the methyl acene dimer, that is, DMAD for 910DMA, 9MAD for 9MA and DMND for 14DMN. Selectivity of the heavy products decreased when going from 910DMA to 9MA to 14DMN; with $S(HVY)_{910DMA} = 0.15$, $S(HVY)_{9MA} = 0.13$ and $S(HVY)_{14DMN} = 0.060$.

Part (c) of Table 8.3 refers to the product ratios of the hydrogenated to demethylated products and methylated to demethylated products. The product ratios of hydrogenated to demethylated products for 910DMA, R[DHDMA/9MA], and for 9MA, R[DHMA/ANT], started out at maximum value, respectively 0.21 and 0.43 at X ~ 0.06, but both ratios dropped rapidly by X = 0.20 and remained roughly constant at ~ 0.05 each over 0.2 < X < 1.0. The product ratios of methylated to demethylated products of 910DMA, R[TMA/9MA], of 9MA, R[DMA/ANT] and of

751

14DMN, R[TMN/1MN], all started out at high values, respectively 0.35, 0.69 and 0.54 at X ~ 0.05, and then decreased somewhat with increasing conversion, reflecting the faster decomposition of the X+1 methyl acene in the numerator relative to the X-1 acene in the denominator.

8.4 Comparison of Numerical Solutions

The proposed mechanisms for thermolysis of 910DMA, 9MA and 14DMN each contains the same basic type of elementary reactions, the total number of elementary steps being 10 for 910DMA and 14DMN but 19 for 9MA, for which there are 2 possible intermediate hydrogenated radical species. Each of the proposed mechanisms can be simplified to three limiting cases, namely (P1) pure hydrogenation, which leads to the dihydroacene and dimer with selectivities 1/3 each; (P2) pure demethylation, which leads to the demethylated product, methane and dimer, with selectivities 1/3 each; and (P3) pure methylation, which leads to the methylated product and dimer, each with selectivities of 1/3. The foregoing show that the present mechanism is inherently incapable of matching observed product selectivities > 0.33.

Table 8.4 displays numerical solution results in terms of substrate decay half-life, product selectivities and product ratios at T = 370°C and initial concentrations of ~ 0.85 mol/l in a manner analogous to that of Table 8.3 for the experimental results. In part (a) of Table 8.4, the substrate decay half-lifes, t^*, for the numerical

Table 8.4

COMPARISON OF NUMERICAL SOLUTION RESULTS FOR 910DMA, 9MA AND 14DMN AT T =370°C AND INITIAL CONCENTRATIONS OF ~ 0.85 mol/l

Part:		Conversion X Range:	910DMA	9MA	14DMN
a	Substrate Decay Half-Life, t^* (s)		34300	53700	376000000
b	Selectivity to:				
	demethylated product	0.20	S(9MA) = 0.21	S(ANT) = 0.16	S(1MN) = 0.34
		0.80	0.35	0.37	0.38
	methylated product	0.20	S(TMAs) = 0.046	S(DMAs) = 0.13	S(TMNs) = 0.015
		0.80	0.052	0.13[1]	0.14
	hydrogenated product	~ 0.05	S(DHDMA) = 0.15	S(DHMA) = 0.23	S(DHDMN) = 0.000013
		0.80	0.0023	0.0017	0
	heavy products	0.20	S(DMAD) = 0.30	S(9MAD) = 0.24	S(DMND) = 0.32
		0.80	0.30	0.25[2]	0.24
c	Product ratios of:				
	hydrogenated/ demethylated products	0.06	R[DHDMA/9MA] 0.77	R[DHMA/ANT] 1.92	R[DHDMN/1MN] ~ 0.00005
		0.80	0.014	0.0045	0
	methylated/ demethylated products	~ 0.05	R[TMA/9MA] 0.23	R[DMA/ANT] 0.79	R[TMN/1MN] 0.015
		0.80	0.15	0.34	0.37

[1]   goes through maximum S(DMAs) = 0.25 at X = 0.60

[2]   goes through minimum S(DMAD) = 0.16 at X = 0.60

solutions increase as one goes from 910DMA to 9MA to 14DMN. This is the same trend as seen in the experimental results in part (a) of Table 8.3, but for each substrate the predicted model kinetics were slower than experimentally observed.

Part (b) of Table 8.4 refers to the selectivities of the major demethylated, methylated, hydrogenated and heavy products from the numerical solutions. The major demethylated product of 910DMA was 9MA, of 9MA was ANT, and of 14DMN was 1MN. Selectivity to the demethylated products generally increased as conversion increased from 0.20 to 0.80 for all model compounds. From the 910DMA numerical solution, S(9MA) increased from 0.21 at X = 0.20 to 0.35 at X = 0.80. Even the highest value of S(9MA) = 0.35 from the numerical solution was somewhat lower than the S(9MA) = 0.42 seen in the experiments for 0.2 < X < 1.0. From the 9MA numerical solution, S(ANT) increased from 0.16 at X = 0.20 to 0.37 at X = 0.80. The maximum value of S(ANT) = 0.37 from the numerical solution was comparable to the S(ANT) = 0.37 seen in the experiments for 0.2 < X < 1.0. From the 14DMN numerical solution, S(1MN) increased slightly from 0.34 at X = 0.20 to 0.38 at X = 0.80. The minimum value of S(1MN) = 0.34 from the numerical solution was slightly higher than the S(1MN) = 0.32 seen in the experiments for 0.2 < X < 1.0. The major methylated product of 910DMA was all TMAs, of 9MA was all DMAs, and of 14DMN was all TMNs. Selectivity to the methylated products generally increased as conversion increased from 0.20 to 0.80 for all substrates. From the 910DMA numerical solution, S(TMAs) increased slightly from 0.046 at X = 0.20

to 0.052 at X = 0.80. Even the maximum value of S(TMA) = 0.052 from the numerical solution was lower than the S(TMA) = 0.10 seen in the experiments for 0.2 < X < 1.0. From the 9MA numerical solution, S(DMAs) increased from 0.13 at X = 0.20 to 0.25 at X = 0.60 and then decreased to 0.13 at X = 0.80. The maximum value of S(DMAs) = 0.25 from the numerical solution was slightly higher than the S(DMAs) = 0.22 seen in the experiments for 0.2 < X < 1.0. From the 14DMN numerical solution, S(TMNs) increased from 0.015 at X = 0.20 to 0.15 at X = 0.80. The maximum value of S(TMNs) = 0.14 from the numerical solution was higher than the S(TMN) = 0.10 seen in the experiments for 0.2 < X < 1.0. The major hydrogenated product of 910DMA was DHDMA, of 9MA was DHMA and of 14DMN was DHDMN. Model selectivities to hydrogenated products DHDMA and DHMA started out at high values respectively 0.15 and 0.23 at X ~ 0.05 and decreased linearly to ~ 0.002 with X = 0.80. The values at low (X = 0.05) and high (X = 0.80) conversions from the numerical solutions for the 910DMA and 9MA substrates were close to the corresponding experimental values, but whereas S(DHDMA) and S(DHMA) in the experiments decreased rapidly by X = 0.20, the numerical solution showed them to decrease more gradually from low to high conversions. Finally, although the hydrogenated product DHDMN of 14DMN was not detected in the experiments, the numerical results predicted a low S(DHDMN) = 13E-06 at X ~ 0.05; this is consistent with the absence of DHDMN among the products that were experimentally detected. The heavy product of the model

compounds include methyl acene dimers, methyl-hydrogenated acene dimers and hydrogenated acene dimers. The dominant dimer in all cases was the methyl acene dimer, that is, DMAD for 910DMA, 9MAD for 9MA and DMND for 14DMN. Selectivity to the heavy products during the numerical solution of 910DMA remained roughly constant at S(DMAD) = 0.30 for 0.2 < X < 0.8. For 9MA, S(9MAD) decreased from 0.24 at X = 0.20 to 0.16 at X = 0.60 and then increased slightly to 0.25 at X = 0.80. For 14DMN, S(DMND) decreased from 0.32 at X = 0.20 to 0.24 at X = 0.80. For all substrates, the selectivities to dimers from the numerical solutions were greater than actually seen experimentally.

Part (c) of Table 8.4 refers to the product ratios of the hydrogenated to demethylated products and methylated to demethylated products. The predicted product ratio R[DHDMN/1MN] from 14DMN was not detected at any initial concentration or temperature. The product ratio of hydrogenated to demethylated products for anthracene compounds started out at maximum value, R[DHDMA/9MA] = 0.77 for 910DMA and R[DHMA/ANT] = 1.92 for 9MA at X = 0.06, and decreased linearly to R[DHDMA/9MA] = 0.014 for 910DMA and R[DHMA/ANT] = 0.0045 for 9MA at X = 0.80. The values from the numerical solutions were too high at low conversions as compared to the experiments, but were comparable to the experiments at high conversion, although again the slope of the decrease was much slower in the numerical solutions than from the experimental observations. For 14DMN, the model predicted the ratio [DHDMA]/[1MA] ~

$0.0005 \approx 0$ at $X \sim 0.05$; this is consistent with the absence of DHDMN among the products detected. The product ratios of methylated to demethylated products of 910DMA were R[TMA/9MA], 9MA were R[DMA/ANT] and 14DMN were R[TMN/1MN]. The product ratio of methylated to demethylated products started out at high values and decreased linearly with increasing conversion for the anthracene compounds; thus R[TMA/9MA] = 0.23 at X = 0.05 and decreased to 0.15 at X = 0.80 while R[DMA/ANT] = 0.79 at X = 0.05 and decreased to 0.34 at X = 0.80. The foregoing values from the numerical solutions at low conversions were higher than seen experimentally, whereas the values from the numerical solutions at high conversions were slightly lower than seen experimentally. For the 14DMN substrate, the model predicted R[TMN/1MN] = 0.015 at X = 0.05 and increased to 0.37 at X = 0.80; the trend seen from the numerical solution was opposite of the experimental observations which showed R[TMN/1MN] $\sim$ 0.54 at $X \sim 0.05$ and ~ 0 at $X \sim 0.80$.

8.5 Extended 910DMA and 9MA Mechanistic Models

Combining the models separately developed for 910DMA and 9MA, and accounting for the additional elementary reactions arising from their interactions, should permit an extended numerical simulation of 910DMA thermolysis. In this section we consider first a comparison between the basic 10-step 910DMA model and experiments at T = 370°C for $[910DMA]_0$ = 0.82 mol/l. Then an extended 48-step

757

model of 910DMA thermolysis is developed and numerically solved at the same conditions. Results of the extended 48-step model are finally compared with both those of the basic 10-step model and the experiments.

8.5.1 Basic 910DMA Thermolysis Model

Table 8.5 presents the rates of radical and stable species formation as calculated from the basic model at low, $X = 0.001$, and moderate, $X = 0.31$, conversions. The table also lists the elementary steps contributing to each species, as well as the most important of these steps.

Figure 8.5 compares the substrate and product histories (upper panel) and product selectivities (lower panel) as obtained from the numerical solution of the basic 10-step 910DMA thermolysis model to the experimental data for 910DMA, 9MA, ANT, TMA, and CH4 at $[910DMA]_o = 0.82$ mol/l and $T = 370°C$. In the upper panel of Figure 8.5, the model is seen to predict 910DMA decay, the solid line, that is too slow compared to the experimental observations, shown as asterisks. The model half-life, $t^* = 34264$ s, is 1.6-fold slower than the experimental $t^* = 21912$ s. The upper panel of Figure 8.5 also shows that the absolute amounts of 9MA, the short-dashed line versus the circles; TMA, the long dashed line versus the triangles; and of CH4, the short dashed lines versus the solid circles, formed by the model are all lower than observed in the experiments. ANT, shown as squares of the graph, was not formed using this model. The lower panel of Figure 8.5 shows that the

Table 8.5

CALCULATED RATES OF FORMATION OF RADICAL AND STABLE SPECIES AT X = 0.001 AND 0.33 AT T = 370°C AND [910DMA]$_o$ = 0.82 mol/l

	CONTRIBUTING REACTIONS	r (mol/l s) at X = 0.001	Major Contribution	r (mol/l s) at X = 0.33	Major Contribution
r(910DMA*)	R1 - R-1 + R2 - R-2 + R4 - R-4 - 2R7 + 2R-7 - R8 + R-8	5.0E-08		1.3E-07	
r(HDMA*)	R1 - R-1 - R2 + R-2 - R3 + R-3 + R6 - R-6 - R8 + R-8 - 2R9 + 2R-9 - 2R10 + 2R-10	1.7E-08		2.5E-08	
r(CH3*)	R3 - R-3 - R4 + R-4 - R5 + R-5	-1.5E-08		-1.5E-08	
r(HTMA*)	R5 - R-5 - R6 + R-6	1.1E-08		8.9E-09	
r(910DMA)	-2R1 + 2R-1 - R2 + R-2 - R4 + R-4 - R5 + R-5 - R6 + R-6 + R10 - R-10	-2.9E-05	R1, R2, R4, R5, R-5	-1.5E-05	R1, R2, R-2, R4, R5, R-5
r(9MA)	R3 - R-3	5.1E-06	R3	3.8E-06	R3
r(TMA)	R6 - R-6	1.2E-06	R6	6.6E-07	R6
r(CH4)	R4 - R-4	3.9E-06	R4	3.1E-06	R4
r(DHDMA)	R2 - R-2 + R10 - R-10	4.1E-06	R2	3.3E-07	R2, R-2
r(DMAD)	R7 - R-7	8.0E-06	R7	3.4E-06	R7, R-7
r(DMAHDMAD)	R8 - R-8	9.2E-07	R8	1.5E-08	R8, R-8
r(HDMAD)	R9 - R-9	6.7E-08	R9	-3.5E-10	R9, R-9

759
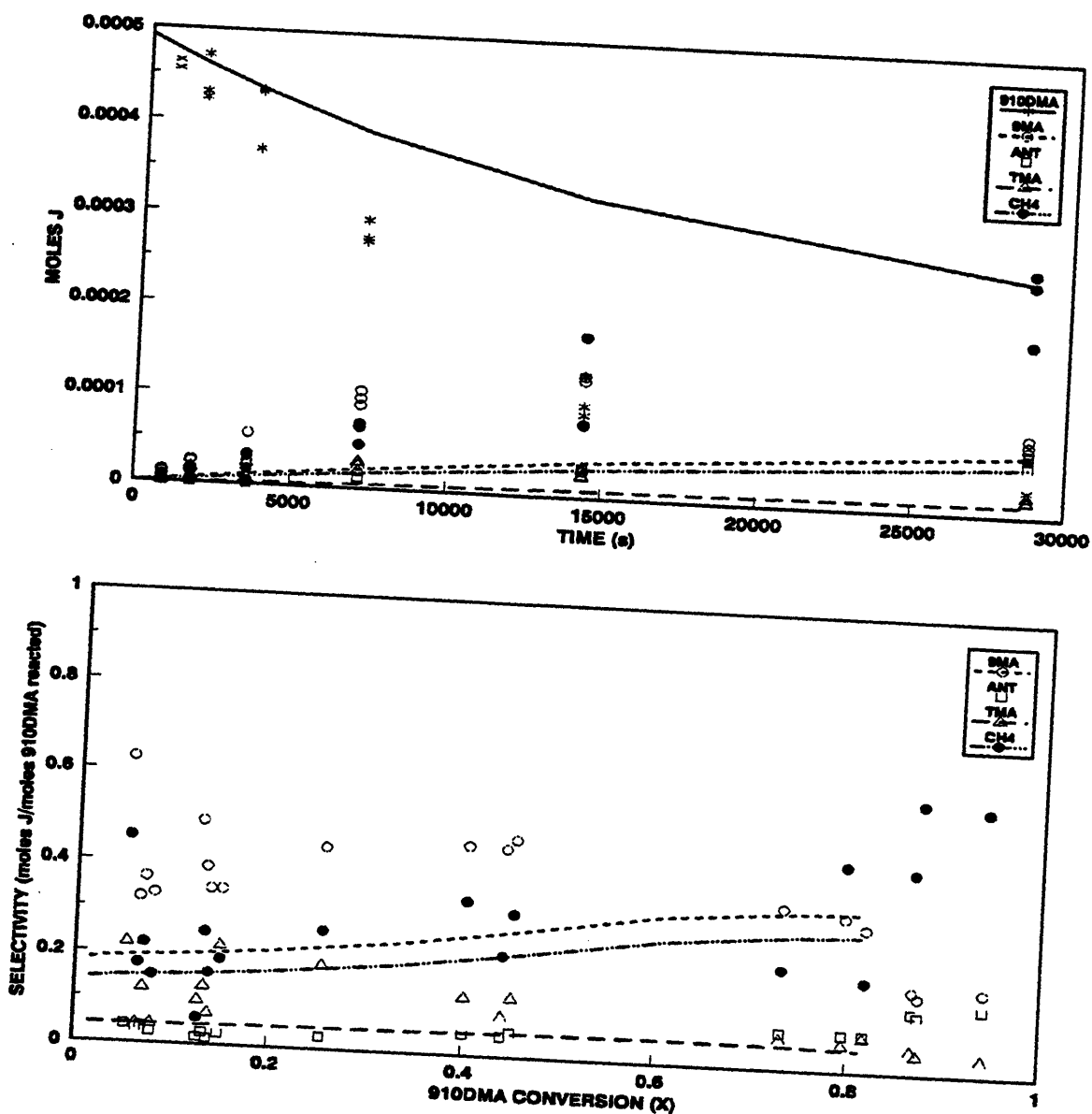
Figure 8.5: Product histories (top) and selectivity diagram (bottom) comparing basic model results (lines) to experiments (symbols) for 910DMA, 9MA, TMA, ANT and CH4 at T = 370°C with $[910DMA]_o$ = 0.82 mol/l.

selectivities S(9MA), S(TMA) and S(CH4) from the model are respectively 2.0-1.2, 2.2 and 1.5-fold too low compared to the average values of S(9MA), S(TMA) and S(CH4) observed from the experiments.

Figure 8.6 continues the comparison between model (lines) and experimental (symbols) product histories and selectivities for DHDMA and DHMA products. In the upper panel of Figure 8.6, the model (solid line) is seen to predict DHDMA amounts too high compared to experimental observations (circles) at all times. Both the model and experimental observations show a maximum followed by a decrease with increasing time. This basic model did not predict DHMA (squares). In the lower panel of Figure 8.6, it is seen that, relative to experiments, S(DHDMA) from the model is 2.0-fold too high at low conversions X = 0.05, comparable to the experimental observations at high conversions, and the slope of the line does not correspond to the trend of the experimental data.

Figure 8.7 compares the model calculations (lines) to the experimental data (symbols) for heavies (910DMAD, 9MAD and 910DMA9MAD). All the possible heavies were predicted by the model for 910DMA thermolysis (910DMAD, HDMAD, DMAHDMAD), but only 910DMAD was predicted by this model and included since it was 2 orders of magnitude greater than any of the other dimer species formed. In the upper panel of Figure 8.7, the model is seen to predict heavies production comparable to the experiments at all reaction times. The lower panel of Figure 8.7 shows that the dimer selectivity S(910DMAD) ~ 0.29 calculated
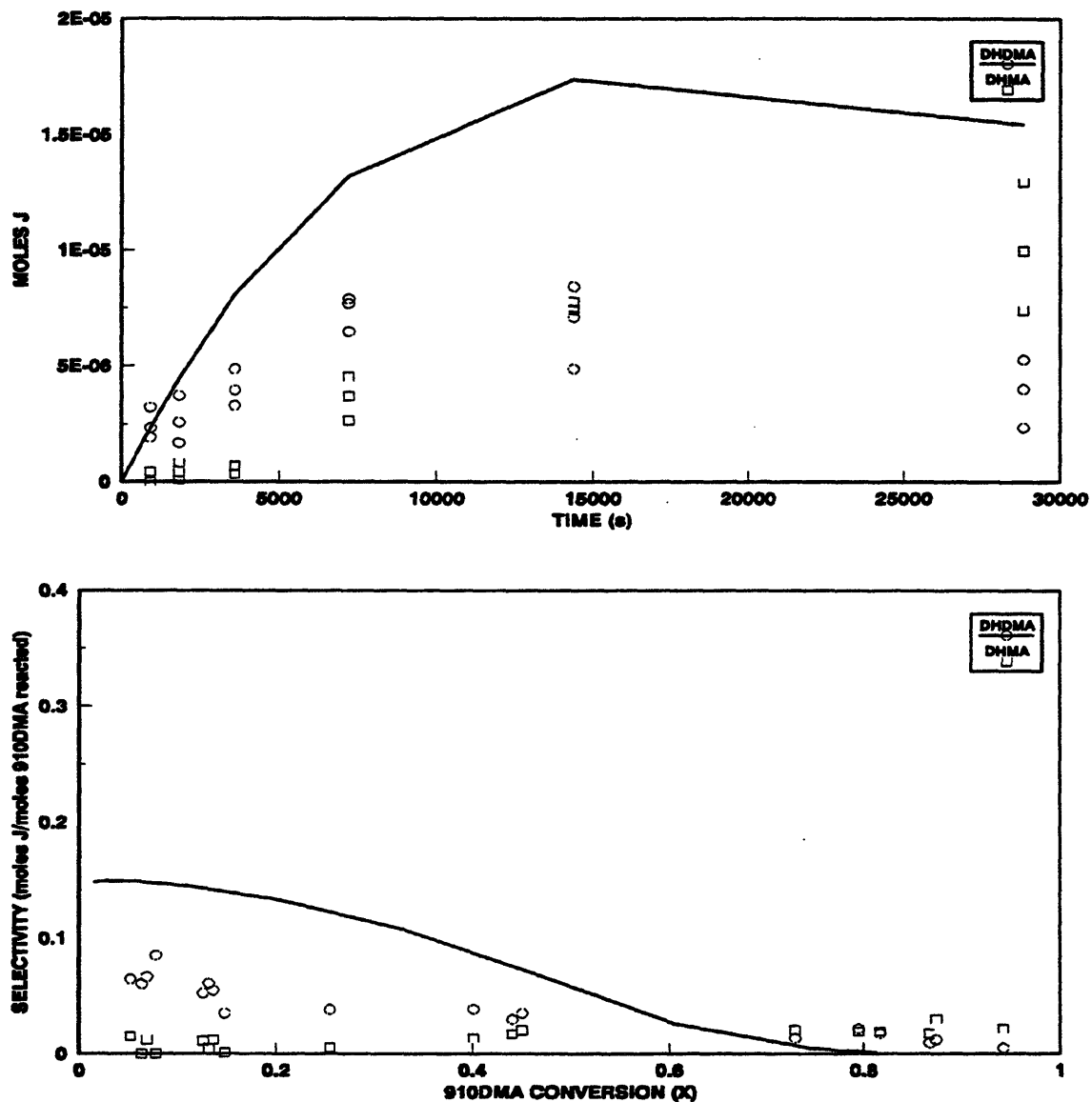
Figure 8.6: Product histories (top) and selectivity diagram (bottom) comparing basic model results (lines) to experimental data (symbols) for DHDMA and DHMA at T = 370°C with $[910DMA]_o$ = 0.82 mol/l.
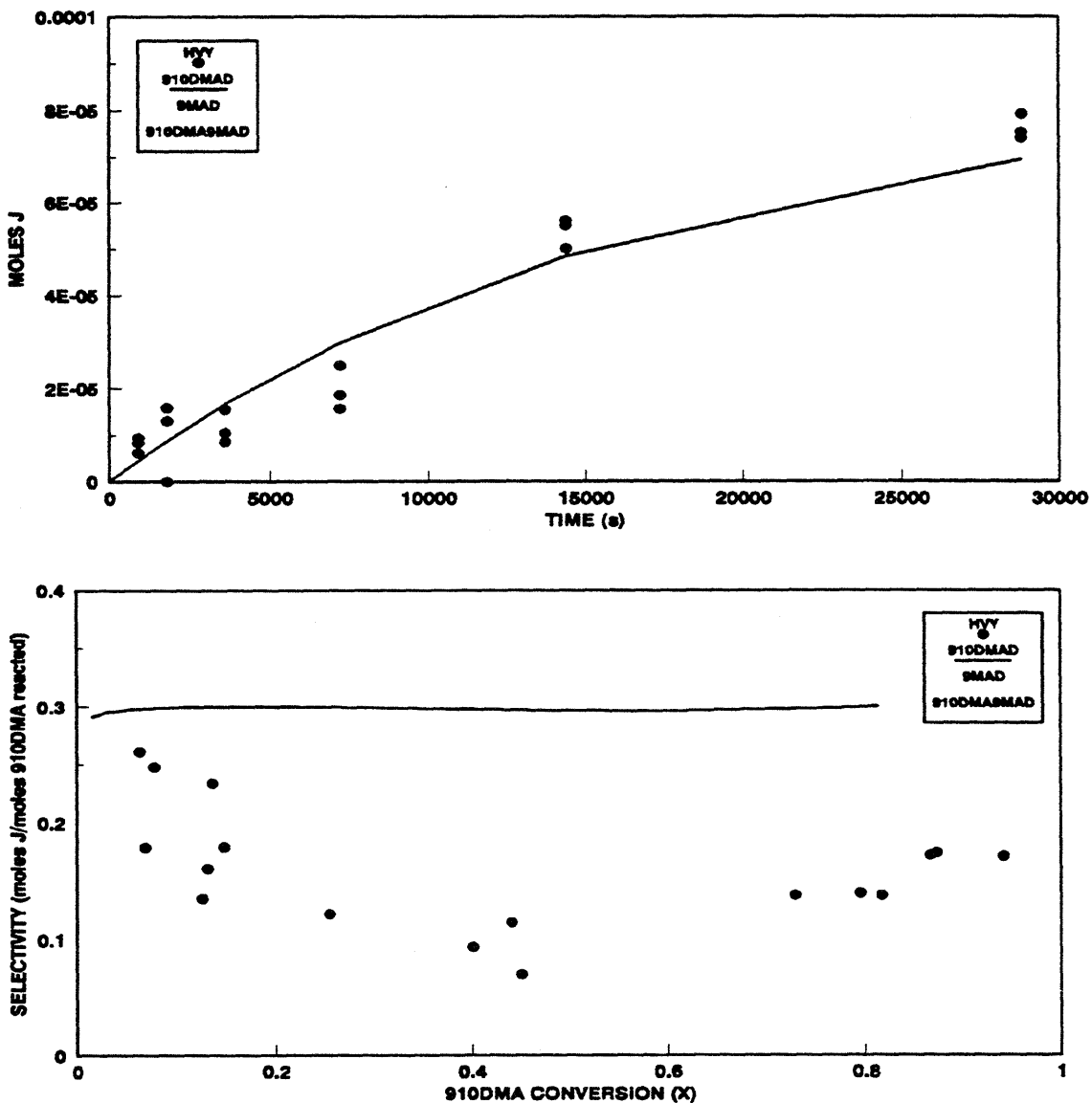
Figure 8.7: Product histories (top) and selectivity diagram (bottom) comparing basic model results (lines) to experimental data (symbols) for heavies at T = 370°C and [910DMA]$_o$ = 0.82 mol/l.

763

from the model is close to the experimental S(HVY) ~ 0.25 at low X < 0.1, but whereas the S(HVY) in the experiments decreases to ~ 0.10 with increasing conversions, S(910DMAD) from the basic model remains at S(910DMAD) ~ 0.29 to X = 0.81. For X > 0.20, S(910DMAD) is approximately 2.7-fold higher than the experimental S(HVY).

Figure 8.8 compares the product ratios R[DHDMA/9MA] and R[TMA/9MA] as functions of 910DMA conversion (X) derived from the model (lines) to those observed experimentally (symbols). In the upper panel of Figure 8.8, the model is seen to predict R[DHDMA/9MA] about 4.1-fold higher than experimental at low conversions, X ~ 0.05, and comparable to the experiments at higher conversions, X ~ 0.80, although the slope is not the same in the model as in the experimental observations. In the lower panel of Figure 8.8, the model is seen to predict R[TMA/9MA] approximately equal to that experimentally observed at all conversion 0 < X < 0.81.

8.5.2 Extended 910DMA Thermolysis Model

Conservation relations derived from the mechanistic models of 910DMA and 9MA thermolysis were combined and reactions representing interactions between
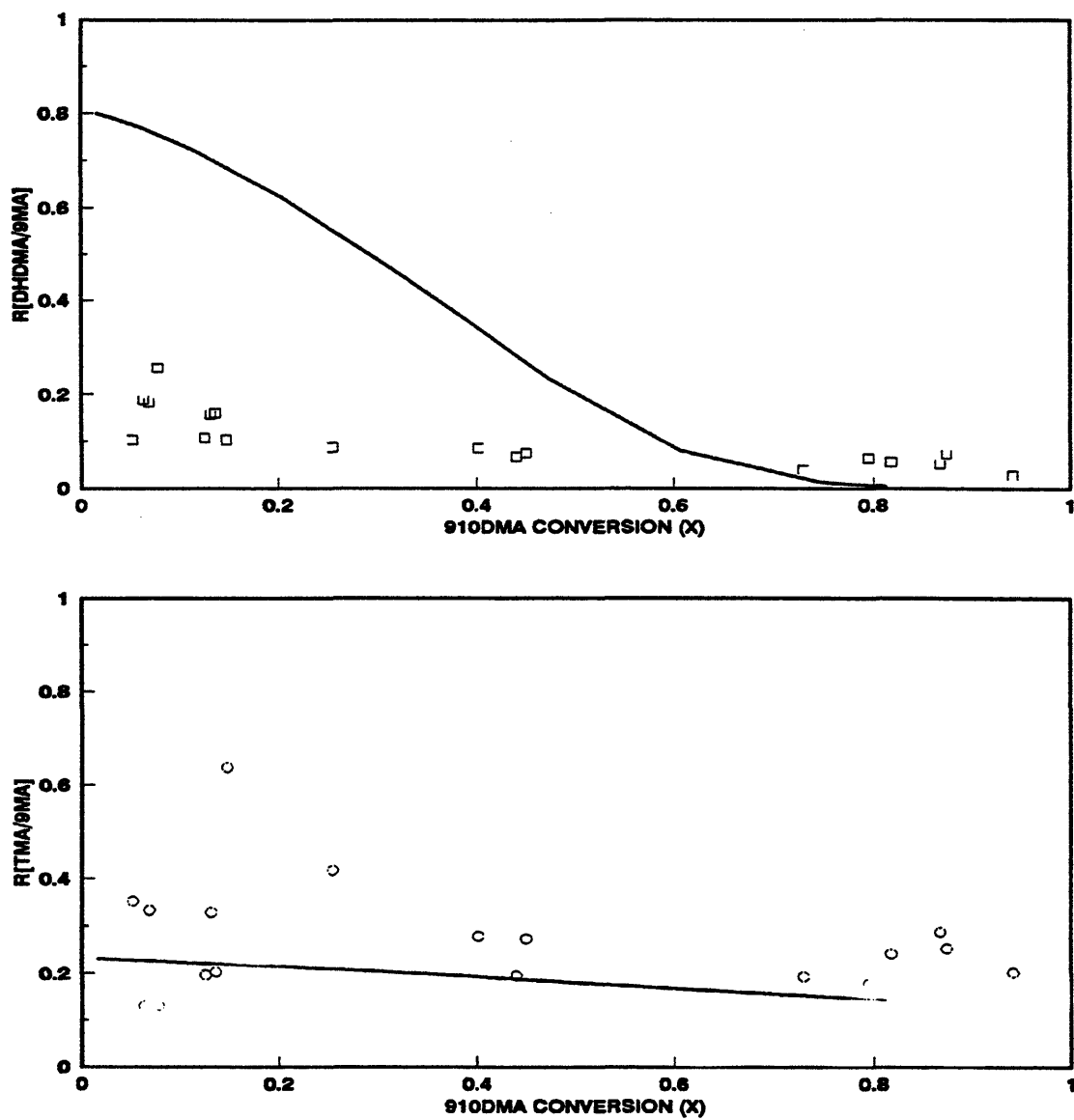
Figure 8.8: Ratio of moles TMA to moles 9MA produced vs. 910DMA conversion (X) (top) and ratio of moles ANT to moles 9MA vs. 910DMA conversion (X) (bottom) at $T = 370°C$ and $[910DMA]_o = 0.82$ mol/l.

species in the individual mechanisms were added to generate the extended 910DMA

and 9MA thermolysis model. Figure 8.9 displays the ten elementary steps in the

basic 910DMA mechanism, Figure 8.10 and Figure 8.11 display the 19 elementary

steps in the 9MA mechanism, and Figure 8.12, Figure 8.13 and Figure 8.14 display

the 20 additional elementary steps arising in the extended 910DMA and 9MA

mechanism. The 20 elementary steps added for the extended model include

initiation, propagation, isomerization and termination reactions. R33 - R35 are

initiation steps that involve the disproportionation of 910DMA and 9MA. R36 - R39

are propagation steps that involve the hydrogenated radicals HMA9* and HMA10*

reacting with the substrate 910DMA and the hydrogenated radical HTMA* reacting

with primary demethylated product 9MA. R40 - R41 are isomerization reactions that

involve the hydrogenated radicals HMA9* and HMA10* reacting with 910DMA

substrate. Finally, R42 - R51 are both pure- and cross-termination and

disproportionation reactions of all radicals in the mechanism.

Arrhenius expressions, of the form $\log_{10} k = \log_{10} A - E^*/\theta$, with rate constant

k and pre-exponential factor A in units of $(1 \text{ mol}^{-1} \text{ s}^{-1})$ and activation energy E^* in

kcal/mol were generated for each elementary step R1 - R51 of the extended

910DMA and 9MA thermolysis mechanism shown in Figure 8.9, Figure 8.10,

Figure 8.11, Figure 8.12 and Figure 8.13. These expressions, and information

regarding their deviation, are summarized in Table 8.6, Table 8.7, Table 8.8,

Table 8.9, and Table 8.10, as follows. Each elementary reaction was classified
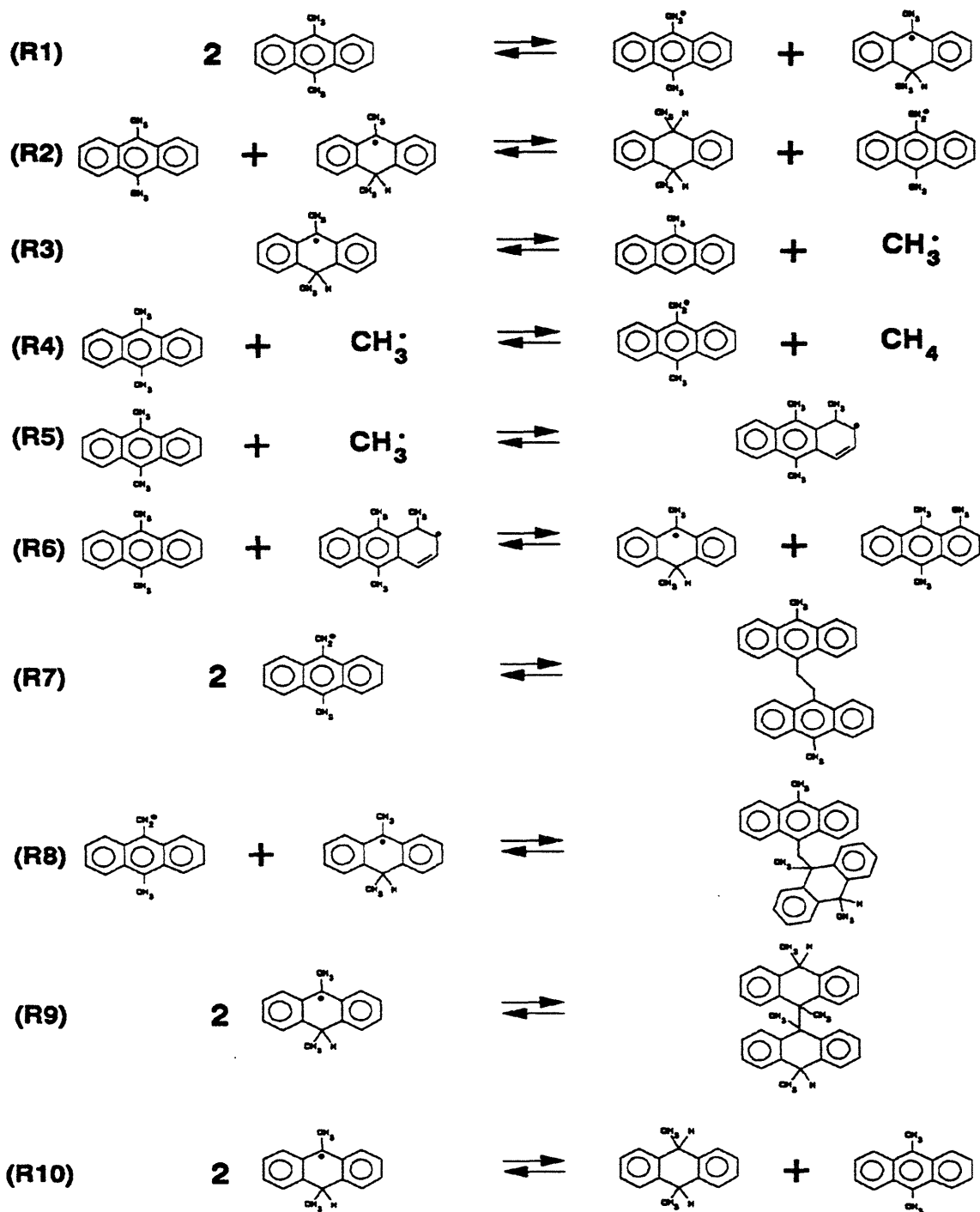
Figure 8.9: Elementary steps for the 910DMA thermolysis mechanism.
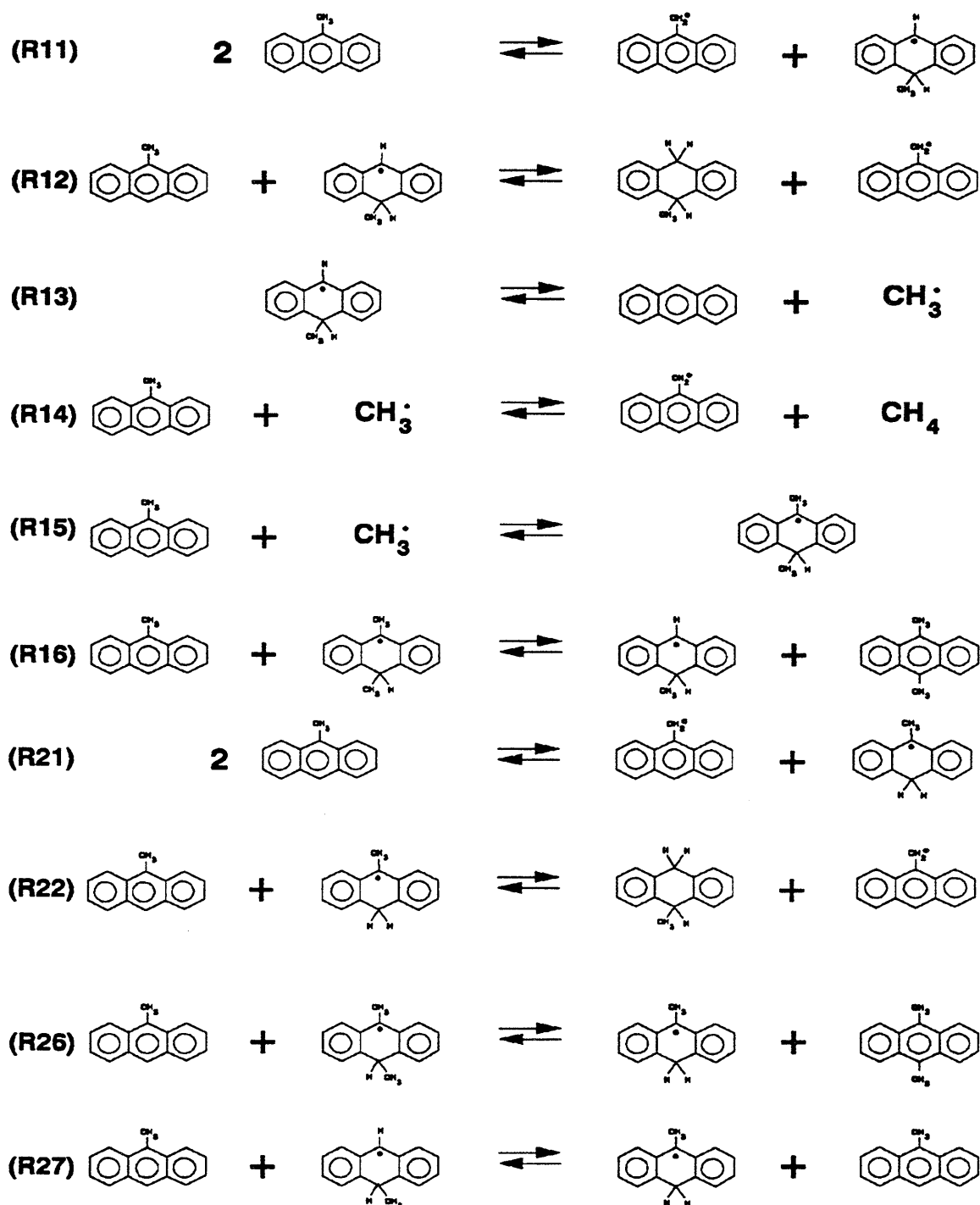
Figure 8.10: Elementary reactions for initiation and propagation steps in 9MA decomposition.
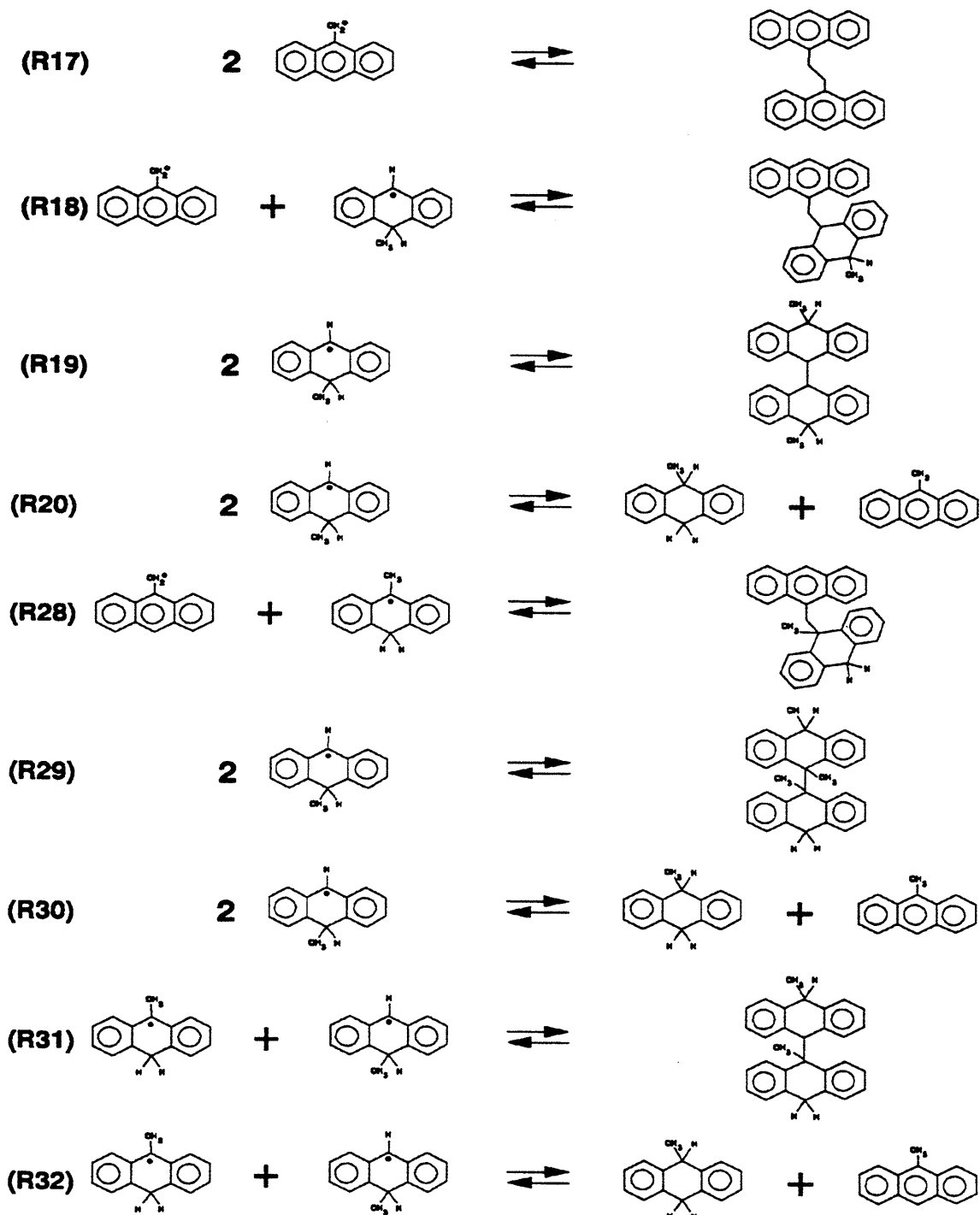
Figure 8.11: Elementary reactions for the terminations steps in 9MA decomposition.
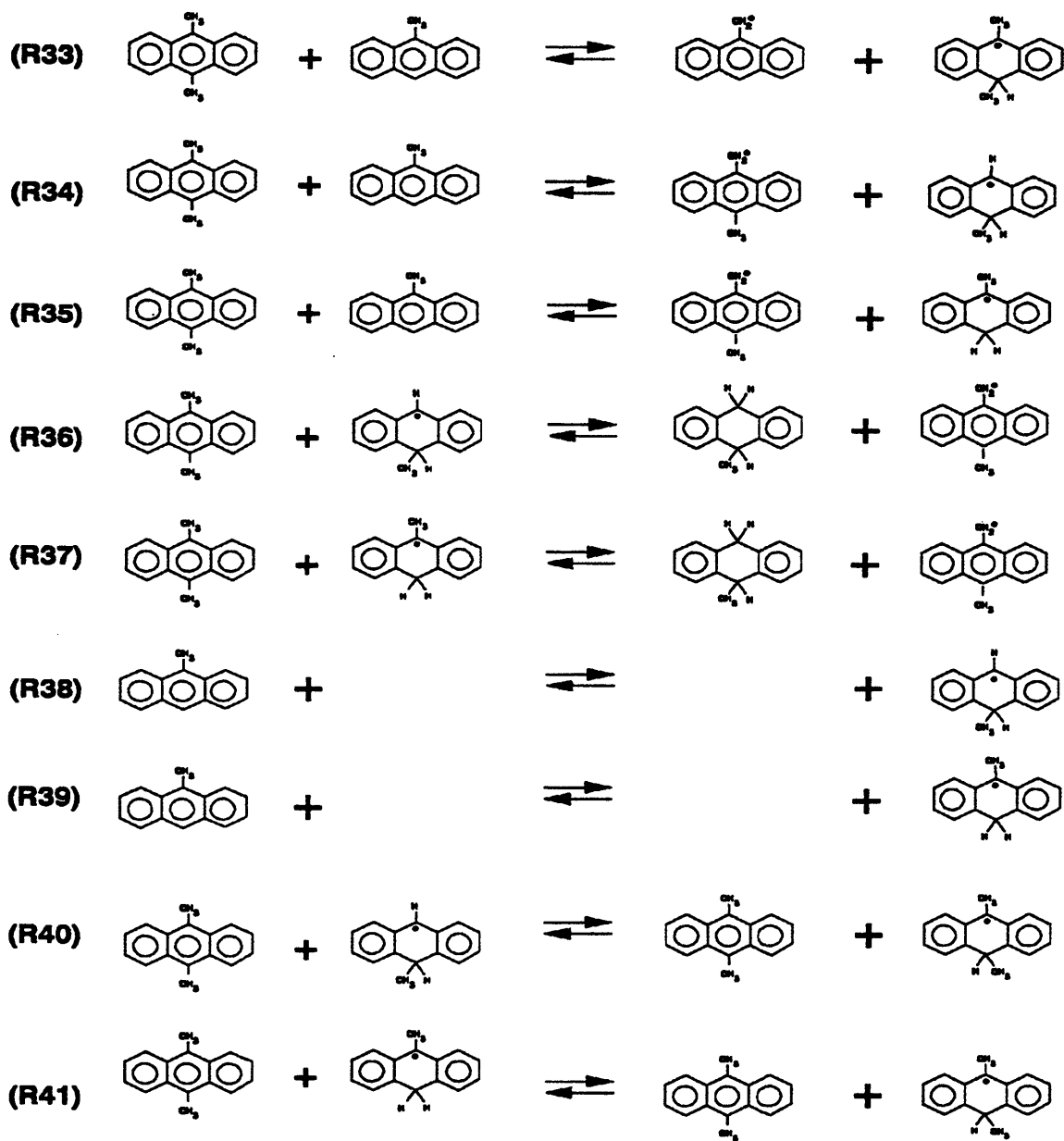
Figure 8.12: Elementary reactions for initiation, propagation and isomerization steps in combined 910DMA and 9MA decomposition.
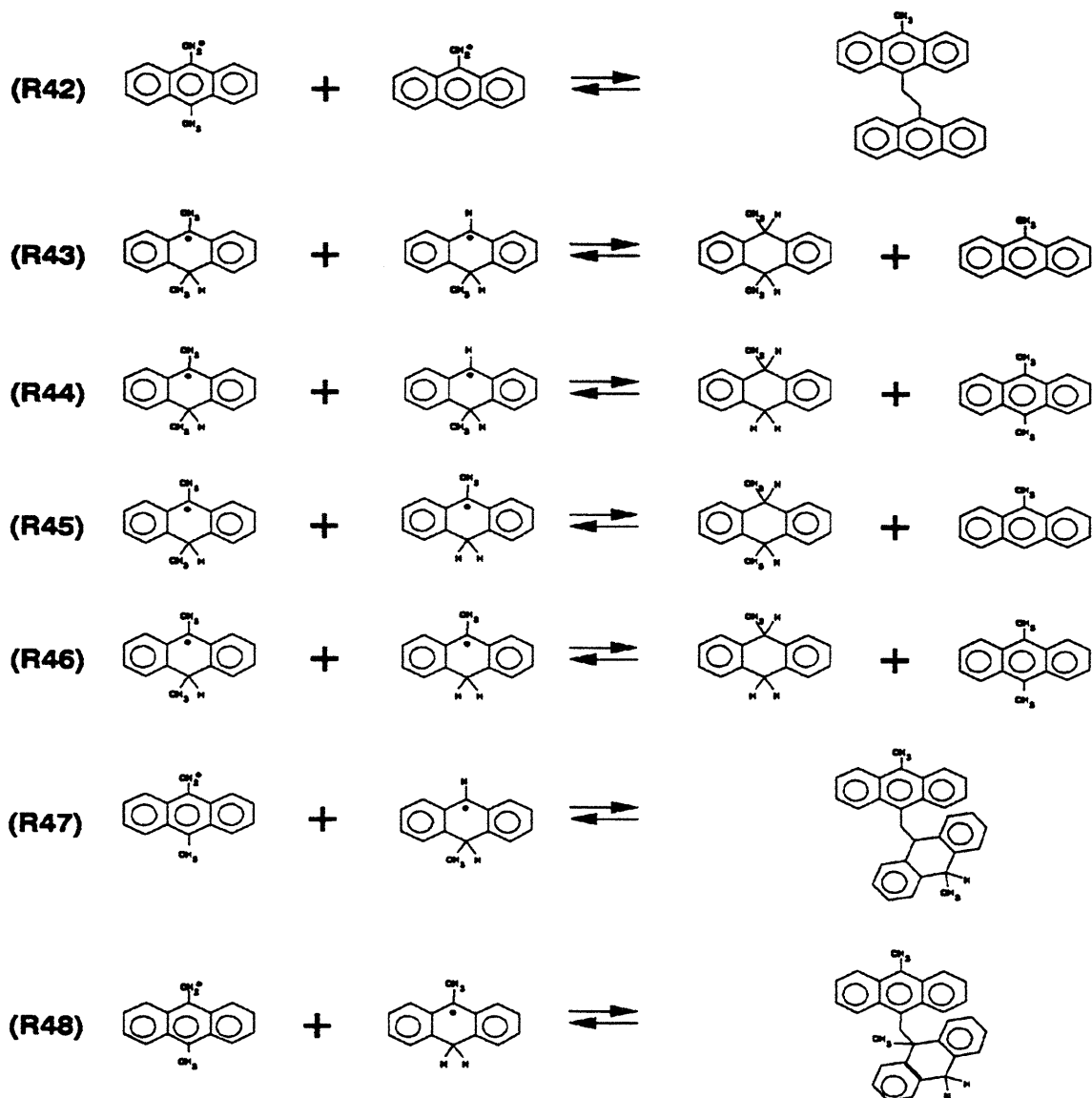
Figure 8.13: Elementary reactions for the terminations steps in combined 910DMA and 9MA decomposition.

(R49)

(R50)

(R51)
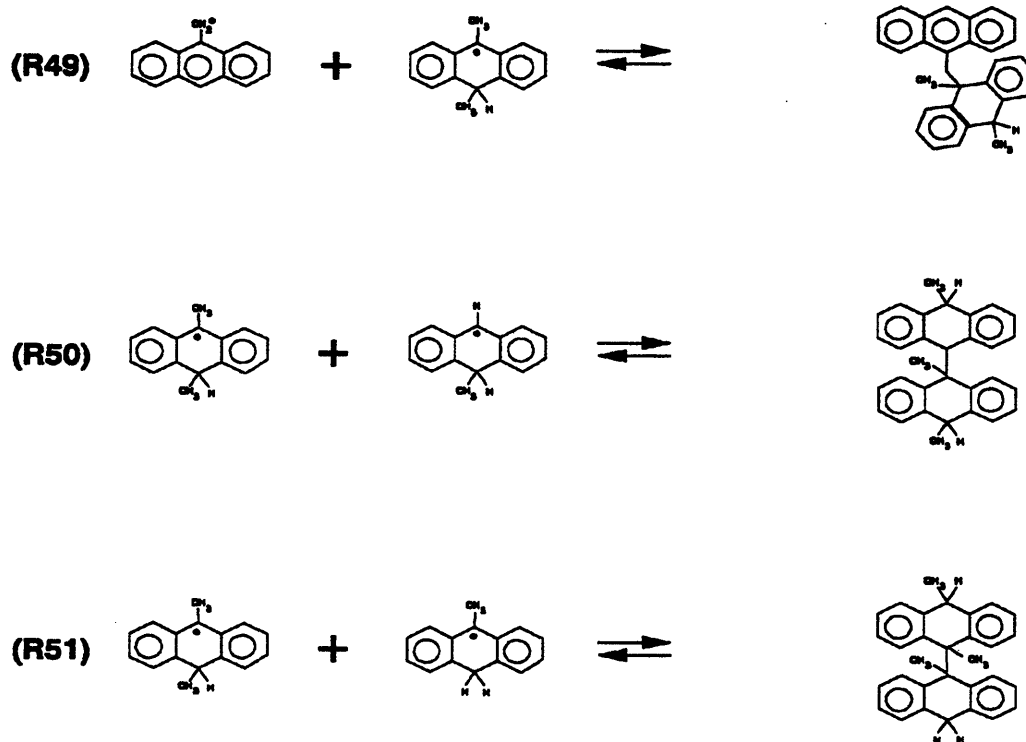
Figure 8.14: Elementary reactions for the terminations steps in combined 910DMA and 9MA decomposition.

Table 8.6

ARRHENIUS EXPRESSIONS FOR ELEMENTARY STEPS OF EXTENDED 910DMA & 9MA THERMOLYSIS MECHANISM

	Type of Reaction	$\log_{10} A_{int}$ $l\ mol^{-1}\ s^{-1}$	rpd	Evans-Polanyi Relation: $E^* =$	ΔH_r° kcal/mol	E^* kcal/mol	Arrhenius Expression: $\log_{10} k =$
R1	molecular disproportionation	8.5	24	ΔH_r°	43.4	43.4	9.9 - 43.4/θ
R-1	radical disproportionation	8.5	1	0	-43.4	0	8.5
R2	H-abstraction	8.1	6	$17.5 + \Delta H_r^\circ/2$	1.2	18.1	8.9 - 18.1/θ
R-2	H-abstraction	8.1	2	$17.5 + \Delta H_r^\circ/2$	-1.2	16.9	8.4 - 16.9/θ
R3	methyl scission	13.5	1	$2.1 + \Delta H_r^\circ$	29.5	31.6	13.5 - 31.6/θ
R-3	CH3* addition	8.3	1	2.1	-29.5	2.1	8.3 - 2.1/θ
R4	H-abstraction	8.1	6	$17.5 + \Delta H_r^\circ/2$	-22.7	6.2	8.9 - 6.2/θ
R-4	H-abstraction	8.1	4	$17.5 + \Delta H_r^\circ/2$	22.7	28.9	8.7 - 28.9/θ
R5	CH3* addition	8.3	4	5.1	-18.6	5.1	8.9 - 5.1/θ
R-5	methyl scission	13.5	1	$5.1 + \Delta H_r^\circ$	18.6	23.7	13.5 - 23.7/θ
R6	radical H transfer	8.1	2	$17.5 + \Delta H_r^\circ/2$	-13.2	10.9	8.4 - 10.9/θ
R-6	radical H transfer	8.1	1	$17.5 + \Delta H_r^\circ/2$	13.2	24.1	8.1 - 24.1/θ
R7	radical combination	9.3	1	0	-54.2	0	9.3
R-7	homolytic dissociation	15.5	1	ΔH_r°	54.2	54.2	15.5 - 54.2/θ
R8	radical combination	9.3	1	0	-52.4	0	9.3
R-8	homolytic dissociation	15.5	1	ΔH_r°	52.4	52.4	15.5 - 52.4/θ
R9	radical combination	9.3	1	0	-50.7	0	9.3
R-9	homolytic dissociation	15.5	1	ΔH_r°	50.7	50.7	15.5 - 50.7/θ
R10	radical disproportionation	8.5	1	0	-42.2	0	8.5
R-10	molecular disproportionation	8.5	4	ΔH_r°	42.2	42.2	9.1 - 42.2/θ

Table 8.7

ARRHENIUS EXPRESSIONS FOR ELEMENTARY STEPS OF EXTENDED 910DMA & 9MA THERMOLYSIS MECHANISM

	Type of Reaction	$\log_{10} A_{int}$ $l\ mol^{-1}\ s^{-1}$	rpd	Evans-Polanyi Relation: $E^* =$	ΔH_r kcal/mol	E^* kcal/mol	Arrhenius Expression: $\log_{10} k =$
R11	molecular disproportionation	8.5	6	ΔH_r°	43.7	43.7	9.3 - 43.7/θ
R-11	radical disproportionation	8.5	1	0	-43.7	0	8.5
R12	H-abstraction	8.1	3	$17.5 + \Delta H_r^\circ/2$	-0.2	17.4	8.6 - 17.4/θ
R-12	H-abstraction	8.1	2	$17.5 + \Delta H_r^\circ/2$	0.2	17.6	8.4 - 17.6/θ
R13	methyl scission	13.5	1	$2.1 + \Delta H_r^\circ$	29.2	31.3	13.5 - 31.3/θ
R-13	CH3* addition	8.3	2	2.1	-29.2	2.1	8.6 - 2.1/θ
R14	H-abstraction	8.1	3	$17.5 + \Delta H_r^\circ/2$	-22.7	6.2	8.6 - 6.2/θ
R-14	H-abstraction	8.1	4	$17.5 + \Delta H_r^\circ/2$	22.7	28.9	8.7 - 28.9/θ
R15	CH3* addition	8.3	1	2.1	-29.5	2.1	8.3 - 2.1/θ
R-15	methyl scission	13.5	1	$2.1 + \Delta H_r^\circ$	29.5	31.6	13.5 - 31.6/θ
R16	radical H transfer	8.1	1	$17.5 + \Delta H_r^\circ/2$	0.3	17.65	8.1 - 17.7/θ
R-16	radical H transfer	8.1	1	$17.5 + \Delta H_r^\circ/2$	-0.3	17.35	8.1 - 17.4/θ
R17	radical combination	9.3	1	0	-54.7	0	9.3
R-17	homolytic dissociation	15.5	1	ΔH_r°	54.7	54.7	15.5 - 54.7/θ
R18	radical combination	9.3	1	0	-53.4	0	9.3
R-18	homolytic dissociation	15.5	1	ΔH_r°	53.4	53.4	15.5 - 53.4/θ
R19	radical combination	9.3	1	0	-52.1	0	9.3
R-19	homolytic dissociation	15.5	1	ΔH_r°	52.1	52.1	15.5 - 52.1/θ
R20	radical disproportionation	8.5	1	0	-43.9	0	8.5
R-20	molecular disproportionation	8.5	2	ΔH_r°	43.9	43.9	8.8 - 43.9/θ

Table 8.8

ARRHENIUS EXPRESSIONS FOR ELEMENTARY STEPS OF EXTENDED 910DMA & 9MA THERMOLYSIS MECHANISM

	Type of Reaction	$\log_{10} A_{int}$ $1\ mol^{-1}\ s^{-1}$	rpd	Evans-Polanyi Relation: $E^* =$	ΔH_r° kcal/mol	E^* kcal/mol	Arrhenius Expression: $\log_{10} k =$
R21	molecular disproportionation	8.5	6	ΔH°_r	42.5	42.5	9.3 - 42.5/θ
R-21	radical disproportionation	8.5	2	0	-42.5	0	8.8
R22	H-abstraction	8.1	3	$17.5 + \Delta H^{\circ}_r/2$	1.0	18.0	8.6 - 18.0/θ
R-22	H-abstraction	8.1	1	$17.5 + \Delta H^{\circ}_r/2$	-1.0	17.0	8.1 - 17.0/θ
R26	radical H transfer	8.1	1	$17.5 + \Delta H^{\circ}_r/2$	-0.9	17.05	8.1 - 17.1/θ
R-26	radical H transfer	8.1	2	$17.5 + \Delta H^{\circ}_r/2$	0.9	17.95	8.4 - 18.0/θ
R27	radical H transfer	8.1	1	$17.5 + \Delta H^{\circ}_r/2$	-1.2	16.9	8.1 - 16.9/θ
R-27	radical H transfer	8.1	2	$17.5 + \Delta H^{\circ}_r/2$	1.2	18.1	8.4 - 18.1/θ
R28	radical combination	9.3	1	0	-52.8	0	9.3
R-28	homolytic dissociation	15.5	1	ΔH°_r	52.8	52.8	15.5 - 52.8/θ
R29	radical combination	9.3	1	0	-50.9	0	9.3
R-29	homolytic dissociation	15.5	1	ΔH°_r	50.9	50.9	15.5 - 50.9/θ
R30	radical disproportionation	8.5	1	0	-41.5	0	8.5
R-30	molecular disproportionation	8.5	1	ΔH°_r	41.5	41.5	9.1 - 41.5/θ
R31	radical combination	9.3	1	0	-51.5	0	9.3
R-31	homolytic dissociation	15.5	1	ΔH°_r	51.5	51.5	15.5 - 51.5/θ
R32	radical disproportionation	8.5	1	0	-42.7	0	8.5 - 42.7/θ
R-32	molecular disproportionation	8.5	2	ΔH°_r	42.7	42.7	8.8 - 42.7/θ

Table 8.9

ARRHENIUS EXPRESSIONS FOR ELEMENTARY STEPS OF EXTENDED 910DMA & 9MA THERMOLYSIS MECHANISM

	Type of Reaction	$\log_{10} A_{int}$ l mol^{-1} s^{-1}	rpd	Evans-Polanyi Relation: $E^* =$	ΔH°_r kcal/mol	E^* kcal/mol	Arrhenius Expression: $\log_{10} k =$
R33	molecular disproportionation	8.5	12	ΔH_r°	43.4	43.4	9.6 - 43.4/θ
R-33	radical disproportionation	8.5	1	0	-43.4	0	8.5
R34	molecular disproportionation	8.5	6	ΔH_r°	42.5	42.5	9.3 - 42.5/θ
R-34	radical disproportionation	8.5	1	0	-42.5	0	8.5
R35	molecular disproportionation	8.5	6	ΔH_r°	43.7	43.7	9.3 - 43.7/θ
R-35	radical disproportionation	8.5	2	0	-43.7	0	8.8
R36	H-abstraction	8.1	6	$17.5 + \Delta H_r^\circ/2$	1.0	18.0	8.9 - 18.0/θ
R-36	H-abstraction	8.1	1	$17.5 + \Delta H_r^\circ/2$	-1.0	17.0	8.1 - 17.0/θ
R37	H-abstraction	8.1	6	$17.5 + \Delta H_r^\circ/2$	-0.2	17.4	8.9 - 17.4/θ
R-37	H-abstraction	8.1	1	$17.5 + \Delta H_r^\circ/2$	0.2	17.6	8.1 - 17.6/θ
R38	radical H transfer	8.1	1	$17.5 + \Delta H_r^\circ/2$	-14.1	10.55	8.1 - 10.6/θ
R-38	radical H transfer	8.1	1	$17.5 + \Delta H_r^\circ/2$	14.1	24.45	8.1 - 24.5/θ
R39	radical H transfer	8.1	1	$17.5 + \Delta H_r^\circ/2$	-12.9	11.05	8.1 - 11.1/θ
R-39	radical H transfer	8.1	2	$17.5 + \Delta H_r^\circ/2$	12.9	23.95	8.4 - 24.0/θ
R40	radical H transfer	8.1	2	$17.5 + \Delta H_r^\circ/2$	0.9	17.95	8.4 - 18.0/θ
R-40	radical H transfer	8.1	1	$17.5 + \Delta H_r^\circ/2$	-0.9	17.05	8.1 - 17.1/θ
R41	radical H transfer	8.1	2	$17.5 + \Delta H_r^\circ/2$	-0.3	17.35	8.4 - 17.4/θ
R-41	radical H transfer	8.1	4	$17.5 + \Delta H_r^\circ/2$	0.3	17.85	8.7 - 17.9/θ
R42	radical combination	9.3	1	0	-54.45	0	9.3
R-42	homolytic dissociation	15.5	1	ΔH_r°	54.45	54.45	15.5 - 54.5/θ

Table 8.10

		$\log_{10} A_{int}$ 1 mol^{-1} s^{-1}	rpd	Evans-Polanyi Relation: $E^* =$	ΔH_r° kcal/mol	E^* kcal/mol	Arrhenius Expression: $\log_{10} k =$
	Type of Reaction						
R43	radical disproportionation	8.5	1	0	-41.3	0	8.5
R-43	molecular disproportionation	8.5	2	ΔH_r°	41.3	41.3	8.8 - 41.3/θ
R44	radical disproportionation	8.5	1	0	-42.4	0	8.5
R-44	molecular disproportionation	8.5	1	ΔH_r°	42.4	42.4	8.5 - 42.4/θ
R45	radical disproportionation	8.5	1	0	-42.5	0	8.5
R-45	molecular disproportionation	8.5	2	ΔH_r°	42.5	42.5	8.8 - 42.5/θ
R46	radical disproportionation	8.5	1	0	-43.6	0	8.5
R-46	molecular disproportionation	8.5	1	ΔH_r°	43.6	43.6	8.5 - 43.6/θ
R47	radical combination	9.3	1	0	-52.55	0	9.3
R-47	homolytic dissociation	15.5	1	ΔH_r°	52.55	52.55	15.5 - 52.6/θ
R48	radical combination	9.3	1	0	-53.15	0	9.3
R-48	homolytic dissociation	15.5	1	ΔH_r°	53.15	53.15	15.5 - 53.2/θ
R49	radical combination	9.3	1	0	-52.7	0	9.3
R-49	homolytic dissociation	15.5	1	ΔH_r°	52.7	52.7	15.5 - 52.7/θ
R50	radical combination	9.3	1	0	-50.8	0	9.3
R-50	homolytic dissociation	15.5	1	ΔH_r°	50.8	50.8	15.5 - 50.8/θ
R51	radical combination	9.3	1	0	-51.4	0	9.3
R-51	homolytic dissociation	15.5	1	ΔH_r°	51.4	51.4	15.5 - 51.4/θ

ARRHENIUS EXPRESSIONS FOR ELEMENTARY STEPS OF EXTENDED 910DMA & 9MA THERMOLYSIS MECHANISM

777

according to type (column 2), using standard free-radical reaction notation. Next, kinetic data reported in the literature for that type of reaction was analyzed to ascertain its activation parameters. Of these, $\log_{10} A$ was decomposed into an intrinsic portion, $\log_{10} A_{int}$ (column 3) and a reaction path degeneracy, rpd (column 4), with $\log_{10} A = \log_{10} A_{int} + \log_{10} (rpd)$. The activation energy E^* was described by an Evans-Polanyi expression (column 5), of form $E^* = E_o + \alpha \Delta H^\circ_r$. Values of the enthalpy of reaction ΔH°_r (column 6), derived from the data of Sections 5.4.3 and 6.4.3, then led to E^* (column 7). Final Arrhenius expressions are summarized in column 8 of Table 8.6, Table 8.7, Table 8.8, Table 8.9, and Table 8.10. Representative results from numerical solution of the extended model at two conversions are presented in Table 8.11, Table 8.12 and Table 8.13 which show the rates of formation of all radical and stable species, along with the elementary steps contributing to each species and an indication of which steps make the major contributions.

Figure 8.15 compares the substrate and product histories (upper panel) and product selectivities (lower panel) as obtained from the numerical solution of the extended thermolysis model to the experimental data for 910DMA, 9MA, TMA, ANT and CH4 at $[910DMA]_o = 0.82$ mol/l and $T = 370°C$. In the upper panel of Figure 8.15, the extended model is seen to predict 910DMA decay, the solid line, that is too slow compared to the experimental observations, shown as asterisks. The model half-life, $t^* = 27358$ s, is 1.2-fold longer than the experimental $t^* = 21912$ s,

Table 8.11

CALCULATED RATES OF FORMATION OF RADICAL SPECIES AT X = 0.001 AND 0.31 AT T = 370°C WITH [910DMA]$_0$ = 0.82 mol/l

	CONTRIBUTING REACTIONS	r(mol/l s) X=0.001	Major Contribution	r(mol/l s) X = 0.31	Major Contribution
r(910DMA*)	R1 - R-1 + R2 - R-2 + R4 - R-4 - 2R7 + 2R-7 - R8 + R-8 + R34 - R-34 + R35 - R-35 + R36 - R-36 + R37 - R-37 - R42 + R-42 - R47 + R-47 - R48 + R-48	-7.9E-07	R1, R-1, R2, R4, R7, R-7, R8, R-8	3.7E-06	R1, R-1, R2, R-2, R4, R7, R-7, R8, R-8
r(9MA*)	R11 - R-11 + R12 - R-12 + R14 - R-14 - 2R17 + 2R-17 - R18 + R-18 + R21 - R-21 + R22 - R-22 - R28 + R-28 + R33 + R-33 - R42 + R-42 - R49 + R-49	-8.4E-07	R42	3.0E-06	R42, R-42
r(HDMA*)	R1 - R-1 - R2 + R-2 - R3 + R-3 + R6 - R-6 - R8 + R-8 - 2R9 + 2R-9 - 2R10 + 2R-10 + R15 - R-15 - R16 + R-16 + R33 - R-33 + R40 - R-40 + R41 - R-41 - R43 + R-43 - R44 + R-44 - R45 + R-45 - R46 + R-46 - R49 + R-49 - R50 + R-50 - R51 + R-51	1.6E-08	R1, R-1, R2, R-2, R3, R-3, R8, R-8, R9, R-9, R10, R15, R-15	2.4E-08	ALL
r(HMA9*)	R21 - R-21 - R22 + R-22 + R27 - R-27 - R28 + R-28 - 2R29 + 2R-29 - 2R30 + 2R-30 - R31 - R-31 - R32 + R-32 + R34 - R-34 - R36 + R-36 + R38 - R-38 - R40 + R-40 - R43 + R-43 - R44 + R-44 - R47 + R-47 - R50 + R-50	-2.7E-10	R34, R-34, R36	-9.8E-08	R21, R-21, R22, R-22, R27, R-27, R34, R-34, R36, R-36, R40, R-40, R47, R-47, R50, R-50
r(HMA10*)	R11 - R-11 - R12 + R-12 - R13 + R-13 - R16 + R-16 - R18 + R-18 - 2R19 + 2R-19 - 2R20 + R-20 - R27 + R-27 - R31 + R-31 - R32 + R-32 + R35 - R-35 -R37 + R-37 + R39 - R-39 - R41 + R-41 - R45 + R-45 - R46 + R-46 - R48 + R-48 - R51 + R-51	-3.0E-11	R13, R-13, R16, R-16, R35, R-35, R37, R39, R41, R-41, R49, R-49	-3.5E-08	R11, R-11, R12, R-12, R13, R-13, R16, R-16, R-27, R35, R-35, R37, R-37, R41, R-41, R48, R-48
r(CH3*)	R3 - R-3 - R4 + R-4 - R5 + R-5 + R13 - R-13 - R14 + R-14 - R15 + R-15	-2.1E-08	R3, R4, R5, R-5	-2.0E-08	R3, R-3, R4, R5, R-5, R13, R14, R15, R-
r(HTMA*)	R5 - R-5 - R6 + R-6 - R38 + R-38 - R39 + R-39	1.9E-08	R5, R-5	1.1E-08	R5, R-5, R6, R38, R39

Table 8.12

CALCULATED RATES OF FORMATION OF STABLE SPECIES AT X = 0.001 AND 0.31 AT T = 370°C WITH [910DMA]$_o$ = 0.82 mol/l

	CONTRIBUTING REACTIONS	r (mol/l s) at X = 0.001	Major Contribution	r (mol/l s) at X = 0.31	Major Contribution
r(910DMA)	-2R1 + 2R-1 - R2 + R-2 - R4 + R-4 - R5 + R-5 - R6 + R-6 + R10 - R-10 + R16 - R-16 - R33 + R-33 - R34 + R-34 - R35 + R-35 - R36 + R-36 - R37 + R-37 - R40 + R-40 - R41 + R-41 + R44 - R-44 + R45 - R-45	-3.0E-05	R1, R2, R4, R5, R-5	-1.2E-05	R1, R2, R-2, R4, R5, R-5
r(9MA)	R3 - R-3 - 2R11 + 2R-11 - R12 + R-12 - R14 + R-14 - R15 + R-15 - R16 + R-16 + R20 - R-20 - 2R21 + 2R-21 - R22 + R-22 - R26 + R-26 +R32 - R-32 - R33 + R-33 - R34 + R-34 - R35 + R-35 - R38 + R-38 - R39 + R-39 + R40 - R-40 + R41 - R-41 + R43 - R-43 + R45 - R-45	7.1E-06	R3, R-15	3.2E-06	R3, R-3, R15, R-15
r(ANT)	R13 - R-13	5.1E-10	R13	1.2E-07	R13, R-13
r(TMA)	R6 - R-6 + R38 - R-38 + R39 - R-39	1.7E-06	R6	7.4E-07	R6
r(CH4)	R4 - R-4 + R14 - R-14	5.5E-06	R4	3.4E-06	R4, R14
r(DHDMA)	R2 - R-2 + R10 - R-10 + R43 - R-43 + R45 - R-45	2.9E-06	R2	2.7E-07	R2, R-2
r(DHMA)	R12 - R-12 + R20 - R-20 + R22 - R-22 + R30 - R-30 + R32 - R-32 + R36 - R-36 + R37 - R-37 - R44 + R-44 - R46 + R-46	2.3E-09	R36, R37	3.0E-07	R22, R-22, R36, R-36, R37, R-37

Table 8.13

CALCULATED RATES OF FORMATION OF STABLE SPECIES AT X = 0.001 AND 0.31 AT T = 370°C WITH [910DMA]$_o$ = 0.82 mol/l

	CONTRIBUTING REACTIONS	r (mol/l s) at X = 0.001	Major Contribution	r (mol/l s) at X = 0.31	Major Contribution
r(910DMAD)	R7 - R-7	8.4E-06	R7	3.2E-06	R7, R-7
r(HDMAD)	R9 - R-9	3.3E-08	R9	-2.0E-10	R9, R-9
r(DMAHDMAD)	R8 - R-8	6.7E-07	R8	1.1E-08	R8, R-8
r(9MAD)	R17 - R-17	3.5E-12	R17	8.1E-08	R17, R-17
r(9MAHMA9D)	R28 - R-28	2.8E-13	R28	1.5E-09	R28, R-28
r(9MAHMA10D)	R18 - R-18	5.8E-14	R18	5.5E-10	R18, R-18
r(HMA9D)	R29 - R-29	2.0E-14	R29	2.6E-11	R29, R-29
r(HMA10D)	R19 - R-19	9.2E-16	R19	3.7E-12	R19, R-19
r(HMA910D)	R31 - R-31	4.3E-15	R31	8.9E-12	R31, R-31
r(910DMA9MAD)	R42 - R-42	8.6E-11	R42	6.2E-06	R42, R-42
r(910DMAHMA9D)	R47 - R-47	4.3E-10	R47	1.2E-08	R47, R-47
r(910DMAHMA10D)	R48 - R-48	8.9E-11	R48	4.7E-09	R48, R-48
r(9MAHDMAD)	R49 - R-49	4.9E-10	R49	5.3E-09	R49, R-49
r(HDMAHMA9D)	R50 - R-50	3.1E-11	R50	9.7E-11	R50, R-50
r(HDMAHMA10D)	R51 - R-51	7.1E-12	R51	3.8E-11	R51, R-51
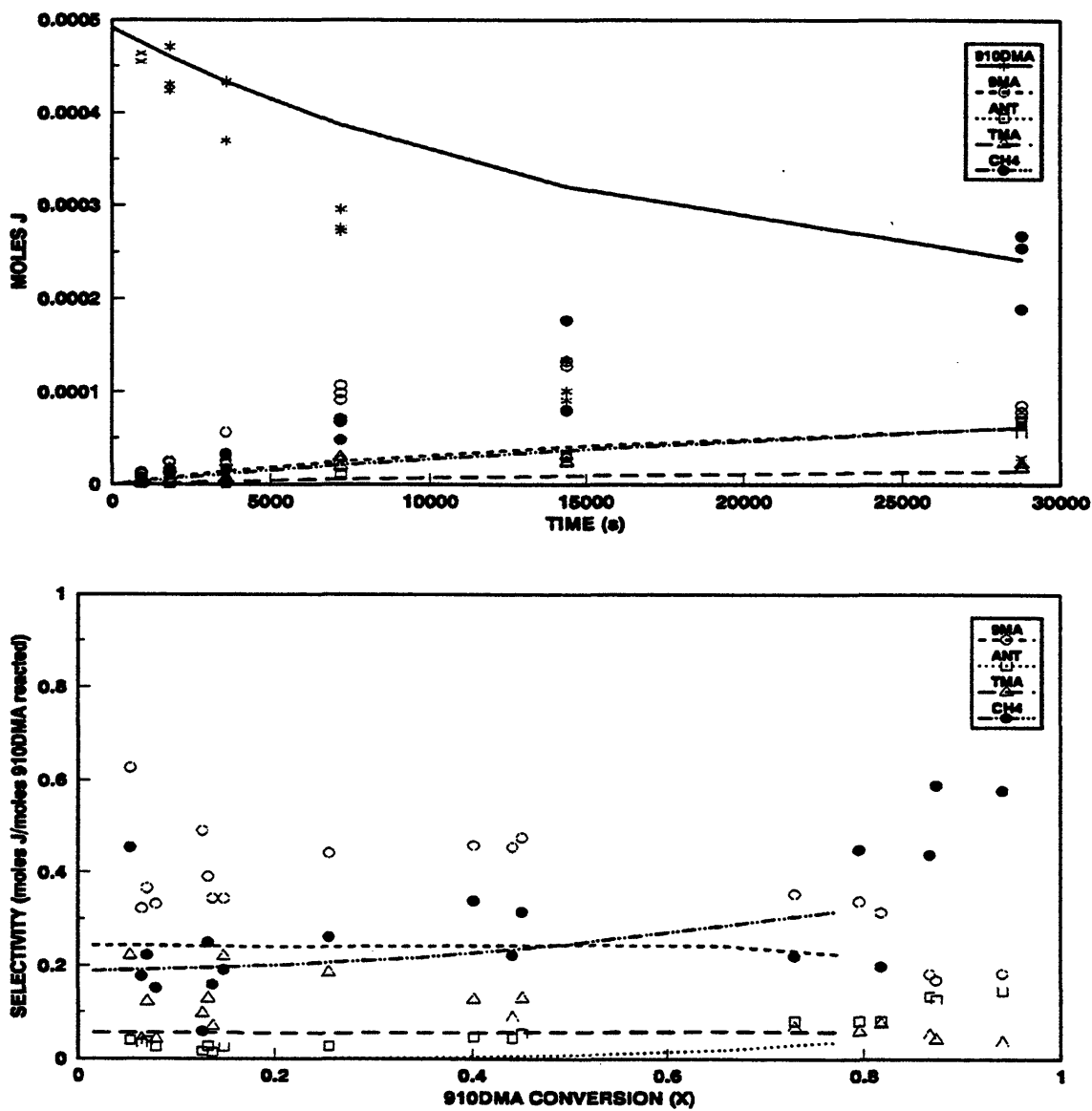
Figure 8.15: Product histories (top) and selectivity diagram (bottom) comparing extended model results(lines) to experiments(symbols) for 910DMA, 9MA, TMA, ANT and CH4 at T = 370°C with [910DMA]$_o$ = 0.82 mol/l.

782

but still shorter than t^* = 34264 s predicted by the basic 910DMA model. The upper

panel of Figure 8.15 also shows that the absolute amounts of 9MA, the short-dashed

line versus the circles; TMA, the long dashed line versus the triangles; CH4, the short

dashed lines versus the solid circles; and of ANT, the dotted line versus the squares;

formed by the model are all lower than observed in the experiments. The lower

panel of Figure 8.15 shows that the selectivities S(9MA), S(TMA), S(CH4) and

S(ANT) from the model are respectively 1.8, 2.0, 1.2 and 6.7-fold too low compared

to the average values of S(9MA), S(TMA), S(CH4) and S(ANT) observed from the

experiments. Relative to the basic model, the extended model produced more 9MA

and TMA at all conversions, and the S(9MA) and S(TMA) in the extended model

remained roughly constant for 0.05 < X < 0.6, after which both declined with

increasing conversion. The extended model produced more CH4 at all conversions,

with S(CH4) in the extended model increasing with increasing conversion. S(ANT)

remained low until X = 0.6, after which it also increased with increasing conversion;

the basic model, restricted to primary products, did not consider ANT at all.

Figure 8.16 continues the comparison between model (lines) and experimental

(symbols) product histories and selectivities for DHDMA and DHMA products. In

the upper panel of Figure 8.16, the extended model (solid line) is seen to predict

DHDMA amounts comparable to experimental observations (circles) at t < 10000

s, but for t > 10000 s, the extended model is seen to predict DHDMA amounts

generally higher than experimentally observed, the more so at longer times. Both the
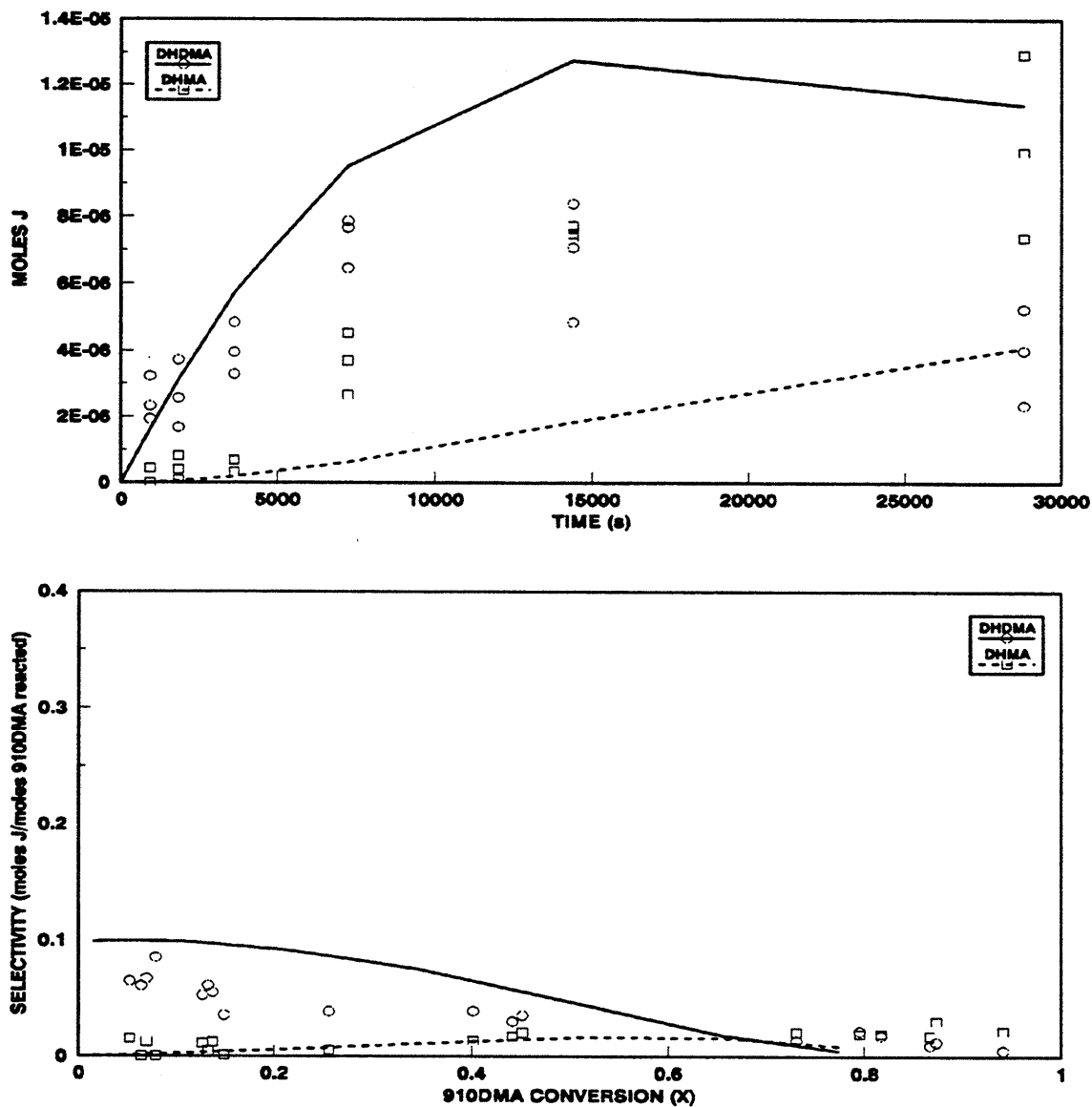
Figure 8.16: Product histories (top) and selectivity diagram (bottom) comparing extended model results (lines) to experimental data (symbols) for DHDMA and DHMA at T = 370°C with $[910DMA]_o$ = 0.82 mol/l.

extended model and experimental observations show a maximum followed by a decrease with increasing time. The rate of DHDMA production is slower in the extended model than in the basic 910DMA model, therefore the maximum DHDMA in the extended model was lower than in the basic 910DMA model and matches the experimental observations more closely. The extended model (dashed line) is seen to predict DHMA amounts generally lower than experimentally observed (squares); the basic model did not consider DHMA at all. In the lower panel of Figure 8.15, it is seen that, relative to experiments, S(DHDMA) from the model has the correct values at low and high conversions, but the curvature of the model line does not well follow the trend of the experimental data. At all X, S(DHDMA) predicted by the extended model is closer to experiments then S(DHDMA) predicted by the basic model. S(DHMA) from the extended model is comparable to experimental observations at both low and high conversions; the basic model was unable to predict S(DHMA).

Figure 8.17 compares the model calculations (lines) to the experimental data (symbols) for heavies (910DMAD, 9MAD and 910DMA9MAD). All the possible heavies were predicted by the extended model for 910DMA and 9MA thermolysis (HDMAD, DMAHDMAD, 9MAHMA10D, 9MAHMA9D, HMA10D, HMA9D, HMA910D, 910DMAHMA9D, 910DMAHMA10D, 9MAHDMAD, HDMAHMA9D, and HDMAHMA10D), but only 910DMAD, 9MAD and 910DMA9MAD were included since they were 2 orders of magnitude greater than any of the other dimer

785
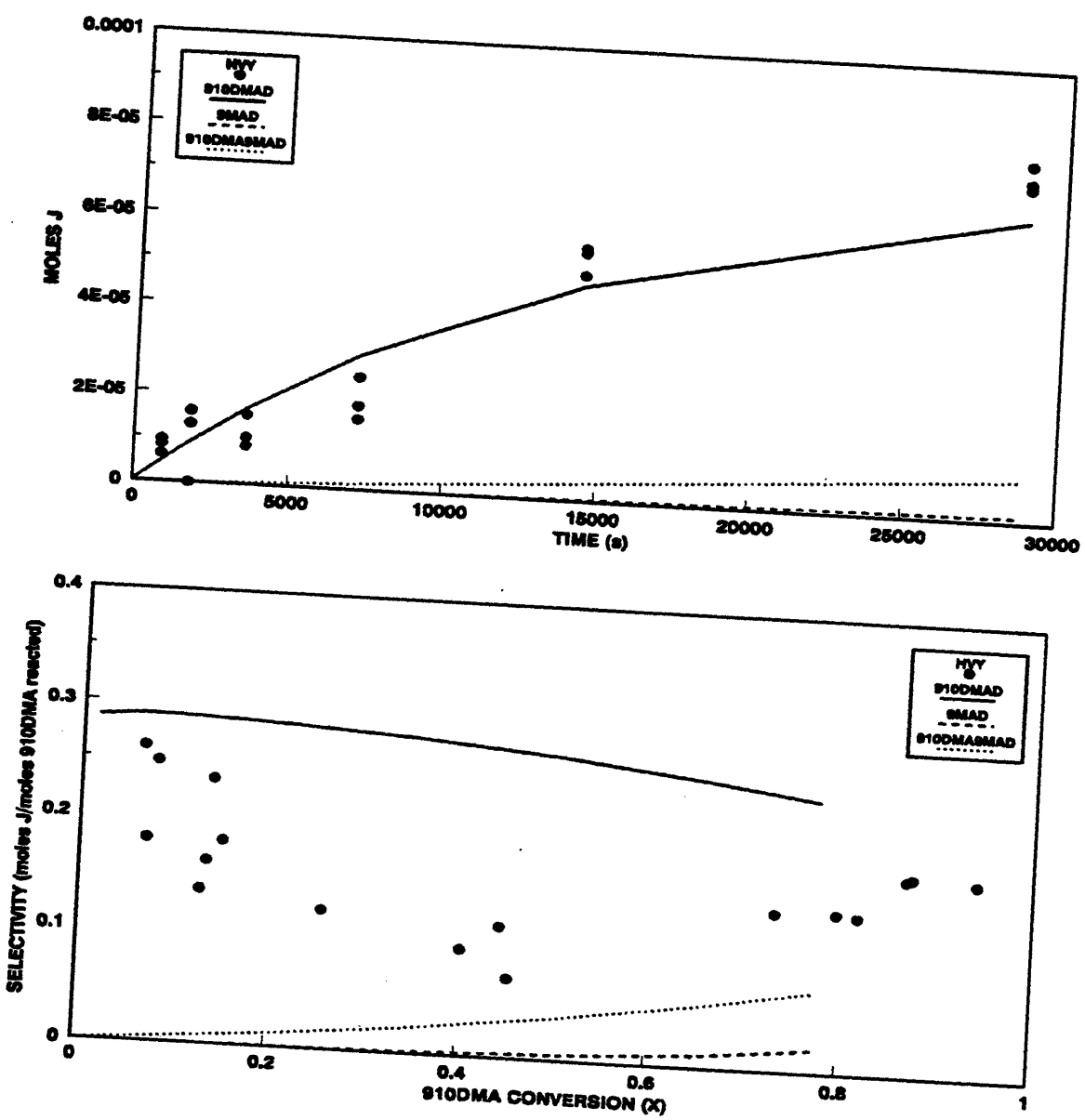
Figure 8.17: Product histories (top) and selectivity diagram (bottom) comparing extended model results (lines) to experimental data (symbols) for heavies at T = 370°C with $[910DMA]_o$ = 0.82 mol/l.

species formed. In the upper panel of Figure 8.17, the extended model is seen to predict heavies production comparable to the experiments at all reaction times. The extended model predicts the dominant heavy dimer to be 910DMAD. The rate of 910DMAD production was slightly higher in the extended model than in the basic 910DMA model. The lower panel of Figure 8.17 shows that the dimer selectivity S(910DMAD) ~ 0.29 calculated from the extended model is close to the experimental S(HVY) ~ 0.25 at low X < 0.1, but whereas the S(HVY) in the experiments decreases to ~ 0.10 with increasing conversions, S(910DMAD) from the extended model decreases very slowly to S(910DMAD) ~ 0.24 at X = 0.77. For X > 0.20, S(910DMAD) from the extended model is ~ 2.2-fold higher than the experimental S(HVY); this is nevertheless a slight improvement over the basic model which predicted S(910DMAD) ~ 2.7-fold higher than experiment.

Figure 8.18 compares the product ratios R[TMA/9MA] and R[ANT/9MA] as functions of 910DMA conversion (X) derived from the extended model (lines) to those observed experimentally (symbols). In the upper panel of Figure 8.18, the extended model is seen to predict R[TMA/9MA] approximately equal to that experimentally observed at all conversion 0 < X < 0.77. The rates of production of 9MA and TMA were both higher in the extended model than in the basic 910DMA model, but their ratio R[TMA/9MA] remained roughly constant over all conversion in both models. In the lower panel of Figure 8.18, the extended model is seen to predict R[ANT/9MA] about 100-fold lower than experimental at low conversions, X
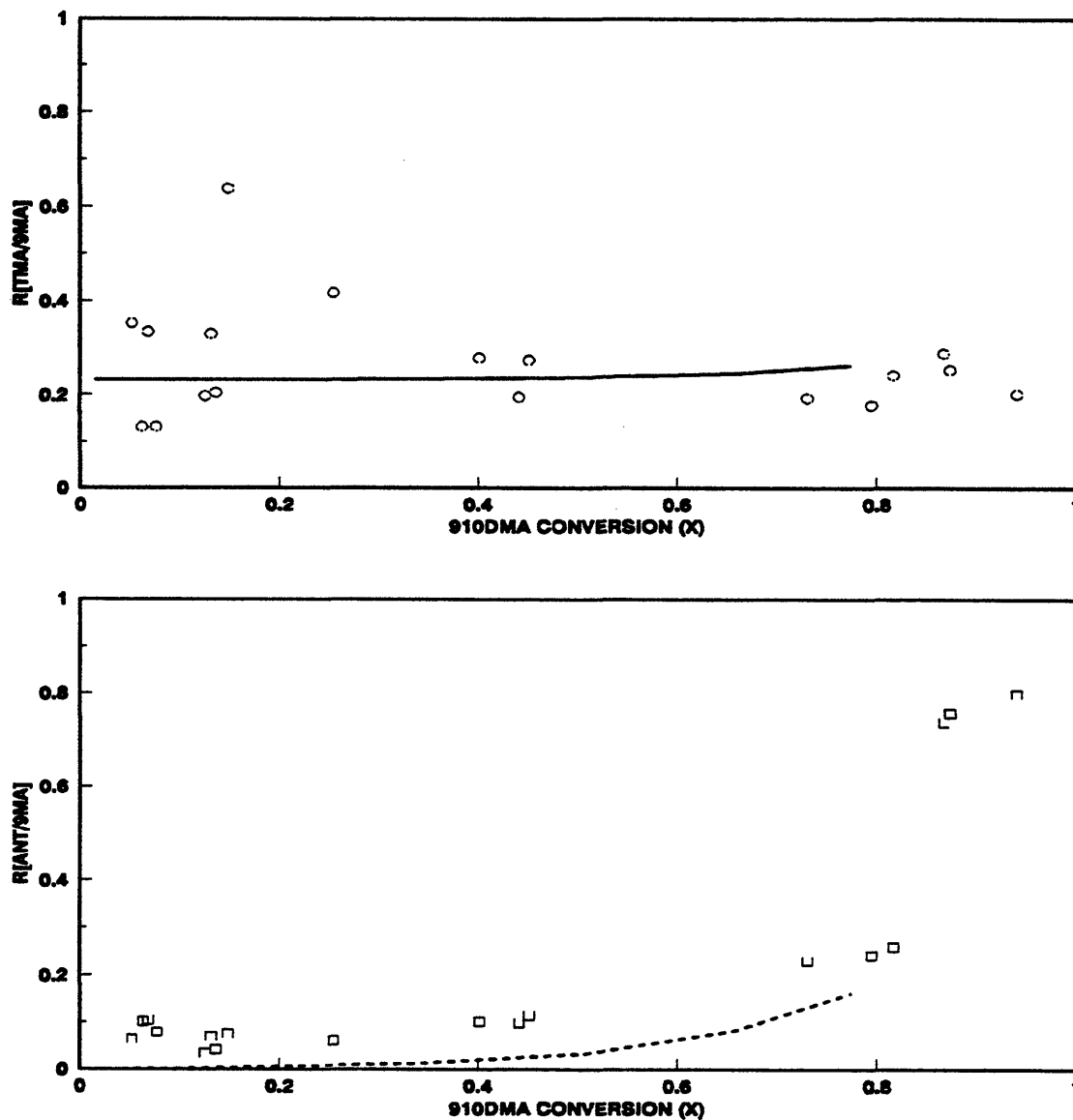
Figure 8.18: Ratio of moles TMA to moles 9MA produced vs. 910DMA conversion (X) (top) and ratio of moles ANT to moles 9MA vs. 910DMA conversion (X) (bottom) at T = 370°C with $[910DMA]_o$ = 0.82 mol/l.

788

~ 0.05, and only 1.5-fold lower than experimental at higher conversions, X ~ 0.80; the basic model did not address ANT production.

Figure 8.19 compares the product ratios R[DHDMA/9MA] and R[DHMA/ANT] as functions of 910DMA conversion (X) derived from the extended model (lines) to those observed experimentally (symbols). In the upper panel of Figure 8.19, the extended model is seen to predict R[DHDMA/9MA] about 2-fold higher than experimental at low conversions, X ~ 0.05, and comparable to the experiments at higher conversions, X ~ 0.80, although the slope is not the same in the extended model as in the experimental observations. The ratio R[DHDMA/9MA] from the extended model is closer to experimental than that predicted by the basic model, which was 4-fold higher than experiment at low X ~ 0.05. In the lower panel of Figure 8.19, at low conversions X ~ 0.05, the extended model is seen to predict R[DHMA/ANT] about 4.6-fold higher than experiments. At higher conversions, X ~ 0.80, the product ratio R[DHMA/ANT] from the extended model is close to that obtained in the experiments.

8.6 Frontier Molecular Orbital Theory Interpretations

The observed formation of the dimethyl acene isomers from the methyl acene isomers and of methyl acene isomers from the parent acenes were earlier interpreted by frontier molecular orbital theory, as examples of periselective methyl radical attack on the aromatic acene nucleus. Here we compare the minor methylated
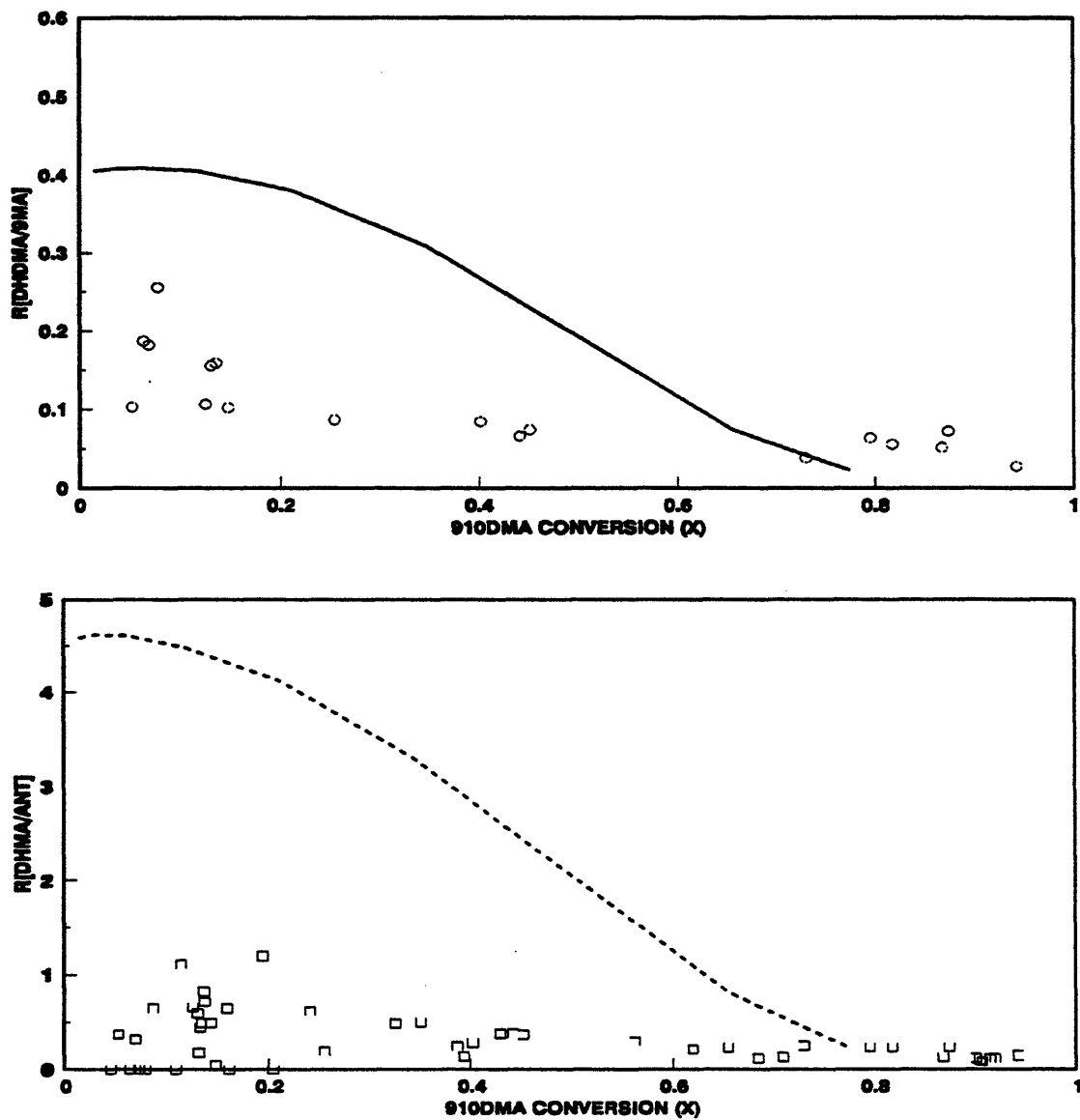
Figure 8.19: Ratio of moles DHDMA to moles 9MA produced vs. 910DMA conversion (X) (top) and ratio of moles DHMA to moles ANT vs. 910DMA conversion (X) (bottom) at T = 370°C with $[910DMA]_o$ = 0.82 mol/l.

product ratios obtained from the three substrates both by isomer position on the ring as well as by aromatic ring type.

8.6.1 Comparison of Observed Minor Product Ratios by Position

Table 8.14 shows the observed product ratios obtained over the entire range of substrate conversions from the 910DMA and 9MA thermolysis experiments. In the case of 910DMA substrate, the ratios of (2,9- + 3,9-)DMA/(1,9- + 1,10-)DMA and 2MA/1MA both represent the relative kinetics of the radical attack on the 2-position of the anthracene nucleus to the on its 1-position. The magnitudes of these ratios, respectively 0.25 and 0.50 show the 2-position to be 4- to 2-fold less reactive than the 1-position. For 9MA substrate, the ratios of (2,9- + 3,9-)DMA/(1,9- + 1,10-)DMA and 2MA/1MA have the same interpretation as described above for 910DMA, the data showing the 2-position of ANT being 4- to 3-fold less prone to methyl attack than the 1-position. In addition, the ratio (2,9- + 3,9-)DMA/910DMA ~ 0.12 shows that the 2-position of anthracene to be ~ 30-fold less reactive than the 9-position, because there are 4-times as many 2-type positions on 9MA as there was 9-type positions. Similarly, the ratio (1,9- + 1,10-)DMA/910DMA ~ 0.45 shows the 1-position to be about 10-fold less reactive than the 9-position.

Table 8.14

OBSERVED PRODUCT RATIOS FROM			
910DMA AND 9MA THERMOLYSIS			
Model Compound	Product Ratio	For Varying Initial Concentration	For Varying Temperature
910DMA	29+39DMA/19+110DMA	0.29 ± 0.07	0.24 ± 0.06
	2MA/1MA	0.49 ± 0.12	0.51 ± 0.15
9MA	29+39DMA/19+110DMA	0.23 ± 0.07	0.22 ± 0.04
	29+39DMA/910DMA	0.13 ± 0.05	0.11 ± 0.04
	19+110DMA/910DMA	0.46 ± 0.11	0.43 ± 0.11
	2MA/1MA	0.36 ± 0.11	0.38 ± 0.19

8.6.2 Comparison of Observed Minor Product Kinetics

We can roughly estimate the apparent kinetics of the formation of an (X+1) methyl acene from an X methyl acene from the difference expression:

$$k_{app} = k \ V \ [CH3*] = \frac{[\dfrac{J_{X+1 \ methyl \ acene}(t_k) - J_{X+1 \ methyl \ acene}(t_{k-1})}{t_k - t_{k-1}}]}{[\dfrac{J_{X \ methyl \ acene}(t_k) + J_{X \ methyl \ acene}(t_{k-1})}{2}]} \qquad (8.1)$$

where:

k_{app} = apparent rate constant, s^{-1}

k = true rate constant

V = reactor volume

$[CH3*]$ = methyl radical concentration

$J_i(t_k)$ = amount, in moles, of species i at time k in reactor volume V

t_k = time in seconds

Values of k_{app} calculated from experimental data at T = 409°C for all substrates are shown in Table 8.15, which also lists the product (X+1) methyl acene formed, the reaction path degeneracy (rpd) at its position and the corresponding "methyl affinity" $m_{aff} = k_{app}/rpd$.

8.6.3 Comparison of FMO Treatment using Hückel MOs

Theoretically, following Fukui (1975) for the interaction between the frontier orbitals of a radical and a molecule, the favorable, non-dimensional FMO

793

Table 8.15

VALUES OF k_{app} FOR MULTIPLY-METHYLATED ACENES AT T = 409°C

Model Compound	Product Ratio	Position 1	Position 2	Position 9
910DMA	TMA/910DMA	-4.80		
	2MA/ANT		-4.54	
	1MA/ANT	-4.73		
9MA	TMA/910DMA		-6.20	
	DMA/9MA			-4.14
	2MA/ANT		-5.01	
	1MA/ANT	-5.01		
14DMN	TMN/14DMN	-6.91		
	2MN/NAP		-5.20	

stabilization energy E'(t) is given by the interaction between the singly-occupied MO

(SOMO) of the CH3* radical and the highest-occupied and lowest-unoccupied MOs

(HOMO and LUMO) of the ANT at position t:

$$E'(t) = \frac{c_{t,HO}{}^2}{-X_{HO}} + \frac{c_{t,LU}{}^2}{X_{LU}} = \frac{2c_{t,HO}{}^2}{-X_{HO}} \tag{8.2}$$

where:

c_t =   MO coefficient at position t (Coulson and Streitwieser, 1960)

X_{HOorLU} = nondimensionalized Hückel MO energy and the subscripts HO and LU

refer to the frontier orbitals (Coulson and Streitwieser, 1960).

Figure 8.20 is an orbital interaction diagram for the system comprising ANT and

CH3*, with energy as ordinate and the molecules confined to separate columns.

Equation (8.2) reduces to one term because, in the Hückel approximation, alterant

hydrocarbons such as ANT have $X_{LU} = -X_{HO}$ and radicals such as CH3* have X_{SO}

= 0. It should also be noted that the nondimensional stabilization energy E'(t) is the

same as Fukui's (1975) "superdelocalizability". The dominant FMO interaction fixes

the denominator of Equation (8.2), but since ANT possesses multiple reaction sites,

the numerator can take several different values. The evaluation of these expressions

is graphically depicted in Figure 8.21, a "periselectivity diagram" in which each

position on the ANT ring framework is decorated with its HOMO coefficients, $C_{t(HO)}$,

and then positions equivalent to the three distinct positions 9, 1, and 2, are shown

interacting with the methyl radical SOMO, having $C_{u(SO)} = 1$. Figure 8.22 shows the
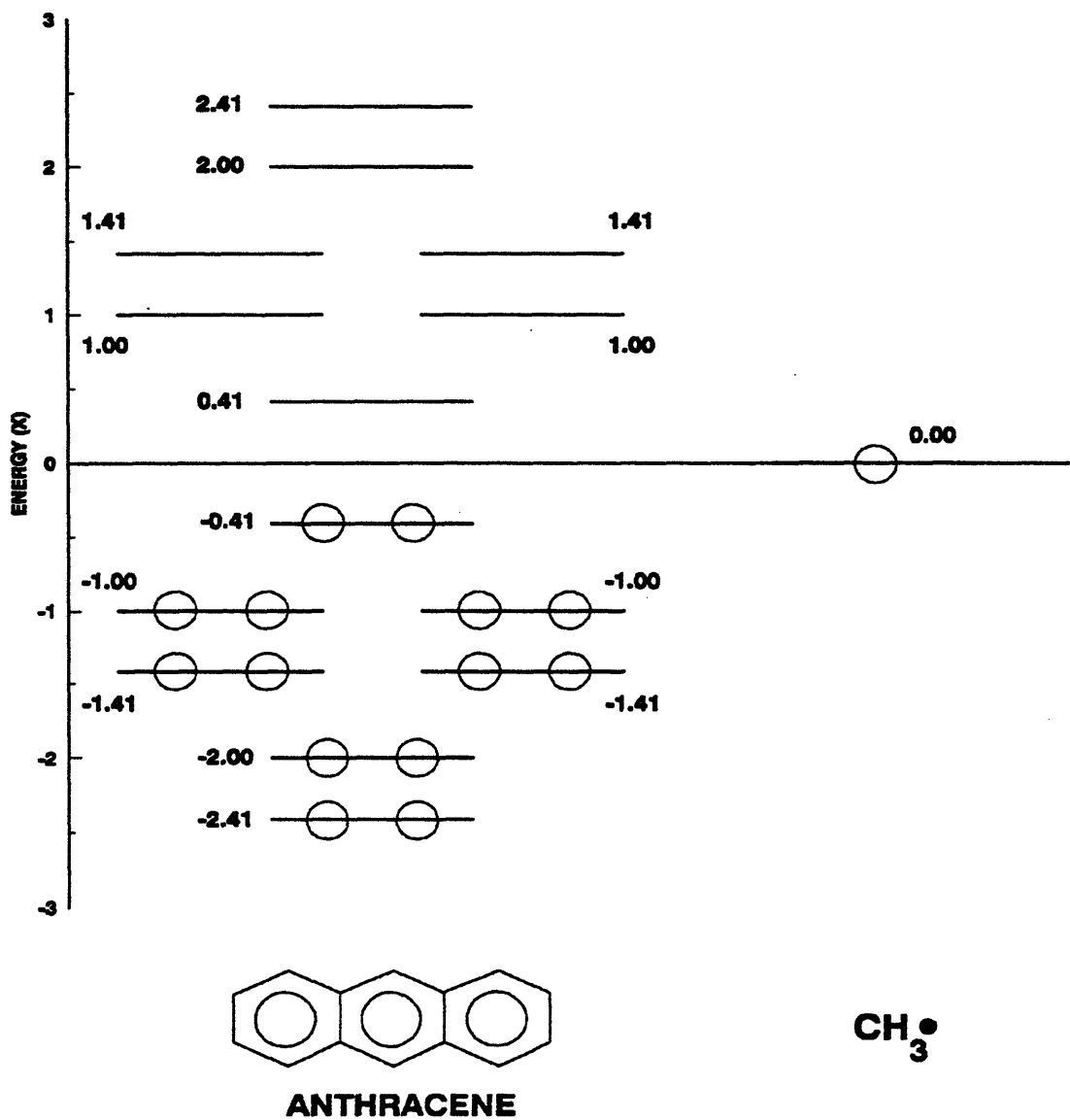
Figure 8.20: Frontier orbital interaction diagram for addition of methyl radical to anthracene using Hückel MOs.
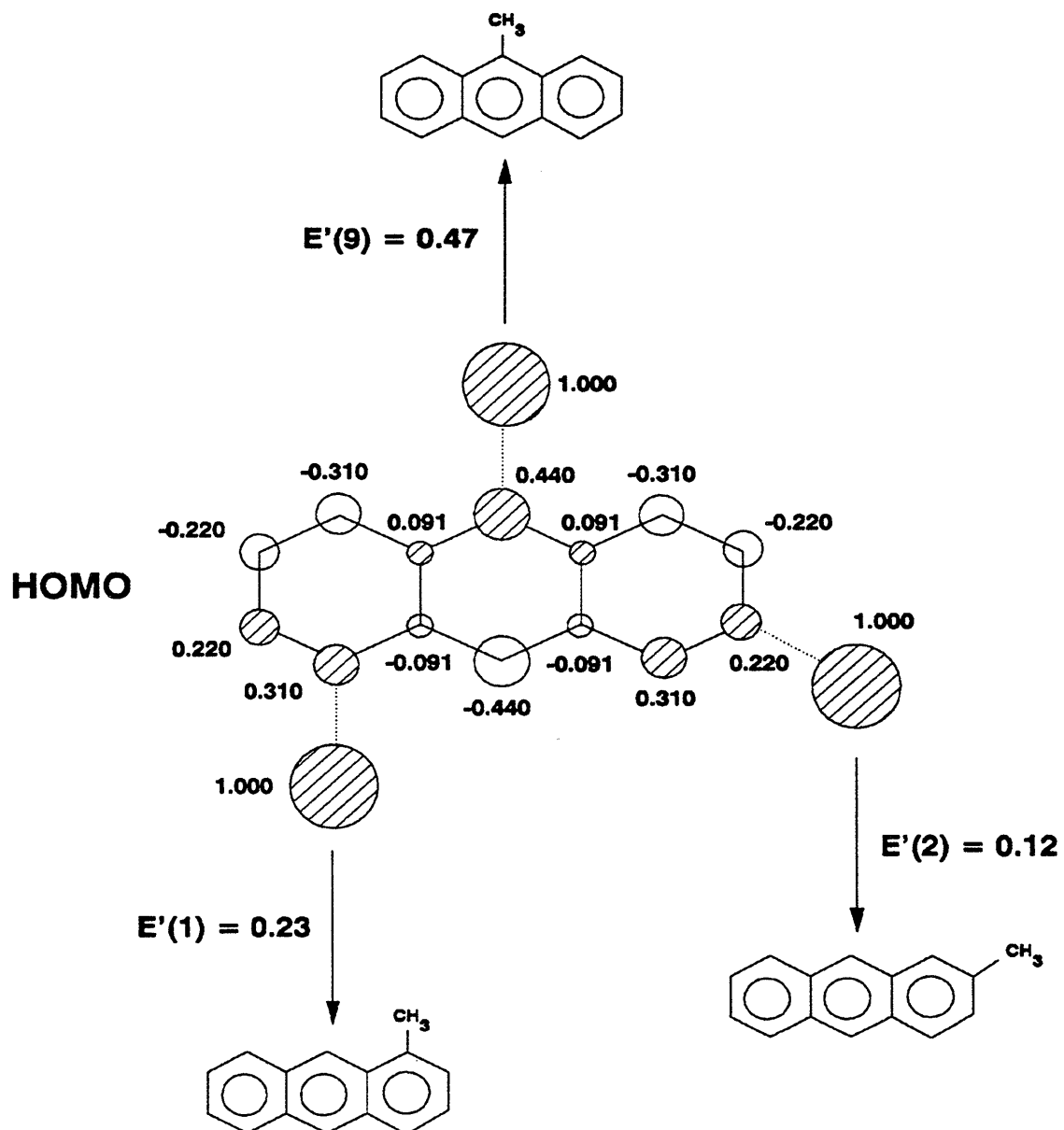
Figure 8.21: Estimation of isomer periselectivity by FMO theory using Hückel MOs for addition of methyl radical to anthracene to form 9-, 2- and 1-methylanthracene.
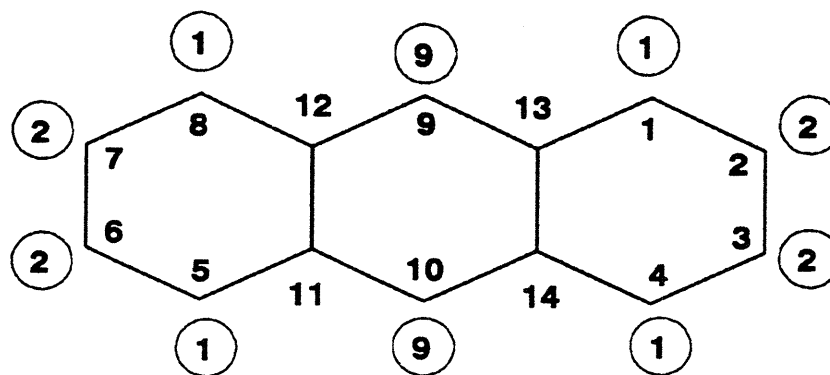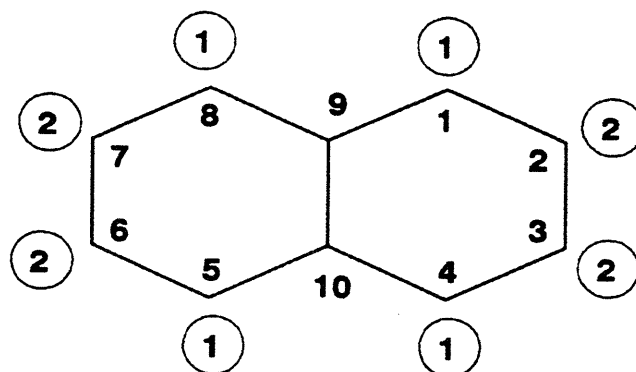
ANTHRACENE

NAPHTHALENE

Figure 8.22: Positions in parent acenes: anthracene and naphthalene.

798

positions that a methyl radical can attack on either the anthracene or naphthalene nucleus; the numbers inside the rings are the position numbers of the acene and the numbers outside the acene in the circles are the type of position. Table 8.16 displays the favorable, non-dimensional FMO stabilization energy E'(t) for the various position of the anthracene and naphthalene nucleus. It can be seen from the table that of the three possible position at which CH3* can add to the ANT (or 9MA) nucleus, FMO theory predicts CH3* attack favored in the order of positions 2 < 1 < 9. There are only two possible positions that CH3* can add to the NAP (or 1MN or 14DMN) nucleus, with FMO theory predicting CH3* attack in the order of positions 2 < 1. The predicted inequality between E'(t) at positions 2, 1 and 9 on anthracene in Table 8.16 accord with the experimentally observed product ratios seen in Table 8.14. Finally Figure 8.23 is a semi-log plot of log m_{aff} versus E'(t) derived from the data in Table 8.15. It can be seen that log m_{aff} increases almost linearly with E'(t), exhibiting slope ~ 1.5. By way of comparison, Dickerman (1973) reports phenyl affinities at T = 30°C in the ratio [0.28:1.00:14.3] for the [2,1,9] positions of anthracene, which translate to a slope ~ 1.9 on the coordinates of Figure 8.23.

8.7 Comparison of Multiply-Methylated Acene Thermolysis with Literature

Table 8.17 summarizes investigators of methyl aromatic substrate thermolyses given in the literature, listing the substrate, author, reaction temperature or

Table 8.16

COMPARISON OF FMO STABILIZATION
ENERGIES FOR METHYLATED AND PARENT ACENES

Hückel Values

Parent Acene	X	Position 1	Position 2	Position 9
ANT	-0.414	0.46	0.24	0.93
NAP	-0.618	0.59	0.22	-

PM3 Values

Methylated and Parent Acene	E_{HO} (eV)	Position 1	Position 2	Position 9
ANT	-8.25	0.29	0.23	0.43
9MA	-8.13	0.28	0.22 (3,6), 0.23 (2,7)	0.44
NAP	-8.84	0.42	0.28	-
1MN	-8.69	0.43 (4), 0.38 (5,8)	0.31 (2), 0.26 (3), 0.25 (6), 0.27 (7)	-
14DMN	-8.54	0.35	0.29 (2,3), 0.24 (6,7)	-
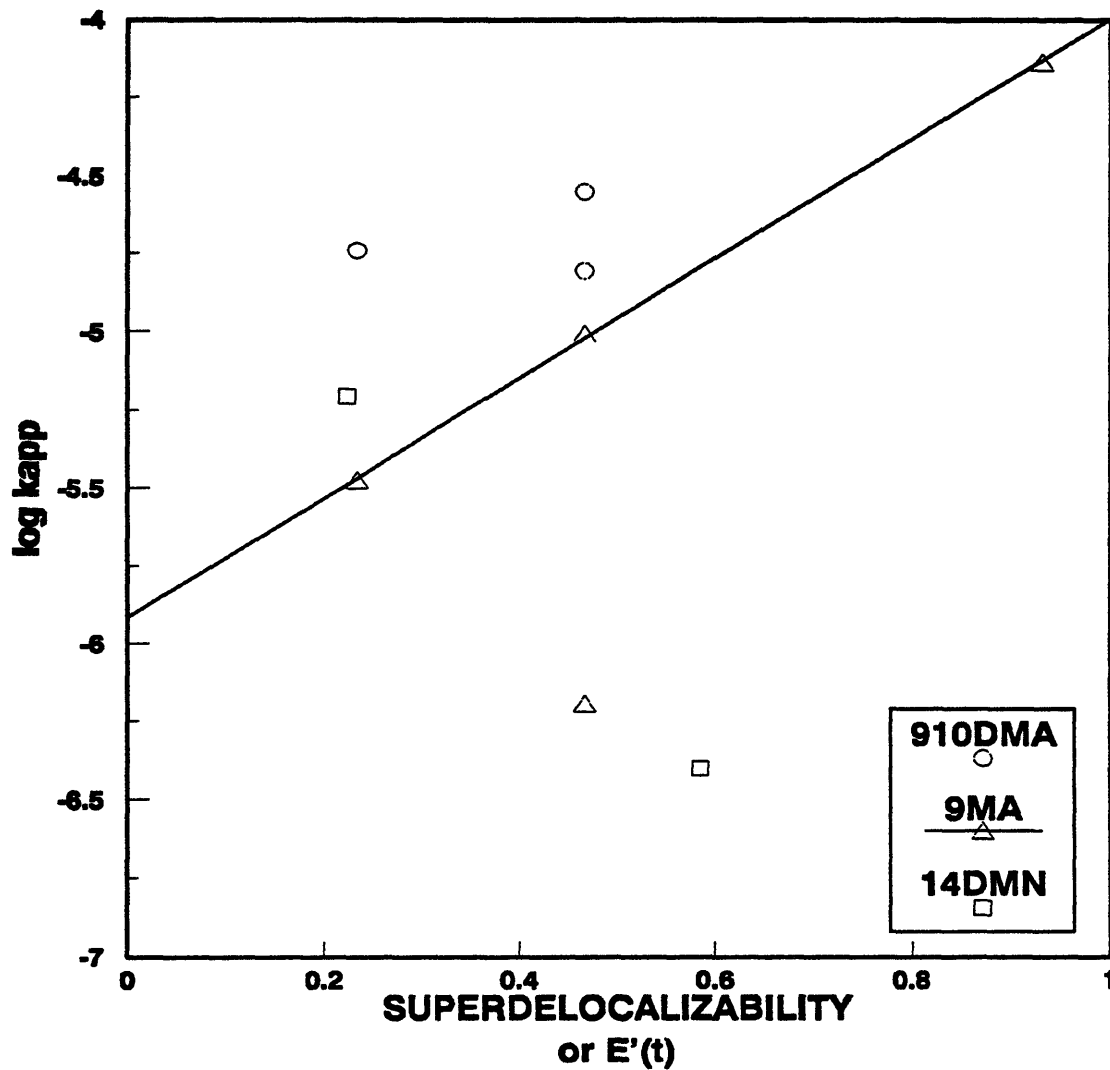
Figure 8.23: Log k_{app} vs. superdelocalizability or E'(t) for X+1 methyl acene to X methyl acene product ratios.

Table 8.17

EXPERIMENTAL CONDITIONS OF LITERATURE SOURCES

Substrate	Reference	Reaction Temperature (Range) °C	Initial Concentration (mol/l)	Reaction Order	Symbol on Graph
toluene	Badger and Spotswood (1960)	700	0.012		□
p-xylene	Schaefgen (1955)	795-872	0.011		o
14DMN	**this thesis**	**370-550**	**0.87**	**2**	▲
1MA	Smith and Savage (1993)	400-450	0.077		o
2MA	Smith and Savage (1993)	400-450	0.087		□
9MA	Smith and Savage (1993)	350-400	0.087		△
9MA	Pomerantz et al. (1980)	400	0.16		∗
9MA	**this thesis**	**315-409**	**0.82**	**3/2**	■
910DMA	Pope (1987)	300-380	2.0	2	∗
910DMA	**this thesis**	**315-409**	**0.82**	**3/2**	●
methylpyrene	Smith and Savage (1991)	400	0.077		△

temperature range, initial substrate concentration and the symbol and line style used to depict these data in Figure 8.24. Thermolysis kinetics derived in the present work are compared to the literature data in Figure 8.24, a semi-log plot of the effective-first-order rate constant for decomposition of methylated aromatics in s^{-1}, versus $1/\theta$, where $\theta = 0.004573*T$. Data from this thesis for 9,10-dimethylanthracene ($\cdot$ point, dashed line), 9-methylanthracene ($\square$ point, dotted line) and 1,4-dimethylnaphthalene ($\triangle$ point, dashed-dotted line) are shown on the graph with the temperature ranges from the experiments highlighted with solid lines. Literature data at single temperatures on the graph include the data of Schaefgen ($\circ$ point, dotted line) for p-xylene at 795°C, Badger and Spotswood ($\square$ point) for toluene at 700°C, Pomerantz (* point) for 9-methylanthracene at 400°C, and Savage and Smith for 1-methylpyrene ($\blacksquare$ point) at 400°C. Literature data over temperatures ranges on the graph include the data of Pope (* point, chain-dotted line) for 910DMA between 300-380°C and Smith and Savage for 1MA ($\circ$ point, long-dashed line) and 2MA ($\square$ point, dotted line) between 400-450°C and for 9MA ($\triangle$ point, dashed line) between 350-400°C. For 910DMA thermolyses, the data on Pope (1987), in our lab, accord closely with the present work. For 9MA, the point of Pomerantz et al. (1980) lies about 0.5 $\log_{10}$ k units below the present data, while the points of Smith and Savage (1993) are, on average, 0.5 $\log_{10}$ k units above our line. Since both these investigators used initial concentrations about 10-fold lower then those in the present work, and the overall reaction order $\sim$ 3/2, it would appear that the kinetics of Pomerantz accord with
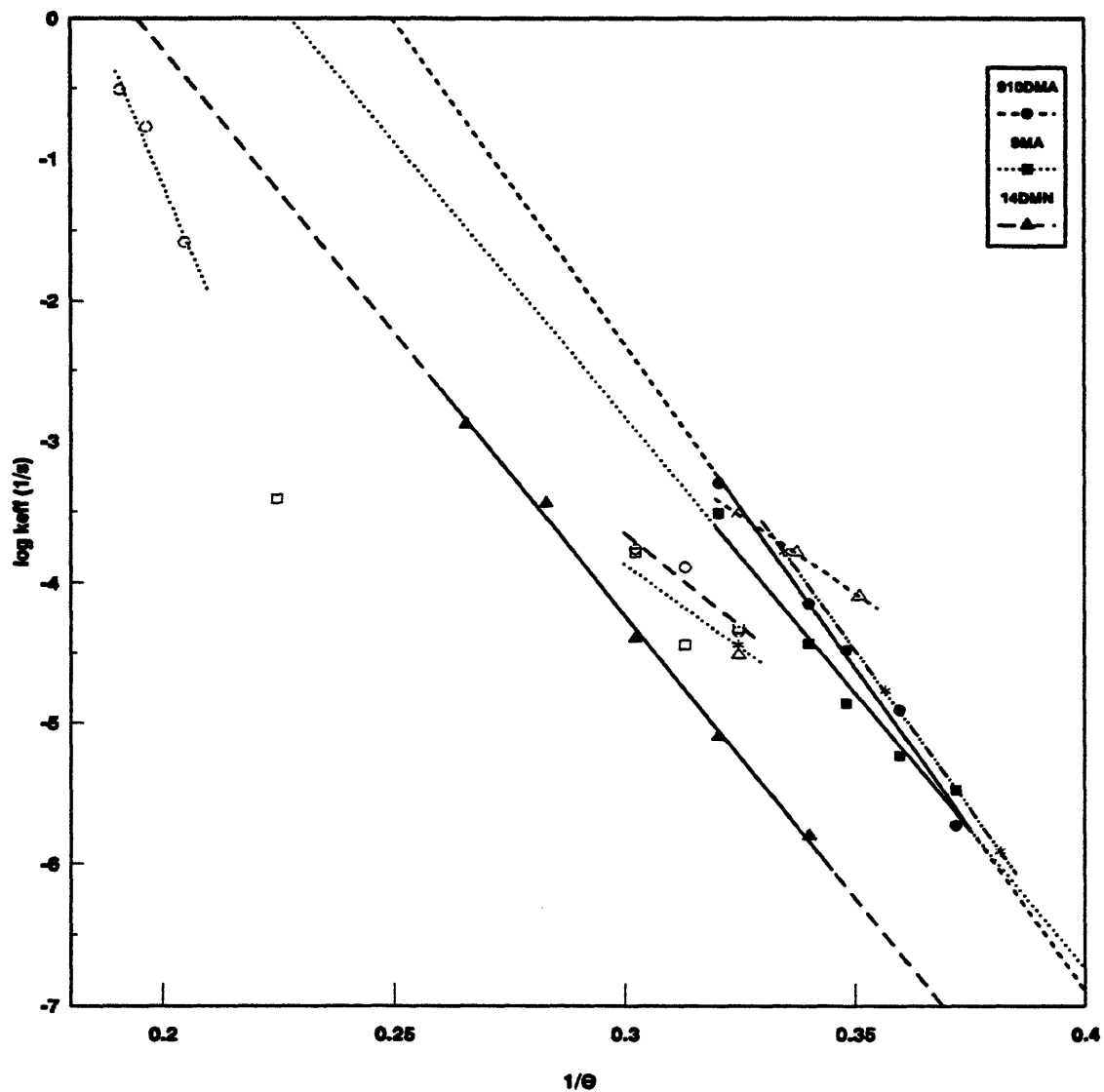
Figure 8.24: Comparison of effective first order rate constant (log k_{eff}) versus $1/\theta$ for methyl aromatic substrate thermolysis.

ours, while the kinetics reported by Smith and Savage lie a factor of 10 higher than both.

Finally, it is worth noting that the reaction pathways and product spectra reported by previous investigators can all be reasonably accommodated by the generalized methyl acene thermolysis scheme in Section 8.2 and shown in Figure 8.3 and Figure 8.4.

Chapter 9.

Conclusions

1. 9,10-dimethylanthracene (910DMA) was thermolyzed at temperatures from 315 - 409°C initial concentrations from 0.082 - 2.47 mol/l, and fractional conversions, X, from 0.05 - 0.99. All gaseous and up to 19 liquid thermolysis products were assayed by GC and certain heavy products were also detected and identified by GC/MS. The experiments provided, for the first time, quantitative experimental information concerning 910DMA thermolysis kinetics and reaction pathways.

2. 910DMA thermolysis kinetics were found, overall, to be of 3/2 order in substrate with activation energy ~45 kcal/mol. Arrhenius parameters for the thermolysis were $[\log_{10} A, E^*] = [11.1 \pm 0.1, 44.6 \pm 2.1]$.

3. Three primary parallel pathways were identified for 910DMA thermolysis, namely: (P1) Hydrogenation, to 9,10-dihydro-9,10-dimethylanthracene (DHDMA), (P2) Demethylation to 9-methylanthracene (9MA), and (P3) Methylation, to 1,9,10-trimethylanthracene (and other isomers, TMA). This pathway triad secondarily operates upon the primary products, forming 9,10-dihydro-9-methylanthracene (DHMA), a host of dimethylanthracenes (1,9-, 1,10-, 2,9- and 3,9-isomers), and anthracene (ANT), as well as minor amounts of 9,10-dihydroanthracene and 1- and 2-methylanthracenes (1MA, 2MA).

4. A 10-elementary step free-radical mechanism was formulated for the early stages of 910DMA thermolysis. Initiation occurs by substrate disproportionation, to form respectively dehydrogenated and hydrogenated radicals, 910DMA* and HDMA*. Of these, HDMA* propagates the reaction. It can either abstract H from substrate or undergo β-scission, controlling the pathway ratio P1/P2. The methyl radical formed by β-scission of HDMA* can subsequently either abstract H from substrate or add to it, setting the pathway ratio P2/P3. Termination occurs by pure- and cross-combination of the 910DMA* and HDMA* radicals.

5. The preceding mechanism served as the platform for the quantitative numerical simulation and modelling of 910DMA thermolysis kinetics and product selectivities. Thermochemical and kinetic parameters required for the model were derived from first principles and the system of stiff differential conservation relations comprising the model was numerically solved with an appropriately stable computer

code called ACUCHEM (Braun, 1988). A sensitivity analysis was performed to estimate the inherent uncertainties in model predictions. An optimized model was finally developed to best-fit the experimental observations. At $T = 355°C$ with $[910DMA]_o = 0.82$ mol/l, the optimized model was able to match within a factor of 2 the observed substrate decay half-life, the product selectivities of 9MA, DHDMA, TMA and dimers, and the product ratios R[DHDMA/9MA] and R[TMA/9MA].

6. The relative amounts of minor methylated products formed during 910DMA thermolyses were modelled as arising from periselective methyl radical attack on an arene ring position, governed by the single-center FMO stabilization energy. This approach predicted the relative abundances of both the minor dimethylanthracene isomers (2,9- + 3,9-)DMA/(1,9- + 1,10-)DMA as well as the minor methylanthracene isomers 2MA/1MA.

7. 9-methylanthracene (9MA) was thermolyzed at temperatures from 315 - 409°C initial concentrations from 0.082 - 2.06 mol/l, and fractional conversions, X, from 0.05 - 0.99. All gaseous and up to 40 liquid thermolysis products were assayed by GC and certain heavy products were also detected and identified by GC/MS. The experiments provided, for the first time, quantitative experimental information concerning 9MA thermolysis kinetics and reaction pathways.

8. 9MA thermolysis kinetics were found, overall, to be of 3/2 order in substrate with activation energy ~40 kcal/mol. Arrhenius parameters for the thermolysis were $[\log_{10} A, E^*] = [9.2 \pm 0.15, 39.7 \pm 3.9]$.

9. Three primary parallel pathways were identified for 9MA thermolysis, namely: (P1) Hydrogenation, to 9,10-dihydro-9-methylanthracene (DHMA), (P2) Demethylation to anthracene (ANT), and (P3) Methylation, to 9,10-dimethylanthracene, 1,9-dimethylanthracene, 1,10-dimethylanthracene, 2,9-dimethylanthracene and 3,9-dimethylanthracene. This pathway triad secondarily operates upon the primary products, forming 9,10-dihydro-9,10-dimethylanthracene (DHDMA), trimethylanthracenes, as well as minor amounts of 9,10-dihydroanthracene and 1- and 2-methylanthracenes (1MA, 2MA).

10. A 19-elementary step free-radical mechanism was formulated for the early stages of 9MA thermolysis. Initiation occurs by substrate disproportionation, to form respectively dehydrogenated and hydrogenated radicals, 9MA* and HMA9* or HMA10*. Of these, HMA10* propagates the reaction. It can either abstract H from substrate or undergo β-scission, controlling the pathway ratio P1/P2. The methyl radical formed by β-scission of HMA10* can subsequently either abstract H from substrate or add to it, setting the pathway ratio P2/P3. HMA9* can react with a molecule of substrate and isomerize to HMA10*. Termination occurs by pure- and cross-combination of the 9MA*, HMA9* and HMA10* radicals.

11. The preceding mechanism served as the platform for the quantitative numerical simulation and modelling of 9MA thermolysis kinetics and product selectivities. Thermochemical and kinetic parameters required for the model were derived from first principles and the system of stiff differential conservation relations

comprising the model was numerically solved with an appropriately stable computer code called ACUCHEM (Braun, 1988). A sensitivity analysis was performed to estimate the inherent uncertainties in model predictions. An optimized model was finally developed to best-fit the experimental observations. At T = 370°C with $[9MA]_o$ = 0.82 mol/l, the optimized model was able to match within a factor of 2 the observed substrate decay half-life, the product selectivities of ANT, DHMA, 910DMA and dimers, and the product ratios R[DHMA/ANT] and R[910DMA/ANT].

12. The relative amounts of minor methylated products formed during 9MA thermolyses were modelled as arising from periselective methyl radical attack on an arene ring position, governed by the single-center FMO stabilization energy. This approach predicted the relative abundances of the minor dimethylanthracene isomers (2,9- + 3,9-)DMA/(1,9- + 1,10-)DMA, (2,9- + 3,9-)DMA/910DMA and (1,9- + 1,10-)DMA/910DMA as well as the minor methylanthracene isomers 2MA/1MA.

13. 1,4-dimethylnaphthalene (14DMN) was thermolyzed at temperatures from 370 - 550°C initial concentrations from 0.081 - 2.07 mol/l, and fractional conversions, X, from 0.05 - 0.99. All gaseous and up to 15 liquid thermolysis products were assayed by GC and certain heavy products were also detected and identified by GC/MS. The experiments provided, for the first time, quantitative experimental information concerning 14DMN thermolysis kinetics and reaction pathways.

14. 14DMN thermolysis kinetics were found, overall, to be of 2nd order in substrate with activation energy ~42 kcal/mol. Arrhenius parameters for the thermolysis were [$\log_{10}$ A, E*] = [7.9±0.14, 40.1±2.3].

15. Three primary parallel pathways were identified for 14DMN thermolysis, namely: (P1) Hydrogenation, to 1,4-dihydro-1,4-dimethylnaphthalene (DHDMN), (P2) Demethylation to 1-methylnaphthalene (1MN), and (P3) Methylation, to 1,4,5-trimethylnaphthalene, 1,4,6-trimethylnaphthalene and other isomers, TMN. This pathway triad secondarily operates upon the primary products, a host of dimethylanthracenes (1,3-, 1,2-, and 2,6-isomers), and naphthalene (NAP), as well as minor amounts of 2-methylnaphthalene (2MN).

16. A 10-elementary step free-radical mechanism was formulated for the early stages of 14DMN thermolysis. Initiation occurs by substrate disproportionation, to form respectively dehydrogenated and hydrogenated radicals, 14DMN* and HDMN*. Of these, HDMN* propagates the reaction. It can either abstract H from substrate or undergo β-scission, controlling the pathway ratio P1/P2. The methyl radical formed by β-scission of HDMN* can subsequently either abstract H from substrate or add to it, setting the pathway ratio P2/P3. Termination occurs by pure- and cross-combination of the 14DMN* and HDMN* radicals.

17. The preceding mechanism served as the platform for the quantitative numerical simulation and modelling of 14DMN thermolysis kinetics and product selectivities. Thermochemical and kinetic parameters required for the model were

derived from first principles and the system of stiff differential conservation relations comprising the model was numerically solved with an appropriately stable computer code called ACUCHEM (Braun, 1988). A sensitivity analysis was performed to estimate the inherent uncertainties in model predictions. An optimized model was finally developed to best-fit the experimental observations. At T = 450°C with $[14DMN]_o$ = 0.87 mol/l, the optimized model was able to match within a factor of 10 the observed substrate decay half-life, the product selectivities of 1MN, DHDMN, TMN and dimers, and the product ratio R[TMN/1MN].

18. A 48-step extended model of 910DMA thermolysis was developed by combining the basic 10-step 910DMA and 19-step 9MA models and accounting for additional reactions between the species therein. Numerical solution of the extended model at T = 370°C and $[910DMA]_o$ = 0.82 mol/l showed to predict decay half-lifes, major product selectivities, namely S(9MA), S(TMA), S(DHDMA), S(DHMA), S(HVY), S(CH4) and S(ANT), and major product ratios R[TMA/9MA], R[DHDMA/9MA], R[ANT/9MA] and R[DHMA/ANT] that were significantly closer to experimental observations than the corresponding prediction of these quantities by the basic 910DMA thermolysis model.

Appendix A. References

REFERENCES

Badger, G.M.: "Pyrolysis of Hydrocarbons" (pp 1-40) in Progress in Physical Organic Chemistry, Cohen, S.G.; Streitwieser, A.; and Taft, R.W.; Eds., Interscience, New York (1965).

Badger, G.M. and Spotswood, T.M.: "The Formation of Aromatic Hydrocarbons at High Temperatures. Part IX. The Pyrolysis of Toluene, Ethylbenzene, Propylbenzene, and Butylbenzene", J. Chem. Soc., 4420 (1960).

Bass, D.H.: Model Compound Studies in Coal Liquefaction: The Kinetics and Mechanism of Hydrogen Transfer from Hydronaphthalene Donors, Sc.D. Thesis, Massachusetts Institute of Technology, Cambridge, MA. (1982).

Benson, S.W.: Thermochemical Kinetics, 2nd Ed., John-Wiley and Sons, New York (1976).

Benson, S.W.; Cruickshank, F.R.; Golden, D.M.; Haugen, G.R.; O'Neal, H.E.; Rodgers, A.S; Shaw, R. and Walsh, R.: "Additivity Rules for the Estimates of Thermochemical Properties", Chem. Rev., 69, 279 (1969).

Billmers, R.; Griffith, L.L. and Stein, S.E.: "Hydrogen Transfer between Anthracene Structures", J. Phys. Chem., 90, 517 (1986).

Bordwell, F.G.; Cheng, J.P. and Harrelson, Jr., J.A.: "Homolytic Bond Dissociation Energies in Solution from Equilibrium Acidity and Electrochemical Data", J. Am. Chem. Soc., 110, 1229 (1988).

Braun, W.; Herron, J.T. and Kahaner, D.K.: "Acuchem: A Computer Program for Modeling Complex Chemical Reaction Systems", Int. J. Chem. Kinet., 20, 51 (1988).

Clark, T.: A Handbook of Computational Chemistry, John-Wiley and Sons, New York (1985).

Coulson, C.A. and Streitwieser, A.: Dictionary of Pi-Electron Calculations, Pergammon Press, London (1960).

Cox, J.D. and Pilcher, G.: Thermochemistry of Organic and Organometallic Compounds, Academic Press, New York (1970).

Dean, A.M.: "Predictions of Pressure and Temperature Effects upon Radical Addition and Recombination Reactions", J. Phys. Chem., 89, 4600 (1985).

Dewar, M.J.S. and Dougherty, R.C.: The PMO Theory of Organic Chemistry, Plenum Press, New York (1975).

Dias, J.R. : Handbook of Polycyclic Hydrocarbons; Part A; Benzenoid Hydrocarbons, Elsevier, Amsterdam (1987).

Dickerman, S.C.; Feigenbaum, W.M.; Fryd, M.; Milstein, N.; Vermont, G.B.; Zimmerman, I.; and McOmie, J.F.W.: "Homolytic Aromatic Substitution. VIII. Phenylation of Polycyclic Aromatic Hydrocarbons", J. Amer. Chem. Soc., 95, 14 (1973).

Fleming, I.: Frontier Orbitals and Organic Chemical Reactions, John Wiley and Sons, London (1976).

Fujimoto H. and Fukui, K.: "Intermolecular Interactions and Chemical Reactivity", Chapter 3 (pp 23-54) in Chemical Reactivity and Reaction Pathways, G. Klopman, Ed., Wiley, New York (1974).

Fukui, K.: Theory of Orientation and Stereoselection, Springer-Verlag, Berlin (1975).

Gear, C.W.: Numerical Initial Value Problems in Ordinary Differential Equations, Prentice-Hill, Englewood Cliffs, N.J., 1971.

Hammond, G.S.: J. Amer. Chem. Soc., 77, 334 (1955).

Harris, J.: lecture notes from 10.610 (1992).

Holt, P.M.and Kerr, J.A.: "Kinetics of Gas-Phase Addition Reactions of Methyl Radicals. I. Addition to Ethylene, Acetylene and Benzene", Int. J. Chem. Kinet., 9, 185 (1977).

Hudson, R.F.: "Nucleophilic Reactivity", Chapter 5 (pp 167-252) in Chemical Reactivity and Reaction Pathways, G. Klopman, Ed., Wiley, New York (1974).

Ingold, K.U.: "Rate Constants for Free Radical Reaction in Solution" (pp 37-66) in Free Radicals, Vol. I, Kochi, J.K.; Ed., John Wiley and Sons, New York (1973).

Kerr, J.A.: "Rate Processes in the Gas Phase" (pp 1-36) in Free Radicals, Vol. I, Kochi, J.K.; Ed., John Wiley and Sons, New York (1973).

Klein, M.T.: Model Pathways in Lignin Thermolysis, Ph.D. Thesis, Massachusetts Institute of Technology, Cambridge, MA. (1981).

Klopman, G.: "The Generalized Perturbation Theory of Chemical Reactivity and Its Applications", Chapter 4 (pp 55-166) in Chemical Reactivity and Reaction Pathways, G. Klopman, Ed., Wiley, New York (1974).

Lias, S.G.; Bartmess, J.E.; Liebman, J.F.; Holmes, J.L.; Levin, R.D. and Mallard, W. G.: "Gas-Phase Ion and Neutral Thermochemistry", Journal of Physical and Chemical Reference Data, Vol. 17, Suppl. 1, National Bureau of Standards (1988).

Mason, R.: Acta. Crystallogr., 17, 547 (1964).

Miller, R.E.and Stein, S.E.: "Liquid-Phase Pyrolysis of 1,2-Diphenylethylane", J. Phys. Chem., 85, 580 (1981).

Pedley, J.B.; Naylor, R.D. and Kirby, S.P.: Thermochemical Data of Organic Compounds, Chapman and Hall, London (1986).

Pomerantz, M.; Combs Jr., G.L. and Fink, R.: "Thermal Extrusion of a One-Carbon Species from 1,2-Benzotropilidene (5H-Benzocycloheptene), the Benzotropyl (Benzocycloheptenyl) Free Radical, 1,2:5,6-Dibenzotropilidene (5H-dibenzo[a,d]cycloheptene), and the 1,2:4,5-Dibenzotropyl (Dibenzo[a,d]cycloheptenyl) Free Radical", J. Org. Chem., 45, 143 (1980).

Pope, J.M.: The Kinetics and Mechanism of Thermal Hydrogen Transfer Reactions Between Aromatic and Hydroaromatic Hydrocarbons, Sc.D. Thesis, Massachusetts Institute of Technology, Cambridge, MA. (1987).

Reid, R.C.; Prausnitz, J.M. and Poling, B.E.: The Properties of Liquids and Gases, Fourth Edition, McGraw-Hill Co., New York (1987).

Ritter, E.R. and Bozzelli, J.W.: "THERM: Thermodynamic Property Estimation of Radicals and Molecules", Int. J. Chem. Kinet., 8, (1991).

Robaugh, D. and Tsang, W.: "Mechanism and Rate of Hydrogen Atom Attack on Toluene at High Temperatures", J. Phys. Chem., 90, 4159 (1986).

Rossi, M.J.; McMillan, D.F. and Golden, D.M.: "Aliphatic C-H Bond Scission Processes in Diphenylmethane and 2-Benzyl- and 4-Benzylpyridine. The Heat of Formation of the Diphenylmethane and α-Phenylethyl Radical in the Gas Phase", J. Phys. Chem., 88, 5031 (1984).

Sarofim, A.F.; Longwell, J.P. and Wornat, M.J.: "Studies of Mutagen Formation During the Devolatilization and Oxidative Pyrolysis of Coal", pp 293-325 in 1986 Annual Report of Progress to the National Institute of Environmental Health Sciences, Submitted by W.G. Thilly, Director, MIT Center for Environmental Health Sciences (1987).

Savage, P.E.; Jacobs, G.E. and Javanmardian, M.: "Autocatalysis and Aryl-Alkyl Bond Cleavage in 1-Dodecylpyrene Pyrolysis", Ind. Eng. Chem. Res., 28, 645 (1989).

Savage, P.E. and Klein, M.T.: "Discrimination between Molecular and Free-Radical Models of 1-Phenyldodecane Pyrolysis", Ind. Eng. Chem. Res., 26, 374 (1987a).

Savage, P.E. and Klein, M.T.: "Asphaltene Reaction Pathways - II. Pyrolysis of n-Pentadecylbenzene", Ind. Eng. Chem. Res., 26, 488 (1987b).

Savage, P.E. and Klein, M.T.: "Asphaltene Reaction Pathways - III. Effect of Reaction Environment", Energy & Fuels, 2, 619 (1988a).

Savage, P.E. and Klein, M.T.: "Asphaltene Reaction Pathways - IV. Pyrolysis of Tridecylcyclohexane and 2-Ethyltetralin", Ind. Eng. Chem. Res., 27, 1348 (1988b).

Savage, P.E. and Klein, M.T.: "Asphaltene Reaction Pathways - V. Chemical and Mathematical Modeling", Chem. Eng. Sci., 26, 393 (1989a).

Savage, P.E. and Klein, M.T.: "Kinetics of Coupled Reactions: Lumping Pentadecylbenzene Pyrolysis into Three Parallel Chains", Chem. Eng. Sci., 44, 985 (1989b).

Savage, P.E.; Klein, M.T. and Kukes, S.G.: "Asphaltene Reaction Pathways - I. Thermolysis", Ind. Eng. Chem. Process Des. Dev, 24, 1169 (1985).

Schaefgen, J.R.: "The Pyrolysis of p-Xylene", J. Polym. Sci., 15, 203 (1955).

Shaw, R., Golden, D.M. and Benson, S.W.: "Thermochemistry of Some Six-Membered Cyclic and Polycyclic Compounds Related to Coal", J. Phys. Chem., 81, 1716 (1977).

Smith, C.M. and Savage, P.E.: "Reactions of Polycyclic Alkylaromatics: Structure and Reactivity", A.I.Ch.E. J., 37, 1613 (1991a).

Smith, C.M. and Savage, P.E.: "Reactions of Polycyclic Alkylaromatics. 1. Pathways, Kinetics, and Mechanisms for 1-Dodecylpyrene Pyrolysis", Ind. Eng. Chem. Res., 37, 331 (1991b).

Smith, C.M. and Savage, P.E.: "Reactions of Polycyclic Alkylaromatics. 4. Hydrogenolysis Mechanisms in 1-Alkylpyrene Pyrolysis", Energy and Fuels, 6, 195 (1992).

Smith, C.M. and Savage, P.E.: "Reactions of Polycyclic Alkylaromatics. 5. Pyrolysis of Methylanthracenes", A.I.Ch.E. J., 39, 1355 (1993).

Stephani, A.P. and Szwarc, M.: "Addition of CF_3 Radicals to Aromatic Hydrocarbons. The Relative Selectivity of CF_3", J. Am. Chem. Soc., 84, 3661 (1962).

Stein, S.E.: "A Fundamental Chemical Kinetics Approach to Coal Conversion" (pp 97-129) in New Approaches in Coal Chemistry, Blaustein, B.D.; Bockrath, B.C.; and Friedman, S.; Eds., ACS Symposium Series 169, Washington, D.C. (1981).

Stein, S.E. and Brown, R.L.: "Prediction of Carbon-Hydrogen Bond Dissociation Energies for Polycyclic Aromatic Hydrocarbons of Arbitrary Size", J. Am. Chem. Soc., 113, 787 (1991).

Stein, S.E.; Rukkers, J.M. and Brown, R.L.: NIST Structures and Properties Database and Estimation Program, Ver. 1.1, Chemical Kinetics and Thermodynamics Division, National Institute of Standards and Technology, (1991).

Stein, S.E., Golden D.M. and Benson, S.W.: "Predictive Scheme for Thermochemical Properties of Polycyclic Aromatic Hydrocarbons", J. Phys. Chem., 81, 314 (1977).

Stewart, J.J.P.: "MOPAC: A Semiempirical Molecular Orbital Program", J. Computer-Aided Molecular Design, 4, 1 (1990a).

Stewart, J.J.P.: "Semiempirical Molecular Orbital Methods" (Chapter 2) in Reviews in Computational Chemistry, Vol. 1, Lipkowitz, K.B. and Boyd, D.B., eds.: VCH Publishers (1990b).

Stull, D.R.; Westrum, Jr., E.F. and Sinke, G.C.: The Chemical Thermodynamics of Organic Compounds, John Wiley and Sons, New York (1969).

White, C.: "Prediction of the Boiling Point, Heat of Vaporization, and Vapor Pressure at Various Temperatures for Polycyclic Aromatic Hydrocarbons", J. Chem. Eng. Data, 31, 198 (1988).

Wojnarovtis, L. and Foldiak, G.: "Electron-Capture Detection of Aromatic Hydrocarbons", J. of Chromatography, 206, 511 (1981).

Wornat, M.J.: Pyrolysis-Induced Changes in the Composition of Polycyclic Aromatic Compounds from a Bituminous Coal, Ph.D. Thesis, Massachusetts Institute of Technology, Cambridge, MA. (1988).

ESTIMATION OF STATE PROPERTIES

The state properties of the model compounds and the biphenyl diluent were estimated using the procedure of Bass (1982), Section 9.2.1 and with estimated methods from The Properties of Gases and Liquids, Fourth Ed. by Reid, Prausnitz and Poling (1987).

Critical properties are estimated using Joback modification of Lydersen's method (Reid et al., 1987). The equations for the critical properties in units of kelvins, bars, and cubic centimeters per mole, respectively; are:

$$T_c = T_b [0.584 + 0.965\Sigma\Delta_T - (\Sigma\Delta_T)^2]^{-1} \qquad (B.1)$$

$$P_c = (0.113 + 0.0032n_A - \Sigma\Delta_P)^{-2} \qquad (B.2)$$

$$V_c = 17.5 + \Sigma\Delta_V \qquad (B.3)$$

where T_b is the normal boiling point at 1 atm, n_A is the number of atoms in the molecule, and relevant group contributions (Δ_i) for the model compounds and biphenyl are given in Table B.1. Errors in the critical values should not exceed 5% for the calculated values. In the case of the model compounds where the experimental T_b is not available, the normal boiling point (K) is estimated using the linear relationship between boiling point and linear-temperature-programmed gas chromatographic polycyclic aromatic hydrocarbon (PAH) retention indices (White,

Table B.1

Joback Group Contributions for Critical Properties and Values and Estimated Boiling Points for Model Compounds and Biphenyl

	Δ_T	Δ_P	Δ_V	T_b(exp)	T_b(pred)
Non-ring: -CH$_3$	0.0141	-0.0012	65		
Ring: =C<	0.0143	0.0008	32		
=CH-	0.0082	0.0011	41		
Biphenyl	0.1106	0.0126	474	528	527
1,4-dimethylnaphthalene	0.1346	0.0074	504	543	541
9-methylanthracene	0.1594	0.0127	594		634
9,10-dimethylanthracene	0.1796	0.0112	650		662

1988) using the following expression:

$$T_b = 1.0672I + 282.82 \qquad \text{(B.4)}$$

where I is the PAH retention index. The linear least-squared regression line between the literature value of the boiling point and the experimentally determined PAH retention index has a correlation coefficient of 0.997, a standard error of estimate of 6.78 K, and the average percent deviation is 0.68. The critical compressibilities are calculated from the gas law:

$$Z_c = \frac{P_c V_c}{R T_c} \qquad \text{(B.5)}$$

Vapor pressures are calculated using the Gomez-Thodos vapor pressure equation (Reid et al., 1987):

$$\ln P_{vp_r} = \beta[\frac{1}{T_r^m} - 1] + \gamma[T_r^7 - 1] \qquad \text{(B.6)}$$

which is necessarily satisfied at the critical point. The normal boiling point provides as additional equation which relates the constants β, γ, and m to each other. This leads to:

$$\gamma = ah + b\beta \qquad \text{(B.7)}$$

where:

$$h = T_{b_r} \frac{\ln (P_c/1.01325)}{1 - T_{b_r}} \tag{B.8}$$

$$a = \frac{1 - 1/T_{b_r}}{T_{b_r}^7 - 1} \tag{B.9}$$

$$b = \frac{1 - 1/T_{b_r}^m}{T_{b_r}^7 - 1} \tag{B.10}$$

$$\beta = -4.26700 - \frac{221.79}{h^{2.5} \exp 0.0384h^{2.5}} + \frac{3.8126}{\exp (2272.44/h^3)} \tag{B.11}$$

$$m = 0.78425 \exp (0.089315h) - \frac{8.5217}{\exp (0.74826h)} \tag{B.12}$$

with $T_{b_r} = T_b/T_c$. Vapor pressure data are tabulated in Table B.2 for the experimental temperatures. Acentric factors are taken directly from these data, in accordance with its definition (Reid et al., 1987):

$$\omega = -\log [P_{vp_r}(at \ T_r = 0.7)] - 1.000 \tag{B.13}$$

Acentric factors are also given in Table B.2.

Table B.2

Vapor Pressures (bars) and Acentric Factor of Model Compounds and Biphenyl

Compound	Temperature (°C)								κ
	315	335	355	370	409	450	500	550	
Biphenyl	3.13	4.31	5.81	7.18	11.86	19.03	32.12	-	0.378
1,4-dimethyl-naphthalene				5.54	9.21	14.88	25.33	-	0.398
9-methyl-anthracene	1.91	2.70	3.71	4.65	7.96				0.478
9,10-dimethyl-anthracene	1.59	2.27	3.15	3.97	6.91				0.525

Liquid densities are estimated using the method of Bhirud (Reid et al., 1987) defined below:

$$\ln \frac{P_c V_s}{RT} = \ln V^{(0)} + \omega \ln V^{(1)} \tag{B.14}$$

where

$$\ln V^{(0)} = 1.39644 - 24.076T_r + 103.615T_r^2 - 255.719T_r^3 \\ + 355.805T_r^4 - 256.671T_r^5 + 75.1088T_r^6 \tag{B.15}$$

$$\ln V^{(1)} = 13.4412 - 135.7437T_r + 533.380T_r^2 - 1091.453T_r^3 \\ + 1231.43T_r^4 - 728.227T_r^5 + 176.737T_r^6 \tag{B.16}$$

Liquid densities for the model compounds and biphenyl are tabulated in Table B.3 for the experimental temperatures.

Since the reactions of the model compounds are likely to display kinetics with order greater than 1, careful control of the absolute reactant concentrations is essential. It is desirable for most of the material within the reactor to be liquid, so that the reactions may be modeled as single phase systems with component concentrations relatively insensitive to small variations in temperature and size of reactant charge. Simultaneously, care must be taken not to over-charge the reactor, so that at elevated temperatures the liquid volume of the reactants do not exceed the volume of the reactor.

It is necessary to calculated the distribution of the reactants between the

Table B.3

Liquid Densities (moles/liter) of Model Compounds and Biphenyl							

Compound	Temperature (°C)							
	315	335	355	370	409	450	500	550
Biphenyl	5.09	4.96	4.82	4.71	4.39	3.92	3.03	-
1,4-dimethyl-naphthalene				3.76	3.50	3.13	2.42	-
9-methyl-anthracene	3.89	3.78	3.68	3.59	3.35			
9,10-dimethyl-anthracene	3.59	3.49	3.39	3.31	3.09			

liquid and gas phases as a function of temperature and size of reactant charge (given the reactor volume), and to select conditions that meet the above specifications. Vapor pressures, compressibility factors and liquid densities are all estimable as a function of temperature and the total reactor volume is also known. From this information, it can be shown that the charge of each component and the diluent biphenyl is in the liquid phase and within the volume of the reactor for safety purposes.

Figure B.1 outlines the procedure to calculate the distribution of the reactants between the liquid and gas phases as a function of temperature and size of reactant charge (given the reactor volume). This calculation was done for the limiting cases that all of the charge was pure component, either model compound or biphenyl, at each reaction temperature. First, the pressure inside the reactor was calculated assuming all the of charge was in the gas phase using the ideal gas law. The pressure obtained from this calculation was much greater than the vapor pressure in all cases, therefore indicating most of the charge was in the liquid phase. Next, an estimate was made for how much of the charge was in the gas phase, again using the ideal gas law with vapor pressure for the specific temperature of the calculation. This value was then corrected by including the compressibility factor, which is a factor of reduced temperature and reduced pressure. The reduced pressured was calculated with the vapor pressure at the experimental temperature. Compressibility factors were estimated from a generalized compressibility chart in Reid et. al. (1987). The

Calculate P assuming all charge in gas phase:

$$P^o = \frac{nRT}{V}$$

↓

Is $P^o >> P_{vp}$?

yes ↙   ↘ *no*

Most charge in liquid phase   *Most charge in gas phase*

Calculate amount in gas phase:

$$n_{gas}^o = \frac{P_{vp}V}{RT}$$

↓

Is $n_{gas}^o << n_{total}$?

yes ↙   ↘ *no*

Calculate n_{gas} *using Z:*

$$n_{gas} = \frac{P_{vp}V}{ZRT}$$

Calculate n_{liq}:

$$n_{liq} = n_{total} - n_{gas}$$

↓

Calculate V_{liq} *of* n_{liq}:

$$V_{liq} = \frac{n_{liq}}{V_s}$$

↓

Is $V_{liq} > 1/2 \ V_{reactor}$?

yes ↙   ↘ *no*

n_{total} *ok*   *change* n_{total}

Figure B.1: Flowchart for calculating number of moles in liquid and gas phase inside reactors.

total moles in the liquid phase was then computed by subtracting the number of

moles in the gas phase from the total number of moles charged to the reactor. The

volume of the number of moles in the liquid phase was then checked to assure that

it occupied greater than one-half of the reactor volume. The results of these

calculations are shown in Table B.4.

Table B.4

Values Used in Calculating Distribution Between Liquid and

	Temperature (°C)	P° (bar)	P_{vp} (bar)	Z	n_{gas} (moles)	n_{liq} (moles)	% in liquid phase	vol. in reactor (cm³)
BIP	315	159	3.2	0.91	4.27E-5	1.90E-5	98	0.37
	335	164	4.4	0.90	5.76E-5	1.89E-5	97	0.38
	355	169	5.9	0.88	7.69E-5	1.87E-3	96	0.39
	370	173	7.3	0.86	9.49E-5	1.85E-3	95	0.39
	409	184	12.0	0.81	1.57E-4	1.79E-3	92	0.41
	450	195	19.3	0.70	2.74E-4	1.67E-3	86	0.43
	500	208	32.5	0.45	6.74E-4	1.27E-3	65	0.42
	550	222	-					
910	315	118	0.23	0.99	6.06E-6	1.45E-3	100	0.43
DMA	335	123	0.36	0.98	9.59E-6	1.44E-3	99	0.43
	355	127	0.54	0.96	1.48E-5	1.44E-3	99	0.44
	370	130	0.72	0.95	2.00E-5	1.43E-3	99	0.45
	409	137	1.42	0.92	4.07E-3	1.41E-3	97	0.46
9MA	315	127	0.37	0.98	9.88E-6	1.44E-3	99	0.39
	335	131	0.56	0.96	1.53E-5	1.44E-3	99	0.40
	355	136	0.82	0.95	2.27E-5	1.43E-3	98	0.40
	370	139	1.07	0.94	3.01E-5	1.42E-3	98	0.41
	409	147	2.02	0.92	5.80E-5	1.40E-3	96	0.42
14	370	171	4.7	0.88	1.40E-4	1.31E-3	90	0.35
DMN	409	181	7.8	0.82	2.50E-4	1.20E-3	83	0.34
	450	192	12.5	0.75	4.42E-4	1.01E-3	70	0.32
	500	206	31.4	0.47	1.20E-3	2.53E-4	17	0.11
	550	219	-					

910DMA THERMOLYSIS - 315°C - 0.82 mol/l - TRIAL #1 - 6/25/90

[910DMA]o	0.825	0.830	0.828	0.827	0.827	0.825	0.822	0.822
Time(s)	450	900	1800	3600	7200	14400	28800	57600
X	0.0341	0.0340	0.0584	0.0589	0.0645	0.0657	0.1025	0.1038
-ln(1-X)/t	7.71e-05	3.84e-05	3.34e-05	1.69e-05	9.26e-06	4.72e-06	3.75e-06	1.90e-06
log keff	-4.1129	-4.4153	-4.4759	-4.7731	-5.0334	-5.3261	-5.4254	-5.7206

ID	RRF	MOLES	MOLES	MOLES	MOLES	MOLES	MOLES	MOLES	MOLES
BIP	1.0000	1.29e-03	1.29e-03	1.28e-03	1.29e-03	1.28e-03	1.28e-03	1.28e-03	1.29e-03
c-DHDMA	1.3333					5.45e-07	8.14e-07	8.77e-07	1.81e-06
DHMA	1.2500								8.51e-07
t-DHDMA	1.3333					8.77e-07	9.37e-07	1.15e-06	7.35e-07
ANTHR	1.1904								1.75e-06
9MA	1.2586	5.07e-06	5.97e-06	5.88e-06	6.74e-06	8.08e-06	1.09e-05	1.71e-05	2.57e-05
DMA	1.3333								1.72e-06
DMA	1.3333								9.22e-07
19DMA	1.3333								3.09e-07
110DMA	1.3333					5.03e-07	7.23e-07	8.08e-07	1.81e-06
910DMA	1.3239	4.78e-04	4.81e-04	4.68e-04	4.67e-04	4.64e-04	4.62e-04	4.43e-04	4.42e-04
TMA	1.4167								2.16e-06
TMA	1.4167					4.93e-07	1.50e-06	2.51e-06	6.31e-06
TMA	1.4167								1.65e-06

MATERIAL BALANCE ON:

wt %C	0.976	0.977	0.953	0.954	0.956	0.963	0.941	0.987
wt %H	0.975	0.976	0.952	0.953	0.955	0.962	0.940	0.984
3-RING SYSTEM	0.976	0.978	0.953	0.955	0.957	0.964	0.943	0.989
METHYL GROUPS	0.971	0.972	0.948	0.948	0.949	0.955	0.928	0.969

half-life t* = 480960 s

910DMA THERMOLYSIS - 315°C - 0.82 mol/l - TRIAL #2 - 8/11/92

[910DMA]o	0.827	0.827	0.827	0.825	0.827	0.822
Time(s)	1800	3600	7200	14400	28800	57600
X	0.0628	0.0433	0.0374	0.0380	0.0494	0.1011
-ln(1-X)/t	3.60e-05	1.23e-05	5.29e-06	2.69e-06	1.76e-06	1.85e-06
log keff	-4.4433	-4.9102	-5.2762	-5.5702	-5.7547	-5.7327

ID	RRF	MOLES	MOLES	MOLES	MOLES	MOLES	MOLES
BIP	1.0000	1.29e-03	1.29e-03	1.28e-03	1.29e-03	1.28e-03	1.29e-03
c-DHDMA	1.3333	3.00e-07	5.83e-07	7.98e-07	1.11e-06	1.54e-06	1.71e-06
DHMA	1.2500		6.41e-07	1.38e-06			
t-DHDMA	1.3333		3.94e-07	4.17e-07	4.55e-07	6.21e-07	6.98e-07
ANT	1.1904		3.25e-07	5.96e-07	1.04e-06	1.49e-06	1.66e-06
9MA	1.2586	1.86e-06	2.53e-06	3.22e-06	7.24e-06	1.42e-05	2.64e-05
UNK210	1.3333		3.94e-07	8.50e-07	7.79e-07	1.09e-06	
DMA	1.3333		5.26e-07	1.74e-06	4.30e-07	1.19e-06	7.77e-07
DMA	1.3333			5.11e-07			3.12e-07
110DMA	1.3333		4.15e-07	4.95e-07	6.83e-07	1.24e-06	1.50e-06
910DMA	1.3239	4.65e-04	4.75e-04	4.78e-04	4.77e-04	4.72e-04	4.43e-04
TMA	1.4167				1.48e-06	1.83e-06	2.06e-06
TMA	1.4167			3.84e-07	1.29e-06	3.03e-06	6.33e-06
TMA	1.4167				4.65e-07	8.54e-07	1.33e-06

MATERIAL BALANCE ON:

wt %C	0.941	0.968	0.984	0.992	1.004	0.983
wt %H	0.941	0.968	0.984	0.991	1.003	0.981
3-RING SYSTEM	0.942	0.968	0.985	0.992	1.005	0.986
METHYL GROUPS	0.940	0.965	0.978	0.986	0.994	0.965

half-life t* = 260229 s

910DMA THERMOLYSIS - 335°C - 0.82 mol/l - TRIAL #1 - 6/29/90

ID	RRF								
	[910DMA]o	0.828	0.827	0.822	0.820	0.828	0.818	0.828	0.823
	Time(s)	450	900	1800	3600	7200	14400	28800	57600
	X	0.0298	0.0382	0.0407	0.0747	0.0985	0.1985	0.2567	0.4624
	-ln(1-X)/t	6.72e-05	4.33e-05	2.31e-05	2.16e-05	1.44e-05	1.54e-05	1.03e-05	1.08e-05
	log keff	-4.1724	-4.3637	-4.6367	-4.6662	-4.8416	-4.8134	-4.9871	-4.9676
		MOLES	MOLES	MOLES	MOLES	MOLES	MOLES	MOLES	MOLES
BIP	1.0000	1.28e-03	1.29e-03	1.29e-03	1.29e-03	1.28e-03	1.29e-03	1.28e-03	1.29e-03
DHMA	1.2500							4.14e-07	1.82e-06
c-DHDMA	1.3333		8.01e-07	6.28e-07	4.36e-07	5.40e-07	9.63e-07	1.88e-06	3.15e-06
DHMA	1.2500						5.63e-07		7.08e-07
t-DHDMA	1.3333				8.29e-07	1.34e-06	1.04e-06	9.58e-07	1.27e-06
ANT	1.1904						1.50e-06	1.45e-06	7.44e-06
UNK196	1.2500								4.44e-07
UNK196	1.2500								3.23e-07
2MA	1.2062								6.12e-07
1MA	1.2027								1.68e-06
9MA	1.2586	6.38e-06	6.81e-06	7.96e-06	1.08e-05	1.64e-05	3.10e-05	6.07e-05	1.08e-04
DMA	1.3333							3.12e-07	
DMA	1.3333						6.57e-06	2.87e-06	
DMA	1.3333						5.79e-06	2.67e-06	8.23e-07
29&39DMA	1.3333							8.19e-07	3.69e-06
19DMA	1.3333						4.27e-07	1.29e-06	5.39e-06
110DMA	1.3333		4.83e-07	5.99e-07	6.34e-07	7.64e-07	7.82e-07	2.65e-06	1.23e-05
910DMA	1.3239	4.82e-04	4.77e-04	4.73e-04	4.55e-04	4.48e-04	3.94e-04	3.69e-04	2.66e-04
TMA	1.4167							1.64e-06	3.03e-06
TMA	1.4167		2.79e-07	5.93e-07	1.29e-06	2.16e-06	5.14e-06	1.25e-05	2.32e-05
TMA	1.4167							8.44e-07	1.29e-06
TMA	1.4167						1.67e-06	1.98e-06	2.29e-06
TMA	1.4167						3.42e-07	4.45e-07	
MATERIAL BALANCE ON:									
wt %C		0.982	0.978	0.978	0.953	0.942	0.915	0.927	0.886
wt %H		0.981	0.977	0.977	0.951	0.941	0.911	0.920	0.872
3-RING SYSTEM		0.983	0.979	0.979	0.954	0.944	0.918	0.933	0.898
METHYL GROUPS		0.977	0.972	0.971	0.944	0.930	0.891	0.885	0.798

half-life t* = 62913 s

832

910DMA THERMOLYSIS - 335°C - 0.82 mol/l - TRIAL #2 - 8/27/92

	[910DMA]o	0.825	0.823	0.828	0.825	0.828	0.823
	Time(s)	1800	3600	7200	14400	28800	57600
	X	0.0238	0.0605	0.0905	0.1404	0.2935	0.4757
	-ln(1-X)/t	1.34e-05	1.73e-05	1.32e-05	1.05e-05	1.21e-05	1.12e-05
	log keff	-4.8735	-4.7611	-4.8802	-4.9786	-4.9185	-4.9504
ID	RRF	MOLES	MOLES	MOLES	MOLES	MOLES	MOLES
BIP	1.0000	1.28e-03	1.29e-03	1.28e-03	1.28e-03	1.29e-03	1.29e-03
DHMA	1.2500					5.52e-07	1.85e-06
c-DHDMA	1.3333	8.34e-07	9.07e-07	8.34e-07	1.16e-06	2.14e-06	3.12e-06
DHMA	1.2500				7.08e-07		1.36e-06
t-DHDMA	1.3333	4.48e-07	3.41e-07	2.90e-07	4.45e-07	8.23e-07	1.26e-06
ANT	1.1904	6.34e-07	9.85e-07	1.09e-06	1.27e-06	2.45e-06	7.92e-06
UNK196	1.2500						4.95e-06
UNK196	1.2500						3.32e-06
2MA	1.2062						5.96e-06
1MA	1.2027						1.69e-06
9MA	1.2586	4.97e-06	8.02e-06	1.20e-05	3.09e-05	6.47e-05	1.06e-04
DMA	1.3333				1.61e-06		
DMA	1.3333				6.18e-07	6.21e-07	9.33e-07
29&39DMA	1.3333					1.01e-06	3.48e-06
19DMA	1.3333					1.61e-06	5.33e-06
110DMA	1.3333	5.10e-07	6.43e-07	7.52e-07	1.97e-06	4.19e-06	1.24e-05
910DMA	1.3239	4.84e-04	4.64e-04	4.52e-04	4.26e-04	3.51e-04	2.59e-04
TMA	1.4167		3.23e-06	3.00e-06	4.09e-06	3.70e-06	3.43e-06
TMA	1.4167						1.45e-06
TMA	1.4167	5.05e-07	1.14e-06	2.13e-06	6.65e-06	1.46e-05	2.27e-05
TMA	1.4167			6.13e-07	1.62e-06	2.28e-06	2.42e-06
TMA	1.4167						5.45e-07
MATERIAL BALANCE ON:							
wt %C		0.991	0.970	0.951	0.953	0.893	0.874
wt %H		0.991	0.969	0.950	0.950	0.886	0.861
3-RING SYSTEM		0.992	0.970	0.952	0.955	0.899	0.886
METHYL GROUPS		0.986	0.965	0.943	0.942	0.850	0.787

half-life t* = 61357 s

833

910DMA THERMOLYSIS - 335°C - 0.82 mol/l - GAS TRIAL #2 - 3/5/91

[910DMA]o		0.825	0.832	0.822	0.833	0.820	0.832
Time(s)		900	1800	3600	7200	14400	28800
X		0.0024	0.0336	0.0441	0.0512	0.1479	0.1082
-ln(1-X)/t		2.67e-06	1.90e-05	1.25e-05	7.30e-06	1.11e-05	3.98e-06
log keff		-5.57351	-4.72153	-4.90211	-5.1367	-4.9541	-5.40054
ID	RRF	MOLES	MOLES	MOLES	MOLES	MOLES	MOLES
BIP	1.0000	1.29e-03	1.28e-03	1.28e-03	1.28e-03	1.28e-03	1.29e-03
c-DHDMA	1.3333		6.23e-07	6.96e-07	8.38e-07	4.35e-06	1.66e-06
t-DHDMA	1.3333	3.61e-07	7.45e-07	9.54e-07	1.37e-06	5.51e-06	2.39e-06
ANT	1.1904			4.29e-07	5.04e-07	9.91e-07	1.29e-06
9MA	1.2586	4.74e-06	5.53e-06	7.72e-06	1.37e-05	3.78e-05	4.96e-05
UNK210	1.3333	5.88e-07					
DMA	1.3333					1.00e-06	7.92e-07
110DMA	1.3333	3.61e-07	3.55e-07	4.47e-07	5.92e-07	2.93e-06	2.97e-06
910DMA	1.3239	4.94e-04	4.82e-04	4.72e-04	4.74e-04	4.19e-04	4.45e-04
TMA	1.4167					7.30e-06	1.03e-05
TMA	1.4167		3.29e-07	6.81e-07	1.46e-06	2.11e-06	2.50e-06
CH4	-					3.12e-05	3.25e-06
MATERIAL BALANCE ON:							
wt %C		1.009	0.981	0.977	0.984	0.978	1.031
wt %H		1.009	0.981	0.976	0.983	0.990	1.027
3-RING SYSTEM		1.010	0.982	0.978	0.986	0.978	1.035
METHYL GROUPS		1.005	0.976	0.970	0.972	0.979	0.999

half-life t* = 62069 s

910DMA THERMOLYSIS - 335°C - 0.82 mol/l - GAS TRIAL #3 - 3/11/91

[910DMA]o		0.823	0.828	0.822	0.828	0.827	0.827
Time(s)		900	1800	3600	7200	14400	28800
X		0.0124	0.0531	0.0694	0.1059	0.1835	0.3396
-ln(1-X)/t		1.39e-05	3.03e-05	2.00e-05	1.55e-05	1.41e-05	1.44e-05
log keff		-4.85811	-4.51838	-4.69942	-4.80836	-4.85145	-4.84144
ID	RRF	MOLES	MOLES	MOLES	MOLES	MOLES	MOLES
BIP	1.0000	1.29e-03	1.28e-03	1.28e-03	1.29e-03	1.28e-03	1.29e-03
DHMA	1.2500						1.26e-06
c-DHDMA	1.3333	3.18e-07	7.23e-07	1.13e-06	2.11e-06	3.77e-06	4.55e-06
DHMA	1.2500						3.98e-07
t-DHDMA	1.3333	3.68e-07	9.12e-07	1.08e-06	2.95e-06	4.17e-06	4.37e-06
ANT	1.1904				6.60e-06	9.71e-07	3.27e-06
9MA	1.2586	4.50e-06	3.96e-06	6.21e-06	1.72e-05	3.12e-05	7.06e-05
DMA	1.3333				5.59e-07	5.04e-07	7.67e-07
19DMA	1.3333						2.92e-06
110DMA	1.3333			3.70e-07	7.65e-07	1.80e-06	5.74e-06
910DMA	1.3239	4.88e-04	4.71e-04	4.58e-04	4.44e-04	4.05e-04	3.28e-04
TMA	1.4167					5.77e-06	1.45e-05
TMA	1.4167			8.97e-07	2.67e-06	1.73e-06	1.92e-06
CH4	-		1.24e-06	6.78e-07	8.11e-07	2.60e-05	4.38e-05
C2H6	-						1.43e-06
MATERIAL BALANCE ON:							
wt %C		0.998	0.958	0.950	0.946	0.917	0.878
wt %H		0.997	0.958	0.950	0.946	0.927	0.892
3-RING SYSTEM		0.998	0.958	0.950	0.948	0.916	0.883
METHYL GROUPS		0.994	0.956	0.946	0.933	0.916	0.867

half-life t* = 66426 s

910DMA THERMOLYSIS - 335°C - 0.82 mol/l - GAS TRIAL #4 - 4/3/91

ID	RRF	MOLES	MOLES	MOLES	MOLES	MOLES	MOLES
[910DMA]o		0.825	0.825	0.828	0.828	0.828	0.827
Time(s)		900	1800	3600	7200	14400	28800
X		0.0145	0.0378	0.0540	0.1072	0.2010	0.3244
-ln(1-X)/t		1.62e-05	2.14e-05	1.54e-05	1.57e-05	1.56e-05	1.36e-05
log keff		-4.78971	-4.66944	-4.81191	-4.80275	-4.80735	-4.86594
BIP	1.0000	1.28e-03	1.28e-03	1.28e-03	1.29e-03	1.29e-03	1.29e-03
DHMA	1.2500					4.61e-07	1.70e-06
c-DHDMA	1.3333	5.78e-07	1.28e-06	1.44e-06	2.56e-06	3.91e-06	5.55e-06
DHMA	1.2500					6.53e-07	9.09e-07
t-DHDMA	1.3333	4.82e-07	7.64e-07	7.35e-07	1.18e-06	1.71e-06	2.35e-06
ANT	1.1904	3.94e-07	7.02e-07	1.11e-06	2.27e-06	3.24e-06	5.72e-06
UNK196	1.2500						5.09e-07
UNK196	1.2500						5.00e-07
2MA	1.2062						2.84e-07
1MA	1.2027						3.58e-07
9MA	1.2586	4.85e-06	6.37e-06	9.29e-06	1.89e-05	3.63e-05	7.87e-05
UNK210	1.3333					5.44e-07	
DMA	1.3333				6.59e-07	9.98e-07	1.13e-06
29&39DMA	1.3333						1.76e-06
19DMA	1.3333					6.07e-07	2.96e-06
110DMA	1.3333	3.46e-07	6.07e-07	7.06e-07	1.04e-06	1.54e-06	5.59e-06
910DMA	1.3239	4.88e-04	4.76e-04	4.70e-04	4.44e-04	3.97e-04	3.35e-04
TMA	1.4167			1.46e-06	1.79e-06	2.41e-06	2.83e-06
TMA	1.4167		3.78e-07	1.01e-06	3.30e-06	7.86e-06	1.73e-05
TMA	1.4167				3.67e-07	6.57e-07	9.86e-07
TMA	1.4167			3.49e-07	9.98e-07	2.00e-06	2.43e-06
TMA	1.4167						7.34e-07
CH4	-		1.02e-06	3.15e-06	1.02e-05	2.09e-05	6.33e-05
C2H4	-						5.07e-07
C2H6	-						2.29e-06
MATERIAL BALANCE ON:							
wt %C		0.999	0.982	0.977	0.959	0.924	0.943
wt %H		0.999	0.982	0.978	0.961	0.931	0.965
3-RING SYSTEM		0.999	0.983	0.978	0.959	0.926	0.943
METHYL GROUPS		0.993	0.976	0.973	0.947	0.915	0.942

half-life t* = 62088 s

910DMA THERMOLYSIS - 355°C - 0.082 mol/l - TRIAL #1 - 5/1/90

	[910DMA]o	0.083	0.081	0.081	0.082	0.082	0.082
	Time(s)	1800	3600	7200	14400	28800	57600
	X	0.0689	0.0924	0.0883	0.1963	0.2018	0.3944
	-ln(1-X)/t	3.97e-05	2.69e-05	1.28e-05	1.52e-05	7.83e-06	8.71e-06
	log keff	-4.4016	-4.5697	-4.8915	-4.8189	-5.1064	-5.0601
ID	RRF	MOLES	MOLES	MOLES	MOLES	MOLES	MOLES
BIP	1.0000	1.88e-03	1.88e-03	1.88e-03	1.88e-03	1.88e-03	1.88e-03
ANT	1.1904						4.22e-07
9MA	1.2586			3.73e-06	4.61e-06	8.88e-06	9.88e-06
910DMA	1.3239	4.65e-05	4.40e-05	4.42e-05	3.94e-05	3.91e-05	2.97e-05
TMA	1.4167						6.13e-07
MATERIAL BALANCE ON:							
wt %C		0.931	0.908	0.984	0.892	0.968	0.815
wt %H		0.931	0.908	0.977	0.884	0.954	0.799
3-RING SYSTEM		0.931	0.908	0.989	0.898	0.980	0.828
METHYL GROUPS		0.931	0.908	0.950	0.851	0.889	0.725

half-life t* = 73532 s

910DMA THERMOLYSIS - 355°C - 0.082 mol/l - TRIAL #3 - 6/14/90

	[910DMA]o	0.082	0.084	0.088	0.088	0.085
	Time(s)	1800	3600	7200	14400	28800
	X	0.2425	0.2220	0.2652	0.3315	0.3789
	-ln(1-X)/t	1.54e-04	6.97e-05	4.28e-05	2.80e-05	1.65e-05
	log keff	-3.8116	-4.1566	-4.3686	-4.5534	-4.7815
ID	RRF	MOLES	MOLES	MOLES	MOLES	MOLES
BIP	1.0000	1.88e-03	1.88e-03	1.88e-03	1.88e-03	1.88e-03
9MA	1.2586			1.62e-06	3.18e-06	8.15e-06
910DMA	1.3239	3.75e-05	3.92e-05	3.88e-05	3.53e-05	3.16e-05
MATERIAL BALANCE ON:						
wt %C		0.758	0.778	0.762	0.725	0.771
wt %H		0.758	0.778	0.761	0.720	0.758
3-RING SYSTEM		0.758	0.778	0.765	0.729	0.781
METHYL GROUPS		0.758	0.778	0.750	0.699	0.701

910DMA THERMOLYSIS - 355°C - 0.082 mol/l - TRIAL #4 - 6/22/90

[910DMA]o		0.087	0.082	0.082	0.083	0.085	0.083
Time(s)		1800	3600	7200	14400	28800	57600
X		0.2886	0.2995	0.2121	0.2848	0.3789	0.4008
-ln(1-X)/t		1.89e-04	9.89e-05	3.31e-05	2.33e-05	1.65e-05	8.89e-06
log keff		-3.7231	-4.0049	-4.4801	-4.6331	-4.7815	-5.0510
ID	RRF	MOLES	MOLES	MOLES	MOLES	MOLES	MOLES
BIP	1.0000	1.88e-03	1.88e-03	1.88e-03	1.88e-03	1.88e-03	1.88e-03
ANT	1.1904						9.01e-07
1MA	1.2026						8.71e-07
9MA	1.2586			1.67e-06	3.42e-06	8.15e-06	1.52e-05
29&39DMA	1.3333						4.53e-07
19DMA	1.3333						3.43e-07
110DMA	1.3333						6.77e-07
910DMA	1.3239	3.69e-05	3.43e-05	3.86e-05	3.57e-05	3.16e-05	2.99e-05
TMA	1.4167						3.30e-07
TMA	1.4167						1.17e-06
MATERIAL BALANCE ON:							
wt %C		0.711	0.701	0.818	0.779	0.771	0.979
wt %H		0.711	0.701	0.817	0.774	0.758	0.953
3-RING SYSTEM		0.711	0.701	0.822	0.784	0.781	1.000
METHYL GROUPS		0.711	0.701	0.805	0.750	0.701	0.835

910DMA THERMOLYSIS - 355°C - 0.082 mol/l - TRIAL #5 - 9/11/92

[910DMA]o		0.083	0.080	0.085	0.083	0.084	0.084
Time(s)		1800	3600	7200	14400	28800	57600
X		0.0730	0.0118	0.0240	0.1206	0.3414	0.5641
-ln(1-X)/t		4.21e-05	3.30e-06	3.37e-06	8.92e-06	1.45e-05	1.44e-05
log keff		-4.3756	-5.4818	-5.4719	-5.0494	-4.8386	-4.8412
ID	RRF	MOLES	MOLES	MOLES	MOLES	MOLES	MOLES
BIP	1.0000	1.88e-03	1.88e-03	1.88e-03	1.88e-03	1.88e-03	1.88e-03
c-DHDMA	1.3333	3.21e-07			3.90e-07	2.87e-07	4.85e-07
ANT	1.1904					5.03e-07	1.63e-06
9MA	1.2586	1.34e-06	1.82e-06	2.72e-06	4.26e-06	1.19e-05	1.83e-05
29&39DMA	1.3333						6.85e-07
19DMA	1.3333						6.70e-07
110DMA	1.3333					4.61e-07	1.29e-06
910DMA	1.3239	4.63e-05	4.74e-05	4.97e-05	4.39e-05	3.32e-05	2.20e-05
TMA	1.4167	6.86e-07	9.92e-07		2.71e-07	1.00e-06	1.51e-06
MATERIAL BALANCE ON:							
wt %C		0.973	1.047	1.026	0.973	0.925	0.914
wt %H		0.969	1.044	1.022	0.968	0.906	0.882
3-RING SYSTEM		0.974	1.047	1.030	0.978	0.939	0.940
METHYL GROUPS		0.967	1.038	1.003	0.938	0.821	0.733

half-life t* = 51171 s

910DMA THERMOLYSIS - 355°C - 0.082 mol/l - TRIAL #6 - 10/1/92

	[910DMA]o	0.086	0.082	0.082	0.084	0.083	0.084
	Time(s)	1800	3600	7200	14400	28800	57600
	X	0.0786	0.1078	0.1033	0.2292	0.2493	0.5702
	-ln(1-X)/t	4.55e-05	3.17e-05	1.51e-05	1.81e-05	9.96e-06	1.47e-05
	log keff	-4.3422	-4.4992	-4.8198	-4.7428	-5.0019	-4.8339
ID	RRF	MOLES	MOLES	MOLES	MOLES	MOLES	MOLES
BIP	1.0000	1.88e-03	1.88e-03	1.88e-03	1.88e-03	1.88e-03	1.88e-03
c-DHDMA	1.3333				4.83e-07	3.34e-07	
ANT	1.1904						1.18e-06
9MA	1.2586	5.17e-07	8.27e-07	1.94e-06	5.73e-06	6.54e-06	1.53e-05
29&39DMA	1.3333						4.76e-07
19DMA	1.3333						4.63e-07
110DMA	1.3333						1.17e-06
910DMA	1.3239	4.74e-05	4.37e-05	4.39e-05	3.89e-05	3.75e-05	2.17e-05
TMA	1.4167					4.22e-07	
TMA	1.4167				4.65e-07	5.25e-07	1.18e-06
MATERIAL BALANCE ON:							
wt %C		0.931	0.908	0.931	0.890	0.892	0.802
wt %H		0.930	0.907	0.931	0.890	0.892	0.823
3-RING SYSTEM		0.931	0.909	0.936	0.903	0.907	0.823
METHYL GROUPS		0.926	0.901	0.897	0.794	0.851	0.682

half-life t* = 52496 s

910DMA THERMOLYSIS - 355°C - 0.25 mol/l - TRIAL #1 - 4/19/90

	[910DMA]o	0.247	0.248	0.248	0.248	0.248	0.250
	Time(s)	900	3600	7200	14400	28800	57600
	X	0.0106	0.0445	0.0655	0.2261	0.4360	0.5943
	-ln(1-X)/t	1.18e-05	1.26e-05	9.41e-06	1.78e-05	1.99e-05	1.57e-05
	log keff	-4.9266	-4.8981	-5.0265	-4.7496	-4.7015	-4.8051
ID	RRF	MOLES	MOLES	MOLES	MOLES	MOLES	MOLES
BIP	1.0000	1.75e-03	1.76e-03	1.76e-03	1.75e-03	1.75e-03	1.75e-03
ANT	1.1904					2.05e-06	4.76e-06
9MA	1.2586	3.22e-06	6.32e-06	1.09e-05	2.28e-05	3.49e-05	5.16e-05
29&39DMA	1.3333						2.66e-06
19DMA	1.3333						2.86e-06
110DMA	1.3333					2.42e-06	4.68e-06
910DMA	1.3239	1.46e-04	1.43e-04	1.40e-04	1.15e-04	8.38e-05	6.10e-05
TMA	1.4167				1.80e-06	3.47e-06	7.17e-06
MATERIAL BALANCE ON:							
wt %C		1.010	0.995	1.003	0.930	0.834	0.874
wt %H		1.008	0.992	0.997	0.919	0.815	0.845
3-RING SYSTEM		1.012	0.998	1.008	0.939	0.848	0.896
METHYL GROUPS		1.000	0.977	0.971	0.869	0.730	0.717

half-life t* = 40547

910DMA THERMOLYSIS - 355°C - 0.25 mol/l - TRIAL #2 - 5/8/90

[910DMA]o		0.245	0.245	0.243	0.247	0.250	0.247	0.248	0.245
Time(s)		450	900	1800	3600	7200	14400	28800	57600
X		0.0848	0.0880	0.1512	0.1703	0.2425	0.3305	0.3367	0.6152
-ln(1-X)/t		1.97e-04	1.02e-04	9.11e-05	5.19e-05	3.86e-05	2.79e-05	1.43e-05	1.66e-05
log keff		-3.7057	-3.9899	-4.0406	-4.2852	-4.4137	-4.5550	-4.8460	-4.7804
ID	RRF	MOLES	MOLES	MOLES	MOLES	MOLES	MOLES	MOLES	MOLES
BIP	1.0000	1.75e-03	1.75e-03	1.75e-03	1.74e-03	1.75e-03	1.75e-03	1.75e-03	1.75e-03
ANT	1.1904								6.27e-06
1MA	1.2027								2.16e-06
9MA	1.2586	1.64e-06	1.93e-06	3.71e-06	4.32e-06	1.31e-05	1.81e-05	3.51e-05	5.49e-05
29&39DMA	1.3333								3.00e-06
19DMA	1.3333								3.35e-06
110DMA	1.3333							1.97e-06	5.37e-06
910DMA	1.3239	1.35e-04	1.34e-04	1.24e-04	1.23e-04	1.13e-04	9.90e-05	9.87e-05	5.67e-05
TMA	1.4167							5.31e-06	7.24e-06
MATERIAL BALANCE ON:									
wt %C		0.926	0.924	0.873	0.857	0.839	0.784	0.936	0.936
wt %H		0.925	0.923	0.871	0.855	0.832	0.774	0.920	0.920
3-RING SYSTEM		0.926	0.925	0.874	0.859	0.845	0.792	0.948	0.948
METHYL GROUPS		0.921	0.919	0.862	0.844	0.801	0.731	0.848	0.848

half-life t* = 45394

910DMA THERMOLYSIS - 355°C - 0.25 mol/l - TRIAL #3 - 5/28/90

[910DMA]o		0.250	0.250	0.243	0.252	0.243	0.247	0.247	0.248
Time(s)		450	900	1800	3600	7200	14400	28800	57600
X		0.0631	0.0634	0.0733	0.1036	0.1513	0.2370	0.4417	0.5703
-ln(1-X)/t		1.45e-04	7.28e-05	4.23e-05	3.04e-05	2.28e-05	1.88e-05	2.02e-05	1.47e-05
log keff		-3.8391	-4.1380	-4.3737	-4.5174	-4.6424	-4.7262	-4.6938	-4.8337
ID	RRF	MOLES	MOLES	MOLES	MOLES	MOLES	MOLES	MOLES	MOLES
BIP	1.0000	1.74e-03	1.75e-03	1.75e-03	1.75e-03	1.75e-03	1.75e-03	1.75e-03	1.75e-03
c-DHDMA	1.3333		2.55e-07			3.31e-07	4.03e-07		2.65e-07
ANT	1.1904						4.38e-07	1.77e-06	4.39e-06
9MA	1.2586	1.85e-06	2.31e-06	3.05e-06	4.81e-06	8.02e-06	1.77e-05	3.49e-05	4.87e-05
29&39DMA	1.3333							8.88e-07	2.06e-06
19DMA	1.3333							1.04e-06	2.72e-06
110DMA	1.3333						5.36e-07	2.05e-06	4.79e-06
910DMA	1.3239	1.40e-04	1.40e-04	1.35e-04	1.35e-04	1.24e-04	1.13e-04	8.28e-05	6.42e-05
TMA	1.4167					9.64e-07	1.28e-06	1.35e-06	
TMA	1.4167					7.71e-07	2.22e-06	4.73e-06	6.56e-06
MATERIAL BALANCE ON:									
wt %C		0.949	0.953	0.946	0.926	0.915	0.910	0.860	0.873
wt %H		0.948	0.952	0.945	0.924	0.912	0.902	0.842	0.845
3-RING SYSTEM		0.949	0.954	0.948	0.928	0.918	0.916	0.873	0.894
METHYL GROUPS		0.943	0.946	0.937	0.912	0.896	0.865	0.764	0.724

half-life t* = 41652 s

910DMA THERMOLYSIS - 355°C - 0.25 mol/l - TRIAL #5 - 10/1/92

	[910DMA]o	0.245	0.247	0.250	0.248	0.250
	Time(s)	3600	7200	14400	28800	57600
	X	0.0291	0.0726	0.1189	0.3745	0.5765
	$-\ln(1-X)/t$	8.20e-06	1.05e-05	8.79e-06	1.63e-05	1.49e-05
	log keff	-5.0860	-4.9801	-5.0560	-4.7880	-4.8263
ID	RRF	MOLES	MOLES	MOLES	MOLES	MOLES
BIP	1.0000	1.75e-03	1.75e-03	1.75e-03	1.75e-03	1.75e-03
c-DHDMA	1.3333	3.13e-07	3.87e-07	3.48e-07	3.94e-07	2.54e-07
ANT	1.1904				1.59e-06	4.44e-06
2MA	1.2027					4.82e-07
1MA	1.2062					1.13e-06
9MA	1.2586	4.22e-06	7.51e-06	1.24e-05	3.43e-05	4.87e-05
UNK210	1.3333			4.67e-07	1.18e-06	1.34e-06
DMA	1.3333				4.53e-07	6.86e-07
29&39DMA	1.3333				1.07e-06	2.34e-06
19DMA	1.3333				1.17e-06	2.77e-06
110DMA	1.3333			3.15e-07	2.15e-06	4.68e-06
910DMA	1.3239	1.43e-04	1.37e-04	1.32e-04	9.34e-05	6.36e-05
TMA	1.4167		9.70e-07	1.07e-06	1.31e-06	7.92e-07
TMA	1.4167		7.97e-07	1.74e-06	5.73e-06	6.75e-06
TMA	1.4167					8.38e-07

MATERIAL BALANCE ON:

wt %C	1.000	0.990	0.986	0.941	0.903
wt %H	0.998	0.988	0.982	0.927	0.878
3-RING SYSTEM	1.002	0.993	0.990	0.953	0.924
METHYL GROUPS	0.987	0.973	0.958	0.850	0.755

half-life t* = 47066 s

910DMA THERMOLYSIS - 355°C - 0.82 mol/l - TRIAL #1 - 3/26/90

ID	RRF	MOLES	MOLES	MOLES	MOLES	MOLES	MOLES	MOLES
	[910DMA]o	0.830	0.830	0.832	0.818	0.830	0.835	0.825
	Time(s)	450	900	1800	3600	7200	14400	28800
	X	0.0589	0.0922	0.1658	0.1903	0.3884	0.6190	0.7349
	-ln(1-X)/t	1.35e-04	1.07e-04	1.01e-04	5.86e-05	6.83e-05	6.70e-05	4.61e-05
	log keff	-3.8700	-3.9687	-3.9969	-4.2318	-4.1657	-4.1739	-4.3363
BIP	1.0000	1.29e-03	1.28e-03	1.29e-03	1.29e-03	1.29e-03	1.28e-03	1.29e-03
DHMA	1.2500						1.63e-06	2.90e-06
c-DHDMA	1.3333					1.58e-06	2.10e-06	2.20e-06
DHMA	1.2500				1.93e-06	4.19e-06	3.24e-06	4.07e-06
t-DHDMA	1.3333					1.27e-06	1.68e-06	1.90e-06
ANT	1.1904				2.02e-06	2.13e-06	1.16e-05	1.90e-05
UNK196	1.2500					1.36e-06		1.79e-06
2MA	1.2062						1.39e-06	3.28e-06
1MA	1.2027						2.36e-06	5.96e-06
9MA	1.2586	1.51e-05	2.11e-05	2.91e-05	5.16e-05	7.91e-05	1.24e-04	1.47e-04
UNK210	1.3333				3.18e-06	3.95e-06	3.67e-06	4.88e-06
DMA	1.3333				5.70e-06	1.25e-06	1.36e-06	1.70e-06
DMA	1.3333				1.35e-06	8.49e-06	7.42e-06	7.87e-06
DMA	1.3333				1.18e-05	1.33e-05	1.10e-05	1.23e-05
DMA	1.3333					2.41e-06	1.42e-06	
29&39DMA	1.3333					1.25e-06	5.36e-06	9.37e-06
19DMA	1.3333				2.73e-06	8.09e-06	8.78e-06	1.13e-05
110DMA	1.3333				3.50e-06	5.23e-06	1.25e-05	1.92e-05
910DMA	1.3239	4.69e-04	4.52e-04	4.17e-04	3.97e-04	3.05e-04	1.91e-04	1.31e-04
TMA	1.4167				2.95e-06	7.46e-06	5.17e-06	5.52e-06
TMA	1.4167				1.59e-06	1.26e-05	1.85e-05	2.66e-06
TMA	1.4167				5.23e-06	1.34e-06	1.31e-06	1.86e-05
TMA	1.4167			2.07e-06	1.55e-06			

MATERIAL BALANCE ON:

wt %C		0.970	0.948	0.893	0.998	0.932	0.824	0.825
wt %H		0.967	0.944	0.889	0.993	0.929	0.809	0.805
3-RING SYSTEM		0.971	0.950	0.897	1.004	0.938	0.839	0.846
METHYL GROUPS		0.956	0.929	0.870	0.958	0.886	0.717	0.677

half-life t* = 10863 s

910DMA THERMOLYSIS - 355°C - 0.82 mol/l - TRIAL #2 - 3/28/90

	[910DMA]o	0.828	0.818	0.828	0.835	0.837	0.817	0.822
	Time(s)	450	900	1800	3600	7200	14400	28800
	X	0.0610	0.0941	0.0906	0.1639	0.4299	0.6075	0.6932
	-ln(1-X)/t	1.40e-04	1.10e-04	5.28e-05	4.97e-05	7.80e-05	6.49e-05	4.10e-05
	log keff	-3.8543	-3.9594	-4.2777	-4.3034	-4.1076	-4.1874	-4.3869
ID	**RRF**	**MOLES**	**MOLES**	**MOLES**	**MOLES**	**MOLES**	**MOLES**	**MOLES**
BIP	1.0000	1.29e-03	1.30e-03	1.29e-03	1.28e-03	1.28e-03	1.30e-03	1.28e-03
DHMA	1.2500						1.41e-06	3.12e-06
c-DHDMA	1.3333				1.53e-06	1.74e-06	2.33e-06	2.08e-06
DHMA	1.2500				1.82e-06	6.73e-06	4.51e-06	
t-DHDMA	1.3333		2.34e-06	2.26e-06	1.71e-06	1.85e-06	2.02e-06	
DHDMA	1.3333					1.79e-06		
ANT	1.1904				1.54e-06	3.19e-06	9.00e-06	2.25e-05
UNK196	1.2500						1.44e-06	
2MA	1.2062						1.79e-06	3.52e-06
1MA	1.2027						2.39e-06	7.66e-06
9MA	1.2586	1.53e-05	1.75e-05	2.61e-05	5.99e-05	8.20e-05	1.12e-04	1.65e-04
UNK210	1.3333				1.39e-06	6.03e-06	3.41e-06	
DMA	1.3333						1.39e-06	
DMA	1.3333						2.00e-06	
DMA	1.3333				3.91e-06		1.24e-06	
DMA	1.3333				6.89e-06	9.12e-06	1.79e-05	
DMA	1.3333					1.66e-05	2.24e-05	
DMA	1.3333						3.27e-06	
29&39DMA	1.3333					3.73e-06	4.82e-06	9.54e-06
19DMA	1.3333					1.67e-06	5.14e-06	1.34e-05
110DMA	1.3333				7.11e-06	1.06e-05	1.40e-05	2.29e-05
910DMA	1.3239	4.67e-04	4.45e-04	4.52e-04	4.19e-04	2.86e-04	2.66e-04	1.51e-04
TMA	1.4167				2.43e-06	7.44e-06	6.21e-06	7.02e-06
TMA	1.4167					1.34e-05	2.03e-06	3.70e-06
TMA	1.4167						1.65e-05	6.12e-06
TMA	1.4167				9.75e-06	1.38e-06	1.23e-06	2.54e-05
TMA	1.4167			1.97e-06	3.47e-06		2.01e-06	3.11e-06

MATERIAL BALANCE ON:

wt %C		0.968	0.944	0.967	1.033	0.915	0.907	0.884
wt %H		0.966	0.942	0.962	1.027	0.913	0.899	0.856
3-RING SYSTEM		0.970	0.946	0.970	1.039	0.922	0.918	0.906
METHYL GROUPS		0.954	0.929	0.946	0.990	0.868	0.817	0.725

half-life t* = 10187 s

910DMA THERMOLYSIS - 355°C - 0.82 mol/l - TRIAL #3 - 7/21/92

	[910DMA]o	0.823	0.827	0.820	0.822	0.825	0.825	0.823
	Time(s)	450	900	1800	3600	7200	14400	28800
	X	0.0462	0.0347	0.0548	0.0989	0.1517	0.3117	0.5782
	$-\ln(1-X)/t$	1.05e-04	3.92e-05	3.13e-05	2.89e-05	2.29e-05	2.59e-05	3.00e-05
	log keff	-3.9783	-4.4063	-4.5043	-4.5387	-4.6411	-4.5860	-4.5233
ID	RRF	MOLES	MOLES	MOLES	MOLES	MOLES	MOLES	MOLES
BIP	1.0000	1.29e-03	1.28e-03	1.29e-03	1.29e-03	1.28e-03	1.28e-03	1.29e-03
DHMA	1.2500							2.54e-06
c-DHDMA	1.3333					1.53e-06	1.92e-06	2.46e-06
ANT	1.1904						3.91e-06	1.54e-05
2MA	1.2062							2.09e-06
1MA	1.2027							4.39e-06
9MA	1.2586	3.16e-06	6.98e-06	1.10e-05	2.12e-05	4.82e-05	8.39e-05	1.46e-04
UNK210	1.3333					2.94e-06	3.64e-06	1.71e-06
29&39DMA	1.3333						2.10e-06	8.70e-06
19DMA	1.3333						2.80e-06	1.04e-05
110DMA	1.3333					2.79e-07	5.28e-05	1.74e-05
910DMA	1.3239	4.72e-04	4.79e-04	4.65e-04	4.44e-04	4.20e-04	3.41e-04	2.09e-04
TMA	1.4167					3.65e-06	2.34e-06	1.82e-06
TMA	1.4167							1.97e-06
TMA	1.4167			1.72e-06	3.73e-06	9.91e-06	1.82e-05	2.74e-05
TMA	1.4167					1.48e-06	1.96e-06	1.88e-06
MATERIAL BALANCE ON:								
wt %C		0.960	0.979	0.970	0.950	0.987	0.930	0.897
wt %H		0.959	0.977	0.968	0.947	0.983	0.921	0.874
3-RING SYSTEM		0.960	0.979	0.971	0.952	0.991	0.939	0.911
METHYL GROUPS		0.957	0.972	0.962	0.934	0.957	0.869	0.761

half-life $t^* = 24655$ s

910DMA THERMOLYSIS - 355°C - 0.82 mol/l - TRIAL #4 - 10/8/92

	[910DMA]o	0.825	0.827	0.827	0.822	0.822	0.825	0.822
	Time(s)	450	900	1800	3600	7200	14400	28800
	X	0.0180	0.0286	0.0663	0.1124	0.1608	0.3977	0.6777
	$-\ln(1-X)/t$	4.04e-05	3.22e-05	3.81e-05	3.31e-05	2.43e-05	3.52e-05	3.93e-05
	log keff	-4.3940	-4.4916	-4.4189	-4.4799	-4.6135	-4.4534	-4.4054
ID	RRF	MOLES	MOLES	MOLES	MOLES	MOLES	MOLES	MOLES
BIP	1.0000	1.29e-03	1.28e-03	1.29e-03	1.28e-03	1.28e-03	1.28e-03	1.28e-03
DHA	1.1667							3.91e-07
DHMA	1.2500						9.32e-07	2.96e-06
c-DHDMA	1.3333	3.95e-07	6.66e-07	9.49e-07	1.04e-06	1.04e-06	2.20e-06	2.31e-06
t-DHDMA	1.3333	2.90e-07	3.27e-07	3.42e-07	4.69e-06	4.19e-07	1.07e-06	1.03e-06
ANT	1.1904	6.85e-07	6.51e-07	7.73e-07	7.84e-07	1.06e-06	4.24e-06	1.68e-05
2MA	1.2062						7.06e-07	2.92e-06
1MA	1.2027			3.82e-07	6.68e-07	6.74e-07	1.08e-06	7.20e-06
9MA	1.2586	2.88e-06	4.68e-06	1.34e-05	2.74e-05	3.52e-05	9.34e-05	1.39e-04
UNK210	1.3333	4.87e-07	4.75e-07	7.63e-07	3.17e-06	1.36e-06	2.34e-06	1.37e-06
DMA	1.3333			3.11e-07	3.70e-07	4.99e-07	8.73e-07	8.72e-07
DMA	1.3333				3.40e-06	6.85e-07	9.27e-07	1.10e-06
29&39DMA	1.3333					6.85e-07	2.76e-06	1.01e-05
19DMA	1.3333					7.73e-07	3.71e-06	1.20e-05
110DMA	1.3333		6.19e-07	1.11e-06	1.72e-06	2.11e-06	8.10e-06	2.16e-05
910DMA	1.3239	4.86e-04	4.81e-04	4.63e-04	4.38e-04	4.14e-04	2.98e-04	1.59e-04
TMA	1.4167			2.41e-06	4.30e-06	3.77e-06	2.93e-06	2.62e-06
TMA	1.4167							2.62e-06
TMA	1.4167		4.45e-07	2.02e-06	4.86e-06	7.44e-06	2.01e-05	2.56e-05
TMA	1.4167						3.06e-07	9.98e-07
TMA	1.4167			6.06e-07	1.01e-06	1.45e-06	2.04e-06	1.39e-06
TMA	1.4167						3.92e-07	9.75e-07
MATERIAL BALANCE ON:								
wt %C		0.991	0.986	0.979	0.993	1.016	0.891	0.827
wt %H		0.991	0.986	0.978	0.994	1.013	0.881	0.805
3-RING SYSTEM		0.992	0.987	0.980	0.996	1.020	0.901	0.846
METHYL GROUPS		0.987	0.982	0.970	0.976	0.992	0.826	0.694

half-life t* = 19169 s

910DMA THERMOLYSIS - 355°C - 2.06 mol/l - TRIAL #1 - 4/15/90

	[910DMA]o	2.050	2.067	2.050	2.050	2.067	2.067	2.050
	Time(s)	450	900	1800	3600	7200	14400	21600
	X	0.0871	0.1115	0.0992	0.2061	0.3958	0.6580	0.7767
	-ln(1-X)/t	2.03e-04	1.31e-04	5.80e-05	6.41e-05	7.00e-05	7.45e-05	6.94e-05
	log keff	-3.6936	-3.8815	-4.2363	-4.1931	-4.1550	-4.1278	-4.1586
ID	RRF	MOLES	MOLES	MOLES	MOLES	MOLES	MOLES	MOLES
BIP	1.0000	2.89e-04	2.90e-04	2.97e-04	2.99e-04	2.96e-04	2.93e-04	2.98e-04
DHMA	1.2500					4.10e-06	1.37e-05	2.11e-05
c-DHDMA	1.3333	2.55e-06	3.13e-06	3.14e-06	4.16e-06	8.73e-06	9.30e-06	8.55e-06
t-DHDMA	1.3333	2.58e-06						
ANT	1.1904	4.12e-06	6.95e-06	8.82e-06	1.06e-05	2.38e-05	5.98e-05	9.05e-05
1MA	1.2027					2.58e-06	2.30e-05	5.03e-05
9MA	1.2586	2.52e-05	3.46e-05	6.48e-05	1.20e-04	2.38e-04	3.60e-04	3.80e-04
110DMA	1.3333			2.44e-06	6.12e-06	2.97e-05	1.00e-04	1.50e-04
910DMA	1.3239	1.13e-03	1.10e-03	1.11e-03	9.77e-04	7.47e-04	4.24e-04	2.76e-04
TMA	1.4167						6.13e-06	1.67e-05
TMA	1.4167	1.25e-06	3.74e-06	1.01e-05	2.40e-05	4.98e-05	6.77e-05	6.35e-05
TMA	1.4167			2.04e-06	5.90e-06	7.43e-06		
TMA	1.4167						4.90e-06	3.00e-06
MATERIAL BALANCE ON:								
wt %C		0.940	0.926	0.972	0.927	0.887	0.840	0.830
wt %H		0.939	0.923	0.967	0.920	0.873	0.814	0.797
3-RING SYSTEM		0.942	0.928	0.975	0.933	0.899	0.862	0.858
METHYL GROUPS		0.929	0.910	0.947	0.888	0.804	0.685	0.635

half-life t* = 10031 s

910DMA THERMOLYSIS - 355°C - 2.06 mol/l - TRIAL #2 - 5/3/90

ID	RRF	MOLES	MOLES	MOLES	MOLES	MOLES	MOLES	MOLES
[910DMA]o		2.067	2.067	2.050	2.050	2.067	2.067	2.050
Time(s)		450	900	1800	3600	7200	14400	28800
X		0.0306	0.0562	0.1691	0.1760	0.4843	0.5533	0.8276
-ln(1-X)/t		6.91e-05	6.43e-05	1.03e-04	5.38e-05	9.20e-05	5.60e-05	6.10e-05
log keff		-4.1608	-4.1920	-3.9875	-4.2694	-4.0363	-4.2521	-4.2144
BIP	1.0000	2.99e-04	2.96e-04	3.03e-04	2.95e-04	3.02e-04	2.93e-04	2.90e-04
DHA	1.1667							7.19e-06
DHMA	1.2500					8.00e-06	1.03e-05	2.20e-05
c-DHDMA	1.3333	2.39e-06	5.67e-06	8.53e-06	3.98e-06	1.11e-05	1.05e-05	7.58e-06
DHMA	1.2500							4.01e-06
ANT	1.1904	5.09e-06	8.69e-06	1.44e-05	6.11e-06	3.33e-05	4.57e-05	1.22e-04
DHMA	1.2500				2.80e-06			2.37e-06
UNK196	1.2500							2.89e-06
2MA	1.2062							3.76e-05
1MA	1.2027					1.13e-05	1.21e-05	6.08e-05
9MA	1.2586	2.22e-05	3.97e-05	1.07e-04	9.32e-05	2.93e-04	3.37e-04	4.27e-04
DMA	1.3333							4.05e-06
DMA	1.3333							2.67e-06
DMA	1.3333							5.02e-06
DMA	1.3333							9.80e-06
DMA	1.3333							6.66e-06
29&39DMA	1.3333							1.09e-04
19DMA	1.3333							8.33e-05
110DMA	1.3333		1.73e-06	1.06e-05	4.80e-06	7.24e-05	6.87e-05	3.65e-06
910DMA	1.3239	1.20e-03	1.17e-03	1.03e-03	1.02e-03	6.38e-04	5.53e-04	2.13e-04
TMA	1.4167				1.13e-05			1.00e-05
TMA	1.4167							5.02e-06
TMA	1.4167							4.08e-06
TMA	1.4167							1.47e-05
TMA	1.4167							6.76e-06
TMA	1.4167		4.47e-06	2.40e-05	2.01e-05	7.23e-05	6.87e-05	5.89e-05
TMA	1.4167		2.59e-06	8.28e-06	3.93e-06	4.90e-06	4.94e-06	4.25e-06
MATERIAL BALANCE ON:								
wt %C		0.992	0.992	0.966	0.939	0.909	0.880	0.969
wt %H		0.990	0.990	0.960	0.935	0.892	0.858	0.929
3-RING SYSTEM		0.993	0.995	0.971	0.943	0.925	0.899	1.005
METHYL GROUPS		0.980	0.974	0.929	0.913	0.803	0.747	0.715

half-life t* = 8725 s

910DMA THERMOLYSIS - 355°C - 2.06 mol/l - TRIAL #3 - 9/6/92

	[910DMA]o	2.050	2.067	2.067	2.050	2.067	2.050	2.050
	Time(s)	450	900	1800	3600	7200	14400	28800
	X	0.0947	0.0522	0.1033	0.1894	0.3809	0.5768	0.8204
	-ln(1-X)/t	2.21e-04	5.96e-05	6.06e-05	5.83e-05	6.66e-05	5.97e-05	5.96e-05
	log keff	-3.6554	-4.2250	-4.2177	-4.2341	-4.1766	-4.2239	-4.2246
ID	RRF	MOLES	MOLES	MOLES	MOLES	MOLES	MOLES	MOLES
BIP	1.0000	2.92e-04	2.92e-04	2.90e-04	2.92e-04	2.90e-04	2.90e-04	2.90e-04
DHA	1.1667							4.71e-06
DHMA	1.2500					4.09e-06	1.05e-05	1.87e-05
c-DHDMA	1.3333	1.01e-05	5.18e-06	5.41e-06	6.72e-06	9.98e-06	1.11e-05	7.72e-06
UNK182	1.1667							1.49e-06
DHMA	1.2500					1.71e-06	1.99e-06	2.04e-06
t-DHDMA	1.3333	5.99e-06	2.09e-06	1.84e-06	2.30e-06	3.78e-06		
ANT	1.1904	4.67e-06	4.62e-06	6.19e-06	7.36e-06	1.67e-05	3.92e-05	8.21e-05
DHMA	1.2500	.	1.64e-06	1.60e-06	1.49e-06			
DHDMA	1.3333						2.53e-06	5.49e-06
UNK222	1.4167						1.88e-06	2.59e-06
UNK222	1.4167						1.67e-06	1.52e-06
UNK196	1.2500						1.62e-06	2.43e-06
2MA	1.2062					1.94e-06	4.94e-06	1.78e-05
1MA	1.2027			2.16e-06	1.77e-06	2.77e-06	1.65e-05	4.92e-05
9MA	1.2586	4.65e-05	2.96e-05	5.33e-05	8.65e-05	2.10e-04	3.25e-04	3.38e-04
DMA	1.3333					2.28e-06	3.43e-06	4.72e-06
DMA	1.3333	1.43e-06		2.42e-06	1.58e-06	2.89e-06	3.21e-06	2.07e-06
DMA	1.3333							4.94e-06
DMA	1.3333						1.54e-06	7.01e-06
DMA	1.3333						1.45e-06	5.27e-06
19&29&39DMA	1.3333					1.36e-05	3.96e-05	7.66e-05
110DMA	1.3333	3.68e-06	2.70e-06	6.60e-06	9.10e-06	2.31e-05	5.40e-05	7.26e-05
910DMA	1.3239	1.12e-03	1.17e-03	1.11e-03	1.00e-03	7.65e-04	5.22e-04	2.22e-04
TMA	1.4167	5.10e-06	4.66e-06	7.59e-06	9.33e-06	9.51e-06	1.10e-05	1.24e-05
TMA	1.4167							5.01e-06
TMA	1.4167						5.00e-06	3.86e-06
TMA	1.4167					2.75e-06	9.24e-06	1.98e-05
TMA	1.4167	8.04e-06	4.95e-06	1.02e-05	2.05e-05	5.25e-05	7.03e-05	5.54e-05
TMA	1.4167		1.49e-06	3.38e-06	5.37e-06	7.27e-06	8.45e-06	7.63e-06
TMA	1.4167					2.27e-06	4.34e-06	3.57e-06
TMA	1.4167						3.03e-06	4.93e-06
TMA	1.4167						1.48e-06	1.89e-06
MATERIAL BALANCE ON:								
wt %C		0.972	0.992	0.976	0.930	0.907	0.919	0.821
wt %H		0.972	0.992	0.974	0.927	0.898	0.902	0.795
3-RING SYSTEM		0.975	0.994	0.978	0.934	0.916	0.936	0.845
METHYL GROUPS		0.957	0.982	0.959	0.906	0.841	0.800	0.640

half-life t* = 11496 s

847

910DMA THERMOLYSIS - 355°C - 2.47 mol/l - TRIAL #1 - 11/28/90

	[910DMA]o	2.467	2.467	2.483	2.467	2.467
	Time(s)	900	1800	3600	7200	14400
	X	0.0146	0.0249	0.1575	0.3348	0.6906
	-ln(1-X)/t	1.63e-05	1.40e-05	4.76e-05	5.66e-05	8.15e-05
	log keff	-4.7867	-4.8536	-4.3223	-4.2470	-4.0890
ID	RRF	MOLES	MOLES	MOLES	MOLES	MOLES
BIP	1.0000	1.13e-04	1.11e-04	1.13e-04	1.13e-04	1.12e-04
DHMA	1.2500				3.28e-06	9.09e-06
c-DHDMA	1.3333	5.19e-06	5.02e-06	5.50e-06	1.03e-05	9.59e-06
DHMA	1.2500					1.34e-06
t-DHDMA	1.3333	6.54e-06	7.65e-06	1.03e-05	1.18e-05	4.82e-06
ANT	1.1904			9.90e-06	1.06e-05	3.13e-05
DHMA	1.2500	2.49e-06	2.54e-06			2.16e-06
DHDMA	1.3333					1.57e-06
UNK196	1.2500				1.03e-06	1.41e-06
UNK196	1.2500					1.77e-06
2MA	1.2062			4.94e-06		5.57e-06
1MA	1.2027	1.79e-06	1.25e-06	1.79e-06	2.71e-06	1.21e-05
9MA	1.2586	3.89e-05	6.55e-05	1.21e-04	2.28e-04	2.85e-04
UNK210	1.3333					4.82e-06
DMA	1.3333				2.30e-06	2.84e-06
DMA	1.3333				1.18e-06	1.62e-06
DMA	1.3333	1.32e-06	1.96e-06	3.00e-06	4.74e-06	5.50e-06
29&39DMA	1.3333					4.27e-06
19DMA	1.3333			9.93e-07	8.49e-06	3.72e-05
110DMA	1.3333	2.76e-06	3.65e-06	4.80e-06	1.46e-05	4.03e-05
910DMA	1.3239	1.46e-03	1.45e-03	1.25e-03	9.86e-04	4.58e-04
TMA	1.4167					4.02e-06
TMA	1.4167		9.44e-06	9.72e-06	1.15e-05	5.45e-06
TMA	1.4167					2.14e-06
TMA	1.4167					1.60e-06
TMA	1.4167				2.38e-06	6.58e-06
TMA	1.4167	5.78e-06	1.17e-05	2.34e-05	4.94e-05	5.55e-05
TMA	1.4167			8.80e-07	2.37e-06	1.47e-06
TMA	1.4167	1.16e-06	2.04e-06	4.03e-06	7.82e-06	6.19e-06
TMA	1.4167				2.00e-06	3.35e-06
TMA	1.4167					1.95e-06

MATERIAL BALANCE ON:

wt %C	1.028	1.050	0.973	0.913	0.665
wt %H	1.028	1.047	0.968	0.906	0.651
3-RING SYSTEM	1.030	1.050	0.977	0.921	0.678
METHYL GROUPS	1.018	1.034	0.941	0.860	0.576

half-life t* = 10486

848

910DMA THERMOLYSIS - 355°C - 2.47 mol/l - TRIAL #2 - 5/1/91

	[DMA]o	2.467	2.467	2.483	2.483	2.467	2.467	2.483
	Time(s)	450	900	1800	3600	7200	14400	28800
	X	0.0524	0.0451	0.1290	0.1402	0.2996	0.5264	0.7976
	-ln(1-X)/t	1.20e-04	5.13e-05	7.67e-05	4.20e-05	4.95e-05	5.19e-05	5.55e-05
	log keff	-3.9222	-4.2901	-4.1150	-4.3772	-4.3058	-4.2848	-4.2559
ID	RRF	MOLES	MOLES	MOLES	MOLES	MOLES	MOLES	MOLES
BIP	1.0000	1.13e-04	1.20e-04	1.13e-04	1.13e-04	1.14e-04	1.13e-04	1.15e-04
DHA	1.1667							6.26e-06
DHMA	1.2500						1.20e-05	2.48e-05
c-DHDMA	1.3333	3.83e-06	4.92e-06	4.80e-06	5.99e-06	1.09e-05	1.42e-05	1.06e-05
DHMA	1.2500						2.13e-06	2.18e-06
t-DHDMA	1.3333	2.27e-06					5.76e-06	
ANT	1.1904	2.31e-06	6.62e-06	7.76e-06	9.61e-06	2.19e-05	4.18e-05	1.07e-04
DHMA	1.2500	1.95e-06	1.75e-06	1.86e-06	2.12e-06		2.55e-06	6.79e-06
UNK196	1.2500						2.09e-06	3.23e-06
UNK196	1.2500						2.09e-06	2.69e-06
2MA	1.2062						5.44e-06	2.55e-05
1MA	1.2027					2.78e-06	1.47e-05	5.76e-05
9MA	1.2586	1.90e-05	3.05e-05	3.15e-05	1.14e-04	2.19e-04	3.86e-04	4.45e-04
UNK210	1.3333	3.27e-06	4.53e-06			1.95e-06	3.21e-06	5.29e-06
DMA	1.3333							2.21e-06
DMA	1.3333							4.17e-06
DMA	1.3333						2.14e-06	7.78e-06
29&39DMA	1.3333							5.37e-06
19DMA	1.3333					9.40e-06	4.07e-05	9.06e-05
110DMA	1.3333	1.73e-06	2.57e-06	3.15e-06	6.60e-06	1.44e-05	5.25e-05	9.03e-05
910DMA	1.3239	1.40e-03	1.42e-03	1.29e-03	1.28e-03	1.04e-03	7.03e-04	3.01e-04
TMA	1.4167			1.54e-05	2.22e-05	2.41e-05	1.75e-05	1.69e-05
TMA	1.4167						7.01e-06	6.71e-06
TMA	1.4167							5.17e-06
TMA	1.4167						1.04e-05	2.44e-05
TMA	1.4167	1.85e-06	5.05e-06	1.06e-05	2.53e-05	4.88e-05	7.73e-05	6.96e-05
TMA	1.4167					2.51e-06	2.94e-06	
TMA	1.4167					8.10e-06	1.04e-05	1.12e-05
TMA	1.4167						4.63e-06	3.97e-06
TMA	1.4167						3.46e-06	4.90e-06
MATERIAL BALANCE ON:								
wt %C		0.971	0.991	0.935	0.986	0.938	0.943	0.875
wt %H		0.971	0.990	0.934	0.982	0.929	0.927	0.847
3-RING SYSTEM		0.972	0.993	0.937	0.989	0.945	0.959	0.903
METHYL GROUPS		0.964	0.979	0.922	0.961	0.884	0.832	0.683

half-life t* = 13503 s

910DMA THERMOLYSIS - 355°C - 2.47 mol/l - TRIAL #4 - 7/8/91

	[910DMA]o	2.467	2.467	2.467	2.483
	Time(s)	450	1800	3600	7200
	X	0.0599	0.0306	0.1022	0.3410
	-ln(1-X)/t	1.37e-04	1.73e-05	2.99e-05	5.79e-05
	log keff	-3.8624	-4.7628	-4.5237	-4.2372
ID	RRF	MOLES	MOLES	MOLES	MOLES
BIP	1.0000	1.19e-04	1.15e-04	1.20e-04	1.16e-04
DHMA	1.2500				3.42e-06
c-DHDMA	1.3333	3.63e-06	5.05e-06	5.97e-06	1.06e-05
DHMA	1.2500		1.50e-06	1.25e-06	2.34e-06
t-DHDMA	1.3333	2.03e-06	2.35e-06	1.10e-05	5.18e-06
ANT	1.1904	2.13e-06	6.11e-06	6.96e-06	1.34e-05
DHMA	1.2500	1.44e-06	2.02e-06	2.15e-06	2.61e-06
1MA	1.2027			1.43e-06	2.35e-06
9MA	1.2586	1.51e-05	5.18e-05	1.03e-04	2.17e-04
UNK210	1.3333	5.29e-06	1.17e-05	1.05e-05	1.92e-06
DMA	1.3333				1.49e-06
DMA	1.3333	1.14e-06	2.42e-06	1.72e-06	3.95e-06
29&39DMA	1.3333				3.65e-06
19DMA	1.3333			1.61e-06	7.10e-06
110DMA	1.3333	1.59e-06	3.66e-06	5.38e-06	1.30e-05
910DMA	1.3239	1.40e-03	1.44e-03	1.33e-03	9.79e-04
TMA	1.4167			1.49e-05	1.09e-05
TMA	1.4167	2.34e-06	1.17e-05	2.40e-05	4.77e-05
TMA	1.4167		1.05e-06	1.56e-06	2.68e-06
TMA	1.4167		2.65e-06	5.46e-06	8.14e-06
TMA	1.4167				1.64e-06
MATERIAL BALANCE ON:					
wt %C		0.963	1.036	1.027	0.893
wt %H		0.963	1.037	1.027	0.886
3-RING SYSTEM		0.964	1.038	1.031	0.901
METHYL GROUPS		0.957	1.021	1.005	0.837

half-life t* = 9208 s

910DMA THERMOLYSIS - 355°C - 2.47 mol/l - TRIAL #5 - 7/10/91

[910DMA]o		2.467	2.467	2.467	2.467	2.467
Time(s)		900	1800	3600	14400	28800
X		0.0329	0.0695	0.1391	0.5488	0.7981
-ln(1-X)/t		3.72e-05	4.00e-05	4.16e-05	5.53e-05	5.56e-05
log keff		-4.4298	-4.3977	-4.3809	-4.2575	-4.2553

ID	RRF	MOLES	MOLES	MOLES	MOLES	MOLES
BIP	1.0000	1.13e-04	1.12e-04	1.14e-04	1.11e-04	1.12e-04
DHA	1.1667					5.77e-06
DHMA	1.2500				1.24e-05	2.39e-05
c-DHDMA	1.3333	4.89e-06	4.86e-06	5.98e-06	1.37e-05	9.88e-06
DHMA	1.2500	1.19e-06	1.68e-06	1.80e-06	2.49e-06	7.48e-06
t-DHDMA	1.3333	2.32e-06	2.26e-06	2.87e-06	5.93e-06	3.56e-06
ANT	1.1904	4.35e-06	6.19e-06	7.15e-06	4.17e-05	1.00e-04
DHMA	1.2500	1.62e-06	1.73e-06	1.94e-06	2.49e-06	
DHDMA	1.3333					7.40e-06
UNK196	1.2500				2.22e-06	4.76e-06
UNK196	1.2500				2.03e-06	
UNK196	1.2500				1.64e-06	6.13e-06
2MA	1.2062				6.56e-06	2.67e-05
1MA	1.2027			1.54e-06	1.59e-05	5.37e-05
9MA	1.2586	2.56e-05	4.40e-05	9.73e-05	3.88e-04	4.43e-04
UNK210	1.3333	6.84e-06	1.17e-05	1.33e-05	3.81e-06	7.86e-06
DMA	1.3333			1.59e-06	3.94e-06	4.84e-06
DMA	1.3333		3.71e-06	4.71e-06	4.59e-06	1.36e-05
DMA	1.3333					1.17e-05
19&29&39DMA	1.3333				4.80e-05	8.64e-05
110DMA	1.3333	2.61e-06	4.09e-06	7.57e-06	5.19e-05	9.98e-05
910DMA	1.3239	1.44e-03	1.38e-03	1.28e-03	6.69e-04	3.00e-04
TMA	1.4167			1.38e-05	1.25e-05	1.95e-05
TMA	1.4167				5.10e-06	6.24e-06
TMA	1.4167					6.58e-06
TMA	1.4167				8.48e-06	2.78e-05
TMA	1.4167	4.17e-06	9.82e-06	2.42e-05	8.00e-05	6.67e-05
TMA	1.4167				2.21e-06	3.72e-06
TMA	1.4167			1.37e-06	9.06e-06	
TMA	1.4167		2.28e-06	5.38e-06	4.99e-06	
TMA	1.4167				3.00e-06	3.66e-06
TMA	1.4167				2.51e-06	

MATERIAL BALANCE ON:

wt %C		1.003	0.991	0.986	0.930	0.883
wt %H		1.004	0.989	0.986	0.913	0.857
3-RING SYSTEM		1.005	0.993	0.989	0.947	0.910
METHYL GROUPS		0.994	0.977	0.965	0.816	0.693

half-life t* =13057 s

910DMA THERMOLYSIS - 355°C - 2.47 mol/l - TRIAL #6 - 7/19/91

	[910DMA]o	2.467	2.467	2.467	2.483	2.467	2.467	2.467
	Time(s)	450	900	1800	3600	7200	14400	28800
	X	0.0293	0.0172	0.0332	0.1663	0.2884	0.5387	0.7936
	-ln(1-X)/t	6.61e-05	1.93e-05	1.88e-05	5.05e-05	4.73e-05	5.37e-05	5.48e-05
	log keff	-4.1799	-4.7150	-4.7268	-4.2965	-4.3255	-4.2698	-4.2613
ID	RRF	MOLES	MOLES	MOLES	MOLES	MOLES	MOLES	MOLES
BIP	1.0000	1.12e-04	1.14e-04	1.12e-04	1.13e-04	1.16e-04	1.15e-04	1.11e-04
DHA	1.1667						1.34e-06	6.20e-06
DHMA	1.2500					2.99e-06	1.25e-05	2.45e-05
c-DHDMA	1.3333	3.82e-06	4.97e-06	5.08e-06	5.67e-06	1.02e-05	1.40e-05	1.07e-05
UNK182	1.1667							2.05e-06
DHMA	1.2500			1.13e-06	2.41e-06	2.00e-06	3.37e-06	2.40e-06
t-DHDMA	1.3333	2.19e-06	1.92e-06		2.89e-06	4.30e-06	5.56e-06	
ANT	1.1904	2.15e-06	4.49e-06	8.25e-06	8.17e-06	1.58e-05	4.49e-05	1.05e-04
DHMA	1.2500	1.75e-06	1.67e-06	1.80e-06				
DHDMA	1.3333						2.30e-06	6.02e-06
UNK196	1.2500						2.08e-06	3.51e-06
UNK196	1.2500						2.04e-06	2.25e-06
UNK196	1.2500						1.95e-06	3.13e-06
2MA	1.2062						5.63e-06	2.71e-05
1MA	1.2027					2.31e-06	1.84e-05	5.52e-05
9MA	1.2586	1.90e-05	2.69e-05	4.84e-05	1.03e-04	2.09e-04	3.99e-04	4.45e-04
UNK210	1.3333	4.39e-06	6.18e-06	8.93e-06	2.60e-06	2.14e-06	3.99e-06	6.89e-06
UNK210	1.3333						3.15e-06	
DMA	1.3333						2.72e-06	2.98e-06
DMA	1.3333							5.36e-06
DMA	1.3333	1.48e-06	1.37e-06	1.94e-06	3.05e-06	4.74e-06	6.96e-06	9.29e-06
DMA	1.3333							6.37e-06
19&29&39DMA	1.3333					8.41e-06	4.30e-05	9.75e-05
110DMA	1.3333	1.82e-06	2.49e-06	3.96e-06	6.39e-06	1.18e-05	6.06e-05	9.06e-05
910DMA	1.3239	1.44e-03	1.46e-03	1.44e-03	1.24e-03	1.05e-03	6.84e-04	3.06e-04
TMA	1.4167				1.68e-05	1.41e-05	1.50e-05	1.67e-05
TMA	1.4167						6.34e-06	1.24e-05
TMA	1.4167						9.91e-06	2.50e-05
TMA	1.4167	1.79e-06	4.68e-06	1.11e-05	2.26e-05	4.67e-05	8.03e-05	7.11e-05
TMA	1.4167		1.06e-06	2.51e-06	6.14e-06	2.11e-06	2.33e-06	2.70e-05
TMA	1.4167					8.14e-06	9.50e-06	1.04e-05
TMA	1.4167					1.34e-06	5.06e-06	4.73e-06
TMA	1.4167						2.97e-06	5.77e-06
TMA	1.4167						1.51e-06	3.59e-06

MATERIAL BALANCE ON:

wt %C		0.996	1.019	1.027	0.951	0.938	0.961	0.896
wt %H		0.996	1.019	1.027	0.949	0.931	0.944	0.870
3-RING SYSTEM		0.997	1.020	1.030	0.954	0.943	0.962	0.923
METHYL GROUPS		0.989	1.010	1.011	0.929	0.886	0.842	0.709

half-life t* = 13200 s

910DMA THERMOLYSIS - 370°C - 0.82 mol/l - TRIAL #1 - 7/12/90

ID	RRF	MOLES	MOLES	MOLES	MOLES	MOLES	MOLES	MOLES
[910DMA]o		0.820	0.823	0.830	0.825	0.822	0.830	0.825
Time(s)		450	900	1800	3600	7200	14400	28800
X		0.0724	0.1589	0.1431	0.2395	0.4283	0.7098	0.9174
-ln(1-X)/t		1.67e-04	1.92e-04	8.58e-05	7.60e-05	7.77e-05	8.59e-05	8.66e-05
log keff		-3.7773	-3.7161	-4.0665	-4.1189	-4.1098	-4.0659	-4.0625
BIP	1.0000	1.29e-03	1.29e-03	1.28e-03	1.29e-03	1.29e-03	1.28e-03	1.29e-03
DHA	1.1667						3.74e-07	1.81e-06
DHMA	1.2500					7.22e-07	2.54e-06	3.91e-06
c-DHDMA	1.3333	4.11e-07	4.16e-07	4.59e-07	8.25e-07	1.52e-06	1.67e-06	8.11e-07
DHMA	1.2500		4.26e-07	3.58e-07	4.68e-07		3.10e-07	2.26e-07
t-DHDMA	1.3333	3.17e-07	2.65e-07	3.07e-07	5.31e-07	7.52e-07	9.14e-07	4.81e-07
ANT	1.1904	5.16e-07	6.61e-07	7.31e-07	7.60e-07	4.92e-06	2.15e-05	5.34e-05
DHMA	1.2500					1.15e-06		1.68e-06
DHDMA	1.3333						6.28e-07	1.41e-06
UNK196	1.2500						2.92e-07	3.21e-07
UNK196	1.2500							2.58e-06
2MA	1.2062					4.36e-07	3.43e-06	1.52e-05
1MA	1.2027					7.31e-07	6.26e-06	2.39e-05
DHDMA	1.3333					5.46e-07		
9MA	1.2586	8.31e-06	1.29e-05	2.35e-05	4.85e-05	9.89e-05	1.49e-04	1.30e-04
UNK210	1.3333		5.51e-07	1.06e-06	1.38e-06	1.47e-06	1.77e-06	1.31e-06
DMA	1.3333			4.04e-07	6.81e-07	9.40e-07	1.15e-06	1.07e-06
DMA	1.3333							6.37e-07
DMA	1.3333						4.76e-07	2.26e-06
DMA	1.3333		6.89e-07	6.82e-07	8.36e-07	6.55e-07	1.88e-06	4.64e-06
DMA	1.3333						4.62e-07	2.25e-06
29&39DMA	1.3333				4.61e-07	3.03e-06	1.08e-05	1.61e-05
19DMA	1.3333				6.29e-07	3.79e-06	1.25e-05	1.99e-05
110DMA	1.3333	5.33e-07	5.25e-07	7.27e-07	1.71e-06	6.62e-06	1.91e-05	2.51e-05
910DMA	1.3239	4.56e-04	4.15e-04	4.27e-04	3.77e-04	2.82e-04	1.44e-04	4.09e-05
TMA	1.4167	3.75e-07	6.47e-07	1.22e-06	2.10e-06	2.94e-06	2.44e-06	1.85e-06
TMA	1.4167						7.81e-07	1.20e-06
TMA	1.4167						5.31e-07	1.28e-06
TMA	1.4167					6.14e-07	2.16e-06	4.83e-06
TMA	1.4167						7.59e-07	1.99e-06
TMA	1.4167	5.42e-07	1.43e-06	3.24e-06	8.49e-06	1.90e-05	2.30e-05	1.05e-05
TMA	1.4167	4.30e-07	6.95e-06			7.72e-07	3.92e-07	3.15e-06
TMA	1.4167	3.19e-07		1.17e-06	1.90e-06	2.03e-06	1.37e-06	1.08e-06
TMA	1.4167						2.52e-07	3.44e-07
TMA	1.4167							8.13e-07
TMA	1.4167					4.51e-07	7.90e-07	3.97e-07
TMA	1.4167					2.74e-07	7.60e-07	7.83e-07
TMA	1.4167					2.11e-07	3.30e-07	9.58e-07
TMA	1.4167					2.69e-07	5.80e-07	4.88e-07

MATERIAL BALANCE ON:

wt %C		0.951	0.878	0.922	0.896	0.871	0.809	0.736
wt %H		0.950	0.877	0.920	0.891	0.859	0.785	0.697
3-RING SYSTEM		0.952	0.880	0.925	0.900	0.882	0.831	0.770
METHYL GROUPS		0.944	0.866	0.905	0.861	0.795	0.659	0.501

half-life t* = 9145 s

910DMA THERMOLYSIS - 370°C - 0.82 mol/l - GAS TRIAL #1 - 1/17/91

	[910DMA]o	0.820	0.827	0.825	0.828	0.828	0.823
	Time(s)	900	1800	3600	7200	14400	28800
	X	0.0448	0.1369	0.1929	0.3493	0.6549	0.9023
	-ln(1-X)/t	5.09e-05	8.18e-05	5.95e-05	5.97e-05	7.39e-05	8.08e-05
	log keff	-4.2930	-4.0873	-4.2253	-4.2242	-4.1315	-4.0928
ID	RRF	MOLES	MOLES	MOLES	MOLES	MOLES	MOLES
BIP	1.0000	1.29e-03	1.28e-03	1.29e-03	1.28e-03	1.28e-03	1.28e-03
DHA	1.1667						2.10e-06
DHMA	1.2500				1.09e-06	2.26e-06	4.77e-06
c-DHDMA	1.3333	1.30e-06	8.57e-07	5.87e-07	2.50e-06	1.95e-06	1.02e-06
UNK182	1.1667						3.08e-07
DHMA	1.2500		8.08e-07	1.71e-06	2.45e-06	1.88e-06	8.07e-07
t-DHDMA	1.3333	1.73e-06	1.35e-06	1.47e-06	3.46e-06	2.15e-06	
ANT	1.1904	1.00e-06	1.13e-06	1.43e-06	7.10e-06	1.79e-05	5.58e-05
UNK196	1.2500					3.30e-07	4.99e-06
UNK196	1.2500					4.32e-07	4.51e-07
2MA	1.2062				2.92e-07	1.74e-06	1.11e-05
1MA	1.2027				1.16e-06	5.35e-06	2.82e-05
9MA	1.2586	1.47e-05	3.12e-05	3.44e-05	1.16e-04	1.45e-04	1.31e-04
UNK210	1.3333		1.45e-06	2.52e-06			
DMA	1.3333			1.62e-06	2.48e-06	3.17e-06	
DMA	1.3333						2.30e-06
DMA	1.3333		5.23e-07	2.04e-06	3.98e-06	2.91e-06	4.24e-06
29&39DMA	1.3333				2.78e-06	5.64e-06	3.67e-06
19DMA	1.3333			3.07e-07	3.78e-06	8.22e-06	2.32e-05
110DMA	1.3333	9.55e-07	2.27e-06	1.67e-06	1.00e-05	2.19e-05	3.61e-05
910DMA	1.3239	4.70e-04	4.28e-04	3.99e-04	3.24e-04	1.72e-04	4.83e-05
TMA	1.4167						9.27e-06
TMA	1.4167	2.74e-06	4.71e-06	5.78e-06	2.24e-05	2.24e-05	1.43e-05
TMA	1.4167		1.81e-06	1.34e-06			
CH4	-			1.29e-06	7.17e-06	9.90e-06	2.01e-05
C2H6	-						8.87e-07

MATERIAL BALANCE ON:

wt %C		0.999	0.953	0.914	0.998	0.814	0.732
wt %H		0.998	0.950	0.911	0.987	0.796	0.701
3-RING SYSTEM		1.001	0.956	0.918	1.011	0.834	0.763
METHYL GROUPS		0.987	0.928	0.887	0.905	0.673	0.512

half-life t* = 10847 s

910DMA THERMOLYSIS - 370°C - 0.82 mol/l - GAS TRIAL #2 - 2/14/91

[910DMA]o		0.832	0.823	0.822	0.820	0.828	0.820
Time(s)		900	1800	3600	7200	14400	28800
X		0.0864	0.1331	0.1606	0.3861	0.6194	0.9048
-ln(1-X)/t		1.00e-04	7.94e-05	4.86e-05	6.78e-05	6.71e-05	8.17e-05
log keff		-3.9983	-4.1004	-4.3131	-4.1690	-4.1734	-4.0880
ID	**RRF**	**MOLES**	**MOLES**	**MOLES**	**MOLES**	**MOLES**	**MOLES**
BIP	1.0000	1.29e-03	1.28e-03	1.29e-03	1.28e-03	1.29e-03	1.29e-03
DHA	1.1667					7.30e-07	1.86e-06
DHMA	1.2500				5.25e-07	4.66e-06	4.29e-06
c-DHDMA	1.3333	5.59e-07	4.02e-07	5.83e-07	1.44e-06	2.94e-06	
DHMA	1.2500	4.97e-07	3.73e-07		4.75e-07	7.46e-07	
t-DHDMA	1.3333	1.32e-06	8.56e-07	8.42e-07	1.42e-06	1.23e-06	
UNK182	1.1667						1.17e-06
ANT	1.1904	7.71e-07	8.45e-07	1.23e-06	4.10e-06	3.18e-05	5.16e-05
DHMA	1.2500					1.31e-06	
DHDMA	1.3333					4.82e-07	1.21e-06
UNK196	1.2500					4.10e-07	
2MA	1.2062					5.22e-06	1.21e-05
1MA	1.2027					1.10e-05	2.26e-05
9MA	1.2586	1.02e-05	1.66e-05	3.67e-05	8.04e-05	2.02e-04	1.28e-04
UNK210	1.3333	7.32e-07	8.11e-07	8.76e-07	1.30e-06		
DMA	1.3333	3.98e-07	2.97e-07	5.35e-07	8.71e-07	1.31e-06	1.46e-06
DMA	1.3333						6.25e-07
DMA	1.3333	1.47e-06	8.67e-07	6.56e-07	6.89e-07	6.28e-07	1.75e-06
DMA	1.3333					2.16e-06	3.78e-06
DMA	1.3333					1.10e-06	2.25e-06
29&39DMA	1.3333			2.47e-07	1.63e-06	1.41e-05	1.20e-05
19DMA	1.3333			3.04e-07	2.29e-06	1.80e-05	1.83e-05
110DMA	1.3333	9.04e-07	6.82e-07	1.02e-06	4.45e-06	2.87e-05	2.50e-05
910DMA	1.3239	4.56e-04	4.28e-04	4.13e-04	3.02e-04	1.89e-04	4.68e-05
TMA	1.4167		2.26e-06	2.88e-06	3.01e-06	4.58e-06	2.65e-06
TMA	1.4167					2.24e-06	1.67e-06
TMA	1.4167					5.66e-06	5.87e-06
TMA	1.4167	1.09e-06	1.78e-06	8.69e-06	1.60e-05	3.22e-05	1.28e-05
TMA	1.4167			1.19e-06	1.99e-06	3.53e-06	5.96e-08
TMA	1.4167					1.06e-06	
TMA	1.4167					1.04e-06	
CH4	-			1.15e-06	6.77e-06	1.79e-05	2.55e-05
C2H6	-						1.08e-06
MATERIAL BALANCE ON:							
wt %C		0.948	0.917	0.950	0.852	1.115	0.700
wt %H		0.947	0.916	0.947	0.845	1.089	0.674
3-RING SYSTEM		0.947	0.919	0.953	0.860	1.143	0.728
METHYL GROUPS		0.938	0.902	0.927	0.794	0.919	0.500

half-life t* = 10736 s

910DMA THERMOLYSIS - 370°C - 0.82 mol/l - GAS TRIAL #3 - 2/21/91

	[910DMA]o	0.822	0.822	0.822	0.828	0.823	0.822
	Time(s)	900	1800	3600	7200	14400	28800
	X	0.1143	0.1340	0.2032	0.3924	0.6845	0.9126
	-ln(1-X)/t	1.35e-04	7.99e-05	6.31e-05	6.92e-05	8.01e-05	8.46e-05
	log keff	-3.8701	-4.0973	-4.2000	-4.1599	-4.0963	-4.0725
ID	RRF	MOLES	MOLES	MOLES	MOLES	MOLES	MOLES
BIP	1.0000	1.29e-03	1.29e-03	1.28e-03	1.29e-03	1.29e-03	1.29e-03
DHA	1.1667						2.49e-06
DHMA	1.2500				5.83e-07	2.39e-06	5.44e-06
c-DHDMA	1.3333	4.36e-07	4.53e-07	4.94e-07	1.51e-06	1.75e-06	1.41e-06
DHMA	1.2500	7.54e-07	4.02e-07				5.64e-07
t-DHDMA	1.3333	8.10e-07	8.18e-07	7.85e-07	1.46e-06	7.28e-07	3.88e-07
ANT	1.1904	6.78e-07	8.23e-07	1.03e-06	4.22e-06	2.01e-05	5.34e-05
2MA	1.2062					2.40e-06	1.18e-05
1MA	1.2027					6.27e-06	2.43e-05
9MA	1.2586	8.18e-06	2.30e-05	2.98e-05	8.84e-05	1.47e-04	1.17e-04
UNK210	1.3333	6.26e-07	7.13e-07	1.08e-06			
DMA	1.3333						1.95e-06
DMA	1.3333						7.71e-07
DMA	1.3333		1.91e-07	4.88e-07	8.82e-07	1.24e-06	1.91e-06
DMA	1.3333	6.50e-07	4.02e-07	4.36e-07	6.36e-07	6.65e-07	3.99e-06
DMA	1.3333						2.71e-06
29&39DMA	1.3333				1.88e-06	7.73e-06	8.55e-06
19DMA	1.3333				2.53e-06	1.10e-05	1.95e-05
110DMA	1.3333	6.90e-07	8.76e-07	1.13e-06	4.98e-06	1.91e-05	2.61e-05
910DMA	1.3239	4.37e-04	4.27e-04	3.92e-04	3.02e-04	1.56e-04	4.31e-05
TMA	1.4167		5.96e-06	5.22e-06	5.01e-06	2.95e-06	2.55e-06
TMA	1.4167					1.99e-06	1.69e-06
TMA	1.4167						5.93e-06
TMA	1.4167	9.87e-07	3.26e-06	4.95e-06	1.64e-05	2.33e-05	1.13e-05
TMA	1.4167				1.94e-06		
CH4	-			1.70e-06	1.02e-05	3.01e-05	5.12e-05
C2H6	-					1.05e-06	1.84e-06
MATERIAL BALANCE ON:							
wt %C		0.913	0.939	0.887	0.862	0.801	0.678
wt %H		0.912	0.937	0.884	0.856	0.789	0.664
3-RING SYSTEM		0.914	0.941	0.889	0.870	0.818	0.702
METHYL GROUPS		0.903	0.925	0.869	0.806	0.679	0.506

half-life t* = 9912 s

910DMA THERMOLYSIS - 370°C - 0.82 mol/l - GAS TRIAL #4 - 3/7/91

	[910DMA]o	0.825	0.830	0.822	0.823	0.830	0.822
	Time(s)	900	1800	3600	7200	14400	28800
	X	0.0728	0.1088	0.1302	0.3242	0.5611	0.8993
	$-\ln(1-X)/t$	8.40e-05	6.40e-05	3.87e-05	5.44e-05	5.72e-05	7.97e-05
	log keff	-4.0758	-4.1939	-4.4118	-4.2642	-4.2427	-4.0985
ID	RRF	MOLES	MOLES	MOLES	MOLES	MOLES	MOLES
BIP	1.0000	1.28e-03	1.29e-03	1.28e-03	1.29e-03	1.28e-03	1.29e-03
DHA	1.1667					7.65e-07	4.34e-06
DHMA	1.2500				2.39e-06	5.55e-06	7.28e-06
c-DHDMA	1.3333	8.80e-07	7.64e-07	1.34e-06	8.04e-06	4.88e-06	1.92e-06
UNK182	1.1667					2.24e-07	3.01e-06
DHMA	1.2500			5.66e-07	3.41e-07	8.96e-07	
t-DHDMA	1.3333	1.26e-06	1.23e-06	1.45e-06	7.22e-06	3.03e-06	
ANT	1.1904	8.52e-07	5.47e-07	9.54e-07	5.62e-06	2.16e-05	6.17e-05
2MA	1.2062				3.82e-07	3.32e-06	1.15e-05
1MA	1.2027				1.56e-06	1.08e-05	4.15e-05
9MA	1.2586	1.04e-05	1.77e-05	2.52e-05	7.03e-05	8.55e-05	8.22e-05
DMA	1.3333						1.77e-06
DMA	1.3333					2.44e-06	
29&39DMA	1.3333					1.41e-06	1.52e-05
19DMA	1.3333				3.82e-06	1.09e-05	1.41e-05
110DMA	1.3333	5.38e-07	7.89e-07	3.29e-06	9.15e-06	1.98e-05	2.87e-05
910DMA	1.3239	4.59e-04	4.44e-04	4.29e-04	3.34e-04	2.19e-04	4.96e-05
TMA	1.4167					5.82e-06	8.07e-06
TMA	1.4167	1.24e-06	2.25e-06	4.68e-06	1.26e-05	1.13e-05	8.35e-06
CH4	-	1.92e-06	4.68e-06	3.52e-06	5.57e-06	7.89e-05	8.50e-05
C2H4	-					7.41e-07	
C2H6	-					3.94e-06	3.43e-06
MATERIAL BALANCE ON:							
wt %C		0.957	0.936	0.943	0.913	0.811	0.667
wt %H		0.956	0.936	0.942	0.909	0.832	0.670
3-RING SYSTEM		0.958	0.938	0.946	0.921	0.817	0.689
METHYL GROUPS		0.949	0.926	0.926	0.853	0.771	0.514

half-life t* = 12647 s

910DMA THERMOLYSIS - 370°C - 0.82 mol/l - GAS TRIAL #5 - 3/13/91

[910DMA]o		0.822	0.830	0.828	0.822	0.827	0.822
Time(s)		900	1800	3600	7200	14400	28800
X		0.0783	0.1364	0.1257	0.4408	0.7304	0.9410
-ln(1-X)/t		9.06e-05	8.15e-05	3.73e-05	8.07e-05	9.10e-05	9.83e-05
log keff		-4.0429	-4.0890	-4.4281	-4.0930	-4.0408	-4.0076
ID	RRF	MOLES	MOLES	MOLES	MOLES	MOLES	MOLES
BIP	1.0000	1.28e-03	1.28e-03	1.29e-03	1.29e-03	1.29e-03	1.28e-03
DHA	1.1667					8.28e-07	4.64e-06
DHMA	1.2500				2.95e-06	6.57e-06	9.47e-06
c-DHDMA	1.3333	1.38e-06	1.48e-06	1.57e-06	3.73e-06	4.85e-06	2.35e-06
DHMA	1.2500		8.08e-07	6.83e-07	7.41e-07	8.29e-07	5.00e-07
UNK182	1.1667						2.80e-06
t-DHDMA	1.3333	1.84e-06	2.23e-06	1.72e-06	2.73e-06		
ANT	1.1904	9.93e-07	9.85e-07	1.04e-06	9.80e-06	2.95e-05	6.80e-05
2MA	1.2062				9.04e-07	3.80e-06	1.27e-05
1MA	1.2027				3.28e-06	1.28e-05	4.10e-05
9MA	1.2586	1.26e-05	2.34e-05	3.09e-05	9.87e-05	1.28e-04	8.52e-05
DMA	1.3333					1.10e-06	
DMA	1.3333				1.27e-06	1.93e-06	9.07e-06
DMA	1.3333		1.14e-06	9.87e-07	1.25e-06	1.54e-06	5.90e-06
19DMA	1.3333				8.56e-06	1.70e-05	1.75e-05
110DMA	1.3333	6.81e-07	1.43e-06	2.96e-06	1.41e-05	2.85e-05	2.93e-05
910DMA	1.3239	4.55e-04	4.30e-04	4.34e-04	2.76e-04	1.34e-04	2.91e-05
TMA	1.4167					5.43e-06	9.09e-06
TMA	1.4167	1.65e-06	4.21e-06	5.27e-06	1.92e-05	1.92e-05	8.04e-06
TMA	1.4167		5.49e-07	8.09e-07			
CH4	-	5.76e-06	1.08e-05	3.72e-06	4.82e-05	7.96e-05	2.68e-04
C2H4	-					9.16e-07	2.35e-06
C2H6	-				5.61e-06	3.89e-06	1.03e-05

MATERIAL BALANCE ON:

wt %C	0.960	0.935	0.964	0.892	0.786	0.680
wt %H	0.961	0.938	0.962	0.903	0.798	0.769
3-RING SYSTEM	0.960	0.936	0.967	0.898	0.799	0.679
METHYL GROUPS	0.953	0.926	0.943	0.849	0.699	0.692

half-life t* = 8670 s

910DMA THERMOLYSIS - 370°C - 0.82 mol/l - GAS TRIAL #6 - 4/11/91

	[910DMA]o	0.832	0.828	0.828	0.825	0.830	0.825
	Time(s)	900	1800	3600	7200	14400	28800
	X	0.0693	0.0524	0.1315	0.4012	0.8172	0.8732
	-ln(1-X)/t	7.98e-05	2.99e-05	3.92e-05	7.12e-05	1.18e-04	7.17e-05
	log keff	-4.0980	-4.5243	-4.4071	-4.1474	-3.9281	-4.1444
ID	RRF	MOLES	MOLES	MOLES	MOLES	MOLES	MOLES
BIP	1.0000	1.29e-03	1.29e-03	1.29e-03	1.29e-03	1.28e-03	1.29e-03
DHA	1.1667					1.77e-06	6.02e-06
DHMA	1.2500			3.12e-07	2.65e-06	6.87e-06	9.00e-06
c-DHDMA	1.3333	1.53e-06	1.13e-06	2.56e-06	5.38e-06	3.76e-06	3.18e-06
UNK182	1.1667					4.07e-07	3.01e-06
DHMA	1.2500	4.25e-07	3.88e-07	8.56e-07	8.52e-07	8.60e-07	5.68e-07
t-DHDMA	1.3333	7.93e-06	5.42e-07	1.38e-06	2.29e-06	1.54e-06	
ANT	1.1904	1.34e-06	1.05e-06	1.77e-06	9.32e-06	3.32e-05	5.53e-05
DHMA	1.2500						3.37e-06
DHDMA	1.3333					1.78e-06	2.07e-06
UNK222	1.4167					6.60e-07	
UNK196	1.2500				3.80e-07	4.23e-07	5.08e-07
UNK196	1.2500				5.31e-07	4.20e-07	8.77e-07
2MA	1.2062				1.05e-06	9.23e-06	2.05e-05
1MA	1.2027				1.72e-06	1.43e-05	2.91e-05
9MA	1.2586	1.28e-05	1.63e-05	2.54e-05	9.12e-05	1.28e-04	7.31e-05
UNK210	1.3333		4.92e-07	8.65e-07	1.45e-06	1.76e-06	
DMA	1.3333				7.12e-07	1.48e-06	1.70e-06
DMA	1.3333					5.93e-07	1.24e-06
DMA	1.3333					1.08e-06	3.20e-06
DMA	1.3333	5.57e-07	5.17e-07	1.05e-06		2.64e-06	6.90e-06
DMA	1.3333					1.45e-06	3.82e-06
29&39DMA	1.3333			3.47e-07	3.88e-06	1.18e-05	7.74e-06
19DMA	1.3333			6.11e-07	5.95e-06	1.66e-05	1.50e-05
110DMA	1.3333	7.77e-07	9.48e-07	1.40e-06	1.00e-05	2.34e-05	1.73e-05
910DMA	1.3239	4.64e-04	4.71e-04	4.32e-04	2.96e-04	9.10e-05	6.27e-05
TMA	1.4167	1.89e-06	2.35e-06	2.63e-06	3.39e-06	3.64e-06	3.17e-06
TMA	1.4167				8.62e-07	1.35e-06	2.75e-06
TMA	1.4167					1.10e-06	
TMA	1.4167				1.00e-06	4.23e-06	6.69e-06
TMA	1.4167					1.54e-06	
TMA	1.4167	1.80e-06	2.68e-06	4.58e-06	1.69e-05	1.68e-05	5.81e-06
TMA	1.4167			3.21e-07	5.24e-07		
TMA	1.4167	5.81e-07	7.17e-07	8.41e-07	1.91e-05	8.87e-07	
TMA	1.4167				8.02e-07	7.13e-07	
TMA	1.4167					6.11e-07	
CH4	-	7.76e-06	1.18e-05	1.62e-05	6.74e-05	8.08e-05	2.55e-04
C2H4	-					7.29e-07	2.46e-06
C2H6	-				3.18e-06	3.58e-06	9.26e-06
MATERIAL BALANCE ON:							
wt %C		0.975	1.002	0.958	0.926	0.761	0.700
wt %H		0.978	1.006	0.964	0.948	0.774	0.791
3-RING SYSTEM		0.976	1.002	0.959	0.928	0.775	0.697
METHYL GROUPS		0.972	1.001	0.953	0.910	0.665	0.728

half-life t* = 8951 s

859

910DMA THERMOLYSIS - 370°C - 0.82 mol/l - GAS TRIAL #7 - 4/17/91

	[910DMA]o	0.827	0.828	0.828	0.830	0.825	0.828
	Time(s)	900	1800	3600	7200	14400	28800
	X	0.0638	0.1479	0.2544	0.4510	0.7952	0.8668
	-ln(1-X)/t	7.33e-05	8.89e-05	8.15e-05	8.33e-05	1.10e-04	7.00e-05
	log keff	-4.1352	-4.0510	-4.0886	-4.0794	-3.9581	-4.1549
ID	RRF	MOLES	MOLES	MOLES	MOLES	MOLES	MOLES
BIP	1.0000	1.29e-03	1.28e-03	1.28e-03	1.28e-03	1.29e-03	1.29e-03
DHA	1.1667					1.51e-06	5.05e-06
DHMA	1.2500			6.60e-07	2.92e-06	7.49e-06	7.38e-06
c-DHDMA	1.3333	1.29e-06	1.79e-06	3.29e-06	5.45e-06	4.90e-06	1.79e-06
UNK182	1.1667					8.81e-07	2.82e-06
DHMA	1.2500		8.58e-07	8.40e-07	1.60e-06		
t-DHDMA	1.3333	6.34e-07	7.70e-07	1.55e-06	2.42e-06	1.64e-06	
ANT	1.1904	1.05e-06	1.89e-06	3.45e-06	1.23e-05	3.22e-05	5.78e-05
DHDMA	1.3333					1.90e-06	2.21e-06
UNK222	1.4167					6.75e-07	
UNK196	1.2500				3.92e-07	5.17e-07	4.55e-07
UNK196	1.2500				7.00e-07	6.75e-07	9.60e-07
2MA	1.2062				1.40e-06	7.46e-06	1.85e-05
1MA	1.2027				2.88e-06	1.38e-05	3.33e-05
9MA	1.2586	1.03e-05	2.51e-05	5.61e-05	1.07e-04	1.33e-04	7.84e-05
UNK210	1.3333			1.56e-06	2.39e-06		
DMA	1.3333			5.18e-07	1.11e-06	1.54e-06	1.87e-06
DMA	1.3333						1.15e-06
DMA	1.3333					7.40e-07	3.09e-06
DMA	1.3333			8.24e-07	8.94e-07	1.75e-06	6.50e-06
DMA	1.3333					1.14e-06	4.35e-06
29&39DMA	1.3333			8.39e-07	3.61e-06	7.24e-06	
19DMA	1.3333			1.74e-06	7.08e-06	1.60e-05	2.11e-05
110DMA	1.3333	6.74e-07	1.23e-06	2.89e-06	1.24e-05	2.52e-05	2.21e-05
910DMA	1.3239	4.64e-04	4.24e-04	3.70e-04	2.73e-04	1.01e-04	6.62e-05
TMA	1.4167		9.94e-06	9.77e-06	6.88e-06	4.10e-06	4.28e-06
TMA	1.4167						3.11e-06
TMA	1.4167					4.71e-06	8.15e-06
TMA	1.4167	1.35e-06	4.91e-06	1.12e-05	1.91e-05	1.48e-05	7.01e-06
TMA	1.4167			5.09e-07	6.40e-07		
TMA	1.4167		1.14e-06	1.93e-06	2.21e-06		
TMA	1.4167				4.22e-07		
CH4	-	5.66e-06	1.39e-05	3.31e-05	7.09e-05	1.77e-04	1.89e-04
C2H6	-			8.75e-07	3.16e-06	1.61e-06	1.45e-06
C2H4	-					7.91e-06	7.42e-06
MATERIAL BALANCE ON:							
wt %C		0.966	0.948	0.941	0.933	0.778	0.714
wt %H		0.968	0.953	0.953	0.955	0.836	0.771
3-RING SYSTEM		0.967	0.948	0.942	0.938	0.779	0.720
METHYL GROUPS		0.962	0.948	0.936	0.903	0.767	0.678

half-life t* = 8330 s

910DMA THERMOLYSIS - 409°C - 0.82 mol/l - TRIAL #1 - 6/18/90

[910DMA]o		0.823	0.830	0.828	0.830	0.830	0.827	0.825
Time(s)		450	900	1800	3600	7200	10800	21600
X		0.1227	0.2683	0.6186	0.8992	0.9827	0.9950	0.9966
-ln(1-X)/t		2.91e-04	3.47e-04	5.36e-04	6.37e-04	5.63e-04	4.91e-04	2.63e-04
log keff		-3.5363	-3.4596	-3.2712	-3.1956	-3.2491	-3.3093	-3.5798
ID	RRF	MOLES	MOLES	MOLES	MOLES	MOLES	MOLES	MOLES
BIP	1.0000	1.29e-03	1.28e-03	1.29e-03	1.28e-03	1.28e-03	1.28e-03	1.28e-03
DHA	1.1667				1.02e-06	3.40e-06	5.61e-06	8.89e-06
DHMA	1.2500			1.24e-06	2.43e-06	2.03e-06	1.10e-06	4.51e-07
c-DHDMA	1.3333		5.97e-07	9.46e-07	5.36e-07			
DHMA	1.2500		6.69e-07	5.51e-07				
UNK182	1.1667					4.49e-07	1.22e-06	3.35e-06
t-DHDMA	1.3333	4.17e-07	7.15e-07	4.22e-07	2.33e-07			
ANT	1.1904	1.29e-06	3.21e-06	1.89e-05	6.06e-05	1.20e-04	1.38e-04	1.44e-04
UNK196	1.2500						5.23e-07	1.13e-06
UNK196	1.2500						4.66e-07	1.15e-06
2MA	1.2062			1.94e-06	1.38e-05	3.73e-05	4.51e-05	4.80e-05
1MA	1.2027		3.36e-07	3.63e-06	2.29e-05	5.78e-05	7.19e-05	7.29e-05
9MA	1.2586	2.76e-05	7.39e-05	1.57e-04	1.52e-04	7.20e-05	2.94e-05	1.03e-05
UNK210	1.3333		1.71e-06	1.73e-06				
DMA	1.3333	7.31e-07	1.72e-06	2.07e-06	1.97e-06			
DMA	1.3333					2.12e-06	1.61e-06	1.26e-06
DMA	1.3333				7.71e-07	1.76e-06	1.73e-06	1.74e-06
DMA	1.3333	4.02e-07	8.92e-07	6.64e-07	1.82e-06	5.82e-06	6.88e-06	6.28e-06
DMA	1.3333				3.54e-06	1.26e-05	1.70e-05	2.85e-05
DMA	1.3333				2.09e-06	6.87e-06	9.62e-06	
29&39DMA	1.3333		9.17e-07	7.48e-06	1.43e-05			
19DMA	1.3333		1.21e-06	9.32e-06	1.97e-05	2.61e-05	1.55e-05	
110DMA	1.3333	7.62e-07	2.38e-06	1.46e-05	2.68e-05	1.95e-05	1.01e-05	1.28e-05
910DMA	1.3239	4.34e-04	3.66e-04	1.90e-04	5.02e-05	8.63e-06	2.50e-06	1.67e-06
TMA	1.4167						1.38e-06	1.51e-06
TMA	1.4167	4.62e-06	6.56e-06	5.13e-06	2.77e-06	1.64e-06	2.10e-06	2.13e-06
TMA	1.4167					1.84e-06	1.77e-06	1.97e-06
TMA	1.4167			1.02e-06	2.03e-06	1.74e-06		
TMA	1.4167			1.75e-06	6.37e-06	7.53e-06	5.40e-06	2.20e-06
TMA	1.4167	2.50e-06	1.01e-05	2.12e-05	1.40e-05	5.66e-06		
TMA	1.4167			5.29e-07				
TMA	1.4167	6.09e-07	1.74e-06	1.94e-06	7.24e-07			
TMA	1.4167			4.34e-07				
TMA	1.4167			4.13e-07	6.55e-07			
TMA	1.4167		5.38e-07	6.90e-07	8.76e-07			

MATERIAL BALANCE ON:

wt %C		0.954	0.939	0.869	0.771	0.743	0.689	0.651
wt %H		0.950	0.925	0.844	0.726	0.681	0.623	0.586
3-RING SYSTEM		0.957	0.947	0.891	0.807	0.793	0.742	0.706
METHYL GROUPS		0.934	0.883	0.721	0.519	0.393	0.313	0.264

half-life t* = 1507 s

910DMA THERMOLYSIS - 409°C - 0.82 mol/l - TRIAL #2 - 8/1/92

	[910DMA]o	0.820	0.823	0.828	0.822	0.822	0.822	0.823
	Time(s)	450	900	1800	3600	7200	10800	21600
	X	0.2368	0.3965	0.8408	0.9329	0.9786	0.9928	0.9980
	-ln(1-X)/t	6.01e-04	5.61e-04	1.02e-03	7.50e-04	5.34e-04	4.57e-04	8.53e-04
	log keff	-3.2215	-3.2509	-2.9910	-3.1247	-3.2725	-3.3403	-3.0691
ID	RRF	MOLES	MOLES	MOLES	MOLES	MOLES	MOLES	MOLES
BIP	1.0000	1.28e-03	1.29e-03	1.29e-03	1.28e-03	1.28e-03	1.28e-03	1.29e-03
DHA	1.1667			5.40e-07	1.25e-06	2.75e-06	5.01e-06	8.01e-06
DHMA	1.2500		3.19e-07	1.85e-06	2.18e-06	2.21e-06	1.18e-06	
c-DHDMA	1.3333	3.44e-06	7.14e-07	6.63e-07	3.58e-07			
DHMA	1.2500							
UNK182	1.1667						1.01e-06	2.77e-06
t-DHDMA	1.3333		2.70e-07					
ANT	1.1904	1.06e-06	4.64e-06	4.04e-05	6.60e-05	9.46e-05	1.15e-04	1.18e-04
DHMA	1.2500					1.39e-06	7.90e-06	1.30e-05
UNK196	1.2500							6.41e-07
UNK196	1.2500							6.70e-07
2MA	1.2062		2.48e-07	7.78e-06	1.69e-05	3.03e-05	4.42e-05	4.76e-05
1MA	1.2027		4.13e-07	1.29e-05	2.66e-05	4.61e-05	6.53e-05	6.88e-05
9MA	1.2586	4.12e-05	9.20e-05	1.55e-04	1.28e-04	8.26e-05	3.32e-05	1.16e-05
DMA	1.3333	1.62e-06	2.34e-06	2.99e-06	1.06e-06	2.14e-06	1.63e-06	
DMA	1.3333				1.10e-06			
DMA	1.3333				9.48e-07	1.36e-06	1.65e-06	1.43e-06
DMA	1.3333			1.05e-06	2.42e-06	4.77e-06	7.03e-06	6.75e-06
DMA	1.3333			1.79e-06	4.51e-06	9.59e-05	1.54e-05	1.66e-05
DMA	1.3333			1.07e-06	2.36e-06	5.07e-06	8.33e-06	9.14e-06
29&39DMA	1.3333		1.65e-06	1.24e-05	1.37e-05	1.03e-05	4.09e-06	
19DMA	1.3333	3.61e-07	2.37e-06	1.59e-05	1.86e-05	1.83e-05	1.30e-05	1.44e-05
110DMA	1.3333	1.06e-06	3.90e-06	2.26e-05	2.34e-05	1.92e-05	9.55e-06	
910DMA	1.3239	3.75e-04	2.98e-04	7.92e-05	3.31e-05	1.05e-05	3.53e-06	9.83e-07
TMA	1.4167					1.21e-06	1.22e-06	
TMA	1.4167					1.26e-06	1.89e-06	1.68e-06
TMA	1.4167	6.16e-06	5.98e-06	2.65e-06	2.62e-06	1.79e-06	1.77e-06	1.46e-06
TMA	1.4167			8.54e-07	1.01e-06			
TMA	1.4167			7.28e-07	1.14e-06	2.21e-06	1.32e-06	
TMA	1.4167			2.80e-06	4.04e-06	4.39e-06		
TMA	1.4167				2.00e-06	2.66e-06	5.32e-06	2.30e-06
TMA	1.4167	5.07e-06	1.38e-05	1.60e-05	1.03e-05	3.38e-06		
TMA	1.4167	3.19e-07	6.15e-07	7.96e-07	6.44e-07	2.70e-06	1.80e-06	
TMA	1.4167	9.63e-07	1.18e-06					
TMA	1.4167				3.71e-07	9.36e-07	1.24e-06	1.79e-06
MATERIAL BALANCE ON:								
wt %C		0.878	0.857	0.733	0.704	0.690	0.665	0.613
wt %H		0.873	0.845	0.694	0.658	0.637	0.608	0.558
3-RING SYSTEM		0.881	0.868	0.755	0.740	0.731	0.713	0.662
METHYL GROUPS		0.850	0.786	0.527	0.450	0.392	0.324	0.266

half-life t* = 1110 s

9MA THERMOLYSIS - 315°C - 0.82 mol/l - TRIAL #1 - 8/11/92

	[9MA]o	0.823	0.828	0.820	0.823	0.820	0.827
	Time(s)	1800	3600	7200	14400	28800	57600
	X	0.1094	0.1254	0.0834	0.0929	0.1216	0.0964
	-ln(1-X)/t	6.44e-05	3.72e-05	1.21e-05	6.77e-06	4.50e-06	1.76e-06
	log keff	-4.1913	-4.4292	-4.9174	-5.1693	-5.3466	-5.7545
ID	RRF	MOLES	MOLES	MOLES	MOLES	MOLES	MOLES
BIP	1.0000	1.33e-03	1.33e-03	1.33e-03	1.33e-03	1.33e-03	1.33e-03
DHMA	1.2500	3.35e-07	7.23e-07	1.06e-06	1.50e-06	1.97e-06	2.80e-06
ANTHR	1.1904		2.93e-07	6.43e-07	1.42e-06	2.86e-06	7.75e-06
1MA	1.2027	1.88e-06	2.07e-06	2.03e-06	2.15e-06	2.06e-06	2.25e-06
9MA	1.2586	4.39e-04	4.34e-04	4.53e-04	4.48e-04	4.32e-04	4.48e-04
29&39DMA	1.3333						3.99e-07
19DMA	1.3333						4.98e-07
110DMA	1.3333	3.38e-07			3.47e-07	5.93e-07	1.33e-06
910DMA	1.3239	4.52e-07	6.84e-07	9.14e-07	1.50e-06	2.46e-06	4.84e-06
MATERIAL BALANCE ON:							
wt %C		0.897	0.882	0.926	0.921	0.899	0.944
wt %H		0.897	0.883	0.926	0.922	0.899	0.944
3-RING SYSTEM		0.897	0.882	0.926	0.921	0.899	0.944
METHYL GROUPS		0.898	0.883	0.927	0.922	0.899	0.942

half-life t* = 458900 s

9MA THERMOLYSIS - 315°C - 0.82 mol/l - TRIAL #2 - 8/11/92

	[9MA]o	0.822	0.820	0.822	0.828	0.828	0.830
	Time(s)	1800	3600	7200	14400	28800	57600
	X	0.1494	0.1205	0.0859	0.1226	0.1384	0.1344
	-ln(1-X)/t	8.99e-05	3.57e-05	1.25e-05	9.08e-06	5.17e-06	2.51e-06
	log keff	-4.0463	-4.4477	-4.9040	-5.0418	-5.2863	-5.6011
ID	RRF	MOLES	MOLES	MOLES	MOLES	MOLES	MOLES
BIP	1.0000	1.33e-03	1.33e-03	1.33e-03	1.33e-03	1.33e-03	1.33e-03
DHMA	1.2500	3.83e-07	6.37e-07	8.33e-07	1.05e-06	1.77e-06	2.52e-06
ANT	1.1904		2.99e-07	7.83e-07	1.21e-06	2.90e-06	6.11e-06
1MA	1.2027	2.44e-06	2.29e-06	2.45e-06	2.02e-06	2.19e-06	2.02e-06
9MA	1.2586	4.19e-04	4.33e-04	4.51e-04	4.36e-04	4.28e-04	4.31e-04
29&39DMA	1.3333						3.09e-07
19DMA	1.3333						4.00e-07
110DMA	1.3333				3.04e-07	5.36e-07	1.12e-06
910DMA	1.3239	6.38e-07	6.37e-07	1.06e-06	1.71e-06	2.29e-06	4.10e-06
MATERIAL BALANCE ON:							
wt %C		0.858	0.887	0.925	0.890	0.881	0.899
wt %H		0.858	0.888	0.925	0.891	0.882	0.900
3-RING SYSTEM		0.858	0.887	0.925	0.890	0.881	0.899
METHYL GROUPS		0.859	0.888	0.925	0.892	0.881	0.899

half-life t* = 318819 s

9MA THERMOLYSIS - 335°C - 0.82 mol/l - TRIAL #1 - 8/27/92

	[9MA]o	0.823	0.823	0.827	0.822	0.823	0.828
	Time(s)	1800	3600	7200	14400	28800	57600
	X	0.0917	0.0935	0.1089	0.1277	0.1773	0.2290
	-ln(1-X)/t	5.34e-05	2.73e-05	1.60e-05	9.49e-06	6.78e-06	4.52e-06
	log keff	-4.2722	-4.5643	-4.7955	-5.0228	-5.1690	-5.3453
ID	RRF	MOLES	MOLES	MOLES	MOLES	MOLES	MOLES
BIP	1.0000	1.33e-03	1.33e-03	1.33e-03	1.33e-03	1.33e-03	1.33e-03
DHMA	1.2500	6.96e-07	9.74e-07	1.35e-06	2.10e-06	2.91e-06	3.58e-06
ANT	1.1904	4.83e-07	1.12e-06	2.64e-06	6.22e-06	2.08e-05	3.45e-05
2MA	1.2062						4.63e-07
1MA	1.2027	2.06e-06	1.69e-06	1.83e-06	1.81e-06	2.12e-06	2.41e-06
9MA	1.2586	4.49e-04	4.47e-04	4.42e-04	4.30e-04	4.07e-04	3.83e-04
DMA	1.3333					1.89e-06	1.93e-06
29&39DMA	1.3333				2.94e-07	9.27e-07	1.49e-06
19DMA	1.3333			6.57e-07	7.26e-07	1.21e-06	1.81e-06
110DMA	1.3333		4.33e-07	8.32e-07	1.33e-06	3.48e-06	5.56e-06
910DMA	1.3239	2.11e-06	1.74e-06	2.60e-06	4.70e-06	1.15e-05	1.70e-05
MATERIAL BALANCE ON:							
wt %C		0.919	0.920	0.911	0.907	0.913	0.908
wt %H		0.920	0.919	0.912	0.908	0.914	0.908
3-RING SYSTEM		0.919	0.919	0.911	0.907	0.913	0.909
METHYL GROUPS		0.922	0.921	0.914	0.909	0.910	0.896

half-life t* = 196305 s

9MA THERMOLYSIS - 335°C - 0.82 mol/l - TRIAL #2 - 8/27/92

	[9MA]o	0.825	0.828	0.823	0.825	0.823	0.820
	Time(s)	1800	3600	7200	14400	28800	57600
	X	0.0972	0.0993	0.0955	0.1187	0.1720	0.2408
	-ln(1-X)/t	5.68e-05	2.91e-05	1.39e-05	8.77e-06	6.55e-06	4.78e-06
	log keff	-4.2456	-4.5368	-4.8557	-5.0568	-5.1835	-5.3203
ID	RRF	MOLES	MOLES	MOLES	MOLES	MOLES	MOLES
BIP	1.0000	1.33e-03	1.33e-03	1.33e-03	1.33e-03	1.33e-03	1.33e-03
DHMA	1.2500	6.92e-07	9.11e-07	1.32e-06	2.08e-06	2.93e-06	3.39e-06
ANT	1.1904	4.35e-07	1.30e-06	2.92e-06	5.72e-06	1.69e-05	3.09e-05
2MA	1.2062						3.58e-07
1MA	1.2027	1.62e-06	1.74e-06	1.63e-06	1.81e-06	1.51e-06	2.44e-06
9MA	1.2586	4.47e-04	4.48e-04	4.47e-04	4.36e-04	4.09e-04	3.74e-04
29&39DMA	1.3333					7.73e-07	1.59e-06
19DMA	1.3333				1.07e-06	9.61e-07	1.84e-06
110DMA	1.3333			7.40e-07	1.52e-06	2.95e-06	6.29e-06
910DMA	1.3239	1.61e-06	1.50e-06	2.74e-06	5.33e-06	9.61e-06	1.71e-05
MATERIAL BALANCE ON:							
wt %C		0.912	0.912	0.923	0.917	0.900	0.889
wt %H		0.912	0.912	0.924	0.918	0.900	0.889
3-RING SYSTEM		0.912	0.912	0.923	0.917	0.900	0.889
METHYL GROUPS		0.914	0.912	0.925	0.921	0.895	0.881

half-life t* = 161828 s

9MA THERMOLYSIS - 355°C - 0.82 mol/l - TRIAL #1 - 10/11/92

ID	RRF	MOLES	MOLES	MOLES	MOLES	MOLES	MOLES	MOLES
[9MA]o		0.823	0.823	0.825	0.825	0.823	0.823	0.823
Time(s)		450	900	1800	3600	7200	14400	28800
X		0.0113	0.0207	0.0110	0.0603	0.0811	0.2093	0.3007
-ln(1-X)/t		2.53e-05	2.32e-05	6.14e-06	1.73e-05	1.17e-05	1.63e-05	1.24e-05
log keff		-4.5977	-4.6337	-5.2115	-4.7625	-4.9301	-4.7876	-4.9059
BIP	1.0000	1.33e-03	1.33e-03	1.33e-03	1.33e-03	1.33e-03	1.33e-03	1.33e-03
DHA	1.1667						2.93e-07	4.11e-07
DHMA	1.2500	4.61e-07	1.05e-06	9.58e-07	1.51e-06	2.40e-06	3.17e-06	2.69e-06
ANT	1.1904	6.83e-07	2.21e-06	2.92e-06	7.70e-06	1.76e-05	3.39e-05	5.01e-05
UNK196	1.2500						4.13e-07	
2MA	1.2062						1.05e-06	6.35e-07
1MA	1.2027	1.94e-06	1.99e-06	1.89e-06	1.81e-06	2.54e-06	1.98e-06	4.18e-06
9MA	1.2586	4.88e-04	4.84e-04	4.89e-04	4.65e-04	4.54e-04	3.90e-04	3.46e-04
DMA	1.3333						5.16e-07	
DMA	1.3333						3.84e-07	
29&39DMA	1.3333				3.42e-07	6.80e-07	1.82e-06	1.85e-06
19DMA	1.3333				3.52e-07	8.72e-07	1.82e-06	2.86e-06
110DMA	1.3333		5.21e-07	4.95e-07	1.41e-06	3.34e-06	5.84e-06	8.61e-06
910DMA	1.3239	1.16e-06	1.69e-06	2.00e-06	5.06e-06	1.08e-05	1.46e-05	2.42e-05

MATERIAL BALANCE ON:

wt %C		0.997	0.994	1.006	0.976	0.996	0.923	0.891
wt %H		0.998	0.995	1.006	0.977	0.997	0.922	0.889
3-RING SYSTEM		0.997	0.994	1.006	0.977	0.996	0.924	0.893
METHYL GROUPS		0.998	0.994	1.005	0.975	0.993	0.906	0.867

half-life t* = 61059 s

9MA THERMOLYSIS - 355°C - 0.82 mol/l - TRIAL #2 - 10/11/92

ID	RRF	MOLES	MOLES	MOLES	MOLES	MOLES	MOLES	MOLES
[9MA]o		0.827	0.822	0.827	0.827	0.825	0.822	0.823
Time(s)		450	900	1800	3600	7200	14400	28800
X		0.0153	0.0755	0.0334	0.0590	0.0987	0.1505	0.2935
-ln(1-X)/t		3.43e-05	8.72e-05	1.89e-05	1.69e-05	1.44e-05	1.13e-05	1.21e-05
log keff		-4.4652	-4.0594	-4.7242	-4.7723	-4.8406	-4.9459	-4.9185
BIP	1.0000	1.33e-03	1.33e-03	1.33e-03	1.33e-03	1.33e-03	1.33e-03	1.33e-03
DHA	1.1667							5.76e-07
DHMA	1.2500	7.55e-07	9.85e-07	1.33e-06	1.15e-06	1.58e-06	2.21e-06	3.03e-06
ANT	1.1904	5.92e-07	9.87e-07	2.66e-06	5.85e-06	1.23e-05	2.08e-05	5.57e-05
UNK196	1.2500							4.53e-07
2MA	1.2062						2.65e-07	1.04e-06
1MA	1.2027	5.56e-07	4.70e-07	4.34e-07	5.77e-07	6.04e-07	5.01e-07	3.10e-06
9MA	1.2586	4.88e-04	4.56e-04	4.79e-04	4.66e-04	4.46e-04	4.19e-04	3.49e-04
DMA	1.3333							2.72e-06
29&39DMA	1.3333						8.53e-07	2.55e-06
19DMA	1.3333			7.89e-07	2.89e-06	1.28e-06	8.12e-07	2.63e-06
110DMA	1.3333		4.49e-07	1.00e-06	2.13e-06	2.58e-06	3.01e-06	8.75e-06
910DMA	1.3239	4.38e-07	6.51e-07	1.78e-06	5.03e-06	7.62e-06	1.13e-05	2.69e-05
TMA	1.4167							4.43e-07
TMA	1.4167							3.06e-07

MATERIAL BALANCE ON:

wt %C		0.989	0.932	0.983	0.977	0.954	0.929	0.924
wt %H		0.990	0.932	0.983	0.978	0.954	0.929	0.923
3-RING SYSTEM		0.990	0.932	0.983	0.977	0.954	0.930	0.926
METHYL GROUPS		0.989	0.932	0.985	0.985	0.952	0.920	0.902

half-life t* = 56331 s

9MA THERMOLYSIS - 370°C - 0.082 mol/l - TRIAL #1 - 5/18/92

	[9MA]o	0.085	0.082	0.085	0.085	0.083	0.082	0.085	0.082
	Time(s)	450	900	1800	3600	7200	14400	28800	57600
	X	0.2164	0.1013	0.1136	0.1093	0.1986	0.2216	0.3288	0.4269
	$-\ln(1-X)/t$	5.42e-04	1.19e-04	6.70e-05	3.22e-05	3.07e-05	1.74e-05	1.38e-05	9.66e-06
	log keff	-3.2661	-3.9256	-4.1740	-4.4928	-4.5122	-4.7595	-4.8588	-5.0148
ID	RRF	MOLES	MOLES	MOLES	MOLES	MOLES	MOLES	MOLES	MOLES
BIP	1.0000	1.89e-03	1.89e-03	1.88e-03	1.88e-03	1.88e-03	1.88e-03	1.88e-03	1.88e-03
ANT	1.1904	2.38e-07	3.91e-07	4.54e-07	2.96e-07	1.13e-06	5.12e-06	5.97e-06	9.28e-06
1MA	1.2027							6.81e-07	4.29e-07
9MA	1.2586	3.99e-05	4.39e-05	4.52e-05	4.54e-05	3.92e-05	3.81e-05	3.42e-05	2.83e-05
110DMA	1.3333					1.55e-07		4.47e-07	6.22e-07
910DMA	1.3239	8.40e-07		5.78e-07		4.30e-07	1.23e-06	1.93e-06	2.25e-06
TMA	1.4167	4.54e-07	5.03e-07	5.81e-07					
TMA	1.4167			3.07e-07					

MATERIAL BALANCE ON:

wt %C		0.816	0.918	0.927	0.897	0.836	0.903	0.844	0.819
wt %H		0.819	0.919	0.930	0.897	0.835	0.895	0.837	0.806
3-RING SYSTEM		0.814	0.917	0.924	0.897	0.837	0.908	0.848	0.828
METHYL GROUPS		0.843	0.930	0.961	0.891	0.825	0.829	0.778	0.698

half-life t* = 74756 s

9MA THERMOLYSIS - 370°C - 0.082 mol/l - TRIAL #2 - 7/26/92

	[9MA]o	0.088	0.082	0.084	0.086	0.083	0.088	0.088	0.082
	Time(s)	450	900	1800	3600	7200	14400	28800	57600
	X	0.1044	0.0699	0.0908	0.0866	0.1496	0.2259	0.3104	0.4537
	$-\ln(1-X)/t$	2.45e-04	8.05e-05	5.29e-05	2.52e-05	2.25e-05	1.78e-05	1.29e-05	1.05e-05
	log keff	-3.6108	-4.0941	-4.2767	-4.5993	-4.6477	-4.7500	-4.8893	-4.9790
ID	RRF	MOLES	MOLES	MOLES	MOLES	MOLES	MOLES	MOLES	MOLES
BIP	1.0000	1.88e-03	1.89e-03	1.88e-03	1.89e-03	1.88e-03	1.89e-03	1.88e-03	1.88e-03
ANT	1.1904			3.97e-07	8.96e-07	7.45e-07	3.04e-06	7.41e-06	1.03e-05
1MA	1.2027								7.99e-07
9MA	1.2586	4.71e-05	4.55e-05	4.59e-05	4.70e-05	4.25e-05	4.07e-05	3.62e-05	2.70e-05
110DMA	1.3333						4.89e-07	6.02e-07	7.91e-07
910DMA	1.3239					3.69e-07	1.33e-06	2.14e-06	2.35e-06

MATERIAL BALANCE ON:

wt %C		0.896	0.930	0.917	0.930	0.872	0.865	0.877	0.824
wt %H		0.896	0.930	0.916	0.928	0.871	0.863	0.868	0.810
3-RING SYSTEM		0.896	0.930	0.917	0.931	0.873	0.867	0.883	0.834
METHYL GROUPS		0.896	0.930	0.909	0.913	0.865	0.843	0.794	0.690

half-life t* = 66198 s

9MA THERMOLYSIS - 370°C - 0.25 mol/l - TRIAL #1 - 5/26/92

	[9MA]o	0.252	0.247	0.245	0.252	0.250	0.245
	Time(s)	1800	3600	7200	14400	28800	57600
	X	0.1517	0.1809	0.2455	0.4697	0.5520	0.6025
	-ln(1-X)/t	9.14e-05	5.54e-05	3.91e-05	4.40e-05	2.79e-05	1.60e-05
	log keff	-4.0391	-4.2563	-4.4075	-4.3561	-4.5547	-4.7954
ID	RRF	MOLES	MOLES	MOLES	MOLES	MOLES	MOLES
BIP	1.0000	1.76e-03	1.76e-03	1.76e-03	1.76e-03	1.76e-03	1.76e-03
DHA	1.1667				2.81e-07		
DHMA	1.2500	8.73e-07	6.01e-07	5.52e-07	1.01e-06	4.13e-07	2.15e-07
ANT	1.1904	4.94e-06	7.21e-06	1.08e-05	2.70e-05	3.46e-05	4.35e-05
DHMA	1.2500		9.46e-07	1.11e-06			
2MA	1.2062				8.61e-07	1.22e-06	2.26e-06
1MA	1.2027	6.81e-07	6.38e-07	6.84e-07	3.18e-06	4.86e-06	7.49e-06
9MA	1.2586	1.28e-04	1.21e-04	1.11e-04	8.00e-05	6.73e-05	5.85e-05
29&39DMA	1.3333				9.00e-07	1.02e-06	1.40e-06
19DMA	1.3333	6.44e-07	5.73e-07	7.12e-07	1.12e-06	1.34e-06	1.73e-06
110DMA	1.3333	8.77e-07	1.22e-06	1.90e-06	3.62e-06	4.57e-06	4.98e-06
910DMA	1.3239	1.36e-06	2.90e-06	5.22e-06	7.24e-06	7.81e-06	7.20e-06
TMA	1.4167						4.30e-07
MATERIAL BALANCE ON:							
wt %C		0.910	0.913	0.896	0.824	0.811	0.856
wt %H		0.909	0.913	0.896	0.816	0.798	0.837
3-RING SYSTEM		0.910	0.914	0.898	0.830	0.819	0.868
METHYL GROUPS		0.897	0.897	0.877	0.730	0.688	0.682

half-life t* = 21203 s

9MA THERMOLYSIS - 370°C - 0.25 mol/l - TRIAL #2 - 7/26/92

	[9MA]o	0.247	0.245	0.250	0.245	0.247	0.247	0.248	0.245
	Time(s)	450	1800	1800	3600	7200	14400	28800	57600
	X	0.0790	0.0552	0.0893	0.1504	0.1739	0.1971	0.4030	0.6270
	-ln(1-X)/t	1.83e-04	3.15e-05	5.20e-05	4.53e-05	2.65e-05	1.52e-05	1.79e-05	1.71e-05
	log keff	-3.7378	-4.5011	-4.2843	-4.3441	-4.5762	-4.8169	-4.7469	-4.7665
ID	RRF	MOLES	MOLES	MOLES	MOLES	MOLES	MOLES	MOLES	MOLES
BIP	1.0000	1.76e-03	1.76e-03	1.76e-03	1.76e-03	1.76e-03	1.76e-03	1.76e-03	1.76e-03
DHMA	1.2500				2.65e-07	4.64e-07			
ANTHR	1.1904	3.78e-07	4.97e-07	1.50e-06	3.36e-06	9.39e-06	1.38e-05	2.59e-05	4.25e-05
2MA	1.2062							4.01e-07	2.15e-06
1MA	1.2027	2.60e-07	2.63e-07		2.49e-07	3.97e-07	5.63e-07	1.79e-06	7.19e-06
9MA	1.2586	1.37e-04	1.39e-04	1.37e-04	1.25e-04	1.22e-04	1.19e-04	8.88e-05	5.49e-05
29&39DMA	1.3333								1.28e-06
19DMA	1.3333					4.60e-07	6.84e-07	1.32e-06	1.65e-06
110DMA	1.3333				5.44e-07	1.25e-06	1.91e-06	3.69e-06	4.68e-06
910DMA	1.3239			7.16e-07	1.92e-06	4.50e-06	6.46e-06	9.37e-06	6.40e-06
TMA	1.4167								4.06e-07
MATERIAL BALANCE ON:									
wt %C		0.925	0.950	0.926	0.892	0.936	0.960	0.877	0.810
wt %H		0.925	0.949	0.926	0.892	0.934	0.956	0.870	0.792
3-RING SYSTEM		0.925	0.950	0.925	0.893	0.937	0.962	0.883	0.823
METHYL GROUPS		0.923	0.947	0.920	0.887	0.916	0.929	0.805	0.635

half-life t* = 41373 s

867

9MA THERMOLYSIS - 370°C - 0.82 mol/l - TRIAL #1 - 5/26/92

ID	RRF							
[9MA]o		0.825	0.825	0.820	0.825	0.823	0.827	0.823
Time(s)		450	900	1800	3600	7200	14400	28800
X		0.0711	0.0768	0.0985	0.1436	0.2284	0.4024	0.5539
-ln(1-X)/t		1.64e-04	8.88e-05	5.76e-05	4.31e-05	3.60e-05	3.58e-05	2.80e-05
log keff		-3.7854	-4.0516	-4.2395	-4.3659	-4.4435	-4.4467	-4.5524
		MOLES	MOLES	MOLES	MOLES	MOLES	MOLES	MOLES
BIP	1.0000	1.33e-03	1.33e-03	1.33e-03	1.33e-03	1.33e-03	1.33e-03	1.33e-03
DHA	1.1667						7.79e-07	1.71e-06
DHMA	1.2500	7.60e-07	8.76e-07	1.26e-06	2.19e-06	2.43e-06	2.73e-06	2.87e-06
c-DHDMA	1.3333						2.21e-07	2.74e-07
DHMA	1.2500					3.08e-07	4.02e-07	3.74e-07
ANT	1.1904	1.44e-06	2.94e-06	5.93e-06	2.09e-05	3.79e-05	8.02e-05	1.17e-04
DHMA	1.2500					3.03e-07	3.22e-07	
2MA	1.2062					4.78e-07	2.31e-06	6.53e-06
1MA	1.2027	2.02e-06	2.49e-06	2.44e-06	2.86e-06	3.64e-06	8.55e-06	2.04e-05
9MA	1.2586	4.60e-04	4.57e-04	4.43e-04	4.24e-04	3.81e-04	2.96e-04	2.20e-04
DMA	1.3333					8.20e-07	9.21e-07	1.68e-06
DMA	1.3333				5.42e-07	6.04e-07	1.12e-06	
DMA	1.3333				4.06e-07	5.87e-07		
DMA	1.3333						4.31e-07	6.02e-07
DMA	1.3333							8.74e-07
DMA	1.3333							6.63e-07
29&39DMA	1.3333			3.07e-07	1.10e-06	1.98e-06	3.61e-06	4.86e-06
19DMA	1.3333	6.44e-07	7.24e-07	6.73e-07	1.30e-06	2.16e-06	4.06e-06	6.72e-06
110DMA	1.3333	2.92e-07	5.78e-07	1.06e-06	3.38e-06	6.00e-06	1.22e-05	1.82e-05
910DMA	1.3239	2.10e-06	2.66e-06	4.21e-06	1.26e-05	1.90e-05	2.87e-05	2.84e-05
TMA	1.4167					3.18e-07		1.21e-06
TMA	1.4167						1.13e-06	2.01e-06
MATERIAL BALANCE ON:								
wt %C		0.944	0.944	0.934	0.948	0.925	0.891	0.873
wt %H		0.944	0.945	0.934	0.947	0.923	0.885	0.863
3-RING SYSTEM		0.944	0.944	0.934	0.948	0.926	0.895	0.881
METHYL GROUPS		0.947	0.946	0.934	0.945	0.914	0.839	0.779

half-life t* = 23684 s

9MA THERMOLYSIS - 370°C - 0.82 mol/l - TRIAL #2 - 5/16/92

	$[9MA]_o$	0.823	0.825	0.823	0.825	0.825	0.823	0.828
	Time(s)	450	900	1800	3600	7200	14400	28800
	X	0.0978	0.1274	0.1636	0.1809	0.3501	0.4204	0.5383
	$-\ln(1-X)/t$	2.29e-04	1.51e-04	9.92e-05	5.54e-05	5.99e-05	3.79e-05	2.68e-05
	log keff	-3.6407	-3.8198	-4.0033	-4.2563	-4.2229	-4.4216	-4.5713
ID	RRF	MOLES	MOLES	MOLES	MOLES	MOLES	MOLES	MOLES
BIP	1.0000	1.33e-03	1.33e-03	1.34e-03	1.33e-03	1.33e-03	1.33e-03	1.34e-03
DHA	1.1667					9.40e-07	8.18e-07	1.74e-06
DHMA	1.2500	5.56e-07	1.34e-06	2.04e-06	1.92e-06	4.22e-06	2.56e-06	2.98e-06
c-DHDMA	1.3333					2.68e-07	2.11e-07	2.78e-07
ANT	1.1904	8.03e-07	5.55e-06	1.43e-05	2.03e-05	6.49e-05	8.14e-05	1.21e-04
DHMA	1.2500		4.36e-07	3.03e-07	8.43e-07			
UNK196	1.2500					2.60e-07		
2MA	1.2062					1.83e-06	2.42e-06	6.68e-06
1MA	1.2027	2.18e-06	3.26e-06	2.86e-06	2.86e-06	7.25e-06	8.43e-06	1.99e-05
9MA	1.2586	4.46e-04	4.32e-04	4.13e-04	4.05e-04	3.22e-04	2.86e-04	2.30e-04
DMA	1.3333			1.13e-06	9.98e-07		1.70e-06	1.50e-06
DMA	1.3333							5.23e-07
DMA	1.3333							8.35e-07
DMA	1.3333			1.06e-06	1.46e-06	1.73e-06		6.40e-07
29&39DMA	1.3333		2.81e-07	7.16e-07	9.38e-07	3.59e-06	3.54e-06	5.40e-06
19DMA	1.3333	1.21e-06	5.79e-07	8.85e-07	1.15e-06	3.81e-06	4.20e-06	6.68e-06
110DMA	1.3333		1.07e-06	2.28e-06	3.58e-06	1.04e-05	1.27e-05	1.85e-05
910DMA	1.3239		3.24e-06	7.35e-06	1.14e-05	2.58e-05	2.90e-05	2.97e-05
TMA	1.4167					7.49e-07		1.09e-06
TMA	1.4167					6.23e-07	9.23e-07	1.96e-06

MATERIAL BALANCE ON:

wt %C	0.912	0.904	0.903	0.911	0.903	0.875	0.895
wt %H	0.912	0.905	0.902	0.910	0.901	0.869	0.886
3-RING SYSTEM	0.912	0.905	0.903	0.911	0.905	0.879	0.902
METHYL GROUPS	0.913	0.904	0.901	0.910	0.870	0.820	0.797

half-life $t^* = 24429$ s

869

9MA THERMOLYSIS - 370°C - 0.82 mol/l - TRIAL #G1 - 11/15/92

[9MA]o		0.827	0.823	0.828	0.823	0.823	0.825
Time(s)		900	1800	3600	7200	14400	28800
X		0.0933	0.0969	0.1491	0.2460	0.3424	0.6009
$-\ln(1-X)/t$		1.09e-04	5.66e-05	4.49e-05	3.92e-05	2.91e-05	3.19e-05
log keff		-3.9633	-4.2470	-4.3482	-4.4065	-4.5360	-4.4963
ID	**RRF**	**MOLES**	**MOLES**	**MOLES**	**MOLES**	**MOLES**	**MOLES**
BIP	1.0000	1.33e-03	1.33e-03	1.33e-03	1.33e-03	1.33e-03	1.33e-03
DHA	1.1667				1.48e-06	3.04e-06	4.83e-06
DHMA	1.2500	1.23e-06	1.11e-06	1.27e-06	1.77e-05	9.30e-06	7.12e-06
c-DHDMA	1.3333				4.12e-07	3.67e-07	6.02e-07
ANT	1.1904	2.89e-06	4.29e-06	9.79e-06	3.44e-05	5.71e-05	1.24e-04
UNK196	1.2500				4.12e-07		2.89e-06
2MA	1.2062				5.47e-07	2.20e-06	1.07e-05
1MA	1.2027	1.90e-06	1.63e-06	1.42e-06	1.43e-06	4.44e-06	2.22e-05
9MA	1.2586	4.49e-04	4.46e-04	4.23e-04	3.73e-04	3.25e-04	1.98e-04
DMA	1.3333						8.71e-07
DMA	1.3333	8.66e-07	1.05e-06	3.97e-07	4.37e-06	3.83e-06	1.75e-06
DMA	1.3333						7.52e-07
DMA	1.3333						9.62e-07
DMA	1.3333						1.39e-06
DMA	1.3333						1.13e-06
29&39DMA	1.3333		4.39e-07	6.53e-07	1.61e-06	2.94e-06	6.66e-06
19DMA	1.3333		3.41e-07	5.55e-07	1.74e-06	3.22e-06	7.78e-06
110DMA	1.3333	7.95e-07	1.22e-06	1.81e-06	4.70e-06	8.50e-06	1.77e-05
910DMA	1.3239	2.09e-06	2.53e-06	4.14e-06	1.24e-05	1.98e-05	2.45e-05
TMA	1.4167					6.45e-07	1.27e-06
TMA	1.4167						1.03e-06
TMA	1.4167					5.96e-07	1.97e-06
CH4	-	4.80e-07	1.02e-06	1.99e-06	6.59e-06	1.28e-05	4.69e-05
C2H4	-						6.12e-07
C2H6	-		3.18e-07	4.36e-07	6.31e-07	9.94e-07	1.30e-06
MATERIAL BALANCE ON:							
wt %C		0.927	0.929	0.891	0.918	0.892	0.884
wt %H		0.927	0.931	0.893	0.927	0.900	0.905
3-RING SYSTEM		0.926	0.929	0.891	0.918	0.892	0.884
METHYL GROUPS		0.929	0.934	0.892	0.911	0.881	0.868

half-life t* = 23244 s

9MA THERMOLYSIS - 370°C - 0.82 mol/l - TRIAL #G2 - 1/3/93

[9MA]o		0.823	0.823	0.822	0.823	0.825	0.822
Time(s)		900	1800	3600	7200	14400	28800
X		0.0976	0.0665	0.0999	0.1944	0.3108	0.6539
-ln(1-X)/t		1.14e-04	3.82e-05	2.92e-05	3.00e-05	2.58e-05	3.68e-05
log keff		-3.9427	-4.4176	-4.5341	-4.5225	-4.5876	-4.4337
ID	RRF	MOLES	MOLES	MOLES	MOLES	MOLES	MOLES
BIP	1.0000	1.33e-03	1.33e-03	1.33e-03	1.33e-03	1.33e-03	1.33e-03
DHA	1.1667				5.83e-07	1.64e-06	5.59e-06
DHMA	1.2500	1.07e-06	1.30e-06	2.18e-06	6.69e-06	5.88e-06	8.66e-06
c-DHDMA	1.3333					3.30e-07	6.67e-07
ANT	1.1904	2.46e-06	3.64e-06	1.17e-05	3.56e-05	5.10e-05	1.15e-04
UNK196	1.2500				\		8.79e-07
2MA	1.2062			3.48e-07	7.82e-07	2.30e-06	1.10e-05
1MA	1.2027	7.27e-07	5.23e-07	3.03e-07	1.67e-06	4.48e-06	2.03e-05
9MA	1.2586	4.45e-04	4.61e-04	4.43e-04	3.98e-04	3.41e-04	1.71e-04
DMA	1.3333						9.25e-07
DMA	1.3333			4.26e-07	7.42e-07	6.69e-07	1.02e-06
DMA	1.3333						3.40e-07
DMA	1.3333						5.83e-07
DMA	1.3333						1.11e-06
DMA	1.3333						7.51e-07
29&39DMA	1.3333			7.79e-07	2.28e-06	3.28e-06	6.48e-06
19DMA	1.3333			6.25e-07	1.98e-06	3.00e-06	7.14e-06
110DMA	1.3333	5.50e-07	7.65e-07	1.75e-06	5.73e-06	7.71e-06	1.49e-05
910DMA	1.3239	1.70e-06	2.46e-06	5.13e-06	1.66e-05	1.84e-05	2.07e-05
TMA	1.4167					4.93e-07	7.52e-07
TMA	1.4167						3.18e-07
TMA	1.4167						7.41e-07
TMA	1.4167						3.08e-07
TMA	1.4167					5.53e-07	1.64e-06
TMA	1.4167						4.27e-07
CH4	-	4.85e-07	9.44e-07	1.93e-06	5.94e-06	6.66e-06	4.75e-05
C2H4	-						7.05e-07
C2H6	-			2.73e-07		4.10e-07	1.71e-06
MATERIAL BALANCE ON:							
wt %C		0.916	0.951	0.947	0.952	0.890	0.791
wt %H		0.916	0.952	0.949	0.956	0.893	0.813
3-RING SYSTEM		0.916	0.951	0.947	0.953	0.891	0.792
METHYL GROUPS		0.916	0.952	0.946	0.947	0.870	0.776

half-life t* = 22362 s

9MA PYRLOYSIS - 370°C - 2.06 mol/l - TRIAL #1 - 6/10/92

	[9MA]o	2.050	2.067	2.050	2.067	2.067	2.050	2.050
	Time(s)	450	900	1800	3600	7200	14400	28800
	X	0.0827	0.1398	0.1456	0.2070	0.3778	0.5654	0.7249
	-ln(1-X)/t	1.92e-04	1.67e-04	8.74e-05	6.44e-05	6.59e-05	5.79e-05	4.48e-05
	log keff	-3.7171	-3.7764	-4.0584	-4.1909	-4.1811	-4.2375	-4.3486
ID	RRF	MOLES	MOLES	MOLES	MOLES	MOLES	MOLES	MOLES
BIP	1.0000	4.07e-04	4.09e-04	4.08e-04	4.11e-04	4.08e-04	4.08e-04	4.06e-04
DHA	1.1667				1.26e-06	3.40e-06	9.96e-06	1.88e-05
DHMA	1.2500	4.03e-06	5.30e-06	7.73e-06	1.11e-05	1.31e-05	1.61e-05	1.51e-05
c-DHDMA	1.3333				3.93e-07	8.12e-07	1.36e-06	1.00e-06
UNK182	1.2500					2.74e-07	1.86e-06	5.60e-06
DHMA	1.2500		4.67e-07	4.30e-07	5.83e-07	7.42e-07	7.51e-07	6.94e-07
ANT	1.1904	6.81e-06	1.89e-05	3.74e-05	9.35e-05	1.66e-04	2.77e-04	3.79e-04
DHMA	1.2500					1.83e-06	2.72e-06	4.61e-06
UNK196	1.2500	6.30e-07	7.07e-07	9.49e-07	1.13e-06			5.18e-07
UNK196	1.2500			4.64e-07	4.19e-07			9.00e-07
2MA	1.2062		2.70e-07	4.22e-07	1.53e-06	5.31e-06	2.03e-05	4.71e-05
1MA	1.2027	6.50e-06	6.99e-06	9.23e-06	1.16e-05	1.92e-05	4.93e-05	9.75e-05
9MA	1.2586	1.13e-03	1.06e-03	1.05e-03	9.80e-04	7.69e-04	5.36e-04	3.40e-04
DMA	1.3333					1.25e-06	1.51e-06	
DMA	1.3333	1.26e-06	1.82e-06	1.89e-06	1.99e-06	1.41e-06	2.30e-06	5.15e-06
DMA	1.3333	1.78e-06	3.18e-06	3.09e-06	3.46e-06	3.32e-06	1.06e-06	2.16e-06
DMA	1.3333	1.01e-06	9.59e-07			1.50e-06	1.68e-06	4.75e-06
DMA	1.3333						2.31e-06	7.51e-06
DMA	1.3333						1.85e-06	5.71e-06
29&39DMA	1.3333	2.67e-07	7.67e-07	1.78e-06	4.89e-06	1.04e-05	1.65e-05	1.60e-05
19DMA	1.3333	9.60e-07	1.93e-06	2.08e-06	5.18e-06	1.02e-05	1.77e-05	2.20e-05
110DMA	1.3333	1.62e-06	3.51e-06	5.87e-06	1.45e-05	2.76e-05	4.09e-05	4.17e-05
910DMA	1.3239	4.16e-06	9.54e-06	1.82e-05	4.11e-05	6.71e-05	6.65e-05	3.46e-05
TMA	1.4167			8.77e-07	1.33e-06	2.17e-06	3.29e-06	2.91e-06
TMA	1.4167					1.09e-06	1.37e-06	
TMA	1.4167					1.90e-06	2.92e-06	2.01e-06
TMA	1.4167						5.12e-06	5.41e-06

MATERIAL BALANCE ON:

wt %C		0.941	0.904	0.928	0.949	0.895	0.871	0.846
wt %H		0.942	0.906	0.929	0.949	0.894	0.866	0.834
3-RING SYSTEM		0.941	0.904	0.928	0.950	0.896	0.876	0.859
METHYL GROUPS		0.944	0.907	0.926	0.933	0.864	0.787	0.663

half-life t* = 11959 s

9MA PYRLOYSIS - 370°C - 2.06 mol/l - TRIAL #2 - 6/10/92

ID	RRF	MOLES	MOLES	MOLES	MOLES	MOLES	MOLES	MOLES
[9MA]o		2.050	2.067	2.050	2.067	2.067	2.067	2.050
Time(s)		450	900	1800	3600	7200	14400	28800
X		0.1102	0.1260	0.1466	0.1715	0.4479	0.5155	0.7013
$-\ln(1-X)/t$		2.59e-04	1.50e-04	8.81e-05	5.23e-05	8.25e-05	5.03e-05	4.20e-05
log keff		-3.5859	-3.8250	-4.0552	-4.2818	-4.0835	-4.2982	-4.3772
BIP	1.0000	4.08e-04	4.10e-04	4.07e-04	4.10e-04	4.07e-04	4.03e-04	4.05e-04
DHA	1.1667			4.72e-07	8.73e-07	2.96e-06	8.82e-06	1.89e-05
DHMA	1.2500	3.96e-06	5.09e-06	9.69e-06	1.09e-05	1.25e-05	1.60e-05	1.60e-05
c-DHDMA	1.3333				3.06e-07	7.22e-07	1.36e-06	1.13e-06
UNK182	1.2500						1.47e-06	5.49e-06
DHMA	1.2500	2.75e-07	2.90e-07	4.88e-07	5.94e-07	3.11e-06	7.41e-07	6.51e-07
ANT	1.1904	6.33e-06	1.63e-05	4.50e-05	7.04e-05	1.40e-04	2.74e-04	3.88e-04
DHMA	1.2500	9.43e-07						
DHDMA	1.3333	5.61e-07	6.75e-07	9.02e-07	1.08e-06	1.69e-06	2.75e-06	4.34e-06
UNK196	1.2500			5.80e-07	5.32e-07	3.79e-07	5.74e-07	8.23e-07
2MA	1.2062	2.35e-06	2.30e-07	5.55e-07	1.05e-06	4.51e-06	1.62e-05	4.47e-05
1MA	1.2027	6.28e-06	5.95e-06	8.50e-06	9.98e-06	1.58e-05	4.49e-05	9.69e-05
9MA	1.2586	1.10e-03	1.08e-03	1.05e-03	1.02e-03	6.83e-04	5.99e-04	3.69e-04
DMA	1.3333						2.03e-06	
DMA	1.3333	1.43e-06	1.97e-06	1.71e-06	1.22e-06	3.98e-06	2.03e-06	6.12e-06
DMA	1.3333	1.76e-06	2.95e-06	2.78e-06	2.45e-06	1.08e-05	2.17e-06	2.60e-06
DMA	1.3333				5.60e-07	8.58e-06	1.79e-06	4.38e-06
DMA	1.3333						1.04e-06	
DMA	1.3333					5.46e-06	1.91e-06	6.94e-06
DMA	1.3333						1.48e-06	5.46e-06
29&39DMA	1.3333	2.58e-07	6.39e-07	2.46e-06	3.65e-06	8.38e-06	1.55e-05	1.53e-05
19DMA	1.3333	1.04e-06	9.65e-07	2.64e-06	4.14e-06	9.68e-06	1.64e-05	2.11e-05
110DMA	1.3333	1.54e-06	2.57e-06	6.61e-06	1.16e-05	2.29e-05	4.08e-05	4.40e-05
910DMA	1.3239	4.10e-06	7.90e-06	2.04e-05	3.58e-05	4.43e-05	7.20e-05	3.94e-05
TMA	1.4167			1.11e-06		1.91e-06	3.97e-06	3.66e-06
TMA	1.4167					1.07e-06	1.68e-06	2.38e-06
TMA	1.4167						3.01e-06	5.47e-06
TMA	1.4167					1.0e-06	4.78e-06	
MATERIAL BALANCE ON:								
wt %C		0.913	0.911	0.937	0.953	0.794	0.914	0.880
wt %H		0.914	0.912	0.939	0.955	0.795	0.911	0.868
3-RING SYSTEM		0.913	0.911	0.938	0.954	0.795	0.919	0.893
METHYL GROUPS		0.917	0.912	0.933	0.944	0.780	0.842	0.697

half-life t* = 13029 s

9MA THERMOLYSIS - 409°C - 0.82 mol/l - TRIAL #1 - 8/1/92

	[9MA]o	0.825	0.830	0.830	0.828	0.828	0.825	0.822
	Time(s)	450	900	1800	3600	7200	14400	28800
	X	0.1530	0.2294	0.4303	0.6180	0.7535	0.8356	0.9644
	-ln(1-X)/t	3.69e-04	2.90e-04	3.13e-04	2.67e-04	1.94e-04	1.25e-04	1.16e-04
	log keff	-3.4330	-3.5383	-3.5050	-3.5730	-3.7111	-3.9018	-3.9362
ID	**RRF**	**MOLES**	**MOLES**	**MOLES**	**MOLES**	**MOLES**	**MOLES**	**MOLES**
BIP	1.0000	1.33e-03	1.33e-03	1.33e-03	1.33e-03	1.33e-03	1.33e-03	1.32e-03
DHA	1.1667			5.00e-07	1.14e-06	2.32e-06	3.44e-06	8.20e-06
DHMA	1.2500	9.46e-07	1.26e-06	1.45e-06	1.38e-06	1.55e-06	1.45e-06	6.88e-07
UNK182	1.1667							1.67e-06
ANT	1.1904	1.18e-05	3.05e-05	7.81e-05	1.35e-04	1.65e-04	1.84e-04	2.12e-04
UNK196	1.2500	4.04e-07	5.99e-07	7.49e-07				
UNK196	1.2500							
2MA	1.2062			1.90e-06	8.29e-06	1.64e-05	2.22e-05	3.43e-05
1MA	1.2027	1.11e-06	1.75e-06	6.11e-06	2.30e-05	4.39e-05	6.21e-05	8.05e-05
DHMA	1.2500				1.84e-06	2.53e-06		
9MA	1.2586	4.20e-04	3.84e-04	2.84e-04	1.90e-04	1.22e-04	8.13e-05	1.76e-05
DMA	1.3333		2.23e-06	2.29e-06	3.01e-06	1.56e-06		
DMA	1.3333					1.94e-06	1.78e-06	1.03e-06
DMA	1.3333	3.65e-07			7.77e-07	2.06e-06	2.91e-06	3.56e-06
DMA	1.3333				1.06e-06	3.40e-06	5.26e-06	8.38e-06
DMA	1.3333				7.18e-07	3.05e-06	4.80e-06	6.85e-06
29&39DMA	1.3333	4.80e-07	1.22e-06	2.96e-06	4.58e-06	4.82e-06	3.72e-06	
19DMA	1.3333	7.54e-07	1.41e-06	3.35e-06	5.88e-06	7.54e-06	7.14e-06	4.91e-06
110DMA	1.3333	1.74e-06	4.22e-06	1.02e-05	1.54e-05	1.63e-05	1.28e-05	2.58e-06
910DMA	1.3239	7.26e-06	1.52e-05	2.68e-05	2.07e-05	1.12e-05	5.16e-06	
TMA	1.4167			5.27e-07	6.95e-07	2.13e-06	1.39e-06	2.17e-07
TMA	1.4167			6.89e-07	1.34e-06	1.78e-06	1.22e-06	1.52e-06

MATERIAL BALANCE ON:

wt %C		0.897	0.887	0.838	0.824	0.812	0.791	0.755
wt %H		0.897	0.887	0.833	0.810	0.792	0.765	0.721
3-RING SYSTEM		0.897	0.888	0.842	0.835	0.826	0.810	0.781
METHYL GROUPS		0.895	0.875	0.781	0.677	0.614	0.530	0.395

half-life $t^* = 2509$ s

9MA THERMOLYSIS - 409°C - 0.82 mol/l - TRIAL #2 - 9/4/92

	[9MA]o	0.828	0.825	0.825	0.828	0.827	0.827	0.825
	Time(s)	450	900	1800	3600	7200	14400	28800
	X	0.1686	0.2438	0.3638	0.5501	0.7087	0.8289	0.9442
	-ln(1-X)/t	4.10e-04	3.10e-04	2.51e-04	2.22e-04	1.71e-04	1.23e-04	1.00e-04
	log keff	-3.3869	-3.5079	-3.5999	-3.6539	-3.7662	-3.9115	-3.9991
ID	RRF	MOLES	MOLES	MOLES	MOLES	MOLES	MOLES	MOLES
BIP	1.0000	1.33e-03	1.33e-03	1.33e-03	1.33e-03	1.33e-03	1.33e-03	1.33e-03
DHA	1.1667			2.46e-07	7.36e-07	1.90e-06	3.52e-06	7.10e-06
DHMA	1.2500	5.97e-07	1.32e-06	1.51e-06	1.56e-06	1.66e-06	1.52e-06	8.61e-07
UNK182	1.1667							1.26e-06
ANT	1.1904	9.51e-06	3.30e-05	6.62e-05	1.11e-04	1.56e-04	1.81e-04	1.99e-04
DHMA	1.2500	1.06e-06	4.71e-07					
UNK196	1.2500	2.92e-07						
2MA	1.2062			1.16e-06	4.83e-06	1.38e-05	2.43e-05	3.46e-05
1MA	1.2027	1.73e-06	2.13e-06	4.85e-06	1.54e-05	3.91e-05	6.03e-05	8.19e-05
DHDMA	1.3333			4.63e-07	1.10e-06		2.59e-06	
9MA	1.2586	4.13e-04	3.74e-04	3.15e-04	2.24e-04	1.45e-04	8.48e-05	2.77e-05
DMA	1.3333	1.21e-06	1.09e-06	9.70e-07				
DMA	1.3333	4.99e-07	1.03e-06	1.46e-06	2.74e-06	2.09e-06	1.70e-06	1.53e-06
DMA	1.3333					1.21e-06	9.17e-07	9.98e-07
DMA	1.3333					2.33e-06	3.46e-06	6.62e-06
DMA	1.3333					3.12e-06	5.98e-06	1.06e-05
DMA	1.3333					2.80e-06	4.93e-06	7.85e-06
29&39DMA	1.3333	5.01e-07	1.49e-06	2.91e-06	4.87e-06	6.27e-06	4.62e-06	
19DMA	1.3333	7.16e-07	1.57e-06	3.04e-06	5.63e-06	8.70e-06	8.74e-06	8.29e-06
110DMA	1.3333	1.82e-06	4.99e-06	9.62e-06	1.59e-05	1.90e-05	1.35e-05	4.85e-06
910DMA	1.3239	6.59e-06	1.71e-05	2.77e-05	2.90e-05	1.71e-05	1.30e-05	8.08e-06
TMA	1.4167						9.43e-07	1.64e-06
TMA	1.4167					2.23e-06	2.50e-06	1.83e-06
TMA	1.4167			5.30e-07	1.54e-06	2.04e-06	7.80e-07	1.73e-06
TMA	1.4167						4.80e-07	
MATERIAL BALANCE ON:								
wt %C		0.880	0.885	0.877	0.834	0.842	0.831	0.800
wt %H		0.881	0.885	0.874	0.825	0.826	0.810	0.773
3-RING SYSTEM		0.880	0.886	0.880	0.840	0.854	0.846	0.820
METHYL GROUPS		0.869	0.874	0.841	0.741	0.680	0.613	0.519

half-life t* = 3145 s

14DMN THERMOLYSIS - 370°C - 0.87 mol/l - TRIAL #1 - 9/1/91

	[14DMN]o	0.867	0.867	0.867	0.867	0.867
	Time(s)	3600	7200	57600	86400	115200
	X	0.0433	0.0821	0.0709	0.1405	0.1532
	-ln(1-X)/t	1.23e-05	1.19e-05	1.28e-06	1.75e-06	1.44e-06
	log keff	-4.9102	-4.9245	-5.8939	-5.7564	-5.8406
ID	RRF	MOLES	MOLES	MOLES	MOLES	MOLES
BIP	1.0000	1.42e-03	1.42e-03	1.42e-03	1.42e-03	1.42e-03
1MN	1.0364	6.97e-06	7.45e-06	1.72e-05	2.33e-05	2.56e-05
13DMN	1.1398	2.30e-06	2.40e-06	4.23e-06	5.31e-06	4.97e-06
14DMN	1.0510	4.98e-04	4.78e-04	4.83e-04	4.47e-04	4.41e-04
12DMN	1.0991	1.21e-05	1.26e-05	1.19e-05	1.30e-05	1.21e-05
145TMN	1.0833	2.64e-06	2.37e-06	2.69e-06	2.07e-06	2.38e-06
146TMN	1.0833			7.58e-07	1.60e-06	1.70e-06
TMN	1.0833	1.14e-06	1.47e-06	1.95e-06	3.79e-06	3.81e-06
MATERIAL BALANCE ON:						
wt %C		1.005	0.968	1.002	0.951	0.941
wt %H		1.004	0.967	1.000	0.949	0.938
2-RING SYSTEM		1.005	0.969	1.004	0.954	0.944
METHYL GROUPS		1.002	0.965	0.992	0.938	0.927

half-life t* = 502723 s

14DMN THERMOLYSIS - 370°C - 0.87 mol/l - TRIAL #2 - 9/1/91

	[14DMN]o	0.867	0.867	0.867	0.867	0.867	0.867	0.867
	Time(s)	3600	7200	14400	28800	57600	86400	115200
	X	0.0455	0.0303	0.0325	0.0480	0.0654	0.1308	0.1379
	-ln(1-X)/t	1.29e-05	4.27e-06	2.29e-06	1.71e-06	1.17e-06	1.62e-06	1.29e-06
	log keff	-4.8882	-5.3692	-5.6393	-5.7675	-5.9302	-5.7898	-5.8901
ID	RRF	MOLES	MOLES	MOLES	MOLES	MOLES	MOLES	MOLES
BIP	1.0000	1.42e-03	1.42e-03	1.42e-03	1.42e-03	1.42e-03	1.42e-03	1.42e-03
2MN	0.9068							3.39e-07
1MN	1.0364	6.72e-06	7.34e-06	8.01e-06	9.65e-06	1.76e-05	1.78e-05	2.65e-05
13DMN	1.1398	1.75e-06	2.24e-06	2.03e-06	3.29e-06	5.37e-06	4.60e-06	5.27e-06
14DMN	1.0510	4.97e-04	5.05e-04	5.03e-04	4.95e-04	4.86e-04	4.52e-04	4.49e-04
12DMN	1.0991	1.05e-05	1.15e-05	1.11e-05	1.39e-05	1.31e-05	1.40e-05	1.21e-05
TMN	1.0833					1.08e-06	8.41e-07	
145TMN	1.0833	2.13e-06	2.63e-06	2.38e-06	3.21e-06	3.41e-06	2.64e-06	2.42e-06
146TMN	1.0833	8.81e-07	4.62e-07	3.00e-07	5.23e-07	1.23e-06	1.04e-06	1.79e-06
TMN	1.0833	9.43e-07	1.44e-06	1.51e-06	1.59e-06	2.18e-06	2.37e-06	3.94e-06
MATERIAL BALANCE ON:								
wt %C		0.998	1.018	1.017	1.016	1.017	0.948	0.960
wt %H		0.998	1.018	1.016	1.015	1.016	0.945	0.957
2-RING SYSTEM		0.999	1.019	1.017	1.016	1.019	0.951	0.963
METHYL GROUPS		0.996	1.016	1.014	1.013	1.009	0.939	0.945

half-life t* = 556249 s

14DMN THERMOLYSIS - 409°C - 0.87 mol/l - TRIAL #1 - 10/13/91

	[14DMN]o	0.867	0.867	0.867	0.867
	Time(s)	3600	7200	28800	57600
	X	0.0391	0.0767	0.1458	0.4235
	-ln(1-X)/t	1.11e-05	1.11e-05	5.47e-06	9.56e-06
	log keff	-4.9555	-4.9553	-5.2619	-5.0194
ID	RRF	MOLES	MOLES	MOLES	MOLES
BIP	1.0000	1.42e-03	1.42e-03	1.42e-03	1.42e-03
NAPH	0.7818		5.81e-07	7.11e-07	6.10e-06
2MN	0.9068			5.83e-07	2.95e-06
1MN	1.0364	1.15e-05	1.60e-05	4.16e-05	1.21e-04
26DMN	0.9930				2.13e-06
13DMN	1.1398	2.51e-06	5.71e-06	9.78e-06	2.04e-05
14DMN	1.0510	5.00e-04	4.80e-04	4.44e-04	3.00e-04
12DMN	1.0991	7.86e-06	1.20e-05	8.03e-06	7.72e-06
TMN	1.0833		9.28e-07	4.16e-07	1.26e-06
TMN	1.0833				3.43e-07
145TMN	1.0833	2.78e-06	2.97e-06	2.67e-06	2.13e-06
TMN	1.0833				6.90e-07
TMN	1.0833				6.65e-07
146TMN	1.0833	8.16e-07	1.15e-06	3.34e-06	9.06e-06
TMN	1.0833				4.43e-07
TMN	1.0833	3.07e-06	2.62e-06	5.39e-06	1.02e-05
TMN	1.0833			4.33e-07	7.33e-07
TMN	1.0833				3.97e-07
MATERIAL BALANCE ON:					
wt %C		1.015	1.003	0.989	0.916
wt %H		1.014	1.001	0.984	0.898
2-RING SYSTEM		1.016	1.004	0.994	0.933
METHYL GROUPS		1.011	0.995	0.964	0.828

half-life t* = 70427 s

877

14DMN THERMOLYSIS - 409°C - 0.87 mol/l - TRIAL #2 - 10/13/91

	[14DMN]o	0.867	0.867	0.867	0.867	0.867
	Time(s)	3600	7200	14400	28800	57600
	X	0.0604	0.0761	0.1076	0.2092	0.4198
	-ln(1-X)/t	1.73e-05	1.10e-05	7.91e-06	8.15e-06	9.45e-06
	log keff	-4.7618	-4.9589	-5.1021	-5.0889	-5.0245
ID	RRF	MOLES	MOLES	MOLES	MOLES	MOLES
BIP	1.0000	1.42e-03	1.42e-03	1.42e-03	1.42e-03	1.42e-03
NAPH	0.7818			5.05e-07	9.53e-07	6.01e-06
2MN	0.9068			4.29e-07	7.52e-07	2.93e-06
1MN	1.0364	1.09e-05	1.59e-05	3.19e-05	4.98e-05	1.21e-04
26DMN	0.9930					1.72e-06
13DMN	1.1398	4.78e-06	5.60e-06	7.13e-06	9.31e-06	2.02e-05
14DMN	1.0510	4.89e-04	4.81e-04	4.64e-04	4.11e-04	3.02e-04
12DMN	1.0991	1.44e-05	1.18e-05	7.26e-06	8.29e-06	7.16e-06
TMN	1.0833	3.67e-07	5.96e-07	3.82e-07	6.19e-07	7.77e-07
145TMN	1.0833	2.41e-06	2.91e-06	2.73e-06	2.29e-06	2.04e-06
TMN	1.0833					6.11e-07
TMN	1.0833					5.20e-07
146TMN	1.0833	5.29e-07	1.17e-06	3.00e-06	3.99e-06	8.99e-06
TMN	1.0833					3.66e-07
TMN	1.0833	1.95e-06	2.58e-06	5.18e-06	5.58e-06	1.04e-05
TMN	1.0833			4.20e-07	5.01e-07	7.36e-07
TMN	1.0833					3.91e-07

MATERIAL BALANCE ON:

wt %C		1.007	1.000	0.999	0.937	0.912
wt %H		1.006	0.999	0.996	0.931	0.894
2-RING SYSTEM		1.008	1.002	1.002	0.943	0.930
METHYL GROUPS		1.002	0.994	0.982	0.907	0.821

half-life t* = 72481 s

14DMN THERMOLYSIS - 450°C - 0.081 mol/l - TRIAL #1 - 12/29/91

	[14DMN]o	0.081	0.081	0.081	0.081	0.081
	Time(s)	3600	7200	14400	28800	57600
	X	0.1368	0.1194	0.1471	0.1638	0.2508
	-ln(1-X)/t	4.09e-05	1.77e-05	1.10e-05	6.21e-06	5.01e-06
	log keff	-4.3887	-4.7530	-4.9567	-5.2068	-5.2999
ID	**RRF**	**MOLES**	**MOLES**	**MOLES**	**MOLES**	**MOLES**
BIP	1.0000	1.42e-03	1.42e-03	1.42e-03	1.42e-03	1.42e-03
NAPH	0.7818				3.52e-07	7.18e-07
1MN	1.0364	1.33e-06	2.15e-06	3.09e-06	5.13e-06	9.25e-06
13DMN	1.1398	1.16e-06	1.49e-06	1.58e-06	2.13e-06	2.55e-06
14DMN	1.0510	4.21e-05	4.30e-05	4.16e-05	4.08e-05	3.65e-05
12DMN	1.0991	3.24e-06	2.30e-06	2.31e-06		

MATERIAL BALANCE ON:

wt %C	0.978	0.999	0.991	0.982	0.988
wt %H	0.976	0.995	0.985	0.972	0.969
2-RING SYSTEM	0.981	1.002	0.996	0.992	1.006
METHYL GROUPS	0.967	0.980	0.964	0.933	0.896

half-life t* = 139917 s

14DMN THERMOLYSIS - 450°C - 0.081 mol/l - TRIAL #1 - 12/29/91

	[14DMN]o	0.081	0.081	0.081	0.081	0.081
	Time(s)	3600	7200	14400	28800	57600
	X	0.0988	0.0574	0.1329	0.2352	0.3556
	-ln(1-X)/t	2.89e-05	8.21e-06	9.90e-06	9.31e-06	7.63e-06
	log keff	-4.5392	-5.0856	-5.0042	-5.0310	-5.1175
ID	**RRF**	**MOLES**	**MOLES**	**MOLES**	**MOLES**	**MOLES**
BIP	1.0000	1.42e-03	1.42e-03	1.42e-03	1.42e-03	1.42e-03
NAPH	0.7818					1.16e-06
1MN	1.0364	1.47e-06	2.17e-06	3.43e-06	8.04e-06	1.33e-05
13DMN	1.1398		6.54e-07	1.63e-06	2.23e-06	3.47e-06
14DMN	1.0510	4.40e-05	4.60e-05	4.23e-05	3.73e-05	3.14e-05
12DMN	1.0991	1.06e-06	1.11e-06	2.17e-06		
145TMN	1.0833		3.16e-07			

MATERIAL BALANCE ON:

wt %C	0.951	1.027	1.010	0.962	0.985
wt %H	0.948	1.024	1.004	0.948	0.958
2-RING SYSTEM	0.953	1.030	1.015	0.975	1.011
METHYL GROUPS	0.938	1.011	0.980	0.893	0.852

half-life t* = 90670 s

14DMN THERMOLYSIS - 450°C - 0.24 mol/l - TRIAL #1 - 12/29/91

	[14DMN]o	0.243	0.243	0.243	0.243	0.243
	Time(s)	3600	7200	14400	28800	57600
	X	0.1256	0.1431	0.2241	0.3262	0.4890
	-ln(1-X)/t	3.73e-05	2.14e-05	1.76e-05	1.37e-05	1.17e-05
	log keff	-4.4285	-4.6686	-4.7540	-4.8630	-4.9335
ID	RRF	MOLES	MOLES	MOLES	MOLES	MOLES
BIP	1.0000	1.42e-03	1.42e-03	1.42e-03	1.42e-03	1.41e-03
NAPH	0.7818			6.14e-07	1.40e-06	5.88e-06
2MN	0.9068			3.34e-07	4.05e-07	8.25e-07
1MN	1.0364	4.53e-06	6.08e-06	1.18e-05	2.63e-05	4.92e-05
13DMN	1.1398	1.62e-06	1.85e-06	2.43e-06	2.88e-06	3.48e-06
14DMN	1.0510	1.28e-04	1.25e-04	1.14e-04	9.86e-05	7.48e-05
12DMN	1.0991	5.81e-06	5.19e-06	5.31e-06	4.75e-06	
TMN	1.0833		3.09e-07			5.84e-07
145TMN	1.0833		6.28e-07	4.68e-07	5.75e-07	

MATERIAL BALANCE ON:

wt %C		0.954	0.950	0.912	0.906	0.886
wt %H		0.951	0.947	0.904	0.889	0.851
2-RING SYSTEM		0.956	0.953	0.919	0.922	0.921
METHYL GROUPS		0.941	0.935	0.875	0.823	0.712

half-life t* = 59778 s

14DMN THERMOLYSIS - 450°C - 0.24 mol/l - TRIAL #2 - 2/16/92

	[14DMN]o	0.243	0.243	0.243	0.243	0.243
	Time(s)	3600	7200	14400	28800	57600
	X	0.1179	0.3026	0.1849	0.3575	0.6716
	-ln(1-X)/t	3.48e-05	5.01e-05	1.42e-05	1.54e-05	1.93e-05
	log keff	-4.4578	-4.3006	-4.8478	-4.8136	-4.7137
ID	RRF	MOLES	MOLES	MOLES	MOLES	MOLES
BIP	1.0000	1.42e-03	1.42e-03	1.42e-03	1.42e-03	1.41e-03
NAPH	0.7818				1.99e-06	1.07e-05
2MN	0.9068				5.35e-07	1.35e-06
1MN	1.0364	4.01e-06	7.77e-06	1.17e-05	3.26e-05	6.14e-05
13DMN	1.1398	8.72e-07	2.57e-06	1.01e-06	2.52e-06	4.25e-06
14DMN	1.0510	1.29e-04	1.02e-04	1.19e-04	9.40e-05	4.81e-05
12DMN	1.0991	3.13e-06	4.47e-06	2.74e-06	2.74e-06	2.60e-07
145TMN	1.0833	6.56e-07		5.67e-07	4.43e-07	
146TMN	1.0833				2.89e-07	
TMN	1.0833	3.81e-07		4.14e-07	6.59e-07	8.82e-07

MATERIAL BALANCE ON:

wt %C		0.942	0.794	0.921	0.908	0.836
wt %H		0.941	0.790	0.915	0.888	0.788
2-RING SYSTEM		0.944	0.799	0.928	0.928	0.883
METHYL GROUPS		0.934	0.772	0.891	0.806	0.599

half-life t* = 41976 s

14DMN THERMOLYSIS - 450°C - 0.87 mol/l - TRIAL #1 - 7/28/91

	[14DMN]o	0.867	0.867	0.867	0.867	0.867
	Time(s)	1800	3600	7200	14400	28800
	X	0.0805	0.1157	0.2154	0.3862	0.8033
	-ln(1-X)/t	4.66e-05	3.42e-05	3.37e-05	3.39e-05	5.65e-05
	log keff	-4.3314	-4.4665	-4.4725	-4.4699	-4.2483
ID	RRF	MOLES	MOLES	MOLES	MOLES	MOLES
BIP	1.0000	1.42e-03	1.42e-03	1.42e-03	1.42e-03	1.42e-03
NAPH	0.7818	3.56e-07	4.98e-07	1.89e-06	7.91e-06	6.74e-05
2MN	0.9068		3.48e-07	8.62e-07	1.74e-06	8.67e-06
1MN	1.0364	1.37e-05	2.58e-05	6.48e-05	1.25e-04	2.23e-04
13DMN	1.1398	5.72e-06	5.31e-06	6.81e-06	6.60e-06	1.55e-05
14DMN	1.0510	4.78e-04	4.60e-04	4.08e-04	3.19e-04	1.02e-04
12DMN	1.0991	1.75e-05	1.57e-05	1.25e-05	1.08e-05	6.23e-06
TMN	1.0833	9.27e-07	1.46e-06	1.09e-06	9.73e-07	
145TMN	1.0833	3.36e-06	3.38e-06	2.92e-06	2.75e-06	1.43e-06
146TMN	1.0833	6.48e-07	9.31e-07	2.20e-06	2.72e-06	2.57e-06
TMN	1.0833	1.57e-06	1.62e-06	2.19e-06	2.30e-06	4.17e-06
TMN	1.0833			4.80e-07		6.54e-06
MATERIAL BALANCE ON:						
wt %C		1.003	0.987	0.959	0.901	0.786
wt %H		1.001	0.984	0.949	0.880	0.729
2-RING SYSTEM		1.004	0.990	0.968	0.922	0.842
METHYL GROUPS		0.996	0.971	0.910	0.794	0.504

half-life t* = 18315 s

14DMN THERMOLYSIS - 450°C - 0.87 mol/l - TRIAL #3 - 8/28/91

	[14DMN]o	0.867	0.867	0.867	0.867	0.867
	Time(s)	1800	3600	7200	14400	28800
	X	0.0599	0.0865	0.1800	0.4448	0.7747
	-ln(1-X)/t	3.43e-05	2.51e-05	2.76e-05	4.09e-05	5.17e-05
	log keff	-4.4645	-4.5998	-4.5597	-4.3887	-4.2861
ID	RRF	MOLES	MOLES	MOLES	MOLES	MOLES
BIP	1.0000	1.42e-03	1.42e-03	1.42e-03	1.42e-03	1.42e-03
NAPH	0.7818		4.99e-07	1.48e-06	1.11e-05	5.26e-05
2MN	0.9068		4.35e-07	7.93e-07	2.72e-06	9.06e-06
1MN	1.0364	1.33e-05	3.17e-05	5.94e-05	1.45e-04	2.08e-04
26DMN	0.9930					2.08e-06
13DMN	1.1398	2.76e-06	4.91e-06	6.01e-06	1.04e-05	1.60e-05
14DMN	1.0510	4.89e-04	4.75e-04	4.27e-04	2.89e-04	1.17e-04
12DMN	1.0991	8.76e-06	8.69e-06	8.52e-06	5.97e-06	4.23e-06
TMN	1.0833	8.07e-07	6.97e-07	7.60e-07	6.75e-07	
145TMN	1.0833	2.70e-06	2.95e-06	2.81e-06	2.37e-06	
146TMN	1.0833	6.53e-07	1.43e-06	1.96e-06	4.51e-06	3.44e-06
TMN	1.0833	1.33e-06	1.96e-06	1.75e-06	3.84e-06	4.79e-06
TMN	1.0833				5.98e-07	
MATERIAL BALANCE ON:						
wt %C		0.997	1.012	0.972	0.890	0.752
wt %H		0.995	1.008	0.963	0.865	0.702
2-RING SYSTEM		0.998	1.016	0.981	0.915	0.803
METHYL GROUPS		0.991	0.991	0.927	0.763	0.501

half-life t* = 16828 s

14DMN THERMOLYSIS - 450°C - 2.07 mol/l - TRIAL #1 - 10/27/91

	[14DMN]o	2.067	2.067	2.067	2.067	2.067
	Time(s)	1800	3600	7200	14400	28800
	X	0.2472	0.4131	0.6793	0.8769	0.9296
	-ln(1-X)/t	1.58e-04	1.48e-04	1.58e-04	1.45e-04	9.21e-05
	log keff	-3.8020	-3.8297	-3.8015	-3.8372	-4.0356
ID	RRF	MOLES	MOLES	MOLES	MOLES	MOLES
BIP	1.0000	1.42e-03	1.42e-03	1.42e-03	1.42e-03	1.42e-03
NAPH	0.7818	1.30e-06	5.99e-06	3.60e-05	1.43e-04	2.26e-04
2MN	0.9068	1.54e-06	5.04e-06	1.87e-05	5.49e-05	7.50e-05
1MN	1.0364	9.81e-05	1.95e-04	3.35e-04	4.02e-04	3.79e-04
26DMN	0.9930		1.74e-06	3.58e-06	8.03e-06	9.62e-06
13DMN	1.1398	2.64e-05	5.02e-05	8.22e-05	8.85e-05	7.51e-05
14DMN	1.0510	9.30e-04	7.25e-04	3.96e-04	1.52e-04	8.70e-05
12DMN	1.0991	1.74e-05	1.61e-05	1.68e-05	1.15e-05	8.54e-06
TMN	1.0833					1.38e-06
TMN	1.0833	9.19e-07	1.65e-06	2.06e-06	1.52e-06	1.32e-06
145TMN	1.0833	5.80e-06	6.35e-06	2.81e-06	5.59e-06	3.87e-06
TMN	1.0833			4.53e-06	4.16e-06	4.15e-06
TMN	1.0833		1.33e-06	3.51e-06		
146TMN	1.0833	1.14e-05	2.26e-05	2.59e-05	1.49e-05	1.04e-05
TMN	1.0833	4.31e-07	7.32e-07	2.71e-06	2.75e-06	3.25e-06
TMN	1.0833	3.96e-07	3.65e-07			
TMN	1.0833	1.49e-05	2.44e-05	2.50e-05	1.69e-05	1.41e-05
TMN	1.0833					1.10e-06
TMN	1.0833	1.24e-06	1.80e-06	2.94e-06	3.19e-06	2.35e-06
TMN	1.0833					9.15e-07

MATERIAL BALANCE ON:

wt %C		0.894	0.847	0.751	0.689	0.673
wt %H		0.889	0.836	0.727	0.642	0.615
2-RING SYSTEM		0.898	0.857	0.775	0.735	0.731
METHYL GROUPS		0.871	0.795	0.631	0.445	0.382

half-life t* = 4749 s

882

14DMN THERMOLYSIS - 450°C - 2.07 mol/l - TRIAL #2 - 2/16/92

	[14DMN]o	2.067	2.067	2.067	2.067	2.067
	Time(s)	1800	3600	7200	14400	28800
	X	0.2088	0.3540	0.6313	0.9147	0.9505
	-ln(1-X)/t	1.30e-04	1.21e-04	1.39e-04	1.71e-04	1.04e-04
	log keff	-3.8857	-3.9159	-3.8583	-3.7671	-3.9814
ID	RRF	MOLES	MOLES	MOLES	MOLES	MOLES
BIP	1.0000	1.42e-03	1.42e-03	1.42e-03	1.42e-03	1.42e-03
NAPH	0.7818	1.16e-06	3.80e-06	2.71e-05	1.95e-04	2.75e-04
2MN	0.9068	1.64e-06	3.13e-06	1.15e-05	6.48e-05	8.23e-05
1MN	1.0364	8.33e-05	1.60e-04	3.11e-04	3.92e-04	3.56e-04
26DMN	0.9930			2.02e-06	8.24e-06	1.08e-05
13DMN	1.1398	1.97e-05	3.42e-05	5.40e-05	7.72e-05	6.55e-05
14DMN	1.0510	9.78e-04	7.98e-04	4.56e-04	1.05e-04	6.11e-05
12DMN	1.0991	1.65e-05	1.48e-05	1.32e-05	9.47e-06	7.93e-06
TMN	1.0833	5.29e-07	4.83e-07	7.47e-07		
145TMN	1.0833	6.33e-06	6.46e-06	4.02e-06	4.26e-06	2.60e-06
TMN	1.0833			2.26e-06	3.66e-06	3.35e-06
TMN	1.0833			1.85e-06		
146TMN	1.0833	9.60e-06	1.74e-05	2.09e-05	1.06e-05	6.14e-06
TMN	1.0833			1.08e-06	2.11e-06	1.19e-06
TMN	1.0833	1.35e-05	1.91e-05	1.77e-05	1.38e-05	1.33e-05
TMN	1.0833	8.60e-07	1.41e-06	1.43e-06	1.34e-06	
TMN	1.0833	8.42e-07				
MATERIAL BALANCE ON:						
wt %C		0.912	0.848	0.726	0.664	0.652
wt %H		0.908	0.840	0.704	0.609	0.587
2-RING SYSTEM		0.916	0.857	0.748	0.719	0.717
METHYL GROUPS		0.893	0.806	0.616	0.390	0.327

half-life $t^* = 5474$ s

14DMN THERMOLYSIS - 500°C - 0.87 mol/l - TRIAL #1 - 9/10/91

	[14DMN]o	0.867	0.867	0.867	0.867
	Time(s)	900	3600	7200	14400
	X	0.2774	0.7952	0.9763	0.9801
	-ln(1-X)/t	3.61e-04	4.40e-04	5.20e-04	2.72e-04
	log keff	-3.4425	-3.3561	-3.2842	-3.5654
ID	RRF	MOLES	MOLES	MOLES	MOLES
BIP	1.0000	1.42e-03	1.42e-03	1.42e-03	1.42e-03
NAPH	0.7818	2.37e-06	6.55e-05	2.03e-04	3.28e-04
2MN	0.9068	1.29e-06	9.80e-06	3.41e-05	4.01e-05
1MN	1.0364	7.63e-05	2.28e-04	1.42e-04	2.64e-05
26DMN	0.9930		2.44e-06	8.26e-06	1.88e-05
13DMN	1.1398	1.10e-05	1.62e-05	1.70e-05	1.44e-05
14DMN	1.0510	3.76e-04	1.07e-04	1.23e-05	1.04e-05
12DMN	1.0991	1.02e-05	4.69e-06	2.06e-06	2.92e-05
TMN	1.0833		1.23e-06	1.73e-06	
145TMN	1.0833	2.49e-06	1.19e-06		
146TMN	1.0833	3.38e-06	2.45e-06	3.72e-07	
TMN	1.0833				5.76e-07
TMN	1.0833	3.29e-06	4.42e-06	9.60e-06	1.34e-05
TMN	1.0833	7.14e-07			
MATERIAL BALANCE ON:					
wt %C		0.925	0.794	0.733	0.812
wt %H		0.913	0.736	0.642	0.699
2-RING SYSTEM		0.936	0.851	0.824	0.926
METHYL GROUPS		0.866	0.506	0.277	0.244

half-life t* = 2064 s

14DMN THERMOLYSIS - 500°C - 0.87 mol/l - TRIAL #2 - 9/10/91

	[14DMN]o	0.867	0.867	0.867	0.867	0.867
	Time(s)	900	1800	3600	7200	14400
	X	0.1369	0.5465	0.8615	0.9769	1.0000
	$-\ln(1-X)/t$	1.64e-04	4.39e-04	5.49e-04	5.23e-04	1.76e-03
	log keff	-3.7863	-3.3572	-3.2603	-3.2812	-2.7548
ID	RRF	MOLES	MOLES	MOLES	MOLES	MOLES
BIP	1.0000	1.42e-03	1.42e-03	1.42e-03	1.42e-03	1.42e-03
NAPH	0.7818	1.01e-06	1.53e-05	8.19e-05	2.22e-04	3.07e-04
2MN	0.9068	6.10e-07	4.81e-06	1.67e-05	3.50e-05	3.76e-05
1MN	1.0364	4.56e-05	1.62e-04	2.20e-04	1.29e-04	2.31e-05
26DMN	0.9930		2.19e-06	4.66e-06	1.25e-05	
13DMN	1.1398	5.47e-06	1.97e-05	2.36e-05	1.83e-05	3.78e-05
14DMN	1.0510	4.49e-04	2.36e-04	7.20e-05	1.20e-05	
12DMN	1.0991	1.19e-05	8.18e-06	5.68e-06	3.68e-06	
TMN	1.0833				5.66e-06	
145TMN	1.0833	2.85e-06	2.55e-06	5.84e-07		
146TMN	1.0833	1.33e-06	6.14e-06	2.41e-06		
TMN	1.0833					5.07e-07
TMN	1.0833	1.65e-06	5.90e-06	6.35e-06	9.04e-06	1.21e-05
TMN	1.0833	6.90e-07	8.39e-07			
MATERIAL BALANCE ON:						
wt %C		0.993	0.862	0.771	0.765	0.697
wt %H		0.986	0.833	0.708	0.670	0.591
2-RING SYSTEM		1.000	0.892	0.833	0.860	0.803
METHYL GROUPS		0.960	0.716	0.458	0.289	0.167

half-life t* = 1699 s

14DMN THERMOLYSIS - 500°C - 0.87 mol/l - TRIAL #3 - 3/9/92

	[14DMN]o	0.867	0.867	0.867	0.867	0.867
	Time(s)	150	300	450	900	1800
	X	0.0291	0.1052	0.1458	0.2932	0.5911
	$-\ln(1-X)/t$	1.97e-04	3.71e-04	3.50e-04	3.86e-04	4.97e-04
	log keff	-3.7058	-3.4312	-3.4557	-3.4139	-3.3038
ID	RRF	MOLES	MOLES	MOLES	MOLES	MOLES
BIP	1.0000	1.42e-03	1.42e-03	1.42e-03	1.42e-03	1.42e-03
NAPH	0.7818		5.05e-07	9.72e-07	2.88e-06	1.70e-05
2MN	0.9068			4.35e-07	1.33e-06	4.29e-06
1MN	1.0364	9.39e-06	1.57e-05	3.04e-05	8.09e-05	1.58e-05
26DMN	0.9930					1.24e-06
13DMN	1.1398	2.44e-06	2.97e-06	4.89e-06	9.68e-06	1.52e-05
14DMN	1.0510	5.05e-04	4.66e-04	4.44e-04	3.68e-04	2.13e-04
12DMN	1.0991	1.08e-05	9.56e-06	9.57e-06	8.98e-06	6.34e-06
TMN	1.0833	5.31e-07			1.06e-06	
145TMN	1.0833	2.95e-06	2.34e-06	2.45e-06	3.19e-06	2.26e-06
146TMN	1.0833	1.18e-06	6.18e-07	1.12e-06	3.87e-06	4.60e-06
TMN	1.0833	1.07e-06	1.29e-06	1.55e-06	3.37e-05	4.26e-06
TMN	1.0833				1.38e-06	8.18e-07
MATERIAL BALANCE ON:						
wt %C		1.025	0.956	0.949	0.919	0.790
wt %H		1.024	0.954	0.944	0.907	0.761
2-RING SYSTEM		1.026	0.958	0.953	0.931	0.820
METHYL GROUPS		1.022	0.946	0.926	0.859	0.643

half-life t* = 1527 s

14DMN THERMOLYSIS - 550°C - 0.87 mol/l - TRIAL #1 - 10/2/91

[14DMN]o		0.867	0.867	0.867	0.867	0.867
Time(s)		450	900	1800	3600	7200
X		0.4421	0.9053	0.9758	1.0000	1.0000
-ln(1-X)/t		1.30e-03	2.62e-03	2.07e-03	7.04e-03	3.52e-03
log keff		-2.8871	-2.5819	-2.6846	-2.1527	-2.4537
ID	RRF	MOLES	MOLES	MOLES	MOLES	MOLES
BIP	1.0000	1.42e-03	1.42e-03	1.42e-03	1.42e-03	1.42e-03
NAPH	0.7818	1.12e-05	1.43e-04	3.48e-04	3.48e-04	2.93e-04
2MN	0.9068	2.20e-06	1.45e-05	2.87e-05	2.21e-05	1.85e-05
1MN	1.0364	1.38e-04	2.23e-04	7.31e-05	2.15e-05	6.43e-06
13DMN	1.1398	1.26e-05	2.26e-05	9.23e-06		
14DMN	1.0510	2.90e-04	4.93e-05	3.70e-06		
12DMN	1.0991	2.15e-05	1.10e-05			
145TMN	1.0833	5.58e-06				
146TMN	1.0833	3.48e-06	6.01e-07			
TMN	1.0833					4.49e-06
TMN	1.0833	2.05e-06	6.14e-06	1.24e-05	1.04e-05	3.98e-05
MATERIAL BALANCE ON:						
wt %C		0.912	0.822	0.788	0.656	0.606
wt %H		0.888	0.739	0.662	0.539	0.515
2-RING SYSTEM		0.936	0.905	0.914	0.773	0.697
METHYL GROUPS		0.790	0.407	0.159	0.072	0.152

half-life t* = 506 s

14DMN THERMOLYSIS - 550°C - 0.87 mol/l - TRIAL #2 - 10/2/91

[14DMN]o		0.867	0.867	0.867
Time(s)		450	3600	7200
X		0.4887	1.0000	1.0000
-ln(1-X)/t		1.49e-03	7.04e-03	3.52e-03
log keff		-2.8266	-2.1527	-2.4537
ID	RRF	MOLES	MOLES	MOLES
BIP	1.0000	1.42e-03	1.42e-03	1.42e-03
NAPH	0.7818	1.52e-05	3.77e-04	2.95e-04
2MN	0.9068	2.71e-06	2.53e-05	1.76e-05
1MN	1.0364	1.57e-04	9.67e-06	5.88e-06
13DMN	1.1398	1.27e-05		
14DMN	1.0510	2.66e-04		
12DMN	1.0991	2.01e-05		
TMN	1.0833	2.95e-06		3.21e-05
145TMN	1.0833	4.85e-06		
146TMN	1.0833	3.31e-06		
TMN	1.0833		1.96e-06	3.74e-06
TMN	1.0833	2.32e-06	1.87e-05	3.55e-05
MATERIAL BALANCE ON:				
wt %C		0.908	0.708	0.663
wt %H		0.879	0.585	0.576
2-RING SYSTEM		0.936	0.831	0.750
METHYL GROUPS		0.766	0.093	0.228

half-life t* = 521 s

14DMN THERMOLYSIS - 550°C - 0.87 mol/l - TRIAL #3 - 3/3/92

	[14DMN]o	0.867	0.867	0.867	0.867	0.867
	Time(s)	150	300	450	900	1800
	X	0.1532	0.2856	0.5416	0.8679	0.9730
	-ln(1-X)/t	1.11e-03	1.12e-03	1.73e-03	2.25e-03	2.01e-03
	log keff	-2.9552	-2.9504	-2.7611	-2.6480	-2.6975
ID	RRF	MOLES	MOLES	MOLES	MOLES	MOLES
BIP	1.0000	1.42e-03	1.42e-03	1.42e-03	1.42e-03	1.42e-03
NAPH	0.7818		2.98e-06	2.10e-05	1.18e-04	3.05e-04
2MN	0.9068	3.68e-07	1.11e-06	3.33e-06	1.17e-05	2.49e-05
1MN	1.0364	2.90e-05	8.15e-05	1.74e-04	2.30e-04	9.36e-05
13DMN	1.1398	4.80e-05	7.23e-06	1.08e-05	1.25e-05	1.04e-05
14DMN	1.0510	4.41e-04	3.72e-04	2.38e-04	6.87e-05	1.40e-05
12DMN	1.0991	1.64e-05	1.50e-05	1.21e-05		
145TMN	1.0833	2.90e-06	3.91e-06	3.82e-06		
146TMN	1.0833	9.26e-07	1.85e-06	3.95e-06	1.19e-06	
TMN	1.0833	5.99e-07	1.64e-06	4.58e-06	5.70e-06	1.01e-05
MATERIAL BALANCE ON:						
wt %C		0.949	0.923	0.875	0.787	0.765
wt %H		0.945	0.910	0.842	0.711	0.650
2-RING SYSTEM		0.953	0.936	0.908	0.862	0.880
METHYL GROUPS		0.929	0.848	0.709	0.409	0.190

half-life t* = 425 s